Christian Julien · Alain Mauger
Ashok Vijh · Karim Zaghib

Lithium Batteries

Science and Technology

Springer

Lithium Batteries

Christian Julien • Alain Mauger • Ashok Vijh
Karim Zaghib

Lithium Batteries

Science and Technology

Springer

Christian Julien
Physicochimie des Electrolytes et Nanosystèmes Interfaciaux (PHENIX) UMR 8234
Sorbonne Universités UPMC Univ. Paris 06
Paris, France

Ashok Vijh
Institut de Recherches d'Hydro-Québec (IREQ)
Quebec, Québec, Canada

Alain Mauger
Institut de Minéralogie, de Physique des Matériaux et de Cosmochimie (IMPMC) Muséum d'Histoire Naturelle, Institut de Recherche pour le Développement IRD UMR 7590 et 206
Sorbonne Universités, UPMC Univ Paris 06
Paris, France

Karim Zaghib
Institut de Recherches d'Hydro-Québec (IREQ)
Quebec, Québec, Canada

ISBN 978-3-319-19107-2 ISBN 978-3-319-19108-9 (eBook)
DOI 10.1007/978-3-319-19108-9

Library of Congress Control Number: 2015946613

Springer Cham Heidelberg New York Dordrecht London

Printed on acid-free paper

Springer International Publishing AG Switzerland is part of Springer Science+Business Media (www.springer.com)

Preface

Energy storage by rechargeable batteries has come to occupy a central stage in the last couple of decades, because of the ubiquitous availability of internet-based devices such as laptop computers, smartphones, computing tablets, digital cameras, and e-book readers.

The importance of batteries has been further augmented because of their use in power tools and a variety of other portable devices including those used in tele-medicine and tele-learning and in other needs of instant communication. And finally, the drive to replace fossil fuel based cars, buses, etc. by hybrid vehicles and electric vehicles has pushed the crucial role of these batteries to the societal forefront where the conjuncture of energy and environmental issues is the most vital concern.

In this context, the research, development, and commercialization of increasingly more efficient and durable batteries of higher energy and power densities have led to an immense field of intense activity. The number of published papers and patents is staggering with a concomitant vast industrial activity on a variety of batteries, especially those based on lithium.

Countless symposia and conferences have been devoted to this field. Also, over the years, a number of excellent books have been published, mostly edited volumes containing chapters by leading workers in the field.

Thus, the question arises, why another book on batteries? There are different reasons: First, a major center of pure and applied research on modern lithium batteries has formed at Hydro-Québec Research Institute, which employs the authors of this book: we wish to present the field in terms of our experience and understanding of this subject. Second, the previous books have been written by battery scientists; the backgrounds of the present authors, however, permit a look at this area through different prisms: Christian Julien and Alain Mauger are solid-state physicists working on the materials aspects of batteries; Ashok Vijh is an interfacial electrochemist who is new to this field and thus has a different perspective; Karim Zaghib is trained as a electrochemical engineer and has a vast experience in battery science and technology. Third, the battery fires experienced not only in ground

transport but also in air transport give us the proof that the warnings of the scientific community have not been heard, or have not been taken into consideration by the commercial car and plane companies in charge of the implementation and the choice of lithium-ion batteries. The present authors, among others, have discussed these safety problems in different scientific reviews that obviously were not read by the engineers in the Procurement department and in charge of the management of these companies. In this context, we felt useful to focus more attention on the safety aspects in a book that is also intended to reach a broader audience in the industrial community than the scientific reviews.

Fourth, important progress in the laboratories has been made in the last 4 years in the nanotechnology to synthesize porous nanoparticles and/or prepare composites of nanoparticles with a conductive element such as graphene or carbon nanotubes, or by nano-painting the particles by a conductive layer. Some of these techniques are scalable, and we hope that they will permit the development of a new generation of Li-ion batteries in a very near future. One goal of this book is also to inform the reader of this advance in research and discuss the scaling aspect.

Finally, we wanted to write a book that emphasizes the materials aspects, both their bulk and interfacial properties, as distinct from many other aspects of battery technology. Thus this book reflects our belief that any future progress in the further study of batteries will be based on the fundamental physicochemical aspects of battery materials. In this context, it is not out of place to point out here that even in the past, the major strides in lithium batteries were also based on a fundamental understanding of the physics and chemistry of battery materials: the supreme example of this approach is the work of John Goodenough.

Paris, France — Christian Julien
Paris, France — Alain Mauger
Quebec, Québec, Canada — Ashok Vijh
Quebec, Québec, Canada — Karim Zaghib

Contents

Chapter 1
Basic Elements for Energy Storage and Conversion

1.1 Energy Storage Ability

One of the main challenges of the modern society is the so-called *energy transition for reducing the global warming* due to the great amount of exhausted carbon dioxide that will devastate our planet. The energy transition consists in replacing fossil fuels such as coal, gas, oil and to some extend nuclear energy by alternative renewable sources of energy that are solar radiation, wind, ocean, biomass, geothermal and hydro-electricity, which are less polluting. Moreover, this *green energy* is abundant except hydro-electricity which is limited by the number of available sites. Photovoltaic cells and wind mills are attracting due to the huge production of electricity coming from solar radiation conversion that is around one to two billion kWh, but they are intermittent sources and storage systems are required to satisfy the consumer demand at any time. Depending on the design of the system, the battery could supply energy for extended dark or cloudy or windless periods. Similar problem occurs with the capture of energy from ocean surface waves. Consequently, the main trend is the growing market not only for small-scale wind systems, but also for grid connected projects. From 1996 to 2009, the existing world capacity produced by wind power increased from 5 to 160 GW [1]. In February 2014, the installed wind energy capacity in the EU was 117.3 GW: 110.7 GW onshore and 6.6 GW offshore with the largest installed capacity (29 %) in Germany [2]. As society becomes increasingly more dependent on electricity, the development of systems capable of storing directly or indirectly this secondary energy form will be a crucial issue for the twenty-first century. As an example of the fast growth of electronics, six billion people out of the world's seven billion have access to mobile phones, equivalent to more than 85 % of global population [3].

The subject of energy storage is a major development in high technology, which bears considerable industrial potential. Batteries, which are devices converting the energy released by spontaneous chemical reactions to electricity work, have some extraordinary properties in these regards. They store and release electrical energy;

C. Julien et al., *Lithium Batteries*, DOI 10.1007/978-3-319-19108-9_1

they are portable and can be used flexibly with a short lead time in manufacture. Today, the high-tech mobile world including mobile phones, laptops, cameras depends on lithium-ion batteries with a quantity of five billion units sale in 2013 [4]. From the view point of energy consumption of portable electronics, operating currents vary from microamps to more than one ampere: cellular phone (200–800 mA), camcorder (700–1000 mA), notebook (500–1500 mA), video games (20–200 mA), remote control (10–60 mA), etc.

In this brief introduction, we provide a brief overview on energy storage systems from the conventional to the update systems before further going into the technology. Energy storage (ES) can be obtained through various ways depending on the stored energy:

- *Mechanical*, like water stored behind a dam (potential energy) or like high speed heavy wheel used to start marine engines (kinetic energy).
- *Electrical* in capacities (voltage is equivalent to potential energy) or in superconductive coils provided that high currents (equivalent to kinetic energy) can be used, which is not the case for high-*Tc* superconductors, while the limit for the others is the low temperature of the transition to the normal state.
- *Chemical* by storing separately two chemical elements like Li and F, or molecules like H_2SO_4 and H_2O able to react when in contact, producing a high value bonding energy. ES in explosives where the energy is obtained by chemical reorganization pertains to this class. In all these cases, the process uses some kind of stored potential energy, and differences in chemical potentials.
- *Electrochemical* storage is a variant of the chemical one where the stored energy depends on the difference of bonding energy between two different compounds of the same element, one used as anode, the other one as a cathode. Classical example is the lead-acid battery, where the oxidation degree of lead changes from one electrode to the other one. Now, a new very important component appears in the form of the electrolyte able to transport the ion that is $(SO_4)^{2-}$.

Note that in all the electrochemical systems, the flow of ions is always from anode to cathode for both charge and discharge process. In rechargeable batteries (as Li-ion cells), there is a confusing meaning when negative and positive electrodes are named anode and cathode either on charge or discharge. They are respectively the anode and cathode and reverse on charge to discharge and vice versa. Many battery engineers use this mistaken nomenclature for the electrodes as a historical artifact of primary (nonrechargeable) batteries which operate only in the discharge mode.

Two configurations exist for ES systems: In the first case, the chemical components are compressed together with a mechanical separator between the electrodes, and they are able to give only one discharge. Such systems are referred as primary batteries. In the other case of secondary batteries the system is reversible, as these cells can be recharged electrically, just as we do pump water at the top of a dam. A recent strategy is to use the high surface area of nano-structured active particles assembled in thin layers of charged species of high value capacities. The high

surface area is also used to obtain super-capacitances. Several F g^{-1} are now easily produced with the constraints due to double-layer formation and potential stability (remain the earth capacity in space is ~1 F).

1.2 The Sustained Energy

It is well known that the present production on use of energy is responsible for serious problems to the global environment, particularly in relation to greenhouse gas emission such as carbon dioxide which provokes climate modification. The challenge in moving towards global energy sustainability can be assessed by the trends in the use of fuels for primary energy supplies. Table 1.1 gives statistics reported by the International Energy Agency (IEA) [5]. The total primary energy supply in the world, in megatons oil equivalent (Mtoe), was 5096 Mtoe in 1998. The IEA's forecast of the world demand is 13700 Mtoe in 2020.

The consequence of the big consumption of fossil energy is the global climate change. The *concentration of greenhouse gases (GHG)* in the atmosphere (including CO_2, CH_4, O_3, N_2O, and CFC) has increased very fast since the end of the nineteenth century. In 2011, the atmospheric concentration of CO_2 was 391 ppm against 278 ppm in 1750. Each year, 5 metric tons of carbon dioxide are added to the atmosphere for each person in the US but they are not included in the chart to ensure consistency with the other greenhouse gas figures [6].

Table 1.2 summarized the electricity production in TWh in the world in 2013. The total energy consumed at all power plants for the generation of electricity was approximately 4.4×10^6 ktoe (1 ktoe—kilo tonne of oil equivalent- is equal to 11630 MWh) [5]. The world's largest producer of electricity since 2011, China, has definitely outpaced the USA in 2012 with 4936.5 TWh against 4298.9 TWh. Chinese production increased by 11.5 % per year from 2002 to 2012, a tripling in 10 years. The thermal generation remains dominant, but renewable energy grew faster (12.5 % per year), increasing from 17.6 to 19.2 %. China is the world leader in the production of electricity from renewable sources with 949.2 TWh in 2012, far ahead of the USA (536.9 TWh) and Brazil (462.2 TWh).

Table 1.1 Total primary energy supply by fuel (in % terms) for the world and forecast (IEA data [5])

Energy supply	1973	1998	2010	2020
Oil	44.9	53.2	38.8	38.3
Coal, biomass, and waste	36.1	24.4	28.4	28.7
Gas	16.3	18.8	23.6	25.2
Nuclear	0.9	1.3	5.8	4.4
Hydroelectric power	1.8	2.1	2.6	2.6
Geothermal, wind, solar, and heat	0.1	0.2	0.7	0.8

Table 1.2 Electricity production in TWh in the world in 2013

Power source	Europe	North America	OCDE Asia Oceania	China[a]	India[b]
Fossil fuels	1661	3232	1462	3889	794
Nuclear	831	899	145	98	131
Hydroelectricity	601	724	135	823	29
Renewables	336	222	41	126	31
Total (TWh)	3429	5077	1783	4936	985

OCDE Asia includes Australia, Japan, Korea, and New Zealand
[a]Year 2012
[b]Year 2011

The goal of global energy sustainability implies the replacement of all fossil fuels (oil, coal, natural gas) by renewable energy sources (geothermal, biomass, hydrogen, batteries, etc.). The large explosion of systems capable to store energy may be considered to be due to influences related to economy and connected to basic problems in industrialized countries from the economical, environmental, technological, and political points of view. To meet the rapid development of energy storage devices, extensive researches are currently devoted to develop power sources, such as lithium-ion batteries (LiBs), supercapacitors (SCs), solar cells, and fuel cells. These devices require new technologies such as *nanotechnology* for light-weight and even implantable applications [7].

1.3 Energy Storage for Nano-electronics

The performance of devices reached today is the result of intensive research to reduce the size of the particles to the nanoscale. The use of nanotechnology has been increasing in modern electronics devices using CMOS semiconductors (Si or GaAs), which allow very high frequency. As an example, microprocessors today run at 1 GHz. It is important, however, to specify what "nano" means here. In electronics, for instance, it signifies particles that are so small the electronic or the magnetic properties are modified by quantum confinement of the electrons. It means particles smaller than 10 nm. In the physics and electrochemistry of the cathode elements of Li-ion batteries, the term is used to signify particles so small that their properties depend importantly on surface effects. Consider nano-grains of materials for batteries, typically, the surface layer of a grain is about 3 nm thick, so that particles are labelled "nano" in the literature if their size is smaller than 100 nm, and usually in the range 20–100 nm. More sophisticated assemblies combining for instance such particles with nano-forms of carbon such as graphene are encountered in the formation of negative electrodes in Chap. 10.

As the power consumption of a CMOS circuit, operating in a switching fashion, is proportional to the square of its supply voltage, such circuits should operate at the lowest possible supply voltage to extend the battery life. Meanwhile, electrical

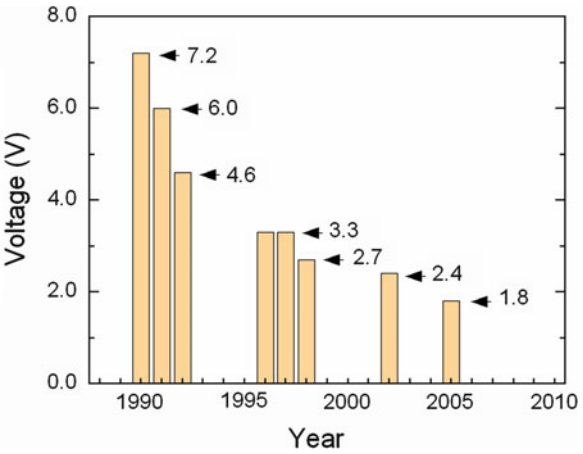

Fig. 1.1 The evolution of the voltage (in volt) at which the semiconductor devices operate in a cellular phone

energy storage is required to power microelectronics, i.e., cell phones and pagers, stand-by power systems. This context has guided the recent evolution of the technology. Figure 1.1 shows the evolution of voltage at which the semiconductor devices operate in a cellular phone. The voltage decrease is related to the thickness of integrated circuits. This picture demonstrates that the powering voltage could reach the range 2–3 V for integrated circuit with a thickness of ~0.2 mm. Of course, this issue led to the design of new batteries for telecommunication devices.

Let us take the case of mobile phones. Most of them today operate on a single cell Li-ion battery, which has a 4.2 V maximum fully charged voltage. Power management system (PMS) is needed because the different components require different voltages: 1.8 V for the digital base band (with a tolerance of ± 5 %) and memory, 2.5 V for the analogous base band, 2.8 V for the SIM card and the RF block. The PMS is also acting as a battery management system (BMS) to control the battery charging, monitoring and fuel gauging. From the view point of energy demand of the new generation GSM phone (GSM = Global System for Mobile Communications), the total typical current consumption during talk time is ~275 mA, so that 150 min talk time is available using 700-mAh Li-ion battery. The same device will consume only ~2.25 mA during standby waiting for a call that corresponds a time of 310 h (~13 days) for the same battery [8].

1.4 Energy Storage

In physics, energy is a scalar physical quantity that describes the amount of work that can be performed by a force. During a 1961 lecture for undergraduate students at the California Institute of Technology, Professor Feynman said this about the concept of energy: “There is a fact, or if you wish, a law, governing natural phenomena that are known to date. There is no known exception to this law; it is exact, so far we know. The law is called conservation of energy; it states that there

is a certain quantity, which we call energy that does not change in manifold changes which nature undergoes. That is a most abstract idea, because it is a mathematical principle; it says that there is a numerical quantity, which does not change when something happens. It is not a description of a mechanism, or anything concrete; it is just a strange fact that we can calculate some number, and when we finish watching nature go through her tricks and calculate the number again, it is the same" [9].

Excepted geothermal, there are two forms of energy, both of them originating from solar energy: the ancient storage energy, fossil energy, which has been produced during many millions of years and the on-time energy that could be trapped by photovoltaic or wing systems as listed in Table 1.3.

Historically, energy has been stored by containment of raw fuel that is satisfactory for the transportation sector since petroleum; fuel and liquefied gas are portable and readily converted into the desired result: motion. In the electric sector, the necessity to supply energy on demand, which fluctuates weekly and daily, has been accomplished by using different classes of generators in nuclear reactor or firing coal, fuel, gas, biomass. The high cost and limited reserves of oil are forcing a reconsideration of these approaches. Figure 1.2 shows the discharge time vs. energy stored for various energy storage technologies including flywheel, batteries, compressed air, pumped water, hydrogen and gas storage. The use of pumped-hydro is the traditional large scale way to store electricity via gravimetric energy. Both flywheel and batteries are systems capable to deliver the storage energy in few seconds. For instance it has been recently demonstrated that Li-ion batteries including lithium-iron phosphate as positive electrode and lithium titanate as negative electrode can be cycled over 30000 cycles for faster charge rate at 15C (4 min), and the discharge rate at 5C (12 min) [10]. In practice, it means that a battery made with such cells to power an electric car (EV) will be guaranteed for the life of the

Table 1.3 Classification of energy storage methods

Chemical $\Delta G = \Delta H - T\Delta S$ Hydrogen Biofuels Liquid nitrogen Oxyhydrogen Hydrogen peroxide	Biological Starch Glycogen	Electrochemical Batteries Flow batteries Fuel cells
Electrical $E_{\mathrm{p,e}} = \frac{1}{4\pi\varepsilon_0}\frac{Q_1 Q_2}{r}$ Batteries Supercapacitor Superconducting magnetic energy storage	Mechanical $E_{\mathrm{p}} = -\int F dS$ Compressed air Flywheel Hydraulic accumulator Hydroelectric Spring	Thermal $\Delta q = \int C_{\mathrm{v}} dT$ Ice storage Molten salt Cryogenic liquid air Seasonal thermal store Solar pond Steam accumulator Fireless locomotive

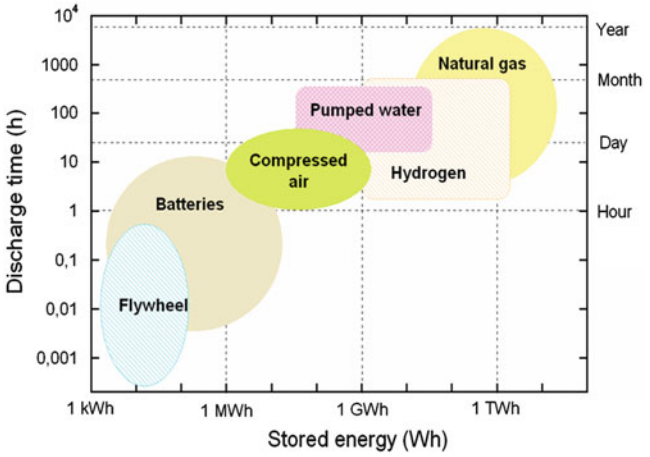

Fig. 1.2 Discharge time vs. energy stored for various energy storage technologies

car, a performance that is expected to boost this market. Note that most of the energy storage systems involve the power-to-gas technology that converts electrical power to gas fuel, including natural and synthetic gas and hydrogen. As shown in Fig. 1.2, time of discharge is very long, which implies the need of grid balancing. Regarding the energy stored requested by consumers, 2 W is needed for cellular phone, while 20–30 W for laptop and 20 kW for electric cars.

Energy storage media are systems storing some form of energy that can be drawn upon at a later time to perform some useful operation. A device that stores energy is sometimes called an accumulator. All forms of energy are either potential energy (e.g., chemical, gravitational or electrical energy) or kinetic energy (e.g., thermal energy). A wind up clock stores potential energy (in this case mechanical, in the spring tension), a battery stores readily convertible chemical energy to keep a clock chip in a computer running (electrically) even when the computer is turned off, and a hydroelectric dam stores power in a reservoir as gravitational potential energy. Ice storage tanks store ice (thermal energy) at night to meet peak demand for cooling. Fossil cells such as coal and gasoline store ancient energy from sunlight. Even food (which is made by the same process as was fossil fuel) is a form of energy stored in chemical form.

Several aspects must be considered for a comparison of energy sources that generate electricity. The first one is the quantity of carbon dioxide equivalent/kWh rejected by energy sources. Figure 1.3 shows the relationship between the CO_2 production and the reaction (response time) for a number of electric power suppliers [11]. It is evident that the response time of nuclear plant (48 h) is bigger than hydro-electric dam or renewable systems such as wind mill and photovoltaic (few seconds). In the middle are the electric power stations using coal, oil or gas.

The second aspect is the gravimetric energy density that is stored (Fig. 1.4a). Let us consider the specific energy available for hydrogen (10^5 Wh kg^{-1}) and gasoline

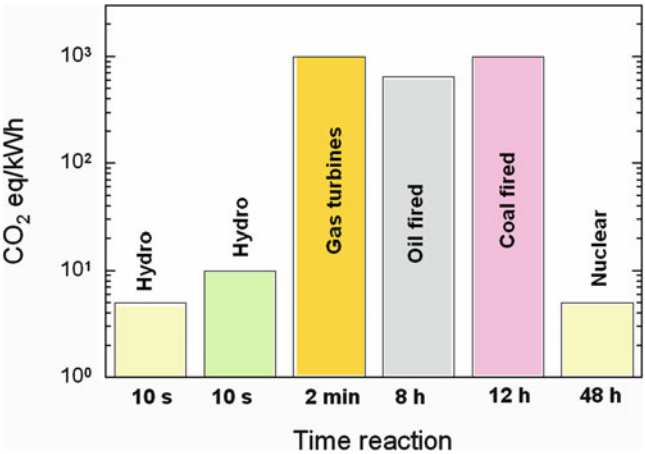

Fig. 1.3 Relationship between the CO_2 production and the time reaction for electric power suppliers

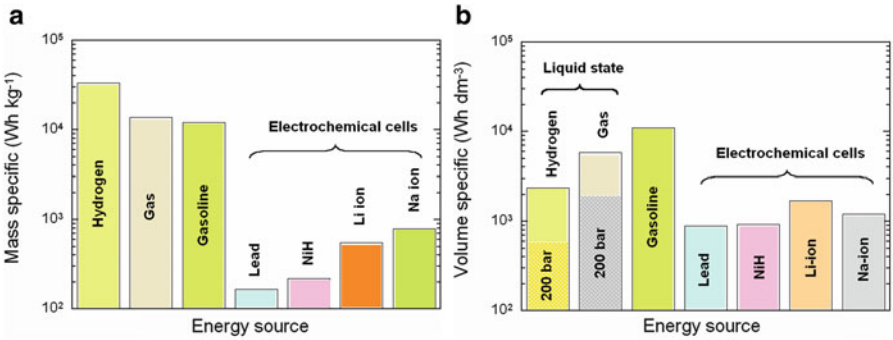

Fig. 1.4 Comparison of various sources of energy (**a**) gravimetric energy density and (**b**) volumetric energy density

(10^4 Wh kg^{-1}). They provide the largest energy density compared to electrochemical cells (~10^3 Wh kg^{-1}), but if a lithium-ion battery is operating for 1000 cycles, we get a total stored energy of ~10^6 Wh kg^{-1} with the same quantity of matter, so that the lithium-ion battery is winning against fossil energies. The third aspect is the volumetric energy density (in Wh dm^{-3}), but the situation is more complex because of the difficulties to store gas and hydrogen by either compression at 200 bar that requires heavy cylinders or by liquefaction that requires cryogenic tanks. Thus, for such a parameter, gasoline is the best source of energy (Fig. 1.4b).

From the foregoing discussion, Birk [12] has suggested three objectives for storage energy, namely: (1) meet discrepancies that can exist between the supplier and the consumer and meet the fluctuating demands for power (it will be the subject of Chap. 19), (2) provide for a more versatile source of energy than can be achieved with the conversion of raw fuels, and (3) change the relative use of the various raw fuels.

1.5 Brief History of Electrochemical Cells

1.5.1 Milestones

Some milestones in electrochemical systems are listed in Tables 1.4 and 1.5 [13, 14]. The history of batteries run from the invention of Alessendro Volta cell in 1800 to the commercialization of Li-ion battery in 1992, via the well-known Leclanché cell, lead-acid battery, nickel-cadmium accumulator and numerous other systems. Generally, the electrochemical cells are classified into two broad categories:

Table 1.4 Primary battery developments

Date	Inventor	Cell design
1000 BC	Baghdad cell	Jar containing an iron rod surrounded by a copper cylinder
1782	Volta	Stack of zinc and silver disks
1813	Davy	First public demonstration of electric lighting
1836	Daniell	$Zn/ZnSO_4/CuSO_4/Cu$
1839	Grove	Nitric acid battery
1866	G. Leclanché	Zinc/manganese dioxide cell
1878	Zinc air cell	$Zn/NaOH/O_2$
1945	Ruben and Mallory	Mercury button-type cell
1949	Lew Urry	Alkaline dry cell commercialized by Eveready Batteries Co.
1961	Silver-zinc cell	$Zn/KOH/Ag_2O$
1970–1980	Lithium-iodine	$Li/Li/I_2$ developed for pace-maker
	Coin cell	Li/aprotic electrolyte/MnO_2
	Li soluble cathode	$Li/SOCl_2$

Table 1.5 Secondary battery developments

Date	Inventor	Cell design
1859	Planté	PbO_2/dilute H_2SO_4/Pb
1899	Waldemar Jungner	Nickel-cadmium cell Ni/2NiOOH/Cd
1905	Edison	Nickel-iron cell Ni/2NiOOH/Fe
1949	Lew Urry	Alkaline dry cell commercialized by Eveready Batteries Co.
1959	Francis Bacon	First practical fuel cell using Ni electrodes
1960s	Volkswagen	Nickel-metal hydride cell with $LaNi_5$ or ZrNi hydrogen sponges
1965	Ford	Beta cell Na/β-Al_2O_3/S
1980s	Li polymer	Li/PEO-$LiClO_4$/Ic (Ic=V_6O_{13}, TiS_2, V_2O_5)[a]
	Microbattery	Li/Li^+ fast ion conductor/TiS_2
1990s	Sony Corp.	Lithium-ion cell based on graphite/$LiCoO_2$ electrodes

[a]*Ic* insertion compound

– *Primary cells* irreversibly (within limits of practicality) transform chemical energy to electrical energy. When the initial supply of reactants is exhausted, energy cannot be readily restored to the electrochemical cell by electrical means.
– *Secondary cells* can be recharged that is, they can have their chemical reactions reversed by supplying electrical energy to the cell, restoring their original composition.

1.5.2 Battery Designs

Interestingly, researches are still carried on to attain maximum performance and reliability in Leclanché cell [15]. At present, a cell includes several elements for safety because gases are evolved from the manganese dioxide oxidation of the hydrolyzed products formed by the gel (Fig. 1.5). For example, engineers at Rayovac Co. patented a new separator that comprises a Kraft paper separator and a corrosion-inhibiting coating thereupon selected to prevent corrosion of a zinc anode of the Leclanché cell [16].

Batteries design can be compared in view of the three main components; the electrode A, the electrolyte, and the electrode B. A possible battery classification can be deduced from the nature of these components: liquid, soft or solid. This is the figure of the Rubik's cube shown in Fig. 1.6 [13]. All these media can be liquid, plastic (soft) or solid. This is crucial because certain interfaces are difficult to handle. Common batteries have a solid–liquid–solid configuration; the liquid–solid–liquid system corresponds to the Na-S battery using β-alumina as the electrolyte, which permits relatively easy manufacture. On the other side, the all-solid

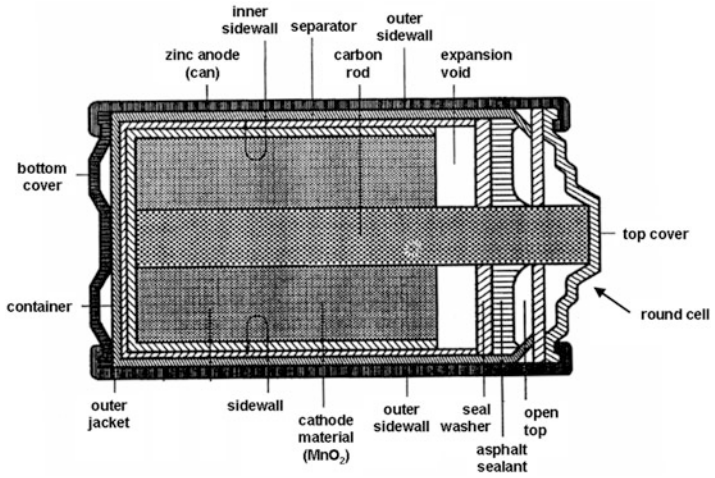

Fig. 1.5 Cross-sectional view of a round Leclanché cell (http://sciencescollege3eme.blogspot.fr/2008/12/histoire-de-pile.htm)

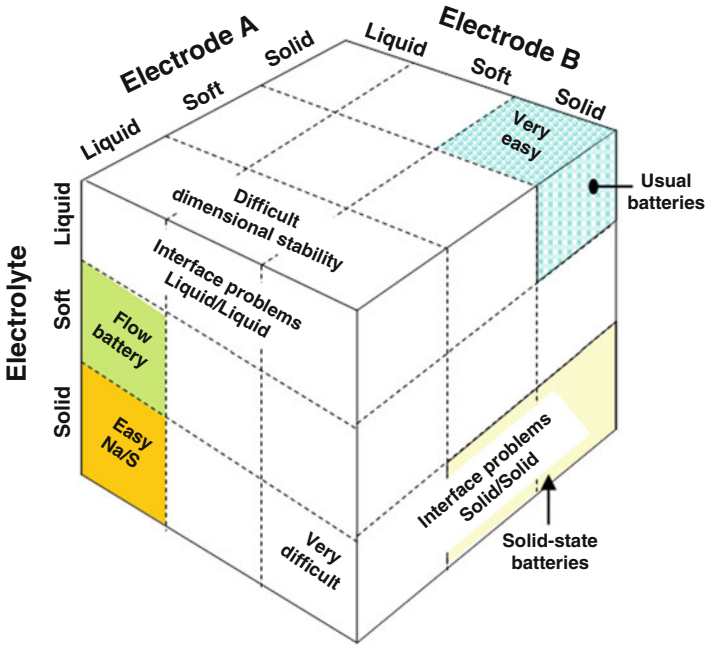

Fig. 1.6 Rubik's cube showing the association of the three components in the solid, soft, and liquid state of electrochemical cells. Reproduced with permission from [13]. Copyright 1994 Wiley

system involves difficult interface problems with crucial dimensional stability at each interface. These difficulties can be solved by using a polymer film as a plastic electrolyte; also, polyethylene oxide (PEO) membranes are the key to Li metal-polymer batteries such as those commercialized by Batscap [17]. Micro-solid state batteries built by successive deposition of thin films partly avoid the interface contact difficulty and can be used as power sources associated to microelectronics [18]. Ultrathin-film solid-state lithium batteries have been fabricated using a thin solid polymer electrolyte membrane prepared by complexion of a plasma polymer and lithium perchlorate [19].

1.6 Key Parameters of Batteries

Battery's users request several high-grades that are long life, high energy density, deep cycle, quick charge and others. With regard to the battery operation, there are several important parameters which are required by consumers: (1) gravimetric specific energy in (Wh g^{-1}), (2) volumetric capacity in (Ah cm^{-3}), (3) rate capability, (4) cyclability (life shelf), and (5) self-discharge. These quantities are fixed by the electrochemical characteristics of the active elements: positive (cathode) and

negative (anode) electrodes. Note that in rechargeable batteries the word cathode is not appropriate in terms of electrochemistry because the positive electrode is cathode on discharge and anode on charge, and so forth. A necessary condition in selecting materials for use in batteries is their ability for *redox* properties, i.e., reduction–oxidation reaction, which is more or less the case of almost every inorganic compound in appropriate electrolytes. In addition, one has to select the materials according to key parameters that condition the properties we have listed.

1.6.1 Basic Parameters

Let us discuss the parameters that govern the design of electrochemical power sources. The electrochemical potential, sometimes abbreviated to ECP, is a thermodynamic measure that combines the concepts of energy stored in the form of chemical potential and electrostatics. It is common in both solid-state physics and electrochemistry to discuss the chemical potential and electrochemical potential of an electron. In an electrochemical cell, the chemical reactions take place at the sites of electrodes represented by the generalized relations [20]:

$$\mathrm{a}A + ne \leftrightarrows \mathrm{b}B, \tag{1.1}$$

$$\mathrm{c}C - ne \leftrightarrows \mathrm{d}D, \tag{1.2}$$

$$\mathrm{a}A + \mathrm{c}C \leftrightarrows \mathrm{b}B + \mathrm{d}D, \tag{1.3}$$

where a molecules of A take up n electrons e^- to form b molecules of B at one electrode and similarly to the second. Eqs (1.1) and (1.2) express the reduction and oxidation reaction, respectively, and Eq. (1.3) is the overall reaction in the cell given by addition of the two half-cell reaction. The change in the standard free energy, ΔG^0, of this reaction is:

$$\Delta G^0 = -nFE^0, \tag{1.4}$$

where F is Faraday's constant ($F = eN_\mathrm{A} = 96485$ C mol^{-1}) and E^0 is the standard electromotive force (emf) When conditions are other than in the standard state, the potential V_oc of the cell is given by the Nernst equation:

$$V_\mathrm{oc} = E^0 - \frac{RT}{nF}\ln\frac{\mu_\mathrm{B}^i \mu_\mathrm{D}^i}{\mu_\mathrm{A}^i \mu_\mathrm{C}^i}, \tag{1.5}$$

where μ^i is the activity of relevant species, R the gas constant (8.314 JK^{-1} mol^{-1}), and T the absolute temperature.

In the case of two electrodes with a semiconducting character, the *operating voltage* of a cell is limited by the open-circuit voltage, V_{oc}, which is the potential difference across terminals of the battery when no current is being drawn:

$$V_{oc} = -\frac{1}{nF}\left(\mu_A^i - \mu_C^i\right), \tag{1.6}$$

where $\left(\mu_A^i - \mu_C^i\right)$ is the difference in the chemical potential of the anode (A) and the cathode (C), n is the number of electronic charge involved in the chemical reaction of the cell. The nominal voltage is determined by the energies involved in both electronic and ionic transfer. It is the work function that determines the energy for electron transfer, while the crystallographic structure determines the energy for the transfer of ions. Thus both the electronic band structure and the barrier height for ion motion should be considered. The magnitude of the open-circuit voltage is constrained to $V_{oc}<5$ V not only by the attainable difference $\mu_A - \mu_C$ of the electrochemical potentials of the anode reductant and the cathode oxidant, but also by either the energy gap E_g between the HOMO (highest occupied molecular orbital) and the LUMO (lowest unoccupied molecular orbital) of a liquid electrolyte, or by the energy gap E_g between the top of the valence band and the bottom of the conduction band of a solid electrolyte [21].

The *energy density* is a common measure in evaluating battery systems. Specific energy stored (in Wh kg^{-1}) in a battery is measured by discharging a battery at an appropriate current:

$$E_{pr} = V_{oc}\, Q_{dis}, \tag{1.7}$$

where V_{oc} is the operating potential in volt (V) obtained from the energy change for the cell reaction and Q_{th} is the specific capacity in ampere-hour per mass (Ah kg^{-1}), or equivalently in mAh g^{-1}. Its theoretical value is obtained from the Faraday'law:

$$Q_{th} = \frac{1000 \times nF}{3600 \times M_w} = \frac{26.8}{M_w} \times n, \tag{1.8}$$

where M_w is the molecular mass of the "limiting" electrode material. As an example, let consider the case of lithium insertion process into the vanadium oxide lattice ($M_w = 542$ g mol^{-1}) that can reversibly accommodate $4Li^+$ ions per formula unit at an experimental mid-discharge potential 2.4 V vs. Li^0/Li^+ at $C/3$ rate according the reaction:

$$4Li^+ + 4e^- + V_6O_{13} \leftrightarrows Li_4V_6O_{13}. \tag{1.9}$$

According to Eq. (1.9), the theoretical specific capacity is 197.8 mAh g^{-1} and the theoretical energy density of 475 Wh kg^{-1}.

The theoretical energy of the battery depends on the capacity of the material and average potential of each electrode material:

$$E_{\text{batt}} = \left(\frac{1}{Q^+} - \frac{1}{Q^-}\right)^{-1}(E^+ - E^-), \tag{1.10}$$

where Q^+ and Q^- are the capacity of the active materials of the positive and negative electrodes in the battery, respectively.

The C-rate is a parameter used to express the discharge (charge) current in order to normalize the data against the capacity that depends on the battery. A C-rate is a measure of the rate at which a battery is discharged relative to its maximum capacity. A charge at nC rate means a full charge in a time $1/n$ hours [22]. For instance, a $1C$ rate means that the discharge current will discharge the entire battery in 1 h. For a battery with a capacity of 50 Ah, this equates to a discharge current of 50 A. At $C/2$ rate would be 25 A.

The *power output* P_{out} of a battery is the product of the electric current I_{dis} delivered by the discharging battery and the voltage V_{dis} across the negative and positive external contacts:

$$P_{\text{out}} = I_{\text{dis}} V_{\text{dis}}. \tag{1.11}$$

The voltage V_{dis} is reduced from its open-circuit value V_{oc} ($I_{\text{dis}} = 0$) by the voltage drop $I_{\text{dis}}R_{\text{b}}$ due to the internal resistance R_{b} of the battery and the *polarization losses* occur at each electrode and result in a decreased cell potential during discharge (V_{dis}) and an increased cell potential on charge (V_{ch}) that are expressed by:

$$V_{\text{dis}} = V_{\text{oc}} - I_{\text{dis}}R_{\text{b}}, \tag{1.12}$$

$$V_{\text{ch}} = V_{\text{oc}} + I_{\text{ch}}R_{\text{b}}, \tag{1.13}$$

which have the form of Ohm's law. In addition the Joule heating effect of the I^2R_{b} losses in the internal resistance of the cell will rise the temperature. It follows from Eqs. (1.11) and (1.13) that realization of a high maximum power P_{max} requires, in addition to as high a V_{oc} as possible, a low internal battery resistance R_{b} expressed by:

$$P_{\text{max}} = I_{\text{max}} V_{\text{max}}, \tag{1.14}$$

$$R_{\text{b}} = R_{\text{e1}} + R_{\text{in}}(A) + R_{\text{in}}(C) + R_{\text{c}}(A) + R_{\text{c}}(C), \tag{1.15}$$

where $R_{\text{in}}(A)$, $R_{\text{in}}(C)$ are the resistances to transport of the working ion across the electrolyte–electrode interface and $R_{\text{c}}(A)$, $R_{\text{c}}(C)$ are the intrinsic resistance of electrodes. The electrolyte resistance R_{e1} to the ionic current is proportional to the ratio of the effective thickness L to the geometrical area A of the inter-electrode space that is filled with an electrolyte of ionic conductivity σ_i as:

$$R_{\text{el}} = \frac{L}{A\sigma_i}. \tag{1.16}$$

The resistance to transport of the working ion across the electrolyte–electrode interfaces is proportional to the ratio of the geometrical and interfacial areas at each electrode:

$$R_{\text{in}} \sim A/A_{\text{in}}. \tag{1.17}$$

Since the chemical reaction of the cell involves ionic transport across an interface, Eq. (1.17) dictates the construction of a porous, small-particle electrode. Achievement and retention of a high electrode capacity, i.e., use of a high fraction of the electrode material in the reversible reaction, requires the achievement and retention of good electronic contact between particles as well as a large particle–electrolyte interface area over many discharge–charge cycles. If the reversible reaction involves a first-order phase change, the particles may fracture or lose contact with one another upon cycling, breaking a continuous electronic pathway to the current collector.

The battery voltage V_{dis} vs. the discharge current I_{dis} delivered across a load is called the polarization curve. The voltage drop $(V_{\text{oc}} - V) = \eta(I)$ of a typical curve (Fig. 1.7) is a measure of the battery resistance:

$$R_{\text{b}}(I) = \eta(I)/I. \tag{1.18}$$

On charging, $\eta(I_{\text{ch}}) = (V_{\text{ch}} - V_{\text{oc}})$ is referred to as an overvoltage. The interfacial voltage drops saturate in region (I) of Fig. 1.7; therefore in region (II) the slope of the curve is:

$$dV/dI \approx R_{\text{e1}} + R_{\text{c}}(A) + R_{\text{c}}(C) \tag{1.19}$$

Region (III) is diffusion-limited; at the higher currents, normal processes do not bring ions to or remove them from the electrode–electrolyte interfaces rapidly enough to sustain an equilibrium reaction. The battery voltage V vs. the state of charge, or the time during which a constant current I has been delivered, is called a discharge curve.

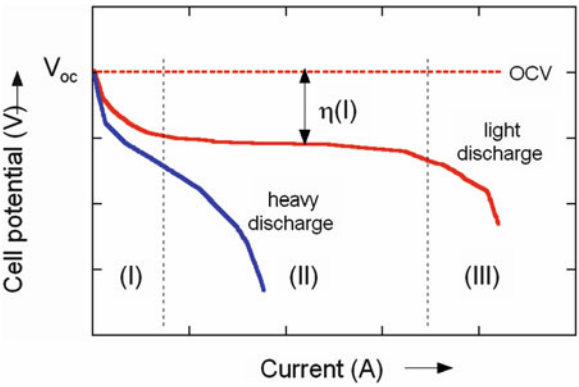

Fig. 1.7 Typical polarization curve for the battery voltage V vs. the I delivered across a load. The voltage drop $(V_{\text{oc}} - V) = \eta(I)$ of a typical curve is a measure of the battery resistance $R_{\text{b}}(I)$

The state-of-charge (SOC) of a battery is the fraction (in %) of available charge capacity to the total capacity of the battery:

$$\mathrm{SOC} = 100\% - \frac{Q_\mathrm{e}}{Q_0}, \tag{1.20}$$

where Q_e is the battery charge and Q_0 the nominal battery capacity (in Ah). The SOC of a battery is the main parameter because the user needs to know the remaining available energy before the next charge. The knowledge of SOC is very challenging; that requires battery modelling [23, 24].

The *self-discharge rate* (SDR) is the percentage of capacity that a battery loses in open-circuit conditions. From usual terms, the SDR is estimated from the lost discharge capacity after 2 days storage in normal conditions to the maximum cell capacity as:

$$\mathrm{SDR}(\%) = \frac{Q_\mathrm{max} - Q_\mathrm{ret}}{Q_\mathrm{max}} \times 100\%, \tag{1.21}$$

where Q_max is the maximum discharge capacity at a discharge current density C/n and Q_ret the retained capacity at a discharge C/n rate. As an example, experimental profiles of charge–discharge for a Li//$LiNi_{1/3}Mn_{1/3}Co_{1/3}O_2$ cell operating at various C-rate are illustrated in Fig. 1.8.

1.6.2 Cycle Life and Calendar Life

Usually, the aging of the battery performance has two origins: (1) the *cycle fade* and (2) the *calendar fade* that is the elapsed time before the battery is not usable at all. An increase in the temperature whether the battery is in active use or not and an increase of the SOC severely affect the degree of degradation. The net result is an increase of the internal resistance and capacity loss $L(t)$, which can be expressed by an empirical law as [25]:

$$L(t) = A\sqrt{t}, \tag{1.22}$$

where A is a constant. Electrochemical impedance spectroscopy (EIS) is a powerful tool to determine the interfacial resistance of a cell as a function of temperature, state-of-charge (SOC) and cycle number [26]. Equation (1.22) yields the formation of the passivation film at the electrode surface. The solvent diffusion model presented by Ploehn et al. [25] predicts, in all cases, passivation films growing to several tens of nanometers in thickness over time periods in excess of 1 year under float potential conditions (the float potential is the voltage at which a battery is maintained after being fully charged to maintain its capacity by compensating for

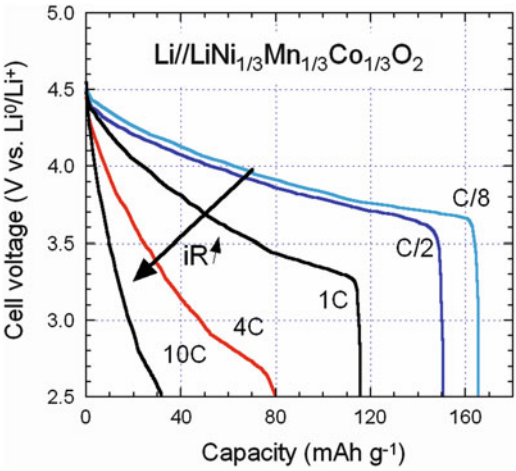

Fig. 1.8 Discharge curves for a $Li//LiNi_{1/3}Mn_{1/3}Co_{1/3}O_2$ cell operating at various *C*-rates

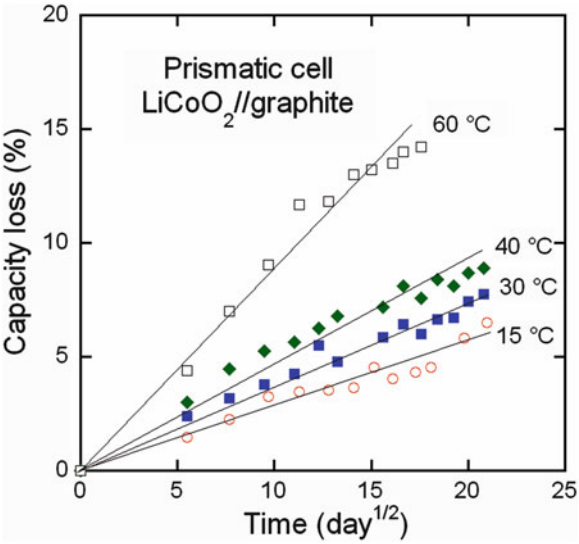

Fig. 1.9 Capacity fade of a prismatic $LiCoO_2$//synthetic graphite cell with 1 mol L^{-1} $LiPF_6$ in solvent EC:DEC:DMC as electrolyte. The cell was stored at different temperatures in the range 15–60 °C at float potential of 3.8 V. Reproduced with permission from [25]. Copyright 2004 The Electrochemical Society

self-discharge). Figure 1.9 illustrates the time evolution of the capacity fade for a prismatic prototype cell $LiCoO_2$//synthetic graphite stored a float potential of 3.8 V.

The *cycle life* corresponds to the number of charge–discharge processes a battery can fulfill before its nominal capacity falls below 80 %. The relationship between cycle life and depth-of-discharge (DOD) appears to be logarithmic. The *shelf life* is the time spent before a battery is out of use during storage. Wright et al. [27] presented the tests and analysis of the capacity fade resulting from the cycle life experiments at 25 and 45 °C for 18650-sized Li-ion batteries including $LiNi_{0.8}Co_{0.15}Al_{0.05}O_2$ cathode materials. The number of test cycles for up to 44 weeks were 369000 cycles at 1*C* and *C*/25 discharge rate. Broussely et al. [26]

studied the long-term calendar life of Li-ion cells containing either $LiCoO_2$ or $LiNi_yMn_{1-y}O_2$ cathodes tested in the temperature range 15–60 °C.

The *coulombic efficiency*, CE in %, is the ratio between the discharge capacity and the charge capacity for each cycle:

$$\mathrm{CE}(\%) = \frac{Q_{\mathrm{disch}}}{Q_{\mathrm{ch}}} \times 100\%, \tag{1.23}$$

thus the rate of capacity loss is inverse proportional to the duration of the test, t_{ts}, given by:

$$\psi = \frac{1 - \mathrm{CE}}{t_{\mathrm{ts}}}, \tag{1.24}$$

The rate of capacity loss is representative of numerous effects such as the growth of the solid electrolyte interphase (SEI) layer, the aging of the crystallographic structure of electrode materials, impurities dissolved in the electrolyte, unwanted chemical reactions, side effects, and generation of other compounds.

1.6.3 Energy, Capacity and Power

1.6.3.1 Modified Peukert Plot

How long does a battery last? The problem with quantifying the stored specific capacity is its discharge rate dependence. The faster the discharge *C*-rate, the lower remaining capacity, so a battery rated for 120 Ah actually provides a lower capacity when drained at rate higher than *C*/20 that is the typical rate for a lead acid battery (PbBat). The lithium-nanophosphate (Li-nP) chemistry exhibits this effect to a much lesser extent. These two batteries are equivalent at rate *C*/20. At faster rate, however, the Li-nP battery demonstrates higher capacities than PbBats. A Li-nP battery rated at 120 Ah will deliver 114 Ah when discharge at 1*C* rate, or 95 % of the rated capacity; in similar conditions a PbBat provides only 88 Ah [28]. Thus, calculating the discharge of a 120-Ah battery will run 12 h under a 10 A load is a false notion of order. This phenomenon can be considered using the Peukert's law (from the name of the German engineer who tested lead acid batteries), which is the simplest model for predicting battery lifetimes taking into account part of the nonlinear properties of the battery. The modified Peukert formula figures the discharge current I_n (in A) into the relation [29]:

$$I_n^k t = \Gamma, \tag{1.25}$$

where t is the maximum discharge time (in A), k is the Peukert exponent that is different from a battery to another one and Γ is a constant. From the derivation of

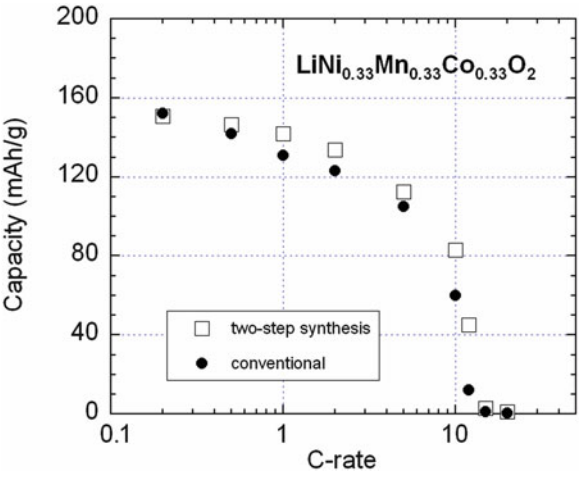

Fig. 1.10 Modified Peukert plots of the $Li//LiNi_{1/3}Mn_{1/3}Co_{1/3}O_2$ cells using solution 1 mol L^{-1} $LiPF_6$ in EC-DEC as electrolyte. Cells were cycled between 2.5 and 4.5 V vs. Li^0/Li^+. Cathode materials were synthesized by (**a**) the conventional wet-chemical method assisted by oxalic acid and (**b**) the two-step oxalate route. Reproduced with permission from [30]. Copyright 2012 Springer

the Eq. (1.21), the available capacity Q_m at different discharge rate I_{m1} is expressed by [29]:

$$Q_m = Q_n \left(\frac{I_n}{I_m}\right)^{k-1}. \tag{1.26}$$

The total discharge time will be m hours. For flooded lead acid batteries it ranges as $1.2 \leq k \leq 1.6$, while Ni-MH batteries have a smaller value of k, and that of Li-ion batteries is even better. The Peukert exponent is generally affected by several factors, among them the temperature and the age of the battery. Figure 1.10 shows the modified Peukert plot for Li cells including $LiNi_{1/3}Mn_{1/3}Co_{1/3}O_2$ (NMC) electrode materials synthesized by different routes. The tests were carried out after five cycles under the same conditions. The Peukert analysis evidences the difference between the powders synthesized using the conventional wet-chemistry assisted by oxalic acid, which results in a material with 3.2 % cationic disorder (fraction of Ni^{2+} on the 3*b* Li sites), and the two-step oxalate method for which $Ni^{2+}(3b) = 2.6$ %. It is obvious that the lower cationic disorder improves the capacity retention: even at the high rate of 10*C*, the capacity reversible capacity was 83 mAh g^{-1}, which is 50 % of the initial discharge capacity [30].

1.6.3.2 Ragone Figure

The Ragone concept is based on the equivalent circuit of an electrical storage system connected to a load or a generator. The battery can be modeled by a pure power source of uniform potential V_{oc} in series with the internal resistance, R_s, generating ohmic losses when the current i draws the load represented by the resistance R_L so that the potential across the load is given by the basic Ohm's law:

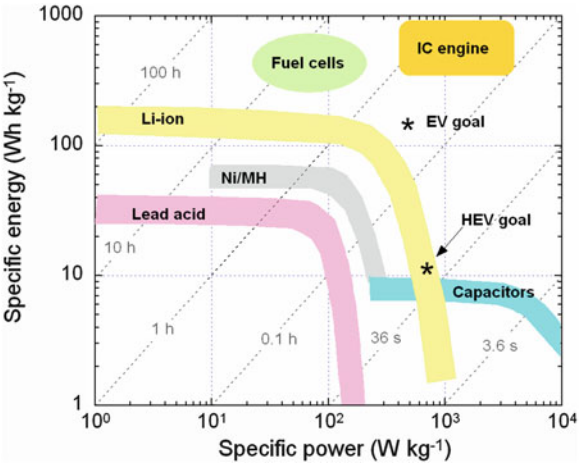

Fig. 1.11 Ragone charts of various electrochemical energy-storage devices. Association of Li-ion batteries and supercapacitors should provide a significant impact on performance of electrical vehicles: acceleration and long range

$$V_{\text{dis}} = R_{\text{L}} i. \tag{1.27}$$

Combining Eqs. (1.12) and (1.27), the cell voltage is given by:

$$V_{\text{oc}} = V_{\text{L}} \left(1 + \frac{R_{\text{S}}}{R_{\text{L}}} \right). \tag{1.28}$$

We can distinguish different energy terms: the energy W_{L} that is supplied to the load and the energy W_{s} that is dissipated in heat by the internal resistance [31, 32]. Currently, Ragone chart is plotted with log-log scales of the available specific energy (in Wh kg^{-1}) against specific power (in W kg^{-1}). Volumetric quantities are also considered in the case of electrochemical capacitors [33]. Figure 1.11 illustrates the Ragone plots of various electrochemical energy-storage devices [34]. It is shown that capacitors have higher specific power but modest specific energy compared to batteries. In terms of transportation, capacitors offer good acceleration but poor range; it is opposite for batteries [35].

1.7 Electrochemical Systems

1.7.1 Batteries

The main electricity storage options appropriate to power any modern system are: (1) electrochemical devices (batteries) using chemical reactions to generate power, (2) hydrogen production, compression, storage and power generation through fuel cells and (3) super-capacitors and ultra-capacitors that store energy in the form of accumulated charge. In this section, we briefly compare batteries and supercapacitors (commonly names "supercaps") [36]. The main targeted

technology is the obtaining of devices both smaller and lighter, which are the typical qualities requested for portable and electric transportation systems. Figure 1.12 displays various electrochemical systems in a plot of specific volumetric energy against gravimetric volumetric energy.

Electrochemical batteries are currently classified into different classes from the view point of the principle, nature of components (see Fig. 1.6), design and working conditions: nonrechargeable (primary) vs. rechargeable (secondary) systems (Table 1.6); aqueous vs. nonaqueous cells; liquid vs. solid electrolyte cells; low vs. high temperature batteries, etc. Since a battery has its own properties according the chemistry used for electrodes and electrolyte, the characterization of all the parameters is requested by consumers. For instance, zinc/silver oxide batteries developed by the US Navy for powering torpedo provide the highest energy per unit weight and volume among any commercially available aqueous secondary battery system. Note that lead-acid batteries are the most popular low cost secondary batteries produced worldwide so far; they represent approximately 45 % of the

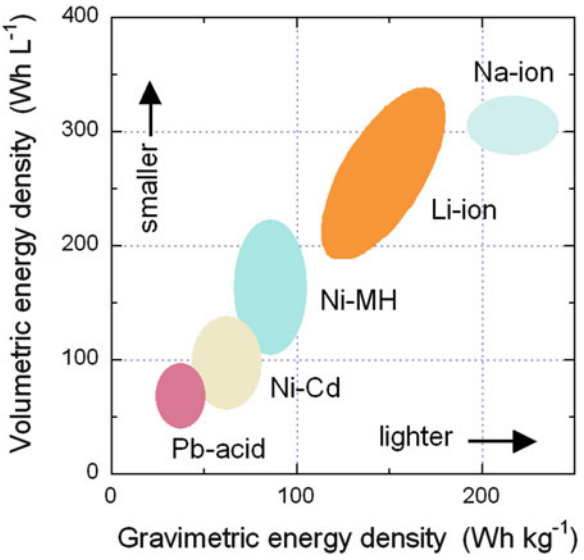

Fig. 1.12 Figures of merit of electrochemical batteries

Table 1.6 Classification of batteries

	Aqueous cell	Nonaqueous cell
Primary battery	Manganese dry cell	Metallic lithium battery
	Alkaline dry cell	
	Magnesium cell	
Secondary battery	Lead-acid battery	Li polymer battery
	Ni-Cd battery	Li-ion battery
	Ni-MH battery	

sales volume of all electrochemical systems. Characteristics of primary and secondary battery systems with their reaction mechanism can be found in Refs. [37, 38].

Batteries as energy storage systems (ESS) are essential for electric drive vehicles, such as hybrid electric vehicles (HEVs) plug-in hybrid electric vehicles (PHEVs) and all-electric vehicles (EVs). HEVs used currently Ni-MH batteries, which show longer life cycle than lead-acid batteries. Despite their high cost, lithium-ion batteries with an adequate chemistry (lithium-phosphate is the most popular) are powering PHEVs and EVs. Supercapacitors can provide additional power to vehicles (see Fig. 1.11) during acceleration and hill climbing. Supercaps are also used as devices to recover braking energy and to assist level load power of batteries. According the US Office of Energy Efficiency & Renewable Energy as part of the Department of Energy (DOE), the transition to a light-duty fleet of HEVs and EVs could reduce US foreign oil dependence by 30–60 % and greenhouse gas emissions by 30–45 % dependent of the exact mix technologies. The "EV Everywhere Blueprint" program gives the 10-year vision of DOE for plug-in electric vehicles (PEVs). The goals is the lowering cost of electric drive batteries from $500 to $125/kWh, and increasing density from 100 to 250 Wh kg^{-1}, 200 to 400 Wh L^{-1}, and 400 to 2000 W kg^{-1}. Note that, in the USA, 97000 PEVs were sold in 2013 [39]. The mission of the US Advanced Battery Consortium LLC (USABC), a collaborative organization operated by the three US car industries, Chrysler Group LLC, Ford Motor Company, and General Motors, is the development of electrochemical storage technologies that support commercialization of fuel cell, hybrid and electric vehicles, with the goal of reduction cost to $20/kW and extend life to 15 years. The total funding of USABC was $21.6 million in 2012 [40].

1.7.2 Electrochromics and Smart Windows

Electrochromic devices act to modulate incident radiation via transmission, absorption, or reflection of the light. Typically, an electrochromic device can be thought of a series of five thin films deposited on glass: a transparent conductor, an electrochromic material (working electrode), an ion conductor (separator/electrolyte), an electrochromic material (counter-electrode) and a transparent conductor (Fig. 1.13). By applying an electric field across the electrodes, the optical transmission and/or reflection of the working electrode can be modulated with a dynamic control of the radiation. The electrodes used in the devices are dependent of the type of device: absorptive/transmissive or absorptive/reflective [41]. Although, working electrode materials include WO_3, MoO_3, NiO, Ni_2O_3, In_2O_3, SnO_2:Sn, SnO_2:F, VO_2, PEDOT/PSS, single-walled carbon nanotubes (SWNT), etc. [42]. The optical modulation is due to the reduction or oxidation of the electrode material that allows reversible insertion/extraction of ions (proton, Li^+, Na^+) into/from its host lattice. Upon insertion, the host changes its color, which makes possible an electrochromic display or a smart window. For example, white-transparent WO_3 film associated

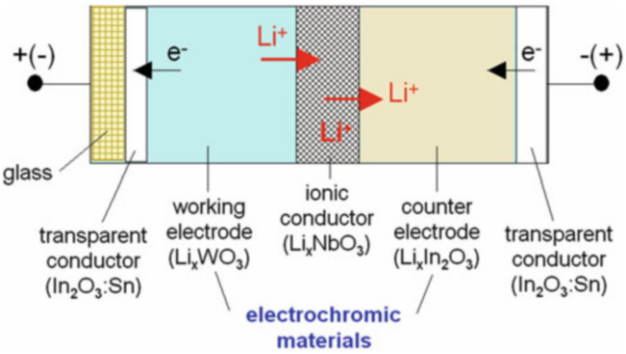

Fig. 1.13 Schematic view of an electrochromic device

with an acidic electrolyte can be used in an electrochromic display according to the reversible reaction:

$$xH^+ + xe^- + WO_3 \leftrightarrow H_xWO_3, \tag{1.29}$$

that products a dark-blue tungsten bronze, H_xWO_3, with the reduction of the transition metal from W^{6+} to W^{5+} [43]. Note that similar electron transfer occurs for lithium insertion. In practice, small cations such as H^+ and Li^+ can be easily inserted into the layered compounds and in the tunnel-like frameworks as well [44].

In any structure, traditional windows are the largest consumer of energy. Commonly, metallic coatings that reflect light and heat are used but they are not versatile and cannot be adjusted. Low-energy glasses named *smart windows* (introduced in the late 1990s) are based on paired electrochromic reactions that change light and heat transmission properties in response to voltage. They are automatically monitored when the exterior environment goes above the transition temperature. This type of low-power consuming technology could potentially save billions of dollars on heating, cooling, and lighting costs. The DOE estimates that windows currently cost $40 billion a year in energy use, which amounts to one quarter of the total energy spent in the USA. [45]. A smart window is composed of two standard float glasses (one has an electrochromic coating applied on one of the surfaces) sealed to form a single insulating glass unit (IGU) with an air space between each slice. The coating provides selective control over visible light and heat-producing near-infrared (NIR) light. Recently researchers reported the introduction of tin-doped indium oxide nanocrystals into niobium oxide glass (NbO_x), and realized a new amorphous structure as a consequence of linking it to the nanocrystals. Unprecedented optical switching and excellent electrochromic stability, with 96 % of charge capacity retained after 2000 cycles were demonstrated [46]. Smart windows are currently in use in architectures (commercial, office, private); Boeing has used them on its new "787 Dreamliner" aircraft.

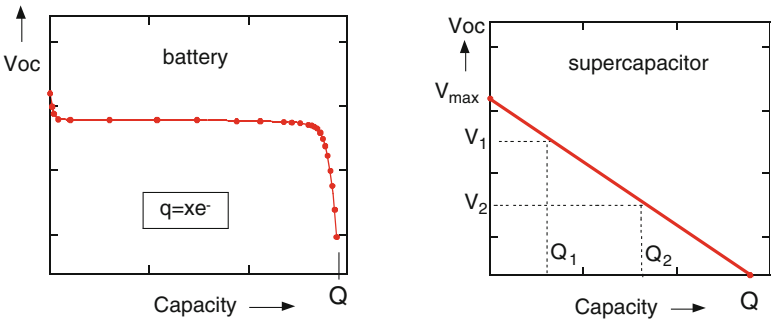

Fig. 1.14 V_{oc} vs. capacity of battery and supercapacitor

1.7.3 Supercapacitors

Supercapacitors, also known as electric double-layer capacitors (EDLCs) or ultracapacitors, have a high energy density when compared to conventional electrolytic capacitors. Larger supercaps have capacitance up to 5000 F. [47]. For applications in which significant energy is needed in pulse form, traditional capacitors used in electronic circuits cannot store enough energy in the volume and weight available. For these applications, the development of high energy density capacitors has been undertaken by various groups around the world [48]. Figure 1.14 shows the fundamental difference between V_{oc} of a battery compared to that of supercap. The simplest capacitors store energy by charge separation in a thin layer of dielectric material that is supported by metal plates that act as the terminals for the device. The energy stored in a capacitor is given by $1/2CV^2$, where C is its capacitance and V is the voltage between the plates. The capacitance value is calculated using the following expression:

$$C = \frac{\Delta Q}{\Delta V} = \frac{I\Delta t}{\Delta V}, \tag{1.30}$$

where I is the constant discharging current, $\Delta t = t_2 - t_1$ and $\Delta V = V_1 - V_2$, $V_1 = 80\ \%\ V_{max}$, $V_2 = 40\ \%\ V_{max}$ and V_{max} is the maximum voltage of the supercapacitor.

In an ultracapacitor, the electrodes are fabricated from high surface area, porous material having pores of diameter in the nanometer range. There are: activated carbon black, aerogel carbon, anhydrous RuO_2, transition-metal oxides (for instance MnO_2) or doped conducting polymers providing capacitance in the range 100–1300 F cm^{-3}. Projections of future developments using carbon indicate that energy densities of 10 mWh g^{-1} or higher are likely with power densities of 1–2 W g^{-1}.

1.8 Concluding Remarks

In this chapter, we have evoked briefly the fundamentals of the storage energy that are daily applied to face the problems associated with the use of fossil fuels (oil, gas and coal), the release of greenhouse gases and the devastating effects of raising the planet temperature as well. Also, energy can be stored in different forms having their own technologies. The use of electricity as power source requests new devices. Several examples can be cited. Electricity production from renewable energy sources needs to store electricity when lack of sunshine or wind is experienced. The integration of these new primary sources requires more attention in the design, control and management of the electric grid. Less-polluting automobiles necessitate the replacement of electric energy for oil. This is a great challenge because of the need of efficient, cheap and reliable batteries. Behind such a technology, the field of storage energy constitutes a multidisciplinary research of modern material science, including the development of new concepts. These days, there is a considerable global research activity on materials related to insertion reactions that constitute a breakthrough in extended applications, with the synthesis of these multi-component devices for storage energy. The fascination with electrical energy storage is driven by the potential superior performance of materials, by environmental necessity, and by the fundamental challenges these technologies present.

The most advanced technology for energy storage uses advanced materials and high performing systems include metal-hydride batteries, lithium-ion batteries, electrochromics, supercaps, etc., all of them need to be optimized for higher specific energy and power requirements. Recently, application of the nanotechnology to storage systems and especially in batteries and supercaps has opened the way for novel enterprise. For instance, lithium-ion batteries are used in large facilities to support energy storage, the load leveling and frequency regulation. With the ability to inject electricity contained in the batteries of cars on the grid, the Vehicle-to-Grid (V2G) technology will emerge.

References

1. El-Ashry M (2010) Renewvable energy policy network for the 21st century. http://www.harbortaxgroup.com/wp-content. Accessed Sept 2010
2. The European Wind Energy Association (2014) Wind in power 2013 European statistics. http://www.ewea.org/fileadmin/files/library/publications/statistics/EWEA_Annual_Statistics_2013.pdf. Accessed Feb 2014
3. Schneider EL, Oliveira CT, Brito RM, Malfatti CF (2014) Classification of discarded MIMH and Li-ion batteries and reuse of the cells still in operational conditions in prototypes. J Power Sourc 262:1–9
4. Van Noorden R (2014) A better battery. Nature 507:26–28
5. International Energy Agency (IEA) (2014) http://www.iea.org/statistics

6. European Environment Agency (2013) Atmospheric greenhouse gas concentrations. http://www.eea.europa.eu/data-and-maps/indicators/atmospheric-greenhouse-gas-concentrations-3/assessment. Accessed Feb 2014
7. Zaghib K, Guerfi A, Hovington P, Vijh A, Trudeau M, Mauger A, Goodenough JB, Julien CM (2013) Review and analysis of nanostructured olivine-based lithium rechargeable batteries: status and trends. J Power Sourc 232:357–369
8. Szepesi T, Shum K (2002) http://www.eetimes.com/document.asp?doc_id=1225408. Accessed 20 Feb 2002
9. Feynman R (1964) The Feynman lectures on physics, vol 1. Addison Wesley, New York
10. Zaghib K, Dontigny M, Guerfi A, Charest P, Mauger A, Julien CM (2011) Safe and fast-charging Li-ion battery with long shelf life for power applications. J Power Sourc 196:3949–3954
11. ITM Power (2014) www.itm-power.com
12. Birk JR (1976) Energy storage, batteries, and solid electrolytes: prospects and problems. In: Mahan GD, Roth WL (eds) Superionic conductors. Plenum, New York, pp 1–14
13. Julien C, Nazri GA (1994) Solid state batteries: materials design and optimization. Kluwer, Boston
14. Julien C, Nazri GA (2001) Intercalation compounds for advanced lithium batteries. In: Nalwa HS (ed) Handbook of advanced electronic and photonic materials, vol 10. Academic Press, San Diego, pp 99–184, chap 3
15. Augustynski J, Dalard F, Machat JY, Sohm JC (1975) Electric cells of the Leclanché type. US Patent 3,902,921, 2 Sept 1975
16. Ekern RJ, Armacanqui ME, Rose JI (1997) Reduced environmental hazard Leclanché cell having improved performance ionically permeable separator. US Patent 5,604,054, 18 Feb 1997
17. Bascap (2009) http://www.batscap.com. Accessed 5 Mar 2009
18. Julien C (1997) Solid state batteries. In: Gellings PJ, Bouwmeester HJM (eds) The CRC handbook of solid state electrochemistry. CRC Press, Boca Raton, pp 372–406
19. Ogumi Z, Uchimoto Y, Takehara Z, Kamanori Y (1988) Thin all-solid-state lithium batteries utilizing solid polymer electrolyte prepared by plasma polymerization. J Electrochem Soc 135:2649–2650
20. Weppner W, Huggins R (1977) Determination of the kinetic parameters of mixed-conducting electrodes and applications to the system Li_3Sb. J Electrochem Soc 124:1569–1578
21. Goodenough JB, Kim Y (2010) Challenges for rechargeable Li batteries. Chem Mater 22:587–603
22. Julien CM, Mauger A, Zaghib K, Vijh A (2010) Lectures of the workshop on materials science for energy storage, Chennai, India, 18–22 Jan 2010
23. Linden D, Reddy TB (2001) Handbook of batteries, 3rd edn. McGraw-Hill, New York
24. Bergveld HJ, Kruijt WS, Notten PHL (2002) Battery management systems, design by modelling. Kluwer Academic Publishers, Dordrecht
25. Ploehn HJ, Ramadass P, White RE (2004) Solvent diffusion model for aging of lithium-ion battery cells. J Electrochem Soc 151:A456–A462
26. Broussely M, Herreyre S, Biensan P, Kasztejna P, Nechev K, Staniewicz RJ (2001) Aging mechanism in Li ion cells and calendar life predictions. J Power Sourc 97–98:13–21
27. Wright RB, Christopherden JP, Motloch CG, Belt JR, Ho CD, Battaglia VS, Barnes JA, Duong TQ, Sutula RA (2003) Power fade and capacity fade resulting from cycle-life testing of advanced technology development program lithium-ion batteries. J Power Sourc 119–121:865–869
28. Mike M, Les A, Knakal T (2011) Lithium ion vehicle start batteries, power for the future. In: Proc NDIA ground vehicle systems engineering and technology symposium, Dearborn, MI, Accessed 9–11 Aug 2011
29. Doerffel D, Sharkh SA (2006) A critical review of using the Peukert equation for determining the remaining capacity of lead-acid and lithium-ion batteries. J Power Sourc 155:395–400

30. Hashem AM, El-Taweel RS, Abuzeid HM, Abdel-Ghany AE, Eid AE, Groult H, Mauger A, Julien CM (2012) Structural and electrochemical properties of $LiNi_{1/3}Co_{1/3}Mn_{1/3}O_2$ material prepared a two-step synthesis via oxalate precursor. Ionics 18:1–9
31. Gallay R (2014) Energy storage. Ragone. http://www.garmanage.com/atelier/index.cgi?path=public/Energy_storage/Ragone
32. Christen T, Carlen MW (2000) Theory of Ragone plots. J Power Sourc 91:210–216
33. Pech D, Brunet M, Durou H, Huang P, Mochalin V, Gogotsi Y, Taberna PL, Simon P (2010) Ultrahigh-power micrometer sized supercapacitors based on onion-like carbon. Nat Nanotechnol 5:651–654
34. Srinivasan V (2011) The three laws of batteries and a bonus Zeroth law. http://gigaom.com/2011/03/18/the-three-laws-of-batteries-and-a-bonus-zeroth-law. Accessed 18 Mar 2011
35. Scherson DA, Palencsar A (2006) Batteries and electrochemical capacitors. Interface Spring 2006:17–22
36. Winter M, Brodd RJ (2004) What are batteries, fuel cells and supercapacitors? Chem Rev 104:4245–4269
37. Linden D, Reddy T (2002) The handbook of batteries, 3rd edn. The McGraw-Hill, New York
38. Colin V, Scrosati B (1997) Modern batteries, 2nd edn. Wiley, Portland
39. Office of Energy Efficiency & Renewable Energy (2014) http://energy.gov/eere/vehicles/vehicle-technologies-office-batteries. Accessed July 2014
40. Snyder K (2012) Overview and progress of United States Advanced Battery Consortium (USABC) activity. http://www1.eere.energy.gov/vehiclesandfuels/pdfs/merit_review_2012/energy_storage/es097_snyder_2012_o.pdf. Accessed 15 May 2012
41. Granqvist CG, Azens A, Hjelm A, Kullman L, Niklasson GA, Rönnow D, Mattsson MS, Veszelei M, Vaivars G (1998) Recent advances in electrochromics for smart windows applications. Sol Energ 63:199–216
42. Niklasson GA, Granqvisr CG (2006) Electrochromics for smart windows: thin films of tungsten oxide and nickel oxide, and devices based on these. J Mater Chem 17:127–156
43. Cogan SF, Plante TD, Parker MA, Rauh RD (1986) Free-electron electrochromic modulation in crystalline Li_xWO_3. J Appl Phys 60:2735–3738
44. Castro-Garcia S, Pecquenard B, Bender A, Livage J, Julien C (1997) Electrochromic properties of tungsten oxides synthesized from aqueous solutions. Ionics 3:104–109
45. Hatt A (2013) Raising the IQ of smart windows. http://www.eurekalert.org/pub_releases/2013-08/dbnl-rti081413.php. Accessed 14 Aug 2013
46. Llordés A, Garcia G, Gazquez J, Milliron DJ (2013) Tunable near-infrared and visible-light transmittance in nanocrystal-in-glass composites. Nature 500:323–326
47. Al-Sakka M, Gualous H, Omar N, Van Mierlo J (2012) Batteries and supercapacitors for electric vehicles. http://cdn.intechopen.com/pdfs-wm/41417.pdf
48. Burke A (2000) Ultracapitors: why, how, and where is the technology. J Power Sourc 91:37–50

Chapter 2
Lithium Batteries

2.1 Introduction

By placing a very pure lithium-metal foil as anode element and a lithium salt in a nonaqueous solution as electrolyte, a new generation of electrochemical generators was born in the mid-1960s. Basically, the charge transport is identical to nickel-metal hydride (Ni-MH) or nickel-cadmium (Ni-Cd) batteries, except that Li^+ ions are created by the simple reaction

$$Li \rightarrow Li^+ + e^-, \tag{2.1}$$

liberating one electron through the external circuit and one ion introduced into the porous structure of the cathode. As discussed in the first chapter, the main parameters of energy storage systems are energy density (gravimetric and volumetric), power density, energy efficiency, and energy quality [1]. The great attractiveness of the lithium technology comes from the fact that Li is a lighter metal (molar weight $M_w = 6.941$ g mol^{-1} and density 0.51 g cm^{-3}), with the electronic configuration $(He)2s^1$. The specific capacity of Li metal is 3860 mAh g^{-1} and the couple Li^0 has the highest electroactivity with standard redox potential -3.04 V against H_2/H^+. Consequently, the voltage of lithium batteries is also significantly higher than that of the Pb-acid and Ni-metal hydride, because lithium is the most electropositive element found in nature.

Primary and secondary lithium batteries using a nonaqueous electrolyte, exhibit higher energy density than aqueous electrolyte-based batteries due to the cell potential higher than 1.23 V, the thermodynamic limitation of water at 25 °C. The excellent performances of nonaqueous lithium batteries may meet the need for high power batteries in micro-devices, portable equipment, and even electrical vehicles.

Lithium does not exist in the form of pure metal in nature due to a very high reactivity with air, nitrogen and water. It is extracted from ore or brine salt marsh

C. Julien et al., *Lithium Batteries*, DOI 10.1007/978-3-319-19108-9_2

(lithium chloride LiCl, lithium hydroxide LiOH, lithium carbonate Li_2CO_3). Since we only have 112.7 g of lithium in one kilo of Li_2CO_3, the extraction of one kilogram of lithium requires 5.3 kg of lithium carbonate. According to the US Geological survey (January 2010), Bolivia would house 32 % of world reserves of lithium carbonate (Li_2CO_3), and Chile nearly 27 %. However, Chile, China, and Argentina are the largest producers [2]. Note that 0.8 kg of lithium metal is produced per second in the world that is 25000 tons a year, mainly to produce lithium-ion batteries for electric cars or cell phones. In the US Geologican survey, Goonan said that it would take 1.4–3.0 kg of lithium equivalent (7.5–16.0 kg of lithium carbonate) to support a 40-mile trip in an electric vehicle before requiring recharge [2].

In this chapter, attention is focused on the technology of the lithium batteries. After a brief historical overview, we draw most of the primary and secondary lithium batteries. To get further information on the interest of these power sources, we invite the readers to consult works in references as there have been published numerous excellent books on LiBs based on various different viewpoints [3–16]. However, there are few books available on the state-of-the-art and future of next generation LiBs, particularly eventually for EVs and HEVs.

2.2 Historical Overview

Research in lithium batteries began in 1912 under G.N. Lewis, but the breakthrough came in 1958 when Harris noticed the stability of Li-metal in a number of nonaqueous (aprotic) electrolytes such as fused salts, liquid SO_2, or lithium salt into an organic solvent such as $LiClO_4$ in propylene carbonate ($C_4H_6O_3$). The formation of a passivation layer that prevents the direct chemical reaction between lithium metal and the electrolyte but still allows for ionic transport is at the origin of the stability of lithium batteries [17].

These researches opened the door to the fabrication and commercialization of varieties of primary lithium batteries; since the late 1960s nonaqueous lithium cells, especially the 3-V primary systems, have been developed. These systems include lithium-sulfur dioxide (Li//SO_2) cells, lithium-polycarbon monofluoride (Li//$(CF_x)_n$) cells introduced by Matsuschita in 1973, lithium-manganese oxide (Li//MnO_2) cells commercialized by Sanyo in 1975, lithium-copper oxide (Li//CuO) cells, lithium-iodine (Li//$(P2VP)I_n$) cells. During the same period, molten salt systems (LiCl-KCl eutecticum) using a Li-Al alloy anode and a FeS cathode were introduced [1]. The lithium-iodine battery has been used to power more than four million cardiac pacemakers since its introduction in 1972. During this time the lithium-iodine system has established a record of reliability and performance unsurpassed by any other electrochemical power source [18].

In the early 1970s was discovered the reversible insertion of guest species (ions, organic molecules, organometallics) into an host lattice that maintains its structural features but exhibits new physical properties. The first work was initiated by

Table 2.1 Rechargeable lithium metal batteries using TM oxides as positive electrodes

Battery	Potential (V)	Specific energy (Wh kg^{-1})	Company/year
Li//V_2O_5	1.5	10	Toshiba 1989
Li//CDMO[a]	3.0	–	Sanyo 1989
Li//$Li_{0.33}MnO_2$	3.0	50	Taridan 1989
Li/VO_x	3.2	200	Hydro-Québec 1990

[a]Composite dimensional manganese dioxide

Armand at Stanford [19] on the properties of Prussian blue (iron cyanide bronzes $M_{0.5}Fe(CN)_3$). Among a great variety of inorganic materials, transition-metal oxide (TMOs) as CrO_3 was investigated by Armand at Grenoble [20] and transition-metal dichalcogenides (TMDs) were studied by DiSalvo at Bell Laboratories [21], and later by researchers at EXXON [22–25]. Rechargeable lithium cells using Li-insertion compounds as positive electrodes were developed in the mid 1970s, when Winn and Steele [26, 27] at Chloride Technical Ltd reported solid-solution electrode of TiS_2 with lithium and sodium as well, followed by the announcement of Exxon (USA) for its intention to commercialize the Li//TiS_2 system [28]; Bell Laboratories (USA) reported the development of lithium cells constructed with either $NbSe_3$ or TiS_3 [29], while transition-metal oxides such as V_2O_5, V_6O_{13} were investigated by Dickens in the UK [30]. Table 2.1 documents the numerous efforts toward the development of rechargeable lithium batteries using TMOs as positive electrode and Li metal as anode.

Prototype cells using the principle of lithium intercalation showed promising characteristics of very high energy density (for instance, 3 times that of Ni-MH cells), moderate cycle life and higher voltage (~3 V) than aqueous technologies. Beside the development of positive electrodes, Li alloys (for instance, Li-Al) were envisaged as negative electrodes. Among them, the first commercially available rechargeable lithium power source system, the Li//MoS_2 type battery (MOLICEL™) was manufactured by Moli Energy Ltd. in Canada. This cell delivers performance with sustained drain rates of several amperes at a cell voltage between 2.3 and 1.3 V. The energy density was in the 60–65 Wh kg^{-1} range at a discharge rate of *C*/3 (approximately 800 mA). The total capacity of a *C*-size cell was 3.7 Ah and the number of realizable cycles is dependent upon the charge and discharge conditions [10]. Especially manufactured as the power source for pocket telephones in Japan, the first attempt to fabricate rechargeable batteries has proven very difficult ensuing safety concerns including fires due to the formation of dendrites. All the products were recalled [31].

At Eveready Battery Co. (USA) a Li/chalcogenide glass/TiS_2 was designed for the CMOS memory backup market. This cell is based on phosphorous chalcogenide glasses $Li_8P_4O_{0.25}S_{13.75}$ mixed with LiI and on solid-solution composite electrode TiS_2-solid electrolyte-black carbon with the percentage by weight of 51:42:7. The cathode capacity ranges from 1.0 to 9.5 mAh. The cell packaging is a standard sized XR2016 coin cell. The impedance of the cell at 21 °C is between 25 and 100 Ω depending upon where the cell is in the charge–discharge cycle. More than

200 cycles have been obtained in experimental cells [32]. A spirally wound AA-size Li//TiS_2 cell has been constructed by Grace Co. (USA). At 200 mA discharge rate, 1 Ah is delivered to 1.7 V [33]. In *C*-size, a Li//TiS_2 cell built by EIC Laboratories Inc. (USA), a capacity of 1.6 Ah was obtained. This cell operates in the temperature range from −20 to +20 °C [34].

The concept of lithium rocking-chair cells or lithium-ion batteries (LiBs) is not new. It has been proposed in the late 1970s by Armand who suggested *to use two different intercalation compounds as a positive and negative electrode, in the so-called rocking-chair battery, the lithium ions being transferred from one side to the other* [35]. Practically they were demonstrated in the early 1980s [36].

However, this concept has gained renewed attention following the success of Japanese industries. Sony and Sanyo in 1985 and 1988, respectively [37, 38], started to apply new electrodes materials following the fundamental researches of Goodenough in Oxford [39, 40] and of Armand and Touzain in Grenoble [41], who evidenced the fast motion of lithium ions in layered host structures (named as *lithium intercalation compounds*). A LiB contains a high-voltage (cathode) and a low voltage (anode) host versus Li^0/Li^+ redox couple. Exploiting the idea for large-scale production, Sony Energytec Inc. has commercialized in June 1991 a Li-ion battery including a lithium cobaltate ($LiCoO_2$) and a non-graphitic carbon (lithiated coke LiC_6), as cathode and anode, respectively; target was powering mobile phones. The Li-ion battery by Sony was an 18650-type (253 Wh L^{-1} energy density) using $LiPF_6$ in propylene carbonate/diethyl carbonate electrolyte solution [42]. Table 2.2 lists the initial applied patents for the invention of LiBs. The first patent related to the construction of a LiB, issued on 5 October 1985, is the property of the Japanese company Asahi Chemical Ind.

During the following decades, active R&D was directed towards alternative electrode materials resulting in small, light and high energy density batteries that have subsequently allowed the rapid development of small portable electronics.

Table 2.2 Prior patents related to Li-ion batteries

Inventor/company	Patent title	Patent number	Application date
Goodenough JB, Mizushima K (Kingdom Atomic Energy)	Fast ion conductors ($A_xM_yO_2$)	US 4,357,215 A	5 Avr 1979
Goodenough JB, Mizushima K (Kingdom Atomic Energy)	Electrochemical cell with new fast ion conductors	US 4,302,518	31 March 1980
Ikeda H, Narukawa K, Nakashima H (Sanyo)	Graphite/Li in nonaqueous solvents	Japan 1,769,661	18 June 1981
Basu S (Bell Labs)	Graphite/Li in nonaqueous solvents	US 4,423,125	13 Sept 1982
Yoshino A, Jitsuchika K, Nakajima T (Asahi Chemical Ind.)	Li-ion battery based on carbonaceous material	Japan 1,989,293	5 Oct 1985
Nishi N, Azuma H, Omaru A (Sony Corp.)	Non aqueous electrolyte cell	US 4,959,281	29 Aug 1989

Table 2.3 Energy densities at a *C*/5 discharge rate of some commercialized Li-ion batteries

Cell	Energy density	
	Gravimetric (Wh kg^{-1})	Volumetric (Wh dm^{-3})
Sony US 18650	103	245
A&T LSR 18650	130	321
Sanyo UR 18650	126	288
Moli ICR 18650	113	287
Matsushita CGR 17500	129	269
SAFT VL18650	108	260

Table 2.4 Chemistry of various primary lithium batteries. Reproduced with permission from [45]. Copyright 1997 CRC Press

Liquid electrolyte cells		Solid electrolyte cells
Solid cathode	Liquid cathode	Solid cathode
Iron disulfide (FeS_2)	Sulfur dioxide (SO_2)	Iodine (I_2)
Carbon fluoride (CF_x)	Thionyl chloride ($SOCl_2$)	Lead iodide (PbI_2)
Manganese dioxide (MnO_2) Silver chromate (Ag_2CrO_4)	Sulfur chloride (SO_2Cl_2)	Me_4NI_5-C cell Bromine trifluoride (BrF_3)
Copper oxide (CuO)		

Li-ion cells have been marketed later (Table 2.3) by several battery companies in the world (Sanyo, Matsushita, Hitachi, Yuasa, Moli, A&T, SAFT, etc.). Lithium-ion chemistries represent a significant step forward in battery technology. As an example, designed for sophisticated portable applications, the VL18650 from SAFT delivers a rated capacity of 1.2 Ah within stable operating conditions of discharge temperature in the range between −20 and +60 °C. Now, scientists and engineers have to throw down the challenge of developing high power LiBs for electric vehicles. Different varieties of Li-ion batteries were launched to power EV cars: in 1995, the 100-Ah $LiCoO_2$//graphite battery from Sony Corp. supplied energy for traveling 200 km at maximum speed up to 120 km h^{-1}; in 1996, the car launched by Mitsubishi Motors used $LiMn_2O_4$ spinel as cathode powering a trip of 250 km.

2.3 Primary Lithium Batteries

Developed in the early 1970s, primary lithium batteries are the most energy-dense electrochemical cells made for watches, film cameras, medical devices, and military purposes. Lithium primary cells have a typical gravimetric density 250 Wh kg^{-1}, against only 150 Wh kg^{-1} for Li-ion batteries. Various technologies that differ in chemistry and construction have been used to develop primary lithium batteries. In Table 2.4, they are classified into three groups, according to the form and the type of cathode and electrolyte used. Frost and Sullivan said that in 2009,

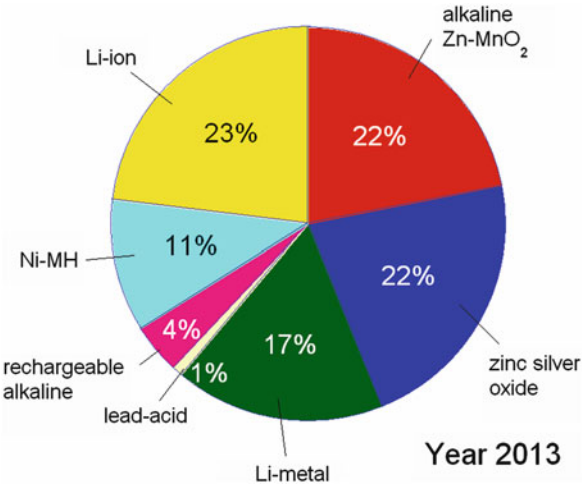

Fig. 2.1 Battery production in Japan for the year 2013. Primary batteries amounted to 61 %, including 17 % of lithium batteries

primary batteries including alkaline that were leading the market, carbon-zinc and lithium cells made 23.6 % of the global market with 3 % for primary lithium cells; it has been predicted a 7.4 % decline in 2015 due to the development of rechargeable batteries [43]. According the Freedonia's studies, the production of primary batteries doubled between 2002 and 2012. US demand for primary and secondary batteries are expected to grow 4.2 % per year to $17.1 billion in 2017. Lithium batteries will offer the best growth opportunities in both the rechargeable and primary battery segments [44]. Figure 2.1 presents the Japanese battery market in the year 2013, in which lithium-metal technology is 17 % segment of the total battery revenue.

2.3.1 High Temperature Lithium Cells

2.3.1.1 Lithium Iron Disulfide Battery

The lithium iron sulfide battery operates at about 400–500 °C using a fused halide eutectic electrolyte immobilized in the pores of a suitable separator. This battery displays a number of attractive features compared to the sodium-sulfur battery, including prismatic flat-plate construction, ability to withstand numerous freeze-thaw cycles, cell failures in short-circuit conditions, ability to withstand overcharge and low-cost materials with available construction techniques. The major disadvantage is a somewhat lower performance. This battery is suitable for load-leveling applications. Attention has also focused on battery designs suitable for electric propulsion [46]. Energizer successfully produced the first commercially available AA-size 1.5 V Li-FeS_2 battery in 1989 (specific energy density ~297 Wh kg^{-1}). The 1.5 V AAA-size followed in 2005.

The most commonly used electrolytes are the LiCl-KCl binary eutectic and the ternary LiF-LiCl-LiI lithium halides. With Li-Al alloy anode and FeS_2 cathode the discharge occurs in several discrete steps:

$$4Li + 3FeS_2 \rightarrow Li_4Fe_2S_5 + FeS, \tag{2.2}$$

$$2Li + Li_4Fe_2S_5 + FeS \rightarrow 3Li_2FeS_2, \tag{2.3}$$

$$6Li + 3Li_2FeS_2 \rightarrow 6Li_2S + 3Fe, \tag{2.4}$$

giving voltage plateaus at 2.1, 1.9, and 1.6 V, respectively. The use of Li-Al results in almost 50 % decrease in the theoretical specific energy, but much better stability is achieved. Most of the development was focussed on the LiAl/FeS couple; the Varta Battery Company (Germany) has produced a series of 140-Ah cells with a specific energy of 100 Wh kg^{-1} at a low discharge rate of 80 mA cm^{-2}, falling to 50 Wh kg^{-1} at high current density 250 mA cm^{-2}. Another version of LiAl/LiCl-LiBr-KBr/FeS_2 utilizes a dense FeS_2 electrode that only discharges to a stoichiometry corresponding to FeS (rather than to elemental Fe, which was the case of prior versions) [47]. The melting point of LiCl-LiBr-KBr at 310 °C allows cell operation at about 400 °C. These innovations have resulted in greatly improved capacity retention, and cells cycling for more than 1000 times. These cells are also developed in the USA and manufactured by Eagle-Picher, by Gould, and by SAFT America. Cells of 150- to 350-Ah capacity yield specific energies of 70–95 Wh kg^{-1} available at a 4-h discharge rate. There are still a number of unresolved scientific questions about the chemistry of LiAl/FeS cells and the mechanism of degradation and failure. In this system the separator is clearly a crucial component, which must not only keep the electrode materials apart but also allow good permeation of the electrolyte. The most suitable materials are found to be boron nitride and zirconia in the form of woven cloths, but they are obviously very expensive options.

2.3.1.2 Lithium Chloride Battery

Similar designs have been used in lithium chloride batteries, which operate at a temperature of 650 °C. The cell has the form Li(liq)/LiCl(liq)/Cl_2(g), carbon. The two electrodes, liquid Li anode and the porous carbon cathode in which the chlorine gas is fed under pressure, are separated by a molten lithium chloride electrolyte. The overall cell reaction is:

$$Li(liq) + ½\ Cl_2(g) \rightarrow LiCl(liq), \tag{2.5}$$

with an OCV of 3.46 V. This system delivers a theoretical energy density 2.18 kWh kg^{-1} at the working temperature. The most serious problems with this battery, however, are the corrosion of cell components and the development of satisfactory seals.

2.3.2 Solid-State Electrolyte Lithium Batteries

Solid-electrolyte batteries generally exhibit high thermal stability, low rates of self-discharge (shelf life of 5–10 years or better), ability to operate over a wide range of environmental conditions (temperature, pressure, and acceleration), and high energy densities of 0.3–0.7 Wh cm^{-3}. However, limitations include relatively low power density due to the high impedance of most lithium-conducting solid electrolytes. The three commercial solid electrolyte battery systems are based on the solid electrolyte LiI, either formed in situ during cell manufacture or dispersed with alumina.

2.3.2.1 Lithium-Iodine Cells

From the first pacemaker implant in 1958 by Dr Ake Senning surgeon at the Karolinska Hospital in Stockholm, numerous engineering developments have faced challenges in battery power. In 1972, a primary lithium-iodine battery replacing the mercury-zinc cells greatly extended the cardiac pacemaker life (about 10 years). More details on the history of this battery can be found in ref. [48]. The most important factor for a cardiac pacemaker battery is its reliability [49]. The terminal voltage decay characteristic is well behaved, falling slowly enough for battery end-of-life (EOL) to be anticipated in routine follow up. The lithium-iodine battery has a solid anode of lithium and a polyphase cathode of poly-vinyl-pyridine (PVP), which is largely iodine (at 90 % by weight). The solid electrolyte is constituted by a thin film of LiI. The discharge reaction is given by:

$$2\mathrm{Li} + n\mathrm{I}_2(\mathrm{PVP}) \rightarrow (n-1)\mathrm{I}_2(\mathrm{PVP}) + 2\mathrm{LiI}. \tag{2.6}$$

The cathode material is thus formed by the thermal reaction of iodine and polyvinyl-pyridine. This cell has an open-circuit voltage of 2.8 V. The theoretical specific energy for the $Li/LiI/I_2(PVP)$ cell is 1.9 Wh $cm^{-3.}$ The electrolyte ionic conductivity is $\sim 6.5 \times 10^{-7}$ S cm^{-1} at 25 °C, and the energy density is 100–200 Wh kg^{-1} [50]. The ratio of iodine to PVP is typically between 30/1 and 50/1, depending on the manufacturer. Phillips and Untereker have studied the phase diagram of the iodine/PVP material [51]. They demonstrated that at the application temperature (37 °C), the material passes through three phases—a two-phase region comprising a eutectic melt and pure iodine, a single phase liquid region, and a two-phase system wherein the iodine/monomer unit adduct phase coexists with the melt. An interesting and useful feature of the cathode material is that it is an electronic conductor. The conductivity is a function of the ratio of iodine to PVP. The maximum conductivity occurs at the I2/PVP weight ratio of 8/1. Since the initial ratio is much greater than this, the electronic conductivity increases until it reaches the weight ratio of 8/1, and then decreases gradually as the cell reaction continues. The increase in cell impedance caused by this decrease, together with the

increase due to the formation of the lithium/iodine reaction product, leads to a gradual and predictable decrease in cell voltage that is easily detected by the electronic circuitry of the pacemaker. This feature allows the clinical personnel to detect the onset of the end-of-service point of the battery well before that point is reached, making it possible to schedule replacement surgery in a timely manner by routine checking of the battery status by telemetry. The volume change accompanying the cell discharge is ~12 % if the cathode is 91 % iodide by weight. This volume change may be accommodated by the formation of a porous discharge product or by the formation of macroscopic voids in the cell. Such batteries are used as power sources for implantable cardiac pacemakers, operating at 37 °C. They are commercialized by Catalyst Research Co., Wilson Greatbatch Inc., and Medtronic Inc. The lithium-iodine batteries have extended system lives up to 10 years for 120- to 250-mAh capacities. For use as power sources for portable monitoring or recording instruments, they have a nominal capacity of 15 Ah or less, and most have deliverable capacities under 5 Ah.

Batteries of medium capacities, i.e., up to around 1 Ah, can be used for random-access memory power supplies in electronics. Similar batteries using Li//Br have also been built. The greater electronegativity of bromine gives rise to voltages the order of 3.5 V and energy densities as high as 1.25 Wh cm^{-3}. Their practical application is, however, limited by the low conductivity of the LiBr films that are formed.

2.3.2.2 Li/LiI-Al_2O_3/PbI_2 Cells

These batteries are recommended for low-rate operations and they are particularly suited for applications requiring long life under low drain or open-circuit conditions. Different cathodes have been used in these commercial solid-state cells, including a mixture of $PbI_2 + Pb$ or $PbI_2 + PbS + Pb$, and a new system under development uses a mixture of $TiS_2 + S$ or As_2S_3, which increases the energy density. The solid electrolyte is a dispersion of LiI and LiOH with alumina. Lithium ionic conductivities as high as 10^{-4} S cm^{-1} have been reported in such a dispersion at temperature of 25 °C [52]. The discharge properties are characterized by an open-circuit voltage of 1.9 V and an energy density of 75–150 Wh kg^{-1}. A three-cell battery design manufactured by Duracell International delivers 6 V and offers a capacity of 140 mAh as a pacemaker power source. In typical complementary metal oxide semiconductor (CMOS) memory applications, the 350-mAh battery can be used with 1.0-V cutoff potential.

2.3.2.3 Carbon Tetramethyl-Ammonium Penta-Iodide Batteries

The Li/LiI (SiO_2, H_2O)/$Me_4NI_5 + C$ cells were evaluated for use in cardiac pulse generators. They exhibited a voltage of 2.75 V and were projected to have a volumetric energy density of 0.4 Wh cm^{-3} [53]. The cathode is a mixture of carbon and tetramethyl-ammonium penta-iodide (Me_4NI_5).

2.3.2.4 Lithium Bromine Trifluoride Battery

Great advances have been made on the unconventional approach of combining alkali metals with strongly oxidizing liquid, e.g., SO_2, $SOCl_2$, or BrF_3, which acts simultaneously as electrolyte solvent and cathode depolarizer. BrF_3 is a very reactive liquid at room temperature, and the concept of a Li//BrF_3 cell has appeared [45, 53, 54]. A super high energy density battery which includes a lithium anode, a catalyst with liquid bromine trifluoride, and an electrolyte of antimony pentafluoride has been invented [55]. The cell reaction proceeds by the bromine trifluoride that disproportionates according the following equation:

$$4Li + BrF_3 \rightarrow 3Li^+F^- + Li^+Br^-. \tag{2.7}$$

Consequently, no electrolyte salt is necessary because lithium was found to be stable in BrF_3 due to the formation of the protective surface layer. Upon cell activation a potential of 5 V is established, giving theoretical energy densities of 2680 Wh kg^{-1} and 4480 Wh dm^{-3}. A typical discharge of a Li/BrF_3/C cell is achieved at 5 mA cm^{-2} current density, and a capacity of 5 mAh cm^{-2} has been measured. The cell performance is controlled by the formation of the reaction product layer at the anode–electrolyte interface, leading to an increase in impedance. The BrF_3 electrolyte can also be modified by dissolution of various fluorides, e.g., $LiAsF_6$, $LiPF_6$, $LiSbF_6$, or $LiBF_4$. Such a cell is actually strongly developed by EIC Laboratories Inc. in the USA.

2.3.3 Liquid Cathode Lithium Batteries

2.3.3.1 Lithium Thionyl-Chloride Batteries

The lithium thionyl-chloride battery uses liquid thionyl chloride ($SOCl_2$) as its positive active material, and lithium metal as its negative active material [56]. The overall reaction of the battery is expressed as:

$$2SOCl_2 + 4Li \rightarrow 4LiCl + S + SO_2. \tag{2.8}$$

The Li//$SOCl_2$ battery achieves a high voltage of 3.6 V and provides high volumetric energy density of 970 Wh dm^{-3} with discharge current of 100 μA. It can be used over a wide temperature range from −55 to +85 °C. This cell displays remarkably lower self-discharge than conventional batteries owing to the formation of a LiCl protective layer over the Li-metal anode surface. Main applications of Li//$SOCl_2$ batteries are: medical instruments, cash registers, measuring instruments, onboard microcomputers, sensors, electronic meters (gas, water, electricity, etc. Bipower® commercialized Li//$SOCl_2$ batteries with nominal voltage 3.6 V. The 1.6-Ah prismatic cell (BL–16PN-64) can be discharged at continuous current

20 mA. Applications include RF transmitters, military GPS systems, data loggers, alarm and security systems, CMOS memory backup and medical equipment. Li//$SOCl_2$ batteries from SAFT are bobbin (LS) or spiral (LSH) cells that operate at 3.6 V and show lowest self-discharge for extended operating life in the temperature range −60 to +150 °C. LS cells are designed specifically for long-term (5–20+ years) applications featuring a few μA base currents and periodic pulses, typically in the (−150 mA range, while. LSH cells are designed for applications requiring continuous current in the range 0.1–0.8 A. Taridan Batteries GmbH commercializes the SL-500 Li//$SOCl_2$ series exhibiting an extended temperature range up to +130 °C. These batteries have excellent shelf life (10 years) and extremely low self-discharge (1 % or less per year).

2.3.3.2 Lithium-Sulfur Dioxide Batteries

The cathode of the lithium-sulfur dioxide (Li-SO_2) batteries consists of a gas under pressure with another chemical as electrolyte salt; this is analogous to the thionyl chloride electrolyte and its liquid cathode [57]. Applications of these systems include emergency power units for aircraft and military cold-weather applications (e.g., radio operation). NASA is using Li-SO_2 cells for balloon and flight equipments. Features of Li-SO_2 batteries are as follows [58]: (1) high energy density up to 280 Wh kg^{-1}, (2) open-circuit voltage 2.95 V, operation voltage is between 2.7 and 2.9 V depending upon loading resistance, (3) long storage life, less than 2 % of self-discharging rate per year, could be stored for 10 years at room temperature, (4) spiral-wound construction may be discharged at higher rates, and (5) wide operation temperature range, −54 to +71 ° C. Spiral-wound Li-SO_2 battery from SAFT operates at 3 V in the temperature range −40 to +70 °C. This battery shows excellent capacity above 1 A. Its main advantage is the superior power at −40 °C and the low-self discharge during storage. The 11.5-Ah cell (model LO39SHX) can deliver 60 A maximum pulse discharge rate.

2.3.4 Solid Cathode Lithium Batteries

The semiconductive properties and tunnel structure of sulfide and transition-metal oxides led to the use of these materials in lithium power sources (Table 2.5). Several lithium-based chemistries were successfully applied to replace the prior system Zn/AgO and later the lithium-iodine batteries in implantable medical devices [59–61]. For example, Li//CuO, Li//V_2O_5, Li//CF_x, and more recently Li//$Ag_2V_4O_{11}$ couples have been adopted to power cardiac pacemakers requiring less that 200 μW [62, 63]. The lithium/carbon monofluoride (Li//CF_x) primary cells are very attractive in several applications because of the double energy density with respect to the state-of-the-art Li//MnO_2 primary batteries (theoretically 2203 against 847 Wh kg^{-1}).

Table 2.5 Primary lithium batteries with solid cathodes

Systems	OCV (V)	Comments
Li//CF_x	3.1	Developed by Matsushita (1973)
Li//MnO_2	3.3	Sanyo (1975)
Li//Ag_2CrO_4	3.25	For implanted pacemakers
Li//CuS	2.0–1.5	Two voltage plateaus
Li//CuO	2.4	Can operate at 150 °C
Li//FeS_2	1.8	Variant is Li//$CuFeS_2$
Li//$Ag_2V_4O_{11}$	2.75–2.50	For implanted pacemakers

2.3.4.1 Lithium Polycarbon Fluoride Cells

Polycarbon fluorides of the general formula $(CF_x)_n$ can be obtained by direct fluorination of carbon black or other varieties of carbon at high temperatures. Theoretical specific energy density 2600 Wh kg^{-1} can be achieved with these materials. Lithium cells with polycarbon fluoride cathodes have an open-circuit voltage in the range of 2.8–3.3 V, depending on the composition of the cathode material. A typical cell reaction may be written [64]:

$$nx\mathrm{Li} + (\mathrm{CF}x)n \rightarrow n\mathrm{C} + nx\mathrm{LiF}. \tag{2.9}$$

Thus, the theoretical specific discharge capacity Q_{th} (in mAh g^{-1}) is expressed by:

$$Q_{\mathrm{th}}(x) = \frac{xF}{3.6(12 + 19x)}. \tag{2.10}$$

The graph in Fig. 2.2 displays the experimental specific capacity of the $(CF_x)_n$ materials as a function of the stoichiometry ($0.5 \leq x \leq 1.0$). The theoretical capacity is calculated according to Eq. (2.11).

The crystal structure of graphite fluorides $(CF_x)_n$ compounds with $x > 0.5$ was investigated by Touhara et al. who proposed two phases: a stage-1 $(CF_1)_n$ and a stage-2 $(CF_{0.5})_n$, also commonly referred to as $(C_2F)_n$ [65]. In stage-1 compounds, the fluorine is intercalated between each carbon layers to yield –CFCF- layers stacking, whereas in stage-2 (hexagonal, C_{3h} symmetry) according to their model, fluorine occupies every other layer with a stacking sequence of –CCFCCF–. The hexagonal symmetry is preserved in both $(CF_1)_n$ and $(CF_{0.5})_n$ phases. Theoretical crystal structure calculations were also carried out and different layers stacking sequences were compared from their total energy. Due to electron localization in the C–F bond, a huge drop of the electrical conductivity occurs ~10^{-14} S cm^{-1} in $(CF)_n$ compared with ~1.7×10^4 S cm^{-1} in graphite.

Cells based on polycarbon fluorides are manufactured commercially in various forms. System developed by Matsushita Electric Industrial Co. is designed as a BR 435 cylindrical cell. Cells constructed by Nippon Steel Co. use carbon fibers as electrodes; they are found to be rechargeable. Cells for military applications have

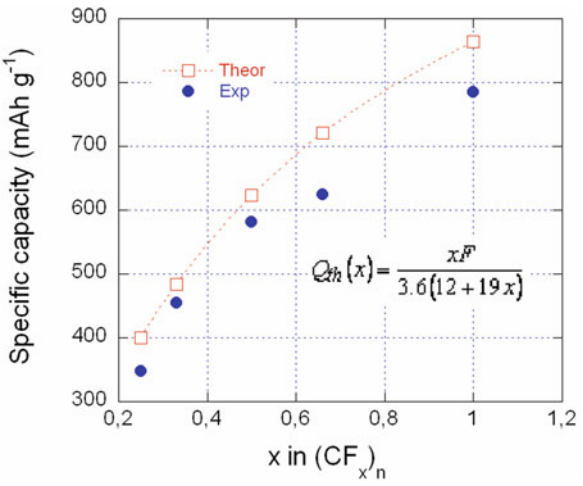

Fig. 2.2 Composition dependence of the experimental theoretical specific capacity of $(CF_x)_n$ cathode materials for primary lithium batteries. The theoretical capacity is calculated according to Eq. (2.11)

been produced in the USA by Eagle Picher and by Yardney Electric. There are spiral-wound cylindrical cells with a largest cell capacity of 5 Ah.

Lam and Yazami prepared sub-fluorinated graphite fluorides $(CF_x)_n$ compounds $(0.33 < x < 0.63)$ from natural graphite. The cathode behavior in lithium batteries investigated under low discharge rate shows that the energy density increases with the fluorine content x. However, at higher rates, sub-fluorinated compounds performed better than commercial $(CF_x)_n$ synthesized from petroleum coke. Specific capacity 400 mAh g^{-1} was obtained for Li//$CF_{0.52}$ coin cell discharged at 2.5*C* [66]. The rate capabilities of Li//$(CF_x)_n$ 18650-type 3.6-Ah cells using 1 mol L^{-1} $LiBF_4$ in EC:PC:EMC (1:1:3) as electrolyte were tested at Sandia Natinal Labs in the temperature range −40 to +72 °C [67]. The Li//CF_x system was fabricated by Wilson Greatbatch as an alternative electrical source for advanced pacemaker systems [68]. Li//CF_x-MnO_2 hybrid cells are commercialized by Ultralife. These cells are fabricated for at least 15 years shelf life and deliver 40 % or more capacity than the same-sized Li//MnO_2 system. Li//CF_x is estimated to be ~9 % of the world's primary battery market that is mainly shared by Panasonic (50 %), Greatbatch Medical (20 %), Spectrum Brands (20 %) and Eagle-Picher [69].

2.3.4.2 Lithium Manganese Oxide Batteries

Lithium manganese oxide (Li-MnO_2) battery is the most common consumer grade battery that covers about 80 % of the lithium battery market. This system includes heat-treated MnO_2 as cathode, lithium metal as anode and $LiClO_4$ in propylene carbonate/dimethoxyethane as aprotic electrolyte. The overall battery reaction is:

$$Mn^{IV}O_2 + Li \rightarrow Mn^{III}OOLi. \tag{2.11}$$

The cell reaction involves reduction of the MnO_2 without gases exhaustion and the product remains in the cathode. The system Li-MnO_2 displays several advantages: (1) the energy density is 150–250 Wh kg^{-1} and 500–650 Wh dm^{-3}, (2) the operating temperature ranges from −40 to +60 °C, (3) manganese dioxide is a low cost and safe material. Batteries are leading the market at approximately 50 % as estimated by Frost and Sullivan.

Many companies (Panasonic, Sony Energytec, Sanyo, Fuji, NTT, Matsushita, Varta, SAFT, etc.) embarked on ambitious programs to develop small rechargeable high-energy density, low cost Li-MnO_2 cells. Panasonic sales various battery sizes, from 30-mAh coin cells (CR1025) to cylindrical 2.4-Ah batteries. Duracell® Li/MnO_2 batteries are being used in a wide range of applications, from powering all functions of fully automatic 35-mm flash cameras to providing long-term standby power for computer clock/calendars. The button cell and spiral-wound cylindrical cell Maxell® Li//MnO_2 batteries have long-term reliability of 10 years; self-discharge rate is about 0.5 % per year. The cylindrical-type CR17450 model weighting 22 g has a nominal capacity 2500 mAh, $V_{oc} = 3$ V, and operates in the temperature range −40 to +85 °C. Typical voltage profiles of Li//MnO_2 batteries during discharge continuously at 40 mA are shown at different temperatures in Fig. 2.3 (from Maxell flyer). Scrap Li//MnO_2 batteries by Energizer® meet US Department of Transportation (DOT) requirements of the 49CFR173.185 standard: limit of 12 g of Li per cell, strong outer packaging, external short circuits prevented. Sony has commercialized a button-type CR2025 cell tested at 23 °C under a load of 15 kΩ for 900 h. Excellent long-term storage reliability was demonstrated: at 60 °C for 120 days is the equivalent of storage at room temperature for 6 years. PowerStream fabricate CR series of primary Li//MnO_2 button cells with nominal capacity from 25 to 1000 mAh. The price of the CR2477 1 Ah-cell is $3.00. The cylindrical Li//MnO_2 3-V battery by Bipower® (model CR34615) of nominal capacity 8 Ah weights 120 g. Panasonic sells a varieties of light button cells; the

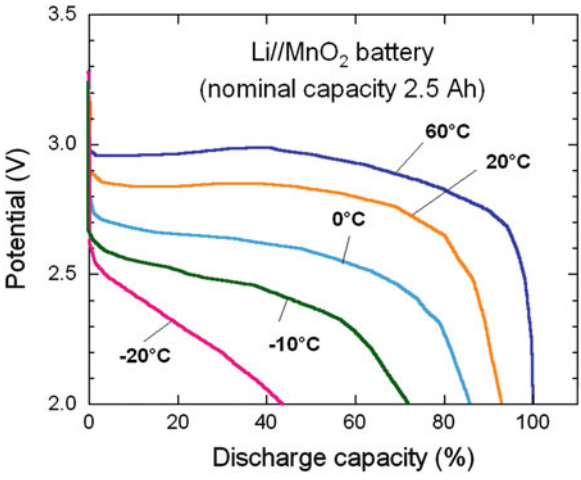

Fig. 2.3 Typical voltage profiles Li//MnO_2 batteries discharged continuously at 40 mA at different temperatures

CR2025 items of capacity 165 mAh weight 2.3 g. Since 1976, Sanyo Electric Co. has developed a wide variety of primary Li-MnO_2 cells to meet the demands of a large diversified market. Coin-type CR1220 36-mAh cell weighting 0.8 g delivers a maximum continuous discharge current 2 mA. The high-power cylindrical 2.6-Ah cell (spiral structure) weighting 23 g delivers 500 mA.

2.3.4.3 Low Temperature Lithium Iron Batteries

Room temperature primary Li//FeS_2 batteries use nonaqueous electrolyte, such as a lithium/iron disulfide, with good low temperature performance characteristics. The electrolyte has a solute including lithium iodide dissolved in an ether-containing solvent including a 1,2-dimethoxypropane based solvent component and no more than 30 vol% 1,2-dimethoxyethane [70, 71]. Commercial Li//FeS_2 AA primary batteries have offered substantially longer runtime than equivalent sized Zn//MnO_2 alkaline AA cells for high-power applications and below ambient temperature [72]. The electrolyte consisted of 1 mol L^{-1} $LiCF_3SO_3$ dissolved in 24.95 vol.% dioxolane, 74.85 vol.% dimethoxyethane, and 0.2 vol.% dimethylisoxazole. However, the rate capability of commercial Li//FeS_2 batteries may be limited by the ion conductivity of the electrolyte when FeS_2 samples have crystal sizes smaller than 1 μm. It has been demonstrated that the electrochemical performances are strongly dependent on the FeS_2 cathode particle size. Reducing crystal size of FeS_2 from 10 μm down to 100 nm increases the presence of crystal boundaries or surfaces per unit volume of FeS_2, provides a large number of nucleation sites for lithiated products, and thus promotes the kinetics of the heterogeneous (not intercalation) lithiation process of FeS_2 [73]. For a loading cathode of 14 mg cm^{-2}, the discharge voltage profiles of Li//nano-FeS_2 cells show a two-voltage-step reaction at 1.7 and 1.5 V at current densities lower than 3 mA g^{-1} (0.042 mA cm^{-2}). The 1.7-V lithiation plateau was attributed to the formation of pyrrhotite $Fe_{1-x}S$ ($0 < x < 0.2$) and $Li_{2+x}Fe_{1-x}S_2$ ($0 < x < 0.33$) intermediate phases, and the 1.5 V reaction produced a mixture of plate-shaped Li_2S and amorphous Fe as final products.

2.3.4.4 Silver Vanadium Oxide Cells

$Ag_2V_4O_{11}$ (SVO) is an interesting cathode material for lithium primary batteries used as a power source for implantable cardiac defibrillators (ICDs). Li//SVO cells have traditionally been designed by Medtronic Inc. to discharge the cathode to a composition of $>6Li{:}Ag_2V_4O_{11}$ [74]. The SVO tunnel-like structure (C-centered monoclinic) consists of vanadium oxide layers with silver located between the layers. Li//SVO batteries have a distinctive discharge curve with two plateaus, one at 3.24 V and one at 2.6 V. In the fully discharged state, the composition of the cathode is $Li_6Ag_2V_4O_{11}$. This composition corresponds to reduction of silver to Ag^0 and reduction of V^{5+} to V^{4+} [75, 76]. Lithium batteries with hybrid cathodes of $Ag_2V_4O_{11}$ and CF_x have been developed by Medtronic Inc. that combine the best

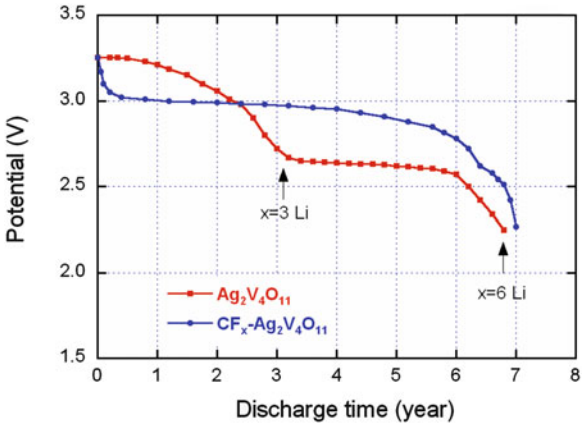

Fig. 2.4 The discharge profile of Li//SVO and Li//SVO-CF_x composite cells used to power medical devices

features of both cathode components. Figure 2.4 compares the discharge profile of Li//SVO and Li//SVO-CF_x composite cells. Silver chromate, Ag_2CrO_4 was also used as a cathode material in Li primary battery for pacemaker. The cell reaction is identical to that of SVO with the formation of metallic silver and final solid product Li_2CrO_4. The nominal voltage is 3.5 V and the specific energy is 200 or 575 Wh dm^{-3} for a 2.5-V cutoff. Button cells were produced by SAFT.

2.3.4.5 Other Primary Lithium Batteries

In many cases the discharge mechanisms involved in lithium oxide cells are still not fully understood. The discharge reaction can be described as a formal displacement process:

$$2\mathrm{Li} + MO \rightarrow \mathrm{Li_2O} + M, \tag{2.12}$$

where MO is an oxide such as CuO, Mn_2O_3, Bi_2O_3, or Pb_3O_4 with theoretical capacity of 670, 310, 350, and 310 mAh g^{-1}, respectively. OCV are in the range 3.0–3.5 V and a practical energy density of 500 Wh dm^{-3} is obtained. Varta has developed a CR 2025-type cell and SAFT has manufactured an LM 2020-type cell. The Li//CuO button cell (LC01) constructed by SAFT exhibits a single step which may be attributed to the simple displacement reaction (Eq. 2.12). This Li//CuO cell delivers an OCV of 1.5 V and has the highest specific energy of all solid cathode-based lithium cells. Practical value of 750 Wh dm^{-3} is obtained. The liquid electrolyte varies from manufacturer to manufacturer, but $LiClO_4$ in dioxolane is very often used. The cylindrical cells manufactured by SAFT have practical capacities in the range 0.5–3.9 Ah.

Sulfide electrodes have the advantage over the corresponding oxides that most of them are good electronic conductors, so that sulfide-based batteries usually do not

require the addition of carbon into the cathode. Batteries based on cupric sulfide cells (three in series) have been developed for use in a cardiac pacemaker. Li//CuS undergoes in two steps, so that the discharge curve exhibits two plateaus at 2.12 and 1.75 V during the first discharge to 1.5 V with a capacity of 530 mAh g^{-1}. The reduction of CuS results in the formation of Li_xCuS during the first voltage plateau, and $Cu_{1.96}S$, Li_2S and metallic Cu during the second voltage plateau [77].

2.4 Secondary Lithium Batteries

Basically, the idea of using materials that undergo insertion reactions as the electrochemically active component at the positive electrodes began to be explored in the 1970s, giving birth to the rechargeable lithium batteries (RLB). Two approaches consist in the design of RLB as shown in Fig. 2.4. The first system utilizes an insertion compound as positive material and a lithium-metal foil as the negative electrode, the so-called lithium-metal battery (Fig. 2.4a). The second system consists in using two open-structured materials as electrodes, in which the lithium ions can be shuttled from one intercalation compound acting as lithium-ion source to another receiving lithium-ion and vice versa for the discharge process. This is the commonly known lithium-ion battery (Fig. 2.4b) that was initially named "rocking chair battery," "swing battery" or "shuttlecock battery." Sometimes, LiBs are also named "lithium metal-free rechargeable batteries" [10] (Fig. 2.5).

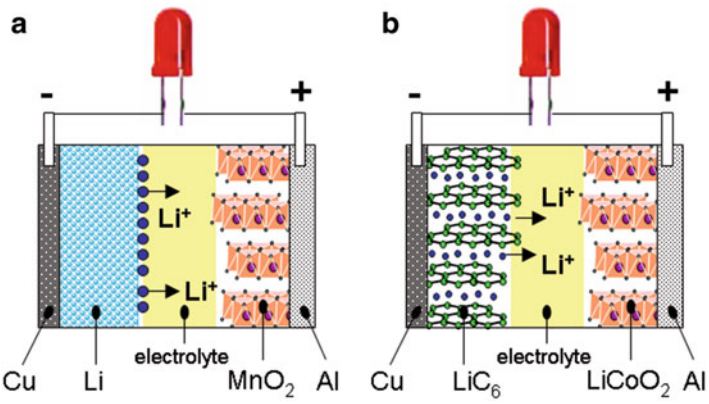

Fig. 2.5 Schematic representation of rechargeable lithium batteries. There are two systems according the nature of the negative electrode either Li metal (**a**) or Li insertion compound (**b**). In both cases, the positive electrode is constituted by an insertion compound, in which the redox reaction occurs at high potential versus Li^0/Li^+

2.4.1 Lithium-Metal Batteries

The first electrochemical applications of intercalation compounds appeared on lithium-metal batteries (LMBs). The idea of using materials that undergo insertion reactions as the electrochemically active components of batteries began to be explored and accepted in the early 1970s [8]. Of particular interest was the case of an electron donor mechanism that takes place in transition-metal dichalcogenides MX_2 ($X = S$, Se). The prototype is the Li//Li_xTiS_2 system [24]. Then, a series of studies of the transition metals of the first and second row were reported. Basically, batteries using MX_2 compounds can be considered as concentration cells, in which the activity of lithium varies in the composition range $0 \leq x \leq 1$. For $x = 0$, TiS_2 is at the pristine state and the cell is fully charged, while, for $x = 1$, the fully intercalated $LiTiS_2$ state corresponds to the discharged state. In Li_xTiS_2, for instance, the inherent reversibility of intercalation mechanism suggests the following reactions

$$xLi^+ + xe^- + TiS_2 \leftrightarrows Li_xTiS_2. \tag{2.13}$$

As the intercalation of lithium occurs as ionic species Li^+, the electro-neutrality of the host is maintained by the ejection into the external circuit of an electron generated by a reduction reaction of the transition-metal cation, the oxidation state of which switches from Ti^{4+} to Ti^{3+}. The cell potential decreases upon the Li uptake into the host framework, which follows the simple Nernst equation:

$$V(x) = E^0 - \frac{RT}{F} \ln a(Li^+), \tag{2.14}$$

where $a(Li^+)$ is the activity of Li^+ ions in Li_xTiS_2. Note that the decrease of the cell potential with increasing of Li^+ ion activity is a typical feature of Li-intercalation batteries. In the limits of the structural stability of the host, the electrochemical reaction is fully reversible.

Whittingham reported that the reversibility of the Li//TiS_2 couple permitted deep cycling for close to 1000 cycles with minimal capacity loss, less than 0.05 % per cycle, with excess lithium anode [78]. Two noticeable batteries with LiAl anode [79] that improves the safety were constructed by Exxon: the LiAl//TiS_2 cells were commercialized to power small devices such as watches and the largest lithium-metal prismatic-type cell using a $LiB(CH_3)_4$ salt in dioxolane was exhibited at the Electric Vehicle Show in Chicago en 1977 [78]. Because TiS_2 is a degenerate semiconductor that exhibits a high electronic conductivity, the use of this compound as cathode does not require the fabrication of composite electrode including conductive additive like carbon black. Despite the excellent performance of TiS_2, the great efforts of the Exxon'group were in vain, due to the formation of dendrites at the metallic anode in liquid electrolytes upon the cycling process, which is related to the non uniform change in the morphology of the anode surface as shown in Fig. 2.7. As pointed out by Xu [80], serious safety hazards are often

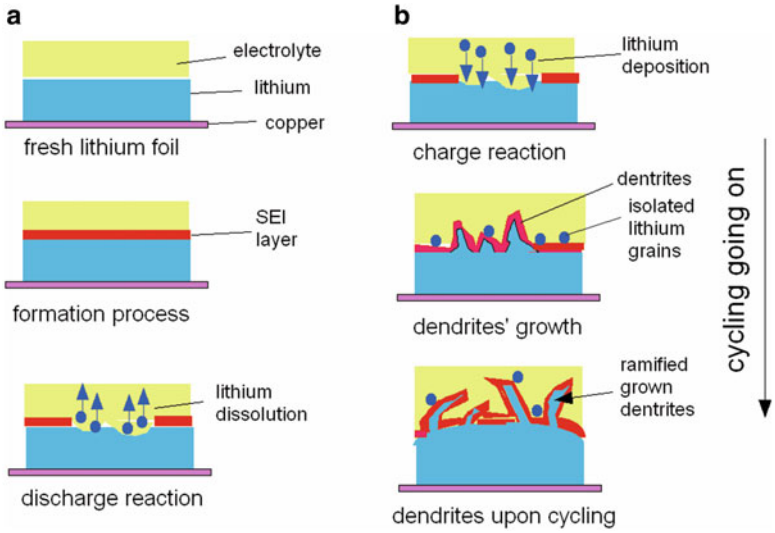

Fig. 2.6 Sketch of the formation of dendrites and deposition of lithium grains at the surface of the electrode (**a**) for the first discharge process with formation of the SEI and (**b**) upon cycling

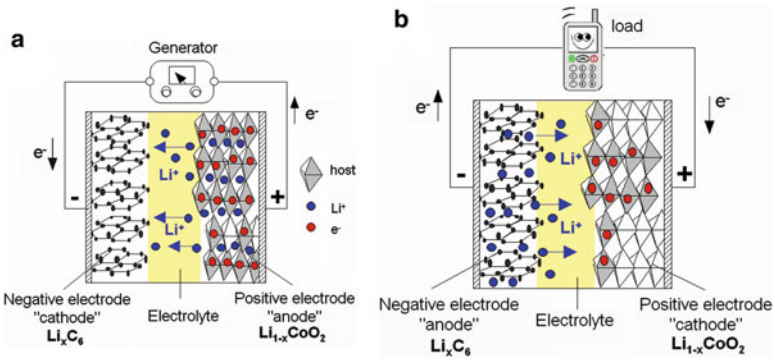

Fig. 2.7 Principle of the lithium-ion battery (**a**) charge process, (**b**) discharge process

caused by the generation of both dendrites and isolated lithium crystals (Fig. 2.6). The former creates internal shorts, and the latter is chemically active with the electrolyte solvents due to the huge surface areas of these lithium crystals. For the first discharge, that is the formation process, a passivation layer is formed at the surface of the lithium anode; this the solid electrolyte interphase (SEI), which is a poor ionic conductor in nature (Fig. 2.6a). This SEI is also growing upon repeated cycles. After the departure from the anode surface during discharge, the Li particles migrate to the cathode; the phenomenon is reverse for the charge. The deposition of Li^+ ions coming from the cathode participates to the nucleation of dendrites,

because particles do not have memory to seat back on the same site as before (Fig. 2.6b). Finally, the continuous dissolution and dendrite formation occur at the expense of the mechanical stability of the anode, which damages the whole battery operation.

The use of LMBs remains inefficient because several factors that are: (1) the unresolved control of the reactivity of lithium toward electrolyte, (2) the difficult mastery of the SEI layer, (3) the formation of large dendrites causes internal short circuiting, and (4) the increasing surface area upon cycling poses risks of overheating. It is a fact that LMBs have low coulombic efficiency ~90 % with carbonate solvents, and low cycle life due to the ceaseless growth of the passivation layer [81]. Von Sacken et al. [82] reported the thermal runaway of anode materials and showed that reactions between lithium metal and electrolyte are exothermic. These aspects are developed in the following, in the chapter related to anode materials.

Beside TiS_2, several transition-metal chalcogenide MX_2 or MX_3 ($X = S$, Se) compounds with a layered structure (case of MX_2) of one-dimensional structure ($NbSe_3$ has been the model system for quasi-1D charge density waves) have been studied as cathode materials in LMBs. Most of them display a single-phase behavior upon lithium intercalation. Li_xVSe_2 is the unique material showing a two-phase behavior that is evidenced by the appearance of two voltage plateaus in the discharge curve [83]. Three systems had emerged using TiS_2, MoS_2 and $NbSe_3$. A solid state battery Li/chalcogenide glass/TiS_2-carbon was developed at Eveready Battery Co. (USA) with the target of CMOS memory backup market. The electrolyte is a phosphorous chalcogenide glass $Li_8P4_{0.25}S_{13.75}$ mixed with LiI and on a composite electrode of TiS_2-solid electrolyte-black carbon with percentages in weight 51:42:7. The capacity ranges from 1.0 to 9.5 mAh. The cell packaging is a standard-sized XR2016 coin cell. The resistance of the cell at 21 °C is between 25 and 100 Ω depending on the state of charge [84]. A spirally wound AA-size Li/TiS_2 cell was constructed by Grace Co. (USA). At 200-mA discharge rate, a capacity of l Ah is delivered to 1.7 V [33]. Capacity of 1.6 Ah is obtained from a *C*-size Li/TiS_2 cell built by EIC Laboratories Inc. (USA). This cell operates in the temperature range from −20 to +20 °C [34]. *C*-size 3.7-Ah Li/MoS_2 batteries were especially manufactured by Moli Energy Ltd. (Canada) as the power source for pocket telephones in Japan. This battery uses a lithium anode, a propylene carbonate-based electrolyte solution and a processed MoS_2 cathode. Sustained drain rates of several amperes at a cell voltage between 2.3 and 1.3 V are obtained. The energy density is in the 60- to 65-Wh kg^{-1} range at a discharge rate of *C*/3 (approximately 800 mA) [85]. The Li-$NbSe_3$ system, termed FARADAY cell [86] was developed at AT&T (USA). The AA-size cylindrical cell was designed for operating over 200 cycles at a typical current of 400 mA to a cutoff capacity of 0.7 Ah. The ability to incorporate 3Li per $NbSe_3$ gives a relatively high theoretical energy density of 1600 Wh dm^{-3}. A practical energy density of 200 Wh dm^{-3} was achieved with the possibility of 350 cycles of charge–discharge.

It has long been recognized that lithium can be inserted chemically into metal oxide frameworks. Both molybdenum oxides [87, 88] and vanadium oxides [89] were synthesized for this purpose. The reversibility of insertion reaction in these alkali

metal bronzes Li_xMO_y formed in electrochemical cells allows many of these cells to be rechargeable. Labat et al. [90] disclosed a rechargeable cell having a cathode based on V_2O_5. A C-type Li//V_2O_5 1.4-Ah cell has been commercialized by SAFT. This cell includes a lithium or lithium alloy anode so that the cell is charged to 3.8 V. In the cell constructed by Tracor Applied Science Inc. about 2–20 % by weight of carbon is admixed to V_2O_5 [91]. The Li//V_2O_5 coin cell developed by Matsushita Micro Battery Corp. (Japan) provides power to electronic equipments like memory backup. The cathode is a mixture of V_2O_5 and 5 wt% carbon black. During the discharge, a depth of 3Li per V_2O_5 is obtained with an average voltage about 2 V. This battery delivers a capacity of 36 mA at a discharge rate of 1 mA [92].

2.4.2 Lithium-Ion Batteries

2.4.2.1 Principle

Basically, a lithium-ion battery (LiB) does not contain lithium metal, but only charge species Li^+ ions. These ions swing from one electrode to another throughout the electrolyte that is a good ionic conductor and an electronic insulator. Let us consider the charge and discharge reaction for a LiB with the Li_xCoO_2/$LiPF_6$-EC-DMC/Li_xC_6 electrochemical chain as shown in Fig. 2.7. A fresh cell is in the discharge state, i.e., at low potential. Consequently, in the initial state, the positive electrode framework is full of Li^+ ions (Li_1CoO_2), while the anode is empty (carbon C). As any electrochemical reaction implies the transport of ions and electrons, the redox process in a LiB is as follows. During the charge process, Li^+ ions are generated by the positive electrode (anode at this time), migrate across the electrolyte and penetrate the negative electrode (cathode at this time), while electrons circulate through the external circuit; in the process, the positive electrode is oxidized losing x electrons ($Li_{1-x}CoO_2$) and the negative electrode is reduced capturing x electrons (Li_xC_6) and vice versa for the discharge process.

For a LIB made of $LiCoO_2$ as positive electrode and graphite-like carbon as negative electrode, the chemical reactions for charge and discharge are expressed as shown below:

$$x\mathrm{Li}^+ + xe^- + 6\mathrm{C} \leftrightarrows \mathrm{Li}_x\mathrm{C}_6(\text{at the negative}), \tag{2.15}$$

$$\mathrm{LiCoO}_2 \leftrightarrows \mathrm{Li}_{1-x}\mathrm{CoO}_2 + x\mathrm{Li}^+ + xe^-(\text{at the positive}), \tag{2.16}$$

where the upper arrow represents the discharge process and the lower one the charge process. The overall battery reaction is expressed as:

$$\mathrm{LiCoO}_2 + 6\mathrm{C} \leftrightarrows \mathrm{Li}_{1-x}\mathrm{CoO}_2 + \mathrm{Li}_x\mathrm{C}_6. \tag{2.17}$$

Note that the $LiCoO_2$//C-type cell operates at high voltages, around 4 V, due to the big difference $[\mu(\mathrm{LiCoO_2}) - \mu(\mathrm{C})]$ between the chemical potentials of the electrodes (Eq. 1.2).

Table 2.6 Characteristics of Li-ion against NiMH cell

Characteristics	Ni-MH	Li-ion
Operating voltage (V)	1.3	3.7
Specific energy (Wh kg^{-1})	75	160
Self discharge (% per month)	30	5
Cycle life	Good	Good
Memory effect	Yes	No

Currently, the electrolyte is a mixture of alkyl carbonate solvents (aprotic) with lithium hexafluophosphate salt ($LiPF_6$) to provide ionic conductivity for the back and forth motion of the lithium ions. Generally the transport of ions into a solid-state compound is a slow process that requires optimization by using very well crystallized electrode materials [93, 94]. However, some amorphous substances can be used and this area is receiving increasing attention, in particular in the case of some anode materials that are discussed in Chap. 10. An important strategy in the design and optimization of an electrode is the use of the nanotechnology to reduce the size of active particles as small as possible. The smaller the particle size, the shorter the length of the path of a guest species in the solid, and the smaller the change from the core to the surface of individual particles during discharge–charge cycling [95].

Lithium ion batteries have a high energy density and are ideal for cyclic applications. They allow savings in volume and weight up to 70 % compared to traditional lead acid batteries or Ni-MH batteries (see Table 2.6). One disadvantage of the Li-ion batteries is that Battery Management System (BMS) is inevitable, to control and monitor the battery pack, and automatically compensate imbalances between cells as much as possible. This ensures a constant high capacity and a long life span. The BMS must also test constantly each cell to avoid thermal runaway and the propagation to other cells (battery fires). However, the recent investigations of LiBs with iron phosphate and titanate electrodes have shown the LFP/LTO cell passes successfully the battery tests for safety use in public transportation [96], in which case the role of the BMS is reduced to the control of the balance between the cells in the battery pack. The "18650" battery prepared under such conditions delivers a capacity of 800 mAh. It retains full capacity after 20000 cycles performed at charge rate 10*C* (6 min), discharge rate 5*C* (12 min), and retains 95 % capacity after 30000 cycles at charge rate 15*C* (4 min) and discharge rate 5*C*, both at 100 % depth of discharge (DOD) and 100 % state of charge (SOC). Since the introduction of LiBs using $LiCoO_2$ as the oxidant electrode, several new cell chemistries have been developed and used in commercial batteries.

2.4.2.2 Energy Diagram

The open-circuit energy diagram of a lithium battery has been discussed by Goodenough and Kim [97]. Figure 2.8 represents the energetic configuration of electrodes and electrolyte of a lithium battery at the thermodynamic equilibrium. The anode and cathode electrodes are electronic conductors with electrochemical

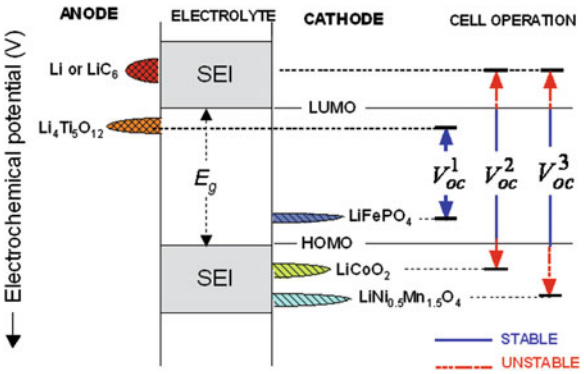

Fig. 2.8 Electronic band diagram of Li-ion batteries with various electrodes: olivine $LiFePO_4$, lamellar $LiCoO_2$, and spinel $LiNi_{1/2}Mn_{3/2}O_4$ as cathodes and lithium-metal and carbon as anodes. E_A and E_C represent the Fermi level of anode and cathode respectively. E_g is the electrolytic window that ensures the thermodynamic stability, while $E_A > E_L$ and $E_C < E_H$ requires a kinetic stability by the formation of an SEI layer

potentials μ_A and μ_C, also called Fermi level energies E_A and E_C, respectively. The electrolyte is an ionic conductor with a band gap E_g, which represents the separation between the lowest unoccupied molecular orbital (LUMO) of energy E_L and the highest occupied molecular orbital (HOMO) of energy E_H. The thermodynamic stability of a lithium cell requires that the electrochemical potentials of electrodes E_A and E_C are located within the energetic window of the electrolyte, which constrains the cell voltage V_{oc} of the electrochemical cell to

$$eV_{oc} = E_C - E_A \geq E_g, \tag{2.18}$$

where e is the elementary electronic charge and $E_g = E_L - E_H$ [14].

It has been suggested that in practical nonaqueous lithium battery systems the anode (Li or graphite) is always covered by a surface layer named the solid electrolyte interphase (SEI), 1–3 nm thick, which is instantly formed by the reaction of the metal with the electrolyte (this is called "formation cycle"). This film, which acts as an interphase between the metal and the solution, has the properties of a solid electrolyte. The SEI acts as a passivating layer at the electrode/electrolyte boundary gives a kinetic stability to the cell only when the condition in Eq. (2.18) is fulfilled. Otherwise, this layer has a corrosive effect and grows with the cycling life of the battery [98]. The design of electrodes must match the LUMO and HOMO level of the electrolyte. In Fig. 2.8, we present the schematic energy diagram of Li-ion cells for three different chemistries that illustrate the different situations: titanate spinel-iron phosphate (LTO//LFP), graphite-lithium cobaltate (C//LCO) and graphite-nickel-manganese spinel (C//LNM). For the couple $Li_4Ti_5O_{12}$// $LiFePO_4$, the voltage cell V_{oc} is smaller than E_g. Therefore, no SEI is formed because the electrode energy levels E_C and E_A match well within the electrolytic window, which insures very high safety. However, the price to be paid is a lower

Table 2.7 The most popular Li-ion technologies developed so far

Acronym	Cathode	Anode	Cell voltage (V)	Energy density (Wh kg^{-1})
LCO	$LiCoO_2$	Graphite	3.7–3.9	140
LNO	$LiNiO_2$	Graphite	3.6	150
NCA	$LiNi_{0.8}Co_{0.15}Al_{0.05}O_2$	Graphite	3.65	130
NMC	$LiNi_xMn_yCo_{1-x-y}O_2$	Graphite	3.8–4.0	170
LMO	$LiMn_2O_4$	Graphite	4.0	120
LNM	$LiNi_{1/2}Mn_{3/2}O_4$	Graphite	4.8	140
LFP	$LiFePO_4$	$Li_4Ti_5O_{12}$	2.3–2.5	100

open-circuit voltage, i.e., 2 V against 4 V for the graphite//$LiCoO_2$ battery. For the graphite//$LiCoO_2$ cell, graphite has E_A lying above the LUMO of used nonaqueous electrolytes and E_C of the cathode lies below the HOMO level. Consequently, the use of both graphite and $LiCoO_2$ electrodes is possible because this combination allows for the growth of the passivating SEI film. The SEI requires properties as follows: (1) it must have good mechanical stability when changes in electrode volume occur upon cycling life, (2) it must allow for fast Li^+-ion transfer from the electrolyte to the electrode, and (3) it must have a good ionic conductivity over the temperature range $-40 < T < 60$ °C [99]. In the case of the graphite//$LiNi_{1/2}Mn_{3/2}O_4$ cell, the situation is worse because E_C lies far from E_H that makes the electrode-electrolyte very instable. Table 2.7 lists a selection of the most popular Li-ion technologies that have been developed so far.

The characteristics of the cathode and anode elements together with a discussion on their advantages and disadvantages are reported in following chapters of this book. In Table 2.7, however, only the $Li_4Ti_5O_{12}$ (LTO) material is reported as an alternative to graphite, since it is being commercialized. LTO has been considered as a viable 1.5 V anode material since some time due to several advantages (see Chap. 10), and LiBs with this anode and various cathodes have been tested, starting with the LTO//$LiMn_2O_4$ combination, with liquid [100] or solid polymer [101] electrolytes. Then, the combinations LTO//$LiNi_{0.8}Co_{0.2}O_2$ and LTO//$LiCoO_2$ have been explored [102], demonstrating their viability for high-power applications. However, the exploration of LTO-based batteries was more or less abandoned for some years, due to the focus of all the research on only one parameter: the energy density and LTO suffered from the lower operating voltage. The interest in LTO was revived by the Ohzuku group [103, 104] who showed that a combination of LTO with a Li mixed oxide as cathode can deliver gravimetric energy densities as high as 250 Wh kg^{-1} and volumetric energy densities of 970 Wh dm^{-3}. The LTO//$LiMn_2O_4$ cell delivers a reversible capacity 90–100 mAh g^{-1} when cycled at 55 °C at 1*C* rate [105, 106]. With LTO particles of diameter 20 nm, the nano-LTO//$LiMn_2O_4$ cell can be cycled up to 1000 cycles at 25 and 55 °C and fast-charge capability was reported [107] up to 80*C* rate. The best results for the LTO//$LiMn_2O_4$ cell have been obtained with micrometer sized (~0.5–2 μm) secondary particles composed of nanosized (≤10 nm) LTO primary particles as the anode, combined with spherical $LiMn_2O_4$ particles [108]. This cell showed nearly

100 % capacity retention up to 1000 cycles when cycled at 5*C* rate at 55 °C. However, the problem with the use of $LiMn_2O_4$ is not the cycling life (number of cycles before aging), but the calendar life, which is very limited by the dissolution of manganese in the electrolyte. In addition, as any chemical process, the kinetics of this dissolution process increases with temperature. An illustration of this effect was given by the failure of $LiMn_2O_4$-based batteries that equipped electric cars in the US after a hot summer in 2013, which forced the car-maker to recall these cars to change the batteries. That is why many efforts were made since 10 years to replace $LiMn_2O_4$ by a compound based on another transition metal that does not dissolve into the electrolyte. The LTO//$LiFePO_4$ (LFP) cell operates at voltage circa 1.75 V and has been first studied in 1994, using a gel-polymer electrolyte [109]. A liquid electrolyte made of Li salt in an ionic liquid, namely, lithiumbis(trifluoromethane) sulfonamide, LiTFSI in Py_{24}TFSI, is also viable [110]. When the $LiFePO_4$ particles used as cathode of the LTO//LFP cell are coated with a conductive layer to increase the electrical conductivity of the LFP powder, the cell delivers a capacity of 155 mAh g^{-1}. In one case, the coat was polyacene [111], but usually it is simply a 2–3 nm thick conductive carbon layer [112]. A breakthrough performance has been obtained with such carbon-coated nano-LFP (particle size, 25 nm) as cathode [96]. The cells retained full capacity after 20000 cycles performed at charge rate of 10*C* and discharge rate of 5*C*, and retained 95 % of the capacity after 30000 cycles at charge rate 15*C* and discharge rate 5*C*, both at 100 % DOD (depth of discharge) and 100 % SOC (state of charge). The performance has even been improved by using carbon-coated LTO particles of size 90 nm, as good rate capability has been observed up to 100*C* rate [113]. In addition, different electrolytes have been tested in this work in order to increase the temperature where the battery can operate, which imposes to get rid of the ethylene carbonate that has a too small boiling temperature. The upper bound of the temperature window where the "18650" battery operates is raised to 80 °C by using 1 mol L^{-1} lithium bis (fluorosulfonyl)imide (LiFSI) in GBL or 1 mol L^{-1} LiFSI in PC+ γ-butyrolactone (GBL) electrolyte. Studies have also been successful to decrease the lower limit of the temperature window. The "18650" cell using the low temperature electrolyte 1 mol L^{-1} $LiPF_6$ and 0.2 mol L^{-1} LiFSI in quaternary blend of aliphatic solvents such as propylene (PC) + methyl propionate (MP) + ethylmethyl carbonate (EMC) + 5 % fluorinated ethylene carbonate (FEC) (1:1:1:1 by volume) displayed a similar electrochemical performance at 25 °C as that of the cell with conventional electrolyte, but in contrast permits to pass the Hybrid pulse power characterization (HPPC) test down to −10 °C, owing to improvement in ionic conductivity of the electrolyte. In addition, accelerated rate calorimetry measurements have shown that this cell benefits from an unprecedented safety [113]. The LTO/LFP combination then appears as the most attractive battery for use in PHEV, and energy storage for wind and solar energy. As mentioned earlier, the $LiNi_{1/2}Mn_{3/2}O_4$ (LNM) cathode, which operates at 4.7 V with respect to Li, cannot be combined with graphite, and LTO has then been considered as an alternative anode by the Ohzuku group [104, 114, 115]. The LNM//LTO cell operates at 3.2 V and delivers a capacity decreasing from 5.4− 4.8 mAh (for mass balanced cells of 0.056 g LTO and 0.049 g LNM)

when the current rate increases from 12.7 to 509 mA g^{-1}. The Amine group found a 86 % capacity retention when the LNM//LTO cell was cycled at *C*-rates from 0.5 to 10*C*, with very good cyclability over 1000 cycles between 2.0 and 3.5 V [116]. A Li$(Ni_{0.45}Co_{0.1}Mn_{1.45})O_4$//LTO with weight ratio of anode to cathode 1.36 in the laminated-type cell delivered a capacity of 124 mAh g^{1} up to 500 cycles at 1*C* rate [117]. Let us recall, however, that the problem with LNM (Co-doped or not) is the dissolution of manganese in the conventional electrolytes (same problem as in the case of the $LiMn_2O_4$) that reduces the calendar life and is still an obstacle to the commercialization of such batteries.

LTO has also been combined with the layered oxides $LiCoO_2$ [102], $Li(Ni_{0.8}Co_{0.2})O_2$, $Li(Co_{1/2}Ni_{1/2})O_2$ [118], $Li(Co_{1/3}Ni_{1/3}Mn_{1/3})O_2$ [104], and $Li_{1+x}[Co_{1/3}Ni_{1/3}Mn_{1/3}]_{1-x}O_2$ [119]. The performance of such batteries is good. The interest in the use of such layered compounds as cathodes is the high energy density. For instance, LTO//$Li(Co_{1/3}Ni_{1/3}Mn_{1/3})O_2$ cell delivered a capacity $<$85 mAh g^{-1} (340 mAh cm^{-3}) and has an energy density of 215 Wh kg^{-1} or 970 Wh dm^{-3} with an average voltage of 2.5 V. The replacement of graphite by LTO improves the power of the battery, since this material does not change volume upon insertion of lithium, and supports much faster charge–discharge rates than graphite. The safety problem with layer compounds, however, remains. Their bad thermal stability has restricted the use of these materials as cathode of LiBs to applications to portable use, with the exception of Boeing and Tesla, who used Al-doped $Li(Ni_{0.8}Co_{0.2})O_2$//graphite, inevitably leading to the battery fires that they have experienced if the BMS cannot manage the intrinsic instability of these batteries. That is why we did not recommend their use in transportation in spite of the temptation of the higher energy density.

Other batteries have been studied at the laboratory scale, using other compounds that are extensively reviewed in Chap. 10 as promising anode elements. They are, however, still too far from commercial use to be listed in Table 2.7. In addition, as we see in Chap. 10, the performance of these materials depend very much on the composition of the anode electrodes, and the research today is focused on their optimization by working on the formation of composites associating for instance carbon under the form of nanotubes or graphene, or coat of the nanoparticles of active elements of different shape (spherical, nanotubes, nanoplates), and different porosity. A review of primary results on such full cells (by opposition to half-cells with Li as the anode studied in Chap. 10) can be found for instance in ref. [120], but they will be fast outdated by the progress on the building of the anodes and the results newly obtained on half-cells discussed in Chap. 10, owing to the progress in nanoscience and materials science.

2.4.2.3 Design and Manufacturing

The elementary electrochemical cell of the lithium-ion battery is based on the assembly of three main components. This cell comprises two reversible electrodes that are slurry deposited onto metallic current collector: the anode provides lithium

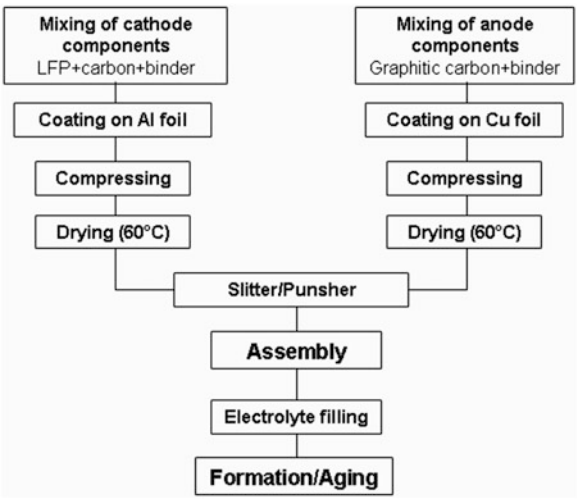

Fig. 2.9 Chart of manufacturing a Li-ion battery

ions during discharge and the cathode receives these charge species which are inserted into its lattice. The two electrodes are separated by a porous membrane with foam structure (separator) [121] soaked with the liquid electrolyte. This electrolyte is a fast ion conductor of lithium ions, but it is also an electronic insulator, because any transport of electron across the electrolyte would result in a self-discharge. The ionic conductivity is achieved by dissolving lithium salts in aprotic solvents. The anode is deposited onto copper foil, while the cathode material that is a mixture of electro-active material, carbon black and binder, is coated onto an aluminum foil. Both metallic foils insure the function of current collector. Each electrode film spread by coating technique has a thickness of a few tens of microns and a width of a few centimeters. Numerous operations are made to construct a cell, from preparation of powders and coating to cell formation and electrical tests (Fig. 2.9). The total thickness of the laminate obtained is about 150 μm, which depends on the electrical characteristics of the required cell. Indeed, changing the film thickness maximizes performance to meet the specific request of the application. So assemble thick film provides a configuration of high-energy type battery, while a thinner element will provide high-power performance. For a brief overview of processing for lithium-ion batteries see Ref. [122]. The sensitive chemistry of the Li-ion cell means that the manufacture must be done in dry room, less than 100 ppm of water. Mass production lies in fully automatic lines.

The manufacture of single cells and modules and packs for large-format power batteries is under development. One thing is inescapable: the manufacturing of cells in a dry room due to the sensitivity of lithium and chemistry to moisture. To satisfy the requirement of the target market of batteries for electric vehicles, the fabrication should be fast and less expensive, which necessitates fully automatic and integrated production lines. Such a solution has been adopted at Hydro-Québec, Canada, manufacturing 10-Ah iron-phosphate lithium-ion cells that are assembled in pack for power applications such as HEV, EVs and stationary storage.

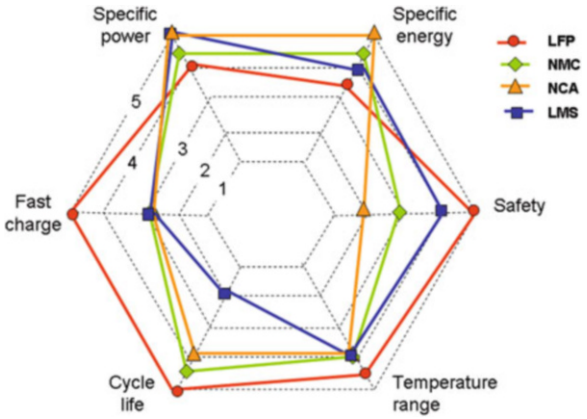

Fig. 2.10 Challenges in electrode materials for Li-ion batteries. *LFP* lithium iron phosphates. *NMC* nickel-manganese-cobalt oxide. *NCA* nickel-cobalt-aluminum oxide. *LMS* lithium-manganese spinel. Ranking: 1 = worst, 5 = best

Figure 2.10 compares the performance of various battery technologies envisaged for HEV and EV applications. Except energy and power density markers, the LFP chemistry shows the best characteristics in terms of fast charge, cycling, temperature runway and safety.

2.4.3 Lithium Polymer Batteries

In the 1980s Armand in collaboration with ELF-Aquitaine (France) and Hydro-Québec (Canada) played a leading role in the development of the lithium polymer battery (LMP) technology. Armand [123] suggested that solid polymer electrolytes derived from polyethylene oxide (PEO) might be used as electrolytes in LMP batteries, and major efforts have been made to produce polymer electrolytes with high conductivities at room temperature. Polymeric electrolytes are formed by complexes between salts of alkali metals and polymers containing solvating heteroatoms localized on the polymer chains. The most common example concerns such complexes with PEO chains that are formed by the repeat unit $–CH_2–CH_2–O–$. The solvating heteroatom, here oxygen, acts as a donor for the cation M^+. The anion X^-, generally of large dimension, stabilizes the PEO-M^+ complex. The first polymer electrolytes had conductivities of less than 10^{-5} S cm^{-1} at 25 °C, far too small for use in normal battery applications. Recently, however, electrolyte compositions have been produced which exhibit conductivity characteristics competitive with the properties of nonaqueous liquid electrolytes [124]. These materials have stimulated major development efforts in polymer electrolyte battery technology. The PEO-*MX* complexes may be considered as plastic electrolytes that are a compromise between liquid and solid crystalline electrolytes. Most of the polymeric batteries are of the form Li/PEO-Li salt/IC, where IC can be an intercalation compound, but also a composite electrode including a large amount of active intercalation material. From an examination of the temperature dependence of the ionic conductivity in polymer

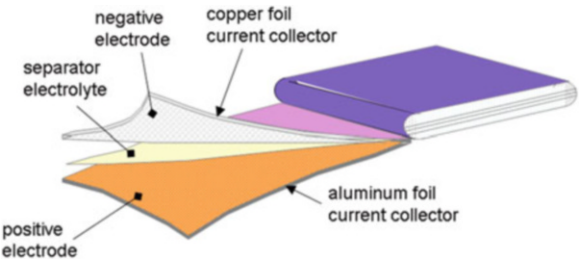

Fig. 2.11 Structure of a prismatic lithium-ion battery

complexes, one can remark the relatively high conductivity at room temperature of the complexes based on polyphosphazene, due to the low value of the vitreous transition temperature, T_g, and thus to the flexibility of the chains of the polymer, in turn related to the small barrier height to rotation of the P-N bond [125].

Positive electrodes of LPM batteries include a lithium-insertion electrode such as V_6O_{13}, TiS_2, MnO_2, Cr_3O_8, or LiV_3O_8 admixed with polymer electrolyte and conducting carbon for enhancement of the ionic and electronic conductivities, respectively. The composite electrode (50- to 75-μm thick) is deposited on a thin copper or nickel foil as current collector of few μm thick, and a film (25–50 μm) of $[(C_2H_4O)_9{\cdot}LiCF_3SO_3]_n$ polymer electrolyte completes the cell (Fig. 2.11). For optimum conductivity, the temperature of the polymer is maintained in the temperature range 80–90 °C. The system examined in the French–Canadian Project considered the following sequence $Li/(PEO)_8{\cdot}LiClO_4/TiS_2 + PEO + C$ [124]. Another system including TiO_2 as the cathode was cycled in the voltage range 3.0–1.2 V at a *C*/8 rate. A comparison of both cells shows similar features.

Recently, a LMP battery pack has been developed by Batscap that aims to demonstrate the feasibility of the high power LMP technology for EV application. It was especially designed to meet the needs for electric vehicles. This module, consisting of 12 cells connected in series is equipped with an electronic system (BMS) that provides thermal management (control of the internal temperature) and the electrical operation. The main information relating to security (alarm management) and the state of charge are managed and communicated to the application. With features in specific and volumetric energy density above 100 Wh kg^{-1} and 100 Wh L^{-1}, respectively, the 2.8-kWh BMP module (rated voltage 31 V) developed by BatScap realizes outstanding performance of lightness (25 kg) and compactness (25 L) and successfully equipped the fully electric Bluecar of the Bollore group.

2.4.4 Lithium-Sulfur Batteries

The lithium-sulfur (Li-S) battery has been under intense scrutiny for over two decades, as it offers the possibility of high gravimetric capacities and theoretical energy densities. Sulfur has a high specific capacity of 1673 mAh g^{-1}, but the rapid

capacity fading due to dissolution of polysulfides poses a significant challenge for practical applications. The discharge process of Li-S cell occurs with lithium dissolution from the anode surface and insertion into alkali-metal polysulfide salts, and reverse lithium plating to the anode while charging [126]. Theoretically, each sulfur atom can host two lithium ions, but experiments show that only 0.5–0.7 Li^+ ions are accommodated. Consequently, polysulfides are reduced while the cell is discharged according the reactions [126–129]:

$$S_8 \rightarrow Li_2S_8 \rightarrow Li_2S_6 \rightarrow Li_2S_4 \rightarrow Li_2S_3, \tag{2.19}$$

across a porous diffusion separator, sulfur polymers form at the cathode as the cell charges:

$$Li_2S \rightarrow Li_2S_2 \rightarrow Li_2S_3 \rightarrow Li_2S_4 \rightarrow Li_2S_6 \rightarrow Li_2S_8 \rightarrow S_8. \tag{2.20}$$

These reactions are analogous to those in the Na/S battery. Octasulfur has three forms: α-sulfur, β-sulfur, and γ-sulfur; the β-sulfur and γ-sulfur are metastable as they convert to α-sulfur in storage at ambient temperature. A typical discharge and charge voltage profile of the first cycle of Li//S cells is shown in Fig. 2.12.

Different configurations of Li//S batteries include silicon or lithium anode and a varieties of sulfur-based cathodes such as pure sulfur, porous TiO_2-encapsulated sulfur nanoparticles, sulfur-coated, disordered carbon nanotubes made from carbohydrates, copolymerized sulfur, sulfur-graphene oxide nanocomposite [129–132]. A 180-Å thick carbon layer was coated onto sulfur cathodes prepared by sputtering method. Charge–discharge tests show a specific capacity 1178 mAh g^{-1} at first discharge, falling to about 500 mAh g^{-1} after 50 cycles [132]. Ji et al. [130] reported the feasibility of a highly ordered nanostructured carbon-sulfur cathode for lithium-sulfur batteries. The conductive mesoporous carbon framework

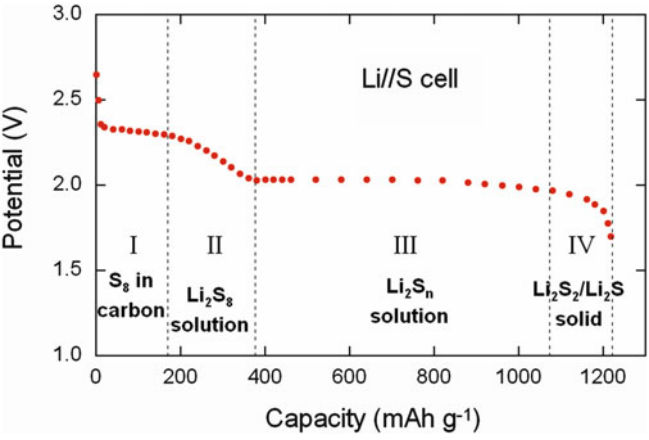

Fig. 2.12 Typical discharge and charge voltage profile of the first cycle of Li//S cells

precisely constrains sulfur nanofiller growth within its channels and generates essential electrical contact to the insulating sulfur. Such a structure favors access to Li reactivity with the sulfur. Reversible capacities up to 1320 mAh g^{-1} were attained. Zheng et al. [131] reported a hollow carbon nanofiber-encapsulated sulfur cathode for effective trapping of polysulfides, fabricated by using anodic aluminum oxide templates, and thermal carbonization of polystyrene. A high specific capacity of about 730 mAh g^{-1} was observed at *C*/5 rate after 150 cycles of charge–discharge. The introduction of $LiNO_3$ additive to the electrolyte was shown to improve the coulombic efficiency to over 99 % at rate *C*/5.

2.5 Economy of Lithium Batteries

Let us consider several aspects of lithium battery managements. Figure 2.13 displays some battery sizes including cylindrical, coin-cell, prismatic and pouch cell. A 2-Ah 18650 Li-ion cell has 0.6 g of lithium content. On a typical 60 Wh laptop battery with 8 cells (4 in series and 2 in parallel), this adds up to 4.8 g. To stay under the 8-g UN limit, the largest battery you can bring is 96 Wh. This pack could include 2.2 Ah cells in a 12 cells arrangement (4 series-3 parallels). If the 2.4-Ah cells were used instead, the pack would need to be limited to 9 cells (3 series-3 parallels). Evidently, the eventual commercial acceptability of lithium rechargeable batteries will depend on their cost effectiveness compared with other types of battery in the same utilization. In France, the cost of domestic electricity is 1.31€ per kWh including VAT and taxes (in January 2014); a AA-size alkaline Leclanché cell delivering, say 5 Wh, currently retails at 1.50€. Thus energy from this primary battery costs 300€/kWh, i.e., more expensive by a factor of over 200 with respect to the energy provided by domestic electricity.

Information from battery manufacturers are rather sparse but prices have now slipped to anywhere from $400 to $750 a kWh that means the 85-kWh pack powering the Tesla electric car costs between $34000 and $6375. A study by the Boston Consulting Group projected that prices would need to come down to

Fig. 2.13 Various battery configurations. (**a**) LS14250- cylindrical Li// $SOCl_2$ battery, (**b**) 4R25-prismatic (container) cell, (**c**–**d**) CR2020 Li-MnO_2 coin cells, (**e**) AA-type Li-ion cylindrical (1.5 Ah, 3.6 V, 12.4 g) cell, and (**f**) 30-Ah pouch ($LiMn_2O_4$-type, 3.8 V, 850 g) cell

$200 or less per kWh to make electric vehicles truly competitive. With a forecast of global demand of 26149 MWh by 2015, Sam Jaffe, research manager at IDC Corporate USA, claims a dramatic reduction in price for Li-ion cells to as low as $400/kWh [133]. Every year over 15 billion electrochemical cells are produced and sold worldwide including 40 % of lithium-based batteries. The global transportation lithium-ion battery market in light duty vehicles will grow from $1.6 billion in 2012 to almost $22 billion in 2020 with a nominal battery pack cost down to $397/kWh. According to Frost and Sullivan, in 2009, lithium battery market made up 40 % of the global revenue, overall 37 % of income for Li-ion batteries and 3 % for primary batteries. Presently, the greater part of general-use LiBs is produced in China, Japan, and the Republic of Korea. From statistics of calendar year 2013 provided by METI, the total battery production by volume was 3.46 billion units that produced a value 683.4 billion yens [134]. This production included 61 % primary batteries and 39 % secondary batteries (Fig. 2.2).

Battery recycling is a necessary issue to avoid hazardous waste and pollution especially when automobiles will be electrically powered. The process could be similar to that used for lead-acid batteries. Estimation made by Chemetall [135] show that recycling could provide 50 % of the lithium requirement for new batteries by 2040. Presently, it costs about $1700 to recycle 1 ton of batteries of any chemistry and size. From calculations by Hsiao and Richter [136], a 100-Ah battery processed through recycling would return 169 kg of Li carbonate, 38 kg of Co and 201 kg of Ni assuming the $LiNi_{0.8}Co_{0.15}Al_{0.05}O_2$ (NCA) cathode chemistry, for a total value of the recovered materials that exceeds $5000.

2.6 Battery Modeling

The constraints encountered by electrified automobiles, HEVs, PHEVs, and EVs, lead to very complex powertrain architectures, which require an optimized energy management obtained by simulation of the batteries. Battery modeling can help to predict, and possibly extend its lifetime. Many battery models can be found in the literature that are electrochemical models and stochastic models; for a review see Jongerden and Haverkort [137, 138]. The open-circuit voltage (thermodynamic property) is the main parameter taken into account in the electrochemical model, in which the charge transfer overvoltage, the diffusion overvoltage and the ohmic drop are considered (Eqs. 1.6 and 1.7). Due to various nonlinear effects the expression of the lifetime $t = Q/i$ does not hold for real battery, thus, a simple approximation for t under constant load i can be made with the Peukert' law (Eq. 1.26). The equivalent circuit used for simulation is obtained from experimental data of electrochemical impedance spectroscopy (EIS) of the battery at given state-of-charge [139].

Electrochemical properties and battery management of lithium metal and lithium-ion cells were analyzed using several different models. The electrochemical model developed by Doyle et al. [140–142] consists of six coupled, nonlinear differential equations whose solutions obtained from the Fortran program named

"Dualfoil" provide, with a very high accuracy, the voltage and current as functions of time and parameters of the battery electrolyte. Hageman has proposed the electrical-circuit models to evaluate Ni-Cd batteries [143]. A typical equivalent circuit includes five components: (1) a capacitor representing the capacity of the battery, (2) a discharge-rate normalizer that determines the lost capacity at high discharge currents, (3) a circuit to discharge the capacity of the battery, (4) a voltage versus state-of-charge lookup table, and (5) a resistor representing the battery's resistance. The Rakhmatov model is an extension of the Peukert's law based on the diffusion process of the active materials in the battery. To determine the lifetime one has to compute the diffusion process described by Fick's laws. This analytical model applied to Li-ion cells does even better, with a 2.7 % maximum error and an average error of less than 1 %.

In the kinetic battery model (KiBaM), Manwell and McGowan [144] used a chemical kinetics process with the battery charge distributed over two wells. For the calculation of the voltage during discharge, the battery is modeled as a voltage source in series with an internal resistance. The KiBaM can be used to model Li-phosphate-type Li-ion batteries because of the flat discharge profile of such a cell. The stochastic model based on discrete-time Markov chains was introduced by Chiasserini and Rao [145]. Modeling of Li-ion batteries has been obtained with a high accuracy, 1 % error. Later, in 2005, Rao et al. [146] proposed a stochastic battery model based on the analytical KiBaM. This simulation was successfully applied to AAA-type Ni-MH batteries with a maximum error of 2.65 %.

Tremblay and Dekkiche [147] presented an easy-to-use battery model applied to dynamic simulation software using the battery state-of-charge (SOC). Such a model is very similar to the Shepherd model that describes the electrochemical behavior of the battery directly in terms of voltage and current, often used in conjunction with the Peukert equation [148, 149]. However, contrary to the Shepherd model, it does not produce an algebraic loop. The battery is modeled using a simple controlled voltage source in series with a constant resistance, as shown in Fig. 1.7. This model assumes the same features for charge and discharge cycles. The open-voltage source is calculated with nonlinear Kalman filter that is an equation based on the actual SOC of the cell:

$$E = E_0 - K\frac{Q}{Q - it} + Ae^{\left(-B\int idt\right)}, \tag{2.21}$$

where E is the now-load voltage (V), E_0 the battery constant voltage (V), K the polarization voltage (V), Q the battery capacity (Ah), A the exponential zone amplitude (V), B the exponential zone time constant inverse $(\text{Ah})^{-1}$, and $\int idt$ the actual battery charge (Ah).

The long term calendar life of lithium ion cells for satellite and standby applications was studied by Broussely et al. [150]. In experiments, the capacity evolution was tracked as a function of storage temperature. Cells containing either $LiCoO_2$ or

$LiNi_xM_yO_2$ positive electrodes coupled with a graphite negative electrode were float-charged at 3.8 or 3.9 V. This study focused on losses at the negative electrode and the data were fit to a model involving a rate-determining step governed by electronic conductivity of the solid electrolyte interphase (SEI) layer, following Arrhenius law as a function of temperature.

References

1. Julien C, Nazri GA (1994) Solid state batteries: materials design and optimization. Kluwer, Boston
2. Goonan TG (2012) Lithium use in batteries. US Geological Survey Circular 1371, Reston, Virginia. http://pubs.usgs.gov/circ/1371/pdf/circ1371_508.pdf
3. Pistoia G (1994) Lithium batteries: new materials, developments and perspectives. Elsevier, Amsterdam
4. Linden D, Reddy TB (2001) Handbook of batteries, 3rd edn. McGraw-Hill, New York
5. Bergveld HJ, Kruijt WS, Notten PHL (2002) Battery management systems, design by modelling. Kluwer Academic Publishers, Dordrecht
6. Van Schalkwijk WA, Scrosati B (2002) Advances in lithium batteries. Kluwer, New York
7. Nazri GA, Pistoia G (2003) Lithium batteries, science and technology. Springer, New York
8. Balbuena PB, Wang Y (2004) Lithium-ion batteries, solid-electrolyte interphase. Imperial College Press, London
9. Wakihara M, Yamamoto O (2008) Lithium ion batteries: fundamentals and performance. Wiley, Weinheim
10. Yoshio M, Brodd RJ, Kozawa A (2009) Lithium batteries, science and technologies. Springer, New York
11. Ozawa K (2009) Lithium ion rechargeable batteries. Wiley, Weinheim
12. Park CR (ed) (2010) Lithium-ion batteries. InTech, Rijeka (Croatia) Open access book. http://www.intechopen.com/books/lithium-ion-batteries
13. Yuan X, Liu H, Jiujun Z (2012) Lithium batteries: advanced materials and technologies. CRC Press, Boca Raton
14. Belharouak I (ed) (2012) Lithium batteries new developments. InTech, Rijeka (Croatia) Open access book. http://www.intechopen.com/books/lithium-ion-batteries-new-developments
15. Abu-Lebdeh Y, Davidson I (2013) Nanotechnology for lithium-ion batteries. Springer, New York
16. Scrosati B, Abraham KM, Van Schalkwijk WA, Hassoun J (2013) Lithium batteries: advanced technologies and applications. Wiley, Hoboken
17. Jasinski R (1967) High-energy batteries. Plenum, New York
18. Julien C (2000) Design considerations for lithium batteries. In: Julien C, Stoynov Z (eds) Materials for lithium-ion batteries. Kluwer, Dordrecht, pp 1–20
19. Armand MB, Whittingham MS, Huggins RA (1972) The iron cyanide bronzes. Mater Res Bull 7:101–108
20. Armand MB (1973) Lithium intercalation in CrO_3 using n-butyllithium. In: Van Gool W (ed) Fast ion transport in solids. North Holland, Amsterdam, pp 665–673
21. Gamble FR, Osiecki JH, Cais M, Pisharody R, DiSalvo FL, Geballe TH (1971) Intercalation complexes of Lewis bases and layered sulfides: a large class of new superconductors. Science 174:493–497
22. Dines MB (1975) Intercalation of metallocenes in the layered transition-metal dichalcogenides. Science 188:1210–1211
23. Dines MB (1975) Lithium intercalation via n-butyllithium of the layered transition metal dichalcogenides. Mater Res Bull 10:287–292

24. Whittingham MS (1978) Chemistry of intercalation compounds: metal guests in chalcogenaide hosts. Prog Solid State Chem 12:41–99
25. Whittingham MS (1982) Intercalation chemistry: an introduction. In: Whittingham MS, Jacobson AJ (eds) Intercalation chemistry. Academic, New York, pp 1–18
26. Winn DA, Steele BCH (1976) Thermodynamic characterization of non-stoichiometric titanium disulphide. Mater Res Bull 11:551–558
27. Winn DA, Shemilt JM, Steele BCH (1976) Titanium disulphide: a solid solution electrode for sodium and lithium. Mater Res Bull 11:559–566
28. Whittingham MS (1977) Preparation of stoichiometric titanium disulfide. US Patent 4,007,055, Accessed 8 Feb 1977
29. Murphy DW, Trumbore FA (1976) The chemistry of TiS_3 and $NbSe_3$ cathodes. J Electrochem Soc 123:960–964
30. Dickens PG, French SJ, Hight AT, Pye MF (1979) Phase relationships in the ambient temperature $Li_xV_2O_5$ system ($0.1 < x < 1.0$). Mater Res Bull 14:1295–1299
31. Toronto Globe and Mail (1989) Cellular phone recall may cause setback for Moli. Accessed 15 Aug 1989
32. Akridge JR, Vourlis H (1986) Solid state batteries using vitreous solid electrolytes. Solid State Ionics 18–19:1082–1087
33. Anderman M, Lunquist JT, Johnson SL, Gionannoi TR (1989) Rechargeable lithium-titanium disulphide cells of spirally-wound design. J Power Sourc 26:309–312
34. Abraham KM, Pasquariello DM, Schwartz DA (1989) Practical rechargeable lithium batteries. J Power Sourc 26:247–255
35. Armand M (1980) Intercalation electrodes. In: Murphy DW, Broadhead J, Steele BCH (eds) Materials for advanced batteries. Plenum Press, New York, pp 145–161
36. Lazzari M, Scrosati B (1980) A cycleable lithium organic electrolyte cell based on two intercalation electrodes. J Electrochem Soc 127:773–774
37. Nagaura T, Nagamine M, Tanabe I, Miyamoto N (1989) Solid state batteries with sulfide-based solid electrolytes. Prog Batteries Sol Cells 8:84–88
38. Nagaura T, Tozawa K (1990) Lithium ion rechargeable battery. Prog Batteries Solar Cells 9:209–212
39. Goodenough JB, Mizuchima K (1981) Electrochemical cell with new fast ion conductors. US Patent 4,302,518, Accessed 24 Nov 1981
40. Mizushima K, Jones PC, Wiseman PJ, Goodenough JB (1980) Li_xCoO_2 ($0 < x < 1$): a new cathode material for batteries of high energy density. Mater Res Bull 15:783–789
41. Armand M, Touzain P (1977) Graphite intercalation compounds as cathode materials. Mater Sci Eng 31:319–329
42. Ozawa K (1994) Lithium-ion rechargeable batteries with $LiCoO_2$ and carbon electrodes: the $LiCoO_2$/C system. Solid State Ionics 69:212–221
43. Frost & Sullivan (2013) Global lithium-ion market to double despite recent issues. http://www.frost.com. Accessed 21 Feb 2013
44. Freedonia (2013) Batteries, study ID 3075. http://www.freedoniagroup.com/industry-category/enrg/energy-and-power-equipment.htm. Accessed Nov 2013
45. Julien C (1997) Solid state batteries. In: Gellings PJ, Bouwmeester HJM (eds) The CRC handbook of solid state electrochemistry. CRC Press, Boca Raton, pp 372–406
46. Ritchie AG, Bowles PG, Scattergood DP (2004) Lithium-iron/iron sulphide rechargeable batteries. J Power Sourc 136:276–280
47. Jensen J (1980) Energy storage. Butterworths, London
48. Holmes CF (2007) The lithium/iodine-polyvinylpyridine battery – 35 years of successful clinical use. ECS Trans 6:1–7
49. Mallela VS, Ilankumaran V, Rao NS (2004) Trends in cardiac pacemaker batteries. Indian Pacing Electrophysiol J 4:201–212
50. Schlaikjer CR, Liang CC (1971) Ionic conduction in calcium doped polycrystalline lithium iodide. J Electrochem Soc 118:1447–1450

51. Phillips GM, Untereker DF (1980) In: Owens BB, Margalit N (eds) Power sources for biomedical implantable applications and ambient temperature lithium batteries. The Electrochem Soc Proc Ser PV 870-4, p 195
52. Liang CC, Joshi AV, Hamilton WE (1978) Solid-state storage batteries. J Appl Electrochem 8:445–454
53. Park KH, Miles MH, Bliss DE, Stilwell D, Hollins RA, Rhein RA (1988) The discharge behaviour of active metal anodes in bromine trifluoride. J Electrochem Soc 135:2901–2902
54. Goodson FR, Shipman WH, McCartney JF (1978) Lithium anode, bromide trifluoride, antimony pentafluoride. US Patent 4,107,401 A, Accessed 15 Aug 1978
55. Crepy G, Buchel JP (1993) Lithium/bromide trifluoride electrochemical cell designed to be discharged after being activated and stored. US Patent 5,188,913 A, Accessed 23 Feb 1993
56. Bowden WL, Dey AN (1980) Primary Li/$SOCl_2$ cells XI. $SOCl_2$ reduction mechanism in a supporting electrolyte. J Electrochem Soc 127:1419–1426
57. Dey AN, Holmes RW (1980) Safety studies on Li/SO_2 cells: investigations of alternative organic electrolytes for improved safety. J Electrochem Soc 127:1886–1890
58. PowerStream (2014) Primary lithium SO_2 cells from PowerStream http://www.powerstream.com/LiPSO2.htm
59. Leising RA, Takeuchi ES (1993) Solid-state cathode materials for lithium batteries: effect of synthesis temperature on the physical and electrochemical properties of silver vanadium oxide. Chem Mater 5:738–742
60. Holmes CF (2001) The role of lithium batteries in modern health care. J Power Sourc 97–98:739–741
61. Root MJ (2010) Lithium-manganese dioxide cells for implantable defibrillator devices, discharge voltage models. J Power Sourc 195:5089–5093
62. Chen K, Meritt DR, Howard WG, Schmidt CL, Skarstad PM (2006) Hybrid cathode lithium batteries for implantable medical applications. J Power Sourc 162:837–840
63. Walk CR (1983) Lithium-vanadium pentoxide cells. In: Gabano JP (ed) Lithium batteries. Academic, London, pp 265–280
64. Whittingham MS (1975) Mechanism of reduction of the fluorographite cathode. J Electrochem Soc 122:526–527
65. Touhara H, Kadono K, Fujii Y, Watanabe N (1987) On the structure of graphite fluoride. Z Anorg Allg Chem 544:7–20
66. Lam P, Yazami R (2006) Physical characteristics and rate performance of $(CF_x)_n$ $(0.33 < x < 0.66)$ in lithium batteries. J Power Sourc 153:354–359
67. Nagasubramanian G (2007) Fabrication and testing capabilities for 18650 Li/$(CF_x)_n$ cells. Int J Electrochem Sci 2:913–922
68. Holmes CF, Takeuchi ES, Ebel SJ (1996) Lithium/carbon monofluoride (Li//CF_x): a new pacemaker battery. Pacing Clin Electrophys 19:1836–1840
69. Shmuel De-Leon (2011) Li/CFx batteries the renaissance. http://www.sdle.co.il/AllSites/810/Assets/li-cfx%20-%20the%20renaissance.pdf. Accessed 8 June 2011
70. Broussely M (1978) Organic solvent electrolytes for high specific energy primary cells. US Patent 4,129,691A, Accessed 12 Dec 1978
71. Webber A (2009) Low temperature Li/FeS_2 battery. US paten 7,510,808B2, Accessed 31 Mar 2009
72. Clark MB (1982) Lithium-iron disulfide cells. Academic, New York
73. Shao-Horn Y, Osmialowski S, Horn QC (2002) Nano-FeS_2 for commercial Li/FeS_2 primary batteries. J Electrochem Soc 149:A1199–A1502
74. West K, Crespi AM (1995) Lithium insertion into silver vanadium oxide $Ag_2V_4O_{11}$. J Power Sourc 54:334–337
75. Crespi AM (1993) Silver vanadium oxide cathode material and method of preparation. US Patent 5,221,453, Accessed 27 Sept 1990
76. Crespi A, Schmildt C, Norton J, Chen K, Skarstad P (2001) Modeling and characterization of the resistance of lithium/SVO for implantable cardioverter-defibrillators. J Electrochem Soc 148:A30–A37

77. Chung JS, Sohn HJ (2002) Electrochemical behaviours of CuS as a cathode material for lithium secondary batteries. J Power Sourc 108:226–231
78. Whittingham MS (2004) Lithium batteries and cathode materials. Chem Rev 104:4271–4301
79. Rao BML, Francis RW, Christopher HA (1977) Lithium-aluminum electrode. J Electrochem Soc 124:1490–1492
80. Xu K (2004) Nonaqueous liquid electrolytes for lithium-based rechargeable batteries. Chem Rev 104:4303–4417
81. Ota H (2004) Characterization of lithium electrodes in lithium imides/ethylene carbonate and cyclic ether electrolytes. Surface chemistry. J Electrochem Soc 151:A437–A446
82. Von Sacken U, Nodwell E, Sundher A, Dahn JR (1990) Comparative thermal stability of carbon intercalation anodes and lithium metal anodes for rechargeable lithium batteries. J Power Sourc 54:240–245
83. Whittingham MS (1978) The electrochemical characteristics of VSe_2 in lithium cells. Mater Res Bul 13:959–965
84. Akridge JR, Vourlis H (1988) Performance of Li/TiS_2 solid state batteries using phosphorous chacogenide network former glasses as solid electrolyte. Solid State Ionics 28–30:841–846
85. Py MA, Haering RR (1983) Structural destabilization induced by lithium intercalation in MoS_2 and related compounds. Can J Phys 61:76–84
86. Trumbore FA (1989) Niobium triselenide: a unique rechargeable positive electrode material. J Power Sourc 26:65–75
87. Schöllhorn R, Kuhlmann R, Besenhard JO (1976) Topotactic redox reactions and ion exchange of layered MoO_3 bronzes. Mater Res Bull 11:83–90
88. Besenhard JO, Schöllhorn R (1976) The discharge reaction mechanism of the MoO_3 electrode in organic electrolytes. J Power Sourc 1:267–276
89. Murphy DW, Christian PA, DiSalvo FJ, Waszczak JV (1979) Lithium incorporation by vanadium pentoxide. Inorg Chem 18:2800–2803
90. Labat J, Cocciantelli JM (1990) Rechargeable electrochemical cell having a cathode based on vanadium oxide. US Patent No. 5,219,677, Accessed 11 Dec 1990
91. Margalit N, Walk CR (1995) Lithium ion battery with lithium vanadium pentoxide positive electrode. World Patent WO 1996006465 A1, Accessed 18 Aug 1995
92. Desilvestro J, Haas O (1990) Metal oxide cathode materials for electrochemical energy storage. J Electrochem Soc 137:5C–22C
93. Zaghib K, Mauger A, Groult H, Goodenough JB, Julien CM (2013) Advanced electrodes for high power Li-ion batteries. Materials 6:1028–1049
94. Julien CM, Mauger A, Zaghib K, Groult H (2014) Comparative issues of cathode materials for Li-ion batteries. Inorganics 2:132–154
95. Zaghib K, Guerfi A, Hovington P, Vijh A, Trudeau M, Mauger A, Goodenough JB, Julien CM (2013) Review and analysis of nanostructured olivine-based lithium rechargeable batteries: status and trends. J Power Sourc 232:357–369
96. Zaghib K, Dontigny M, Guerfi A, Charest P, Rodrigues I, Mauger A, Julien CM (2011) Safe and fast-charging Li-ion battery with long shelf life for power applications. J Power Sourc 196:3949–3954
97. Goodenough JB, Kim Y (2010) Challenges for rechargeable Li batteries. Chem Mat 22:587–603
98. Peled E (1979) The electrochemical behaviour of alkali and alkaline earth metals in nonaqueous battery systems. The solid electrolyte interphase model. J Electrochem Soc 126:2047–2051
99. Aurbach D, Gamolsky K, Markovsky B, Salitra G, Gofer Y, Heider U, Oesten R, Schmidt M (2000) The study of surface phenomena related to electrochemical lithium intercalation into Li_xMO_y host materials (M = Ni, Mn). J Electrochem Soc 147:1322–1331
100. Ferg E, Gummow RJ, Dekock A, Thackeray MM (1994) Spinel anodes for lithium-ion batteries. J Electrochem Soc 141:L147–L150

101. Peramunage D, Abraham KM (1998) Preparation of micron-sized $Li_4Ti_5O_{12}$ and its electrochemistry in polyacrylonitrile electrolyte-based lithium cells. J Electrochem Soc 145:2609–2615
102. Jansen AN, Kahaian AJ, Kepler KD, Nelson PA, Amine K, Dees DW, Vissers DR, Thackeray MM (1999) Development of a high-power lithium-ion battery. J Power Sourc 81:902–905
103. Ohzuku T, Yamato R, Kawai T, Ariyoshi K (2008) Steady-state polarization measurements of lithium insertion electrodes for high-power lithium-ion batteries. J Solid State Electrochem 128:979–985
104. Ariyoshi K, Ohzuku T (2007) Conceptual design for 12 V "lead-free" accumulators for automobile and stationary applications. J Power Sourc 174:1258–1262
105. Lu W, Belharouak I, Liu J, Amine K (2007) Thermal properties of $Li_{4/3}Ti_{5/3}O_4/LiMn_2O_4$ cell. J Power Sourc 174:673–677
106. Belharouak I, Sun YK, Lu W, Amine K (2007) On the safety of the $Li_4Ti_5O_{12}$ /$LiMn_2O_4$ lithium-ion battery system batteries and energy storage. J Electrochem Soc 154:A1083–A1087
107. Du Pasquier A, Huang CC, Spitler T (2009) Nano $Li_4Ti_5O_{12}$-$LiMn_2O_4$ batteries with high power capability and improved cycle-life. J Power Sourc 186:508–514
108. Amine K, Belharouak I, Chen ZH, Tran T, Yumoto H, Ota N, Myung ST, Sun YK (2010) Nanostructured anode material for high-power battery system in electric vehicles. Adv Mater 22:3052–3057
109. Reale P, Panero S, Scrosati B, Garche J, Wohlfahrt-Mehrens M, Wachtler M (2004) A safe, low-cost, and sustainable lithium-ion polymer battery. J Electrochem Soc 151:A2138–A2142
110. Reale P, Fernicola A, Scrosati B (2009) Compatibility of the Py_{24}TFSI-LiTFSI ionic liquid solution with $Li_4Ti_5O_{12}$ and $LiFePO_4$ lithium ion battery electrodes. J Power Sourc 194:182–189
111. Sun LQ, Cui RH, Jalbout AF, Li MJ, Pan XM, Wang RS, Xie HM (2009) $LiFePO_4$ as an optimum power cell material. J Power Sourc 189:522–526
112. Jaiswal A, Horne CR, Chang O, Zhang W, Kong W, Wang E, Chern T, Doeff MM (2009) Nanoscale $LiFePO_4$ and $Li_4Ti_5O_{12}$ for high rate Li-ion batteries and energy storage. J Electrochem Soc 156:A1041–A1046
113. Zaghib K, Dontigny M, Guerfi A, Trottier J, Hamel-Paquet J, Gariepy V, Galoutov K, Hovington P, Mauger A, Julien CM (2012) An improved high-power battery with increased thermal operating range: C-$LiFePO_4$//C-$Li_4Ti_5O_{12}$. J Power Sourc 216:192–200
114. Ohzuku T, Ariyoshi K, Yamamoto S, Makimura Y (2001) A 3-volt lithium-ion cell with Li$[Ni_{1/2}Mn_{3/2}]O_4$ and Li$[Li_{1/3}Ti_{5/3}]O_4$: a method to prepare stable positive-electrode material of highly crystallized Li$[Ni_{1/2}Mn_{3/2}]O_4$. Chem Lett 1270–1271
115. Ariyoshi K, Yamamoto S, Ohzuku T (2003) Three-volt lithium-ion battery with Li$[Ni_{1/2}Mn_{3/2}]O_4$ and the zero-strain insertion material of Li$[Li_{1/3}Ti_{5/3}]O_4$. J Power Sourc 119:959–963
116. Wu HM, Belharouak I, Deng H, Abouimrane A, Sun YK, Amine K (2009) Development of $LiNi_{0.5}Mn_{1.5}O_4/Li_4Ti_5O_{12}$ system with long cycle life batteries and energy storage. J Electrochem Soc 156:A1047–A1050
117. Jung HG, Jang MW, Hassoun J, Sun YK, Scrosati B (2011) A high-rate long-life $Li_4Ti_5O_{12}$/Li$[Ni_{0.45}Co_{0.1}Mn_{1.45}]O_4$ lithium-ion battery. Nat Commun 2:516
118. Sawai K, Yamato R, Ohzuku T (2006) Impedance measurements on lithium-ion battery consisting of Li$[Li_{1/3}Ti_{5/3}]O_4$ and Li$(Co_{1/2}Ni_{1/2})O_2$. Electrochim Acta 51:1651–1655
119. Lu W, Liu J, Sun YK, Amine K (2007) Electrochemical performance of $Li_{4/3}Ti_{5/3}O_4/Li_{1+x}(Ni_{1/3}Co_{1/3}Mn_{1/3})_{1-x}O_2$ cell for high power applications. J Power Sourc 167:212–216
120. Reddy MV, Suba Rao GV, Chowdari BVR (2013) Metal oxides and oxysalts as anode materials for Li ion batteries. Chem Rev 113:5364–5457
121. Arora P, Zhang Z (2004) Battery separators. Chem Rev 104:4419–4462
122. Daniel C (2008) Materials and processing for lithium-ion batteries. JOM 60:43–48
123. Armand MB (1983) Polymer solid electrolytes – an overview. Solid State Ionics 9–10:745–754

124. Gauthier M, Fauteux D, Vassort G, Belanger A, Duval M, Ricoux P, Gabano JP, Muller D, Rigaud P, Armand MB, Deroo D (1985) Assessment of polymer-electrolyte batteries for EV and ambient temperature applications. J Electrochem Soc 132:1333–1340
125. Armand M (1985) Ionically conductive polymers. In: Sequeira CAC, Hooper A (eds) Solid state batteries. Marinus Nijhoff, Dordrecht, pp 63–72
126. Zhang SS (2013) Liquid electrolyte lithium/sulfur battery: fundamental chemistry, problems, and solutions. J Power Sourc 231:153–162
127. Jeong SS, Lim Y, Choi YJ, Cho GB, Kim KW, Ahn HJ, Cho KK (2007) Electrochemical properties of lithium sulfur cells using PEO polymer electrolytes prepared under three different mixing conditions. J Power Sourc 174:745–750
128. Song MK, Zhang Y, Cairns EJ (2013) A long-life, high-rate lithium/sulfur cell: a multifaceted approach to enhancing cell performance. Nano Lett 13:5891–5899
129. Manthiram A, Fu Y, Su YS (2013) Challenges and prospects of lithium-sulfur batteries. Acc Chem Res 46:1125–1134
130. Ji X, Lee KT, Nazar LF (2009) A highly ordered nanostructured carbon-sulphur cathode for lithium-sulphur batteries. Nat Mater 8:500–506
131. Zheng G, Yang Y, Cha JJ, Hong SS, Cui Y (2011) Hollow carbon nanofiber-encapsulated sulfur cathodes for high specific capacity rechargeable lithium batteries. Nano Lett 11:4462–4467
132. Choi YJ, Ahn JH, Ahn HJ (2008) Effects of carbon coating on the electrochemical properties of sulfur cathode for lithium/sulfur cell. J Power Sourc 184:548–552
133. Jaffe S, Talon C, Ishimori K, Bigliani R, Tong F, Nicholson R (2001) Business strategy: lithium ion manufacturing global buildout, supply and demand forecasts. http://www.idc.com/getdoc.jsp?containerId=EI232266. Accessed Dec 2011
134. Battery Association of Japan (2014) Total battery production statistics. http://www.baj.or.jp/e/statistics/01.html
135. Chemetall (2009) Lithium applications and availability: Chemetall statement to investors, July 28. http://www.chemetall.com/fileadmin/files_chemetall/Downloads/Chemetall_Li-Supply_2009_July.pdf. Accessed 4 Jan 2009
136. Hsiao E, Richter C (2008) Electric vehicles special report – Lithium Nirvana – Powering the car of tomorrow. In: CLSA Asia-Pacific Markets. http://www.clsa.com/assets/files/reports/CLAS-Jp-ElectricVehicles20080530.pdf. Accessed 2 Dec 2009
137. Jongerden MR, Haverkort BR (2008) Which battery model to use? In: Dingle NJ, Haeder U, Argent-Katwala A (eds) UKPEW 2008. Imperial College, London, pp 76–88, http://doc.utwente.nl/64866/1/battery-model.pdf
138. Jongerden MR, Haverkort BR (2008) Battery modelling. Tech report TR-CIT-08-01. UTwente, Enschede. http://eprints.eemcs.utwente.nl/11645/01/BatteryRep4.pdf. Accessed 29 Jan 2008
139. Hafsaoui J, Scordia J, Sellier F, Aubret P (2012) Development of an electrochemical battery model and its parameters identification tool. Int J Automobile Eng 3:27–33
140. Doyle M, Fuller TF, Newman J (1993) Modeling of galvanostatic charge and discharge of the lithium/polymer/insertion cell. J Electrochem Soc 140:1526–1533
141. Fuller TF, Doyle M, Newman J (1994) Simulation and optimization of the dual lithium ion insertion cell. J Electrochem Soc 141:1–10
142. Fuller TF, Doyle M, Newman J (1994) Relaxation phenomena in lithium-ion-insertion cells. J Electrochem Soc 141:982–990
143. Hageman SC (1993) Simple PSpice models let you simulate common battery types. Electronic Design News 38:117–129
144. Manwell J, McGowan J (1993) Lead acid battery storage model for hybrid energy systems. Sol Energ 50:399–405
145. Chiasserini C, Rao R (2001) Energy efficient battery management. IEEE J Selected Areas Commun 19:1235–1245

146. Rao V, Singhal G, Kumar A, Navet N (2005) Battery model for embedded systems. In; Proceedings of the 18th international conference on VLSI design held jointly with 4th international conference on embedded systems design (VLSID'05) IEEE Computer Society, pp 105–110
147. Tremblay O, Dessaint LA, Dekkiche AI (2007) A generic battery model for the dynamic simulation of hybrid electric vehicles. In: Proceedings of the vehicle power and propulsion conference. Arlington, TX, IEEE, pp 284–289
148. Moore S, Merhdad E (1996) Texas A&M, an empirically based electrosource horizon lead-acid battery model, Strategies in Electric and Hybrid Vehicle Design, SAE J. SP-1156, paper 960448, pp 135–138
149. Unnewehr LE, Nasar SA (1982) Electric vehicle technology. Wiley, New York, pp 81–91
150. Broussely M, Herreyre S, Biensan P, Kasztejna P, Nechev K, Staniewicz RJ (2001) Aging mechanism in Li ion cells and calendar life predictions. J Power Sourc 97–98:13–21

Chapter 3
Principles of Intercalation

3.1 Introduction

In chemistry, the term intercalation refers to the reversible process of introduction-extraction of species (ions or molecules) into a layered host structure, while the word insertion refers the inclusion in tunnel-like frameworks. Insertion compounds have been classified in various ways, like dimensionality according the passageway of the guest into the host (Fig. 3.1). Examples of one-dimensional (1D) structures are $NbSe_3$, $TiSe_3$, $(CH)_x$ and materials crystallizing in the olivine structure. The most extensively investigated compounds are two-dimensional (2D) lattices such as transition-metal chalcogenides and oxides. Three-dimensional (3D) solids are transition-metal oxides MnO_2, spinels, WO_3, V_6O_{13}, etc. In these compounds the guest species occupy preferential sites with minimum energy that allows easy travelling across the lattice. Low-dimensional materials are particularly susceptible to intercalation reactions due to the presence of the weak van der Waals (vdW) forces between either strongly bonded chains or layers, but three dimensional materials can also be host to intercalation provided that interstitial sites exist and that these are accessible to the incoming guest. This usually implies the presence of channels, which favors fast ionic diffusion.

Intercalation compounds of well-defined stoichiometry are formed by reacting a host matrix $\langle H \rangle$ with so-called intercalate atoms or molecules (A). The product of the heterogeneous reaction,

$$\langle H \rangle + xA \leftrightarrows A_x \langle H \rangle, \tag{3.1}$$

is known as an intercalation compound, where x is the concentration of intercalant. For layered compounds, this process involves breaking of the vdW bonds between lamellae in the pristine material so that the interslab distance increases to permit the introduction of a intercalate layer and formation of a new ordered crystalline compound. Figure 3.2 presents the schematic picture of the intercalation process in the

C. Julien et al., *Lithium Batteries*, DOI 10.1007/978-3-319-19108-9_3

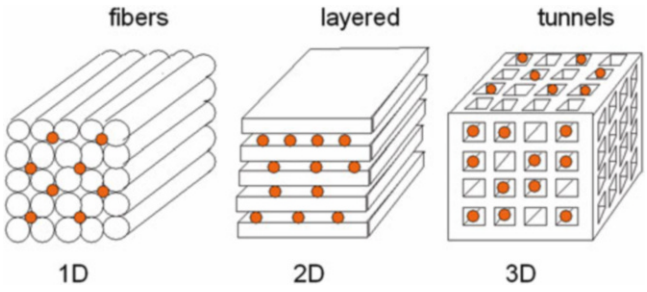

Fig. 3.1 The types of insertion compounds as a function of the dimensionality. *Red circles* are intercalated ions across the host channels

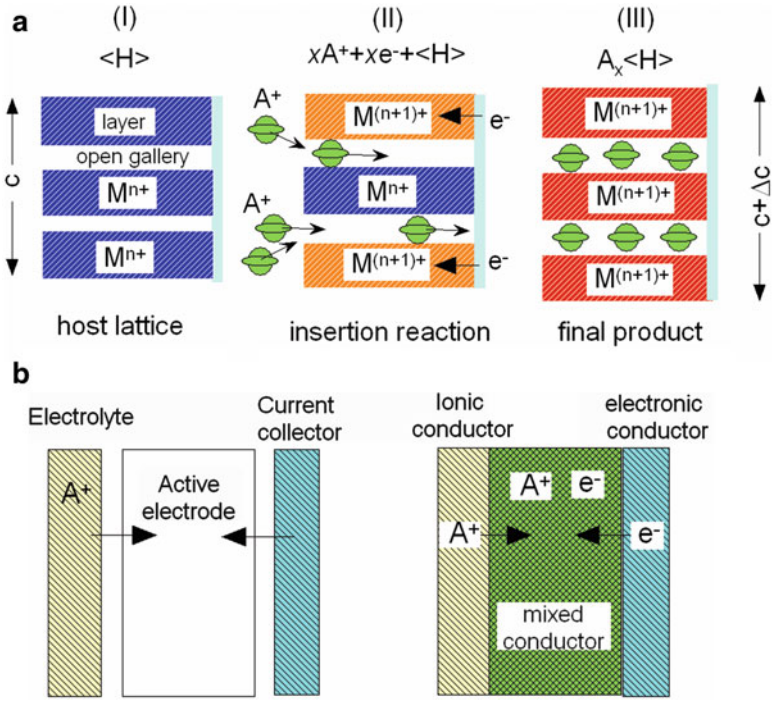

Fig. 3.2 (**a**) Schematic picture of the intercalation process in a host $\langle H \rangle$ with a lamellar structure. Incorporation of A^+ ions implies the opening of the van der Waals gap, modification of the lattice parameters and reduction of the transition-metal *M*. (**b**) The mixed-conductor character of the new product

lamellar matrix $\langle H \rangle$ (a) and the mixed-conductor character of the final product (b). The intercalation process is complicated because the modification of one physical property, i.e., slight change in crystallographic parameters in the intercalate layer inevitably alters other properties. Applications of intercalation materials are multiple: lubricants, batteries [1], catalysts [2], etc.

One of the main limitations in the overall performance of Li-ion batteries depends on the intrinsic performance of the materials working as either positive or negative electrodes. In these materials, the electrochemical reactions occur via a process known as intercalation that can manipulate their properties. One class of electrodes includes the layered compounds considered as prototypes in which Li^+ ions are inserted/extracted into/from the crystal structure. Many reviews have been written concerning this peculiar chemical reaction focusing on the electronic and structural modifications induced by intercalation [3–5]. This phenomenon was early describes in the case of graphite [6], in layered transition-metal dichalcogenides (TMDs) [7–9] and later in layered oxides such as $LiCoO_2$ used in the first commercialized Li-ion batteries [10]. As a result, graphite and transition-metal oxides (TMOs) are the most studied Li insertion hosts because these compounds accept charge transfer, especially transition-metal cations can undergo oxidation or reduction without major changes in their coordination number and then without major changes of the host, which retains basically its integrity in terms of structure and composition [11].

A lamellar compound implies atomic layers in which the atoms are strongly bonded by covalent or ionic forces, while the link between the layers is insured by much weaker forces frequently referred as the vdW interactions [12]. Accordingly, one says intercalation for introduction of ions or molecules into a lamellar compound—the host—while the term insertion is devoted to other frameworks with one-dimensional (1D) and three-dimensional (3D) structure. Two major aspects must be considered for an insertion process taking place (Fig. 3.1):

- A geometric condition that implies an easy access for inserted ions or molecules into the empty sites of the host lattice.
- An energetic condition that requires electronic states for the exchanged electrons.

Consequently, most of the intercalation compounds are mixed-conductors, i.e., electronic and ionic to some extent, in which the charge transfer occurs between the intercalant species and the host structure. The tendency for this charge transfer process is the main driving force for the intercalation reaction and it is one of the basic properties that make the host framework a suitable cathode material. Intercalation is crucial in the working cycle of modern batteries and supercapacitors; it involves complex diffusion processes along and across the layers.

The structural modification with respect to the pristine compound results in changes of the unit cell parameters of the pristine material that are related to the radii of the guest ions, the size of the empty sites of the host lattice and the nature of these sites, i.e., octahedron or tetrahedron. It has been shown that intercalation of alkali ions can induce staging phenomenon due to the minimization of repulsive forces between intercalated cations and a special ordering that results in superstructures [13, 14].

3.2 Intercalation Mechanism

Formally, an electrode is defined as an interface between an ionically conductive electrolyte (A^+ or B^-) and an electronic conductor [15]. At the junction a chemical potential μ_i of the species (A or B) is imposed for the electrochemical reaction):

$$A \leftrightarrows A^+ + e^-, \tag{3.2}$$

$$½B_2 + e \leftrightarrows B^-. \tag{3.3}$$

In this ideal scheme, the electrode is a surface without any capacity. The electrical capacity would be observed only if the surface electrode is expanded in volume, by interposing a material possessing the three properties of the junction: (1) an electronic conductivity (e^-), (2) an ionic conductivity (A^+ or B^-) and (3) a chemical potential (μ_A or μ_{B_2}) imposed. As a consequence, the electrode material must have a host lattice structure, $\langle H \rangle$ and participates to the electrochemical reaction via an intercalation mechanism (Fig. 3.1)

$$xA^+ + xe^- + \square_x\langle H \rangle \leftrightarrows \langle A_xH \rangle, \tag{3.4}$$

$$xB^- + \square_x\langle H \rangle \leftrightarrows \langle B_xH \rangle + xe^-. \tag{3.5}$$

where $\square_x$ designs an empty lattice site. The electrolyte and the current lead have in this case the sole function to carrying charged species, and do not enter the electrochemical process by dissolution and transport of neutral reactants. An intercalation electrode can thus operate in totally solid-state system, the rate depending only on the transport properties in the bulk of the host lattice. From the historical view point, two steps should be evoked: (1) the chemical intercalation in graphite compound recognized by Shaufhautl in 1840 [16] and (2) the concept of electrochemical intercalation and its potential use in compounds for battery electrodes has been clearly defined in 1972 by Steele [17] and Armand [18].

The intercalate acts as a source and a sink of either A or B. In practice, there are very few examples of an anionic intercalation mechanism (graphite salts B_xC), and we mainly restrict ourselves to the intercalation of monopositive species. Among them, Li plays a dominant role, as a large majority of studies deal with compounds of this light element. Synchronous or consecutive intercalation of different guest species may basically occur by the exchange reactions:

$$xA + yB + \square_x\langle H \rangle \rightarrow \langle A_xB_yH \rangle, \tag{3.6}$$

$$xA + \square_xB_y\langle H \rangle \rightarrow \langle A_xB_yH \rangle, \tag{3.7}$$

$$xA + B_x\langle H \rangle \rightarrow xB + \langle A_xH \rangle, \tag{3.8}$$

3.3 The Gibbs' Phase Rule

For a given redox couple, the potential of an intercalation electrode considered as solution of guest A in the host lattice $\langle H \rangle$ is provided by the classical thermodynamic law:

$$V(x) = -\frac{1}{zF}\frac{\partial(\Delta G)}{\partial x} + \text{constant}, \tag{3.9}$$

where ΔG denotes the variation in the Gibbs energy of the system, x is the composition, z the number of electrons involved and F the Faraday's constant. $V(x)$ is thus the electrode potential as a function of the composition x in $\langle A_x H \rangle$.

In a closed system at equilibrium, the Gibbs' phase rule states that the relation between the number of degrees of freedom, f, and the number of independent components, c, is given by:

$$f = c - p + n, \tag{3.10}$$

where p is the number of phases and n is the number of the intensive variables necessary to describe the system, except for the mole fractions of the components in each phase. The number of thermodynamic parameters must be specified in order to determine all of the associated properties. In electrochemical studies, the intensive variables are only temperature and pressure. Hence, Gibbs' phase rule has the simplified form:

$$f = c - p + 2. \tag{3.11}$$

The cathode can be treated as a binary system ($c = 2$) consisting of Li and the host. Since the temperature and the pressure are kept constant in the experiments, the degrees of freedom reduce to:

$$f = (2 - p + 2) - 2 = 2 - p. \tag{3.12}$$

If only one phase exists in a particle, $p = 1$ and $f = 1$; therefore, the potential has a degree of freedom and varies with the lithium concentration. On the other hand, if the particles contain two phases (Fig. 3.3a), $p = 2$ so that $f = 0$, in which case no intensive variable has a degree of freedom, meaning the cell potential cannot change; it is a constant, C^{onst}. A wide voltage plateau is observed in the composition range $\alpha_1 \leq x \leq \beta_1$ as shown in Fig. 3.3b:

$$\frac{\partial(\Delta G)}{\partial x} = C^{\text{onst}} \rightarrow V(x) = C^{\text{onst}}. \tag{3.13}$$

A general feature is the fact that the insertion or deinsertion process for the Li_xMPO_4 (M = Fe, Co, Ni) olivine materials is a two-phase process at temperature

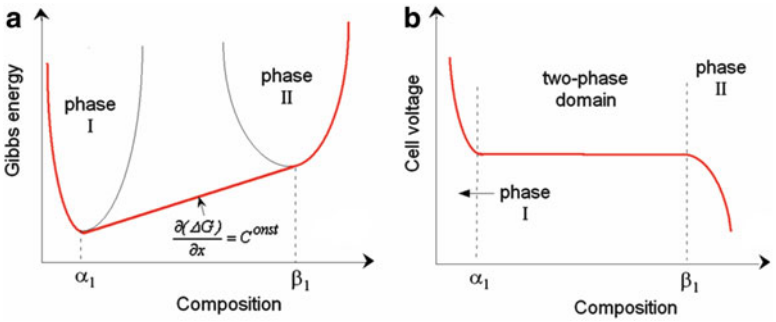

Fig. 3.3 (**a**) Schematic representation of the Gibbs rule for a two-phase system, (**b**) the cell voltage profile shows a plateau in the composition range $\alpha_1 \leq x \leq \beta_1$ for the bulk material

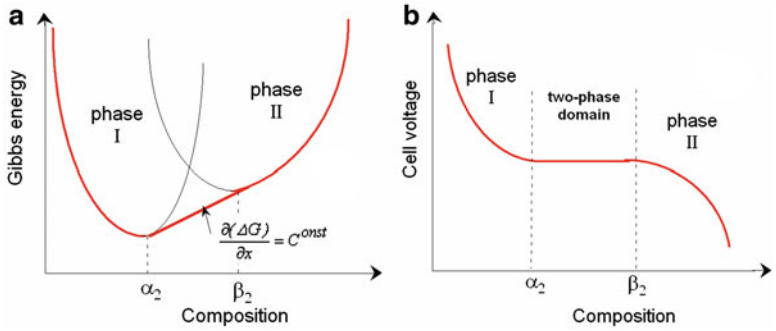

Fig. 3.4 (**a**) Schematic representation of the Gibbs rule for a two-phase system, (**b**) cell voltage vs. composition for nano-sized material

of interest. It means that, for instance, the Li_xFePO_4 solid solution does not exist unless x is close to zero or close to 1. As a consequence, a rapid demixing occurs, and we are left with a two-phase system, namely $Li_{1-\alpha}FePO_4$ (Li-rich) and $Li_\beta FePO_4$ (Li-poor), where α and β denote the width of the single-phase region in Fig. 3.3.

For big (micrometer size) particles, $\alpha \approx \beta \approx 0$, and we can simply write the bulk material at intermediate concentrations under the form $x\text{LiFePO}_4 + (1-x)\text{FePO}_4$. For nanoparticles, the two-phase domain is reported to shrink, so that the Gibbs energy varies according to the scheme represented in Fig. 3.4a. Accordingly, the voltage plateau is shorter (Fig. 3.4b) due to the wider α and β single-phase regions. The corresponding voltage profile for the Li//$LiFePO_4$ half-cell with nanosized cathode particles shown in Fig. 3.4b displays a reduced voltage plateau over the concentration range $\alpha_2 \leq x \leq \beta_2$ with $\alpha_2 > \alpha_1$ and $\beta_2 > \beta_1$.

Figure 3.5a displays a multiphase system with three phases noted I, II, III. The intermediate–single phase emerges at stoichiometric compositions β–γ. Consequently, an energetically favorable interstitial site becomes fully occupied. For

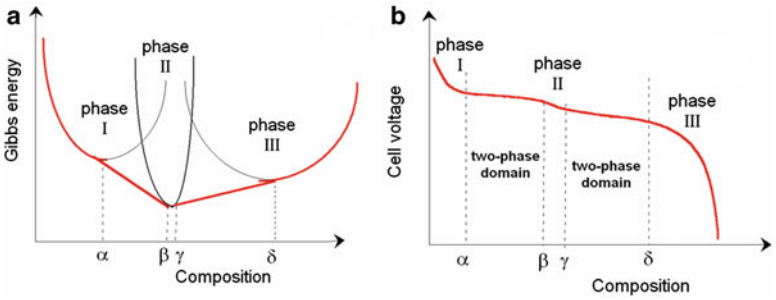

Fig. 3.5 (**a**) Schematic representation of the Gibbs rule for a multiphase system, (**b**) voltage plateaus appear between the phase instabilities

example, this case is met in the $LiNi_{0.5}Mn_{1.5}O_4$ spinel, a high-voltage cathode material for which the potential curve exhibits two plateaus (Fig. 3.5) in the range α–β and γ–δ.

3.4 Classification of Intercalation Reactions

The intercalation process is a dissolution of A (as $A^+ + e^-$) in the solvent $\langle H \rangle$. As discussed by Armand, the properties of the solute $\langle A_x H \rangle$ depend on the host-guest interactions [15]. The different cases are discussed in this section.

3.4.1 The Perfectly Nonstoichiometric Compounds: Type-I Electrode

These compounds are defined by the intercalation reaction, Eq. (3.3) for which the x quantity can vary continuously from zero to a maximum value x_{max} as $0 < x < x_{max}$. We define:

$$y = \frac{x}{x_{max}}, \tag{3.14}$$

as the degree of occupancy. These materials constitute solid-solutions prepared by electrochemical injection of ions into non stoichiometric electrodes as defined by Steele [19]. Selected materials can function as a host lattice for the incorporation of elements such as hydrogen, lithium, sodium which may be employed as the electroactive species in a variety of electrochemical devices. Then these materials can be used as solid solution electrodes (SSEs).

The type I electrode is an ideal case for the reversible electrochemical reaction where the transport of matter occurs through a double flux of charged species

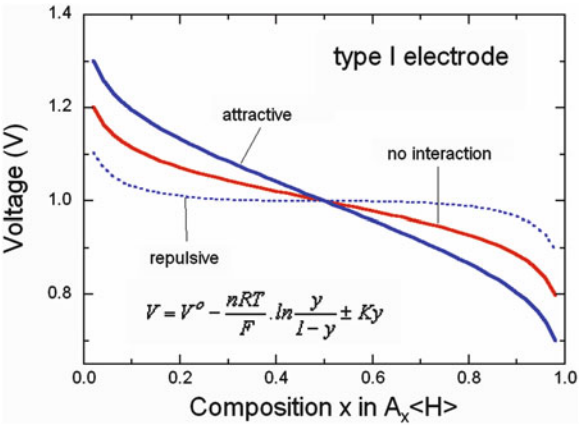

Fig. 3.6 Shape of the potential-composition curve for type-I electrode

(A^++e$^-$) in the bulk of the material whatever the concentration. This case is illustrated in Fig. 3.6. Examples are H_xMnO_2, Li_xTiS_2 and Li_xNbSe_2 ($0 < x < 1$) electrodes. According to Eq. (3.9), the intercalation electrode, considered as solution of A in the host lattice $\langle H \rangle$ has thus a potential written as:

$$V = -\frac{1}{F}\mu(A)_{\langle H \rangle} + C_o, \tag{3.15}$$

where $\mu(A)_{\langle H \rangle}$ denotes the chemical potential of A in the $\langle H \rangle$ phase and C_o is a constant. The electrode potential is a function of the composition x in $\langle A_xH \rangle$. In the simplest ideal case, the potential of A is sum of the chemical potential contribution from the ions and the electrons:

$$\mu(A) = \mu(A^+) + \mu(e^-). \tag{3.16}$$

The host lattice $\langle H \rangle$ keeps this integrity through the intercalation reaction, fixing the concentration of sites available for A^+ ions. The chemical potential of the ionic contribution is:

$$\mu(A^+) = \mu_i^o + \mathrm{RTln}\,\frac{\xi_{os}}{\xi_{es}} = \mu_i^o + \mathrm{RTln}\,\frac{y_i}{1-y_i}. \tag{3.17}$$

where ξ_{os} and ξ_{es} are the number of occupied and empty sites, respectively. The valence electrons are fermions, and are distributed in the lattice in a band of energy width L. Fermi–Dirac statistics have then to be used to determine the total band occupancy y_e:

$$y_e = \frac{\int_{\mu_e^o}^{y_e^o+L} D(E)\cdot f(E)\mathrm{d}E}{\int_{\mu_e^o}^{y_e^o+L} D(E)\mathrm{d}E}, \tag{3.18}$$

where $f(E)$ is the Fermi function and $D(E)$ the density of state. Eq. (3.18) can be simplified with the hypothesis that the electron band is narrow ($L = 0$ for a Dirac function), a logical assumption in the case of ionic crystals:

$$\exp\left[\frac{\mu_e - \mu_e^o}{RT}\right] = \frac{y_e}{1 - y_e}, \tag{3.19}$$

Equation (3.17) thus becomes:

$$\mu_e = \mu_e^o + RT \cdot \ln \frac{y_e}{1 - y_e}. \tag{3.20}$$

Then the electrode potential E is compiled from Eqs. (3.15), (3.16), and (3.20):

$$V = V^o - \frac{RT}{F} \cdot \ln \frac{y_i}{1 - y_i}. \tag{3.21}$$

Equation (3.19) implies two possibilities: one type of site is limiting:

$$y_i = y = \frac{x}{x_{max}}; \text{when } \; y_e \ll y_{i,} \tag{3.22a}$$

and

$$y_e = y = \frac{x}{x_{max}}, \text{when } \; y_i \ll y_e. \tag{3.22b}$$

Or both types of sites are simultaneously limiting $y_i = y_e = y = \frac{x}{x_{max}}$ and finally the potential for the type I electrode is given by:

$$V = V^o - \frac{nRT}{F} \cdot \ln \frac{y}{1 - y}, \tag{3.23}$$

with $n = 1$ or 2.

This basic model takes only into account the entropy term, the enthalpy being supposed constant. Interactions between guest species contribute to a new energy term proportional to the site occupancy, leading to:

$$V = V^o - \frac{nRT}{F} \cdot \ln \frac{y}{1 - y} \pm Ky. \tag{3.24}$$

This is the master equation for which the potential is a smooth decreasing function of the degree of occupancy $\partial E/\partial y < 0$ imposing:

$$K < \frac{4n\mathrm{RT}}{F}. \tag{3.25}$$

Thus, attractive interactions are for positive values of K and repulsive interactions occurs for $K < 0$. Figure 3.6 shows the potential-composition curve for the type-I electrode with no interaction and repulsive-attractive interactions. With $n = 1$, $K = 0$, this corresponds to the experimental determination of the H_xMnO_2 electrode in Leclanché cells [20]. Considering the experimental data in Li_xTiS_2, good agreement is obtained with $n = 2$ and $K = 0.22$ eV [21]. Steele [19] has established the criteria for a nonstoichiometric SSE, A_xMX_y incorporating electroactive species A.

3.4.2 The Pseudo Two-Phase System: Type-II Electrode

The condition expressed by Eq. (3.19) is no longer valid as type II electrode materials have narrow nonstoichiometric domains (Fig. 3.7). When the host lattice contains a transition-metal element M, the electrons injected in the insertion process are distributed in the empty d orbitals. The decrease in the formal oxidation state $M^{n+} \rightarrow M^{(n-1)+}$ results in a change of either the ionic radius of the coordination shell symmetry (Jahn-Teller effect), inducing strains on the $\langle H \rangle$ framework. This situation is expressed as a strong positive interaction term proportional to the number of intercalated species (Eq. 3.19). It appears that the existence of a maximum of potential $V(x)$ implies some instability in the $[\varepsilon–\lambda]$ domain. As a consequence, the voltage composition curve shows a plateau in the "forbidden composition range" due to the equilibrium of the two pseudo-phases.

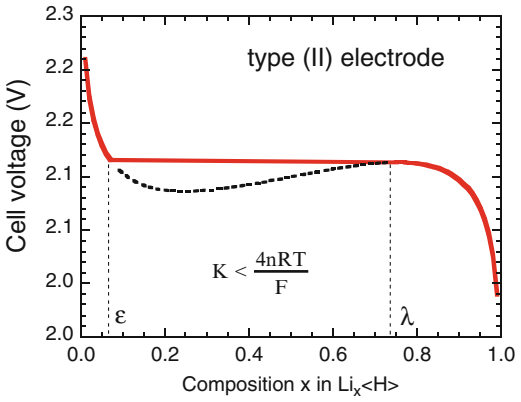

Fig. 3.7 Shape of the potential-composition curve for type-II electrode

3.4.3 The Two-Phase System: Type-III Electrode

Figure 3.8 shows the voltage-composition profile for an electrode in which two-phases A_zBX and BX coexist. This system obeys to the Gibbs phase rule, for which the existence of the forbidden composition-range implies instabilities in the ε–λ domain due to some relaxation of the lattice [22]. As a consequence, the voltage composition curve shows a plateau in the "forbidden composition range" due to the equilibrium of the two pseudo-phases. As the voltage is the derivative of the change in Gibbs energy:

$$V(x) = -\frac{1}{zF}\frac{\partial(\Delta G)}{\partial x}, \tag{3.26}$$

it implies constant value for type-III electrode:

$$\frac{\partial(\Delta G)}{\partial x} = C^{\text{onst}} \rightarrow V(x) = C^{\text{onst}}. \tag{3.27}$$

This is the case of the popular phospho-olivine compound $LiFePO_4$ for with the insertion reaction can be represented by:

$$\begin{aligned} &FePO_4 + x\text{Li}^+ + \text{e}^- \rightarrow \text{Li}_x FePO_4, \quad \text{for } 0 \le x \le \varepsilon, \\ &\text{Li}_\varepsilon FePO_4 + x\text{Li}^+ + \text{e}^- \rightarrow \text{Li}_{\varepsilon+x} FePO_4, \quad \text{for } \varepsilon \le x \le \lambda, \\ &\text{Li}_\lambda FePO_4 + x\text{Li}^+ + \text{e}^- \rightarrow \text{Li}_{\lambda+x} FePO_4, \quad \text{for } \lambda \le x \le 1, \end{aligned} \tag{3.28}$$

for which the eligible parameter that obey the Gibbs rule is $p = 2$, so that $f = 0$, giving no intensive variable in the $\varepsilon \le x \le \lambda$ composition region.

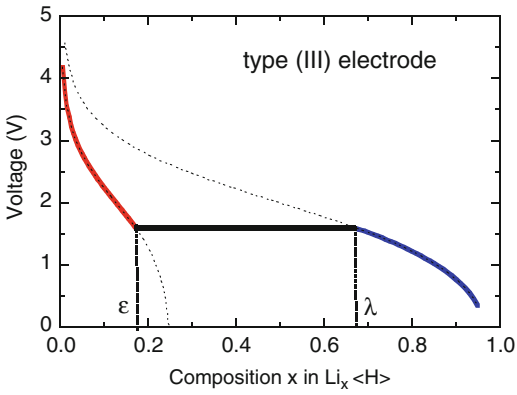

Fig. 3.8 Shape of the potential-composition curve for type-III electrode

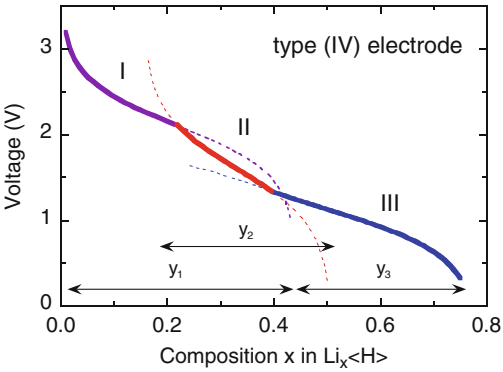

Fig. 3.9 Shape of the potential-composition curve for type-IV electrode

3.4.4 The Adjacent Domain: Type-IV Electrode

Ordered sublattice can appear as the A concentration increases in the host structure, in the range $0 < x < x_1$, for phase 1 and $x_k < x < x_j$ for phase j, with $x_k < x_1$ defining a coexistence domain $[x_k, x_1]$. Each pseudo phase corresponds to a different host-guest interaction. The expression of the potential-composition profile becomes:

$$V_{l,j} = V^{o}_{l,j} - \frac{n\mathrm{RT}}{F} \cdot \ln \frac{y_{l,j}}{1 - y_{l,j}}, \tag{3.29}$$

where $y_{l,j}$ represents the degree of occupancy of the l, j phase sites, respectively. The pseudo-phases are in equilibrium for $V_j = V_l$, thus, we have implicitly access to the chemical potential as a function of the global occupancy y. The corresponding curve is presented in Fig. 3.9. Such profile has been evidenced for Na_xTiS_2 [23].

3.5 Intercalation in Layered Compounds

In this section we limit our discussion to a general presentation of the alkali-metal intercalation compounds; the synthesis of ICs and the geometrical factors affecting the intercalation in lamellar compounds, i.e., transition-metal dichalcogenides and transition-metal oxides are discussed. The electronic side is described in the following Chapter.

3.5.1 Synthesis of ICs

Ternary compounds A_xMX_2 (A = alkali metal; M = transition metal; X = S, Se; $0 < x \leq 1$) were first described by Rüdorff [24] and Omloo and Jellinek [25]. Layered MX_2 compounds probably represent on of the best host structure examples capable

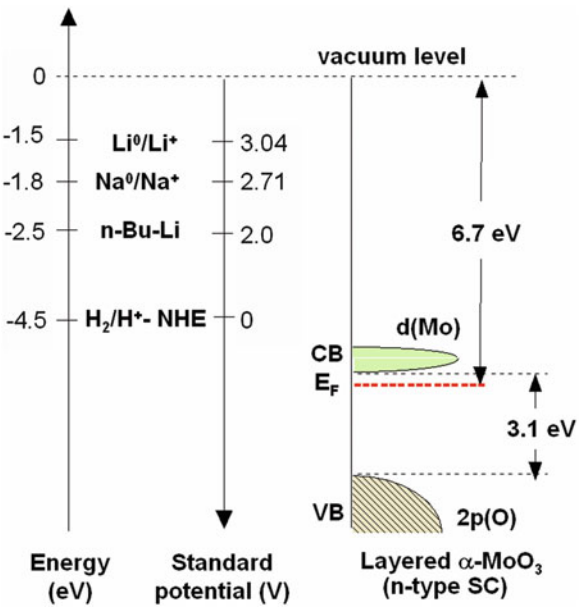

Fig. 3.10 Intercalation of Li^+ ions into MoO_3 using the n-butyllithium technique is very easy as the Fermi level is pinned against the conduction band minimum, indicating a strongly n-type material with $E_i \approx 6.7$ eV and $E_g = 3.1$ eV

of providing intercalation compounds. Several methods were used to prepare alkali intercalation compounds as follows.

- Use of alkali metal solutions in liquid ammonia that leads to fast reactions. A good procedure consists of using thick-walled sealed Pyrex tubes through chosen temperature gradients to separate ammonia from IC product [26].
- Solution of butyllithium (C_4H_9Li) in hexane (0.4 M or less) serves as a good reagent to perform the intercalation [18, 27]. Intercalation starts from the edges of the sample exposed to the solution, and further proceeds to the core. As shown in Fig. 3.10, the relative energetic levels of the n-type semiconductor MoO_3, with bandgap E_g and ionization energy E_i are compared to the decomposition potential of n-butyllithium [28].
- Solid state reactions [29].
- Electrochemical insertion in which the host is employed as cathode. This method has been intensively used to prepared alkali metal bronzes [23].
- Redox reactions in alkali halide melts [30].
- Growth of single crystal via solutions in liquid ammonia [30].
- In situ decomposition of alkali metal derivatives using lithium hydride heated at 900 °C.

3.5.2 Alkali Intercalation into Layered Compounds

In a battery operation there will be repeated charging and discharging. The alkali ion insertion/extraction process of a solid-state host matrix undergoes reduction–

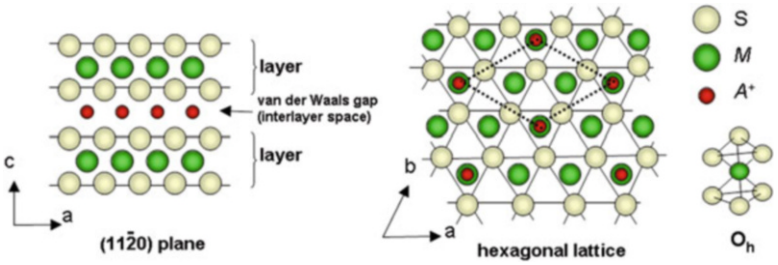

Fig. 3.11 The lithium ions intercalation into the van der Waals gap between the slabs of a layered compound

oxidation (redox) reactions. This concept was first illustrated with compounds that have a layer structure [4]. Figure 3.11 shows the scheme of the reversible lithium ions intercalation into the vdW gap or interlayer space between the sulfide layers in host matrix MS_2. The structure of a transition-metal disulfide MS_2 can be easily visualized by removing alternative metal (M) layers from otherwise regular stacks of 2D close-packed structure …S-M-S-(M)-S-M-S… The void thus created becomes the vdW gap, naturally separating the S-M-S sandwiches. Intercalation results in the occupation of the voids by foreign species (ions or molecules). For mechanical rigidity it is important to ensure a minimum perturbation to the structure of the electrode material in such processes. Two structural modifications generally occur when a layered framework is intercalated. One is the increase in the vdW gap due to extra space needed to accommodate the intercalant Li^+ ions, and this can be minimized by choosing small ions such as lithium. The second is a more subtle change taking place in the internal structure of the sandwich layer as the total number of valence electrons in the host layer is altered [12]. This change of valence electrons is, of course, a direct consequence of the charge transfer from the intercalant ions, and the additional electron will have to be accommodated within the host's electronic configuration. Let consider the case of TiS_2. During the discharge process of the Li//TiS_2 battery, the charge balance is maintained by a reduction of the Ti^{4+} ions to Ti^{3+} according the reaction:

$$x\mathrm{Li}^+ + x\mathrm{e}^- + \square_x \mathrm{Ti}^{\mathrm{IV}}\mathrm{S}_2 \leftrightarrows \mathrm{Li}_x\left[\mathrm{Ti}^{\mathrm{III}}{}_x\mathrm{Ti}^{\mathrm{IV}}{}_{1-x}\right]\mathrm{S}_2. \tag{3.30}$$

This reaction is energetically favored, giving an open-circuit voltage which varies between 2.4 V ($x = 0$) and 1.8 V ($x = 1$). The decrease of V_{oc} is in part due to the increase in the Fermi energy in the titanium d band, but it is limited to only 0.6 V as a consequence of the high value of the density of states in this d band. As the electrons flow to the cathode the latter acquires a negative electric potential, which in turn provides an electric field within the electrochemical cell, driving the positive ions to the cathode. Then, the transition-metal cation is reduced from M^{IV} to M^{III} (Eq. 3.29), which modifies the atomic distances in the S-M-S slab with the change of the ionic radii of M. As a general rule, the voltage-composition profile of the electrochemical process is governed by several factors: the nature and the energy of

the site occupied by the foreign species, the size of the intercalants, the amount of intercalation, the ionicity of the bonds, and the ability of the host to accommodate the electronic exchange [26]. Note that intercalation of very electro-positive elements such as alkali metals determine the ionization the MX_n host as $A^+[MX_n]^-$.

The filling of empty sites in the host introduces geometrical aspects regarding local structural effects such as (1) symmetry of the occupied site, (2) ordering in the van der Waals gap and (3) a global change in the structure with the c-axis expansion in the direction perpendicular to the basal plane of slabs. From the structural view point, the intercalated species can occupy either octahedral or trigonal prismatic sites between slabs of a layered compound.

The intercalation of A^+ ion into the MX_2 matrix implies a delocalization of the electrons, which leads to the ionization following the scheme $A_x^+(MX_2)^-$. Under these conditions, the parameter variations can result from the action of two conflicting factors: a geometric space factor related to the size of the inserted ion, which tends to cause the exaltation Δc parallel to the c-axis, but also an electric attraction between ionized sheets $(MX_2)^-$ and A^+ layers, which tends to counteract the previous effect. A trigonal-prismatic phase corresponds to a weak bonding of A. The effect due to the electric increases with the amount of alkali inserted and reflects the apparently abnormal contraction of c as x increases. Octahedral phase represents instead a compact structure: an increase in the alkali content can cause contraction due to more stringent geometric requirements, the parameter c increases slightly with x.

3.6 Electronic Energy in ICs

The operating potential of a cell is limited by the open-circuit voltage V_{oc}. The potential difference across terminals of the battery when no current is being drawn (Eq. 1.6), is the difference in the electrochemical potential of the anode μ_A and the cathode μ_C. For a high-voltage cathode that is a semiconductor in nature, μ_C is the Fermi level [31]. Let consider the case of the 4.7-V $LiNi_{1/2}Mn_{3/2}O_2$ (LNM). If the active transition-metal cation contains a localized d-electron manifold, the manifold acts as a redox couple, e.g., $Ni^{2+/4+}$ in LNM. Successive redox couples are separated by an on-site effective Coulomb correlation energy U (Hubbard potential) that can be large when augmented by either a crystal-field splitting or an intra-atomic exchange splitting [32]. However, when the Fermi energy E_{FC} of the cathode material approaches the top of the anion p bands of the host, the p-d covalent mixing may transform the correlated d electrons at E_{FC} into band electrons occupying one-electron states. In the absence of a crystal-field splitting of the d orbitals at E_{FC}, which is the case for Ni(IV) to Ni(II), the one-electron states are not separated by any on-site energy U and there is no step in the voltage of the battery. E_{FC} is moved from one formal valence state to another upon the reduction or oxidation of the host.

Figure 3.12 shows a comparison of the schematic density of states and Fermi energies for (a) $Li_xNi_{0.5}Mn_{1.5}O_4$ spinel and (b) Li_xNiPO_4 olivine cathodes. Access to Ni(III) and (Ni(IV) valence states is possible in the spinel case, while the

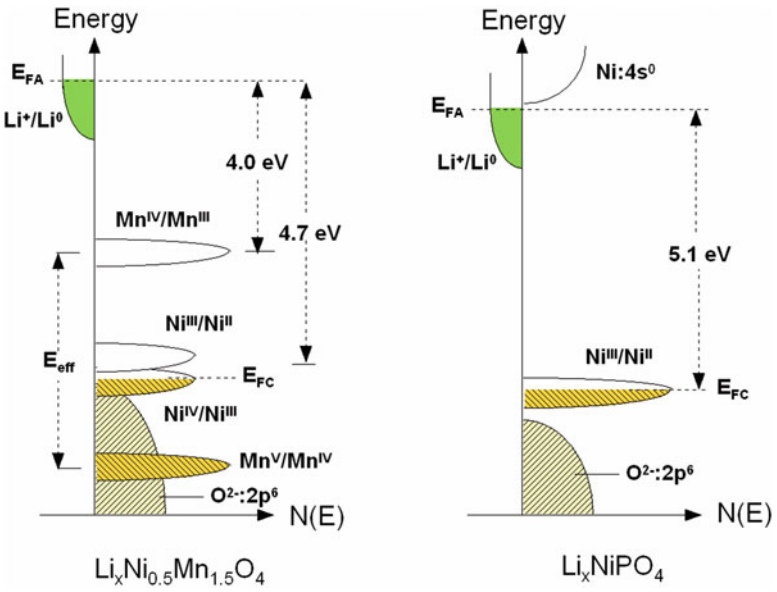

Fig. 3.12 Schematic density of states and Fermi energies for (**a**) $Li_xNi_{0.5}Mn_{1.5}O_4$ spinel and (**b**) Li_xNiPO_4 olivine cathodes. The origin of energies is chosen at the Fermi energy of lithium metal

Mn^{5+}/Mn^{4+} couple lies well-below the top of the O 2*p* bands; the solid electrolyte interphase (SEI) layer formed at voltage $V > 4.3$ V is self-limiting and Li-permeable. On the other hand, the properties of Li_xNiPO_4 (LNP) are greatly influenced by the counteraction of the $(PO_4)^{3-}$ polyanion on the Ni^{2+}/Ni^{3+} couple that is pinned at the top of the O 2*p* bands, which provides an intrinsic voltage limit for this cathode.

3.7 Origin of the High Voltage in ICs

Let consider the electrochemical reaction in the high-voltage cathode $Li_xNi_yMn_{2-y}O_4$ [31–35]. Using ultraviolet photoelectron spectroscopy, Gao et al. [34] studied the top of the valence band of $LiNi_yMn_{2-y}O_4$ spinel structure for a series of samples with $0.0 < y < 0.5$. A partial density of states attributed to Ni 3*d* electrons is located about 0.5-eV above that of the Mn 3*d* e_g electrons. When $y = 0$, the voltage plateau of Li//$LiMn_2O_4$ is located at 4.1 V. As *y* increases, the capacity associated to the 4.1 V plateau decreases as 1–2*y* Li per formula unit and a new plateau at 4.7 V appears. The capacity associated to the 4.7 V plateau increases as 2*y* Li per formula unit, so that the total capacity of the samples (the sum of the contributions from the 4.1 and 4.7 V plateau) is constant. This is taken as evidence that the oxidation state of Ni in these samples is +2, and therefore they can be written as $Li^+Ni_y^{2+}Mn_{1-2y}^{3+}Mn_{1+y}^{4+}O_4^{2-}$ [36].

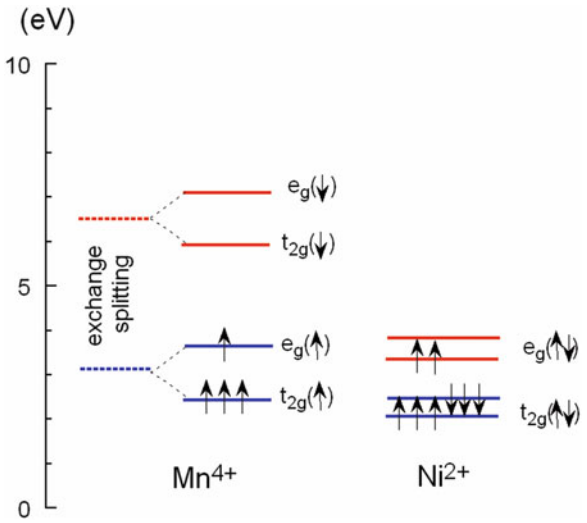

Fig. 3.13 Schematic diagram showing the 3*d* electronic levels of Mn^{3+} and Ni^{2+} in $LiNi_yMn_{2-y}O_4$ spinel. It is noted that Ni^{2+} favors the low-spin configuration in $LiNi_yMn_{2-y}O_4$

The 4.1 V plateau is related to the oxidation of Mn^{3+} to Mn^{4+} and the 4.7 V plateau to the oxidation of Ni^{2+} to Ni^{4+}. The reason for this behavior is shown in Fig. 3.13. The crystal field splits the 3*d* levels of Mn and Ni octahedrally coordinated with oxygen into e_g and t_{2g} levels [36]. For Mn^{3+}, among the four $3d^4$ electrons with majority spin (↑) three electrons are on $t_{2g}(\uparrow)$ and one electron is on $e_g(\uparrow)$. In the low-spin configuration, the $3d^8$ electrons of Ni^{2+} have six electrons on the $t_{2g}(\uparrow\downarrow)$ level and two electrons on the $e_g(\uparrow\downarrow)$ level. As an electron is removed from Mn^{3+}, it is removed from Mn $e_g(\uparrow)$, which has an electron binding energy at around 1.5–1.6 eV, and this is on the 4.1-V plateau. When there are no more electrons left on Mn $e_g(\uparrow)$ (all Mn are oxidized to Mn^{4+}), electrons are removed from Ni $e_g(\uparrow\downarrow)$ which has an electron binding energy of about 2.1 eV, and the voltage plateau moves up to 4.7 V because of the increased energy needed to remove electrons. Table 3.1 lists the electrochemical data of the high-voltage cathode materials.

3.8 Lithium Battery Cathodes

In order for a lithium insertion compound to be a successful cathode in secondary lithium cells, it should have several features:

1. The insertion compound $Li_xM_yX_z$ ($X =$ anion) should have a high lithium chemical potential ($\mu_{Li(c)}$) to maximize the cell voltage. This implies that the transition metal ion M^{n+} in $Li_xM_yX_z$ should have a high oxidation state.
2. The insertion compound $Li_xM_yO_z$ should allow an insertion/extraction of a large amount of lithium x to maximize the cell capacity. This depends on the number

Table 3.1 Electrochemical data for high-voltage cathode materials

Cathode material	High-voltage plateau redox couple	Discharge voltage[a] (V vs. Li^+/Li)	Theoretical capacity (mAh g^{-1})
$LiNi_{0.5}Mn_{1.5}O_4$	$Ni^{2+/4+}$	4.7	147
$LiNi_{0.45}Mn_{1.45}Cr_{0.1}O_4$	$Ni^{2+/4+}/Cr^{3+/4+}$	4.7/4.8	145
$LiCr_{0.5}Mn_{1.5}O_4$	$Cr^{3+/4+}$	4.8	149
$LiCrMnO_4$[b]	$Cr^{3+/4+}$	4.8	151
$LiCu_{0.5}Mn_{1.5}O_4$	$Cu^{2+/3+}$	4.9	147
$LiCoMnO_4$[b]	$Co^{3+/4+}$	5.0	147
$LiFeMnO_4$[b]	$Fe^{3+/4+}$	5.1	148
$LiNiVO_4$	$Ni^{2+/3+}$	4.8	148
$LiNiPO_4$	$Ni^{2+/3+}$	5.1	167
$LiCoPO_4$	$Co^{2+/3+}$	4.8	167
Li_2CoPO_4F	$Co^{2+/4+}$	5.1	115

[a]Voltage of the upper plateau
[b]A partial delithiation occurs at ca. 4 V vs. Li^+/Li due to the $Mn^{3+/4+}$ redox couple

of available lithium sites and the accessibility of multiple valences for M in the insertion host.

3. The lithium insertion/extraction process should be reversible with no or minimal changes in the host structure over the entire range x of lithium insertion/extraction in order to provide good cycle life for the cell.
4. The insertion compound should have good electronic conductivity σ_e and lithium-ion conductivity σ_{Li} to minimize polarization losses during the discharge/charge process and thereby to support a high current density and power density.
5. The insertion compound should be chemically stable without undergoing any reaction with the electrolyte over the entire range x of lithium insertion/extraction.
6. The redox energy of the cathode in the entire range x of lithium insertion/extraction should lie within the band gap of the electrolyte to prevent any unwanted oxidation or reduction of the electrolyte.
7. From a commercial point of view, the insertion compound should be inexpensive, environmentally benign, and lightweight. This implies that the M^{n+} ion should be preferably from the 3*d* transition series.

Figure 3.14 shows the cell voltage vs. capacity for various intercalation compounds used in lithium batteries. In the past few years, Li-ion batteries have been introduced into the consumer market, particularly the cellular phone and camcorder segments. Li-ion batteries excel through their high cell voltage, low weight and volume for given stored energy, favorable power output, and long cycle life. These outstanding features have led to considering Li-ion batteries for EV applications [37].

The energy μ_C or μ_A is given by the Fermi energy of an itinerant electron in a metallic electrode like in carbon, or by the energy of a localized *d*-electron

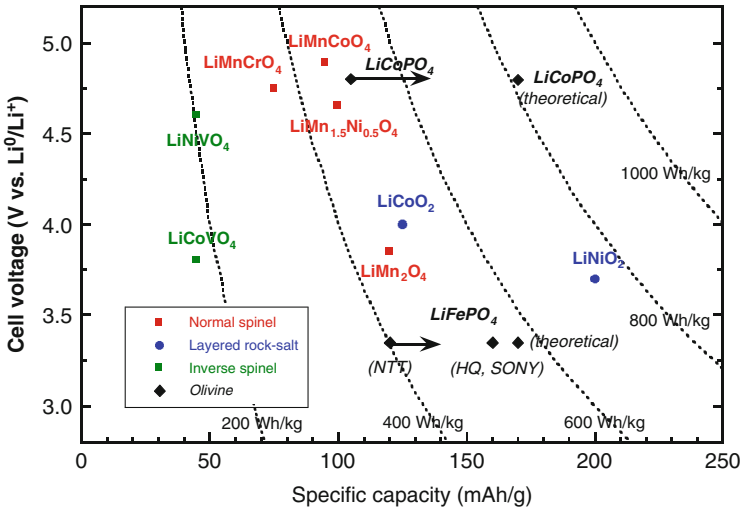

Fig. 3.14 Cell voltage vs. capacity for various intercalation compounds used in lithium batteries

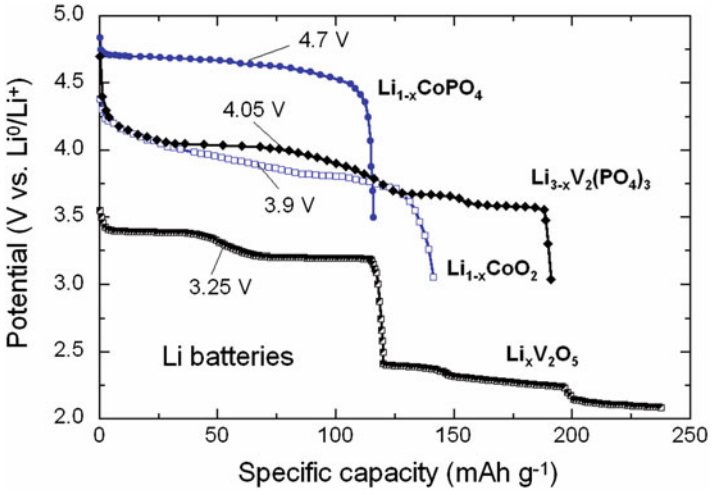

Fig. 3.15 Discharge profiles of lithium cells with cobalt- and vanadium-contained cathodes. The average discharge potential is reported

associated to the redox couple $M^{n+}/M^{(1+n)+}$ of a transition-metal cation. The energy of $M^{n+}/M^{(1+n)+}$ is dependent of two factors: (1) the formal valence state of the cation and (2) the covalent component of its nearest-neighbor bonding. Thus, the structure influences the site and character of the counter-cation and the Madelung energy of the ionic component of the atom bonding. As a consequence, the intrinsic voltage vs. Li^0/Li^+ is determined by the position of the redox couple relative to the top of an anion p band or to the bottom of a conduction band. As an example, Fig. 3.15

illustrates the role of polyanions against a layered framework in cobalt- and vanadium-containing lithium insertion hosts, for which positions of the redox energies relative to the Li^0/Li^+ changes as a function of the iron environment. However, the ranges of cell potentials that are exhibited by host structures into/from which Li^+ ions are reversibly inserted/extracted. $LiCoO_2$ and V_2O_5 are lamellar compounds and the $LiCoPO_4$ olivine and $Li_3V_2(PO_4)_3$ Nasicon-like show the influence of the $(PO_4)^{-3}$ polyanion on the $Co^{3+/2+}$ couple relative to the $Co^{4+/3+}$ couple in the layered structure. The upper voltage of $Li_3V_2(PO_4)_3$ comes from the $V^{4+/3+}$ couple, while $V^{5+/4+}$ for V_2O_5.

3.9 Conversion Reaction

A new reactivity concept has taken the advantage of nanostructured materials in which a change of the reaction pathway is noticed, affording high capacities and good cycling behavior of battery systems. One such reaction pathway is referred to as a "conversion reaction." By using a binary transition-metal M_yX_z compound ($M = $ Fe, Mn, Ni, Co, Cu; $X = $ O, S, P, S), the conversion reaction is expressed as:

$$M_xX_y + yne^- + yn\mathrm{Li}^+ \leftrightarrow xM^0 + y\mathrm{Li}_nX, \tag{3.31}$$

where n is the formal oxidation state of the anion. The conversion mechanism implies 3*d* metal nanoparticles M^0 as final product embedded in a Li_2O matrix. The conversion reaction exhibits two fingerprints: (1) a representative voltage plateau with length typically equivalent to the amount of electrons required to fully reduce the compound and (2) a large voltage difference between charge and discharge that results in poor energy efficiency [38]. Remark that conversion reactions have long been proposed for use in primary battery systems (see Chap. 2) that are still utilized today, for instance, the Li/CuO and Li/CF_x systems [39]. In advanced lithium rechargeable batteries, materials presenting conversion reactions have already been reported such as oxides (e.g., CoO, NiO, Fe_2O_3, MoO_2), sulfides (e.g., CuS, FeS, NI_3S_2), fluorides (e.g., FeF_3, CoF_2, NiF_2), and phosphides (e.g., NiP_3, Cu_3P, FeP_2) with different degrees of reversibility [40]. The key of reversibility of the conversion reaction lied in the morphology of the binary *M*–*X* compounds, the decomposition to nanoparticles (5–12 nm in diameter) upon complete reduction of the metal M^0 (during first discharge) and the formation of the lithium binary Li_nX compound. Generally, the nanometric character of the M^0 particles is maintained after few reduction-oxidation cycles. Materials that undergo a conversion reaction with lithium often accommodate more than one Li atom per transition-metal cation, and are promising candidates for high-capacity electrodes for lithium ion batteries. More complex systems have recently shown new insights into their electrochemical features such as the $Ni_{0.5}TiOPO_4$/C composite battery anode material suggesting a

combination of intercalation and conversion reactions [41]. Finally, notice that a conversion reaction implies an electrochemical process via the formation of a binary lithium-based compound Li_nX such as Li_2O, LiF, or Li_2S. This aspect is widely exposed in Chap. 10 on negative electrode materials.

3.10 Alloying Reaction

For more than three decades, lithium metal alloys Li_xM_y (M = Al, Sb, Si, Sn, etc.) have been extensively studied such as negative electrode materials for Li-ion batteries. They exhibit specific capacities higher than conventional graphite anode, i.e., 372 mAh g^{-1}, for instance $Li_{4.4}Sn$ and $Li_{4.4}Si$ have 993 and 4200 mAh g^{-1}, respectively. Drawback of alloy formation is a large volume expansion–contraction inducing cracks and pulverization that can be reduced replacing bulk material with nanostructured particles. As an example, the alloying process of Li with Sb is expressed by [42, 43]:

$$Sb + 3Li^+ + 3e^- \rightarrow Li_3Sb, \tag{3.32}$$

with a theoretical specific capacity of 660 mAh g^{-1}.

An alternative approach consists in the replacement of the single metal alloy with an intermediate phase $M'M''$ formed by an intermetallic compound for which the electrochemical process includes the displacement of one metal to form the expected alloy Li_xM'', while the other metal, M', which is electrochemically inactive plays the role of matrix to buffer the volume changes during the alloying process. This approach, first suggested by Huggins [44] and Besenhard [45], has been applied to several systems. As an example, let consider the case of the intermetallic compound Ni_3Sn_4 for which the electrochemical process occurs via two steps:

$$Ni_3Sn_4 + 17.6Li^+ + 17.6e^- \rightarrow 4Li_{4.4}Sn + 3Ni, \tag{3.33}$$

$$4Li_{4.4}Sn \rightarrow Sn + 4.4Li^+ + 4.4e^-, \tag{3.34}$$

$$Sn + 4.4Li^+ + 4.4e^- \rightarrow 4Li_{4.4}Sn. \tag{3.35}$$

The initial step, Eq. (3.33), consists of the activation of Li alloy, $Li_{4.4}Sn$, with the formation of a nickel matrix followed by the reversible electrochemical reactions, while Eqs. (3.34) and (3.35) represent the steady-state process with the theoretical specific capacity of 993 mAh g^{-1}. Currently, 50-nm sized Ni_3Sn_4 nanoparticles delivered a practical capacity of ca. 500 mAh g^{-1} after 200 cycles [46].

References

1. Haering R, Stiles JAR (1980) Electrical storage device. US Patent 4,233,377, 11 Nov 1980
2. Meitzner G, Kharas K (2012) Methods for promoting syngas-to-alcohol catalysts. US Patent 8,110,522, 7 Feb 2012
3. Rouxel J (1978) Alkali metal intercalation compounds of transition metal chalcogenides: TX_2, TX_3 and TX_4 chacogenides. In: Levy F (ed) Intercalated layer materials. Reidel, Dordrecht, pp 201–250
4. Whittingham MS (1978) Chemistry of intercalation compounds: metal guests in chalcogenide hosts. Prog Solid State Chem 12:41–99
5. Friend RH, Yoffe AD (1987) Electronic properties of intercalation complexes of the transition metal dichalcogenides. Adv Phys 36:1–94
6. Dresselhaus MS, Dresselhaus G (1981) Intercalation compounds of graphite. Adv Phys 30:139–326
7. Whittingham MS (1982) Intercalation chemistry: an introduction. In: Whittingham MS, Jacobson AJ (eds) Intercalation chemistry. Academic, New York, NY, pp 1–18
8. Julien C, Nazri GA (2001) Intercalation compounds for advanced lithium batteries. In: Nalwa HS (ed) Handbook of advanced electronic and photonic materials, vol 10. Academic, San Diego, CA, pp 99–184
9. Julien CM (2003) Lithium intercalated compounds charge transfer and related properties. Mater Sci Eng R 40:47–102
10. Mizushima K, Jones PC, Wiseman PJ, Goodenough JB (1980) Li_xCoO_2 $(0 < x < 1)$: a new cathode material for batteries of high energy density. Mater Res Bull 15:783–789
11. Schöllhorn R (1980) Intercalation chemistry. Physica B 99:89–99
12. Liang WY (1986) Electronic properties of transition metal dichalcogenides and their intercalation complexes. In: Dresselhaus MS (ed) Intercalation in layered materials. Plenum, New York, NY, pp 31–73
13. Rouxel J (1976) Sur un diagramme ionicity-structure pour les composes intercalaires alcalins des sulfures. J Solid State Chem 17:223–229
14. Hibma TJ (1980) X-ray study of the ordering of the alkali ions in the intercalation compounds Na_xTiS_2 and Li_xTiS_2. J Solid State Chem 34:97–106
15. Armand M (1980) Intercalation electrodes. In: Murphy DW, Broadhead J, Steele BCH (eds) Materials for advanced batteries. Plenum, New York, NY, pp 145–161
16. Schafhaeutl C (1840) Ueber die verbindungen des kohlenstoffes mi silicium, eisen und andern metallen. J Prakt Chem 19:159–1740
17. Steele BCH (1973) In: van Gool W (ed) Fast ion transport in solids. North-Holland, Amsterdam, pp 103–109
18. Armand MB (1973) Lithium intercalation in CrO_3 using n-butyllithium. In: van Gool W (ed) Fast ion transport in solids. North-Holland, Amsterdam, pp 665–673
19. Steele BCH (1976) Properties and applications of solid solution electrodes. In: Mahan GD (ed) Superionic conductors. Plenum, New York, NY, pp 47–64
20. Vosburgh WC (1959) The manganese dioxide electrode. J Electrochem Soc 106:839–845
21. Whittingham MS (1976) The role of ternary phases in cathode reactions. J Electrochem Soc 123:315–320
22. Ramana CV, Mauger A, Zaghib K, Gendron F, Julien C (2009) Study of the Li-insertion/extraction process in $LiFePO_4/FePO_4$. J Power Sourc 187:555–564
23. Winn DA, Shemilt JM, Steele BCH (1976) Titanium disulphide: a solid solution electrode for sodium and lithium. Mater Res Bull 11:559–566
24. Rüdorff W (1965) Inclusion of base metals in graphite and in metallic chalcogenides of the type MeX_2. Chimia [Zürich] 19:489–499
25. Omloo WP, Jellinek F (1970) Intercalation compounds of alkali metals with niobium and tantalum dichalcogenides. J Less Common Met 20:121–129

26. Rouxel J, Trichet L, Chevalier P, Colombet P, Abou-Ghaloun O (1979) Preparation and structure of alkali intercalation compounds. J Solid State Chem 29:311–321
27. Julien C, Nazri GA (1994) Transport properties of lithium-intercalated MoO_3. Solid State Ionics 68:111–116
28. Julien C, Hatzikraniotis E, Balkanski M (1986) Electrical properties of lithium intercalated p-type GaSe. Mater Lett 4:401–403
29. Parkin SSP, Friend RH (1980) Magnetic and transport properties of 3d transition metal intercalates of some group Va transition metal dichalcogenides. Physica B 99:219–223
30. Schölhorn R, Lerf A (1975) Redox reactions of layered metal disulfides in alkali halide melts. J Less Common Met 42:89–100
31. Goodenough JB, Kim Y (2010) Challenges for rechargeable Li batteries. Chem Mater 22:587–603
32. Goodenough JB (2002) Oxides cathodes. In: van Schalkwijk W, Scrosati B (eds) Advances in lithium-ion batteries. Kluwer, New York, NY, pp 135–154
33. Zhong QM, Bonakdarpour A, Zhang MJ, Gao Y, Dahn JR (1997) Synthesis and electrochemistry of $LiNi_xMn_{2-x}O_4$. J Electrochem Soc 144:205–213
34. Gao Y, Myrtle K, Zhang MJ, Reimers JN, Dahn JR (1996) Valence band of $LiNi_xMn_{2-x}O_4$ and its effects on the voltage profiles of $LiNi_xMn_{2-x}O_4$/Li electrochemical cells. Phys Rev B Condens Matter 54:16670–16675
35. Shin Y, Manthiram A (2003) Origin of the high voltage (>4.5 V) capacity of spinel lithium manganese oxides. Electrochim Acta 48:3583–3592
36. Julien CM, Mauger A (2013) Review of 5-V electrodes for Li-ion batteries: status and rends. Ionics 19:951–988
37. Zaghib K, Guerfi A, Hovington P, Vijh A, Trudeau M, Mauger A, Goodenough JB, Julien CM (2013) Review and analysis of nanostructured olivine-based lithium rechargeable batteries: status and trends. J Power Sourc 232:357–369
38. Armand M, Tarascon JM (2008) Building better batteries. Nature 451:652–657
39. Goodenough JB (2013) Battery components, active materials for. In: Brodd RJ (ed) Batteries for sustainability: selected entries from the encyclopedia of sustainability science and technology. Springer Sci, New York, NY, pp 51–92
40. Cabana J, Monconduit L, Larcher D, Palacin MR (2010) Beyond intercalation-based Li-ion batteries: the state of the art and challenges of electrode materials reacting through conversion reactions. Adv Mater 22:E170–E192
41. Lasri K, Dahbi M, Liivat A, Brandell D, Edström K, Saadoune I (2013) Intercalation and conversion reactions in $Ni_{0.5}TiOPO_4$/C Li-ion battery anode materials. J Power Sourc 229:265–271
42. Weppner W, Huggins RA (1977) Determination of the kinetic parameters of mixed-conducting electrodes and application to the system Li_3Sb. J Electrochem Soc 124:1569–1578
43. Weppner W, Huggins RA (1978) Thermodynamic properties of the intermetallic systems lithium antimony and lithium bismth. J Electrochem Soc 125:7–14
44. Huggins RA, Boukamp BA (1984) All-solid electrodes with mixed conductor matrix. US Patent 4,436,796, 13 March 1984
45. Yang J, Winter M, Besenhard JO (1996) Small particle size multiphase Li-alloy anodes for lithium-ion batteries. Solid State Ionics 90:281–287
46. Timmons A, Dahn JR (2007) Isotropic volume expansion of particles of amorphous metallic alloys in composite negative electrodes for Li-ion batteries. J Electrochem Soc 154:A444–A448

Chapter 4
Reliability of the Rigid-Band Model in Lithium Intercalation Compounds

4.1 Introduction

Layered compounds, in particular the transition-metal dichalcogenides (TMDs) and transition-metal oxides (TMOs), can be intercalated with a wide range of both organic and inorganic materials which may have a profound influence on the physical properties of the host compound [1]. The intercalation reaction in these compounds is driven by charge transfer from the intercalant to the host layered compound conduction band and thus electron-donating species can take place in such a reaction. The reversible ion-electron transfer reaction is classically represented by the scheme:

$$xA^{+} + xe^{-} + \langle H \rangle \Leftrightarrow A_x^{+}\langle H \rangle^{x-}, \tag{4.1}$$

in the usual case where $\langle H \rangle$ is the host material, A an alkali metal and x the molar intercalation fraction. The electronic transport plays an important role in such reaction toward the formation of intercalation compounds. It also governs the phase transitions as the parameter expansion of the host structure has an electronic component. Consequently, it is possible to consider three classes of intercalation reaction that correspond to the different steps in the delocalization of the transferred electrons. The level of acceptance can be either a discrete atomic state, or a molecular level of a discrete polyatomic entity existing in the structure, or part of a conduction band.

In this chapter, we present the physical properties of cathodes materials and verify the applicability of the rigid-band model for intercalation compounds with a layered structure namely transition-metal chalcogenides MX_2 ($M =$ Ti, Ta, Mo, W; $X =$ S, Se) and oxides $LiMO_2$ ($M =$ Co, Ni) as well. Electrical and optical properties are investigated. For some materials, we observe different degrees of irreversibility in the intercalation process and lattice evolution to the complete destruction of the host. Since the purpose here is the study of the materials in the framework of

C. Julien et al., *Lithium Batteries*, DOI 10.1007/978-3-319-19108-9_4

materials science, all the electrochemical properties reported in this chapter have been recorded at low rate $C/12$ or $C/24$ to be close to thermodynamic equilibrium so that they can be related to the physical properties.

4.2 Evolution of the Fermi Level

Let consider the schematic representation of Fig. 4.1 providing an easy way to visualize the energetic levels of the three active components of a lithium battery that are the negative and positive electrodes and the electrolyte. Taking into account the description of physicists, the vacuum refers the zero-energy level. The electronic band structure of a material is characterized by three energies: the work function W that is the minimum thermodynamic energy to remove an electron from the Fermi level of a solid to the vacuum $W = E_{vac} - E_F$, the electron affinity $E_{EA} = E_{vac} - E_{cb}$ that is the energy obtained by moving an electron from the bottom of the conduction band to the vacuum and the band gap $E_g = E_{vb} - E_{cb}$ is the energy separation between the valence band E_{vb} and the conduction band E_{cb}. The negative electrode is lithium metal, which is an infinite reservoir of electrons; so electrons in a metal can be viewed as free electrons in a conduction band with $W_{(Li)} = E_{EA(Li)} \approx 1.5$ eV. The electrolyte is an electronic insulating medium characterized by a wide band gap $E_g > 4$ eV, which is the separation between the occupied and unoccupied molecular orbital energies that are HOMO and LUMO level, respectively. The case of the positive electrode is more complex as it is a semiconductor with various locations for the Fermi level that is not necessarily at the position $E_F = (E_{cb} + E_{vb})/2$. For instance, TiS_2 is a degenerate semiconductor with $E_g \approx 0.2$ eV [2], while $LiCoO_2$ is a p-type semiconductor with $E_g \approx 2.4$ eV and $W = 4.36$ eV that makes the Fermi level 0.4 eV above the top of the valence band [3].

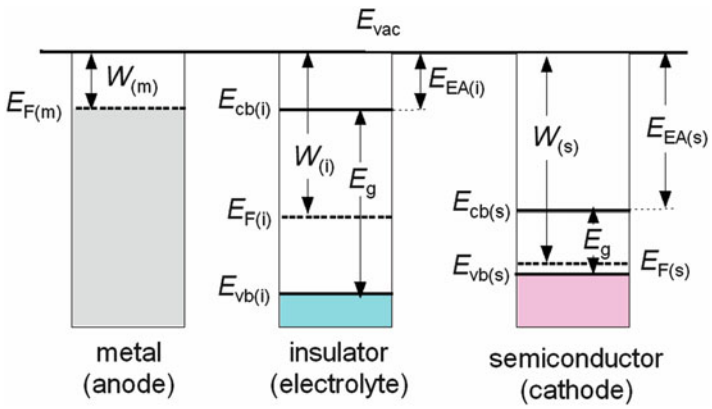

Fig. 4.1 Schematic representation of the electronic structure of the active elements of a lithium battery. E_{EA} indicates the electron affinity, W represents the work function and E_g is the band gap energy of the materials

The rigid-band model (RBM) is a useful approximation for describing the changes in electronic properties of the host material with intercalation. Sellmyer [4] distinguishes two versions of the rigid-band model for dilute solid solutions, which might be called the electron-gas RBM and the screened-impurity RBM. In the former, described mainly by Jones [5], the valence electrons are regarded essentially as in plane wave states and the only effect of alloying with an element having a valence difference ΔZ, is to change the free electron density to a new value, that obtained simply by scaling the valences of the solvent and solute according to their atomic fractions in the alloy. In this case, the Fermi energy in the material has changed accordingly, but E_{BC} remains unchanged. In the screened-impurity RBM of Friedel [6], it is recognized that the electron gas cannot support an electric field at long distances from the charge impurity. The reason is that the conduction electrons will redistribute themselves to screen out the Coulomb field, an effect that is measured by the dielectric constant, which is large in conducting materials. In this case, any charged impurity added to a solid will polarize the solid, which generates a Coulomb potential. Therefore, the Fermi energy is unchanged, but the whole conduction band has been shifted by this potential (Fig. 4.2).

The concept of rigid-bands implies chemical stability of the system. From the energetic point of view, this means the total energy of the substance is little affected by the addition of intercalated electrons. The consequence is that the structure too is stable, and the only energy band involved in intercalation is the narrow *d*-conduction band in TMDs. These are precisely the properties most desirable in a good cathode material, which provide features such as stable voltage against aging and mechanical durability [1]. It is most important, therefore, to investigate theoretically and experimentally how well the approximation can apply in a system employed for the lithium battery cathode.

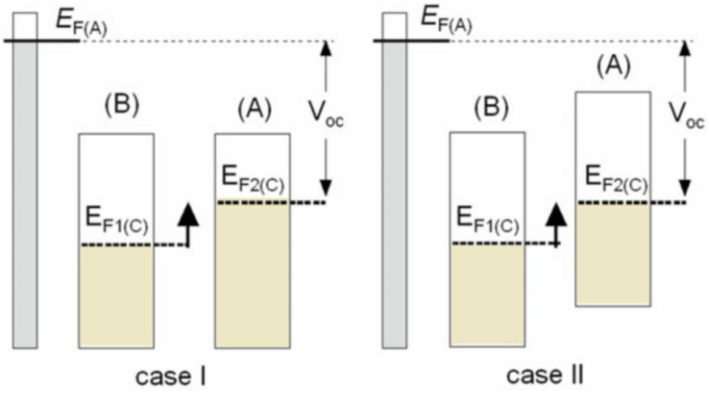

Fig. 4.2 Scheme of the Fermi level evolution in the frame of the rigid-band model (RBM). Two situations are considered: case I represents the electron-gas RBM, case II shows the screened-impurity RBM. (B) and (A) mean before and after lithium insertion, respectively. In both cases, the cell voltage V_{oc} is the same

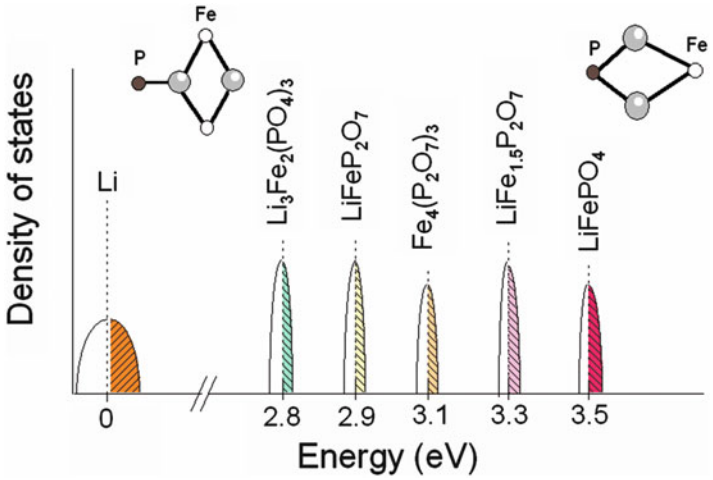

Fig. 4.3 Position of the iron redox energies to the Li^0/Li^+ in various Fe-containing lithium insertion hosts and consequent changes in cell voltages, illustrating the role of polyanions

As the potential of an insertion compound-based lithium battery is determined by the difference between the chemical potentials of electrodes (Eq. 1.6), the crystal chemistry of the cathode governs the cell voltage. As an example, Fig. 4.3 illustrates the role of the polyanions, i.e., $(PO_4)^{3-}$ and $(P_2O_7)^{4-}$, in iron-containing lithium insertion compounds, for which positions of the iron redox energies relative to Li^0/Li^+ changes as a function of the cation environment. This phenomenon has been described as the inductive effect by Goodenough [7]. It depends on the framework connectivity. For instance, the fluorophosphate compounds are expected to exhibit a high cell potential as a result of both the inductive effect of $(PO_4)^{3-}$ group and the electron-withdrawing character of the F^- ion.

4.3 Electronic Structure of TMDs

Considerations of the structural and chemical similarities in the layer structure of TMDs led Wilson and Yoffe [8–10] to suggest that the electronic energy band structures of the materials might also be similar and that the range of observed optical and electrical properties results from differences in the filling of band subgroups as the number of valence electrons is changed. While a completely rigid band model of the TMD compounds cannot account for all properties, theoretical calculations and experiments show that the basic view of the materials is probably correct: the character and the order of the various band subgroups remain the same, while their separations and widths vary slightly with changes in the constituents and the type of coordination unit in the crystal structure.

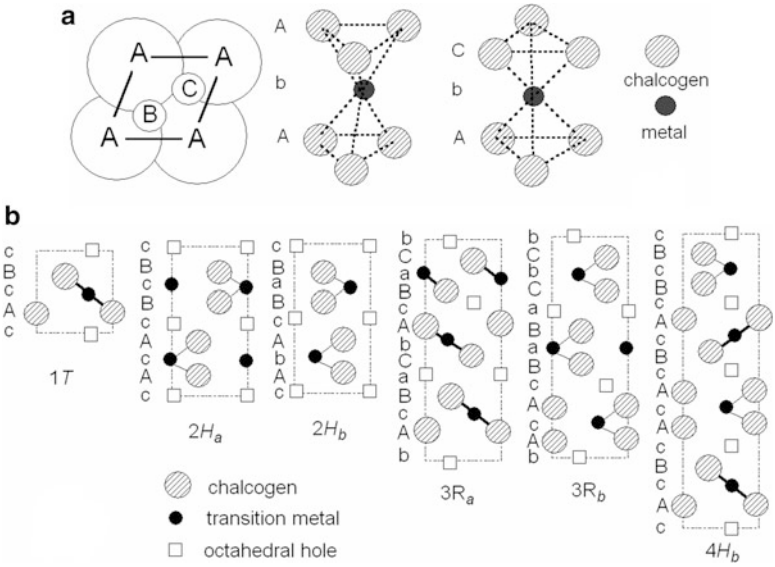

Fig. 4.4 (**a**) The octahedral and trigonal prismatic structures of MX_2 compounds. A, B, C represent the three nonequivalent positions for a close-packed stacking. In octahedron and tetrahedron, capital letters denote the chalcogen atoms and lower case letters the metal atoms. (**b**) Elementary unit cell of simple polytypes of TMDs in the <1120> projection

TMDs have a layered structure made up of a sheet of metal atoms M sandwiched between two sheets of chalcogen atoms X (Fig. 4.4). The X-M-X layers are held together by weak van der Waals forces. Each sheet consists of atoms in a hexagonally close-packed network as shown in Fig. 4.4a. This structure allows almost unlimited expansion of the interslab distance upon insertion of electron-donating species in the layer. Although initial interest in these intercalation compounds was driven by their superconducting properties (at very low temperature), these were used as the active electrode of secondary lithium batteries [8]. Three nonequivalent hexagonally close-packed positions are noted A, B, and C. Two types of coordination structure are possible, either one or both can form the basic unit of the crystal. In the trigonal prismatic coordination, the sandwich of X-M-X follows the AbA sequence and in the octahedral coordination it follows the AbC sequence (Fig. 4.4a). Capital letters denote the chalcogen atoms and lower case letters the metal atoms.

A rational nomenclature adopted for naming the different polymorphs and polytypes proposed Brown and Beerntsen [11] is presented in Fig. 4.4b. In designating the polytypes, one first indicates the number of sandwiches required to obtain a unit cell perpendicular to the plane of the layers, then the overall symmetry of the structure: trigonal T, hexagonal H, or rhombohedral R. Lower case subscripts are used to distinguish polytype otherwise similarly labeled, e.g., 2Ha and 2Hb. Thus the simplest polytype with octahedral coordination, labeled 1T, has a repeat of the sandwich perpendicular to the layer, i.e., this polytype is obtained by piling the

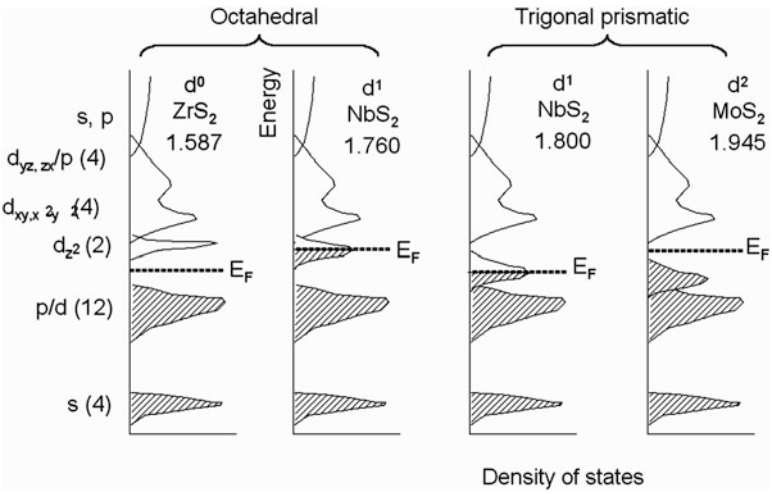

Fig. 4.5 Schematic band structures for all the TMDs compounds with octahedral and trigonal prismatic coordination. Sketches show the electronic structures before (**a**) and after (**b**) lithium intercalation with the respective position of the Fermi level

sandwich units. In the trigonal symmetry and the simplest trigonal prismatic coordination, polytypes have two sandwich repeats, and are designated 2Ha and 2Hb. The 2Ha structure is adopted by metallic group V materials such as NbS_2 and stocks the metal atoms directly above each other along the *c*-axis, while in the 2Hb structure, adopted by semiconducting group VI materials such as MoS_2, the metal atoms are staggered. In the 4Hb and 6R polytypes, the coordination within successive sandwiches alternates between octahedral and trigonal prism, i.e., a mixed coordination. The six best known polytypes of transition metal dichalcogenides are shown in Fig. 4.4b. Octahedral interstitial (vacant) sites between sandwiches are represented by square sites, into which intercalation atoms may enter.

The electronic band structure of TMDs have been generally calculated using simplest molecular-orbital arguments [5] and experimentally established from the optical properties for the group IV, V, and VI TMDs. Figure 4.5 shows the schematic band structure of the MX_2 compounds having octahedral and trigonal prismatic coordination. The basic features of the band model are shown for the regular trigonal prismatic structure (groups VI and V) and the regular octahedral structure (groups IV and V). The chalcogen *p* states with different degrees of admixture of metal states form the main valence band, while the energy of the chalcogen *s* states is located 10–15 eV below. The metal *d* states, with possible admixture of chalcogen states, lie immediately above the *p* valence band, and the next higher bands are made up of metal *s* and *p* states. The *d* band is subdivided in accordance with the ligand field splitting. The lowest of these sub-bands can hold two electrons and is called the "d_{z^2}" band after Wilson and Yoffe [8]. The reason is that the d_{z^2} is split off the $d_{xy}-d_{x^2-y^2}$ band towards lower energy by the trigonal distortion. The same band-labeling scheme is used here in spite of the hybridization

between d and p states, and between the various d states. In all the compounds of the group IV to group VI transition metals, the p- and s-valence bands are completely filled, and the variations of the electrical and optical properties are largely accounted for by the gradual filling of the d_{z2} band [12].

On the whole the band structure of an octahedrally coordinated material is characterized by greater charge transfer from the metal atom to the chalcogen atom. The p-valence band is relatively narrow (about 2.5 eV wide), while the d_{z2} band forms part of the d band manifold which is separated from the p-valence bands by about 2 eV. This is the case for all the group IV compounds and for some of the group V compounds. The band structure of a trigonal prism coordinated material, on the other hand, has a wider p-valence band (about 5 eV wide) and there is more mixing between p and d states, while the d_{z2} band lies close to or overlaps with the p bands and is now well separated from the rest of the d band manifold. This is the case for all the regular group VI compounds and the rest of the group V compounds.

The position of the d_{z2} band is thus determined by the symmetry of the coordination unit. It is interesting to consider the total energy for a given coordination. This is basically determined by two competing terms: the electrostatic potential energy and the energy of the d_{z2} electrons. In the group IV compounds, the d_{z2} band is empty and the electrostatic energy term favors octahedral coordination, where the chalcogen atoms on two sides of the metal atoms in a sandwich are staggered, while in the group VI compounds where the d_{z2} band is full and the bonding is predominantly covalent, it is energetically advantageous to depress the d_{z2} band by adopting the trigonal prism coordination where the chalcogen atoms are in the eclipsed position. In the group V compounds, the d_{z2} band is only half full, so it is not surprising that neither term necessarily dominates completely and both coordination units occur.

In the simple picture, during intercalation, the donating-electrons will occupy one of the empty d-bands. The simplest approximation to the band structure of an intercalation compound is just that of the parent host compound with the Fermi level moved up to accommodate the extra electrons.

Many techniques have been used to obtain information on the optical absorption α, the reflectivity R and dielectric constants ε_1 and ε_2. Visible and ultra-violet absorption spectroscopy gives us the joint density of states of valence and conduction bands. Soft X-rays and synchrotron radiation give us information on conduction bands, while photoemission experiments (UPS, XPS, ESCA) can tell us about density of states in valence band and give the energies relative to the Fermi level. Typical absorption spectra for the semiconductor MoS_2 (d^2, group VI), metal NbS_2 (d^1, group V), and wide-band gap semiconductor ZrS_2 (d^0, group IV) are given in Fig. 4.6. The prominent features A and B for MoS_2 are excitons, while in the metal NbS_2 one observes the characteristic free carrier absorption at about 1 eV.

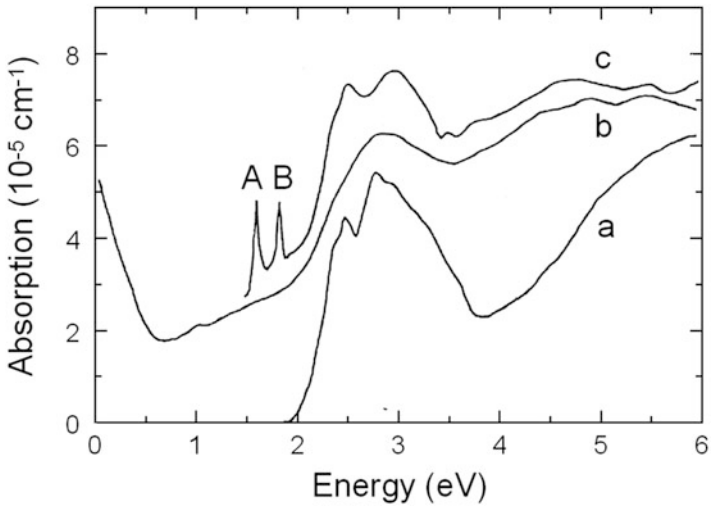

Fig. 4.6 Absorption spectra of two-dimensional TMDs: (**a**) 1T-ZrS_2, (**b**) 2*H*-NbS_2, and (**c**) 2*H*-MoS_2. The prominent features A and B for MoS_2 are excitonic transitions

4.4 Lithium Intercalation in TiS_2

For TMDs, the temperature dependence of the electron mobility is usually formed to be much stronger than expected for acoustic phonon scattering. The resistivity for materials with a temperature independent extrinsic carrier concentration is usually fit by the empirical relation:

$$\rho = \rho_0 + AT^{\alpha}, \tag{4.2}$$

where ρ_0 is the temperature-independent contribution form impurity scattering and A is a constant [13]. The exponent α is found to vary from 2.3 in good-stoichiometry TiS_2 sample (with carrier concentration $n = 1.1 \times 10^{20}$ cm^{-3}) to 1.6 in poor-stoichiometry sample ($n = 2.9 \times 10^{21}$ cm^{-3}); α is found to be as large as 2.2 for $ZrSe_2$.

In Li_xTiS_2 the magnitude of the Hall coefficient decreases with increasing lithium content, confirming the occurrence of electron transfer from intercalates to the host [6–8]. The electron concentration is TiS_2 before intercalation is 3.1×10^{20} cm^{-3} indicating that this material is of stoichiometry $Ti_{1.0044}S_2$ [14]. Upon lithium intercalation we observe a large decrease of the resistivity as well as of the Hall coefficient. The carrier concentration in electro-intercalated samples increases to 5×10^{21} and 9.6×10^{21} cm^{-3} for $x = 0.25$ and 0.5, respectively. The Hall coefficient R_H of all the samples is nearly temperature independent, as would be expected for a normal metal.

Klipstein et al. [15, 16] explain this behavior by a model involving the interplay between inter-pocket and intra-pocket scattering of electrons by longitudinal

acoustic phonons, whereby the increase in Fermi surface dimensions reduces the restriction on the wave-vector of phonons that may take part in the scattering process, implying that, as the carrier concentration increases, α should tend towards unity, which is the limit for a metal when the resistivity is solely due to a scattering of the electrons by LA-acoustic phonons. Simultaneously, the temperature T_{min} below which the $\ln(\rho - \rho_0)$ vs. $\ln(T)$ curve starts deviating from linearity, should increase, since this deviation originates from incomplete momentum relaxation when the phonon wave-vectors characteristic of these temperatures are too short to span the Fermi surface. This model, which was originally based on studies in pristine TiS_2 with a varying degree of stoichiometry, was later verified to remain valid for higher carrier concentrations, such as in TiS_2 intercalated with lithium via the n-butyllithium technique [16] or intercalated with hydrazine [17].

Electron transfer is also apparent in the optical properties of this system. Figure 4.7 shows the absorption spectra, in the energy range 0.5–6.0 eV of pure

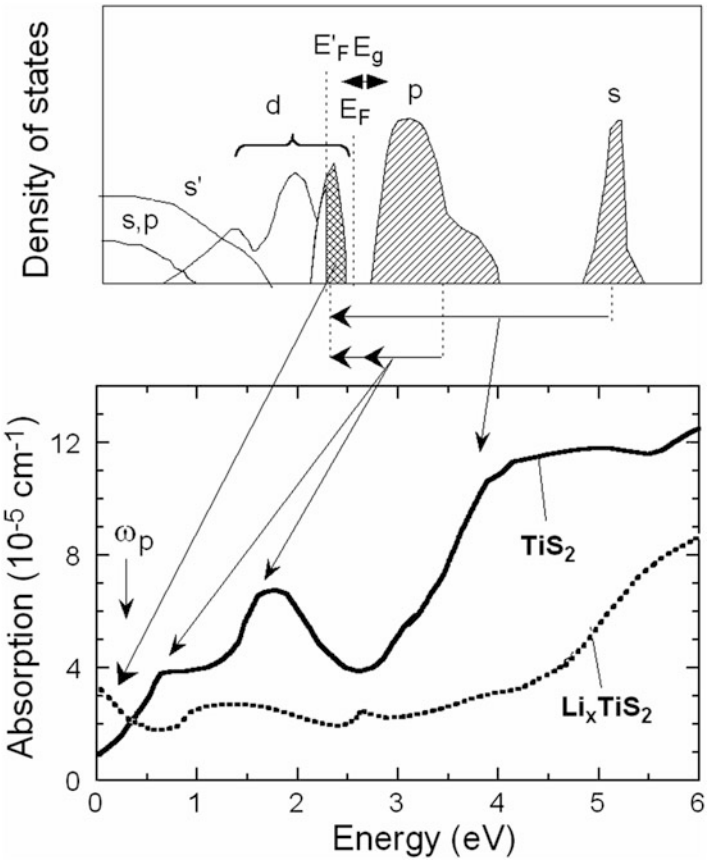

Fig. 4.7 Room-temperature absorption spectra of TiS_2 and $LiTiS_2$. The schematic band structure shows that the rigid-band model may be used for the intercalation complexes

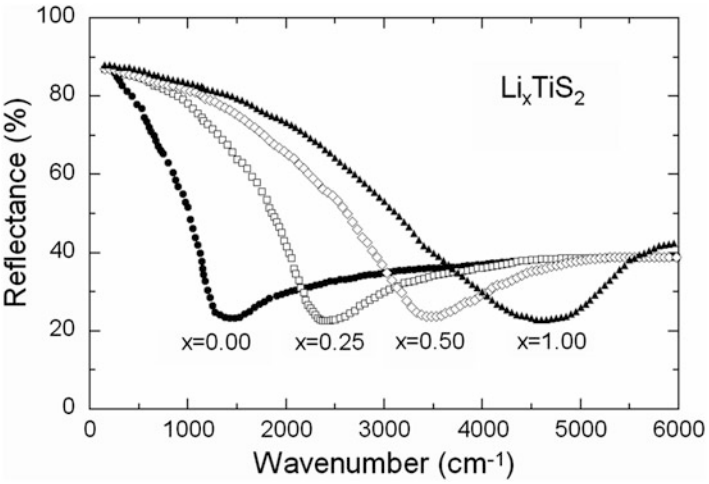

Fig. 4.8 FTIR reflectivity spectra of Li_xTiS_2 as a function of lithium content

and Li-intercalated TiS_2 [18]. In the spectrum of the intercalation complex $LiTiS_2$, the free carrier absorption is evidenced below 1 eV as it is responsible for the increase of the absorption when decreasing the photon frequency in the vicinity of the plasma frequency ω_p. We also observe interband transitions which are the first direct allowed transitions from the p valence to the d conduction band at the L point of the Brillouin zone. Moving into the spectrum of Li_xTiS_2, the onset of inter-band transitions is seen to have shifted to higher energies and the oscillator strength under the absorption band is roughly halved. Beal and Nulsen [18] argue that this is exactly what one would expect as the d_{z2} band is now half-full following saturation of the intercalation complexes.

Another optical experiment, infrared reflectivity was carried out on Li-electro-intercalated TiS_2 [15]. Figure 4.8 shows the FTIR reflectivity spectra of Li intercalated TiS_2 single crystals as a function of x(Li) in the range $0 \leq x \leq 1$. We observe a large shift in the plasma edge for $Li_{1.0}TiS_2$ with respect to pure TiS_2. According to the free-carrier Drude model (see Chap. 13), the analysis of the dielectric function gives the values as follows. In TiS_2, the plasma edge lies around 1200 cm^{-1}, whereas in $LiTiS_2$ the plasma edge occurs at about 4000 cm^{-1} giving plasma frequencies of 1360 and 4100 cm^{-1}, respectively, if we take into account that the high-frequency dielectric constant remains similar to that of the pristine material and if we consider the electron effective mass as obtained by Isomaki et al. [19]. At the L-point of the Brillouin zone, Isomaki et al. estimate $m_a = 0.4\, m_0$ along the a-axis. This assumption implies that the optical effective mass m_{opt} has a value higher than $1.3\, m_0$. In the present studies, the Drude analysis gives a carrier concentration of 1.7×10^{22} cm^{-3} for complete intercalation of TiS_2 at $x = 1$. This is in excellent agreement with the theoretically expected value of 1.75×10^{22} cm^{-3} and very close to the value of 2.2×10^{22} cm^{-3} determined from Hall measurements.

We assume in the spirit of the rigid-band model [1] that intercalation changes appreciably neither the effective mass of the conduction band, nor the high-frequency dielectric constant of the host material. The charge transfer Δn from the alkali-metal atoms to the *d*-conduction band of the host compound can be directly calculated from the difference between ${\omega_p}^2$ before and after intercalation. Here Δn is expressed in terms of the number of electrons transferred per Ti atoms. Using this method we have $\Delta n = 0.9 \pm 0.1$ electrons. The uncertainty of 0.1 electrons is thought to be a reasonable estimate in view of the assumptions made. It is interesting to note the large increase of the plasma damping factor from 310 to 2160 cm^{-1} in $Ti_{1.005}S_2$ and $Li_{1.0}Ti_{1.005}S_2$, respectively. This increase is observed in the energy-loss function by the broadening of the plasmon peak. The damping factor can be expressed as follows:

$$\Gamma = 1/\tau = q/m^*\mu_H, \tag{4.3}$$

where μ_H is the Hall mobility of free carriers. The observed increase of Γ suggests a decrease of the Hall mobility or a modification of the effective mass tin the intercalated sample. In $Li_{1.0}Ti_{1.005}S_2$ the electron mobility measured by Hall effect has a value of 1.9 cm^2V^{-1} s^{-1} at room temperature [14]. This value can be related with those given in the literature, namely 13.5 and 0.35 cm^2 V^{-1} s^{-1} for TiS_2 and $LiTiS_2$, respectively [16].

The temperature dependence of the IR reflectivity spectra of the $Li_{1.0}Ti_{1.005}S_2$ sample is similar to those of the pure material. The spectra show a dip close to the plasma frequency $\omega_p = 4180$ cm^{-1} extracted from analysis of the data using a Drude-like model with a frequency dependent relaxation time, as:

$$1/\tau(x, T, \omega) = x\ \tau_0 + \alpha\left[(pT)^2 + \omega^2\right]. \tag{4.4}$$

A good fit to the optical data is achieved with the scattering rate given by Eq. (4.4) [20], with $p = 13.6$, against 2π in the ideal isotropic three-dimensional effective mass model [21], while the second term in ω^2 is due to the electron-electron scattering. For Li intercalated TiS_2 sample, the temperature and frequency components of Eq. (4.4) are strongly screened by the first term ($x\tau_0$) as shown in Fig. 4.9. This may be due to the complete filling of the *d*-band associated with a very low Hall mobility. In this case, it is difficult to evaluate the optical mobility because the quantity $\omega\tau >> 1$ is no longer valid.

Considering that Hall measurements on the $Li_{1.0}Ti_{1.005}S_2$ sample give $N_H = 1.8 \times 10^{22}$ cm^{-3} and that the Fermi energy obtained by optical reflectivity measurements is $E_F = 4180$ $cm^{-1} = 0.52$ eV, we may estimate the electron effective mass $m^* = 0.49\, m_0$. This value is very close to the value reported for the pure material by Isomaki et al. [19]. In conclusion, it can be seen from the electrical and optical properties of the Li-intercalated TiS_2 presented above that they all can be explained in terms of the rigid-band model. It is worth mentioning here that optical absorption results by Scholz and Frindt [22] on Ag-intercalated TiS_2 also agreed with this model.

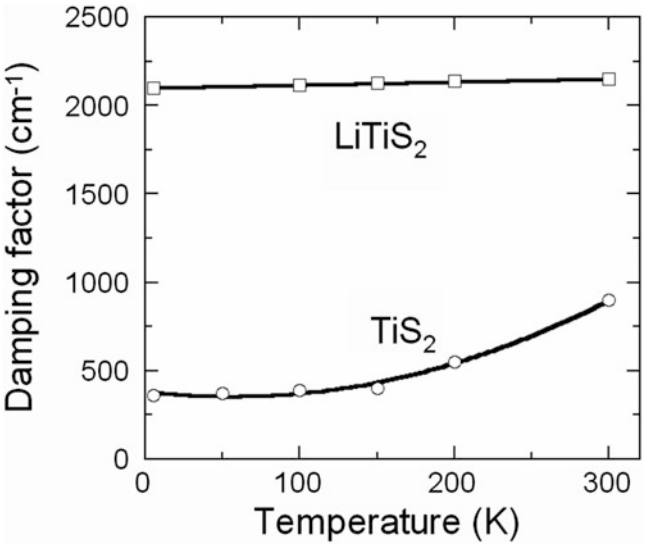

Fig. 4.9 Temperature dependence of the damping factor (inverse relaxation time) for TiS_2 and $LiTiS_2$

The reliability of the rigid-band model is due to the excellent structural stability of TiS_2. From the electrochemical view point, TiS_2 was considered as the best positive electrode for lithium batteries due to its high electronic conductivity, which avoids carbon additive, and the high mobility of Li^+ ions into van der Waals planes. Unfortunately, problems came from the anode side. Note that the Li//TiS_2 electrochemical cell was invented by Broadhead and Butherus at Bell Telephone Labs, who filed their patent on 24 July 1972 [23].

4.5 Lithium Intercalation in TaS_2

Among the group-V TMDs, TaS_2 has perhaps been the subject of greatest interest, because of the fascinating structural and electronic properties that this material exhibits. Due to valence electron occupying their d_{z^2} band, this metallic compound can exist in either 1T-, 2H-, or 4H-structure [24]. As a consequence of the switching from octahedral (Oh) to trigonal prismatic (TP) coordination, the shift of the d_{z^2} band to lower energies occurs gradually. The absorption spectrum of pure 2H-TaS_2 shows a Drude edge below 1 eV associated with the free-carrier absorption in this material owing to the half-filled d_{z^2} band. After intercalation, the Drude edge disappears and the first $d_{z^2} \rightarrow d$ transition shifts toward lower energy. These changes are attributed to the gradual filling of the d_{z^2} band by electron transferred from lithium.

The absorption spectrum of 1T-TaS_2 is shown in Fig. 4.10. Near 1.5 eV, the absorption bands are associated with the $d_{z^2 1} \rightarrow d_{z^2 2}$ and $d_{z^2 1} \rightarrow d$ transitions,

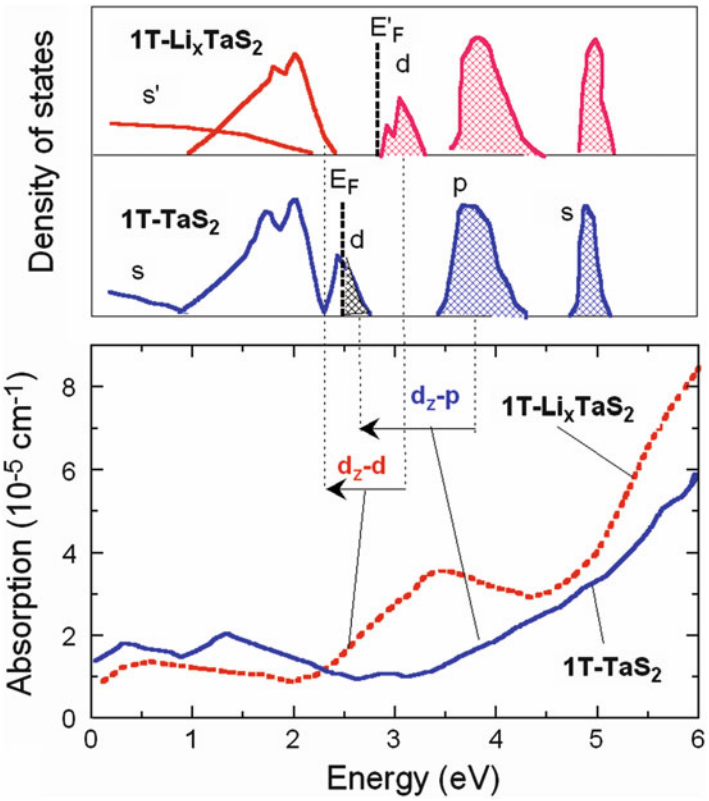

Fig. 4.10 Absorption spectra of pure 1T-TaS_2 and 1T-Li_xTaS_2. The schematic band structure shows the lowering of the d_z band upon Li intercalation. Reproduced with permission from [24]. Copyright 1986 Kluwer Academic Press

whereas the band above ~3.5 eV owing to $p \rightarrow d_{z^2}$ transition. Charge transfer from Li to the host lattice increases the population of the d_{z^2} band and raises the Fermi level E_F to a new energy, $E_{F'}$. The displacement of the strong absorption edge around ~3 eV indicates a considerable lowering of the d_{z^2} band with respect to its position in the pristine material. The lowering of the d_{z^2} band is attributed to the filling with electrons donated by Li, as well as the modification of the crystal structure that is an increase of the c/a ratio after intercalation [25]. These results provide further support to the argument that, upon lithium intercalation the rigid-band model is not entirely applicable in 1T-TaS_2.

4.6 Lithium Intercalation in 2H-MoS_2

Among the group-VI TMDs, MoS_2 is one of the materials where intercalation reactions induce a transition of the host related to local ligand field modification. In this particular case, molybdenum presents a trigonal prismatic sulfur

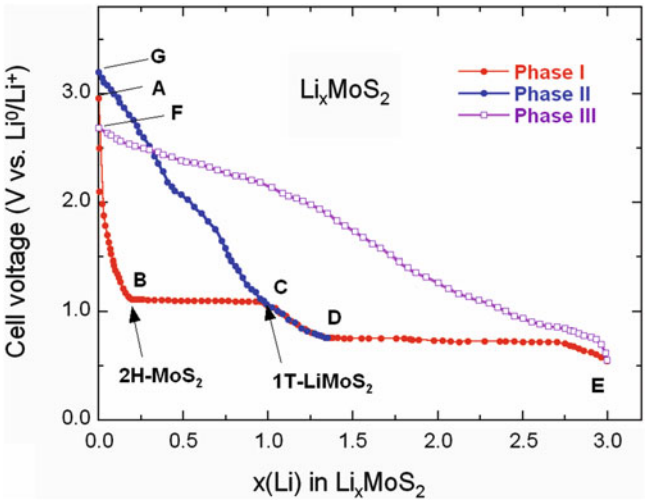

Fig. 4.11 Electrochemical profile of the Li-MoS_2 system as a function of the Li content in Li_xMoS_2. Reproduced with permission from [29]. Copyright 2002 Elsevier

coordination that changes the octahedral one (TP → Oh transition) [26–28]. The structure modification is accompanied by an increase of the *M-X* band ionicity in agreement with the respective stability of the new atomic arrangement, the Coulomb repulsion between partially charged ligands favoring the octahedral form. Also, the comparison of the *d*-band density of states of 2H-MoS_2 and hypothetical 1T-$LiMoS_2$ shows that the occupied bands, which contain six states, are lower in the case of the Oh phase. This effect corresponds to the glide process between Mo and S atoms. This is a fine example of destabilization through lithium reduction.

Figure 4.11 shows the voltage profile vs. composition x(Li) of the Li//Li_xMoS_2 cell using 1 mol L^{-1} $LiClO_4$ in propylene carbonate as electrolyte [29]. The Li-MoS_2 system exhibit three distinct phases in good agreement with the work of Hearing et al. [30]. The discharge reaction of a fresh cell occurs in the range 3.0–0.55 V with two voltage plateaus at 1.1 and ~0.7 V when 3Li are intercalated in the layered MoS_2 lattice. The first discharge curve (phase I) exhibits a plateau in the range $0.25 \leq x \leq 1$ that corresponds to a two-phase system including both 2H-$Li_{0.25}MoS_2$ and 1T-$LiMoS_2$ structures. For $x = 1$ the complete transformation from (TP) to (Oh) coordination is attributed to a process, which is driven by a lowering of the electronic energy for the octahedral structure when electrons are donated from Li to the MoS_2 layer upon intercalation. The octahedral transformation starting at $x \approx 0.25$ completes around $x = 1.0$ and is not preserved on subsequent cycling [1, 26, 27]. For $x > 1$, the phase II is formed, which appears to be reversible in the range 0.75–3.2 V without plateau formation. This phase II is a preferred phase (path D-G in Fig. 4.11) for battery use that requires the so-called battery formation process, i.e., first discharge down to 0.75 V. The phase III (path E-F) occurs at the end of the second plateau. This phase is not suitable because the poor reversibility [30].

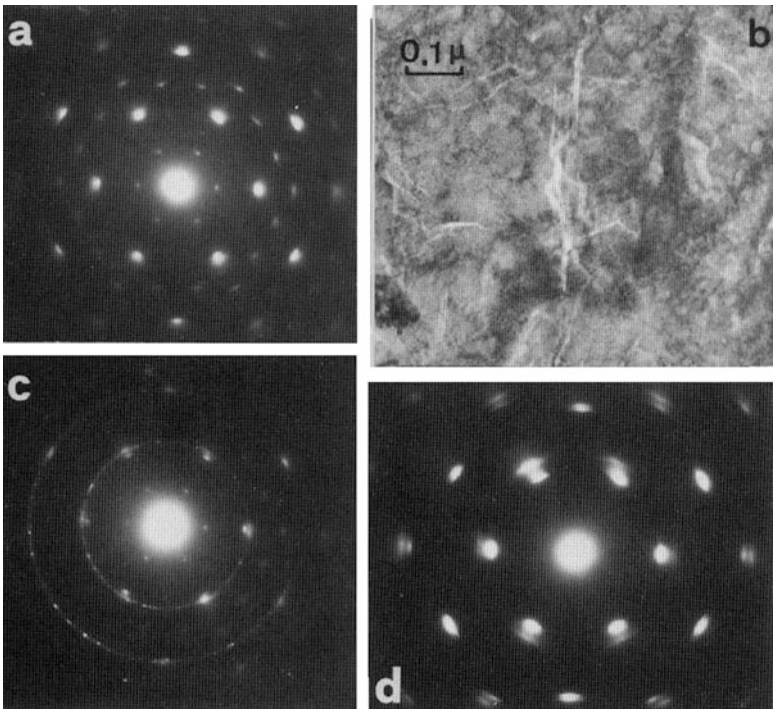

Fig. 4.12 Li intercalation of MoS_2 in n-butyllithium. (**a**) After 10 min, defects are created near the edges and in the steps of the specimen denoted by *arrows*. (**b**) After 2 h intercalation, superlattice spots appear (denoted by the letter s), which are indexed as (1/201/20). Notice also the splitting of the main spots (denoted by the letter M). (**c**) A micrograph taken from the same area reveals that the specimen is heavily defected owing to intercalation. (**d**) Distribution of lithium vs. Distance from the edges of the specimen as revealed by SSNTD images. Reproduced with permission from [29]. Copyright 2002 Elsevier

Electron diffraction studies on the Li-MoS_2 system have shown that the structural transformation is accompanied by a $2a_0 \times 2a_0$ superlattice formation observed for the composition $x \approx 0.25$, which is interpreted as a pseudo-staging on the basal hexagonal lattice (Fig. 4.12) [31]. This superlattice formation was also observed in the incremental capacity dQ/dV obtained from electrochemical measurements [28] and in the Raman scattering spectra of $Li_{0.3}MoS_2$ [32, 33]. However, we do expect that the lithiation process is accompanied by the raising of the Fermi level due to the charge transfer from Li intercalation. This is depicted in Fig. 4.13, where the temperature dependence of the electrical conductivity of lithium intercalated MoS_2. Undoped MoS_2 is a n-type semiconductor with $\sigma \sim \exp(-E_a/k_B T)$, where $E_a = 0.05$ eV, and $Li_{0.3}MoS_2$ is a highly degenerate semiconductor with $\sigma \sim T^{-1.4}$. Here, we must be aware of the limitations of the rigid band model. It is probably non appropriate for Li_xMoS_2 because the fully occupied d_{z^2} states in the pristine material imply new electrons to enter the next higher d band with a change of the c/a ratio associated with the destabilization of the host lattice.

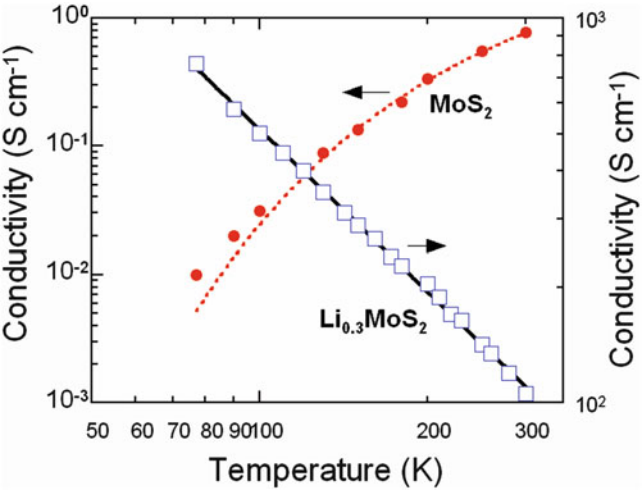

Fig. 4.13 Temperature dependence of the electrical conductivity of lithium intercalated MoS_2. Reproduced with permission from [29]. Copyright 2002 Elsevier

Following the above structural transformation, phonon spectroscopy offers an excellent way of quantifying the degree of anisotropy not only by distinguishing between inter- and intra-layer normal modes but also by determining the shear moduli in different directions. The Raman spectrum of 2H-MoS_2 at room temperature is shown in Fig. 4.14. It exhibits four Raman-active bands that are the intra-layer A_{1g} mode at 407 cm^{-1} involving motion along the c-axis, the intra-layer E_{2g} mode at 382 cm^{-1} involving motion in the based plane, the E_{1g} mode at 286 cm^{-1} and the rigid-layer (RL) mode at 32 cm^{-1} of E_{2g} symmetry. This last mode is of interlayer type involving rigid motion of neighboring sandwiches in opposite phase.

The Raman spectra of Li_xMoS_2 with $x \approx 0.1$ and $x = 0.3$ (Fig. 4.14) display the structural changes from the ß-phase (2H structure) to a α-phase (1T structure) upon Li intercalation [32]. This transformation from trigonal prismatic to octahedral coordination has been attributed to a process which is driven by a lowering of the electronic energy for the octahedral structure when electrons are donated from Li to the MoS_2 layer during intercalation [33]. The octahedral transformation in Li_xMoS_2 starts at $x = 0.1$ and completes around $x = 1$. For a degree of intercalation $x \approx 0.1$, the Raman intensity is considerably reduced (by a factor 5) and we observe two new bands: a broad peak located at 153 cm^{-1} (A-line) and a weak peak situated at 205 cm^{-1} (B-line) and the intensity of the RL mode is reduced. The two pristine intra-layer modes can still be observed, with little shift in frequency, but both of them are split to give weak additional side bands towards lower energies (C- and D-line). These bands are attributed to the Davydov pairs of the optical phonon branches. For $x = 0.3$, the spectrum of Li_xMoS_2 is modified with respect to the former ones. The RL mode is no longer recorded. All the other lines are still observed. In addition, a small shift in frequency of the lattice modes of MoS_2 can be observed [33].

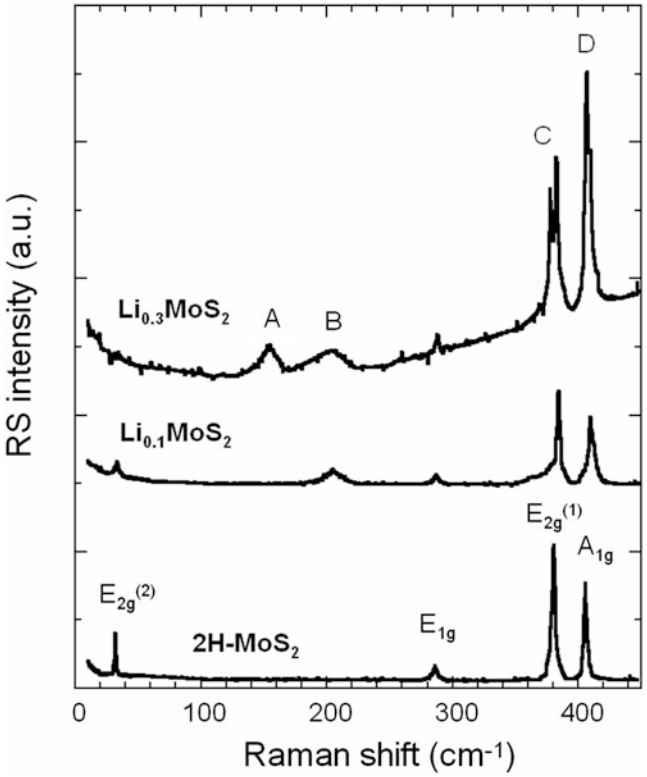

Fig. 4.14 Raman spectra of 2H-MoS_2 natural crystal as a function of Li content lithium

A simple model has been used to calculate the frequencies of the new modes appearing after Li intercalation. The intercalation mode is given by:

$$\omega_{\text{int}}(\text{o}) = [k(2m_1 + m_2)/m_1 m_2]^{1/2}, \tag{4.5}$$

where m_1 and m_2 are the masses of the MoS_2 molecule and of the Li atom, respectively, and k is the force constant between the S and Li atoms. We estimate $k = 8.23 \times 10^3$ dyn cm^{-1}, which is much smaller than the intra-layer force constants. For a degree of intercalation $x = 0.3$, we assume that Li_xMoS_2 is a two-phase system. The following changes on the lattice dynamics can be expected. The RL mode disappears because the elementary cell of the 1T-structure contains only one molecular unit (3 atoms per sandwich). The symmetry changes from D_{6h} to D_{3d} and the new symmetry allows only the two Raman active A_{1g} and E_g modes representative of the intra-layer atomic motions. The weak spacing expansion observed upon Li intercalation and the difference of the molybdenum coordination do not modify significantly the frequency of these modes. A simplest calculation gives a change of about 6 % in frequency. Thus, we can trust the validity of the lattice dynamics model using a 2H-structure [33]. Finally, it is obvious that Li intercalation into molybdenum disulfides does not satisfy the concept of rigid-band model.

4.7 Lithium Intercalation in WS_2

Among the TMDs materials, WS_2, which belongs to the group VIb transition metal, crystallizes into a layered structure identical to MoS_2. Two polytypes hexagonal (2H) and rhombohedral (3R) are commonly found among the materials with trigonal-prismatic coordination. Varieties of other polymorphic structures have been described such as o-WS_2 and 2M-WS_2 [34]. Orthorhombic ß-WS_2 (1T-structure) has been prepared by removing Na from Na_xWS_2 [35]. WS_2 is a grey-black indirect-gap semiconductor with a n-type character and an energy gap of 1.35 eV due to electronic transition of the $d \rightarrow d$ type. In terms of the two-dimensional WS_2 band structure direct low energy transitions at about 1.9–2.5 eV are characterized by A and B exciton pairs and its narrow d_{z2} subband is completely filled. The conduction band based on $d_{x^2-y^2}$, d_{xy} orbitals is empty and can thus be populated by electron donors. The observation by Rüdorff [36] that WS_2 forms metal intercalated products when the dichalcogenide is treated with liquid ammonia solutions of alkali metals prompted us to examine more generally the features of electrochemically Li-intercalated WS_2. Somoano et al. [37] have also shown that intercalation compounds are found in the case of tungsten derivatives. Omloo and Jellinek [38] made an attempt to understand the unstability of WS_2 and WSe_2 intercalated by alkali metals and alkaline earths. The electrochemical features of the intercalation-deintercalation reaction of Li_xWS_2 is shown in Fig. 4.15a [39]. The voltage-composition curve displays features as follows: (a) the initial OCV of 3.0 V, (b) the emf decreases smoothly from 3.0 to 2.2 V in the range $0 \leq x \leq 0.2$ and a break is clearly observed at about $x = 0.2$, (c) for $x > 0.2$ the discharge curve occurs with a pseudo-plateau at about 2.1 V, (d) the cell voltage drops to 0.5 V for $x = 0.6$ giving a specific energy density of 140 Wh kg^{-1}. The incremental capacity $-(\partial x/\partial V)$ curve recorded at the first discharge (Fig. 4.15b) shows patterns comparable to a double-site energy system [40]. This should be the evidence of either increasing repulsive forces between inserted ions or formation of a new phase. During the insertion process the alkali metal transfers electron to the

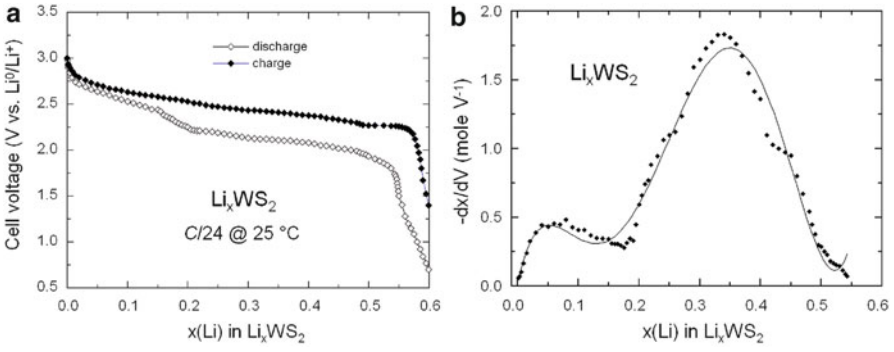

Fig. 4.15 (**a**) Discharge–charge curves of an electrochemical Li//WS_2 cell using the 3R-WS_2 polymorph as cathode material. (**b**) Incremental capacity dx/dV vs. composition

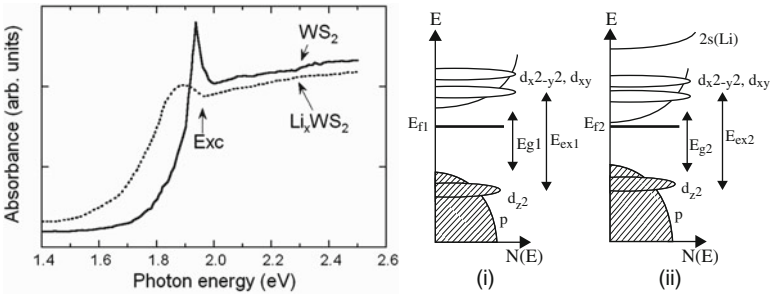

Fig. 4.16 (*Left*) The absorbance spectra recorded at 5 K of pure WS_2 and Li-intercalated WS_2 single crystal containing a small amount of lithium $x = 0.1$. (*Right*) Electronic band structure of trigonal prismatic dichalcogenide (i) pure WS_2 and (ii) $Li_{0.1}WS_2$

empty conduction band based on $d_{x^2-y^2}$, d_{xy} orbitals of W. Intercalation with electron donors is expected to populate these higher energy bands and give metallic properties. According to molecular-orbital calculations [25] with the d_{z^2} band already full and intercalation increasing the d band population from d^2 to d^3, the electron energy can be lowered by a trigonal. Indeed, for the W layered compounds, the number of d electrons exceeds d^2 during intercalation. The stability of intercalates of WS_2 is clearly related to the ionization potentials of the inserted metals and the affinity of the layer compound [38] and the prismatic coordination is destabilized on addition of lithium ions for $x > 0.2$. It was suggested that the result is a structural transformation from 3R-WS_2 to 2H-Li_xWS_2 due to the instabilities in the interlayer structure. Later in the discussion it will be demonstrated that upon Li^+ insertion the interlayer spacing increases with a small expansion [41].

Figure 4.16a shows the absorbance spectra recorded at 5 K of pristine WS_2 and $Li_{0.1}WS_2$ samples in the energy range 1.4–2.5 eV. In these spectra, we observe absorption edge at 1.9 and 1.7 eV and side-band at 1.93 and 1.88 eV corresponding to the absorption edge and the excitonic peak of WS_2 and $Li_{0.1}WS_2$, respectively. The exciton transition at about 1.93 eV is attributed to the smallest direct gap at K (the zone-edge point in the (110) direction) in between the d_{z^2} valence states and the $d_{x^2-y^2}$, d_{xy} conduction states, split by interlayer interactions and spin-orbit coupling [42]. Upon Li intercalation, modifications in the absorption spectrum are observed, with a red shift of absoption edge and the vanishing of the exciton peak (located at E_{ex} on the curves) due to free carrier screening. In this process the free carriers arise from band filling above the full d_{z^2} band. For Li_xWS_2 the donated electrons should go into the empty conduction band based on the $d_{x^2-y^2}$, d_{xy} orbitals. The half width at half-maximum (HWHM) of the exciton of pure WS_2 at 5 K is about 20 meV, whereas one observes a HWHM of 55 meV for Li_xWS_2. The primary phenomenon associated with the lithium intercalation in WS_2 is the donation of x electrons from the guest to the host matrix. The second effect is that the interband absorption edge around 1.9 eV shifts to lower energies with Li insertion (Fig. 4.16b). This result can be understood in terms of a destabilization of the electronic band structure. The shift of the fundamental absorption edge toward lower energies can be attributed to

an interaction between the conduction band made up of *s* and *p* orbitals and the 2*s* orbitals of lithium. Thus, the net effect is a decrease of the optical band gap of about 0.22 eV. Optical effects in Li-intercalated WS_2 can be satisfactory interpreted in terms of electron donation but the rigid-band model is essentially inadequate in such a compound. One may note that, in the studied energy range (1.4–2.5 eV), intercalation of Li ions did not give rise to extra absorption bands [42].

4.8 Lithium Intercalation in InSe

The intercalation of lithium in InSe has been extensively studied. Indium monoselenide is a layered semiconductor in which each layer consists of four close-packed, covalently bounded, monoatomic sheets in the sequence Se-In-In-Se. When material is grown by the Bridgman method, the 3R polytype (γ-InSe) crystallizes in a rhombohedral system with the R3m space group (C^5_{6v}) with the primitive unit cell containing three layers but only one molecule [43, 44]. The layers are stacked in the sequence *CBA*□*ABC* separated by weak interlayer interaction (often referred to as van der Waals-like). The square symbol represents the empty site available for insertion. The interaction of cleaved InSe crystals with lithium was investigated by electrochemical titration, in situ X-ray diffractometry, and by X-ray photoemission spectroscopy showing a competition between intercalation and chemical decomposition reactions expressed as [45–47]:

$$x\mathrm{Li} + \mathrm{InSe} \rightarrow \mathrm{Li}_x\mathrm{InSe}, \tag{4.7}$$

$$2\mathrm{Li} + \mathrm{InSe} \rightarrow \mathrm{Li}_2\mathrm{Se} + \mathrm{In}^0. \tag{4.8}$$

The effect of Li insertion on the electronic structure of InSe has been evidenced by photoluminescence, Raman scattering, and absorption measurements [48, 49]. Upon lithium insertion, one observes different features in the optical spectra of Li_xInSe, which appear to be strongly dependent on the Li concentration. For $x \approx 0.1$, a blue shift of the fundamental absorption threshold is due to the destabilization of both the highest valence band and the lowest conduction band. This is attributed to the (s, p_z) character of these energy states which interact with the lithium *s*-orbital. New broad bands appeared at 1.278 and 1.206 eV in the photoluminescence spectrum of $Li_{0.1}$InSe, which were attributed to transitions associated with the lattice deformations introduced by the expansion perpendicular to the basal plane and to those associated with the lithium donor levels, respectively [49].

Figure 4.17 displays the evolution of Raman spectra of Li_xInSe. The structural modification due to lithium insertion is clearly shown from these experiments. The vibrational feature of γ-InSe (C^5_{3v} symmetry) includes six Raman-active modes such as $3A_1 + 3E$ [50]. The Raman spectrum displays a low-frequency band at 41 cm^{-1} (*E* species), a strong band at 117 cm^{-1} (A_1 species), three bands located in the polar phonon domain at 177, 199, and 211 cm^{-1} (LO and TO modes), and a

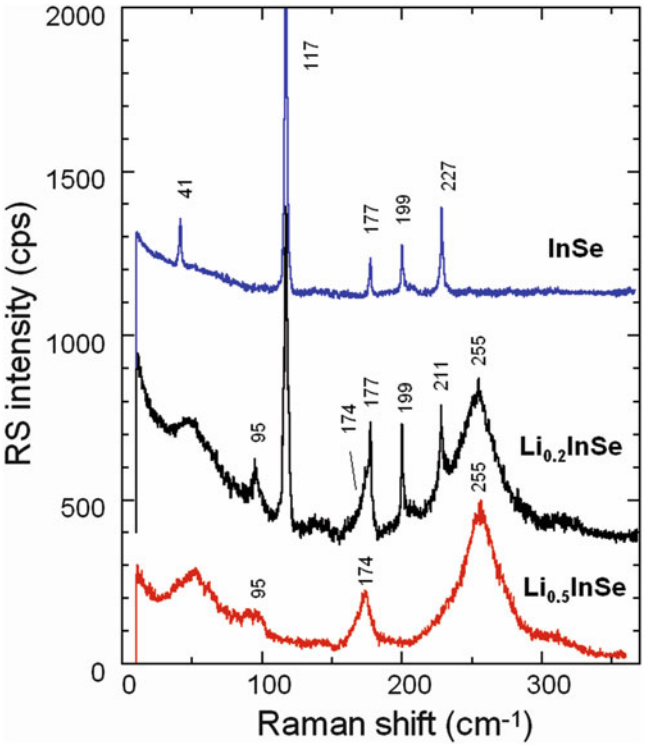

Fig. 4.17 Raman scattering spectra of pristine and Li intercalated γ-InSe single crystal. The intercalated samples were prepared by galvanostatic method in lithium cell

nonpolar mode at 225 cm^{-1} (A_1 species). After intercalation ($x \approx 0.2$), the Raman spectrum is drastically modified. It displays vanishing bands of the pristine material and additional broad peaks centered at 95, 174 and 257 cm^{-1}. These bands, which are attributed to the presence of Li_2Se and amorphous Se in the host lattice, respectively, dominate the RS spectrum for $x = 0.5$. Here, the bending mode, ν(Se-Li-Se), appears at 174 cm^{-1} in Li_xInSe. At this stage, the crystal is partially decomposed in the presence of Li producing Li_2Se, amorphous Se and In metal. At this stage, we explain these experimental data by the simple schematic band structure presented in Fig. 4.18. At relatively low lithium concentration ($x \approx 0.1$), we assume the picture (Fig. 4.18a) where the principal electronic states are grouped into two categories (s, p_z) and (p_x, p_y). The electronic lithium-like s-orbital, which is located at the higher position energy into the conduction band, repulses the lower levels of same symmetry (Fig. 4.18b). The effect of Li intercalation on the interband optical transitions is rather weak but nevertheless clearly observable [52]. These results suggesting a decomposition process are in good accordance with the potential-composition curve (not shown) in which the plateau represents

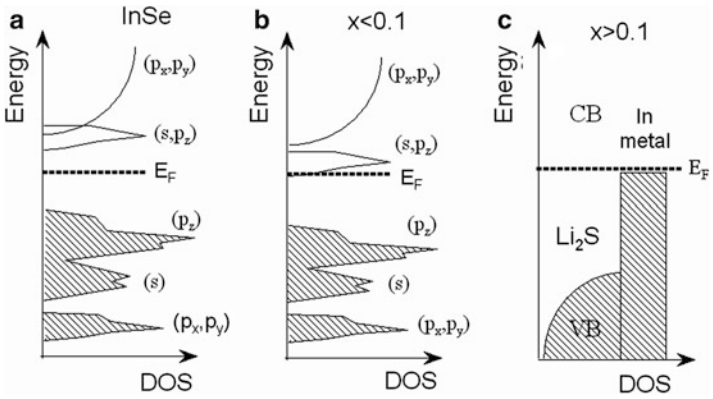

Fig. 4.18 Schematic representation of the electronic band structure evolution of InSe upon Li insertion. (**a**) pristine material, (**b**) Li_xInSe for $x \leq 0.1$, and (**c**) Li_xInSe for $x \geq 0.1$ showing the chemical decomposition

the Gibbs free energy $\Delta G_{react} = -140$ kJ mol^{-1} for the decomposition reaction of InSe by Li. This means for $x > 0.1$, a chemical decomposition of InSe occurs with two competitive reactions given by Eqs. (4.1) and (4.2).

4.9 Electrochemical Properties of TMCs

Figure 4.19 compares the discharge profile of prior nonaqueous rechargeable lithium batteries including lithium metal as anode, 1 mol L^{-1} $LiClO_2$ in propylene carbonate (PC) as electrolyte and MX_2 dichalcogenide as cathode. Such positive electrodes have several advantages: (1) they deliver high voltage, (2) water hydrogen is not liberated by electrolytic reduction, (3) materials exhibit high conductivity, and (4) these electrodes are insoluble in electrolyte solvents such as PC [51]. Note that PC cannot be used with graphitic carbon as negative electrode, but we consider in this chapter only half-cells, i.e., lithium metal is the negative electrode. The change of the cell voltage depends in general on the electronic states of the material. During the runaway, the voltage is also a function of the electrode composition x, which represents the fraction of electrons in the $Li_x<H>$ host. Also, Li–Li interactions play a role in determining the magnitude of the voltage. It is therefore instructive to analyze the dependence of the voltage, V vs. x. Operating voltage of a solid-state redox reaction associated with lithium ions insertion or extraction usually exhibits subtle dependence on the concentration of lithium ions and electrons in a solid matrix, which does not follow the simple Nernst equation. Problems that have limited the usefulness of these batteries are associated to the dendritic growth which eventually generate short circuit between the negative and the positive electrodes.

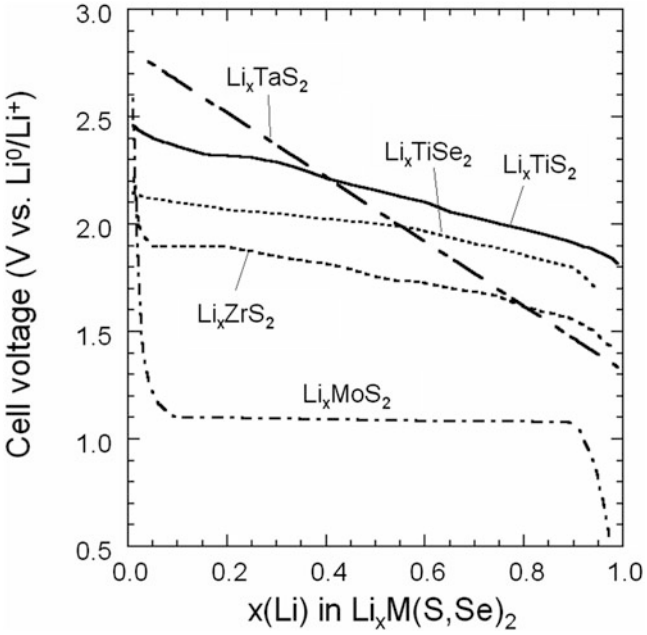

Fig. 4.19 Discharge voltage curves of the Li intercalation reaction into several TMD frameworks

4.10 Concluding Remarks

In this chapter we have shown that intercalation is a heterogeneous process in layered materials. Consequently, the rigid-band model leaving the electronic band structure of the host mostly unchanged can only be rarely applied. The electronic band structure of transition-metal dichalcogenides of group IV with the octahedral coordination in their *X*-*M*-X sandwich is not really affected by the lithium intercalation. There are two main energy terms to be considered in relation to the stability of a given coordination structure. These are the lattice energy term on the one hand which is based on ionicity and the Coulomb interactions between ions (the Madelung energy), and the electronic band energy term on the other, which depends on the energy position of the filled bands, particularly that of the occupied d_{z2} band (the lowest lying *d* sub-band of the *d*-band manifold).

The striking example is the reactivity of lithium with III-VI layered compounds such as the decomposition of Li intercalated InSe with the formation of lithium selenide, Li_2Se, observed by Raman spectroscopy on specimens prepared by various intercalation methods. The insertion of Li into MoS_2 appears more stable with the occurrence of a superlattice formation at $x(\mathrm{Li}) \approx 0.25$ but a structural transformation from 2H-MoS_2 (β-phase) to 1T-MoS_2 (α-phase) occurs for $x \approx 1$. This process is irreversible but the intercalation-deintercalation reaction is possible with the 1T-MoS_2, which could act as a positive electrode in rechargeable lithium batteries after formation of the cells.

References

1. Liang WY (1989) Electronic properties of intercalation compounds. Mater Sci Eng B 3:139–143
2. Wilson JA (1977) Concerning the semimetallic characters of TiS_2 and $TiSe_2$. Solid State Commun 22:551–553
3. Laubach S, Schmidt PC, Ensling D, Schmid S, Jaegermann W, Thisen A, Nikolowskid K, Ehrenberg H (2009) Changes in the crystal and electronic structure of $LiCoO_2$ and $LiNiO_2$ upon Li intercalation and de-intercalation. Phys Chem Chem Phys 11:3278–3289
4. Sellmyer DJ (1978) Electronic structure of metallic compounds and alloys. Solid State Phys 33:83–248
5. Jones H (1934) The theory of alloys in the γ-phase. Proc R Soc London Ser A 144:225–234
6. Friedel J (1954) Electronic structure of primary solid solutions in metals. Adv Phys 3:446–507
7. Goodenough JB, Kim Y (2010) Challenges for rechargeable Li batteries. Chem Mater 22:587–603
8. Wilson JA, Yoffe AD (1969) The transition metal dichalcogenides discussion and interpretation of the observed optical, electrical and structural properties. Adv Phys 18:193–335
9. Huisman R, de Jong R, Haas C (1971) Trigonal-prismatic coordination in solid compounds of transition metals. J Solid State Chem 3:56–66
10. Williams PM (1976) Photoemission studies of materials with layered structures. In: Lee PA (ed) Physics and chemistry of materials with layered structure, vol 4. Reidel, Dordrecht, pp 273–341
11. Brown BE, Beerntsen DJ (1965) Layer structure polytypism among niobium and tantalum selenides. Acta Crystallogr 18:31–36
12. Hibma TJ (1982) Structural aspects of monovalent cation intercalates of layered dichacogenides. In: Whittingham MS, Jacobson AJ (eds) Intercalation chemistry. Academic, New York, pp 285–313
13. Julien C, Balkanski M (1993) Is the rigid band model applicable in lithium intercalation compounds? Mater Res Soc Symp Proc 293:27–37
14. Julien C, Samaras I, Gorochov O, Ghorayeb AM (1992) Optical and electrical-transport studies on lithium-intercalated TiS_2. Phys Rev B 45:13390–13395
15. Klipstein PC, Pereira CM, Friend RH (1984) Transport and Raman investigation of the group IV layered compounds and their lithium intercalates. In: Acrivos JV, Mott NF, Yoffe AD (eds) Physics and chemistry of electrons and ions in condensed matter, NATO-ASI Series, Ser. C 130. Reidel, Dordrecht, pp 549–559
16. Klipstein PC, Friend RH (1987) Transport properties of Li_xTiS_2 ($0 < x < 1$): a metal with a tunable Fermi level. J Phys C 20:4169–4180
17. Ghorayeb AM, Friend RH (1987) Transport and optical properties of the hydrazine intercalation complexes of TiS_2, $TiSe_2$ and ZrS_2. J Phys C 20:4181–4200
18. Beal AR, Nulsen S (1981) Transmission spectra of lithium intercalation complexes of some layered transition-metal dichalcogenides. Phil Mag B 43:965–983
19. Isomaki H, von Boehm J, Krusius P (1979) Band structure of group IVA transition-metal dichacogenides. J Phys C 12:3239–3252
20. Julien C, Ruvalds J, Virosztek A, Gorochov O (1991) Fermi liquid reflectivity of TiS_2. Solid State Commun 79:875–878
21. Virosztek A, Ruvalds J (1990) Nested-Fermi-liquid theory. Phys Rev B 42:4064–4072
22. Scholz GA, Frindt RF (1983) Transmission spectra of silver intercalated 2H-TaS_2 and 1T-TiS_2. Can J Phys 61:965–970
23. Broadhead J, Butherus AD (1972) Rechargeable nonaqueous battery. US Patent 3,791,867, Accessed 12 Feb 1974
24. Ghorayeb AM, Liang WY, Yoffe AD (1986) Band structure changes upon lithium intercalation. In: Dresselhaus MS (ed) Intercalation in layered compounds, NATO-ASI Series, Ser B 148. Plenum, New York, pp 135–138

25. Liang WY (1986) Electronic properties of transition metal dichalcogenides and their intercalation complexes. In: Dresselhaus MS (ed) Intercalation in layered compounds, NATO-ASI Series, Ser. B 148. Plenum, New York, pp 31–73
26. Py MA, Haering RR (1983) Structural destabilization induced by lithium intercalation in MoS_2 and related compounds. Can J Phys 61:76–84
27. Selwyn LS, McKinnon WR, von Sacken U, Jones CA (1987) Lithium electrochemical cells at low voltage. Decomposition of Mo and W dichalcogenides. Solid State Ionics 22:337–344
28. Samaras I, Saikh I, Julien C, Balkanski M (1989) Lithium insertion in layered materials as battery cathodes. Mater Sci Eng B 3:209–214
29. Julien CM (2002) Lithium intercalated compounds: charge transfer and related properties. Mater Sci Eng R 40:47–102
30. Hearing RR, Stiles JAR, Brandt Klaus (1979) Lithium molybdenum disulphide battery cathode. US Patent 4,224,390, Accessed 23 Sep 1980
31. Chrissafis K, Zamani M, Kambas K, Stoemenos J, Economou NA, Samaras I, Julien C (1989) Structural studies of MoS_2 intercalated by lithium. Mater Sci Eng B 3:145–151
32. Sekine T, Julien C, Samaras I, Jouanne M, Balkanski M (1989) Vibrational modifications on lithium intercalation in MoS_2. Mater Sci Eng B 3:153–158
33. Julien C, Sekine T, Balkanski M (1991) Lattice dynamics of lithium intercalated MoS_2. Solid State Ionics 48:225–229
34. Mattheis LF (1973) Band structure of transition-metal-dichalcogenide layer compounds. Phys Rev B 8:3719–3740
35. Tsai HL, Heising J, Schindler JL, Kannewurf CT, Kanatzidis MG (1997) Exfoliated-restacked phase of WS_2. Chem Mater 9:879–882
36. Rüdorff W (1966) Reaktionen stark elktropositiver metalle mit graphit und mit metalldichalcogeniden. Angew Chem 78:948
37. Somoano RB, Hadek V, Rembaum A (1973) Alkali metal intercalates of molybdenum disulphide. J Chem Phys 58:697–701
38. Omloo WPF, Jellinek F (1970) Intercalation compounds of alkali metals with niobium and tantalum dichalcogenides. J Less Common Metals 20:121–129
39. Julien C, Yebka B (1996) Studies of lithium intercalation in 3R-WS_2. Solid State Ionics 90:141–149
40. DiSalvo FJ, Bagley BG, Voorhoeve JM, Waszczak JV (1973) Preparation and properties of a new polytype of tantalum disulfide (4Hb-TaS_2). J Phys Chem Solids 34:1357–1362
41. Julien C (1990) Technological applications of solid state ionics. Mater Sci Eng B 6:9–28
42. Julien C, Yebka B, Porte C (1998) Effects of the lithium intercalation on the optical band edge of WS_2. Solid State Ionics 110:29–34
43. Likforman A, Carre D, Etienne J, Bachet B (1975) Structure cristalline du monosélénium d'indium InSe. Acta Crystallogr B 31:1252–1254
44. Ikari T, Shigetomi S, Hashimoto K (1982) Crystal structure and Raman spectra of InSe. Phys Status Sol (b) 111:477–481
45. Levy-Clement C, Rioux J, Dahn JR, McKinnon WR (1984) In-situ X-ray characterization of the reaction of lithium with InSe. Mater Res Bull 19:1629–1634
46. Schellenberger A, Lehman J, Pettenkofer C, Jaegermann W (1994) Electronic structure of in-situ (in UHV) prepared Li/InSe insertion compounds. Solid State Ionics 74:255–262
47. Schellenberger A, Jaegermann W, Pettenkofer C, Tomm Y (1995) Electronic structure and electrochemical potential of electrons during alkali intercalation in layered materials. Ionics 1:115–124
48. Julien C, Jouanne M, Burret PA, Balkanski M (1989) Effects of lithium intercalation on the optical properties of InSe. Mater Sci Eng B 3:39–44
49. Burret PA, Jouanne M, Julien C (1989) Theoretical calculations and Raman spectrum of intercalation modes in Li_xInSe. Z Phys B Condensed Matter 76:451–455
50. Kuroda N, Nishina Y (1978) Resonant Raman scattering at higher M_0 exciton edge in layer compound InSe. Solid State Commun 28:439–443
51. Julien C, Nazri GA (2001) Intercalation compounds for advanced lithium batteries. In: Nalwa HS (ed) Handbook of advanced electronic and photonic materials, vol 10. Academic Press, San Diego, pp 99–184

Chapter 5
Cathode Materials with Two-Dimensional Structure

5.1 Introduction

For over 40 years, researchers have actively focused their works on the study of physicochemical properties of the so-called low-dimensional solids. Indeed these compounds find major applications in the conversion and storage of energy. Different steps in the progress in this field can be identified. DiSalvo in 1971, investigated the properties of transition-metal chalcogenides (TMCs) as intercalation complexes for advanced devices such as superconductors [1]. Broadhead invented, in July 1972, the first rechargeable nonaqueous battery in which the active material is incorporated in the layer structure; his patent suggests the use of TMCs such as TiS_2 and WS_2 [2]. Goodenough has established the ability of fast-ion conduction of certain metal oxides [3]; his discovery was soon followed by Japanese companies that commercialized the first lithium-ion batteries (LiBs). The lithium-ion technology has opened a wide research field both in physics and chemistry to find a class of materials for high voltage cells [1–3]. However, there remain several key materials issues such as the structural stability over several hundreds of cycles, which need to be solved. In the area of positive electrode materials, extensive investigations on the requirements of optimum-ideal electrode system have shown that transition-metal oxides, $A_xM_yO_n$ ($A =$ Li, Na; $M =$ Ni, Co, Mn, Cr, Fe) are the most promising systems with great potential for structural improvements for long cycle life.

This chapter provides the relationships between structural and electrochemical properties of lamellar compounds: the 3d-transition metal oxides currently studied as for their potential use in LiBs. First, we examine briefly three binary layered oxides, MoO_3, V_2O_5, and LiV_3O_8 which were proposed as intercalation compounds since at the end of 1970s. Then, the ternary layered oxides are considered. Starting from the historical and prototype compound $LiCoO_2$, which is the dominant positive electrode material employed by all Li-ion cell manufacturers so far, we state the broad family of layered oxides such as LiM_xO_y and their derivatives: the

C. Julien et al., *Lithium Batteries*, DOI 10.1007/978-3-319-19108-9_5

metal-doped oxides $LiM_xM'_zO_y$, the solid-solutions LiM_xO_y-LiM'_xO_y and the composite materials such as the Li-rich oxides. For each class of materials, we review their electrochemical properties and discuss them as a function of the structural stability of the lattices. The surface modification (coating or encapsulation) of active particles that has led recently to encouraging results is also reviewed and discussed.

5.2 Binary Layered Oxides

5.2.1 MoO_3

The oxides and oxide-hydrates of molybdenum in its highest oxidation state display a variety of structural types involving linked MoO_6 octahedra. MoO_3 is such a host. Of the anhydrous MoO_3, the well-known orthorhombic form (α-MoO_3) is the stable form in normal conditions, which possesses a layered structure as shown in Fig. 5.1

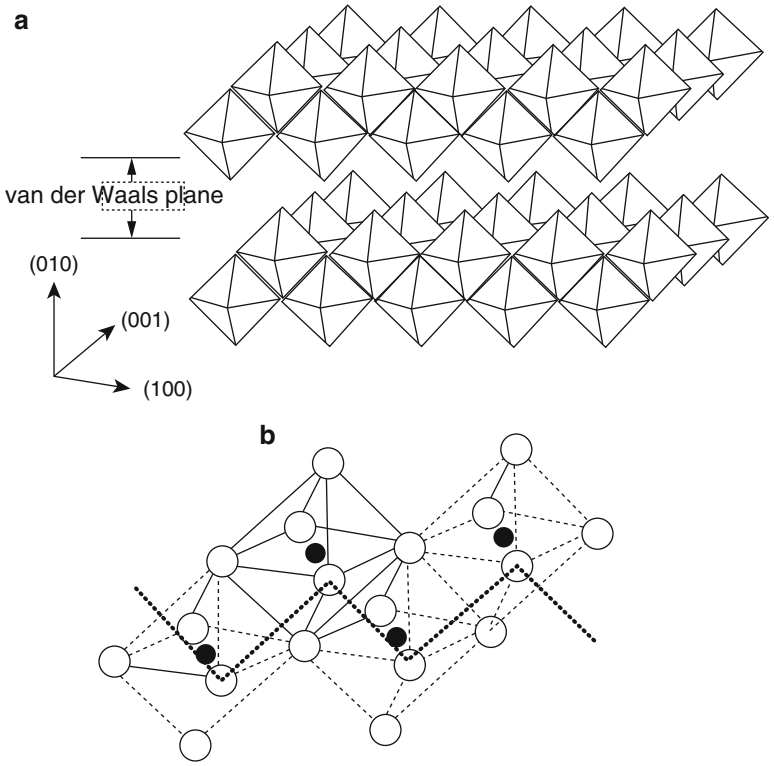

Fig. 5.1 (**a**) The layered structure at α-MoO_3 showing the interlayer van der Waals gap. (**b**) Detail of the Mo coordination

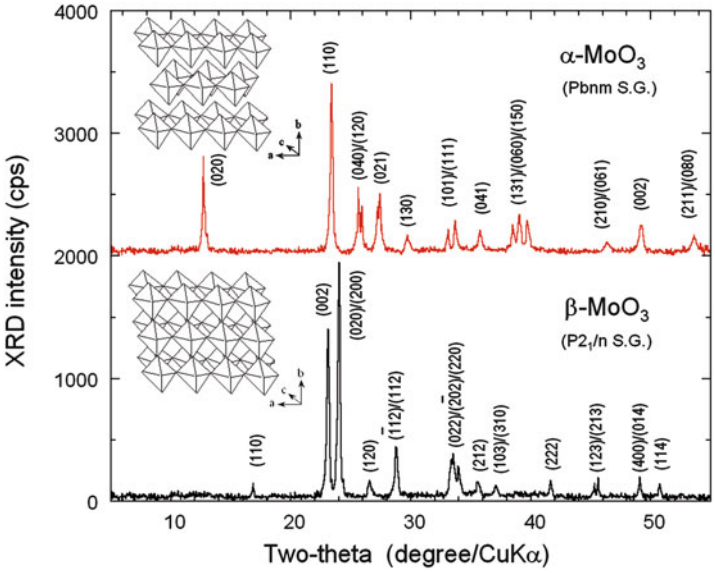

Fig. 5.2 XRD patterns of α-MoO_3 and β-MoO_3 crystals indexed in the monoclinic ($P2_1/n$ S.G.) and orthorhombic (*Pbnm* S.G.) system, respectively

[4] and three metastable phases: the β-MoO_3 phase which adopts the ReO_3-related structure, the MoO_3-II or ε-MoO_3 ($P2_1/m$ S.G.) metastable high pressure phase and the hexagonal MoO_3 form (h-MoO_3). Among the three stoichiometric solid hydrates of MoO_3 or "molybdic acids," white $MoO_3 \cdot H_2O$ has a structure closely related to that of α-MoO_3 [5], consisting of isolated double chains of edge-sharing MoO_6 octahedra with each molybdenum atom bearing a coordinated water molecule.

Figure 5.2 shows the XRD patterns of α-MoO_3 and β-MoO_3 crystalline samples with the main features of the XRD patterns indexed in the orthorhombic (*Pbnm* S.G.) system with lattice parameters $a = 3.9621(4)$ Å, $b = 13.858(8)$ Å, $c = 3.972(1)$ Å and in the monoclinic ($P2_1/n$ S.G.) system with lattice parameters $a = 7.118(7)$ Å, $b = 5.379(2)$ Å, $c = 5.566(6)$ Å, $\beta = 91.87°$, respectively. Single crystals of α-MoO_3 have the shape of elongated platelets with the (010) axis perpendicular to the basal plane and the (001) axis along the longest edge. The orthorhombic structure was formed above 500 °C. The layered arrangement causes van der Waals interactions between parallel layers formed by MoO_6 octahedra that share edges in the (001) direction and are connected by corners in the (100) direction. The (0 *k*0) intense Bragg lines suggest that this compound is a layered structure packed in the direction of the *b*-axis. The hexagonal MoO_3 is commonly synthesized using the chemical precipitation method and crystallizes with lattice parameters $a = 10.55$ Å and $c = 14.89$ Å ($P6_3/m$ S.G.).

Molybdenum oxides display a variety of structural types involving linked MoO_6 octahedra whose arrangements are favorable for intercalation process. Several studies have shown that Li^+ ions can be reversibly incorporated in Mo-O compounds [6–9]. The Li//α-MoO_3 system undergoes redox reactions with high reversibility, accommodating up to 1.5 Li per Mo atom and giving rise to a theoretical energy density of 745 Wh kg^{-1}, whereas the theoretical energy density of $MoO_{2.765}$ (~490 Wh kg^{-1}) is comparable to that of TiS_2. Despite the apparent diversity of the structural types shown by the Mo(VI) oxides and molybdenum-oxide hydrates, it is evident that they possess a number of common features in their reactions with lithium. Mo oxides offer high voltages and wide composition intervals accessible for lithium intercalation. The interest of α-MoO_3 arises from its layered structure presenting open channels for fast Li-ions diffusion, a higher electrochemical activity vs. Li^0/Li^+ than that of chalcogenides and the highest chemical stability among the oxide lattices [10].

The electrochemical lithium insertion into the MoO_3 framework can be described according the following reaction:

$$x\mathrm{Li}^+ + xe^- + \left[\mathrm{Mo}^{\mathrm{VI}}\right]\mathrm{O}_3 \leftrightarrows \mathrm{Li}_x^+\left[\mathrm{Mo}^{(6-x)+}\right]\mathrm{O}_3, \tag{5.1}$$

Assuming the reduction from Mo^{VI} to Mo^{V} and Mo^{IV} valence states, the maximum Li uptake occurs at $x = 1.5$. Figure 5.3 shows the discharge–charge curves of the Li//MoO_3 cell using anhydrous well-crystallized powders of the α-phase [11]. The electrochemical lithium insertion into the MoO_3 framework can be described assuming the reduction from Mo(VI) to Mo(V) and Mo(IV) oxidation states. The

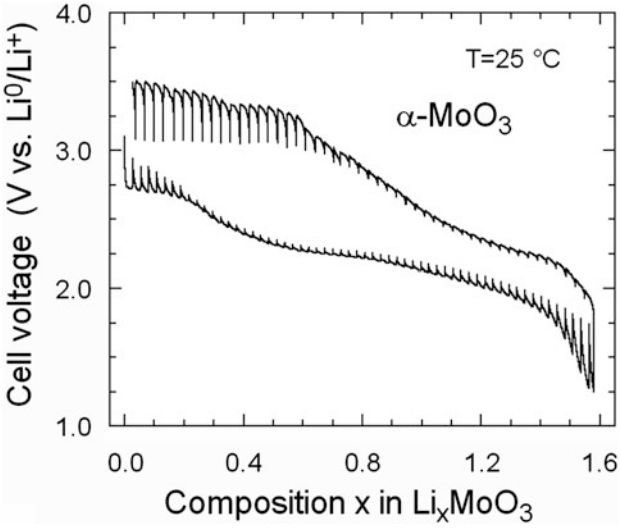

Fig. 5.3 Discharge–charge curves of the Li//MoO_3 cell using anhydrous well-crystallized powders of the α-phase. Reproduced with permission from [11]. Copyright 1997 Springer

capacity of MoO_3 observed here is approximately in agreement with the theoretical gravimetric capacity 280 mAh g^{-1}. α-MoO_3 is a very advantageous cathode material because it acts as a self-limiting voltage element at the end of the charge as reoxidation of Mo produces a resistive effect which induces a large polarization of the cell for potential of ≈3.5 V (Fig. 5.3).

Nadkarni and Simmons [12] studied the electrical properties of MoO_3 and reported that there is a donor band between the conduction and the valence bands due to oxygen vacancies. MoO_3 has the outer electron configuration $4s^5\ 5s^1$. If MoO_3 is considered to be ionic, i.e., composed only of Mo^{VI} and O^{2-} ions, the valence band would be composed of oxygen 2p states and the conduction band of empty 4*d* and 5*s* states [13]. Figure 5.4 shows the temperature dependence of the electrical conductivity of Li_xMoO_3 ($0.0 \leq x \leq 0.3$) intercalated by electrochemical titration. Upon Li intercalation the electrical conductivity of Li_xMoO_3 increases by two orders of magnitude and the temperature dependence of σ shows important changes in the conduction mechanism. The semiconducting character of MoO_3 gradually disappears and a degenerate semiconductor behavior is observed. For a degree of intercalation of $x = 0.3$, the material exhibits a metallic behavior. The metallic features are also observed in the temperature dependence of the Hall coefficient. This variation of mass is detected by the analysis of the absorption spectra near the plasma frequency. It is admitted that the mechanism for the conductivity of MoO_3 is the electron hopping between Mo^{6+} and Mo^{5+} sites. The increase of the conductivity with the addition of intercalants observed in Fig. 5.4 is linked to the diminution of the valence state of molybdenum ions by transfer of electrons from lithium to molybdenum. Further experiments are needed to elucidate the mechanism of the charge transfer occurring in transition-metal oxide compounds but the rigid-band model seems adequate in Li_xMoO_3 which found technological application in electrochromic rear mirror in automotive industry.

In MoO_3, electrical conductivity comes from the hopping of electrons forming small polarons between Mo^{6+} and Mo^{5+} ions. Infrared absorption studies of Li_xMoO_3 compounds revealed a transition small polaron to metallic features [14],

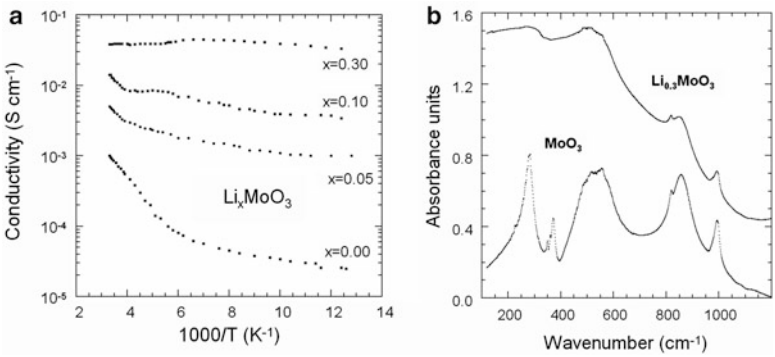

Fig. 5.4 (**a**) Arrhenius plot of the electrical conductivity of α-MoO_3 and Li_xMoO_3 and (**b**) FTIR absorption spectra of α-MoO_3 and $Li_{0.3}MoO_3$

in agreement with the analysis of the electrical conductivity. After intercalation the lattice vibration spectrum is completely screened by the free electrons in the host material. The Drude edge contribution, i.e., plasmon feature, is responsible for the metallic absorption due to high electron density in $Li_{0.3}MoO_3$ as shown in Fig. 5.4. The free-carrier absorption coefficient can be expressed by:

$$\alpha = \omega_p^2 \, \tau \left[n \;\; c\left(1 + \omega^2 \tau^2\right)\right], \tag{5.2}$$

where ω_p is the plasma frequency, τ is the relaxation time of the free carrier, n is the refractive index, and c is the light velocity. Using Eq. (5.2), the fit of experimental data gives a carrier concentration of 5×10^{16} cm^{-3} in $Li_{0.3}MoO_3$. This value is in good agreement with the Hall measurements. In MoO_3, the bonding framework is composed of five O(p_π) and three Mo(t_{2g}) orbitals, which interact to form π and π* bands [5]. As the extra electrons supplied by the inserted lithium are in the antibonding π* states, $Li_{0.3}MoO_3$ is expected to exhibit a two-dimensional type of electronic conductivity. The narrowing of the conduction band leads to an increase in the effective electron mass which affects the position of the Drude edge in Li_xMoO_3 phases. The temperature dependence of the absorption coefficient shows a small increase of α with temperature, which can be attributed to the fact that Li-intercalated MoO_3 is a degenerate semiconductor for $x = 0.3$.

5.2.2 V_2O_5

Vanadium pentoxide, V_2O_5, was one of the earliest studied ICs that can exhibit several different phases upon intercalation of 3Li per formula. V_2O_5 crystallizes with an orthorhombic unit cell structure and belongs to the *Pmnm* space group with lattice parameters $a = 11.510$ Å, $b = 3.563$ Å, and $c = 4.369$ Å [15, 16]. The crystal structure of orthorhombic V_2O_5 is usually described as made up of chains of edge-sharing VO_5 square pyramids (Fig. 5.5a). These chains are linked together via corner sharing. The distorted polyhedra have a short vanadyl bond (1.54 Å) and four oxygen atoms located in the basal plane at distances ranging from 1.78 to 2.02 Å (Fig. 5.5b). Here, the oxygen atoms surrounding a vanadium atom are geometrically labelled O_1, O_{21}, O_{23}, O'_{23}, and O_3, respectively. In the deformed octahedron including the O'_1 atom, a V–O_1 bond length is the shortest: 1.54 Å, and a V–O'_1 distance is 2.81 Å. The deformed octahedrons, which have common corners in the b direction are linked by common edges, giving rise to chains in the a-direction.

The complex phase diagram of lithia-vanadium pentoxide had been described by several groups [17–19] employing electrochemical and chemical synthesis. Figure 5.6 shows a schematic representation of the α- and γ-$Li_xV_2O_5$ structure and the Li-V_2O_5 phase diagram proposed by Galy [20]. The discharge curve of a Li// $Li_xV_2O_5$ cell in the range $0 \leq x \leq 3$ is shown in Fig. 5.7. It is seen that insertion of up to 1 Li per formula unit proceeds in two distinct steps, each accounting for

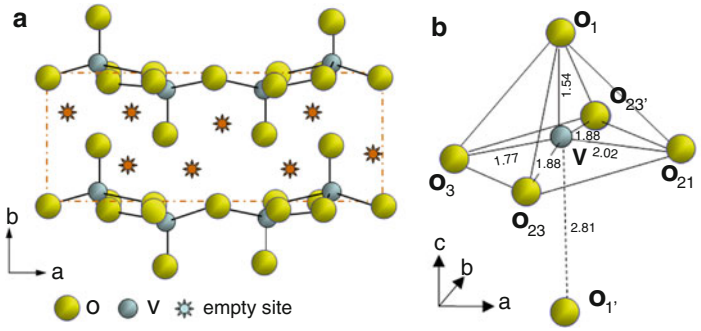

Fig. 5.5 (**a**) Projection of the layered structure of V_2O_5 on (001). Superimposed oxygen atoms are symmetrically displaced. (**b**) The deformed pyramid of the V_2O_5 structure, shown with the coordinate system and labels of V, O_1, O_{21}, O_{23}, and O_3 atoms. The *solid* and *dashed lines* schematically represent the chemical bonds, and numerical values indicate the bonding length (Å) between atoms. The O'_1 atom is the O_1 type atom belonging to the neighbor pyramid painting at opposite direction

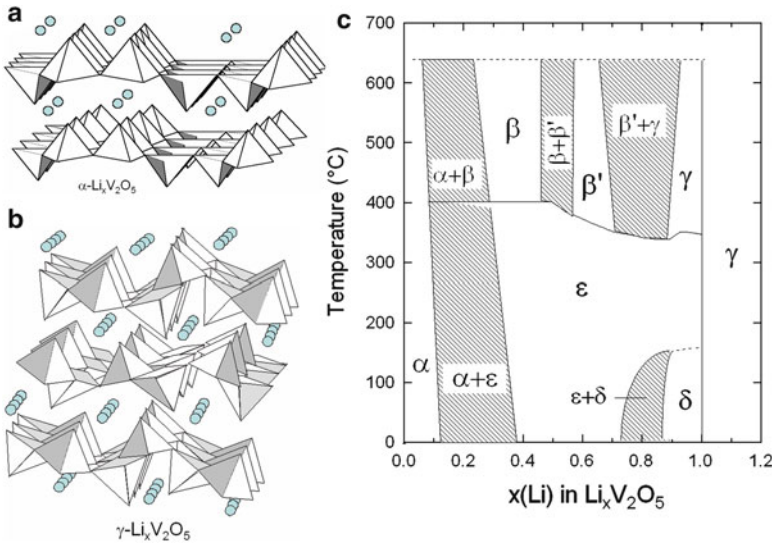

Fig. 5.6 Schematic representation of (**a**) α-$Li_xV_2O_5$, (**b**) γ-$Li_xV_2O_5$, and (**c**) the Li-V_2O_5 phase diagram

half the charge. Upon lithium intercalation up to $x = 3$ in $Li_xV_2O_5$, a series a structural rearrangement (α-, ε-, δ-, and γ-$Li_xV_2O_5$ phases) emerges that corresponds to a theoretical specific capacity of 442 mAh g^{-1}.

When the amount of lithium content is increased beyond $x = 1$, the discharge curve exhibits a sharp potential drop followed by a region with a plateau characteristic of a two-phase domain, for which the δ- and γ-$Li_xV_2O_5$ phases are in

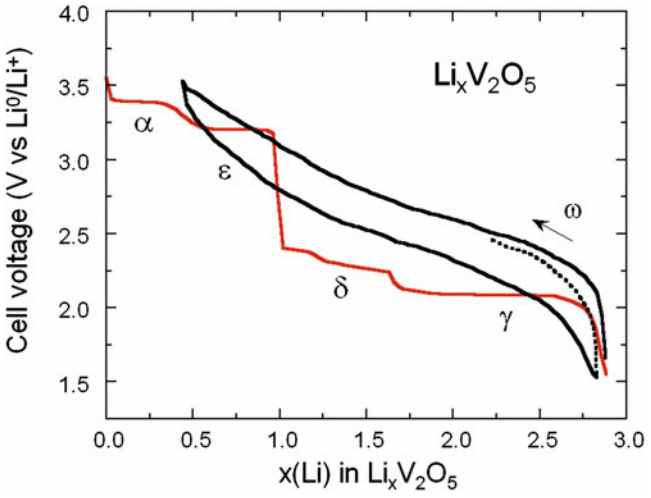

Fig. 5.7 Discharge curve of the Li//$Li_xV_2O_5$ electrochemical cell. At $x = 3$, the system reaches the NaCl-like ω-$Li_{3-x}V_2O_5$ phase (*black curve*)

equilibrium. When the amount of lithium inserted is restricted to $x < 2$, the reversibility in the composition range $0 < x < 1$ is not much affected [21]. At $x \approx 3$, the new ω-V_2O_5 phase appears [22, 23]. This phase has a NaCl-like structure with high number of vacancies. In shear vanadium oxide, V_2O_5, the O^{2-} along the shear planes are bonded to three cations and, indeed, high values of the chemical diffusion coefficient have been measured. $Li_xV_2O_5$ shows values of 10^{-8} cm^2 s^{-1} in the range 0.01–0.98 [24]. Recently, Li et al. [25] reported the lithium insertion in the β-$Li_xV_2O_5$ phases ($0 < x \leq 3$) for powders synthesized by the hydrothermal treatment of α-V_2O_5 at 220 °C for 24 h followed by post-heating at 650 °C for 3 h. The rigid 3D host lattice of the monoclinic tunnel-like β-V_2O_5 shows desirable reversibility upon 3Li uptake per formula unit and a discharge capacity exceeding 330 mAh g^{-1} at current density 10 mA g^{-1} in the potential range 4.0–1.8 V.

5.2.3 *LiV_3O_8*

Lithium trivanadate, LiV_3O_8, is a mixed-valence oxide. Firstly reported by Wadsley [26], LiV_3O_8 is a quasi-layered compound, which can be regarded as a lithia-stabilized V_2O_5 compound. It crystallizes in a monoclinic symmetry ($P2_1/m$ S.G.) and consists of octahedral (VO_6) octahedral and trigonal bipyramidal (VO_5) ribbons. In this structure, distorted (VO_6) octahedra are connected by shared edges and vertices to form $(V_3O_8)^-$ anions that stack one upon another to form quasi layers (Fig. 5.8). The spacing between slabs is sufficiently flexible to accommodate guest species on octahedral and tetrahedral interstitial sites [27, 28].

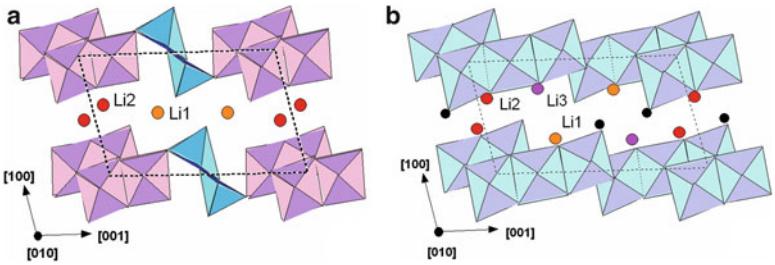

Fig. 5.8 (**a**) Representation of [010] view of the layered structure of LiV_3O_8 ($P2_1/m$ S.G.). The *circles* represent the octahedral site Li(1) and the tetrahedral site Li(2) between the layers. (**b**) [010] View of the structure of $Li_4V_3O_8$. The *c*-axis is horizontal within a V_3O_8 layer

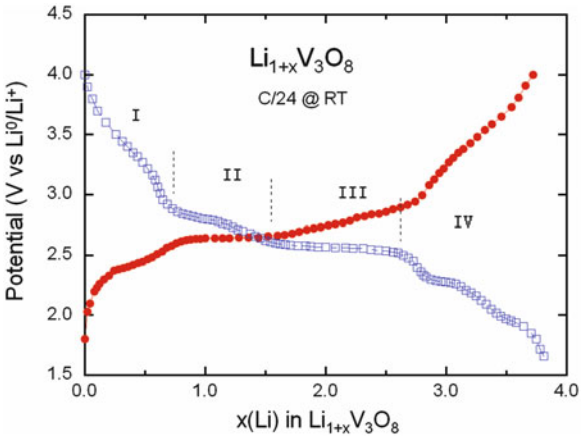

Fig. 5.9 The typical voltage vs. composition *x*(Li) curve for Li//LiV_3O_8 cell. The discharge–charge processes is rather complex reactions that correspond to multistep Li insertion–extraction associated with the reduction–oxidation of vanadium ions. The different steps are indicated

When intercalating Li^+ ions into the LiV_3O_8 framework to the composition of $Li_4V_3O_8$, the V_3O_8 framework remains intact and the monoclinic unit cell parameters vary isotropically with phase changes [29]. As reported by several workers [28, 30–34], the V_3O_8 sublattice is very stable upon lithiation leading to composition $Li_{3.8}V_3O_8$ owing to the availability of the 2D interstitial space for the transport of Li^+ ions. This feature makes LiV_3O_8 an attractive cathode candidate for lithium secondary batteries with a specific capacity higher than 300 mAh g^{-1}. Electrochemical intercalation mechanism was investigated including long-term cycling and kinetics Li^+ ions [35–37]. LiV_3O_8 has a lower Li-ion diffusion coefficient (~10^{-13} cm^2 s^{-1}) than $Li_xV_2O_5$ (~10^{-10} cm^2 s^{-1}) [37]. Jouanneau et al. [38] reported that the dissolution of a small quantity of V^{III} in the electrolyte occurring during the reduction at 2.3 V depends on the morphology of the powders. Figure 5.9 shows the typical voltage vs. composition *x*(Li) curve for Li//$Li_{1.2+x}V_3O_8$ cell. Initial discharge capacity of 308 mAh g^{-1} at 20 mA g^{-1} corresponds at $x = 3.8$Li uptake. The discharge curve shows a rather complex process, at first the open circuit voltage of $Li_{1.2+x}V_3O_8$ drops rapidly to 2.85 V for the composition $x \leq 0.8$ (S-shape region), where the lithium is

inserted into the interstitial sites Li(2). Then, the voltage drops less rapidly from 2.85 to 2.7 V in the domain $0.8 \leq x \leq 1.7$, where the lithium is inserted into the interstitial space of the $Li_2V_3O_8$ structure, possibly in the $S_t(1)$ and $S_t(2)$ tetrahedral sites. At $x > 1.7$, the voltage curve shows a plateau at 2.5 V characteristics of a two-phase system, with the coexistence of $Li_{2.9}V_3O_8$ compound and the defect rock-salt structure of nominal composition $Li_4V_3O_8$. $Li_{1+\delta}V_3O_8$ is a semiconductor that exhibits a polaronic conduction ($\sigma_e = 10^{-5}$ S cm^{-1} at room temperature, $E_a = 0.25$ eV).

As for all ICs, the method of preparation of LiV_3O_8 appears to be important to its electrochemical features. Synthesis technique include: the traditional solid-state reaction using Li_2VO_3 and V_2O_5 at high temperature (680 °C) [38], sol–gel method [39], precipitation technique [40], hydrothermal method [41], freeze-drying technique [42], combustion synthesis [43], spray pyrolysis route [44] and polymer assisted method [45]. West et al. [32] have compared the capacity and cycling behavior of several samples. Nanostructured LiV_3O_8 cathode materials were synthesized under several forms including nanocrystals [46, 47], nanowires [48, 49], nanorods [41, 50], and nanoflakes [51]. Improvement of the intercalation process was also achieved by effective doping [52]. Nanosheets with a thickness of 15–30 nm width were synthesized by hydrothermal method combined with a solid-state process using uniform $(NH_4)_{0.5}V_2O_5$ nanosheets as the precursor. Good cycling stability of 149 mAh g^{-1} at 5*C* was demonstrated by the stability retention of 85 % [53]. Surface modification with conducting materials appears to be efficient to enhance the electrochemical properties of LiV_3O_8 via suppressing the dissolution of active materials and the overall phase change [54]. Kumagai et al. [55] reported the use of LiV_3O_8 powders ultrasonically treated.

5.3 Ternary Layered Oxides

This class of materials include the $LiMO_2$ compounds (M = Co, Ni, Cr) and the related oxides $LiCoM'O_2$ where M' is a substituting trivalent or divalent element (M' = Ni, Cr, Fe, Al, B, Mg, etc.). $LiMO_2$ oxides adopt the α-$NaFeO_2$-type crystallographic structure that belongs to $R\bar{3}m$ (D_{3d}^5) space group. This structure derives from the NaCl structure with a stacking of Li ions between adjacent MO_2 slabs [56]. The individual coordination octahedron is face-sharing. They show higher operating voltage than the conventional 3-V systems; a relationship between the level of operating voltage of transition-metal oxides and their *d*-electron character has been recognized. Among them, $LiNiO_2$ and $LiCoO_2$, as well as their solid solutions $LiN_{1-y}Co_yO_2$, are isostructural with α-$NaFeO_2$. Crystal radius for Co^{3+} ion (68 pm) is almost the same as that of Ni^{3+} ion (70 pm) (ions in octahedral sites in the low-spin state), so that a solid solution of $LiNiO_2$ and $LiCoO_2$ may be obtained [57]. Schematic crystal structures of P2-, P3-, O2-, and O3-$LiMO_2$ are shown in Fig. 5.10. The labels "O2" and "O3" indicate that the Li environment is octahedral in both cases, but the stacking sequences of the oxygen layers are *ABCB* and *ABCABC*, leading to two and three sets of Co and Li layers in the hexagonal unit

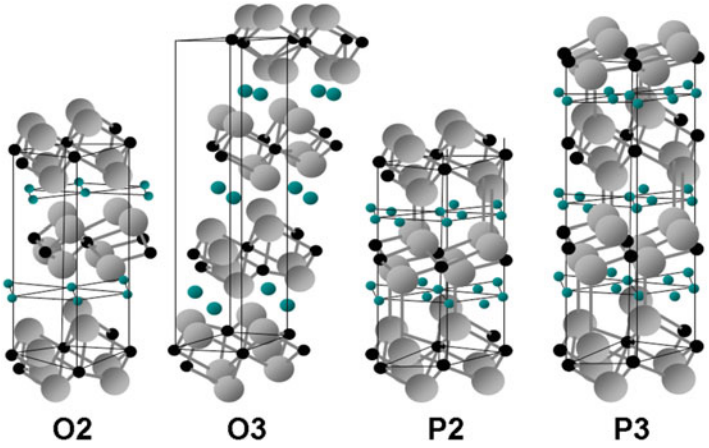

Fig. 5.10 Crystal structures of P2-, P3-, O2-, and O3-type LiMO_2. Here O states for octahedral coordination of the cation and the number corresponds to the number of layers building the unit cell. In O3-type each layer is related to the others by translation whereas in O2-type every second layer is rotated by 60°

cell, respectively. The electrochemical performance of O2-$LiCoO_2$ is competitive to that of conventional O3-$LiCoO_2$, but its synthesis is more difficult and it is thus not convenient for industrial application [58].

Studies of structural properties of the α-$NaFeO_2$ type structure have shown that the oxygen sublattice can be considered as distorted from the *fcc* array in the direction of the hexagonal *c* axis [59, 60]. Considering the XRD patterns, the trigonal distortion gives rise to a splitting of the (006, 102) and (108, 110) Bragg lines that are characteristic of the lamellar framework. When the distortion in the *c* direction is absent, the ratio of the lattice parameters, *c*/*a* is $\sqrt{24}$ (4.899), and the (006, 102) and (108, 110) lines will merge into single peaks [61].

5.3.1 *$LiCoO_2$ (LCO)*

Identified and tested by Goodenough et al. [3, 62] $LiCoO_2$ (LCO) is considered as the prototypal cathode oxide in which fast charge–discharge reaction occurs in the potential range 3.6–4.2 V [63]. After almost three decades, this material and its derivatives were still used in commercial lithium-ion batteries in the form of "normal" thermodynamically stable O3-structure as well as in the O2-structure. In the O3-$LiCoO_2$ lattice, *M* cations are located in octahedral 3*a* (000) sites and oxygen anions are in a cubic close-packing (*ccp*), occupying the 6*c* (00*z*, 000*z*) sites. Li ions reside at Wyckoff 3*b* (00½) sites. The transition-metal and lithium ions are occupying the alternating (111) planes. The Bravais cell contains one molecule ($Z = 1$). The lattice constants ($a = 2.806$ Å, $c = 9.52$ Å) show that

O2-$LiCoO_2$ has a slightly larger interlayer spacing than the conventional O3-$LiCoO_2$ lattice ($a = 2.816$ Å, $c = 14.08$ Å). This former material has a more pronounced layered structure. For the refinement of the O2-$LiCoO_2$ lattice, the $P6_3mc$ (no. 186) space group was used with oxygen and cobalt atoms located on 2*a* and 2*b* sites, respectively. The strong covalent bond in $LiCoO_2$, with reduced Co–O bond distance, results in stabilization of Co^{3+} in low-spin ground state that is $d^6 = (t_{2g})^6(e_g)^0$, $S = 0$, and reduces the electronic conductivity of the compound.

A wide range of techniques were used to prepare LCO with different characteristics: morphology, size (from micron to nanometer), and size distribution of grains, all important factors in the development of efficient cathode materials. In the synthesis of LCO, the rhombohedral structure is obtained at high temperature $T > 850$ °C (called HT-LCO), while a low temperature phase (LT-LCO) was prepared around 400 °C with a spinel structure $Li_2Co_2O_4$ [64]. Shao-Horn et al. [65] found that LT-LCO nucleates from an intermediate $Li_xCo_{1-x}[Co_2]O_4$ spinel product before transforming more slowly to HT-LCO.

The traditional solid-state process is very popular [56, 66, 67]. It consists in sintering the mixture of cobalt carbonate (or oxide) and lithium carbonate (or hydroxide) at high temperature $T \approx 850$–900 °C in air for several hours. Numerous other techniques of LCO preparation, aiming to obtain fine grains with narrower size distribution, include: sol–gel method using various chelating agents [68, 69], combustion synthesis [70], molten salt synthesis [71], mechanical activation [72], freeze-dried salt synthesis [73], hydrothermal route [74], and microwave synthesis [75]. Akimoto et al. [76] succeeded to grow $LiCoO_2$ single-crystal by a flux method of the slow cooling from 900 °C in a gold crucible.

In Fig. 5.11a, the charge–discharge characteristics of the Li//$LiCoO_2$ cell is reported with the various phase in Li_xCoO_2 in the range $0 < x < 1$ [67, 77]. In the

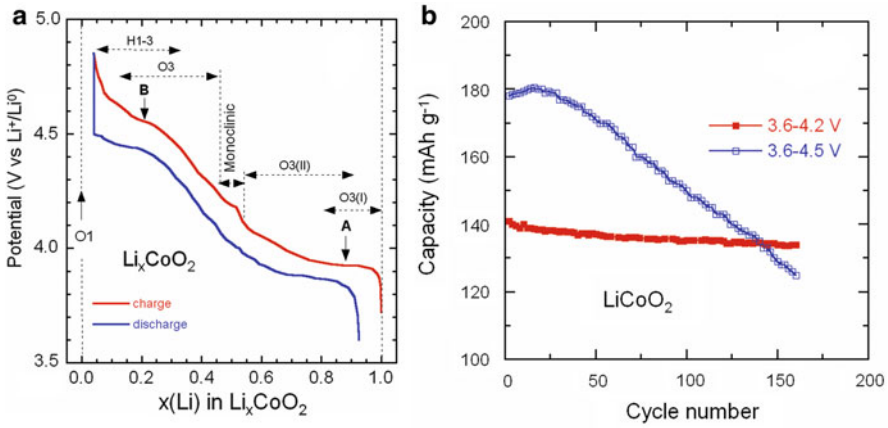

Fig. 5.11 (**a**) Electrochemical features of the Li//$LiCoO_2$ cycled in the voltage range 3.0–4.8 V. Powders were synthesized by sol–gel method. (**b**) Capacity retention as a function of the working region. When the $LiCoO_2$ electrode is operating with the cutoff voltage 3.6–4.5 V, the capacity fading becomes very important

potential domain 2.5–4.3 V, the voltage profile of $LiCoO_2$ displays the typical plateau at ca. 3.92 V, which is the characteristic feature of the first phase transition denoted H1 ↔ H2. This transition has been associated to a semiconductor-metal transition. The capacity retention of $LiCoO_2$ electrode is clearly depicted as a function of the working region. For a cell working between 3.6 and 4.2 V, the capacity is quite stable, while for a voltage cutoff 3.6–4.5 V the capacity decreases drastically with the cycle number due to the loss of oxygen at deep lithium extraction (Fig. 5.11b). The tendency to lose oxygen at lower lithium contents appears to limit the practical capacity of the Li//$LiCoO_2$ system to 140 mAh g^{-1}. Both O2-LCO and O3-LCO materials exhibit similar reversible phase transition as a function of the x(Li) [78, 79]. The first transition (at 3.90 V for O3 and 3.73 V for O2) is connected with a large change in lattice constant but minor change in crystal structure; this modification is noted H1 ↔ H2 in O3-$LiCoO_2$ and $O2_1 \leftrightarrow O2_2$ in O2-$LiCoO_2$. When Li_xCoO_2 approaches $x = 0.5$, both materials exhibit a phase transition that possibly is due to lithium ordering. This is a continuous phase transition (H2 ↔ M) to the monoclinic phase in O3. If more Li is removed, another continuous transition M ↔ H3 occurs in O3-$LiCoO_2$. However, there are some controversies on the crystal chemistry and the phase diagram of delithiated Li_xCoO_2 [80].

The structural evolution of the $LiCoO_2$ phase during Li extraction (charge process) is still subject to debate (Fig. 5.12). Structural and chemical stabilities of $Li_{1-x}CoO_{2-\delta}$ and $Li_{1-x}Ni_{0.85}Co_{0.15}O_{2-\delta}$ with $0 \leq (1-x) \leq 1$ electrode materials have been investigated by chemically extracting lithium using acetonitrile solution of NO_2BF_4 [81]. This technique has the advantage of using samples free of carbon and binder. The $Li_xCoO_{2-\delta}$ and $Li_{1-x}Ni_{0.85}Co_{0.15}O_{2-\delta}$ systems maintain the initial O3-type structure, for $0.5 \leq x \leq 1$ and $0.3 \leq x \leq 1$, respectively. While $Li_xCoO_{2-\delta}$ begins to form a P3-type phase for $x < 0.5$, $Li_{1-x}Ni_{0.85}Co_{0.15}O_{2-\delta}$ begins to form a new O3-type phase, designated as O3′ phase, for $x < 0.3$. The P3-type and the O3′ phases have smaller c parameters than do the O3-type phase and oxygen contents lower than 2, resulting in a loss of oxygen from the lattice for $x < 0.5$ and $x < 0.3$, respectively, for $Li_xCoO_{2-\delta}$ and $Li_xNi_{0.85}Co_{0.15}O_{2-\delta}$. The formation of the P3-type and O3′ phase is related to the introduction of holes into the O:2p band and the O–O interaction. The loss of oxygen was also confirmed for electrochemically charged samples. Unfortunately, only 50 % of the theoretical capacity of $LiCoO_2$ could be practically utilized. This corresponds to a reversible extraction/insertion of 0.5 Li per cobalt and a practical capacity of 140 mAh g^{-1} because capacity fade occurs below $x < 0.5$ in Li_xCoO_2. Reimers et al. [82] attributed the limitation in practical capacity to an ordering of lithium ions and consequent structural distortions around $x = 0.5$ in Li_xCoO_2. However, Chebiam et al. [78] believed that the limited capacity could be due to chemical instability of Li_xCoO_2 at deep charge with $x < 0.5$. One way to overcome the chemical instability of $Li_xCoO_{2-\delta}$ could be the modification of its surface with nanophase inert oxides such as Al_2O_3 and ZrO_2 [83]. A set of experiments, XRD, photoelectron spectroscopy and band structure calculations, shows that the degradation and fatigue of Li_xCoO_2 and Li_xNiO_2 ($0.5 < x < 1$) are due to the broadening of the Co/Ni 3d states upon Li deintercalation [84].

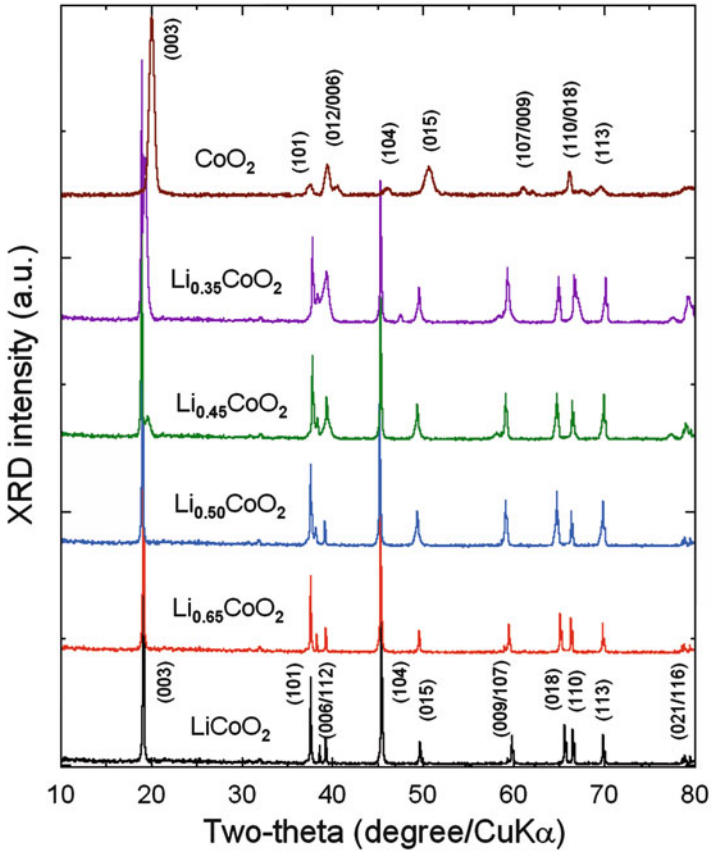

Fig. 5.12 XRD patterns of $LiCoO_2$ and chemically delithiated using with a required amount of the NO_2BF_4 oxidizing agent and anhydrous acetonitrile mixture. Note that the (003) reflection of the end member CoO_2-d occurs at a slightly higher $2q$ value than that of the new phase formed at $x = 0.45$, which could be due to a small lithium solid solubility range for the P3-type phase and/or changes in the oxygen content of the P3-type phase with the overall lithium content

5.3.2 *$LiNiO_2$ (LNO)*

$LiNiO_2$ (LNO) is isostructural with $LiCoO_2$ and has the O3 layer structure. The $Ni^{3+/4+}$ couple with a high lithium chemical potential $\mu_{Li(c)}$ provides a high cell voltage of around 4 V (Fig. 5.13) like $LiCoO_2$. However, $LiNiO_2$ suffers from a few drawbacks: (1) the difficulty to synthesize $LiNiO_2$ with all the nickel ions in the Ni^{3+} valence state and crystallized in a perfectly ordered phase without a mixing of cations Li^+ and Ni^{2+} ions in the insterslab space to form the $[Li_{1-x}Ni_x]_{3b}[Ni]_{3a}O_2$, where $3a$ and $3b$ are the site occupancy into the intra- and inter-layer space, respectively [85], (2) the Jahn–Teller distortion (tetragonal structural distortion) associated with the low spin Ni^{3+}:d^7 ($t_{2g}{}^6e_g{}^1$) ion [86], (3) irreversible phase transitions occurring during the charge–discharge process [87], and (4) exothermic

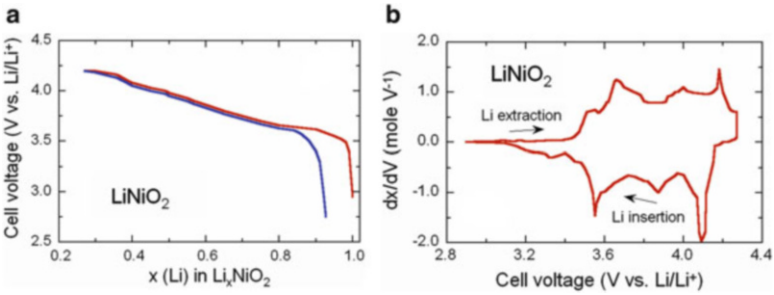

Fig. 5.13 Electrochemical features of $LiNiO_2$ powders: (**a**) first charge-discharge profile and (**b**) the incremental capacity

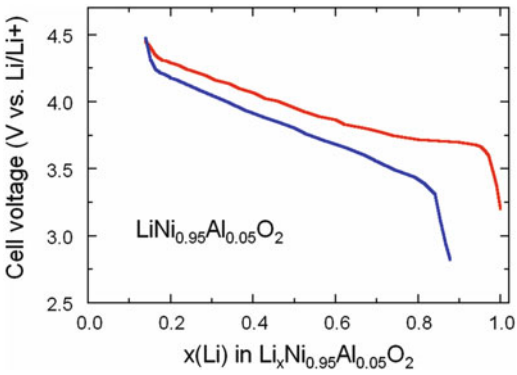

Fig. 5.14 The charge discharge profile of aluminum doped $LiNi_{1-y}Al_yO_2$ with $y = 0.05$

release of oxygen at elevated temperatures and safety concerns in the charged state [88]. The deviation of $Li_{1-x}Ni_{1+x}O_2$ from stoichiometry was studied by magnetic measurements [89]. We return to the magnetic properties of this material in Chap. 13 devoted to experimental technics.

As a result, pure $LiNiO_2$ is not a promising material for commercial lithium-ion cells although nickel is slightly less expensive and less toxic than cobalt. The formation of low lithium content Li_xNiO_2 ($x < 0.2$) causes cycle life failure. In addition, the material becomes highly catalytic toward electrolyte oxidation and some of the nickel ions may migrate to lithium sites. LNO is considered as thermally unstable in its charged state [90]. The formation of pure LNO is difficult, and residual Ni^{II} (up to 1–2 %) exist between the NiO_6 slabs. In fact, the irreversibility during the first cycle of charge–discharge is mainly related to the amount of Ni^{II} between the slabs, which require extra charge for oxidation to higher valency state [91], when electrolyte decomposition is controlled. Through careful synthesis and adjustment of lithium concentration in the material during heat treatment, it was obtained LNO very close to stoichiometry. In order to stabilize the structure of $LiNiO_2$ at low lithium content, sp elements such as B and Al were used as dopant of the LNO materials. These doping elements do not participate in oxidation reduction processes during charge–discharge of the cell. Figure 5.14 shows the

charge–discharge of aluminum doped $LiNi_{1-y}Al_yO_2$ with $y = 0.05$. The specific capacity of the cell reduces as a function of Al content, as the Al does not participate in the redox process. The capacity changes almost linearly with respect to the Al content up to 25 at%. This result may indicate a solubility limit in the formation of a solid solution between $LiAlO_2$ and $LiNiO_2$. It is also observed that the first charge–discharge irreversibility also increases as the amounts of Al in the samples were increased. The extra nickel in the lithium sites may cause the increase in first cycle irreversibility [92]. Ohzuku et al. [93] suggested the composition $LiNi_{3/4}Al_{1/5}O_2$ as more stable compound for lithium-ion batteries.

5.3.3 $LiNi_{1-y}Co_yO_2$ (NCO)

Efforts are currently done to improve the electrochemical performance of electrodes based on $LiNiO_2$ oxides, by forming the $LiNi_{1-y}Co_yO_2$ (NCO) solid solutions that are considered as Ni-rich compounds. Delmas et al. [94] pioneered studies of the NCO system. These solid solutions lead to successful results and progress has already been made to overcome the capacity fading by doping with several cations; it was noticed that the cationic mixing in the lithium sites still remains but at lower extent [95–99]. Many techniques were utilized for the NCO preparation. Julien et al. [100] synthesized $LiNi_{0.3}Co_{0.7}O_2$ powders of 510 nm particle size by the glycine–nitrate combustion process. This sample had significantly higher capacity (140 mAh g^{-1}) than samples synthesized by the sol–gel method (125 mAh g^{-1}). Julien et al. [69] prepared NCO by sol–gel technique assisted by citric acid as chelating agent. The structural properties of NCOs are found to be similar to their parent oxide, O3-$LiCoO_2$. A slight increase of the $(Co,Ni)O_2$ slab covalency is observed in $LiNi_{1-y}Co_yO_2$ powders. FTIR absorption spectra indicate the slight modification in the local structure related to the short-range environment of oxygen coordination around the cations in oxide lattices [101]. The variation of the lattice parameters as a function of the substitution of Co for Ni in $LiNi_{1-y}Co_yO_2$ reported in Fig. 5.15 These graphs follow the Vegard's law showing that the solid-solution is completed in these compounds. An interesting point to emphasize is the variation of the (c/a) ratio, which characterizes the degree of anisotropy of the layered structure. This criterion establishes the deviation from the hexagonal-close-packed structure when $(c/a) > 4.92$ for $y = 0$ and $(c/a) < 4.99$ for $y = 1$ [97]. Such graphs are also plotted in Fig. 5.15 for $LiNi_{1-y}Co_yO_2$ synthesized by wet chemistry via citrate route. From the plot (c/a) vs. y, we can appreciate the cation mixing effect. The binding energy of the Co–O bond being higher than that of the Ni–O bond, the strong Co–O skeleton can contribute to the stability of $LiNi_{1-y}Co_yO_2$ in the charged state.

In the case of $LiNi_{1-y}Co_yO_2$, even a small cobalt content shows the effect of reducing the amount of Ni^{3+} present in the 3*a* sites, stabilizing the layered structure and enhancing electrochemical capacity and the reversibility of the charge–discharge process. The same effect may occur when iron is partially

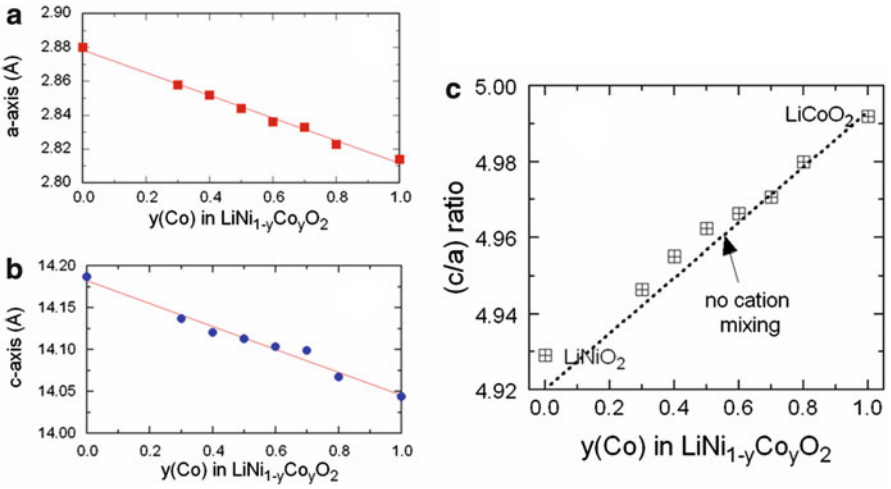

Fig. 5.15 (**a**) and (**b**) The variation of hexagonal unit-cell parameters with cobalt concentration y in $LiCo_yNi_{1-y}O_2$ solid solution. (**c**) The variation of the (c/a) ratio as a function of cobalt content. *Dashed line* represents the (c/a) vs. y relationship without cation mixing effect

substituted for cobalt in $LiFeO_2$: the layered structure is thought to be stabilized by cobalt ions present, reducing the amount of Fe^{3+} present in the 3*a* sites, thus facilitating lithium diffusion and rendering lithium deintercalation possible. The cathode layered structure enables fast 2D Li^+-ion diffusion and direct metal–metal intercation across the shared octahedral edges, which supports high operating voltage (>4.0 V vs. Li^0/Li^+). As experimental facts, the iron-enrichment on the cathode surface of $LiNi_{1-y}Fe_yO_2$ and $LiCo_{1-y}Fe_yO_2$ prevents surface-electrolyte instability at these high operating voltages and Fe-substituted cathodes exhibit superior rate capability and lower surface resistance (R_s) and charge transfer resistance (R_{ct}) compared to the unsubstituted cathode. In $LiNi_{1-y}Fe_yO_2$, Li sites are reportedly Ni and Fe, and their oxidation states are 2+ and 3+, respectively and Fe^{3+} occupies Li sites preferentially, compared to Ni^{2+}; this suggests the chemical formula for the Fe-substituted samples as follows: $\left[Li_{1-z}Ni^{2+}_{z-a}Fe^{3+}_{a}\right]_{\text{inter-slab}}\left[Ni^{3+}_{1-y}Fe^{3+}_{y-a}Ni^{2+}_{z+a}\right]_{\text{slab}}O_2$. Variations of the trigonal distortion and cation mixing could be estimated from XRD patterns using two factors involving the Bragg line intensity. It is known that the smaller value of the ratio $(I_{006}+I_{102})/I_{101}$, called the R_1-factor, is related to higher hexagonal ordering and the large value of the ratio $R_2 = I_{003}/I_{104}$ is related to the smaller cation mixing. The $Li(Ni_{0.5}Co_{0.5})_{1-y}Fe_yO_2$ cathodes synthesized under mild conditions (sol–gel technique) shows the smallest R_1-factor $[(I_{006}+I_{102})/I_{101}]$ and the largest I_{003}/I_{104}, indicating better hexagonal ordering and less cation mixing, respectively, for $y = 0.1$ (Fig. 5.16). The direction of the *c*-axis distorted in the $R\bar{3}m$ structure is reflected by the splitting of the (006) and (102) peaks, and (108) and (110) peaks in the XRD patterns (see Fig. 5.12).

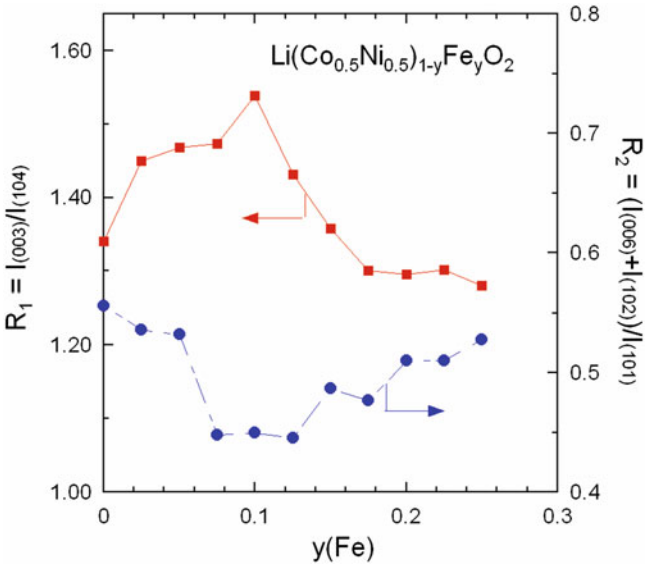

Fig. 5.16 Variation of the *R*-factors indicating better hexagonal ordering and less cation mixing for $y = 0.1$ in $Li(Ni_{0.5}Co_{0.5})_{1-y}Fe_yO_2$

Since the voltage-composition curves for LCO and LNO are similar, the NCO solid solution could be expected to give a cathode performance similar to that of Li_xCoO_2, but with a significant reduction of cobalt and partly elimination of the Ni^{II} from the lithium layers for $y > 0.3$. It was demonstrated that the Ni^{4+}/Ni^{3+} couple lies about 0.35 eV above the Co^{4+}/Co^{3+} couple, which gives a somewhat larger capacity [102]. Although the capacity of $LiCoO_2$ is about 130 mAh g^{-1}, the capacity of $LiNi_{1-y}Co_yO_2$ with part of the Co substituted by Ni increases to about 180 mAh g^{-1} but the discharge voltage falls slightly (suppression of the H1 ↔ H2 transformation). This solid solution system, especially the composition $LiNi_{0.8}Co_{0.2}O_2$, appears to replace $LiCoO_2$. A charge–discharge voltage profile for this composition is shown in Fig. 5.17. The $LiNi_{0.8}Co_{0.2}O_2$ electrode showed a high discharge capacity of 200 mAh g^{-1} at 25 °C. Investigations of the physical-chemistry of $LiNi_{1-y}Co_yO_2$ compounds include structure and morphology [101], vibrational spectroscopy [103], magnetism [104, 105], electronic transport [97], nuclear magnetic resonance [106] as a function of the composition. Chebiam et al. [107] showed that cobalt-rich phases tend to lose oxygen on deep lithium extraction due to the overlap of the $Co^{3+/4+}$:t_{2g} band with the top of the O:2*p* band in $Li_{1-x}Ni_{1-y}Co_yO_{2-\delta}$.

Thin films $LiNi_{1-y}Co_yO_2$ compounds were also prepared [108]. Highly oriented $LiNi_{0.8}Co_{0.2}O_2$ films grown by pulsed-laser were fabricated for application in microbatteries [109]. Electrochemical titration curve shows a specific capacity of 85 μAh μm^{-1} cm^{-2} at current density 4 μA cm^{-2} in the potential range 2.5–4.3 V.

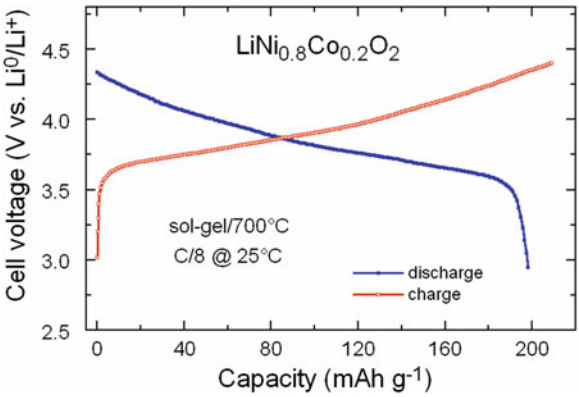

Fig. 5.17 Typical charge–discharge characteristics of Li//$LiNi_{0.8}Co_{0.2}O_2$ nonaqueous cells using the electrolyte of composition 1 mol L^{-1} $LiClO_4$ in PC at 25 °C. Charge and discharge were obtained at current densities 0.1 mA/cm^2. $LiNi_{0.8}Co_{0.2}O_2$ powders were fired at 700 °C for 4 h in air

5.3.4 *Doped $LiCoO_2$ (d-LCO)*

LCO was doped with several elements to stabilize the layered lattice at $x(\mathrm{Li}) < ½$ and extend the specific discharge capacity of $LiCo_{1-y}M'_yO_2$ [110, 111] Doping elements include $M' = \mathrm{Al}$ [112, 113], $M' = \mathrm{Mg}$ [99], $M' = \mathrm{B}$ [114], $M' = \mathrm{Cr}$ [115]. They were mainly prepared by soft-chemistry via dicarboxylic acid-assisted sol–gel method [116, 117]. In this technique, the chelating agent, $C_nH_mO_4$, with COOH groups, plays the role of oxidant starting from high purity metal acetates dissolved in a minimum volume of distilled water. The concentration of the chelate was adjusted carefully to get a solution with the pH in the range 3–4. The paste was further dried at 120 °C to obtain the dried precursor mass. The decomposition of the precursor was made in air at around 400 °C followed by calcination at 800 °C. Scanning electron microscopy (SEM) studies reveal the nano-structured morphology of the powders. The influence of Al doping on particle size and morphologies has been clearly evidenced [118]. The layered structure of boron-substituted $LiCo_{1-y}B_yO_2$ is preserved upon a large amount of B^{III} incorporation ($y \leq 0.25$), for which no residual impurity phases were detected [114]. The limit of solubility of boron is also the composition that optimizes the electrochemical properties. Up to $y \leq 0.2$ the boron improves importantly the cycling performance of the battery, as the dopant favors lattice adaptation to the insertion/extraction of Li^+ ions and prevents the onset of the structural first-order transition associated with the Verwey transition in $Li_{0.5}CoO_2$. Abuzeid et al. [119] reported the synthesis of $LiCo_{0.8}Mn_{0.2}O_2$ using a wet-chemical method via citric-acid route. This cathode material has the ability to free Li^+ ions from its structure by chemical process analogous to the first step of the charge transfer reaction in an electrochemical cell. Both the concentration of Mn^{3+}–Mn^{4+} pairs and that of Mn^{4+}–Mn^{4+} pairs formed in the delithiation process have been determined, together with that of the Mn^{3+}–Mn^{3+} pairs. The results indicate a random distribution of the Li ions that are removed from the matrix upon delithiation, which then undergo a diffusion process. Testing the material as cathode in lithium batteries revealed a capacity of ~170 mAh g^{-1} with lower polarization and high coulombic efficiency [120].

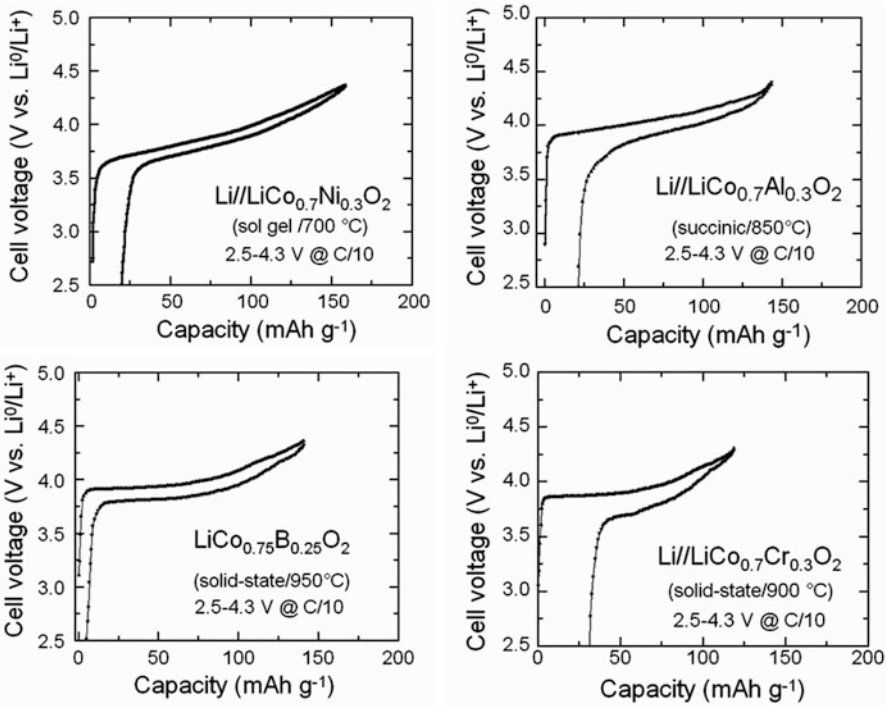

Fig. 5.18 Electrochemical features of Li//$LiCo_{1-y}M'_yO_2$ cells during the first charge–discharge cycle carried out in the range 2.5–4.4 V at $C/10$ rate. (**a**) $M' = Ni$, (**b**) $M' = Al$, (**c**) $M' = B$, and (**d**) $M' = Cr$

In Fig. 5.18, the electrochemical features of synthesized $LiCo_{0.7}M'_{0.3}O_2$ ($M' = Ni$, Al, B and Cr) layered oxides are compared. The electrochemical features of the layered $LiCo_{0.7}Ni_{0.3}O_2$, $LiCo_{0.7}Al_{0.3}O_2$, and $LiCo_{0.65}B_{0.35}O_2$, oxides resemble to that of $LiCoO_2$. Replacing a small amount of Co demonstrates the disappearance of the voltage plateau at 3.85 V in the charge curve. This is attributed to the absence of the semiconductor-metal transition with M' substitution [121]. Chemical substitution of products improves electrochemical properties for Al- and Ni-based materials, which exhibit good capacity retention. The efficiency in maintaining capacity retention is observed over a large number of cycles without sacrificing initial reversible capacity. However, the electrochemical profile of the $LiCo_{0.7}Cr_{0.3}O_2$ cell displays a large capacity fading attributed to the structural distortion upon substitution [115]. The electrochemical profiles of Li//$LiCo_{1-y}B_yO_2$ cells including various levels of boron substitution ($0.05 \leq y \leq 0.35$) in their positive electrode provide very low polarization during charge–discharge cycling, with capacity over 130 mAh g^{-1} when charged up to 4.3 V vs. lithium anode. Capacity of the $LiCoO_2$ doped with 15 % boron remains over 125 mAh g^{-1} after 100 charge–discharge cycles. It appears that a less electrolyte decomposition occurs with boron or aluminum substitution in $LiNiO_2$ and $LiCoO_2$ cathodes in lithium batteries [99].

5.3.5 $LiNi_{1-y-z}Co_yAl_zO_2$ (NCA)

Among the Ni-rich layered compounds, $LiNi_{1-y-z}Co_yAl_zO_2$ (NCA) exhibits enhanced electrochemical performance compared with non Al-doped $LiNi_{1-y}Co_yO_2$ mixed materials because of its structural and thermal stability [122–125]. The specific composition $LiNi_{0.80}Co_{0.15}Al_{0.15}O_2$ is currently used in the 85-kWh battery pack to power the EV Roadster by Tesla at high speed. Note that NCA-type materials are currently used in SAFT commercial batteries for various applications (EV, HEV, space, military, etc.) [126]. Majumdar et al. [127] synthesized NCA powders via wet-chemical route using metal acetates and aluminum nitrate. The electrochemical features carried out in the potential range 3.2–4.2 V at a current density 0.45 mA cm^{-2} showed a specific capacity of ~136 mAh g^{-1}. NCA prepared by a co-precipitation method showed a quasi-ideal lamellar structure with less than 1 % extra-nickel ions in the interslab space [92]. Bang et al. [124] investigated the structural change of the delithiated cathode $LiNi_{0.80}Co_{0.15}Al_{0.05}O_2$ during thermal decomposition, the XRD analysis was carried out with different states-of-charge (SOCs). As the SOC increases, the (018) and (110) Bragg lines at $2\theta = 65°$ move toward lower higher angles, respectively. An increase in the distance between these reflections indicated an increase in the *c/a* ratio of the NCA lattice [128]. Improvement of the electrochemical performance at high temperature (60 °C) was obtained by coating the NCA powders with metal oxides. Cho et al. [129, 130] stabilized the surface of nanoparticles by SiO_2 and TiO_2 dry coating. Surface modification of NCA nonapowders has been also obtained with various other coatings such as $Ni_3(PO_4)_2$ [131], AlF_3 [132], Li_2O-$2B_2O_3$ (LBO) glass [133], and carbon [134]. Enhancement of the capacity retention (169 mAh g^{-1} at current density 360 mA g^{-1}) at high temperature of $LiNi_{0.80}Co_{0.15}Al_{0.05}O_2$ has been obtained with a 2 wt% LBO coating [133]. Belharouak et al. [135] studied the thermal degradation of deintercalated NCA samples. They reported that the oxygen release from these delithiated powders was associated with the occurrence of several structural transformations, ranging from the $R\bar{3}m \rightarrow Fd3m$ (layered → spinel) transition to the $Fd3m \rightarrow Fm3m$ (spinel → NiO-type) transition.

5.3.6 $LiNi_{0.5}Mn_{0.5}O_2$ (NMO)

Layered, monoclinic $LiMnO_2$ is isostructural with $LiCoO_2$ but transforms on cycling at 3–4 V vs. Li^0/Li^+ to more thermodynamically stable spinel phase. Cation doping (e.g., Ni^{2+} or Cr^{3+}) can be used to stabilize the layered phase with some success. The layered oxide $LiNi_{0.5}Mn_{0.5}O_2$ (NMO) was reported to be a promising positive electrode material [136, 137]. $LiNi_{0.5}Mn_{0.5}O_2$ adopts a hexagonal unit cell (α-$NaFeO_2$-like). XANES experiments have demonstrated that transition-metal ions adopt the Ni^{3+} and Mn^{4+} state with a small fraction of divalent Ni^{2+} ions. The manganese remaining in the +4 valence state at all times prevents the instabilities

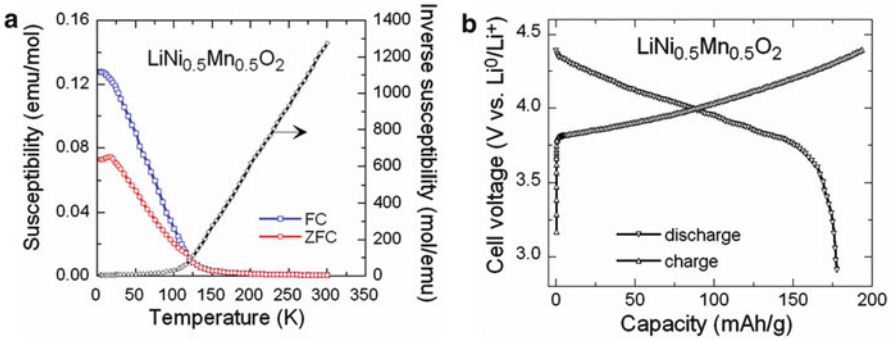

Fig. 5.19 (**a**) Temperature dependence of the magnetic susceptibility of $LiNi_{0.5}Mn_{0.5}O_2$ powders for zero-field cooling (ZFC) and field-cooling (FC). (**b**) Charge and discharge curves of the $Li//LiNi_{0.5}Mn_{0.5}O_2$ cell with a current density of 0.12 mA/cm^2 and cutoff voltage of 2.6 and 4.2 V. The cathode material was synthesized by citric acid assisted sol–gel method

associated with Jahn–Teller Mn^{3+} ions. This material shows a reversible capacity 150 mAh g^{-1} in the voltage range 2.5–4.3 V and exhibits the superior characteristics of a larger capacity than $LiMn_2O_4$ and better thermal stability than $LiNiO_2$. Structural analysis have shown that the lattice parameters of $LiNi_{0.5}Mn_{0.5}O_2$ are $a = 2.896$ Å and $c = 14.306$ Å and the chemical composition can be expressed by referring to the Wyckoff positions 3*a* and 3*b* of the space group $R\overline{3}m$ as $[Li_{0.92}Ni_{0.07}]_{3a}[Li_{0.08}Mn_{0.5}Ni_{0.43}]_{3b}O_2$. Figure 5.19a shows the magnetic properties of $LiNi_{0.5}Mn_{0.5}O_2$ [138] with the plot of the molar spin susceptibility, $\chi(T)$ as a function of the temperature in the range 4–300 K. A cusp in $\chi(T)$ is observed close to 15 K that is similar to the spin-glass behavior reported for $LiNiO_2$ [139, 140]. A large deviation between ZFC and FC curves below 100 K indicates the existence of ferromagnet. The ferromagnetic interaction is associated with the random occupancy of 3*a* and 3*b* sites by 7 % Ni^{2+} and 50 % Mn^{4+}, respectively. The 180° Ni^{2+}-O-Mn^{4+}-O-Ni^{2+} superexchange interaction is assumed to be ferromagnetic in $LiNi_{0.5}Mn_{0.5}O_2$. In this layered compound the almost linear 180° M_{3a}-O-M_{3b}-O-M_{3a} bond is expected to be stronger than the interlayer 90° M_{3b}-O-M_{3b} bond when the 3*a* site is partially occupied by *M* cations [139]. Figure 5.19b shows the charge and discharge curves of the $LiNi_{0.5}Mn_{0.5}O_2$ cell with a current density of 0.12 mA cm^{-2} and cutoff voltage of 2.6 and 4.2 V. This electrochemical profile indicates that the lithium deintercalation process in $LiNi_{0.5}Mn_{0.5}O_2$ proceeds via a single-phase reaction.

5.3.7 $LiNi_{1-y-z}Mn_yCo_zO_2$ (NMC)

In search of high-power lithium-ion batteries with excellent calendar life and better thermal abuse tolerance to replace the $Li//LiCoO_2$ system, the new chemistry $Li(Ni,Mn,Co)O_2$ (NMC) was first synthesized by Liu et al. [141]. These compounds of various compositions, which look like the simple solid solution

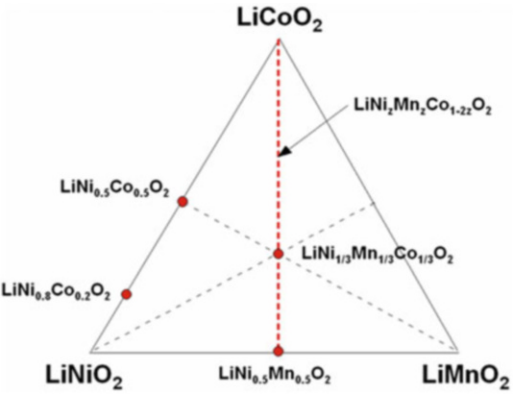

Fig. 5.20 The triangular phase diagram of the $LiCoO_2$-$LiNiO_2$-$LiMnO_2$ solid solution

$LiCoO_2$-$LiNiO_2$-$LiMnO_2$ (Fig. 5.20), have been intensively studied with ultimate goals of large enhancement of the thermal and structural stability and appreciable increase of the capacity retention because the combination of nickel, manganese, and cobalt can provide many advantages. The $LiNi_{1-y-z}Mn_yCo_zO_2$ compounds crystallize with the α-$NaFeO_2$-type structure ($R\overline{3}m$ space group). The pioneering work of the Dahn's group demonstrated the high performance of the $Li//LiNi_yMn_yCo_{1-2x}O_2$ and suggested the valence state of transition-metal cations such as divalent (Ni^{2+}), trivalent (Co^{3+}) and tetravalent (Mn^{4+}), respectively [142, 143]. Note that to keep the charge neutrality and avoid the Mn^{3+} Jahn–Teller ions, the amount of Ni and Mn ions must be equal. It was reported that $LiNi_yMn_yCo_{1-2x}O_2$ showed a specific capacity of 160 mAh g^{-1} over 2.5–4.4 V [144] and the thermal behavior of charged $LiNi_yMn_yCo_{1-2x}O_2$ was milder than that of charged LCO and LNO [145]. There are many factors that influence the electrochemical features of $LiNi_{1-y-z}Mn_yCo_zO_2$ such as synthesis preparation, structural defects, morphology, composition, operation voltage domain. Lee et al. [146] have investigated the defect chemistry and doping effects of NMCs in terms of energetics and dynamics with special attention of the antisite pair defects. Properties of NMCs were summarized in several review papers [147–149]. NMR studies have evidenced for a nonrandom distribution of the transition-metal cations in $LiNi_{1-x-y}Mn_xCo_yO_2$ [150]. The insulator-to-metal transition observed with $LiCoO_2$ disappeared at $y \geq 0.2$ due to the loss of contact between Co ions that interrupts the cooperative effect. Various synthetic methods have been applied to elaborate $LiNi_{1-y-z}Mn_yCo_zO_2$ compounds such as traditional solid-state reaction [151, 152], supercritical water method [153], sol–gel technique [154], co-precipitation synthesis [155–157], spray-drying method [121, 158, 159], radiated polymer gel method [160], solvent evaporation method [161], molten-salt synthesis [162], polymer template route [163], and Pechini method [164]. Among these synthetic methods, co-precipitation and sol–gel route have been found powerful, economic, and easy for large scale fabrication, because the TM ions are precipitated in an homogeneous manner and oxidized in the aqueous solution at the molecular level. Fujii et al. [165] indicated that high calcination temperature results

in the formation of vacancies in the TM slabs, lowers the specific capacity and degrades the cycle performance. The optimum calcination temperature is 900 °C in order to obtain the electrochemically active and dense packed oxide particles.

Electrochemical performance of $LiNi_{1-y-z}Mn_yCo_zO_2$ cathode materials were improved by doping cations [166, 167] and anion substitution of fluoride for oxygen [168]. The long-range and local structure and cationic environment in $LiNi_{1-y-z}Mn_yCo_zO_2$ were studied by FTIR and EPR spectroscopy [169]. Cation ordering was investigated by using a combination of ^6Li magic angle spinning (MAS) nuclear magnetic resonance (NMR) spectroscopy and neutron pair distribution function (PDF) analysis [150]. For $Li[Ni_xMn_yCo_z]O_2$ lamellar compounds, the electronic conductivity is not a problem but these materials have poor cycling stability at high rate or high cutoff voltage, which limits their use to portable applications. Aurbach et al. [170] have suggested that the capacity retention is strongly dependent on the surface chemistry of the particles because of resistive SEI layer. That is why many attempts have been made to protect the surface of NMC materials with metal oxides such as Al_2O_3, TiO_2, ZrO_2, and MgO, or other compounds such as $FePO_4$, $LiFePO_4$, and $Li_4Ti_5O_{12}$ [83]. The improvement of the electrochemical performance due to the crystallization of the surface layer can be understood as follows. First, the electronic conductivity is affected by the structural disorder. This has been evidenced by transport experiments that have shown an increase of conductivity when the calcination temperature used in the synthesis process increases from 800 up to around 1000 °C, owing to improved crystallinity of the materials [164]. In fact, a high crystallinity is essential to obtain good electrical conductivity. In another approach, direct UV-assisted conformal coating of poly(tris(2-(acryloyloxy)ethyl) phosphate) (PTAEP) gel polymer electrolyte on as-formed $LiNi_{1/3}Mn_{1/3}Co_{1/3}O_2$ (NMC) cathode is quite a new process. A smooth and continuous PTAEP coating layer with thickness 20 nm was obtained, which improved the 4.6 V cycling performance, without impairing discharge capability [171]. The authors, however, were too optimistic when claiming that it suppressed the exothermic reaction. It only shifted the exothermic peak temperature from 284 to 294 °C and reduced the exothermic peak from 649 to 576 J g^{-1}. This is, however, a new conformal coating strategy that has to be explored on other electrodes.

Nowadays, the magic composition $LiNi_{1/3}Mn_{1/3}Co_{1/3}O_2$ with hexagonal structure, first introduced by the Ohzuku's group in 2001, has attracted more significant interest as a candidate of cathode materials because the good stability during cycling even at elevated temperature, and high reversible capacity [155]. The lithium excess cathode $Li_{1+x}(Ni_{1/3}Mn_{1/3}Co_{1/3})_{1-x}O_2$ was found to exhibit better cyclability and rate capability than the stoichiometric material up to a cutoff charge voltage of 4.6 V vs. Li^0/Li^+ [172–174]. Ligneel found that NMC structural stability [174]. Zhang et al. [173] have explored the co-precipitation route to synthesize the $Li_{1+x}(NMC)_{1-x}O_2$ powders and optimize its structure by adjusting one parameter of the synthesis, namely the lithium–transition metal ratio (κ), so as to minimize the cation mixing. The synthesis of NMC powders was performed by a hydroxide route using transition-metal hydroxide and lithium carbonate as with Li excess

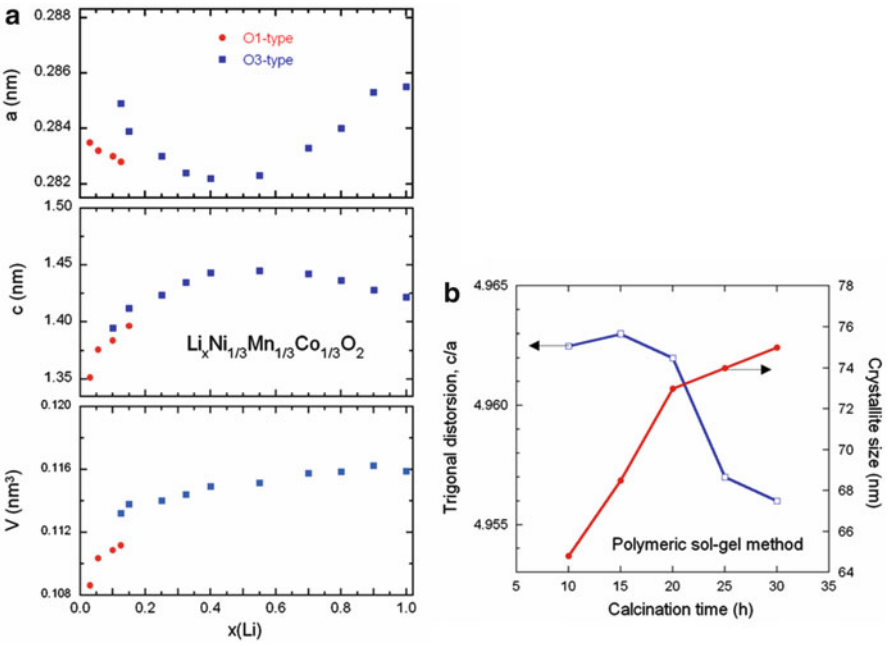

Fig. 5.21 (**a**) Evolution of the lattice parameters vs. x(Li) in $Li_xNi_{1/3}Mn_{1/3}Co_{1/3}O_2$. Powders were prepared by citrate gel method with molar ratio Li/(Ni + Mn + Co) = 1. (**b**) Evolution of the trigonal distortion, i.e., the c/a ratio and particle size of $Li_xNi_{1/3}Mn_{1/3}Co_{1/3}O_2$ powders as a function of the calcination time at the optimum temperature of 900 °C

$0.04 \leq x \leq 0.12$ shows a strong starting materials. The final products were fired at 950 °C for 10 h in air. The samples described here were obtained with nominal values: $\kappa = \text{Li}/M = 1.05$ (sample-A) and $\kappa = 1.10$ (sample-B) with $M = \text{Ni} + \text{Mn} + \text{Co}$. The Rietveld refinement of the XRD spectra and the analysis of the magnetic properties showed that the concentration of cation mixing for sample-A and sample-B were below 2 %. Figure 5.21 shows the evolution of the structural properties of $Li_xNi_{1/3}Mn_{1/3}Co_{1/3}O_2$ powders prepared by the citrate gel method with metal molar ratio Li/(Ni + Mn + Co) = 1. The evolution of the lattice parameters vs. x(Li) in $Li_xNi_{1/3}Mn_{1/3}Co_{1/3}O_2$ displays the two structural O1- and O3-phase. The curves of the trigonal distortion measured from the c/a ratio, and particle size as a function of the calcination temperature for $Li_xNi_{1/3}Mn_{1/3}Co_{1/3}O_2$ show that heat treatment for 20 h is sufficient. The electrochemical features of are displayed in Fig. 5.22a for $Li_{1+x}(NMC)_{1-x}Co_{1/3}O_2$ powders synthesized by the co-precipitation method with $\kappa = 1.05$. Results show a loss rate of 0.15 % per cycle for the NMC electrodes synthesized by co-precipitation method. More than 95 % of its initial capacity was retained after 30 cycles in the cutoff voltage of 3.0–4.3 V at 1 C-rate. Note that a cation mixing below 2 % can be considered as the threshold for which the electrochemical performance does not change for NMC. The diagram of the discharge capacity against thermal stability for a series of NMC cathode materials

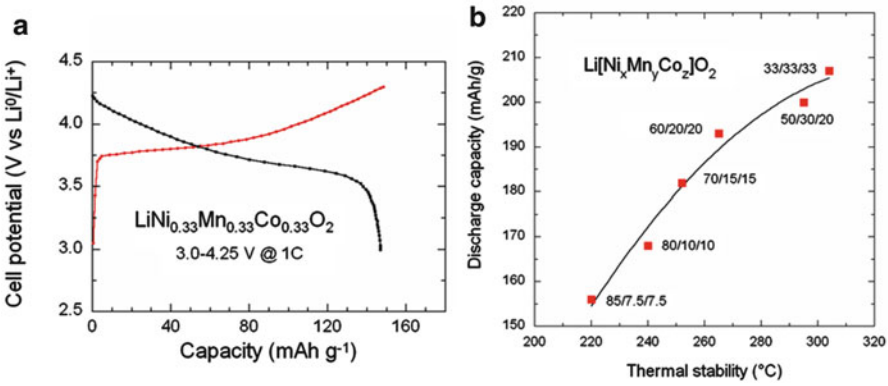

Fig. 5.22 (**a**) The electrochemical features of $Li_{1+x}(NMC)_{1-x}Co_{1/3}O_2$ powders synthesized by the co-precipitation method. The structure was optimized by adjusting the lithium–transition metal ratio to $\kappa = Li/M = 1.05$. Results indicated a rate of 0.15 % per cycle for the NMC electrodes. (**b**) Diagram discharge capacity against thermal stability measured by the exothermic peak temperature for a series of $LiNi_xMn_yCo_zO_2$ cathode materials. The number indicates the amount of Ni/Mn/Co

is shown in Fig. 5.22b. The number indicates the amount of Ni/Mn/Co in $LiNi_xMn_yCo_zO_2$. This graph shows clearly that the more stable cathode is $LiNi_{0.33}Mn_{0.33}Co_{0.33}O_2$.

5.3.8 Li_2MnO_3

Lithium manganate Li_2MnO_3 attracts an ever-growing attention of researchers and is still the object of debates since, among the family of manganese oxides, it is one of the most interesting compounds from the view point of electrochemical behavior and structural evolution upon charge/discharge [175–179]. Li_2MnO_3 possesses an O3-type structure that can be represented in conventional layered $LiMO_2$ notation as $Li_{3a}[Li_{1/3}Mn_{2/3}]_{3b}O_2$, where interslab octahedral sites are only occupied by Li^+-ions while Li^+ and Mn^{4+}-ions (in a ratio of 1:2) occupy slab octahedral sites, and 3*a* and 3*b* refer to the octahedral sites of the trigonal lattice [180]. In other words, in Li_2MnO_3, 1/3 of the Mn-ions in the transition metal layer is replaced with Li. Layers of lithium ions and alternating layers of manganese ions are separated from one another by layers of cubic-close packed oxygen planes, thus resembling the ideal layered structure of $LiCoO_2$. It should be noted that Li_2MnO_3 is an integrated part of the so-called high-energy cathode $xLi_2MnO_3{\cdot}(1-x)Li[M]O_2$ materials (M = Mn, Ni, Co) for Li-ion batteries that provide reversible capacities >200 mAh g^{-1} [181]. In these materials, Li_2MnO_3 component plays an important role of supplying lithium and stabilizing the electrode structure. Li_2MnO_3 is rich in mobile Li^+ ions and theoretically can deliver a high capacity of 460 mAh g^{-1} for

total Li extraction when charged up to 4.6 V. However, manganese cannot be oxidized beyond +4 in an octahedral environment and Li_2MnO_3, especially in its microcrystalline form, is considered electrochemically inactive for lithium insertion and extraction. It was shown that Li^+ extraction from Li_2MnO_3 is possible not by oxidation of Mn^{4+} but by other mechanisms. They may involve simultaneous removal of oxygen (Li_2O) to balance the charge [182] or exchange of Li^+ ions by protons generated from oxidation reactions of the nonaqueous electrolyte solutions at elevated temperatures [183]. Actually, Li_2MnO_3 becomes electrochemically active in electrodes comprising its nano-sized particles and these electrodes demonstrate much higher electrochemical activity in terms of capacity and cycling behavior [178]. This can be due to decreasing the potential of the Li^+-ions extraction from the host structure in the first charge associated with the higher surface-to-volume ratio, much shorter distances for the electrons and the Li-ion transport in nanoparticles, the increased surface concentration of the electrochemically active sites, and with a better accommodation of strain during Li^+ extraction/insertion. Recently, Okamoto related a substantial decrease of the potential of the Li^+-ions extraction to the increasing concentration of oxygen vacancies in Li_2MnO_3, which activate the Mn sites as the redox centers in the Li deintercalation reaction [184]. There are many reports [185, 186] dedicated to structural transformations of layered cathode materials $LiMO_2$ for Li-cells (M = transition metal, like Mn, Ni, Co) from the layered to spinel-type ordering upon Li electrochemical or chemical deintercalation. Amalraj [179] reported this structural transformation upon charging Li_2MnO_3 electrodes that comprises micro- or nano-sized particles at high anodic potentials (4.6–4.7 V). Ito et al. [187] have shown that in the first charge of $xLi_2MnO_3 \cdot (1-x)Li[M]O_2$ integrated materials, the formation of the spinel-type ordering started just at the potential plateau around 4.5 V, at the same time as the electrochemical activation of Li_2MnO_3 ($Li_2MnO_3 \rightarrow Li_2O + MnO_2$) occurs at this potential. On the other hand, we have established that in the above materials, in which the structurally compatible Li_2MnO_3 (layered monoclinic) and $LiMO_2$ (layered rhombohedral) components are closely interconnected with one another and coexist side by side in the structure, partial layered-to-spinel transition occurred even at the early stages of the first charge (Li^+-extraction), at 4.1–4.4 V [188]. In this potential range, the Li^+ ions are extracted (deintercalated) only from the electrochemically active $LiMO_2$ component, while Li_2MnO_3 remains inactive until 4.5 V (Fig. 5.23). Therefore one can suggest that $LiMO_2$ is "responsible" for the observed partial transformation of the layered-type to spinel-type structural ordering in electrodes comprising $xLi_2MnO_3 \cdot (1-x)Li[M]O_2$ materials. This transformation is supposed to be due to the partial irreversible migration of transition metal cations into interlayer Li sites by the electrochemical charging the electrode or by chemical delithiation (leaching) of the layered material in acidic media [175, 178, 183, 185].

The structural transformations from the layered-type to spinel-type ordering was investigated at various states-of-charge of Li_2MnO_3 electrodes, even at the early stages around 4.3 V far beyond the electrochemical decomposition of Li_2MnO_3, and at 4.5 V (potential plateau) where it decomposes into Li_2O and MnO_2 [189]. This

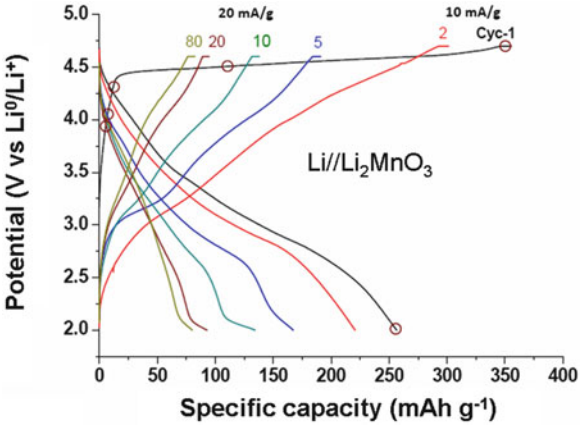

Fig. 5.23 Typical potential profiles measured in the ranges of 2.0–4.7 V (first 2 cycles) and 2.0–4.6 V (rest of the cycles) from a Li_2MnO_3 electrode at 30 °C in coin-type cells. Cycle numbers are indicated on the curves. The cycling mode was CC–CV, potentiostatic steps were 1 h at 4.7 V and 0.5 h at 4.6 V. The first 2 cycles were performed by applying the current density of $i = 25$ mA g^{-1}. For cycles 3–100 the current density was $i = 20$ mA g^{-1} and for the subsequent cycles $i = 10$ mA g^{-1}. Empty circles on the charge–discharge profiles of the first cycle indicate potentials, at which electrochemical cells were terminated and Li_2MnO_3 electrodes studied for possible structural transformations

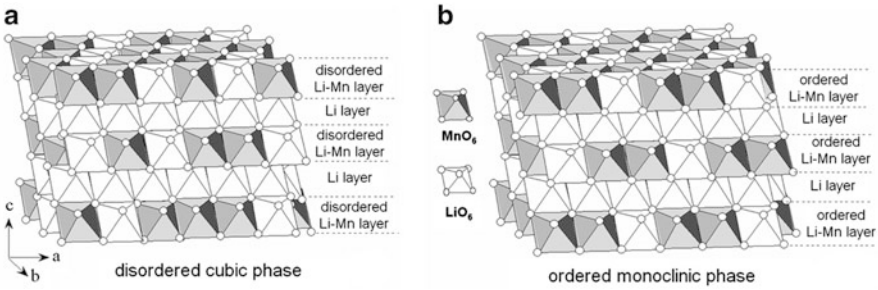

Fig. 5.24 (**a**) Schematic representation of the Li_2MnO_3 crystallographic structures showing the α-phase with randomly distributed cation sites in the Li-Mn layers, (**b**) the β-phase corresponding to the case where the cations are ordered

layered-to-spinel transformation was examined by means of X-ray and electron diffraction techniques, Raman spectroscopy, and the study of the magnetic properties of Li_2MnO_3, which is an efficient tool to probe structural ordering. The novelty of this work is that layered-to-spinel structural transformations were detected and studied at the initial states-of-charge, prior to the electrochemical activation of Li_2MnO_3 electrodes. In addition, the prior works related to this cathode material miss the polymorphism of Li_2MnO_3 that is able to crystallize in α- and β-phases (Fig. 5.24) depending on the sintering temperature during the synthesis process [190].

5.3.9 Li-Rich Layered Compounds (LNMC)

Novel Li-rich layered cathode materials, the "layered-rocksalt" Li$[Li_xNi_yCo_yMn_{1-x-y}]O_2$ frameworks (LNMC) have received great attention because of their ability to deliver capacities of 250 mAh g^{-1} when electrochemically activated at 4.6 V [191–205]. Layered-rocksalt compounds can be regarded, in a homogeneous phase approach, as a solid solution series between $Li[Li_{1/3}Mn_{2/3}]O_2$ and $LiNi_zCo_{1-z}O_2$ [191] as shown by the phase diagram in Fig. 5.25 and on the other hand it is regarded, in a two-phase approach as a kind of composite electrode with nanoclusters of Li_2MnO_3 and $Li(Ni,Co)O_2$ in localized regions [192]. Various synthesis techniques used to fabricate high-capacity LNMC composite materials include ion-exchange reaction [206], solid-state reaction of metal hydroxide with calcination at 900 °C for 24 h [207], co-precipitation method [208], sol–gel method [209], molten salt method [210], and template-free method [211].

Figure 5.26 compares the charge–discharge profiles of the Li-rich layered compounds of composition $Li_{1.134}Ni_{0.3}Mn_{0.566}O_2$ and $Li_{1.2}Ni_{0.13}Mn_{0.54}Co_{0.13}O_2$ synthesized by sol–gel method assisted by citric acid as chelating agent. Measurements were carried out at *C*/10 rate in the potential range 4.8–2.0 V. The electrochemical curves exhibit two regions (I and II) during the first charge (separated by a dashed line in Fig. 5.26). The region (I), below 4.6 V, corresponds to the oxidation of the transition-metal cation (TM) to tetravalent state M^{4+}, while the plateau (region II) at around 4.6 V corresponds to an oxidation of O^{2-} ions and the irreversible loss of oxygen from the lattice [212]. The oxygen loss leads to a lowering of the oxidation states of the TM ions at the end of the first discharge, which makes easier the reversibility of subsequent cycles. As reported by Wu and Manthiram [213], the irreversible loss of oxygen from the LNMC framework can be reduced by a substitution of small amount of Al^{3+} for Li^+ or F^- for O^{2-}, which

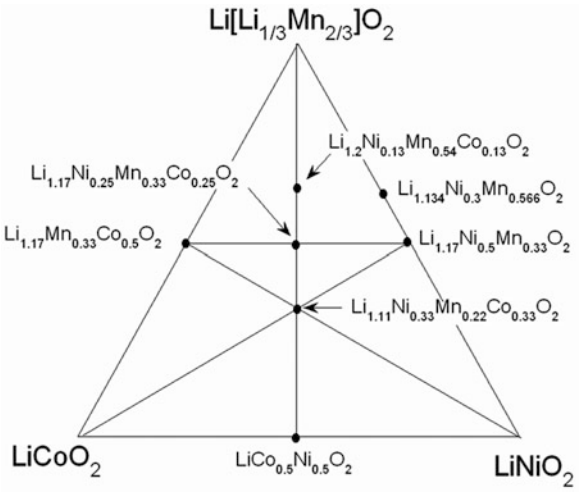

Fig. 5.25 Ternary phase diagram of the "layered-rocksalt" $Li[Li_{1/3}Mn_{2/3}]O_2$-$LiCoO_2$-$LiNiO_2$ solid solution systems

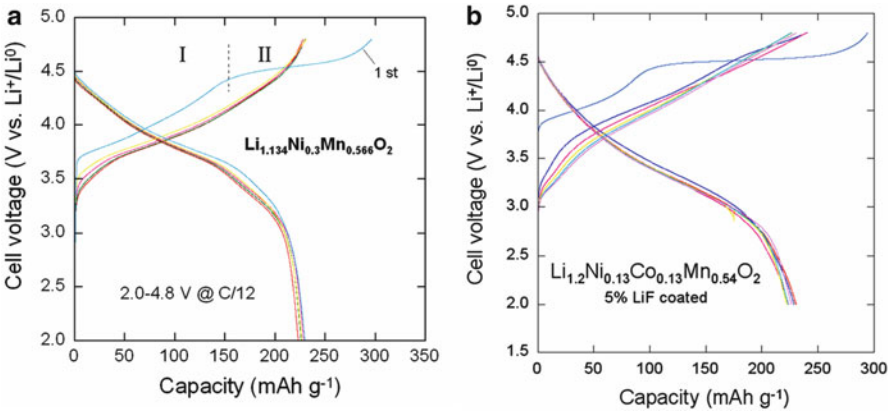

Fig. 5.26 Charge–discharge curves of Li-rich layered-rocksalt composite electrodes. (**a**) $Li_{1.134}Ni_{0.3}Mn_{0.566}O_2$ and (**b**) 5 % LiF-coated $Li_{1.2}Ni_{0.13}Mn_{0.54}Co_{0.13}O_2$. Measurements were carried out in the galvanostatic mode at *C*/12 rate in the potential range 2.0–4.8 V

lowers significantly the irreversible capacity loss (ICL). High capacity of $Li[Li_{(1-x)/3}Mn_{(2-x)/3}Ni_{x/3}Co_{x/3}]O_2$ can be obtained by surface modification with Al_2O_3. For instance, surface modified $Li[Li_{0.2}Ni_{0.13}Mn_{0.54}Co_{0.13}]O_2$ shows a remarkably high capacity of 285 mAh g^{-1} with an ICL of 41 mAh g^{-1} and good rate capability [213]. Mechanisms associated with the plateau observed at high voltage for the overlithiated $Li_{1.12}(Ni_{0.425}Mn_{0.425}Co_{0.15})_{0.88}O_2$ system have been discussed by Tran et al. [214].

$Li(Li_{0.17}Ni_{0.2}Co_{0.05}Mn_{0.58})O_2$ particles synthesized by a spray-drying method were modified subsequently with CeO_2 nanoparticles, which results in smaller surface charge transfer resistance and larger discharge capacity [195]. Fluorine doping in $Li_2MnO_3{\cdot}LiMO_2$ can create polaron states in the Li_2MnO_3 lattice with a migration energy barrier about 0.27 eV. The polaron state is strongly trapped by fluorine atom, which decreases the efficiency of the doping effect to enhance the electronic conductivity [196]. Novel $Li_{1.2}Mn_{0.5}Co_{0.25}Ni_{0.05}O_2$ microcube prepared through a simple binary template method with calcination at 800 °C [205] providing high reversible discharge capacities of 208 mAh g^{-1} at a current density of 200 mA g^{-1}. In general, owning to oxygen extraction at the first cycle and insulation phase of Li_2MnO_3, the pristine Li-rich layered cathode materials experience high irreversible capacity loss at the first cycle, accompanied with gradual capacity fade and poor rate capability during cycling [196]. The surface modification [215], acid treatment [216], doping [217] as well as blending with other cathode materials [218] have been found to alleviate the irreversible capacity loss at the first cycle. In particular, the irreversible capacity loss at the first cycle was eliminated by blending with other lithium insertion hosts, such as $Li_4Mn_5O_{12}$, LiV_3O_8, V_2O_5 [219].

5.3.10 Other Layered Compounds

5.3.10.1 Mn-Based Oxides

The difficulties met with $LiMn_2O_4$ spinel have also motivated the investigation of several non-spinel manganese oxides [220]. Although $LiMnO_2$ obtained by conventional synthesis procedures adopts an orthorhombic rock-salt structure (*Pmmn* S.G.), in which the oxygen array is distorted from the ideal cubic close packing [221], layered (monoclinic) $LiMnO_2$ isostructural with the layered $LiCoO_2$ (O3 structure) can be obtained by an ion-exchange of $NaMnO_2$ [222] or by a partial substitution of Mn by Cr or Al [223]. Unfortunately, both the orthorhombic and the monoclinic $LiMnO_2$ with a close-packed oxygen array tend to transform to spinel-like phase that is completed within a few charge–discharge cycles [224]. In this regard, $Na_{0.5}MnO_2$—designated as $Na_{0.44}MnO_2$ in the literature—adopting a non-close-packed tunnel structure has drawn some attention as it does not transform to spinel-like phases and shows extraordinary structural stability to temperatures as high as 300 °C [225, 226]

However, only a small amount of lithium could be extracted from the ion-exchanged sample $Na_{0.5-x}Li_xMnO_2$ although additional lithium could be inserted into $Na_{0.5-x}Li_xMnO_2$. Therefore, it is not attractive for lithium-ion cells fabricated with carbon anodes. Nevertheless, it has been shown to be a promising candidate for lithium polymer batteries employing metallic lithium anode [225]. Additionally, amorphous manganese oxides have been shown to exhibit high capacity (300 mAh g^{-1}) with good cyclability [227]. However, the capacity occurs over a wide voltage range extending from 4.3 to 1.5 V with a continuously sloping discharge profile and not much lithium could be extracted from the initial material. Therefore these amorphous oxides are not attractive for lithium-ion cells fabricated with carbon anodes. However, they may become viable with the development of new lithium-containing counter-electrodes.

5.3.10.2 Chromium Oxides

$LiCrO_2$ also crystallizes in the O3 structure of $LiCoO_2$. Although one would expect $Li_{1-x}CrO_2$ to exhibit good structural stability due to the strong preference of Cr^{3+} ions for octahedral sites, it is difficult to extract lithium from $LiCrO_2$. However, a number of chromium oxides such as Cr_2O_5, Cr_6O_{15}, and Cr_3O_8 having a Cr oxidation state of $\geq$5+ show high capacities and energy densities as high as 1200 mWh g^{-1} above a cutoff voltage of 2 V [228]. Also, amorphous Cr_3O_8 has been found to show high energy density with good rechargeability [229]. However, the synthesis of these oxides generally requires decomposition of CrO_3 in an autoclave or under high oxygen pressure and the products are often contaminated with non decomposed CrO_3. Additionally, amorphous $CrO_{2-\delta}(0 \leq \delta \leq 0.5)$ synthesized under ambient conditions by a reduction of potassium chromate solution with

borohydride followed by heat treatment at moderate temperatures have been shown to exhibit >150 mAh g^{-1} capacity [230]. However, the absence of lithium in these materials makes them unsuitable to be employed with carbon anodes in lithium-ion cells.

5.3.10.3 Iron-Based Oxides

Iron oxides offer significant advantages compared to other 3*d*-transition-metal oxides from both cost and toxicity points of view. Although $LiFeO_2$ obtained by conventional procedures adopts the cubic structure (*Fm*3*m* S.G.), the O3-type layered α-$LiFeO_2$ can be obtained by following the same procedure as in the case of $LiMnO_2$, i.e., by ion-exchange reactions of NaMO_2. Unfortunately, the layered $LiFeO_2$ does not exhibit good electrochemical properties as the high spin Fe^{3+}:$3d^5$ ion having no particular preference for octahedral coordination tends to migrate to the lithium planes via the neighboring tetrahedral sites [231]. The cubic phase synthesized via solid state reaction exhibits well-formed crystallites of 0.55 μm size. Magnetic measurements have evidenced that α-$LiFeO_2$ exhibits deviation from the Curie–Weiss law with $\mu_{eff} << 5.9\ \mu_B$ at room temperature. The cationic disorder seems to affect the magnetic properties. This compound is expected to belong to the class of Fe-diluted magnetic semiconductors regarding its magnetic properties. Electrochemical texts show severe structural changes that occurred during the first charge–discharge process of the cells. The structural transformation from α-$LiFeO_2$ to $LiFe_5O_8$ spinel phase has been evidenced by ex situ X-ray diffraction and Raman spectroscopy [231].

5.4 Concluding Remarks

Numerous efforts are done to replace the lithium-cobalt oxide used in the first generation of commercial lithium-ion batteries by materials with low cost and environmental concerns. The development of new materials needs new synthesis procedure such as sol–gel processing, ion-exchange reaction, and hydrothermal reaction. The chemical and structural stabilities of the transition-metal oxide electrodes have been compared by studying bulk samples. In this respect, the various physicochemical techniques are welcome to design the best structure. Synthesis of amorphous compounds could help the knowledge of microstructures in this regard.

The search for layered materials that exhibit superior cycling performance has led to the study of transition-metal- and cation-substituted materials of the series LiMO_2 with M = (Ni, Co), (Ni, Co, Al), (Ni, Mn, Co) and composite materials. Doping was successful in many cases such as $LiNiO_2$, $LiCoO_2$, and $LiMnO_2$. The $LiCo_{1-y}M_yO_2$ system showing relatively better chemical stability can replace the conventional $LiCoO_2$ with respect to oxygen loss. New systems such as

$LiNi_{0.5}Mn_{0.5}O_2$ and $LiNi_{0.33}Mn_{0.33}Co_{0.33}O_4$ show interesting electrochemical features but need better control of their crystal chemistry. Frameworks built with layered-rocksalt solid solution are very promising materials but the irreversible capacity loss must controlled by anionic substitution or surface modification. Some progress has been recently done with carbon-coating or aluminum doping. In view of maximizing the cell voltage and energy density, transition metal oxide hosts have emerged as the choice for cathodes [232–235]. The electrode properties of some of the 3*d* transition-metal oxides are summarized in Table 5.1. However, only 70 % of the theoretical capacity is currently delivered by the layered $LiMO_2$ oxides. The high capacity delivered by the $xLi_2MnO_3 \cdot (1-x)LiMO_2$ cathodes (>250 mAh g^{-1}) has been attributed to the electrochemical activation of the Li_2MnO_3 component within the crystal lattice but the studies of structural instabilities such as phase separation of Li_2MnO_3 should be clarified.

The future challenge is to develop cathodes with simple transition-metal layered oxides in which at least one lithium ion per transition-metal ion could be reversibly extracted/inserted while keeping the materials cost and toxicity low; such a cathode can nearly double the energy density compared to the present level. There are also possibilities to increase the capacity of cathode hosts perhaps by focusing on nanosized powders and amorphous materials. From a safety, cycle and shelf life points of view, such cathodes with a voltage lower than 4.5 V, but with a significantly increased capacity are desirable for future applications.

Table 5.1 Comparison of the electrode characteristics of some 3*d* transition-metal layered oxides

Compound	First discharge capacity (mAh g^{-1})	Average voltage (V vs. Li)	Li uptake	Energy density (Wh kg^{-1})
$Li_xV_2O_5$	420	2.25	3.0	923
$Li_{1+x}V_3O_8$	308	2.50	4.0	770
Li_xMoO_3	250	2.30	1.5	575
$Li_{1-x}CoO_2$	140	3.70	0.5	520
$Li_{1-x}NiO_2$	160	3.80	0.5	530
$Li_{1-x}Ni_{0.70}Co_{0.30}O_2$	180	3.75	0.6	675
$Li_{1-x}Ni_{0.80}Co_{0.15}Al_{0.05}O_2$	120	3.60	0.8	400
$Li_{1-x}Ni_{1/3}Mn_{1/3}Co_{1/3}O_2$	170	3.30	1.0	560
$Li_{1.2}Ni_{0.2}Mn_{0.6}O_2$	178	3.50	1.0	623
$Li_{1.17}Mn_{0.33}Co_{0.5}O_2$	254	3.50	1.0	889
$Li_{1.17}Ni_{0.125}Mn_{0.33}Co_{0.375}O_2$	265	3.50	1.0	927

References

1. Gamble FR, Osiecki JH, Cais M, Pisharody R, DiSalvo FL, Geballe TH (1971) Intercalation complexes of Lewis bases and layered sulfides: a large class of new superconductors. Science 174:493–497
2. Broadhead J, Butherus AD (1972) Rechargeable nonaqueous battery. US Patent 3,791,867. Accessed 24 July 1972
3. Mizushima K, Jones PC, Wiseman PJ, Goodenough JB (1980) Li_xCoO_2 ($0 < x < 1$): a new cathode material for batteries of high energy density. Mater Res Bull 15:783–789
4. Julien C, Nazri GA (1994) Transport properties of lithium-intercalated MoO_3. Solid State Ionics 68:111–116
5. Crouch-Baker S, Dickens PG (1989) Qualitative bonding models for some molybdenum oxide phases. Solid State Ionics 32–33:219–227
6. Julien C (1990) Technological applications of solid state ionics. Mater Sci Eng B 6:9–15
7. Julien C, Hussain OM, El-Farh L, Balkanski M (1992) Electrochemical studies of lithium insertion in MoO_3 films. Solid State Ionics 53–56:400–404
8. Campanella L, Pistoia G (1971) MoO_3: a new electrode material for nonaqueous secondary battery applications. J Electrochem Soc 118:1905–1908
9. Besenhard JO, Heydecke J, Wudy E, Fritz HP, Foag W (1983) Characteristics of molybdenum oxide and chromium oxide cathodes in primary and secondary organic electrolyte batteries. II. Transport properties. Solid State Ionics 8:61–71
10. Goodenough JB (1990) Designing a reversible solid electrode. In: Akridge JR, Balkanski M (eds) Solid state microbatteries, NATO-ASI Series, Ser. B 217. Plenum, New York, pp 213–232
11. Yebka B, Julien C (1997) Lithium intercalation in sputtered MoO_3 films. Ionics 3:83–88
12. Nadkarni GS, Simmons JG (1970) Electrical properties of evaporated molybdenum oxide films. J Appl Phys 41:545
13. Goodenough JB (1971) Metallic oxides. Prog Solid State Chem 5:145–399
14. Julien C, Nazri GA (2001) Intercalation compounds for advanced lithium batteries. In: Nalwa HS (ed) Handbook of advanced electronic and photonic materials, vol 10. Academic Press, San Diego, pp 99–184
15. Bystrom A, Wilhelmi KA, Brotzen O (1950) Vanadium pentoxide a compound with five-coordinated vanadium atoms. Acta Chem Scand 4:1119–1130
16. Bachmann HG, Ahmed FR, Barnes WH (1961) The crystal structure of vanadium pentoxide. Z Kristallogr 115:110–116
17. Cava RJ, Santoro A, Murphy DW, Zahurak SM, Fleming RM, Marsh P, Roth RS (1986) he structure of the lithium-inserted metal oxide LiV_2O_5. J Solid State Chem 65:63–71
18. Murphy DW, Christian PA, DiSalvo FJ, Carides JN, Waszczak JV (1981) Lithium incorporation by V_6O_{13} and related vanadium (+4,+5) oxide cathode materials. J Electrochem Soc 128:2053–2060
19. Dickens PG, French SJ, Hight AT, Pye MF (1979) Phase relationship in the ambient temperature $Li_xV_2O_5$ system ($0.1 < x < 1.0$). Mater Res Bull 14:1295–1299
20. Galy J (1992) Vanadium pentoxide and vanadium oxide bronzes – structural chemistry of single (S) and double (D) layer $M_xV_2O_5$ phases. J Solid State Chem 100:229–245
21. West K, Zachau-Christiansen B, Jacobsen T, Skaarup S (1991) Vanadium oxides as host materials for lithium and sodium intercalation. Mater Res Soc Symp Proc 210:449–460
22. Delmas C, Brethes S, Ménétrier M (1991) ω-$Li_xV_2O_5$ a new electrode material for rechargeable lithium batteries. J Power Sourc 34:113–118
23. Leger C, Bach S, Soudan P, Pereira-Ramos JP (2005) Structural and electrochemical properties of ω-$Li_xV_2O_5$ ($0.4 \leq x \leq 3$) as rechargeable cathodic material for lithium batteries. J Electrochem Soc 152:A236–A241
24. Dickens PG, Reynolds GJ (1981) Thermodynamics and kinetics of the electrochemical insertion of lithium into tungsten. Solid State Ionics 5:351–354

25. Li WD, Xu CX, Du Y, Fang HT, Feng YJ, Zhen L (2014) Electrochemical lithium insertion behavior of β-$Li_xV_2O_5$ phases ($0 < x \leq 3$) as cathode material for secondary lithium batteries. J Electrochem Soc 161:A75–A83
26. Wadsley AD (1957) Crystal chemistry of non-stoichiometric pentavalent vanadium oxides: crystal structure of $Li_{1+x}V_3O_8$. Acta Crystallogr 10:261–267
27. Pistoia G, Panero S, Tocci M, Moshtev R, Manev V (1984) Solid solutions $Li_{1+x}V_3O_8$ as cathodes for high rate secondary Li batteries. Solid State Ionics 13:311–318
28. Pasquali M, Pistoia G, Manev V, Moshtev RV (1986) Li/$Li_{1+x}V_3O_8$ batteries. J Electrochem Soc 133:2454–2458
29. Pistoia G, Pasquali M, Tocci M, Moshtev RV, Manev V (1985) Li/$Li_{1+x}V_3O_8$ secondary batteries. III. Further characterization of the mechanism of Li^+ insertion and of the cycling behavior. J Electrochem Soc 132:281–284
30. Besenhard JO, Schöllhorn R (1976/1977) The discharge reaction mechanism of the MoO3 electrode in organic electrolytes. J Power Sourc 1:267–276
31. Schöllhorn R, Klein-Reesink F, Reimold R (1979) Formation, structure and topotactic exchange reactions of the layered hydrogen bronze $H_xV_3O_8$. J Chem Soc Chem Commun 398–399
32. Nassau K, Murphy DW (1981) The quenching and electrochemical behaviour of Li_2O-V_2O_5 glasses. J Non Cryst Solids 44:297–304
33. West K, Zachau-Christiansen B, Skaarup S, Saidi Y, Barker L, Olsen II, Pynenburg R, Koksbang R (1996) Comparison of LiV_3O_8 cathode materials prepared by different methods. J Electrochem Soc 143:820–826
34. Winter M, Besenhard JO, Sparhr ME, Novak P (1998) Insertion electrode materials for rechargeable lithium batteries. Adv Mater 10:725–763
35. Pistoia G, Li L, Wang G (1992) Direct comparison of cathode materials of interest for secondary high-rate lithium cells. Electrochim Acta 37:63–68
36. Kawakita J, Miura T, Kishi T (1999) Lithium insertion and extraction kinetics of $Li_{1+x}V_3O_8$. J Power Sourc 83:79–83
37. Jouanneau S, Verbaere A, Lascaud S, Guyomard D (2006) Improvement of the lithium insertion properties of $Li_{1.1}V_3O_8$. Solid State Ionics 177:311–315
38. Jouanneau S, Le Gal La Salle A, Verbaere A, Guyomard D (2005) The origin of capacity fading upon lithium cycling in $Li_{1.1}V_3O_8$. J Electrochem Soc 152:A1660–A1667
39. Xie JG, Li JX, Zhan H, Zhou YH (2003) Low-temperature sol-gel synthesis of $Li_{1.2}V_3O_8$ from V_2O_5 gel. Mater Lett 57:2682–2687
40. Kawakita J, Katayama Y, Miura T, Kishi T (1998) Lithium insertion behavior of $Li_{1+x}V_3O_8$ prepared by precipitation technique in CH_3OH. Solid State Ionics 110:199–207
41. Liu HM, Wang YG, Wang KX, Wang YR, Zhou HS (2009) Synthesis and electrochemical properties of single-crystalline LiV_3O_8 nanorods as cathode materials for rechargeable lithium batteries. J Power Sourc 192:668–673
42. Liu HM, Wang YG, Wang WS, Zhou HS (2011) A large capacity of LiV_3O_8 cathode material for rechargeable lithium-based batteries. Electrochim Acta 56:1392–1398
43. Si YC, Jiao LF, Yan HT, Li HX, Wang YM (2009) Structural and electrochemical properties of LiV_3O_8 prepared by combustion synthesis. J Alloys Compd 486:400–405
44. Ju SH, Kang YC (2010) Morphological and electrochemical properties of LiV_3O_8 cathode powders prepared by spray pyrolysis. Electrochim Acta 55:6088–6092
45. Sakunthala A, Reddy MV, Selvasekarapandian S, Chowdari BVR, Selvin PC (2010) Preparation, characterization and electrochemical performance of lithium trivanadate rods by a surfactant-assisted olymer precursor method for lithium batteries. J Phys Chem C 114:8099–8107
46. Hui Y, Juan L, Zhang JG, Jia DZ (2007) Synthesis and properties of LiV_3O_8 nanomaterials as the cathode material for Li-ion battery. J Inorg Mater 22:447–450
47. Yang H, Li J, Zhang XG, Jin YL (2008) Synthesis of LiV_3O_8 nanocrystallites as cathode materials for lithium ion batteries. J Mater Process Technol 207:265–270

48. Liu XH, Wang JQ, Zhang JY, Yang SR (2007) Sol-gel template synthesis of LiV_3O_8 nanowires. J Mater Sci 42:867–871
49. Lee KP, Manesh KM, Kim KS, Gopalan AY (2009) Synthesis and characterization of nanostructured wires (1D) to plates (3D) LiV_3O_8 combining sol-gel and electrospinning processes. J Nanosci Nanotechnol 9:417–422
50. Xu HY, Wang H, Song ZQ, Wang YW, Yan H, Yoshimura M (2004) Novel chemical method for synthesis of LiV_3O_8 nanorods as cathode materials for lithium ion batteries. Electrochim Acta 49:349–353
51. Sun D, Jin G, Wang H, Huang X, Ren Y, Jiang J, He H, Tang Y (2014) $Li_xV_2O_5/LiV_3O_8$ nanoflakes with significantly improved electrochemical performance for Li-ion batteries. J Mater Chem A 2:8009–8016
52. Liu L, Jiao LF, Sun JL, Zhang YH, Zhao M, Yuan HT, Wang YM (2008) Electrochemical performance of $LiV_{3-x}Ni_xO_8$ cathode materials synthesized by a novel low-temperature solid-state method. Electrochim Acta 53:7321–7325
53. Wang H, Ren Y, Wang Y, Wang W, Liu S (2012) Synthesis of LiV_3O_8 nanosheets as a high-rate cathode material for rechargeable lithium batteries. Cryst Eng Comm 14:2831–2836
54. Feng CQ, Chew SY, Guo ZP, Wang JZ, Liu HK (2007) An investigation of polypyrrole-LiV_3O_8 composite cathode materials for lithium-ion batteries. J Power Sourc 174:1095–1099
55. Kumagai N, Yu A (1997) Ultrasonically treated LiV_3O_8 as a cathode material for secondary lithium batteries. J Electrochem Soc 144:830–835
56. Orman HJ, Wiseman PJ (1984) Cobalt(III) lithium oxide, $CoLiO_2$: structure refinement by powder neutron diffraction. Acta Crystallogr C 40:12–14
57. Delmas C, Fouassier C, Hagenmuller P (1980) Structural classification and properties of the layered oxides. Physica B 99:81–85
58. Venkatraman S, Manthiram A (2002) Synthesis and characterization of P3-type $CoO_{2-\delta}$. Chem Mater 14:3907–3912
59. Gao Y, Yakovleva MV, Ebner WB (1998) Novel $LiNi_{1-x}Ti_{x/2}Mg_{x/2}O_2$ compounds as cathode materials for safer lithium-ion batteries. Electrochem Solid State Lett 1:117–119
60. Cho J, Kim G, Lim HS (1999) Effect of preparation methods of $LiNi_{1-x}Co_xO_2$ cathode materials on their chemical structure of electrode performance. J Electrochem Soc 146:3571–3576
61. Mueller-Neuhaus JR, Dunlap RA, Dahn JR (2000) Understanding irreversible capacity in $LiNi_{1-y}Fe_yO_2$ cathode materials. J Electrochem Soc 147:3598–3605
62. Goodenough JB, Mizuchima K (1981) Electrochemical cell with new fast ion conductors. US Patent 4,302,518. Accessed 24 Nov 1981
63. Nagaura T, Tozawa K (1990) Lithium ion rechargeable battery. Prog Batteries Solar Cells 9:209–212
64. Gummow RJ, Thackeray MM, David WIF, Hull S (1992) Structure and electrochemistry of lithium cobalt oxide synthesized at 400 °C. Mater Res Bull 27:327–337
65. Shao-Horn Y, Hackney SA, Kahaian AJ, Thackeray MM (2002) Structural stability of $LiCoO_2$ at 400 °C. J Solid State Chem 168:60–68
66. Johnston WD, Heikes RR, Sestrich D (1958) The preparation, crystallography and magnetic properties of the $Li_xCo_{(1-x)}O$ system. J Phys Chem Solids 7:1–13
67. Ohzuku T, Ueda A (1994) Solid-state redox reactions of $LiCoO_2$ (R-3 m) for 4 volt secondary lithium cells. J Electrochem Soc 141:2972–2977
68. Oh IH, Hong YS, Sun YK (1997) Low-temperature preparation of ultrafine $LiCoO_2$ powders by the sol-gel method. J Mater Sci 32:3177–3182
69. Julien C, El-Farh L, Rangan S, Massot M (1999) Synthesis of $LiNi_{1-y}Co_yO_2$ cathode materials prepared by a citric acid-assisted sol-gel method for lithium batteries. J Sol Gel Sci Technol 15:63–72
70. Santiago EI, Andrade AVC, Paiva-Santos CO, Bulhoes LOS (2003) Structural and electrochemical properties of $LiCoO_2$ prepared by combustion synthesis. Solid State Ionics 158:91–102

71. Han CH, Hong YS, Park CM, Kim K (2001) Synthesis and electrochemical properties of lithium cobalt oxides prepared by molten-salt synthesis using the eutectic mixture of LiCl-Li_2CO_3. J Power Sourc 92:95–101
72. Kosova NV, Anufrienko VF, Larina TV, Rougier A, Aymard L, Tarascon JM (2002) Disordering and electronic state of cobalt ions in mechanochemically synthesized $LiCoO_2$. J Solid State Chem 165:56–64
73. Brylev OA, Shlyakhtin OA, Kulova TL, Skundin AM, Tretyakov YD (2003) Influence of chemical prehistory on the phase formation and electrochemical performance of $LiCoO_2$ materials. Solid State Ionics 156:291–299
74. Larcher D, Polacin MR, Amatucci GG, Tarascon JM (1997) Electrochemically active $LiCoO_2$ and $LiNiO_2$ made by cationic exchange under hydrothermal conditions. J Electrochem Soc 144:408–417
75. Yan H, Huang X, Zhonghua L, Huang H, Xue R, Chen L (1997) Microwave synthesis of $LiCoO_2$ cathode materials. J Power Sourc 68:530–532
76. Akimoto J, Gotoh Y, Oosawa Y (1998) Synthesis and structure refinement of $LiCoO_2$ single crystals. J Solid State Chem 141:298–302
77. Amatucci GG, Tarascon JM, Klein LC (1996) CoO_2, the end member of the Li_xCoO_2 solid solution. J Electrochem Soc 143:1114–1123
78. Chebiam RV, Prado F, Manthiram A (2001) Soft chemistry synthesis and characterization of layered $Li_{1-x}Ni_{1-y}Co_yO_{2-\delta}$ ($0 \leq x \leq 1$ and $0 \leq y \leq 1$). Chem Mater 13:2951–2957
79. Chebiam RV, Kannan AM, Prado F, Manthiram A (2001) Comparison of the chemical stability of the high energy density cathodes of lithium-ion batteries. Electrochem Commun 3:624–627
80. Delmas C, Saadoune I (1992) Electrochemical and physical properties of the $Li_xNi_{1-y}Co_yO_2$ phases. Solid State Ionics 53–56:370–375
81. Venkatraman S, Shin Y, Manthiram A (2003) Phase relationships and structural and chemical stabilities of charged $Li_{1-x}CoO_{2-\delta}$ and $Li_{1-x}Ni_{0.85}Co_{0.15}O_{2-\delta}$ cathodes. Electrochem Solid State Lett 6:A9–A12
82. Reimers JN, Dahn JR (1992) Electrochemical and in situ X-ray diffraction studies of lithium intercalation in Li_xCoO_2. J Electrochem Soc 139:2091–2097
83. Mauger A, Julien CM (2014) Surface modifications of electrode materials for lithium-ion batteries: status and trends. Ionics 20:751–787
84. Laubach S, Laubach S, Schmidt C, Ensling D, Schmid S, Jaegermann W, Thissen A, Nikolowski K, Erhenberg H (2009) Changes in the crystal end electronic structure of $LiCoO_2$ and $LiNiO_2$ upon Li intercalation and de-intercalation. Phys Chem Chem Phys 11:3278–3289
85. Hirano A, Kanno R, Kawamoto Y, Takeda Y, Yamamura K, Takano M, Ohyama K, Ohashi M, Yamaguchi Y (1995) Relationship between non-stoichiometry and physical properties in $LiNiO_2$. Solid State Ionics 78:123–131
86. Ohzuku T, Ueda A, Nagayama M, Iwakashi Y, Komori H (1993) Comparative study of $LiCoO_2$, $LiNi_{1/2}Co_{1/2}O_2$ and $LiNiO_2$ for 4 volt secondary lithium cells. Electrochim Acta 38:1159–1167
87. Dahn JR, Fuller EW, Obrovac M, von Sacken U (1994) Thermal stability of Li_xCoO_2, Li_xNiO_2 and λ-MnO_2 and consequence for the safety of Li-ion cells. Solid State Ionics 69:265–270
88. Zhang Z, Fouchard D, Rea JR (1998) Differential scanning calorimetry material studies: implications for the safety of lithium-ion cells. J Power Sourc 70:16–20
89. Bianchi V, Caurant D, Baffier N, Belhomme C, Chappel E, Chouteau G, Bach S, Pereira-Ramos JP, Sulpice A, Wilmann P (2001) Synthesis, structural characterization and magnetic properties of quasistoichiometric $LiNiO_2$. Solid State Ionics 140:1–17
90. Arai H, Okada S, Yamaki J (1998) Thermal behavior of $Li_{1-y}NiO_2$ and the decomposition mechanism. Solid State Ionics 109:295–302

91. Li W, Curie J (1997) Morphology effects on the electrochemical performance of $LiNi_{1-x}Co_xO_2$. J Electrochem Soc 144:2773–2779
92. Guilmard M, Pouillerie C, Croguennec L, Delmas C (2003) Structural and electrochemical properties of $LiNi_{0.70}Co_{0.15}Al_{0.15}O_2$. Solid State Ionics 160:39–50
93. Ohzuku T, Ueda A, Kouguchi M (1995) Synthesis and characterization of $LiAl_{1/4}Ni_{3/4}O_2$ (R-3 m) for lithium-ion (shuttlecock) batteries. J Electrochem Soc 142:4033–4039
94. Delmas C, Saadoune I, Rougier A (1993) The cycling properties of the $Li_xNi_{1-y}Co_yO_2$ electrode. J Power Sourc 44:595–602
95. Kannan AM, Manthiram A (2002) Degradation of $LiNi_{0.8}Co_{0.2}O_2$ cathode surfaces in high-power lithium-ion batteries. Electrochem Solid State Lett 5:A164–A166
96. Gummow RJ, Thackeray MM (1993) Characterization of LT-$Li_xCo_{1-y}Ni_yO_2$ electrodes for rechargeable lithium cells. J Electrochem Soc 140:3365–3368
97. Julien C, Letranchant C, Rangan S, Lemal M, Ziolkiewicz S, Castro-Garcia S, El-Farh L, Benkaddour M (2000) Layered $LiNi_{0.5}Co_{0.5}O_2$ cathode materials grown by soft-chemistry via various solution methods. Mater Sci Eng B 76:145–155
98. Ohzuku T, Yanagawa T, Kouguchi M, Ueda A (1997) Innovative insertion material of $LiAl_{1/4}Ni_{3/4}O_2$ (R-3 m) for lithium-ion (shuttlecock) batteries. J Power Sourc 68:131–134
99. Julien C, Nazri GA, Rougier A (2000) Electrochemical performances of layered $LiM_{1-y}M_y'O_2$ (M = Ni, Co; M′ = Mg, Al, B) oxides in lithium batteries. Solid State Ionics 135:121–130
100. Julien C, Michael SS, Ziolkiewicz S (1999) Structural and electrochemical properties of $LiNi_{0.3}Co_{0.7}O_2$ synthesized by different low-temperature techniques. Int J Inorg Mat 1:29–34
101. Abdel-Ghany AE, Hashem AMA, Abuzeid HAM, Eid AE, Bayoumi HA, Julien CM (2009) Synthesis, structure characterization and magnetic properties of nanosized $LiCo_{1-y}Ni_yO_2$ prepared by sol-gel citric acid route. Ionics 15:49–59
102. Goodenough JB (1999) Oxide engineering for advanced power sources. Electrochem Soc Proc 99–24:1–14
103. Julien C (2000) Local cationic environment in lithium nickel-cobalt oxides used as cathode materials for lithium batteries. Solid State Ionics 136–137:887–896
104. Senaris-Rodriguez MA, Castro-Garcia S, Castro-Couceiro A, Julien C, Hueso LE, Rivas J (2003) Magnetic clusters in $LiNi_{1-y}Co_yO_2$ nanomaterials used as cathodes in lithium-ion batteries. Nanotechnology 14:277–282
105. Zhang X, Julien CM, Mauger A, Gendron F (2011) Magnetic analysis of lamellar oxides for Li-ions batteries. Solid State Ionics 188:148–155
106. Delmas C, Ménétrier M, Croguennec L, Saadoune I, Rougier A, Pouillerie C, Prado G, Grüne M, Fournès L (1999) An overview of the Li(Ni, M)O2 systems: synthesis, structure and properties. Electrochim Acta 45:243–253
107. Caurant D, Baffier N, Bianchi V, Grégoire G, Bach S (1996) Preparation by a chimie douce route and characterization of $LiNi_zMn_{1-z}O_2$ ($0.5 \leq z \leq 1$) cathode materials. J Mater Chem 6:1149–1155
108. Julien C, Castro-Garcia S (2001) Lithiated cobaltates for Li-ion batteries. Structure, morphology and electrochemistry of oxides grown by solid-state reaction, wet chemistry and film deposition. J Power Sourc 97–98:290–293
109. Ramana CV, Zaghib K, Julien CM (2006) Highly oriented growth of pulsed-laser deposited $LiNi_{0.8}Co_{0.2}O_2$ films for application in microbatteries. Chem Mater 18:1397–1400
110. Julien C (2000) Structure, morphology and electrochemistry of doped lithium cobalt oxides. Ionics 6:451–460
111. Julien C (2003) Local structure and electrochemistry of lithium cobalt oxides and their doped compounds. Solid State Ionics 157:57–71
112. Julien C, Camacho-Lopez MA, Lemal M, Ziolkiewicz S (2002) $LiCo_{1-y}M_yO_2$ positive electrodes for rechargeable lithium batteries. I. Aluminium doped materials. Mater Sci Eng B 95:6–13

113. Amdouni N, Zarrouk H, Soulette F, Julien C (2003) $LiAl_yCo_{1-y}O_2$ ($0.0 \leq y \leq 0.3$) intercalation compounds synthesized from the citrate precursors. Mater Chem Phys 80:205–214
114. Julien CM, Mauger A, Groult H, Zhang X, Gendron F (2011) $LiCo_{1-y}B_yO_2$ as cathode materials for rechargeable lithium batteries. Chem Mater 23:208–218
115. Amdouni N, Zarrouk H, Julien C (2003) Low temperature synthesis of $LiCr_{0.3}Co_{0.7}O_2$ intercalation compounds using citrate, oxalate, succinate and glycinate precursors. British Ceram Trans 102:27–30
116. Julien C, Letranchant C, Lemal M, Ziolkiewicz S, Castro-Garcia S (2002) Layered $LiNi_{1-y}Co_yO_2$ compounds synthesized by a glycine-assisted combustion method for lithium batteries. J Mater Sci 37:2367–2375
117. Mazas-Brandariz D, Senaris-Rodriguez MA, Castro-Garcia S, Camacho-Lopez MA, Julien C (1999) Structural properties of $LiNi_{1-y}Co_yO_2$ ($0 \leq y \leq 1$) synthesized by wet chemistry via malic acid-assisted technique. Ionics 5:345–350
118. Castro-Couceiro A, Castro-Garcia S, Senaris-Rodriguez MA, Soulette F, Julien C (2002) Effects of the aluminum doping on the microstructure and morphology of $LiNi_{0.5}Co_{0.5}O_2$ oxides. Ionics 8:192–200
119. Abuzeid HA, Hashem AM, Abdel-Ghany AE, Eid AE, Mauger A, Groult H, Julien CM (2011) Study of the delithiation of $LiMn_{0.2}Co_{0.8}O_2$ cathode material for lithium batteries. ECS Trans 35–34:95–102
120. Abuzeid HAM, Hashem AMA, Abdel-Ghany AE, Eid AE, Mauger A, Groult H, Julien CM (2011) De-intercalation of $LiCo_{0.8}Mn_{0.2}O_2$: a magnetic approach. J Power Sourc 196:6440–6448
121. Wang GX, Bewlay S, Yao J (2003) Multiple-ion doped lithium nickel oxides as cathode materials for lithium-ion batteries. J Power Sourc 119–121:189–194
122. Kostecki R, McLarnon F (2004) Local-probe studies of degradation of composite $LiNi_{0.80}Co_{0.15}Al_{0.05}O_2$ cathodes in high-power lithium-ion cells. Electrochem Solid State Lett 7:A380–A383
123. Weaving J, Coowar F, Teagle D, Cullen J, Dass V, Bindin P, Green R, Macklin W (2001) Development of high energy density Li-ion batteries based on $LiNi_{1-x-y}Co_xAl_yO_2$. J Power Sourc 97:733–735
124. Bang HJ, Joachin H, Yang H, Amine K, Prakash J (2006) Contribution of the structural changes of $LiNi_{0.80}Co_{0.15}Al_{0.05}O_2$ cathodes on the exothermic reactions in Li-ion cells. J Electrochem Soc 153:A731–A737
125. Ju S, Jang H, Kang Y (2007) Al-doped Ni-rich cathode powders prepared from the precursor powders with fine size and spherical shape. Electrochim Acta 52:7286–7292
126. Biensan P, Simon B, Pérès JP, de Guilbert A, Broussely M, Bodet JM, Perton F (1999) On safety of lithium-ion cells. J Power Sourc 81:906–912
127. Majumdar SB, Nieto S, Katiyar RS (2006) Synthesis and electrochemical properties of $LiNi_{0.80}(Co_{0.20-x}Al_x)O_2$ ($x = 0.0$ and 0.05) cathodes for Li ion rechargeable batteries. J Power Sourc 154:262–267
128. Chebiam RV, Prado F, Manthiram A (2001) Structural instability of delithiated $Li_{1-x}Ni_{1-y}Co_yO_2$ cathodes. J Electrochem Soc 148:A49–A53
129. Cho Y, Cho J (2010) Significant improvement of $LiNi_{0.80}Co_{0.15}Al_{0.05}O_2$ cathodes at 60 °C by SiO_2 dry coating for Li-ion batteries. J Electrochem Soc 157:A625–A629
130. Cho Y, Lee YS, Park SA, Lee Y, Cho J (2010) $LiNi_{0.80}Co_{0.15}Al_{0.05}O_2$ cathodes materials prepared by TiO_2 nanoparticle coatings on $Ni_{0.80}Co_{0.15}Al_{0.05}(OH)_2$ precursors. Electrochim Acta 56:333–339
131. Lee DJ, Scrosati B, Sun YK (2011) $Ni_3(PO_4)_2$-coated $Li(Ni_{0.80}Co_{0.15}Al_{0.05})O_2$ lithium battery electrode with improved cycling performance at 55 °C. J Power Sourc 196:7742–7746
132. Lee SH, Yoon CS, Amine K, Sun YK (2013) Improvement of long-term cycling performance of $Li(Ni_{0.80}Co_{0.15}Al_{0.05})O_2$ by AlF_3 coating. J Power Sourc 234:201–207

133. Lim SN, Ahn W, Yeon SH, Park SB (2014) Enhanced elevated-temperature performance of $LiNi_{0.80}Co_{0.15}Al_{0.05}O_2$ electrodes coated with Li_2O-$2B_2O_3$ glass. Electrochim Acta 136:1–9
134. Ju JH, Chung YM, Bak YR, Hwang MJ, Ryu KS (2010) The effects of carbon nano-coating on $Li(Ni_{0.80}Co_{0.15}Al_{0.05})O_2$ cathode material using organic carbon for Li-ion battery. Surf Rev Lett 17:51–58
135. Belharouak I, Lu W, Vissers D, Amine K (2006) Safety characteristics of $Li(Ni_{0.8}Co_{0.15}Al_{0.05})O_2$ and $Li(Ni_{1/3}Co_{1/3}Mn_{1/3})O_2$. Electrochem Commun 8:329–335
136. Ohzuku T, Makimura Y (2001) Layered lithium insertion material of $LiNi_{1/2}Mn_{1/2}O_2$: a possible alternative to $LiCoO_2$ for advanced lithium-ion batteries. Chem Lett 30:744–745
137. Liu Y, Chen B, Cao F, Zhao X, Yuan J (2011) Synthesis of nanoarchitectured $LiNi_{0.5}Mn_{0.5}O_2$ spheres for high-performance rechargeable lithium-ion batteries via an in situ conversion route. J Mater Chem 21:10437–10441
138. Abdel-Ghany A, Zaghib K, Gendron F, Mauger A, Julien CM (2007) Structural, magnetic and electrochemical properties of $LiNi_{0.5}Mn_{0.5}O_2$ as positive electrode for Li-ion batteries. Electrochim Acta 52:4092–4100
139. Yamaura K, Takano M, Hirano A, Kanno R (1996) Magnetic properties of $Li_{1-x}Ni_{1+x}O_2$ ($0 \leq x \leq 0.08$). J Solid State Chem 127:109–118
140. Goodenough JB (1963) Magnetism and the chemical bond. Wiley-Interscience, New York
141. Liu Z, Yu A, Lee JY (1999) Synthesis and characterization of $LiNi_{1-x-y}Co_yMn_yO_2$ as the cathode materials secondary lithium batteries. J Power Sourc 81–82:416–419
142. Lu Z, MacNeil DD, Dahn JR (2001) Layred $Li[Ni_xCo_{1-2x}Mn_x]O_2$ cathode materials for lithium-ion batterie. Electrochem Solid State Lett 4:A200–A203
143. MacNeil DD, Lu Z, Dahn JR (2002) Structure and electrochemistry of $Li[Ni_xCo_{1-2x}Mn_x]O_2$ ($0 \leq x \leq 1/2$). J Electrochem Soc 149:A1332–A1336
144. Shaju KM, Subba-Rao GV, Chowdari BVR (2002) Performance of layered $Li(Ni_{1/3}Co_{1/3}Mn_{1/3})O_2$ as cathode for Li-ion batteries. Electrochim Acta 48:145–151
145. Yabuuchi N, Ohzuku T (2003) Novel lithium insertion material of Li $Ni_{1/3}Co_{1/3}Mn_{1/3}O_2$ for advanced lithium-ion batteries. J Power Sourc 119–121:171–174
146. Lee S, Park SS (2012) Atomistic simulation study of mixed-metal oxide ($LiNi_{1/3}Mn_{1/3}Co_{1/3}O_2$) cathode material for lithium ion battery. J Phys Chem C 116:6484–6489
147. Wang L, Li J, He X, Pu W, Wan C, Jiang C (2005) Recent advances in layered $LiNi_xCo_yMn_{1-x-y}O_2$ cathode materials for lithium ion batteries. J Solid State Electrochem 13:1157–1164
148. Fergus JW (2010) Recent developments in cathode materials for lithium ion batteries. J Power Sourc 195:939–954
149. Zhu JP, Xu QB, Yang HW, Zhao JJ, Yang G (2011) Recent development of $LiNi_{1/3}Co_{1/3}Mn_{1/3}O_2$ as cathode material of lithium ion battery. J Nanosci Nanotechnol 11:10357–10368
150. Zeng D, Cabana J, Bréger J, Yoon WS, Grey CP (2007) Cation ordering in $Li[Ni_xMn_xCo_{(1-2x)}]O_2$-layered cathode materials. Chem Mater 19:6277–6289
151. Liao PY, Duh JG, Sheen SR (2005) Microstructure and electrochemical performance of $LiNi_{0.6}Co_{0.4-x}Mn_xO_2$ cathode materials. J Power Sourc 143:212–218
152. Gan CL, Hu XH, Zhan H (2005) Synthesis and characterization of $Li_{1.2}Ni_{0.6}Co_{0.2}Mn_{0.2}O_{2+\delta}$ as cathode material for secondary lithium batteries. Solid State Ionics 176:687–692
153. Lee JW, Lee JH, Tan-Viet T, Lee JY, Kim JS, Lee CH (2010) Synthesis of $LiNi_{1/3}Mn_{1/3}Co_{1/3}O_2$ cathode materials by using a supercritical water method in a bath reactor. Electrochim Acta 55:3015–3021
154. Na SH, Kim HS, Moon SI (2005) The effect of Si doping on the electrochemical characteristics of $LiNi_xMn_yCo_{(1-x-y)}O_2$. Solid State Ionics 176:313–317
155. Ohzuku T, Makimura Y (2001) Layered lithium insertion material $LiNi_{1/3}Mn_{1/3}Co_{1/3}O_2$ for lithium-ion batteries. Chem Lett 30:642–643

156. Ngala JK, Chernova NA, Ma M, Mamak M, Zavalij PY, Whittingham MS (2004) The synthesis, characterization and electrochemical behavior of the layered $LiNi_{0.4}Mn_{0.4}Co_{0.2}O_2$ compound. J Mater Chem 14:214–220
157. Lee MH, Kang YJ, Myung ST, Sun YK (2004) Synthetic optimization of $Li[Ni_{1/3}Mn_{1/3}Co_{1/3}]O_2$ via co-precipitation. Electrochim Acta 50:939–948
158. Oh SW, Park SH, Park CW, Sun YK (2004) Structural and electrochemical properties of layered $Li(Ni_{0.5}Mn_{0.5})_{1-x}Co_xO_2$ positive materials synthesized by ultrasonic spray pyrolysis method. Solid State Ionics 171:167–172
159. Li DC, Noguchi H, Yoshio M (2004) Electrochemical characteristics of $LiNi_{0.5-x}Mn_{0.5-x}Co_{2x}O_2$ ($0 \leq x \leq 0.1$) prepared by spray dry method. Electrochim Acta 50:427–430
160. Wen JW, Liu J, Wu H, Chen CH (2007) Synthesis and electrochemical characterization of $LiCo_{1/3}Ni_{1/3}Mn_{1/3}O_2$ by radiated polymer gel method. J Mater Sci 42:7696–7701
161. Ren H, Li X, Peng Z (2011) Electrochemical properties of $Li[Ni_{1/3}Mn_{1/3}Al_{1/3-x}Co_x]O_2$ as a catode material for litium ion battery. Electrochim Acta 56:7088–7091
162. Du K, Peng Z, Hu G, Yang Y, Qi L (2009) Synthesis of $LiMn_{1/3}Ni_{1/3}Co_{1/3}O_2$ in molten KCl for rechargeable lithium-ion batteries. J Alloy Comp 476:329–334
163. Sinha NN, Munichandriaah N (2010) High rate capability of porous $LiNi_{1/3}Mn_{1/3}Co_{1/3}O_2$ synthesized by polymer template route. J Electrochem Soc 157:A647–A653
164. Samarasingh P, Tran-Nguyen DH, Behm M, Wijayasinghe A (2008) $LiNi_{1/3}Mn_{1/3}Co_{1/3}O_2$ synthesized by the Pechini method for the positive electrode in Li-ion batteries: material characteristics and electrochemical behaviour. Electrochim Acta 53:7995–8000
165. Fujii Y, Miura H, Suzuki N, Shoji T, Nakayama N (2007) Structural and electrochemical properties of $LiNi_{1/3}$ $Co_{1/3}Mn_{1/3}O_2$: calcinations temperature dependence. J Power Sourc 171:894–903
166. Park SH, Oh SW, Sun YK (2005) Synthesis and structural characterization of layered $Li[Li_{1/3+x}Co_{1/3}Mn_{1/3-2x}Mo_x]O_2$ cathode materials by ultrasonic spray pyrolysis. J Power Sourc 146:622–625
167. Li DC, Sasaki Y, Kobayakawa K (2006) Morphological, structural and electrochemical characteristics of $LiNi_{0.5}Mn_{0.4}M_{0.1}O_2$ (M = Li, Mg, Co, Al). J Power Sourc 157:488–493
168. Kim GH, Kim JH, Myung ST (2005) Improvement of high-voltage cycling behavior of surface-modified $Li[Ni_{1/3}Co_{1/3}Mn_{1/3}]O_2$ cathodes by fluorine substitution for Li-ion batteries. J Electrochem Soc 152:A1707–A1713
169. Ben-Kamel K, Amdouni N, Abdel-Ghany A, Zaghib K, Mauger A, Gendron F, Julien CM (2008) Local structure and electrochemistry of $LiNi_yMn_yCo_{1-2y}O_2$ electrode materials for Li-ion batteries. Ionics 14:89–97
170. Aurbach D, Gamolsky K, Markovsky B, Salitra G, Gofer GY, Heider U, Oesten R, Schmidt M (2000) The study of surface phenomena related to the electrochemical intercalation into Li_xMO_y host materials (M = Ni, Mn). J Electrochem Soc 147:1322–1331
171. Lee EH, Park JH, Cho JH, Cho SJ, Kim DW, Dan H, Kang Y, Lee SY (2013) Direct ultraviolet-assisted conformal coating of nanometer-thick poly(tri(2-(acryloyloxy)ethyl) phosphate gel polymer electrolytes on high-voltage $LiNi_{1/3}Co_{1/3}Mn_{1/3}O_2$ cathodes. J Power Sourc 244:389–394
172. Choi J, Manthiram A (2004) Comparison of the electrochemical behaviours of stoichiometric $Li_{1.03}(Ni_{1/3}Mn_{1/3}Co_{1/3})_{0.97}O_2$ and lithium excess $LiNi_{1/3}Mn_{1/3}Co_{1/3}O_2$. Electrochem Solid State Lett 7:A365–A368
173. Zhang X, Jiang WJ, Mauger A, Qi L, Gendron F, Julien CM (2010) Minimization of the cation mixing in $Li_{1+x}(NMC)_{1-x}Co_{1/3}O_2$ as cathode material. J Power Sourc 195:1292–1301
174. Ligneel E, Nazri GA (2009) Improvement of $LiNi_{1/3}Mn_{1/3}Co_{1/3}O_2$ by a cationic substitution and effect of over-lithiation. ECS Trans 16–50:21–29
175. Robertson AD, Bruce PG (2003) Mechanism of electrochemical activity in Li_2MnO_3. Chem Mater 15:1984–1992
176. Gan C, Zhan H, Hu X, Zhou Y (2005) Origin of the irreversible plateau (4.5 V) of Li $[Li_{0.182}Ni_{0.182}Co_{0.091}Mn_{0.545}]O_2$ layered material (2005). Electrochem Commun 7:1318–1322

177. Lei CH, Wen JG, Sardela M, Bareno J, Petrov I, Kang SH, Abraham DP (2009) Structural study of Li_2MnO_3 by electron microscopy. J Mater Sci 44:5579–5587
178. Yu DYW, Yanagida K, Kato Y, Nakamura H (2009) Electrochemical activities in Li_2MnO_3 batteries and energy storage. J Electrochem Soc 156:A417–A424
179. Amalraj F, Markovsky B, Sharon D, Talianker M, Zinigrad E, Persky R, Haik O, Grinblat J, Lampert J, Schulz-Dobrick M, Garsuch A, Burlaka L, Aurbach D (2012) Study of the electrochemical behavior of the "inactive" Li_2MnO_3. Electrochim Acta 78:32–39
180. Julien CM, Massot M (2003) Lattice vibrations of materials for lithium rechargeable batteries III. Lithium manganese oxides. Mater Sci Eng B 100:69–78
181. Johnson CS, Li N, Lefief C, Vaughey JT, Thackeray MM (2008) Synthesis, characterization and electrochemistry of lithium battery electrodes: xLi_2MnO_3-(1-x)$LiMn_{0.333}Ni_{0.333}Co_{0.333}O_2$ ($0 \leq x \leq 0.7$). Chem Mater 20:6095–6106
182. Lu ZH, Dahn JR (2002) Understanding the anomalous capacity of Li/Li[$Ni_xLi_{(1/3-2x/3)}Mn_{(2/3-x/3)}$]$O_2$ cells using in situ X-ray diffraction and electrochemical studies. J Electrochem Soc 149:A815–A822
183. Armstrong AR, Robertson AD, Bruce PG (2005) Overcharging manganese oxides: extracting lithium beyond Mn^{4+}. J Power Sourc 146:275–280
184. Okamoto Y (2012) Ambivalent effect of oxygen vacancies on Li_2MnO_3: a first principles study. J Electrochem Soc 159:A152–A157
185. Gabrisch H, Yi T, Yazami R (2008) Transmission electron microscope studies of $LiNi_{1/3}Mn_{1/3}Co_{1/3}O_2$ before and after long-term aging at 70 °C. Electrochem Solid State Lett 11:A119–A124
186. Meng YS, de Dompablo EA (2009) First principles computational materials design for energy storage materials in lithium ion batteries. Energy Environ Sci 2:589–609
187. Ito A, Shoda K, Sato Y, Hatano M, Horie H, Ohsawa Y (2011) Direct observation of the partial formation of a framework structure for Li-rich layered cathode material Li[$Ni_{0.17}Li_{0.2}Co_{0.17}Mn_{0.56}$]$O_2$ upon the first charge and discharge. J Power Sourc 196:4785–4790
188. Amalraj F, Talianker M, Markovsky B, Sharon D, Burlaka L, Shafir G, Zinigrad E, Haik O, Aurbach D, Lampert J, Schulz-Dobrick M, Garsuch A (2013) Studies of Li and Mn-rich Li_x[MnNoCo]O_2 electrodes: electrochemical performance, structure, and the effect of the aluminum fluoride coating. J Electrochem Soc 160:A2220–A2233
189. Amalraj SF, Burlaka L, Julien CM, Mauger A, Kovacheva D, Talianker M, Markovsky B, Auirbach D (2014) Phase transitions in Li_2MnO_3 electrodes at various states-of-charge. Electrochim Acta 123:395–404
190. Von Meyer G, Hoppe R (1976) ZuV thermischen verhalten von Li_3MnO_4. Uber α- und β-Li_2MnO_3. Z Anorg Allg Chem 424:257–261
191. Jonson CS, Kim JS, Lefief C, Li N, Vaughey JT, Thackeray MM (2004) The significance of the Li_2MnO_3 component in composite $xLi_2MnO_3 \cdot (1\text{-}x)LiMn_{0.5}Ni_{0.5}O_2$ electrodes. Electrochem Commun 6:1085–1091
192. Thackeray MM, Kang SH, Johnson CS, Vaughey JT, Hackney SA (2006) Comments on the structural complexity of lithium-rich $Li_{1+x}M_{1-x}O_2$ electrodes (M = Mn, Ni, Co) for lithium batteries. Electrochem Commun 8:1531–1538
193. Deng H, Belharouak I, Yoon CS, Amine K (2010) High temperatura performance of surface-treated $Li_{1.1}(Ni_{0.15}Co_{0.1}Mn_{0.55})O_{1.95}$ layered oxide. J Electrochem Soc 157:A1035–A1039
194. Armstrong AR, Holzapfel M, Novák P, Johnson CS, Kang SH, Thackeray MM, Bruce PG (2006) Demonstrating oxygen loss and associated structural reorganization in the lithium battery cathode Li[$Ni_{0.2}Li_{0.2}Mn_{0.6}$]O_2. J Am Chem Soc 128:8694–8698
195. Yuan W, Zahng HZ, Liu Q, Li GR, Gao XP (2014) Surface modification of $Li(Li_{0.17}Ni_{0.2}Co_{0.05}Mn_{0.58})O_2$ with CeO_2 as cathode material for Li-ion batteries. Electrochim Acta 135:199–207
196. Wang ZQ, Chen YC, Ouyang CY (2015) Polaron states and migration in F-doped Li_2MnO_3. Phys Lett A 378:2449–2452

197. Röder P, Baba N, Wiemhöfer HD (2014) A detailed thermal study of a Li[$Ni_{0.33}Co_{0.33}Mn_{0.33}$]$O_2$-$LiMn_2O_4$-based lithium ion cell by accelerating rate and differential scanning calorimetry. J Power Sourc 248:978–987
198. Shi SJ, Tu JP, Tang YY, Liu XY, Zhao XY, Wang XL, Gu CD (2013) Morphology and electrochemical performance of Li[$Li_{0.2}Mn_{0.54}Ni_{0.13}Co_{0.13}$]$O_2$ cathode materials treated in molten salts. J Power Sourc 241:186–195
199. Toprakci O, Toprakci HAK, Li Y, Ji LW, Xue LG, Lee H, Zhang S, Zhang XW (2013) Synthesis and characterization of $x Li_2MnO_3 \cdot (1-x) LiMn_{1/3}Ni_{1/3}Co_{1/3}O_2$ composite cathode materials for rechargeable lithium-ion batteries. J Power Sourc 241:522–526
200. Shi SJ, Tu JP, Tang YY, Zhang YQ, Wang XL, Gu CD (2013) Preparation and characterization of macroporous $Li_{1.2}Mn_{0.54}Ni_{0.13}Co_{0.13}O_2$ cathode material for lithium-ion batteries via aerogel template. J Power Sourc 240:140–148
201. Zhenyao W, Biao L, Jin M, Dingguo X (2014) Molten salt synthesis and high-performance of nanocrystalline Li-rich cathode materials. RSC Adv 4:15825–15829
202. Zhang HZ, Qiao QQ, Li GR, Gao XP (2014) PO_4^{3-} polyanion-doping for stabilizing Li-rich layered oxides as cathode materials for advanced lithium-ion batteries. J Mater Chem A 2:7454–7460
203. Myung ST, Lee KS, Sun YK, Yashiro H (2011) Development of high power lithium-ion batteries: layer Li[$Ni_{0.4}Co_{0.2}Mn_{0.4}$]O_2 and spinel Li[$Li_{0.1}Al_{0.05}Mn_{1.85}$]$O_4$. J Power Sources 196:7039–7043
204. Zhu Z, Zhu L (2014) Synthesis of layered cathode material $0.5Li_2MnO_3$-$0.5LiMn_{1/3}Ni_{1/3}Co_{1/3}O_2$ by an improved co-precipitation method for lithium-ion battery. J Power Sourc 256:178–182
205. Shi SJ, Lou ZR, Xia TF, Gu CD, Tu JP (2014) Hollow $Li_{1.2}Mn_{0.5}Co_{0.25}Ni_{0.05}O_2$ microcube prepared by binary template method as a cathode material for lithium ion batteries. J Power Sourc 257:198–204
206. Croy KSH, Balasubramanian M, Thackeray MM (2011) Li_2MnO_3-based composite cathodes for lithium batteries: a novel synthesis approach and new structures. Electrochem Commun 13:1063–1066
207. Li J, Klöpsch R, Stan MC, Nowak S, Kunze M, Winter M, Passerini S (2011) Synthesis and electrochemical performance of the high voltage cathode material Li[$Li_{0.2}Mn_{0.56}Ni_{0.16}Co_{0.08}$]$O_2$ with improved rate capability. J Power Sourc 196:4821–4825
208. Chen Y, Xu G, Li J, Zhang Y, Chen Z, Kang F (2013) High capacity $0.5Li_2MnO_3$-$0.5LiNi_{0.33}Co_{0.33}Mn_{0.33}O_2$ cathode material via a fast co-precipitation method. Electrochim Acta 87:686–892
209. Kim JH, Sun YK (2003) Electrochemical performance of Li[$Li_xNi_{(1-3x)/2}Mn_{(1+x)/2}$]$O_2$ cathode materials synthesized by a sol-gel method. J Power Sourc 119:166–170
210. Zhao X, Cui Y, Xiao L, Liang H, Liu H (2011) Molten salt synthesis of $Li_{1+x}(Ni_{0.5}Mn_{0.5})_{1-x}O_2$ as cathode material for Li-ion batteries. Solid State Ionics 192:321–325
211. Kim MG, Jo M, Hong YS, Cho J (2009) Template-free synthesis of Li[$Ni_{0.25}Li_{0.15}Mn_{0.6}$]$O_2$ nanowires for high performance lithium battery cathode. Chem Commun 218–220
212. Lu Z, MacNeil DD, Dahn JR (2001) Layered cathode materials Li[$Ni_xLi_{(1/3-2x/3)}Mn_{(1/3-x/3)}$]$O_2$ for lithium-ion batteries. Electrochem Solid State Lett 4:A191–A194
213. Wu Y, Manthiram A (2007) Effect of Al^{3+} and F^- doping on the irreversible oxygen loss from layered Li[$Li_{0.17}Mn_{0.58}Ni_{0.25}$]$O_2$ cathodes. Electrochem Solid State Lett 10:A151–A154
214. Tran N, Croguennec L, Menetrier M, Weill F, Biensan P, Jordy C, Delmas C (2008) Mechanisms associated with the plateau observed at high voltage for the overlithiated $Li_{1.12}(Ni_{0.425}Mn_{0.425}Co_{0.15})_{0.88}O_2$ system. Chem Mater 20:4815–4825
215. Wang ZY, Liu EZ, He CN, Shi CS, Li JJ, Zhao NQ (2013) Effect of amorphous $FePO_4$ coating on structure and electrochemical performance of $Li_{1.2}Ni_{0.13}Co_{0.13}Mn_{0.54}O_2$ cathode material for Li-ion batteries. J Power Sourc 236:25–32

216. Kang SH, Johnson CS, Vaughey JT, Amine K, Thackeray MM (2006) The effects of acid treatment on the electrochemical properties of $0.5Li_2MnO_3{\cdot}0.5LiNi_{0.44}Co_{0.25}Mn_{0.31}O_2$ electrodes in lithium cells. J Electrochem Soc 153:A1186–A1192
217. Tang JH, Wang ZX, Li XH, Peng WJ (2012) Preparation and electrochemical properties of Co-doped and none-doped $Li[Li_xMn_{0.65(1-x)}Ni_{0.35(1-x)}]O_2$ cathode materials for lithium batteries. J Power Sourc 204:187–192
218. Tran HY, Täubert C, Fleischhammer M, Axmann P, Küppers L, Wohlfahrt-Mehrens M (2011) $LiMn_2O_4$ spinel/$LiNi_{0.8}Co_{0.15}Al_{0.05}O_2$ blends as cathode materials for lithium-ion batteries. J Electrochem Soc 158:A556–A561
219. Gao J, Manthiram A (2009) Eliminating the irreversible capacity loss of high capacity layered $Li[Li_{0.2}Mn_{0.54}Ni_{0.13}Co_{0.13}]O_2$ cathode by blending with other lithium insertion hosts. J Power Sourc 191:644–647
220. Thackeray MM (1997) Manganese oxides for lithium batteries. Prog Solid State Chem 25:1–71
221. Gummow RJ, Liles DC, Thackeray MM (1993) Lithium extraction from orthorhombic lithium manganese oxide and the phase transformation to spinel. Mater Res Bull 28:1249–1256
222. Armstrong AR, Bruce PG (1996) Synthesis of layered $LiMnO_2$ as an electrode for rechargeable lithium batteries. Nature 381:499–500
223. Davidson IJ, McMillan RS, Murray JJ (1995) Rechargeable cathodes based on $Li_2Cr_xMn_{2-x}O_4$. J Power Sourc 54:205–208
224. Choi S, Manthiram A (2002) Factors influencing the layered to spinel-like phase transition in layered oxide cathodes. J Electrochem Soc 149:A1157–A1163
225. Doeff MM, Richardson TJ, Kepley L (1996) Lithium insertion processes of orthorhombic Na_xMnO_2-based electrode materials. J Electrochem Soc 143:2507–2516
226. Jeong YU, Manthiram A (1999) Synthesis and lithium intercalation properties of $Na_{0.5-x}Li_xMnO_{2+\delta}$ and $Na_{0.5-x}MnO_{2+\delta}$ cathodes. Electrochem Solid State Lett 2:421–424
227. Kim J, Manthiram A (1999) Amorphous manganese oxyiodides exhibiting high lithium intercalation capacity at higher current density. Electrochem Solid State Lett 2:55–57
228. Takeda Y, Kanno R, Tsuji Y, Yamamoto O (1983) Chromium oxides as cathodes for lithium cells. J Power Sourc 9:325–328
229. Yamamoto O, Takeda Y, Kanno R, Oyabe Y, Shinya Y (1987) Amorphous chromium oxide, a new lithium battery cathode. J Power Sourc 20:151–156
230. Kim J, Manthiram A (1997) Synthesis, characterization, and electrochemical properties of amorphous $CrO_{2-\delta}$ ($0 \leq \delta \leq 0.5$) cathodes. J Electrochem Soc 144:3077–3081
231. Abdel-Ghany AE, Mauger A, Groult H, Zaghib K, Julien CM (2012) Structural properties and electrochemistry of α-$LiFeO_2$. J Power Sourc 197:285–291
232. Wang W, Wang H, Liu S, Huang J (2010) Synthesis of γ-LiV_2O_5 nanorods as high-performance cathode for Li ion battery. J Solid State Electrochem 16:2555–2561
233. Yang G, Wang G, Hou W (2005) Microwave solid-state synthesis of LiV_3O_8 as cathode material for lithium batteries. J Phys Chem B 109:11186–11196
234. Delmas C, Braconnier JJ, Hagenmuller P (1982) A new variety of $LiCoO_2$ with an unusual packing obtained by exchange reaction. Mater Res Bull 17:117–123
235. Paulsen JM, Mueller-Neuhaus JM, Dahn JR (2000) Layered $LiCoO_2$ with a different oxygen stacking (O2 structure) as a cathode material for rechargeable lithium batteries. J Electrochem Soc 147:508–516

Chapter 6
Cathode Materials with Monoatomic Ions in a Three-Dimensional Framework

6.1 Introduction

Cathodes materials for lithium batteries with a three-dimensional (3D) structure have been the subject of intense researches for a number of years. 3D materials are binary transition-metal oxides (TMOs) and lithiated TMOs. Historically, manganese oxide was used in primary lithium batteries introduced in the market by Sanyo in 1975 as low-power supplies for watches [1]. Further developments were directed toward the cyclability of electrolytic manganese dioxide (EMD) in secondary Li batteries [2]. In the early 1980s several groups at University of Münster, Germany, at University of Oxford, UK, and at Bell Laboratories, NJ, USA have intensively studied the insertion of Li^+ ions into MO_n oxides including MoO_3 and its derivatives such as the Magneli phase Mo_8O_{23}, V_2O_5 formed by shearing ReO_3-type chains and related compounds V_6O_{13} and LiV_3O_8, WO_3 and TiO_2 [3–5]. The next step was the discovery of the properties of mixed ionic-electronic conduction in lithiated manganese oxide spinels as cathode materials for secondary batteries [6]. Table 6.1 documents the industrial efforts for developing rechargeable lithium batteries using TM oxides as positive electrode, Li metal as anode and a solution of $LiClO_4$ in propylene carbonate as a nonaqueous electrolyte.

Li-Mn-O electrodes are attractive materials due to their noticeable advantages such as low toxicity, low cost, environmentally benign, higher thermal stability than $LiCoO_2$. The cost of manganese is less than 1 % of that of cobalt and it is less toxic. For example, in the charge state, $Li_xMn_2O_4$ shows a low reactivity with an onset temperature over 220 °C and low heat release [7, 8]. Also, the wide abundance on the Earth makes manganese as a very attractive transition-metal. However, manganese oxides display relatively low specific capacity.

Let us consider the change of the structural properties of Li-Mn oxides with the different oxidation states of Mn. The change of size of Mn ions at octahedral sites in a close-packed oxygen (CPO) array (MnO_6) during the electrochemical reaction must be considered because enlargement of ions can destroyed the lattice. As a

C. Julien et al., *Lithium Batteries*, DOI 10.1007/978-3-319-19108-9_6

Table 6.1 Rechargeable lithium metal batteries using TM oxides as positive electrodes

Battery	Potential (V)	Specific energy (Wh kg^{-1})	Company/year
Li//V_2O_5	1.5	10	Toshiba 1989
Li//CDMO[a]	3.0	–	Sanyo 1989
Li//$Li_{0.33}MnO_2$	3.0	50	Taridan 1989
Li//VO_x	3.2	200	Hydro-Québec 1990
C//$LiMn_2O_4$	4.0	400	Duracell 1999

[a]Composite dimensional manganese dioxide

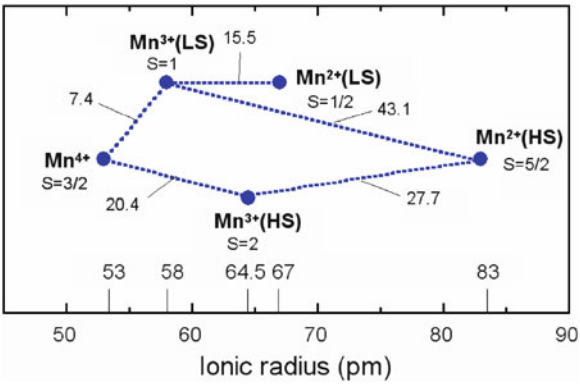

Fig. 6.1 Ionic radii of Mn^{n+} ions for CN = 6. LS and HS denote the low and high spin states. The enlargement in percent between two redox species and the spin *S* are also given

general rule of the solid-state chemistry, the octahedral coordination in the CPO array is realized for the ratio of ion radii of Mn and O in the range 0.4–0.7. Figure 6.1 presents the changes in ionic radii of Mn^{n+} ions for coordination number CN = 6, where LS and HS denote the low and high spin states [9]. As shown in Fig. 6.1, the ionic radii of Mn ions located in octahedral sites are in the range 53–83 pm compared with 140 pm for O^{2-} ion, thus the ratios $r(Mn^{n+})/r(O^{2-})$ are satisfied. As a consequence, the ionic radii of Mn ions in tetravalent and trivalent states suggest that Mn^{4+} can accept electrons forming Mn^{3+} without destruction of octahedral coordination that allows the redox reaction upon Li insertion/extraction process. Ohzuku [10] has discussed the Li^+-ion motion in solid frameworks in which the transition-metal ions must be immobile at octahedral sites when the Mn-O covalency forming $(MnO_6)^{8-/9-}$ units is strong enough and Li-O bonding are considered to be more ionic. For instance, a necessary condition of stability of the structure of manganese dioxides is that vacant sites in $\square MnO_2$ (where $\square$ is a crystallographic empty site) should be linked as 3D tunnels or channels to accommodate Li^+-ions motion.

The purpose of this chapter is to summarize the current status of materials with 3D-tunnel structure that have a cubic-close packed (ccp) array. These materials belong to the class of 3- and 4-V cathodes. Non-lithiated $\square M_xO_y$ and lithiated LiM_xO_y lattices are considered. The first group includes the different polymorphs of MnO_2, V_6O_{13}, WO_3, and its derivatives, while the second class includes $LiMnO_2$, $Li_{0.33}MnO_2$, $LiMn_2O_4$ spinel, and its derivatives.

6.2 Manganese Dioxides

Manganese dioxide, MnO_2, (MDO) is a widely used as material in primary electrochemical cells. It is the positive electrode of the zinc-MnO_2 cell, invented in 1866 by the French engineer Georges-Lionel Leclanché [11]. Li-MnO_2 battery was developed by Sanyo in 1975 [12] as low-power supplies for watches, calculators and memory backups. The poor cyclability of MDOs observed at that time [13] has been improved by preparing composite dimensional manganese oxides (CDMOs) for the development of flat-type secondary batteries. Table 6.2 lists the chemical formula of selected Li-Mn-O compounds used in Li batteries.

6.2.1 MnO_2

Manganese oxides with tunnel and layered crystal structures constitute a large family of porous materials [14]. Manganese dioxide can exist in different crystal structures, including α-, β-, γ-, ε-, η-, δ-, and λ-MnO_2, etc., where the basic structural unit [MnO_6] is linked in different manners [15–17]. Most of the frameworks are built by MnO_6 octahedral units shared by corners and/or edges, which define structural voids for cation insertion. According to different octahedron links, the MnO_2 structures can be divided into three categories: the chain-like tunnel structure such as α-, β-, and γ-crystalline form; the sheet-like or layered structure such as δ-type MnO_2; and the third category that is composed of three-dimensional structures such as λ-MnO_2. The different crystalline structures of manganese dioxide exhibit different properties and life cycles [18, 19]. In addition to the crystal structure, the size and morphologies of MnO_2 particles also play a key role in determining the properties for practical applications. In this regard, many efforts have been made to prepare nanocrystalline MnO_2 with different structures

Table 6.2 Designation and chemical formula of various Li-Mn-O compounds

Designation	Compound	Formula
Birnessite	$MnO_{1.86}{\cdot}0.6H_2O$	$[Mn^{4+}]_{0.84}[Mn^{2+}]_{0.16}O_{1.84}{\cdot}0.6H_2O$
Na-birnessite	$Na_{0.32}MnO_2{\cdot}0.6H_2O$	$Na_{0.32}[Mn^{4+}]_{0.68}[Mn^{3+}]_{0.32}O_2{\cdot}0.6H_2O$
Li-birnessite	$Li_{0.32}MnO_2{\cdot}0.6H_2O$	$Li_{0.32}[Mn^{4+}]_{0.68}[Mn^{3+}]_{0.32}O_2{\cdot}0.6H_2O$
Co-birnessite	$Mn_{0.85}Co_{0.15}O_2{\cdot}0.6H_2O$	$[Co^{3+}]_{0.15}[Mn^{4+}]_{0.72}[Mn^{2+}]_{0.13}O_{1.80}{\cdot}0.6H_2O$
Spinel	λ-$LiMn_2O_4$	$Li[Mn^{4+}Mn^{3+}]O_4$
NMD	Romanechite	$(R)_2Mn_5O_{10}{\cdot}xH_2O$
EMD	γ-MnO_2	$MnO_2{\cdot}0.16H_2O$
CDMO	MnO_2-based composite	γ-β-$MnO_2 + Li_2MnO_3$
m-LMO	$LiMnO_2$	Monoclinic phase $Li[Mn^{3+}]O_2$
LT-LMO	$Li_{0.52}MnO_2$	Spinel-contained phase
HT-LMO	$Li_{0.52}MnO_2$	Layered phase

and shapes. Up to now, various nanostructures of MnO_2, such as nanoparticles, nanorods, belts, wires, tubes, fibers, urchins/orchids, mesoporous and branched structures, have been synthesized by different methods [18].

The excellent electrochemical properties of several MnO_2 phases are attracting attention for positive electrodes in lithium batteries [20–23]. There is a wide variety of battery-grade MDOs, whose structures have been extensively investigated [24]. Among the MDOs, most attention has been focused on synthetic products prepared by either electrolytic (EMD) or chemical (CMD) method that belong to the nsutite (γ-MnO_2) group [25]. The electrochemical behavior of EMD compounds has been investigated by Ohzuku et al. [26]. Besides the γ-MnO_2 form, particular attention has been paid to other stoichiometric compounds. As an example, the sodium-free birnessite, $MnO_{1.85}$–$0.6H_2O$, displays a layered structure with larger interlayer distance and trigonal prismatic sites favorable for easy lithium insertion [27]. The manganese dioxides can be classified according the nature of the polymerization of MnO_6 units and the number of MnO_6 octahedral chains between two basal layers to form tunnel ($T_{m,n}$) openings. The $T_{1,n}$ group includes two chemically pure forms, the pyrolusite β-MnO_2 ($T_{1,1}$) and the ramsdellite *R*-MnO_2 ($T_{1,2}$). The $T_{m,\infty}$ group includes the layered phyllomanganates such as birnessite, buserite, and rancieite. Figure 6.2 shows the schematic structure of various MnO_2 polymorph showing the variation in the chain and tunnel ($m \times n$) structures [28].

The discharge curves of different forms of manganese dioxide such as single-phase α-MnO_2, β-MnO_2, *R*-MnO_2, and the stabilized phase α/β-MnO_2 are shown in Fig. 6.3. These data show that the stabilized two-phase α/β-MnO_2 sample delivers higher discharge capacity than the single-phase α-MnO_2. Furthermore ramsdellite *R*-MnO_2 and pyrolusite β-MnO_2 display the highest discharge capacities. These materials present flat discharge curves while hollandite structure shows an S-shaped discharge curve. On the initial discharge the stabilized α/β-MnO_2 material delivers a specific capacity 230 mAh g^{-1}. This electrode shows good recharge ability with capacity retention 150 mAh g^{-1} after 20 cycles. The initial capacity loss of 33 % suggests that $\approx$0.3 mol of inserted lithium ions is used [27].

6.2.2 *MnO_2-Based Composites*

Nohma et al. [29] have shown that, if MnO_2 contained a small amount of lithium in its crystal structure beforehand, the electrochemical reversibility would be improved. Several *composite dimensional manganese oxides* (CDMOs) were prepared by reacting LiOH with MnO_2. The XRD patterns of the product prepared from various Li/Mn atomic ratios are shown in Fig. 6.4.

From these results, the structural model of heat-treated $LiOH{\cdot}MnO_2$ precursor at 375 °C is considered to be a composite formed by the mixture of the Li_2MnO_3 and γ-β-MnO_2 phases. γ-β-MnO_2 phases has one-dimensional channels while Li_2MnO_3

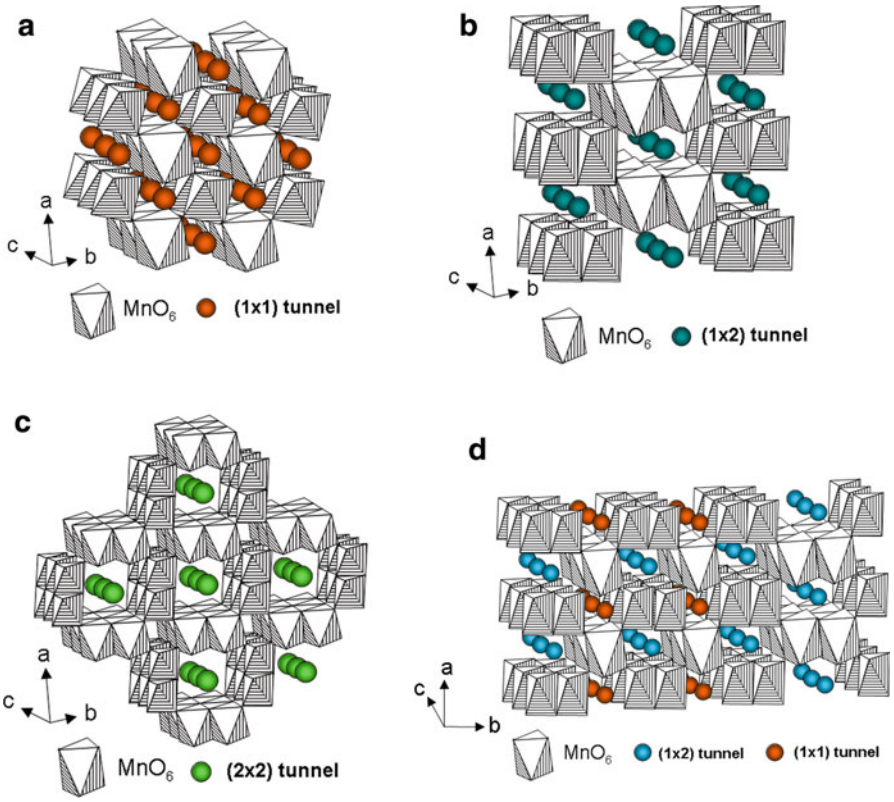

Fig. 6.2 Schematic view of the tunnel structure of MnO_2 polymorph (**a**) pyrolusite β-MnO2 ($T_{1,1}$) and (**b**) ramsdellite R-MnO_2 ($T_{1,2}$), hollandite α-MnO_2 ($T_{2,2}$) and (**c**) nsutite γ-MnO_2 (intergrowth $T_{1,1} + T_{1,2}$)

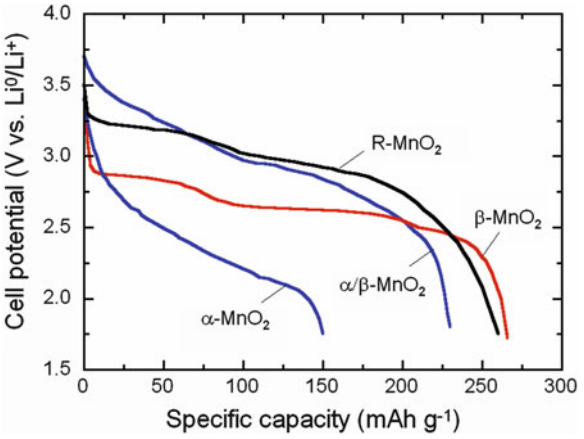

Fig. 6.3 Discharge curves of single-phase manganese dioxides: α-MnO_2, β-MnO_2, *R*-MnO_2, and the stabilized phase α/β-MnO_2

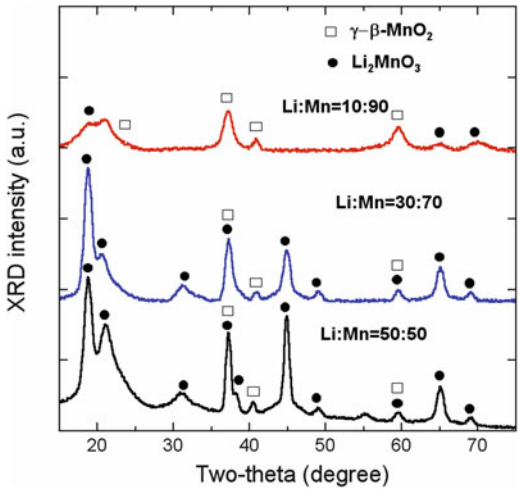

Fig. 6.4 X-ray diffraction patterns of CDMO at several Li/Mn atomic ratios. The LiOH·MnO_2 precursor was heated at 375 °C

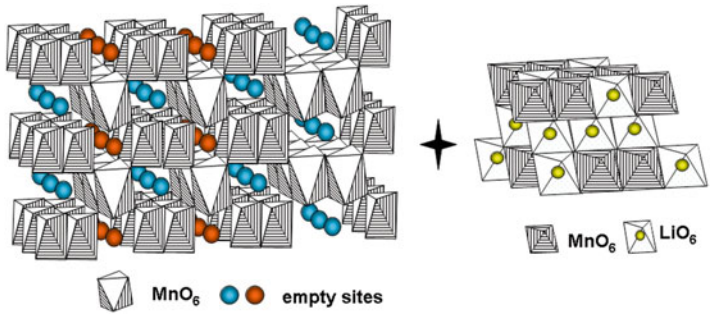

Fig. 6.5 Schematic view of the CDMO structure formed by the composite of γ-β-MnO_2 and Li_2MnO_3

is a layered compound, namely $Li[Li_{1/3}Mn_{2/3}]O_2$ (Fig. 6.5). As a result, the CDMO prepared at 375 °C with a Li/(Li + Mn) = 0.3 yielded the largest discharge capacity 200 mAh g^{-1} for electrode cycled in the potential range 3.6–2.0 V at current density 1.1 mA cm^{-2} [30].

6.2.3 *MnO_2 Nanorods*

Nano-sized MnO_2 samples with the shape of nanorod were prepared by hydrothermal reaction between ammonium persulfate and Mn(II) salts [31]. XRD measurements revealed the α-MnO_2 phase for the sample prepared from manganese sulfate and the β-MnO_2 structure for the sample prepared from manganese nitrate

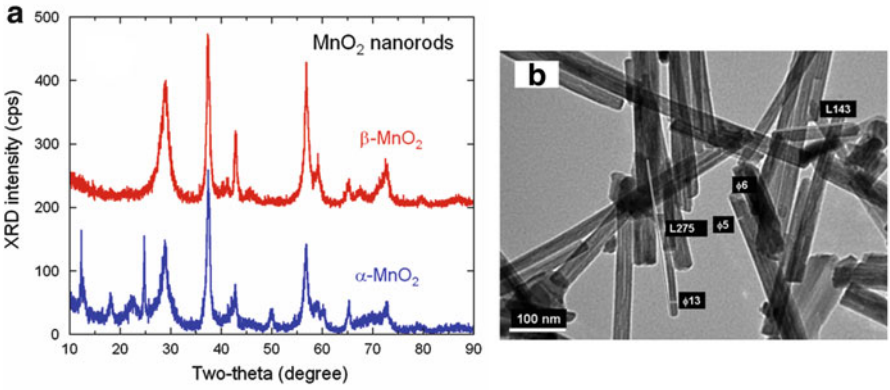

Fig. 6.6 (**a**) XRD patterns of α-MnO_2 and β-MnO_2 nanorods prepared through redox reaction between $(NH_4)_2S_2O_8$ and $MnSO_4{\cdot}4H_2O$, and through redox reaction between $(NH_4)_2S_2O_8$ and $Mn(NO_3)_2{\cdot}4H_2O$, respectively (**b**) TEM images of α-MnO_2 nanorods. Values of diameter and length of nanorods are in nanometer

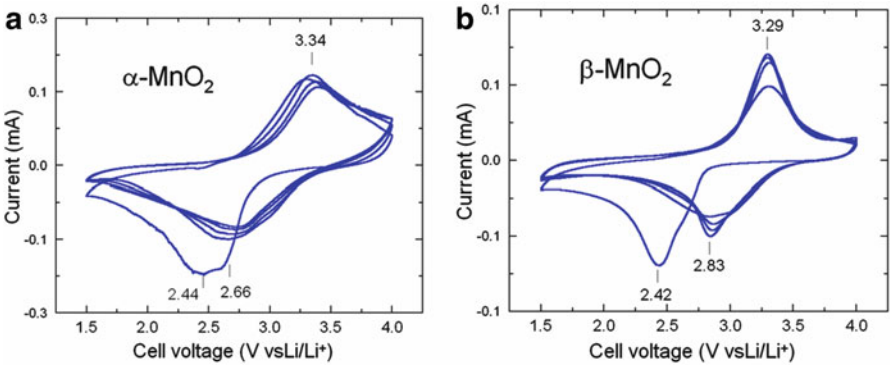

Fig. 6.7 Cyclic voltamograms of (**a**) α-MnO_2 and (**b**) β-MnO_2. Data were recorded in lithium cells using a scan rate 0.05 V s^{-1} in the voltage range 1.5–4.0 V vs. Li^0/Li^+. Redox potentials are indicated in volt

(Fig. 6.6). TGA analysis has confirmed the MnO_2 structure for both samples showing three weight losses without thermal stabilization due to the absence of K^+ ions in the tunnels. It seems that the difference in the nature and size of tunnels between α-MnO_2 ($T_{2,2}$) and β-MnO_2 ($T_{1,1}$) affect the specific capacity. Nanorods structures exhibit good electrochemical performance, evidenced by cyclic voltammetry (Fig. 6.7). There is a structural evolution after the first cycle. This can be observed clearly from the reduction in the potential polarization after the first cycle and also the reduction in capacity fading. Shao-Horn et al. [32] have demonstrated that crystals with a small aspect ratio have a large electrochemically active surface because of the large exposed $T_{2,2}$-type tunnel cross-sectional area per unit

volume available for lithium insertion. β-MnO_2 nanorods yield a specific discharge capacity of 180 and 130 mAh g^{-1} in the first and 45th cycle respectively, while α-MnO_2 nanorods deliver 210 mAh g^{-1} at first cycle that decreases to 115 mAh g^{-1} in the 45th cycle.

The electrochemical behavior of β-MnO_2 may be attributed to the nature of nanorods of this sample, which alleviates the stress and provides flexibility for lithium insertion/extraction in/from 1 × 1 tunnels [33]. The capacity loss observed after the first cycle is attributed to the small amount of lithium ions inserted in the MnO_2 electrode that cannot be easily removed from the structure. The second reason for this degradation in the capacity upon cycling may be related to significant amount of Mn^{2+} ions formed at the end of discharge. The Mn^{2+} ions can be dissolved into the electrolyte causing significant increase in the capacity fading of lithium manganese oxides [34].

6.2.4 *Birnessite*

One class of MDO polymorphs crystallizes in a layered structure (monoclinic, *C*/2*m* S.G.), namely birnessite (δ-MnO_2) or phylomanganates [27, 35]. The birnessite-type manganese oxides are found in nature (soils, ore deposits, marine nodules, etc.) and produced synthetically (hydrothermal, sol–gel, etc.). The lamellar framework is built of edge-sharing MnO_6 octahedra with water molecules and/or metal cations occupying the interlayer region as shown in Fig. 6.8 [36].

Depending on the synthesis route, a combination of Mn(IV)/Mn(III) or Mn(IV)/Mn(II) is found in birnessite (BR). For example, the mean oxidation state of manganese in sol–gel materials and classical BR (prepared from Stähli's method) varies in the range $3.6 < Z_{Mn} < 3.8$. In the case of sol–gel birnessite (SG-BR) and Co-doped sol–gel birnessite (SGCo-BR) [37], we have a mixture of Mn(IV) and Mn

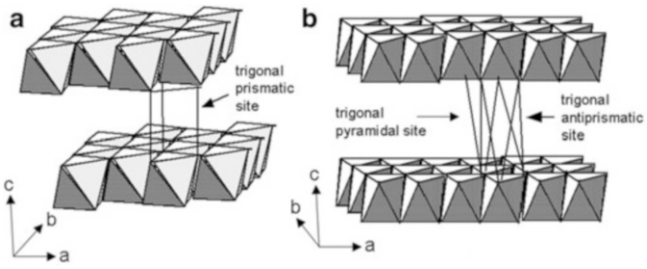

Fig. 6.8 Layered structure of sodium birnessite. (**a**) The interlayer distance $d = 7.1$ Å corresponds to two consecutive superposable MnO_6 octahedral sheets. The trigonal prismatic sites are occupied by sodium ions. (**b**) Layered structure of alkali-free birnessite. The interlayer distance $d = 7.25$ Å corresponds to two consecutive non-superposable MnO_6 octahedral sheets. The interlayer space defines trigonal antiprismatic and trigonal pyramidal sites

(II) while a combination of Mn(IV) and Mn(III) is found for the classical birnessites. These phases have a hexagonal or monoclinic symmetry. One of them is like the layered CdI_2-type structure and consists in single sheets of edge-sharing $[MnO_6]$ octahedra and water molecules between layers and Mn^{2+} or Mn^{3+} located between the water layer and oxygen of the $[MnO_6]$ slab in order to counterbalance the charge defects in MnO_6 sheets. The sequence along the c axis is:

$$O - Mn^{IV} - O - Mn^{III(+)\text{or } II(*)} - H_2O - Mn^{III(+)\text{or } II(*)} - O - Mn^{IV} - O, \quad (6.1)$$

where (+) denotes classical BR and (*) SG-BR compounds. The orthogonal distance between two consecutive slabs of $[MnO_6]$ is around 7 Å. In the case of SGCo-BR, we have previously shown that Co^{3+} ions are incorporated into the MnO_6 sheets as Co^{3+} is substituting for Mn ions [38] (see chemical formula in Table 6.1).

The maximum Li uptake in SG-BR $x(\text{Li}) = 0.85$ is in good agreement with the concentration of Mn^{4+} ions (the average valence of Mn ions is $Z_{\text{Mn}} = 3.68$), which are reduced to Mn^{3+} during the intercalation reaction (discharge process) that occurs with a significant contraction 7.5 % of the host lattice. Pereira-Ramos et al. [39] reported that the faradaic yield recovered for SG-BRr is twofold greater than that of BR. Such a result can be understood in terms of faster Li^+-ion kinetics, as its diffusion coefficient was estimated to be $D_{\text{Li}}^* = 10^{-10}$–$10^{-11}$ $\text{cm}^2\ \text{s}^{-1}$. In the potential range 4.2–2.0 V, the Li//SG-BR cells exhibit good cycling behavior with a specific capacity of 150 mAh g^{-1} at the 50th cycle.

6.3 Lithiated Manganese Dioxides

The phase diagram of the Li-Mn-O system in air between 350 and 1060 °C according to Paulsen and Dahn [40] is shown in Fig. 6.9. Lithium doped single-phase spinels $Li_{1+z}Mn_{2-z}O_4$ ($0 \leq z \leq 0.33$) are stable between 400 and 880 °C (with an average Mn valence between 3.5 and 4). Above the upper critical temperature line, Tc_1, the spinel coexists with the monoclinic Li_2MnO_3, and below the lower critical temperature line, Tc_2, with Mn_2O_3 or MnO_2. Most of the manganese oxides are confronted with two major difficulties: (1) lattice distortions occurring during the charge–discharge processes due to the presence of Jahn–Teller (JT) distortion associated with the single electron in the e_g orbitals of the Mn^{3+} cation [6] and (2) manganese dissolution from the cathode framework into the electrolyte particularly at higher temperature and in the high voltage charge state due to the disproportionation reactions of Mn^{3+} into Mn^{2+} and Mn^{4+} induced by acids generated by reactions of fluorinated anions with water impurities and by oxidation of solvents [41].

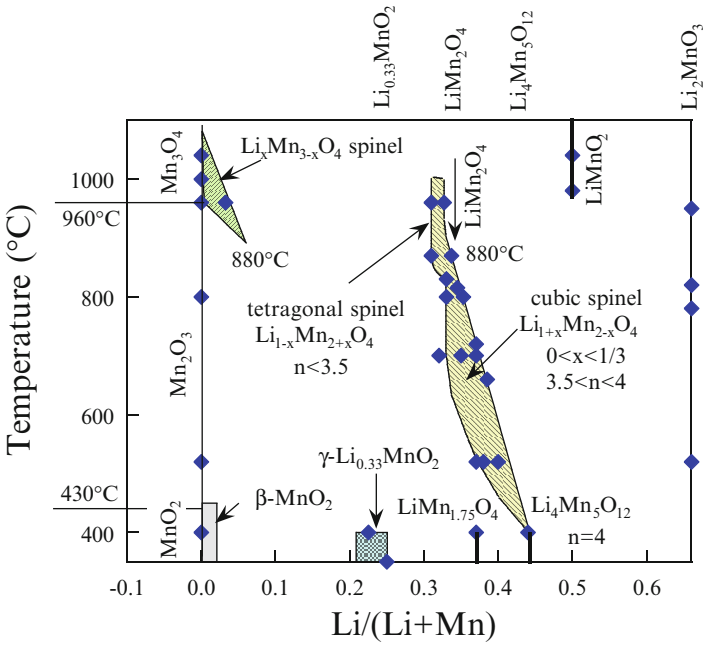

Fig. 6.9 Phase diagram of the Li-Mn-O system in air between 350 and 1060 °C

6.3.1 $Li_{0.33}MnO_2$

Lithiated Li_xMnO_2 with $x = 0.33$ obtained by heat treatment of a mixture of LiOH-MnO_2 and $LiNO_3$-MnO_2 at low temperature, has been studied extensively as a 3-V cathode material in liquid-electrolyte lithium batteries. This compound delivered a rechargeable capacity of 180 mAh g^{-1} after 50 cycles with a flat potential of 2.9 V vs. Li^0/Li^+ [42, 43]. $Li_{0.33}MnO_2$ crystallizes in the monoclinic structure (*C*2/*m* S.G.). According to the structural considerations of Levi et al. [44] Li ions are located in the octahedral sites of (1×2) channels that produce weak bonding for the lithium cations in the MnO_2 lattice. Figure 6.10 shows the first discharge–charge curves for the Li//$Li_{0.33+x}MnO_2$ cells in the voltage range 4.0–1.5 V vs. Li^0/Li^+ at a current density 0.14 mA cm^{-2} [45]. Positive electrodes synthesized by solid state reaction of CMD and Li salt were tested at 25 and 50 °C showing a faradaic yield 0.62Li/Mn achieved upon discharge, which leads to a specific capacity of 194 mAh g^{-1}. For the first discharge–charge process, the voltage profile occurs with an S-shape that indicates the formation of a single-phase $Li_{0.33+x}MnO_2$. Since the reduction process of $Li_{0.33}MnO_2$ is reversible, the construction of rechargeable cells is possible. Satisfactory charge–discharge efficiency and storage capability are other favorable features of this cell. Upon lithiation of $Li_{0.33+x}MnO_2$, the electronic conductivity increases slightly from 1×10^{-4} S cm^{-1} for $x = 0$ to ca. 5×10^{-3} S cm^{-1} for $x = 0.55$.

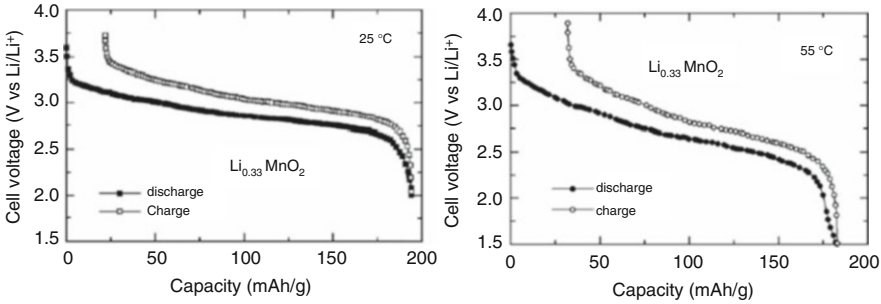

Fig. 6.10 First discharge–charge curves for the Li//$Li_{0.33+x}MnO_2$ cells tested at 25 and 50 °C in the voltage range 4.0–1.5 V vs. Li^0/Li^+ at a current density 0.14 mA cm^{-2}

6.3.2 $Li_{0.44}MnO_2$

Lithium manganese oxide, $Li_{0.44}MnO_2$, has been extensively investigated as a positive electrode material for secondary lithium batteries [46–49]. This compound can be prepared by a soft-chemical method using the corresponding sodium manganese oxide as the parent compound. $Li_{0.44}MnO_2$ crystallizes in the orthorhombic structure (*Pbam* S.G.) that maintains the parent $Na_{0.44}MnO_2$-type tunnel structure [47]. It consists of double and triple rutile-type chains of edge-sharing MnO_6 octahedra and a single chain of edge-sharing MnO_5 producing a framework containing large and small tunnels along the *c*-axis direction, with three lattice sies of Li ions located in the tunnels. The $Li_{0.44}MnO_2$ lattice differs from that of the well-known rocksalt-related lithium manganese oxides such as spinel-type $LiMn_2O_4$ and layered $LiMnO_2$. The electrochemical measurements for the Li//$Li_{0.44}MnO_2$ cell showed a novel high potential plateau region at around 4.3 V on both charge and discharge with an average discharge voltage of 3.57 V, and an initial discharge capacity of 166 mAh g^{-1} between 2.5 and 4.8 V. The tunnel structure can reversibly intercalate up to 0.55–0.6 Li/Mn at moderate current densities, corresponding to capacities of 160–180 mAh g^{-1}. The 4-V plateau was observed in all the Li//$Li_{0.44}Mn_{1-y}Ti_yO_2$ $(0 < y < 0.55)$ cells with different Ti contents [49, 50]. The maximum discharge capacity (179 mAh g^{-1}) was observed in the Li//$Li_{0.44}Mn_{0.89}Ti_{0.11}O_2$ cell. Li/PEO/$Na_{0.2}Li_xMnO_2$ cells were cycled at 0.1 mA cm^{-2}, with excellent capacity retention [46].

6.3.3 $LiMnO_2$

The difficulties met with the $LiMn_2O_4$ spinel that are reported in the next section have also motivated the investigation of several non-spinel manganese oxides [16].$LiMnO_2$ is known to exist in several phases. Two of them are the high

temperature orthorhombic (hereafter referred to as o-$LiMnO_2$) form and the monoclinic (hereafter referred to as m-$LiMnO_2$) form; both of them involve distorted oxygen arrays from the ideal cubic close packing [51]. The third form is the tetragonal λ-$Li_2Mn_2O_4$ phase. The o-$LiMnO_2$ (*Pmnm* S.G.) material that has the advantages of being easy to prepare and air stable, exhibits a high gravimetric capacity (286 mAh g^{-1}) and high potential against lithium. Ohzuku et al. [52] have prepared a low temperature o-$LiMnO_2$ form by reacting γ-MnOOH and LiOH at 450 °C, while a very low temperature (100 °C) was used by ion exchange [53]. Gummow et al. [51] investigated o-$LiMnO_2$ obtained at moderate (~600 °C) temperature from γ-MnO_2 and LiOH in argon with carbon as a reducing agent. Synthesis by hydrothermal route [54] and quenching method [55] have also been reported. Liu et al. [56] prepared o-$LiMnO_2$ nanorods by hydrothermal conversion of MnOOH needles. At *C*/20 discharge rate, two voltage plateaus appeared at 4.0 and 2.9 V, which can be ascribed to the phase transition during the cycling from o-$LiMnO_2$ to spinel phase [51]. Cyclic voltammetry reveals the reactions occurring during the transformation of o-$LiMnO_2$ to the spinel $LiMn_2O_4$ phase [55]. The m-$LiMnO_2$ phase (*C*2/*m* S.G.) with the same layered structure as $LiCoO_2$ was considered very difficult to obtain. The lithium content of the synthesized material can vary from $x = 0$ to 1 in $LiMnO_2$, depending on the synthesis approach used [57, 58]. Capitaine et al. [58] prepared this phase by *chimie douce* reaction from α-$NaMnO_2$ precursor via Li/Na exchange. For the O_2 structure, the monoclinic unit cell parameters are $a = 5.439(3)$ Å, $b = 2.809(2)$ Å, $c = 5.395(4)$ Å and $\beta = 115.9(4)$ Å. Layered $LiMnO_2$ suffers from structural instability during electrochemical cycling and as a result, exhibits significant capacity fade [16]. The transformation to spinel-like phases for the $Li_{0.5}MnO_2$ composition is due to a migration of the Mn ions from the Mn plane to the Li plane. Substantial efforts have been made to stabilize the layered structure by substituting Mn with cation dopants, such as Al and Co [59–61]. The tetragonal phase ($I4_1/amd$ S.G.) is obtained by electrochemical or chemical lithiation of the λ-$LiMn_2O_4$ spinel. $LiMnO_2$ rechargeable AA-type batteries have been developed at Taridan (Israel). The insertion reaction $LiMn_3O_6 + 2Li \leftrightarrows 3LiMnO_2$ was suggested that delivered an average voltage 2.8 V. Typical cycle life a fast charging (250 mA, *C*/2–*C*/3 rate) demonstrated at least 150 cycles at about 100 % DOD. The high cycle life obtained in these cells is attributed to the very smooth morphology of Li deposition in 1,3-dioxolane-$LiAsF_6$ solutions [62]. Unfortunately, both *o*- and *m*-$LiMnO_2$ with a close-packed oxygen array tend to transform irreversibly to spinel-like structures upon electrochemical cycling. This is consistent with the appearance of two plateaus at ≈4.0 and ≈2.9 V vs. Li^0/Li^+, as the parent space groups *Pmnm* and *C*2/*m* are subgroups of the $Fd\bar{3}m$ spinel. Figure 6.11 is a schematic representation of the structural transformation from *o*- and *m*-$LiMnO_2$ to spinel upon electrochemical cycling.

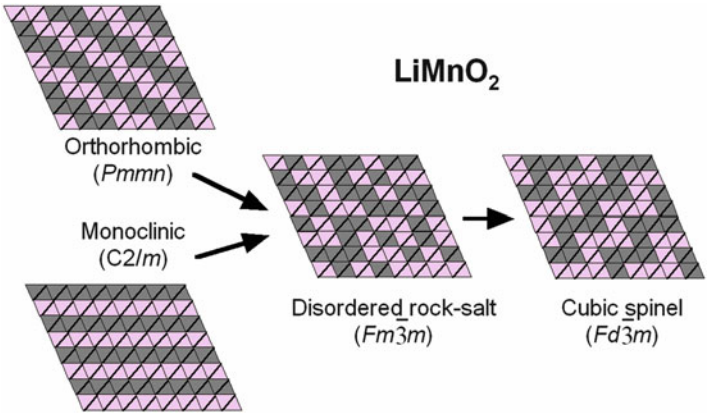

Fig. 6.11 Schematic representation of the structural transformation from *o*- and *m*-$LiMnO_2$ to $LiMn_2O_4$ spinel upon electrochemical cycling. $Fd\bar{3}m$ is a klassengleiche (*k*-) subgroup of $Fm\bar{3}m$

6.3.4 $Li_xNa_{0.5-x}MnO_2$

$Na_{0.5}MnO_2$ (designated as $Na_{0.44}MnO_2$ in the literature) adopting a non-close-packed tunnel structure has drawn some attention for Li insertion host as it does not transform to spinel-like phases and it shows extraordinary structural stability up to temperatures as high as 300 °C [48, 63, 64]. The structure consists of MnO_5 square pyramids and MnO_6 octahedra that are connected together by sharing edges and corners. However, only a small amount of lithium could be extracted from the ion-exchanged sample $Li_xNa_{0.5-x}MnO_2$ although additional lithium could be inserted into $Li_xNa_{0.5-x}MnO_2$. Therefore, it is not attractive for lithium-ion cells fabricated with carbon anodes. Nevertheless, it has been shown to be a promising candidate for lithium polymer batteries employing metallic lithium anode [63]. Additionally, amorphous manganese oxides deliver high capacity (300 mAh g^{-1}) with good cyclability [64]. However, the capacity occurs over a wide voltage range of 4.3 to 1.5 V with a continuously sloping discharge profile and not much lithium could be extracted from the initial material. Therefore these amorphous oxides are not attractive for lithium-ion cells fabricated with carbon anodes. However, they may become viable with the development of new lithium-containing anodes.

6.4 Lithium Manganese Spinels

6.4.1 $LiMn_2O_4$ (LMO)

Among the lithium manganates, which are known to ionically conduct, perhaps the best studied is the lithium manganese oxide, $LiMn_2O_4$ as an intercalation compound. $LiMn_2O_4$ (LMO) belongs to the class of 4-V intercalation hosts, and

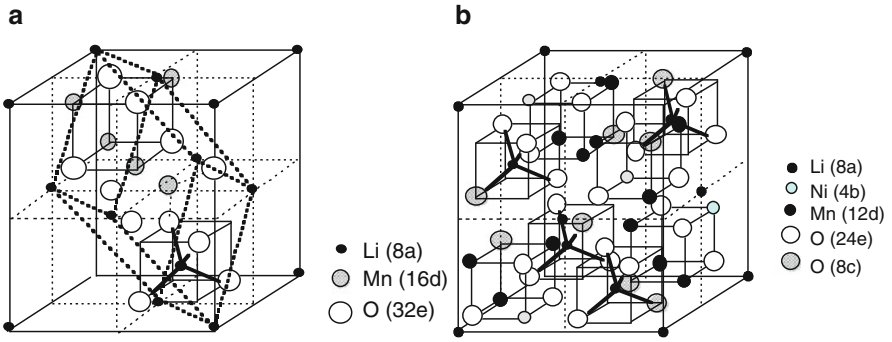

Fig. 6.12 Schematic representation of the structure of AB_2O_4 spinel lattices. (**a**) the smallest (primitive) cubic unit cell of normal spinel (*Fd3m* S.G.) and (**b**) the unit cell of the 1:3 ordered spinel ($P4_132$ S.G.). The structure is composed of alternating octants of AO_4 tetrahedra and B_4O_4 cubes to build the *fcc* unit cell

crystallizes with a cubic spinel-like structure. The structural relationship between the spinel $Li[Mn_2]O_4$ and the lithium deficient materials was described by Hunter [21]. Its crystallographic structure possesses the symmetry *Fd3m* and has a general structural formula $(A)_{8a}[B_2]_{16d}O_4$, where the *B* cations reside on the octahedral 16*d* sites, the oxygen anions on the 32*e* sites, and the *A* cations occupy the tetrahedral 8*a* sites. The approximately cubic close-packed (ccp) array of oxide ions incorporates MnO_6 octahedra sharing two opposing corners with LiO_4 tetrahedra. The spinel structure is primarily characterized by structural groups as follows. (1) MnO_6 octahedra, connected to one another in three dimensions by edge sharing. (2) LiO_4 tetrahedra, sharing each of their four corners with a different MnO_6 unit but essentially isolated from one another. (3) A three-dimensional network of octahedral (16*c*) and tetrahedral (primarily 8*a*) sites, lithium ions moving through the (1×1) channels of the spinel lattice [65]. The atomic arrangements of normal (*Fd3m* S.G.) and ordered ($P4_132$ S.G.) spinel lattices are illustrated in Fig. 6.12.

Early proposed to replace $LiCoO_2$, LMO has several advantages; (1) lower cost resulting from natural abundant manganese compared to Co and Ni, (2) lower toxicity and (3) high cell voltage. However, LMO is confronted with two major difficulties: (1) it is difficult to prepare samples of good quality, (2) although the LMO spinel is expected not to undergo JT distortion in the 4-V domain, the formation of tetragonal $Li_2Mn_2O_4$ layer has been observed at the surface of the LMO particles due to local conditions of discharge [66], (3) $LiMn_2O_4$ transforms into a tetragonal phase upon lithium insertion of more than one Li per Mn. Spectroscopic studies have confirmed that the cooperative JT effect from the $(Mn^{3+}O_6)$ octahedral is the mechanism for this transition. The capacity fade mechanism in this material concerns the large volume expansion associated with this structural modification that is problematic as both cubic and tetragonal phases coexist. As we show below, this coexistence is confirmed by the presence of a voltage plateau at 3 V. Limiting the cycling to the 4 V plateau reduced but did not

eliminate the structural distortion, while reducing the available theoretical capacity to 140 mAh g^{-1}.

Various techniques were used for the synthesis of LMO such as solid-state reaction by heating at ≈800 °C a stoichiometric mixture of Li_2CO_3 and EMD-MnO_2 in air for 24 h [67], sol–gel [68], Pechini technique [69, 70], emulsion dry method [71, 72], ultrasonic spray pyrolysis [73], precipitation method [74]. LMO was prepared by various wet-chemical techniques such as sol–gel method assisted by succinic acid as chelating agent [75]. LMO was also synthesized by chemical insertion of threefold excess Li into γ-MnO_2 followed by heat-treatment in oxygen [76]. Among the nanostructured LMO materials, nanoparticles were prepared by combustion method [77, 78], and by high-energy ball milling method [79]. Mesoporous LMO spinels were synthesized by polymer template method [80]; nanospheres LMO, 35 nm diameter, were prepared by ultrasonic method using LiOH and nano-MnO_2 [81]. Kim et al. [82] successfully fabricated highly ordered mesoporous LMO nanospheres through a chemical reaction in combination with ultrasonic waves. LMO nanorods, 300 nm diameter, were obtained by hydrothermal method using β-MnO_2 as precursor [83, 84]; LMO nanowires have been shown to grow in the (220 direction [85]. Fluorination as a means of changing the structure and electronic properties of oxides became an established route to stabilize their structure. It was used in the quest for improved high temperature storage and cycling of LMO spinels [86, 87]. Improvement of the cycling performance of LMO was also realized by coating the surface of particles by various oxides such as $LiCoO_2$ [88], V_2O_5 [89], Al_2O_3 [90], SiO_2 [91], MgO [92], carried out through chemical processes, solution based techniques such as) sol–gel transformation, solution precipitation, and micro-emulsion. Such a surface modification avoids the formation of polymeric species occurring intensively at high temperature (50–60 °C), which increase the electrode impedance and even isolate electrically part of the active mass [93]. The electrochemical properties of quaternary spinel solid-solution phases $LiM_yMn_{2-y}O_4$ (M = Co, Cr, Ni, Al, Ti, Ge, Fe, Zn) were studied for different conditions of sample preparation and different degrees of cation substitution [94, 95]. Several hundred papers reported the physical properties of $LiMn_2O_4$ such as structural evolution on charging and discharging [96], electrical conductivity driven by the small polaronic mechanism [97], lattice dynamics [98, 99], magnetic properties [100, 101], electronic properties [102]. Wang et al. [103] reported the effect of the annealing temperature on the cubic lattice parameter of $LiMn_2O_4$ synthesized by a sol–gel precipitation method.

Figure 6.13 shows the charge–discharge curves at the first cycle of Li//$LiMn_2O_4$ cell, under galvanostatic conditions at 22 °C. The cell was charged and discharged at current densities of 1 mA cm^{-2}, while the voltage was monitored between 3.0 and 4.4 V. In this potential domain, the charge–discharge curves correspond to the voltage profiles characteristic of the spinel material associated with lithium occupancy of tetrahedral sites [104]. The variation of the potential for the complete cell reveals the presence of two regions during the lithium insertion-extraction processes. The first region (I) is characterized by an S-shaped voltage curve, whereas the second region (II) corresponds to a plateau portion. In region I, the charge

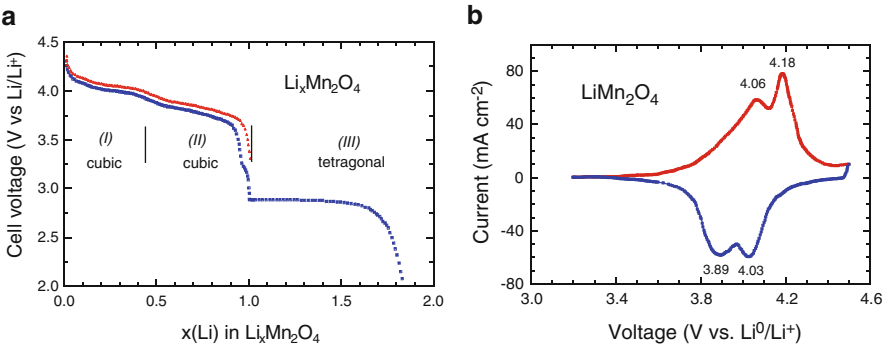

Fig. 6.13 (**a**) First charge–discharge profile of Li//$LiMn_2O_4$ cell in the 4-V and 3-V region and (**b**) cyclic voltammogram carried out at sweep rate 1 mV min^{-1}

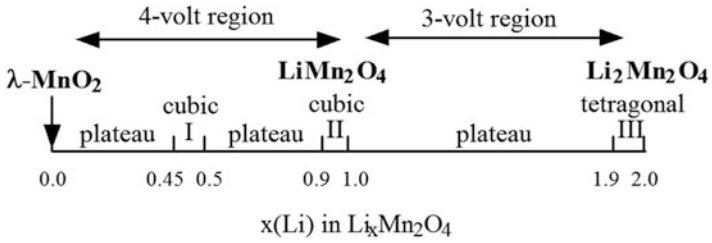

Fig. 6.14 Phase diagram of $Li_xMn_2O_4$ showing the plateaus occurring in the 4- and 3-V region

voltage increases continuously in the voltage range of 3.80–4.05 V. In region II, the charge voltage is stable around 4.15 V. Furthermore, these results describe the phase diagram of $Li_xMn_2O_4$ compounds against the lithium content.

The phase diagram of the $Li_xMn_2O_4$ ($0 \leq x \leq 2$) system showing the plateaus occurring in the 4- and 3-V domains is reported in Fig. 6.14. From the results shown in Fig. 6.14, a two-phase system is recognized in the region II corresponding to the upper voltage plateau, whereas the region I can be attributed to a single phase characterized by an S-shaped voltage curve. The two regimes of intercalation are clearly depicted when the derivative voltage, $-dx/dV$, is plotted vs. cell voltage. For the Li//$Li_xMn_2O_4$ cell, the upper 4-V plateau that is the region available for cycling provides a capacity over 120 mAh g^{-1} [105]. The lithium extraction/insertion from/into the 8*a* tetrahedral sites occurs at around 4 V (Fig. 6.13) with the maintenance of the initial cubic spinel symmetry, while the extraction/insertion from/into the 16*c* octahedral sites occurs at around 3 V by a two-phase mechanism involving the cubic spinel $Li[Mn_2]O_4$ and the tetragonal lithiated spinel $Li_2[Mn_2]O_4$. Palacin et al. [106] found two additional steps at 4.5 and 3.3 V, characteristics of double hexagonal layers upon oxidation. Although they both involve the same $Mn^{3+/4+}$ couple, the 1-V difference between the two processes is a reflection of the differences in the site energies [107]. A deep energy well for the 8*a* tetrahedral Li^+ ions and the high activation energy required for the Li^+ ions to move from one 8*a*

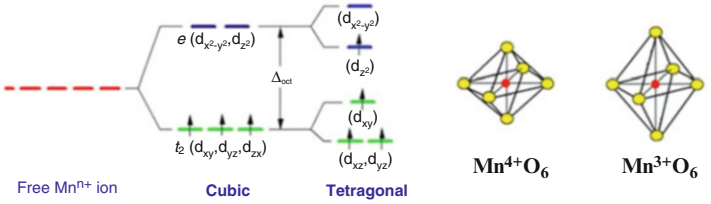

Fig. 6.15 Illustration of the JT distortion in manganese oxides: (**a**) Mn^{4+}:$3d^3$ with cubic symmetry (no JT distortion) and (**b**) Mn^{3+}:$3d^4$ with tetragonal symmetry (JT distortion)

tetrahedral site to another via an energetically unfavorable neighboring 16*c* site lead to a higher voltage of 4 V. The cubic to tetragonal transition when going from Li $[Mn_2]O_4$ to $Li_2[Mn_2]O_4$ is due to the Jahn–Teller (JT) distortion associated with the single electron in the e_g orbitals of a high spin Mn^{3+} : $3d^4\left(t_{2g}^3 e_g^1\right)$ ion (Fig. 6.15). A cooperative distortion of the MnO_6 octahedra with long Mn-O bonds along the *c* axis and short Mn-O bonds along the *a* and *b* axes results in a macroscopic tetragonal symmetry for $Li_2[Mn_2]O_4$ shown in Fig. 6.15.

Although two lithium ions per $LiMn_2O_4$ formula unit could be reversibly extracted/inserted, the cubic to tetragonal transition is accompanied by a 16 % increase in the *c*/*a* ratio of the unit cell parameters and 6.5 % increase in unit cell volume. Let us recall that this change is too severe for the electrodes to maintain structural integrity during the discharge/charge cycle and so $LiMn_2O_4$ exhibits rapid capacity fade in the 3-V region. As a result, $LiMn_2O_4$ could be utilized only in the 4-V region with a limited practical capacity of around 120 mAh g^{-1} (Fig. 6.13), which corresponds to an)extraction/insertion of 0.4 lithium per Mn and compared well with the theoretical capacity of 140 mAh g^{-1} we have mentioned earlier. Unfortunately, even with a limited capacity, $LiMn_2O_4$ tends to exhibit capacity fade in the 4-V region as well, particularly at elevated temperatures (50 °C). Various reasons have been attributed to the capacity fade in the 4-V region. For example, the dissolution of manganese into the electrolyte originating from a disproportionation of Mn^{3+} into Mn^{4+} and Mn^{2+} [108] and the formation of tetragonal $Li_2[Mn_2]O_4$ on the surface of the particles under conditions of non-equilibrium cycling [66] have been thought to be the source of)capacity fade. In addition, the 4-V region involves the formation of two cubic phases and that may also play a role in the capacity fade. The difficulties of lattice distortions in $LiMn_2O_4$ spinel have motivated strategies to suppress JT distortion. One way to suppress the JT distortion is to increase the average oxidation state of manganese since Mn^{4+} : $3d^3\left(t_{2g}^3 e_g^0\right)$ does not undergo JT distortion. The oxidation state of manganese can be increased either by aliovalent cationic substitutions or by increasing the oxygen content in $LiMn_2O_{4+\delta}$ [109–112]. Additionally, cationic substitutions with other transition metals $M = Cr$, Co, Ni and Cu in $LiMn_{2-y}M_yO_4$ have been pursued to improve the capacity retention of spinel manganese oxides [113–116]. This strategy is linked to the fact that the substitution of some Mn

cations for another ion of valence $\leq +3$ (bulk doping) will keep the Mn oxidation state above 3.5 during cycling over the 4-V plateau, thus reducing the)JT distortion on discharge. In addition, surface doping can decrease the manganese dissolution by reducing the apparent contact area with the electrolyte and inhibiting the surface Jahn–Teller distortion. Many efforts have been made recently to synthesize doped LMO. The numerous works on the preparation and doping modes (bulk, surface, and combined doping) of doped LMO have been recently reviewed [117]; therefore, they are not reviewed here, and we simply redirect the reader to this paper for the different doping elements and processes and a discussion on there effectiveness to reduce the capacity fading of LMO. However, such a strategy leads to a decrease in capacity in the 4-V region with a development of two plateaus for the extraction/insertion of lithium from/into the 8*a* tetrahedral sites: one around 4 V corresponding to the oxidation of Mn^{3+} to Mn^{4+} and the other around 5 V corresponding to the oxidation of the other transition metal ions. Although an increase in the cell voltage to 5 V is attractive from an energy density point of view, the $LiMn_{2-y}M_yO_4$ oxides are prone to suffer from oxygen loss from the lattice and safety concerns in the 5-V region.

6.4.2 *Surface Modified LMO*

The dissolution of manganese in the electrolyte is of major concern [118]. The reaction of $LiMn_2O_4$ with the electrolyte increases with the temperature, so that $LiMn_2O_4$-based batteries need being maintained at room temperature. In this context, the study of surface modifications of LMO is of primary importance to protect the material against reactions with the electrolyte and avoid the dissolution of Mn^{3+} in order to achieve two goals: (1) improve the calendar life and cycling life to make it competitive with other cathode elements, in order to get rid of the lamellar component in the cathode, (2) restore the thermal safety of the battery. The most commonly used coating materials are metal oxides such as Al_2O_3, ZrO_2, ZnO, SiO_2, and Bi_2O_3, which can successfully protect electrode from HT attack. A review of developments in the surface modification of $LiMn_2O_4$ as cathode material of power lithium-ion battery can be seen in ref. [119]. To explore the change in the electrochemical properties of the spinel electrodes, electrochemical impedance spectroscopy (EIS) was carried out for the pristine and coated material upon cycling in the charged state for cells maintained at 55 °C. Nyquist plots derived from the analyses of uncoated and ZrO_2-coated $LiMn_2O_4$ are shown in Fig. 6.16a, b, respectively. Each EIS spectrum consists of two semicircles and a slope. The first semicircle in the high-to-medium frequency region is attributed to resistance of surface film (R_{sf}) that covers the electrode particle. The semicircle at medium-to-low frequency region is associated with the charge transfer resistance (R_{ct}) coupled with a double-layer capacitance. The slope at the low-frequency region is assigned to lithium-ion diffusion in the bulk material. On the basis of this mechanism, the equivalent circuit used for analysis is given as insert. R_w represents the electrolyte

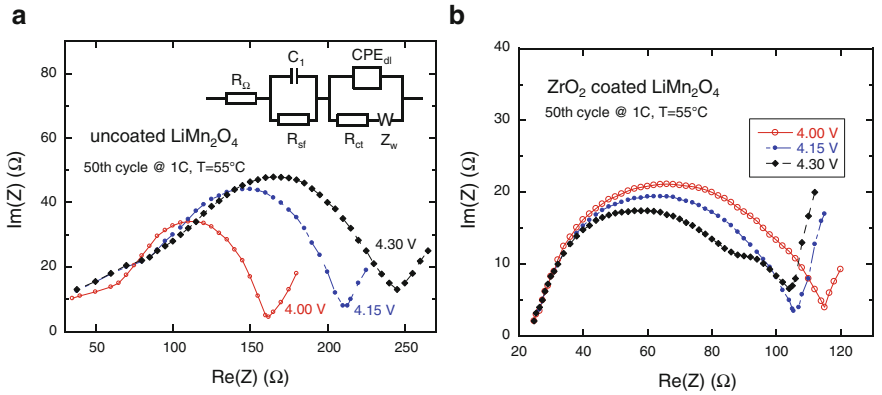

Fig. 6.16 Nyquist diagrams of (**a**) uncoated $LiMn_2O_4$ as a function of the state-of-charge after 50 cycles in the potential range 4.0–4.3 V and (**b**) after ZrO_2 coating. Cells were cycled at 1*C* rate and maintained at $T = 55$ °C. The equivalent circuit used for the analysis is shown as insert (see text for symbol meaning)

resistance, CPE_{dl} is a constant phase element and W_z is the Warburg element corresponding to the Li^+ ion diffusion in the host material. After 50 cycles, the increase of R_{ct} of the uncoated material is due to the chemical evolution at the electrode–electrolyte interface rather than Mn(II) migration. The impedance spectra of ZrO_2-coated $LiMn_2O_4$ clearly display the contribution of the low frequency element due to the modified SEI layer, which reduces the Li^+-ion transport through the coating.

It has been reported that LMO particles coated with either borate glass Li_2O–$2B_2O_3$ (LBO) or with fluorine exhibit good high-temperature electrochemical performance. LBO-coated LMO electrode via solution method has an excellent cycling behavior (112 mAh g^{-1}) without any capacity loss even after 30 cycles at 1*C* rate [120]. Fluoride is also used to coat LMO to improve its cyclability because it is very stable even in HF. Lee et al. [121] reported that the BiOF-coated spinel electrode had excellent capacity retention at 55 °C, maintaining its initial discharge capacity of 96 % after 100 cycles against 84 % for the pristine material because the oxyfluoride layer provides a strong protection against HF attack and scavenges HF.

6.4.3 Defect Spinels

The technological interest of the defect spinels $Li_{1-\delta}Mn_{2-\delta}O_4$ as positive electrodes comes from their ability to reversibly intercalate/deintercalate lithium. Considering the Li-Mn-O phase diagram (Fig. 6.17), the area that falls within the MnO_2-$LiMn_2O_4$-$Li_4Mn_5O_{12}$ tie triangle constitutes a region of defect spinel compositions. The defective $Li_{1-\delta}Mn_{2-\delta}O_4$ manganospinels, which contain vacancies at both tetrahedral and octahedral manganese sites can lead to high capacity

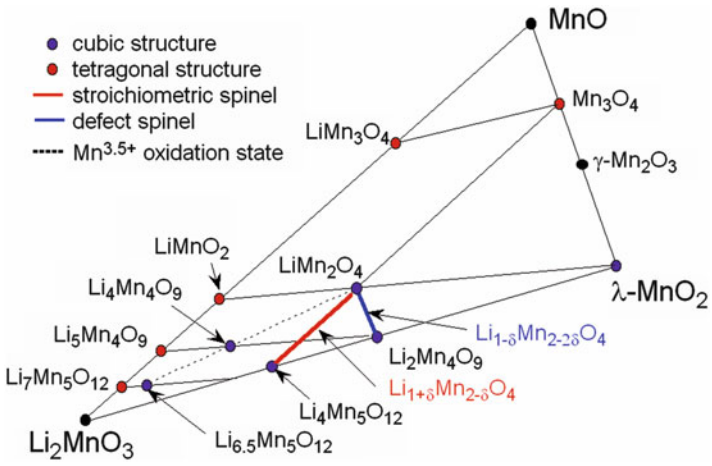

Fig. 6.17 Expanded region of the Li-Mn-O phase diagram. The MnO_2-$LiMnO_2$-Li_2MnO_3 tie triangle includes the region of defect spinel compositions

(>230 mAh g^{-1}). Such compounds also have a Li/Mn ratio of 0.5 and have an average Mn^{+} valence state varying from 3.5 to 4 (depending on the value of δ) [16, 122]. For a value of $\delta = 0.11$, this compound, $Li_2Mn_4O_9$, is a nonstoichiometric form with Mn^{+} oxidation state of 4.0. The higher is the value of δ, the lower is the capacity at 4 V, the smaller is the lattice parameter, and the better is the cyclability in the 3-V region. It was then speculated that the oxygen-rich lithium manganospinels can deliver high steady capacities in excess of 150 mAh g^{-1} (Fig. 6.17).

Defect spinel with the formula $Li_{0.50}MnO_{2.25}$ ($Li_2Mn_4O_9$) and $Li_{0.51}MnO_{2.20}$ were synthesized by sol–gel method via the citrate route. The structure analysis yielded powders of cubic structure (*Fd3m* S.G.) with lattice parameters $a = 8.193$ Å for $Li_{0.52}MnO_{2.1}$ and $a = 8.162$ Å for $Li_2Mn_4O_9$ that can be compared with that of stoichiometric $LiMn_2O_4$ ($a = 8.248$ Å) and that of $Li_4Mn_5O_{12}$ ($a = 8.137$ Å). The formula of $Li_2Mn_4O_9$ is written $(\square_{0.11}Li_{0.89})_{8a}[\square_{0.22}Mn_{1.78}]_{16d}O_4$ in spinel notation. $Li_2Mn_4O_9$ accommodates 0.95Li/Mn to a cutoff of 2.0 V and shows a slight transformation from cubic to tetragonal for 0.9Li (Fig. 6.18). This was evidenced by the appearance of a second phase in the Raman spectrum of $Li_{4.4}Mn_4O_9$. Similar features are observed for $Li_{0.51}MnO_{2.20}$, which can insert 0.86Li/Mn.

6.4.4 Li Doped Spinels

For wide scale application, the major drawback of $LiMn_2O_4$ comes from the difficulty to prepare samples of good quality because the Jahn–Teller Mn^{3+} ion favors lattice distortions. Several investigations have been made to overcome the

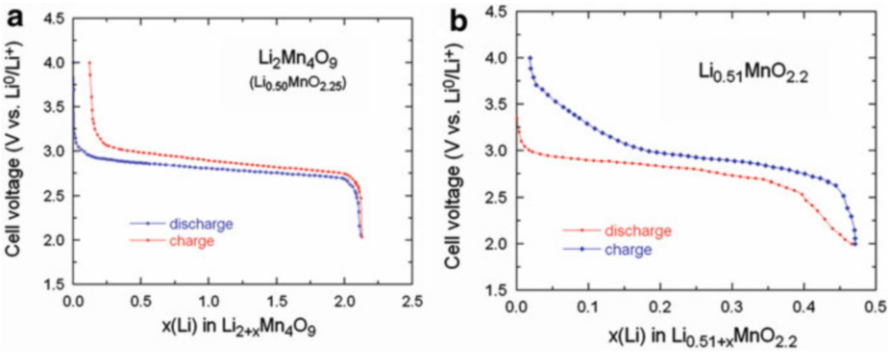

Fig. 6.18 Charge–discharge profiles of defect spinels (**a**) $Li_{0.5}MnO_{2.25}$ ($Li_2Mn_4O_9$) and (**b**) $Li_{0.51}MnO_{2.2}$. Measurements were carried out at *C*/20 rate in the potential range 2–4 V

capacity fading by replacing Li for Mn [16]. The reduction of Mn^{3+} concentration has been obtained by substitution of monovalent ions, which enhances the stability of the $LiMn_2O_4$ spinel phase. In the system Li-Mn-O, $Li_{1+x}Mn_{2-x}O_4$ spinels exist as a continuous series of solid solution in the range $0.00 \leq x \leq 0.33$. It is generally accepted that Li-rich spinels behave with improved electrochemical performance. Recently, numerous papers reported the physical properties of such materials [100, 101, 123]. Both structural and magnetic analyses reveal that the physical and electrochemical properties are importantly influenced by the presence of Li_2MnO_3 impurity phase. The presence of this additional phase reduces the average oxidation state of manganese according to disproportionation reaction, so that the final composition of the spinel phase is $Li_{3.8}Mn_{5.2}O_{12}$ (or $Li_{1.27}Mn_{1.73}O_4$). Due to the important geometric frustration of the magnetic interactions, and dilution of the antiferromagnetic interactions, no magnetic ordering is observed in the temperature range investigated. The anomalous magnetic properties, including the Dysonian profile of the ESR line, show that the material is metallic. The Sommerfeld constant deduced from the specific heat measurements is 308 mJ K^{-2} per mole of $Li_{1.27}Mn_{1.73}O_4$, which shows that this material belongs to the class of heavy-fermion systems like LiV_2O_4 or $LiTi_2O_4$. These heavy fermions are the minority-spin $t_g\downarrow$ electrons of Mn^{3+} ions that have a reduced effective masse $m/m_0 = 467$. The electrochemical properties show that the specific capacity of 163 mAh g^{-1} for $Li_{3.8}Mn_{5.2}O_{12}$ at charge rate 1*C* is a large value due to the possible insertion of Li up to the composition $Li_{6.8}Mn_{5.2}O_{12}$. The origin of the disproportionation, and the flat voltage in the lithiation process have been discussed in the framework of the stability of the Mott insulator phase with respect to the metallic phase [75].

Figure 6.19a displays the discharge–charge curve of Li//$Li_4Mn_5O_4$ cell. As reported previously [16, 124], the $[Mn^{IV}]O_6$ framework of $Li[Li_{1/3}Mn_{5/3}]O_4$ spinel is an attractive host structure for lithium insertion-extraction reactions because it provides a three-dimensional network of face-sharing tetrahedra and octahedra for lithium-ion diffusion. $Li_{4/3}Mn_{5/3}O_4$ has a capacity of 163 mAh g^{-1} in the potential

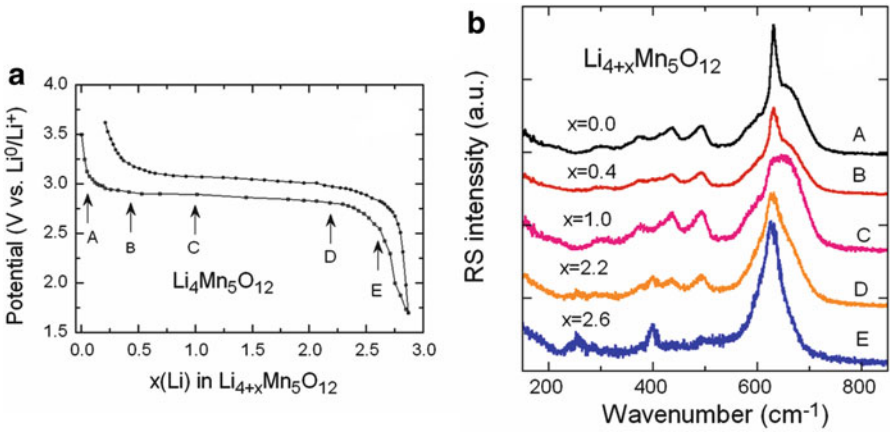

Fig. 6.19 (**a**) Charge–discharge curves as a function of the lithium content in $Li_{4+x}Mn_5O_{12}$ cell. *Arrows* indicate the composition for analysis. (**b**) The Raman spectra of $Li_{4+x}Mn_5O_{12}$ electrode materials at different amounts of lithium insertion. The spectrum of the final product shows the features of the tetragonal structure

range 3.5–1.5 V. Upon intercalation (discharge) the phase transition process from spinel to rock-salt type phase with 3Li uptake in $Li_4Mn_5O_{12}$:

$$Li_4Mn_5O_{12} + xLi + + xe^- \leftrightarrows Li_7Mn_5O_{12}. \tag{6.2}$$

Note that this phase transformation starts to dominate the electrode kinetics. The OCV curve vs. x(Li) displays a voltage plateau in the Li composition range $0.05 \leq x \leq 0.85$. This curve slightly decreases from 0.9 before to drop sharply at $x \approx 0.95$. A two-phase electrochemical reaction occurs as a flat voltage response; in this reaction, a distinct change in voltage is evident as one phase becomes depleted, thus providing an end-of-charge indicator [125]. Figure 6.19b shows the phase evolution upon Li insertion studied by Raman scattering (RS) spectroscopy. Spectra (curves A-E) of electrochemically lithiated $Li_{4+x}Mn_5O_{12}$ spinels were recorded on material taken from a cell discharged in the range 3.2–2.5 V. The RS spectrum of $Li_{6.5}Mn_5O_{12}$ shows clearly the structural change that occurred in $Li_{4/3}Mn_{5/3}O_4$ upon Li insertion from cubic (O_h^7) to tetragonal (D_{4h}^{19}) structure. This structural modification induces three typical RS bands at wave numbers 255, 282 and 397 cm^{-1}. The high-frequency band appears at 628 cm^{-1} with a shoulder at 592 cm^{-1}. Similarly to $Li_7Ti_5O_{12}$, spectral features $Li_{6.5}Mn_5O_{12}$ are consistent with the tetragonal $I4_1/amd$ symmetry. A tetragonal distortion is expected to occur with the Li insertion in $Li_{4/3}Mn_{5/3}O_4$ because of appearance of the Mn^{3+} Jahn–Teller ions at the end of the discharge. The net effect is a lowering in the crystal symmetry from cubic $Fd3m$ to tetragonal $I4_1/amd$ [126].

6.5 Five-Volt Spinels

To improve the poor cycling performance of $LiMn_2O_4$, several works have reported transition metal substituted spinel materials $LiM_yMn_{2-y}O_4$ with $M = Ni$, Co, Fe, Cr, etc. For a review see ref. [127]. Their electrochemical properties strongly depend on the kind and content of 3*d*-transition metal. However, they exhibit high-voltage plateau at around 5 V vs. Li^0/Li^+ [128, 129]. Among them, $LiNi_{0.5}Mn_{1.5}O_4$ is of special interest for its dominant potential at around 4.7 V. The plateau at 4.7 V results from Ni^{2+}/Ni^{4+} redox couple while the plateau at 4.1 V is due to the Mn^{3+}/Mn^{4+} redox couple. In contrast to the tetragonal structure formation upon insertion of Li^+ into undoped spinel, the spinel $LiNi_{0.5}Mn_{1.5}O_4$ remains cubic to form $Li_2Ni_{0.5}Mn_{1.5}O_4$.

The structure is identified as a primitive cubic cell $a = 8.166$ Å with a space group $P4_132$ instead of $Fd3m$ for normal spinel lattice. The space group $P4_132$ allows to place the larger Ni^{2+} ions (ionic radius 0.69 Å) in bigger 4*b* site instead of 16*d* site of normal spinel structure (Fig. 6.12). The smaller unit cell dimension is primarily due to the change in Mn valence state. Despite the replacement of a fraction of Mn ions by bigger Ni^{2+} ions, the Mn valence change effect is prevailing. Figure 6.20 presents the RS spectra of $LiNi_{0.5}Mn_{1.5}O_4$ powders synthesized by wet chemical method. Using different procedure of calcination, two types of materials are obtained, i.e., the ordered- and the normal-spinel framework. The former compound exhibits additional Raman bands due to the symmetry lowering [130].

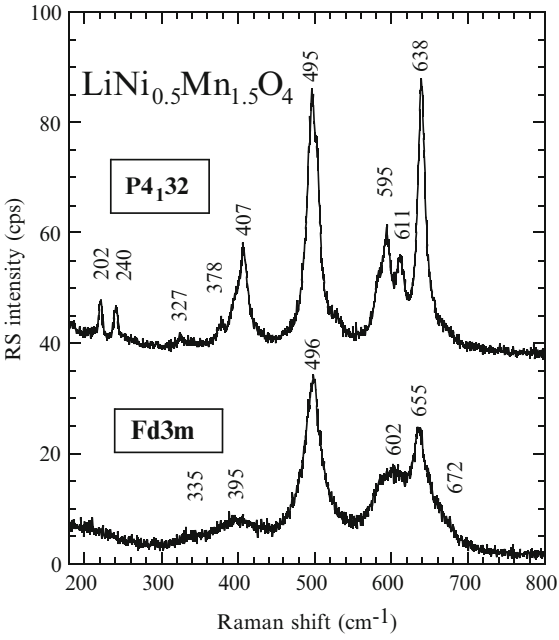

Fig. 6.20 Raman spectra of $LiNi_{0.5}Mn_{1.5}O_4$ powders with the ordered- and the normal-spinel framework

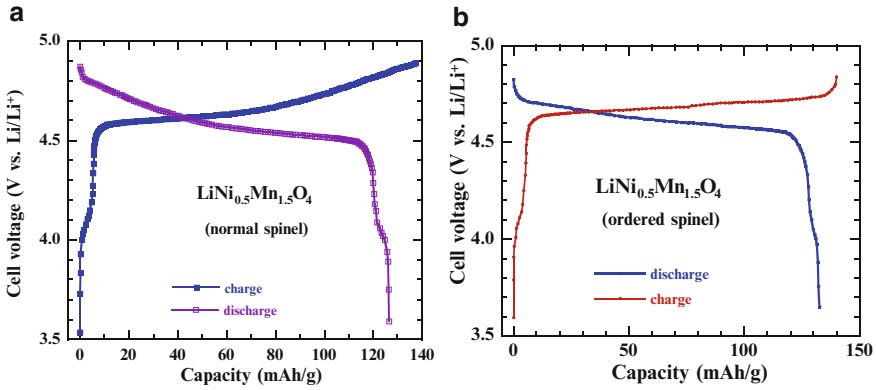

Fig. 6.21 Charge–discharge curves of Li//$LiNi_{0.5}Mn_{1.5}O_4$ cells with (**a**) normal-spinel and (**b**) ordered-spinel framework

Figure 6.21 shows the first charge–discharge profile of the spinel Li// $LiNi_{0.5}Mn_{1.5}O_4$ cells in the voltage range 3.5 to 4.9 V vs. Li^0/Li^+ for (a) normal $A[B_2]O_4$ spinel lattice and (b) ordered 1:3 spinel framework [130]. Our data are consistent with these of prior results in terms of their high-voltage characteristics. As can be seen in Fig. 6.21, the $LiNi_{0.5}Mn_{1.5}O_4$ samples reveal operating voltage higher than 4.5 V. The curves are characteristic of a two-step lithium intercalation–deintercalation behavior. The small plateau around 4.0 V is related to the redox couple Mn^{3+}/Mn^{4+}. Pure and stoichiometric $LiNi_{0.5}Mn_{1.5}O_4$ should not contain Mn^{3+} ions. However, due to a small loss of oxygen during the synthesis at high temperature, part of the inactive Mn^{4+} ions are reduced to active Mn^{3+} due to charge neutrality. The plateau around 4.7 V has been attributed to the oxidation of Ni^{2+} to Ni^{4+}. The normal-spinel phase shows predominantly one-step reaction at 4.65 V. The voltage profile of the ordered-spinel structure transforms from a sloping curve to flat curve at 4.72 V. In the voltage range 3.5–4.9 V, the Li//$LiNi_{0.5}Mn_{1.5}O_4$ delivers a capacity 133 mAh g^{-1} during the first discharge. The capacity retention is over 97 % of the initial capacity for cells discharged at $C/10$ in the voltage range 3.5–4.9 V.

The cycling performance of the normal $LiNi_{0.5}Mn_{1.5}O_4$ is better than that of the ordered spinel material due to the higher diffusion coefficient of Li^+ in the former. Unfortunately, the disordered state favors the oxygen deficiency responsible for the presence of the Mn^{3+} Jahn–Teller and the presence of $Li_yNi_{1-y}O$ impurity, which is damageable to the electrochemical properties. Therefore, different cation substitutions have been made aiming to overcome this problem. The best result has been obtained with substitution of Cr for Mn. In particular, $LiMn_{1.45}Cr_{0.1}Ni_{0.45}O_4$ spinel prepared by a co-precipitation method assisted by a post-annealing at 600 °C that reoxidizes the manganese to the Mn^{+4} state showed improved capacity at any C-rate up to $5C$, with only 6 % capacity lost after 125 cycles [131].

6.6 Vanadium Oxides

Vanadium shows versatile oxide phases of mixed valence states between V^{4+} and V^{5+}. They have higher electronic conductivity arising from the hopping mechanism from V^{4+} to V^{5+} and can be denoted by the nominal formula of V_nO_{2n+1} ($n > 2$). Lithium insertion reaction has been shown in vanadium oxides such as V_2O_5, VO_2(B), V_6O_{13} and LiV_3O_8. Their structure consists of edge-shared octahedra forming single zig-zag strings and double zig-zag ribbons with infinite extension normal to the plane of the paper. The single and double sheets are then joined together by sharing corners to give a three-dimensional lattice. Murphy et al. [132, 133] have investigated some distinct phases of vanadium oxides such as V_3O_7, V_4O_9, and V_6O_{13}.

6.6.1 V_6O_{13}

V_6O_{13} is a black material which derives from the ReO_3 structure and is intermediate in composition between VO_2 and V_2O_5. In this family, V_3O_7 and V_4O_9 appear to have an intermediate structure between that of V_6O_{13} and V_2O_5. The monoclinic structure of V_6O_{13} contains edge-shared distorted VO_6 octahedra forming single and double zig-zag chains linked together by further edge sharing corner-shared (Fig. 6.22). The resulting sheets (single and double) are interconnected by corner sharing, thus giving a 3D framework [134]. This structure contains tri-capped cavities joined through shared square faces. The three open faces of the cavity should permit lithium-ion diffusion along (010) with the possibility of exchange between pairs of adjacent channels. Stoichiometric V_6O_{13} can be written as $(V^{4+})_4(V^{5+})_2(O^{2-})_{13}$ as far as the valency state of the vanadium ions are concerned.

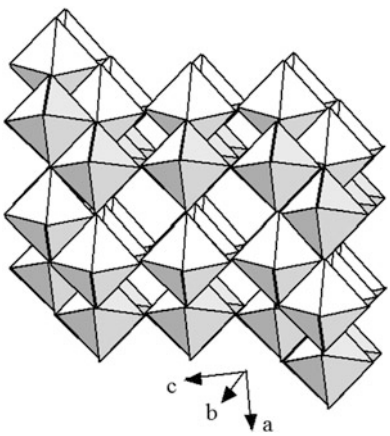

Fig. 6.22 The crystallographic structure of V_6O_{13} showing the shear lattice derived from the ReO_3. The structure consists of distorted VO_6 octahedra sharing corners and edges

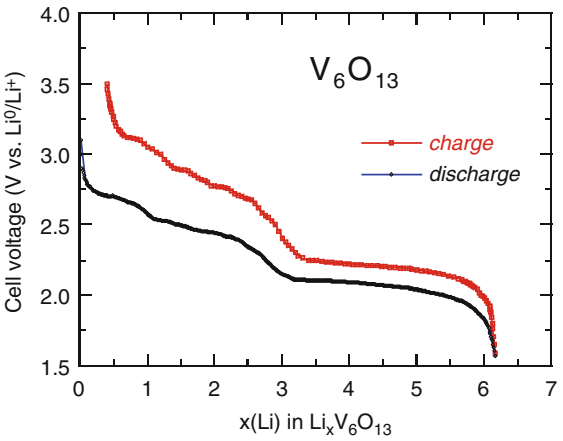

Fig. 6.23 The discharge–charge curve of the Li// V_6O_{13} cell carried out at *C*/24 in the potential range 1.5–3.5 V. The plateaus correspond to the various redox states of vanadium in the ReO_3-like structure. Reproduced with permission from [135]. Copyright 1983 Elsevier

The structure of V_6O_{13} is interesting from an electrochemical viewpoint due to the theoretical maximum limit of lithium uptake giving an energy density of 890 Wh kg^{-1}. The stoichiometric V_6O_{13} structure is believed to accommodate 8 Li per formula unit as determined by the available electronic sites rather than the structural cavities [135]. The limit corresponds to a situation when all the vanadium ions are present in the trivalent V^{3+} state. As a function of the stoichiometry, the maximum uptake goes to 1.35 Li for $VO_{2.18}$ oxide. Reversible chemical and electrochemical insertion of lithium into V_6O_{13} was first demonstrated by Murphy et al. [132, 136], and its potential as an active cathode material in practical batteries has since been more fully investigated [135]. The discharge curve exhibits three distinct plateaus, reflecting the sequential filling of non-equivalent sites in the host structure (Fig. 6.23) [137].

Figure 6.24a shows the Arrhenius plot of the electrical conductivity of V_6O_{13} and $Li_xV_6O_{13}$ ($0 \leq x \leq 6$). The pure material has a conductivity of 1×10^{-2} S cm^{-1} at room temperature and exhibits a semiconductor behavior. The electronic conduction in V_6O_{13} is due to the electron hopping between V^{4+} and V^{5+} states. The decreasing conductivity corresponds to a steadily decrease with addition of Li-ions in the $Li_xV_6O_{13}$ framework. Intercalation of Li-ions is believed to lower the valence state of vanadium ions by transfer of electrons. The relative concentration of reduced cations results in the lowering of the conductivity towards a poor electronic semiconductor. Electronic conductivity of pressed V_6O_{13} powders indicates a sharp fall in two steps with increasing Li content [138, 139]. For lithiated V_6O_{13}, we observe a continuous decrease of the electrical conductivity. Lowest conductivity of 5×10^{-4} S cm^{-1} has been measured in $Li_6V_6O_{13}$. This is also accompanied by an increase in activation energy, a general phenomenon observed in any oxide with small-polaron conduction. Fourier transform infrared (FTIR) spectra of $Li_xV_6O_{13}$ ($x = 0.0$ and 3.2) compounds reveals the transition from metal-like to small-polaron features (Fig. 6.24b). In pure V_6O_{13}, a Drude edge is observed around 200 cm^{-1}, which is the contribution of the free charge-carriers in the 3*d* band. For lithiated

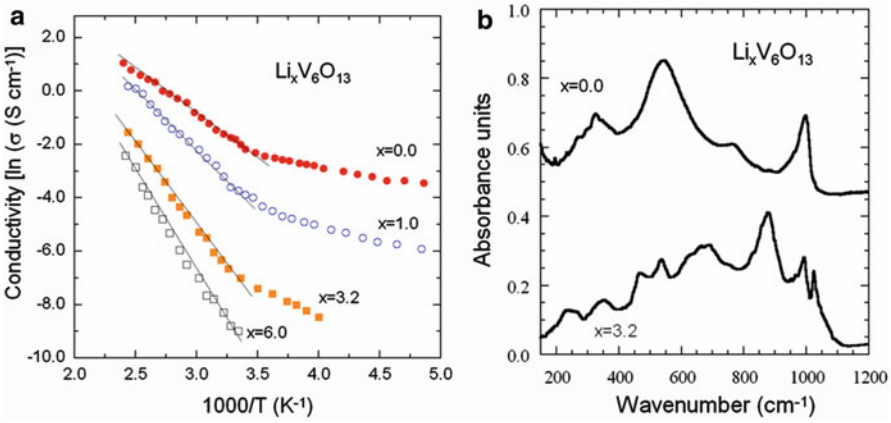

Fig. 6.24 (**a**) Arrhenius plot of the electrical conductivity of V_6O_{13} and $Li_xV_6O_{13}$ in the composition range $0 \leq x \leq 6$. Measurements were carried out on pellets using the van der Pauw method. (**b**) FTIR absorption spectra of V_6O_{13} and $Li_{3.2}V_6O_{13}$

V_6O_{13}, we observe a continuous decrease of the electrical conductivity, which is also recorded in the far-infrared spectrum by the disappearance of the Drude absorption [137].

6.6.2 $LiVO_2$

$LiVO_2$ adopts the O_3 structure of $LiCoO_2$. Although lithium could be readily extracted from $LiVO_2$, the vanadium ions migrate to the lithium planes for $(1-x) < 0.67$ in $Li_{1-x}VO_2$ [140, 141]. Similarly, the LiV_2O_4 spinel suffers from the migration of vanadium ions during the charge–discharge process.

6.6.3 $VO_2(B)$

The VO_2(B) phase is a metastable form of VO_2 [142] that exhibits high capacity with good cyclability. The shear structure derived from the hypothetical VO_3, ReO_3-like structure consists of distorted VO_6 octahedra sharing corners and edges [143–145]. Additionally, VO_2(B) contains one dimensional tunnel for alkali insertion. Metastable VO_2(B) crystallizes in a monoclinic structure clearly identified ($a = 12.03$, $b = 3.693$, $c = 6.42$ Å, $\beta = 106°$) and distinct from the closely related structure of V_6O_{13}. However, VO_2 (B) is very difficult to prepare by conventional high temperature route because the phase change from metastable to thermodynamically more stable rutile phase VO_2(R). Two other VO_2 phases are known: VO_2(A) which exhibits the shift of oxygen vacancies in the fcc lattice and the

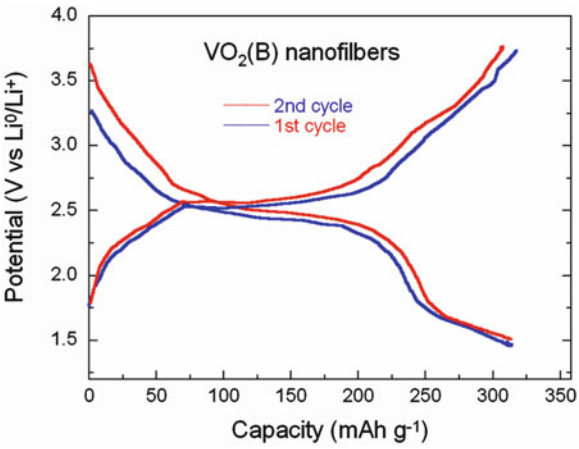

Fig. 6.25 The initial two charge–discharge curves of Li//VO_2(B) cell cycled at *C*/12 rate

metallic VO_2(M) phase [142]. Nanostructured VO_2(B) material was prepared in various forms such as nanowires, nanobelts, nanoribbons, nanoneedles, and nanorods [146–150]. The synthesis of VO_2(B) by slow reduction of V^{5+} in V_2O_5 shows a preferential growth in platelets with surfaces parallel to the *ab*-plane [151]. Nanorods VO_2(B) were prepared by solvothermal reduction of V_2O_5 by formaldehyde or isopropanol [152]. Vanadium oxide aerogels were used as a precursor for preparing nanotextured VO_2(B) by low-temperature heat treatment under vacuum. The VO_2(B) material prepared from aerogel precursor retains the fibrous morphology and high surface area of the aerogel. The electrochemical behavior of VO_2(B) shows specific capacity for lithium as high as 500 mAh g^{-1} and good stability when cycled between 4 and 2.4 V vs. Li^0/Li^+ [153]. Nanoflower-like VO_2(B) synthesized via one-step hydrothermal process had the first discharge capacity of 180 mAh g^{-1} [154]. VO_2(B) nanobelts synthesized by simple hydrothermal route have rectangular cross-section with mean length ~1 μm, mean width ~80 nm and thickness ~50 nm. Electrochemical tests show an initial discharge capacity of 321 mAh g^{-1} with voltage plateau near 2.5 V [155]. Figure 6.25 presents the initial two charge–discharge curves of Li//VO_2(B) cell cycled at *C*/12 rate.

6.7 Concluding Remarks

Numerous efforts are done to replace the cobalt oxide used in commercial lithium-ion batteries by materials with low cost and environmental concerns. The development of new materials needs new synthesis procedure such as sol–gel processing, ion-exchange reaction, hydrothermal reaction, etc. The chemical and structural stabilities of the transition-metal oxide electrodes have been compared by studying bulk samples. In this respect, the various physicochemical techniques are welcome

Table 6.3 Comparison of the electrode characteristics of some 3*d* transition-metal oxides

Oxide	Practical capacity $(\text{mAh g})^{-1}$	Average voltage (V)	Reversible Li^+ per *M* atom	Energy density (mWh g^{-1})
Li_xVO_2	290	2.6	0.9	750
$Li_{1-x}Mn_2O_4$	120	3.8	0.4	455
$Li_xNa_yMnO_zI_\eta$ (amorphous)	275	2.6	1.5	715
$Li_{1-x}CoO_2$	140	3.7	0.5	520
$Li_{1-x}MnCoO_4$	125	4.8	0.4	600
$Li_{1-x}NiO_2$	140	3.8	0.5	530
$Li_{1-x}Ni_{0.85}Co_{0.15}O_2$	180	3.75	0.6	675
$Li_xFe_2(SO_4)_3$	110	3.6	0.8	400
Li_xFePO_4	170	3.3	1.0	560

to design the best structure. Synthesis of amorphous compounds could help in the knowledge of microstructures in this regard.

The search for materials that exhibit superior cycling performance has led to the study of transition-metal- and cation-substituted materials; Effect of doping have been successful in many cases such as $LiNiO_2$, $LiCoO_2$, $LiMnO_2$, $LiMn_2O_4$. The $LiCo_{1-y}M_yO_2$ system showing relatively better chemical stability can replace the conventional $LiCoO_2$ with respect to oxygen loss. However, the problem of thermal instability of these lamellar compounds is not solved [156]. New systems such as $LiNi_{0.5}Mn_{0.5}O_2$ and $LiNi_{0.5}Mn_{1.5}O_4$ show interesting electrochemical features but need better control of their crystal chemistry.

In view of maximizing the cell voltage and energy density, transition metal oxide hosts have emerged as the choice for cathodes. The electrode properties of some of the 3*d* transition metal oxides are summarized in Table 6.3. Among the various oxide hosts, the layered $LiMO_2$ ($M =$ Co and Ni), spinel $LiMn_2O_4$, and olivine $LiFePO_4$ containing lithium have emerged as the leading cathode candidates as they can be coupled with the presently available anode host carbon, which does not contain lithium. However, only 40–65 % of the theoretical capacity of the layered $LiMO_2$ and spinel $LiMn_2O_4$ could be practically utilized due to various difficulties such as chemical and structural instabilities, which are discussed in a later chapter.

The future challenge is to develop simple oxide cathodes without having other elements such as P or Na in which at least one lithium ion per transition metal ion could be reversibly extracted/inserted while keeping the materials cost and toxicity low; such a cathode can nearly double the energy density compared to the present level. There are also possibilities to increase the capacity of anode hosts perhaps by focusing on amorphous materials. An alternative approach is to develop cells with lithium-containing anodes and lithium-free cathodes. This strategy will allow the use of some of the already known high capacity cathodes such as the vanadium oxides that have better chemical stability and safety characteristics. From a safety, and cycle and shelf life points of view, cathodes with a lower voltage (3–4 V) are

preferred, but this is at expense of the energy density. In particular, we see in the next chapter that frameworks built with $(PO_4)^{3-}$ polyanions are very promising materials. The phospho-olivine structure $LiFePO_4$ exhibits a very stable framework upon electrochemical cycling, and carbon-coated $LiFePO_4$ is an excellent cathode element for high-power batteries, but its energy density is smaller than that of lamellar compounds, although recent studies indicate that 100 % of the theoretical capacity of $LiFePO_4$ can be utilized.

References

1. Ikeda H, Saito T, Tamura H (1975) In: Kozawa A, Brodd RH (eds) Proceedings manganese dioxide symposium, vol 1. IC Sample Office, Cleveland, OH, p 384
2. Gabano JP (1983) Lithium batteries. Academic, London
3. Schöllhorn R (1982) Solvated intercalation compounds of layered chacogenide and oxide bronzes. In: Whittingham MS, Jacobson AJ (eds) Intercalation chemistry. Academic, New York, pp 315–360
4. Dickens PG, Pye MF (1982) Oxide insertion compounds. In: Whittingham MS, Jacobson AJ (eds) Intercalation chemistry. Academic, New York, pp 539–561
5. Murphy DW (1982) Lithium intercalation compounds of vanadium chalcogenides. In: Whittingham MS, Jacobson AJ (eds) Intercalation chemistry. Academic, New York, pp 563–572
6. Thackeray MM, David WIF, Bruce PG, Goodenough JB (1983) Lithium insertion into manganese spinels. Mater Res Bull 18:461–472
7. MacNeil DD, Dahn JR (2001) The reaction of charged cathodes with nonaqueous solvents and electrolytes: II. $LiMn_2O_4$ charged at 4 V. J Electrochem Soc 148:A1211–A1215
8. MacNeil DD, Lu Z, Chen Z, Dahn JR (2002) A comparison of the electrode/electrolyte reaction at elevated temperatures for various Li-ion battery cathodes. J Power Sourc 108:8–14
9. Shannon RD (1976) Revised effective ionoic radii and systematic studies of interatomic distances in halides and chalcogenides. Crystallogr Acta A 32:751–767
10. Ohzuku T (1994) Four-volt cathodes for lithium accumulators and the Li-ion batteries concept. In: Pistoia G (ed) Lithium batteries: new materials, developments, and perspectives. Elsevier, Amsterdam, pp 239–280
11. Leclanché GL (1866) Pile au peroxide de manganèse à seul liquide. Fr Pat 71,865. Brit Pat 2623
12. Ikeda H, Saito T, Tamura H (1977) Manganese dioxide symposium, vol 1. Cleveland Section of the Electrochem Society, Pennington
13. Dampier FW (1974) The cathodic behaviour of CuS, MoO_3 and MnO_2 in lithium cells. J Electrochem Soc 121:656–660
14. Feng Q, Kanoh H, Ooi K (1999) Manganese oxides porous crystals. J Mater Chem 9:319–333
15. Chabre Y, Pannetier J (1995) Structural and electrochemical properties of the proton/γ-MnO_2 system. J Prog Solid State Chem 23:1–130
16. Thackeray MM (1997) Manganese oxides for lithium batteries. Prog Solid State Chem 25:1–71
17. Julien CM, Massot M, Poinsignon C (2004) Lattice vibrations of manganese oxides. Part I. Periodic structure. Spectrochim Acta A 60:689–700
18. Chen Y, Hong Y, Ma Y, Li J (2010) Synthesis and formation mechanism of urchin-like nano/micro-hybrid α-MnO_2. J Alloys Compd 490:331–335
19. Abuzeid HM, Hashem AM, Narayanan N, Ehrenberg H, Julien CM (2011) Nanosized silver-coated and doped manganese dioxide for rechargeable lithium batteries. Solid State Ionics 182:108–115

20. Le Goff P, Baffier N, Bach S, Pereira-Ramos JP (1996) Synthesis, ion exchange and electrochemical properties of lamellar phyllomanganates of the birnessite group. Mater Res Bull 31:63–75
21. Hunter JC (1981) Preparation of a new crystal form of manganese dioxide λ-MnO_2. J Solid State Chem 39:142–147
22. Thackeray MM, de Kock A, de Piocciotto LA, Pistoia G (1989) Synthesis and characterization of γ-MnO_2 from $LiMn_2O_4$. J Power Sourc 26:355–363
23. Nardi JC (1985) Characterization of the Li/MnO_2 multistep discharge. J Electrochem Soc 132:1787–1791
24. Palache C, Berman H, Frondel C (1963) The system of mineralogy, vol 1, 7th edn. Wiley, New York
25. Julien C, Massot M, Rangan S, Lemal M, Guyomard D (2002) Study of structural defects in γ-MnO_2 by Raman spectroscopy. J Raman Spectr 33:223–228
26. Ohzuku T, Kitagawa M, Hirai T (1989) Electrochemistry of manganese dioxide in lithium nonaqueous cell. I. X-ray diffractional study on the reduction of electrolytic manganese dioxide. J Electrochem Soc 136:3169–3174
27. Le Goff P, Baffier N, Bach S, Pereira-Ramos JP (1994) Structural and electrochemical properties of layered manganese dioxides in relation to their synthesis: classical and sol-gel routes. J Mater Chem 4:875–881
28. Julien CM, Massot M (2004) Vibrational spectroscopy of electrode materials for rechargeable lithium batteries. III. Oxide frameworks. In: Stoynov Z, Vladikova D (eds) Proceedings of the international workshop on advanced techniques for energy sources investigation and testing, Bulgarian Academy of Sciences, Sofia, pp 1–17
29. Nohma T, Yoshimura S, Nishio K, Saito T (1994) Commercial cells based on MnO_2 and MnO_2-related cathodes. In: Pistoia G (ed) Lithium batteries. Elsevier, Amsterdam, pp 417–456
30. Nohma T, Saito T, Furukawa N, Ikada H (1989) Manganese oxides for a lithium secondary battery. Composite dimensional manganese oxide (CDMO). J Power Sourc 26:389–396
31. Hashem AM, Abuzeid HM, Abdel-Latif AM, Abbas HM, Ehrenberg H, Indris S, Mauger A, Julien CM (2013) MnO_2 nanorods prepared by redox reaction as cathodes in lithium batteries. ECS Trans 50–24:125–130
32. Shao-Horn Y, Hackney SA, Johnson CS, Thacheray MM (1998) Microstructural features of α-MnO_2 electrodes for lithium batteries. J Electrochem Soc 145:582–589
33. Huang X, Lv D, Zhang Q, Chang H, Gan J, Yang Y (2010) Highly crystalline macroporous β-MnO_2: hydrothermal synthesis and application in lithium battery. Electrochim Acta 55:4915–4920
34. Hashem AM, Abuzeid HM, Nikolowski K, Ehrenberg H (2010) Table sugar as preparation and carbon coating reagent for facile synthesis and coating of rod-shaped MnO_2. J Alloys Compd 497:300–303
35. Renuka R, Ramamurthy S (2000) An investigation on layered birnessite type manganese oxides for battery applications. J Power Sourc 87:144–152
36. Julien C, Massot M, Baddour-Hadjean R, Franger S, Bach S, Pereira-Ramos JP (2003) Raman spectra of birnessite manganese dioxides. Solid State Ionics 159:345–356
37. Strobel P, Mouget C (1993) Electrochemical lithium insertion into layered manganates. Mater Res Bull 28:93–100
38. Franger S, Bach S, Pereira-Ramos JP, Baffier N (2000) Influence of cobalt ions on the electrochemical properties of lamellar manganese oxides. Ionics 6:470–476
39. Bach S, Pereira-Ramos JP, Baffier N, Messina R (1991) Birnessite manganese dioxide synthesized via a sol-gel process: a new rechargeable cathodic material for lithium batteries. Electrochim Acta 36:1595–1603
40. Paulsen JM, Dahn JR (1999) Phase diagram of Li-Mn-O spinel in air. Chem Mater 11:3065–3079

41. Wen SJ, Richardson TJ, Ma L, Striebel KA, Ross PN, Cairns EJ (1996) FTIR spectroscopy of metal oxide insertion electrodes: a new diagnostic tool for analysis of capacity fading in secondary Li/$LiMn_2O_4$ cells. J Electrochem Soc 143:L136–L138
42. Banov B, Momchilov A, Massot M, Julien CM (2003) Lattice vibrations of materials for lithium rechargeable batteries V. Local structure of $Li_{0.3}MnO_2$. Mater Sci Eng B 100:87–92
43. Yoshio M, Nakamura H, Xia Y (1999) Lithiated manganese dioxide $Li_{0.33}MnO_2$ as a 3 V cathode for lithium batteries. Electrochim Acta 45:273–283
44. Levi E, Zinigrad E, Teller H, Levi MD, Aurbach D (1998) Common electroanalytical behaviour of Li intercalation processes into graphite and transition metal oxides. J Electrochem Soc 145:3024–3034
45. Julien CM, Banov B, Momchilov A, Zaghib K (2006) Lithiated manganese oxide $Li_{0.33}MnO_2$ as electrode material for lithium batteries. J Power Sourc 159:1365–1369
46. Doeff MM, Peng MY, Ma Y, De Jonghe LC (1994) Orthorhombic Na_xMnO_2 as a cathode material for secondary sodium and lithium polymer batteries. J Electrochem Soc 141: L145–L147
47. Armstrong AR, Huang H, Jennings RA, Bruce PG (1998) $Li_{0.44}MnO_2$: an intercalation electrode with a tunnel structure and excellent cyclability. J Mater Chem 8:255–259
48. Jeong YU, Manthiram A (1999) Synthesis and lithium intercalation properties of $Na_{0.5-x}Li_x$ $MnO_{2+\delta}$and $Na_{0.5-x}MnO_{2+\delta}$ cathodes. Electrochem Solid State Lett 2:421–424
49. Akimoto J, Awaka J, Takahashi Y, Kijima N, Tabuchi M, Nakashima A, Sakaebe H, Tatsumi K (2005) Synthesis and electrochemical properties of $Li_{0.44}MnO_2$ as a novel 4 V cathode material. Electrochem Solid State Lett 8:A554–A557
50. Akimoto J, Awaka J, Hayakawa H, Takahashi Y, Kijima N, Tabuchi M, Sakaebe H, Tatsumi K (2007) Structural and electrochemical properties of $Li_{0.44}Mn_{1-y}Ti_yO_2$ as a novel 4-V positive electrode material. J Power Sourc 174:1218–1223
51. Gummow RJ, Liles DC, Thackeray MM (1993) Lithium extraction from orthorhombic lithium manganese oxide and the phase transformation to spinel. Mater Res Bull 28:1249–1256
52. Ohzuku T, Kitano S, Iwanaga M, Matsuno H, Ueda A (1997) Comparative study of Li $[Li_xMn_{2-x}]O_4$ and LT-$LiMnO_2$ for lithium-ion batteries. J Power Sourc 68:646–651
53. Reimers JN, Fuller EW, Rossen E, Dahn JR (1993) Synthesis and electrochemistry studies of $LiMnO_2$ prepared at low temperatures. J Electochem Soc 140:3396–3401
54. Zhou F, Zhao X, Liu Y, Li L, Yuan C (2008) Size-controlled hydrothermal synthesis and electrochemical behaviour of orthorhombic $LiMnO_2$ nanorods. J Phys Chem Solids 69:2061–2065
55. Jin EM, Jin B, Jeon YS, Park KH, Gu HB (2009) Electrochemical properties of $LiMnO_2$ for lithium polymer battery. J Power Sourc 189:620–623
56. Liu Q, Mao D, Chang C, Huang F (2007) Phase conversion and morphology evolution during hydrothermal preparation of orthorhombic $LiMnO_2$ nanorods for lithium ion battery application. J Power Sourc 173:538–544
57. Armstrong AR, Bruce PG (1996) Synthesis of layered $LiMnO_2$ as an electrode for rechargeable lithium batteries. Nature 381:499–500
58. Capitaine F, Gravereau P, Delmas C (1996) A new variety of $LiMnO_2$ with a layered structure. Solid State Ionics 89:197–202
59. Singhal A, Skandan G, Amatucci G, Pereira N (2000) Nanostructured electrodes for rechargeable Li batteries. In: Proceedings of electrochemical society workshop on interfaces, phenomena and nanostructures in lithium batteries, Argonne, Accessed 11–13 Dec 2000
60. Paulsen JM, Thomas CL, Dahn JR (1999) Layered Li-Mn-Oxide with O2 structure: a cathode material for Li-ion cells which does not convert to spine. J Electrochem Soc 146:3560–3565
61. Chiang YM, Wang H, Jang YI (2001) Electrochemically induced cation disorder and phase transformations in lithium intercalation oxides. Chem Mater 13:53–63
62. Dan P, Mengeritsky E, Aurbach D, Weissman I, Zinigrad E (1997) More details on the new $LiMnO_2$ rechargeable battery technology developed at Taridan. J Power Sourc 68:443–447

63. Doeff MM, Richardson TJ, Kepley L (1996) Lithium insertion processes of orthorhombic Na_xMnO_2-base electrode materials. J Electrochem Soc 143:2507–2516
64. Kim J, Manthiram A (1997) A manganese oxyiodide cathode for rechargeable lithium batteries. Nature 390:265–267
65. Wickham DG, Croft WJ (1958) Crystallographic and magnetic properties of several spinels containing trivalent JA-1044 manganese. J Phys Chem Solids 7:351–360
66. Thackeray MM, Shao-Horn Y, Kahaian AJ, Kepler KD, Skinner E, Vaughey JT, Hackney SA (1998) Structural fatigue in spinel electrodes in high voltage (4 V) $Li/Li_xMn_2O_4$ cells. Electrochem Solid State Lett 1:7–9
67. Wang E, Bowden W, Gionet P (1998) Method of preparation of lithium manganese oxide spinel. US Patent 5,753,202. Accessed 8 Apr 1996
68. Rho YH, Dokko K, Kanamura K (2006) Li^+ ion diffusion in $LiMn_2O_4$ thin film prepared by PVP sol-gel method. J Power Sourc 157:471–476
69. Liu W, Farrington GC, Chaput F, Duhn B (1996) Synthesis and electrochemical studies of spinel phase $LiMn_2O_4$ cathode materials prepared by the Pechini process. J Electrochem Soc 143:879–884
70. Wu SH, Su HJ (2002) Electrochemical characteristics of partially cobalt-substituted $LiMn_{2-y}Co_yO_4$ spinels synthesized by Pechini process. Mater Chem Phys 78:189–195
71. Kim BH, Choi YK, Choa YH (2003) Synthesis of $LiFe_xMn_{2-x}O_4$ cathode materials by emulsion method and their electrochemical properties. Solid State Ionics 158:281–285
72. Komaba S, Oikawa K, Myung ST, Kumagai N, Tamiyama T (2002) Neutron powder diffraction studies of $LiMn_{2-y}Al_yO_4$ synthesized by the emulsion drying method. Solid State Ionics 149:47–52
73. Taniguchi I, Lim CK, Song D, Wakihara M (2002) Particle morphology and electrochemical performances of spinel $LiMn_2O_4$ powders synthesized using ultrasonic spray pyrolysis method. Solid State Ionics 146:239–247
74. Barboux P, Tarascon JM, Shokoohi FK (1991) The use of acetates as precursors for the low-temperature synthesis of $LiMn_2O_4$ and $LiCoO_2$ intercalation compounds. J Solid State Chem 94:185–196
75. Kopeć M, Dygas JR, Krok F, Mauger A, Gendron F, Jaszczak-Figiel B, Pietraszko A, Zaghib K, Julien CM (2009) Heavy-fermion behaviour and electrochemistry of $Li_{1.27}Mn_{1.73}O_4$. Chem Mater 21:2525–2533
76. Ammundesn B, Jones DJ, Rosière J, Berg H, Tellgren, Thomas JO (1998) Ion exchange in manganese dioxide spinel: proton, deuteron and lithium sites determined from neutron powder diffraction data. Chem Mater 10:1680–1687
77. Kovacheva D, Gadjov H, Petrov K, Mandal S, Lazarraga MG, Pascual L, Amarilla JM, Rojas RM, Herrero P, Rojo JM (2002) Synthesizing nanocrystalline $LiMn_2O_4$ by a combustion route. J Mater Chem 12:1184–1188
78. Chitra S, Kalyani P, Mohan T, Gangadharan R, Yebka B, Castro-Garcia S, Massot M, Julien C, Eddrief M (1999) Characterization and electrochemical studies of $LiMn_2O_4$ cathode materials prepared by combustion method. J Electroceram 3:433–441
79. Kamarulzaman N, Yusoff R, Kamarudin N, Shaari NH, Abdul-Aziz NA, Bustam MA, Blagojevic N, Elcombe M, Blackford M, Avdeev M, Arof AK (2009) Investigation of cell parameters, microstructures and electrochemical behaviour of $LiMn_2O_4$ normal and nano powders. J Power Sourc 188:274–280
80. Liu HK, Wang GX, Guo Z, Wanq J, Konstantinov K (2006) Nanomaterials for lithium-ion rechargeable batteries. J Nanosci Nanotechnol 6:1–15
81. Kiani MA, Mousavi MF, Rahmanifar MS (2011) Synthesis of ano- and micro-particles of $LiMn_2O_4$: electrochemical investigation and assessment as a cathode in Li battery. Int J Electrochem Sci 6:2581–2595
82. Kim JM, Lee G, Kim BH, Huh YS, Lee GW, Kim HJ (2012) Ultrasound-assisted synthesis of Li-rich mesoporous $LiMn_2O_4$ nanospheres for enhancing the electrochemical performance in Li-ion secondary batteries. Ultrason Sonochem 19:627–631

83. Yung DK, Kim MP, Lee HW, Riccardo R (2009) Spinel $LiMn_2O_4$ nanorods as lithium-ion battery cathodes. Nano Lett 8:3948–3952
84. Chen ZH, Huang KL, Liu SQ, Wang HY (2010) Preparation and characterization of spinel $LiMn_2O_4$ nanorods as lithium-ion battery cathodes. Trans Nonferrous Met Soc China 20:2309–2313
85. Hosono E, Kudo T, Honma I, Matsuda H, Zhou H (2009) Synthesis of single crystalline spinel $LiMn_2O_4$ nanowires for a lithium ion battery with high power density. Nano Lett 9:1045–1051
86. Amatucci GG, Tarascon JM (1997) Lithium manganese oxy-fluorides for Li-ion rechargeable battery electrodes. US Patent 5,674,645. Accessed 7 Oct 1997
87. Xia Y, Hideshima Y, Kumada N, Nagano M, Yoshio M (1998) J Power Sourc 24:24–28
88. Liu Z, Wang H, Fang L, Lee JY, Gan LM (2002) Improving high-temperature performance of $LiMn_2O_4$ spinel by micro-emulsion coating of $LiCoO_2$. J Power Sourc 104:101–107
89. Kweon H, Kim G, Paark D (2001) Positive active material for rechargeable lithium batteries. US Patent 6,183,911. Accessed 6 Feb 2001
90. Cho J, Kim YJ, Kim TJ, Park B (2001) Enhanced structural stability of o-$LiMnO_2$ by sol-gel coating of Al_2O_3. Chem Mater 13:18–20
91. Zheng Z, Tang Z, Zhang Z, Shen W, Lin Y (2002) Surface modification of $Li_{1.03}Mn_{1.97}O_4$ spinels for improved capacity retention. Solid State Ionics 148:317–321
92. Kannan AM, Manthiram A (2002) Surface/chemically modified $LiMn_2O_4$ cathodes for lithium-ion batteries. Electrochem Solid State Lett 5:A167–L169
93. Aurbach D, Markovsky B, Rodkin A, Cojocaru M, Levi E, Kim HJ (2002) An analysis of rechargeable lithium-ion batteries after prolonged cycling. Electrochim Acta 47:1899–1911
94. Tarascon JM, Wang E, Shokoohi FK, McKinnon WR, Colson S (1991) The spinel phase of $LiMn_2O_4$ as a cathode in secondary lithium cells. J Electrochem Soc 138:2859–2864
95. Wakihara M (2005) Lithium manganese oxides with spinel structure and their cathode properties for lithium ion battery. Electrochem 73:328–335
96. Lee YJ, Wanf F, Mukerjee S, McBreen J, Grey CP (2000) ^6Li and ^7Li magic-angle spinning nuclear magnetic resonance and in situ X-ray diffraction studies of the charging and discharging of $Li_xMn_2O_4$ at 4 V. J Electrochem Soc 147:803–812
97. Ziolkiewicz S, Rougier A, Nazri GA, Julien C (1998) Electrical conductivity of $Li_xMn_2O_4$ with $0.60 \leq x \leq 1.18$. Electrochem Soc Meeting Proc 97–24:145–150
98. Julien C, Rougier A, Nazri GA (1997) Synthesis, structure and lattice dynamics of lithiated manganese spinel $LiMn_2O_4$. Mater Res Soc Symp Proc 453:647–653
99. Julien C, Rougier A, Haro-Poniatowski E, Nazri GA (1998) Vibrational spectroscopy of lithium manganese spinel oxides. Mol Cryst Liq Cryst 311:81–86
100. Dygas JR, Kopeć M, Krok F, Gendron F, Mauger A, Julien CM (2007) Electronic, structural and magnetic properties of nanocrystalline $Li_{1+x}Mn_{2-x}O_4$ spinels. ECS Trans 3–36:179–190
101. Kopec M, Dygas JR, Krok F, Mauger A, Gendron F, Julien CM (2008) Magnetic characterization of $Li_{1+x}Mn_{2-x}O_4$ spinel ($0 \leq x \leq 1/3$). J Phys Chem Solids 69:955–966
102. Bagci S, Tutuncu HM, Duman S, Bulut E, Ozacar M, Srivastava GP (2014) Physical properties of the cubic spinel $LiMn_2O_4$. J Phys Chem Solids 75:463–469
103. Wang GG, Wang JM, Mao WQ, Shao HB, Zhang JQ, Cao CN (2005) Physical properties and electrochemical performance of $LiMn_2O_4$ cathode materials prepared by a precipitation method. J Solid State Electrochem 9:524–553
104. Ohzuku T, Kitagawa M, Hirai T (1990) Electrochemistry of manganese dioxide in lithium nonaqueous cell. III X-ray diffraction study on the reduction of spinel-related manganese dioxide. J Electrochem Soc 137:769–775
105. Julien C, Ziolkiewicz S, Lemal M, Massot M (2001) Synthesis, structure and electrochemistry of $LiMn_{2-y}Al_yO_4$ prepared by wet chemistry. J Mater Chem 11:1837–1842
106. Palacin MR, Chabre Y, Dupont L, Hervieu M, Strobel P, Rousse G, Masquelier C, Anne M, Amatucci GG, Tarascon JM (2000) On the origin of the 3.3 and 4.5 V steps observed in $LiMn_2O_4$-based spinels. J Electrochem Soc 147:845–853

107. Aydinol MK, Ceder G (1997) Firs-principles prediction of insertion potentials in Li-Mn oxides for secondary Li batteries. J Electrochem Soc 144:3832–3835
108. Jang DH, Shin JY, Oh SM (1996) Dissolution of spinel oxides and capacity losses in 4 V $Li/Li_xMn_2O_4$ cells. J Electrochem Soc 143:2204–2211
109. Thackeray MM, de Kock A, Rossouw MH, Liles DC, Hoge D, Bittihn R (1992) Spinel electrodes from the Li-Mn-O system for rechargeable lithium battery applications. J Electrochem Soc 139:363–366
110. de Gummow RJ, Kock A, Thackeray MM (1994) Improved capacity retention in rechargeable 4 V lithium/lithium-manganese oxide (spinel) cells. Solid State Ionics 69:59–67
111. Kim J, Manthiram A (1998) Low temperature synthesis and electrode properties of $Li_4Mn_5O_{12}$. J Electrochem Soc 145:L53–L55
112. Choi S, Manthiram A (2000) Synthesis and electrode properties of metastable $Li_2Mn_4O_{9-\delta}$ spinel oxides. J Electrochem Soc 147:1623–1629
113. Sigala C, Guyomard D, Verbaere A, Piffard Y, Tournoux M (1995) Positive electrode materials with high operating voltage for lithium batteries $LiCr_yMn_{2-y}O_4$ ($0 \leq y \leq 1$). Solid State Ionics 81:167–170
114. Kawai H, Nagata M, Takamoto H, West AR (1998) A new lithium cathode $LiCoMnO_4$: toward practical 5 V lithium batteries. Electrochem Solid State Lett 1:212–214
115. Zhong Q, Bonakdarpour A, Zhang M, Gao Y, Dahn JR (1997) Synthesis and electrochemistry of $LiNi_xMn_{2-x}O_4$. J Electrochem Soc 144:L205–L207
116. Ein-Eli Y, Howard WF Jr, Lu SH, Mukerjee S, McBreen J, Vaughey JT, Thackeray MM (1998) $LiMn_{2-x}Cu_xO_4$ spinels ($0.1 \leq x \leq 0.5$): a new class of 5 V cathode materials for Li batteries. I. Electrochemical, structural, and spectroscopic studies. J Electrochem Soc 145:1238–1244
117. Liu Q, Wang S, Tan H, Yang Z, Zeng J (2013) Preparation and doping mode of doped $LiMn_2O_4$ for Li-ion batteries. Energies 6:1718–1730
118. Amatucci GG, Schmutz CN, Blyr A, Sigala C, Gozdz AS, Larcher D, Tarascon JM (1997) Materials effects on the elevated and room temperature performance of $C/LiMn_2O_4$ Li-ion batteries. J Power Sourc 69:11–25
119. Yi TF, Zhu YR, Zhu XD, Shu J, Yue CB, Zhou AN (2009) A review of recent developments in the surface modification of $LiMn_2O_4$ as cathode material of power lithium-ion battery. Ionics 15:779–784
120. Sahan H, Göktepe H, Patat S, Ülgen A (2008) The effect of LBO coating method on electrochemical performance of $LiMn_2O_4$ cathode material. Solid State Ionics 178:1837–1842
121. Lee KS, Myung ST, Amine K, Yashiro H, Sun YK (2009) Dual functioned BiOF-coated Li $[Li_{0.1}Al_{0.05}Mn_{1.85}]O_4$ for lithium batteries. J Mater Chem 19:1995–2005
122. Franger S, Bach S, Pereira-Ramos JP, Baffier N (2001) Highly rechargeable $Li_xMnO_{2+\delta}$ oxides synthesized via low temperatures techniques. J Power Sourc 97–98:344–348
123. Dygas JR, Kopec M, Krok F, Julien CM (2007) Relaxation of polaronic charge carriers in lithium manganese spinels. J Non-Cryst Solids 353:4384–4389
124. Takada T, Hayakawa H, Akiba E, Izumi F, Chakoumakos BC (1997) Novel synthesis process and structure refinements of $Li_4Mn_5O_{12}$. J Power Sourc 68:613–617
125. Endres P, Fuchs B, Kemmler-Sack S, Brandt K, Faust-Becker G, Praas HW (1996) Influence of processing on the Li:Mn ratio in spinel phases of the system $Li_{1+x}Mn_{2-x}O_{4-\delta}$. Solid State Ionics 89:221–231
126. Julien CM, Zaghib K (2004) Electrochemistry and local structure of nano-sized $Li_{4/3}Me_{5/3}O_4$ (Me = Ti, Mn) spinels. Electrochim Acta 50:411–416
127. Julien CM, Mauger A (2013) Review of 5-V electrodes for Li-ion batteries: status and trends. Ionics 19:951–988
128. Amine K, Tukamoto H, Yasuda H, Fujita Y (1996) A new three-volt spinel $Li_{1+x}Mn_{1.5}Ni_{0.5}O_4$ for secondary lithium batteries. J Electrochem Soc 143:1607–1613

129. Ohzuku T, Takeda S, Iwanaga M (1999) Solid-state redox potentials for $Li[Me_{1/2}Mn_{3/2}]O_4$ (Me: 3d-transition metal) having spinel-framework structures: a series of 5 volt materials for advanced lithium-ion batteries. J Power Sourc 81–82:90–94
130. Amdouni N, Zaghib K, Gendron F, Mauger A, Julien CM (2006) Structure and insertion properties of disordered and ordered $LiNi_{0.5}Mn_{1.5}O_4$ spinels prepared by wet chemistry. Ionics 12:117–126
131. Liu D, Hamel-Paquet J, Trottier J, Barray F, Gariépy V, Hovington P, Guerfi A, Mauger A, Julien CM, Goodenough JB, Zaghib K (2012) Synthesis of pure phase disordered $LiMn_{1.45}Cr_{0.1}Ni_{0.45}O_4$ by a post-annealing method. J Power Sourc 217:400–406
132. Murphy DW, Christian PA, DiSalvo FJ, Carides JN, Waszczak JV (1981) Lithium incorporation by V_6O_{13} and related (+4,+5) oxide cathodes materials. J Electrochem Soc 128:2053–2058
133. Christian PA, DiSalvo FJ, Murphy DW (1980) Nonaqueous secondary cell using vanadium oxide positive electrode. US Patent 4,228,226. Accessed 14 Oct 1980
134. Wilhelmi KA, Waltersson K, Kihlborg L (1971) A refinement of the crystal structure of V_6O_{13}. Acta Chem Scand 25:2675–2687
135. West K, Zachau-Christiansen B, Jacobsen T (1983) Electrochemical properties of non-stoichiometric V_6O_{13}. Electrochim Acta 28:1829–1833
136. Murphy DW, Christian PA, Carides JN, DiSalvo FJ (1979) Topochemical reactions of metal oxides with lithium. In: Vashishta P, Mundy JN, Shenoy GK (eds) Fast ion transport in solids. North-Holland, Amsterdam, pp 137–140
137. Julien C, Nazri GA (2001) Intercalation compounds for advanced lithium batteries. In: Nalwa HS (ed) Handbook of advanced electronic and photonic materials, vol 10. Academic, San Diego, pp 99–184
138. Julien C, Balkanski M (1993) Is the rigid band model applicable in lithium intercalation compounds? Mater Res Soc Symp Proc 293:27–37
139. Chaklanabish NC, Maiti HS (1986) Phase stability and electrical conductivity of lithium intercalated nonstoichiometric V_6O_{13}. Solid State Ionics 21:207–212
140. De Picciotto LA, Thackeray MM, David WF, Bruce PG, Goodenough JB (1984) Structural characterization of delithiated $LiVO_2$. Mater Res Bull 19:1497–1506
141. De Picciotto LA, Thackeray MM (1985) Insertion/extraction reactions of lithium with LiV_2O_4. Mater Res Bull 20:1409–1420
142. Tsang C, Manthiram A (1997) Synthesis of nanocrystalline VO_2 and its electrochemical behavior in lithium batteries. J Electrochem Soc 144:520–524
143. Theobald F, Cabala R, Bernard J (1976) Essai sur la structure de VO_2(B). J Solid State Chem 17:431–438
144. Grymonprez G, Fiermans L, Vennik J (1977) Structural properties of vanadium oxides. Acta Crystallogr A 33:834–837
145. Oka Y, Yao T, Tamamoto N (1991) Structural phase transition of VO_2(B) to VO_2(A). J Mater Chem 1:815–818
146. Armstrong G, Canales J, Armstrong AR, Bruce PG (2008) The synthesis and lithium intercalation electrochemistry of VO_2(B) ultra-thin nanowires. J Power Sourc 178:723–728
147. Liu X, Xie G, Huang C, Xu Q, Zhang Y, Luo Y (2008) A facile method for preparing VO_2 nanobelts. Mater Lett 62:1878–1880
148. Mao L, Liu C (2008) A new route for synthesizing VO_2(B) nanoribbons and 1D vanadium-based nanostructures. Mater Res Bull 43:1384–1392
149. Sediri F, Touati F, Gharbi N (2006) From V_2O_5 foam to VO_2(B) nanoneedles. Mater Sci Eng B 129:251–255
150. Reddy CVS, Walker EH, Wicher SA, Williams QL, Kalluru RR (2009) Synthesis of VO_2(B) nanorods for Li battery application. Curr Appl Phys 9:1195–1198
151. Valmalette JC, Gavarri JR (1998) High efficiency thermochromic VO_2(R) resulting from the irreversible transformation of VO_2(B). Mater Sci Eng B 54:168–173

152. Corr SA, Grossman M, Shi Y, Heier KR, Stucky GD, Seshadri R (2009) VO_2 (B) nanorods: solvothermal preparation, electrical properties and conversion to rutile VO_2 and V_2O_3. J Mater Chem 19:4362–4367
153. Baudrin E, Sudant G, Larcher D, Dunn B, Tarascon JM (2006) Preparation of nanostructured VO_2(B) from vanadium oxide aerogels. Chem Mater 18:4369–4374
154. Ni J, Jiang W, Yu K, Sun F, Zhu Z (2011) Electrochemical performance of B and M phases VO_2 nanoflowers. Cryst Res Technol 46:507–510
155. Ni S, Zeng H, Yang X (2011) Fabrication of VO_2(B) nanobelts and their application in lithium ion batteries. J Nanomater 2011(961389):1–4
156. Zaghib K, Dubé J, Dallaire A, Galoustov K, Guerfi A, Ramanathan M, Benmayza A, Prakash J, Mauger A, Julien CM (2012) Enhanced thermal safety and high power performance of carbon-coated $LiFePO_4$ olivine cathode for Li-ion batteries. J Power Sourc 219:36–44

Chapter 7
Polyanionic Compounds as Cathode Materials

7.1 Introduction

Since the discovery of the Goodenough's group, the lithium insertion compounds built with polyanionic groups such as $(SO_4)^{2-}$, $(PO_4)^{3-}$, $(P_2O_7)^{4-}$, $(MoO_4)^{2-}$, or $(WO_4)^{2-}$ are considered as potential positive electrode materials for use in lithium rechargeable batteries [1, 2]. Yet in this family, olivine phosphate and Nasicon-like frameworks are currently the subject of many investigations. $LiFePO_4$ (LFP) has received a special attention, because this cathode material realizes the highest capacity ($\approx$170 mAh g^{-1}) at moderate current densities [3]. In addition, it presents several advantages with regard to low cost, non-toxicity, environmental friendliness, and high safety that are determinant with respect to cobalt-oxide-based materials for large-scaled applications such as hybrid electric vehicles (HEV). Nevertheless, the bulk electronic conductivity of LFP is quite low, which may result in losses in capacity during high-rate discharge. To increase the electronic conductivity, it is a common practice in the production of Li-ion battery cathodes to add carbon to a LFP powder [1, 4], and surface coating of LFP particles with thin layers of carbon [5–7]. On a technical point of view, however, the amount of carbon added to the powder cannot exceed few wt%, so that the coating of the particles by a thin (typically 3 nm thick) carbon layer is definitely the solution. A seven-order-of-magnitude increase in the electronic conductivity can be reached by the addition of an organic material as a carbon precursor, such as sucrose, to produce a carbon coat to $LiFePO_4$ raw particles by a spray pyrolysis technique [7]. The addition of carbon has then the advantage of combining much better electronic conductivity and high capacity. In particular, a capacity of about 160 mAh g^{-1} has been found in ref. [5] for LFP coated with 1 wt% carbon.

Ravet et al. [6] reported two ways to coat carbon: mixing $LiFePO_4$ powder with sugar solution and heating the mixture at 700 °C, or synthesizing $LiFePO_4$ with some organic materials added before heating. Although the way to add carbon is not fully optimized yet [8], the synthesis and the effects of carbon deposition process on

C. Julien et al., *Lithium Batteries*, DOI 10.1007/978-3-319-19108-9_7

$LiFePO_4$ are now well understood [9]. The electrochemical properties of LFP are known to be sensitive to the mode of preparation and the structural properties. This can be an advantage for potential applications since it allows for an optimization of the material if we can correlate the mode of preparation with the structural and the physical properties. Aiming to this problem, we have first investigated this correlation in $LiFePO_4$ that had been grown by three different techniques [10]. Different clustering effects have been evidenced. A firing temperature larger than 800 °C increases the fraction of Fe_2P [11], with Fe_2P nanoparticles in such large concentration that they drive superferromagnetism has been detected in samples that have been heated to such high temperatures [10]. On the one hand, the presence of Fe_2P can increase the electronic conductivity because it is metallic, but on the other hand, it also decreases the ionic conductivity so that both the capacity and cycling rates are degraded with respect to the carbon-coated LFP free of impurity. Most of all, Fe_2P dissolves into the electrolyte, thus reducing importantly the life of the battery. It is thus desirable to optimize the preparation of the samples so that such clustering effects do not occur. This can be done easily for Fe_2P clusters by decreasing the synthesis temperature, but it is more difficult to avoid the presence of a small concentration (1.0×10^{-6} per chemical formula) of γ-Fe_2O_3 nanoparticles [10, 12]. We know from the iron industry that hydrogen, carbon monoxide or carbon can reduce Fe_2O_3 through different reduction steps that depend on temperature and other physical parameters such as particle sizes. Nearly all iron produced commercially is made using a blast furnace process covered by most chemistry text books. In essence, at high temperature, Fe_2O_3, is reduced with carbon (as coke) according to the reaction $2Fe_2O_3 + 3C \rightarrow 4Fe + 3CO_2$. This is one of the most significant industrial processes in history, and the origins of the modern process are traceable back to a small town called Coalbrookdale in Shropshire (England) around the year 1773. This is known as the carbothermal effect. Although we might then expect that carbon would reduce Fe^{3+} ions directly over 1000 °C or through the formation of CO gas, thus preventing the formation of γ-Fe_2O_3, this process is impossible at the lower synthesis temperature used for LFP. The proof is given by the fact that adding carbon to the precursors of LFP fails to synthesize LFP when the synthesis can be achieved by adding any organic compound as the carbon precursor [13]. Actually the decomposition of the organic compound produces carbon that deposits on the LFP particles and forms the carbon coat, and also reductive hydrogenous gases that are active kinetically to reduce Fe^{3+} impurities in the 500–700 °C temperature range used in the synthesis process. This effect is also favored by the fact that the organic precursor is usually mixed with the LFP material or with the LFP chemical precursors by solution processes at a molecular size level. For overview on olivine phosphate material see the reviews recently published [14–16].

The aim of the present chapter is to investigate the physico-chemical properties of optimized of LFP and Nasicon-like electrode materials. One approach to provide insight into the structural and electronic properties of electrode materials involves a systematic study by a combination of techniques including structural, magnetic and spectroscopic measurements. Furthermore, advantage can be taken of the high sensitivity of some analytical tools for the detection of parasitic impurities that can be grown

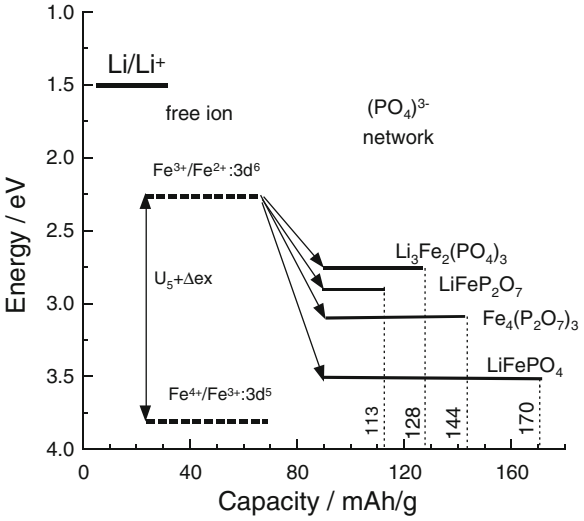

Fig. 7.1 Energy diagram of the redox couple relative to lithium and iron phosphate frameworks. The graph presents the theoretical capacity for each compound

during synthesis of solid phases. These principles were fully exploited to optimize lithium iron phosphate compounds. Both carbon-free and carbon-coated LFP samples are examined in order to investigate the effect of carbon on their structural properties.

Electrochemical extraction of Li from $LiFePO_4$ gives (Fe^{2+}/Fe^{3+}) redox potential at ca. 3.5 V vs. Li^0/Li^+. A small but first-order displacive structural change of the framework gives a two-phase separation over most of the solid-solution range $0 < x < 1$ for Li_xFePO_4 and therefore a flat V–x curve. A reversible capacity of 160 mAh g^{-1} is delivered by the nano-structured cathode particles coated with carbon. Electrochemical characteristics of $LiFePO_4$ are compared with those of other Fe-containing phosphates in Fig. 7.1. This graph presents the energy of the redox couples against the specific capacity relative to lithium and iron in various phosphate frameworks. Electrochemical tests of optimized $LiFePO_4$ have been conducted under various conditions to assess the influence of the electrolyte on stability and the influence of electrode processing. Post-mortem analysis, i.e., ICP, XRD, SEM, showed that no iron species were detected at the separator-negative electrode interface in cells with anode of lithium metal, graphite, or C-$Li_4Ti_5O_{12}$ [12, 17, 18]. This result is attributed to the high quality of the "optimized" $LiFePO_4$, impurity-free materials used as positive electrodes.

This chapter is organized as follows. First, we expose in Sect. 7.2, the synthesis route and crystal chemistry of LFP. Section 7.3 presents the structure and morphology of optimized $LiFePO_4$ particles deduced from the analysis of data including X-ray powder diffractometry (XRD), Scanning Electron Microscopy (SEM), High Resolution Transmission Electron Microscopy (HRTEM), Fourier transform infrared (FTIR) and Raman scattering (RS) spectroscopy. However, these techniques do not allow the detection of impurities or nanometer-sized clusters in concentration lower than 1 %. We then complete the analysis (Sect. 7.4) with magnetic measurements: magnetization curves and electron spin resonance (ESR), since they are powerful

tools to characterize the strongly ferrimagnetic nanoparticles of γ-Fe_2O_3 (both in size and concentration) even at concentrations as small as the ppm [10, 11]. Yet this set of experiments is not sufficient to characterize the carbon-coated compounds. First, carbon is nonmagnetic. Second, the sensitivity of FTIR spectroscopy, which is a probe of bulk properties, is not sensitive enough to detect the carbon. Therefore, we have added Raman spectroscopy to characterize the carbon coat. Since the penetration depth of the light inside the LFP particles in such experiments is very small, these experiments are a probe of the first layers at the surface of these particles and allow for the detection of carbon coat. They also give evidence that the carbon does not penetrate inside the particles and remains stuck at their surface. As a result, we find that the carbon-coated sample can be prepared free of γ-Fe_2O_3 and any Fe^{3+}-based impurity. In Sect. 7.5, we explore the effects of the exposition of carbon-coated $LiFePO_4$ particles to H_2O. The deterioration of the carbon coat is found to be dependent on the synthesis process, either hydrothermal or solid-state reaction. In case the particles are simply exposed to humid air, the carbon coat protects more efficiently the particles. In this case, the exposure to H_2O mainly results in the delithiation of the surface layer, due to the hydrophilic nature of Li. Again, however, this process only affects the surface layer, at least for a reasonable time (weeks) of exposure to humid air. In addition, within this timescale, the surface layer can be chemically lithiated again, and the samples can be dried to remove the moisture, restoring the electrochemical properties that are then reversible. Finally, Sect. 7.6 shows the electrochemical performance of the optimized LFP particles. We demonstrate the electrochemical ability of the material operating at high temperature, ca. 60 °C, which justifies its use as a cathode element in the new generation of lithium secondary batteries powering Electric Vehicles (EV). We report a Li-ion battery that can be charged within a minute, passes the safety tests, and has a very long shelf life. The active materials are nanoparticles of $LiFePO_4$ and $Li_4Ti_5O_{12}$ for the positive and negative electrodes, respectively. The "18650" battery prepared under such conditions delivers a capacity of 800 mAh. It retains full capacity after 20000 cycles performed at charge rate 10*C*, discharge rate 5*C*, and retains 95 % capacity after 30000 cycles at charge rate 15*C* and discharge rate 5*C*.

7.2 Synthesis Routes

Many synthesis routes have been used for the preparation of $LiFePO_4$ materials. They are reviewed in this section as follows.

7.2.1 Solid-State Reaction

An important parameter in this synthesis route is the choice of precursors [19–22]. For instance, $LiFePO_4$ specimens were prepared by mixing iron

(II) oxalate [$Fe(C_2O_4)\cdot 2H_2O$], ammonium di-hydrogen phosphate [$NH_4H_2PO_4$], and lithium carbonate [Li_2CO_3] in the molar ratio 1:1:1. However, with this choice a residual concentration of γ-Fe_2O_3 was detected by magnetic experiments [10, 23]. The concentration of iron involved in this impurity is very small (0.3 at.%) so that it cannot be detected by X-ray diffraction analysis for instance, but is it damageable to the electrochemical properties, because it is located at the surface of the $LiFePO_4$ particles, where it can be an obstacle to the electron and ion transfer. Samples free of any impurity were obtained with another choice of precursors, namely $FePO_4(H_2O)_2$ and Li_2CO_3 in stoichiometric amount. These precursors were then thoroughly mixed together in isopropanol. After drying, the blend was heated at 700 °C for 8 h under reducing atmosphere. This sintering temperature is also an important parameter. Heating at $T \leq 500$ °C is not sufficient to prevent the formation of secondary phases with Fe^{3+} ions, since the presence of Fe^{3+} has been detected by Mössbauer experiments. On the other hand, both trivalent Fe_2O_3 and $Li_3Fe_2(PO_4)_3$ are formed in such large quantities that they are detected by X-rays after heating above 800 °C [22]. The heating temperature 700–750 °C thus appears as the best compromise: high enough to obtain well-crystallized samples, small enough to avoid the formation of impurities. With this choice of precursors, the particles are not carbon-coated. As it has been specified in the introduction, the very small electric conductivity requires a coating of the particles with a conducting agent, usually carbon (although a coating with conductive polymer is also possible, as we shall see below with the polyol synthesis). The carbon coating was performed as follows. Sucrose and cellulose acetate were chosen as the carbon precursors in acetone solution. The carbon-free powder was mixed with the carbon precursors. The dry additive corresponded to 5 wt % carbon in $LiFePO_4$. After drying, the blend was heated at 700 °C for 4 h under argon atmosphere. We have shown elsewhere that this is the minimum temperature needed to make the carbon layer conductive [24]. Note also that in the solid-state technique, it is not needed to use a two-step process in which the $LiFePO_4$ are first synthesized, before the carbon coating is performed in a second step. It can be done in a one-step process, by including the carbon precursor to the precursors of $LiFePO_4$ and following the procedure described above. The result is the same, namely C-$LiFePO_4$, which means $LiFePO_4$ particles covered with a thin layer (about 3 nm thick) of conductive carbon. Also, the choice of sucrose or cellulose is not critical. Other sources of carbon have been chosen, like polystyrene, or malonic acid, although in this particular case, the thickness of the carbon layer is larger (between 4 and 9 nm) [25].

7.2.2 Sol–Gel Method

The sol–gel method was also successful [26, 27]. As a starting precursor, iron (III) citrate and two parts of citric acid were dissolved at 60 °C in water. Separately, an equimolar water solution of LiH_2PO_4 was prepared from lithium phosphate and phosphoric (V) acid. Clear solutions were mixed together and dried at 60 °C for

24 h. After thorough grinding with a mortar and pestle, the obtained xerogel was fired in an inert (pure argon) atmosphere at 700 °C for 10 h. Note this is the same temperature as in the case of the solid-state reaction route, for the same reason. Also in both synthesis routes, micro-sized particles are obtained. LiMPO$_4$/C (M = Mn, Fe) composite particles are obtained in both cases. In the sol–gel technique, this is due to the fact that the remaining solid products of citrate degradation (basically pure carbon) are deposited on all surfaces of the LiFePO$_4$ particles [28, 29]. The sol–gel technique leads to particles that are more or less spherical, like the solid-state technique. There is, however, a difference in the morphology. Contrary to the result of the solid-state reaction, the sol–gel technique generates particles that are porous and their interior has large voids due to development of gases during degradation of citrate anions. Nevertheless, the particles are well crystallized. Also, the carbon coat is also less regular and less uniform than in the case of the solid-state reactions.

7.2.3 Hydrothermal Method

Among the various synthesis approaches pursued in the past few years, the hydrothermal route is particularly successful with respect to controlling the chemical composition and crystallite size [13, 30–33]. The conventional hydrothermal process involves a reaction time 5–12 h to synthesize LiFePO$_4$ [34–40]. With respect to the previous techniques, the hydrothermal process has the advantage that the synthesis temperature can be as small as 230 °C [33]. Brochu et al. [41] demonstrated the beneficial effect of choosing adapted complexing agent in the hydrothermal solution. Even at this mild temperature the coating of the particles by conductive carbon could be achieved by an in situ hydrothermal carbonization of glucose during the synthesis process. The heating temperature to get the particles coated with *conductive* carbon was still 700 °C, but good results were obtained upon heating during 1 h only. Note however that this is linked to the microwave assistance, reviewed later on in this section.

7.2.4 Coprecipitation Method

The co-precipitation method was chosen as the synthetic method of LiFePO$_4$, because it allows for a control of the morphology and the accessibility of cheap raw materials [42, 43]. Recently, Wang et al. [44] succeeded in preparing nano-sized LiFePO$_4$ by co-precipitation combined with in situ polymerization. During the previous co-precipitation process, aniline monomers were polymerized and covered the surface of each newly formed FePO$_4$ particle, thus hindering the further growth of nuclei. The morphology of the LiFePO$_4$ consisted of primary particles (40–50 nm) more or less spherical, only slightly agglomerated with secondary

particles of 100–110 nm. Each particle was evenly coated with an amorphous carbon layer, which has a thickness around 3–5 nm. Graphene-$LiFePO_4$ composites of spherical shape and size about 100 nm were also obtained using a previous co-precipitation method in de-ionized water at room temperature [45]. The composite in that case was obtained with graphene nanosheets used as additives, and sintering at 700 °C for 18 h in a tubular furnace under argon flow.

7.2.5 Microwave Synthesis

Microwave-assisted synthesis approach is appealing because it can shorten the reaction time to a few minutes with significant energy savings. Park et al. [46] reported that the single-phase $LiFePO_4$ was synthesized by microwave heating using carbon as a microwave absorber and a reducing agent, and the precursor of $LiFePO_4$ was prepared by a method of co-precipitation. Higuchi et al. [47] reported on $LiFePO_4$ prepared in a domestic microwave oven; the mixture of starting materials was prepared by manual grinding. However, the main problem arises from the nonuniformity of components in the precursor, especially after the addition of carbon. Recently, Beninati et al. [48] and Wang et al. [49] reported the synthesis of $LiFePO_4$ by irradiating the solid-state raw materials with carbon in a domestic microwave oven. However, they were unable to control the particle size, and the electrochemical properties were not as good as expected. C-$LiFePO_4$ particles under the form of rods with diameter about 200 nm have been obtained [33] within a short reaction time (15 min) by a simple microwave-assisted hydrothermal (MW-HT) method. This offers significant energy and cost savings for large-scale industrial manufacturing [50–52]. Although attention is more focused on nanoparticles, it should be noticed that micron-sized and sub-micron particles can also been obtained by a one-step microwave method with the domestic or the laboratory microwave oven [53, 54].

7.2.6 Polyol and Solvothermal Process

A polyol process has been developed first by Kim to synthesize $LiFePO_4$ particles under the form of rods with average width 20 nm and length 50 nm [55], but different shapes ranging from rods to plates can be obtained [56] with average size of 100–300 nm. Note the polyol process makes possible the synthesis of $LiFePO_4$ at low temperature just like the hydrothermal process. Bigger particles can be obtained by the solvothermal process in a polyol medium of diethylene glycol, but still under the form of plates or rods. The advantage of this process is that the polyol medium acts not only like a solvent but also as a reducing agent and stabilizer that limits the particle growth and prevents agglomeration [55–58]. In general, the solvothermal process leads to the formation of $LiFePO_4$ under the form

of plates, about 50 nm-thick [59], which can be self-assembled by using poly(vinyl pyrrolidone) (PVP) as the surfactant in a benzyl alcohol system [60].

7.2.7 Micro-emulsion

An emulsion drying method allows for the synthesis of particles in a more spherical shape, even at 300 °C [61]. However, the crystallinity is low and well-crystallized C-$LiFePO_4$ powders were obtained only after calcinations at 750 °C. In addition, the particles are big (only sub-micron sized), unless burning-out the emulsion-dried precipitates under such conditions that lead to a very high carbon concentration coming from the burning of the oil.

7.2.8 Spray Technique

Spray pyrolysis is a method that can be used to obtain a powder with particle size distribution that is narrow and controllable from micrometer to sub-micrometer order [62]. The size of the particles is reduced to 300 nm by a combination of spray pyrolysis with dry ball milling [63]. To decrease the size of the particles down to 150 nm on average, a wet milling is needed, and performed owing to 45 ml zirconia vial, ethanol being used as a medium [64].

7.2.9 Template Method

Porous $LiFePO_4$ can also be prepared via a solution-based template technique [65–67]. Nanowire $LiFePO_4$ has been obtained by this process, using the two-dimensional hexagonal SBA-15 silica template with *P6mm* symmetry. However, the performance as a cathode element is not as good as the three-dimensional porous $LiFePO_4$ obtained when using hard templates KIT-6 for instance [66]. Using poly(methyl methacrylate) (PMMA) colloidal crystals as templates, porous $LiFePO_4$ has been obtained with a range of pore sizes, enabling the pore sizes to be tailored in the (2–50 nm), (20–80 nm), and (50–120 nm) size range, depending on the diameter of the initial PMMA template [67]. The thermal heating is 700 °C, like in the other synthesis routes except hydrothermal and microwave synthesis. We have already mentioned that porous samples have also been obtained by the sol–gel technique, but the template technique has the advantage of the monitoring of the pore size, so that the morphology can be adapted to optimize the electrochemical properties. However, nano-structured electrode materials prepared from template synthesis routes use polycarbonate filtration membranes followed by removal of membranes. Thus, template synthesis method suffers from disadvantages related to

high cost and complicated synthetic procedures that are difficult to expand to large-scale commercial applications. That was the motivation to use a template-free reverse micelle process for the synthesis of rod-like C-$LiFePO_4$ particles [68].

7.2.10 Mechanical Activation

Mechanical activation involves the blending of ingredients by high-energy ball milling followed by thermal treatment at high temperature. The ball milling can reduce the particle size and create close contact of the reactants. The mechanical activation process also allows the in situ formation of a carbon coat on the $LiFePO_4$ particles when a suitable organic/polymeric compound is incorporated as the carbon source during the synthesis. Thereby, a decrease in the thermal treatment time and temperature is usually experienced during the following calcination to obtain a pure phase product. That is why mechanical activation has been commonly used [63, 69–73] to synthesize $LiFePO_4$. However, in the present case, the mechanical activation of the synthesis of C-$LiFePO_4$ composites does not make possible a reduction or the temperature of the heating treatment nor even its duration, because these parameters are imposed by the coating with conductive carbon.

All the synthesis routes above described produce $LiFePO_4$ powder with capacity close to the theoretical value provided the synthesis is performed under reducing atmosphere to avoid oxidation of iron generating Fe^{3+}-based impurity phases [10]. The multiplicity of the synthesis routes that have been investigated gives evidence of the efforts to find which one would be the best to obtain particles with good crystallinity and small size at the industrial scale. As we have reported, small crystallized particles can be obtained by different techniques. Yet the size is not the only parameter of interest; the shape of the particles matters too, since the ionic motion is very anisotropic. The Li^+ ions preferably slalom along the *b*-axis of the crystal with orthorhombic *Pnma* S.G. [74, 75]. It is then desirable to reduce the crystallite size along this axis. However, this is a difficult problem because there is a tendency of the particles to grow in the form of plates in the (*ab*) plane [76], although the thickness along the *b*-axis is reduced to 30–40 nm in some cases [59, 77–79]. As we have recalled, for some synthesis routes, the reduction in size occurs at the expense of crystallinity and the formation of a large concentration of defects [78], which reduces the electrochemical performance. These difficulties have been overcome in the framework of a preparation process in which the mechanical assistance is used only to reduce the size of the particles [80]. In a first step, the $LiFePO_4$ particles are prepared by a solid-state reaction at 700 °C under inert (nitrogen) atmosphere using the polymeric synthetic route described elsewhere [81]. The starting materials were Fe(III) phosphate ($FePO_4(H_2O)_2$) and lithium carbonate (Li_2CO_3) as precursors. Then, the mixture was heated to 1050 °C for 5 min in a graphite crucible and then cooled under N_2 atmosphere. This mode of preparation does not allow us to obtain nano-sized particles. On the other hand, it makes possible the synthesis of big samples, even ingots of few tens of centimeters

in size, with high crystallinity and free of defects. The next step is to decrease the size of the particles down to the desired value, anywhere in the range from the centimeter down to 40 nm. For this purpose, the ingot is first crushed into centimeter-size particles by using a jaw-crusher with ceramic liner to avoid metal contamination. Then, the roll crusher (ceramic type) is used to obtain millimeter-size particles. The millimeter-size particles are further ground by jet-mill to achieve micrometer-size particles. In the process, the grains enter the grading wheel and are blasted to the collector. The particles obtained at this step are referred as "jet-mill" in the following. There size is the order of 1 μm. To obtain smaller particles, these micrometer-size powders were dispersed in isopropyl alcohol (IPA) solution at 10–15 % of solid concentration and then ground on a bead mill using 0.2-mm zirconia beads to obtain nanometer-size particles [80]. This final product is referred "wet mill" in the following. One advantage of the process is that we can investigate the properties of the same particles at different stages of the milling for comparison, so that any difference is a size effect. The particles can be considered as uncoated particles because of the great damage caused by the milling process. In the case of the particles used to obtain the experimental results illustrated in the figures of this review, the carbon-coated particles have been obtained with lactose as the carbon precursor in acetone solution according to the following procedure. The uncoated particles were mixed with the carbon precursor. The dry additive corresponded to 5 wt% carbon in $LiFePO_4$. After drying, the blend was heated at 750 or 700 °C [69, 81] for 4 h under argon atmosphere. This range of temperature is dictated by two considerations. On the one hand, below 700 °C, the carbon deposit is not conductive enough [81]. On the other hand, TEM images recorded in situ as a function of temperature show that above 750 °C, the shape of the particles changes so that inter-diffusion phenomena take place [80]. The quantity of carbon represents about 2 wt% of the final product (C-detector, LECO Co., CS 444). The whole procedure has many advantages. The ingot has been prepared with a procedure that makes it free of impurity and with good crystallinity. No defect is introduced in the milling process. At the end, the wet-milled nanoparticles are crystallites, since the coherence length measured from the Rietveld refinement of the XRD spectrum using the Scherrer's law is the same as the size of the primary particles observed by TEM.

A major effect of the carbon deposition process has been to reduce Fe^{3+}, most probably through a gas-phase reduction process involving hydrogen from the organic carbon precursor. The hydrogen prevents formation of γ-Fe_2O_3 nanoparticles in which iron is in the trivalent state. The cartoon shown in Fig. 7.2 summarizes the conditions of synthesis of LFP powders as positive materials for lithium-ion batteries. Although the heating of our sample in the preparation process did not exceed 700 °C, the amorphous carbon film is expected to have properties similar to carbon-pyrolyzed photoresists prepared at a pyrolysis temperature $T_p = 830 \pm 30$ °C. This feature is essential to explain the performance of the carbon coating since increasing the sintering temperature degrades LFP, and increases the amount of Fe_2O_3 clusters (or even Fe_2P clusters in some cases) in the material. On the other hand, decrease of the pyrolysis temperature below 800 °C degrades dramatically the electronic conductivity of the carbon. The carbon deposit can be

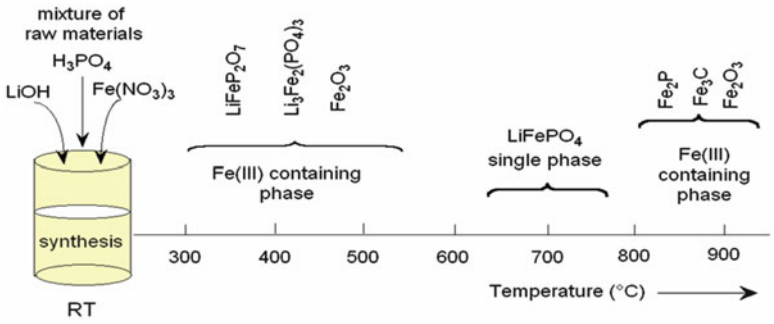

Fig. 7.2 Cartoon of the synthesis of $LiFePO_4$ powders as positive materials for Li-ion batteries

viewed as a film of irregular thickness, 30 nm thick on average, eventually with gaps. The gaps might actually be fortunate as the lithium can pass through them without having to tunnel through the carbon film, which could be one reason why the ionic conductivity is not affected by the coating. Finally, it is also possible to prepare nano-crystalline $LiFePO_4$ starting from $FePO_4$ [82].

7.3 Crystal Chemistry

7.3.1 Structure of Olivine Phosphate

Triphylite is a rather scarce orthophosphate primary mineral found in phosphatic pegmatites and pegmatite dikes. Its formula is $Li(Mn,Fe)PO_4$ and differs from the other mineral, lithiophilite, by being rich in iron instead of manganese. The structures of the two minerals are the same and form a solid solution, referred as the triphylite series, isomorphous with olivine. Therefore, any difference in physical properties along the series would be related to the iron/manganese percentage. These differences are best evidenced by comparing the physical properties of the two end members, namely $LiFePO_4$ and the often associated material $LiMnPO_4$, which, in contrast with triphylite and lithiophilite, are artificial ceramics [83]. In addition, triphylite in Greek means "family of three" (referring to iron, manganese, and lithium). Any confusion between $LiFePO_4$ and triphylite met sometimes in the literature should then be avoided. Triphylite alters easily into other phosphate minerals, and geologists show it a lot of respect for making the other phosphate minerals possible. This easy alteration, however, means that it is difficult to make good quality, well-crystallized samples. This feature, which makes geologists happy, is thus only bad news for physicists and chemists who also devote a lot of attention to the triphylite series although their effort has been focused on the definite compounds $LiFePO_4$ and $LiMnPO_4$ rather than their solid solutions. These materials belong to the rich family of olivines of the Mg_2SiO_4-type with the general formula B_2AX_4 [84].

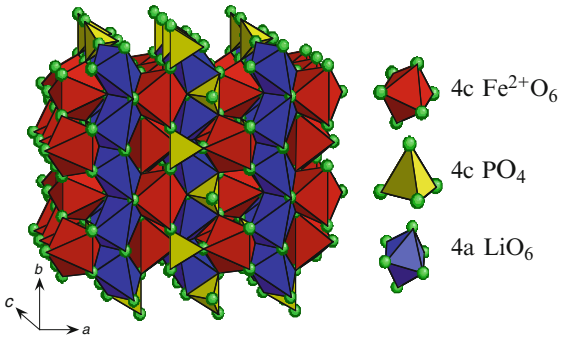

Fig. 7.3 Crystal structure of $LiFePO_4$ olivine. Corner-shared FeO_6 octahedra are linked together in the *bc*-plane; LiO_6 octahedra form edge-sharing chains along the *b*-axis. The tetrahedral PO_4 groups bridge neighboring layers of FeO_6 octahedra by sharing a common edge with one FeO_6 octahedra and two edges with LiO_6 octahedra

The crystal structure of lithium-iron phosphate materials has been studied by several authors [84–91]. As a member of the olivine family, $LiFePO_4$ crystallizes in the orthorhombic system (No. 62) with *Pnma* S.G. It consists of a distorted hexagonal-close-packed oxygen framework containing Li and Fe located in half the octahedral sites and P ions in one-eighth of the tetrahedral sites [86]. The FeO_6 octahedra, however, are distorted, lowering their local cubic-octahedral O_h to the C_s symmetry. Corner-shared FeO_6 octahedra are linked together in the *bc*-plane; the LiO_6 octahedra form edge-sharing chains along the *b*-axis. The tetrahedral PO_4 groups bridge neighboring layers of FeO_6 octahedra by sharing a common edge with one FeO_6 octahedron and two edges with LiO_6 octahedra. Remarkably short O-O bonds at the shared PO_4 and FeO_6 edges help to screen the cation charges from one another. This structure is illustrated in Fig. 7.3 showing the 1-D channels via which the lithium ions can be removed. Corner-shared FeO_6 octahedra are linked together in the *bc*-plane, while LiO_6 octahedra from edge-sharing chains along the *b*-axis. The tetrahedral PO_4 groups bridge neighboring layers of FeO_6 octahedra by sharing a common edge with one FeO_6 octahedra and two edges with LiO_6 octahedra.

The $LiFePO_4$ structure consists in three nonequivalent O sites. Most of the atoms of the olivine structure occupy the 4*c* Wyckoff position except O(3) which lies in the general 8*d* position and Li^+ ions occupying only the 4*a* Wyckoff position (M1 site on an inversion center). The iron is in the divalent Fe^{2+} state in FeO_6 units octahedra isolated from each other in $TeOc_2$ layers perpendicular to the (001) hexagonal direction [87]. In addition, the lattice has a strong two-dimensional character, since above a $TeOc_2$ layer comes another one at the vertical of the previous one, to build (100) layers of FeO_6 octahedra sharing corners and mixed layers of LiO_6 octahedra and PO_4 tetrahedra.

On a fundamental point of view, the main interest lies in the fact that the olivine structure generates geometric frustration of the magnetic interactions [92]. However, three olivine structure classes can be distinguished as a function of the site

occupation by magnetic ions. In Mn_2SiS_4 and Fe_2SiS_4, the magnetic ion (Mn, Fe) lies in the M1 and the M2 site [93], while in $NaCoPO_4$ and $NaFePO_4$, the magnetic ion lies on the M1 site only [94]. The third class is the phospho-olivine $LiMPO_4$ (M = Ni, Co, Mn, Fe) where the magnetic ion lies in the M2 site with the M1 site occupied by the nonmagnetic ion (Li^+).

We use the structural data determined by Streltsov et al. [86] as a standard reference (Table 7.1). The orthorhombic unit cell of the olivine structure contains 28 atoms ($Z = 4$). Structural parameters and interatomic distances are listed in Tables 7.2 and 7.3. Fe-O distances range from 2.064 to 2.251 Å. The Fe-Fe separation in $LiFePO_4$ is large (3.87 Å).

The $LiFePO_4$ lattice consists of six oxygen atoms that surround the Fe 3*d* transition metal atom in an octahedral environment. The primarily O_h local symmetry is decreases to C_s symmetry due to the split of the 3*d* levels into e_g and t_{2g} states under the crystal field of oxygen. As shown in Fig. 7.4, the oxygen atoms can roughly be grouped into axial (O_{ax}) and equatorial (O_{eq}) types. The angle of O_{ax}-Fe-O_{ax} is roughly 180°; on the plane perpendicular to the O_{ax}-Fe-O_{ax}, the O_2FeO_2 forms roughly a scissor structure. In the equatorial plane, the Fe-O bond length

Table 7.1 Lattice constants for stoichiometric $LiFePO_4$ materials in the *Pnma* (62) structure

a (Å)	*b* (Å)	*c* (Å)	Unit cell volume (Å^3)	Reference
10.332(4)	6.010(5)	4.692(2)	291.4(3)	Herle [11]
10.334	6.008	4.693	291.39	Yamada [22]
10.329(0)	6.006(5)	4.690(8)	291.02	Geller [84]
10.31	5.997	4.686	289.73	Santoro [85]
10.3298	6.0079	4.6921	291.19	Andersson [92]
10.322(3)	6.008(1)	4.690(2)	290.8(4)	Junod [93]

Table 7.2 Fractional coordinates and site symmetry of atoms in $LiFePO_4$ (*Pnma* S.G.)

Atom	*x*	*y*	*z*	Site symmetry
Li	0	0	0	$\bar{1}$(4*a*)
Fe	0.28222	¼	0.97472	*m*(4*c*)
P	0.09486	¼	0.41820	*m*(4*c*)
O(1)	0.09678	¼	0.74279	*m*(4*c*)
O(2)	0.45710	¼	0.20602	*m*(4*c*)
O(3)	0.16558	0.04646	0.28478	1(8*d*)

Table 7.3 Interatomic distance (in Å) in $LiFePO_4$ (*Pnma* S.G.)

Fe octahedron		Li octahedron		P tetrahedron	
Fe-O(1)	1 × 2.204(2)	Li-O(1)	2 × 2.171(1)	P-O(1)	1.524(2)
Fe-O(2)	1 × 2.108(2)	Li-O(2)	2 × 2.087(1)	P-O(2)	1.538(2)
Fe-O(3)	2 × 2.251(1)	Li-O(3)	2 × 2.189(1)	P-O(3)	2 × 1.556(1)
Fe-O(3)	2 × 2.064(2)				

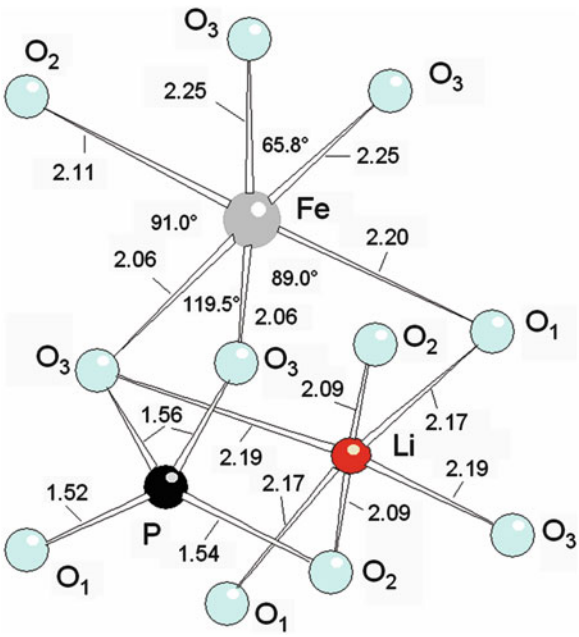

Fig. 7.4 Schematic view of the cation coordination in the $LiFePO_4$ olivine lattice. There are three nonequivalent oxygen atoms noted O_1 to O_3. The distorted FeO_6 octahedron lowers its symmetry from O_h to C_s in the strong crystal field of oxygen atoms

differs by as much as 0.2 Å, and the O-Fe-O angle is far from 90°. Remarkable structural features include the short O-O distances in the PO_4 tetrahedron, and that three of the six edges are shared with the metal octahedral.

7.3.2 The Inductive Effect

Another aspect of tuning the redox potential of an electrode material has been demonstrated by Goodenough et al. [1, 95] who have shown that the use of polyanions $(XO_4)^{n-}$ such as $(SO_4)^{2-}$, $(PO_4)^{3-}$, $(AsO_4)^{3-}$, or even $(WO_4)^{2-}$ lowers 3*d*-metals redox energy to useful levels compared to the Fermi level of the Li anode. Thus, the most attractive key point of the polyanion frameworks can be seen in the strong *X*-O covalency, which results in a decrease of the Fe-O covalency. This inductive effect is responsible for a decrease of the redox potential in comparison to the oxides [95, 96]. The polyanion PO_4^{3-} unit stabilizes the olivine structure of $LiFePO_4$ and lowers the Fermi level of the $Fe^{2+/3+}$ redox couple through the Fe-O-P inductive effect which results in a higher potential for the olivine material. The discharge voltage 3.45 V is almost 650 mV higher than that of $Li_3Fe_2(PO_4)_3$ [1]. It is also 350 mV higher than that of $Fe_2(SO_4)_3$ [97], which is consistent with the stronger Bronsted acidity of sulphuric vs. phosphoric acid. In the case of Li_2FeSiO_4, the lower electronegativity of Si vs. P results in a lowering of the $Fe^{2+/3+}$ redox couple [98]. On the other hand, the higher thermal stability of the

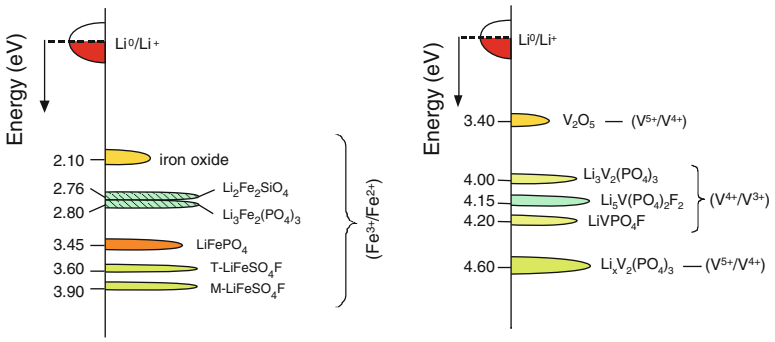

Fig. 7.5 Energy of the redox couples of iron (*left*) and vanadium (*right*) phosphate frameworks relative to the Fermi level of metallic lithium

phospho-olivines and their lower tendency to release oxygen is explained by the strong *X*-O covalency and the rigid $(XO_4)^{n-}$ units decreasing the safety risks. However, $AMXO_4$ compounds and $AM(XO_4)_3$ as well (*A* is an alkali ion) exhibit a very low electronic conductivity because of the separation between MO_6 octahedra and XO_4 tetrahedra that induces a large polarization effect during charge–discharge reaction [99]. Figure 7.5 illustrates the changes in redox energies relative to the Fermi level of Li for the $Fe^{2+/3+}$ and $V^{n+/(n+1)+}$ couples. For instance, the electrochemical insertion properties of lithium vanadium fluorophosphate, $LiVPO_4F$, indicate that the V^{3+}/V^{4+} redox couple in $LiVPO_4F$ is located at a potential around 0.3 V higher than in the lithium vanadium phosphate, $Li_3V_2(PO_4)_3$ [99]. This property characterizes the impact of structural fluorine on the inductive effect of the PO_4^{3-} polyanion.

7.4 Structure and Morphology of Optimized $LiFePO_4$ Particles

We report in this section the typical results obtained on one of our samples, chosen because it is representative of the product that is now used as a cathode element of commercial $LiFePO_4$ batteries.

7.4.1 XRD Patterns of LFP

The X-ray diffraction patterns of the carbon-free and carbon-coated samples are shown in Fig. 7.6. The pattern of the carbon-free sample is characteristic of $LiFePO_4$. The introduction of carbon by spray pyrolysis generates a broad amorphous hump in the count baseline centered at about $2\theta = 22°$ [7]. This broad peak

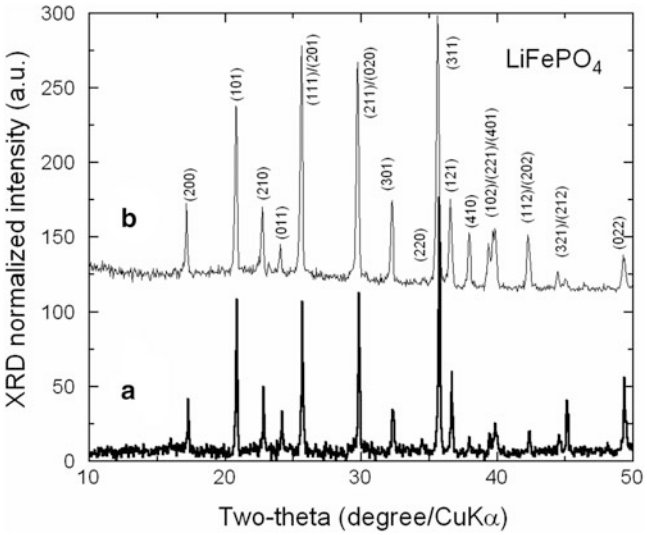

Fig. 7.6 X-ray diffraction diagrams for (**a**) carbon-free and (**b**) carbon-coated $LiFePO_4$ samples. XRD lines are indexed in the rhombohedral system, *Pnma* space group. XRD features are dominated by the four (101), (111) + (201), (211) + (020), and (311) lines. According to the Scherrer analysis the particle size is estimated to be 36 and 32 nm for the CF and the CC samples, respectively

gives evidence of the amorphous nature of the carbon coat [100]. On the other hand, the introduction of carbon by our process does not alter the crystallinity of the $LiFePO_4$ particles, which is evidenced by the crystalline peaks superposed on the amorphous background. The position of the peaks are the same in both samples, which means that the lattice parameters are unaffected by the carbon, a first evidence that the carbon does not penetrate into $LiFePO_4$. In addition, the width of the XRD peaks is about the same in the two samples. According to Scherrer's law, this width is inversely proportional to the mean diameter d of the crystallites. We can then infer that the size of the $LiFePO_4$ crystallites, hereafter called primary particles, is roughly the same in both samples. More precisely, the size of the crystallites estimated from Scherrer's law is 36 and 32 nm for the carbon-free and the carbon-coated samples, respectively. There are two equivalent ways to index the lines of the XRD, depending on the choice of space group *Pnma* or *Pnmb* and therefore of what is called the a or the b axis. Both are listed in the X-ray Powder Diffraction data files (88-2092, 40-1499) by the American Society for Testing Materials (ASTM). We have chosen the notation corresponding to *Pnma* S.G. ($a = 10.33$, $b = 6.010$, $c = 4.693$ Å). The only difference between the XRD pattern of the carbon-free and carbon-coated samples is the relative intensity of the Bragg peaks. The spectrum of $LiFePO_4$ is dominated by the four (101), (111) + (201), (211) + (020), and (311) lines. Which one of the four lines has the largest intensity is sample-dependent. It may be the (211) + (020) line as in the case of the carbon-free sample (also the case reported in the ASTM file 40-1499) or it may be

the (311) line as in the XRD pattern of the carbon-coated sample (also the case reported in the ASTM file 83-2092 and in ref. [101]). These differences, however, relate to the disorder of the Li; the common feature of all the $LiFePO_4$ materials investigated in the past is that these four lines have comparable intensities [102].

7.4.2 Morphology of Optimized LFP

The surface morphology of the $LiFePO_4$ powders and the shape of the carbon coat have been investigated by scanning electron microscopy (SEM) and high-resolution transmission electron microscopy (HRTEM). Typical SEM images for the carbon-coated sample are reported in Fig. 7.7a, b. The powders are composed of well-dispersed secondary particles that are slightly agglomerated and show a small quantity of fragments as displayed in the SEM images. The SEM observation shows similar images at any part of the sample, which is homogeneous at a scale large with respect to the area investigated. Figure 7.6a, b is then representative of the secondary particle size distribution, and the average size is 200 nm. Each of the secondary particles is made of a large number of small primary particles that are observed by TEM. The TEM images for the carbon-coated sample are illustrated in Fig. 7.7c, d. They show poly-dispersed primary particles with a mean size $\approx$90 nm, which is larger by a factor 3 than the average size of the monocrystallite grains deduced from the application of the Scherrer's law on the XRD pattern. Therefore, the primary particles are polycrystallites of $LiFePO_4$ made of a few (3 on average) monocrystallites of $LiFePO_4$. The amorphous carbon layer covering the primary particles can be seen in the TEM pictures (Fig. 7.7c, d). In the micrographs, the $LiFePO_4$ crystallites appear as the darker regions while the carbon is surrounding the primary particles as the greyish region. An average thickness is estimated to 30 nm. The carbon film is highly porous, which results in an irregular coating of the crystallites well-observed on the SEM and TEM images but the important point for the electronic conductivity is that it connects the particles. To summarize these results, the SEM and TEM images clearly depict a carbon layer coating the $LiFePO_4$ crystallites. XRD and HRTEM data are consistent [81].

7.4.3 Local Structure, Lattice Dynamics

Fourier transform infrared (FTIR) spectroscopy probes bulk properties [103, 104], while Raman scattering (RS) spectroscopy is the tool to perform surface analysis [105, 106]; for instance, the amount of carbon on $LiFePO_4$ is too small to be detected by FTIR, but it is well-characterized by RS experiments [23]. The vibrational modes of $LiFePO_4$ are primarily due to motion associated with phosphate and iron the other modes show some lithium contribution [13, 107, 108].

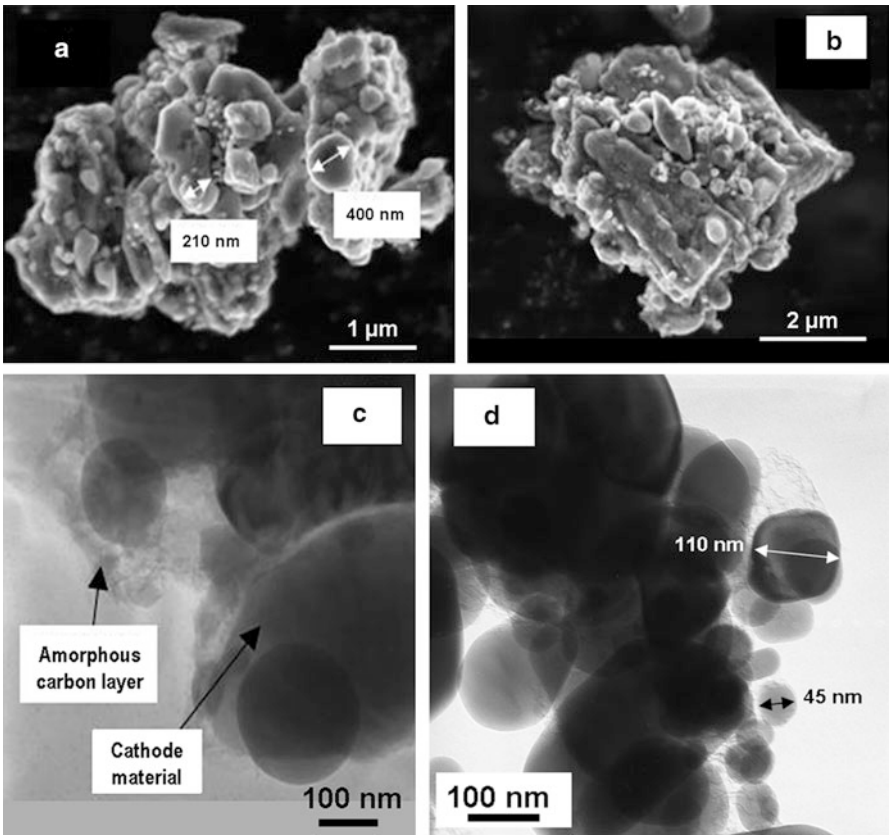

Fig. 7.7 SEM image (**a**–**b**) showing the shape of the secondary particles. There are slight agglomeration and small quantity of fragments. Values of the grain size are given in nm. TEM images (**c**–**d**) showing the amorphous carbon layer deposited onto the $LiFePO_4$ crystallite

The FTIR spectra of the)samples are reported in Fig. 7.8. We have also reported the position of the peaks intrinsic to this material, already identified in earlier works [103, 104]. Let us recall that the spectra result from absorption measurements, so that they are a probe of the bulk properties, and the amount of carbon in the powder is too small to be detected by such experiments. This is the basic reason why the FTIR spectra are characteristics of the $LiFePO_4$ part. The position of all the IR bands is in agreement with those listed in Table 1 in ref. [103]. No extra line is observed with respect to pure $LiFePO_4$. The bands in the range 372–647 cm^{-1} are bending modes (ν_2 and ν_4) involving O-P-O symmetric and asymmetric modes and Li vibrations [108]. In particular, the line at 230 cm^{-1} corresponds to the same cage mode of the lithium ions that undergo translation vibrations inside the cage formed by the six nearest neighbor oxygen atoms [109]. The bands in this range 372–647 cm^{-1} are thus the part of the spectrum that is sensitive to the local lithium environment. This is also the part of the spectrum that is the same in both the carbon-free and carbon-coated samples. We can

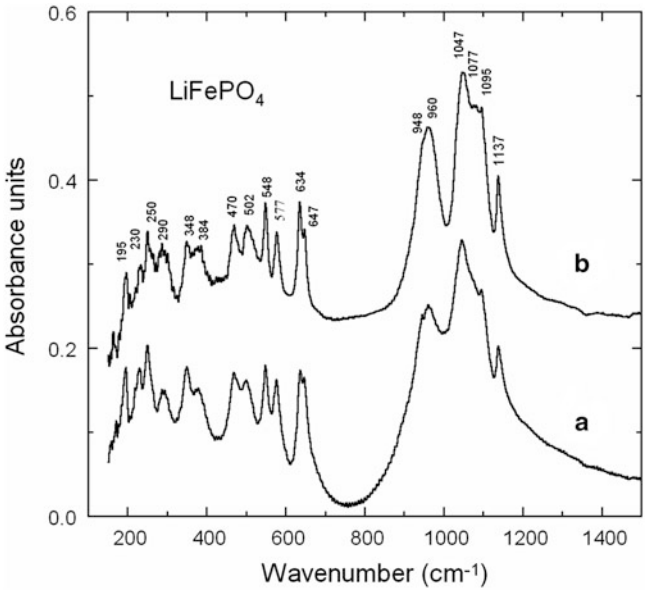

Fig. 7.8 FTIR absorption spectra of (**a**) carbon-free and (**b**) carbon-coated $LiFePO_4$ samples. Peak positions are marked (in cm^{-1}). Infrared spectra were recorded on pellet of $LiFePO_4$ powders diluted into ICs matrix (1:300)

then infer from this result that the lithium ions do not "see" the carbon ions, one other evidence that the carbon did not penetrate inside the $LiFePO_4$ particles. The part of the spectrum in the range 945–1139 cm^{-1} corresponds to the stretching modes of the $(PO_4)^{3-}$ units. They involve symmetric and asymmetric modes of the P-O bonds, at frequencies closely related to those of the free molecule, which explains that the frequencies of these modes are the same in both samples. However, the modes in the carbon-free sample are significantly broader than in the carbon-coated sample. This broadening gives evidence of a decrease in the lifetime of the phonons, and thus the existence of defects breaking the periodicity of the lattice sites inside the $LiFePO_4$ crystallites of the carbon-free sample. The analysis of magnetic properties in the next section allows us to identify these defects as γ-Fe_2O_3 nanoparticles.

To explore the surface properties of the $LiFePO_4$ particles, Raman spectra have been measured; the penetration depth for carbon with Raman spectroscopy is approximately 30 nm [107]. This is one order of magnitude larger than the thickness of the carbon coat deposited at the surface of the $LiFePO_4$ particles in case of a uniform carbon distribution. Therefore, any screening effect of carbon on the $LiFePO_4$ spectra is not expected. The penetration depth inside $LiFePO_4$ is unknown, but it should be small, so that the detector in the Raman experiments collects the signal within the light penetration depth, which basically represents the total amount of carbon and a few per cent of the amount of $LiFePO_4$. Since the total amount of carbon is itself 5 wt% of $LiFePO_4$, we can expect that comparable amounts of carbon and $LiFePO_4$ are probed by the sampling depth. This is

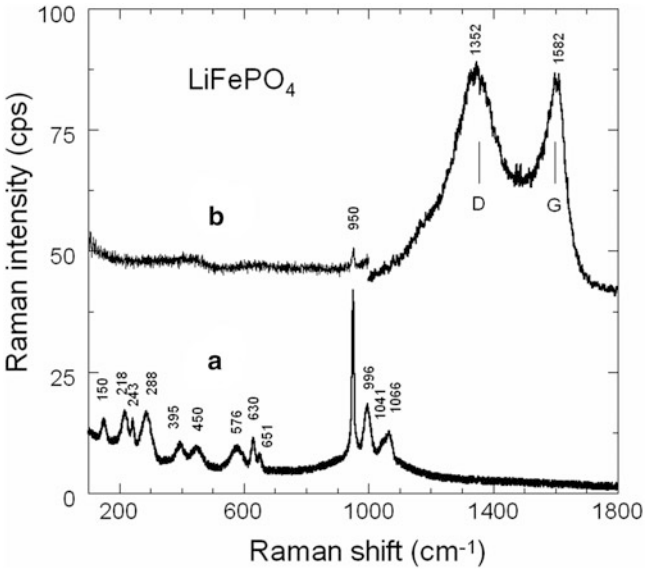

Fig. 7.9 Raman spectra of the carbon-free and carbon-coated $LiFePO_4$ samples. Spectra were recorded using the 514.5 nm laser line at the spectral resolution 2 cm^{-1}. RS features of the $LiFePO_4$ bulk material are screened by the carbon deposit for which the G- and D-band are observed

confirmed by the Raman spectra reported in Fig. 7.9. The part of the spectrum in the wave number range 100–1100 cm^{-1} is the same in the carbon-free and the carbon-coated sample and only the lines characteristics of $LiFePO_4$ are detected in this range. The peak positions reported in Fig. 7.9 in this range are within a few cm^{-1} the same as those that have been reported in ref. [103], and we refer to this prior work for their assignment. The largest difference is for the line at 395 cm^{-1}, which is reported at 410 cm^{-1} in ref. [108]. This line is associated with the PO_4 bending modes ν_2, ν_4 which are strongly coupled. However, we cannot consider this difference as significant since all the other lines associated with PO_4 have the same position. This is the case in particular for the lines at 620, 940, 986 and 1058 cm^{-1} associated with ν_4, ν_1, ν_3, and ν_2 intramolecular stretching modes of PO_4, respectively. The only difference in this range of wave numbers is a shift of the Raman lines by about 10 cm^{-1} towards lower frequencies in the carbon-coated sample. This shift of the Raman lines is in contrast with the absence of any shift of the FTIR lines, which gives evidence that it is a surface effect. This shift of the Raman lines is attributable to the increase of the bonding length in the first layers of $LiFePO_4$ particles near the interface with the carbon, taking its origin in the strain induced by the adhesion of the carbon film. For samples with a different mode of preparation, carbon was reported to be responsible for a screening of the signal from $LiFePO_4$, so that only a weak band at 942 cm^{-1} associated with $LiFePO_4$ could still be detected [105]. Again, such a screening is not expected for the reasons above mentioned, and it is not observed in the present case.

7.5 Magnetic and Electronic Features

7.5.1 Intrinsic Magnetic Properties

The magnetic interactions between Fe ions are antiferromagnetic superexchange interactions of the form -Fe-O-Fe- and -Fe-O-P-O-Fe-, and well-crystallized $LiFePO_4$ is antiferromagnetic (AF), with a Néel temperature $T_N = 52$ K [83, 85, 110, 111]. The topology of the AF order has been determined by neutron experiments from which the magnetic interactions have been determined [112]. The dominant interactions that fully account for this structure is the intralayer superexchange Fe-O-Fe interaction J_1, and two super-superexchange interactions Fe-O···O-Fe, namely an interlayer interaction J_2 and an intralayer interaction J_b. Other interactions envisioned in earlier works [113] turn out to be negligible. All the interactions J_1, J_2 and J_b are antiferromagnetic, and their estimated value is [112]:

$$J_1 = -1.08 \text{ meV}, \; J_2 = -0.92 \text{ meV}, \; J_b = -0.4 \text{ meV}. \tag{7.1}$$

Interesting enough, this recent result shows that the FeO_4 layers are strongly coupled antiferromagnetically. This is in essence why the system undergoes a true transition to three-dimensional antiferromagnetic ordering, while a 2D-magnetic system does not order because of enhanced quantum spin fluctuations. In addition, the J_2, J_b cannot cause geometric frustration of the magnetic interactions, in contrast with prior claims, because J_b is significantly smaller than J_1. Therefore, for a pure $LiFePO_4$ sample, the magnetization curve $M(H)$ is simply linear in H. This case is illustrated by the sample named B-10 in Fig. 7.10a. The magnetic susceptibility satisfies the Curie–Weiss law in the paramagnetic regime, i.e., H/M varies linearly

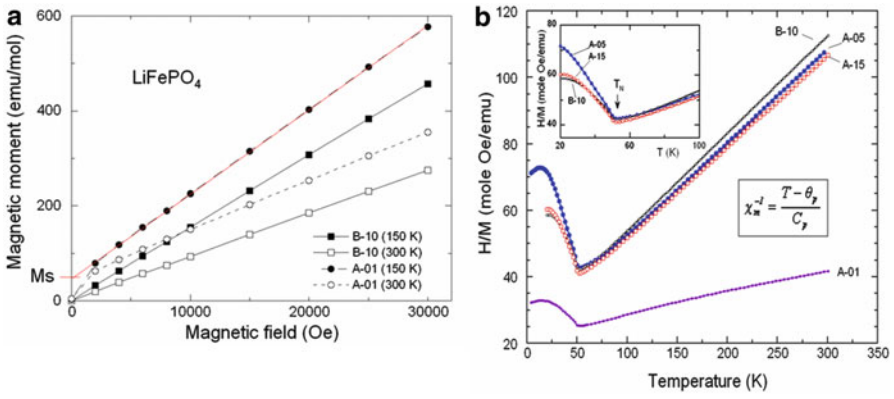

Fig. 7.10 (**a**) Isothermal curves of the magnetic moment vs. applied magnetic field as a function of temperature for A-type and optimized B-type $LiFePO_4$ sample. *Symbols* are experimental data, the *straight continuous lines* are guides for the eyes. (**b**) Temperature dependence of H/M measured at $H = 10$ kOe for $LiFePO_4$ samples. The best material (B-10) has the lowest Curie constant 3.41 emu K mol^{-1}. *Insert* shows the cusp at the Néel temperature $T_N = 52$ K

with temperature as it can be seen for this sample in Fig. 7.10b, and the effective magnetic moment deduced from this Curie constant is $\mu_{\text{eff}} = 5.22\,\mu_{\text{B}}$, close to the theoretical value $4.90\,\mu_{\text{B}}$ calculated from the spin-only value of Fe^{2+} in its high-spin configuration [114]. The insert shows the cusp of the transition from antiferromagnetic ordering to the paramagnetic range at $T_{\text{N}} = 52$ K.

7.5.2 *Effect of the γ-Fe_2O_3 Impurity*

On the other hand, the magnetic properties of $LiFePO_4$ samples may be different in presence of impurities. The case is illustrated by the sample named sample A in Fig. 7.10, with a magnetization curve that deviates strongly from a linear behavior at low fields. This curvature is the signature of ferrimagnetic impurities [10, 109, 114] under the form of nano-sized clusters. In this case, the magnetization $M(H)$ is the superposition of two contributions:

$$M(H) = \chi_{\text{m}} H + M_{\text{extrin}}. \tag{7.2}$$

The intrinsic part, $\chi_{\text{m}} H$, is linear in the applied magnetic H and is just the contribution of pure $LiFePO_4$. The extrinsic component that is easily saturated in H is the contribution of the ferrimagnetic nanoclusters, which can be estimated in a simple superparamagnetic model [10]. It can be written under the form:

$$M_{\text{extrin}} = Nn\mu £(\xi), \tag{7.3}$$

where $£(\xi) = £(n\mu H/k_{\text{B}}T)$ is the Langevin function, N is the number of magnetic clusters, and each cluster contains n magnetic ions of average moment μ. T is the absolute temperature and k_{B} the Boltzmann constant. At high fields, M_{extrin} saturates to $Nn\mu$, and is readily determined as the ordinate at $H = 0$ of the intersection of the tangent to the magnetization curves at large fields.

As a result, we find that $Nn\mu$ does not depend significantly on temperature below 300 K. We are in the situation where the cluster magnetization is temperature-independent, which amounts to say that the Curie temperature Tc inside the clusters is much larger than 300 K, which identifies the clusters as ferrimagnetic maghemite impurities (γ-Fe_2O_3). Since the value of μ for this material is known, it is then easy to determine n from the fit of the $M_{\text{extrin}}(H)$ curve according to Eq. (7.3), and N from the saturation value $Nn\mu$. As a result, we find that the impurity clusters are 1 nm in size, and their concentration is a few tenths of a ppm. This is small, but it is sufficient to alter the electrochemical properties, and the control of the synthesis to obtain pure samples is crucial [10, 114]. Indeed, the 1-D Li channels make the olivine performance sensitive not only to particle size but also to impurities and stacking faults that block the channels. That is why it is crucial to get rid of this impurity which takes its origin in the fact that iron prefers to be in the trivalent state. This can be done by a synthesis of LFP in a reducing atmosphere like hydrogen. In a

one step synthesis of carbon-coated LFP, the hydrogeneous gases coming from the decomposition of the organic material chosen as the precursor of the carbon coat does the job. Figure 7.10b shows the temperature dependence of the reciprocal magnetic susceptibility of a series of A-samples with different concentrations of impurities. The data reported in the figure are raw data H/M at $H = 10$ kOe, measured with a SQUID magnetometer. At this large magnetic field, M_{extrin} is saturate, so that $M/H = \chi_{\text{m}} + (Nn\mu/H)$. The second term is responsible for the deviation of the curves for the A-samples from the $H/M \sim \chi_{\text{m}}{}^{-1}(T)$ curve of sample B in Fig. 7.10b.

Another means of investigation of the magnetic contribution of γ-Fe_2O_3 is provided by the electron spin resonance (ESR). The derivative signals of the ESR absorption spectra of a sample A are reported in Fig. 7.11. The EPR signal detected in $LiFePO_4$ in the absence of impurities is orders of magnitude smaller [83]. The EPR signal is then attributed solely to the magnetic impurity, the reason why ESR experiment is an efficient tool to determine its contribution [10, 109]. For uncorrelated magnetic clusters, one expects a signal characteristics of a gyromagnetic factor $g = 2$. At the frequency used in the experiments, such a signal is centered at $H = 3300$ G. Indeed, this signal, already detected in other $LiFePO_4$ samples that contained ferrimagnetic particles [10, 109], is also detected in the present work and has a comparable shape. The structure at 3300 G has the same width. Its integration allows us to derive the magnetization associated to the impurity clusters, and thus their concentration, which is found to be consistent with the analysis of the magnetization curves we have described above.

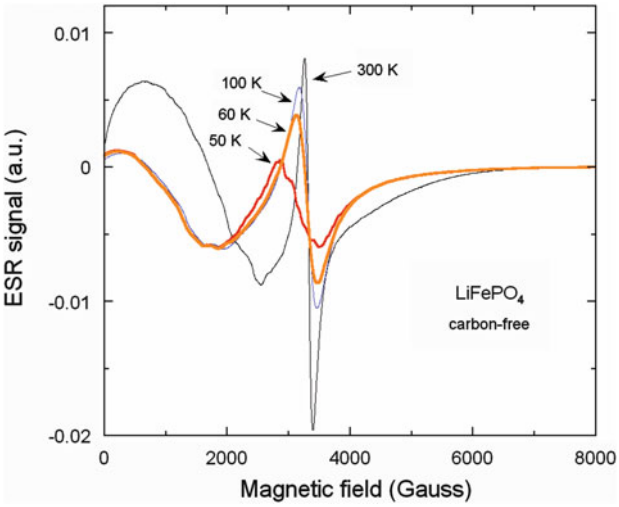

Fig. 7.11 Electron spin resonance spectrum for the carbon-free $LiFePO_4$ sample at several temperatures indicated in the figure. Note the unit is arbitrary, but it is the same one as in the previous figure, so that the relative intensity between the spectra of the two samples is given by the ratio of the ordinates between the spectra in the two figures

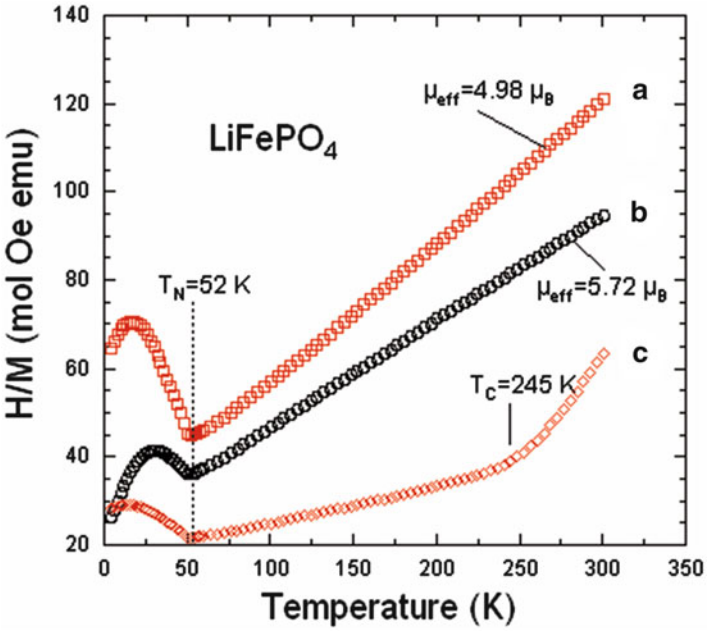

Fig. 7.12 Temperature dependence of the reciprocal magnetic susceptibility of different $LiFePO_4$ samples. (**a**) optimized pure $LiFePO_4$, (**b**) Fe_2O_3-containing sample, and (**c**) Fe_2P-containing sample

7.5.3 Effect of the Fe_2P Impurity

Other iron-based impurities have been identified in the olivine framework, including $Li_3Fe_2(PO_4)_3$, $Fe_2P_2O_7$, Fe_2P, depending on the synthesis conditions [10, 13, 81, 114]. For instance, we have reported in Fig. 7.12 the $H/M(T)$ curve measured again at 10 kOe for a different sample, which shows an abrupt change of the slope of the curve near $T_C = 265$ K. Since this is the Curie temperature of the ferromagnet Fe_2P, this feature identifies the impurity contained in this sample as Fe_2P. The quantitative analysis of the magnetization curve of this particular sample analysis of the magnetic properties shows that the proportion of iron contained in this impurity is Fe_2P is 0.5 %. Data obtained on a pure sample and a sample containing Fe_2O_3 impurity are also reported for comparison.

Since Fe_2P is metallic, its presence increases the electronic conductivity, but on the other hand, it also decreases the ionic conductivity so that both the capacity and cycling rates are degraded with respect to C-LFP. This is evidenced in Fig. 7.13 that shows the Arrhenius plot of the electronic conductivity, σ_{elec}, of three $LiFePO_4$ samples: an uncoated material without impurity, a Fe_2P-containing uncoated sample, and a C-LFP. It is obvious that addition of either iron phosphide or carbon enhances greatly σ_{elec}. For this reason, some authors have even intentionally

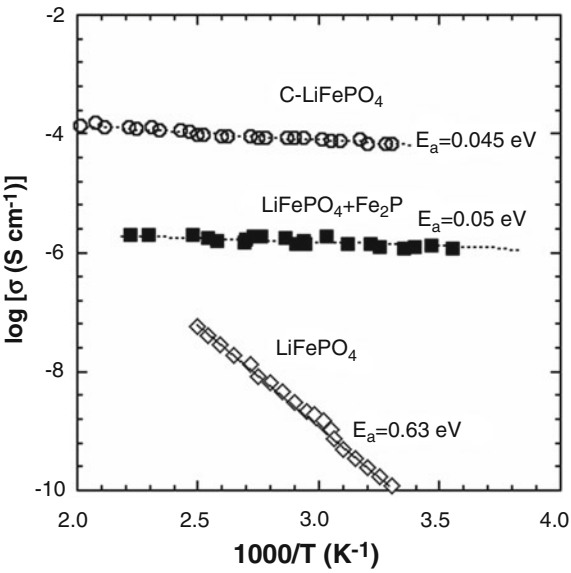

Fig. 7.13 Electronic conductivity of $LiFePO_4$ samples: (**a**) uncoated material without impurities (*open squares*), (**b**) Fe_2P-containing uncoated sample (*full squares*), and (**c**) carbon-coated $LiFePO_4$ (*open circles*)

introduced this impurity. However, this is detrimental to the electrochemical properties for reasons that are discussed hereunder.

Figure 7.13 also shows that the carbon coating greatly enhances the electronic conductivity of the LFP particles that allows high rate for the charge–discharge process. The electrical conductivity of LFP with Fe_2P impurity is intermediate between coated and uncoated pure LFP. This results explains why fanciful results for conductivity of LFP have been published by different authors that did not detect impurities in their material because they failed to do the magnetic measurements that would have detected them, in particular in samples that were supposed to be doped with different metal ion elements, while the doping elements did not enter into the matrix but segregated under the form of metallic impurities at the surface of the particles.

Figure 7.14 displays the electrochemical charge–discharge profiles of Li//LFP cells cycled at room temperature with pure $LiFePO_4$ and with Fe_2P-containing electrode material. It is obvious that at the rate 2C, the capacity retention decreases significantly for the material containing few % of Fe_2P. A close examination was made for the detection of any iron dissolution that could occur after long-term cycling. The analysis of iron species was investigated at the separator/lithium (SL) interface by SEM cross-section (slice view) as shown in Fig. 7.15a, b. The micrograph (Fig. 7.15a) obtained from evaluation of the earlier generation material shows the presence of iron islands at the SL interface. Obviously, some iron particles (or ions) migrate through the electrolyte from the $LiFePO_4$ positive electrode to the lithium negative. The net effect of this migration is a large decrease in capacity retention of the Li//LFP cell. Figure 7.15b shows the post-mortem micrograph obtained from tests with an optimized electrode in a Li cell with a lithium foil negative. In this case, there is no iron detected at the SL interface, which

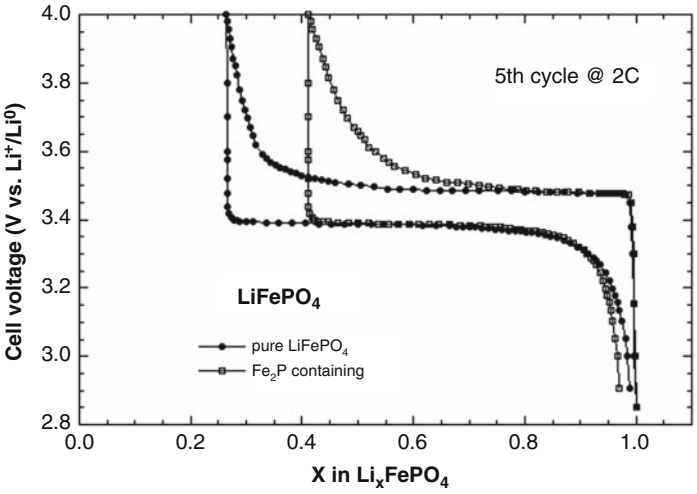

Fig. 7.14 Electrochemical charge–discharge profiles of Li//$LiFePO_4$ cells cycled at room temperature. (**a**) with pure $LiFePO_4$ and (**b**) with Fe_2P-containing electrode material

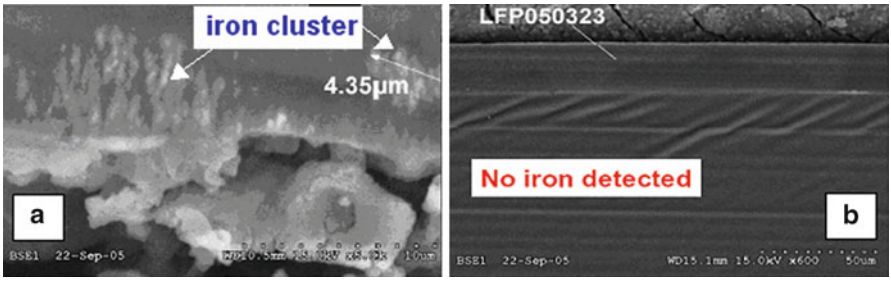

Fig. 7.15 Post-mortem SEM images of the detection of iron species at the interface between the separator and lithium metal anode. (**a**) Formation of iron islands at the interface when an earlier generation of $LiFePO_4$ cathode is used. (**b**) No iron was detected at the surface of Li foil when the design of the $LiFePO_4$ cathode was optimized

remained intact after 100 cycles. These results show that the iron of the Fe_2P impurity dissolves into the electrolyte, which destroys the battery and shorten its calendar life. Therefore, it is mandatory to get rid of this impurity, which can be done by reducing the synthesis temperature to 700 °C.

The results we have reported for two impurities, namely γ-Fe_2O_3 and Fe_2P illustrates the necessity of adjusting the synthesis parameters in order to obtain pure samples free of any impurity, and insuring a strict control of the structural quality of the materials. Several physical methods were utilized to analyze the local structure and the electronic properties of the phospho-olivine framework [115]. The quality control of the product is the key to obtain high-performing LFP Li-ion batteries.

7.5.4 Magnetic Polaron Effects

The intrinsic electrical conductivity of $LiFePO_4$ is of a polaronic type, as in many ionic compounds. The polaron in the present case is linked to the existence of Fe^{3+} ions that maintain the charge neutrality in presence of lithium vacancies. According to the Mott formula, the conductivity $\sigma(T)$ is [116]:

$$\sigma = c(1-c)\frac{ev}{RkT}\exp(-2\alpha R)\exp\left(\frac{-E_a}{kT}\right), \tag{7.4}$$

where c is the concentration of polarons per magnetic ion, i.e., the probability that a Fe^{3+} ion can be found, so that $c(c-1)$ is the probability to find a Fe^{3+} ion with a Fe^{2+} ion nearest neighbor at distance R to exchange the outer electron. The wavefunction of the orbital of the $t_g\downarrow$ 3d-electron is represented by an exponential with a rate of decay α, so that the first exponential proportional to the square of the wave function is the probability of jumping of the electron (hole). Ea is the activation energy, i.e., the energy barrier that the electron (hole) has to overcome to jump, and ν is an atomic frequency. For iron ions, $\alpha = 1.5$ Å^{-1}, $R = 3.87$ Å, $\nu = 10^{-15}$ Hz. After Fig. 7.13, $E_a = 0.6$ eV. It is then straightforward to determine c from the fit of the experimental curve of pure uncoated LFP in Fig. 7.13 with Eq. (7.1), to find $c = 3 \times 10^{-3}$ [117].

In the conduction process, an electron jumps from a Fe^{2+} site to a neighboring Fe^{3+} site. This electron is the $t_g\downarrow$ 3d-electron of Fe^{2+} since it is in the high spin multi-electronic state $(t_g\uparrow)^3(e_g\uparrow)^2t_g\downarrow$, while the state of lowest energy for Fe^{3+} is the high spin multi-electronic state $(t_g\uparrow)^3(e_g\uparrow)^2$, as shown in Fig. 7.16a. The "up" and "down" symbols refer to a majority spin direction. In band structure calculations

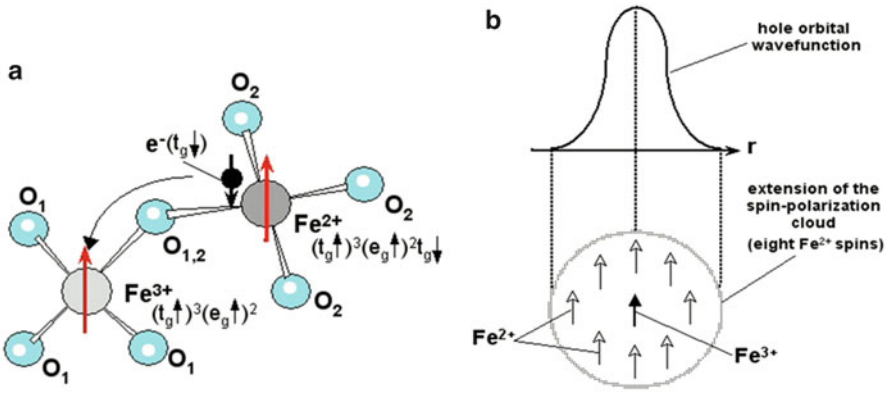

Fig. 7.16 (**a**) Small magnetic polaron in $LiFePO_4$. The hopping process is illustrated in (**a**). The $t_g\downarrow$ "hole" on the Fe^{3+} site 1 is shifted to a neighboring iron site 2 by transfer of one $t_g\downarrow$ electron from site 2 to site 1. (**b**) The indirect exchange interaction is responsible for the spin-polarization of the iron ions inside the electronic $t_g\downarrow$ "hole" wave function (in the direction opposite to that of the t_g electron)

performed in the ferromagnetic configuration [118], this is simply the direction of the spontaneous magnetization. Indeed, in the range of temperature where the electronic conductivity is measured, $LiFePO_4$ is paramagnetic; it orders only at 52 K, and yet in the antiferromagnetic phase. It is not very important as far as the electronic structure is concerned, because the magnetic exchange energy is negligible with respect to the Coulomb energy in this ionic material. But of course, this difference is crucial when one is concerned with magnetic properties. In a paramagnetic configuration, this majority spin direction has to be taken in the Hartree–Fock sense, i.e., as the direction of the local magnetic moment carried by one iron ion resulting from the uncompensated moment of the electrons that occupy the 3*d*-shell of the ion under consideration. Therefore, the $t_g\downarrow$ electron of one Fe^{2+} ion on site i is spin-polarized in the direction opposite to the local spin $\vec{S}_i$ carried by the iron ion on site i. In a hopping process, this electron jumps by tunneling effect on nearest neighboring (nn) Fe^{3+} ion on site j in the initial state $(t_g\uparrow)^3(e_g\uparrow)^2$ to make it a Fe^{2+} in the final state $(t_g\uparrow)^3(e_g\uparrow)^2 t_g\downarrow$. But in this final state, the spin polarization refers to the direction of the spin $\vec{S}_j$ carried by the iron ion on site j. This hopping, illustrated in Fig. 7.11a is thus possible only if both iron ions on site i and j are spin polarized in the same direction, due to the Pauli principle. Therefore, the hopping process that couples iron ions at nn sites i and j generates a nn indirect exchange between $\vec{S}_i$ and $\vec{S}_j$ that is ferromagnetic. As a consequence, the spins of the central ion of the polaron and the neighboring iron ions should be spin-polarized. The result is that the moving electron must carry with it not only its distortion cloud but also its spin-polarization cloud, as shown in Fig. 7.11b. This kind of magnetic polaron is a pseudo-particle called a ferron [119]. In usual semiconductors, its formation involving localization of the electron orbital requires a much stronger indirect exchange interaction than expected here. Even in rare earth compounds, the magnetic polaron is actually bound to a donor (or acceptor), owing to the additive effects of the Coulomb attractive potential and the indirect magnetic exchange potential well. This is the bound magnetic polaron. There is, however, an important difference between the bound magnetic polaron we have investigated in the past, and the present case. Prior studies of magnetic polarons concerned nonionic materials with important indirect exchange interactions, in which case the magnetic polaron may have tremendous effects on electronic transport properties [120], and the effective magnetic moment μ_{pol} carried by a magnetic polaron can be large [119]. Here, the orbital of the excess charge carrier is strongly localized by the distortion of its surroundings, because the material is ionic. The consequence is that the contribution of the indirect exchange interaction to the activation energy is negligible, so that the spin-polarization process does not significantly influence the transport properties. The other consequence, closely linked to the previous one, is that the magnetic moment associated to the spin-polarization of the cloud is small, because the orbital is much more localized than in nonionic compounds so that only the neighbors of the central polaron site can be spin-polarized. The actual moment depends on how many neighbors the excess carrier can spin-polarize. A reasonable approximation is to take into account the neighbors that are effectively

magnetically coupled to a given iron ion in the lattice. These magnetic interactions according to Eq. (7.1) are the four Fe ions coupled by the intra-layer Fe-O-Fe interaction J_1, the two ions coupled by an interlayer interaction J_2 super-super exchange interactions Fe-O···O-Fe, and the two ions coupled by an intra-layer interaction J_b. The number of neighboring Fe^{2+} ions spin –polarized by the excess carrier centered on an Fe^{3+} site should then be 8 in total. Since the spin of the central Fe^{3+} ion is $S = 5/2$ and the spin of the nn Fe^{2+} ions is $S = 2$, we expect the macro-spin associated to the polaron to be $S_{pol} = 5/2 + 8 \times 2 = 18.5$, hence a magnetic moment $\mu_{pol} = gS_{pol} = 37$ in Bohr magneton unit (we take $\mu_B = 1$ throughout this work), while $\mu(Fe^{2+}) = 4.9\,\mu_B$. This moment can be detected by magnetic measurements. In the paramagnetic regime where the Curie–Weiss law is satisfied, the Curie constant per magnetic ion $C = {\mu_{eff}}^2/(3k_B)$ will be the sum of the intrinsic contribution of $LiFePO_4$ plus the contribution of the polarons, so that:

$$ {\mu_{eff}}^2 = (1-c)\left[\mu\left(Fe^{2+}\right)\right]^2 + c\left(\mu_{pol}\right)^2 - 4c\left[\mu\left(Fe^{2+}\right)\right]^2, \tag{7.5} $$

where c is the concentration of polarons (i.e., the concentration of Li vacancies) per iron ion. The last (negative) term in Eq. (7.5) comes from the fact that the contribution of the four Fe^{2+} involved in the polarons have their contribution included in the μ_{pol} term, so that they must be subtracted from the contribution of the intrinsic contribution from the host (first term). The experimental effective moment μ_{eff} can be deduced from the slope of the $\chi^{-1}(T)$ experimental curve in the paramagnetic regime where the Curie–Weiss law is satisfied:

$$ \begin{aligned} \chi &= C/(T-\theta), \\ C &= {\mu_{eff}}^2/(3k_B). \end{aligned} \tag{7.6} $$

In pure samples that do not contain any impurity, the magnetic susceptibility χ is defined unambiguously since M is linear in H. For samples that contain a residual concentration of magnetic impurity, like for the samples B in Fig. 7.10 for instance, the susceptibility χ entering Eq. (7.6) must be defined as the slope of the magnetization curves $M(H)$, i.e., $\chi = dM/dH$ measured at $H = 10$ kOe, not to be confused with the ratio M/H reported in Fig. 7.10b. At this large magnetic field, the superparamagnetic contribution of the impurity phases to M is saturated to M_{extrin} (see Eq. 7.3), so that the impurity phases, if any, do not contribute to χ [10]. The experimental value of μ_{eff} we have found for our carbon free sample is $\mu_{pol} = 5.3\,\mu_B$. That is in excess with respect to the intrinsic value $\mu(Fe^{2+}) = 4.9\,\mu_B$ expected for the pure stoichiometric sample, because of the contribution of the polarons. Using this value in Eq. (7.1) and (7.5), we find, for $c = 3 \times 10^{-3}$ in quantitative agreement with the value determined from the analysis of the elec. The description of the optical, electronic, and magnetic properties of $LiFePO_4$ is then fully self-consistent. The indirect exchange interaction is responsible for the spin-polarization of the iron ions inside the electronic $t_g\downarrow$ "hole" wave function (in the direction opposite to that of the t_g electron), as it is illustrated in Fig. 7.16b. As the charge in excess hops from

site to site, it brings with it not only a local lattice deformation cloud associated to the Coulomb potential but also its spin-polarization cloud.

We have already mentioned that a magnetic polaron is formed by a Li vacancy, so that c is also the concentration of Li vacancies that almost always exist in LFP, whether it is carbon-coated or not. We systematically find μ_{eff} in the range 5.1–5.3, depending on the sample. The magnetic susceptibility associated to the carbon itself is negligible, so the excess in the effective magnetic moment with respect to the value 4.9 observed only in stoichiometric samples is the same as in the carbon-free sample and has the same origin, namely a proportion a few 10^{-3} of Li vacancies. In the carbon-coated sample, the electronic conductivity through the powder product is insured by the carbon and not by the small polarons, with the consequence that is no longer possible to detect the small polarons by transport experiments. In this latter case, only magnetic measurements reveal their existence, by the excess in μ_{eff}. We already know that the hydrogen contained in the organic additive has a reducing power on iron that prevents the formation of impurity phases including Fe_2O_3, Fe_2P, and $Li_3Fe_2(PO_4)_3$. But the fact the μ_{eff} is the same whether the synthesis has been made with or without this organic compound now gives the proof that the organic compound has no effect on the native defects at the origin of the presence of a small proportion $c = 3 \times 10^{-3}$ of iron in the trivalent state. This result is consistent with the idea that the native defects are not be related to iron itself, but are related to Li vacancies.

7.6 Carbon Coating

To increase the electronic conductivity, it is a common practice in the production of Li-ion battery electrodes, to add carbon, not only to add carbon to the $LiFePO_4$ matrix [3] but also by surface coating of $LiFePO_4$ particles with a thin layer of carbon [5, 6]. A seven-order-of-magnitude increase in the electronic conductivity has been reached by adding sucrose to produce carbon in $LiFePO_4$ raw materials by a spray pyrolysis technique [7] (see also Fig. 7.13). The addition of carbon has then the advantage of combining much better electronic conductivity, and thus high rate capability, and high capacity. In particular, a capacity of about 160 mAh g^{-1} has been found for $LiFePO_4$ coated with 1 wt% carbon [81]. Ravet et al. [5, 6] reported two ways to coat carbon: (1) mixing $LiFePO_4$ powder with sugar solution and heating the mixture at 700 °C, and (2) synthesizing $LiFePO_4$ with some organic materials added before heating. Although the way to add carbon is not fully optimized yet [6], the approach that consists in adding a carbon source at the beginning of the synthesis whenever it is possible is thought being more promising [6–8]. In the case of hydrothermal synthesis, however, the sintering temperature is too small to obtain a conductive carbon coat and a two-step process is inevitable, in which the carbon coating is made at a sintering temperature of 700 °C. Recently, Zaghib et al. [117] demonstrated that better performance was obtained at high-rate discharge (3C) with 6 % carbon additive in the $LiFePO_4$ electrode. This material is suitable for HEV application.

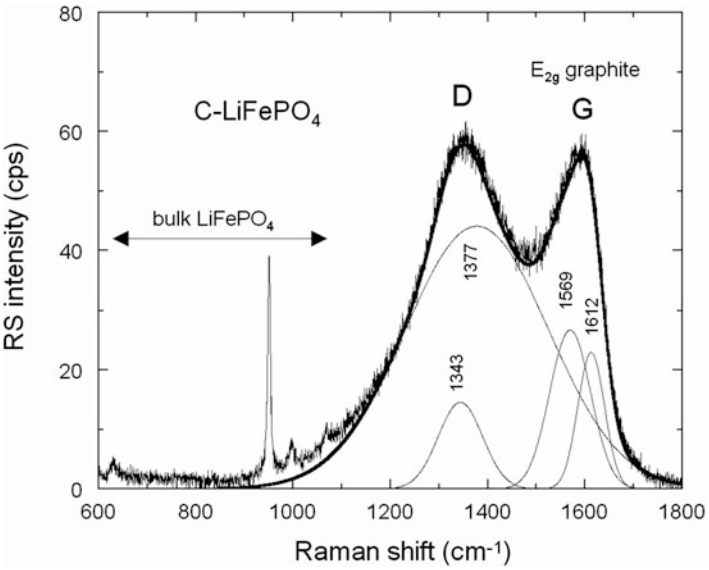

Fig. 7.17 Fit (*thick line*) showing the deconvolution of the Raman spectrum by Gaussians (*thin lines*, identified by their position) of the D and G carbon structures of the Raman spectrum of the carbon coated $LiFePO_4$ sample

7.6.1 Characterization of the Carbon Layer

To explore the surface properties of the $LiFePO_4$ particles, Raman spectroscopy proved to be a powerful tool [24, 121, 122]. Two broad lines at 1345 and 1583 cm^{-1} are found in the carbon-coated sample only, as can be seen in Fig. 7.17. These broad lines are a fingerprint of amorphous carbon films. Since they constitute protective optical or tribological coatings [123], a tremendous amount of work has been devoted to amorphous carbon films deposited by a wide variety of methods. Different methods affect both local the bonding and intermediate-range order, so that they lead to a wide variety of films, including amorphous diamond, hydrogenated "diamond-like" carbon, and plasma polymers. All these films have in common the existence of these two broad lines in the Raman spectra. The structure at 1583 cm^{-1} mainly corresponds to the G-line associated with the optically allowed E_{2g} zone-center mode of crystalline graphite. The structure at 1345 cm^{-1} mainly corresponds to the D-line associated with disorder-allowed zone-edge modes of graphite. The exact position of the structures in amorphous films depends on the probe-laser wavelength [123–126], so that a quantitative comparison between spectra in the literature is possible only between experiments using the same wavelength. Tamor and Vassell [127] have compared Raman spectra of nearly one hundred amorphous carbon films obtained with the same probe-laser wavelength (Ar-line) as the one we have chosen.

First of all, we note that the Raman spectra of hydrogen-free carbon films can be distinguished from those of hydrogenated films by an additional broad feature centered at 600 cm^{-1} [128]. Since this structure never exists in hydrogenated carbon and always exists in hydrogen-free films, this criterion is considered to be robust [127]. In the present case, this structure is not observed. Therefore, the carbon is hydrogenated, which is actually not surprising, since the preparation process involved different organic additives. As we shall see, however, the amount of hydrogen is only small. Second, the spectrum is characteristics of amorphous graphitic carbon, meaning that the carbon atoms are essentially three-coordinated and bound by sp^2-type hybrid orbitals, in opposition to diamond-like carbon [128]. This result explains why the carbon coating was found to be efficient to increase the electronic conductivity in our material, since the graphitic carbon is the only carbon type that can be conductive. We report hereunder a more complete analysis of the D and G bands since they have been recognized as predictive of the structural as well as physical properties [128]. In particular, a comprehensive study to relate the D and G features in the Raman spectrum to the structure of the disordered graphitic films can be found in ref. [129], while the relation to the physical properties can be found in ref. [127].

The analysis of the D and G lines in such films is always done by fitting the Raman curves in the region from 1000 to 2000 cm^{-1} with Gaussians. The number of Gaussians varies from two [127] to four [105]. In our case, we found that the deconvolution of the Raman spectra with two Gaussians (one for the D-line, one for the G-line) did not give good results, and four Gaussians were necessary to account for the Raman spectra. The result of this fit is shown in Fig. 7.16 and Table 7.4. The band at 1569 cm^{-1} can be assigned to the E_g mode of graphite while the very broad, dominant band centered at 1378 cm^{-1}, which extends over the entire spectral range of carbon vibrations, is the disorder-induced peak characteristic of highly defective graphite. If two Gaussians only are used in the fitting procedure, those are the only structures identified. Among the two extra structures identified in the fit of the spectra by four Gaussians, the band at 1612 cm^{-1} is typical for severely disordered carbonaceous materials [130, 131]. The origin of the other line at 1344 cm^{-1} is more questionable. Such a line has been observed in the Raman spectra of polypara-phenylene (PPP)-based carbon prepared at heat-treatment temperatures below 750 °C [132]. For this PPP-based carbon, this line was attributed to a quinoid-like inter-ring stretching mode due to a contraction in inter-ring bond length as the PPP chains are converted into graphitic ribbons, or to a "bridging" of the aromatic rings along the chain by more than one C–C bond [132]. The initial idea that this line was

Table 7.4 Parameters of the Gaussians which fit the G and D lines of the Raman spectrum

Raman band	Position (cm^{-1})	Amplitude	Width (cm^{-1})
D-band	1343.7	14.6	107.4
	1377.7	44.1	347.6
G-band	1569.4	26.7	99.4
	1612.7	22.9	64.6

related somehow to the nature of the initial polymer comes from the fact that it is not observed in PPP-based carbon films heated at higher temperatures ($T > 750$ °C), which suggests the reminiscence of some PPP domains at lower temperature. However, the fact that the same peak is observed in carbon films prepared by pyrolyzed photoresists and now in our C-$LiFePO_4$ shows that it is not related to the existence of PPP and should be related to some aromatic rings preferentially formed, irrespective of the original polymer, in the course of the conversion of the carbon into disordered graphite. The fact that the original polymer is unimportant is also evident by the fact that the peak has been observed in many pyrolyzed photoresists, irrespective of the pyrolysis temperature, which could be as high as 1000 °C [105].

7.6.2 Quality of the Carbon Layer

Let us now analyze the other parameter of interest to characterize the carbon film, namely the intensity of the Raman lines. The ratios of the Raman intensities, defined as the integral of the Gaussians in Fig. 7.17 and Table 7.4, are $I_{1343.7}/I_{1377} = 0.102$, and $I_{1569}/I_{1612} = 1.789$. If we compare these intensities with the values determined for pyrolyzed photoresists [105], we find that the carbon coating of $LiFePO_4$ has the Raman spectrum of a carbon film deposited on silicon wafers by spin coating and then pyrolyzed at a temperature in the range 800–860 °C. The remarkable result is that our carbon film in the present case has been obtained by heating at 700 °C only. This temperature difference is critical for the electric conductivity of the carbon film since a pyrolyzed carbon sheet is highly resistive when the carbon film has been prepared at a pyrolysis temperature $T_p = 700$ °C; the resistivity decreases dramatically for higher pyrolysis temperatures to reach a sheet resistivity of 10 Ω-per-square at $T_p = 1000$ °C. We can then expect, on the basis of the Raman spectra, that the conductivity of the carbon in the carbon-coated $LiFePO_4$ is comparable to that of the carbon deposited by pyrolysis at 850 °C, which means reasonably good electrical conductivity. It explains the successful increase in the electronic conductivity that has been reported in the literature for carbon-coated $LiFePO_4$. Incidentally, it shows that if the efficiency of the carbon coating process on $LiFePO_4$ would not have been improved with respect to the pyrolysis technique, the result would have been a total failure because it is not possible to heat $LiFePO_4$ above 800 °C without damaging the material, resulting in the growth of inclusions of different chemical compositions as mentioned earlier in this work.

The width of the G-line at 1569 cm^{-1} is 99.3 cm^{-1}, characteristic of hydrogen-free amorphous carbon layers and markedly larger than the width of this line in the hydrogenated amorphous carbon(a-C:H) [128]. This result gives evidence that although there is some hydrogen in the carbon deposited on $LiFePO_4$ the H/C ratio is very small. This is actually consistent with the fact that the dramatic increase in the electronic conductivity after pyrolysis at temperatures above

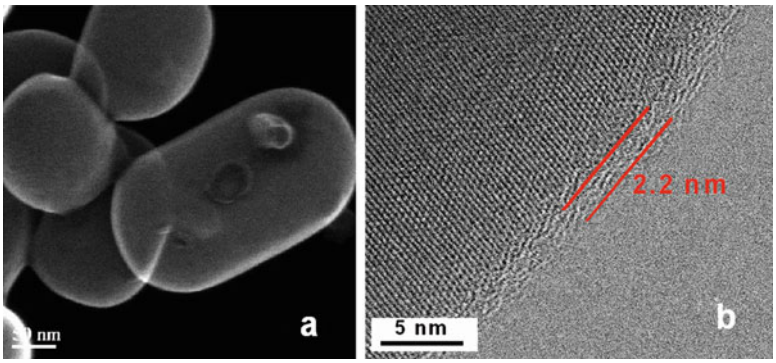

Fig. 7.18 HRTEM of carbon-coated LFP particles synthesized by hydrothermal method. The carbon coating, ~2-nm thick was realized using the lactose route

700 °C is due to a decrease in the H/C ratio [105]. Since the Raman spectrum is that of pyrolyzed carbon obtained at a significantly higher temperature of 800–860 °C, the ratio H/C must be the same, i.e., small. For the same reason, we expect the hardness of the carbon deposit is comparable to that of a-C films. However, the carbon films investigated in the literature are thick, so that the hardness is an intrinsic property that does not depend on the substrate. The average thickness of the carbon coat is in the range 3–5 nm at is can be seen in Fig. 7.18. This thickness is not large enough to guarantee that the adherence on the $LiFePO_4$ particles does not quantitatively affect the hardness of the a-C film since the strain interactions are long range, but it is large enough to insure that the order of magnitude of the hardness is unaffected. Although the hardness of the a-C:H films increases from 0 up to 20 GPa when the G-line width increases from 50 to 80 cm^{-1}, the hardness of a-C films with a G-line width 100 cm^{-1} is just in the middle, namely 10 GPa [127]. This hardness can be considered small. For instance, hardness up to 80 GPa has been reported for "diamond-like i-C" carbon-films. We therefore take the hardness of the carbon deposited on the $LiFePO_4$ to be small. This is actually expected, especially as the substrate on which the carbon is deposited is not flat as in the case of silicon wafers, but is the bent surface of nanoparticles. We can even consider that this a-C structure chosen by the carbon is an example of self-adaptation to allow for an adhesion on such a surface, which would be impossible with a strong hardness.

The D/G intensity ratio has been used in the literature to determine the size of the graphite particles in polycrystalline carbon. Some extension has often been made to use the same relation to determine the correlation length of the graphitic order. This extension is, however, a confusion already outlined in ref. [130]. The D/G intensity ratio gives the size of particles in the absence of any disorder and should not be confused with the loss of long-range order in amorphous materials. In disordered carbon, the information on the disorder is provided by the optical gap, according to the Robertson and O'Reilly law, which allows for an estimate of the number of carbon rings inside a local cluster [133]. In particular, the simultaneous study of

both the optical gaps and the Raman D/G ratio has revealed contradictions that show the D/G intensity ratio is determined by factors other than the graphitic cluster size in amorphous carbon [133]. This point is sometimes missed, and we can find recent analyses on C-$LiFePO_4$ that postulate that a decreasing D/G intensity ratio is related to the carbon disorder. In this same analysis, it is postulated that a decreasing D/G intensity also means decreasing sp^3/sp^2 ratio. This is not justified either, and it is not possible to evaluate the content of sp^2- and sp^3-coordinated carbon in a material that is dominantly graphitic because the intrinsic Raman intensity of the graphite spectrum is 50 times that of the diamond spectrum. Therefore, Raman spectroscopy is a sensitive tool to detect residual sp^2 bonds in diamond, but it is not a reliable test of the presence of sp^3 bonds in a dominantly graphitic carbon [127, 128]. In the carbon-coated samples investigated in this work, we did not investigate the optical gaps, but we note that the width (not the intensity) of the Raman lines is related to the degree of carbon disorder, which shows that in the present case, the carbon is amorphous. We do not know the sp^3/sp^2 ratio, but we know that the amount of sp^3 is small. In addition, this is always the case for disordered carbon. Even in diamond-like carbon films, the percentage of tetrahedral carbon is small [105]. In the present case, however, the percentage should be even smaller than in most cases because the position of the D and G lines are quite close to those of graphite. A bending of a graphite sheet is expected to induce some sp^3 character into the sp^2 bonds, which are planar. Therefore, the small amount of sp^3 gives evidence that the bending is small, i.e., that the radius of curvature is large at the scale of the bond length. This is consistent with the HRTEM images in Fig. 7.18, which show that the carbon coats the secondary particles with a typical radius of 100 nm and does not penetrate into the $LiFePO_4$ particles [41].

7.7 Effects of Deviation from Stoichiometry

In the previous section, we have found that a very small Li deficiency results in the formation of Li vacancies, with the conversion of Fe^{2+} in Fe^{3+} to maintain the Coulomb charge neutrality giving rise to the magnetic polaron. We thus have a solid solution $Li_{1-x}FePO_4$ where x is simply the concentration of magnetic polarons we had called c in this section. This, however, is true for a very small value of $x = 0.003$, which was the case explored above. For significantly larger values of x, the situation will be different (Fig. 7.19) because we have already mentioned that the delithiation processes in a two-phase system at temperatures of interest, which means that solution is no longer stable above some critical value ε of x that is larger than 0.003. The case $x \gg 0.003$ has been explored in ref. [134] by decreasing the amount of Li precursor in the synthesis process. Both inductive coupled plasma spectroscopy (ICP) and the Rietveld refinement of the XRD have shown that the chemical composition of the Li-deficient samples is $Li_{1-2x}Fe_xFePO_4$ or, in closed

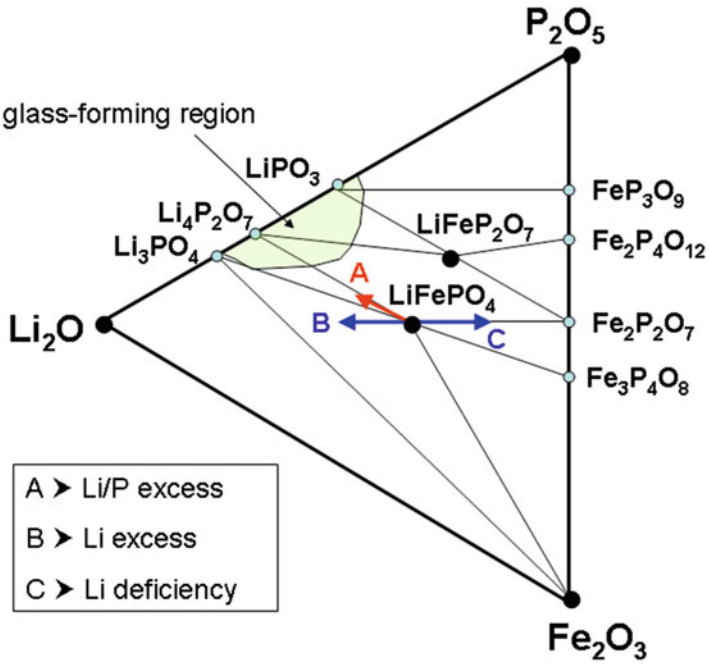

Fig. 7.19 Ternary phase diagram of off-stoichiometric $LiFePO_4$. The composition moves toward three directions such as *A* for Li/P excess, *B* for Li excess only, and *C* for Li deficient

form, $Li_{1-2x}Fe_{1+x}PO_4$, which identifies the defect generated by the Li-deficiency as the complex:

$$Fe^{\bullet}_{Li} + V'_{Li}, \tag{7.7}$$

in Kröger–Vink notation, in the range of x values $1 \leq x \leq 6$ % [134]. This is a neutral defect with an iron on a Li site, and a Li vacancy for charge compensation. The iron on Li site has also been observed in a synthesis of the material by hydrothermal process below 200 °C [135, 136]. The formation of the solid solution $Li_{1-2x}Fe_{1+x}PO_4$ is confirmed by the linear variation of the volume of the unit cell of the lattice with x. This sets an upper limit of 1 % for ϵ, in agreement with other estimates of this limit of stability for the solution $Li_{1-x}FePO_4$ [137]. At $x \geq 1$ %, this solution is unstable with respect to the solid solution $Li_{1-2x}Fe_xFePO_4$. In the delithiation process starting from $LiFePO_4$, the $Li_{1-2x}Fe_xFePO_4$ solution cannot be formed because the heavy iron ion cannot move on a Li site, and in this case a two-phase system is preferred. Yet the limit of solubility for the complex defect is 6.8 %. For larger deficiencies, the ICP and XRD analyses shows a decomposition in $Li_{1-2x}Fe_{1+x}PO_4$ with $x = 6.8$ %, and a $Fe_3(PO_4)_2$ impurity, known as sarcopside [134].

On the other hand, an excess of lithium does not result in the formation of any solid solution. Instead, it results in the formation of Li_3PO_4. This impurity has been detected by XRD, ICS, and also indirectly by magnetic measurements, because Li_3PO_4 has a magnetic contribution that is negligible with respect to $LiFePO_4$ so that the amount of Li_3PO_4 can be quantified by the measurement of the deficit in magnetization [134]. In addition, the lattice parameters of $LiFePO_4$ and the volume of the unit cell are independent of the amount of Li in excess, which is another proof that the Li in excess does not penetrate into the $LiFePO_4$ matrix, and simply forms Li_3PO_4 at the surface, and even form a Li_3PO_4 coating of the LFP particles. This difference between excess and deficiency of lithium implies that the energy of formation of the antisite defect iron on Li site is small, while that of Li on iron site is large so that this defect cannot be formed during the synthesis process so that the Li in excess can only precipitate under the form of Li_3PO_4.

The effects of an excess and a deficiency of lithium on the electrochemical properties are also very different. They are shown in Fig. 7.20.

The capacity falls dramatically with x in $Li_{1-2x}Fe_xFePO_4$, because one iron ion on a Li site blocks the whole Li channel in which it is located, and thus prevents all the Li^+ ions in this channel from contributing to the electrochemical process. On the other hand, in the case of Li excess, the Li_3PO_4 component simply does not participate to the electrochemical process. It just acts as an inert mass since the capacity is found equal to that of the $LiFePO_4$ part in $LiFePO_4 + xLi_3PO_4$. Sometimes, the deposition of a thin film of Li_3PO_4 is even made on purpose to protect the active particles. Recently, very thin films of Li_3PO_4 have also been deposited onto thin film Si anodes and it was found that these layers effectively suppress the SEI formation and dramatically improve the cycle performance of Si film anodes [138].

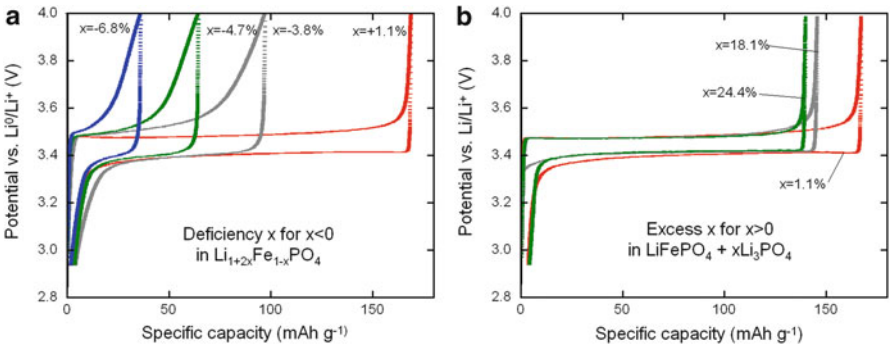

Fig. 7.20 *Left*: Electrochemical charge/discharge curves (second cycle) of LFP samples with Li deficiency defined by $Li_{1-2x}Fe_xFePO_4$. *Right*: The same for LFP samples with Li deficiency defined by $LiFePO_4 + xLi_3PO_4$

7.8 Aging of LFP Particles Exposed to Water

It has been well-known for decades that all the lithium-ion batteries need to be protected against humidity. The main reason is that lithium is very reactive with water according to the chemical reaction:

$$\mathrm{Li} + \mathrm{H_2O} \rightarrow \mathrm{LiOH} + \tfrac{1}{2}\,\mathrm{H_2}. \tag{7.8}$$

Lithium hydroxide (LiOH) is a corrosive alkali hydroxide. When crystallized, it is a white hygroscopic material. It is also soluble in water, a property that has been used to investigate aqueous lithium hydroxide as a potential electrolyte in Li-ion batteries with a $LiFePO_4$ cathode. Since the carbon coat is not a barrier for Li^+-ion transport (the reason for the success of C-$LiFePO_4$ as a cathode element of Li-ion batteries), we expect the reaction (7.8) to be effective, implying extraction of Li from the $LiFePO_4$ to interact with water. We have shown that this delithiation is the only effect that is observed after exposure to H_2O in air; moreover, it affects only the surface layer of the particles [139]. When a C-$LiFePO_4$ powder is dropped into water, part of the carbon that links the particles unties and floats to the surface, retaining with it some of the particles, while the major part sinks. In the present work, we investigate the effect of water on carbon-coated $LiFePO_4$ particles and analyze both the particles that have sunk and the floating part. We report that the water attacks the particles and that the carbon coat is not a protection because it detaches and is not watertight. We find that Fe is not the only element that reacts with the water, which contains also P and Li species after immersion of the $LiFePO_4$. A strong interaction between $LiFePO_4$ with H_2O molecules was not necessarily expected. After all, "parkerization" of iron is an industrial process that amounts to dropping iron into a hot bath with manganese phosphide, which results in the formation of a thin layer of $FePO_4$ at the surface. Since iron phosphate is hydrophobic, this layer protects the iron against oxidation and corrosion. Intuition would then have suggested that, upon immersion of $LiFePO_4$ in water, a delithiation in a thin layer at the surface would lead to the formation of a $FePO_4$ layer that would protect the particles against any other damage. Our investigations, however, show that the situation is slightly more complicated. Porcher et al. [140] have determined that the exposure of C-$LiFePO_4$ particles to water after some time results in the formation of a thin layer of Li_3PO_4 (few nm thick) at the surface of the particles as a result of migration of Fe into the water.

7.8.1 Water-Immersed LFP Particles

A series of LFP particles synthesized by solid-state reaction (SSR) and hydrothermal method (HTR) were characterized before and after immersion in water, using various techniques: XRD, Raman spectroscopy, magnetic measurements and

voltammetry. Zaghib et al. [139] reported the hygrometry of $LiFePO_4$ and its consequence on the aging of the electrochemical performance of this material upon exposure to the moisture of ambient atmosphere at the scale of a few months.

Magnetic measurements have been used to detect surface effects [69]. After immersion in water, the magnetic moment μ_{eff} of the sinking part increases by $0.04\,\mu_B$ in both SSR and HTR samples to reach $\mu_{eff} = 5.42$ and $5.40\,\mu_B$, respectively. These values of the magnetic moment are obtained very rapidly. For technical reasons, the shortest time in which the samples have been investigated is 15 min, where this limit for μ_{eff} was already achieved. The magnetic moment stays at this value even when the samples stay in water for longer times (up to 1 h). This increase of μ_{eff} in the short time limit is the signature of an oxidation of iron from Fe^{2+} to Fe^{3+} at the surface of the samples, the evidence of a delithiation of the surface layer. Quantification of this effect shows that the thickness of the delithiated surface layer is ~3 nm.

The voltammetry measurements of the SSR and HTR samples (sinking part) after immersion for 1 h in water are reported in Fig. 7.21. In these measurements, an initial 3.2 V working potential is applied. Then, the voltage was varied at the rate 1.25 mV per minute, as shown in the figure: a voltage increase up to 4 V is followed by a decrease to 2.2 V and an increase again up to 3.2 V. Besides the peak associated with Fe^{2+}, the part of the curve obtained by decreasing the voltage shows a secondary peak at 2.63 V that is characteristic of the Fe^{3+} in iron oxide (versus more than 3.5 V in phosphate) [56]. The presence of Fe^{3+} ions in both SSR and HTR samples confirms the delithiation of the surface layer evident in the previous sections. On the other hand, upon increasing the voltage again, this signal disappeared, which shows that the voltammetry curve of the samples before exposure to H_2O was recovered. Therefore, the surface layer was lithiated again during Li insertion, and the effect of immersion in water was reversed.

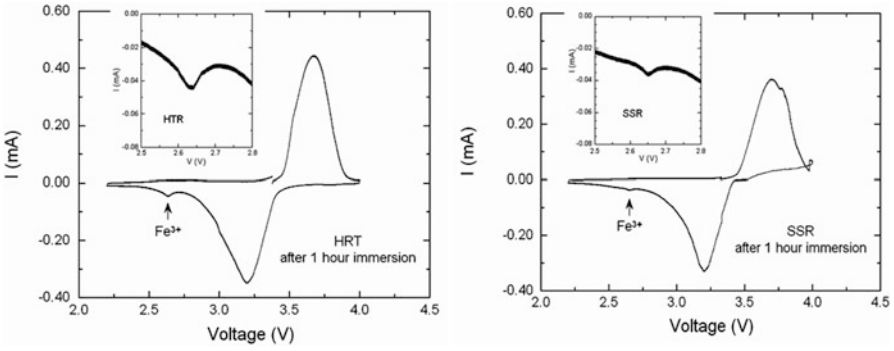

Fig. 7.21 Electrochemical performance of the C-$LiFePO_4$ (HTR sample)/$LiPF_6$-EC-DEC/Li cells at room temperature. The results are shown before immersion of this sample in water, and after immersion during 63 h, then dried during 48 h at 85 °C

7.8.2 *Long-Term Water-Exposed LFP Particles*

The same effect holds true for longer immersion times of a few days. In the following experiments, the samples were immersed during 63 h. Then, the samples were dried for 48 h at 85 °C [139]. The open-circuit voltage (OCV) decreased by 2.3 % on immersion in water. Since the OCV is directly related to the state of charge of the battery, it can be viewed as an indirect measurement of the delithiation rate of the battery. Indeed, this result is fully consistent with the 4 % delithiation rate deduced from the magnetization measurements, and the 1 and 3 % loss of Fe and P, respectively, during the immersion process, as estimated from the physical and chemical analyses. These results also confirm that the delithiation process is located in the surface layer. The effect of H_2O on the electrochemical properties was also evaluated by exposure of the sample to ambient air. This effect is illustrated for the HTR sample in Fig. 7.22, which shows the change of the capacity as a function of time at different temperatures in dry atmosphere and in ambient air (55 % relative humidity).

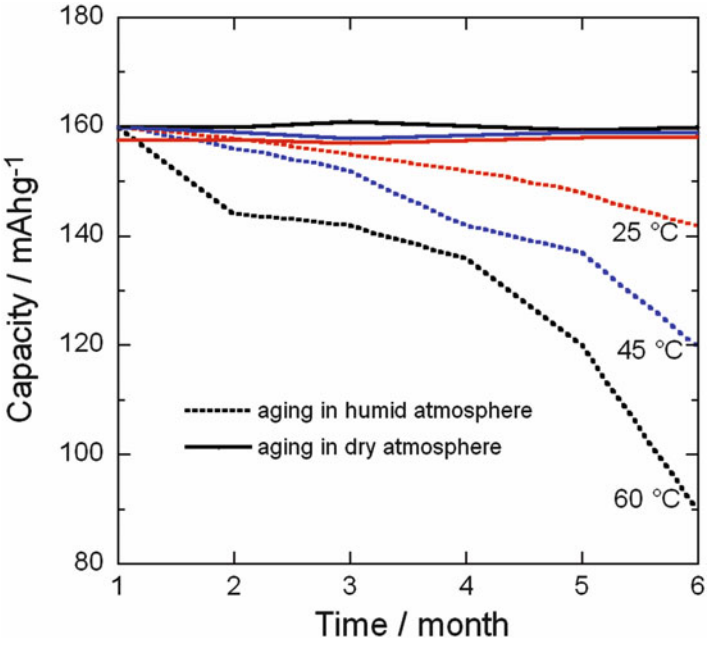

Fig. 7.22 Capacity of the C-$LiFePO_4$ (HTR sample)/$LiPF_6$-EC-DEC/Li cells as a function of time spent in dry atmosphere and in ambient atmosphere (55 % relative humidity), at three different temperatures. The temperatures at which the full curves (in dry atmosphere) have been obtained (in *color* in the web version) can be distinguished by the fact that they do not overlap, and the property that the lower the temperature, the higher the capacity is

7.9 Electrochemical Performance of LFP

7.9.1 Cycling Behavior

Here, we present an overview of the high-temperature performance for an optimized $LiFePO_4$ sample, i.e., carbon-coated (C-LFP). The coffee-bag cell was charged and discharged at *C*/8 for the first cycle followed by 12 cycles at *C*/4 with 1 h rest before each charge and discharge. This high-temperature test was made at 60 °C, which is the appropriate condition to investigate possible iron dissolution in nonaqueous electrolytes. Figure 7.23 shows the XRD patterns of the new generation of C-LFP after 200 cycles (47 days) at 60 °C. There is no change in the olivine structure after cycling at 60 °C. We observed Bragg lines with the same intensity as that for the pristine material. The capacity loss was below 3 % in 100 cycles for this optimized electrode material. A close examination was made for the detection of any iron dissolution that could occur after long-term cycling by post-mortem SEM analysis. No iron detected on the Li foil of the cell with optimized cathode, which remained intact after 100 cycles. In fact, this high performance was possible not only because of the optimized synthesis of the $LiFePO_4$ powders but also because of strict control of the structural quality of the materials. Similar results were observed in graphite//LFP Li-ion cell. EDX analysis of the graphite electrode confirms this last observation. No iron, even at the ppm level, was found in the electrolyte solution. Thus, all these data converge to the conclusion that the optimized $LiFePO_4$ is not soluble, even at 60 °C.

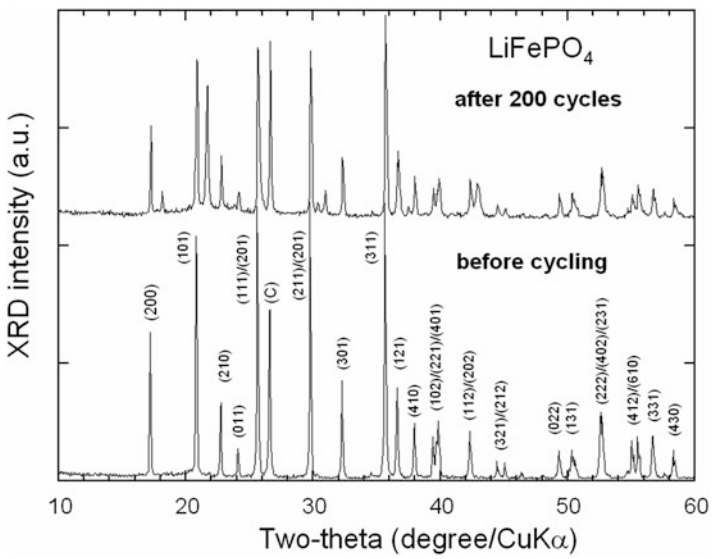

Fig. 7.23 XRD pattern of as-prepared $LiFePO_4$ material (*lower curve*) and positive electrode after 200 cycles (*lower curves*). *Bragg lines* are indexed in the *Pmna* S.G. Notice that the olivine framework remains intact after cycling at 60 °C

7.9.2 *Electrochemical Features vs. Temperature*

To study the capacity fade of $LiFePO_4$ at high temperature (60 °C), three different negative electrodes were used, namely lithium metal, graphite, and $Li_4Ti_5O_{12}$. A lithium metal anode gave exact capacity during charge–discharge process with Li metal excess 2.5 times to $LiFePO_4$ cathode material. Due to the large excess of lithium metal, it was difficult to observe the capacity fade with this anode at 60 °C. Graphite anode was 5 % of excess to $LiFePO_4$ cathode. This type of anode can detect easily the dissolution of iron because the passivation layer of the graphite anode is a ionic conductor and an electrical insulator; so the dissolution of iron from the cathode side to the anode increases the electronic conductivity of the passivation layer of graphite that results in the capacity fade of the cell. LTO has been used because no passivation layer formed at its surface, and also it is a zero strain material as the volume does not change with the lithium concentration during cycling. In this case, the anode has 0 % excess to the cathode that gives the high stability of the cycling and also prevents side reactions or reduction of electrolyte to the potential of LTO (1.5 V vs. Li^0/Li^+) (see also Chap. 3 regarding the formation of SEI, and the chapter devoted to the technology concerning the balance of a cell).

Figure 7.24a presents the electrochemical performance of cell in two configurations using LFP as positive electrode, aiming to better understand the role of the carbon coating on nanoparticles. In-situ high-resolution transmission electron microscopy synthesis observation of nanostructured $LiFePO_4$ [141] has given evidence of the following properties. Before carbon coating, the surface layer of the nanoparticles is strongly disordered. During the carbon coating process, the carbon coat is formed in the temperature range 600–700 °C, and a crystallization of the surface layer is observed simultaneously. To separate between the effect of the re-crystallization of the surface layer and the effect of the carbon coating on the electrochemical properties, a first coin cell has been prepared with LFP particles of average size 40 nm, which are not carbon-coated, but have been submitted to the same thermal treatment at 700 °C during 4 h used in the carbon coating process. Therefore, the crystallization of the particles has been allowed by annealing effect at 700 °C, but the particles are not coated because the carbon precursor was not added. A second coin cell has been prepared with the same particles that have been submitted to the same treatment in presence of the carbon precursor (lactose in the occurrence), so that they are carbon-coated. The same powder was used to avoid any size effect of the particles on the electrochemical particles, and the same electrolyte was used, namely 1 mol L^{-1} $LiPF_6$-EC-DEC, and the counter-electrode was Li in both cases. The voltage profiles of the two cells, measured at rate C/12 at room temperature are reported in Fig. 7.24a for comparison. The results show that the capacity of the cell prepared with LFP heated at 700 °C without carbon additive is very small despite the crystallization of the surface layer of the $LiFePO_4$ particles. The capacity only reaches ca. 55 % of its theoretical value, while, after carbon coating, the capacity of these particles is close to the theoretical value. This is indeed the evidence that, even in the case of nano-scaled particles, the carbon

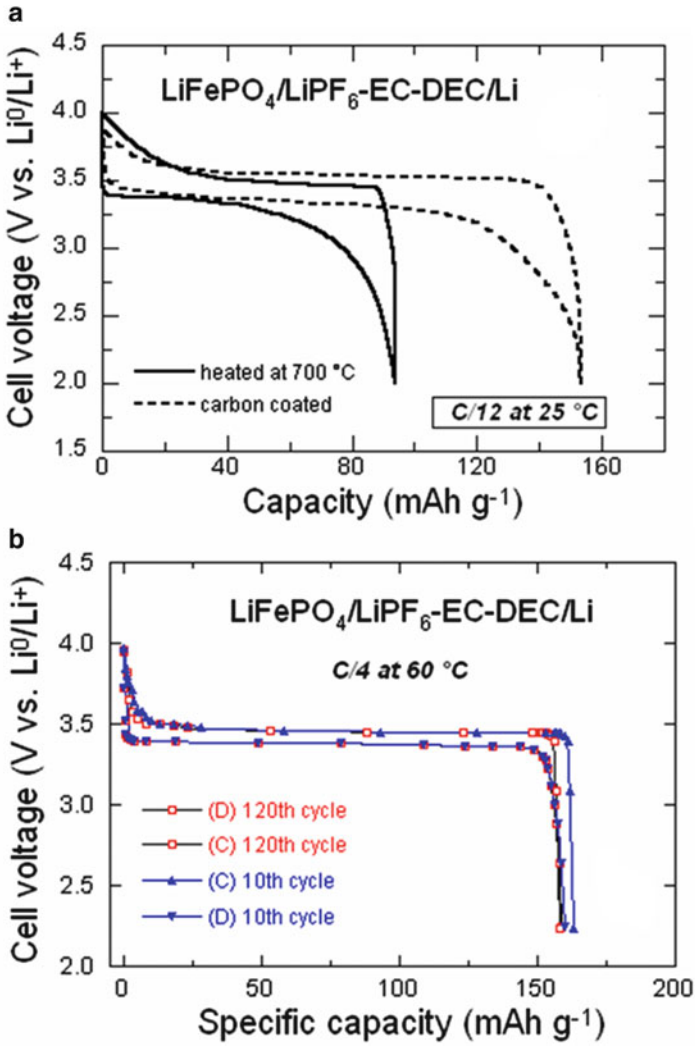

Fig. 7.24 (**a**) Electrochemical performance of the lithium-LFP coin cell cycled at 25 °C at *C*/12 rate. Cathode was (1) non-coated and heated at 700 °C (2) carbon-coated. (**b**) Voltage-capacity cycle for Li//LFP 18650-type cell. All the cells used 1 mol L^{-1} $LiPF_6$ in EC:DEC (1:1) as electrolyte

coating is mandatory to recover the full capacity of C-LFP, for the reasons we have recalled in the introduction. The small amount of carbon coating (<2 wt%) can be viewed as a 3 nm thick film on average, observed by TEM.

The typical electrochemical profile of the C-LFP/1 mol L^{-1} $LiPF_6$-EC-DEC/Li 18650-type cell cycled at 60 °C is shown in Fig. 7.24b. Under these experimental conditions, this type of C-LFP electrode can be cycled without significant capacity loss for over 200 cycles [142]. Actually, this result shows that the cycling life of the

cell is very long, even at 60 °C. Note that the calendar life would be reduced at this temperature with this choice of electrolyte, because the $LiPF_6$ tends to decompose at high temperature, but other electrolytes and salts tested with $Li_4Ti_5O_{12}$ are available, which avoid this problem [143]. Optimized particle size in the range 200–300 nm agrees well with the average diameter of grains L that validates the characteristic diffusion time $\tau = L^2/4\pi^2 D^*$, where D^* is the chemical diffusion coefficient of Li^+ ions in the $LiFePO_4$ matrix (typically 10^{-14} cm^2 s^{-1}) when compared with the experimental discharge rate up to 5*C*. The 10th and 120th cycle show a similar specific capacity of 160 mAh g^{-1}. These results illustrate the excellent electrochemical performance of the carbon-coated olivine material. The electrode can be fully charged up to 4 V, which is its most reactive state. This remarkable performance is attributed to the optimized carbon-coated particles and their structural integrity under a large current in the electrode. Even at such a high cycling rate, C-$LiFePO_4$ exhibits rapid kinetics of lithium extraction, and realizes most of its theoretical capacity (170 mAh g^{-1}). The discharge profile appears with the typical voltage plateau (at ca. 3.45 V vs. Li^0/Li^+) attributed to the two-phase reaction of the $(1-x)FePO_4 + xLiFePO_4$ system. The Peukert plots of cell cycled at 25 and 60 °C are shown in Fig. 7.25. The cells were cycled in the potential range 2.5–4.0 V. The discharge capacity and electrochemical utilization, i.e., the ratio discharge/charge, vs. cycle number are excellent for the C-$LiFePO_4$/$LiPF_6$-EC-DEC/Li cells. At 10*C* rate, these Li-ion cells provide coulombic efficiencies 85 % at 60 °C.

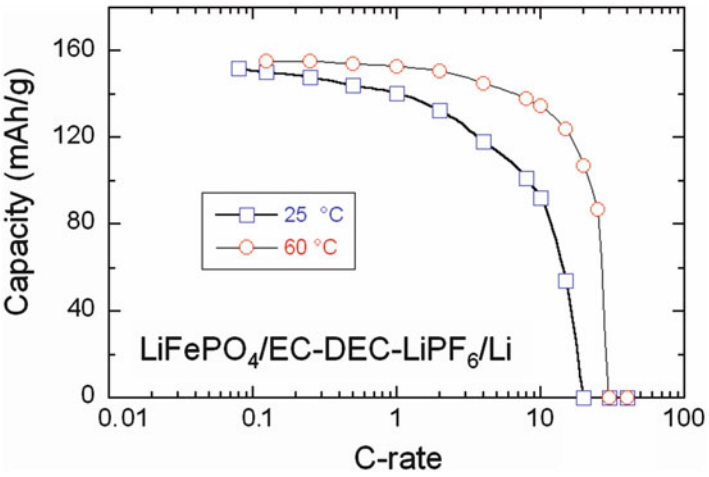

Fig. 7.25 Peukert plots of the C-$LiFePO_4$/$LiPF_6$-EC-DEC/Li cells as a function of the working temperature 25 and 60 °C

7.10 $LiMnPO_4$ as a 4-V Cathode

Since the redox potential of Mn is 4.1 V instead the 3.45 V of Fe, The theoretical energy density of $LiMnPO_4$ is larger, ad many efforts have been made to find a way to extract lithium from this material. Unfortunately, the electrical conductivity is even smaller than that of LFP, so that the electron path inside the particles must be reduced as much as possible. Even when they are carbon coated, the C-$LiMnPO_4$ particles are electrochemically active only when the size is reduced to circa 50 nm. Particles of this size have been successfully synthesized by different techniques, such as solid-state reaction in molten hydrocarbon [144], spray pyrolysis plus ball milling [145], and polyol synthesis [146, 147]. Another difficulty with this material comes from the fact that it is more difficult to coat $LiMnPO_4$ with carbon than the iron counterpart. The reason is that Fe interacts strongly with carbon, which is fortunate since it has many applications in biology. We believe that the result of this affinity is the facility with which a conductive carbon layer can be deposited on the surface of LFP. To the contrary, Mn has no particular affinity with Fe, and the carbon coating of $LiMnPO_4$ is much more difficult. Nevertheless, C-$LiMnPO_4$ has been successfully synthesized [148–150]. Still, the results are disappointing as the carbon coating was found to be less efficient than in the case of LFP. At best discharge capacity of 130–140 mAh g^{-1} could be achieved, but only when the particles are immersed in a huge quantity of conductive carbon, namely 20 wt% [151] or 30 wt% [145, 152]. However, only few % can be added to the powder in commercialized batteries, in which case the capacity of C-$LiMnPO_4$ is small [153]. This gives evidence that the carbon coat is not as conductive as in the case of C-$LiFePO_4$, for two reasons. First, $LiMnPO_4$ deteriorates when it is heated above 600–650 °C, while the temperature could be raised to 700 °C for the carbon coating of LFP. As we have noticed in the previous sections, the conductivity of the carbon increases strongly with the temperature of the deposit. The second reason os that, as there is no affinity between Mn and Fe, we suspect that the conductivity of the carbon deposited at the surface of $LiMnPO_4$ is the same as in the case of a carbon deposit on silicon wafers at the same temperature, and at 600 °C, this conductivity is small (we have shown in Sect. 7.6.2 that the conductivity of the carbon layer deposited on LFP at 600 °C is the same as that of carbon deposited on a silicon wafer at 800 °C). In such a case, the conductivity of the carbon coat of $LiMnPO_4$ is not sufficient to conduct efficiently the electrons to the current collector, inasmuch as the carbon coat is not uniform, and the large quantity of conductive carbon added to the powder is needed to do the job. This is at difference with C-LFP where the conductive carbon coat that percolates through the powder can drive the electrons to the current collector.

These difficulties met with $LiMnPO_4$ were the motivation for trying other strategies. One of them is to find a compromise between $LiFePO_4$ and $LiMnPO_4$ with the solid solution $LiMn_yFe_{1-y}PO_4$, and find the maximum value of y that can be used before the problems outlined for $LiMnPO_4$ will take over [154]. Indeed, the carbon coating is easier and C-$LiMn_yFe_{1-y}PO_4$ has been synthesized using different techniques [155–160]. The best compromise turns out to be $y \sim 0.7$ in which case the capacity is still 160 mAh g^{-1}, close to the theoretical value, and the voltage versus

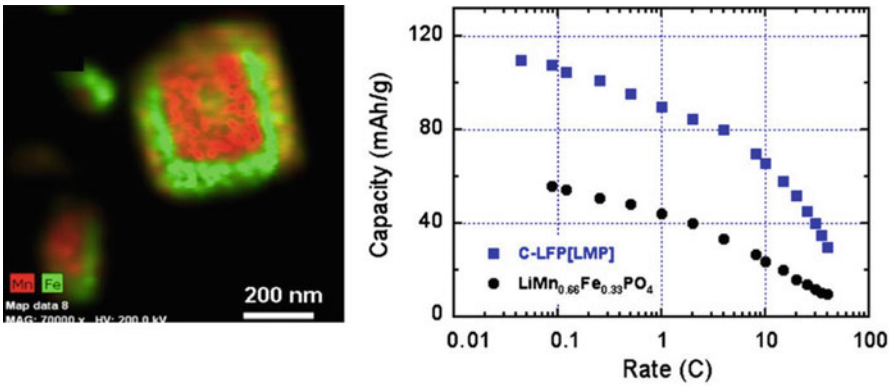

Fig. 7.26 *Left*: EDX map of a particle of $LiMnPO_4$ (core region) coated with a $LiFePO_4$ layer (green shell). *Right*: modified Peuckert plot obtained with these particles after carbon coating with Li counter-electrode (*squares*). The same result obtained with $LiMn_yFe_{1-y}PO_4$ particles of same size and same proportion of Mn and Fe: $y = 2/3$ (*full circles*), for comparison

capacity profile shows the two plateaus at 3.45 and 4.1 V characteristics of the Fe^{2+}/Fe^{3+} and Mn^{2+}/Mn^{3+} redox potentials vs. Li^0/Li^+, respectively, so that both Fe and Mn are active [157]. However, this capacity is delivered only at low *C*-rate. At 1*C* rate, the capacity is reduced to 120 mAh g^{-1}, due to the very small electrical conductivity of the polaron in Mn-rich $LiMn_yFe_{1-y}PO_4$.

Since it is easy to coat $LiFePO_4$ with conductive carbon, another strategy has been to coat $LiMnPO_4$ with a $LiFePO_4$ layer first, and then coat the $LiFePO_4$ layer with carbon. The carbon layer acts as a buffer that has two advantages: (1) it protects the $LiMnPO_4$ particles from the side reactions with the electrolyte, including the dissolution of Mn into the electrolyte that is a recurrent problem with Mn-based active particles. (2) The carbon coat is now deposited on $LiFePO_4$. A first attempt has been done successfully [161]. In this work, the $LiMnPO_4$ particles of size 200 nm were covered with a $LiMnPO_4$ layer. The layer, however, was not regular, with holes, and its average thickness was the order of 10 nm. Thus synthesized, the multi-composite particles contained 1/3 $LiFePO_4$ and 2/3 $LiMnPO_4$. The electrochemical measurements reported in Fig. 7.26 together with the results obtained with a solid solution $LiMn_yFe_{1-y}PO_4$ with the same ratio [Fe]/[Mn], i.e., $y = 2/3$, show that the multicomponent material is much more efficient than the solid solution, since both the capacity and the rate capability have been improved importantly.

7.11 Polyanionic High-Voltage Cathodes

The third family of 5-V cathode materials is based on poly-anionic frameworks with the olivine and olivine-related structures. Recently, a short review on these materials as cathodes for advanced lithium-ion batteries has been published [162]. Since the discovery of the electrochemical activity of $LiMPO_4$

(M = Fe, Mn) olivines with $Fe^{3+/2+}$ and $Mn^{3+/2+}$ redox potentials 3.5 and 4.1 V vs. Li^0/Li^+, respectively, and theoretical capacity 170 mAh g^{-1} [1], there are intensive researches to develop cathode materials with higher intercalation voltages over 4.5 V that deliver specific energy density as high as 800 Wh kg^{-1}. Candidates for high-voltage electrodes are polyanionic materials containing either nickel or cobalt (for structure description, see ref. [163]). Li$M$$PO_4$ compounds crystallize in the olivine structure belonging to the orthorhombic symmetry (*Pnma* S.G.). According to this structure, the lithium ions are distributed along channels and the ionic conductivity is a 1-D diffusion of the lithium ions along these channels. We know from the transport theory that any impurity or defect along a 1-D lattice can lead to localization. This is in essence the reason why the electrochemical properties are so sensitive to any structural defect, as we have shown in the previous section. Another common feature to all olivine materials is their poor electronic conductivity. Therefore, the active element of the cathode is always a nanocomposite C-Li$M$$PO_4$, which designates the nanoparticle with its carbon coat [164]. On the other hand, the ability to suppress thermal runaway of Li$M$$PO_4$ olivine frameworks is attributed to the high covalent feature of the P-O bonds in the tetrahedral (PO_4) units, which stabilizes the olivine structure and prevents oxygen release from the charged (delithiated) olivine materials up to 600 °C. However, it is still controversial for the delithiated state of $LiCoPO_4$ [165].

7.11.1 Synthesis of Olivine Materials

In this section, we consider the various techniques used for the growth of $LiNiPO_4$ (LNP) and $LiCoPO_4$ (LCP) isostructural olivines. Synthetic methods include solid state reaction with a final heat treatment at 775 °C for 48 h in argon [166–173], ball milling mixing carbon with the precursors [174], freeze-drying process assisted by formic acid [175], polyvinyl-pyrrolidone assisted sol–gel route [176], precipitation method [177], Pechini method [178, 179], polyol method using 1,2 propanediol and ethylene glycol [180], thin film deposition [181]. LCP powders were prepared by an original solid-state synthesis procedure based on the use of an alternative cobalt-containing precursor $CoNH_4PO_4$ and a lithium excess synthesis with carbon black as temporal dispersing agent, later eliminated as CO_2 [181]. The sol–gel technique in ethylene glycol [182, 183] appeared to be a simple method to prepare submicron size and uniform size distribution for carbon-coated LNP and LCP. Bramnik et al. [165] reported the effect of different synthesis routes on Li extraction–insertion from $LiCoPO_4$; samples prepared by SSR method at high temperature demonstrated unsatisfactory electrochemical performance [169], although improvement was observed by a synthetic approach based on the precursor $NH_4CoPO_4{\cdot}H_2O$ [181]. Surface modification of LCP particle was realized via a thin layer of Al_2O_3 deposited (~10 nm) by a sputtering method [177] or via a thin layer of LiFePO4 (~4 nm) by SSR method [173].

7.11.2 $LiNiPO_4$ as 5-V Cathode

Wolfenstine and Allen [166, 184] determined the Ni^{3+}/Ni^{2+} redox potential in $LiNiPO_4$ between 5.1 and 5.3 V. To overcome the problems with low electrolyte stability, a 1 mol L^{-1} $LiPF_6$ in tetramethylene sulfone electrolyte was used because of its high oxidative stability, around 5.8 V vs. Li^0/Li^+. These experimental values are in excellent agreement with the theoretical predictions [185–187]. The absence of redox peaks when LNP was heated under argon atmosphere suggests that this material has a very low intrinsic electrical conductivity. Therefore, additional treatments such as carbon coating are required for LNP to exhibit Li insertion/deinsertion. Actually, the electrical conductivity of $LiNiPO_4$ is 2–3 decades lower than that for $LiCoPO_4$ and $LiMnPO_4$ [188]. Magnetic anisotropy in Li-phosphates and the origin of their magneto-electric properties have been investigated [189, 190]. Magnetic properties of LCP and LNP show that antiferromagnetic M-O-M superexchange interactions couple the spins closely in planes parallel to (100) [111]. Local environment and bonding strength of cations were studied by vibrational spectroscopies, i.e., Raman and FTIR [190, 191]. The information available about the electrochemical performance of LNP is very limited. Few reports have shown that LNP is not electrochemically active if it is charged over 5.2 V [192–194]. However, Wolfenstine and Allen [166] mentioned the electrochemical activity of LNP powders prepared by SSR method under high purity argon with addition of a thin layer of carbon coat. The voltammetry displayed an oxidation peak at ~5.3 V and a reduction peak at ~5.1 V. Recently, Jaegermann et al. [195, 196] have reported the preparation of LNP and LCP by a Pechini assisted sol–gel process that provides material exhibiting redox peaks at ~5.2 and ~4.9 V vs. Li^0/Li^+. Mg-substituted LNP/graphitic carbon foams composite was also synthesized by the same method, which delivered a discharge capacity of 126 mAh g^{-1} at $C/10$ rate when substituting 0.2 Mg for Ni [197].

7.11.3 $LiCoPO_4$ as 5-V Cathode

In the early work by Amine et al. [184], it is demonstrated that Li can be reversibly removed from LCP at an average voltage of 4.8 V vs. Li^0/Li^+ with only a small contraction in the unit cell volume of the olivine lattice and the formation of a second olivine-like phase upon Li extraction from Li_xCoPO_4 with limited $\Delta x = 0.42$ lithium per formula unit. The electrochemical properties of $LiCoPO_4$ have been studied as a function of several parameters. Effects on the discharge capacity have and capability improvements include: mixing LNP-LCP to obtained solid solutions as cathodes [198], carbon coating [199, 200], effect of oxygen partial pressure on the discharge capacity [201]. Wolfenstine et al. have studied the structural evolution of $LiCoPO_4$ delithiated by the chemical oxidation [202]. Okada et al. [172] have shown that $LiCoPO_4$ exhibited the highest 4.8 V

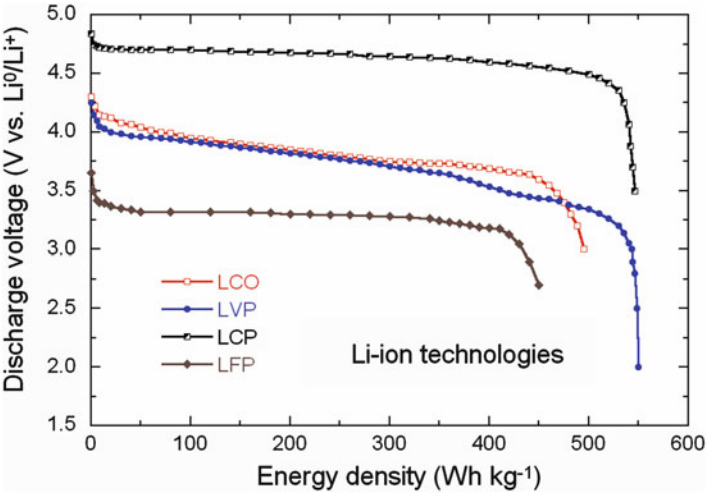

Fig. 7.27 Comparison of discharge curve of several cathode materials: $LiCoPO_4$ (LCP), $LiCoO_2$ (LCO), $LiFePO_4$ (LFP), and $Li_3V_2(PO_4)_3$ (LVP)

discharge plateau of 100 mAh g^{-1} after initial charging to 5.1 V giving an energy density of 480 Wh kg^{-1} comparable to that of $LiCoO_2$. Electrical conductivity of LCP by alloying (Co, Ni), (Co, Mn) [203], and doping [204]. Like any member of the olivine family, LNP has low electron conductivity, so that its use as the cathodic material is possible only under the form of the C-$LiCoPO_4$ composite [205]. Such composites can be discharged at the potentials of 4.7–4.8 V. However, their cyclability is very low, because the decomposition of liquid electrolyte occurs under charging in the potential range of 4.8–5.1 V simultaneously with oxidation of Co^{2+} to Co^{3+}. The initial discharge capacity of C-$LiCoPO_4$ is close to the theoretical one that is about 167 mAh g^{-1}. Figure 7.27 compares the discharge curves of various lithium cells including $LiCoPO_4$ (LCP), $LiCoO_2$ (LCO), $LiFePO_4$ (LFP), and $Li_3V_2(PO_4)_3$ (LVP).

The phase transitions occurring upon lithium insertion–extraction of $LiCoPO_4$ have been investigated by several groups [206]. A two phase mechanism was confirmed by in situ synchrotron diffraction [168]. An amorphization of the phosphate was observed after electrochemical or chemical oxidation [204]. Nagayama et al. [206] suggested from X-ray absorption spectroscopy a hybridization effect between the Co 3*d* and O 2*p* orbitals and the polarization effect introduced by Li ions. Bramnik et al. [171] revealed the appearance of two orthorhombic phases upon electrochemical Li extraction. The $LiCoPO_4$ and the Li deficient phases, $Li_{0.7}CoPO_4$ and $CoPO_4$, are responsible for the two voltage plateaus at 4.8 and 4.9 V vs. Li^0/Li^+. The hedgehog-like $LiCoPO_4$ microstructures in the size of about 5–8 μm are composed of large numbers of nanorods in diameter of ca. 40 nm and length of ca. 1 μm, which are coated with a carbon layer of ca. 8 nm in thickness by in situ carbonization of glucose during the solvothermal reaction. As a 5-V positive

electrode material for rechargeable lithium battery, the hedgehog-like $LiCoPO_4$ delivers an initial discharge capacity of 136 mAh g^{-1} at $C/10$ rate and retains its 91 % after 50 cycles [168]. Surface modification of LCP particles provides a satisfactory cyclability for $LiCoPO_4$ to be used as a 5 V cathode material [177]. The capacity retention of Al_2O_3-coated LCP was 105 mAh g^{-1} after 50 cycles at $T = 55$ °C. Jang et al. [173] claimed that $LiFePO_4$ coated LCP particles prepared by SSR method (~100–150 nm) show improved battery performance with an initial discharge capacity of 132 mAh g^{-1} but did neither mention the C-rate nor the current density. Another problem comes from the fact that the thermal stability of the metal oxides is known to be a decreasing function of the voltage of the redox potential [207]. In the case of LMP with M = Fe, Mn, the redox potential is still small enough so that the covalent feature of the P-O bonds in the tetrahedral (PO_4) units is sufficient to stabilize the olivine structure and prevents oxygen release from the charged (delithiated) olivine materials up to 600 °C. For M = Ni, Co, however, the 5 V redox potential is so large that the P-O bonding may be not sufficient to stabilize the structure. In particular, a thermal instability has been reported in the charged (i.e., delithiated) state of $LiCoPO_4$ [165]. Both olivine-like phases Li_zCoPO_4 ($z = 0.6$) and $CoPO_4$ appearing during the delithiation of $LiCoPO_4$ are unstable upon heating, and decompose readily in the range 100–200 °C. The decomposition of lithium-poor phases leads to gas evolution and the crystallization of $Co_2P_2O_7$. Incorporation of lithium bis(oxalato)borate (LiBOB) as additive in conventional electrolyte solutions enhances the electrochemical performance of LCP electrode [208]. Nevertheless, $LiCoPO_4$ is a good example of the conflict that is met with Li-ion batteries: more energy density means less thermal stability and is thus detrimental to safety.

7.12 NASICON-Like Compounds

NASICON (for Na^+ SuperIonic CONductor)-related compounds have been studied as cathode materials for Li-ion batteries due to the high Li^+ mobility and acceptable discharge capacities [96]. Table 7.5 details the relevant characteristics of several NASICON-related cathode materials. Note that the most useful redox potentials are $Fe^{2+/3+}$ in a sulfate framework and $Fe^{3+/4+}$ in a phosphate framework [209].

Table 7.5 Properties of lithium-insertion compounds with the NASICON-type structure

Compound	Structure	Redox couple	Potential (V)	Li uptake
$Fe_2(SO_4)_3$	R/M	$Fe^{3+/2+}$	3.6	2
$V_2Fe_2(SO_4)_3$	R	$V^{3+/2+}$	2.6	1.8
$LiTi_2(PO_4)_3$	R	$Ti^{4+/3+}$	2.5	2.3
$Li_{3-x}Fe_2(PO_4)_3$	M	$Fe^{3+/2+}$	2.8	1.6
$Li_{3-x}FeV(PO_4)_3$	M	$V^{4+/3+}$	3.8	1.6

R rhombohedral ($R\bar{3}$ S.G.), *M* monoclinic ($P2_1/n$ S.G.)

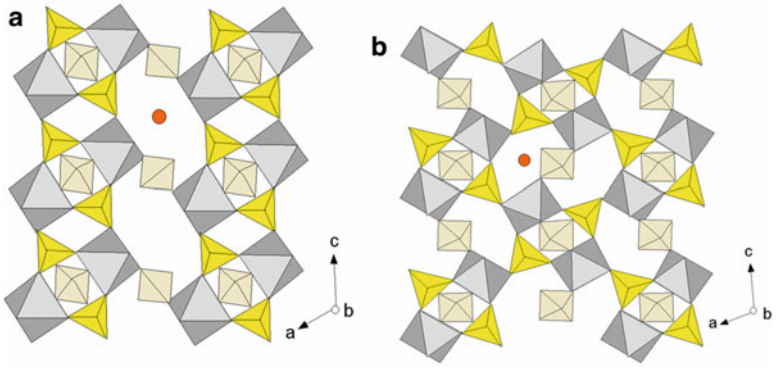

Fig. 7.28 Schematic representation of NASICON-type structure (**a**) rhombohedral and (**b**) monoclinic

As pointed out by Cushing and Goodenough [209], the NASICON-related compounds with the highest ionic mobility possess rhombohedral ($R\bar{3}$) symmetry [210]. The $M_2(XO_4)_3$ framework is built of $(XO_4)_n$ ($X = Si^{4+}$, P^{5+}, S^{6+}, Mo^{6+}, etc.) tetrahedral corner-linked to octahedral-site M^{m+} (M = transition metal). The alkali ions can occupy two different sites. At low alkali content $x \leq 1$ in $A_xM_2(XO_4)_3$), an octahedral site, $A1$, is selectively occupied (Fig. 7.28). With $x > 1$, the alkali ions are randomly distributed among the $A1$ and three 8-coordinate sites, $A2$. The open, 3-D nature of the structure allows easy migration of the alkali ions between $A1$ and $A2$, and the exceptional ionic mobility of the alkali ions is well documented [211]. Li insertion into NASICON-like frameworks were experimented into hexagonal $Fe_2(SO_4)_3$ and compared with that for isostructural $Fe_2(MoO_4)_3$ and $Fe_2(WO_4)_3$. These substances contain Fe^{3+} ions in the octahedral sites, which allows insertion of 2Li per formula unit by converting the Fe^{3+} to Fe^{2+} ions. $Li_xFe_2(SO_4)_3$ had an open-circuit voltage $V_{oc} = 3.6$ V whereas $Fe_2(MoO_4)_3$ and $Fe_2(WO_4)_3$ have $V_{oc} = 3.0$ V. The voltage profile, V_{oc} vs. x, of $Li_xFe_2(SO_4)_3$ occurs as a flat plateau due to a dispersive structural change between the hexagonal $Fe_2(SO_4)_3$ and the orthorhombic $Li_2Fe_2(SO_4)_3$ insulating phases. The insertion mechanism occurs as a front mobility between the Li-rich and Li-poor phases giving a reversible capacity loss that increased with the C-rate. From these studies several conclusions can be drawn: the mixed-valent electronic transport through a polyanion is not too small, the position of the $Fe^{3+/2+}$ redox energy is lowered by the counter-cation of the (XO_4) units, and finally this energy of the octahedral site is a function of the cation X. Consequently, V_{oc} is increased with the weak covalency of the Fe-O bonds due to the more acidic (XO_4) groups. With the greater acidity of the $(SO_4)^{2-}$ anion, the voltage raises by 0.8 V with respect to the case of the $(PO_4)^{3-}$ anion. Contrary to the spinel frameworks, the redox energies in the NASICON lattice do not vary with the location of Li^+ ions in the interstitial sites.

At room temperature $Li_3Fe_2(PO_4)_3$ can be stabilized in one of the three distinct crystallographic structures. According to Bykov et al. [212], they are monoclinic

α-$Li_3Fe_2(PO_4)_3$ ($P2_1/n$ S.G.), rhombohedral Nasicon-like ($R\bar{3}$ S.G.) and γ-$Li_3Fe_2(PO_4)_3$ orthorhombic (*Pcan* S.G.) lattice that symmetry depending on the technique of preparation [213]. The rhombohedral phase crystallizes with the Nasicon-like ($Na_3Zr_2Si_2PO_{12}$) structure [214]. Such polyanionic framework structures containing an interconnected interstitial space are potentially fast ionic conductors, especially if the energetically equivalent sites are connected. Recent magnetic susceptibility and the Mössbauer effect studies of α-$Li_3Fe_2(PO_4)_3$ (monoclinic phase) by Goni et al. [215] showed that the magnetic Fe(III) system undergoes an antiferromagnetic phase transition below $T_N = 29$ K, while the magnetic structure of the rhombohedral phase has been reported by Anderson et al. [216]. The γ-form $Li_3Fe_2(PO_4)_3$ material was prepared using a standard wet chemical method (sol–gel) using the nitrate route [217, 218]. The elementary cell parameters are $a = 8.827$ Å, $b = 12.3929$ Å and $c = 8.818$ Å. The framework structure consists of FeO_6 octahedra and PO_4 tetrahedra linked through common corners forming [$Fe_2P_3O_{12}$] lantern units. The asymmetric unit cell contains three PO_4 tetrahedra and two FeO_6 octahedra. The lithium ions occupy the 8*d* Wyckoff sites forming infinite chains of the Li-O-Fe-O-Li type of edge-sharing LiO_4 tetrahedra and FeO_6 octahedra. Figure 7.29 shows the discharge–charge curves of the Li//$Li_3Fe_2(PO_4)_3$ cell. Electrochemical insertion of Li^+ into $Li_3Fe_2(PO_4)_3$ leads to $Li_5Fe_2(PO_4)_3$ for a complete iron reduction ($Fe^{3+} \rightarrow Fe^{2+}$) delivering a theoretical capacity 128 mAh g^{-1}.

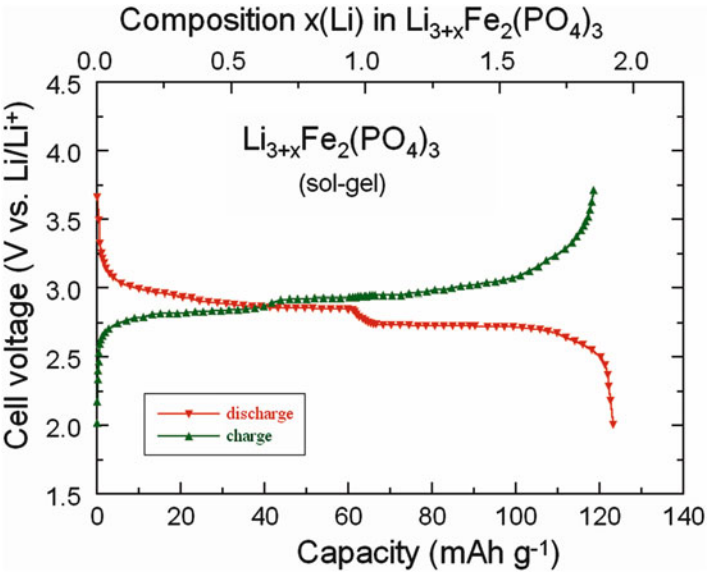

Fig. 7.29 The discharge–charge curves of the Li//$Li_3Fe_2(PO_4)_3$ cell. The cathode material prepared by sol–gel method has the γ-form

7.13 The Silicates Li_2MSiO_4 (M = Fe, Mn, Co)

According to their formula, this family of materials can theoretically exchange two electrons per transition ion. This has been the motivation of many investigations, following the pioneering report of the Armand's group showing the reversible lithium extraction in Li_2FeSiO_4 [98, 219]. Like in the case of $LiFePO_4$, the problem of the low electrical conductivity has been solved by reducing the size of the particles to the nano-range, and carbon coating [220]. Even under such conditions, the capacity is low, i.e., 91 and 78 mAh g^{-1}, at rates higher than 1C; it can be obtained at 5 and 10C rate for particles of 40–80 nm in thickness [221]. At lower rate, however, the performance is improved. The capacity retention reaches 135 mAh g^{-1} at rate C/16, and is stable over 40 cycles [222]. Porous Li_2FeSiO_4/C nanocomposite with 8.06 wt% carbon showed a capacity of 176.8 mAh g^{-1} at 0.5C in the first cycle and a reversible capacity of 132 mAh g^{-1} at 1C ($1C = 160$ mA g^{-1}) in the 50th cycle [223]. If the voltage range extends from 1.5 to 4.8 V, a capacity of 220 mAh g^{-1} has been reported at low current density 10 mA g^{-1}, but after three cycles, the capacity was already decreased to circa 190 mAh g^{-1} [224], because the deintercalation of the second lithium (Fe^{3+}/Fe^{4+} redox couple) is predicted to occur at a very high voltage (4.7 V vs. Li^0/Li^+) with severe structural distortions, being detrimental to reversible cycling of the second lithium ion. Therefore, in practice, only one Li can be extracted reversibly in Li_2FeSiO_4.

Li_2FeSiO_4 has a rich polymorphism, due to many variations between the connectivity of tetrahedral sites occupied by Li^+, Si^{4+} , and M^{2+} that have been revealed by electronic structure calculations [225]. Depending on the synthesis conditions, the *Cmma* space group with $a = 10.66$ Å, $b = 12.54$ Å, $c = 5.02$ Å has been obtained [226] and monoclinic symmetry with $a = 8.23$ Å, $b = 5.02$ Å, $c = 8.23$ Å, $\beta = 99.20°$ [227, 228] have been obtained for Li_2FeSiO_4 annealed at 800 °C, while another polymorph has been found upon quenching from 900 °C to room temperature [229]. All of the polymorphs have comparable energies [225], which explain that the material is difficult to synthesize in a single phase. This, however, is not necessarily dramatic, because they have very similar electrochemical properties. On the other hand, impurities can poison this material and affect the electrochemical properties. In particular, it is difficult to avoid lithium-silicate phases such as Li_2SiO_3 or, just like in the case of $LiFePO_4$, the partial oxidation of Fe^{2+} into Fe^{3+}, and many synthesis processes have been used for this purpose: direct precipitation in H_2O [226], hydrothermal reaction [230, 231], Pechini sol–gel [230, 232], hydrothermal-assisted sol–gel [221], ceramic synthesis [229], microwave-assisted solvo-thermal process [233], spray pyrolysis [234].

The best results have been obtained with porous C-coated nanoparticles prepared by sol–gel process [235]: at C/5 rate, the initial charge and discharge capacities were 164 and 134 mAh g^{-1}. Starting from 53th cycle, the charge/discharge capacities continuously increase and reach 157.7 and 155.0 mAh g^{-1} in the 190th electrochemical cycle. The explanation for the increase of capacity upon cycling

was attributed to the fact that active materials in the pores can be gradually activated during electrochemical cycling. We recover here a general property that is also encountered in Chap. 10 devoted to negative electrodes, namely the important role of the porosity to gain in electrochemical performance, and the possibility to increase the capacity upon cycling associated with the increasing number of active sites. Another important parameter is the aggregation of the nanoparticles. In the present case, the primary particles of size ~100 nm were agglomerated in secondary particles of 5 μm. Indeed, we have found in the study of $LiFePO_4$ powders that agglomeration improved the electrochemical performance when the secondary are large enough to increase the tape density, but small enough to let the electrolyte penetrate into the secondary particles [236]. Since the conductivity is very small due to the isolated FeO_4 tetrahedra and tightly bound Li^+ cations in tetrahedral sites, most of the data reported in the literature have been measured at 60 °C [220, 232, 237] to improve both the electrical and ionic transport. However, the data in ref. [235] have been obtained at room temperature, which outlines the performance of this electrode.

Nevertheless, Li_2FeSiO_4 is not yet competing with $LiFePO_4$ for instance, for several reasons. The rate capability is smaller, and so is the operating voltage. If the first charge plateau is located at 3.1 V, the first discharge plateau is located at only 2.8 V vs. Li^0/Li^+, and it is this lower operating voltage that is usually observed in further cycles. This lowering is attributed to a structural rearrangement in which some of the Li^+ ions and Fe atoms become interchanged within their respective crystallographic sites [234, 238]. In addition, this material is sensitive not only to moisture, like $LiFePO_4$, but also to oxygen, so that it must be stored in inert atmosphere [239].

To increase the operating voltage, Fe can be substituted for Mn. Li_2MnSiO_4 has also a polymorphism [239, 240]. However, both of them have a very poor conductivity, although differences in intrinsic Li mobility between the monoclinic and orthorhombic polymorphs are expected [241]. The operating voltage is 4.2 and 4.4 V for the first and second lithium [242], but until recently the electrochemical properties of Li_2MnSiO_4 were very bad, with an important loss of crystallinity occurring during the first oxidation [239]. The situation encountered here is thus the same as the situation met when substituting Fe for Mn in $LiFePO_4$, and has presumably the same origin, namely a structural instability linked to the Jah–Teller Mn^{3+} ions. Therefore, attempts have been made to use the same strategy as in the olivine family, i.e., try an only partial substitution of Fe for Mn to find a compromise to stabilize the unstable local environment of Mn^{3+} in tetrahedral coordination by Fe [243–245]. However, even if this substitution improved the stability, the overall change in oxidation state did not exceed more than 0.8 electron per both transition metals in $Li_2Fe_{0.8}Mn_{0.2}SiO_4$ [246]. Recently, however, the interest in Li_2MnSiO_4 has been renewed by a new synthesis process [247]. To avoid the problem of the Jahn–Teller distortion, the particles must be not only nano-sized but also porous. For this purpose, the authors started with monodispersed $MnCO_3$ nanocubes were prepared through a water-in-oil microemulsion process under ambient conditions. $MnCO_3$ @ SiO_2 core–shell nanocubes were then obtained via

a modified Stöber silica coating recipe under mild wet-chemistry conditions [248]. The next step is to mix the $MnCO_3$ @ SiO_2 nanocubes with lithium acetate (LiAc) and lactose, followed by calcination under inert atmosphere. The resulting MnO would further react with SiO_2 and LiAc in the shells as templates to produce Li_2MnSiO_4 nanoboxes, and CO_2 gas would be released to generate pores in the walls of the hollow structures [249]. Meanwhile a carbon coating would be formed in situ on the surface of Li_2MnSiO_4, resulting from the carbonization of lactose. The result was then phase-pure Li_2MnSiO_4 @ nanoboxes. Finally, under magnetic stirring, 100 mg of these nanoboxes were added to 10 mg of glucose, 10 mg of cellulose acetate, and a graphene oxide (GO) suspension prepared by ultrasonically dispersing 5 mg of GO in 2.5 mL water. Finally, the water was removed bu vacuum-rotary evaporation. The resulting dried powder was annealed in Ar at 400 °C for 4 h to form porous Li_2MnSiO_4 @ C/reduced graphene oxide particles about 200 nm in size, with Li_2MnSiO_4 crystallized in a pure $Pmn2_1$ phase without any impurity, and a pore size of 4 nm. The electrochemical tests performed at 40 °C at very low 0.02C rate in the voltage range 1.5–4.8 V showed that this product still delivers a capacity of 220 mAh g^{-1} after 50 cycles [248]. On the one hand, the nano-sized plus porosity allowed to overcome the problem of the structural instability associated with Mn^{3+}, and the carbon coating plus the RGO could solve the problem of the conductivity, at least at very low C-rate, at a mild temperature of 40 °C. Still the stability over 50 cycles is far from requirements for commercialization, and the performance will presumably decrease at higher C-rates. Nevertheless, this novel synthesis process leading to an important progress for this material could be useful to enhance the electrochemical properties of other cathode elements as well. It should be noted, however, that the preparation process involves many steps, so that the price will be another obstacle to industrial production (a problem that is also encountered in Chap. 10 devoted to the anodes).

7.14 Summary and Outlook

An important part of this chapter is a thorough report on $LiFePO_4$ synthesized by several methods since this compound is winning an important part of the market of Li-ion batteries. We have followed a logical structure starting with synthesis, crystallographic properties, the characterization of the crucial carbon-coating layer at the surface of LFP particles, magnetic properties, reaction with water and humidity, and finally electrochemical performance of optimized material at room temperature, 60 °C, and in full Li-ion cells. Depending of the synthesis procedure, the fundamental properties can be modified because of impurities poisoning this material. These impurities are identified, and quantitative estimate of their concentrations is deduced from the combination of analytical methods. The most powerful technique used so far is the SQUID magnetometry, which is very sensitive to detect Fe^{3+} ions. Note that such iron-based impurities may be at the origin of iron dissolution in the electrolyte producing short circuit of the battery. Thus an

optimized preparation provides materials with carbon-coated particles free of any impurity phase, insuring structural stability and electrochemical performance. Raman scattering spectroscopy is the tool to probe the quality of the carbon layer, especially its degree of graphitization.

The structural properties have been correlated with the electrochemical performance of the positive electrode materials. It appears that a severe control of synthesis conditions is needed to obtain materials with good performance under high current density.

The product reacts with water, but not with dry atmosphere, so that storage of the LFP powder in a dry chamber at 5 % relative humidity is needed, which is sufficient to guarantee that the product does not age before manufacturing the battery. The carbon coat is not protective. Exposure to humidity induces delithiation of the surface layer. However, the resulting $FePO_4$ layer that is formed within minutes of exposure to humidity is very protective, so that the damage remains limited to the surface layer (about 3 nm thick) unless the time of exposure to humid atmosphere is very large (months).

All these researches justify the use of the $LiFePO_4$ material as a cathode element in new generation of lithium secondary batteries operating for powering hybrid electric vehicles and full electric vehicles, and also to store the energy from windmills or photoelectric plants to solve the intermittence problem on smart grids.

Only the phosphate polyanion has been considered here. For completeness, we can also mention a pyrophosphate, $Li_2CoP_2O_8$, considered as a 4.9 V cathode [218]. This pyrophosphate crystallizes in the monoclinic structure ($P2_1/c$ S.G.), in which Li occupies five sites; two are tetrahedrally coordinated, one forms bipyramidal sites, and two Li share them occupancy with Co bipyramids. The material synthesized using a two-step solid-state method delivered a discharge capacity of ca. 80 mAh g^{-1} at $C/20$ rate, which illustrates the superiority of the phosphate compounds as active cathode elements. The fluoro-polyanionic compounds, however, deserve a special attention, and the next chapter is devoted to them.

In addition to the phosphate polyanion compounds we have considered, we can also mention for completeness a pyrophosphate, $Li_2CoP_2O_8$, considered as a 4.9 V cathode [218]. This pyrophosphate crystallizes in the monoclinic structure ($P2_1/c$ S.G.), in which Li occupies five sites; two are tetrahedrally coordinated, one forms bipyramidal sites, and two Li share them occupancy with Co bipyramids. The material synthesized using a two-step solid-state method delivered a discharge capacity of ca. 80 mAh g^{-1} at $C/20$ rate, which illustrates the superiority of the phosphate compounds as active cathode elements. Among the other XO_4 ($X = S, Si, Mo, W$)-based compounds, we have selected the silicates $X = Si$, because recent progress revive the interest in these materials; a more exhaustive review on other polyionic compounds can be found in a review [250]. The fluoro-polyanionic compounds, however, deserve a special attention, and the next chapter is devoted to them.

References

1. Padhi K, Nanjundaswamy KS, Goodenough JB (1997) Phospho-olivines as positive-electrode materials for rechargeable lithium batteries. J Electrochem Soc 144:1188–1194
2. Padhi K, Nanjundaswamy KS, Masquelier C, Okada S, Goodenough JB (1997) Effect of structure on the Fe^{3+}/Fe^{2+} redox couple in iron phosphates. J Electrochem Soc 144:1609–1613
3. Huang H, Yin SC, Nazar LF (2001) Approaching theoretical capacity of $LiFePO_4$ at room temperature at high rates. Electrochem Solid State Lett 4:A170–A172
4. Dominko D, Gaberscek M, Drofenik J, Bele M, Jamnik J (2003) Influence of carbon black distribution on performance of oxide cathodes for Li ion batteries. Electrochim Acta 48:3709–3716
5. Ravet N, Goodenough JB, Besner S, Simoneau M, Hovington P, Armand M (1999) Improved iron based cathode material. In: Proceedings of the 196th ECS meeting, Honolulu, Oct 1999, extended abstract n° 127
6. Ravet N, Chouinard Y, Magnan JF, Besner S, Gauthier M, Armand M (2001) Electroactivity of natural and synthetic triphylite. J Power Sourc 97:503–507
7. Bewlay SL, Konstantinov K, Wang GX, Dou SX, Liu HK (2004) Conductivity improvements to spray-produced $LiFePO_4$ by addition of a carbon source. Mater Lett 58:1788–1791
8. Chen Z, Dahn JR (2002) Reducing carbon in $LiFePO_4$/C composite electrodes to maximize specific energy, volumetric energy and tap density. J Electrochem Soc 149:A1184–A1189
9. Ravet N, Besner S, Simoneau M, Vallée A, Armand M, Magnan JF (2005) Electrode materials with high surface conductivity. US Patent 6,962,666, 8 Nov 2005
10. Ait-Salah A, Mauger A, Julien CM, Gendron F (2006) Nanosized impurity phases in relation to the mode of preparation of $LiFeO_4$. effects. Mater Sci Eng B 129:232–244
11. Herle PS, Ellis B, Coombs N, Nazar LF (2004) Nano-network electronic conduction in iron and nickel olivine phosphates. Nat Mater 3:147–152
12. Ait-Salah A, Dodd J, Mauger A, Yazami R, Gendron F, Julien CM (2006) Structural and magnetic properties of $LiFePO_4$ and lithium extraction effects. Z Allg Inorg Chem 632:1598–1605
13. Ravet N, Gauthier M, Zaghib K, Goodenough JB, Mauger A, Gendron F, Julien CM (2007) Mechanism of the Fe^{3+} reduction at low temperature for $LiFePO_4$ synthesis from a polymeric additive. Chem Mater 19:2595–2602
14. Ellis BL, Lee KT, Nazar LF (2010) Positive electrode materials for Li-ion and Li-batteries. Chem Mater 22:691–714
15. Fergus JW (2010) Recent developments in cathode materials for lithium ion batteries. J Power Sourc 195:939–954
16. Zaghib K, Mauger A, Julien CM (2012) Overwiew of olivines in lithium batteries for green transportation and energy storage. J Solid State Electrochem 16:835–845
17. Zaghib K, Shim J, Guerfi A, Charest P, Striebel KA (2005) Effect of carbon source as additive in $LiFePO_4$ as positive electrode for Li-ion batteries. Electrochem Solid State Lett 8:A207–A210
18. Zaghib K, Armand M (2002) Electrode covered with a film obtained from an aqueous solution containing a water soluble binder, manufacturing process and uses thereof. Canadian Patent CA 2,411,695
19. Cho YD, Frey GTK, Kao HM (2009) The effect of carbon coating thickness on the capacity of $LiFePO_4$/C composite cathodes. J Power Sourc 189:256–262
20. Lu CZ, Frey GTK, Kao HM (2009) Study of $LiFePO_4$ cathode materials coated with high surface area carbon. J Power Sourc 189:155–162
21. Zaghib K, Mauger A, Gendron F, Julien CM (2008) Magnetic studies of phospho-olivine electrodes in relation with their electrochemical performance in Li-ion batteries. Solid State Ionics 179:16–23

22. Yamada A, Chung SC, Hinokuma K (2001) Optimized $LiFePO_4$ for lithium battery cathodes. J Electrochem Soc 148:A224–A229
23. Julien CM, Mauger A, Ait-Salah A, Massot M, Gendron F, Zaghib K (2007) Nanoscopic scale studies of $LiFePO_4$ as cathode material in lithium-ion batteries for HEV application. Ionics 13:395–411
24. Julien CM, Zaghib K, Mauger A, Massot M, Ait-Salah A, Selmane M, Gendron F (2006) Characterization of the carbon-coating onto $LiFePO_4$ particles used in lithium batteries. J Appl Phys 100:063511
25. Doeff MM, Wilcox JD, Kostecki R, Lau G (2006) Optimization of carbon coatings on $LiFePO_4$. J Power Sourc 163:180–184
26. Dominko R, Bele M, Gaberscek M, Remskar M, Hanzel D, Goupil JM, Pejovnik S, Jamnik J (2006) Porous olivine composites synthesized by sol–gel technique. J Power Sourc 153:274–280
27. Gaberscek M, Dominko R, Bele M, Remskar M, Hanzel D, Jamnik J (2005) Porous, carbon-decorated $LiFePO_4$ prepared by sol–gel method based on citric acid. Solid State Ionics 176:1801–1805
28. Dominko R, Goupil JM, Bele M, Gaberscek M, Remskar M, Hanzel D, Jamnik J (2005) Impact of $LiFePO_4$/C composites porosity on their electrochemical performance. J Electrochem Soc 152:A858–A863
29. Dominko R, Bele M, Gaberscek M, Remskar M, Hanzel D, Pejovnik S, Jamnik J (2005) Impact of the carbon coating thickness on the electrochemical performance of $LiFePO_4$/C composites. J Electrochem Soc 152:A607–A610
30. Yang S, Zavajil PY, Whittingham MS (2001) Hydrothermal synthesis of lithium iron phosphate cathodes. Electrochem Commun 3:505–508
31. Sato M, Tajimi S, Okawa H, Uematsu K, Toda K (2002) Preparation of iron phosphate cathode material of $Li_3Fe_2(PO_4)_3$ by hydrothermal reaction and thermal decomposition processes. Solid State Ionics 152–153:247–251
32. Dokko K, Koizumi S, Kanamura K (2006) Electrochemical reactivity of $LiFePO_4$ prepared by hydrothermal method. Chem Lett 35:338–339
33. Murugan AV, Muraliganth T, Manthiram A (2009) One-pot microwave-hydrothermal synthesis and characterization of carbon-coated $LiMPO_4$ (M = Mn, Fe, and Co) cathodes. Electrochem Soc 156:A79–A83
34. Meligrana G, Gerbaldi C, Tuel A, Bodoardo S, Penazzi N (2006) Hydrothermal synthesis of high surface $LiFePO_4$ powders as cathode for Li-ion cells. J Power Sourc 160:516–522
35. Shiraishi K, Dokko K, Kanamura K (2005) Formation of impurities on phospho-olivine $LiFePO_4$ during hydrothermal synthesis. J Power Sourc 146:555–558
36. Franger S, Le Cras F, Bourbon C, Rouanlt H (2003) Comparison between different $LiFePO_4$ synthesis routes and their influence on its physico-chemical properties. J Power Sourc 119–121:252–257
37. Tajimi S, Ikeda Y, Uematsu K, Toda K, Sato M (2004) Enhanced electrochemical performance of $LiFePO_4$ prepared by hydrothermal reaction. Solid State Ionics 175:287–290
38. Lee J, Teja AS (2006) Synthesis of $LiFePO_4$ micro and nanoparticles in supercritical water. Mater Lett 60:2105–2109
39. Dokko K, Koizumi S, Sharaishi K, Kananura K (2007) Electrochemical properties of $LiFePO_4$ prepared via hydrothermal route. J Power Sourc 165:656–659
40. Jin B, Gu HB (2008) Preparation and characterization of $LiFePO_4$ cathode materials by hydrothermal method. Solid State Ionics 178:1907–1914
41. Brochu F, Guerfi A, Trottier J, Kopeć M, Mauger A, Groult H, Julien CM, Zaghib K (2012) Structure and electrochemistry of scaling nano C-$LiFePO_4$ synthesized by hydrothermal route: complexing agent effect. J Power Sourc 214:1–6
42. Delacourt C, Poizot P, Levasseur S, Masquelier C (2009) Size effects on carbon-free $LiFePO_4$ powders. Electrochem Solid State Lett 9:A352–A355

43. Arnold G, Garche J, Hemmer R, Ströbele S, Vogler C, Wohlfgang-Mehrens M (2003) Fine-particle lithium iron phosphate $LiFePO_4$ synthesized by a new low-cost aqueous precipitation technique. J Power Sourc 119–121:247–251
44. Wang Y, Sun B, Park J, Kim WS, Kim HS, Wang G (2011) Morphology control and electrochemical properties of nanosize $LiFePO_4$ cathode material synthesized by co-precipitation combined with in situ polymerization. J Alloys Compd 509:1040–1044
45. Ding Y, Jiang Y, Xu F, Yin J, Ren H, Zhuo Q, Long Z, Zhang P (2010) Preparation of nano-structured $LiFePO_4$/graphene composites by co-precipitation method. Electrochem Commun 12:10–13
46. Park KS, Son JT, Chung HT, Kim SJ, Lee CH, Kim HG (2003) Synthesis of $LiFePO_4$ by co-precipitation and microwave heating. Electrochem Commun 5:839–842
47. Higuchi M, Katayama K, Azuma Y, Yukawa M, Suhara M (2003) Synthesis of $LiFePO_4$ cathode material by microwave processing. J Power Sourc 119–121:258–261
48. Beninati S, Damen L, Mastragostino M (2008) MW-assisted synthesis of $LiFePO_4$ for high power applications. J Power Sourc 180:875–879
49. Wang L, Huang Y, Jiang R, Jia D (2007) Preparation and characterization of nano-sized $LiFePO_4$ by low heating solid-state coordination method and microwave heating. Electrochim Acta 52:6778–6783
50. Hu X, Yu JC (2008) Continous aspect-ratio tuning and fine shape control of monodisperse α-Fe_2O_3 nanocrystals by a programmed microwave-hydrothermal method. Adv Funct Mater 18:880–887
51. Qin X, Wang X, Xiang H, Xie J, Li J, Zhou Y (2010) Mechanism for hydrothermal synthesis of LiFePO4 platelets as cathode material for lithuium-ion batteries. J Phys Chem C 114:16806–16812
52. Gerbec JA, Morgan D, Washington A, Strouse GF (2005) Microwave-enhanced reaction rates for nanoparticle synthesis. J Am Chem Soc 127:15791–15800
53. Feng H, Zhang Y, Wu X, Wang L, Zhang A, Xia T, Dong H, Liu M (2009) One-step microwave synthesis and characterization of carbon-modified nanocrystalline $LiFePO_4$. Electrochim Acta 54:3206–3210
54. Bileka I, Hintennach A, Djerdj I, Novak P, Niederberger M (2009) Efficient microwave-assisted synthesis of $LiFePO_4$ mesocrystals with high cycling stability. J Mater Chem 19:5125–5128
55. Kim DH, Kim J (2006) Synthesis of $LiFePO_4$ nanoparticles in polyol medium and their electrochemical properties. Electrochem Solid State Lett 9:A439–A442
56. Kim DH, Kim J (2007) Synthesis of $LiFePO_4$ nanoparticles and their electrochemical properties. J Phys Chem Solids 68:734–737
57. Kim DH, Kang JW, Jung IO, Lim JS, Kim EJ, Song SJ, Lee JS, Kim J (2008) Microwave assisted synthesis of nanocrystalline Fe-phosphates electrode materials and their electrochemical propperties. J Nanosci Nanotechnol 8:5376–5379
58. Kim DH, Lim JS, Kang JW, Kang JW, Kim EJ, Ahn HY, Kim J (2007) A new synthesis route to nanocrystalline olivine phosphates and their electrochemical properties. J Nanosci Nanotechnol 7:3949–3953
59. Saravanan K, Reddy MV, Balaya P, Gong H, Chowvari BVR, Vittal JJ (2009) Storage performance of $LiFePO_4$ nanoplates. J Mater Chem 19:605–610
60. Yang H, Wu XL, Cao MH, Guo YG (2009) Solvothermal synthesis of $LiFePO_4$ hierarchically dumbbell-like microstructures by nanoplate self-assembly and their application as a cathode material in lithium-ion batteries. J Phys Chem C 113:3345–3351
61. Myung ST, Komaba S, Hirosaki N, Yashiro H, Kumagai N (2004) Emulsion drying synthesis of olivine $LiFePO_4$/C composite and its electrochemical properties as lithium intercalation material. Electrochim Acta 49:4213–4222
62. Konstantinov K, Bewlay S, Wang GX, Lindsay M, Wang JZ (2004) New approach for synthesis of carbon-mixed $LiFePO_4$ cathode materials. Electrochim Acta 50:421–426

63. Konarova M, Taniguchi I (2009) Preparation of carbon coated $LiFePO_4$ by a combination of spray pyrolysis with planetary ball-milling followed by heat treatment and their electrochemical properties. Powder Technol 191:111–116
64. Konarova M, Taniguchi I (2010) Synthesis of carbon-coated $LiFePO_4$ nanoparticles with high rate performance in lithium secondary batteries. J Power Sourc 195:3661–3667
65. Cides CR, Croce F, Young VY, Martin CR, Scrosati B (2005) A high-rate, nanocomposite $LiFePO_4$/carbon cathode. Electrochem Solid State Lett 8:A484–A487
66. Lim S, Yoon CS, Cho J (2008) Synthesis of nanowire and hollow $LiFePO_4$ cathodes for high-performance lithium batteries. Chem Mater 20:4560–4564
67. Doherty CM, Caruso RA, Smarsly BM, Drummond CJ (2009) Colloidal crystal templating to produce hierarchically porous $LiFePO_4$ electrode materials for high power lithium ion batteries. Chem Mater 21:2895–2903
68. Hwang BJ, Hsu KF, Hu SK, Cheng MY, Chou TC (2009) Template-free reverse micelle process for the synthesis of a rod-like $LiFePO_4$/C composite cathode for lithium batteries. J Power Sourc 194:515–519
69. Zaghib K, Mauger A, Gendron F, Julien CM (2008) Surface effects on the physical and electrochemical properties of thin $LiFePO_4$ particles. Chem Mater 20:462–469
70. Kim JK, Cheruvally G, Choi JW, Kim JU, Ahn JH, Cho GB, Kim KW, Ahn H-J (2007) Effect of mechanical activation process parameters on the properties of $LiFePO_4$ cathode material. J Power Sourc 166:211–218
71. Shin HC, Cho WI, Jang H (2006) Electrochemical properties of carbon-coated $LiFePO_4$ cathode using graphite, carbon black, and acetylene black. Electrochim Acta 52:1472–1476
72. Kim JK, Choi JW, Cheruvally G, Kim JU, Ahn JH, Cho GB, Kim KW, Ahn HJ (2007) A modified mechanical activation synthesis for carbon-coated $LiFePO_4$ cathode in lithium batteries. Mater Lett 61:3822–3825
73. Kang HC, Jun DK, Jin B, Jin EM, Park KH, Gu HB, Kim KW (2008) Optimized solid-state synthesis of $LiFePO_4$ cathode materials using ball-milling. J Power Sourc 179:340–346
74. Maxisch T, Zhou F, Ceder G (2006) Ab initio study of the migration of small polarons in olivine Li_xFePO_4 and their association with lithium ions and vacancies. Phys Rev B 73:104301
75. Islam MS, Driscoll DJ, Fischer CA, Slater PR (2005) Atomic scale investigation of defects, dopants, and lithium transport in the $LiFePO_4$ olivine-type battery material. Chem Mater 17:5085–5092
76. Chen G, Song X, Richardson TJ (2007) Metastable solid-solution phases in the $LiFePO_4$/$FePO_4$ system. J Electrochem Soc 154:A627–A632
77. Chen G, Song X, Richardson TJ (2006) Electron microscopy study of the $LiFePO_4$ to $FePO_4$ phase transition. J Electrochem Solid State Lett 9:A295–A298
78. Laffont L, Delacourt C, Gibot P, Wu MY, Kooyman P, Masquelier C, Tarascon JM (2006) Study of the $LiFePO_4$/$FePO_4$ two-phase system by high-resolution electron energy loss spectroscopy. Chem Mater 18:5520–5529
79. Dokko K, Koizumi S, Nakano H, Kanamura K (2007) Particle morphology, crystal orientation, and electrochemical reactivity of $LiFePO_4$ synthesized by the hydrothermal method at 443 K. J Mater Chem 17:4803–4810
80. Zaghib K, Dontigny M, Charest P, Labrecque JF, Guerfi A, Kopec M, Mauger A, Gendron F, Julien CM (2010) $LiFePO_4$: from molten ingot to nanoparticles with high-rate performance in Li-ion batteries. J Power Sourc 195:8280–8288
81. Ait-Salah A, Mauger A, Zaghib K, Goodenough JB, Ravet N, Gauthier M, Gendron F, Julien CM (2006) Reduction of Fe^{3+} impurities in $LiFePO_4$ from the pyrolysis of organic precursor used for carbon deposition. J Electrochem Soc 153:A1692–A1701
82. Prosini PP, Carewska M, Scaccia S, Wisniewski P, Passerini S, Pasquali M (2002) A new synthetic route for preparing $LiFePO_4$ with enhanced electrochemical performance. J Electrochem Soc 149:A886–A890

83. Arcon D, Zorko A, Dominko R, Jaglicic Z (2004) A comparative studies of magnetic properties of $LiFePO_4$ and $LiMnPO_4$. J Phys C Condens Matter 16:5531–5548
84. Geller S, Durand JL (1960) Refinement of the structure of $LiMnPO_4$. Acta Crystallogr 13:325–329
85. Santorro RP, Newnham RE (1987) Antiferromagnetism in $LiFePO_4$. Acta Crystallogr 22:344–347
86. Streltsov VA, Belokoneva EL, Tsirelson VG, Hansen NK (1993) Multipole analysis of the electron density in triphylite $LiFePO_4$ using X-ray diffraction data. Acta Crystallogr B 49:147–153
87. Rousse G, Rodriguez-Carvajal J, Patoux S, Masquelier C (2003) Magnetic structures of the triphylite $LiFePO_4$ and its delithiated form $FePO_4$. Chem Mater 15:4082–4090
88. Losey A, Rakovan J, Huges J, Francis CA, Dyar MD (2004) Structural variation in the lithiophilite-triphylite series and other olivine-group structures. Canad Mineral 42:1105–1109
89. Junod A, Wang KQ, Triscone G, Lamarche G (1995) Specific heat, magnetic properties and critical bahaviour of Mn_2SiS_4 and Fe_2GeS_4. J Magn Magn Mater 146:21–29
90. Moring J, Kostiner E (1986) The crystal structure of $NaMnPO_4$. J Solid State Chem 61:379–383
91. Nakamura T, Miwa Y, Tabuchi M, Yamada Y (2006) Structural and surface modifications of $LiFePO_4$ olivine particles and their electrochemical properties. J Electrochem Soc 153:1108
92. Andersson AS, Thomas JO (2001) The source of first-cycle capacity loss in $LiFePO_4$. J Power Sourc 97–98:498–502
93. Nyten A, Thomas JO (2006) A neutron powder diffraction study of $LiCo_xFe_{1-x}PO_4$ for $x = 0$, 0.25, 0.40, 0.60 and 0.75. Solid State Ionics 177:1327–1330
94. Beale AM, Sankar G (2002) Following the structural changes in iron phosphate catalysts by in situ combined XRD/QuEXAFS technique. J Mater Chem 12:3064–3072
95. Nanjundaswamy KS, Padhi AK, Goodenough JB, Okada S, Ohtsuka H, Arai H, Yamaki J (1996) Synthesis, redox potential evaluation and electrochemical characteristics of NASICON-related-3D framework compounds. Solid State Ionics 92:1–10
96. Pahdi AK, Manivannan M, Goodenough JB (1998) Tuning the position of the redox couples in materials with NASICON structure by anionic substitution. J Electrochem Soc 145:1518–1520
97. Manthiram A, Goodenough JB (1989) Lithium insertion into $Fe_2(SO_4)_3$ frameworks. J Power Sourc 26:403–408
98. Nyten A, Abouimrane A, Armand M, Gustafsson T, Thomas JO (2005) Electrochemical performance of Li_2FeSiO_4 as a new Li-battery cathode material. Electrochem Commun 7:156–160
99. Barker J, Saidi MY, Swoyer JL (2003) Electrochemical insertion properties of the novel lithium vanadium fluorophosphate, $LiVPO_4F$. J Electrochem Soc 150:A1394–A1398
100. Armand M, Gauthier M, Magnan JF, Ravet (2002) Method for synthesis of carbon-coated redox materials with controlled size. Word Patent 02/27823 A1
101. Zaghib K, Armand M Guerfi A, Perrier M, Dupuis E (2004) Electrode covered with a film obtained from an aqueous solution containing a water soluble binder, manufacturing process and usesthereof. Canadian Patent CA 2,411,695, 13 May 2004
102. Striebel K, Shim J, Srinivasan V, Newman J (2005) Comparison of $LiFePO_4$ from different sources. J Electrochem Soc 152:A664–A670
103. Paques-Ledent MT, Tarte P (1974) Vibrational studies of olivine-type compounds – II orthophosphates, -arsenates and -vanadates $A^IB^{II}X^VO_4$. Spectrochim Acta Part A 30:673–689
104. Burma CM, Frech R (2004) Raman and FTIR spectroscopic study of Li_xFePO_4 ($0 \leq x \leq 1$). J Electrochem Soc 151:A1032–A1038
105. Kostecki R, Schnyder B, Alliata D, Song X, Kinoshita K, Kotz R (2001) Surface studies of carbon films from pyrolyzed photoresist. Thin Solid Films 396:36–43

106. Julien CM, Massot M (2004) Structure of electrode materials for Li-ion batteries: the Raman spectroscopy investigations. In: Vladikova D, Stoynov Z (eds) Portable and emergency energy sources. Academic, Waltham, MA, pp 37–70
107. Burba CM, Frech R (2006) In situ transmission FTIR spectroelectrochemistry: a new technique for studying lithium batteries. Electrochem Acta 52:780–785
108. Ait-Salah A, Jozwiak P, Zaghib K, Garbarczyk J, Gendron F, Mauger A, Julien CM (2006) Spectrochim Acta A 65:1007–1013
109. Julien CM, Ait-Salah A, Gendron F, Morhange JF, Mauger A, Ramana CV (2006) Microstructure of $LiXPO_4$ ($X = $Ni, Co, Mn) prepared by solid-state chemical reaction. Scripta Mater 55:1179–1182
110. Santorro RP, Newnham RE, Nomura S (1966) Magnetic properties of Mn_2SiO_4 and Fe_2SiO_4. J Phys Chem Solids 27:655–666
111. Santoro RP, Segal DJ, Newnham RE (1966) Magnetic properties of $LiCoPO_4$ and $LiNiPO_4$. J Phys Chem Solids 27:1192–1193
112. Dai D, Koo HJ, Rocquefelte X, Jobic S (2005) Analysis of the spin exchange interactions and the ordered magnetic structures of lithium transition metal phosphates $LiMPO_4$ (M = Mn, Fe, Co, Ni) with the olivine structure. Inorg Chem 44:2407–2413
113. Mays JM (1963) Nuclear magnetic resonances and Mn-O-P-O-Mn superexchange linkages in paramagnetic and antiferrmagnetic $LiMnPO_4$. Phys Rev 131:38–53
114. Zaghib K, Ravet N, Gauthier M, Gendron F, Mauger A, Goodenough JB, Julien CM (2006) Optimized electrochemical performance of $LiFePO_4$ at 60 °C with purity controlled by SQUID magnetometry. J Power Sourc 163:560–566
115. Julien CM, Zaghib K, Mauger A, Groult H (2012) Enhanced electrochemical properties of $LiFePO_4$ as positive electrode of Li-ion batteries for HEV application. Adv Chem Eng and Sci 2:321–329
116. Mott NF (1968) Conduction in glasses containing transition metal ion. J Non-Cryst Solids 1:1–17
117. Zaghib K, Mauger A, Goodenough JB, Gendron F, Julien CM (2007) Electronic, optical, and magnetic properties of $LiFePO_4$: small magnetic polaron effects. Chem Mater 19:3740–3747
118. Zhou F, Kang K, Maxisch T, Ceder G, Morgan D (2004) The electronic structure and band gap of $LiFePO_4$ and $LiMnPO_4$. Solid State Commun 132:181–186
119. Mauger A, Godart C (1986) The magnetic, optical and transport properties of representatives of a class of magnetic semiconductors: the europium chalcogenides. Phys Reports 141:51–176
120. Mauger A, Godart C (1980) Metal-insulator transition in Eu rich EuO. Solid State Commun 35:785–788
121. Wilcox JW, Doeff MM, Marcinek M, Kostecki R (2007) Factors influencing the quality of carbon coatings on $LiFePO_4$. J Electrochem Soc 154:A389–A395
122. Doeff MM, Hu Y, McLarnon F, Kostecki R (2003) Effect of surface carbon structure on the electrochemical performance of $LiFePO_4$. Electrochem Solid State Lett 6:A207–A209
123. Geis MW, Tamor MA (1993) Diamond and diamondlike carbon. In: Trigg GL (ed) The encyclopedia of applied physics, vol 5. VCH, New York, NY, p 1
124. Robertson J (1992) Properties of diamond-like carbon. Surf Coatings Technol 50:185–203
125. Ramsteiner M, Wagner J (1987) Resonant Raman scattering of hydrogenated amorphous carbon: evidence for π-bonded carbon clusters. Appl Phys Lett 51:1355–1357
126. Yoshikawa M, Katagani G, Ishida H, Ishitami A, Akamatsu T (1988) Resonant Raman scattering of diamondlike amorphous carbon films. Appl Phys Lett 52:1639–1641
127. Tamor MA, Vassell WC (1994) Raman fingerprinting of amorphous carbon films. J Appl Phys 76:3823–3830
128. Wada N, Gaczi PJ, Solin SA (1980) Diamond-like 3-fold coordinated amorphous carbon. J Non-Cryst Solids 35–36:543–548
129. Lespade P, Marchand A, Cousi M, Cruege F (1984) Caractérisation de matériaux carbonés par microspectrométrie Raman. Carbon 22:375–385

130. Knight DS, White WB (1989) Characterization of diamond films by Raman spectroscopy. J Mater Res 4:385–393
131. Nakamizo M, Tamai K (1984) Raman spectra of the oxidized and polished surfaces of carbon. Carbon 22:197–198
132. Matthews MJ, Bi XX, Dresselhaus MS, Endo M, Takahashi T (1996) Raman spectra of polyparaphenylene-based carbon prepared at low heat-treatment temperatures. Appl Phys Lett 68:1078–1080
133. Robertson J, O'Reilly EP (1987) Electronic and atomic structure of amorphous carbon. Phys Rev B 35:2946–2957
134. Axmann P, Stinner C, Wohlfahrt-Mehrens M, Mauger A, Gendron F, Julien CM (2009) Non-stoichiometric $LiFePO_4$: defects and related properties. Chem Mater 21:1636–1644
135. Chen J, Whittingham MS (2006) Hydrothermal synthesis of lithium iron phosphate. Electrochem Commun 6:855–858
136. Yang S, Song Y, Zavalij PY, Whittingham MS (2002) Reactivity, stability and electrochemical behavior of lithium iron phosphates. Electrochem Commun 4:239–244
137. Yamada A, Koizumi H, Sonoyma N, Kanno R (2005) Phase change in Li_xFePO_4. Electrochem Solid State Lett 5:A409–A413
138. Xie J, Oudenhoven FM, Harks PRML, Li D, Notten PHL (2015) Chemical vapor deposition of lithium phosphate thin-films for 3D all-solid-state Li-ion batteries. J Electro Chem 162: A249–A254
139. Zaghib K, Dontigny M, Charest P, Labrecque JF, Guerfi A, Kopec M, Mauger A, Gendron F, Julien CM (2008) Aging of $LiFePO_4$ upon exposure to H_2O. J Power Sourc 185:698–710
140. Porcher W, Moreau P, Lestriez B, Jouanneau S, Guyomard D (2008) Is $LiFePO_4$ stable in water? Toward greener Li-ion batteries. Electrochem Solid State Lett 11:A4–A8
141. Trudeau ML, Laul D, Veillette R, Serventi AM, Zaghib K, Mauger A, Julien CM (2011) In situ high-resolution transmission electron microscopy synthesis observation of nanostructured $LiFePO_4$. J Power Sourc 196:7383–7394
142. Zaghib K, Ravet N, Mauger A, Gauthier M, Goodenough JB, Julien CM (2007) $LiFePO_4$ high electrochemical performance at 60 °C with purity controlled by SQUID magnetometry. ECS Trans 3–27:119–129
143. Zaghib K, Dontigny M, Guerfy A, Trottier J, Hamel-Paquet J, Gariepy V, Galoutov K, Hovington P, Mauger A, Groult H, Julien CM (2012) J Power Sourc 216:192–200
144. Choi D, Wan D, Bae LT, Xiao J, Nie Z, Wang W, Viswanathan VV, Lee YJ, Zhang JG, Graff GL, Yang Z, Liu J (2010) $LiMnPO_4$ nanoplate grown via solid-state reaction in molten hydrocarbon for Li-ion battery cathode. Nano Lett 10:2799–2805
145. Oh SM, Oh SW, Yoon CS, Scrosati B, Amine K, Sun YK (2010) High-performance carbon-LiMnPO4 nanocomposite cathode for lithium batteries. Adv Funct Mater 20:3260–3265
146. Wang D, Buqa H, Crouzet M, Deghenghi G, Drezen T, Exnar I, Kwon N-H, Miners JH, Poletto L, Grätzel M (2009) High-performance, nano-structured $LiMnPO_4$ synthesized via a polyol method. J Power Sourc 189:624–628
147. Martha K, Markovski B, Grinblat J, Gofer Y, Haik O, Zinigrad E, Aurbach D, Drezen T, Wang D, Deghenghi G, Exnar I (2009) $LiMnPO_4$ as an advanced cathode material for rechargeable lithium batteries. J Electochem Soc 156:A541–A552
148. Kuroda S, Tobori N, Sakuraba M, Sato Y (2003) Charge–discharge properties of a cathode prepared with ketjen black as the electroconductive additive in lithium ion batteries. J Power Sourc 119–121:924–928
149. Xing W, Qiao SZ, Ding RG, Li F, Lu GQ, Yan ZF, Cheng HM (2006) Superior electric double layer capacitors using ordered mesoporous carbons. Carbon 44:216–224
150. Bakenov Z, Taniguchi I (2010) $LiMg_xMn_{1-x}PO_4$/C cathodes for lithium batteries prepared by a combination of spray pyrolysis with wet ball milling. J Electrochem Soc 157:430–436
151. Bakenov Z, Taniguchi I (2005) Electrochemical performance of nanostructured $LiM_xMn_{2-x}O_4$ (M = Co and Al) powders at high charge–discharge operations. Solid State Ionics 176:1027–1034

152. Oh SM, Jung HG, Yoon CS, Myung ST, Chen ZH, Amine K, Sun YK (2011) Enhanced electrochemical performance of carbon-$LiMn_{1-x}Fe_xPO_4$ nanocomposite cathode for lithium-ion batteries. J Power Sourc 196:6924–6928
153. Oh SM, Oh SW, Myung ST, Lee SM, Sun YK (2010) The effects of calcination temperature on the electrochemical performance of $LiMnPO_4$ prepared by ultrasonic spray pyrolysis. J Alloy Compd 506:372–376
154. Yamada A, Chung S-C (2001) Crystal chemistry of the olivine-type $LiMn_yFe_{1-y}PO_4$ and $Mn_yFe_{1-y}PO_4$ as possible 4 V cathode materials for lithium batteries. J Electrochem Soc 148: A960–A967
155. Nakamura T, Sakumoto K, Okamoto M, Seki S, Kobayashi Y, Takeuchi T, Tabuchi M, Yamada Y (2007) Electrochemical study on Mn^{2+}-substitution in $LiFePO_4$ olivine compound. J Power Sourc 174:435–441
156. Molenda J, Ojczyk W, Marzec J (2007) Electrical conductivity and reaction with lithium of $LiFe_{1-y}Mn_yPO_4$ olivine-type cathode materials. J Power Sourc 174:689–694
157. Kopec M, Yamada A, Kobayashi G, Nishimura S, Kanno R, Mauger A, Gendron F, Julien CM (2009) Structural and magnetic properties of $Li_xMn_yFe_{1-y}PO_4$ electrode materials for Li-ion batteries. J Power Sourc 189:1154–1163
158. Bramnik NN, Bramnik KG, Nikolowski K, Hinterstein M, Baehtz C, Ehrenberg H (2005) Synchrotron diffraction study of lithium extraction from $LiMn_{0.6}Fe_{0.4}PO_4$. Electrochem Solid State Lett 8:A379–A381
159. Bini M, Mozzati MC, Galinetto P, Capsoni D, Ferrari S, Grandi MS, Massarotti V (2009) Structural, spectroscopic and magnetic investigation of the $LiFe_{1-x}Mn_xPO_4$ ($0 \leq x \leq 1$) solid solution. J Solid State Chem 182:1972–1981
160. Yoncheva M, Koleva V, Mladenov M, Sendova-Vassileva M, Nikolaeva-Dimitrova M, Stoyanova R, Zhecheva E (2011) Carbon-coated nano-sized $LiFe_{1-x}Mn_xPO_4$ solid solutions ($0 \leq x \leq 1$) obtained from phosphate–formate precursors. J Mater Sci 46:7082–7089
161. Zaghib K, Trudeau M, Guerfi A, Trottier J, Mauger A, Veillette R, Julien CM (2012) New advanced cathode material: LiMnPO4 encapsulated with $LiFePO_4$. J Power Sourc 204:177–181
162. Kraytsberg A, Ein-Eli Y (2012) Higher, stronger, better. A review of 5 volt cathode materials for advanced lithium-ion batteries. Adv Energy Mater 2:922–939
163. Zaghib K, Mauger A, Goodenough JB, Gendron F, Julien CM (2009) Positive electrode: Lithium iron phosphate. In: Garche J (ed) Encyclopedia of electrochemical power sources, vol 5. Elsevier, Amsterdam, pp 264–296
164. Zhu QB, Li XH, Wang ZW, Guo HJ (2006) Novel synthesis of $LiFePO_4$ by aqueous precipitation and carbothermal reduction. Mater Chem Phys 98:373–376
165. Bramnik NN, Nikolowski K, Trots DM, Ehrenberg H (2008) Thermal stability of $LiCoPO_4$ cathodes. Electrochem Solid State Lett 11:A89–A93
166. Wolfenstine J, Allen J (2005) Ni^{3+}/Ni^{2+} redox potential in $LiNiPO_4$. J Power Sourc 142:389–390
167. Minakshi M, Sharma N, Ralph D, Appadoo D, Nallathamby K (2011) Synthesis and characterization of $Li(Co_{0.5}Ni_{0.5})PO_4$ cathode for Li-ion aqueous battery applications. Electrochem Solid State Lett 14:A86–A89
168. Bramnik NN, Bramnik KG, Baehtz C, Ehrenberg H (2005) Study of the effect of different synthesis routes on Li extraction–insertion from $LiCoPO_4$. J Power Sourc 145:74–81
169. Bramnik NN, Bramnik KG, Buhrmester T, Baehtz C, Ehrenberg H, Fuess H (2004) Electrochemical and structural study of $LiCoPO_4$-based electrodes. J Solid State Electrochem 8:558–564
170. Nakayama M, Goto S, Uchimoto Y, Wakihara M, Kitayama Y (2004) Changes in electronic structure between cobalt and oxide ions of lithium cobalt phosphate as 4.8-V positive electrode material. Chem Mater 16:3399–3401
171. Bramnik NN, Nikolowski K, Baehtz C, Bramnik KG, Ehrenberg H (2007) Phase transition occurring upon lithium insertion-extraction of $LiCoPO_4$. Chem Mater 19:908–915

172. Okada S, Sawa S, Egashira M, Yamaki JI, Tabuchi M, Kageyama H, Konishi T, Yoshino A (2001) Cathode properties of phospho-olivine $LiMPO_4$ for lithium secondary batteries. J Power Sourc 97–98:430–432
173. Jang IC, Lim HH, Lee SB, Karthikeyan K, Aravindan V, Kang KS, Yoon WS, Cho WI, Lee YS (2010) Preparation of $LiCoPO_4$ and $LiFePO_4$ coated $LiCoPO_4$ materials with improved battery performance. J Alloys Compd 497:321–324
174. Rabanal ME, Gutierrez MC, Garcia-Alvarado F, Gonzalo EC, Arroyo-de Dompablo ME (2006) Improved electrode characteristics of olivine–$LiCoPO_4$ processed by high energy milling. J Power Sourc 160:523–528
175. Koleva V, Zhecheva E, Stoyanova R (2010) Ordered olivine-type lithium-cobalt and lithium-nickel phosphates prepared by a new precursor method. Eur J Inorg Chem 26:4091–4099
176. Kandhasamy S, Pandey A, Minakshi M (2012) Polyvinyl-pyrrolidone assisted sol-gel route $LiCo_{1/3}Mn_{1/3}Ni_{1/3}PO_4$ composite cathode for aqueous rechargeable battery. Electrochim Acta 60:170–176
177. Eftekhari A (2004) Surface modification of thin-film based $LiCoPO_4$ 5 V cathode with metal oxide. J Electrochem Soc 151:A1456–A1460
178. Deniard P, Dulac AM, Rocquefelte X, Grigorova V, Lebacq O, Pasturel A, Jobic S (2004) High potential positive materials for lithium-ion batteries: transition metal phosphates. J Phys Chem Solids 65:229–233
179. Prabu M, Selvasekarapandian S, Kulkarni AR, Karthikeyan S, Hirankumar G, Sanjeeviraja C (2011) Structural, dielectric, and conductivity studies of yttrium-doped $LiNiPO_4$ cathode materials. Ionics 17:201–207
180. Karthickprabhu S, Hirankumar G, Maheswaran A, Sanjeeviraja C, Daries-Bella RS (2013) Structural and conductivity studies on $LiNiPO_4$ synthesized by the polyol method. J Alloys Compd 548:65–69
181. Lloris JM, Pérez-Vicente C, Tirado JL (2002) Improvement of the electrochemical performance of $LiCoPO_4$ 5 V material using a novel synthesis procedure. Electrochem Solid State Lett 5:A234–A237
182. Yang J, Xu JJ (2006) Synthesis and characterization of carbon-coated lithium transition metal phosphates $LiMPO_4$ (M = Fe, Mn, Co, Ni) prepared via a nonaqueous sol-gel route batteries, fuel cells, and energy conversion. J Electrochem Soc 153:A716–A723
183. Gangulibabu N, Bhuvaneswari D, Kalaiselvi N, Jayaprakash N, Periasamy P (2009) CAM sol-gel synthesized $LiMPO_4$ (M = Co, Ni) cathodes for rechargeable lithium batteries. J Sol-Gel Sci Technol 49:137–144
184. Amine K, Yasuda H, Yamachi M (2000) Olivine $LiCoPO_4$ as 4.8-V electrode material for lithium batteries. Electrochem Solid State Lett 3:178–179
185. Zhou F, Cococcioni M, Kang K, Ceder G (2004) The Li intercalation potential of $LiMPO_4$ and $LiMSiO_4$ olivines with M = Fe, Mn, Co, Ni. Electrochem Commun 6:1144–1148
186. Howard WF, Spotnitz RM (2007) Theoretical evaluation of high-energy lithium metal phosphate cathode materials in Li-ion batteries. J Power Sourc 165:887–891
187. Chevrier VL, Ong SP, Armiento R, Chan MKY, Ceder G (2010) Hybrid density functional calculations of redox potentials and formation energies of transition metal compounds. Phys Rev B 82:075122
188. Rissouli K, Benkhouja K, Ramos-Barrado JR, Julien C (2003) Electrical conductivity in lithium orthophosphates. Mater Sci Eng B 98:185–189
189. Goñi A, Lezama L, Barberis GE, Pizarro JL, Arriortua MI, Rojo T (1996) Magnetic properties of the $LiMPO_4$ (M = Co, Ni) compounds. J Magn Magn Mater 164:251–255
190. Julien CM, Mauger A, Zaghib K, Veillette R, Groult H (2012) Structural and electronic properties of the $LiNiPO_4$ orthophosphate. Ionics 18:625–633
191. Fomin VI, Gnezdilov VP, Kurnosov VS, Peschanskii AV, Yeremenko AV, Schmid H, Rivera JP, Gentil S (2002) Raman scattering in a $LiNiPO_4$ single crystal. Low Temp Phys 28:203–209

192. Ficher CAJ, Prieto VMH, Islam MS (2008) Lithium battery materials $LiMPO_4$ (M = Mn, Fe, Co and Ni): insights into defect association, transport mechanisms and doping behaviour. Chem Mater 20:5907–5915
193. Garcia-Moreno O, Alvarez-Vega M, Garcia-Alvarado F, Garcia-Jaca J, Garcia-Amores JM, Sanjuan ML, Amador U (2001) Influence of the structure on the electrochemical performance of lithium transition metal phosphates as cathodic materials in rechargeable lithium batteries: a new high-pressure form of $LMPO_4$ (M = Fe and Ni). Chem Mater 13:1570–1576
194. Piana M, Arrabito M, Bodoardo S, D'Epifanio A, Satolli D, Croce F, Scrosati B (2002) Characterization of phospho-olivines as materials for Li-ion cell cathodes. Ionics 8:17–26
195. Dimesso L, Jacke S, Spanheimer C, Jaegermann W (2012) Investigation on $LiCoPO_4$ powders as cathode materials annealed under different atmospheres. J Solid State Electrochem 16:3911–3919
196. Dimesso L, Becker D, Spanheimer C, Jaegermann W (2012) Investigation of graphitic carbon foams/$LiNiPO_4$ composites. J Solid State Electrochem 16:3791–3798
197. Dimesso L, Spanheimer C, Jaegermann W (2013) Effect of the Mg-substitution on the graphitic carbon foams – $LiNi_{1-y}Mg_yPO_4$ composites as possible cathodes materials for 5 V applications. Mater Res Bull 48:559–565
198. Wolfenstine J, Allen J (2004) $LiNiPO_4$–$LiCoPO_4$ solid solutions as cathodes. J Power Sourc 136:150–153
199. Ni J, Gao L, Lu L (2013) Carbon coated lithium cobalt phosphate for Li-ion batteries: comparison of three coating techniques. J Power Sourc 221:35–41
200. Wolfenstine J, Read J, Allen J (2007) Effect of carbon on the electronic conductivity and discharge capacity $LiCoPO_4$. J Power Sourc 163:1070–1073
201. Wolfenstine J, Lee U, Poese B, Allen J (2005) Effect of oxygen partial pressure on the discharge capacity of $LiCoPO_4$. J Power Sourc 144:226–230
202. Wolfenstine J, Poese B, Allen J (2004) Chemical oxidation of $LiCoPO_4$. J Power Sourc 138:281–282
203. Ruffo R, Mari CM, Morazzoni F, Rosciano F, Scotti R (2007) Electrical and electrochemical behavior of several $LiFe_xCo_{1-x}PO_4$ solid solutions as cathode materials for lithium ion batteries. Ionics 13:287–291
204. Wolfenstine J (2006) Electrical conductivity of doped $LiCoPO_4$. J Power Sourc 158:1431–1435
205. Wang F, Yang J, Li YN, Wang J (2011) Novel hedgehog-like 5 V $LiCoPO_4$ positive electrode material for rechargeable lithium battery. J Power Sourc 196:4806–4810
206. Nakayama M, Goto S, Uchimoto Y, Wakihara M, Kitayama Y, Miyanaga T, Watanabe I (2005) X-ray absorption spectroscopic study on the electronic structure of $Li_{1-x}CoPO_4$ electrodes as 4.8 V positive electrodes for rechargeable lithium ion batteries. J Phys Chem B 109:11197–11203
207. Huggins RA (2013) Do you really want an unsafe battery? J Electrochem Soc 160:A3001–A3005
208. Aravindan V, Cheah YL, Chui Ling WC, Madhavi S (2012) Effect of LiBOB additive on the electrochemical performance of $LiCoPO_4$. J Electrochem Soc 159:A1435–A1439
209. Cushing BL, Goodenough JB (2002) $Li_2NaV_2(PO_4)_3$: a 3.7 V lithium-insertion cathode with the rhombohedral NASICON structure. J Solid State Chem 162:176–181
210. Goodenough JB, Hong HYP, Kafalas JA (1976) Fast Na^+-ion transport in skeleton structures. Mat Res Bull 11:203–220
211. Anantharamulu N, Rao K, Rambabu G, Kumar B, Radha V, Vithal M (2011) A wide-ranging review on Nasicon type materials. J Mater Sci 46:2821–2837
212. Bykov B, Chirkin AP, Demyanets LN, Doronin SN, Genkina EA, Ivanov-Shits AK, Kondratyuk IP, Maksimov BA, Melnikov OK, Muradyan LN, Simonov VI, Timofeeva VA (1990) Superionic conductors $Li_3M_2(PO_4)_3$ (M = Fe, Sr, Cr): synthesis, structure and electrophysical properties. Solid State Ionics 38:31–52

213. D'Yvoire F, Pintard-Scrépel M, Bretey E, De la Rochère M (1983) Phase transitions and ionic conduction in 3D skeleton phosphates $A_3M_2(PO_4)_3$: A = Li, Na, Ag, K; M = Cr, Fe. Solid State Ionics 9–10:851–857
214. Barj M, Lucazeau G, Delmas C (1992) Raman and infrared spectra of some chromium Nasicon-type materials: short-range disorder characterization. J Solid State Chemistry 100:141–150
215. Goni A, Lezama L, Moreno NO, Fournes L, Olazcuaga R, Barberis GE, Rojo T (2000) Spectrocopic and magnetic properties of α-$Li_3Fe_2(PO_4)_3$: a two-submattice ferrimagnet. Chem Mater 12:62–66
216. Anderson AS, Kalska B, Jonsson P, Haggstrom L, Nordblad P, Tellgren R, Thomas JO (2000) The magnetic structure and properties of rhombohedral $Li_3Fe_2(PO_4)_3$. J Mater Chem 10:2542–2547
217. Ait-Salah A, Jozwiak P, Garbarczyk J, Gendron F, Mauger A, Julien CM (2006) Magnetic properties of orthorhombic $Li_3Fe_2(PO_4)_3$ phase. Electrochem Soc Symp Proc 2006–19:173–181
218. Kim H, Lee S, Park YU, Kim H, Kim J, Jeon S, Kang K (2011) Neutron and X-ray diffraction study of pyrophosphate-based $Li_{2-x}MP_2O_8$ (M = Fe, Co) for lithium rechargeable battery electrodes. Chem Mater 23:3930–3938
219. Armand M, Michot C, Ravet N, Simoneau M, Hovington P (2000) New lithium insertion electrode based on orthosilicate derivatives. European patent EP1134 826 A1
220. Dominko R, Conte DE, Hanzel D, Gaberscek M, Jamnik J (2008) Impact of synthesis conditions on the structure and performance of Li_2FeSiO_4. J Power Sourc 178:842–847
221. Gong ZL, He GN, Li J, Yang Y (2008) Nanostructured Li_2FeSiO_4 electrode material synthesized through hydrothermal-assisted sol-gel process. Electrochem Solid-State Lett 11 (5):A60–A63
222. Yan Z, Cai S, Miao L, Zhou X, Zhao Y (2012) Synthesis and characterization of in situ carbon-coated Li_2FeSiO_4 cathode materials for lithium ion battery. J Alloys Compd 511:101–106
223. Zheng Z, Wang Y, Zhang A, Zhang T, Cheng F, Tao Z, Chen J (2012) Porous Li_2FeSiO_4/C nanocomposite as the cathode material of lithium-ion batteries. J Power Sourc 198:229–235
224. Lv D, Wen W, Huang X, Bai J, Mi J, Wu S, Yang Y (2011) A novel Li_2FeSiO_4/C composite: synthesis, characterization and high storage capacity. J Mater Chem 21:9506–9512
225. Saracibar A, Van Der Ven A, Arroyo-De Dompablo ME (2012) Crystal structure, energetics, and electrochemistry of Li_2FeSiO_4 polymorphs from first principles calculations. Chem Mater 24(3):495–503
226. Quoirin G, Tarascon JM, Masquelier C, Delacourt C, Poizot P, Taulelle F (2008) Mixed lithium silicates. World Patent WO 2008/107571 A2
227. Nishimura S, Hayase S, Kanno R, Yashima M, Nakayama N, Yamada A (2008) Structure of Li_2FeSiO_4. J Am Chem Soc 130:13212–13213
228. Boulineau A, Sirisopanaporn C, Dominko R, Armstrong AR, Bruce P, Masquelier C (2010) Polymorphism and structural defects in Li_2FeSiO_4. Dalton Trans 27:6310–6316
229. Sirisopanaporn C, Boulineau A, Dominko R, Hanzel D, Armstrong AR, Bruce P, Masquelier C (2010) Crystal structure of a new polymorphism in Li_2FeSiO_4. Inorg Chem 49:7446–7451
230. Dominko R, Bele M, Gaberscek M, Meden A, Remskar M, Jamnik J (2006) Structure and electrochemical performance of Li_2MnSiO_4 and Li_2FeSiO_4 as potential Li-battery cathode materials. Electrochem Commun 8:217–222
231. Nadherna M, Dominko R, Hanzel D, Relter J, Gaberscek M (2009) Electrochemical behavior of Li_2FeSiO_4 with ionic liquids at elevated temperature. J Electrochem Soc 156:A619–A626
232. Dominko R (2008) Li_2MSiO_4 (M = Fe and/or Mn) cathode materials. J Power Sourc 184:462–468
233. Muraliganth T, Stroukoff KR, Manthiram A (2010) Microwave-solvothermal synthesis of nanostructured Li_2MSiO_4/C (M = Mn and Fe) cathodes for lithium-ion batteries. Chem Mater 22:5754–5761

234. Shao B, Taniguchi I (2012) Synthesis of Li_2FeSiO_4/C nanocomposite cathodes for lithium batteries by a novel synthesis route and their electrochemical properties. J Power Sourc 199:278–286
235. Fan X-Y, Li Y, Wang JJ, Gou L, Zhao P, Li D-L, Huang L, Sun S-G (2010) Synthesis and electrochemical performance of porous Li_2FeSiO_4/C cathode material for long-life lithium-ion batteries. J Alloys Compd 493:77–80
236. Vediappan K, Guerfi A, Gariépy V, Demopoulos GP, Hovington P, Trottier J, Mauger A, Zaghib K, Julien CM (2014) Stirring effect in hydrothermal synthesis of C-$LiFePO_4$. J Power Sourc 266:99–106
237. Zaghib K, Salah AA, Ravet N, Mauger A, Gendron F, Julien CM (2006) Structural, magnetic and electrochemical properties of lithium iron orthosilicate. J Power Sourc 160:1381–1386
238. Nyten A, Kamali S, Häggström L, Gustafsson T, Thomas JO (2006) The lithium extraction/insertion mechanism in Li_2FeSiO_4. J Mater Chem 16:2266–2272
239. Nyten A, Stjerndahl M, Rensmo H, Armand M, Gustafsson T, Edström K, Thomas JO (2006) Surface characterization and stability phenomena in Li_2FeSiO_4 studied by PES/XPS. J Mater Chem 16:3483–3488
240. Duncan H, Kondamreddy A, Mercier PHJ, Le Page Y, Abu-Lebdeh Y, Couillard M, Whitfield PS, Davidson I (2011) Novel *Pn* polymorph for Li_2MnSiO_4 and its electrochemical activity as a cathode material in Li-ion batteries. Chem Mater 23:5446–5456
241. Kuganathan N, Islam MS (2009) Li_2MnSiO_4 lithium battery material: atomic-scale study of defects, lithium mobility, and trivalent dopants. Chem Mater 21:5196–5202
242. Arroyo-de Dompablo ME, Armand M, Tarascon JM, Amador U (2006) On-demand design of polyoxianionic cathode materials based on electronegativity correlations: an exploration of the Li_2MSiO_4 system (M = Fe, Mn, Co, Ni). Electrochem Commun 8:1292–1298
243. Gong ZL, Li XY, Yang Y (2006) Synthesis and characterization of $Li_2Mn_xFe_{1-x}SiO_4$ as a cathode material for lithium-ion batteries. Electrochem Solid State Lett 9:A542–A544
244. Kokalj A, Dominko R, Mali G, Meden A, Gaberscek M, Jamnik J (2007) Beyond one-electron reaction in Li cathode materials: designing $Li_2Mn_xFe_{1-x}SiO_4$. Chem Mater 19:3633–3640
245. Deng C, Zhang S, Yang SY (2009) Effect of Mn substitution on the structural, morphological and electrochemical behaviors of $Li_2Mn_xFe_{1-x}SiO_4$ synthesized via citric acid assisted sol–gel method. J Alloys Compd 487:L18–L23
246. Dominko R, Sirisopanaporn C, Masquelier C, Hanzel D, Arcon I, Gaberscek M (2010) On the origin of the electrochemical capacity of $Li_2Fe_{0.8}Mn_{0.2}SiO_4$. J Electrochem Soc 157:A1309–A1316
247. Yang X-F, Yang J-H, Zaghib K, Trudeau ML, Ying JY (2015) Synthesis of pure Li_2MnSiO_4 @ C porous nanoboxes for high-capacity Li-ion battery cathodes. Nano Energy 12:305–313
248. Graf C, Vossen DLJ, Imhof A, Van Blaaderen A (2003) A general method to coat colloidal particles with silica. Langmuir 19:6693–6700
249. Biernacki L, Pokrzywnicki S (1999) The thermal decomposition of manganese carbonate thermogravimetry and exoemission of electrons. J Therm Anal Calorim 55:227–232
250. Masquelier C, Croguennec L (2013) Polyanionic (phosphates, silicates, sulfates) frameworks as electrode materials for rechargeable Li (or Na) batteries. Chem Rev 113:6552–6591

Chapter 8
Fluoro-polyanionic Compounds

8.1 Introduction

During the last decade, numerous studies have been devoted to replace oxides by materials with a polyanion-based framework that are considered as safe alternatives for the traditional oxide electrodes [1]. For instance, $M_x(SO_4)_y$ sulfate-based and $M_x(PO_4)_y$ phosphate-based compounds (M is a transition-metal ion) that house interstitial Li^+ ions such as $LiFe_2(SO_4)_3$ [2], $LiFePO_4$ [3], $Li_3V_2(PO_4)_3$ [4], $Li_{2.5}V_2(PO_4)_3$ [5], $LiVOPO_4$ [6–8], and $LiVP_2O_8$ [8, 9] have all been considered as thermally stable. All these materials usually exhibit excellent stability on long-term cycling by comparison to lithium metal oxides and essentially no release of oxygen from the lattice or reactivity with the electrolyte. However, the materials were found to be poor electronic conductors [3].

The search of new cathode materials aiming to maintain a good mix of properties, with focus on electrochemical and safety parameters, has resulted in the improvement of the electrochemical performance using two strategies: (1) substitution of fluorine for oxygen or (2) fluorine coating of the active particles. As a result, fluorinated compounds display several advantages such as high voltage redox reactions, stabilization of the host lattice, protection the electrode particle surface from HF attack and electrolyte decomposition that impedes a side reaction, and easy transport of mobile Li^+ ions [10–15]. Accordingly, anion substitution is expected as an effective way to enhance the electrochemical performance of spinel and layered compounds, especially for NMC materials [16] due to the strong electronegativity of the F^- anion, which will make the structure more stable. Among the metal fluorides as surface fluorination (coating) agents of oxide-based cathode particles, the most popular are ZrF_x [17], AlF_3 [18], CaF_2 [19], and LiF [20]. While these materials are treated in the first and third chapters, attention hereunder is focussed on technological developments of fluorophosphates and fluorosulfates [21–23]. The present chapter gives the state of the art in the understanding of the properties of these F-containing materials. Owing to the progress in

C. Julien et al., *Lithium Batteries*, DOI 10.1007/978-3-319-19108-9_8

this field, these compounds are promising active cathode elements for the next generation of Li-ion batteries to improve the technology of the energy storage and electric transportation. This chapter is organized as follows. The preliminary considerations are dedicated to a brief recall of the energetic properties of these compounds. The second section is devoted to the structural and electrochemical properties of fluorophosphate materials. Then the fluorosulfates are treated in Sect. 8.3. Finally, some concluding remarks are given with emphasis on the quality that insures the reliability and the optimum electrochemical performance of these materials.

8.2 Properties of Polyanionic Compounds

According Eq. (1.5), the average voltage of an intercalation compound is directly related to the energies of the end states (charged and discharged), the voltage depends on the structure of the cathode element [24]. Several computer simulation techniques have been employed to address the voltage, diffusion and nano-structural properties of cathode materials [25, 26]. DFT + U methods have also been used recently to investigate the structural and electronic properties of both tavorite and triplite $LiFeSO_4F$ polymorphs. Islam and Fisher [25] have pointed out that the difference in voltage is mainly due to the difference in the stabilities of the delithiated states $FeSO_4F$, which can be rationalized in terms of the Fe^{3+}-Fe^{3+} repulsion in the edge-sharing geometry of the triplite structure [27].

Considering the crystal field concept developed by Goodenough [28], the redox potential of an insertion electrode material is governed by the ionocovalency of the *M*-*X* bond: the more ionic bonds, the higher potential. Thus, the redox potential strongly depends on the electronegative ion: substitution of fluorine F^- for oxygen O^{2-} results in higher potential, while the opposite is observed for sulfur. As an example, the redox potential of the $LiFePO_4F$ tavorite phase is 850 mV higher than that of the $LiFePO_4$ olivine phase, because the ionicity in Fe-F bonds is larger than that of Fe-O bonds. A computational investigation on fluorinated-polyanionic compounds has demonstrated that the more ionic *M*-F bond and the resulting stabilization of the energy of the antibonding 3*d* orbitals of the transition-metal ion by fluorine substitution for oxygen is the law acting on the electrochemical properties [28].

Another aspect of tuning the redox potential of an electrode material has been demonstrated by Goodenough et al. [3, 29]. They have shown that the use of polyanions $(XO_4)^{n-}$ such as $(SO_4)^{2-}$, $(PO_4)^{3-}$, $(AsO_4)^{3-}$, or even $(WO_4)^{2-}$ lowers 3*d*-metals redox energy to useful levels compared to the Fermi level of the Li anode. Thus, the most attractive key point of the polyanion frameworks can be seen in the strong *X*-O covalency, which results in a decrease of the Fe-O covalency. This inductive effect is responsible for a decrease of the redox potential in comparison to the oxides [29, 30]. The polyanion PO_4^{3-} unit stabilizes the olivine structure of $LiFePO_4$ and lowers the Fermi level of the $Fe^{2+/3+}$ redox couple through

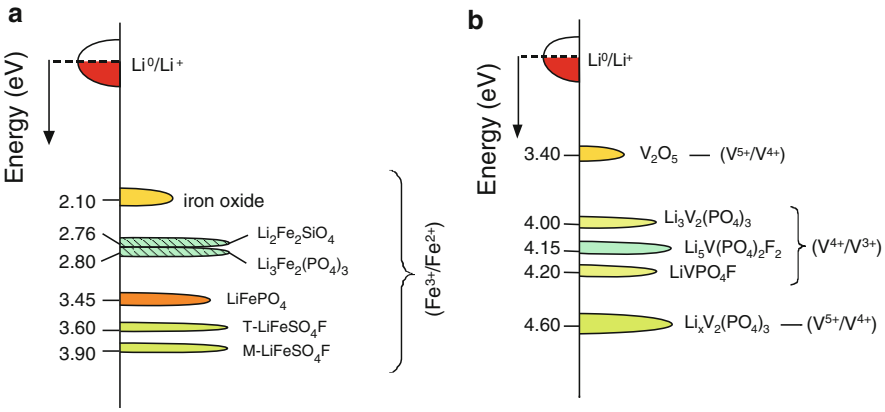

Fig. 8.1 Energy of the redox couples of iron (**a**) and vanadium (**b**) phosphate frameworks relative to the Fermi level of metallic lithium

the Fe-O-P inductive effect which results in a higher potential for the olivine material. The discharge voltage 3.45 V is almost 650 mV higher than that of $Li_3Fe_2(PO_4)_3$ [3]. It is also 350 mV higher than that of $Fe_2(SO_4)_3$ [2], which is consistent with the stronger Bronsted acidity of sulfuric vs. phosphoric acid. In the case of Li_2FeSiO_4, the lower electronegativity of Si vs. P results in a lowering of the $Fe^{2+/3+}$ redox couple [31]. On the other hand, the higher thermal stability of the phospho-olivines and their lower tendency to release oxygen is explained by the strong *X*-O covalency and the rigid $(XO_4)^{n-}$ units decreasing the safety risks. However, $AMXO_4$ compounds and $AM(XO_4)_3$ as well (*A* is an alkali ion) exhibit a very low electronic conductivity because of the separation between MO_6 octahedra and XO_4 tetrahedra that induces a large polarization effect during charge–discharge reaction [32]. Figure 8.1 illustrates the changes in redox energies relative to the Fermi level of Li for the $Fe^{2+/3+}$ and $V^{n+/(n+1)+}$ couples. For instance, the electrochemical insertion properties of lithium vanadium fluorophosphate, $LiVPO_4F$, indicate that the V^{3+}/V^{4+} redox couple in $LiVPO_4F$ is located at a potential around 0.3 V higher than in the lithium vanadium phosphate, $Li_3V_2(PO_4)_3$ [32]. This property characterizes the impact of structural fluorine on the inductive effect of the PO_4^{3-} polyanion. The electrochemical characteristics of various lithiated compounds with polyanionic framework are listed in Table 8.1 [32–36].

Most of these compounds crystallize in a structure similar to tavorite $LiFe(PO_4)(OH)$ [37]. Using high-throughput density-functional-theory calculations, Mueller et al. [38] have evaluated tavorite-structured oxyphosphates, fluorophosphates, oxysulfates, and fluorosulfates. The activation energies for lithium diffusion through the tavorite frameworks of $LiVO(PO_4)$, $LiV(PO_4)F$, and $Li_2V(SO_4)F$ showed that these materials are capable of reversibly inserting two lithium ions per redox active metal at very high rates.

Table 8.1 Electrochemical characteristics of lithiated compounds with polyanionic framework

Compounds lithiated state	Compounds delithiated state	Redox potential (V)	Capacity (mAh g^{-1})	References
$LiVPO_4F$	VPO_4F	4.2	115	[32]
Li_2VPO_4F	$LiVPO_4F$	1.8	130	[33]
Li_2FePO_4F	$LiFePO_4F$	2.9	288	[34]
$Li_{1+x}TiPO_4F$	$LiTiPO_4F$	1.8	145	[35]
$LiFeSO_4F$	$FeSO_4F$	3.6	140	[35]
$LiNiSO_4F$	$NiSO_4F$	5.4 (?)	142	[36]

8.3 Fluorophosphates

Numerous inorganic material factors including the nature of the transition-metal ion and its number of valence states affect the structural and transport properties. For instance, lithium fluorophosphates glasses (LFG) formed by P_2O_5 glass former and LiF glass modifier with addition of dopant are well known to exhibit enhancement of their conductivity and decrease of their glass transition temperature without altering the phosphate network [38, 39]. The crystallized materials with the framework-structured Li-containing fluorophosphates of 3*d*-metals, described by general formulae $LiMPO_4F$ and Li_2MPO_4F, have been explored as perspective high-voltage cathode materials for rechargeable lithium batteries [22]. The crystallographic parameters of $LiMPO_4F$ (M = Fe, Co, Ni) compounds are listed in Table 8.2.

8.3.1 Fluorine-Doped $LiFePO_4$

With the goal of increasing the voltage of the redox reaction, Liao et al. [44] were among the first groups who investigated the effects of fluorine substitution on electrochemical behavior of $LiFePO_4$/C composite electrode material. $LiFe(PO_4)_{1-x}F_{3x}$/C ($x = 0.01$, 0.05, 0.1, 0.2) was synthesized by a solid-state carbothermal reduction route at 650 °C using NH_4F as dopant. F-doped $LiFePO_4$/C nanoparticles were prepared either via a low-temperature hydrothermal reaction followed by high-temperature treatment at 850 °C for 5 h under Ar atmosphere [45, 46] or via sol–gel process using LiF [48]. Nanostructured C-$LiFePO_{3.98}F_{0.02}$ composite was synthesized by an aqueous precipitation of precursor material in molten stearic acid [48]. The excessively F-substituted $LiFe(PO_4)_{0.9}F_{0.3}$/C composite showed the most attractive high rate performance and the cycling life at high temperatures ($T > 50$ °C) due to the fact that the more ionic Fe-F bond stabilizes the energy of the antibonding 3*d* orbitals of the transition-metal ion.

However, two proposals about the fluorine ion occupy were given: (1) the first one suggested that $3F^-$ ions replace PO_4^{3-} group as a whole [44, 45], and

Table 8.2 Crystallographic parameters of LiMPO$_4$F (M = Fe, Co, Ni) compounds

Compound	Space group	a (Å)	b (Å)	c (Å)	α (°)	β (°)	γ (°)	V (Å^3)	References
VPO$_4$F	$C2/c$	8.1553(2)	8.1014(1)	8.1160(2)	90	118.089(1)	90	319.00(8)	[35]
LiVPO$_4$F	$P\bar{1}$	5.1830(8)	5.3090(6)	8.2500(3)	82.489(4)	108.868(8)	84.385(8)	184.35(0)	[32]
LiFePO$_4$F	$P\bar{1}$	5.15510(3)	5.3044(3)	8.2612(4)	108.358(5)	108.855(6)	98.618(5)	1832.91(2)	[40]
LiTiPO$_4$F	$P\bar{1}$	5.1991(2)	5.3139(2)	8.2428(3)	106.985(3)	108.262(4)	98.655(4)	186.10(2)	[40]
Li$_2$VPO$_4$F	$C2/c$	8.2255(1)	8.9450(1)	8.3085(1)	90	116.881(1)	90	384.53(8)	[38]
Li$_2$FePO$_4$F	$P\bar{1}$	5.3846(3)	8.4438(3)	5.3256(4)	109.038(2)	94.423(6)	108.259(9)	189.03(4)	[34]
Li$_2$FePO$_4$F	$Pbcn$	5.0550(2)	13.5610(2)	11.0520(3)	90	90	90	858.62(1)	[41]
Li$_2$CoPO$_4$F	$Pnma$	10.4520(2)	6.3911(8)	10.8840(2)	90	90	90	826.40(3)	[42]
Li$_2$NiPO$_4$F	$Pnma$	10.4830(3)	6.2888(8)	10.8460(1)	90	90	90	814.33(2)	[43]

(2) the second one declared that F^- could only be replaced at the oxygen sites [46–48]. Considering the second proposition, there are three nonequivalent randomly occupied O sites, namely the O(1), O(2), and O(3) site, in the crystalline elementary cell of $LiFePO_4$. As compared with the pure olivine material, its discharge capacity at 10*C* rate was 110 mAh g^{-1} with a flat discharge voltage plateau of 3.3–3.0 V vs. Li^0/Li^+. Lu et al. [46] reported that the length of Li–O bonds increased and those of P–O bonds decreased due to F doping. This implies that Li^+ diffusion between lithiated phase and delithiated phase could be improved, due to the F-doping that weakens the Li–O bonds. Fluorine ions preferably occupy specific O(2) oxygen sites. It seems that fluorine doping leads to additional electron density on the lithium sites indicating the formation of Fe_{Li+}-Li_{Fe-} antisite pairs. Such fluorine doping closes the gap in the electronic structure, which results in a finite density of states at the Fermi level. Enhanced high rate performance and improved cycle stability of F-doped olivine-phosphate was also reported in more recent studies [46–48]. C-$LiFePO_{3.98}F_{0.02}$ composite delivered the capacity of 164 mAh g^{-1} at *C*/10 rate. The first principles computational results indicate that electronic properties, the lithium insertion voltage, and general electrochemical behavior, are very sensitive to the placement of fluorine ions in the structure of this compound [48]. It was suggested that $LiVSiO_4F$ and $Li_{0.5}FePO_{3.5}F_{0.5}$ lithium deinsertion causes a too large *M*-F distance (indicative of *M*-F bond breaking), being the predicted lithium insertion voltage about 0.3 V lower than that of the parent compound.

8.3.2 $LiVPO_4F$

The vanadium-containing phosphate polyanion $LiVPO_4F$ has been initially proposed and described in detail by Barker et al. [32, 49–59] as a novel 4-V positive electrode materials for Li-ion batteries. Initial testing of $LiVPO_4F$ has shown that this material is substantially safer than the traditional oxide materials, and therefore should also be considered as a cathode replacement for the current generation of Li ion cells [32]. $LiVPO_4F$ is isostructural with the native mineral tavorite, which belongs to the lithium-bearing pegmatite family with favorite $LiFe^{3+}(PO_4)\cdot(OH)$, amblylgonite $(Li,Na)AlPO_4\cdot(F,OH)$, and montebrasite $LiAlPO_4\cdot(F,OH)$ polymorphs. The tavorite phase crystallizes in a triclinic structure ($P\bar{1}$ S.G.) and its framework consists of $V^{3+}O_4F_2$ octahedra linked by fluorine vertices forming $(V^{3+}O_4F_2)_\infty$ chains along the *c*-axis (Fig. 8.2). The connection of these chains with corner-sharing PO_4 tetrahedra form an open three-dimensional lattice with wide tunnels along the *a*, *b*, and *c* directions that accommodate the Li ions in two sites, i.e., Li(1) is five coordinated with low occupancy (~18 %) and Li(2) adopts a six coordination with high occupancy (~82 %) on the 2*i* Wyckoff positions [60–63].

In the early work of Barker et al. [32] the synthesis of $LiVPO_4F$ was made by a two-step approach involving the initial carbothermal preparation of a VPO_4

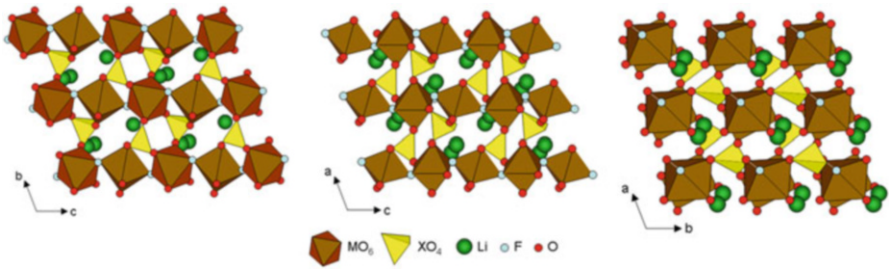

Fig. 8.2 Schematic view of the tavorite structure ($P\bar{1}$ S.G.) along the *a*-, *b*-, and *c*-crystallographic directions

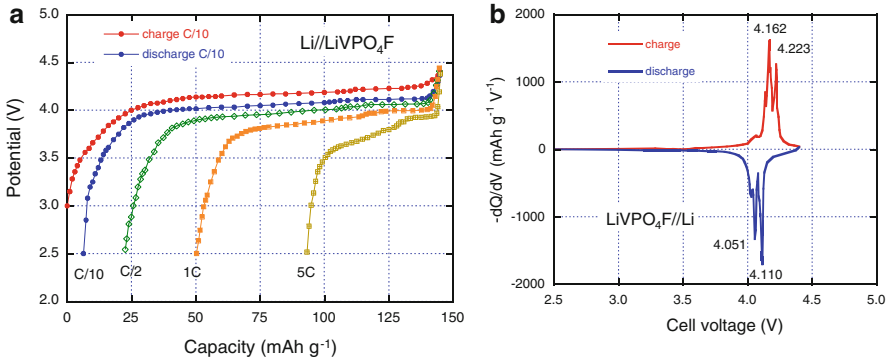

Fig. 8.3 (**a**) Charge–discharge profile of $LiVPO_4F$//Li cell cycled at different C-rates with 1 mol L^{-1} $LiPF_6$ solution in EC-DEC (1:1) as electrolyte. The first charge curve (*red*) is shown for comparison. (**b**) Variation of the derivative capacity ($-dQ/dV$) as a function of the voltage during extraction (charge) and insertion (discharge) of Li^+ ions into the $LiVPO_4F$ host

intermediate using V_2O_5, $NH_4H_2PO_4$, and particulate carbon (super P grade) precursors, followed by a simple LiF incorporation process. The single tavorite phase displays lattice parameters such as $a = 5.1830(8)$ Å, $b = 5.3090(6)$ Å, $c = 8.2500(3)$ Å, $\alpha = 82.489(4)°$, $\beta = 108.868(8)°$, $\gamma = 81.385(8)°$, and $V = 184.35(0)$ $Å^3$. Preliminary electrochemical studies of the $LiVPO_4F$ cathode material demonstrate a reversible lithium extraction/insertion reaction based on the $V^{3+/4+}$ redox couple that indicates: (1) a discharge potential centered at around 4.19 V vs. Li^0/Li^+, (2) a two-phase reaction mechanism coupled to phase nucleation behavior, (3) a reversible specific capacity around 115 mAh g^{-1}, a performance roughly equivalent to cycling of $x = 0.84$ in $Li_{1-x}VPO_4F$. In Fig. 8.3a, we present the charge–discharge profile of $LiVPO_4F$//Li cell cycled at different *C*-rates with 1 mol L^{-1} $LiPF_6$ solution in EC-DEC (1:1) as electrolyte. The first charge curve (red) is shown for comparison. The variation of the derivative capacity ($-dQ/dV$) as a function of the voltage during extraction (charge) and insertion (discharge) of Li^+ ions into the

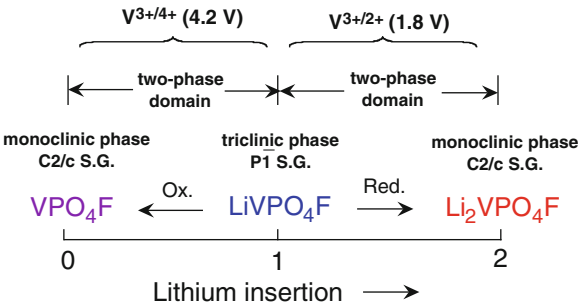

Fig. 8.4 Phase diagram of Li_xVPO_4F ($0 \leq x \leq 2$)

$LiVPO_4F$ host is shown in Fig. 8.3b. In the charge profile, the two distinct peaks with a potential separation ~60 mV correspond to the $V^{3+/4+}$ redox couple with the two Li(1) and Li(2) site occupancies. Typical thermal response of the fully delithiated $Li_{1-x}VPO_4F$ phase obtained by differential scanning calorimetry shows that, with a heat flow of ~205 J g^{-1}, the safety characteristics of $LiVPO_4F$ is vastly superior to known oxide cathode materials (for instance 345 J g^{-1} for $LiMn_2O_4$) [58].

Taking advantage of the multivalency of vanadium ions, an additional lithium insertion reaction at around 1.8 V vs. Li^0/Li^+ was reported to be associated with the $V^{3+/2+}$ redox couple [49, 56–58]. $LiVPO_4F$ has two redox electric potentials based on the $V^{4+/3+}$ ($LiVPO_4F \rightarrow VPO_4F$ reaction) and $V^{3+/2+}$ ($LiVPO_4F \rightarrow Li_2VPO_4F$ reaction) couples, which offers the possibility of using this material for the cathode as well as anode as shown in the diagram presented in Fig. 8.4. Ellis et al. [40] have investigated the end phases combining X-ray and neutron diffraction for VPO_4F and Li_2VPO_4F prepared by chemical oxidation and reduction of the parent compound. The crystal chemistry of these end phases is listed in Table 8.2. The delithiated phase VPO_4F adopts a monoclinic structure (*C*2/*c* S.G.) in which corner-shared ($V^{4+}O_4F_2$) octahedral chains are interconnected by PO_4 tetrahedra. The lithiated Li_2VPO_4F phase displays the same structural change to monoclinic symmetry (*C*2/*c* S.G.) in which lithium ions occupy two sites, Li(1) and Li(2), filled with equal probability [64]. The redox activity between the two $LiVPO_4F$-Li_2VPO_4F compositions is very facile and occurs with an 8 % change in volume and displays a stable specific capacity of 145 mAh g^{-1} [34]. More recently, Ellis et al. [40] and Plashnitsa et al. [65] and have utilized $LiVPO_4F$ as both cathode and anode for fabrication of a symmetric Li-ion $LiVPO_4F$//$LiVPO_4F$ cell with a non-flammable ionic liquid $LiBF_4$-$EMIBF_4$ electrolyte. This symmetrical cell displays a potential window of 2.4 V with a reversible specific capacity of 130 mAh g^{-1} and has shown to be stable and safe at high temperature up to 80 °C.

The incorporation of aluminum into the $LiV_{1-y}Al_yPO_4F$ framework prepared by the two-step carbothermal reduction method has generated some interesting properties: (1) an almost linear decrease of the discharge capacity on the $V^{3+/4+}$ redox couple with Al substitution, (2) a lower polarizability, (3) a gradual upshift in the $V^{3+/4+}$ redox peak of 90 mV, and (4) the ratio of the two charge plateaus remains relatively constant for $0 \leq y \leq 0.25$ [59].

The reactivity of $LiVPO_4F$ charged at $C/5$ rate with 1 mol L^{-1} $LiPF_6$ solution in EC:DEC electrolyte was tested by accelerating rate calorimetry (ARC) at high temperature. The self-heating rate (dT/dt) of the CTR-synthesized $LiVPO_4F$ reacting with electrolyte is lower or about the same as that of $LiFePO_4$ olivine over the entire test temperature range 50–350 °C for powders of identical surface area (15 m^2 g^{-1}) [66, 67]. Ma et al. [68] have investigated the effects of oxidation on the structure and the performance of $LiVPO_4F$ as a cathode material. Two two-phase structural evolutions were detected upon Li^+ electrochemical extraction at average potentials at 4.26 and 4.30 V corresponding to the continuous transformation of $LiVPO_4F \rightarrow Li_{0.82}VPO_4F \rightarrow VPO_4F$ in the first charge process, while the discharge process occurs without the appearance of the intermediate phase. Changes in the Li environment and ion mobility in the tavorite $LiVPO_4F$ lattice have been observed by multinuclear solid-state $^{6/7}Li$ and ^{31}P NMR spectroscopies on chemically and electrochemically delithiated samples [68]. The ionic conductivity determined from electrochemical impedance spectroscopy (EIS) of tavorite-structured $LiVPO_4F$. is $\sigma_\iota = 0.6 \times 10^{-8}$ S cm^{-1} at room temperature with the activation energy of $E_a = 0.85$ eV determined from the Arrhenius plot [69]. These values differ from those of $LiFePO_4F$ $\sigma_\iota = 8 \times 10^{-11}$ S cm^{-1} and $E_a = 0.99$ eV reported by Recham et al. [35].

Various vanadium-based fluorophosphates were evaluated as cathode material for Li-ion batteries [35, 70–83]. Wang et al. [81] reported the electrochemical performance of $LiVPO_4F$/C composite prepared by heating a precursor, obtained through ball milling with slurry of $H_2C_2O_4 \cdot 2H_2O$ as reacting agent and carbon source, $NH_4H_2PO_4$, NH_4VO_3 and LiF. This material shows specific discharge capacities of 151 and 102 mAh g^{-1} at $0.1C$ and $10C$, respectively, in the voltage range of 3.0–4.4 V and displays a discharge coulombic efficiency 90.4 % at 10C-rate after 50 cycles. Reddy et al. [83] have examined the long-term behavior in the potential range 3.0–4.5 V at $0.92C$-rate of $LiVPO_4F$ prepared by CTR method. The capacity degrades slowly over 800–1260 cycles and the total loss is ~14 %.

8.3.3 *$LiMPO_4F$ (M = Fe, Ti)*

Following the discovery of Barker et al. [46], who described the preparation of $LiM_{1-y}M'_yPO_4F$ materials (M and M' are transition metals having a +3 oxidation state) several attempts were made to substitute transition-metal ions of the first raw for vanadium such as Fe and Ti. DFT calculations using plane-wave methods were performed for Li_2MPO_4F, $LiMPO_4F$, and MPO_4F (M = V, Mn, Fe, Co, Ni) to address their feasibility as high-voltage cathode materials (>3.5 V relative to Li metal) for Li-ion batteries [84]. Average open-circuit voltages of 4.9, 5.2 and 5.3 V were calculated for Mn, C, and Ni, respectively.

$LiFePO_4F$ synthesized by CRT method or by a hydrogen reduction reaction crystallizes in the triclinic structure ($P\bar{1}$ S.G.) with lattice parameters $a = 5.1528$ Å, $b = 5.3031$ Å, $c = 8.4966$ Å, $\alpha = 68.001°$, $\beta = 68.164°$, $\gamma = 81.512°$ and cell volume $V = 183.89$ Å^3. $LiCrPO_4F$ prepared by the same methods crystallizes with the $P\bar{1}$ space group with lattice parameters $a = 4.996$ Å, $b = 5.308$ Å, $c = 6.923$ Å, $\alpha = 88.600°$, $\beta = 100.81°$, $\gamma = 88.546°$ and cell volume $V = 164.54$ Å^3. Recham et al. [35] experienced the growth of crystalline $LiFePO_4F$ by either solid-state or ionothermal techniques. For the solid-state synthesis, the mixture of Li_3PO_4 and FeF_3 was heated at 800 °C for 24 h inside a platinum tube. For the ionothermal method, similar mixture stabilized with an ionic liquid and triflate produced nano-structured particles (~20 nm). This material shows a reversible specific capacity of ~145 mAh g^{-1} with the average potential at 2.8 V corresponding to the $Fe^{3+} \rightarrow Fe^{2+}$ redox couples. However, $LiFePO_4F$ cannot be oxidized, which limits its use in Li-ion batteries [21]. The phase transition and electrochemistry of the $LiFePO_4F$-Li_2FePO_4F have been studied by Ramesh et al. [34]. The fully lithium inserted phase, Li_2FePO_4F, adopts a triclinic tavorite-type structure that is closely related to the parent phase (see Table 8.2). Despite the presence of two crystallographic distinct Fe sites (1*a* and 1*c* Wyckoff positions) in the $P\bar{1}$ lattice, the electrochemical features of $LiFePO_4F \rightarrow Li_2FePO_4F$ show an overall potential at 3 V with a reversible capacity of 0.96 Li corresponding to a capacity of 145 mAh g^{-1}.

Ti-based $LiMPO_4F$ is another tavorite structure built by distorted TiO_4F_2 octahedra linked by fluorine ions, which was synthesized by either solid-state or ionothermal techniques [35]. Single-phase $LiTiPO_4F$ powders prepared at low temperature (260 °C) has lattice parameters $a = 5.1991$ Å, $b = 5.3139$ Å, $c = 8.2428$ Å, $\alpha = 106.985°$, $\beta = 108.262°$, $\gamma = 98.655°$ and cell volume $V = 186.10$ Å^3. Li extraction/insertion reaction from/into the $Li_{1+x}TiPO_4F$ framework occurs in the range $-0.5 \leq x \leq 0.5$ with the appearance of two pseudo-plateaus centered at 2.9 and 1.8 V corresponding to the $Ti^{3+} \rightarrow Ti^{4+}$ and $Ti^{3+} \rightarrow Ti^{2+}$ redox couples, respectively. However, due to the sensitivity of electrochemical features upon mild modifications of synthesis, Barpanda and Tarascon [21] conclude that $LiTiPO_4F$ is a poor cathode material for battery applications.

8.3.4 Li_2FePO_4F (M = Fe, Co, Ni)

Fluorophosphates of general formula A_2MPO_4F (A = Li, Na and M = Fe, Mn, Co, Ni) crystallize in three structure types, which differ in the connectivity of (MO_4F_2) octahedra: face-shared (Na_2FePO_4F), edge-shared (Li_2MPO_4F, M = Co, Ni) and corner-shared (Na_2MnPO_4F) [42, 83]. The Li_2MPO_4F (M = Fe, Co, Mn, Ni) crystallize in three different structures types; triclinic (tavorite) and two-dimensional orthorhombic (*Pbcn* S.G.) and tunnel-like monoclinic ($P2_1/n$ S.G.) [85]. In their prior work, Ellis et al. [41] have shown that A_2FePO_4F (A = Na, Li) could serve as a cathode in Li-ion cells. This compound possesses facile two-dimensional pathways

for Li^+ motion, and the structural modifications on redox reactions are minimal with a volume change of only 3.8 % that contributes to the absence of distinct two-phase behavior. Single-phase Li_2FePO_4F was prepared by ion exchange of Na_2FePO_4F in 1 mol L^{-1} LiBr acetonitrile solution. The material $LiNaFePO_4F$ (Li/Na ratio 1:1) was obtained by reducing $NaFePO_4F$ with LiI in acetonitrile for 6 h. Li_2FePO_4F crystallizes in the orthorhombic structure (*Pbcn* S.G.) with lattice parameters $a = 5.055$ Å, $b = 13.561$ Å, $c = 11.0526$ Å, $\beta = 90°$, and cell volume $V = 858.62$ Å^3. The open-circuit voltage is lower than the $LiFePO_4$ olivine (3.0 V vs. 3.45 V); 80 % of the theoretical capacity (135 mAh g^{-1}) is attainable on the first oxidation cycle. Recently, the same group [33] reported the crystal structure and electrochemical properties of Li_2MPO_4F fluorophosphates (M = Fe, Mn, Co, Ni) synthesized by solid-state and hydrothermal synthetic routes. New forms of lithium fluorophosphate cathode materials have been reported such as Li_2FePO_4F obtained by cycling the orthorhombic $NaLiFePO_4F$ phase (*Pnma* S.G.) in an electrochemical lithium cell [85], single phase sub-stoichiometric nanocrystalline $Li_{1-x}Fe_{1-y}M_yPO_4$ (M = Fe, Co) [86], and $Li_{2-x}Na_xFe[PO_4]F$ tavorite structure synthesized by ion exchange using LiBr in ethanol [87].

8.3.5 Li_2MPO_4F (M = Co, Ni)

Several groups reported on high voltage electrochemical performance of Li_2CoPO_4F and Li_2NiPO_4F [86]. Both $LiCoPO_4$ and Li_2CoPO_4F (isostructural with Li_2NiPO_4F) crystallize in the orthorhombic system (S.G. *Pnma*, $Z = 8$). Nevertheless, there are remarkable differences between the structures from a crystallographic point of view. $LiCoPO_4$ has CoO_6 octahedra, LiO_6 octahedra and PO_4 tetrahedra. In contrast, Li_2CoPO_4F has CoO_4F_2 octahedra instead of CoO_6 octahedra. In addition, Li_2CoPO_4F has two kinds of Li sites, 4*c* and 8*d* [43]. It was confirmed that Li_2CoPO_4F is a new class of 5-V cathode materials similar to $LiCoPO_4$ [13, 42, 89]. Dumont Botto et al. [85] have pointed out that, contrary to the Na phases which are quite simple to obtain, the synthesis of Li_2MPO_4F remains difficult and requires either the ion exchange of the Na-counterparts or a lengthy solid-state reaction (at least 10-h heat treatment) [83]. In the search of finding unconventional way to prepare Li_2CoPO_4F, a shorter reaction down to 9 min was done by spark plasma sintering, which favors the formation of submicrometric particles (0.8 μm).

A considerable theoretical upper limit of approximately 310 mAh g^{-1} is expected for Li_2CoPO_4F and Li_2NiPO_4F. The theoretical estimation of the intercalation voltage of ~4.9 V for Li_2CoPO_4F cathode [88] is in good agreement with the voltage plateau observed at ca. 5 V [42]. A fault of both Li_2CoPO_4F and lithiated cobalt phosphate is a high irreversible capacity (especially in the first cycles), which is related to decomposition of electrolyte at high anodic potentials. Experimentally, $LiNiPO_4F$ discharge voltage is demonstrated to be close to 5.3 V [88]. Khasanova

et al. [89] have investigated the electrochemical performance and structural properties of the high-voltage cathode material Li_2CoPO_4F. The cyclic voltammetry and coulometry under potential step mode in the voltage range 3.0–5.1 V vs. Li revealed a structural transformation at potentials above 4.8 V. This transformation occurring upon Li-extraction appears to be irreversible: the subsequent Li-insertion does not result in restoration of the initial structure, but takes place within a new "modified" framework. According to the structure refinement, this modification involves the mutual rotations of (CoO_4F_2) octahedra and (PO_4) tetrahedra accompanied by the considerable unit cell expansion, which is expected to enhance the Li transport upon subsequent cycling. The new framework demonstrates a reversible Li-insertion/extraction in a solid-solution regime with stabilized discharge capacity at around 60 mAh g^{-1}. The Li_2CoPO_4F is prepared by a two step solid state method, followed by the application of wet coating containing various amounts of ZrO_2. Among the samples, the 5 wt% ZrO_2 coated Li_2CoPO_4F material shows the best performance with an initial discharge capacity of up to 144 mAh g^{-1} within the voltage range of 2–5.2 V vs. Li^0/Li^+ at current density 10 mA g^{-1} [83]. XRD patterns of Li_2CoPO_4F electrodes at different stages of cycling during the first charge–discharge cycle were investigated by Wang et al. [83]. Electrodes discharged from 5.0 V maintain the same trend as the fresh electrodes; however, a slight difference indicates that the structural relaxation of the framework of Li_2CoPO_4F occurs at a voltage greater than 5.0 V, which is consistent with the CV measurements.

8.3.6 $Na_3V_2(PO_4)_2F_3$ Hybrid-ion Cathode

The sodium vanadium fluorophosphate materials have demonstrated reversible Li-ion insertion behavior [87, 88]. The $Na_3V_2(PO_4)_2F_3$ phase prepared using a solid-state carbothermal reduction (CTR) approach involving the precursors VPO_4 and NaF crystallizes in the tetragonal space group $P4_2/mnm$ with lattice parameters $a = 0.0388(3)$ Å, $c = 10.8482(4)$ Å and $V = 888.94(6)$ Å^3. The framework structure is best described in terms of ($V_2O_8F_3$) bi-octahedra and (PO_4) tetrahedral. The bi-octahedra are linked by one of the fluorine atoms, whereas the oxygen atoms are all interconnected through the PO_4 units. Electrochemical properties of $Li_xNa_{3-x}V_2(PO_4)_2F_3$ carried out in a metallic Li half-cell in the potential range 3.0–4.6 V vs. Li^0/Li^+ reveal that mobile Na is rapidly exchanged for Li (Fig. 8.5). The voltage response corresponded to the reversible cycling of two alkali ions per formula unit. The associated specific capacity was around 120 mAh g^{-1}, at an average discharge voltage of around 4.1 V vs. Li metal anode [88]. The differential capacity data for the cell cycled at C/20 rate for charge and discharge is shown in Fig. 8.5a. Thus, when fully charged to 4.6 V vs. Li, a cathode composition approximating to $NaV_2(PO_4)_2F_3$ is produced, a condition in which all the vanadium has been oxidized to V^{4+}. Such a hybrid-ion cathode was used in Li-ion battery with

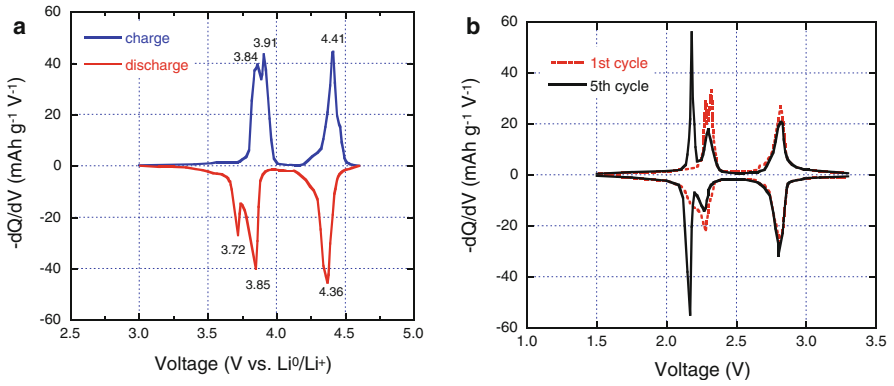

Fig. 8.5 Differential capacity (dQ/dV) curves of (**a**) Li//$Na_3V_2(PO_4)_2F_3$ cell and (**b**) the first and fifth cycle for a $Li_{4/3}Ti_{5/3}O_4$//$Na_3V_2(PO_4)_2F_3$ hybrid-ion cell. The electrolyte comprised a 1 mol L^{-1} $LiPF_6$ solution in ethylene carbonate/dimethyl carbonate (2:1 wt%)

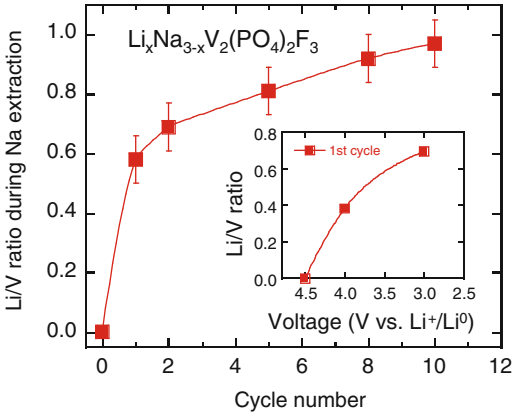

Fig. 8.6 Variation of the Li/V ratio in $Li_xNa_{3-x}V_2(PO_4)_2F_3$ as a function of cycle number showing the Li-Na exchange process. *Insert* presents the change during the first cycle

$Li_{4/3}Ti_{5/3}O_4$ as Li source. The differential capacity ($-dQ/dV$) curves of the first and fifth cycle for a $Li_{4/3}Ti_{5/3}O_4$//$Na_3V_2(PO_4)_2F_3$ hybrid-ion cell cycle are displayed in Fig. 8.5b. During the initial charge of the cell sodium ions are extracted from the $Na_3V_2(PO_4)_2F_3$ cathode. These results show that the $-dQ/dV$ response for the first cycle is broad and symmetrical, confirming the energetic reversibility of the cell chemistry with a capacity of ~120 mAh g^{-1}. However, sodium insertion into $Li_{4/3}Ti_{5/3}O_4$ is not favored. On subsequent cycles, the 2.28/2.23 V redox peaks shift by 100 mV to lower potential due to the Li^+/Na^+ ionic exchange that is now characterized by sharp redox peaks. Thus, change to a predominate lithium insertion mechanism occurred at the cathode [88]. Variation of the Li/V ratio in $Li_xNa_{3-x}V_2(PO_4)_2F_3$ as a function of cycle number showing the Li-Na exchange process is presented in Fig. 8.6. As a result, the almost entire Li/Na exchange was completed after ten cycles. Similar results for Na_2FePO_4F have been reported by

Ellis et al. [31]. By ion-exchange reaction, the entire Na content in Na_2FePO_4F may be replaced with Li to yield Li_2FePO_4F, which exhibits a slightly higher redox potential than the parent compound because of the more electronegative nature of Li compared to Na [43]. Later on, the same authors have shown that $LiVPO_4F$// graphite Li-ion cell delivered a capacity 130 mAh g^{-1} and an average discharge voltage of 4.06 V. Long-term cycling at *C*/5 rate displays a coulombic efficiency around 90 % after 500 cycles [48].

8.3.7 Other Fluorophosphates

To follow the initial investigation of Barker et al., several compounds of the same structure have been proposed. Park et al. [89] have prepared the $Li_{1.1}Na_{0.4}VPO_{4.8}F_{0.8}$ phase from the pseudo-layered structure $Na_{1.5}VPO_5F_{0.5}$ using an ion-exchange process between Na^+ and Li^+ in 1-hexanol at its boiling point (160 °C) under reflux with LiBr as the lithium source. The lattice is made up of VO_5F octahedral and PO_4 tetrahedra units, where two VO_5F are linked by a bridging fluorine ion to form $V_2O_{10}F$ bi-octahedron. These units are repeatedly connected in the *ab* plane via PO_4 units sharing oxygen to construct an open framework having a layer-like spacing into which Na^+/Li^+ ions are inserted [90]. This compound shows reversible extraction and insertion of ~1.1 Li^+ ions at an ideal 4 V vs. Li^0/Li^+ to provide a capacity of 156 mAh g^{-1} with coulombic efficiency 98 % after 100 cycles at 60 °C. Among fluorophosphates used as electrode materials, the layered structure $Li_5M(PO_4)_2F_2$ with $M = V$, Cr operates as 4-V cathodes for lithium-ion batteries [91, 92], but the capacity is lower than 100 mAh g^{-1}.

8.4 Fluorosulfates

Recently, the concept of inductive effect have been applied to replace $(PO_4)^{3-}$ for $(SO_4)^{2-}$ in polyanionic cathode materials [35, 36, 93–119]. Table 8.3 summarizes the structural properties of some fluorosulfate compounds. The fluorosulfates $LiMSO_4F$ constitute a wide family showing a good mix of properties, especially, both electrochemical and safety issues. However, we notice that the electroactive compounds appeared only in 2010 after the synthesis of newest member of the tavorite family $LiFe^{2+}(SO_4)F$ [36]. For instance, a simple substitution in Nasicon $Li_xM_3(XO_4)_3$ networks increases the redox potential by 800 mV independently of the 3*d* transition-metal ion [2]. Recent review by Rousse and Tarascon [119] deals with the crystal chemistry and structural–electrochemical relationship of new fluorosulfate polyanionic $LiMSO_4F$ electrode materials. The lithiated fluorosulfates present an interesting family from the view point of crystal chemistry with the three main types of structure that depend on the nature of the transition-metal ion:

Table 8.3 Crystallographic parameters of LiMSO$_4$F (M = Fe, Co, Ni) compounds

Compound	Space group	a (Å)	b (Å)	c (Å)	α (°)	β (°)	γ (°)	V (Å^3)	References
LiFeSO$_4$F	$P\bar{1}$	5.1848(3)	5.4943(3)	8.2224(3)	106.522(3)	108.210(3)	98.891(3)	182.559(16)	[36]
LiFeSO$_4$F	$C2/c$	13.0238(6)	6.3958(3)	9.8341(5)	90	119.68(5)	90	811.64(1)	[108]
LiNiSO$_4$F	$P\bar{1}$	5.1430(6)	5.3232(8)	8.1404(8)	106.802(9)	108.512(8)	98.395(6)	182.56(4)	[100]
LiCoSO$_4$F	$P\bar{1}$	5.1821(8)	5.4219(8)	8.1842(8)	106.859(6)	108.888(6)	98.986(5)	188.80(4)	[100]
LiMnSO$_4$F	$C2/c$	13.2801(5)	6.4162(2)	10.0393(4)	90	120.586(2)	90	835.85(5)	[102]
LiMgSO$_4$F	$P\bar{1}$	5.1623(8)	5.388(1)	8.083(1)	106.68(1)	108.40(1)	98.50(1)	184.82(5)	[93]
LiZnSO$_4$F	$Pnma$	8.4035(8)	6.3299(5)	8.4201(6)	90	90	90	348.84(0)	[96]

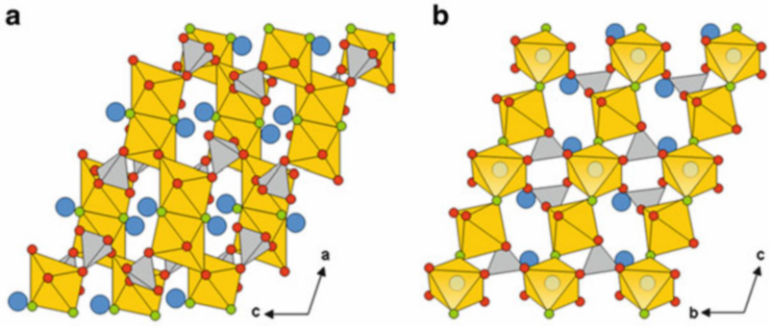

Fig. 8.7 Schematic representation of the crystal chemistry of the triplite (**a**) compared with the tavorite phase (**b**)

tavorite ($M = \text{Fe}$), triplite ($M = \text{Mn}$), or sillimanite ($M = \text{Zn}$). Figure 8.7 shows the difference between the tavorite ($P\bar{1}$ S.G.) and triplite ($P\bar{1}$ S.G.) structure.

8.4.1 $LiFeSO_4F$

Single phase tavorite $LiFeSO_4F$ cannot be prepared by typical solid-state methods because its low thermodynamic stability imposes that the crystallization must be effected at low (<400 °C) temperatures in hydrophobic ionic liquids [36, 100]. Tripathi et al. [99] reported the easy synthesis of $LiFeSO_4F$ by reaction in hydrophobic tetraethylene glycol at 220 °C to give a highly electrochemically active material. Reversible Li insertion is easy because of the close structural similarity of the lattice with that of the tavorite-type monoclinic $FeSO_4F$ ($C2_1/c$ S.G.). $LiFeSO_4F$ can be readily oxidized to produce the empty host $FeSO_4F$ but the volume contraction (from 182.4 to 164.0 $Å^3$) is greater than that of the olivine $LiFePO_4$ framework [99]. The temperature dependence of the magnetic susceptibility gives evidence of a transition to long-range antiferromagnetic order at $T_N = 100$ K in $FeSO_4F$, while such ordering appears at 25 K in $LiFeSO_4F$ [108]. This large increase of T_N upon delithiation is not only linked to the change of valence of the iron ions, since it is not observed in the case of $LiFePO_4$ for instance. Instead, it gives evidence of the shortening of the bonding path responsible for the superexchange interactions and is thus another evidence of the large contraction of the lattice. An ionothermal route (soft chemistry) has been developed for the synthesis of fluorosulfates [35, 100], in which the nucleation is facilitated by ionic liquids decomposing at temperatures ~300 °C. In such a synthesis route the $FeSO_4{\cdot}H_2O$ monohydrate is employed because of the structural similarity with the $LiMgSO_4F$ tavorite [93]. The galvanostatic cycling of ionothermal synthesized $LiFeSO_4F$ at $C/10$ rate shows a reversible capacity 130 mAh g^{-1} involving the $Fe^{2+/3+}$ redox reaction at 3.6 V vs. Li^0/Li^+ [35]. Note that the cell voltage is

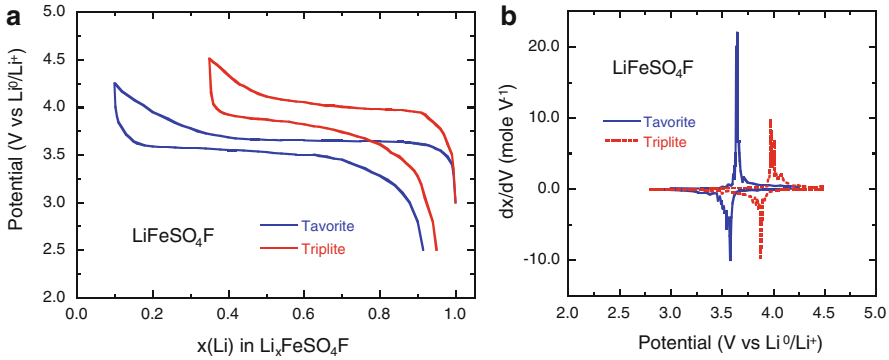

Fig. 8.8 (**a**) Charge–discharge profiles and (**b**) derivative $-dx/dV$ for the tavorite and triplite $LiFeSO_4F$ polymorphs

enhanced by 150 mV over $LiFePO_4$. Ultra-rapid microwave synthesis of triplite $LiFeSO_4F$ has been performed by Tripathi et al. [120]. Using the solid-state reaction method, the triplite was obtained upon long annealing at 320 °C in water-containing autoclaves; after 6 days the complete tavorite → triplite conversion was done [110]. The Fe triplite intercalates Li at 3.9 V, which is 0.3 V higher than its ordered tavorite analogue, attributable to longer Fe-O bond length [113]. The origin of the voltage difference between the tavorite and the triplite phase has been discussed by Ben-Yahia et al. [113] from results of DFT + U calculations. The voltage increase originates from the difference in the anionic networks of the two polymorphs, due to the change in the electrostatic repulsions induced by the configuration of the fluorine atoms around the transition-metal cations. The potential difference between the two $LiFeSO_4F$ polymorphs is illustrated in Fig. 8.8.

Recently, Ati et al. [110] have discussed the nucleation of the triplite phase of $LiFeSO_4F$ using X-ray diffraction and TEM studies. Besides preparing triplite $LiFeSO_4F$ from dry precursors, it was found that this phase could be obtained from the tavorite via a heating process at 320 °C for few days. Sobkowiak et al. [118] demonstrated the dependence of the electrochemical features of the tavorite $LiFeSO_4F$ on the synthesis conditions. The importance of the surface chemistry has been pointed out and the optimized cycling performance can be achieved by removing the unwanted residues and applying a conducting polymer coating such as PEDOT film.

8.4.2 *$LiMSO_4F$ (M = Co, Ni, Mn)*

The redox potential of the fluorosulfates $LiMSO_4F$ (M = Co, Ni, Mn) are expected to exhibit redox potentials of 4.25, 4.95, and 5.25 V, respectively. Barpanda et al. [100] succeeded in preparing the $Li(Fe_{1-x}M_x)SO_4F$ solid solutions only

when we used the corresponding monohydrate solid solutions as precursors, hence providing further evidence for the topotacticity of the synthesis reaction. None of these fluorosufates was shown to present any electrochemical activity up to 5 V. Evidently, Co^{2+}/Co^{3+}, Ni^{2+}/Ni^{3+}, and Mn^{2+}/Mn^{3+} redox reactions do not occur within the explored galvanostatic cycling potential window, contrary to the case of the Fe^{2+}/Fe^{3+} redox reaction. Subsequently, the electrochemical activity of pure $LiMSO_4F$ phases were tested at different rates ($C/2$–$C/10$) by cycling up to 5 V using an aluminum plunger for the cathode. Therefore, even at such high voltages prone to electrolyte oxidation/decomposition, the activity of the corresponding M^{2+}/M^{3+} redox couples did not be triggered. Among the Co-based polyanionic insertion compounds, $Li_2CoP_2O_8$ [121] is considered as a 4.9 V cathode. This pyrophosphate crystallizes in the monoclinic structure ($P2_1/c$ S.G.), in which Li occupies five sites; two are tetrahedally coordinated, one forms bipyramidal sites, and two Li share them occupancy with Co bipyramids. The material synthesized using a two-step solid-state method delivered a discharge capacity of ca. 80 mAh g^{-1} at $C/20$ rate. Sillimanite-structured $LiZnSO_4F$ was produced by low temperature synthesis (<300 °C). The Li^+ ion conductivity has been enhanced by a monolayer of ionic liquid grafting [115]. On the other hand, it has been pointed out that the $LiMnSO_4F$ polymorph is electrochemically inactive [103]. However, the effect of Zn substitution in the $LiFe_{1-y}Zn_ySO_4F$ forms an electrochemically active solid solution. The Fe-rich phase is obtained in the triplite structure, while the Zn-rich phase crystallizes in the sillimanite structure. The redox potentials are observed at 3.6 and 3.9 V vs. Li^0/Li^+ for the $LiFe_{0.8}Zn_{0.2}SO_4F$ (sillimanite) and $LiFe_{0.9}Zn_{0.1}SO_4F$ (triplite), respectively. In the same way, while $LiMnSO_4F$ that crystallizes in the triplite phase is inactive, $LiFe_{1-x}Mn_xSO_4F$ can be electrochemically active. Fe-rich solid solutions ($0 < x < 0.2$) tavorite polymorphs have a redox activity at 3.6 V close to that of $LiFeSO_4F$ and characteristic of the Fe^{2+}/Fe^{3}+ redox potential in the tavorite structure, with a standard two-phase voltage-composition curve [102]. On the other hand, Fe-rich $LiFe_{1-x}Mn_xSO_4F$ triplite solid solution polymorphs show a redox activity at 3.9 V. This value characteristic of the Fe^{2+}/Fe^{3+} redox potential in the triplite structure is large. Unfortunately only the iron shows an activity, so that the capacity decreases linearly with x (120 mAh g^{-1} for $x = 0.2$ [21]).

8.5 Concluding Remarks

The combination high electronegativity of F with the inductive effect of polyanion allows for the tuning of the redox potential of many fluorine-based polyanionic compounds in the electrolytic window, which make them promising electrodes for Li-ion batteries. Among them $LiVPO_4F$ can deliver a capacity of 145–150 mAh g^{-1}, which is comparable to the capacity delivered by $LiFePO_4$, but the operating voltage (4.1 V) is larger than that of the olivine (3.45 V). The $LiVPO_4F//LiVPO_4F$ cell works at 2.4 V with a reversible capacity 130 mAh g^{-1} and is safe at 80 °C,

which is comparable to the $LiFePO_4//Li_4Ti_5O_{12}$ that also works at this temperature [122]. However, the performance of $LiVPO_4F$ at high C-rates is smaller than that of $LiFePO_4$, since the capacity reduces to 100 mAh g^{-1} at 10*C* in the best case (preparation by the CRT method). Even at 1*C* a capacity loss of 14 % is observed between 800 and 1260 cycles, while that of $LiFePO_4$ is stable under such condition. Among the other fluorophosphates that we have reviewed, the best results are obtained with $LiFePO_4F$, which, however cannot be oxidized. Again, the $LiFePO_4F \rightarrow Li_2FePO_4F$ reaction gives a reversible capacity of 145 mAh g^{-1}, but it takes place at an overall potential at 3 V only. An ideal 4 V-battery is obtained with $Li_{1.1}Na_{0.4}VPO_{4.8}F_{0.8}$, providing a capacity of 156 mAh g^{-1} with coulombic efficiency 98 % after 100 cycles at 60 °C. The corresponding energy density is thus better than that of $LiFePO_4$ owing to the larger operating voltage. Again, however, the advantage of $LiFePO_4$ will be its high-rate performance that allows for higher power densities, and the cycling life that exceeds 30000 cycles at room temperature [122].

Among the fluorosulfates, $LiFeSO_4F$ in the triplite phase is promising, owing to the high Fe^{2+}/Fe^{3+} redox potential at 3.9 V, but the kinetics is very sluggish, and only a small fraction of the lithium can be extracted so far. The voltage is decreased to 3.6 V in the tavorite phase, but then the capacity is raised to 130 mAh g^{-1}, and this smaller capacity with respect to $LiFePO_4$ is compensated by the larger voltage. The capacity of $LiFeSO_4F$ tavorite, however, decreases at *C*-rate lager than 1*C*, and this cathode does not operate au 10*C* rate so far.

At present time, the fluorophosphates and fluorosulfates cannot compete in energy density with lamellar compounds, and cannot compete in power density and cycling life with C-$LiFePO_4$. It should be noted, however, that these materials have been studied for Li-ion battery applications only recently, while it took about 15 years to optimize C-$LiFePO_4$ and bring it to the position of winning a part of the market. In addition, the structural relationship between the precursor and the final product underlying the topotactic reaction makes possible the synthesis of many fluorophosphates and sulfates, and many of them have still to be discovered. Therefore, the research in this field will be very active in the years to come, justified by the fact that this family of materials is promising for applications in electrochemical energy storage.

References

1. Julien CM, Mauger A, Zaghib K, Groult H (2014) Comparative issues of cathode materials for Li-ion batteries. Inorganics 2:132–154
2. Manthiram A, Goodenough JB (1989) Lithium insertion into $Fe_2(SO_4)_3$ frameworks. J Power Sourc 26:403–408
3. Padhi AK, Nanjundaswamy KS, Goodenough JB (1998) Phospho-olivines as positive-electrode materials for rechargeable lithium batteries. J Electrochem Soc 144:1188–1194

4. Saidi MY, Barker J, Huang H, Swoyer JL, Adamson G (2002) Electrochemical properties of lithium vanadium phosphate as a cathode material for lithium-ion batteries. Electrochem Solid State Lett 5:A149–A151
5. Yin C, Grondey H, Strobel P, Nazar LF (2004) $Li_{2.5}V_2(PO_4)_3$: a room-temperature analogue to the fast-ion conducting high-temperature γ-phase of $Li_3V_2(PO_4)_3$. Chem Mater 16:1456–1465
6. Azmi BM, Ishihara T, Nishiguchi H, Takita Y (2005) $LiVOPO_4$ as a new cathode materials for Li-ion rechargeable battery. J Power Sourc 146:525–528
7. Gaubicher J, Le Mercier T, Chabre Y, Angenault J, Quarton M (1999) Li/β-$VOPO_4$: a new 4 V system for lithium batteries articles. J Electrochem Soc 146:4385–4389
8. Rousse G, Wurm C, Morcrette M, Rodriguez-Carvajal J, Gaubicher J, Masquelier C (2001) Crystal structure of a new vanadium(IV) diphosphate VP_2O_8, prepared by lithium extraction from $LiVP_2O_8$. Int J Inorg Mater 3:881–888
9. Barker J, Gover RKB, Burns P, Bryan A (2005) $LiVP_2O_8$: a viable lithium-ion cathode material. Electrochem Solid State Lett 8:A446–A448
10. Kim GH, Myung ST, Bang HJ, Prakash J, Sun YK (2004) Synthesis and electrochemical properties of $Li[Ni_{1/3}Co_{1/3}Mn_{(1/3-x)}Mg_x]O_{2-y}F_y$ via coprecipitation. Electrochem Solid State Lett 8:A480–A488
11. Son JT, Kim HG (2005) New investigation of fluorine-substituted spinel $LiMn_2O_{4-x}F_x$ by using sol–gel process. J Power Sourc 148:220–226
12. Luo Q, Muraliganth T, Manthiram A (2009) On the incorporation of fluorine into the manganese spinel cathode lattice. Solid State Ionics 180:803–808
13. Stroukoff KR, Manthiram A (2011) Thermal stability of spinel $Li_{1.1}Mn_{1.9-y}M_yO_{4-z}F_z$ ($M = Ni$, Al, and Li, $0 \le y \le 0.3$, and $0 \le z \le 0.2$) cathodes for lithium ion batteries. J Mater Chem 21:10165–10180
14. Yue P, Wang Z, Guo H, Xiong X, Li X (2013) A low temperature fluorine substitution on the electrochemical performance of layered $LiNi_{0.8}Co_{0.1}Mn_{0.1}O_{2-z}F_z$ cathode materials. Electrochim Acta 92:1–8
15. Yue P, Wang Z, Li X, Xiong X, Wang J, Wu X, Guo H (2013) The enhanced electrochemical performance of $LiNi_{0.6}Co_{0.2}Mn_{0.2}O_2$ cathode materials by low temperature fluorine substitution. Electrochim Acta 95:112–118
16. Fergus JW (2010) Recent developments in cathode materials for lithium ion batteries. J Power Sourc 195:939–954
17. Yun SH, Park KS, Park YJ (2010) The electrochemical property of ZrF_x-coated $Li[Ni_{1/3}Co_{1/3}Mn_{1/3}]O_2$ cathode material. J Power Sourc 195:6108–6115
18. Park BC, Kim HB, Myung ST, Amine K, Belharouak I, Lee SM, Sun YK (2008) Improvement of structural and electrochemical properties of AlF_3-coated $Li[Ni_{1/3}Co_{1/3}Mn_{1/3}]O_2$ cathode materials on high voltage region. J Power Sourc 188:826–831
19. Xu K, Jie Z, Li R, Chen Z, Wu S, Gu J, Chen J (2012) Synthesis and electrochemical properties of CaF_2-coated for long-cycling $Li[Mn_{1/3}Co_{1/3}Ni_{1/3}]O_2$ cathode materials. Electrochim Acta 60:130–133
20. Shi SJ, Tu JP, Tang YY, Zhang YQ, Liu XY, Wang XL, Gu CD (2013) Enhanced electrochemical performance of LiF-modified $LiNi_{1/3}Co_{1/3}Mn_{1/3}O_2$ cathode materials for Li-ion batteries. J Power Sourc 225:338–346
21. Barpanda P, Tarascon JM (2013) Fluorine-based polyanionic compounds for high-voltage electrode materials (Chapter 8). In: Scrosati B, Abraham KM, Van Schalkwijk W, Hassoun J (eds) Lithium batteries: advanced technologies and applications. John Wiley & Sons, New York, NY
22. Julien CM, Mauger A (2013) Review of 5-V electrodes for Li-ion batteries: status and trends. Ionics 19:951–988
23. Hu M, Pang X, Zhou Z (2013) Recent progress in high-voltage lithium ion batteries. J Power Sourc 238:229–242
24. Goodenough JB (1994) Design considerations. Solid State Ionics 69:184–198

25. Islam MS, Fisher CAJ (2013) Lithium and sodium battery cathode materials: computational insights into voltage, diffusion and nanostructural properties. Chem Soc Rev 43:185–204
26. Saubanère M, Ben-Yahia M, Lemoigno F, Doublet ML (2013) Beyond the inductive effect to increase the working voltage of cathode materials for Li-ion batteries. ECS Meeting Abstracts MA2013-02, p 840
27. Goodenough JB (2002) Oxide cathodes (Chapter 4). In: van Schalkwijk W, Scrosati B (eds) Advances in lithium-ion batteries. Kluwer Academic/Plenum, New York, NY
28. Arroyo de Dompablo ME, Amador U, Tarascon JM (2008) A computational investigation on fluorinated-polyanionic compounds as positive electrode for lithium batteries. J Power Sourc 184:1251–1258
29. Nanjundaswamy KS, Padhi AK, Goodenough JB, Okada S, Ohtsuka H, Arai H, Yamaki J (1996) Synthesis, redox potential evaluation and electrochemical characteristics of NASICON-related-3D framework compounds. Solid State Ionics 92:1–10
30. Pahdi AK, Manivannan M, Goodenough JB (1998) Tuning the position of the redox couples in materials with NASICON structure by anionic substitution. J Electrochem Soc 145:1518–1520
31. Nyten A, Abouimrane A, Armand M, Gustafsson T, Thomas JO (2005) Electrochemical performance of Li_2FeSiO_4 as a new Li-battery cathode material. Electrochem Commun 8:156–160
32. Barker J, Saidi MY, Swoyer JL (2003) Electrochemical insertion properties of the novel lithium vanadium fluorophosphate, $LiVPO_4F$. J Electrochem Soc 150:A1394–A1398
33. Ellis BL, Makahnouk WRM, Rowan-Weetaluktuk WN, Ryan DH, Nazar LF (2010) Crystal structure and electrochemical properties of A_2MPO_4F fluorophosphates (A = Na, Li; M = Fe, Mn, Co, Ni). Chem Mater 22:1059–1080
34. Ramesh TN, Lee KT, Ellis BL, Nazar LF (2010) Tavorite lithium iron fluorophosphates cathode materials: phase transition and electrochemistry of $LiFePO_4F$-Li_2FePO_4F. Electrochem Solid State Lett 13:A43–A48
35. Recham N, Dupont L, Courty M, Djellab K, Larcher D, Armand M, Tarascon JM (2009) Ionothermal synthesis of Li-based fluorophosphates electrodes. Chem Mater 22:1142–1148
36. Recham N, Chotard JN, Dupont L, Delacourt C, Walker W, Armand M, Tarascon JM (2010) A 3.6 V lithium-based fluorosulphate insertion positive electrode for lithium-ion batteries. Nat Mater 9:68–84
37. Mueller T, Hautier G, Jain A, Ceder G (2011) Evaluation of tavorite-structured cathode materials for lithium-ion batteries using high-throughput computing. Chem Mater 23:3854–3862
38. Chowdari BVR, Mok KF, Xie JM, Gopalakrishnan R (1995) Electrical and structural studies of lithium fluorophosphates glasses. Solid State Ionics 86:189–198
39. Sreedhar B, Sairam M, Chattopadhyay DK, Kojima K (2005) Preparation and characterization of lithium fluorophosphates glasses doped with MoO_3. Mater Chem Phys 92:492–498
40. Ellis BL, Ramesh TN, Davis LJM, Govard GR, Nazar LF (2011) Structure and electrochemistry of two-electron redox couples in lithium metal fluorophosphates based on the tavorite structure. Chem Mater 23:5138–5148
41. Ellis BL, Makahnouk WRM, Makimura Y, Toghill K, Nazar LF (2008) A multifunctional 3.5 V iron-based phosphate cathode for rechargeable batteries. Nat Mater 6:849–853
42. Okada S, Ueno M, Uebou Y, Yamaki JI (2005) Fluoride phosphate Li_2CoPO_4F as a high-voltage cathode in Li-ion batteries. J Power Sourc 146:565–569
43. Dutreilh M, Chevalier C, El-Ghozzi M, Avignant D, Montel JM (1999) Synthesis and crystal structure of a new lithium nickel fluorophosphates Li_2NiFPO_4 with an ordered mixed anionic framework. J Solid State Chem 142:1–5
44. Liao XZ, He YS, Ma ZF, Zhang XM, Wang L (2008) Effects of fluorine-substitution on the electrochemical behavior of $LiFePO_4$/C cathode materials. J Power Sourc 184:820–825

45. Pan M, Lin X, Zhou Z (2011) Electrochemical performance of $LiFePO_4$/C doped with F synthesized by carbothermal reduction method using NH_4F as dopant. J Solid State Electrochem 16:1615–1621
46. Lu F, Zhou Y, Liu J, Pan Y (2011) Enhancement of F-doping on the electrochemical behavior of carbon-coated $LiFePO_4$ nanoparticles prepared by hydrothermal route. Electrochim Acta 56:8833–8838
47. Pan F, Wang W (2012) Synthesis and characterization of core–shell F-doped $LiFePO_4$/C composite for lithium-ion batteries. J Solid State Electrochem 16:1423–1428
48. Milovic M, Jugovic D, Cvjeticanin N, Uskokovic D, Milosevic AS, Popovic ZS, Vukajlovic FR (2013) Crystal structure analysis and first principle investigation of F doping in $LiFePO_4$. J Power Sourc 241:80–89
49. Barker J, Saidi MY, Swoyer JL (2001) Lithium metal fluorophosphates materials and preparation thereof. International Patent, WO01/084,655
50. Barker J, Saidi MY, and J.L. Swoyer JL (2002) Lithium metal fluorophosphates materials and preparation thereof US Patent, 6,388,568 B1, 14 May 2002
51. Barker J, Saidi MY, Swoyer JL (2003) Electrochemical insertion properties of the novel lithium vanadium fluorophosphate, $LiVPO_4F$. Electrochem Solid State Lett 6:A1–A4
52. Barker J, Saidi MY, Swoyer JL (2004) A Comparative investigation of the Li insertion properties of the novel fluorophosphate phases, $NaVPO_4F$ and $LiVPO_4F$. J Electrochem Soc 151:A1680–A1688
53. Barker J (2005) Lithium-containing phosphate active materials. US Patent, 6,890,686 B1, 10 May 2005
54. Barker J, Gover RKB, Burns P, Bryan AJ (2005) Hybrid-ion, a symmetrical lithium-ion cell based on lithium vanadium fluorophosphates $LiVPO_4F$. Electrochem Solid State Lett 8: A285–A288
55. Barker J, Gover RKB, Burns P, Bryan A, Saidi MY, Swoyer JL (2005) Performance evaluation of lithium vanadium fluorophosphate in lithium metal and lithium-ion cells. J Electrochem Soc 152:A1886–A1889
56. Barker J, Saidi MY, Swoyer JL (2005) Lithium metal fluorophosphates materials and preparation thereof. US Patent, 6,855,462 B2, 15 Feb 2005
57. Barker J, Gover RKB, Burns P, Bryan A, Saidi MY, Swoyer JL (2005) Structural and electrochemical properties of lithium vanadium fluorophosphate, $LiVPO_4F$. J Power Sourc 146:516–520
58. Gover RKB, Burns P, Bryan A, Saidi MY, Swoyer JL, Barker J (2006) $LiVPO_4F$: a new active material for safe lithium-ion batteries. Solid State Ionics 188:2635–2638
59. Barker J, Saidi MY, Gover RKB, Burns P, Bryan A (2008) The effect of Al substitution on the lithium insertion properties of lithium vanadium fluorophosphate $LiVPO_4F$. J Power Sourc 184:928–931
60. Lindberg ML, Pecora WT (1955) Tavorite and barbosalite, two new phosphate minerals from Minas Gerais Brazil. Am Mineral 40:952–966
61. Roberts AC, Dunn PJ, Grice JD, Newbury DE, Dale E, Roberts WL (1988) The X-ray crystallography of tavorite from the tip top pegmatite, custer, South Dakota. Powder Diffr 3:93–95
62. Groat LA, Raudseep M, Hawthorne FC, Ercit TS, Sherriff BL, Hartman JS (1990) The amblygonite-montebrasite series: characterization by single-crystal structure refinement, infrared spectroscopy, and multinuclear MAS-NMR spectroscopy. Am Mineral 85:992–1008
63. Pizarro-Sanz JL, Dance JM, Villeneuve G, Arriortuz-Marcaida ML (1994) The natural and synthetic tavorite minerals: crystal chemistry and magnetic properties. Mater Lett 18:328–330
64. Davis LJM, Ellis BL, Ramesh TN, Nazar LF, Bain AD, Govard GR (2011) 6Li 1D EXSY NMR spectroscopy: a new tool for studying lithium dynamics in paramagnetic materials applied to monoclinic Li_2VPO_4F. J Phys Chem C 115:22603–22608

65. Plashnitsa LS, Kobayashi E, Okada S, Yamaki JI (2011) Symmetric lithium-ion cell based on lithium vanadium fluorophosphate with ionic liquid electrolyte. Electrochim Acta 56:1344–1351
66. Zhou F, Zhao X, Dahn JR (2011) Reactivity of charged $LiVPO_4F$ with 1 M $LiPF_6$ EC:DEC electrolyte at high temperature as studied by accelerating rate calorimetry. Electrochem Commun 11:589–591
67. Ma R, Shao L, Wu K, Shui M, Wang D, Long N, Ren Y, Shu J (2014) Effects of oxidation on structure and performance of $LiVPO_4F$ as cathode material for lithium-ion batteries. J Power Sourc 248:884–885
68. Davis LJ, Cahill LS, Nazar LF, Goward GR (2010) Studies of ion mobility in lithium vanadium fluorophosphates using multinuclear solid state NMR. ECS Meeting Abstracts, MA-2010-01, p 626
69. Prabu M, Reddy MV, Selvasekarapandian S, Subba Rao GV, Chowdari BVR (2012) Synthesis, impedance and electrochemical studies of lithium iron fluorophosphate, $LiFePO_4F$ cathode. Electrochim Acta 85:582–588
70. Zheng JC, Zhang B, Yang ZH (2012) Novel synthesis of $LiVPO_4F$ cathode material by chemical lithiation and postannealing. J Power Sourc 202:380–383
71. Wang JX, Wang ZX, Shen L, Li XH, Guo HJ, Tang WJ, Zhu ZG (2013) Synthesis and performance of $LiVPO_4F$/C-based cathode material for lithium ion battery. Trans Nonferrous Met Soc China 23:1818–1822
72. Zhang QM, Shi ZC, Li YX, Gao D, Chen GH, Yang Y (2011) Recent advances in fluorophosphate and orthosilicate cathode materials for lithium ion batteries. Acta Phys Chim Sin 28:268–284
73. Reddy MV, Subba-Rao GV, Chowdari BVR (2010) Long-term cycling studies on 4 V-cathode lithium vanadium fluorophosphates. J Power Sourc 195:5868–5884
74. Yu J, Rosso KM, Zhang JG, Liu J (2011) Ab initio study of lithium transition metal fluorophosphate cathodes for rechargeable batteries. J Mater Chem 21:12054–12058
75. Khasanova NR, Drozhzhin OA, Storozhilova DA, Delmas C, Antipov EV (2012) New form of Li_2FePO_4F as cathode material for Li-ion batteries. Chem Mater 24:4281–4283
76. Badi SP, Ramesh TN, Ellis B, Lee KT, Nazar LF (2009) Effect of substitution and solid solution behavior in lithium metal polyanion materials for Li-ion battery cathodes. ECS Meeting Abstracts, MA2009-02, p 398
77. Okada S, Ueno M, Uebou Y, Yamaki JI (2004) Electrochemical properties of a new lithium cobalt fluorophosphate $Li_2[CoF(PO_4)]$. IMLB-12 Abstracts, p 301
78. Nagahama M, Hasegawa N, Okada S (2010) High voltage performances of Li_2NiPO_4F cathode with dinitrile-based electrolytes. J Electrochem Soc 158:A848–A852
79. Khasanova NR, Gavrilov AN, Antipov EV, Bramnik KG, Hibst H (2011) Structural transformation of Li_2CoPO_4F upon Li-deintercalation. J Power Sourc 196:355–360
80. Wu X, Gong Z, Tan S, Yang Y (2012) Sol-gel synthesis of Li_2CoPO_4F/C nanocomposite as a high power cathode material for lithium ion batteries. J Power Sourc 220:122–129
81. Kosova NV, Devyatkina ET, Slobodyuk AB (2012) In situ and ex situ X-ray study of formation and decomposition of Li_2CoPO_4F under heating and cooling. Investigation of its local structure and electrochemical properties. Solid State Ionics 225:580–584
82. Karthikeyan K, Amaresh S, Kim KJ, Kim SH, Chung KY, Cho BW, Lee YS (2013) A high performance hybrid capacitor with Li_2CoPO_4F cathode and activated carbon anode. Nanoscale 5:5958–5964
83. Amaresh S, Karthikeyan K, Kim KJ, Kim MC, Chung KY, Cho BW, Lee YS (2013) Facile synthesis of ZrO_2 coated Li_2CoPO_4F cathode materials for lithium secondary batteries with improved electrochemical properties. J Power Sourc 244:395–402
84. Wang D, Xiao J, Xu W, Nie Z, Wang C, Graff G, Zhang JG (2011) Preparation and electrochemical investigation of Li_2CoPO_4F cathode material for Li-ion batteries. J Power Sourc 196:2241–2245
85. Dumont-Botto E, Bourbon C, Patoux S, Rozier P, Dolle M (2011) Synthesis by spark plasma sintering: a new way to obtain electrode materials for lithium ion batteries. J Power Sourc 196:2284–2288

86. Ben-Yahia H, Shikano M, Koike S, Sakaebe H, Tabuchi M, Kobayashi H (2013) New fluorophosphate $Li_{2-x}Na_xFe[PO_4]F$ as cathode material for lithium ion battery. J Power Sourc 244:88–93
87. Gover RKB, Bryan A, Burns P, Barker J (2006) The electrochemical insertion properties of sodium vanadium fluorophosphate, $Na_3V_2(PO_4)_2F_3$. Solid State Ionics 188:1495–1500
88. Barker J, Gover RKB, Burns P, Bryan AJ (2008) $Li_{4/3}Ti_{5/3}O_4$//$Na_3V_2(PO_4)_2F_3$: an example of a hybrid-ion cell using a non-graphitic anode. J Electrochem Soc 154:A882–A888
89. Park YU, Seo DH, Kim B, Hong KP, Kim H, Lee S, Shakoor RA, Miyasaka K, Tarascon JM, Kang K (2012) Tailoring a fluorophosphate as a novel 4 V cathode for lithium-ion batteries. Sci Rep 2:804–811
90. Sauvage F, Quarez E, Tarascon JM, Baudrin E (2006) Crystal structure and electrochemical properties vs. Na^+ of sodium fluorophosphates $Na_{1.5}VPO_5F_{0.5}$. Solid State Sci 8:1215–1221
91. Yin SC, Edwards R, Taylor N, Herle PS, Nazar LF (2006) Dimensional reduction: synthesis and structure of layered $Li_5M(PO_4)_2F_2$ ($M = V$, Cr). Chem Mater 18:1845–1852
92. Makimura Y, Cahill LS, Iriyama Y, Goward GR, Nazar LF (2008) Layered lithium vanadium fluorophosphate, $Li_5V(PO_4)_2F_2$: A 4 V class positive electrode material for lithium-ion batteries. Chem Mater 20:4240–4248
93. Sebastian L, Gopalakrishnan J, Piffard Y (2002) Synthesis crystal structure and lithium ion conductivity of $LiMgFSO_4$. J Mater Chem 12:384–388
94. Ati M, Sougrati MT, Recham N, Barpanda P, Leriche JB, Courty M, Armand M, Jumas JC, Tarascon JM (2010) Fluorosulphate positive electrodes for Li-ion batteries made via a solid-state dry process. J Electrochem Soc 158:A1008–A1015
95. Ati A, Walker WT, Djellab K, Armand M, Recham N, Tarascon JM (2010) Fluorosulfate positive electrode materials made with polymers as reacting media. Electrochem Solid State Lett 13:A150–A153
96. Barpanda P, Chotard JN, Delacourt C, Reynaud M, Filinchuk Y, Armand M, Deschamps M, Tarascon JM (2010) $LiZnSO_4F$ made in an ionic liquid: a new ceramic electrolyte composite for solid-state Li-batteries. Angew Chem Int Ed 50:2526–2531
97. Barpanda P, Chotard JN, Recham N, Delacourt C, Ati M, Dupont L, Armand M, Tarascon JM (2010) Structural, transport and electrochemical investigation of novel $AMSO_4F$ (A = Na, Li; M = Fe, Co, Ni, Mn) metal fluorosulphates prepared using low temperature synthesis routes. Inorg Chem 49:8401–8413
98. Tripathi R, Ramesh TN, Ellis BL, Nazar LF (2010) Scalable synthesis of tavorite $LiFeSO_4F$ and $NaFeSO_4F$ cathode materials. Angew Chem Int Ed 49:8838–8842
99. Tripathi R, Ramesh TN, Ellis BL, Nazar LF (2010) Scalable synthesis of tavorite $LiFeSO_4F$ and $NaFeSO_4F$ cathode materials. Angew Chem 122:8920–8924
100. Barpanda P, Recham N, Chotard JN, Djellab K, Walker W, Armand M, Tarascon JM (2010) Structure and electrochemical properties of novel mixed $Li(Fe_{1-x}M_x)SO_4F$ (M = Co, Ni) phases fabricated by low temperature ionothermal synthesis. J Mater Chem 20:1659–1668
101. Frayret C, Villesuzanne A, Spaldin N, Bousquet E, Chotard JN, Recham N, Tarascon JM (2010) $LiMSO_4F$ (M = Fe, Co and Ni): promising new positive electrode materials through the DFT microscope. Phys Chem Chem Phys 12:15512–15522
102. Barpanda P, Ati M, Melot BC, Rousse G, Chotard JN, Doublet ML, Sougrati MT, Corr SA, Jumas JC, Tarascon JM (2011) A 3.90 V iron-based fluorosulphate material for lithium-ion batteries crystallizing in the triplite structure. Nat Mater 10:882–889
103. Ati M, Melot BC, Rousse G, Chotard JN, Barpanda P, Tarascon JM (2011) Structural and electrochemical diversity in $LiFe_{1-\delta}Zn_\delta SO_4F$ solid solution: a Fe-based 3.9 V positive-electrode material. Angew Chem Int Ed 50:10584–10588
104. Ramzan M, Lebegue S, Kang TW, Ahuja R (2011) Hybrid density functional calculations and molecular dynamics study of lithium fluorosulphate, a cathode material for lithium-ion batteries. J Phys Chem C 115:2600–2603
105. Liu L, Zhang B, Huang XJ (2011) A 3.9 V polyanion-type cathode material for Li-ion batteries. Prog Nat Sci Mater Int 21:211–215

106. Tripath R, Gardiner GR, Islam MS, Nazar LF (2011) Alkali-ion conduction paths in $LiFeSO_4F$ and $NaFeSO_4F$ tavorite-type cathode materials. Chem Mater 23:2284–2288
107. Ati M, Melot BC, Chotard JN, Rousse G, Reynaud M, Tarascon JM (2011) Synthesis and electrochemical properties of pure $LiFeSO_4F$ in the triplite structure. Electrochem Commun 13:1280–1283
108. Melot BC, Rousse G, Chotard JN, Ati M, Rodríguez-Carvajal J, Kemei MC, Tarascon JM (2011) Magnetic structure and properties of the Li-ion battery materials $FeSO_4F$ and $LiFeSO_4F$. Chem Mater 23:2922–2930
109. Tripathi R, Popov G, Ellis BL, Huq A, Nazar LF (2012) Lithium metal fluorosulfate polymorphs as positive electrodes for Li-ion batteries: synthetic strategies and effect of cation ordering. Energ Environ Sci 5:6238–6246
110. Ati M, Sathiya M, Boulineau S, Reynaud M, Abakumov A, Rousse G, Melot B, Van Tendeloo G, Tarascon JM (2012) Understanding and promoting the rapid preparation of the triplite-phase of $LiFeSO_4F$ for use as a large-potential Fe cathode. J Am Chem Soc 134:18380–18388
111. Ati M, Sougrati MT, Rousse G, Recham N, Doublet ML, Jumas JC, Tarascon JM (2012) Single-step synthesis of $FeSO_4F_{1-y}OH_y$ ($0 < y < 1$) positive electrodes for Li-based batteries. Chem Mater 24:1482–1485
112. Recham N, Rousse G, Sougrati MT, Chotard JN, Frayret C, Mariyappan S, Melot BC, Jumas JC, Tarascon JM (2012) Preparation and characterization of a stable $FeSO_4F$-based framework for alkali ion insertion electrodes. Chem Mater 24:4363–4380
113. Ben-Yahia M, Lemoigno F, Rousse G, Boucher F, Tarascon JM, Doublet ML (2012) Origin of the 3.6 V to 3.9 V voltage increase in the $LiFeSO_4F$ cathodes for Li-ion batteries. Energ Environ Sci 5:9584–9594
114. Radha AV, Furman JD, Ati M, Melot BC, Tarascon JM, Navrotsky A (2012) Understanding the stability of fluorosulfate Li-ion battery cathode materials: a thermochemical study of $LiFe_{1-x}Mn_xSO_4F$ ($0 \leq x \leq 1$) polymorphs. J Mater Chem 22:2446–2452
115. Barpanda B, Dedryvère R, Deschamps MP, Delacourt C, Reynaud M, Yamada A, Tarascon JM (2012) Enabling the Li-ion conductivity of Li-metal fluorosulphates by ionic liquid grafting. J Solid State Electrochem 16:1843–1851
116. Tripathi R (2013) Novel high voltage electrodes for Li-ion batteries. PhD thesis, Univ. of Waterloo, Ontario, Canada
117. Sobkowiak A, Roberts MR, Younesi R, Ericsson T, Häggström L, Tai CW, Andersson AM, Edström K, Gustafsson T, Björefors F (2013) Understanding and controlling the surface chemistry of $LiFeSO_4F$ for an enhanced cathode functionality. Chem Mater 25:3020–3029
118. Dong J, Yu X, Sun S, Liu L, Yang X, Huang X (2013) Triplite $LiFeSO_4F$ as cathode material for Li-ion batteries. J Power Sourc 244:816–820
119. Rousse G, Tarascon JM (2014) Sulfate-based polyanionic compounds for Li-ion batteries: synthesis, crystal chemistry, and electrochemistry aspects. Chem Mater 26:394–406
120. Tripathi R, Popov G, Sun X, Ryan DH, Nazar LF (2013) Ultra-rapid microwave synthesis of triplite $LiFeSO_4F$. J Mater Chem A 1:2990–2994
121. Kim H, Lee S, Park YU, Kim H, Kim J, Jeon S, Kang K (2011) Neutron and X-ray diffraction study of pyrophosphate-based $Li_{2-x}MP_2O_8$ (M = Fe, Co) for lithium rechargeable battery electrodes. Chem Mater 23:3930–3938
122. Zaghib K, Dontigny M, Guerfi A, Trottier J, Hamel-Paquet J, Gariepy V, Galoutov K, Hovington P, Mauger A, Groult H, Julien CM (2012) An improved high-power battery with increased thermal operating range: C-$LiFePO_4$//C-$Li_4Ti_5O_{12}$. J Power Sourc 216:192–200

Chapter 9
Disordered Compounds

9.1 Introduction

Until now, the materials investigated to find suitable intercalation host structures for the positive electrode of electrochemical generators with an alkali metal or silver anode have been essentially crystalline structures. Yet the discovery in the 1950s of the semiconducting properties of phosphorus pentoxide-based glasses [1, 2] has opened the area of amorphous and disordered semiconductors. The amorphous material structures were considered merely as "accidents" until only recently. Today, however, they are studied in their own right due to certain interesting characteristics related to the disordered state. The higher capacity of the amorphous over crystalline materials, in MoS_2, for example, has been pointed out by Whittingham et al. [3]. This is presumably associated with either the more open lattice in amorphous compounds or the disordered framework that prevents the decomposition in some materials. The energy-storage capacity of lithium insertion in amorphous materials is very high, and some of them are receiving increasing attention. An intercalation reaction is topotactic in nature, the structure of the host being changed only by atomic displacements; the reaction does not involve diffusive rearrangement of the host atoms. As an example, for a-MoS_3, the initial energy density on discharge is 1.0 Wh g^{-1}; this may be compared with 0.48 and 0.8 Wh g^{-1} for crystalline TiS_2 and V_6O_{13}, respectively. The counterpart of the amorphous state is the low mobility of Li^+-ions in the framework, which is a limitation for high current densities. However, several examples have shown that the amorphous phase of cathode active materials can be used for improvement of cell rechargeability [4–9]. A typical example developed by Sakurai and Yamaki [8] is a $xV_2O_5-(1-x)P_2O_5$ glassy material, but despite good discharge–charge characteristics, a low rate of the Li^+-ion transport has been reported. In the case of $Li_{1.211}Mo_{0.467}Cr_{0.3}O_2$, the high electrochemical performance is due to the facile lithium diffusion in the disordered phase; Lee et al. [10] reported that this unexpected behavior is due to percolation of a certain type of active diffusion channels

C. Julien et al., *Lithium Batteries*, DOI 10.1007/978-3-319-19108-9_9

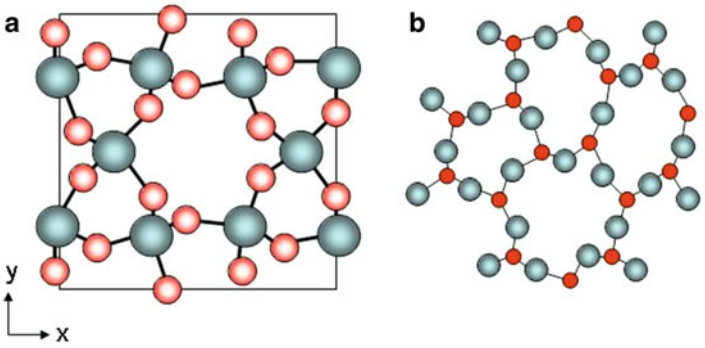

Fig. 9.1 Comparison between structures (**a**) crystalline of quartz and (**b**) SiO_2 glass

in the disordered Li-rich framework. Nano-silicon-based disordered carbon composites prepared by mechanical milling and heat-treated at 800 °C have been examined as anodes of lithium cells showing the charge–discharge capacity 548 mAh g^{-1} [11].

When we evoke disordered or amorphous materials, the first question is: how to define them? The classical definition is "an amorphous material is a solid in which there is no long-range order of the positions of the atoms" (Fig. 9.1). In principle, this class of materials does not display X-ray diffraction patterns, but other techniques such as FTIR and Raman spectroscopy, NMR, ESR, etc. are used to analyze the structure at the short-range scale. As an example, the structure of SiO_2 is such that the tetrahedral formed by the SiO_4 group must touch each other at their corners, but can do so at widely varying angles. The result of the flexibility in the bridge bonds is that SiO_2, while it has many crystalline phases, can easily form glasses. However, amorphous materials have their own characteristics and exhibit new properties after intercalation for two reasons: the modification of the pathways for ions in the host lattice and the change in the electronic structure with the appearance of new states and/or tail of the electronic bands in the energy gap. Since the open-circuit voltage of a Li cell is the difference between Fermi energies, this kind of situation explains the lower V_{oc}(a) of an amorphous material compared with respect to that of the crystalline phase, V_{oc}(c) (Fig. 9.2).

The aim of this chapter is to present a selection of appropriate disordered materials and to illustrate their properties upon lithium intercalation. This chapter is organized in six sections as follows. First, in Sect. 9.2, we show an interesting material of the transition-metal dichalcogenide group (MoS_2). Sections 9.3–9.6 are devoted to transition-metal oxides such as MoO_3, V_2O_5, MnO_2, and $LiCoO_2$; polycrystalline glasses and thin films are examined. Finally, we treat the physicochemical properties of disordered spinel structures ($LiMn_2O_4$ and $LiNiVO_4$).

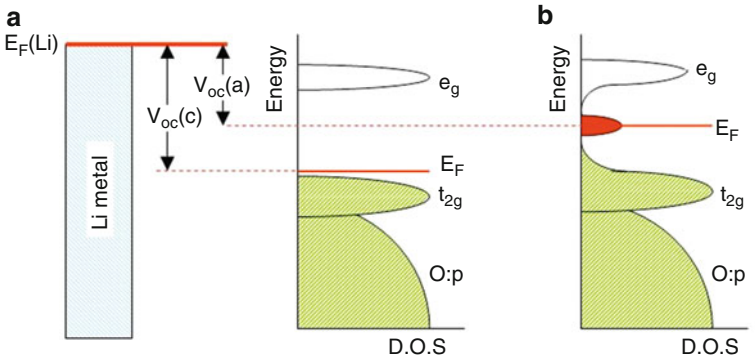

Fig. 9.2 Electronic band structure of crystalline semiconductor (SC) (**a**) and amorphous SC (**b**) vs. Li metal. As the open-circuit voltage is given by the difference of the Fermi's energy, amorphous SC displays lower open circuit voltage, V_{oc}(a) than the crystalline phase, V_{oc}(c)

9.2 Disordered MoS_2

The electrochemical properties of crystalline molybdenum disulfide (c-MoS_2) have been early reported [3, 12, 13]. The specific energy density of a Li//MoS_2 cell is very low, about 100 Wh kg^1, for the utilization as a primary cell. Haering et al. [14] have discovered that a lithium molybdenum disulfide compound exhibits several distinct stages of operation when used as a cathode in a battery having a lithium anode. In this case, the cell is reversible and the specific energy density is twice. The electrochemical properties of a disordered MoS_2 (d-MoS_2) phase has been reported by Jacobson et al. [15] and Julien et al. [16, 17]. It has been demonstrated, that by including such a material in a lithium cell, it is possible to increase the specific energy density for its possible application in a high-rate rechargeable batteries.

A highly disordered sample of MoS_2 was prepared by heat treatment of crystalline MoS_2 (Ventron) at 400 °C for 4 h under 1 Pa pressure. X-ray diffraction patterns show an intense but rather broad diffraction (002) line. The structure is a highly folded but disordered stacking pattern of layered MoS_2 with a tendency to grow in-plane and weak tendency for the layers to stack. The broadness of the diffracted lines manifests the high disorder lattice of the sample. Figure 9.3 shows the temperature dependence of the electrical resistivity of d-MoS_2. The room temperature resistivity is 0.3 Ω cm which is a low value compared with 1.25 Ω cm of c-MoS_2. Similar influence of the disorder on electrical parameter has been reported on sputtered MoS_2 films [18]. The difference between electrical characteristics demonstrates that the transport mechanism is driven by the scattering at inter-crystallite boundaries in d-MoS_2. The band-bending at grain boundaries, which leads to the formation of potential barriers, is responsible for the low resistivity of disordered samples.

The typical discharge curve for electrochemical cell containing d-MoS_2 is shown in Fig. 9.4. An initial $V_{oc} = 2.4$ V was observed which dropped continuously to

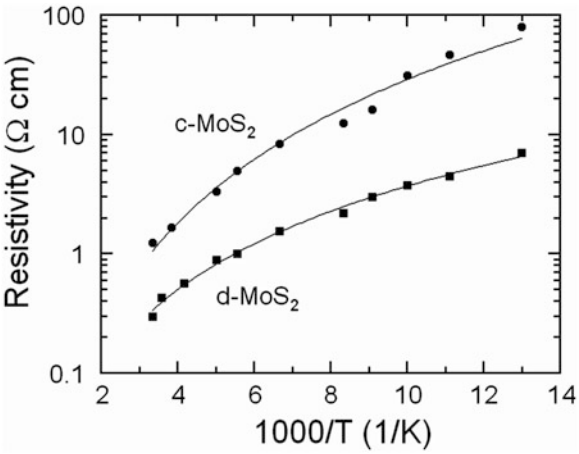

Fig. 9.3 Electrical conductivity of (**a**) disordered MoS_2 compared with (**b**) crystalline MoS_2

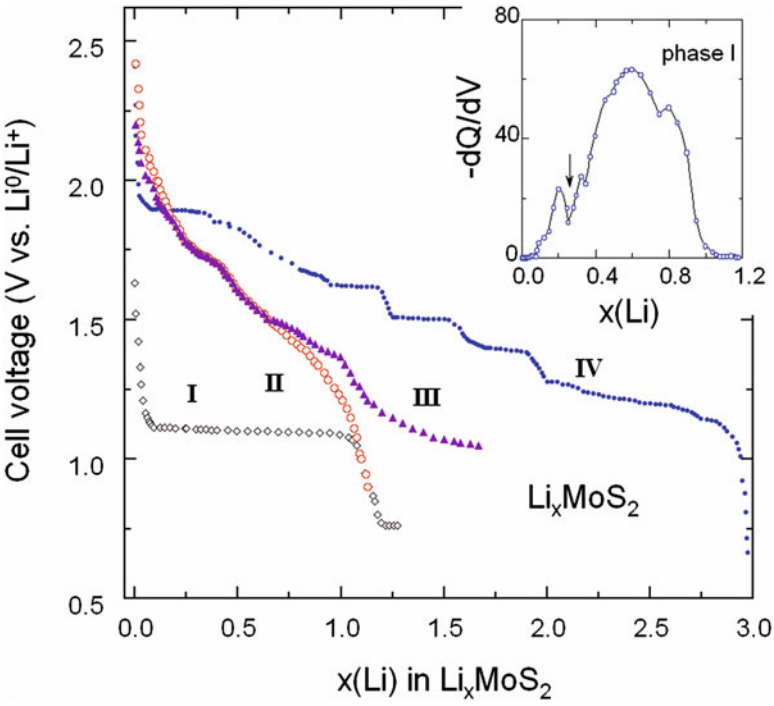

Fig. 9.4 Discharge profiles of several Li//MoS_2 cells as a function x of Li concentration in Li_xMoS_2. Phases I and II are the 2H- and 1T-polytype (β-MoS_2) of crystalline MoS_2, respectively. Phase III is a thin film grown by rf-sputtering and phase IV is the disordered MoS_2 prepared by heat treatment of crystalline phase at 400 °C for 4 h under vacuum. Insert shows the incremental capacity of the crystalline phase

1.1 V at $Li_{3.0}MoS_2$. For comparison, the open circuit voltage (OCV) of the same cell with crystalline MoS_2 cathode is also shown. An abrupt change in OCV vs. x curve at $x \approx 1$ is the indication of the phase transformation discussed above. The constant part of the curve reflects the two-phase region of the material. The disordered phase of MoS_2 shows significantly higher storage charge-capacity compared with that of the crystalline form. The discharge curve of d-MoS_2 resembles the β-phase discharge curve described by Haering et al. [14]. We remark that the discharge is not rigorously smooth, since small plateaus appear at 1.9, 1.7, 1.5, and 1.3 V. However, in the compositional range $0.1 \leq x \leq 3$, the discharge curve can be fit by the linear expression:

$$E(\text{Volt}) = E^* - kx, \tag{9.1}$$

where $E^* = 1.85$ V and $k = 9RT/F$ have been obtained for a Li//d-MoS_2 cell, where R is the ideal gas constant, and F the Faraday constant. Note also that the two characteristic plateaus of the OCV vs. x curve observed at 1.1 and 0.5 V for the 2H-MoS_2 crystalline samples are not observed with d-MoS_2. This result shows that the disorder stabilizes the solid solution with respect to the two-phase structure.

Figure 9.5 displays the chemical diffusion coefficient in d-Li_xMoS_2 as a function of the degree of Li insertion. The apparent D^* in disordered MoS_2 at room temperature has been calculated on the assumption of uniform Li^+ distribution at any composition in the solid solution electrode. We observe a continuous decrease of the value of D^* with the increase of lithium content. The high value 10^{-7} cm^2 s^{-1} of the Li^+ diffusion coefficient at low lithium concentration $0 \leq x \leq 0.2$ may result from the smaller diffusion path length of the lithium ion in the disordered phase compared to that of crystalline sample. The variation in the diffusion coefficient can

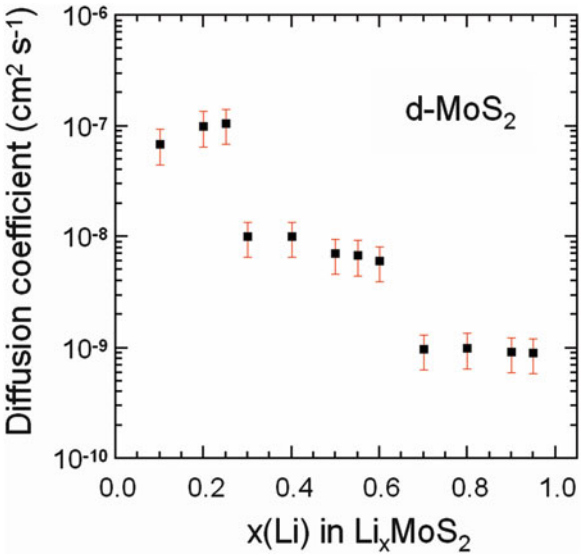

Fig. 9.5 Chemical diffusion coefficient of lithium in d-MoS_2 as a function of lithium concentration. The diffusivity parameter is deduced from the potential step polarization method

be approximated by a relationship of the form $D^* = D_o \exp(-\beta x)$, with $D_o = 1.7 \times 10^{-7}$ cm^2 s^{-1} and $\beta = 2.8$ mol^{-1} for d-MoS_2 [16]. This behavior reflects the loss of structural integrity on repeated cycles of intercalation and deintercalation. Nevertheless, even after long-term cycling the Li^+ mobility remains sufficient for practical application of nano-sized d-MoS_2 cathode materials. In fact this is a general feature of most of the insertion compounds [19].

9.3 Hydrated MoO_3

Molybdenum is known to exist in a number of oxidation states and a variety of oxides, sub-oxides, hydroxides, and hydrated complexes [20]. These oxides and oxide-hydrates of molybdenum in its highest oxidation state display a variety of structural types involving linked MoO_6 octahedra. Of the anhydrous oxides, the well-known orthorhombic form, denoted α-MoO_3 is stable at room temperature and its structure can be described in terms of layered lattice in which distorted MoO_6 octahedra share edges and vertices to form corrugated two-dimensional sheets separated by a van der Waals gap. According to the X-ray data, molybdenum trioxide reacts readily with lithium, forming two well-defined discharge products that are different, but similar to the known high temperature Li_2MoO_3 phase [21]. However, MoO_3 only reacts with about 1.5 Li/Mo. The typical discharge–charge profile of the anhydrous α-MoO_3 phase is compared with that of hydrated $MoO_3 \cdot nH_2O$ ($n = 0.66$, 1.00) materials in Li cell in Fig. 9.6. The electrochemical lithium insertion into the MoO_3 framework can be described assuming the reduction

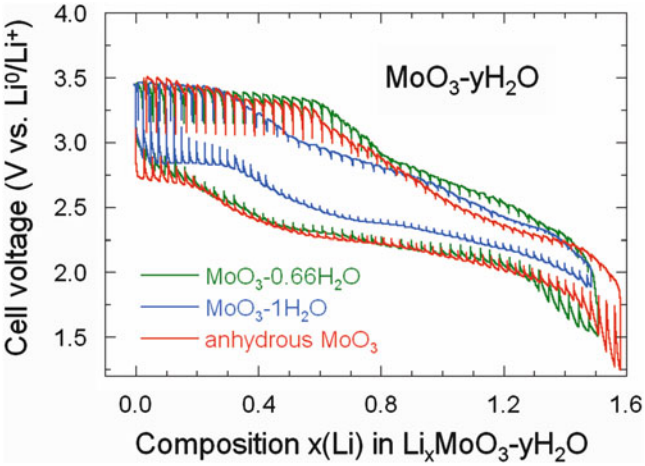

Fig. 9.6 Typical discharge–charge curves of MoO_3-yH_2O cathode materials ($y = 0.0$, 0.66; 1.0). Measurements were carried out at 0.1 mA cm^{-2} in Li cell using nonaqueous electrolyte 1 mol L^{-1} $LiPF_6$ in EC-DEC

from Mo(VI) to Mo(V) and Mo(IV) oxidation states. The capacity of MoO_3 observed here is approximately in agreement with the theoretical gravimetric capacity 280 mAh g^{-1}. Since the MoO_3 reduction process is reversible, the construction of rechargeable cells is possible. Satisfactory charge–discharge efficiency and storage capability are other favorable features for $MoO_3{\cdot}nH_2O$ compounds that exhibit similar electrochemical characteristics. Upon lithiation of Li_xMoO_3, the electronic conductivity increases from 10^{-4} S cm^{-1} for $x = 0$ to ca. 10^{-1} S cm^{-1} for $0.3 \leq x \leq 0.9$ [22]. Li diffusion coefficients in Li_xMoO_3 powder depend on x. A maximum value of ca. 10^{-9} cm^2 s^{-1} has been reported for $x \approx 0.6$. The Li mobility was shown to slightly decrease upon subsequent discharge–charge cycles due to irreversible structural and morphological changes of the host matrix. However, upon recharging, reoxidation of Mo produces a resistive compound which induces a large polarization of the cell for potential of ≈3.5 V (Fig. 9.6). This is very advantageous from the technology point of view, since this material acts as a self-limiting voltage medium at the end of the charge. The suitability of molybdenum oxide-hydrates, $MoO_3{\cdot}nH_2O$, as cathode materials for nonaqueous lithium batteries has been assessed by several workers [23–28]. As a result, the discharge capacity of $MoO_3{\cdot}nH_2O$ increases with decreasing water content, but the cycle life increases with increasing water content in the composition range $0.33 < n < 1.00$. Monoclinic monohydrate, $MoO_3{\cdot}H_2O$, having one coordinated water molecule, showed a discharge capacity of about 200 mAh g^{-1} of acid weight and a discharge potential around 2.5 V vs. Li^0/Li^+. This cathode material displayed a good charge–discharge cyclic behavior at a capacity below 1 e^-/Mo, while keeping the original layered lattice on cycling. The oxide-hydrate material prepared by sol–gel [23] shows a good performance and could be a candidate for practical primary lithium battery. Amorphous $MoO_3{\cdot}H_2O$ cathode exhibits stepwise discharge behavior, including two plateaus; the first step up to 0.3 e^-/Mo and the second one up to 1.0 e^-/Mo. This amorphous phase delivers a discharge capacity of 260 mAh g^{-1} corresponding to 1.5 e^-/Mo. On the other hand, the profile of the discharge cell voltage using the crystalline $MoO_3{\cdot}½H_2O$ cathode is rather monotonous without any plateau. This electrochemical behavior is attributed to the large cavities available for Li ions which prevent repulsive forces between inserted ions. Cathodes formed with this hemihydrate oxide gave a practical energy density of 630 Wh kg^{-1} for 1.5 e^-/Mo. X-ray diffraction patterns of Li_xMoO_3-$½H_2O$ measured after electrochemical titration show that the monoclinic structure remains largely unchanged upon lithiation with the strongest (001) Bragg line shifted toward lower angles. This suggests that during the discharge, Li^+ ions are inserted between the layers, leading to a small increase of the interlayer spacing. This can be explained by a model of rigid hydrated-MoO_3 layers in their original state separated by intercalated Li^+ cations.

The electrochemical behavior of nonstoichiometric molybdenum oxides $MoO_{3-\delta}$ suggests that both channel/site size and electronic conductivity are the predominant factors influencing the extent of reversible lithium incorporation by metal oxides with framework structures shear-related to those of ReO_3 and MoO_3. Distortions and nonequivalence of the sites available for Li^+ accommodation should affect the thermodynamics of the reduction processes. The nonstoichiometric

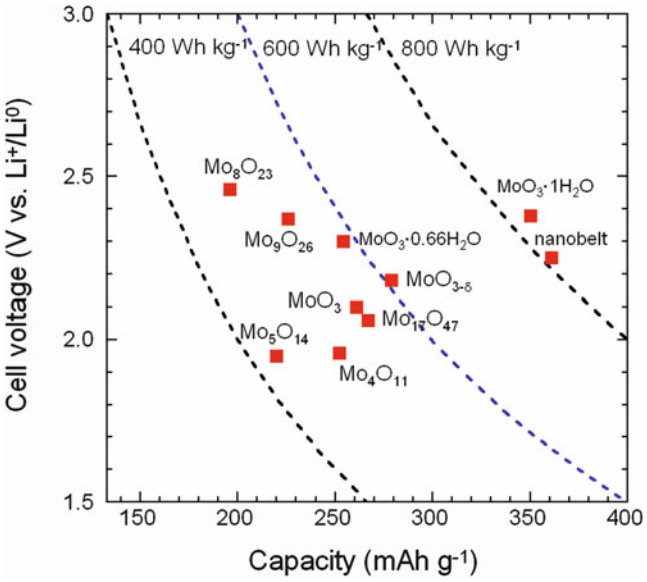

Fig. 9.7 Electrochemical characteristics of lithium/Mo-based cells. Cathode materials can be classified into three classes according their energy density

molybdenum oxide Mo_5O_{14} ($MoO_{2.8}$) with framework structure based on mixed networks of polyhedra is permeated by large open channels [29]. Mo_5O_{14} was obtained by dehydration and annealing treatment of molybdenum monohydrate at 750 °C. The open-circuit voltage is 3.1 V vs. Li^0/Li^+ for the $Li//MoO_{2.8}$ cell. The first discharge displays a stepped behavior with a voltage plateau at ca. 2.2 V followed by a potential decline for $x > 0.7$Li/Mo. The limiting reversible lithium capacity is 1.5 Li/Mo for Mo_5O_{14}. This compound can be assigned the following Mo valence distribution: $Mo_3^{6+}Mo_2^{5+}$. If reversible lithium incorporation produced all Mo^{4+}, the expected lithium uptake would be 8/5(1.6) Li/Mo; a value close to that measured by electrochemical titration. The gravimetric capacity was much higher than the 280 mAh g^{-1} of anhydrous MoO_3. Figure 9.7 summarizes the electrochemical characteristics of Mo-based lithium cells. According the energy density, three classes of materials can be distinguished from the voltage-capacity graph.

9.4 MoO_3 Thin Films

Molybdenum trioxide thin films can be easily grown by various deposition techniques: rf-sputtering, thermal evaporation, flash evaporation, deep-coating, pulse-laser deposition (PLD), atomic layer deposition (ALD), etc. providing various forms of crystal chemistry by tuning the substrate temperatures, T_s, and/or the oxygen partial pressure, $p(O_2)$, in the deposition chamber [30, 31]. For example,

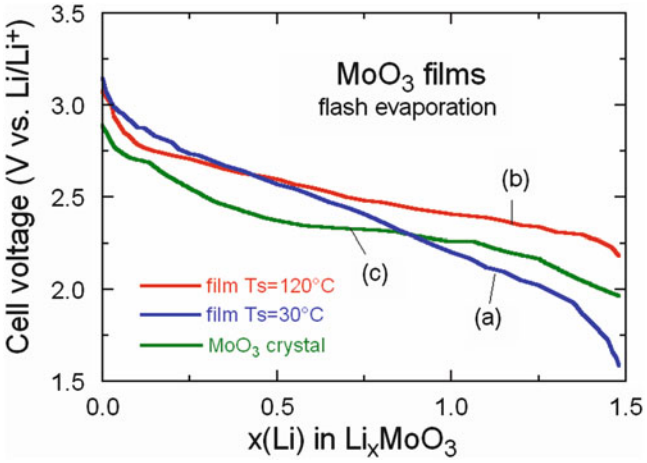

Fig. 9.8 Discharge curves of Li//MoO_3 microbatteries including thin films deposited by flash evaporation method onto silicon substrate maintained at $T_s = 30$ and 120 °C. Measurements were carried out at current densities 10 μA cm^{-2}

MoO_3 films grown by flash-evaporation onto silicon substrates maintained in the temperature range 30–300 °C revealed a predominant α-phase with a well-defined (*0 k0*) orientation. The surface morphological studies show that films prepared in the range 200–300 °C are crystalline with elongated crystal geometry. The layered nature of the film is shown on each crystallite [31–33]. Discharge curves of Li// MoO_3 cells with cathode thin film deposited by flash-evaporation method onto silicon substrate maintained at $T_s = 30$ and 120 °C are shown in Fig. 9.8. These microbatteries display electrochemical features as follows. The initial voltage 3.2 V of a Li-cell with MoO_3 thin-film is higher than that recorded on the galvanic cell using crystalline and stoichiometric material. This could be attributed to the oxygen-deficient structure of $MoO_{3-\delta}$ films. The cell voltage decreases continuously as a function of the degree of Li insertion and the steadily behavior is a function of the structural arrangement in the film, which depends on the substrate deposition temperature [34]. The electrochemical process seems to be a classical intercalation mechanism for the lithium ions with no voltage plateau occurring during the discharge, and 1.5 e^- transferred in the host material. The reduction process is accompanied by coloration of MoO_3 films. These results suggest that the Li^+ diffusion is anisotropic and limited by grain boundary effects which affect the discharge curve. The discharge curve of the cell fabricated with the MoO_3 film deposited at 120 °C (curve b) is quite stable. This can be attributed to the unique layered structure of α-MoO_3 with nanosized grain (43 nm) in the film. A second possibility is the presence of the mixed α–β phase, which would enhance the standard potential by 120 mV. A third explanation may be oxygen-defects in the host structure involving a lower Fermi level in such a semiconducting film that provides higher open-circuit voltage. This hypothesis is verified for MoO_3 films deposited by rf-sputtering in different partial oxygen pressure in the chamber as

shown ion Fig. 9.9. As an experimental result, films deposited under $p(O_2) =$ 150 mTorr exhibits a less disordered lattice.

Investigations of the electronic structure of transition metal-oxides, i.e., MoO_3 and WO_3, have demonstrated that these films show an n-type semiconductor property due to oxygen vacancies with a large electron affinity (6.7 eV) and ionization potential (9.7) eV as well as a high work function (6.8 eV). MoO_3 thin films had a valence band edge at 5.3 eV and the conduction band edge at 2.3 eV [35, 36]. In a simplest semiconductor model, electrochemical properties of Li_xMoO_3 films can be illustrated by an electronic band scheme as shown in Fig. 9.10 [37]. The cell voltage can be viewed as the difference in the Fermi energies between

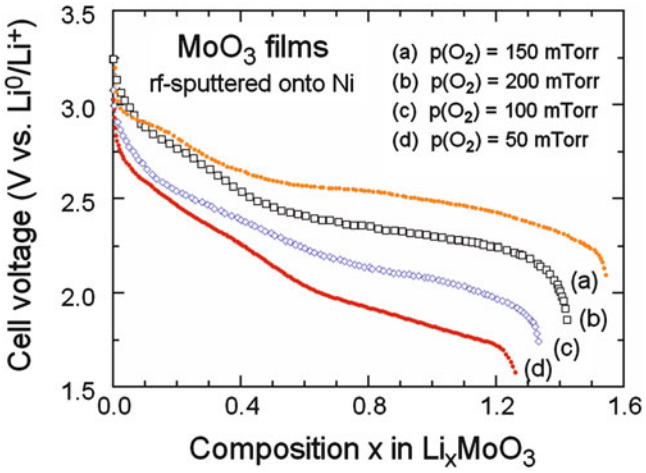

Fig. 9.9 Discharge curves of Li//MoO_3 microcells including thin films deposited by rf-sputtering method onto nickel substrate as a function of the partial oxygen pressure. Measurements were carried out at current densities 20 μA cm^{-2}

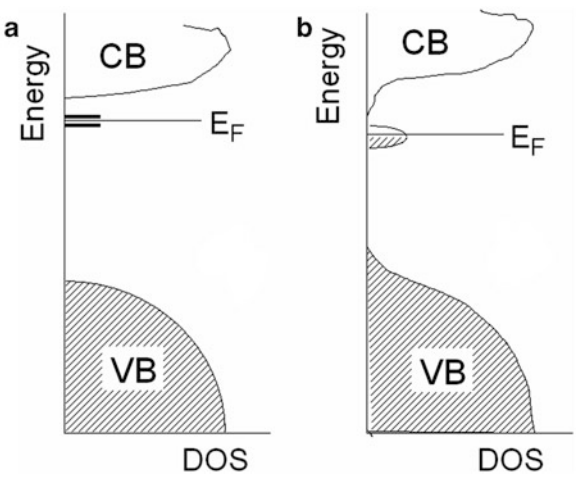

Fig. 9.10 Schematic view of the electronic band structure of (**a**) α-MoO_3 crystal and (**b**) MoO_3 thin film. The energy of the Fermi level E_F lies with the localized electronic band upon Li insertion in the host material

lithium metal and positive electrode. In MoO_3, there are five O(p_π) and three Mo (t_{2g}) orbitals which interact to form π and π* bands forming the valence and conduction bands, respectively [38]. The antibonding π* states hold the extra electrons supplied by the inserted lithium ions. The narrowing of the conduction band is expected to lead to an increase in the effective mass which will affect the position of the Fermi energy in Li_xMoO_3 phases. In Li-intercalated MoO_3 crystal, the Fermi energy lies either with the donor level near the bottom of the conduction band or in the conduction band itself (Fig. 9.10), while in MoO_3 films the density-of-states might show a band in the middle of the gap and the Fermi level lies in the band. This last description is supported by absorption measurements [31]. Thus, as α-MoO_3 is a semiconductor with a wide band gap of 3.1 eV, the higher voltage displayed in thin-film cells is attributed to the difference between Fermi levels (>0.5 eV) in the crystal and thin-film.

The ionic transport properties of Li^+ ions into the MoO_3 film network were investigated by the modified galvanostatic intermittent titration technique (GITT) from the variation of the potential vs. time during a relaxation period following a short pulse of current in the discharge process [39]. Transport parameters such as the Li^+ chemical diffusion coefficient, thermodynamic factor, and ionic conductivity are investigated during the Li^+ insertion process and discussed with respect to the crystallinity of the cathode material. Figure 9.11 shows the chemical diffusion coefficient of Li^+ ions as a function of the degree of intercalation in Li_xMoO_3

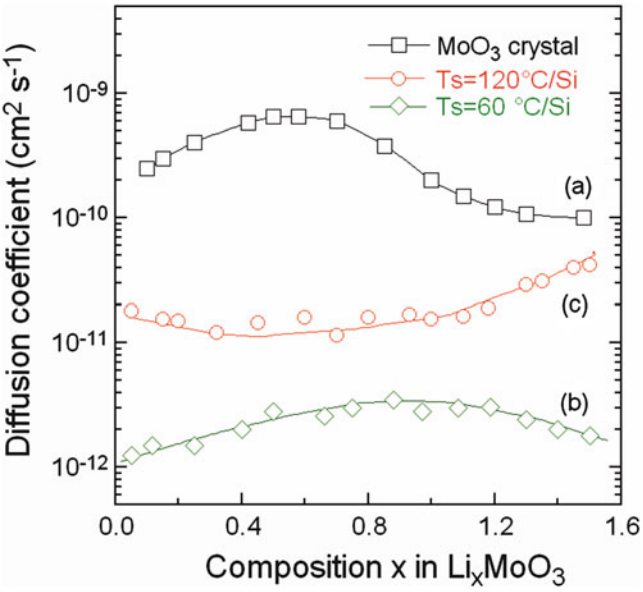

Fig. 9.11 Composition dependence of the chemical diffusion coefficient, D^*, of Li^+ ions in MoO_3 films deposited by flash-evaporation method onto Si substrate maintained at two temperatures T_s. D^* of α-MoO_3 crystal is shown for comparison

materials. In these experiments, the evolution in the voltage E^* after applying a current pulse at $t = 0$ through the cell obeys the relation:

$$E^* = \left(\frac{\mathrm{IWRT}}{F^2 c^* A}\right)\left[\left(\frac{4t}{\pi D^*}\right)^{1/2} - \frac{t}{\delta}\right], \tag{9.2}$$

where I is the current intensity of the pulse, t the time, c^* the Li-ion concentration of the host, W the thermodynamic factor, A and δ the surface and thickness of the electrode, T the absolute temperature, $F = 96485\ \mathrm{A\,s\,mol^{-1}}$ and $R = 8.314\ \mathrm{JK^{-1}\,mol^{-1}}$. The thermodynamic factor is defined as:

$$W = \frac{\partial(\ln a^*)}{\partial(\ln c^*)}, \tag{9.3}$$

which a^* is the activity of the intercalant species in the solid solution electrode. W is the ratio between the chemical diffusion coefficient D^* and the component diffusion coefficient D_0:

$$W = D^*/D_0. \tag{9.4}$$

Equation (9.1) is valid: (1) if the duration of the preceding discharge is longer than a critical time:

$$t_0 = \frac{\delta^2}{4D^*}, \tag{9.5}$$

and (2) for a limited period of relaxation $t < t_0$ of the electrochemical cell. In the compositional range $0.2 \leq x \leq 1.2$ the values of the chemical diffusion coefficient of lithium varies from 9×10^{-11} to 1×10^{-9} $\mathrm{cm^2\ s^{-1}}$ in the MoO_3 crystal. The compositional dependence of D^* is approximately a quadratic function due to the nature of the empty sites in the host structure. According to the model of Basu and Worrell [40], the chemical diffusivity is related to the composition:

$$D^* = \beta x^2(1-x) + x\left(1 - x^2\right), \tag{9.6}$$

where β is an interaction parameter related to the repulsive interaction energy between alkali ions. According to Eq. (9.6) D^* shows a maximum at the half-filling site number. Although the uncertainties in the chemical diffusion data shown in Fig. 9.11 prelude an adequate test of Eq. (9.6), the maximum in the Li_xMoO_3 data suggests an interaction energy lower than 0.2 eV, which is consistent with the value obtained from thermodynamic measurements. The value of the chemical diffusion coefficient in MoO_3 thin films (Fig. 9.11, curves b, c) is lower than in α-MoO_3 single crystal.

For MoO_3 films prepared at $T_s = 60\,^{\circ}C$ a maximum value of $5 \times 10^{-12}\ cm^2\ s^{-1}$ is obtained at $x = 0.8$ (Fig. 9.11, curve b). D^* varies with the composition x according to a quadratic law:

$$D^* = \kappa\left[\left(2x - x^2\right)\right], \tag{9.7}$$

where $\kappa = 2 \times 10^{-12}\ cm^2\ s^{-1}$. The chemical diffusion coefficient behavior in MoO_3 thin film deposited at 250 °C differs from the previous one. We observe that D^* has an almost constant value of $1.5 \times 10^{-11}\ cm^2\ s^{-1}$ in the range $0.1 < x < 1.2$ and increases at higher concentration of intercalant ions. We tentatively attribute this complex behavior to the polycrystalline state of MoO_3 films grown at high substrate temperature for which the enhancement factor is high. In this case, the intercalation process is partly controlled by the number of ion occupancies in the host lattice of the crystallite in the film. Figure 9.12 shows the thermodynamic factor, W (in a logarithmic scale), as a function of the degree of intercalation in the Li_xMoO_3 host material. In the compositional range $0.2 < x < 1.4$, W varies from 1.8 to 30 for MoO_3 crystals (Fig. 9.12, curve a). Considering that MoO_3 is a layered host for the intercalant, the model of ion–ion interaction can be applied. Armand [41] has proposed such a model to describe the variation of the chemical potential in intercalation compounds. The thermodynamic factor is related to the interaction factor, g, as:

$$W = \left[(1 - x)^{-1} + gx\right]. \tag{9.8}$$

Experimental data are well fitted using Eq. (9.8), which provides an interaction factor $g = 7.5$. This value is of the same order as in TiS_2 [42]. The thermodynamic

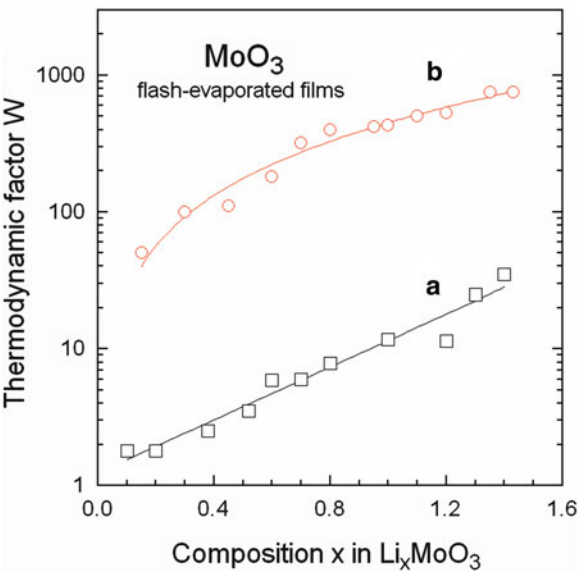

Fig. 9.12 Thermodynamic factor of Li_xMoO_3 cathodes: (**a**) crystalline α-MoO_3 phase and (**b**) thin film grown on a substrate maintained at $T_s = 250\,^{\circ}C$. *Full lines* represent the fit using Eq. (9.8)

factor of MoO_3 thin films varies from 50 to 800 in the compositional range $0.2 < x < 1.5$. We observe a quasi-linear variation of the composition dependence of W which may be associated with the oxygen-defects in the host lattice. It is a fact that numerous of such defects exist in the film structure, even when the crystallinity is improved by different conditions of preparation. Here, we remark that W is two orders of magnitude higher than that for MoO_3 crystal. Using Eq. (9.8) a fit of experimental data is obtained with a high value of the interaction factor ($g = 400$). Considering that MoO_3 films are oxygen-deficient materials, the model of charge transport in internal defect-materials can be applied [43]. Defects are Li interstitials, Li*, and conduction electrons, e′, for example. Maeir [44] showed that, in a solid solution where no internal defect reactions occur, the thermodynamic factor is related to the defect concentration (if dilute defects exist) as:

$$W = \Phi_{\mathrm{Li}}^{-1} + \Phi_{\mathrm{e}'}^{-1}, \tag{9.9}$$

where $\Phi_{\mathrm{Li}}^{-1} = c_{\mathrm{Li}^*}/c_{\mathrm{Li}^+}$ and $\Phi_{\mathrm{e}'}^{-1} = c_{\mathrm{e}'}/c_{\mathrm{Li}^+}$. Equation (9.4) provides a linear variation of the thermodynamic factor with the degree of intercalation, as shown in Fig. 9.12 (curve b). The large increase of W may be also associated with the decrease of the electronic mobility in Li_xMoO_3 film. For the case in which the chemical diffusion is predominantly determined by ionic species, Eq. (9.4) yields, with the substitution of D_0 by the conductivity σ_i and the thermodynamic factor, for the partial conductivity [45]:

$$\sigma_\mathrm{i} t_\mathrm{e} = \frac{F}{\mathrm{RT}}\left(\frac{qc^*D^*}{W}\right), \tag{9.10}$$

where t_e is the transference number defined by:

$$t_\mathrm{e} = \frac{\sigma_\mathrm{e}}{\sigma_\mathrm{e} + \sigma_\mathrm{i}}. \tag{9.11}$$

By combining the chemical diffusion coefficient and the thermodynamic factor values, the lithium ion conductivities σ_i in Li_xMoO_3 materials are shown in Fig. 9.13. Discharging the cell results in the formation of a mixed conductor; the compound is an electronic and ionic conductor. If the sample is predominantly an electronic conductor, i.e., $\sigma_\mathrm{e} >> \sigma_\mathrm{i}$, the ionic conductivity can be deduced from Eq. (9.8). The conductivity is found to increase with lithium concentration in Li_xMoO_3 crystal to reach about 1.5×10^{-4} S cm^{-1} at $x = 0.6$ (Fig. 9.13, curve a). One can remark that the ionic transport parameters in Li_xMoO_3 crystal are comparable with those of Li_xTiS_2 [40]. Figure 9.13 (curve b) displays the lithium ionic conductivity of MoO_3 thin-film cathode. The ionic conductivity is estimated with an average value of 9×10^{-9} S cm^{-1} at $x = 0.8$. We remark that the Li^+ ionic conductivity is much smaller than for MoO_3 crystals. This behavior may be attributed to the disordered structure of the film. In such a material the conduction

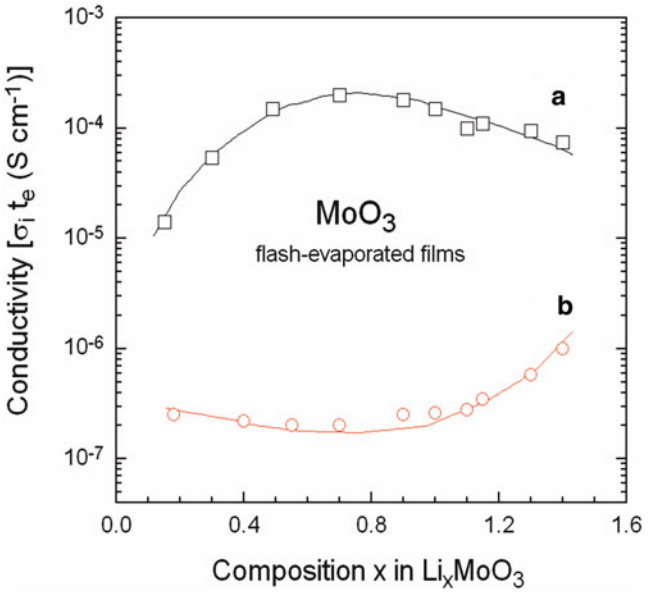

Fig. 9.13 Partial ionic conductivity of Li_xMoO_3 cathodes: (**a**) crystalline α-MoO_3 MoO_3 phase and (**b**) thin film grown at $T_s = 250$ °C

paths are not defined as well as they are in the crystalline material because in thin film: (1) the van der Waals plane is not quasi-infinite, (2) the potential barriers are more important, and (3) the Li^+ ions can be trapped by the structural defects.

9.5 Disordered Vanadium Oxides

Amorphous vanadium oxides were obtained by quenching molten mixtures of V_2O_5 with glass formers such as P_2O_2, TeO_2, and GeO_2. Lower valence transition-metal ions are generally produced due to the loss of oxygen from the melt resulting in a mixed valence in the glass and in an enhanced semiconducting conduction, which occurs by electron hopping between V^{4+} and V^{5+} states. Transition-metal oxides (TMO) glasses have some potential advantages over crystalline solids for use as cathode materials in high energy density lithium batteries [37]. For instance, the superior performance was attributed to the diffusivity of Li^+ ions that is larger in glass V_2O_5 than in polycrystalline materials [46, 47]. Nabavi et al. [48] reported the electrochemical properties of amorphous V_2O_5 positive electrode prepared by splat-cooling from the pure oxide melted at 950 °C in air. The amorphous oxide is able to give $Li_xV_2O_5$ phase via electrochemical insertion of Li^+ ions with reversible uptake of $1.8Li^+$ per V_2O_5. Figure 9.14 displays the discharge curves of various vanadium-based cathodes in lithium cells. These results show clearly the

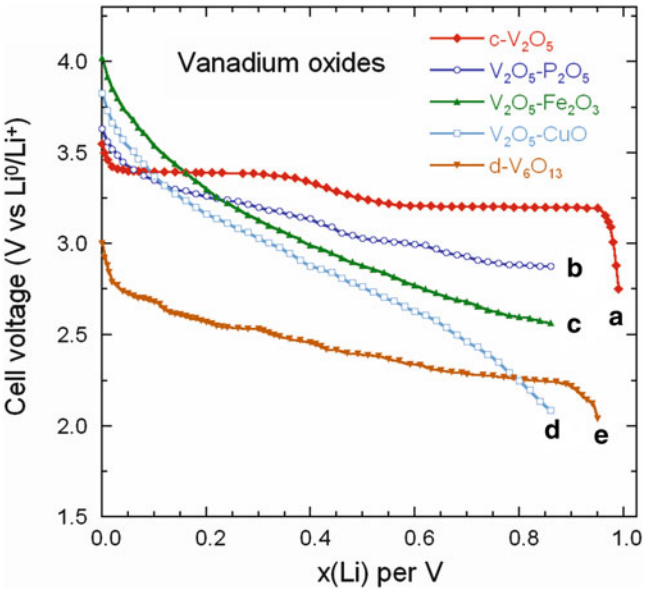

Fig. 9.14 Discharge curves of disordered vanadium oxides compared with crystalline V_2O_5 (**a**): V_2O_5-P_2O_5 glass (**b**), $0.8V_2O_5$-$0.2Fe_2O_3$ glass (**c**), $0.67V_2O_5$-0.33CuO glass (**d**) and disordered V_6O_{13} material

glasses $xV_2O_5-(1-x)P_2O_5$ exhibit good electrochemical features. Contrary to crystalline V_2O_5, the discharge potential continuously decreases with the amount of inserted Li^+ suggesting that no phase transition occurred in the amorphous material. In particular, the composition $0.66V_2O_5-0.4P_2O_5$ showed reversible insertion process leading to a high voltage of 3.6 V vs. Li^0/Li^+, a small degree of lattice expansion of about 2 % in volume and a large stored energy density of 750 Wh dm^{-3}. Sakurai et al. [49] demonstrated the rechargeability of the Li// $xV_2O_5{\cdot}(1-x)P_2O_5$ systems by cycling the 95:60 mol.% V_2O_5 in the voltage range 2.0–3.5 V at current density 0.5 mA cm^{-2}. Figure 9.14 presents the discharge curves of several vanadium-based electrodes including V_2O_5-type glasses and disordered V_6O_{13} compared to crystalline vanadium pentoxide.

Amorphous vanadium oxide thin-film electrodes synthesized by various methods including thermal evaporation [50], flash-evaporation [51], rf-sputtering [52], pulse-laser deposition (PLD) [53], electron-beam evaporation [54], xerogel method [55], sol–gel casting [56] were all investigated for their Li^+ ion intercalation capabilities. The microstructure of V_2O_5 film, which is very sensitive to the growth conditions, strongly influences their performance in thin-film solid-state microbatteries and other electrochemical devices [57]. Among the $V_2O_5{\cdot}nH_2O$ materials with $n=1.6$, 0.6, and 0.3 prepared from the sol−gel route the $V_2O_5{\cdot}0.3H_2O$ film exhibits the best Li^+ intercalation performance, with an initial capacity of 275 mAh g^{-1} and a stabilized capacity of 185 mAh g^{-1} under a high current density of 100 μA cm^{-2} after 50 cycles. Such an enhanced electrochemical

property by thermal treatment is ascribed to the reduced water content, the retained interlayer spacing and the dominant amorphous phase in the film [56]. Specific capacity and cyclic stability of Li^+ ion intercalation in V_2O_5 films could be attributed to surface defects V^{4+} and/or V^{3+} associated to oxygen vacancies in less crystallized vanadium pentoxide. Note that the specific capacity is limited because the valence of the metal cations fixes the number of electrons withdrawn from each metal center [58–61]. Swider-Lyons et al. [62] discussed the point defects introduced into the oxide network using various heat-treatment to modify the defective structure of polycrystalline V_2O_5. The V_2O_5 cathode half-cell reaction can be expressed in the Kröger-Vink notation under the form of the following equilibrium reaction in defective oxides [63]:

$$V_V^x + O_O^x + Li_{(sol)}^+ + e^- \rightarrow V_V^{'} + OLi_O^{\bullet}, \tag{9.12}$$

in which V_V^x designates a V^{5+} ion at a vanadium site in the V_2O_5 lattice, and O_O^x is an O^{2-} ion on an oxygen site. In Eq. (9.7), one considers that one electron is consumed when a Li^+ from an electrolyte solution ($Li_{(sol)}^+$) inserts into a V_2O_5 cathode and a V^{5+} ion is reduced to V^{4+}. The occupation of the V^{5+} site with a V^{4+} ion results in an effective one-negative charge on it, and is denoted by $V_V^{'}$. The inserted Li^+ ion is associated with an oxygen site, $OLi_o^{\bullet}$, and has an effective on-positive charge ($^{\bullet}$). The Li^+ ions are alternatively introduced into an interstitial site, written as $Li_i^{\bullet}$. As an example of electrochemical properties of vanadium oxide thin-films, Figure 9.15 presents the discharge curves of Li//V_6O_{13} microbatteries as

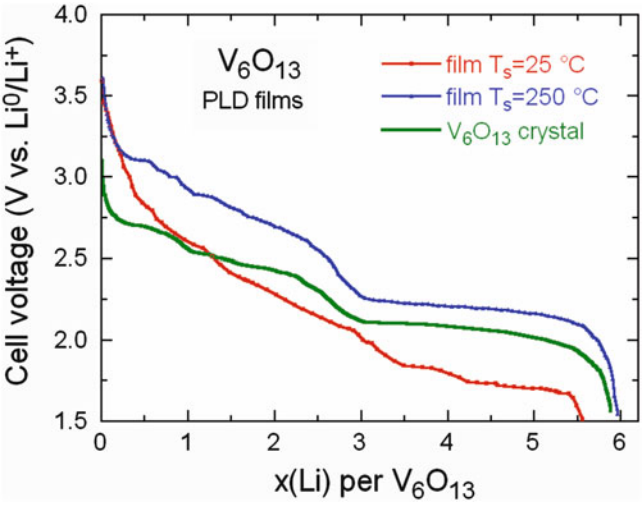

Fig. 9.15 Discharge profiles of Li//V_6O_{13} microbatteries as a function of the substrate temperature, T_s compared to the response of Li//V_6O_{13} crystal. Measurements were carried out at 10 μA cm^{-2}

a function of the substrate temperature T_s compared to the response of Li//V_6O_{13} crystal [58]. It is worth noting the influence of the substrate temperature on the electrochemical characteristics of the active cathode films. The film V_6O_{13} deposited at $T_s = 25$ °C displays the typical discharge curve of an amorphous material with uptake of 1Li per vanadium, while the discharge profile of the film deposited at $T_s = 250$ °C resembles to that of V_6O_{13} crystal with the appearance of a plateau at ~2.2 V vs. Li^0/Li^+. These electrochemical features can be assigned to the modification of the electronic states in the 3d-subband, induced by the distorted V_6O_{13} film structure and the change in V−V distance [64], responsible for the shift of the OCV. The chemical diffusion coefficients of $Li_xV_6O_{13}$ remain constant over the composition range $0 \leq x \leq 6$ with a mean value of 10^{-13} cm^2 s^{-1}. This value is about three orders of magnitude lower than that of the stoichiometric phase, which is typical of less structured material such as in $LiMn_2O_4$ films [65]. Note that the diffusion path through the cavities extending in the (010) direction of the 3D framework of V_6O_{13} is sensitive to the synthesis conditions. The difference between the oxide prepared in crystalline form and the films can thus be ascribed to differences in lattice perfection, i.e., static disorder or short chains with undistorted cavities [58].

9.6 $LiCoO_2$ Thin Films

Polycrystalline thin films of lithium cobalt oxide were grown by PLD technique [66, 67]. Films of $LiCoO_2$ were deposited onto Si substrates heated at temperature lower than 300 °C from a sintered composite target ($LiCoO_2 + Li_2O$) irradiated with a Nd: YAG laser. Under these deposition conditions, i.e., substrate temperature and partial oxygen pressure temperature, $LiCoO_2$ films grown from target without Li_2O additive display the presence of cobalt oxide impurities. In addition to the peaks belonging to $LiCoO_2$, two small peaks attributed to Co_3O_4 are present at $2\theta = 45$ and 59°. Moreover, a large peak around $2\theta = 70°$ is observed that could be mainly associated to the silicon substrate. As the amount of Li_2O increased in the target, the XRD patterns develop features expected for the regular layered phase. They are indexed using the $R\bar{3}m$ symmetry. Figure 9.16 illustrates a highly textured (003) film obtained when a target with 15 % Li_2O was used. The X-ray diffraction pattern displays three sharp and intense peaks at $2\theta = 19$, 38 and 58°, which are unambiguously attributed to the (003), (006), and (009) Bragg lines, respectively. That of $LiCoO_2$ films deposited at low substrate temperature reveals the amorphous nature of the layer. The typical peaks of the polycrystalline layered phase in $LiCoO_2$ films appear upon increasing the substrate temperature ($T_s = 300$ °C) in oxygen partial pressure $P(O_2) = 50$ mTorr using a lithium-rich target. The cobalt-oxygen framework is well defined in this structure [66].

$LiCoO_2$ films obtained by PLD with polycrystalline morphology were successfully used as cathode materials in lithium microbatteries. Typical charge and discharge curves of a Li//$LiCoO_2$ cell using pulsed-laser deposited film grown at

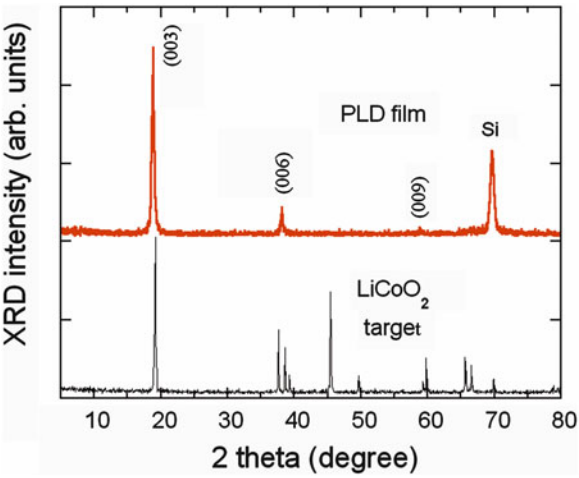

Fig. 9.16 X-ray diffraction patterns of $LiCoO_2$ powder used as PLD target and $LiCoO_2$ textured film grown into 50 mTorr O_2 partial pressure

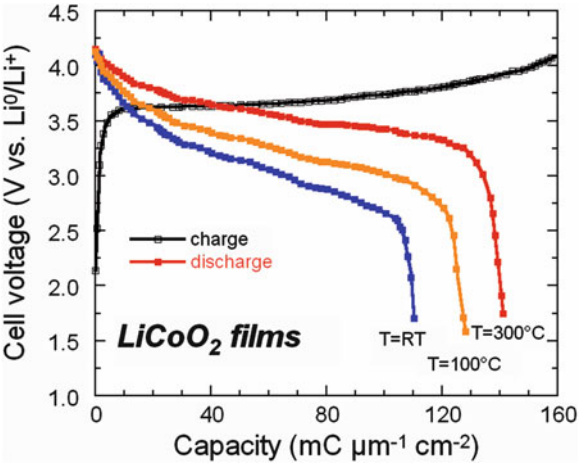

Fig. 9.17 First charge–discharge curves of a Li// $LiCoO_2$ microbatteries using a $LiCoO_2$ films grown by PLD technique in 50 mTorr oxygen pressure onto substrate heated in the range $25 \leq T_s \leq 300$ °C

$T_s = 300$ °C are shown in Fig. 9.17. Electrochemical measurements was carried out at a rate C/100 in the potential range 2.0–4.2 V; as such, the voltage profile should provide a close approximation to the OCV. The cell-voltage profiles display the typical profile currently observed for Li_xCoO_2 cathodes. From the electrochemical features, we can make the following general remarks. An initial voltage about 2.15 V vs. Li^0/Li^+ was measured for $LiCoO_2$ thin-film cathode cells, which is lower than the value recorded on galvanic cell using crystalline cathode [68]. The cell voltage is a function of the structural arrangement in the film and thus depends on the substrate deposition temperature (Fig. 9.17). These potentials slightly increased for films grown at high substrate temperature. This is consistent with many literature data and ensures that at $T_s = 300$ °C the material particles are electrochemically active [68]. Specific capacity as high as 158 mC cm^{-2} µm was

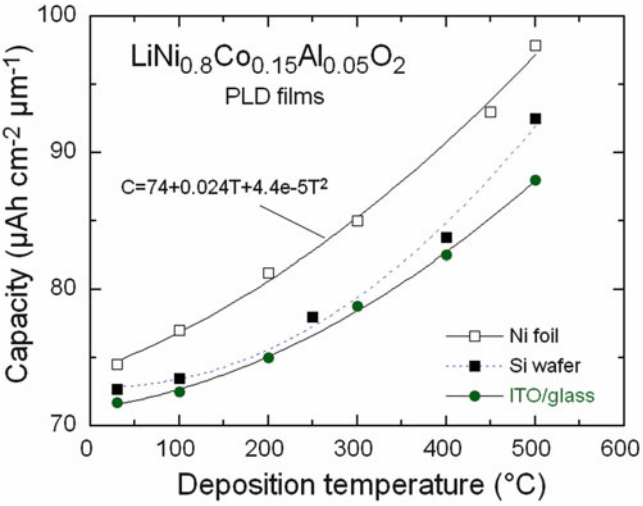

Fig. 9.18 Specific capacity of Li//$LiNi_{0.8}Co_{0.15}Al_{0.05}O_2$ cells as a function of the substrate temperature. PLD films were grown onto various substrates at $25 \leq T_s \leq 300$ °C in $p(O_2) =$ 50 mTorr. Films deposited onto Ni foil exhibit the best discharge capacity

measured on $LiCoO_2$ polycrystalline films [67]. The capacity of films with a layered ($R\overline{3}m$ S.G.) structure appears to be strongly dependent on the morphology that is greatly influenced by the substrate temperature and the nature thereof. As an example, Fig. 9.18 shows the variation of the specific capacity of the Ni-rich $LiNi_{0.80}Co_{0.15}Al_{0.05}O_2$ (NCA) films deposited onto three different substrates: Ni foil, Si wafer and ITO/glass. As an experimental result, NCA cathode deposited onto nickel at $T_s = 500$ °C by PLD technique exhibits the highest specific capacity of ≈100 μA cm^{-2} μm.

9.7 Disordered $LiMn_2O_4$

Among the most promising compounds for Li-ion battery electrodes, the 3D spinel $LiMn_2O_4$ is able to reversibly uptake about 0.5 Li per transition-metal atom [69]. However, there are some problems that postpone its implementation, such as difficulties encountered in controlling cationic order/disorder in these systems during either their synthesis or cycling [70]. Other problems associated to cationic distribution within $LiMn_2O_4$ are also severe because spinel compounds of general formula AB_2O_4 are prone to cationic mixing between tetrahedral and octahedral sites, leading to either normal $[A]_{Tet.}[B_2]_{Oct.}O_4$ or inverse $[B]_{Tet.}[AB]_{Oct.}O_4$ spinels. $LiMn_2O_4$ was shown to be a normal spinel, but deviations from such a cationic distribution exist depending on the synthesis history, namely annealing temperature and cooling rate of the material. Here, we present the properties of two $LiMn_2O_4$

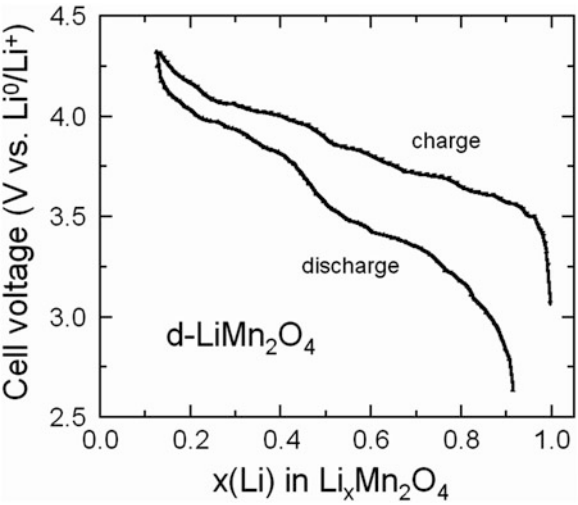

Fig. 9.19 The voltage composition profile for a Li//$LiMn_2O_4$ using a spinel electrode synthesized by the combustion urea-assisted method. The cell was charged and discharged at current density 0.05 mA/cm^2

spinel oxides, the first material was synthesized by the combustion urea-assisted method [71] and the second one was obtained by milling of MnO_2 and Li_2O.

Using a wet-chemical technique assisted by urea as combustion agent, $LiMn_2O_4$ spinel oxides exhibit grains with a quite small domain size of 0.5 μm The voltage composition profile for a Li//$LiMn_2O_4$ using a spinel electrode synthesized by wet-chemical technique assisted by urea as combustion agent is shown in Fig. 9.19. In the voltage domain between 3.0 and 4.5 V, the charge–discharge curves correspond to the voltage profiles characteristic of the spinel $LiMn_2O_4$ cathode material associated with lithium occupation of tetrahedral sites, in agreement with previous works. From the variation of the cell potential with x in $Li_xMn_2O_4$, one can distinguish the presence of two regions. The shape of the voltage curves indicates whether the delithiated $LiMn_2O_4$ exists as a single- or a multiple-phase. In the latter case the potential is expected to be essentially invariant with composition. The first region (I) is characterized by a S-shaped voltage curve, whereas the second region (II) corresponds to a plateau portion. In region I, the charge voltage increases continuously in the voltage range of 3.80–4.05 V. In region II, the charge voltage is stable around 4.10 V. The lithium extraction/insertion reactions in regions I and II proceed in a matrix having a cubic symmetry. In the region II corresponding to the upper voltage plateau, a two-cubic phase system is recognized, whereas the region I is attributed to a single cubic phase characterized by an S-shaped voltage curve. The upper 4-V plateau provides a capacity over 110 mAh g^{-1} based on the active material utilization with an excellent cyclability [71].

Mechano-chemical technique is an efficient method to obtain high dispersed compounds directly during mechanical activation at room temperature [72]. $LiMn_2O_4$ was synthesized by mechanical activation in plenary mill with steel balls from the mixture Li_2O and MnO_2 electrochemically activated (EMD) [73].

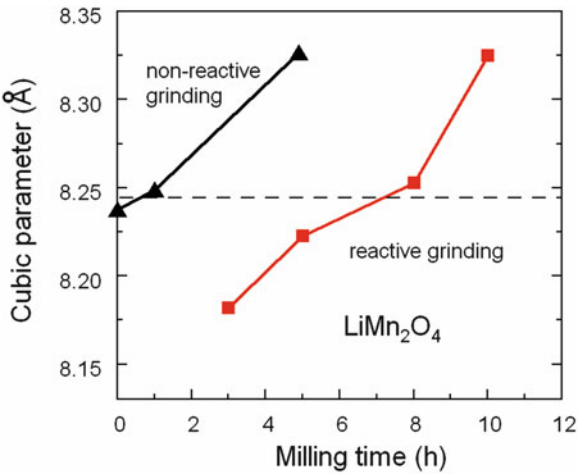

Fig. 9.20 Evolution of the lattice parameters of ceramic $LiMn_2O_4$ (*filled triangle*) and mechano-synthesized Li-Mn-O (*filled square*) with grinding. a_{cub} is given with an accuracy of 0.01 Å, whereas due to a large inaccuracy on its value, the 10-h ground ceramic lattice parameter is not reported. The *dashed line* points out the lattice parameter $a_{cub} = 8.247$ Å for stoichiometric $LiMn_2O_4$

Evolution of the structure upon mechano-milling is as follows. After 1 h of grinding, the major peaks of a spinel-type phase are visible. Higher milling times, between 2 and 8 h, lead to a better crystallization of the materials. The narrowing of the X-ray peaks (i.e., better crystallization) may be correlated to a decrease in the lattice strain and an increase in the crystallite size, which slightly varies from around 20 Å after 1 h of grinding to 80 Å after 8 h of grinding, respectively. Further grindings ($t_m \geq 10$ h) lead to a decomposition of the Li-Mn-O spinel-type oxides coupled with the appearance of new phases mainly identified as Mn_2O_3. The evolution of the cell parameters with milling time for non-reactive and reactive grinding are reported in Fig. 9.20. In both cases, the lattice parameter a_{cub} increased with milling time, and with the synthesis temperature. The 8.238 Å value, slightly smaller than 8.247 Å reported in the literature for stoichiometric $LiMn_2O_4$, indicates a small departure from the Li/Mn = ½ ratio for the ceramic sample [74]. The strong increase in the cell parameter from 8.238 to 8.318 Å after non-reactive grinding during 5 h is still not completely understood. Indeed, to our knowledge, such a high cell parameter value has never been reported for spinel-type lithiated manganese oxides. In the literature, a cubic parameter a_{cub} higher than 8.24 Å is generally attributed either to an excess in lithium or an oxygen deficient spinel. Xia et al. [75] determined an 8.2485 Å value for ceramic $LiMn_2O_4$ heat treated 700 °C for 24 h in air exhibiting an oxygen deficiency of 0.08 (e.g., $Li_{0.938}Mn_2O_{3.92}$).

The product prepared by reactive milling for 5 h shows a rather disordered spinel structure as observed by Raman scattering spectroscopy (Fig. 9.21a). For this compound the Raman active A_{1g} mode at 625 cm^{-1} is shifted to 633 cm^{-1} and broadened in comparison with that of a λ-$LiMn_2O_4$ ceramic. This disordered structure is also at the origin of the electrochemical behavior shown in Fig. 9.21b. The first charge–discharge curve recorded at the *C*/10 rate shows deviation from the standard electrochemical profile of $LiMn_2O_4$ spinel. We do not observe the

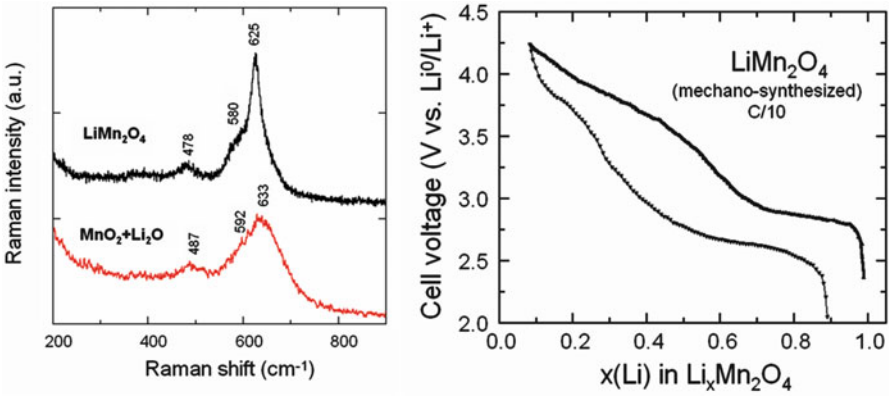

Fig. 9.21 (*Left*) Raman spectra of λ-$LiMn_2O_4$ spinel and disordered spinel grown by mechano-synthesis from the MnO_2-Li_2O mixture. (*Right*) The first charge–discharge of the disordered $LiMn_2O_4$ sample

characteristic plateaus at 4.05 and 4.15 V occurring during in the charge process. This is attributed to the strong distortion of the MnO_6 octahedra as evidenced by the red shift of the A_{1g} Raman mode.

9.8 Disordered $LiNiVO_4$

Among the various vanadates, crystallized $LiNiVO_4$ shows promising electrochemical behavior as a 4-V electrode material [76–78]. Crystallized $LiNiVO_4$ synthesized by the classical high-temperature route can reversibly react with about seven Li ions per transition metal when discharged to voltages lower than 0.2 V [79], so that specific capacities as 800–900 mAh g^{-1} could be achieved. This vanadate was shown to become amorphous upon the first electrochemical discharge, which must be performed at a slow cycling rate to ensure a proper function of the electrode material upon subsequent cycles.

$LiNiVO_4$ has been synthesized by a wet-chemical method, which consists of a low-temperature reaction assisted by glycine as combustion agent. The powder mass was annealed at 350 and 500 °C in air for 6 h for improving the crystallinity of the $LiNiVO_4$ final product. XRD date show that $LiNiVO_4$ belongs to inverse spinel structure (space group $Fd\overline{3}m - O_h^7$) with a cubic lattice parameter of 8.222 Å. The pentavalent vanadium is located on the tetrahedral (8*a*) sites, whereas Li and Ni are distributed on the octahedral (16*d*) sites, the distribution being disordered. Figure 9.22a presents the voltage-composition curve for the Li insertion into an amorphous $LiNiVO_4$. Upon the first reduction, $LiNiVO_4$ reacts with ten Li ions per Ni, while only seven Li/Ni can be removed after subsequent recharges.

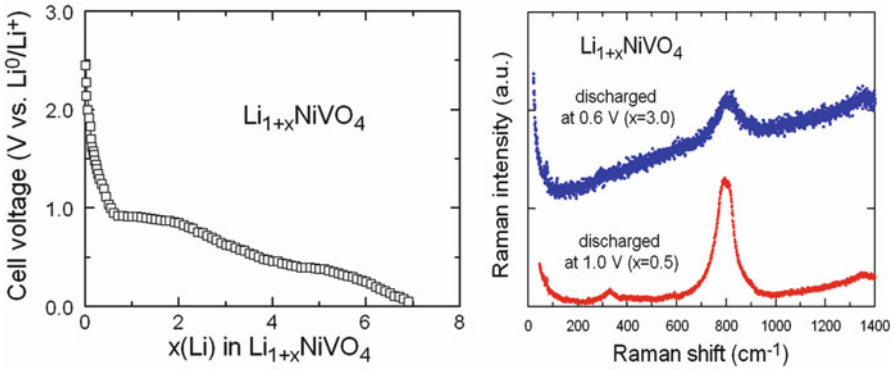

Fig. 9.22 (**a**) The voltage-composition curve for the Li insertion into an amorphous $LiNiVO_4$. (**b**) Raman spectra of a $LiNiVO_4$ cathode discharged at 1.0 and 0.6 V vs. lithium anode

Figure 9.22b shows the Raman spectra of Li intercalated $LiNiVO_4$ phase. Spectra were recorded at the beginning of the two plateaus at 0.9 and 0.4 V occurring during the Li//$LiNiVO_4$ cell discharge (Li intercalation). These plateaus should be at the origin of biphasic transformation due to the high reduction of vanadium ions. The Raman features of $LiNiVO_4$ have been discussed elsewhere [78]. The spectra are dominated by a broad band in the 700–850 cm^{-1} region, which is assigned to a vibration between the oxygen and the highest-valency cation. This vibration corresponds to the stretching mode of VO_4 tetrahedron having the A_1 symmetry, whereas the band situated at 335 cm^{-1} corresponds to the bending mode of VO_4 tetrahedron with an E symmetry. Therefore, one observes either the bending vibrations of VO_4 tetrahedron or the vibrations involving the NiO_6, LiO_6 octahedral environments. If one considers that all the Li ions are accommodated in octahedral LiO_6 environments, the F_{1u} modes are normally split into $(A + 2B)$ Raman-active and IR-active components. Therefore, IR modes having $(A + 2B)$ symmetry are intense, whereas Raman modes are expected to be very weak. These two modes are observed at 416 and 435 cm^{-1}, respectively. As shown in Fig. 9.22b, there are important modifications of the Raman spectra of $LiNiVO_4$ upon Li intercalation. When the cathode is discharged, the stretching mode of VO_4 tetrahedra is shifted toward the low-wave number side corresponding to the reduction of the highest-valency cation. At 0.6 V the Raman efficiency is very weak. Thus, the host lattice is highly intercalated and the Raman peaks of $LiNiVO_4$ decrease and a strong luminescence band appears at about 1.8 eV for Li_5NiVO_4.

References

1. Denton EP, Rawson H, Stanworth JE (1954) Vanadate glasses. Nature 173:1030–1032
2. Baynton PL, Rawson H, Stanworth JE (1957) Semiconducting properties of some vanadate glasses. J Electrochem Soc 104:237–240
3. Whittingham MS, Chianelli RS, Jacobson AJ (1980) Amorphous cathodes for lithium batteries. In: Murphy DW, Broadhead J, Steele BCH (eds) Materials for advanced batteries. Plenum, New York, NY, pp 291–299
4. Jacobson AJ, Rich SM (1980) Electrochemistry of amorphous V_2S_5 in lithium cells. J Electrochem Soc 127:779–781
5. Nassan K, Murphy DW (1981) The quenching and electrochemical behaviour of Li_2O-V_2O_5 glasses. J Non-Cryst Solids 44:297–304
6. Whittingham MS (1981) Lithium incorporation in crystalline and amorphous. J Electroanal Chem 118:229–239
7. Takeda Y, Kanno R, Tsuji Y, Yamamoto O (1984) Rechargeable lithium/chromium oxide cells. J Electrochem Soc 131:2006–2010
8. Sakurai Y, Yamaki J (1985) V_2O_5-P_2O_5 glasses as cathode for lithium secondary battery. J Electrochem Soc 132:512–513
9. Wakihara M, Uchida T, Morishita T, Wakamatsu H, Tanigushi M (1987) A rechargeable lithium battery employing a porous thin film of $Cu_{3+\delta}Mo_6S_{7.9}$. J Power Sourc 20:199–204
10. Lee J, Urban A, Li X, Su D, Hautier G, Ceder G (2014) Unlocking the potential of cation-disordered oxides for rechargeable lithium batteries. Science 343:519–522
11. Zhang XW, Patil PK, Wang C, Appleby AJ, Little FE, Cocke DL (2004) Electrochemical performance of lithium ion battery, nano-silicon-based, disordered carbon composite anodes with different microstructures. J Power Sourc 125:206–213
12. Py MA, Haering RR (1983) Structural destabilization induced by lithium intercalation in MoS_2 and related compounds. Can J Phys 61:76–84
13. Selwyn LS, McKinnon WR, von Sacken U, Jones CA (1987) Lithium electrochemical cells at low voltage. Decomposition of Mo and W dichalcogenides. Solid State Ionics 22:337–344
14. Hearing RR, Stiles JAR, Brandt Klaus (1979) Lithium molybdenum disulphide battery cathode. US Patent 4,224,390, 23 Sep 1980
15. Jacobson AJ, Chianelli RR, Whittingham MS (1979) Amorphous molybdenum disulfide cathodes. J Electrochem Soc 126:2277–2278
16. Julien C, Saikh SI, Nazri GA (1990) Disordered MoS_2 used as cathodic material in Li electrochemical cell. ISSI Lett 1:12–14
17. Julien C, Saikh SI, Nazri GA (1992) Electrochemical studies of disordered MoS_2 as cathode material in lithium batteries. Mater Sci Eng B 15:73–77
18. Bichel R, Levy F (1986) Influence of process conditions on the electrical and optical properties of RF magnetron sputtered MoS_2 films. J Phys D 19:1809–1820
19. Julien C, Nazri GA (1994) Solid state batteries: materials design and optimization. Kluwer, Boston, MA
20. Julien C, Yebka B (2000) Electrochemical features of lithium batteries based on molybdenum-oxide compounds. In: Julien C, Stoynov Z (eds) Materials for lithium-ion batteries, NATO-ASI series, Ser 3–85. Kluwer, Dordrecht, pp 263–277
21. James ACWP, Goodenough JB (1988) Structure and bonding in Li_2MoO_3 and $Li_{2-x}MoO_3$ ($0 \leq x \leq 1.7$). J Solid State Chem 76:87–96
22. Julien C, Nazri GA (1994) Transport properties of lithium-intercalated MoO_3. Solid State Ionics 68:111–116
23. Guzman G, Yebka B, Livage J, Julien C (1996) Lithium intercalation studies in hydrated molybdenum oxides. Solid State Ionics 86–88:407–413
24. Nazri GA, Julien C (1995) Studies of lithium intercalation in heat-treated products obtained from molybdic acid. Ionics 2:1–6

25. Dampier FW (1974) The cathodic behaviour of CuS, MoO_3, and MnO_2 in lithium cells. J Electrochem Soc 121:656–660
26. Margalit N (1974) Discharge behaviour of Li/MoO_3 cells. J Electrochem Soc 121:1460–1461
27. Kumagai N, Kumagai N, Tanno K (1988) Electrochemical characteristics ans structural changes of molybdenum trioxide hydrates as cathode materials for lithium batteries. J Appl Electrochem 18:857–862
28. Sugawara M, Kitada Y, Matsuki K (1989) Molybdic oxides as cathode active materials in secondary lithium batteries. J Power Sourc 26:373–379
29. Ekstrom T (1972) Formation of ternary phases of Mo_5O_{14} and $Mo_{17}O_{47}$ structure in the molybdenum-wolfram-oxygen system. Mater Res Bull 7:19–26
30. Julien C, Nazri GA, Guesdon JP, Gorenstein A, Khelfa A, Hussain OM (1994) Influence of the growth conditions on electrochemical features of MoO_3 film-cathodes in lithium microbatteries. Solid State Ionics 73:319–326
31. Julien C, Khelfa A, Hussain OM, Nazri GA (1995) Synthesis and characterization of flash evaporated MoO_3 thin films. J Cryst Growth 156:235–244
32. Julien C, Hussain OM, El-Farh L, Balkanski M (1992) Electrochemical studies of lithium insertion in MoO_3 films. Solid State Ionics 53–56:400–404
33. Julien C, El-Farh L, Balkanski M, Hussain OM, Nazri GA (1993) The growth and electrochemical properties of metal-oxide thin films: lithium intercalation. Appl Surf Sci 65–66: 325–330
34. Julien C, Yebka B, Guesdon JP (1995) Solid-state lithium microbatteries. Ionics 1:316–327
35. Kröger M, Hamwi S, Meyer J, Riedl T, Kowalsky W, Ouchi Y (2009) Role of the deep-lying electronic states of MoO_3 in the enhancement of hole-injection in organic thin films. Appl Phys Lett 95:123301
36. Kim DY, Subbiah J, Sarasqueta G, So F, Ding H, Gao Y (2009) The effect of molybdenum oxide interlayer on organic photovoltaic cells. Appl Phys Lett 96:093304
37. Julien C (1996) Electrochemical properties of disordered cathode materials. Ionics 2:169–178
38. Goodenough JB, Manthiram A, James ACWP, Strobel P (1989) Lithium insertion compounds. Mater Res Soc Symp Proc 135:391–415
39. Honders A, Broers GHJ (1985) Bounded diffusion in solid solution electrode powder compacts. Part I. The interfacial impedance of a solid solution electrode (M_xSSE) in contact with a m^+-ion conducting electrolyte. Solid State Ionics 15:173–183
40. Basu S, Worrell WL (1979) Chemical diffusion of lithium in Li_xTaS_2 and Li_xTiS_2 at 30 °C. In: Vashishta P, Mindy JN, Shenoy GK (eds) Fast ion transport in solids. North-Holland, Amsterdam, pp 149–152
41. Armand M (1980) Intercalation electrodes. In: Murphy DW, Broadhead J, Steele BCH (eds) Materials for advanced batteries. Plenum, New York, NY, pp 145–161
42. Honders A, der Kinderen JM, van Heeren AH, de Wit JHW, Broers GHJ (1985) Bounded diffusion in solid solution electrode powder compacts. Part II. The simultaneous measurement of the chemical diffusion coefficient and the thermodynamic factor in Li_xTiS_2 and Li_xCoO_2. Solid State Ionics 15:265–276
43. Julien C, El-Farh L, Balkanski M, Samaras I, Saikh SI (1992) Studies of the transport properties in lithium-intercalated $NiPS_3$. Mater Sci Eng B 14:127–132
44. Maeir J (1991) Diffusion in materials with ionic and electronic disorder. In: Nazri GA, Huggins RA, Shriver DF (eds) Solid state ionics II, vol 210. Materials Research Society, Pittsburgh, PA, pp 499–510
45. Weppner W, Huggins RA (1977) Determination of the kinetic parameters of mixed-conducting electrodes and application to the system Li_3Sb. J Electrochem Soc 124:1569–1578
46. Minami T (1984) Fast ion conducting glasses. J Non-Cryst Solids 73:273–284
47. Machina N, Fuchida R, Minami T (1989) Behavior of rapidly quenched V_2O_5 glass as cathode in lithium cells. J Electrochem Soc 136:2133–2136
48. Nabavi M, Sanchez C, Taulette F, Livage J, de Guibert A (1988) Electrochemical properties of amorphous V_2O_5. Solid State Ionics 28–30:1183–1186

49. Sakurai Y, Yamaki J (1985) Electrochemical behaviour of amorphous V_2O_5(-P_2O_5) cathodes for lithium secondary batteries. J Power Sourc 20:173–177
50. Lee SH, Cheong HM, Liu P, Tracy CE (2003) Improving the durability of amorphous vanadium oxide thin-film electrode in a liquid electrolyte. Electrochem Solid State Lett 6: A102–A105
51. Julien C, Guesdon JP, Gorenstein A, Khelfa A, Ivanov I (1995) The growth of V_2O_5 flash-evaporated films. J Mater Sci Lett 14:934–936
52. Oukassi S, Salot R, Pereira-Ramos JP (2009) Eleboration and characterization of crystalline RF-deposited V_2O_5 positive electrode for thin film batteries. Appl Surf Sci 256:149–155
53. Julien C, Haro-Poniatowsk E, Camacho-Lopez MA, Escobar-Alarcon L, Jimenez-Jarquin J (1999) Growth of V_2O_5 thin films by pulsed laser deposition and their applications in lithium microbatteries. Mater Sci Eng B 65:170–176
54. Madhuri KV, Naidu BS, Hussain OM, Eddrief M, Julien C (2001) Physical investigations on electron beam evaporated V_2O_5-MoO_3 thin films. Mater Sci Eng B 86:165–171
55. Liu D, Liu Y, Garcia BB, Zhang Q, Pan A, Jeong YH, Cao G (2009) V_2O_5 xerogel electrodes with much enhanced lithium-ion intercalation properties with N_2 annealing. J Mater Chem 19:8789–8795
56. Wang Y, Shang HM, Chou T, Cao GZ (2005) Effects of thermal annealing on the Li^+ intercalation properties of V_2O_5•nH_2O xerogel films. J Phys Chem B 109:11361–11366
57. Ramana CV, Smith RJ, Hussain OM, Massot M, Julien CM (2005) Surface analysis of pulsed-laser-deposited V_2O_5 films and their lithium intercalated products studied by Raman spectroscopy. Surf Interface Anal 37:406–411
58. Julien C, Gorenstein A (1995) R&D of lithium microbatteries using transition oxide films as cathodes. J Power Sourc 15:373–391
59. Julien C, Gorenstein A, Khelfa A, Guesdon JP, Ivanov I (1995) Fabrication of V_2O_5 thin films and their electrochemical properties in lithium microbatteries. Mater Res Soc Symp Proc 369:639–647
60. Gorenstein A, Khelfa A, Guesdon JP, Julien C (1995) Effect of the crystallinity of V_6O_{13} films on the electrochemical behaviour of lithium microbatteries. Mater Res Soc Symp Proc 369:649–655
61. Gorenstein A, Khelfa A, Guesdon JP, Nazri GA, Hussain OM, Ivanov I, Julien C (1995) The growth and electrochemical properties of V_6O_{13} flash-evaporated films. Solid State Ionics 76:133–141
62. Swider-Lyons KE, Love CT, Rolison DR (2002) Improved lithium capacity of defective V_2O_5 materials. Solid State Ionics 152–153:99–104
63. Kröger FA (1964) Chemistry of imperfect crystals. North-Holland, Amsterdam
64. Abo-el-Soud AM, Mansour B, Soliman LI (1994) Optical and electrical properties of V_2O_5 thin films. Thin Solid Films 247:140–143
65. Liquan C, Schooman J (1994) Polycrystalline, glassy and thin films of $LiMn_2O_4$. Solid State Ionics 67:17–23
66. Escobar-Alarcon L, Haro-Poniatowski E, Jimenez-Jarquin J, Massot M, Julien C (1999) Physical properties of lithium-cobalt oxides grown by laser ablation. Mater Res Soc Symp Proc 548:223–228
67. Julien C, Camacho-Lopez MA, Escobar-Alarcon L, Haro-Poniatowski E (2001) Fabrication of $LiCoO_2$ thin film cathodes for rechargeable lithium microbatteries. Mater Chem Phys 68:210–216
68. Garcia B, Farcy J, Pereira-Ramos JP, Perichon J, Baffier N (1995) Low-temperature cobalt oxide as rechargeable cathodic material for lithium batteries. J Power Sourc 54:373–377
69. Tarascon JM, Guyomard D (1993) The $Li_{1+x}Mn_2O_4$/C rocking-chair system: a review. Electrochim Acta 38:1221–1231
70. Tarascon JM (2000) Better Electrode materials for energy storage applications through chemistry. In: Julien C, Stoynov Z (eds) Materials for lithium-ion batteries, NATO-ASI Series, Ser 3–85. Kluwer, Dordrecht, pp 75–103

71. Chitra S, Kalyani P, Mohan T, Gangadharan R, Yebka B, Castro-Garcia S, Massot M, Julien C, Eddrief M (1999) Characterization and electrochemical studies of $LiMn_2O_4$ cathode materials prepared by combustion method. J Electroceram 3:433–438
72. Kosova NV, Asanov IP, Devyatkina ET, Avvakumov EG (1999) State of manganese atoms during the mechanochemical synthesis of $LiMn_2O_4$. J Solid State Chem 146:184–188
73. Soiron S, Rougier A, Aymard L, Julien C, Moscovici J, Michalowicz A, Hailal I, Taouk B, Nazri GA, Tarascon JM (2003) Relationship between the structural and catalytic properties of mechanosynthesized lithiated manganese oxides. Ionics 9:155–167
74. Endres P, Ott A, Kemmler-Sack S, Jager A, Mayer HA, Praas HW, Brandt K (1997) Extraction of lithium from spinel phases of the system $Li_{1+x}Mn_{2-x}O_{4-\delta}$. J Power Sourc 69:145–156
75. Xia Y, Sakai T, Fujieda T, Yang XQ, Sun X, Ma ZF, McBreen L, Yoshio M (2001) Correlating capacity fading and structural changes in $Li_{1+y}Mn_{2-y}O_{4-\delta}$ spinel cathode materials. J Electrochem Soc 148:A723–A729
76. Bernier JC, Poix P, Michael A (1961) Sur deux vanadates mixtes du type spinelle. CR Acad Sci (Paris) 253:1578
77. Fey GTK, Li W, Dahn JR (1994) $LiNiVO_4$: a 4.8 volt electrode material for lithium cells. J Electrochem Soc 141:2279–2282
78. Prabaharan SRS, Michael MS, Radhakrishna S, Julien C (1997) Novel low-temperature synthesis and characterization of $LiNiVO_4$ for high-voltage Li-ion batteries. J Mater Chem 7:1791–1796
79. Orsini F, Baudrin E, Denis S, Dupont L, Touboul M, Guyomard D, Piffard Y, Tarascon JM (1998) Chimie douce synthesis and electrochemical properties of amorphous and crystallized $LiNiVO_4$. Solid State Ionics 107:123–133

Chapter 10
Anodes for Li-Ion Batteries

10.1 Introduction

Lithium-ion batteries (LiBs) have made considerable progress since the first commercial one by Sony in 1991, which had $LiCoO_2$ and graphite as active elements of the positive and negative electrodes, respectively. The LiBs are now the primary energy storage devices in the transportation and communications, from portable use in computers, up to electric and hybrid vehicles. More recently, they have also been used as back-up supply units, frequency regulators (load leveling) to integrate on smart grids the electricity produced by windmills and photovoltaic plants (for a recent review, see [1]). These applications require high energy densities, high power, and safety among others. Considerable efforts have been made to propose other electrodes to fulfill these requirements. We have recently reviewed the works and progress concerning the materials for the positive electrode [2–6]. The present work is devoted to the materials for the negative electrode counterpart. It is common to use the terminology anode and cathode for the negative and positive electrodes, respectively, although the electrodes play alternatively the role of anode and cathode during the charge and discharge process. We shall use this terminology in the following for conciseness purposes only.

An ideal active anode element should fulfill the following requirements as follows: (1) It must be light and accommodate as much Li as possible to optimize the gravimetric capacity. (2) Its redox potential with respect to Li^0/Li^+ must be as small as possible at any Li-concentration. The reason is that this potential is subtracted to the redox potential of the cathode material to give the overall voltage of the cell, and smaller voltage means smaller energy density. (3) It must possess good electronic and ionic conductivities since faster motion of the lithium ions and the electrons also mean higher power density of the cell. (4) It must not be soluble in the solvents of the electrolyte and not react with the lithium salt. (5) It must be safe, i.e. avoid any thermal runaway of the battery, a criterion that is not independent of the previous one, but deserves special attention, especially for use in transportation

C. Julien et al., *Lithium Batteries*, DOI 10.1007/978-3-319-19108-9_10

such as electric vehicles and planes. (6) It must be cheap and environmentally friendly. The different materials proposed as anode elements for Li-ion batteries must be discussed with respect to these different criteria.

The graphite is still the most used anode material and is still the reference. The first works giving evidence of the insertion of lithium in graphite date from 1955 [7], confirmed by the synthesis of LiC_6 in 1965 [8]. The synthesis of LiC_6, however, was not obtained by electrochemical process at that time. Another decade was spent before Besenhard and Eichinger discovered the reversible intercalation of lithium in graphite, proposing this material as an anode in 1976 [9, 10]. Increasing the Li content in LiC_6 is possible [8], but no reversible cycling beyond LiC_6 could ever be obtained. The graphite anode can thus be cycled between Li and LiC_6, at which the stage I intercalation is achieved with the Li atoms located between the carbon planes. The theoretical capacity associated to the cycles between C and LiC_6 is 372 mAh g^{-1}. Therefore, the requirement labeled (1) in the previous section is not very well satisfied: one goal of the research on anode material is the increase of this capacity. There is a tendency, however, to focus too much attention on this parameter. The reason is that the capacity is limited more by the cathode than the anode element: typically, the capacity of a cathode element is in the range 140–200 mAh g^{-1}. The gain in capacity of the total cell by increasing that of the anode element alone is thus limited [11]. This is illustrated in Fig. 10.1, which shows that the total capacity of an 18,650-type cell as a function of the anode capacity. The total capacity almost saturates when the anode capacity reaches typically 500 mAh g^{-1}. On the one hand, it shows that the tests of anode materials that are usually performed on half-cells (i.e. with lithium metal counter-electrode) are misleading. On the other hand, the capacity 372 mAh g^{-1} of the graphite is significantly below this saturation limit, and the research on anodes with higher capacity is clearly justified. The requirement (2) is well satisfied, since the potential of graphite versus Li metal is only 0.15–0.25 V. So is the requirement (3). Graphite is a semimetal with an electronic conductivity at room temperature that exceeds

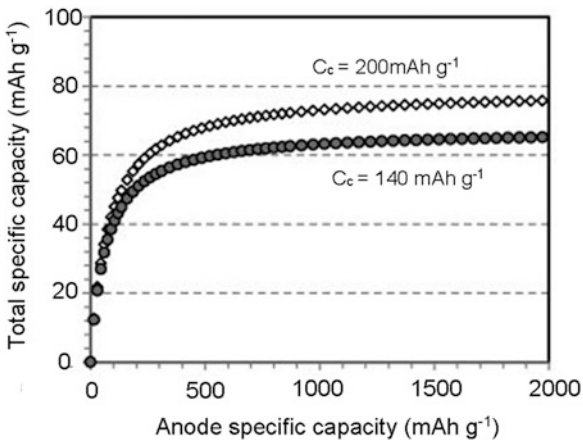

Fig. 10.1 Total capacity of a 18,650 Li-ion cell as a function of the anode capacity, for two cathodes having capacities 140 and 200 mAh g^{-1}. Reproduced with permission from [11]. Copyright 2007 Elsevier

10^{-3} S cm^{-1}, while LiC_6 is a metal with a high Li ion mobility 10^{-8}–10^{-10} cm^2 s^{-1}. Requirement (4) poses questions. The graphite must be protected against side reactions with the electrolyte. This is the role of ethylene carbonate (EC) that is used as a solvent in the electrolyte of batteries with graphite anode. Owing to the EC-based solvent, a solid-electrolyte interface (SEI) is formed at the surface of graphite particles during the first cycles. This SEI prevents excessive solvent intercalation and acts as a good Li ion conductor [12–16]. Moreover, it protects the strongly reducing LiC_6 formed at the end of charge from direct contact with the electrolyte. On another hand, the use of more conductive solvents such as propylene carbonate (PC) is forbidden with graphite, because of side reactions, and the flow of Li ions arriving on the graphite must be small enough to give the ions the time to insert into the graphite, otherwise the Li deposition generates safety issues [17, 18]. Therefore, efforts on the research for new cathode elements also aim to find materials that are more performing with respect to the criteria (4) and (5). Concerning the requirement (6), graphite is not expensive, except specialty graphites like MesoCarbon MicroBeads (MCMB) graphite or microcrystalline graphite that imply expensive manufacturing processes.

One can easily understand from this discussion that it is difficult to replace graphite, since it satisfies many requirements. The only alternative anode that has been introduced on the market is the composite Sn/Co/C developed by Sony in 2005 [19]. Here, Sn is the electro-active element, which exemplifies the efforts that are made in research on the so-called alloy anodes including metals metalloids, and alloy-compounds reviewed in [20]. Cobalt and carbon are inactive matrix elements that help in better cycling. A reversible capacity circa 400 mAh g^{-1} has been achieved, which is comparable to that of graphite, but the advantages are an increase of safety and a lower cost with respect to specialty graphite. Another anode, $Li_4Ti_5O_{12}$, is very promising and this material is already commercialized, but the batteries equipped with this anode are still made at the laboratory scale. Results obtained with this anode prior 2010 have been reviewed in [21]. The active research of topical interest has motivated many reviews on the other anode compounds as well through the last decade [22–67]. They include metal-containing anodes in the form of metals, intermetallics [20], oxides, and oxysalts including phosphates and carbonates [22], vanadium oxides [34], molybdenum oxides [34, 68], TiO_2-based nanostructures [15, 31, 35, 38, 53, 69–73], more generally conversion electrodes [27, 74] including fluorides [27, 75], sulfides [27], selenides [25], nitrides [27], phosphides [25, 27], antimonides [25], and graphene-based nanocomposites [76]. Different reviews have also been focused on silicon anodes [77–86], which illustrates the tremendous amount of works on this very promising anode, boosted by the new nanotechnologies from which various advantages are expected: (1) nano-sized active particles can suffer huge dilatation/contraction upon Li insertion/extraction without damage, contrary to bigger particles. (2) Larger surface to volume ratio implies a larger specific capacity, and a larger contact area with the electrolyte leading to high lithium-ion flux across the electrode/electrolyte interface. (3) Lithium diffusion and electronic conductivity are improved due to the reduction of the electron and Li path length, leading to batteries with enhanced

power capability. Therefore, many works have been devoted to the synthesis and analysis of the properties of the nano-sized anode particles that have been specifically reviewed [49, 87]. Some reviews have been focused on such nano-particles based on carbon (carbon nanotubes, graphene composites) [41, 88–93].

The aim of the present chapter is to review the different works that have been accomplished on the different types of anode materials that have been proposed recently, focusing attention on the tremendous amount of work that has been done in this field during the last 5 years. Elder works can be readily found in the different reviews that have been cited in this introduction. A comparative study is made between the different anodes with respect to the requirements (1)–(5) we have listed.

10.2 Carbon-Based Anodes

Two types of carbon can be used as active anode materials [94, 95]: soft carbon, also called graphitized carbon where crystallites are oriented almost in the same direction, and hard carbon where crystallites have disordered orientations. Both are used in lithium-ion batteries, but they do not have the same properties.

10.2.1 Hard Carbon

Before the recent results obtained with soft carbon anodes, hard carbon had the advantage of higher reversibility and high reversible capacity. Currently, the capacity of hard graphite is in the range 200–600 mAh g^{-1} [96–100]. Usually, the problem with hard carbon is not the capacity, but the poor rate capability coming from the slow diffusion process resulting from the many voids and defects associated to the random alignment of the graphene sheets. This problem seems to have been overcome in nano-porous hard carbons synthesized from pyrolyzed sucrose, which deliver a reversible capacity 500 mAh g^{-1} with a good cycle life and a good rate capability due to the fast lithium diffusion 4.11×10^{-5} cm^2 s^{-1} for hierarchical nanoporous hard carbon [101].

10.2.2 Soft Carbon

The most popular graphite) materials commercialized for anodes are Mesocarbon Microbead (MCMB), Mesophase-pitch-based carbon fiber (MCF), vapor grown carbon fiber (VGCF) and Massive Artificial Graphite (MAG). These soft carbon anodes have a long cycling life and a coulombic efficiency larger than 90 % [54, 102–106]. Their specific capacity is close to the theoretical value 372 mAh g^{-1}

corresponding to the formation of LiC_6, which, as discussed in the introduction, is a limiting factor, and efforts are currently done to improve this capacity [107]. Two approaches are investigated: use porous carbon, and nano-sized carbon. Actually, mesoporous carbon is also a form of nano-sized carbon. For instance, the length of the mesoporous carbon that delivered a capacity of 1100 mAh g^{-1} in the first cycle and 850 mAh g^{-1} in the 20th cycle in [108] was 10.5 nm, the uniform size of the pores was 3.9 nm, and the thickness of the carbon wall was 6.6 nm. Indeed, the nano-sized carbon under its various forms (nanotubes, nanorings, graphene) is most promising. The idea is to decrease the size to such a small scale (typically 10 nm) that quantum confinements of the electron states modify the electronic structure and electronic properties with respect to those of the bulk material. This modification introduces novel properties that are beneficial to the storage capacity by removing the limitation of the capacity to 372 mAh g^{-1} [109–114]. Not only quantum effects, but also the increase of the number of storage sites available for the lithium ions in small closed spaces in nanostructured carbon has been proposed to explain the large capacities that have been observed [99, 115, 116]. One example is provided by carbon nanorings with 20 nm outer diameters and 3.5-nm wall thickness (Fig. 10.2), which deliver a capacity 1200 mAh g^{-1}, and over a hundreds of cycles at the current density of 0.4 A g^{-1}. Even at the higher current rates of 45 A g^{-1}, the capacity is as high as 500 mAh g^{-1} [117].

10.2.3 Carbon Nanotubes

Carbon nanotubes (CNTs) are often used together with other active anode elements to improve the electrochemical performance by taking advantage of their superior electronic conductivity, mechanical and thermal stability [107, 118]. The CNTs are divided into single (SWCNTs) and multiwall (MWCNTs) depending on their thickness and the number of coaxial layers. The highest reversible capacity is predicted for SWCNTs and is estimated to be 1116 mAh g^{-1} in stoichiometry LiC_2 owing to the intercalation of lithium into stable sites located on the surface of pseudographitic layers and inside the central tube as well [119–122]. This theoretical prediction is confirmed by experiments, since purified SWCNTs, produced by laser vaporization procedure, yield a capacity larger than 1050 mAh g^{-1} [123], the largest capacity obtained with SWCNT anodes. This performance has been obtained for a purified SWCNT obtained by laser vaporization. It is very difficult, however, to prepare CNTs that do not contain defects or impurities that degrade importantly the reversible capacity and the coulombic efficiency. Therefore, many efforts are presently devoted to the mode of preparation [107, 119], and the morphology (thickness, porosity, shape) [124, 125].

Until recently, MWCNTs had not reached the same performances as the SGCNTs. Commercial MWCNTs have a typical capacity close to 250 mAh g^{-1}. After purification, the capacity raises to a 400 mAh g^{-1}. However, chemically drilled MWCNT (DMWCNT) has been prepared recently by solid state process [126].

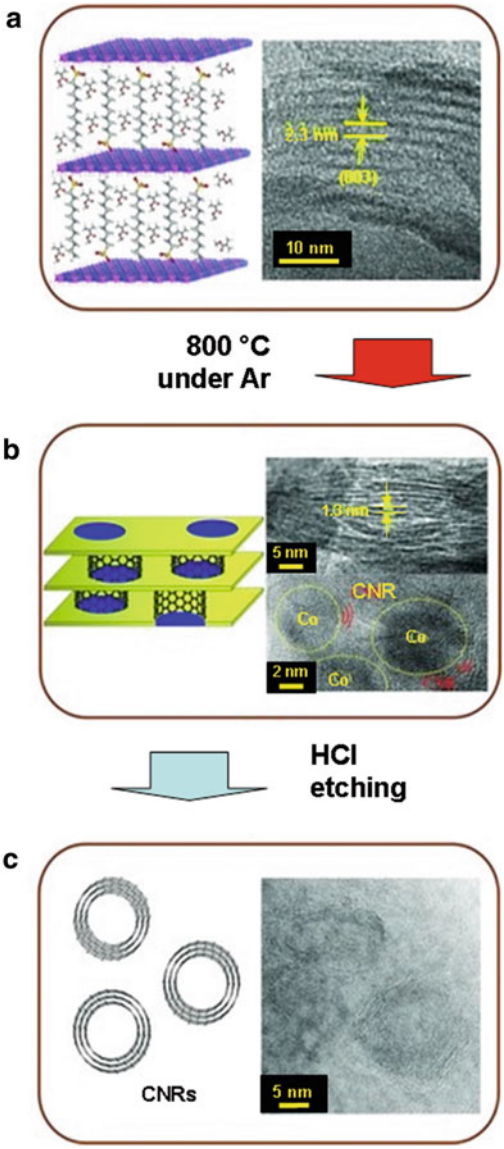

Fig. 10.2 Schematic illustrations and HRTEM images of the different stages in the fabrication of carbon nanorings (CNRs) in the cobalt(II)–aluminum (III) layered double hydroxide (LDH) containing co-intercalated dodecyl sulfonate (DSO) anions and methyl methacrylate (MMA) CoAl–DSO–MMA–LDH matrix: (**a**) the (CoAl–DSO–MMA–LDHCoAl–DSO–MMA–LDH precursor, (**b**) CoAl–DSO–MMA–LDH after calcination in an Ar atmosphere at 800 °C and (**c**) isolated CNRs obtained after dissolution of the matrix. Reproduced with permission from [117]. Copyright 2013 Wiley

In this work, cobalt oxide particles have been deposited on the surface of the nanotubes, and have been removed after an oxidation process, leading to 4 nm-sized holes. The reversible capacity of the DMWCNT cycled between 0.02 and 3.0 V exceeded 600 mAh g^{-1}, remaining constant over the 20 cycles were the material has been tested. An improvement has been achieved for an interface-controlled MWCNT structure, synthesized through a two-step process of catalyst deposition and chemical vapor deposition (CVD) and directly grown on a copper current collector [127],

which delivered a capacity 900 mAh g^{-1} and no capacity degradation up to 50 cycles. The best result with MWCNTs so far has been obtained through directly applying a 10 nm thick layer of Al_2O_3 by atomic layer deposition (ALD) on the MWCNTs anode; the resultant anode demonstrated a stable capacity of 1100 mAh g^{-1} in 50 charge–discharge cycles at the current rate of 372 mA g^{-1} [128]. The effects of the ALD-Al_2O_3 coating have been understood by simulations showing that the coating effectively blocks electron tunneling to the adsorbed EC molecules of the electrolyte, and thus decreases the decomposition of the electrolyte [129]. Therefore, both the experiments and the simulations show that the ALD-Al_2O_3 coat acts as an "artificial" SEI. Note, however, that this outstanding performance is obtained when directly coating the pre-fabricated electrodes made from bare powders. On another hand, bad results are obtained when coating bare electrode materials via ALD and then fabricate the coated materials into electrodes. In this latter case, the poor performance of the power anode is due to the insulating Al_2O_3 film inhibiting theses electron conduction paths between the current collector and the active anode element [130]. The recent results mentioned above show that it is now possible to prepare MWCNTs-based anodes with good electrochemical properties. The drawback of the MWCNTs, however, is their tendency to suffer from Li-induced embrittlement [131]. The reason is that concentric and close structure of MWCNTs does not allow expansion of graphene sheets in the c-axix or radial direction as in graphite, when Li is inserted, thus inducing large stresses. This may cause aging, particularly on board of an automative where high levels of vibrations are anticipated [78]. Good performances have also been achieved in hybrid anodes that combine CNTs with another nanostructured material (Si, Ge, Sn-Sb, M_xO_y with $M =$ Mn, Ni, Mo, Cu, Cr) [93, 103, 107, 113, 132, 133]. The uniform coating of Fe_3O_4 onto aligned CNTs by magnetron sputtering leads to a capacity over 800 mAh g^{-1} with 100 charge discharge cycles [134]; MoS_2/MWCNTs deliver a stable capacity of 1030 mAh g^{-1} at the 60th cycle [135]. Despite these promising results, the CNTs have not found a place in the industry of the lithium-ion batteries, essentially because of their cost and the difficulty to prepare them free of any large structure defects and high voltage hysteresis.

10.2.4 Graphene

Graphene is one atomic sheet of graphite. Its large electronic conductivity, mechanical strength, and large surface area make it attractive for an anode material [33, 112, 113, 136, 137]. As a matter of fact, the amount of lithium that can be absorbed on the surface of a single layer is small [138], but considering several graphene sheets, the theoretical capacity is much larger than that of graphite, namely 780 mAh g^{-1} if Li ions can be absorbed on both sites up to the sotichiometry Li_2C_6, and 1116 mAh g^{-1} if the Li ions can be trapped at the benzene rings in a covalent bonding up to LiC_2 stoichiometry [112, 139, 140]. Experiments have confirmed that the initial capacity delivered by graphene is larger than that of graphite. The problem with graphene,

however, is the aging upon cycling [141–143]. For instance, the oxidized graphene nanoribbons showed the specific discharge capacity of 820 mAh g^{-1} at the first cycle, but decreases to about 550 mAh g^{-1} on the 15th cycle [142]. Large capacities up to 1050 mAh g^{-1} can be obtained with more disordered graphene [140], because the disorder introduces new active sites for lithium storage. The drawback in this case is the small electronic conductivity associated to the disorder, so that the power density is limited and the fading of the capacity upon cycling not solved. The solution, however, has been found in a remarkable work by Wang et al. [144] who fabricated a novel type of doped hierarchically porous graphene (DHPG) electrode through a facile in situ constructing strategy in nickel foam using graphene oxide (GO), sulfonated polystyrene (S-PS) spheres, and poly(vinyl pyrrolidone) (PVP) as precursors. As porous graphene directly grows on the skeletons of nickel foam without the addition of any binder, high electron conductivity in the electrode assembly could be ensured. Nitrogen atoms from PVP and sulfur atoms from S-PS were successfully in situ doped into the graphene during pyrolysis of the precursor. Benefitting from the synergistic effect of structure and doping, the novel electrodes deliver a high-power density of 116 kW kg^{-1} while the energy density remains as high as 322 Wh kg^{-1} at 80 A g^{-1} (only 10 s to full charge), which provides an electrochemical storage level with the power density of a supercapacitor and the energy density of a battery. Furthermore, these optimized electrodes exhibit long-cycling capability with nearly no capacity loss for 3000 cycles and wide temperature features with high capacities ranging from 20 to 55 °C. This is by far the most outstanding performance obtained with a carbon-based anode. The next question will be to investigate if such an anode can be prepared at the industrial scale at a reasonable price, otherwise, it satisfies the criteria that we have listed in the introduction.

This last result shows that doping is beneficial to the performance of graphene as an anode. Nitrogen N, which has five valence electrons and has a comparable atomic size with C, is the most popular dopant, forming a strong covalent C-N bond breaking the charge neutrality on C. This doping generates a disorder in the honeycomb lattice of pristine graphene, which may help in the prevention against re-stacking of the graphene sheets, and it donates more electrons to the carbon network, this increasing the electrical conductivity [145]. Obviously, the synthesis process in ref. [144] has avoided the re-stacking of the graphene sheets that is a major cause of the aging upon cycling. This tendency of graphene to agglomerate has been the motivation to envision composites of graphene with nanoparticles of another electroactive anode material, which will be described in the following sections. Indeed, with each graphitic plane and n-electrons exposed, graphene is an ideal supporting materials for anode [146, 147]. The elastically strong, flexible, and conductive graphene can accommodate the volume changes suffered by the particles upon cycling, thus benefiting the structural stabilization of the nanoparticles and the cycling life. In addition, the grafting of the nanoparticles on the graphene sheets prevents the re-stacking. An example among many others of the improvement of the N-doped grapheme-nanoparticle composite with respect to the bare nanoparticles is illustrated by the choice of Co_3Sn_2/Co nanoparticles in [146],

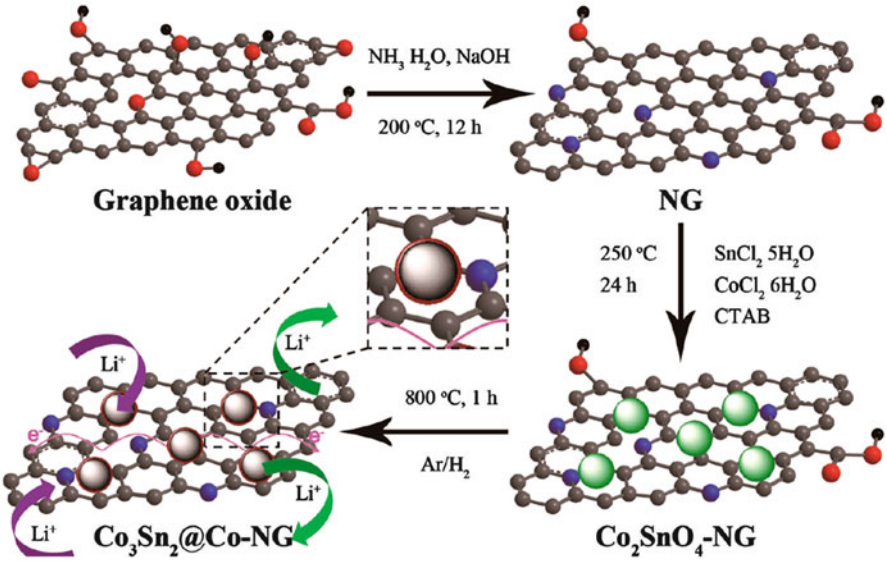

Fig. 10.3 Schematic illustration of synthetic method of Co_3Sn_2-Co-NG hybrid and its electrochemical mechanism for reversible Li^+ storage. Reproduced with permission from [146]. Copyright 2013 American Chemical Society

prepared according to Fig. 10.3. This composite tested as an anode delivered capacities of 1600 and 800 mAh g^{-1} almost constant between the second and the 100th cycle in the voltage range 0.005–3 V, at current densities 250 and 2500 mA g^{-1}, respectively. This performance, both in cyclability and rate capability, makes this composite competitive with the other anode materials that will be considered in this chapter.

10.2.5 Surface-Modified Carbons

We have already mentioned that the presence of EC in the electrolyte makes possible the formation of a SEI that protects the graphite anodes. However, the SEI formed in this case is rather thick. Contrary to some prior claims, this effect is not always an obstacle to obtain very high rate capability, since the DHPG anode supported rates as high as 80 A g^{-1}. However, the SEI depends on the quality of the surface (porosity, defects) and in some cases may affect significantly the electrochemical properties. In addition, the formation of the SEI is not limited to the first cycle in the case of graphite, which may affect the calendar life. Therefore, it may be desirable to protect graphite by a coating. The ALD-Al_2O_3 coating of MWCNTs [127, 128] that we have mentioned earlier in this work is a good example. The ALD is an elegant technique that builds uniform and well controlled coatings of nanostructures, but it is also expensive. It is possible, however, to coat

the particles at less expense with carbon. The difference between carbon-coated and noncoated graphite has been studied in [148]. As a result, the SEI formed on the coated graphite is much thiner than the SEI formed on noncoated graphite (in the range 60–150 nm against 450–980 nm). Moreover, the carbon coat preventing direct contact between the graphite and the electrolyte, the decomposition of propylene carbonate is greatly reduced and the intercalation of electrolyte species (organic carbonates) into graphene layer is prevented [104, 149]. Conversely, a thin layer of soft carbon at the surface of hard carbon has improved the coulombic efficiency and the capacity [150].

10.3 Silicon Anodes

The next element if the group 14 in the Mendeleev table after carbon is the silicon. The motivation for the tremendous amount of work on the Si-base electrodes is sustained by two properties: the material is cheap, and the specific capacity is very large: 4200 mAh g^{-1} when lithiated to $Li_{4.4}Si$ [151]. Moreover, the onset voltage potential is 0.3–0.4 V above the Li^0/Li^+ redox potential, which averts the safety concern of lithium deposition encountered with the graphite anode. The requirements (1), (2), and (4) in the introduction section are thus very well satisfied. We can also add the requirement (3) since Si is a semiconductor. Actually the problem with Si, which will be met also for Sn, Sb, and other anodes later in this review, is the irreversibility and capacity fading. The performance degrades during the first cycles due to the large variations of the volume during the charging/discharging process [152–158]: from Si to $Li_{4.4}Si$, the volume expansion is 420 % [159–163]. This large volume change upon cycling results in the cracking and pulverization of the Si particles and disconnection of some of the particles from the conductive carbon and from the current collector [164–166]. The cracking of the particles has been observed by atomic force microscopy during the Li-extraction [20, 25, 154, 167]. The formation of cracks has also been confirmed by in-situ SEM investigations [168]. Ex-situ experiments have shown that cracks become less frequent for crystallized Si (c-Si) pillars of diameter 240–360 nm [169]. In-situ experiments showed that no cracks for particles below 150 nm in size at high lithiation rate (the order of the minute) [170], and that the size limit before cracking can be raised to 2 μm at low lithiation rate [168]. However, these results are not impressive, if we consider that the cracks of the particles do not occur during the lithiation process, but in the delithiation process. Upon lithiation, both Si and the matrix are under compressive stress, while the initiation and propagation of cracks are the result of tensile stress [20]. Upon lithiation, the Si particles remain intact. The results also depend on the geometry, and even Si-structures 150-nm thick may crack upon cycling [171]. In addition, the disconnection of the particles from the carbon matrix, evidenced by the sharp rise of the internal resistance of Si anodes during the lithium extraction process [172], can be observed even if the particles do not crack [171]. The opposite also holds true: a 150-nm thick Si thin film deposited

on a rigid metal substrate cracked although it did maintain contact with the substrate [171], again emphasizing the importance of the geometry and cycling conditions. Therefore, the decrease of the size to the nano-range is mandatory to relieve the stress [173]. It has been reported that decreasing the size of the particles has no significant effect on the irreversible capacity loss observed during the first cycle, but improves the capacity retention in the following cycles [174]. As a matter of fact, this view is too pessimistic, as it depends on many factors. Nanostructured electrodes can absorb more easily the strains associated to the change of volume, and avoid cracking [157, 175]. The results depend on the geometry of the particles, but for particles of given geometry, say quasi-spherical [168] or pillars [169], for instance, this has been confirmed by experiments. Also, the decrease of the diameter of the particles upon delithiation is proportional to the size of the particles, so that smaller particles can keep contact with the matrix, allowing for full extraction of the lithium. These effects reduce the irreversible capacity loss, and thus improve the capacity retention. In addition, silicon is not a good conductor, so that the smaller length of the electrons and holes inside the nanoparticles improve the rate capacity. On another hand, independently of their chemical formula, nano-particles also have disadvantages, such as high manufacturing cost and handling difficulty [176]. Also the larger surface in contact with the electrolytes results in increasing side reactions with the electrolyte. When the potential of the anode is lower than 1 V with respect to Li^0/Li^+, the decomposition of the organic electrolyte at the surface of the particles forms the solid–electrolyte interface (SEI). Its formation on Si particles has been investigated [16, 177–179], and consists mainly in lithium carbonate, lithium alkylcarbonates, LiF, Li_2O, and nonconductive polymers. The SEI must be dense and stable to prevent further side reactions to occur. However, the large volume change makes it challenging to form a stable SEI, as it can results in a breaking of the SEI. Then a new part of Si can be exposed to the electrolyte, resulting in the formation of another SEI that becomes thicker and thicker upon cycling [180]. These effects can affect both the cycling and calendar life. That is why the efforts on silicon anodes have been focused on the synthesis of nano-particles of different geometries, and also on the protection of the Si particles against side reactions with the electrolyte. These works are reviewed in the following.

Note that a much better cycle life can be obtained with Si simply by limiting the voltage range. The lithiated amorphous Si is converted into crystalline $Li_{15}S_4$ below 50 mV, resulting in capacity fade and high internal stress that reduces the cycling life [181, 182]. A threshold 0.1 V corresponds to the voltage expected for the composition $Li_{12}Si_7$. Indeed, Bridel et al. [183] have reported that the Si-particles do not fracture when they are not solicited entirely (stop of the lithiation at $Li_{12}Si_7$ instead of $Li_{22}Si_5$). On another hand, they crack when the lithiation process is pushed up to the formation of $Li_{22}Si_5$ [168]. Actually, changing the lower cutoff voltage from 0 to 0.2 V increased the cycle life of an amorphous Si anode from 20 to 400 cycles [184]. The drawback of this change is the reduction of the specific capacity from 3000 to 400 mAh g^{-1}. With limited capacity of 1800 mAh cm^{-2} per cycle (corresponds to about 45 % of its theoretical capacity), Si thin films of 6 μm

thick showed very stable cycling performance and a coulombic efficiency of ≈100 % up to 250 cycles [182, 185, 186]. Full cells using 4 and 6 μm thick Si films as the anodes and standard commercial $LiCoO_2$ as the cathodes (70 μm thick) delivered stable capacity of about 1.8 mAh cm^{-2} for 200 cycles. This areal capacity is very close to the requirement of current commercial LiB anodes. We have noted earlier that the specific capacity of a Li-ion battery saturates when that of the anode reaches 500 mAh g^{-1} (see Fig. 10.1), so that the lower capacity resulting from a shorter voltage range does not look dramatic. However, this aspect is usually overviewed, and all the efforts aimed at keeping the voltage range 0–2 V with silicon. Therefore, all the electrochemical properties reported hereunder have been obtained with cycles using this voltage range unless the voltage range is specified.

10.3.1 Si Thin Films

If crystalline, Si expands anisotropically upon lithiation, primarily in the <110> direction [187–189]. This anisotropy contributes to increase the stress and strains in the material. That is why, at least in continuous films, amorphous Si (a-Si) is preferred to the crystalline Si (c-Si), because of the isotropic lithiation on a-Si. This has been confirmed by experimental experiments on thin films [190]. Note that, even when starting with c-Si, the silicon becomes amorphous already after the first cycle [191]; however, for the reasons we have just evoked, starting with a-Si is better as it will reduce the irreversible capacity loss during the first cycle, and all the results reviewed here have been obtained with a-Si.

Remarkable cycling performance has been achieved on thin Si-films. A 50 nm-thick Si film deposited onto a 30 μm-thick Ni foil delivered over 3500 mAh g^{-1} being maintained during 200 cycles under 2*C* charge/discharge rate, while a 1500 Å film revealed around 2200 mAh g^{-1} during 200 cycles under 1*C* rate [192]. By optimizing the synthesis parameters such as the Si deposition rate, and n-doping Si with phosphor to improve the electronic conductivity, the capacity of the 50 nm-thick n-Si was as high as over 3000 mAh g^{-1} for the case of 12*C* test, which could be kept during 1000 cycles. Also in the case of heavy load of 30*C* rate, the charge/discharge capacity was still over 2000 mAh g^{-1} even after 3000th cycle although the capacity fluctuated during cycling [193].

A 250 nm-thick film deposited by radio-frequency (rf) magnetron sputtering on copper foil delivered 3500 mAh g^{-1} when tested over 30 cycles in the voltage range 0.02–1.2 V [194]. Fe-Si multilayer thin films were prepared on a Cu substrate by sequential deposition of Fe (inactive) and Si (active) using electron-beam deposition [195]. After annealing to take advantage of the fact that the Fe–Si phase from the Fe–Si interface is stable for extended cycles and acts as a buffering matrix for alloying reaction of Si with Li [196], the volumetric capacity delivered was stable at 3000 mAh cm^{-3} over the 300 tested cycles using the constant charge and discharge current of 30 A cm^{-2} between 0 and 1.2 V at 30 °C. These results illustrate that the

performance depends importantly on the adhesion with the support, the deposition rate and the temperature of the deposition, the film thickness, and annealing treatment. They also show that long cycle life up to 3000 cycles can be obtained with Si films prepared either by physical vapor deposition [193, 197], or magnetron sputtering [198].

10.3.2 Si Nanowires (Si Nw)

While good results on thin films or nanoparticles have been obtained at low loading, the silicon nanowire (Si Nw) array provides sufficient empty space between the nanowires to accommodate the change in the volume associate to the insertion/extraction of lithium. Each Si Nw can be electrically connected to the current collector so that it can contribute to the total capacitance making conductive carbon additives and polymer binders unnecessary [83]. Growth methods have been reviewed in ref. [199]. The most popular one is the vapor-solid–liquid (VLS) growth performed in a chemical vapor deposition reactor under a flowing Si-bearing gas at temperatures in the range 300–1000 °C, depending on the gas precursor and the type of metal catalyst [199]. The wire diameters range from several nm to hundreds of microns. The first result with long cycling life and full energy density was obtained with interconnected and curved Si nanowires synthesized after Au-catalyzed VLS growth in a hot plate (cold wall) reactor [200]. 3100 mAh g^{-1} capacity retention was obtained after 40 cycles at $C/2$ rate, without charging voltage limitation. The anode could also be cycled at $8C$ rate without damage, in which case the capacity retention is still circa 500 mAh g^{-1}. Since this is typically the capacity that is useful for an anode after Fig. 10.1, we can conclude that this electrode is actually optimized up to this C-rate. Because of the entanglement after the first phase of growth, the quantity of Si was the order of 1.2 mg cm^{-2} of current collector electrode, thus overcoming one of the drawbacks of using nanomaterials in battery electrodes, namely the low volumetric energy density [31]. The first growth step was achieved with PH_3 in the gas phase in order to yield Nws with their core n-doped with phosphor, aiming to improve the electrical conductivity, and thus the rate capability. In addition, the wires were composed of an amorphous shell covering a crystalline core. This is believed to be the best configuration, since the amorphous shell is able to prevent the initial cracking that takes place in the surface layer upon delithiation. With respect to prior works, the major improvements in the cycling life were attributed to the fact that the interconnection between the Nws prevents them from detaching from the substrate. This entanglement was obtained owing to the use of the planar furnace. In this case, the temperature in the gas phase above the furnace decreases rapidly, so that after a short period of vertical growth in the stagnant layer, the wires tend to kink and curve their growth direction towards the substrate. Because of this change in growth directions, the Nws become highly entangled.

Simple Nws grown by VLS-CVD are usually made of a c-Si core and a a-Si shell, like in ref. [200]. There is further experimental evidence that cycle life is indeed improved by lithiating a CVD-deposited a-Si layer over the as-grown c-Si Nws [157, 201]. To avoid cracking and rapid degradation, their diameter must be kept below some critical value between 240 and 360 nm for c-Si Nws [169] and around 900 nm for a-Si Nws, assuming that results obtained on nanoparticles apply to Nws [168, 202]. In particular, in [178], the unreacted Si Nws had an average diameter of 89 nm. After lithiation, the Nws remained intact, although their diameter increased to 141 nm. Si Nws can also be prepared by a scalable supercritical fluid-liquid–solid (SFLS) method. In this method, metal nanoparticles (e.g. Au colloids) are mixed with a saline-based reactant (hexane, toluene, benzene) in a solvent that becomes supercritical under the temperature and pressure conditions. The effects of the binder, electrolyte, and the presence of gold seeds on the performance of anodes based on SFLS-grown Nws have been investigated [203]. The best results were obtained on Au-catalyzed SFLS wires, using a sodium alginate binder [204] for the slurry and adding fluoroethylene carbonate to the electrolyte, in which case the authors reported good cyclability. The role of the alginate will be discussed later in the context of the stabilization of the SEI.

Nws have also been obtained by etching at the laboratory scale (see review in [78]). However, it is difficult to consider their use for industrial development, because of the high cost [78]. However, a refinement of the metal-assisted wet chemical etching (MaCE), technique, which represents an interesting approach towards cost reduction, uses c-Si powders (instead of c-Si wafers) in which NWs can also be etched [205]. Nanoporous silicon nanowires of 5–8 μm length and with a pore size of 10 nm are formed in the bulk silicon particle. These silicon electrodes show a high reversible charge capacity of 2400 mAh g^{-1} with an initial coulombic efficiency of 91 % and stable cycle performance. This synthetic route is not only low-cost, but also mass producible (high yield of 40–50 % in tens of gram scale), and thus, provides an effective method for producing high-performance anode materials. Remarkable results have been obtained with porous doped silicon nanowires synthesized by direct etching of boron-doped silicon wafers, again with sodium alginate binder [151]. Here, the boron doping has two effects: (a) it increases the electrical conductivity, which is needed to improve the rate capability, (b) it provides defective sites facilitating the etching process which leaves holes on the silicon nanowire surface. More details on the synthesis will be provided in Sect. 10.3.3 devoted to porous Si. Both the pore diameter and the wall thickness were about 8 nm. Even after 250 cycles, the capacity of the anodes formed with these Nws was stable above 2000, 1600, and 1100 mAh g^{-1} at current rates of 2, 4, and 18 A g^{-1}, corresponding to rates 0.5, 1, 4.5*C*, respectively. The best battery has recorded 2000 cycles with a capacity remaining above 1000 mAh g^{-1}, even achieved at 18 A g^{-1}. It should be noted that this high rate capability has been obtained at a low mass loading of 0.3 mg cm^{-2}. This is a general property of all the Si anodes: high rate capability can be achieved only at low mass loading.

This last result illustrate two properties: (1) the use of alginate binder greatly improves the cyclic performance of a silicon nanoparticle anode, compared with

using traditional polyvinylidene fluoride (PVdF) binder, already evidenced in [204]; (2) it also illustrates the beneficial effect of the porosity that limits the change in the volume of the particles during cycling, thus improving the anode structural stability and stabilizing the anode SEI. In addition, the results in ref. [151] show that such is also the case for Si nanowires, but in addition, the capacity retention is also increased in this later case. Despite the outstanding recent results obtained on nanowires, the Si Nws anodes are still difficulties to compete with graphite anodes. Typical commercialized graphite-based anodes can store a charge of 4 mAh cm^{-2}, because they use 50 μm thick films on the current collector. So assuming a Si capacity of 3800 mAh g^{-1}, an areal mass of more than 1 mg cm^{-2} of Si is needed, in order to be competitive with graphite anodes. For this condition to be met, Nws with their diameter in the 300 nm range have to be grown, which will limit the rate to around 3*C* [78]. This is the main limit for Nws, due to the difficulty to have both a high rate and a high Si mass. Actually, as we have recalled in the previous section, thin Si film that are able to deliver stable capacity of about 1.8 mAh cm^{-2} for 200 cycles are closer to the performance required to be competitive with graphite anodes.

10.3.3 Porous Silicon

The recent investigations of porous Si porous structures gave encouraging results when used as anodes [206–208]. Porous structured silicon with pores of several nanometers or hollow silicon spheres with a thin shell can dramatically reduce the stress by providing additional free space for volume expansion induced by lithium-ion insertion. This has been evidenced experimentally [206–210], and it is in agreement with simulations [151, 207]. After finite elements calculation, the tensile stress in a hollow Si sphere is five times smaller than in a solid sphere with an equal volume of Si [207], meaning that the hollow nanostructures will fracture less readily. This has been confirmed by experiments [207, 211]. We have just recalled in the previous section that porous nanowires give good results, but their preparation is limited in quantity. Indeed, a more scalable method is desired for the preparation of porous silicon nanostructures, which have been reviewed in [84]. One solution has been to start with commercial silicon nanoparticles available in large quantity as starting material, and treat them in a route involving boron doping and an electroless etching [212]. Boron doping is achieved by mixing the silicon nanoparticles with boric acid in solution and then drying before before annealing at 900 °C in argon atmosphere. Electroless etching generates porosity by taking advantage of a galvanic displacement between noble metal, say Ag, and silicon. This is achieved in the presence of $AgNO_3$ in HF etchant solution. The two reactions taking place simultaneously are:

$$4Ag^{+} + 4e^{-} \rightarrow 4Ag, \tag{10.1}$$

$$Si + 6F^- \rightarrow [SiF_6]^{2-} + 4e^- \quad (10.2)$$

In this reaction, silicon donates electrons to reduce Ag^+ to Ag, and is etched away by F^-. Since the redox potential of Ag^+/Ag lies below the valence band of silicon, for p-type silicon (e.g. boron-doped silicon), Ag^+ preferentially reacts with silicon nanoparticles at defective sites (dopant sites), leaving pores on the surface [213]. Porous nanoparticles with different porosity can be obtained by adjusting the ratio of boric acid and silicon. The cyclic performance of porous silicon nanoparticles after graphene wrapping as a Li-ion battery anode reported in [212] is remarkable: the initial capacity is 2500 mAh g^{-1} at *C*/8 rate, and still 1000 mAh g^{-1} at *C*/2 rate ($1C = 4$ Ah g^{-1}); the capacity remained at 1400 mAh g^{-1} and 1000 mAh g^{-1} after 200 cycles at *C*/4 and *C*/2 rate, respectively. In the same way, porous Si particles have also been obtained from crushed boron-doped silicon wafers [214]. The process in this case differed by the addition of H_2O_2 etchant leading to a hierarchical structure with micro- and nanosized pores uniformly distributed in Si. The final product delivered 1500 mAh g^{-1} for 50 cycles at low *C*-rate. An even better result of 2000 mAh g^{-1} for 50 cycles has been obtained starting with commercial bulk silicon, using a similar procedure to obtain porous silicon with pore size of several hundred nanometers [215].

Porous silicon can also be obtained by electrochemical etching with a HF etching solution. The porosity and depth of porous Si are monitored by the control of the current density and the HF concentration. The porous silicon film obtained by this process can achieve a discharge capacity of 1260 mAh g^{-1} when combined with pyrolyzed polyacrylonitrile (PAN) [216] and above 2000 mAh g^{-1} when coated with gold [217]. The freestanding porous film lifted off from the substrate when the current density is suddenly increased can be converted into a particulate structure and combined with a binder such as PAN to form a slurry self-adapting to a roll-to-roll process for mass production [218]. Porous Si can also be obtained by Si deposition into a porous template. Usually, SiO_2 nanospheres are used to form an opale structure. Then, porous Si can be obtained in the form of an inverse structure by filling the voids of the template. The synthesis can be carried out through chemical vapor deposition (CVD) gaseous silicon source such as Si_2H_6 followed by treatment in HF solution. An interconnected silicon nanosphere film obtained by such a process through a modified CVD method delivered a capacity above 1300 mAh g^{-1} after 700 cycles [207]. Using a different template, namely a porous Ni inverse opal structure prepared by electrodepositing of Ni on a silica opal template, a capacity above 2500 mAh g^{-1} was delivered after 100 cycles [219]. In the same way a conformal coating of a porous Ni film with silicon by the CVD process led to a porous silicon-Ni structure that delivered a reversible capacity of 1650 mAh g^{-1} after 120 cycles [220].

The main concern with the CVD method to grow Si nanostructures is the low yield. For nanowires for instance, it is only 200–250 μg cm^{-2} or 0.75 mg h^{-1} [221], which greatly limits the use of this method for mass production. Instead of the CVD

method, the void space of the template can be filled with the gel-like silicon precursor then annealing at high temperature to solidify the gel to get rigid porous silicon [206]. In this work, the silicon gel composed of fine silicon nanoparticles was first prepared by reducing $SiCl_4$ with sodium naphthalide in glyme and capping this with n -butyl groups by the reaction with LiC_4H_9. This capping was an essential step to protect Si from reacting with SiO_2 to form SiO_{2-x} during annealing. The product demonstrated capacity retention as high as 90 % at 1*C* rate after 100 cycles. Using the same gel, mesoporous Si-carbon core–shell nanowires with a diameter of 6.5 nm were prepared for a lithium battery anode material using a SBA-15 template. These nanowires demonstrated a first charge capacity of 3163 mAh g^{-1} and retained a capacity at 2738 mAh g^{-1} after 80 cycles [222] (see Figs. 10.4 and 10.5).

Instead of filling the void space of the template to get an inverse porous structure, it is also possible to convert the porous silica template into silicon directly by magnesio-thermic reduction. This reduction by magnesium operates at 650 °C, according to the reaction:

$$2\mathrm{Mg(g)} + \mathrm{SiO_2(s)} \rightarrow 2\mathrm{MgO(s)} + \mathrm{Si(s)}. \tag{10.3}$$

The byproducts (MgO, unreacted SiO_2) are removed by washing with HCl and HF, sequentially. A three-dimensional mesoporous silicon with a high surface of 74.2 m^2 g^{-1} has been obtained by this process, using P123 as surfactant and SBA-15 silica as both template and silicon precursor. After carbon coating via a CVD process, this anode material delivered a capacity above 1500 mAh g^{-1} for 100 cycles.

10.3.4 Porous Nanotubes and Nanowires vs. Nanoparticles

The shape of the silicon material matters. One advantage of the nanotubes and nanowires is that it is easier to connect them electrically to the current collector than nanoparticles, for instance. This is one reason for the good performance of porous nanotubes [151, 223–225]. For example, Cho's group fabricated Si nanotube structures by reductive decomposition of Si precursor inside anodic alumina templates [225]. The use of Si nanotubes increased the surface area accessible to the electrolyte, allowing lithium ions to intercalate from both the interior and the exterior of the nanotubes, so that the reversible charge capacity reached 3200 mAh g^{-1} with capacity retention of 89 % after 200 cycles at 1*C* rate. In the case of Si nanoparticles for which the electrical connection to the current collector is more challenging, the traditional slurry coating method exploiting conductive carbon and PVdF binder additive have not worked well. To overcome this problem, Si particle anodes have been prepared, where amorphous Si is deposited onto electrode structure; a-Si acts as an inorganic glue to fuse all the particles together and bind them to the current collector [226]. With a limited charge capacity of 1200 mAh g^{-1}, the prepared 200 nm Si particle anode showed

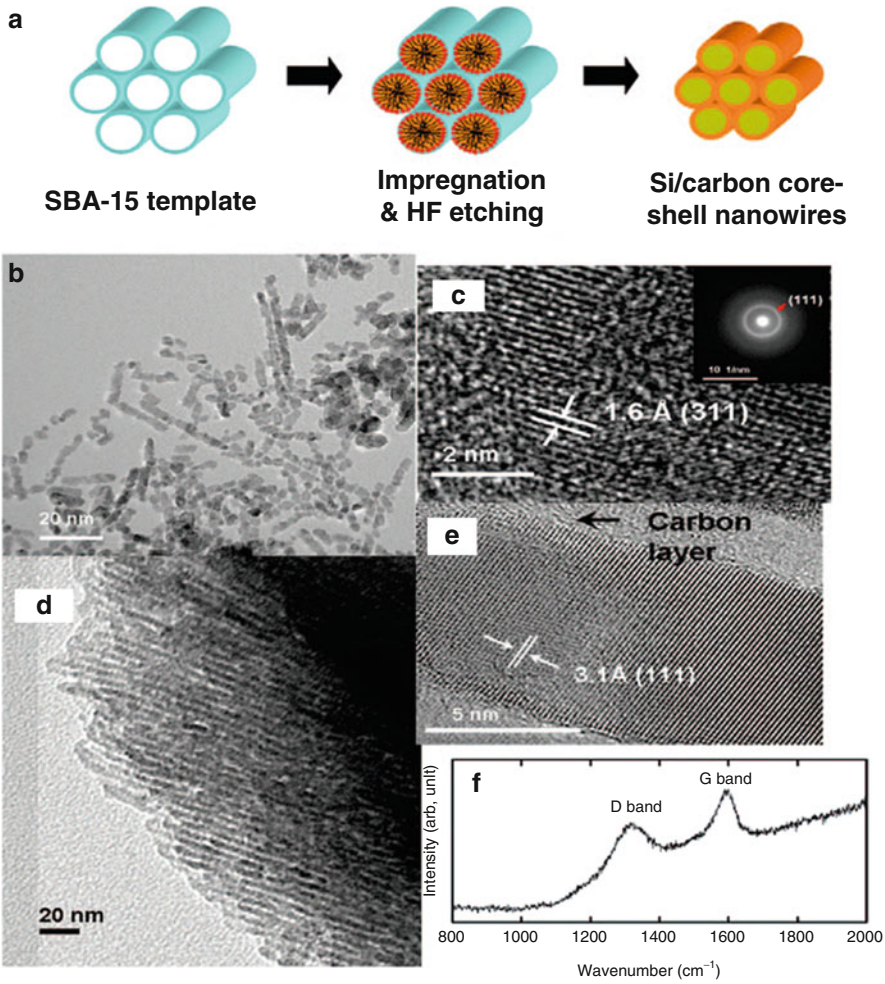

Fig. 10.4 (**a**) Schematic view of the preparation of Si-carbon core-shell nanowires using the SBA-15 (a mesoporous silica sieve) template. (**b**) TEM image of the Si-carbon core-shell nanorods obtained from first impregnation of Butyl-capped Si. (**c**) Expanded TEM image of (**b**) (*inset* is SADP of (**c**)). (**d**) TEM image of the Si-carbon core-shell nanowires obtained from fourth impregnation. (**e**) Expanded TEM image of (**d**) and (**f**) Raman spectrum of Si-carbon core-shell nanowires. Reproduced with permission from [222]. Copyright 2008 American Chemical Society

stable cycling up to 130 cycles. Another way to improve the electrochemical performance of Si nanoparticles has been to explore new binder materials. Composite electrodes based on Si particles and the PFFOMB (poly (9,9-dioctylfluorene-co-fluorenonecomethylbenzoic acid) binder, without any conductive additive, exhibit high capacity, long-term cycling, low overpotential between charge and discharge, and good rate performance [227]. Another example is the use of alginate that we have already mentioned in the context of

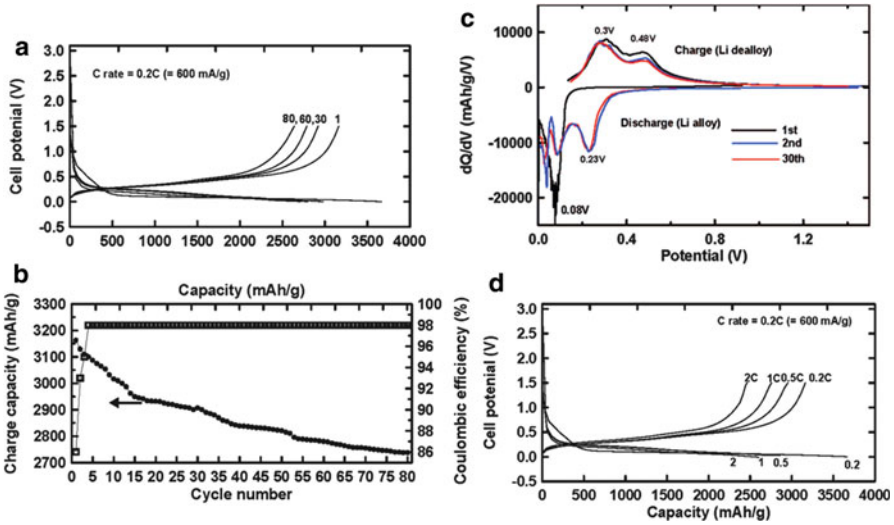

Fig. 10.5 (**a**) Voltage profiles of the Si-carbon core- shell nanowire electrode prepared according to Fig. 10.4, after 1, 30, 60, and 80 cycles at a rate of 0.2*C* between 1.5 and 0 V in coin-type half-cells. (**b**) Plot of charge capacity and Coulombic efficiency of the cell (**a**) vs cycle number. (**c**) Differential curves of the Si-carbon core-shell nanowire electrode after 1, 2, and 30 cycles. (**d**) Voltage profiles of the rate capabilities of the Si-carbon core-shell nanowire electrode at rates of 0.2, 0.5, 1, and 2*C* between 1.5 and 0 V in coin-type half-cells (same charge and discharge rates were used). Reproduced with permission from [222]. Copyright 2008 American Chemical Society

nanowires [204]. The dramatic improvement in electrochemical performance by using the alginate binder is attributed to several reasons. The first reason is the weak interaction between the binder and the electrolyte. The second reason is that the binder can offer access of Li ions to the surface of silicon. The third reason is that the binder is helpful to build a deformable and stable SEI [204].

10.3.5 Coated Si Nanostructures and Stabilization of the SEI

So far, we have reviewed the Si structured materials that successfully addressed the pulverization problem, but they do not prevent the volume changes upon cycling, so that their interface with the electrolyte is not static. Therefore, the problem of the unstable SEI is still unsolved [228], mainly because the SEI formed in the lithiated expanded state can be broken as the nanostructure shrinks during delithiation. This re-exposes the fresh Si surface to the electrolyte and more SEI forms, resulting in a thicker and thicker SEI film upon charge/discharge cycling. Thicker SEI film means electrolyte consumption, increase of the electrical resistivity, longer Li diffusion path through the SEI, degradation caused by the mechanical stress of the thick SEI, in other words aging of the battery. Stabilizing the SEI is thus crucial. One strategy to solve the problem has been to coat the silicon structure

with a protective element. Indeed, when the shell remains unchanged during cycling, it helps in the formation of a stable SEI layer [229, 230]. For an ideal case, a stiff shell could effectively reduce the mechanical stress generated in the Si core during cycling [231]. The actual effect depends strongly on the thickness and Young's modulus of the shell material [232]. Generally, a thick shell is preferred to avert fracture; However, thick shell adds additional weight. Thus, careful engineering of the core and shell materials is required to obtain an optimal balance [233, 234]. With 10 nm thick carbon coating on Si nanowires of 90 nm in diameter, the first cycle coulombic efficiency was greatly enhanced from 70 % (without coating) to 83 %, in addition to the increased capacity from 3125 mAh g^{-1} (without coating) to 3702 mAh g^{-1}, and cycling stability (5 % capacity retention after 15 cycles) [235]. Replacing the carbon coating with 10 nm thick Cu film can further improve the coulombic efficiency of the initial cycle up to 90.3 %, and improve capacity retention up to 86 % after 15 cycles [236]. This improvement is not necessarily due to a better stabilization of the SEI, however, as it can presumably due to the fact that Cu is a better electronic conductor than the carbon coat. Cu-coating on thin films had a similar effect [237]. Coating with conductive polymers such as PEDOT has also improved the cycling properties of Si Nws [238].

Al-coating could not help enhance the initial coulombic efficiency, but it did help to increase the capacity retention after numerous cycles [239]. The improved capacity retention is due to the more stable mechanical structure of electrodes in the presence of Al coating [240, 241]. Similar results were observed on cells comprised of Si nanowires coated with $a \approx 100$ nm layer of Ag/poly (3,4-ethylenedioxythiophene) (PEDOT), which exhibited an improvement of the capacity retention from 30 % (without coating) to 80 % after 100 cycles [238]. While coating with a conductive layer such as Cu and Al may be beneficial to the electrochemical performance partly because of the increase in the electrical conductivity, coating with an oxide has been done only to prevent direct contact with the electrolyte. In particular, Al_2O_3 coatings (<10 nm) obtained by ALD have been tested on Si thin films [242, 243] and Si Nws [244]. Upon the first lithiation, Al_2O_3 transforms into an Al-Li-O glass [245], which is a good ionic conductor and an electronic insulator, thus exhibiting the attributes of a good SEI substitute. Indeed, the Al_2O_3 coating resulted in a 45 % increase of the anode lifetime, and 1280 cycles at 1C have been obtained with Al_2O_3 coated Si Nws [244].

The surface-clamping of the porous structures has also been achieved. A successful control of the SEI growth of porous nanotubes has been obtained by coating them with rigid carbon [246]. In a similar strategy, commercially available Si nanoparticles were completely sealed inside thin, self-supporting carbon shells, with rationally designed void space in between the particles and the shells. The well-defined void space allows the Si particles to expand freely without breaking the outer carbon shell, therefore stabilizing the SEI on the shell surface. High capacity (2800 mAh g^{-1} at $C/10$), long cycle life (1000 cycles with 74 % capacity retention), and high coulombic efficiency (99.84 %) were realized in this yolk-shell structured Si electrode. Other materials such as Ge [223, 247], SnO_2 [248] and TiO_2

[247] have also been deposited at the surface of Si nanotube walls to form the so-called double- or triple-walled silicon nanotube architectures. Almost all these coatings, except Ge, have little effect on improving the initial coulombic efficiency, but they increase importantly the life of the battery. Double walled Si nanotubes have been obtained by coating the Si nanotube with SiO_x [246]. This coat is rigid enough and mechanically strong, so that it can successfully prevent the Si from expanding outward during lithiation, while still allowing lithium ions to pass through. As a result, the SiO_x-coated Si nanotubes in [246] demonstrated a long cycle life (6000 cycles with 88 % capacity retention), high capacity (2970 mAh g^{-1} at *C*/5; 1000 mAh g^{-1} at 12*C*) and fast charging/discharging rates (up to 20C). Using a nanoscale open cell electrochemical device that operates inside a transmission electron microscope (TEM), Liu et al. demonstrated ultrafast and full electrochemical lithiation of individual carbon-coated Si Nws [241, 249]. The Si NWs did not fracture despite the ultrahigh lithiation rates. The lithiation and expansion of a yolk-shell Si nanoparticle has been observed by using a similar approach [229]. After complete lithiation, the diameter of the largest Si particle increased from 185 to 300 nm and it filled the hollow space within the carbon coating.

Various carbon-silicon (C-Si) composite anodes have been used. In particular, 2D-layers of graphite/Si hundred of nanometers in have delivered a capacity of 840 mAh g^{-1} after 100 cycles at *C*/3.4 rate at loading 1.1 mg cm^{-2} [250]. Nevertheless, silicon–carbon composite particles in which silicon nanoparticles are embedded in porous carbon particles [251] and porous Si-C composite spheres [252] achieved similar performance, but at higher rates. Embedding the Si Nws in a network of carbon nanotubes is also a way to improve the conductivity to improve the overall electric conductivity of the anode; moreover the resulting anode is flexible and self standing [253]. Si Nws have also been grown by pulsed laser deposition on a single wall carbon nanotube paper [254]. Si Nws have also be grown by vapor-liquid–solid method, from multiwall naotubes decorated with Au nanoparticles and deposited on stainless steel substrate [255].

Other binary thin-film anodes Si-*M* (*M* = Mg, Al, Sn, Zn, Ag, Fe, Ni, Mn), and ternary thin-film anodes Si-Al-*M* have been studied. These studies that date from the previous decade are referenced in [20], but their electrochemical properties are not competitive with the results we have reported in the present review. More elaborate architectures give better results. For instance, electrodes using vertically aligned carbon nanotubes (VACNTs) uniformly coated with Si and a thin C surface layer demonstrated very good stability for over 250 cycles and high specific capacity approaching theoretical limits (4200 mAh g^{-1}) [256]. Here also, the outer C-coating on the Si surface was critical to achieving good capacity retention and high Coulombic efficiency close to 100 %. This last result also illustrates the progress that is currently made on Si anodes. The works that have been reported in this review already show that the technical problems related to the huge volume change during cycling, such as fracturation, pulverization, stabilization of the SEI have been progressively solved the last 4 years. It is now possible to obtain Si anodes with high capacity and good capacity retention for more than 1000 cycles.

However, the overall electrode thickness and the cost of the proposed processes were still a limiting factor for large size battery applications. The process described in [256] is a scalable method to produce ultrathick, yet highly conductive and stable, Li-ion battery electrodes. Very recently, a robust method to prepare gram-scale Si NTs has been reported using nanorod-like nickel-hydrazine complexes as templates [257]. These different results show that the efforts currently done to find scalable synthesis processes without altering the electrochemical performance of Si anodes open the route to their mass production in the near future. However, the persistent difficulty to combine high-rate performance and high area density will limit their use to batteries that do not require high power.

10.4 Germanium

The next element along the column of the Mendelev table after C and Si is germanium. Among the criteria defined in the introduction, the criterion (6) is clearly not fulfilled. While Silicon is cheap, germanium is very expensive, and did not benefit from the development associated to the market in electronics. Its cost is even prohibitive for most applications. Nevertheless, it has some advantages with respect to Si, in particular with respect to criterion (3): a better electronic conductivity and better lithium diffusivity. But Ge has another major advantage. It can be lithiated until $Li_{15}Ge_4$ is formed [258], while the delithiation results in porous amorphous phase [259–261]. Unlike Si, the whole process is isotropic, and does not lead to the formation of cracks, even at high C rates and particles size 620 nm [261, 262]. That is why Ge is presently receiving increasing interest. Ge thin films demonstrated reversible lithiation at rates as high as 1000*C* [263]. The remarkable rate capability of Ge is also evidenced by the increasing performance at high *C*-rate of Si-Ge alloys as the transition is made from Si to Ge [264]. We have outlined in the previous section that it was not possible to make Si anodes with a thickness of the thin films of the diameter of the nanowires or nanotubes that would make them competitive with graphite-based anodes without sacrificing the high rate performance. This obstacle is smeared out with germanium, since it is possible to increase the size of the Ge particles without cracking, i.e. without increasing the thickness of the SEI layer. Indeed, 500 nm thick Ge particles exhibit stable cycling life at 150 mA g^{-1} rate, delivering 800 mAh g^{-1} [265]. Two hundred nanometer thick Ge sheets on graphene exhibit less than 20 % loss in capacity over 400 cycles at nearly theoretical capacity [266]. After the first cycle the differential capacity plot shows three relatively broad lithiation peaks at 500, 350, and 200 mV corresponding to the lithiation of amorphous Ge [267], so that the amorphous porous phase is preserved upon cycling. Cathode elements cannot accept cycling at *C* rates as high as 40*C* over thousands of cycles, except $LiFePO_4$ [268]. Therefore, to take benefit of the impressive rate capability of Ge, or even to test Ge, the Ge anode should be associated to the $LiFePO_4$. Such a Ge//$LiFePO_4$ full cell has been investigated with mass loading 15 mg cm^{-2} [260]. After 400 cycles at 40*C* rate, the

capacity was 1000 mAh g^{-1}. Surprisingly, most studies on Ge anodes have been performed on nano-Ge with dimensions 100 nm [267, 269–271] or even 3 nm [272] missing the main interest of the germanium element, presumably by continuity with the prior works on Si where the nano-size was mandatory. In particular, Ge nanowires have been grown by CVD [273], like Si nanowires. Reminding that it is an expensive process that yields very small amounts of material after hours of deposition, a better synthesis process for Ge nanowires in large quantities is the growth in solution [267], again like Si Nws. However, the superiority of Ge with respect to Si is clearly the possibility to reach simultaneously high areal density, and very high rate capability. In addition, PVdF binder works well for Ge, at contrast with the Si case, and since Ge is more conductive, the amount of conductive additives needed in the case of Ge anode is small, while 10–30 wt% of conductive carbon powder is mixed with Si in the anode formulation. These properties also explain why coating Si with Ge was found efficient to improve the Si-based anode, as mentioned in the previous section.

The price of Ge may unfortunately be limiting the mass production of Ge-based anodes for Li-ion batteries. Nevertheless, its coupling with $LiFePO_4$ counter-electrode gives rise to an outstanding Li-ion battery. $LiFePO_4$ is the best cathode element in terms of rate capability and safety, and its only disadvantage is its energy density that is limited to 170 mAh g^{-1}; the coupling with Ge anode will compensate this limitation without impacting the rate capability, this giving rise to the Li-ion battery with the highest power density and good energy density.

10.5 Tin and Lead

Next element in column 14 of the Mendeleev table is Sn. The theoretical capacity of pure Sn is 960 mAh g^{-1}, which is larger than many graphite-based anodes. Unfortunately, the huge volume change (360 % volume expansion up to full lithiation) is discouraging, leading to fracturation and decrepitation upon cycling. In addition, theoretical capacity could never be reached, presumably due to brittleness. Taking these problems into account, Sn-based anodes clearly require composite structures to help maintain electrical contact and Li diffusivity, and many works have been devoted to them; they have been reviewed in [43]. Indeed, progress was made in the previous decade by designing composites containing Sn and a stress-accommodating phase. Carbon was found to be an appropriate second phase in these investigations thanks to its excellent stress-relieving properties and also its low reactivity with Sn. Among these C-Sn composites, tin-filled carbon nanofibres or nanotubes [274–276] and a Sn-microporous carbon composite [277] have shown the most promise due to their high reversible capacity and good capacity for retention. In particular, for Sn-CNT with smaller encapsulated Sn particles of 6–10 nm, the contribution from Sn to the overall capacity was about 1050 mAh g^{-1} for the first 20 cycles, which is larger than the theoretical capacity of Sn [275]. The higher-than-theoretical capacities could be attributed to the

additional storage of Li ions in the large interstitial areas formed by the stacking of nanoscale materials. In the same way, the Sn/C encapsuled carbon nanofibres delivered a capacity close to 800 mAh g^{-1} after 200 cycles [274]. However, the multistep processes used to produce these kinds of materials are too complicated and difficult to be used in industrial processes. Therefore, the future of Sn-based anodes is uncertain, as it seems difficult for them to compete with the Si anodes. In addition, metal oxides are usually much easier to handle than the metals themselves, and tin oxide anodes will be reviewed in a forthcoming section.

The last element of the column 14 is Pb. This element suffers from toxicity and low specific capacity, which was discouraging and very few investigation have been done. The best result that has been obtained recently is a SiC-Pb-C composite [278], but still the capacity was too small to raise interest.

10.6 Oxides with Intercalation-Deintercalation Reaction

10.6.1 TiO_2

Titanium oxide is low cost, safe for the environment, and is considered as a promising candidate for use as anode in Li-ion batteries. Its theoretical capacity is 335 mAh g^{-1} based on the reaction:

$$Ti^{4+}O^2 + Li^+ + e^- \leftrightarrow Li_x\left(Ti^{3+}{}_xTi^{4+}{}_{1-x}\right)O_2 (x \leq 1). \tag{10.4}$$

In addition, its thermal stability is very good, and its SEI is stable, so that the TiO_2-anode is recommended for safety issues [279, 280]. The interest in this material has led to a tremendous amount of works devoted to the successful preparation of nano-TiO_2 by all kinds of techniques: hydrothermal [281, 282], sol–gel [283–287], soft template [288], precipitation or solid state method followed by ion exchange [289, 290], urea-mediated hydrolysis/precipitation route [291], anodization [292, 293], molten salt method [294], synthesis by ionic liquids [295] and electrospinning technique [294, 296]. These syntheses of TiO_2 have been reviewed and discussed in [73, 297]. TiO_2 exists in different polymorphic structures: anatase, rutile, brookite, TiO_2-B (bronze), TiO_2-R (ramsdellite) TiO_2-H (hollandite), TiO_2-II (columbite), TiO_2-III (baddeyte). These polymorphs differ by the connections between TiO_6 octahedra. Their structures are illustrated in Fig. 10.6 for those of the polymorphs that are of interest for Li-ions batteries [38]. The Li cycling properties of these polymorphs have been reviewed in [38, 73]. Since the electrochemical properties depend importantly on the type of polymorph, each polymorph must be considered separately.

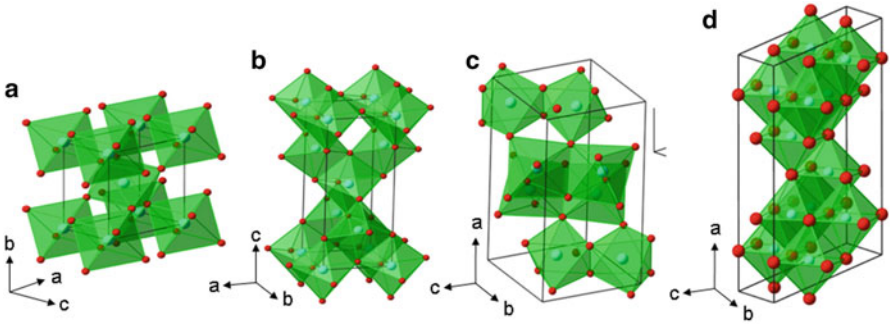

Fig. 10.6 (**a**) Rutile, (**b**) anatase, (**c**) brookite, and (**d**) bronze (B) of TiO_2. Reproduced with permission from [222]. Copyright 2009 Elsevier

10.6.1.1 Anatase TiO_2

The anatase phase crystalizes in a body-centered tetragonal phase that ,contains interstitial sites available to intercalate Li, so that the previous reaction equation applies, so that the theoretical capacity is 335 mAh g^{-1} when the material is cycled to the lower voltage cut-off 1 V vs. Li^0/Li^+. Note the cut-off voltage is higher than that of graphite and Si, which will impact the energy density. Therefore, both criteria (1) and (2), defined in the introduction for good anode element, are moderately satisfied, but the other criteria are very well satisfied. Upon cycling, the anatase is a two-phase system, with separation between $Li_{\sim 0.01}TiO_2$ and $Li_{\sim 0.55}TiO_2$ on the scale of several tens of nanometers [298]. This two-phase region upon lithiation is maintained until all the $Li_{\sim 0.01}TiO_2$ is converted into the $Li_{\sim 0.55}TiO_2$ phase, and is reflected in a voltage plateau in the voltage versus capacity curve. This plateau occurs at 1.72–1.75 V during Li insertion, and 1.8–1.9 V during delithiation, meaning a voltage hysteresis 0.1–0.2 V. However, the $Li_{\sim 0.55}TiO_2$ phase adopts an orthorhombic structure [299], this change of symmetry being accompanied with a 4 % increase in the volume. The group of Wagemaker and Mulder has examined the effect of particle size and structure on the Li-rich orthorhombic and the Li-poor tetragonal phases [298, 300–303]. For big particles, It is possible to cycle Li_xTiO_2 reversibly only in the range $0 \leq x \leq 0.55$, without capacity fading. By decreasing the size of the particles to the nanometer range, it is possible to cycle until $x = 1$. However, the cyclability in the entire range $0 \leq x \leq 1$ is poor, because of the change of symmetry and the volume change associated to it. In addition the Li kinetics at $x = 1$ are very slow. In practice, it is possible to obtain a good cyclability and rate capability of nano-anatase TiO_2 by limiting the upper value of x to ~0.7.

Just like in the case of Si, and for the same reasons (better resistance to strain apposite for enhanced ionic and electronic diffusion), porous material has improved electrochemical properties with respect to nonporous structures. In particular, mesoporous mono-phasic anatase TiO_2 spheres of uniform particle size (ca. 400 nm) encompassing an average crystallite size of 14 nm was synthesized

via the urea-assisted hydrothermal method [304]. Surface area of ca. 116.49 m g^{-1} along with a pore size of 7 nm authenticated the mesoporous nature of the synthesized material. After calcination at 400 °C, this material delivered a reversible capacity of 180 mAh g^{-1} after 80 cycles at *C*/10 rate (cycling range 1.5–3 V). 162, 160, 154, and 147 mAh g^{-1} at 0.5, 1, 5, and 10*C* rate, respectively. Mesoporous anatase TiO_2 with an ordered 3D pore structure was obtained using the silica KIT-6 as a hard template [305]. The ordered pore structure consisted of 11 and 50 nm pores with walls of thickness 6.5 nm with a BET surface area 205 m^2 g^{-1}. A first discharge capacity of 322 mAh g^{-1} (composition $Li_{0.96}TiO_2$ was obtained at 0.09*C* rate, with excellent cycling performance up to 1000 cycles, and very good high rate performance. It is possible to decrease the size and obtain nanoporous TiO_2, using a modified in-situ hydrolysis route [306]. This is a two-step process. The first step is to prepare titanium glycolate spheres by the ethylene glycol mediated process. In the second step, the titanium glycolate is mixed with water at refluxing temperature, and the titanium glycolate reacts with water to form the hierarchically nanoporous TiO_2. The obtained nanoporous anatase TiO_2 shows fully reversible capacities as high as 302 mAh g^{-1} (1*C*; 100th cycle) and 229 mAh g^{-1} (5*C*; 100th cycle) [307]. The galvanostatic curves obtained in this reference are reported in Fig. 10.7, illustrating the overall Li insertion mechanism for the anatase structure. The remarkable high rate performance has been attributed to the fact that the formation of irreversible phases from deep bulk discharge can be avoided at high charge/discharge rates. Good results have also been obtained with

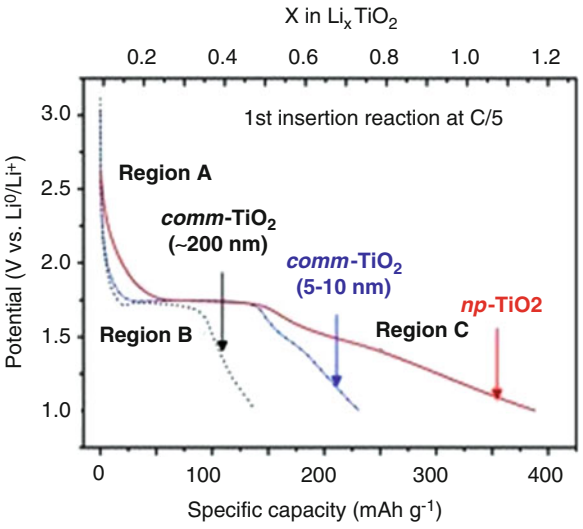

Fig. 10.7 Galvanostatic curves for the two types of commercialized (comm-)anatase TiO_2 particles with different grain sizes (≈200 and ≈5–10 nm) and for the calcined nanoporous (np)-TiO_2 discharged at 0.2*C*, illustrating the three different regions. Region A: V > 1.75 V, *x* in $Li_xTiO_2 < 0.15$, solid solution. Region B: V plateau at 1.75 V, $0.15 < x < 0.5$, two-phase bulk intercalation. Region *C* V < 1.75 V, $x > 0.5$, where the continuous decrease of V indicates interfacial storage pf Li. Reproduced with permission from [307]. Copyright 2011 Wiley

TiO_2 prepared by the molten salt method (MSM) [308, 309]. In particular, nanosized particles obtained by urea-treated MSM delivered a reversible capacity of 250 mAh g^{-1}, and showed a 94 % capacity retention after 60 cycles [309].

Anatase TiO_2 hollow microspheres (400 nm in diameter) with the shell consisting of nanotubes (ca. 30 nm in diameter and 5 nm in wall thickness, 200 nm in length) have been synthesized via a template-free hydrothermal process [281]. After calcination at 450 °C during 5 h to obtain mono-phasic anatase phase, the electrochemical properties of the anatase sample have been investigated by cyclic voltammetry and galvanostatic method. The initial Li insertion/extraction capacity at a current density of 0.2*C* reached 290 and 232 mAh g^{-1} respectively. Moreover, as-prepared TiO_2 delivers a reversible capacity of ca. 150 mAh g^{-1} after 500 cycles at 1*C* (voltage range 1–3 V), and it also shows superior high rate performance (e.g. 90 mAh g^{-1} at 8*C*). Nanotubes of anatase TiO_2 have also been synthesized by the hydrothermal process. Theses nanotubes with thickness 2–3 nm, external diameter 8–10 nm, and length in the range 200–300 nm delivered a maximum capacity at 300 mAh g^{-1}, and good cycling life, with a capacity 250 mAh g^{-1} over 100 cycles. Hollow anatase TiO_2 microspheres were designed from a process employing in suit template-assisted and hydrothermal methods, with controlled size and hierarchical nanostructures via adjusting the hydrothermal reaction time and calcination temperature [310]. The results show that the hollow microspheres composed of mesoporous nanospheres (6 nm size) possess an initial reversible capacity 230 mAh g^{-1}. A stable reversible capacity of 184 mAh g^{-1} ($Li_{0.55}TiO_2$), 172 mAh g^{-1} ($Li_{0.51}TiO_2$) and 122 mAh g^{-1} at 0.25, 1.5, and 10*C* rate, respectively. The superior high-rate and high-capacity performance of the sample is attributed to the efficient hierarchical nanostructures. The hollow structure could shorten the diffusion length for lithium ion in the microspheres. The large mesoporous channels between the mesoporous nanospheres provide an easily-accessed system which facilitates electrolyte transportation and lithium ion diffusion within the electrode materials. The superiority of porous nanosphere over non porous nanospheres has also been proved in [311]. Uniform and dispersed anatase TiO_2 nanoparticles have been synthesized from a triethylene glycol solution of titanium isopropoxide [$Ti(O\text{-}iPi)_4$] by refluxing at 270 °C for 12 h [312]. The particle size varies from 50 to 5 nm, when the temperature used in the preparation decreases from 500 to 100 °C. Depending on the size, the reversible capacity varies from 100 to 250 mAh g^{-1} with capacity retention 85–90 % after 20 cycles at current density 0.1 mA cm^{-2} [312] (1*C* rate = 335 mAh g^{-1}).

Mesoporous material obtained by cetyl trimethylammoniumbromide templated C16-TiO_2 has a high surface area of 135 m^2 g^{-1} and reversible capacity of 288, 220, 138, 134, and 107 mAh g^{-1} at 0.2, 1, 5, 10, and 30*C*, respectively [288]. The storage performance of the as-synthesized mesoporous TiO_2 is nearly five times better than the commercially available TiO_2 nanopowder. The packing density of this meso-TiO_2 is 6.6 times higher than the TiO_2 nanopowder, and the best result obtained so far for anatase TiO_2. Nevertheless, it is possible to increase the performance of anatase nanoparticles by introducing oxygen vacancies by hydrogen reduction to increase the electronic conductivity [313]. In particular,

H_2-1 h-$TiO_{2-\delta}$ anatase nanoparticles, i.e. particles (29 nm in size) thermally annealed under 5 % H_2/95 % Ar ($PO_2 \approx 10^{-25}$ bar) for 1 h, delivered 307 mAh g^{-1} at the first cycle and 131 mAh g^{-1} at the 20th cycle, not only at 1*C* rate, but also at 10*C*-rate [313].

Nanorods have also been successful [314, 315]. In particular, the initial lithium insertion/extraction capacities of mesoporous anatase TiO_2 rods reached 262 and 221 mAh g^{-1}, respectively, at a current density of 0.1 A g^{-1}. A discharge capacity of approximately 161 mAh g^{-1} could be retained after cycling at 1 A g^{-1} for 40 cycles, demonstrating good rate performance and high cycleability [314]. An even larger capacity has been obtained with nanorods obtained by hydrothermal reaction of amorphous TiO_2 in NaOH to form $Na_2Ti_3O_7$ nanorod, followed by ion exchange in HCl solution, to give $H_2Ti_3O_7$ and dehydratation at 400 °C. The rods 40–50 nm in length and 10 nm in diameter had a BET surface area 185.5 m^2 g^{-1}. The first discharge and charge capacities were 320 and 265 mAh g^{-1}, respectively (1–3 V voltage range, 50 mAh g^{-1} current density). A reversible capacity of 225 mAh g^{-1} was observed after 50 cycles.

Nanotubes are also very promising [295, 316–321] when the wall thickness of the nanotube is small for instance 330 mAh g^{-1} when the wall thickness is reduced to 5 nm [317]. The initial large capacity with nano structures indicates interfacial storage of Li. For instance, the first discharge capacity of np-TiO_2 was 388 mAh g^{-1} in [307]. The problem is thus to stabilize this interfacial Li storage to avoid important capacity loss upon cycling. The authors in ref. [307] state that this capacity loss can be overcome by cycling the material at high C-rates without further long rest periods. High-surface-area stable anatase TiO_2 nanosheets comprising nearly 100 % exposed (001) facets have been obtained from spontaneous assembly of the nanosheets into three-dimensional hierarchical spheres, which stabilizes them from collapse [321]. The high surface density of exposed TiO_2 (001) facets leads to fast lithium insertion/deinsertion processes: at a rate of 1*C* and 5C, a reversible capacity of 174 and 135 mAh g^{-1}, respectively was retained after more than 100 charge–discharge cycles.

Due to the low electrical conductivity of TiO_2 ($\approx 10^{-13}$ S cm^{-1}), various metals, metal oxides, and carbonaceous materials with high electrical conductivity have been utilized as matrices or conductive additives to improve the electrochemical performance of anatase TiO_2. Graphene appears promising to improve the rate capability and cycle performance of titania owing to its unique characteristics including superior electrical conductivity, large surface area, and excellent mechanical flexibility. Nevertheless, due to the strong π-interaction of graphene sheets and their intrinsic incompatibility with inorganic components, a homogeneous dispersion of titania nanoparticles onto graphene remains a challenge [141, 322–326]. Nevertheless, good results have been obtained. Wang et al. fabricated a composite of titania and graphene by hydrothermal process. The structure consisted of 10 nm in diameter anatase TiO_2 nanotubes with length from hundreds to thousands of nanometers, built on a graphene layer [327]. The obtained capacity was 350 mAh g^{-1} at the rate of 10 mA g^{-1}. Rate capacities of 150 mAh g^{-1} (at the rate of 4000 mA g^{-1}) after 50 cycles and 80 mAh g^{-1} (at the rate of 8000 mA g^{-1})

after 2000 cycles were observed. The coulombic efficiency was approximately 99.5 %, indicating excellent cycling stability and reversibility. Another example is the successful fabrication of sandwich-like, graphene-based mesoporous titania (G-TiO_2) nanosheets by a nanocasting method has been obtained in [328], owing to a synthetic strategy involving the employment of G-silica nanosheets as template, and $(NH_4)_2TiF_6$ as titania precursor in a sol–gel process. These G-TiO_2 nanosheets retained reversible capacities at 162 and 123 mAh g^{-1} at 1*C* and 10*C*, respectively, and the coulombic efficiencies (calculated from the discharge and charge capacities) approach almost 100 %. Even at the high rate of 50*C* (charge/discharge within 72 s), a capacity of 80 mAh g^{-1} could still be delivered. TiO_2-graphene composites have also been reported to be promising anodes [329–332]. TiO_2-reduced graphene oxide composite (termed as TGC) nanostructures using tetrabutyl titanate as the titanium source via a solvothermal route also gave good results [330]. The sample was made of monodisperse TiO_2 particles of thickness 200–300 nm, resulting from the aggregation of particles of thickness 20–30 nm deposited on graphene oxide sheets. Initial irreversible capacity and a reversible capacity of 386.4 and 152.6 mAh g^{-1} for TGC after 100 cycles at a high charge rate of 5*C* (1000 mA g^{-1}).

Carbon-TiO_2 composites have also been investigated. The combined benefits of mesoporosity and in situ grown conductive amorphous carbon on lithium storage capacity of anatase TiO_2 have been discussed in [333]. Mesoporous carbon-TiO_2 sphere exhibited a first discharge cycle capacity of 334 mAh g^{-1} at 0.2*C* rate, whereas carbon-TiO_2 sphere and mesoporous TiO_2 stored 120 and 270 mAh g^{-1} respectively. The good cyclability in mesoporous carbon-TiO_2 sphere was attributed to the synergy of mesoporosity and in situ grown carbon in the formation of an effective percolation network for the conducting species around the TiO_2 spheres. Mesoporous carbon TiO_2 composites have also been investigated in [334], while anatase TiO_2-carbon nanofibers have been explored in ref. [335], and TiO_2/carbon nanotubes in [336, 337]. The combined benefits of mesoporosity and in situ grown conductive amorphous carbon on lithium storage capacity of anatase TiO_2 have been discussed in [333]. Mesoporous carbon-TiO_2 sphere exhibited a first discharge cycle capacity of 334 mAh g^{-1} at 0.2*C*-rate, whereas carbon-TiO_2 sphere and mesoporous TiO_2 stored 120 and 270 mAh g^{-1} respectively. The good cyclability in mesoporous carbon-TiO_2 sphere is attributed to the synergy of mesoporosity and in situ grown carbon in the formation of an effective percolation network for the conducting species around the TiO_2 spheres.

Different composites made of anatase TiO_2 with a conductive element: TiO_2/Ag [296], mesoporous TiO_2/Cu and TiO_2/Sn [287], TiO_2/RuO_2 [338], have been explored for lithium storage, but the electrochemical properties were competitive with the more recent results obtained with anatase TiO_2. On another hand, a three-dimensional (3-D) Ni/TiO_2 nanowire network was successfully fabricated using a 3-D porous anodic alumina (PAA) template-assisted electrodeposition of Ni followed by TiO_2 coating using atomic layer deposition [339]. With a stable Ni/TiO_2 nanowire network structure, 100 % capacity is retained after 600 cycles. Finally, another way to increase the electric conductivity has been doping anatase NiO_2, N,F co-doping [340], Cu-doping [341], doping with Mn, Sn, Zr, V, Fe, Ni, Nb [309].

10.6.1.2 Rutile TiO_2

Even though anatase is the most electroactive form in the voltage range 1–3 V, rutile as also been widely studied. Nano-phased rutile TiO_2 have demonstrated that circa 0.5 mol of Li per TiO_2 (170 mAh g^{-1}) can be cycled in the voltage range 1–3 V. Cycling rutile TiO_2 is more facile than in the anatase phase, because the Li^+ diffusion coefficient D_{Li} in nano-rutile Li_xTiO_2 is very high. It has been estimated by impedance spectroscopy [342]. At ambient pressure, $D_{Li} = 7 \times 10^{-8}$ cm^2 s^{-1} for $x = 0.1$, decreasing linearly with x to 1×10^{-9} cm^2 s^{-1} at $x = 0.4$. A review and discussion of the physical properties and electrochemical properties of rutile TiO_2 dating from 2009 is reported in [38]. More recently, a simple way to prepare highly flexible self-standing thin-film electrodes composed of mesoporous rutile TiO_2/C nanofibers with low carbon content (<15 wt%) by electro-spinning technique, which can be applied directly as electrodes of lithium-ion batteries without the further use of any additive and binder [343]. After optimization, the diameter of fibers can reach as small as ~110 nm, and the as-prepared rutile TiO_2 films show high initial electrochemical activity with the first discharge capacity as high as 388 mAh g^{-1}. Very stable reversible capacities of ~122, 92, and 70 mAh g^{-1} are achieved respectively at 1, 5, and 10C rates with negligible decay rate within 100 cycling times. Among doped samples (N,F)-co doped rutile TiO_2 delivered a reversible capacity of 210 mAh g^{-1}, and 80 % capacity retention after 60 cycles [340]. The group of Wohlfahrt-Mehrens has made a very interesting work on rutile TiO_2 in a series of papers [279, 286, 344, 345]. There, the nanorutile TiO_2 was prepared by sol gel method using glycerol-modified Ti-precursor in the presence of an anionic surfactant, and heat treatment at 400 °C in air. The rutile whiskers thus obtained are agglomerated to form cauliflower-like aggregates of several micrometer size. The whiskers had a diameter of 4–6 nm in the *ab*-plane and a length of ~50 nm in the c -direction. The BET surface area was 181 m^2 g^{-1}. The Li cyclability was studied in the usual voltage range 1–3 V, but also in the range 0.1–3 V vs. Li^0/Li^+ at various current rates, 0.05–30*C* ($1C = 335$ mA g^{-1}), and at various temperatures from 20 to −40 °C. Normally, amorphization and crystal structure destruction of TiO_2 is expected under deep discharge conditions to 0.1 V vs. Li^0/Li^+. Surprisingly, this was not the case here. At 0.2*C* at 20 °C, large first-discharge capacities of 380 and an extraordinary 660 mAh g^{-1} (2Li mol per TiO_2) were observed for the lower cutoff voltages of 1 and 0.1 V, respectively. These values correspond to 1.1 and 2 mol of Li per mol of TiO_2, respectively. Large irreversible capacity loss was noted in the first discharge–charge cycle in the above voltage ranges. However, after five cycles, the coulombic efficiency improved to 95–97 % and reversible capacities of 183 mAh g^{-1} (0.55 mol of Li) and 324 mAh g^{-1} (0.97 mol of Li) were observed in the voltage ranges 1–3 V and 0.1–3 V vs. Li^0/Li^+, respectively. Even at low temperature, the results were remarkable. At −20 °C, a capacity of 80 and 140 mAh g^{-1} was noted in the above voltage ranges, corresponding to 40 % capacity retention. The *C*-rate capability was also found to be excellent, with 50 and 24 % capacity retention at 20*C*

rate, in comparison to the values at 0.05*C* rate. Long-term cycling studies, up to 1000 cycles at 5C rate and at 20 °C, showed a fading of capacity during the first 200 cycles, from 150 to 120 mAh g^{-1}, a slow degradation up to 750 cycles and finally stabilized at 105 mAh g^{-1} in the range 750–1000 cycles. This corresponds to a capacity retention of 70 %. The reason why the rutile TiO_2 has such outstanding electrochemical properties down to 0.1 V is unknown. It has been suggested [22] that amorphization of nanorutile TiO_2 occurs during the first discharge at least in the few surface layers, resulting in the formation of a composite, $Li_2O \cdot TiO_y$ ($y \leq 1.5$), and Li cycling occurs through a "conversion reaction".

10.6.1.3 TiO_2-B

The bronze polymorph is the last one that accepts insertion of Li. It adopts an open framework structure that enables easy Li transport in it. However, it can only be prepared by the proton exchange of $Na_2Ti_3O_7$, followed by heat treatment at 400–500 °C, and this synthesis leads to residual H_2O in the TiO_2 and formation of nonnegligible amount of the anatase phase. Nevertheless, TiO_2-B is an attractive anode material with large reversible capacity. The fast kinetics are illustrated by the performance of porous TiO_2-B microspheres with 12 nm pore size, which delivered 120 mAh g^{-1} at 60*C* rate [346]. At 10*C* rate, the sixth reversible capacity was 166 mAh g^{-1}, and retained a value 149 mAh g^{-1} after 5000 cycles. This material was obtained by a five-step template-assisted ultrasonic spray pyrolysis followed by refluxing, ion-exchange, and heat treatment at 500 °C. Another example is the mixture of 96 % TiO_2-B nanoribbons, 4 % nanotubes, and 1 % nanospheres obtained by the solution-refluxing method 120° for 1 week, followed by heat treatment at 400 and 500 °C [289]. The nanoribbons were 30 nm width, 6-nm thick, and 1–2 μm in length, and the BET surface area was 115 m^2 g^{-1}. Reversible capacities of 200, 150, and 100 mAh g^{-1} were obtained at rates *C*/3, 3*C*, and 15*C*, respectively ($1C = 330$ mA g^{-1}); the capacity loss up to 500 cycles at 3C rate was only 5 %. Note, however, that these results were obtained in electrodes with 50 wt% carbon black loading, an amount of carbon that is prohibited in any commercialized battery. Hierarchical porous TiO_2–B with 5–10 thick nanosheets and BET surface area 151 m^2 g^{-1} delivered a reversible capacity of 211 mAh g^{-1} at 10*C* rate and retained a capacity at 200 mAh g^{-1} after 200 cycles at 10*C* rate [347]. Nanosheets of pure TiO_2-B were also obtained by using multilamellar tetratitanate nanosheets as the reassembly component when K^+ replaced H^+ as guest ions for the self-reassembly of nanosheets [348]. The nanosheets were 200 nm in width, 1 μm in length and 4-nm thick, with a BET surface area 66 m^2 g^{-1}. They exhibited a large discharge capacity of 258 mAh g^{-1} at the fifth cycle and maintained a large discharge capacity of 253 mAh g^{-1} after ten cycles.

TiO_2-B nanowires encapsulated inside and an amorphous carbon layer coating the outside were obtained by hydrothermal process [349]. These carbon-TiO_2-B nanowires exhibited a high reversible capacity of 560 mAh g^{-1} after 100 cycles at the current density of 30 mA g^{-1}, good cycling stability, and rate capability

(200 mAh g^{-1} when cycled at the current density of 750 mA g^{-1}). TiO_2-B anatase hybrid nanowires with a bicrystalline structure consisting of TiO_2-B core and anatase shell was performed by the hydrothermal process and post treatments [350]. The phase fractions by weight were determined to be 92.8(5)% of TiO_2-B and 7.2(1)% of anatase. The composite electrode exhibited a highly reversible initial specific discharge and charge capacity of over 256.5 and 232 mAh g^{-1}, respectively, in the first cycle. It maintained a high capacity of ~196 mAh g^{-1} after 100 cycles at *C*/10 rate, delivered a capacity 125 mAh g^{-1} at 15*C*, and after the application of 15*C*, recovered to 219.3 mAh g^{-1} at *C*/10. The high rate capability of TiO_2-B has motivated the coupling with $LiFePO_4$ counterelectrode, like in the case of Ge. The $LiFePO_4$//TiO_2-B cell was tested with TiO_2-B nanofiber bundles [351]. The balancing mass ratio of the anode and cathode materials was designed to be 1:1.5 by using the specific capacity of 200 mAh g^{-1} of the prepared TiO_2 and 165 mAh g^{-1} of the $LiFePO_4$, separately. The battery delivered an average voltage 1.8 V with capacities of 200 mAh g^{-1} based on the weight of the TiO_2-B in anode. Typically, the battery studied herein exhibited an initial discharge capacity of 160 mAh g^{-1} at the rate of 1*C*; more than 140 and 120 mAh g^{-1} discharge capacity was delivered at a rate of 2*C* and 5*C*, respectively. The battery studied herein exhibited a discharge capacity of 80 mAh g^{-1} at the high rate of 20*C* and an average capacity loss of no more than 0.05 mAh g^{-1} per cycle. The full lithium battery maintained 81 % of its initial capacity after 300 cycles. In summary, it is difficult for TiO_2 to compete with silicon. Like Si, TiO_2 has a low electronic conductivity, but its reversible capacity is much smaller. Nevertheless, TiO_2 has the advantage of reduced volume change upon cycling, which is beneficial to the safety and cycle life. Anatase has always been considered as the best phase for anode applications. However, the recent results showing remarkable properties in the full voltage range 0–3 V make the rutile phase competitive with respect to anatase. TiO_2-B remains the phase that allows for the highest rate capability. In fact, TiO_2 is suitable for mass production and it is cost effective. The problem is that its electrochemical properties, irrespective of the polymorph phase, require nano sizes and preferentially composites, so that an anode-based TiO_2 at the end is not cheap. Therefore, the titanium oxide will presumably remain a niche market as an anode material, especially as it also has to compete with another titanium compound, namely $Li_4Ti_5O_{12}$.

10.6.2 $Li_4Ti_5O_{12}$

The $Li_4Ti_5O_{12}$ (LTO) spinel is considered as the most appropriate titanium-based oxide for use as anode in Li-ion batteries, and is actually considered as a viable anode for Li-ion batteries. It exhibits excellent Li-ion reversibility according to a two-phase reaction maintaining the constant voltage 1.55 V vs. Li^0/Li^+ with a very small hysteresis between charge and discharge; this potential is high, which guarantees safety conditions as the formation of the SEI is mitigated, and the

development of dendrites observed with carbonaceous, and in particular graphite anodes, is avoided. It is cheap, very safe, environmental friendly, and has a remarkable structural stability. Li cycling involves very little change in the cubic lattice parameter so that LTO is a "zero strain" material ideally suited as an anode material. That is why a huge amount of papers has been devoted to this material, and again we guide the reader to the previous reviews on $Li_4Ti_5O_{12}$ [21, 22, 38] to focus attention here on the progress achieved in the recent years. The lithium insertion/extraction reaction for $Li_4Ti_5O_{12}$ can be summarized as:

$$\begin{aligned}&\left(Li^+\right)_{3(8a)}\cdot\square_{16c}\left[Li^+\left(Ti^{4+}\right)_5\right]_{(16d)}\left(O^{2-}\right)_{12(32e)}+3Li^++3e^-\\&\quad\rightarrow\cdot_{\square(8a)}\left(Li^+\right)_{6(16c)}\left[Li^+\left(Ti^{3+}\right)_3\left(Ti^{4+}\right)_2\right]_{(16d)}\left(O^{2-}\right)_{12(32e)}.\end{aligned}\tag{10.5}$$

This reaction equation shows that the migration of the lithium between the tetrahedral (8*a*) sites and the octahedral (16*d*) sites oxygen coordination. The theoretical capacity according to this equation is 175 mAh g^{-1}. The electronic conductivity of LTO is small ($\sigma_e \sim 10^{-12}$–10^{-13} S cm^{-1} at room temperature), due to the fact that the t_{2g} states of Ti^{4+} that form the conduction band of LTO are empty. Fortunately, it improves upon lithiation, because the reaction equation show that some of the titanium ions shift to the Ti^{3+} valence state, in which one t_{2g} is occupied, enabling the hopping between Ti^{3+} and Ti^{4+} ions. Nevertheless, the consequence of the low value of σ_e of virgin LTO is that the theoretical capacity can be approached only at low *C*-rate, especially as the ionic conductivity is also small (3×10^{-10} S cm^{-1}). To overcome this problem, the solutions have been the same as for any anode element, starting with the decrease of the size of the particles to the nano-range, and favor porous LTO to increase the active surface area while minimizing the length of the electron and ion path.

The electronic spray deposition (ESD) technique is a way of engineering nano-structured anodes [352]. Already in 2005, the ESD spurs the formation of porous nanoscaled LTO by using lithium acetate and titanium butoxide as the precursors [353]. The obtained LTO showed fractal-like morphology. No obvious structure change (see Fig. 10.8) was observed after annealing at a high temperature (700 °C), demonstrating that the LTO film exhibited very good thermal stability. It was found that the anode produced by the ESD provided high energy capacity (175 mAh g^{-1}) at cycling rate *C*/18, close to its theoretical value in the initial cycle. A capacity of about 155 mAh g^{-1} was still achieved after ten cycles and remained constant up to 70 cycles. Mesoporous LTO microspheres (300 nm-spheres made of 20 nm-thick primary particles were prepared by template-free hydrothermal process in ethanol–water mixed solution aimed at the formation of mesoporous structure, and subsequent heat treatment. This material delivered 114 mAh g^{-1} at 30*C* and good capacity retention of 125 mAh g^{-1} after 200 cycles at 20*C* (1*C* = 170 mAh g^{-1}). Next step was to associate the nano-LTO with a conducting element under the form of a composite or a coating to improve the rate capability. Nanocrystalline LTO has also been synthesized by single-step-solution-combustion method in less than 1 min [354].

LTO particles thus synthesized are flaky and highly porous in nature with a surface area of 12 $m^2\ g^{-1}$. The primary particles are agglomerated crystallites of varying size between 20 and 50 nm with a 3-dimensional interconnected porous network. A capacity value close to the theoretical value of 175 mAh g^{-1} has been reached at *C*/2 rate. The electrodes also exhibited promising capacity retention with little capacity loss over 100 cycles at varying discharge rates together with attractive discharge-rate capabilities yielding capacity values of 140 and 70 mAh g^{-1} at 10 and 100*C* discharge rates, respectively. Another synthesis route to fabricate hierarchically porous LTO microspheres made of well-crystalline nanoparticles is a hydrothermal treatment of commercial anatase TiO_2 powder in LiOH solution and a following calcination procedure [355]. The surface area thus obtained was 57.5 $m^2\ g^{-1}$. At rate 2*C*, this material delivered 147 mAh g^{-1} with 95 % retention after 200 cycles. Soft chemistry can also be used to prepare spherical LTO particles made of nanoparticles. In particular, such a sample prepared by solvothermal synthesis based on the "benzyl alcohol route" delivered a capacity of 155 mAh g^{-1} at 1*C* rate, with capacity retention of 95 % over 200 cycles, for a surface area of 8 $m^2\ g^{-1}$. Porous LTO was also synthesized from mixture of LiCl and $TiCl_4$ with 70 wt% oxalic acid by a modified one-step solid state method [356]. In this case, the initial capacity was 167 and 133 mAh g^{-1} at 0.5 and 1*C* charge/discharge rate, respectively, and the capacity retention was maintained above 98 % after 200 cycles. A capacity of 70 mAh g^{-1} at charge/discharge 10*C* rate after 200 cycles.

The morphology of the LTO in all these works was the same, namely spheres made of primary nanoparticles. However, other geometries have also been obtained. Hierarchical mesoporous nest-like LTO prepared by hydrothermal synthesis with large surface area 219.2 $m^2\ g^{-1}$ delivered 135 mAh g^{-1} after 200 cycles at 14*C* rate, and 113.6 mAh g^{-1} were obtained at 57C [357]. Ten nanometer thick nano flower-like LTO has been synthesized by hydrothermally treating amorphous TiO_2 beads under the additive of LiOH precursor [358]. This sample delivered a capacity of 148, 143, 141, 138, 133, 126, and 118 mAh g^{-1} at 0.5, 1, 3, 5, 10, 20, 30*C*, respectively. The reversible capacity at 30*C* even remains over 80 % of that at *C*/2. The superior *C*-rate performance has been associated with the nano flower-like structure, facilitating lithium transportation ability during cycling. To obtain even better results, the nano-LTO (nanorods, hollow spheres, nanoparticles) has been carbon-coated [359, 360]. The results obtained with C-LTO particles of size 90 nm [268] are illustrated in Fig. 10.8. The carbon coat covers the catalytic active sites of LTO particles. Then some authors have deduced that the carbon coat separates the LTO particles from the electrolyte, so that a solid electrolyte interface (SEI) film is formed on the carbon layer during the formation process, which can prevent the further reduction decomposition of electrolyte at around 0.7 V, making possible the extension of the voltage range to lower potential [361]. This explanation, however, is not satisfactory, because the SEI forms on the anodes, whether they are carbon, graphite, or metal oxides, as soon as the voltage is lower than 1 V during Li insertion. This is due to the reduction of the solvents present in the electrolyte, namely ethylene carbonate (EC) and diethyl carbonate (DEC), aided by the presence of the Li

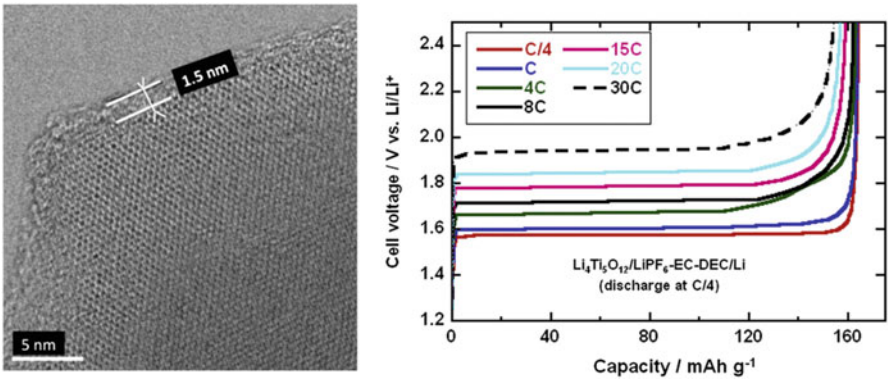

Fig. 10.8 (*Left*) TEM image showing the carbon coat of the C-$Li_4Ti_5O_{12}$ composite (particles of size 90 nm) and (*right*) the charge curves of the C-$Li_4Ti_5O_{12}$/1 mol L^{-1} $LiPF_6$ in EC-DEC (1:1)/Li cell at different *C* rates. Reproduced with permission from [268]. Copyright 2012 Elsevier

salt ($LiPF_6$). That is the reason why all the electrochemical performance reported here have been obtained with the lower voltage at 1 V, unless specified. In addition, the interest in the carbon coating (and actually any coating) is that the coat is porous and does not prevent the contact between the electrolyte and the particles, otherwise the particles would not be active. To the contrary, carbon-coating improves the electrochemical performance. For example, a chain-structured carbon coated LTO prepared by a filter paper templated sol–gel route reached 165 mAh g^{-1} at *C*/5 and 110 mAh g^{-1} at a high rate of 12*C* [362]. 100 nm-sized C-LTO primary particles with surface area 12 m^2 g^{-1} were synthesized by a simple solid-state reaction using TiO_2, Li_2CO_3, and pitch [363]. The 5 wt% C-coated sample had a uniform 3 nm thick carbon coat. At rate 1*C*, the reversible capacity was 165 mAh g^{-1} with 99 % retention over 100 cycles. A very good cyclability was also obtained at 5*C* and 10*C* rates. A 5 wt% carbon-coated LTO has also been prepared by template-free solvothermal synthesis [364]. In this case, the LTO consisted in 0.5–1 μm sized porous microspheres composed of 11 nm-sized crystallites (pore diameter 4.3 nm). When cycled in the range 1–2.5 V, this C-coated LTO delivered 158 and 100 mAh g^{-1} at 1*C* and 50*C*, respectively without noticeable capacity fading. In another work, porous LTO particles prepared by spray drying method have been coated with nitrogen-doped carbon that turns out to give better results than non-doped carbon derived from sugar [365]. The best results were obtained with 7 wt% N-doped carbon–coated LTO made of spherical particles, size 3–5 μm composed of nano-sized aggregates. The capacities at 5*C* and 10*C* rates were 145 and 129 mAh g^{-1}, respectively, stable for at least 20 cycles. At 2*C* rate, the initial capacity was 150 mAh g^{-1}, with a capacity retention of 83 % after 2200 cycles. The reduction of the thickness of the carbon coat to 1 nm owing to the use of cetyltrimethylammonium bromide (CTAB) as a surfactant significantly improved the rate performance of carbon coated LTO by facilitating the diffusion of Li through the carbon layer [366]. The specific capacities of such a C-LTO material with lump

morphology prepared by hydrothermal process at charge and discharge rates of 0.1, 1, 5, 10, and 20*C* were 176, 163, 156, 151, and 136 mAh g^{-1}.

Another process to improve the performance of LTO has been the synthesis of composites. In particular, just as in the case of the other anode materials reviewed in the previous sections, the composite LTO-graphene. Composites of 1 wt% graphene and nano-LTO was prepared with a surface area of 170 mAh g^{-1} by electrospinning [367]. At a discharging and charging rate of 22*C*, the initial reversible specific capacity of the graphene-embedded LTO nanocomposites was around 110 mAh g^{-1}. After 1300 cycles a capacity of 101 mAh g^{-1} was observed (91 % of the initial capacity). Composites with other forms of carbon have also been prepared. Urchin-like LTO–carbon nanofiber delivered 123 mAh g^{-1} when charged/discharged at 15*C* [368]. LTO nano-platelets of size 10–20 nm have been uniformly dispersed on reduced graphite oxide (RGO) to form a nano-hybrid composite (72:38 wt%) by microwave-assisted solvothermal reaction followed by heat treatment at 700 °C [369]. Reversible capacities 154, 142, 128, and 101 mAh g^{-1} have been obtained at 1, 10, 50, and 100*C* rates, respectively. The capacity retention after 100 cycles was 95 % at 1 and 10*C* rates. Carbon nanotubes (CNT)-LTO composites have also been prepared by mechanically mixing LTO with CNTs [370–372]. Better results have been obtained by adding carbon, thus forming a LTO/C/CNT composite, synthesized by solid-state method [373]. For a 6 wt% of total content of C (pitch) and CNTs, the discharge capacities were 163, 148, and 143 mAh g^{-1}, for charge–discharge rate of 0.5, 5, and 10*C*, respectively. After 100 cycles at 5*C*, it remained at 146 mAh g^{-1}. An entanglement structure for an LTO/multiwalled carbon nanotube (MWCNT) composite is prepared by a ball-milling-assisted solid-state reaction [370]. At 10*C* rate, the corresponding electrode delivered 147 mAh g^{-1}, with a capacity retention 97 % over 100 cycles. In a different synthesis approach, Nano-LTO has also been anchored on MWCNT by liquid phase deposition, owing to the controlled hydrolysis of tetrabutyl titanate [374]. The predetermined amount of MWCNT in nano-LTO/MVCNTs composite was 10 wt%. Then, the MWCNTs surfaces was functionalized using concentrated nitric acid that introduces functional groups such as carboxyl (–COOH), hydroxyl (–OH), and carbonyl (CO) groups. Then, the TiO_2 nanoparticles were anchored on the surface of MWCNTs by the controlled hydrolysis of tetrabutyl titanate. Finally, the TiO_2/MWCNTs were converted to LTO/MWCNTs nanocomposite by a short heat-annealing. The LTO particles thus obtained were 50 nm thick. Tested in the voltage window 1–2.5 V, these LTO/MWCNTs delivered a capacity of 171 mAh g^{-1} (per gram of LTO) at 1*C* rate, and still 90 mAh g^{-1} at 30*C* rate, stable over at least 30 cycles. This performance is close to that of the N-doped carbon coated LTO in [365]. MWNT-LTO core/sheath coaxial nanocables (thickness 25 nm) obtained by solid-state synthesis with rich hierarchical pores providing a high surface area of 80 m^2 g^{-1} delivered a capacity of 90 mAh g^{-1} at 40*C* over 100 cycles [375]. These different results give evidence of the important improvement of the electrochemical properties by the use of carbon nanotubes that facilitate the penetration of the electrolyte and improve the electronic conductivity.

The main disadvantage of LTO with respect to TiO_2 being its lower capacity, a dual-phase LTO-TiO_2 consisting of irregular nanocrystals and nanorods has been synthesized by hydrothermal process with adding thiourea to add up the properties of both oxides [376]. After 300 cycles at 1*C* rate, the dual-phase LTO-TiO_2 nanocomposite maintained a capacity of 116 mAh g^{-1}. The large capacity of 132 mAh g^{-1} was also observed at the current density of 1600 mA g^{-1} upon cycling. This high rate capacity has been attributed to the pseudocapacitive affect induced by the presence of abundant phase interfaces in this composite. In another work, the elements of the dual-phase LTO-TiO_2 have been carbon-coated [377], delivering 110 mAh g^{-1} at a current density of 10*C* up to 100 cycles.

Another prominent route to overcome the low conductivity has been to dope LTO. The doping introduces Ti^{3+} ions which contain one conducting electron in the t_{2g} sub-band. In this regard, Shen et al. published a facile template-free route to fabricate LTO nanowire arrays growing directly on Ti foil while creating Ti^{3+} sites through hydrogenation [378]. At a low *C*-rate (e.g. *C*/5), this electrode achieved a first discharge capacity as high as ≈173 mAh g^{-1}. As the current rate increased from 1 to 5 and 10C, the discharge capacity slightly decreased from 166 to 157 and 145 mAh g^{-1}, respectively. At the high rate of 30*C* (5.3 A g^{-1}), the capacity retained 69 % of the value achieved at 0.2*C* with a discharge voltage plateau at 1.33 V, indicating the excellent rate capability of the material. These electrochemical properties are compared in Fig. 10.9 with the capacities delivered by different LTO anodes: TiO_2-coated LTO [379], nano-crystalline LTO [354], mesoporous LTO/C [380], LTO/graphene [381], carbon-coated LTO [382], phosphidated LTO [383], Ni-doped LTO [384] (figure extracted from ref. [380]). It shows that the hydrogenated LTO nanowires growing directly on Ti foil without any additive gives the best results, comparable to commonly conductive coating electrodes. This is due to the increase of the electronic conductivity resulting from the doping by hydrogenation, and the large space that facilitate the fast transfer of Li^+ and small diameter of NW that provides the short diffusion length. LTO has also been doped with supervalent metal ions with respect to Ti^{4+}: Nb^{5+} [385, 386], V^{5+} [387, 388]. More surprising, good results have been obtained by Gu et al. for what the authors called doping with Zr^{4+} [389] to obtain carbon-coated $Li_4Ti_{5-x}Zr_xO_{12}$ ($x = 0, 0.05$). Since Zr^{4+} is isovalent with Ti^{4+}, Zr is not supposed to act as a dopant if it substitutes for Ti; nevertheless, the electronic conductivity increased with this substitution [390], for unknown reason. But most of all, the remarkable electrochemical properties was observed by extending the voltage range from 2.5 V down to 0 V instead of 1 V, which recalls the work of the Wohlfahrt-Mehrens group on rutile TiO_2 in the previous section. The Zr^{4+}-doped $Li_4Ti_5O_{12}$/C delivered a discharge capacity 289 mAh g^{-1} after 50 cycles at 0.2*C* rate, when extending the voltage range to 0–2.5 V, and the capacity was still 212.6 mAh g^{-1} at 5*C*. Like in the case of rutile TiO_2, the reason for this improvement, in particular by extending the voltage range down to 0 V is not understood and more investigations on surface reactions of the titanium oxides are clearly needed. Moreover, we cannot take for granted the possibility to use such low voltages to improve the performance of the anodes. In an analysis made on V-doped LTO [386], it has been noticed that the

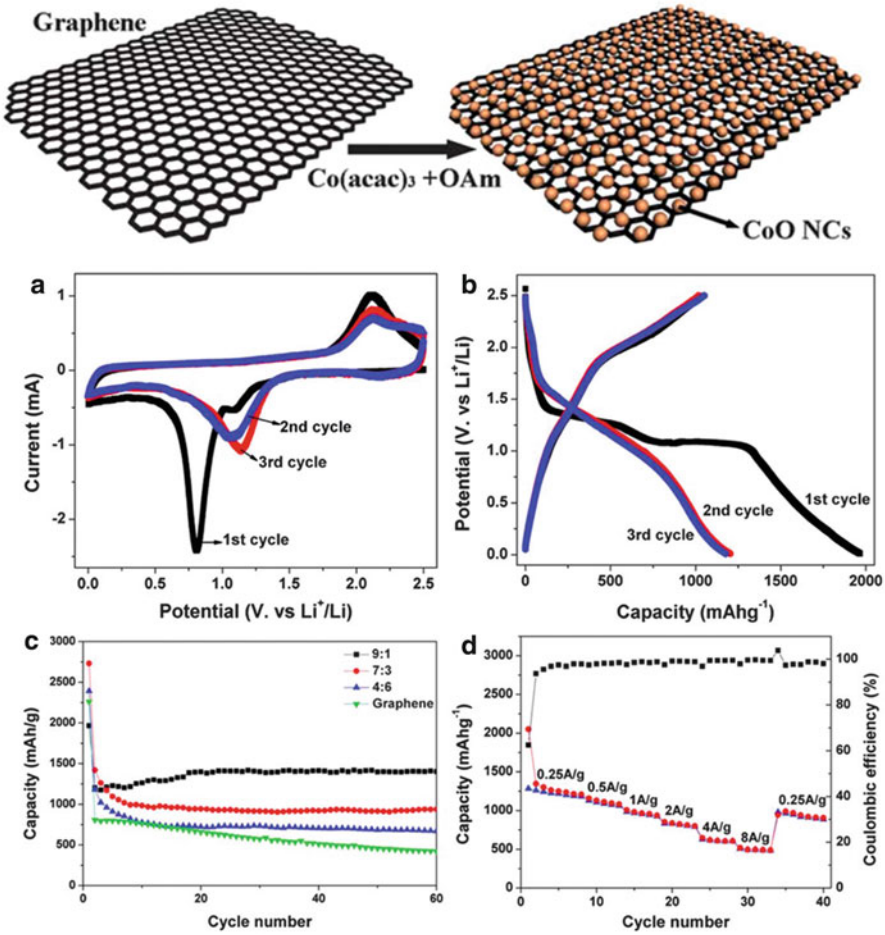

Fig. 10.9 Schematic illustrating the synthetic procedure for making highly loaded CoO/graphene nanocomposites and their electrochemical properties. (**a**) The first three CV curves of the CoO/graphene nanocomposite with a mass ratio of 9:1 in the potential range of 0.0–2.5 V at a scan rate of 0.1 mV s^{-1}. (**b**) The first three discharge–charge curves of the CoO/graphene nanocomposite with a mass ratio of 9:1 at a current density of 100 mA g^{-1} and room temperature. (**c**) Discharge capacities vs. cycle number for the CoO/graphene nanocomposites with mass ratios of 9:1, 7:3, and 4:6, and pure graphene at a current density of 100 mA g^{-1} and room temperature. (**d**) Specific capacities of the CoO/graphene nanocomposite with a mass ratio of 9:1 for different discharge-charge cycles at current rates between 0.25 and 8.0 A g^{-1}. (*Black*: coulombic efficiency; *red*: discharge capacity; *blue*: charge capacity). Reproduced with permission from [494]. Copyright 2013 Royal Chemical Society

electrolyte starts to decompose irreversibly below 1.0 V, and SEI film of LTO is formed at 0.7 V in the first discharge process, thus altering the cycling life. In particular, the cycling life has not been investigated in the Zr-doped LTO discharged at 0 V. Other doping with aliovalent ions have also led to some improvement of the electrochemical properties, but not with the same success:

Mg^{2+} [391], Al^{3+}[392–394], Ni^{2+}[384, 395, 396], Mn^{2+} [395], Cr^{3+} [396], Co^{2+} [394, 395], Fe^{3+} [396], Ga^{3+} [394], La^{3+}[397–400], Zn^{2+} [401, 402], Mo^{6+} [403], Mo^{4+} [404], Sn^{2+} [405], Ta^{5+} [406], Ru^{4+} [407], F^{-} [392] and Br^{-}[408]. Much better results have been obtained recently by choosing a different dopent, namely yttrium [409]. The Y-doped LTO (Y concentration 4 at.%) delivered 141.3 mAh g^{-1} after 1800 cycles at 10*C* rate. Owing to these outstanding properties, LTO has been recognized since some time as a viable anode for Li-ion batteries, and the progress that have been reviewed in this section confirm this ability. In particular, due to safety considerations, LTO is well suited to HEV applications and in load-shedding. Therefore, batteries with LTO anode have been tested with all the cathodes that are envisioned for Li-ion batteries.

10.6.3 Ti-Nb Oxide

The research on new Ti-derived compounds still goes on. Recently, the Goodenough's group worked on $TiNb_2O_7$ (TNO), which crystallizes in a monoclinic layer structure [410]. After carbon-coating, this material a reversible capacity of 285 mAh g^{-1} was obtained and the voltage-capacity profile showed a plateau at 1.6 V. At *C*/5 and after ten cycles in the standard voltage range 1–2.5 V, the capacity retention was 98 % and a capacity 270 mAh g^{-1} was stable up to 20 cycles. The Nb^{4+}-doped carbon-coated TNO (C-$Ti_{0.9}Nb_{2.1}O_7$) gave the best results, with stable performance upon discharge at 2*C* and charge from 2*C* up to 600*C* rate. The safety and structural stability have not been tested, yet.

10.7 Oxides Based on Alloying/De-alloying Reaction

10.7.1 Si Oxides

Since silicon suffers from the huge change of volume upon lithiation-delithiation, SiO has been viewed as an alternative. SiO is a mixture of amorphous Si and amorphous silica. Lithium oxide (Li_2O) is generated during the first lithiation:

$$SiO + 2Li^{+} + 2e^{-} \rightarrow Li_2O + Si, \tag{10.6}$$

thus creating a microstructure in the active material such that Si nanodomains are embedded in the Li_2O matrix [411]. As a result, the Li_2O layers can act as buffer zones and thus suppress the side effects originating from the volume changes of Si. This reaction during the first lithiation also shows that the cycleability in the subsequent cycles is due to the silicon Si that is the only active species, giving reversible capacity via alloying/de-alloying reaction with Li in a matrix of lithium

silicates formed during the first discharge by the reaction between silica and Li. The study of the electrochemical reduction of SiO_2 in hard carbon has shown that SiO_2 is reduced to Si along with the formation of Li_2O and/or Li_4SiO_4 [412]. The works concerning the electrochemistry of SiO and its composites before 2010 have been published in [25]. Progress has still been done since then. Of course, SiO, just like Si and for the same reason, SiO is usually mixed with a conductive element to improve the electrical conductivity of the material, and this element is usually carbon, either by coating, or under the form of composites. The synthesis parameters of SiO, however, also play a role. In particular, disproportionated-SiO (d-SiO) powders obtained by heat-treatment of SiO at 1000 °C has been found to give the best electrochemical performance among the samples tested in terms of the initial Coulombic efficiency and cycle retention [413]. This material milled with graphite powder to obtain a nano-Si/SiO_x/graphite composite delivered a constant capacity of 600 mAh g^{-1} between the 10th cycle and the 200th cycle at rate of 100 mA g^{-1}.

SiO_x/Si composed of Si-suboxide and embedded Si nanocrystallites were prepared via a partial reduction reaction between ball-milled silicon monoxide and magnesium by high-energy mechanical milling [414]. After carbon-coating via a chemical vapor deposition process, the composite showed a stable reversible capacity of ca. 1250 mAh g^{-1} and excellent cycling stability with 90.9 % capacity retention on the 100th cycle versus the 6th one. Coating SiO with N-doped carbon (NC) improves the capacity at any *C*-rate, since it improves the electronic conductivity of the carbon coat. NC-SiO shows 955 mAh g^{-1} after 200 cycles when cycled at 1*C*, corresponding to a capacity retention of 92 % [415]. This result was obtained with SiO particles as large as 20 μm, giving evidence that the side effects (fracture, pulverization of micron-sized Si particles) upon the change in volume of Si have been avoided with SiO. We have already noticed in the previous section, including the section devoted to Si-anodes, that the porosity improves the electrochemical properties by increasing the effective surface area. This is also true for SiO-anodes. Carbon-coated porous SiO have shown an excellent capacity of 1490 mAh g^{-1} over 50 cycles at rate 0.1*C*, and stable capacities of 1100 and 920 mAh g^{-1} have been observed at 3 and 5*C*, respectively [416]. The SiO-carbon composite materials consisting of SiO, graphite, and carbon fiber with carbon coatings showed the smallest irreversible capacity at the first cycle and the best capacity retention among the other silicon-based materials examined, such as carbon-coated silicon, the one-to-one mixture of "SiO" and graphite, or one-to-one mixture of carbon-coated "SiO" and graphite [417]. Capacity of more than 85 % compared to capacities observed for initial ten cycles is retained after 100 cycles when the laminate-type cell with a positive electrode is examined in voltage ranging from 2.5 to 4.2 V. In a different work, Si–SiO_2-C composites have also been synthesized by ball milling the mixture of SiO, graphite, and coal pitch in the mass ratio mass ratio of 3:1.5:1.5, respectively, and subsequent heat treatment at 900 °C in inert atmosphere. This composite delivered a reversible Li-alloying/de-alloying capacity of 700 mAh g^{-1} and excellent cyclic stability even at about the 90th cycle at the current density of 100 mA g^{-1}. An even better result was obtained with a ball-milled SiO and carbon nanofiber (CNF) composite anode that delivered the same

capacity of 700 mAh g^{-1} after 200 cycles [418]. This result comes from the reduction of the irreversible capacity at the first cycle for the SiO/CNF composite electrode was reduced to 2 % by chemically pre-charging with a lithium film attached to the rim of the electrode. Silicon monoxide/graphite/multiwalled carbon nanotubes (SiO/G/CNTs) material prepared by ball milling followed by chemical vapor deposition method exhibited an initial specific discharge capacity of 790 mAh g^{-1} with a columbic efficiency of 65 %. After 100 cycles at a constant current density of 230 mA g^{-1}, a high reversible capacity of 495 mAh g^{-1} was still retained [419]. A novel SiO/graphene composite exhibited a high initial specific capacity of 2285 mAh g^{-1}, excellent cyclic performance of 890 mAh g^{-1} at 100th cycle and good rate capability, which was ascribed to the three-dimensional architecture of SiO/graphene nanocomposite [420].

A different approach comes from the consideration that the SiO_2 in disproportionated SiO has been considered as a main matrix phase and a cause of the initial irreversible reaction [421]. Hence the idea to reform this matrix phase to retain less irreversible electrochemical reactivity and more reinforced mechanical properties. This has been done in ref. [422], where a nanostructured $SiAl_{0.2}O$ composite material has been developed via mechanochemical synthesis. The compositional structure of the matrix is aluminosilica in which most of Si atoms are neighbored with two Al atoms over oxygen. This composite offered a capacity of 800 mAh g^{-1} over 100 cycles at a current density of 120 mA g^{-1}.

It should also be noted that attention should be taken to the fact that the performance of SiO-anodes depend importantly on the choice of binder, which makes difficult the quantitative comparison of the electrochemical performance between different works. The study of the electrochemical properties for different binders has been made by Komaba et al. [423] who showed that the electrochemical reversibility of SiO anodes is drastically improved by using poly(acrylic acid) (PAA) as the binder in comparison to the PVdF, sodium carboxymethyl cellulose (NaCMC), and poly(vinyl alcohol) PVA binders. Polyimide as binder was also found to give very good results [424]. A concern with SiO is the thermal instability due to the sudden exothermic peak in the region of 350–400 °C. This enthalpy peak, however, is importantly reduced (but not suppressed) by coating SiO with anatase TiO_2 [425]. This has been attributed to the thermal stability of lithiated TiO_2 and its SEI [279, 280].

Columnar-shape SiO_x nanoconifers were directly self-assembled on metallic $NiSi_x$ ($0.9 < x < 1$) nanowires by means of chemical vapor deposition technique [426]. The first discharge and charge capacities of these SiO_x nanoconifers were 4058 and 1737 mAh g^{-1} at the current density of 150 mA g^{-1}, which produce the irreversible capacity loss of 57 % at the very first cycle. After the first cycle, the SiO_x nanoconifer cell shows very high coulombic efficiency over 97 % for the subsequent cycles. After 20 cycles, the capacity is measured to be 1375 mAh g^{-1}, which corresponds to 80 % of the initial capacity. Then, its capacity is gradually degraded to about 800 mAh g^{-1} up to the 100th cycle. Other multi-composites have been recently synthesized. Carbon-coated SiO_x and PVdF binder was uniformly coated with Cr by ion beam sputtering [427]. The Cr coating was

found to improve the electrochemical performance of the electrode. The first charge capacity of the coated anode was 1127 mAh g^{-1} at *C*/10. The second discharge capacity was 517 mAh g^{-1}, and after 100 cycles at the *C*/10 rate, the capacity was still 517 mAh g^{-1}. Mechanically alloyed composite anode materials based on SiO–$Sn_xFe_yC_z$ have also been investigated, and the composition *x*, *y*, *z* adjusted to optimize the electrochemical properties [428]. The 50 wt% SiO–50 wt% $Sn_{30}Fe_{30}C_{40}$ composition exhibits high specific capacity (900 mAh g^{-1} at *C*/6 rate) with good cycle life up to 40 cycles, but the capacity decreases at subsequent cycles.

Contrary to the SiO, SiO_2 has not been considered as a competitor to sicon anodes. However, recent efforts have been made to improve the performance of silica. Hollow porous SiO_2 nanocubes prepared via a two-step hard-template process exhibited a reversible capacity of 919 mAh g^{-1} over 30 cycles at the current density of 100 mA g^{-1} between 3 and 0 V [429]. In the same way, SiO_2 nanotubes fabricated via a facile two step hard-template growth method exhibited a highly stable reversible capacity of 1266 mAh g^{-1} after 100 cycles with negligible capacity fading [430]. In both cases, the hollow morphology of the SiO_2 nanotubes or nanocubes accommodates the large volume expansion experienced by Si-based anodes during lithiation and promotes preservation of the solid electrolyte interphase layer.

10.7.2 GeO_2 and Germanates

GeO_2 has been studied since 10 years as a potential anode material [431]. During the first discharge reaction, an amorphous $Li_2O \cdot GeO_2$ phase forms at 0.65 V, and in the range 0.55–0.35 V, crystal structure destruction occurs to form the nano composite $Li_2O \cdot Ge$ and (LiGe). This is followed by the formation of the alloy, $Li_{4.2}Ge$ in the voltage range 0.35–0.05 V. As a result, a drastic capacity fading is observed due, at least partly, to the large change of volume of the unit cell resulting from the alloying/de-alloying reaction $Ge + 4.2Li^+ + 4.2e^- \leftrightarrow Li_{4.2}Ge$. A recent progress, however, has been achieved by using Ge with a conductive carbon coating [432]. GeO_2/Ge/C was prepared in a three steps process, starting with the synthesis of GeO_2 from hydrolysis of $GeCl_4$ and followed by carbon coating with acetylene gas, resulting in GeO_2/C. The last step was the reduction of GeO_2/C to GeO_2/Ge/C through heating at 650 °C. The composite showed high capacities of 1860 and 1680 mAh g^{-1}, at the current rates of 1*C* and 10*C*, respectively, with good cycling stability over 50 cycles at 0.5 discharge rate and 1*C* (2.1 A g^{-1}) charge rate. This improvement in the performance was attributed to the enhancement of the reversibility of the alloying/de-alloying reaction of GeO_2 with lithium by the carbon coating and the catalytic effect of Ge. Among the Ge-based compounds [433, 434], $LiGe_2(PO_4)_3$ has the most promising electrochemical properties. It adopts the Nasicon-type structure containing GeO_6 octahedra and PO_4 tetrahedra, while Li occupies the 3D channels. A reversible capacity of 460 mAh g^{-1} was obtained

when LGP was cycled in the voltage range 0.001–1.5 V at a current rate of 150 mA g^{-1}, and 92 % of the capacity was retained after 25 cycles. At a high current of 1500 mA g^{-1}, 77 % capacity retention was noted after 1000 cycles [433].

10.7.3 Sn Oxides

During the first discharge, SnO and SnO_2 undergo structural destruction (amorphization) and formation of nano Sn-metal dispersed in amorphous Li_2O according to the reactions:

$$SnO + 2Li^+ + 2e^- \leftrightarrow Sn + Li_2O, \tag{10.7}$$

$$SnO_2 + 4Li^+ + 4e^- \leftrightarrow Sn + 2Li_2O. \tag{10.8}$$

These two-phase reactions are irreversible and responsible for an irreversible loss of capacity during the first cycle. This is followed by the reversible reactions that contribute to the reversible capacity:

$$Sn + 4.4Li \leftrightarrow Li_{4,4}Sn. \tag{10.9}$$

Thus, the theoretical reversible capacities of SnO and SnO_2 are 875 and 782 mAh g^{-1}, respectively. The cycling performance is improved with respect to those of Sn metal, owing to the formation of nano-Li_2O that acts as a buffer during alloying/de-alloying of Sn (Eq. 10.9), thus maintaining the integrity of the Sn particles. Nevertheless, the problem of capacity fading has never been solved for SnO, despite the numerous efforts that have been reviewed in ref. [22]. The efforts today are focused on SnO_2 that has better electrochemical properties, also linked to the fact that it is the stable form of tin oxide. The optimum voltage range for the alloying-dealloying reaction of SnO_2 is 0.005–1 V vs. Li^0/Li^+. At higher cut-off voltage, SnO_x forms according to the reaction:

$$Sn + xLi_2O \leftrightarrow SnO_x + 2xLi^+ + 2xe^- (x < 2), \tag{10.10}$$

which invariably gives rise to a capacity fading because of the large change of volume that is associated to this reaction, in addition to the change of volume associated to the alloying-dealloying reaction of Sn in Eq. (10.9). Therefore, until recently, a capacity circa 1494 mAh g^{-1} associated to Eq. (10.10) could be observed only in the first cycles, and fades to the value associated to the reversible reaction (Eq. 10.9). That is why the theoretical capacity of SnO_2 is usually considered to be 782 mAh g^{-1}. The study of SnO_2 upon cycling has been performed by TEM experiments and discussed in detail in some papers [435, 436] and a review [437]. Again, we only refer to the previous reviews (see also [22]) for the studies prior 2009, and focus attention on more recent results. For SnO_2, like for any anode

nowadays, the material is always prepared at the nanoscale to improve the conductivity and optimize the capacity of the material to suffer the change of volume upon cycling without loss of structural integrity.

SnO_2 nanorod arrays of average 60 nm in diameter and 670 nm in length have been prepared on large-area flexible metallic collector substrates via a hydrothermal process [438]. A reversible capacity of 580 mAh g^{-1} after 100 cycles at the 0.1*C* rate (*C* was defined as 4.4 Li^+ per hour; 781 mA g^{-1}) and shows good rate capability (350 mAh g^{-1} at the 5*C* rate). The electrode was obtained by thoroughly mixing 75 wt% active materials, 15 wt% carbon black, and 10 wt% polyvinylidene fluoride (PVdF) in N-methyl-2-pyrrolidene (NMP) solvent. The addition of a large concentration of carbon is always beneficial to the electronic conductivity and acts as a buffer to facilitate the structural stabilization of the active material, but in a commercial battery the concentration of carbon in the electrolyte does not exceed 10 wt%. This is the amount of carbon that has been mixed with ultra-fine porous SnO_2 nanopowder (5 nm) synthesized by a simple, easily scaled-up molten salt method [439]. This electrode delivered a reversible capacity of 410 mAh g^{-1} after 100 cycles in the voltage range of 0.05–1.5 V at 0.1*C*. The reversible charge capacity at the 5 and 10*C* rates during the first cycles is about 400 and 300 mAh g^{-1}, respectively. This result is another example of the efficiency of the combination nano and porous, which we have already evidenced in the case of the Si anode. In the same way, mesoporous SnO_2 spheres in the range of 100–300 nm delivered 761 mAh g^{-1} capacity after 50 cycles at the current density of 200 mA g^{-1}. Even at 2 A g^{-1}, it retained 480 mAh g^{-1} after 50 cycles [440]. The self-assembly of tin dioxide (SnO_2) porous microspheres conducted via a surfactant-free onestep hydrothermal reaction delivered a stable capacity about 690 mAh g^{-1} after 50 cycles at a current density of 500 mA g^{-1}. These results are less spectacular than some others reported hereunder, in particular when combined with graphene, but this anode is also more scalable. Other morphologies have been explored. SnO_2 nanofibers consisting of orderly bonded nanoparticles have been obtained by thermal pyrolysis and oxidization of electrospun tin(II)2-ethylhexanoate/polyacrylonitrile (PAN) polymer nanofibers in air [441]. They delivered a reversible capacity of 446 mAh g^{-1} after 50 cycles at the 100 mAh g^{-1} rate and excellent rate capability of 477.7 mAh g^{-1} at 10*C* rate.

In the form of thin films, the best results have been obtained with Sn-Co-O and Sn-Mn-O films [442, 443]. In particular, at *C*/2 rate, the Sn-Co-O films delivered a reversible capacity of 734 mAh g^{-1}. Interestingly, this capacity increases to 845 mAh g^{-1} after 50 cycles. Such an increase upon cycling has been also observed in other SnO_2-anodes, and we shall return on this property when discussing the case of the SnO_2/N-doped graphene hybrid material.

SnO_2 hollow structures have been reviewed in ref. [53]. Such structures, however, failed to alliavate entirely the capacity fading associated to the large volume change upon cycling, and good results can be obtained only up to circa 30–50 cycles. Coating SnO_2 is another route that has been explored to improve the anode performance. Electrodes have been built with carbon-coated SnO_2 nanoparticles (6–10 nm-thick) prepared by hydrothermal process [444]. The as-prepared

SnO_2-carbon with 8 wt% carbon could deliver a capacity as high as 631 mAh g^{-1} even after 100 charge/discharge cycles at a current drain of 400 mA g^{-1}. This result is actually better than nanoparticles of SiO_2 embedded in 12 wt% carbon matrix [445] despite the porosity of the nanoparticles. More recently, interconnected ultrafine SnO_2–C core–shell (SnO_2-C) nanospheres have been successfully synthesized via a simple one-pot hydrothermal method and subsequent carbonization, giving rise to outstanding electrochemical properties [446]. Discharge capacity reaches as high as 1215 mAh g^{-1} after 200 cycles at a current density of 100 mA g^{-1}, giving evidence that the problem of the aging associated to the volume change associated to the reaction in Eq. (10.11) upon cycling has been solved. Even at 1600 mA g^{-1}, the capacity is still 520 mAh g^{-1} and can be recovered up to 1232 mAh g^{-1} if the current density is turned back to 100 mA g^{-1}. A carbon-coated SnO_2–NiO nanocomposite electrode exhibited a reversible capacity of about 529 mAh g^{-1} at 800 mA g^{-1}, and 265 mAh g^{-1} at 1600 mA g^{-1}, even after 500 cycles [447]. A larger capacity but with larger capacity fading has been obtained with nano-Si-coated nanotube SnO_2 with the composition 40:60 wt%. At 0.5*C* rate in the voltage range 0–1.2 V, this anode delivered an initial reversible capacity of 1800 mAh g^{-1}, slowly degrading to 1600 mAh g^{-1} after 90 cycles. This high capacity is due to the fact that both Si and SnO_2 are electrochemically active. However, since both Si and SnO_2 suffer large volume changes upon cycling, some deterioration of the tube wall structure was evidenced by TEM studies after 90 cycles at 2*C* rate. The best result, however, has been obtained in 2014 by coating SnO_2 with HfO_2 by atomic layer deposition [448]. This anode delivered a capacity of 853 mAh g^{-1} after 100 cycles at a current density of 150 mA g^{-1}. Finally, a novel high performance cathode material for LiBs has been developed by coating V_2O_5 on SnO_2 nanowires, utilizing the better conductivity of SnO_2 nanowires and the short diffusion distance of the thin V_2O_5 layer [449]. This material delivers a high power density of about 60 kW kg^{-1}, while the energy density remains 282 Wh kg^{-1}.

Different composites have been investigated, combining SnO_2 with a metallic compound, such as Cu [450, 451]. Good results have also been obtained with a conductive polymer: SnO_2 nanoparticles uniformly decorated polypyrrole (PPy) nanowires could deliver 690 mAh g^{-1} with 90 % capacity retention between the 2nd and the 80th cycle at current rate 690 mA g^{-1} in the voltage range 0.005–3 V [452]. However the best results have been obtained with carbon under different forms [453–459]. SnO_2/multiwalled carbon nanotubes (MWCNT) made of an uniform layer of SnO_2 nanocrystals with crystal size around 5 nm was deposited on the surface of the carbon nanotubes have been synthesized by the solvothermal method [456]. The reversible capacity was 709 mAh g^{-1} at the first cycle, stabilizing to circa 400 mAh g^{-1} over 100 cycles in the voltage range of 0.01–3 V at a constant current density of 100 mA g^{-1} based on the weight of the composite. A SnO_2/multiwalled carbon nanotubes core-shell structure prepared by wet chemical route delivered an initial discharge capacity and reversible capacity up to 1472.7 and 1020.5 mAh g^{-1}, respectively [456]. Moreover, the reversible capacity still remained above 720 mAh g^{-1} over 35 cycles in the voltage range 0.005–3 V, at

current density 0.2 mA cm^{-2}, and the capacity fading was only 0.8 % per cycle. This performance is attributed to the large surface area of the SnO_2 that is deposited on MWCNTs that are only 3 nm-thick, the high conductivity of the MWCNTs, and the fact that the MWCNTS avoid the agglomeration of the SnO_2 particles. The integrity of SnO_2 in SnO_2/carbon nanotubes is best evidenced by the good capacity retention observed in [458] with a reversible capacity of 540 mAh g^{-1} almost stable over 200 cycles at 0.5*C* rate. A novel ethylene glycol-mediated solvothermal-polyol route for synthesis of highly dispersed 3–5 nm SnO_2 nanocrystals on the surface of MWCNTs showed high rate capability and superior cycling stability with specific capacity of 500 mAh g^{-1} for up to 300 cycles [460]. The capacity of a Sn/SnO_2/MWCNT composite still delivers a capacity of 624 mAh g^{-1} after 100 cycles at *C*/4 rate [460].

Carbon–tin oxide (C-SnO_2) nanofibers have also been synthesized aiming to complement the long cycle life of carbon with the high lithium storage capacity of tin oxide [461]. The composite nanofibrous anodes are binder-free and have first discharge capacities of 788 mAh g^{-1} at 50 mA g^{-1} current density. After this pioneering work, this technology has been improved. In particular, SnO_2-electrodeposited porous carbon nanofibers (PCNF-SnO_2) composites that can maintain their structural stability during repeated charge–discharge cycling have been recently obtained [462]. After coating with amorphous carbon layers by chemical vapor deposition, this PCNF-SnO_2-C composite delivered capacities of 713, 568, 463, and 398 mAh g^{-1}, respectively, at 100, 200, 400, and 800 mA g^{-1} with high capacity retention of 78 % and large coulombic efficiency of 99.8 % at the 100th cycle. The charge capacity value returned to 600 mAh g^{-1} under a reduced current density of 100 mAh g^{-1} after undergoing these cycles at higher current densities. Remarkable results have been obtained owing to the fabrication of ultra-uniform SnO_x/carbon nanohybrids (denoted as U-SnO_x/C) by solvent replacement and subsequent electrospinning homogeneous dispersion of SnO_2 nanoparticles in polyacrylonitrile (PAN)/*N*, *N* dimethylformamide (DMF) solution [463]. The resulting 1D nanostructure U-SnO_x/C holds strong interaction between SnO_x and nitrogen containing carbon nanofiber matrix that effectively confine the uniformly embedded SnO_x. After 200 deep charge/discharge cycles at 0.5 A g^{-1} between 0.005 and 3 V vs. Li^0/Li^+, the U-SnO_x/C electrode still exhibits a reversible capacity of 608 mAh g^{-1}. As the current densities increase stepwise from 0.5 to 1, 2, 5, and 10 A g^{-1}, the electrode delivers stable capacities at each of these rates, varying from 663 to 518, 365, 175, and 80 mAh g^{-1}, respectively. In a different geometry, coaxial SnO_2-carbon hollow nanospheres (carbon content 32 wt%) cycling performance was evaluated between 2 V and 5 mV at a 0.8*C* rate (where C does not have the usual meaning but is defined as 625 mA g^{-1} in this work) stabilizes around 460 mAh g^{-1} for more than 100 cycles [464]. at a high rate of 4.8*C*, the hollow spheres can still deliver a stable capacity of about 210 mAh g^{-1}. We recover here the higher performance when the carbon content is larger.

The extensive and promising study of SnO_2/graphene composites started in 2010–2011 [465–473]. More recently, a composite made from graphene nanoribbons and SnO_2 nanoparticles has been synthesized [474]. This composite

exhibits reversible capacities of over 1520 and 1130 mAh g^{-1} for the first discharge and charge, respectively, which is more than the theoretical capacity of SnO_2. The reversible capacity retains 825 mAh g^{-1} at a current density of 100 mA g^{-1} with a coulombic efficiency of 98 % after 50 cycles. Further, the composite shows good power performance with a reversible capacity of ~580 mAh g^{-1} at the current density of 2 A g^{-1}. A composite made from graphene nanoribbons (GNRs) and SnO_2 nanoparticles has also been tested as an anode [474]. The SnO_2 nanoparticles of diameter 10 nm were synthesized via a simple chemical method, and they were uniformly distributed among the GNR structure layers. The GNRs were made by Na/K unzipping of MWCNTs. The reversible capacity retained 825 mAh g^{-1} at a current density of 100 mA g^{-1} with a coulombic efficiency of 98 % after 50 cycles. Further, the composite shows good power performance with a reversible capacity of 580 mAh g^{-1} at the current density of 2 A g^{-1}. The remarkable performance is due to the fact that GNRs are known to enhance lithium storage through edge effects [142, 474], and in addition can buffer the change of volume of the SnO_2 particles. This property of graphene that also avoids the formation of agglomerates has also been the motivation for using situ hydrazine monohydrate vapor reduction method for binding SnO_2 nanocrystals in graphene sheets by Sn–N bonding to obtain a SnO_2 nanocrystal/nitrogen-doped reduced graphene oxide hybrid material [475, 476]. The 4–5-nm thick SnO_2 particles were synthesized by hydrothermal process. After initial conditioning cycles, the coulombic efficiency increases to more than 97 %, and a stable capacity of 1021 mAh g^{-1} is obtained for the hybrid under a current density of 0.5 A g^{-1} in the voltage range of 0.005–3 V vs. Li^0/Li^+. In this work, the specific capacity values are calculated on the basis of the total mass of the SnO_2/N-doped graphene hybrid material, so that 1021 mAh g^{-1} indicates that a capacity of 1352 mAh g^{-1} for the SnO_2 nanocrystals, which is very close to the theoretical capacity of 1494 mAh g^{-1} for SnO_2 according to the reaction (Eq. 10.10). Moreover, the capacity increases upon cycling, to reach a reversible charge capacity as high as 1346 mAh g^{-1} after 500 cycles. This increase is attributed to the improvement of lithium ion accessibility in the hybrid during the cycling process, which leads to an increased accommodation behavior for lithium [477]. In any case, this large value of the capacity implies the additional capacity contribution from the conversion reaction of Sn with LiO_2 in Eq. (10.10). As the current densities increase from 0.5 to 1, 2, 5, 10, and 20 A g^{-1}, the electrode shows good capacity retention, varying from 1074 to 994, 915, 782, 631, and 417 mAh g^{-1}, respectively. When the current density returns to 0.5 A g^{-1}, the charge capacity reverts to 1034 mAh g^{-1}. The decrease of Sn L3-edge peak intensity observed in the hybrid compared with pure SnO_2 nanocrystals, suggesting a higher electron density at the Sn site in the hybrid, confirming the formation of Sn–N bonds in the hybrid, which is probably indispensable for the high and stable electrochemical performance of the hybrid. This is by far the best result obtained with SnO_2 anode, and the performance is remarkable, since the decrease of the size of the particles to 4–5 nm, plus the high flexibility of graphene, plus the fact that the Sn-N bonding has anchored the nanoparticles on the graphen sheets, avoiding the agglomeration of the particles all result in a hybrid that can accommodate the change of volume

associated to the reaction in Eq. (10.10) during long-term cycling (500 cycles). Most recently, a flexible graphene film decorated with spindle-like Fe_2O_3-SnO_2 nanoparticles was fabricated through vacuum filtration of Fe_2O_3-SnO_2 and GO mixing solution, followed by thermal reduction [478]. The core–shell structured Fe_2O_3-SnO_2 nanoparticles were synthesized through a facile hydrothermal route and uniformly dispersed between layered graphene nanosheets. This anode showed an excellent cycling performance of 1015 mAh g^{-1} even after 200 cycles. Another remarkable result has been obtained with SnO_2 hollow spheres (HS) 140–150 nm in dimensions embedded in graphene oxide (GO) nanosheets and enveloped by a sheath of a conducting polymer, poly(3,4-ethylenedioxythiophene) or PEDOT [479]. Owing to the synergy between the moderately high intrinsic electronic conductivity of GO nanosheets and the ability of PEDOT to buffer the volume change during repetitive Li^+ charge–discharge, the SnO_2 HS/GO/PEDOT hybrid capacity of 608 mAh g^{-1} at a current density of 100 mA g^{-1} to the hybrid, retained at the end of 150 cycles, and the latter value was 1248 mAh g^{-1} when the mass of only the SnO_2 HS in the hybrid was considered. The SnO_2 HS/GO/PEDOT hybrid also showed an excellent rate capability as a capacity of 381 mAh g^{-1} was attained even at a high current density of 2000 mA g^{-1}.

These results clearly upgrade SnO_2 as a prospective anode. The breakthrough in 2013 has been to succeed in the possibility to synthesize diverse nanostructures hybrids that avoid the structural degradation and thus the capacity fading associated to the large changes of volume during the reaction (4). However, it is doubtful that these anodes can be prepared at the industrial scale, because of the price: graphene is expensive, so is the synthesis process. Scaling-up the preparation of such nanostructured composites to quantities required for commercial development also remains challenging, and the key issue to insure the future success of this material as an anode.

10.8 Anodes Based on Conversion Reaction

The conversion or redox, reaction involves the formation and decomposition of Li_2O according to the so-called conversion-displacement reaction [480–483]:

$$MO + 2Li^+ \rightarrow M + Li_2O, \tag{10.11}$$

where M is a 3d-metal: $M =$ Mn, Fe, Co, Ni, Cu. Although electrochemically inert, Li_2O can participate indirectly to the anode performance by catalyzing the reaction. The first discharge reaction with Li metal involves the amorphization of the lattice, followed by the formation of nanoparticles of metal embedded into the Li_2O matrix. During charge, the re-formation of MO is a consequence of the decomposition of Li_2O. Therefore the voltage vs. capacity curve of the MO has the same features. A flat voltage region below 1 V, characteristic of a two-phase reaction due to the coexistence of M and Li_2O during the amorphization process, followed by a sloping

region down to 0.001 V characteristic of a single phase Li insertion reaction. Except FeO that crystallizes in a cubic defect structure, and CuO that adopts a distorted rock salt structure due to a Jahn-Teller (JT) distortion, the *M*O compounds adopt the cubic rock salt structure. The properties of these materials have been reviewed in the past [22], and again, attention is focused here on the progress that have been made in the recent years.

10.8.1 CoO

The theoretical capacity after Eq. (10.11) is 715 mAh g^{-1}, large enough to make CoO a promising anode. Indeed, an experimental capacity close to this value can be achieved at low rate. However, cobalt oxides suffer from poor capacity retention due to their low electrical conductivity and large volume swings during the charge–discharge process. Many efforts have been made to resolve the aforementioned problems by minimizing the volume change of cobalt oxide-based anodes, following the same attempts as in the case of the other anodes we have already reviewed.

In addition to the 3–6 nm thick SEI film that is formed during the first discharge process on the surface of CoO-based anodes, just as in the case of any other anode, a polymeric gel-type film of thickness 50–100 nm forms on the CoO electrode in the fully discharged state, which becomes thiner upon charging above 1.8 V, and fully disappears upon charging to 3 V. The decomposition of this polymer-gel layer is invoked to explain the observation of capacities much larger than the theoretical value (consumption of more than 2.0 mol of Li per mole of CoO noticed during the first discharge) [482]. In addition, the formation of higher oxides (Co_2O_3 and Co_3O_4) by the decomposition of Li_2O contributes to this increase of capacity [484]. This feature has also been invoked to explain the increase of capacity upon cycling that is commonly observed in cobalt oxide [484, 485]. However, we have also noted that this effect is more general as it has been also observed in SnO_2 anodes. In any case, the increase of capacity gives evidence of surface modification upon cycling, also the phenomena is not fully understood.

Reddy et al. have synthesized CoO particles with a coral-like structure by carbothermal reduction with Co_3O_4 as the precursor [486]. The 60th discharge cycle capacity is 895 mAh g^{-1} and the charge cycle capacity is 893 mAh g^{-1} (cycles in the voltage range 0.005–3 V, current density 60 mA g^{-1}). Only few experiments used doping to improve the conductivity of CoO, and thus the rate performance. Cu-doped h-CoO nanorods have been found to deliver a capacity of circa 1000 mAh g^{-1} between 30 and 50 cycles at current density of 72 mA g^{-1}; unfortunately, results at a higher current density have not been reported in this case [487]. Good results at higher *C* rates have been obtained by combining nanoscale and porosity. In particular, the synthesis of CoO porous nanowire arrays with robust mechanical adhesion to a flexible conductive Ti foil exhibit good high-rate capability at a rate of 1*C* (716 mA g^{-1}), 2*C* (1432 mA g^{-1}), 4*C* (2864 mA g^{-1}), and 6*C* (4296 mA g^{-1}), respectively [488]. Hierarchically self-assembled mesoporous CoO

nanodisks synthesized by the reaction of cobalt acetate tetrahydrate with hydrazine hydrate in solution followed by heat treatment in an inert atmosphere delivered a capacity of 1118.6 mAh g^{-1} after 50 discharge–charge cycles at 200 mA g^{-1} and excellent cycling performance: 633.5 mAh g^{-1} after 400 discharge–charge cycles at 800 mA g^{-1} [489]. This remarkable result has been attributed to the he unique hierarchical nanoarchitecture with highly beneficial combination of small primary particles with mesoporous, ultra-thin, large area 2D structure, and orderly self-stacked 3D structure. Actually, this performance is sufficient to make this material a promising anode for the next generation of Li-ion batteries, and this synthesis process is reported to be a facile, cheap, and easily scaled-up strategy, which may compensate for the fact that cobalt is expensive. Nevertheless, at higher *C*-rates, the association with a conductive material under the form of a coating or a composite, just as in the case of the other anode materials.

Among the hybrid coated CoO particles that have been studied, Co-CoO nanoparticles consisting of an unsealed hollow porous CoO shell with a metal Co core with a void between the core and the shell maintained a reversible capacity over 800 mAh g^{-1} after 50 cycles at current density 50 mAh g^{-1} in the potential window 0–3 V, with an initial coulombic efficiency of 74.2 % [490]. Almost the same result has been obtained with a carbon-decorated CoO sample, which also delivered 800 mAh g^{-1} after 70 cycles in the voltage range of 0.01–3.0 V at a current density of 100 mA g^{-1} [491]. CoO/$NiSi_x$ core–shell nanowire arrays synthesized through a facile CVD and subsequent RF-sputtering approach delivered a capacity stabilized at circa 600 mAh g^{-1} at 1C rate, and still 400 mAh g^{-1} at 44C rate [492], increasing importantly the rate capability of CoO anodes. The same group obtained a nano-architectured current collector by growing a 3D array of Cu nanorods onto a Cu foil via electrodeposition assisted by a porous alumina membrane that was subsequently dissolved. Then, the deposition of CoO onto Cu nanorods was achieved by controllable rf-sputtering, to form nanostructured hybrid CoO/Cu electrodes [493]. At a current density of 215 mA g^{-1} (0.3*C*), the anode delivered the first discharge capacity of 1362 mAh g^{-1} and the first charge capacity of 903 mAh g^{-1}. It corresponds to a coulombic efficiency of 66 %, which is a good result for a cobalt oxide where an important irreversible capacity loss is observed during the first cycle, because of the formation of the SEI plus the amorphisation of the particles. A stable reversible capacity of circa 900 mAh g^{-1} was still retained after 200 cycles. This is a remarkable result showing that the problem of the capacity fading arising from the aggregation of Co [441] has been overcome. At 10C rate, the capacity was still larger than 500 mAh g^{-1}. A self-assembled echinus-like nanostructure consisting of mesoporous CoO nanorod-carbon nanotube core–shell material showed high capacities (703–746 mAh g^{-1} in 200 cycles) and a long cycle life (0.029 % capacity loss per cycle) at a high current rate (3580 mA g^{-1}) [494].

We have already seen in the previous sections that graphene sheets have been widely used as an ideal matrix for anchoring a number of active anode materials to form unique nanocomposites. Such has been also the case with CoO. Until recently, however, these cobalt oxide/graphene nanocomposites have a relatively low

loading of cobalt oxides with an unsatisfactory dispersion on graphene nanosheets. Highly loaded, well-dispersed cobalt oxide/graphene nanocomposites have been synthesized only recently [495], by self-assembly in an oil-phase solution. This synthesis involved the thermal decomposition of cobalt acetylacetonate $Co(acac)_3$ by oleylamine in the presence of graphene (see Fig. 10.9). At a current density of 100 mA g^{-1}, CoO/graphene nanocomposites with mass ratio of 9:1 delivered a constant capacity 1400 mAh g^{-1} over 60 cycles. Even at a current density as high as 8 A g^{-1}, the nanocomposite electrode is capable of delivering a stable capacity of about 500 mAh g^{-1}. Indeed, these performances are better than some prior results on CoO-graphene nanosheets [496]. However, an even better result has been obtained by Peng et al. [497]. These authors designed a facile one-step ultrasonic way to synthesize CoO quantum dots (3–8 nm) (Qds) on graphene nanosheets (GNs) by using a metal carbonyl ($Co_4(CO)_{12}$) cluster as the precursor at ambient temperature. This anode delivered a reversible discharge capacity of 996 mAh g^{-1} at the second cycle at current rate of 50 mA g^{-1} (always in the voltage range 0–3 V), increasing with the cycle number to reach 1592 mAh g^{-1} at the 50th cycle. 1008 mAh g^{-1} was still retained after the 50th cycle at 1000 mA g^{-1}. Finally, CoO nanoparticles with size 5 nm densely anchored on graphene nanosheets maintained a stable capacity of 1015 mAh g^{-1} for 520 cycles with 100 % coulombic efficiency [498]. Indeed, transmission electron microscopy analysis has confirmed that the morphology of the CoO particles is preserved along these cycles. The recent improvement of the electrochemical properties give CoO the status of an attractive anode. Nevertheless, CoO suffers form the fact that cobalt is expensive and toxic. In addition, this oxide is not very stable, with a tendency to transform in the more stable spinel phase Co_3O_4.

10.8.2 NiO

Nickel oxide (NiO) is considered to be a promising electrode material for lithium ion batteries and supercapacitors due to its low cost, low toxicity, and superior safety. In addition, the density of NiO is 6.67 g cm^{-3}, leading to high volumetric energy density. For these reasons, considerable efforts have been made in the past to synthesize nano-NiO and its composites (for a review, see ref. [22]). Until 2010, however, the reversible capacities obtained on all kinds of NiO-anodes such as Ni/NiO core shell particles [499], NiO hollow nanospheres [500], NiO microspheres [501], NiO-carbon nanocomposites [502–504], NiO porous thin films [505–507], NiO/poly(3,4-ethylenedioxythiophene) (PEDOT) composites [508] were confined in the range 250–650 mAh g^{-1} after 20–50 cycles at current rate 0.1–1*C* in the voltage range 0.005–3 V. Similar results have been obtained in 2011 with Co-doped NiO Nanoflake arrays showing a capacity of 600 mAh g^{-1} after 50 discharge/charge cycles at low current density of 100 mA g^{-1}, and it retains 471 mAh g^{-1} when the current density is increased to 2 A g^{-1} [509]. The doping is important since the electrochemical performance is significantly improved with

respect to undoped ingle-crystalline NiO nanoflake arrays directly on copper substrates by a modified hydrothermal synthesis and post-annealing [510].

Another important parameter is the porosity. Mesoporous 8 nm-thick NiO particles with an effective surface area measured by BET equal to 96 $m^2\ g^{-1}$ could deliver a capacity of 680 mAh g^{-1} at 0.1*C* after 50 cycles [511]. Rapid progress has been obtained more recently. The promising nanoflake geometry has been confirmed, since NiO nanoflakes with mean size about 2 μm and mean thickness about 20 nm showed a charge and discharge capacities of 1015 and 990 mAh g^{-1}, respectively, after 50 cycles at a current density of 100 mA g^{-1}. There respective value at the 50th cycle at current rate 800 mAh g^{-1} are still 568 and 578 mAh g^{-1} [512]. Nanoporous NiO films directly grown on the foam Ni were fabricated via a facile ammonia-induced route, delivering rate capacity of 280 mAh g^{-1} at 10*C* rate and high reversible capacity of 543 mAh g^{-1} after 100 cycles at *C*/5 rate [513].

More recently, three-dimensional "curved" hierarchical mesoporous NiO nanomembranes made using a simple fabrication technique followed by a thermal oxidation process delivered a high capacity of 721 mAh g^{-1} at 1.5*C*, and a long lifetime of 1400 cycles, making them attractive for high power Li-ion batteries [514]. NiO microspheres with hierarchically porous structures have been synthesized via a facile thermal decomposition of $Ni(CH_3COO)_2 \cdot 4H_2O$ at 500 °C for 10 h [515]. This NiO anode retained a reversible capacity of 800 mAh g^{-1} after 100 cycles at a current density of 500 mA g^{-1}. This is the first report on the mass production of large-surface-area hierarchical architectures for NiO microspheres.

The ensemble of porous structures and one-dimensional shape has also proved to be efficient for NiO-anodes, just as in the other anodes. Mesoporous NiO nanotubes using filter paper as the template presented a reversible capacity of 600 mAh g^{-1} after 100 cycles at current rate 200 mA g^{-1} [516]. Hierarchically porous NiO microtubes synthesized by a high temperature calcination of $Ni(dmg)_2$ (dmg = dimethyl-glyoxime) microtubes obtained by a simple precipitation method of PEG 2000 (poly(ethylene glycol)) to hollow the nanostructure delivered a capacity ~640 mAh g^{-1} after 200 cycles at 1 A g^{-1}. The investigation of the rate capability revealed reversible capacities of 810, 780, 720, 630, and 520 mAh g^{-1} at 50, 200, 500, 1000, and 2000 mA g^{-1}. More importantly, a discharge capacity of 800 mAh g^{-1} can be recovered, while the current density back to 50 mA g^{-1}. It indicates the high stability of NiO microtubes [517].

Coating NiO has not been so successful. To avoid the barrier that a uniform coat of NiO with a metal could rise for the lithium transport, a composite NiO/Co-P has been synthesized with NiO particles 200 nm in size, and 30 nm thick granular plating particles of Co-P [518]. This anode delivered the discharge and charge capacities 560 and 540 mAh g^{-1}, respectively, after 50 cycles at current density 100 mA g^{-1}. At the higher current densities of 200, 500, and 1000 mA g^{-1}, the reversible capacities were 560, 480, and 270 mAh g^{-1}, respectively. Among NiO/Ni composites [519–521], the best results over 50 cycles have been found on self-supported nickel-coated NiO arrays prepared by chemical bath deposition of NiO flake arrays

followed by magnetron sputtering of nickel nanoparticles [521]. For a sputtering time of 60 s, the capacity delivered after 50 cycles at current density 100 mA g^{-1} was 648 mAh g^{-1}. The capacity delivered at current density of 2, 4, and 7.18 A g^{-1} was 455, 316, and 187 mAh g^{-1}, respectively. Composites of NiO with graphene have been synthesized to increase the conductivity, and thus the rate capability. Some of these composites [521–525] did not achieved better rate capability than the best results obtained for instance in [513] on nanopous films. Recent graphene/NiO composites, however, reached the goal. NiO-graphene sheet-on-sheet prepared by hydrothermal process delivered a capacity of 1030 mAh g^{-1} after 50 cycles at 0.1*C* rate, and still retained 492 mAh g^{-1} at 5*C* [526]. A better rate capability has been obtained with a NiO/graphene nanosheet hierarchical structure prepared by electrostatic interaction between positively charged NiO nanosheets and negatively charged graphene oxide in aqueous solution with a pH = 4 and then sintering in Ar gas atmosphere [527], still able to deliver a discharge capacity of 615 mAh g^{-1} at 4000 mA g^{-1} (5.6*C* rate). Reduced graphene oxide and nanosheet-based nickel oxide microsphere composite prepared by homogeneous coprecipitation and subsequent annealing showed a discharge capacity of 1041 mAh g^{-1} after 50 cycles at a current of 100 mA g^{-1}, and a good rate capacity with 727 mAh g^{-1} at a current of 1600 mA g^{-1}, but was not tested at higher rates [528]. Very recently, a powder consisting of core-shell-structured Ni/NiO nanocluster-decorated graphene (Ni/NiO-graphene) was synthesized by the following method: first, a crumpled graphene powder consisting of uniformly distributed Ni nanoclusters was prepared by one-pot spray pyrolysis. This powder was subsequently transformed into the Ni/NiO-graphene composite by annealing at 300 °C in air [529]. Used as an anode, this composite delivered 863 mAh g^{-1} after 300 cycles at 1500 mAh g^{-1}. Even at a high current density of 3000 mA g^{-1}, the discharge capacity of the Ni/NiO-graphene composite powder was as high as 700 mAh g^{-1} after 40 cycles. This is the best result that gives evidence of the remarkable progress achieved on such anodes since 2011, and also that the performance of the NiO/graphene composites depends very much on the synthesis and the architecture of the electrode. The remarkable performance of the Ni/NiO-graphene composite has been attributed to the role of the highly dispersed Ni nanoclusters resulting in the more complete decomposition of the Li_2O formed during the discharging process, plus the fact that these Ni clusters acted as highly conductive pathways for electron transfer during the conversion reaction of NiO with Li. This explains the benefit obtained by the introduction of the Ni metalin Ni/NiO-graphene composites. However, the results we have mentioned on NiO/graphene composites without Ni nanoclusters were already very promising, which means that the NiO can be anchored strongly on the graphene. This bonding has been understood by the analysis of by X-ray photoelectron spectroscopy, Fourier transform infrared spectroscopy, and Raman spectroscopy measurements, which have given evidence of the formation of oxygen bridges originating from the pinning of hydroxyl/epoxy of a Ni adatom on oxygenated graphite in experiments performed on NiO nanosheets/graphene composites [530].

10.8.3 CuO

CuO has also been considered as an attractive material as anode, because it is cheap and environmentally acceptable, in addition of good safety. Its theoretical capacity is only 375 mAh g^{-1}, but fortunately, the intermediate phase Cu_2O always formed during charging, with a theoretical capacity of 674 mAh g^{-1}, and it is thus this value that must be kept as the theoretical capacity for CuO-based anodes. However CuO, like any material for anode based on conversion reaction, suffers from a large volume expansion and dispersion of Cu particles in the Li_2O matrix during cycling, which leads to severe mechanical strain and rapid capacity decay. In addition, CuO has a low electronic conductivity, which is damageable to charge transfer. To reduce these limitations, CuO must be prepared under the form of a nanomaterial. Different forms have been investigated. Recently, the dependence of the performance of CuO anodes on the morphology has been studied [531]. As a result, the reversible capacity of the leaf-like CuO decreases during cycling, which confirms prior results found by different groups on CuO particles with this morphology [532, 533], and such is also the case for oatmeal-like CuO. The same holds for hierarchical structures [534]. The morphologies that avoid this capacity fading are the nanowires [535] and the nanoribbon arrays [536]. The nanowires delivered a capacity of 650 mAh g^{-1} stable over 100 cycles at *C*/2 rate in the voltage range 0.02–3 V. The nanoribbon arrays showed an initial reversible capacity of 500 mAh g^{-1} increasing slowly 610 mAh g^{-1} upon cycling to 275 cycles at *C*/2 rate in the same voltage range, and the capacity still retained at current density 800 mA g^{-1} was 332 mAh g^{-1}. Many other investigations have been made on different CuO anodes, reviewed for instance in [22], but failed to give better results. For comparison, CuO micrometer/nanoflake walls prepared using molten salt synthesis could at best with the optimum choice of the synthesis temperature (750 °C) deliver 620 mAh g^{-1} at the end of the 40th cycle [537]. To compete with the performance we have reported, a composite with a conductive material is needed, in particular with graphene that is the most conductive form of carbon. Still, however, the result is not guaranteed, since some of the graphene/CuO composites have not met this goal [538, 539], so that an optimized nanostructure design is needed even for such composites. Such a design has been proposed by Wang et al. [540], according to a synthesis process they have described in their paper. These authors obtained a basic urchin-like CuO cluster with CuO nanosheet substructure; these CuO flowers were uniformly separated by the surrounding graphene sheets. At current density 65 mAh g^{-1}, this CuO/graphene composite delivered a stabilized reversible capacity of 600 mAh g^{-1} over the 100 cycles that have been tested. The study of the rate capability has revealed that after ten cycles, this capacity decreased only slowly ten cycles; and this value was slowly lowered to 480, 320, and 150 mAh g^{-1} at the current densities 320, 1600, and 6400 mA g^{-1}, respectively. At this highest current density, the capacity was then found to be three times larger than that of graphite, while that of CuO vanishes. Another performing structure has been found by Zhou et al. who synthesized CuO hollow

nanoparticles/graphene-nanosheet composites using the Kirkendall-effect approach [541]. The reversible capacity of the material attains 640 mAh g^{-1} at 50 mA g^{-1} and the capacity retention is ca. 96 % when the current density is increased ten times. At 1 A g^{-1} (ca. 1.7*C*), the reversible capacity reaches 485 mAh g^{-1} and remains at 281 mAh g^{-1} after 500 cycles. Even better results have been obtained with a graphene nanosheet supported shuttle CuO nanostructure prepared by a facile low-temperature solution route [542]. At current density of 700 mAh g^{-1}, this composite retained a stable capacity of 826 mAh g^{-1} after 100 cycles. This capacity is even larger than the capacity of 771 mAh g^{-1} obtained at a lower current density of 70 mA g^{-1}. This higher capacity vs higher current has been also observed in other electrodes, and attributed to the fact that slow Li-ion reactions at a smaller current may lead to more serious electrode pulverization [543]. At least part of this cycling performance is attributable to the fact that the CuO nanoshuttles were distributed uniformly and wrapped well by the graphene nanosheets, another evidence of the importance of the design of the graphene/CuO composites to obtain a performing anode. To our knowledge, these are the best results obtained with CuO-based anodes. Other CuO/graphene composites that have been synthesized did not have this rate capability [525, 544].

The progress made these last 5 years on CuO-based anodes, especially when combined with graphene have reached the cyclability and rate capability that make this material challenging. Nevertheless, the best results are still obtained on composites that need proving that they can be prepared at an industrial scale, and at a reasonable price. Indeed, the research on such material might now focus on this aspect. For instance the very recent synthesis of mesoporous NiO microspheres by a simple method that is more scalable than prior synthesis of hollow structures give electrochemical that are less performant than the best CuO-graphene composites, but sufficient to fulfill the requirements in terms of capacity and rate capability to make it a promising anode. This is just an illustration of the fact that further studies on CuO-based anodes will be exciting in the near future.

10.8.4 MnO

Manganese oxides are also considered as potential anode materials with its high theoretical capacity of 755 mAh g^{-1}, and indeed, constant progress in the electrochemical properties of MnO-based anodes has been obtained in the recent years. The first results that were encouraging date from 2009, when a mixture of MnO and Mn_3O_4 confined to porous carbon nanofibers delivered an initial capacity of 785 mAh g^{-1}, stabilized to 600 mAh g^{-1} between 10 and 50 cycles at current density of 50 mA g^{-1} in the range 0.01–3 V [545]. MnO/C nanocomposites have also been prepared through a simple thermal decomposition of manganese benzoate precursor [546]. Good results have been obtained, but at the price of a large amount of carbon (10–18 wt%), to obtain a capacity in the range 600–680 mAh g^{-1} at a current rate of 100 mAh g^{-1}. More promising, carbon-coated MnO prepared by

ball-milling with sugar an pyrolysis at 600 °C in Ar atmosphere as found to deliver a reversible capacity of 650 mAh g^{-1} at 50 mA g^{-1} (0.08*C*) almost stable up to 150 cycles in the range 0.01–3 V, and could deliver 400 mAh g^{-1} at 400 mA g^{-1} [547]. Note this synthesis process is the same as the process of fabrication of some of the C-$LiFePO_4$ cathodes presently commercialized. In this case, however, the carbon coating is performed at circa 700 °C to obtain a better electronic conductivity of the carbon. This is then also the temperature that should be better used if it is not damageable to the MnO_2 powder. It is thus not clear whether or not the temperature of 600 °C used in this paper is the best choice. This same sintering temperature (600 °C) was used to coat MnO nanotubes with carbon, with C_2H_2 precursor [548], with a result that is comparable, since the capacity was nearly 500 mAh g^{-1} at a current density of 189 mA g^{-1}. However the capacity fading was not solved, since 18 % of the capacity was lost after 25 cycles. Other carbon-coated MnO_2 anodes where the coating was also obtained at 600 °C [549] gave a better cyclability, but less than in case the coating has been made at higher temperature. Carbon-coating of porous MnO microspheres obtained through chemical vapor deposition at 700 °C using toluene as precursor and argon as gas carrier gave better results, as the product delivered a capacity of ~700 mAh g^{-1} almost constant over 50 cycles at a rate of 50 mA g^{-1}; the capacity retained at 1600 mA g^{-1} was 400 mA g^{-1} [550]. Another example is provided by 20 nm-thick MnO particles coated with carbon at 700 °C, using glucose as both the source of carbon and the reducing agent [551]. This anode made from 10.7 wt%-carbon-coated MnO/C shows very stable cycling performance with a high reversible capacity of 939.3 mAh g^{-1} after 30 cycles at *C*/10. This electrode also shows favorable rate performance with specific capacities of 726.7, 686.8, 633.0, and 587.9 mAh g^{-1} at 1, 2, 5, and 10*C*, respectively. On another hand, carbon-coated nanorods prepared at a sintering temperature as small as 500 °C using block copolymer F127 as carbon source has a capacity that decreases almost linearly from 800 to 600 mAh g^{-1} between the second and the 40th cycle at charge current rate of 200 mA g^{-1} [552].

These different results are consistent with our analysis that the conductivity of the carbon layer increases with the sintering temperature and should be raised to 700 °C whenever it is possible. However, this is not the only pertinent parameter since the electrochemical properties depend importantly on the porosity of the particles. This is best evidenced by the good results obtained with porous carbon-coated MnO nanotubes, despite the fact that the coating has been obtained at 500 °C using glucose as the precursor [553]. This porous MnO/C nanotubes could deliver a reversible capacity as high as 763.3 mAh g^{-1} after 100 cycles at a charge/discharge current density of 100 mA g^{-1} (0.13*C*; $1C = 755.6$ mA g^{-1}), and 618.3 mAh g^{-1} after 200 cycles at a rate of 0.66*C*. One explanation might come from the investigation of the structure of the carbon layer coating MnO_2 nanoplates [554]. The ratio of the intensities of D over G bands of the carbon in the Raman spectra was found almost constant when the temperature is raised above 550 °C in the range 550–650 °C so that the graphitic degree of carbon increases with temperature up to 550 °C, but does not change significantly at higher temperature. Indeed, the capacity obtained with the nanoplates with a 8 nm-thick carbon layer, synthesized

at 550 °C during 10 h, was 563 mAh g^{-1} after 30 cycles at a current density of 200 mA g^{-1}. Unfortunately, the cycling life was limited to this small number of cycles. Another example is given by the good results obtained without carbon coating on interconnected porous MnO nanoflakes on nickel foam [555]. A high reversible capacity of 568.7 mAh g^{-1} was obtained at a current density of 246 mA g^{-1} for the second discharge. It retained a capacity of 708.4 mAh g^{-1} at the 200th charge–discharge cycle after cycling with various current densities up to 2460 mA g^{-1} and delivered a capacity of 376 mAh g^{-1} at a current density as high as 2460 mA g^{-1}. This good result is due to the combination of two features. One is the beneficial effect of the porosity. Secondly, the architecture of active material grown directly on metals provides an efficient electron transport channel between the active material and the current collector of metals, which compensates for the absence of coating by conducting carbon.

Inspired by the distinctive features of natural microalgae, a biotemplating method has been developed to synthesize hollow microspheres of MnO/C, which exhibited a specific capacity of 700 mAh g^{-1} after 50 cycles at 100 mA g^{-1} [556]. The high capacity was partially due to the porous carbon matrix. Very recently, hollow nanospheres of MnO have been synthesized, using carbon nanospheres as a template and a reagent [557]. The as-prepared MnO nanospheres were built by aggregated nanoparticles, giving a thin and porous shell. The corresponding anode delivered a reversible capacity of 1515 mAh g^{-1} after 60 cycles at 100 mA g^{-1}. Even at 500 mA g^{-1}, the capacity retained after 100 cycles was still 1050 mAh g^{-1}, illustrating the performance that can be obtained when combining hollow structure, surface porosity, and nanoscale size. This also explains the very good results obtained with MnO nanocrystals embedded in carbon nanofibers (MnO/CNFs), obtained with a porous structure through an electrospinning process [558]. The as-formed MnO/CNFs have diameters of 100–200 nm and lengths up to several millimeters. Until 100 cycles at 100 mA g^{-1}, the discharge capacity of these MnO/CNFs was as high as 1082 mAh g^{-1} with a coulombic efficiency of 99 %, indicating an excellent cyclic performance. Even at a high current density of 1000 mA g^{-1}, the specific capacity is up to 575 mAh g^{-1} after 200 cycles. In addition, the MnO/CNFs electrode cycled at a high current density of 2000 mA g^{-1} presents similar electrochemical performances, which is better than that of previously reported MnO_2/CNTs.

As stated before, graphene uses to be the best form of carbon to associate with an active anode element. This is confirmed also in the case of MnO. A hybrid material consisting of MnO nanocrystals grown on conductive graphene nanosheets exhibits a reversible capacity as high as 2014.1 mAh g^{-1} after 150 discharge/charge cycles at 200 mA g^{-1}, excellent rate capability (625.8 mAh g^{-1} at 3000 mA g^{-1}), and superior cyclability (843.3 mAh g^{-1} even after 400 discharge/charge cycles at 2000 mA g^{-1} with only 0.01 % capacity loss per cycle) [559]. This is to our knowledge, the best performance in terms of rate capacity and cyclability obtained with MnO, which illustrates the constant progress in the synthesis of MnO-graphene composites since 2011 [560–564].

10.8.5 Oxides with Spinel Structure

Many of these oxides have been studied and share common features [22] illustrated in Fig. 10.10. The first discharge reaction may involve Li intercalation into the lattice (single-phase reaction) (Fig. 10.10), followed by crystal structure destruction (amorphization), and finally formation of the respective nanosized metal particles via a two-phase reaction. These three steps correspond to the regions labeled a, b, c, respectively in Fig. 10.10a.

10.8.5.1 Co_3O_4

The theoretical capacity of Co_3O_4 according to the conversion reaction is 890 mAh g^{-1}, and has thus attracted attention. In addition, this is the most stable

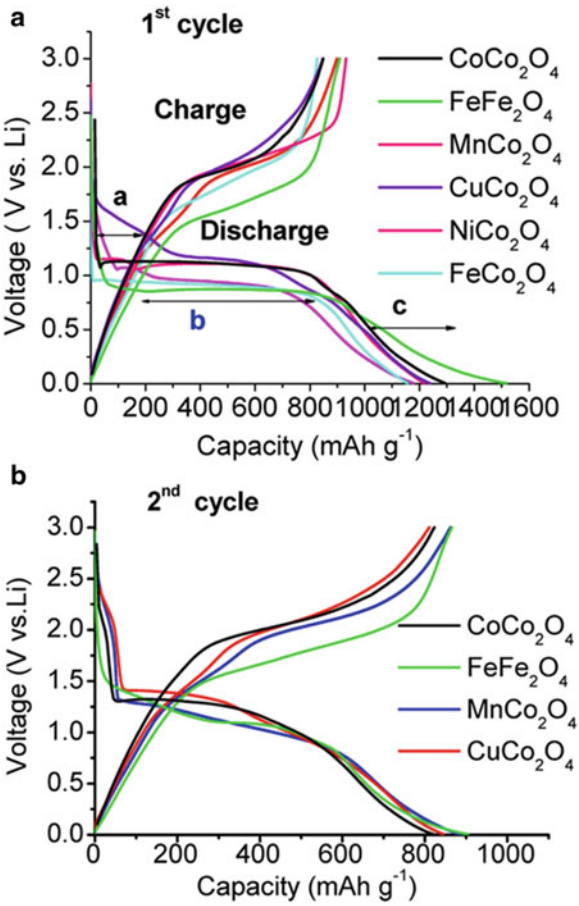

Fig. 10.10 Galvanostatic discharge–charge cycling curves of AB_2O_4 (MM'_2O_4) (A = Co, Fe, Cu, Ni, or Mn, B = Co or Fe). (**a**) First cycle and (**b**) second cycle cycled in the voltage range 0.005–3.0 V at current 60 mA g^{-1}. ACo_2O_4 with A = Co, Cu, Mn prepared by molten salt method at 280 °C; particle size is on the order of submicrometer; A = Ni or Fe (urea combustion method) and Fe_3O_4 carbothermal reduction method. For comparison, binary spinel (Co_3O_4 and Fe_3O_4) discharge–charge cycling curves are also shown

Table 10.1 Comparison of electrochemical performance of Co_3O_4 as anode material for LiB (from ref. [5])

Materials	Current density (mA g^{-1})	Initial charge capacity (mAh g^{-1})	Initial coulombic efficiency (%)	References
Co_3O_4 nanowires	100	892	80	[572]
Needle-like Co_3O_4	50	950	58.7	[573]
Co_3O_4 nanocages	50	741	73.5	[574]
Co_3O_4 nanosheets	150	1031	61	[571]
Network-like Co_3O_4	100	1214	60	[575]

cobalt oxide, so that it is much easier to prepare it than CoO or Co_2O_3, and we can thus expect a stronger structural stability favoring the cycling life. Nevertheless, the large change of volume during the redox reaction implies the necessity of using nano-sized particles like in the case of CoO, so that many efforts have been made to prepare Co_3O_4 under different nano-morphologies: nanowires [565, 566], nanotubes [567, 568], nanobelts [569], nanocapsules [570], nanosheets [571]. A comparison of the first charge and discharge capacities between different morphologies [572–575] has been discussed in ref. [575] and are summarized in Table 10.1. Among the simplest nanostructures, Co_3O_4 nanoparticles synthesized by the thermal decomposition of nanoparticles of cobalt-based Prussian blue analogues at 550 °C could deliver a capacity of 970 mAh g^{-1} after 30 cycles at a current density of 50 mA g^{-1} [574]. This capacity is larger than theoretical, a phenomenon often observed in nano-sized anode materials, owing to the additional contribution of lithium available on the surface sites, a general feature that applies to any anode material, or also the contribution of the polymeric layer that is more specific to Co-based anodes, already discussed for CoO-anodes.

The Co_3O_4-graphene nanosheets have not reached the best electrochemical activities we have reviewed for CoO-graphene. The results include a capacity sweeping from 800 mAh g^{-1} (second cycle) to 1000 mAh g^{-1} after 70 cycles at current rate 74 mAh g^{-1} [576], a capacity of 935 mAh g^{-1} after 30 cycles at current density 50 mA g^{-1} [143], a capacity of 740 mAh g^{-1} after 60 cycles [577], 640 mAh g^{-1} after 50 cycles [578], or ca. 1000 mAh g^{-1} after 50 cycles at current density 50 mA g^{-1} [579]. The synthesis of free-standing one-dimensional anode elements grown directly on conducting substrates in a controlled manner is an important issue to support the large changes of volume without affecting the integrity of the anode. In the particular case of Co_3O_4 the efforts include the synthesis of well-aligned rhombus-shaped Co_3O_4 nanorod arrays grown directly on nickel foil via fluorine-mediated synthesis though a hydrothermal method [580]. These nanorods exhibit the combined properties of meso-porosity and quasi-single-crystalline structure, and meanwhile, exhibit robust mechanical

adhesion to the nickel foil. This anode delivered a reversible capacity of circa 1000 mAh g^{-1} between the second and the 20th cycle at 1*C* rate in the voltage range 0.005–3 V. The combined effects of porosity and crystalline structure are also evidenced by mesoporous and single-crystal Co_3O_4 nanoplates (30 nm in thickness, 1 μm in width) with large surface area (118.6 m^2 g^{-1}) and small average pore size (4.7 nm) [581]. This anode delivered 1000 mAh g^{-1} after 30 cycles at 0.2*C*, corresponding to a current density of 178 mAh g^{-1}. The rate capability however is limited, as this anode delivered only 750 mAh g^{-1} at 1*C* rate instead of 1000 mAh g^{-1} in ref. [580]. The higher rate capability obtained in ref. [580] may be attributable to the fact that one-dimensional structure (nanorods) can better accommodate the volume change upon cycling than the geometry used in ref. [580] (plate-like particles). Coating nano-Co_3O_4 has also been tried to improve the electrochemical properties. Network-like Ppy-coated Co_3O_4 particles delivered a reversible capacity of circa 1000 mAh g^{-1} almost constant between the second and the 50th cycle at current density 100 mA g^{-1} [575].

Porous hollow architectures are well performing to accommodate the large change of volume upon cycling. The most popular method used for Co_3O_4 has been the templating approach [582, 583]. However, these methods usually need strict experimental conditions or sophisticated post-treatment (such as removal of the template, selective etching in an appropriate solvent and cumbersome retreatment process), which not only introduce impurities but also increase the cost. More importantly, those methods are not suitable for large-scale production. Recently, however, a simple and scalable coordination-derived method for the synthesis of porous Co_3O_4 hollow nanospheres has been found [584]. At a current density of 100 mA g^{-1}, the capacity of the anode prepared with these porous hollow nanospheres was maintained almost constant at circa 1100 mAh g^{-1} between the 10th and the 60th cycles. Unfortunately, the capacity decreases at larger cycles: nearly 1000 mAh g^{-1} at the 80th cycle, 820 mAh g^{-1} at the 100th cycle, which is still a good results, but shows the difficulty to overcome the aging of the anode. The rate performance has been investigated by measuring the capacity over ten cycles at successive current densities 100, 200, 400, 600, and 1000 mA g^{-1}. At this highest current density, the capacity was 543 mAh g^{-1}. When returning to a current density of 100 mAh g^{-1}, however, the capacity recovered was 802 mAh g^{-1}, smaller than the 1100 mA h recorded before, so that the anode has aged significantly along the process. This fading of the capacity has been solved recently with anode built with porous Co_3O_4 hexagonal nanodisks (20 nm in thickness, surface area 60 m^2 g^{-1}) prepared with a template-free hydrothermal method [585]. After 100 cycles at current density 100 mA g^{-1} in the usual voltage range 0.01–3 V, the capacity reached 1180 mAh g^{-1}, while the initial capacity was 1417 mAh g^{-1}. The rate capability was investigated by measuring the capacity over 50 cycles at successive current densities 500, 1000, 2000, 4000, and 8000 mA g^{-1}, followed by a final return to 500 mA g^{-1}. At this highest current density 8000 mA g^{-1}, the capacity was still close to 300 mA g^{-1}. Most of all, after returning to the current to 500 mA g^{-1}, i.e. after a total of 250 cycles at these different rates, a capacity of 1086 mAh g^{-1} was restored with almost 100 % coulombic efficiency.

Hierarchical urchin-like Co_3O_4 spheres (5–8 μm in diameter) consisting of many nanowires and nanoparticles (10–50 nm) also possess very good cycling stability (1190 mAh g^{-1} after 100 cycles at *C*/10) and excellent rate capability (796 mAh g^{-1} at 5*C* and 433 mAh g^{-1} at 10*C*, i.e. at current density 8900 mA g^{-1}) [586]. Moreover, the preparation is also template-free, which makes the synthesis process more scalable. Some other shapes are also promising, such as porous hollow multishelled Co_3O_4 microspheres, which delivered 1616 mAh g^{-1} in the 30th cycle [587], but unfortunately, the cyclability has not been explored at more cycles. We also regret that a Co_3O_4 nanobelt array (20–50 nm in width with needle-like tips) prepared with excellent rate capability (530 and 320 mAh g^{-1} after 30 cycles at 15 and 30*C*, respectively) has not been tested beyond 30 cycles [588].

These outstanding recent results, however, should not mask show how difficult it is to improve the cyclability of Co_3O_4. Capacity retention larger than 90 % between the second and the 100th cycle usually does not reach 90 %. Apart the results we have reported above, this goal has been achieved with a graphene-encapsuled Co_3O_4 (amount of Co_3O_4: 91.5 wt%) composite obtained by co-assembly between negatively charged graphene oxide and positively charged oxide nanoparticles. The process is driven by the mutual electrostatic interactions of the two species, and is followed by chemical reduction. The resulting GE–MO possesses flexible and ultrathin graphene shells that effectively enwrap the oxide nanoparticles. This GE-MO delivered a reversible capacity of 1100 mAh g^{-1} with a capacity retention of 91 % between the 2nd and the 130th cycles at current density of 74 mAh g^{-1}, a result that turns out to be significantly better than the results obtained with the standard Co_3O_4/graphene composites where metal oxides are distributed onto the surface of graphene or between the graphene layers. We can also note that porous polyhedral and fusiform Co_3O_4 powders synthesized through the hydrothermal method have shown good capacity rate and good capacity retention at the scale of 70 cycles [589]. They delivered circa 1350 mAh g^{-1} initial discharge capacity, with capacity retention 92 % at 0.1*C* after 70 cycles. The rate capability was better with fusiform particles, in which case the spindles (2.0–5.0 μm in length, 0.5–2.0 μm in width) are composed of irregular nanoparticles (20–200 nm in diameter, 20–40 nm in thickness), which delivered 93.8, 90.1, and 98.9 % of the second discharge capacities after 70 cycles at 0.5, 1, and 2*C*, respectively. Hierarchical heterostructures composed of anatase TiO_2 nanofibers and secondary Co_3O_4 nanosheets with porous surface have been synthesized [590]. As an anode, this composite delivered a high reversible capacity of 632.5 mAh g^{-1} and 95.3 % capacity retention over 480 cycles. In addition, a good rate capability has been observed owing to the TiO_2 component, with capacities of 475.8 and 449.5 mAh g^{-1} at current densities of 400 and 1000 mA g^{-1}, respectively.

To conclude, the difficulty to build a Co_3O_4 with a good cycling life and good rate capability explains that this problem has been solved only recently. The major improvements the last 2 or 3 years now makes possible the fabrication of Co_3O_4-based anodes that deliver capacities the order of 1000 mAh g^{-1} at 100–200 cycles even at high rates, and most of all, some of the synthesis processes are scalable. Therefore, Co_3O_4 remains a promising material as a future anode for Li-ion

batteries, while most of the reviews published on the subject few years ago were not optimistic on its future. Nevertheless, the fact that cobalt is expensive and not environmentally friendly remains a limitation.

10.8.5.2 Fe_3O_4

Fe_3O_4 has some advantages that make it a promising anode. The theoretical reversible capacity is high (928 mAh g^{-1}), it is abundant as it occurs in nature as the mineral magnetite, it is nontoxic; its low cost and high corrosion resistance are other characteristics. The limits come, as usual with all the anode elements based on conversion reactions, the degradation of the battery coming from the large change of volume (200 %) upon cycling. In addition, it is not so simple to prepare the material free from impurity, due to the presence of Fe^{2+} (in addition to Fe^{3+}), while iron likes to be in the III valence state, so that there is a tendency with Fe_3O_4 to contain Fe_2O_3 impurity. This is the same problem we met in the preparation of the $LiFePO_4$ cathode element (see Chap. 8). In the present case, however, the presence of Fe_2O_3 is not dramatic, since Fe_2O_3 is itself a high capacity electro-active materials and undergoes a similar kind of metallic reduction i.e. conversion reaction, as we shall see in a subsequent section.

A lot of efforts have been made on the synthesis of Fe_3O_4 and C-Fe_3O_4 composites under different forms (see ref. [591] for a review), in parallel with the same efforts made on the synthesis of C-$LiFePO_4$. Without carbon coating, nanoparticles usually show important capacity fading [592] and carbon coating, or formation of Fe_3O_4/carbon composites has been considered as necessary to facilitate the charge transfer. Without carbon coat, particles 200 nm in size could still deliver 1000 mAh g^{-1}, but the test has been carried out on 40 cycles only [593]. An intermediate situation is provided by recent experiments on clusters of mesoporous 11–12 nm sized nanoparticles, with carbon-coating through bottom-up self assembly approach [594]. The anode could deliver a capacity of 800 mAh g^{-1} over 100 cycles, but still an important decrease of capacity is observed when increasing the rate. In addition, the carbon must be conducting, so that the carbon must be coated at a high temperature (larger than 600 °C, as already discussed in the case of the chromium spinel in the previous section, or in the case of $LiFePO_4$, as discussed in Chap. 8). For instance, carbon deposited at 400 °C non intentionally owing to the presence of carbon in the precursors during the synthesis of monodisperse mesoporous particles was of little help [595]. Due to their high specific surface area (122.3 m^2 g^{-1}) the initial discharge capacity is vey large (1307 mAh g^{-1}), but the capacity fading remained important (capacity reduced to 450 mAh g^{-1} after 110 cycles at 0.2*C* rate).

The combination of hollow structures that accommodate more easily the changes of volume upon cycling, porosity that increases the surface contact with the electrolyte, and graphene that facilitates the electron conduction and thus the charge transfer has also been experimented on Fe_3O_4. Flexible free-standing (binder-less) hollow Fe_3O_4/graphene (39.6 wt% graphene) hybrid films, fabricated

through vacuum filtration and thermal reduction processes, in which graphene formed a three-dimensional conductive network, with hollow and porous Fe_3O_4 spindles being captured and distributed homogeneously has been fabricated. The anode exhibited a high specific capacity of 1400, 940, and 660 mAh g^{-1} after 50 cycles in the voltage range 0.01–3 V, at current densities 100, 200, and 500 mA g^{-1}, respectively [596]. Yet, no capacity loss was observed at the 50th cycle where the experiments have been stopped, which suggests excellent capacity retention over a larger number of cycles. The synthesis of Fe_3O_4 nanoparticles grafted on graphene usually requires the use of surfactants and solvents to avoid the aggregation of the particles. Their introduction inevitably makes the solid–liquid separation more complex. A new method to synthesize a Fe_3O_4-graphene has been proposed recently [597]. First, the precursor was synthesized through the decomposition of ferric nitrate in the presence of graphene oxide in the mixed solvent of CO_2-expanded ethanol. Then, the precursor was converted to the Fe_3O_4-graphene composite via thermal treatment in N_2 atmosphere. With the help of the CO_2–expanded ethanol, Fe_3O_4 nanoparticles were coated on the surface of GN completely and uniformly with high loading. The resulting Fe_3O_4-graphene composite with 25 wt% graphene delivered a capacity of 826 mAh g^{-1} after 100 cycles at current density of 1 A g^{-1}, almost constant after the two first cycles. At a high current density of 5 A g^{-1}, the composite was still able to deliver a capacity of 460 mAh g^{-1}. This rate capability is better than another composite graphene nanoscroll (GNS)-Fe_3O_4 nanoparticles, where GNS is a spirally wrapped two-dimensional (2D) graphene sheet (GS) with a 1D tubular structure wrapping Fe_3O_4 nanoparticle [598]. Although this composite showed a very large capacity at 0.1 rate (ca. 1100 mA h after 50 cycles), it only retained 300 mA g^{-1} at 5 A g^{-1}. A peculiar nanoarchitecture obtained by coating copper nanoribbons with Fe_3O_4 has given very good anode properties [599]. Here, a CuO nanoribbons array (NRA) was prepared by using a one-step oxidation of Cu sheet in alkaline solution, and a Cu NRA on copper substrate was fabricated by electrochemical reduction of CuO NRA. Then, 3D nanostructured Fe_3O_4 was fabricated by electrodeposition of Fe_3O_4 nanoparticles on the Cu NRA. Used as an anode, this 3D-architecture delivered a reversible capacity of 870 mAh g^{-1} after 280 cycles at a current density of 385 mA g^{-1} (0.42*C*). The capacity retained at high rate of 9*C* (8000 mAh g^{-1}) was still 231 mAh g^{-1}.

10.8.5.3 Mn_3O_4

The energy density of Mn_3O_4 is expected to be larger than those of Co_3O_4 and the Fe_3O_4 spinels because of the lower operational voltage of Mn (1.2 V), and the high theoretical capacity of 936 mAh g^{-1}. Until recently, however, the results obtained with Mn_3O_4 were not competitive with the performance of the other spinel compounds, unless it entered the formation of a composite. Among the best results, spongelike nanosized Mn_3O_4 exhibited a stabilized reversible capacity of about 800 mAh g^{-1} after 40 charge–discharge cycles at a current rate of *C*/4 [600].

Recently, however, the interest in Mn_3O_4 has been renewed, following the fabrication of porous nanorods fabricated through the decomposition of MnOOH nanorods with a high BET surface area of 27.6 $m^2\ g^{-1}$ and a narrow pore size distribution of 3.9 nm [601]. A specific capacity of 901.5 mAh g^{-1} at a current density of 500 mA g^{-1} was retained with long cycling stability (coulombic efficiency of 99.3 % after 150 cycles) and high rate capability (387.5 mAh g^{-1} at 2000 mA g^{-1}). This performance is better than the Mn_3O_4-carbon composites, such as Mn_3O_4 nanocrystals anchored on multiwalled carbon nanotubes (592 mAh g^{-1} after 50 cycles at a current density of 100 mAh g^{-1}) [602] and Mn_3O_4-ordered mesoporous carbon (802 mAh g^{-1} after 50 cycles at a current density of 100 mAh g^{-1}) [603], or Mn_3O_4/reduced graphene oxide composite and Mn_3O_4/graphene-platelets composite (675 and 725 mAh g^{-1} after 100 cycles at 75 mAh g^{-1}, respectively) [604]. The improved performance of the porous nanorods in ref. [601] illustrates the fact that the composite architecture either with graphene or with carbon nanotubes or with any other material is not the only parameter that needs to be taken into consideration, and the porosity of the active Mn_3O_4 nanoparticles is a key parameter.

10.8.6 Oxides with the Corundum Structure: M_2O_3 (M = Fe, Cr, Mn)

10.8.6.1 γ-Fe_2O_3

This compound is cheap material, since it naturally occurs as the mineral hematite. In addition, it is stable, since iron is trivalent, and its theoretical capacity is large as 1005 mAh g^{-1}. These features explain that a huge amount of works has been done to optimize the preparation of γ-Fe_2O_3 as a potential anode for LiBs, which have been reviewed for instance in ref. [22]. We just recall here that the conversion reaction has been demonstrated by the first charge–discharge profile in the range 0–3 V (see for instance [605]), which indicates Li intercalation to give first $Li_2(Fe_2O_3)$ at 1.2 V vs. Li^0/Li^+, followed by amorphisation at 0.75 V by an additional consumption 4 mol of Li to yield Fe^0 and Li_2O via the two-phase reaction. Therefore, the safety of Fe_2O_3 is much better than carbon materials due to the higher voltage plateau for Li ion lithiation, avoiding appearing of lithium dendrite. The first Li extraction profile up to 3 V indicates the conversion reaction to give FeO or Fe_2O_3, as shown by the voltage plateau at 2.1 V. The best results have been obtained with mesoporous particles, a general trend with materials for anodes based on conversion reactions as already shown in previous sections. As soon as in 2007, porous nanoparticles 25 nm in size were found to deliver a reversible capacity of 1000 mAh g^{-1} over 100 cycles at 100 mA g^{-1} with 99 % capacity retention [606]. Then, the efforts have been focused on the improvement of the rate capacity. Again focusing on the progress that has been achieved in the recent years we find that many γ-Fe_2O_3 materials can now accommodate the large variation of volume upon cycling.

An effective, inexpensive, and large-scale production approach to the synthesis of Fe_2O_3 nanoparticles with a favorable configuration that 5 nm iron oxide domains in diameter assembled into a mesoporous network delivered a reversible capacity of up to 1009 mAh g^{-1} at a current density of 100 mA g^{-1} up to 230 cycles [607]. A porous γ-Fe_2O_3 xerogel assembled from nanocrystalline particles (∼5 nm) with abundant mesopores (3 nm) via a simple hydrothermal method delivered capacities 1000, 600, and 200 μAh g^{-1} after 1000 cycles at 0.1, 5, and 10*C* rates, respectively [608]. The capacity retained after 230 cycles at 1000 mA g^{-1} was still 400 mAh g^{-1}, showing that mesoporous Fe_2O_3 nanoparticles without a carbon matrix as a buffer still have an excellent structural stability. Electrospun γ-Fe_2O_3 nanorods (surface area and average pore radius are 27.6 m^2 g^{-1} and 15 nm, respectively) delivered a high reversible capacity of 1095 mAh g^{-1}, with 100 % capacity retention after 50 cycles when cycled in the range of 0.005–3.0 V at a current rate of 0.05*C*, and a capacity of 765 mAh g^{-1} is still obtainable at 2.5*C* (1*C* = 1007 mAh g^{-1}) [609]. It confirms that electrospinning has emerged as a versatile and low cost method for producing long continuous porous fibers with diameters ranging from several micrometers down to a few nanometers by applying a high voltage on a polymer solution or melt. Remarkable results have also been obtained with γ-Fe_2O_3 nanotubes showing a 102.1 m^2 g^{-1} surface area and 0.46 cm^3 g^{-1} total pore volume, although the electrochemical tests have been performed only over 30 cycles [610]. A simple synthesis method for hierarchical spheres with hollow interiors composed of ultrathin nanosheets of has also been reported [611]. These ultrathin nanosheet subunits possess a thickness of around 3.5 nm and the specific surface area of the porous hierarchical γ-Fe_2O_3 spheres was 139.5 m^2 g^{-1}. As a result, a reversible discharge capacity of 815 mAh g^{-1} during the 200th cycle has been delivered at current density of 500 mAh g^{-1}. The best results have been obtained very recently with Fe_2O_3 triple-shelled porous hollow microspheres synthesized using carbonaceous microsphere sacrificial templates [612]. The hollow microspheres had uniform diameters of about 1.2 μm. Control over the shell thickness, porosity, and number of internal multi-shells was achieved by tuning the Fe^{3+} concentration in the carbonaceous microsphere templates. The best results were obtained with average shell thickness of 35 nm containing irregularly shaped 40 nm pores. The hollow shells had a hierarchical structure and are composed of interconnected γ-Fe_2O_3 grains approximately 25–30 nm in diameter. Under such conditions a capacity of 102 mAh g^{-1} has been obtained, constant over the 50 cycles at current density 50 mA g^{-1} that have been tested. The rate capability was also very good, as the anode achieved a stable capacity of 1100 mAh g^{-1} ar current density of 1000 mA g^{-1}. For comparison, let us report the best results obtained with γ-Fe_2O_3-carbon composites. Hierarchical nanostructures composed of carbon-coated γ-Fe_2O_3 hollow nanohorns on carbon nanotube (CNT) backbones delivered a capacity that increases gradually from 660 to 820 mAh g^{-1} within 100 cycles at current density of 500 mAh g^{-1} with a high Coulombic efficiency of around 97–98 %, and the reversible capacity retained at 3000 mA g^{-1} was still 400 mAh g^{-1} [613]. These results are better than the results obtained with γ-Fe_2O_3 nanoparticle-loaded carbon nanofiber composites [614] and other γ-Fe_2O_3-carbon composites

cited therein. It is obvious from the results obtained these recent years that porous α-Fe_2O_3 nanoparticles, coupled with carbon or not, with a capacity in the range 400–1000 mAh g^{-1} over hundreds of cycles and excellent rate capability up to 5*C* rate are very promising anode materials, especially as the material is low-cost en environmentally friendly.

10.8.6.2 Cr_2O_3

Although Cr_2O_3 is the most stable oxide of chromium and adopts the corundum structure, the capacity fading could never be solved entirely. Even mesoporous Cr_2O_3 sheet consisting of 20 nm-sized particles could only deliver a capacity that decreases to ca. 400 mAh g^{-1} after 50 cycles at current density of 100 mAh g^{-1}, despite its high surface area of 162 m^2 g^{-1} [615]. Things have improved with the help of graphene. Graphene-Cr_2O_3 nanosheets have recently been synthesized without foreign templates. Na_2CrO_4 and graphene oxide were chosen as the oxidant and reductant templates, respectively, in a hydrothermal reaction in order to synthesize porous $Cr(OH)_3$ nanosheet precursors. The best results were obtained for the initial mass ratios of graphene oxide and Na_2CrO_4 equal to 1:3. Subsequently, graphene-Cr_2O_3 composites with the mass ratio of graphene to Cr_2O_3 of 0.135 could be obtained by calcinating this precursor [616]. These graphene–Cr_2O_3 nanosheets exhibited a reversible capacity of 850 mAh g^{-1} after 50 cycles at a current density of 200 mA g^{-1}. At higher current densities of 800 mA g^{-1} and 1.6 A g^{-1}, the reversible capacities still remain at 630 and 500 mAh g^{-1}, respectively. Cr_2O_3 nanoparticles, ranging from 10 to 20 nm, well dispersed in the matrix of mesoporous carbon composite delivered a capacity that remained at circa 600 mAh g^{-1} over 80 cycles at current density of 50 mAh g^{-1} [617]. However, this result was obtained owing to a large concentration of porous carbon since the material contained 42 % carbon and 58 % Cr_2O_3.

10.8.6.3 Mn_2O_3

Its theoretical capacity (1018 mAh g^{-1}) is associated to the following reactions:

$$2Li^+ + 3Mn_2O_3 + 2e^- \rightarrow 2Mn_3O_4 + Li_2O, \tag{10.12}$$

$$2Li^+ + Mn_3O_4 + 2e^- \rightarrow 3MnO + Li_2O, \tag{10.13}$$

$$2Li^+ + MnO + 2e^- \rightarrow Mn + Li_2O, \tag{10.14}$$

$$Mn + xLi_2O \leftrightarrow 2xLi^+ + MnO_x + 2xe^- (1.0 < x < 1.5). \tag{10.15}$$

The successful synthesis of porous Mn_2O_3 is recent. In 2011, two kinds of precursor morphologies, oval-shaped and straw-sheaf-shaped, have been selectively prepared by hydrothermal treatment of different functional polyol molecules (oval-shape

with fructose and straw-sheaf-shape with α-cyclodextrin) and potassium permanganate; the morphologies were conserved after decomposition of the precursors [618]. Among them, straw-sheaf-shaped Mn_2O_3 gave the best results, delivering a specific capacity of 550 mAh g^{-1} at a current density of 100 mA g^{-1}, 180 mAh g^{-1} at a current density of 1600 mA g^{-1}. After 36 cycles, however, the capacity recovered at 100 mA g^{-1} had decreased to 430 mAh g^{-1}. The next year, porous microspheres obtained by decomposition of $MnCO_3$ precursor delivered 796 mAh g^{-1} after 50 cycles [619]. An improved control of the porosity of the microsphere by adjusting the temperature at which the $MnCO_3$ precursor has been sintered led to much better results. The best result was obtained at 500 °C, in which case the BET surface area was 28.3 m^2 g^{-1}, with the pore diameter 23.6 nm [620]. At the fourth cycle at current density at 200 mAh g^{-1} the discharge capacity was 529 mAh g^{-1}, remaining at 524 mAh g^{-1} after 200 cycles. At high current density of 1000 mAh g^{-1}, the capacity was still 125 mAh g^{-1}, stable over 1000 cycles. Porous Mn_2O_3 microspheres were also mixed with carbon in wt% ratios Mn_2O_3/carbon/VDF of 60:20:20 to improve the rate capability [621]. This anode delivered 470 mAh g^{-1} after 70 cycles at current density 200 mA g^{-1}. Very recently, porous Mn_2O_3 nanoplates with a surface area of 21.6 m^2 g^{-1} have been prepared by a polyol solution method and post-annealing treatment [622]. As an anode, this material retained a capacity of 814 mAh g^{-1} at current density of 100 mAh g^{-1}. At a current density of 2000 mAh g^{-1}, the retained capacity was 38 % of the theoretical value, i.e. 387 mAh g^{-1}. Despite some progress since 2 years, the Mn_2O_3 is not competitive with the other Mn oxides as a cathode element. Another obstacle experienced with Mn-based anodes (including MnO_2 we did not consider here) is some lack of reproducibility in the results that have been obtained even when the same synthetic methods were used to prepare the Pn-based anode materials, pointed out recently in a review devoted to them [623].

10.8.7 Dioxides

Many other oxides have been explored, will less success so far. This is the case with dioxides MO_2(M = Mn, Mo, Ru), reviewed in ref. [22]. Among them, the best results have been obtained with MoO_2. Indeed, this compound crystallizes in a distorted rutile structure, with a resulting ban structure that makes it a good electrical conductor (the resistivity is 8.8×10^{-5} Ω cm for bulk MoO_2 at room temperature), at contrast will all the other anode materials (except carbon) that we have envisioned so far. We can also mention its good chemical stability, its theoretical capacity (838 mAh g^{-1}), and its affordable cost. However, the problem of low rate capability and rather poor capacity retention has never been solved, unless the MnO_2 particles are nano-sized, and are mixed with carbon. For instance, MnO_2/carbon nanowires delivered an almost constant capacity of 350 mAh g^{-1} up to 20 cycles at a current density of 1000 mAh g^{-1} [624]. Carbon-coated MoO_2 nanospheres (60–80 nm) delivered an initial capacity of 670 mAh g^{-1} at 1C rate in

the voltage range 0.1–3 V, but most of all retained 90 % of it after 30 cycles [625]. In these hybrids, and more complex ones like carbon decorated WO_x-MoO_2 nanorods [626], the good capacity retention and rate capability is attributable to the carbon providing an elastic matrix for absorbing the change of volume during cycling, and preventing the agglomeration of the particles. MoO_2/graphene showed a capacity of 550 mAh g^{-1} after 1000 cycles at current density of 540 mA g^{-1} in the voltage range 0.01–3 V [627]. More recently, MoO_2-ordered mesoporous carbon (MoO_2-OMC) has been prepared through a two-step low-temperature solvothermal chemical reaction route, using SBA-15 as a hard template and sucrose as the carbon source [628]. For a content of 45 wt% MoO, which is the optimized case, a reversible capacity as high as 1049 mAh g^{-1} even after 50 cycles at a current density of 100 mA g^{-1} has been reached, much larger than the theoretical capacity of MnO_2 (838 mAh g^{-1}). At a high current density of 1600 mA g^{-1}, MoO_2-OMC still retains an excellent cyclic performance of 600 mAh g^{-1} after 50 cycles. This is one order of magnitude larger than that of OMC (54 mAh g^{-1}). The outstanding performance of the MoO_2-OMC composite has been attributed to the OMC that acts as branches to connect the MoO_2 nanoparticules and build up a network to ensure the good electrical contact. Meanwhile, the open channels of the ordered mesoporous OMC with MoO_2 nanoparticles modified on the surface allow sufficient infiltration of electrolyte and provide fast diffusion channels of Li^+ the MoO_2 nanoparticles. These results are comparable with other conversion reaction-based anodes.

10.9 Ternary Metal Oxides with Spinel Structure

Since Co_3O_4 and Fe_3O_4 adopt the inverse spinel structure, the substitution of Co or Fe has also been explored. Among them, $NiFe_2O_4$ nano fibers synthesized by an electrospinning approach exhibit a higher charge-storage capacity of 1000 mAh g^{-1} even after 100 cycles with high Coulombic efficiency of 100 % between 10 and 100 cycles at the current density of 100 mA g^{-1} in the voltage range 0.005–3 V [629]. This is by far the best result obtained with this compound. Unfortunately, the electrochemical properties of this anode have not been explored at higher current densities. For comparison, $NiFe_2O_4$/single-wall carbon nanotube (SWNT) composites with 70 wt% loading ratio exhibited a reversible capacity of 776 mAh g^{-1} over 55 cycles under the same conditions [630]. Porous $CoFe_2O_4$ + 20 % reduced graphene oxide, synthesized by a solvothermal process, exhibited a capacity of 1040 mAh g^{-1} at $C/10$ (91 mA g^{-1}), very stable along the 30 cycles that have been tested [631]. Even at the very high rate of $20C$, the discharge capacity was still 380 mAh g^{-1}. Even without graphene support, very good results have been obtained with porous $CoFe_2O_4$ nanosheets, having the thickness of 30–60 nm and lateral size of several microns with numerous penetrating pores, synthesized via thermal decomposition of $(CoFe_2)_{1/3}C_2O_4 \cdot 2H_2O$ nanosheets [632]. At current densities 1000 and 2000 mA g^{-1}, the anode delivered capacities of 806 and

648 mAh g^{-1}, respectively, each for 200 cycles. These results show the superior behavior of $CoFe_2O_4$ with respect to $NiFe_2O_4$, and renew the interest in this spinel compound as a promising anode material. In addition, these nanosheets have been synthesized at a sintering temperature that does not exceed 600 °C, while the obtention of a good capacity retention for $CoFe_2O_4$ (740 mAh g^{-1} after 75 cycles at 1*C* rate) required a sintering temperature as high as 1000 °C in prior works [633]. This gain in the sintering temperature makes the synthesis more scalable for industrial processes.

10.9.1 Molybdenum Compounds

Among molybdenum-containing mixed oxides that adopt the Scheelite structure, the best results have been obtained with $CoMoO_4$. Interconnected networks of $CoMoO_4$ submicrometer particles prepared by thermolysis of polymer matrix based metal precursor solution exhibited a high reversible capacity of 990 ± 10 mAh g^{-1} at a current density of 100 mA g^{-1}, with 100 % capacity retention between 5 and 50 cycles [634]. Hierarchically porous 3D electrode of $CoMoO_4$ prepared by the hydrothermal method resulted in the formation of a $CoMoO_4$ network composed of interconnected porous nanosheets with a lateral length of 1 μm and a thickness of 8–10 nm, each nanosheet consisting of many interconnected nanocrystallites with grain size around 5 nm and voids around 2–4 nm [635]. This structure achieved a discharge capacity of 1063 mAh g^{-1} and a coulombic efficiency of 100 % at the second and second cycles at a current density of 0.1 A g^{-1} (*C*/10; where $1C = 980$ mA g^{-1}) between 0.005 and 3.0 V, and remained steady over 100 cycles. Even at high rates of 2 and 3*C*, the $CoMoO_4$ electrode can still achieve high capacities of 460 and 327 mAh g^{-1}, respectively. After 100 cycles at 0.3*C*, the reversible discharge capacity was 894 mAh g^{-1}, which corresponds to a capacity retention of 87.6 % of the initial capacity. When the current density was increased to 0.5 A g^{-1}, the $CoMoO_4$ electrode delivered a capacity of 758 mAh g^{-1} at the end of 100 cycles, corresponding to 75.7 % retention. These results show that $CoMoO_4$ submicrometer particles with interconnected network like morphology makes it promising as a high capacity anode material for LiBs, as Co and Mo are mutually beneficial elements to buffer the volume change upon Li cycling.

10.9.2 Oxide Bronzes

Molybdenum trioxide α-MoO_3 is also considered as a promising anode material, due to its layer structure and its high theoretical capacity of 1117 mAh g^{-1} by the conversion reaction, assuming 6Li can participate. The interest in this material has been raised by the good performance of nanospheroids of MoO_3 (5–20 nm in size),

prepared by the hotwire chemical vapor deposition [636]. The electrodes were prepared by electrophoretic deposition of these nanospheres onto stainless steel substrates to give 2-μm thick films followed by annealing at 450 °C in air to obtain porous crystalline α-MoO_3. The electrode was then coated with a solid polymer electrolyte PEO-$LiClO_4$. The investigation of the electrochemical properties upon cycling at $C/10$ in the range 0.005–3 V revealed that the capacity was stabilized to 630 mAh g^{-1} between the 30th and the 150th cycles. Since this compound has a poor electronic conductivity, many efforts have been made to fabricate nanoparticles under different forms: wire arrays [637], hollow nanospheres [638], nanobelts [639], and/or by coating the nanoparticles with a conductive layer. Coating the MoO_3 electrode with four monolayers of Al_2O_3 raises the capacity to 900 mAh g^{-1} up to the 50th cycle at the rate $C/2$ [640]. More recently, carbon coated MoO_3 nanobelts maintained its capacity of 1064 mAh g^{-1} after 50 cycles at a rate of $C/10$ [641]. The nanobelts, having a diameter of 150 nm and a length of 5–8 μm, ware prepared by a simple hydrothermal route. It is interesting to note that the carbon coating was done using malic acid as the carbon precursor, dispersed in toluene. The malic acid is decomposed at a temperature of 265 °C, which is sufficient to coat the material with amorphous carbon. The comparison of the electrochemical properties before and after carbon coating gives evidence of major improvements associated with the carbon-coating, which can be considered as the proof that the carbon layer is a good electronic conductor despite the very low sintering temperature, while higher synthesis temperatures are needed with other precursors, as we have already discussed in previous sections. Like in the case of all the anodes, porosity is important to increase the performance of MoO_3. Recently, a porous MoO_3 film was prepared by using a facile hydrothermal route and subsequent calcinations in air. This material had a high capacity (750 mAh g^{-1} at $1C$), long cycle life (120 cycles with 80 % capacity retention) [642]. Recently, a MoO_3/graphene composite electrode (1:1 in weight ratio) delivered discharge capacities of 1437, 967, 688, and 574 mAh g^{-1} for the 1st, 2nd, 50th, and 100th cycles at a current density of 500 mA g^{-1}, respectively, with a coulombic efficiency of 97 % from the second cycle. The electrode still delivered the capacity of 513 mAh g^{-1} even at a high current density of 1000 mA g^{-1} [642]. Taking into account that $1C = 1117$ mA g^{-1}, the rate capability is still smaller than that of the porous MoO_3 film in [643] without the help of graphite, again pointing to the important effect of the porosity in the performance of the electrodes.

10.9.3 $Mn_2Mo_3O_8$

Numerous well-defined Mo triangular cluster oxide compounds exist and have been considered as possible anode materials (see ref. [22] for a review). However, the only one that has a rate capability and capacity competitive with the other materials we have considered above is $Mn_2Mo_3O_8$. Hierarchically nanostructured $Mn_2Mo_3O_8$-graphene composites (10.3 wt% carbon) consisting of graphene-wrapped

secondary microspheres (3–5 μm) synthesized by a two-step reduction method delivered a capacity that increases from 650 to 921 mAh g^{-1} between the second and the 20th cycles at a current density of 200 mA g^{-1}. The capacity reached 950 mAh g^{-1} after the 40th cycle. The rate capability was also very good, as the reversible capacity at was 671 mAh g^{-1} at a current density of 1500 mAh g^{-1} [644]. However, this work dates from 2011, and no further study has been reported on this compound to our knowledge. This is at contrast with the situation met with the other compounds mentioned in this paper, where important progress has been achieved owing to the intensive efforts made in the years 2011–2014.

10.10 Anodes Based on Both Alloying and Conversion Reaction

Different materials in which a Li alloying-dealloying element is added to a conversion of transition metal oxide have been investigated, hoping that the addition of the two effects would improve the electrochemical properties. The most promising materials entering this category are oxides with spinel structure.

10.10.1 $ZnCo_2O_4$

These are not the only spinel that belongs to this family, which include $CdFe_2O_4$, but Cd is toxic. Since the electrochemical properties of $CdFe_2O_4$ are not better than those of ZnM_2O_4 ($M = $ Co, Fe) that are more friendly for the environment, only the Zn-based spinels will be considered here. The reactions that govern the electrochemical properties are written hereunder for $ZnCo_2O_4$ and will also apply with Co replaced by Fe:

$$ZnCo_2O_4 + xLi^+ + xe^- \rightarrow Li_x(ZnCo_2O_4), \tag{10.16}$$

$$Li_x(ZnCo_2O_4) + (8-x)Li^+ + (8-x)e^- \rightarrow Zn + 2Co + 4Li_2O, \tag{10.17}$$

$$Zn + Li^+ + e^- \rightarrow ZnLi(\text{alloying/de-alloying reaction}), \tag{10.18}$$

$$Zn + 2Co + 3Li_2O \rightarrow 2/3Co_3O_4 + 4/3Li^+ + 4/3e^-. \tag{10.19}$$

A reversible capacity corresponding to 8.3 mol of Li per mole of $ZnCo_2O_4$ (ca. 900 mAh g^{-1}) is expected, assuming $x \leq 0.5$ for Li intercalation into the spinel lattice (Eq. 10.16), crystal structure destruction, followed by metal particle formation, and alloy formation with Zn (Eqs. 10.17 and 10.18). The conversion reactions occur during charging (Li extraction, Eq. 10.19). Part of the CoO can also form Co_3O_4 during the charging process (Eq. 10.19). The theoretical capacity has been

achieved with nanosized $ZnCo_2O_4$ (20 nm) prepared by the urea combustion technique, stable up to at least 60 cycles at a current density of 60 mAh g^{-1} (0.07C) in the range 0.005–3 V [645]. Starting with $ZnSO_4 \cdot 4H_2O$ and $Co(OH)_2$ precursors, this stable capacity was raised to 957 mAh g^{-1} for $ZnCo_2O_4$ prepared by the molten salt method at 280 °C in air [646]. However, neither these works nor other nano/microstructures including nanoparticles [647], nanowires [648], nanotubes [649] could meet the rate capability and cyclability needed to be competitive. Again, one had to wait for the synthesis of porous nanoparticles to obtain significant improvements, with the results of uniform mesoporous $ZnCo_2O_4$ microspheres with surrounding nanoparticles (surface area of 26.8 m^2 g^{-1} and a pore volume of 0.12 cm^3 g^{-1}, pore size in the range 2–10 nm) and microspheres [650]. The capacity maintained at 721 mAh g^{-1} after 80 discharge–charge cycles. Even as current density reached to 1000 mA g^{-1}, the initial specific capacity still showed 937 mAh g^{-1} and the discharge capacity of 432 mAh g^{-1} was retained after 40 cycles.

A binder-free flexible anode has been fabricated with hierarchical 3D-$ZnCo_2O_4$ nanowire arrays grown on a carbon cloth by using a hydrothermal route [651]. This anode delivered charge–discharge capacities in the range of about 1200–1340 mAh g^{-1} with 99 % capacity retention from 3 to 160 cycles at current density of 200 mAh g^{-1}. The capacity decreased from 1200, 920, 890, 710, and 605 mAh g^{-1} with increasing *C*-rate ranging from 0.2, 0.5, 1, 2, to 5*C* ($1C = 900$ mA g^{-1}). The capacity was then reversibly back to 105 mAh g^{-1} once the charging/discharging rate was set back to *C*/5 again, revealing that almost 92 % of the initial capacity at *C*/5 was recovered. This anode can be used in many applications such as stretchable/bendable electronic devices, portable energy storage devices, flexible powering sustainable vehicles, photovoltaic devices, and control of commercial available LED and displays.

A facile two-step strategy involving a polyol method and subsequent thermal annealing treatment has been successfully developed for the large-scale preparation of $ZnCo_2O_4$ various hierarchical micro/nanostructures (twin microspheres and microcubes) without surfactant assistance [652]. For the twin microspheres, the surface area was 7.33 m^2 g^{-1} with a relatively narrow pore size distribution ranging from 30 to 80 nm. The pore volume is determined to be 0.0449 cm^3 g^{-1}. The relatively low pore volume is mainly contributed form the small mesopores between the homogeneous nanometer-sized building blocks. After 50 and 100 cycles at current density of 500 mAh g^{-1} in the voltage range 0.01–3 V, the discharge capacities were the same at 1100 mAh g^{-1}. At a current of 1000 mAh g^{-1}, the capacity was 1145 mAh g^{-1}, and still 831.7 mAh g^{-1} after 100 cycles with a coulombic efficiency of 99 % after the second cycle. As the current densities increase from 1.0, 2.0, and 5.0 A g^{-1}, the electrode exhibits excellent capacity retention, slightly varying from 1040, 1005, and 920 mAh g^{-1}. When the rate was further increased to 10 A g^{-1}, the specific capacity recorded is exceptionally high at 790 mAh g^{-1}. Noticeably, when the current rate turns back to 0.5 A g^{-1}, the capacity can be retained as high as 1260 mAh g^{-1} even after 600 cycles without any losses and the coulombic efficiency is almost around 99 %. This effective route to prepare mesoporous $ZnCo_2O_4$ via a topotactic conversion from $Zn_{0.33}Co_{0.67}CO_3$ twin

microspheres according to a multistep-splitting-then in situ dissolution-recrystallization growth process is a facile synthetic approach and gives to $ZnCo_2O_4$ the potential for being a high-energy and high-power anode material for LiBs.

10.10.2 $ZnFe_2O_4$

Another normal spinel oxide, $ZnFe_2O_4$, is cost competitive, with a theoretical capacity of 1072 mAh g^{-1}. Carbon-coated $ZnFe_2O_4$ nanoparticles can also deliver capacities of 1000 mAh g^{-1} at low rate, with only 10 % loss of capacity at a current density of 1000 mAh g^{-1} [653, 654]. The influence of the carbon precursor on the electrochemical properties has been studied in [655]. Between sucrose, citric acid, and oleic acid, the winner is sucrose, which led to a carbon-coated $ZnFe_2O_4$ delivering a capacity stabilized at 1100 mAh g^{-1} after 60 cycles at a current density of 50 mAh g^{-1}. $ZnFe_2O_4$/graphene composite synthesized using urea-assisted auto combustion synthesis followed by an annealing step delivered, with $ZnFe_2O_4$ particles 25–50 nm in size homogeneously distributed on the graphene sheets, delivered 908.6 mAh g^{-1} in the fifth cycle at *C*/10 rate, and 908.6 mAh g^{-1} after 75 cycles. This anode delivered reversible charge capacities of 1002.5, 721.9, 658.8, 595.7, 516.7, 398.6, and 352.3 mAh g^{-1} at the current rates of 0.1, 0.2, 0.4, 0.8, 1.6, 3.2, and 4.0*C*, respectively [656]. Quite similar results have been obtained with another $ZnFe_2O_4$/graphene composite synthesized by hydrothermal process, which delivered a capacity of 956 mAh g^{-1} after 50 cycles at current density 100 mA g^{-1}, and 600 mAh g^{-1} at 1000 mA g^{-1} [657]. Interestingly, nanostructured $ZnFe_2O_4$ (30–70 nm particles) prepared by the polymer pyrolysis method, namely, metal–polyacrylate decomposition at 600 °C in air, had an even better rate capability. For example, at 4*C*, the resulting nano-$ZnFe_2O_4$ anode showed a reversible capacity over 400 mAh g^{-1} [658]. Note we have shown that the best results with $ZnCo_2O_4$ were also obtained with a polyol synthesis route, which actually suggests ta particular role of polyol in its interaction with these spinel compounds. Monodisperse $ZnFe_2O_4$ nanoparticles with sizes less than 10 nm have been successfully assembled on multiwalled carbon nanotubes (MWCNTs) by in situ high-temperature decomposition of the precursor iron(III) acetylacetonate, zinc acetate, and MWCNTs in polyol solution [659]. This anode delivered a larger capacity at slow rate (1152 mAh g^{-1} after 50 cycles at a current density of 60 mA g^{-1}), but a lower rate capability: At current densities of 300, 600, and 1200 mA g^{-1}, the specific capacities were 840, 580, and 270 mAh g^{-1}, respectively. The importance of the porosity, pointed out many times along this chapter is also evident in the results obtained with mesoporous $ZnFe_2O_4$ microspheres embedded into a carbon network [660]. The microspheres were built from nanoparticles in the size of 10–50 nm. The pore size distribution was in the range of 5–20 nm, peaked at 11 nm, and the surface area of the microspheres was 46.8 m^2 g^{-1} on average, coming from both the outer surface of the nanoparticles and the amorphous carbon. The specific reversible capacity was 1100 mAh g^{-1} at the specific

current of 0.05 A g^{-1} after 100 cycles, and more than 500 mAh g^{-1} at the specific current of 1.1 A g^{-1}; the cyclability was also very good, with little fading (97.6 % after 100 cycles). All these results show that $ZnCo_2O_4$ as an anode presently outperforms $ZnFe_2O_4$ as an anode. However, the effective route to prepare mesoporous $ZnCo_2O_4$ via a topotactic conversion from twin microspheres that gave the best results for $ZnCo_2O_4$ is too recent to have been experimented on $ZnFe_2O_4$ yet.

Tin oxides spinels M_2SnO_4 have also been studied to examine whether additional capacity can be obtained by the participation of Sn and Li_2O by conversion reaction to form SnO and SnO_2. The results, which have been reviewed in ref. [22] show drastic capacity fading, even in the case $M = Co$, which, like in the case of ZnM_2O_4, is found to be the most favorable case.

10.11 Concluding Remarks

The efforts to replace graphite as to increase the energy density, and most importantly ensure safety-in-operation of lithium batteries, in particular for use in hybrid and electric vehicles have given rise to a wide variety of metal oxides and oxysalts for use as a negative electrode of Li-ion batteries. Yet, the list that has been reviewed in this chapter is not exhaustive, but the other materials that have been envisioned so far cannot compete. In the intercalation-deintercalation group, soft carbon is a mature technology, but hard carbon can be an option for applications requiring a lot of power. Titanium oxides have the disadvantage of a low energy density than that of graphite, typically 160 mAh g^{-1} for $Li_4Ti_5O_{12}$, 250 mAh g^{-1} for TiO_2 vs. 372 mAh g^{-1}. Also, the voltage at which Li cycling occurs in the titanium oxides is high, namely 1.3–1.6 V, which reduces the operating voltage of the Li-ion battery, and thus its energy density. On another hand, this voltage has the advantage of avoiding the large irreversible capacity lost due to the formation of the SEI on anode particles operating below 1 V. The titanium oxides have other remarkable advantages: low cost, environmental safety, very good stability both in the discharged and charged state, very good cyclability and very high power density, very good abuse tolerance. That is why $Li_4Ti_5O_{12}$ is expected to be accepted for hybrid and electric vehicles in the next few years. Graphene has a very good electronic conductivity, a good mechanical flexibility and high chemical functionality. Therefore, it can serve as an ideal 2D support for assembling nanoparticles with various structures and very good results have been obtained with composites grapheme-nanoparticles of metal oxides. In addition the graphene is able to prevent the agglomeration of the nanoparticles upon cycling, and the nanoparticles prevent the re-stacking of the graphene sheets. The handicap for the development of such anodes is the cost, and a scalable production of graphene. This is a big challenge that hinders the mass production of such anodes until the problem has been solved. Also the composites carbon nanotubes-nanoparticles of metal

oxides can be presently prepared only at the laboratory scale, as production cost does not permit their application in the battery industry.

Alloying materials such as Si, Ge, SiO, SnO_2 can provide much larger capacities, and energy densities than the titanium oxides and the other elements of the previous group, but they suffer from the important capacity loss upon cycling due to the large variation of volume upon Li insertion and de-insertion. The problem can be solved by the reduction of the size to the nanoscale, along with the realization of complex structures such as graphene-based composites, but again we recover the scalability problem we have just outlined for graphene or carbon nanotubes. Si and SnO_2 are the most promising elements of this family, as germanium is expensive and not abundant in nature. The same problem is met with oxide anodes based on conversion reactions. In addition, these anodes exhibit large potential hysteresis between the charge and discharge reactions. This voltage hysteresis, however, is expected to be solved by using some catalysts and surface coating. Important improvements in the cyclability and rate capability of these anodes have been obtained in the last few years.

Both the alloying anode materials and the oxide anodes based on conversion reactions have benefited from the progress in the preparation of porous nanostructures. Until recently, the general strategy for synthesizing porous materials is a hard/soft template-based or de-alloying method, based on removing something from the host materials, and simultaneously generating the porous structures. Those methods are not suitable for large-scale production. Recently, however, other techniques have merged involving thermal decomposition of hydroxide, carbonate, oxalate, etc., which are much more scalable, and have been found to be an effective way to produce porous materials. Indeed porous nanomaterials give results that are comparable to the complex composite we have mentioned, so that the development of few metal oxides based on alloying or conversion reaction, in addition of titanium oxides based on the intercalation process can be expected in the near future.

References

1. Zaghib K, Mauger A, Julien CM (2014) Energy storage for smart grid applications. In: Franco AA (ed) Rechargeable lithium batteries: from fundamentals to applications. Woodhead Publications, Oxford
2. Zaghib K, Mauger A, Julien CM (2012) Overview of olivines in lithium batteries for green transportation and energy storage. J Solid State Electrochem 16:835–845
3. Zaghib K, Guerfi A, Hovington P, Vijh A, Trudeau M, Mauger A, Goodenough JB, Julien CM (2013) Review and analysis of nanostructured olivine-based lithium recheargeable batteries: status and trends. J Power Sourc 232:357–369
4. Julien CM, Mauger A (2013) Review of 5-V electrodes for Li-ion batteries: status and trends. Ionics 19(7):951–988
5. Julien CM, Mauger A, Zaghib K, Groult H (2014) Comparative issues of cathode materials for Li-ion batteries. Inorganics 2:132–154

6. Liu D, Zjhu W, Trottier J, Cagnon C, Barray F, Guerfi A, Mauger A, Groult H, Julien CM, Goodenough JB (2014) Comparative issues of cathode materials for Li-ion batteries. RSC Adv 4:154–167
7. Herold A (1955) Bull Soc Chim Fr 187:999
8. Juza R, Wehle V (1965) Lithium-graphit-einlagerungsverbindungen. Nature 52:560–560
9. Besenhard JO, Eichinger G (1976) High energy density lithium cells. Part I. Electrolytes and anodes. J Electroanal Chem 68:1–18
10. Eichinger G, Besenhard JO (1976) High energy density lithium cells. Part II. Cathodes and complete cells. J Electroanal Chem 72:1–31
11. Kasavajjula U, Wang C, Appleby AJ (2007) Nano- and bulk-silicon-based insertion anodes for lithium-ion secondary cells. J Power Sourc 163:1003–1039
12. Van Schalkwijk WA, Scrosati B (2002) Advances in lithium-ion batteries. Kluwer, New York, NY
13. Nazri GA, Pistoia G (2003) Lithium batteries: science and technology. Kluwer, New York, NY
14. Alifantis KE, Hackney SA, Kumar R (2010) High energy density lithium batteries: materials, engineering, applications. Wiley VCH, Weinheim
15. Arico AS, Bruce P, Scrosati B, Tarascon JM, Van Schalkwijk W (2005) Nanostructured materials for advanced energy conversion and storage devices. Nat Mater 4:366–377
16. Verma P, Maire P, Novak P (2010) A review of the features and analyses of the solid electrolyte interphase in Li-ion batteries. Electrochim Acta 55:6332–6341
17. Shukla AK, Kumar TP (2008) Materials for next generation of lithium batteries. Curr Sci 94:314–331
18. Winter M, Besenhard JO, Spahr ME, Novak P (1998) Insertion electrode materials for rechargeable lithium batteries. Adv Mater 10:725–763
19. Sony press news (2005) www.Sony.net/SonyInfo/News/Press/200502/05-006E/index.html
20. Zhang W-J (2011) A review of the electrochemical performance of alloy anodes for lithium-ion batteries. J Power Sourc 196:13–24
21. Yi TF, Jiang LJ, Shu J, Yue CB, Zhu RS, Qiao HB (2010) Recent development and application of $Li_4Ti_5O_{12}$ as anode material of lithium ion battery. J Phys Chem Solids 71:1236–1242
22. Reddy MV, Subba Rao GV, Chowdari BVR (2013) Metal oxides and oxysalts as anode materials for Li ion batteries. Chem Rev 113:5364–5457
23. Scrosati B, Garche JJ (2010) Lithium batteries: status, prospects and future. J Power Sourc 195:2419–2430
24. Kim MG, Cho J (2009) Reversible and high-capacity nanostructured electrode materials for Li-ion batteries. Adv Funct Mater 19:1497–1514
25. Park CM, Kim JH, Kim H, Sohn HJ (2010) Li-alloy based anode materials for Li secondary batteries. Chem Soc Rev 39:3115–3141
26. Todd ADW, Ferguson PP, Fleischauer MD, Dahn JR (2010) Tin-based materials as negative electrodes for Li-ion batteries: combinatorial approaches and mechanical methods. Int J Energ Res 34:535–555
27. Cabana J, Monconduit L, Larcher D, Palacin MR (2010) Beyond intercalation-based Li-ion batteries: the state of the art and challenges of electrode materials reacting through conversion reactions. Adv Mater 22:E170–E191
28. Bruce PG (2008) Energy storage beyond the horizon: rechargeable lithium batteries. Solid State Ionics 179:752–760
29. Guo Y-G, Hu J-S, Wan LJ (2008) Nanostructured materials for electrochemical energy conversion and storage devices. Adv Mater 20:2878–2887
30. Balaya P (2008) Size effects and nanostructured materials for energy applications. Energ Environ Sci 1:645–654
31. Bruce PG, Scrosati B, Tarascon JM (2008) Nanomaterials for rechargeable lithium batteries. Angew Chem Int Ed 47:2930–2946

32. Cheng F, Tao Z, Liang J, Chen J (2008) Template-directed materials for rechargeable lithium-ion batteries. Chem Mater 20:667–681
33. Wu Z-S, Zhou G, Yin L-C, Ren W, Li F, Cheng H-M (2012) Graphene/metal oxide composite electrode materials for energy storage. Nano Energy 1:107–131
34. Chernova N, Roppolo M, Dillon AC, Whittingham MS (2009) Layered vanadium and molybdenum oxides: batteries and electrochromics. J Mater Chem 19:2526–2552
35. Deng D, Kim MG, Lee JY, Cho J (2009) Green energy storage materials: nanostructured TiO_2 and Sn-based anodes for lithium-ion batteries. Energ Environ Sci 2:818–837
36. Centi G, Perathoner S (2009) The role of nanostructure in improving the performance of electrodes for energy storage and conversion. Eur J Inorg Chem 2009:3851–3878
37. Li H, Wang ZX, Chen LQ, Huang XJ (2009) Research on advanced materials for Li-ion batteries. Adv Mater 21:4593–4607
38. Yang ZG, Choi D, Kerisit S, Rosso KM, Wang DH, Zhang J, Graff G, Liu J (2009) Nanostructures and lithium electrochemical reactivity of lithium titanites and titanium oxides: a review. J Power Sourc 192:588–59
39. Liu C, Li F, Ma LP, Cheng HM (2010) Advanced materials for energy storage. Adv Mater 22: E28–E62
40. Su DS, Schlogl R (2010) Nanostructured carbon and carbon nanocomposites for electrochemical energy storage applications. ChemSusChem 3:13138
41. Luo B, Liu SM, Zhi LJ (2012) Chemical approaches toward graphene-based nanomaterials and their applications in energy-related areas. Small 8:630–646
42. Jiang J, Li Y, Liu J, Huang X (2011) Building one-dimensional oxide nanostructure arrays on conductive metal substrates for lithium-ion battery anodes. Nanoscale 3:45–58
43. Kamali AR, Fray DJ (2011) Tin-based materials as advanced anode materials for lithium ion batteries: a review. Rev Adv Mater Sci 27:14–24
44. Lee KT, Cho J (2011) Roles of nanosize in lithium reactive nanomaterials for lithium ion batteries. Nano Today 6:28–41
45. Li J, Daniel C, Wood D (2011) Materials processing for lithium-ion batteries. J Power Sources 196:2452–2460
46. SongMK PS, Alamgir FM, Cho J, Liu M (2011) Nanostructured electrodes for lithium-ion and lithium-air batteries: the latest developments, challenges, and perspectives. Mater Sci Eng R 72:203–252
47. Zhang X, Ji L, Toprakci O, Liang Y, Alcoutlabi M (2011) Electrospun nanofiber-based anodes, cathodes, and separators for advanced lithium-ion batteries. Polym Rev 51:239–264
48. Jeong G, Kim YU, Kim H, Kim YJ, Sohn HJ (2011) Prospective materials and applications for Li secondary batteries. Energ Environ Sci 4:1986–2002
49. Ji L, Lin Z, Alcoutlabi M, Zhang X (2011) Recent developments in nanostructured anode materials for rechargeable lithium-ion batteries. Energ Environ Sci 4:2682–2699
50. Cavaliere S, Subianto S, Savych I, Jones DJ, Roziere J (2011) Electrospinning: designed architectures for energy conversion and storage devices. Energ Environ Sci 4:4761–4785
51. Yang Z, Zhang J, Kintner-Meyer MCW, Lu X, Choi D, Lemmon JP, Liu J (2011) Electrochemical energy storage for green grid. Chem Rev 111:3577–3613
52. Ji G, Ma Y, Lee JY (2011) Mitigating the initial capacity loss (ICL) problem in high-capacity lithium ion battery anode materials. J Mater Chem 21:9819–9824
53. Chen JS, Archer LA, Lou XW (2011) SnO_2 hollow structures and TiO_2 nanosheets for lithium-ion batteries. J Mater Chem 21:9912–9924
54. Marom R, Amalraj SF, Leifer N, Jacob D, Aurbach D (2011) A review of advanced and practical lithium battery materials. J Mater Chem 21:9938–9954
55. Dunn B, Kamath H, Tarascon JM (2011) Electrical energy storage for the grid: a battery of choices. Science 334:928–935
56. Liu Y, Liu D, Zhang Q, Cao G (2011) Engineering nanostructured electrodes away from equilibrium for lithium-ion batteries. J Mater Chem 21:9969–9983

57. Singh V, Joung D, Zhai L, Das S, Khondaker SI, Seal S (2011) Graphene based materials: past, present and future. Prog Mater Sci 56:1178–1271
58. Zhou Z-Y, Tian N, Li J-T, Broadwell I, Sun S-G (2011) Nanomaterials of high surface energy with exceptional properties in catalysis and energy storage. Chem Soc Rev 40:4167–4185
59. Cheng F, Chen J (2011) Transition metal vanadium oxides and vanadate materials for lithium batteries. J Mater Chem 21:9841–9848
60. Tartaj P, Morales MP, Gonzalez-Carreno T, Veintemillas-Verdaguer S, Serna CJ (2011) The iron oxides strike back: from biomedical applications to energy storage devices and photoelectrochemical water splitting. Adv Mater 23:5243–5249
61. Dillon SJ, Sun K (2012) Microstructural design considerations for Li-ion battery systems. Curr Opin Solid State Mater Sci 16:153–162
62. Li Y, Yang XY, Feng Y, Yuan ZY, Su BL (2012) One-dimensional metal oxide nanotubes, nanowires, nanoribbons, and nanorods: synthesis, characterizations, properties and applications. Crit Rev Solid State Mater Sci 37:1–74
63. Kim T-H, Park J-S, Chang SK, Choi S, Ryu JH, Song H-K (2012) The current move of lithium ion batteries towards the next phase. Adv Energ Mater 2:860–872
64. Devan RS, Patil RA, Lin JH, Ma YR (2012) One-dimensional metal-oxide nanostructures: recent developments in synthesis, characterization, and applications. Adv Funct Mater 22:3326–3370
65. Liu JH, Liu XW (2012) Two-dimensional nanoarchitectures for lithium storage. Adv Mater 24:4097–4111
66. Nishihara H, Kyotani T (2012) Templated nanocarbons for energy storage. Adv Mater 24:4473–4498
67. Tan CW, Tan KH, Ong YT, Mohamed AR, Zein SHS, Tan SH (2012) Energy and environmental applications of carbon nanotubes. Environ Chem Lett 10:265–273
68. Ellefson CA, Marin-Flores O, Ha S, Norton MG (2012) Synthesis and applications of molybdenum (IV) oxide. J Mater Sci 47:2057–2071
69. Djenizian T, Hanzu I, Knauth P (2011) Nanostructured negative electrodes based on titania for Li-ion microbatteries. J Mater Chem 21:9925–9937
70. Zhu GN, Wang YG, Xia YY (2012) Ti-based compounds as anode materials for Li-ion batteries. Energ Environ Sci 5:6652–6667
71. Su X, Wu QL, Zhan X, Wu J, Wei S, Guo Z (2012) Advanced titania nanostructures and composites for lithium ion battery. J Mater Sci 47:2519–2534
72. Berger T, Monllor-Satoca D, Jankulovska M, Lana-Villarreal T, Gomez R (2012) The electrochemistry of nanostructured titanium dioxide electrodes. ChemPhysChem 13: 2824–2875
73. Froschl T, Hormann U, Kubiak P, Kucerova G, Pfanzelt M, Weiss CK, Behm RJ, Husing N, Kaiser U, Landfester K, Wohlfahrt-Mehrens M (2012) High surface area crystalline titanium dioxide: potential and limits in electrochemical energy storage and catalysis. Chem Soc Rev 41:5313–5360
74. Nitta N, Yushin G (2014) High-capacity anode materials for lithium-ion batteries: choice of elements and structures for active particles. Part Syst Charact 31:317–336
75. Li H, Balaya P, Maier J (2004) Li-storage via heterogeneous reaction in sSelected binary metal fluorides and oxides. J Electrochem Soc 151:A1878–A1885
76. Li Q, Mahmood N, Zhu J, Hou Y, Sun S (2014) Graphene and its composites with nanoparticles for electrochemical energy applications. Nano Today 9:668–683
77. Su X, Wu Q, Li J, Xiao X, Lott A, Lu W, Sheldon BW, Wu J (2014) Silicon-based nanomaterials for lithium-ion batteries: a review. Adv Energy Mater 4:1300882
78. Zamfir MR, Nguyen HT, Moyen E, Lee YH, Pribat D (2013) Silicon nanowires for Li-based battery anodes: a review. J Mater Chem A 1:9566–9586
79. Erk C, Brezesinski T, Sommer H, Schneider R, Janek J (2013) ACS toward silicon anodes for next-generation lithium ion batteries: a comparative performance study of various polymer binders and silicon nanopowders. ACS Appl Mater Interfaces 5:7299–7307

80. Chen J (2013) Recent progress in advanced materials for lithium-ion batteries. Materials 6:156–183
81. Kamali AR, Fray DJ (2010) Review on carbon and silicon based materials as anode materials for lithium ion batteries. J New Mat Electr Sys 13:147–160
82. Bogart TD, Chockla AM, Korgel BA (2013) High capacity lithium ion battery anodes of silicon and germanium. Curr Opin Chem Eng 2:286–293
83. Wu H, Cui Y (2012) Designing nanostructured Si anodes for high energy lithium ion batteries. Nano Today 7:414–429
84. Ge M, Fang X, Rong J, Zhou C (2013) Review of porous silicon preparation and its application for lithium-ion battery anodes. Nanotechnology 24:422001
85. Cho J (2010) Porous Si anode materials for lithium rechargeable batteries. J Mater Chem 20:4009–4014
86. Szczech JR, Jin JR (2011) Nanostructured silicon for high capacity lithium battery anodes. Energ Environ Sci 4:56–72
87. Goriparti S, Miele E, De Angellis F, Di Fabrizio E, Zaccaria RP, Capiglia C (2014) Review on recent progress of nanostructured anode materials for Li-ion batteries. J Power Sourc 257:421–443
88. Inagaki M, Yang Y, Kang F (2012) Carbon nanofibers prepared via electrospinning. Adv Mater 24:2547–2566
89. Yan L, Zheng YB, Zhao F, Li S, Gao X, Xu B, Weiss PS, Zhao Y (2012) Chemistry and physics of a single atomic layer: strategies and challenges for functionalization of graphene and graphene-based materials. Chem Soc Rev 41:97–114
90. Liu XM, Huang ZD, Oh SY, Zhang B, Ma PC, Yuen MMF, Kim J-K (2012) Carbon nanotube (CNT)-based composites as electrode material for rechargeable Li-ion batteries: a review. Compos Sci Technol 72:121–144
91. Tiwari JN, Tiwari RN, Kim KS (2012) Zero-dimensional, one-dimensional, two-dimensional and three-dimensional nanostructured materials for advanced electrochemical energy devices. Prog Mater Sci 57:724–803
92. Dai LM, Chang DW, Baek JB, Lu W (2012) Carbon nanomaterials for advanced energy conversion and storage. Small 8:1130–1166
93. De Las Casas C, Li WZ (2012) A review of application of carbon nanotubes for lithium ion battery anode material. J Power Sourc 208:74–85
94. Winter M, Moeller K-C, Besenhard JO (2003) Carbonaceous and graphitic anodes (Chapter 5). In: Pistoia G, Nazri GA (eds) Lithium batteries: science and technology. Springer, New York, NY
95. Park T-H, Yeo J-S, Seo M-H, Miyawaki J, Mochida I, Yoon S-H (2013) Enhancing the rate performance of graphite anodes through addition of natural graphite/carbon nanofibers in lithium-ion batteries. Electrochim Acta 93:236–240
96. Fujimoto H, Tokumitsu K, Mabuchi A, Chinnasamy N, Kasuh T (2010) The anode performance of the hard carbon for the lithium ion battery derived from the oxygen-containing aromatic precursors. J Power Sourc 195:7452–7456
97. Yang J, Zhou XY, Li J, Zou Y-L, Tang JJ (2012) Study of nano-porous hard carbons as anode materials for lithium ion batteries. Mater Chem Phys 135:445–450
98. Bridges CA, Sun X-G, Zhao J, Paranthaman MP, Dai S (2012) In situ observation of solid electrolyte interphase formation in ordered mesoporous hard carbon by small-angle neutron scattering. J Phys Chem C 116:7701–7711
99. Liu Y, Xue JS, Zheng T, Dahn JR (1996) Mechanism of lithium insertion in hard carbons prepared by pyrolysis of epoxy resins. Carbon 34:193–200
100. Hu J, Li H, Huang X (2005) Influence of micropore structure on Li-storage capacity in hard carbon spherules. Solid State Ionics 176:1151–1159
101. Li W, Chen M, Wang C (2011) Spherical hard carbon prepared from potato starch using as anode material for Li-ion batteries. Mater Lett 65:3368–3370

102. Li C-C, Wang YW (2013) Importance of binder compositions to the dispersion and electrochemical properties of water-based $LiCoO_2$ cathodes. J Power Sourc 227:204–210
103. Boyanov S, Annou K, Villevieille C, Pelosi M, Zitoun D, Monconduit L (2008) Nanostructured transition metal phosphide as negative electrode for lithium-ion batteries. Ionics 14:183–190
104. Yashio M, Wang H, Fukuda K, Umeno T, Abe T, Ogumi Z (2004) Improvement of natural graphite as a lithium-ion battery anode material, from raw flake to carbon-coated sphere. J Mater Chem 14:1754–1758
105. Haik O, Ganin S, Gershinsky G, Zinigrad E, Markovsky B, Aurbach D, Halalay I (2011) On the thermal behavior of lithium intercalated graphites batteries and energy storage. J Electrochem Soc 158:A913–A923
106. Wang H, Yoshio M, Abe T, Ogumi Z (2002) Characterization of carbon-coated natural graphite as a lithium-ion battery anode material. J Electrochem Soc 149:A499–A503
107. Li C-C, Zheng H, Qu Q, Zhang L, Liu G, Battaglia VS (2012) Hard carbon: a promising lithium-ion battery anode for high temperature applications with ionic electrolyte. RSC Adv 2:4904–4912
108. Zhou HS, Zhu SM, Hibino M, Honma I, Ichihara M (2003) Lithium storage in ordered mesoporous carbon (CMK-3) with high reversible specific energy capacity and good cycling performance. Adv Mater 15:2107–2111
109. Li CC, Orsini F, du Pasquier A, Beaudouin B, Tarascon JM, Trentin M, Langenhuizen N, de Beer E, Notten P (1999) In situ SEM study of the interfaces in plastic lithium cells. J Power Sourc 81–82:918–921
110. Landi BJ, Ganter MJ, Cress CD, DiLeo RA, Raffaelle RP (2009) Carbon nanotubes for lithium ion batteries. Energ Environ Sci 2:638–654
111. Kim C, Yang KS, Kojima M, Yoshida K, Kim YJ, Kim YA, Endo M (2006) Fabrication of electrospinning-derived carbon nanofiber webs for the anode material of lithium-ion secondary batteries. Adv Funct Mater 16:2393–2397
112. Hou J, Shao Y, Ellis MW, Moore RB, Yi B (2011) Graphene-based electrochemical energy conversion and storage: fuel cells, supercapacitors and lithium ion batteries. Phys Chem Chem Phys 13:15384–15402
113. Cui G, Gu L, Zhi L, Kaskhedikar N, Aken PA, Mullen K, Maier J (2008) A germanium-carbon nanocomposite material for lithium batteries. Adv Mater 20:3079–3083
114. Candelaria SL, Shao Y, Zhou W, Li X, Xiao J, Zhang J-G, Wang Y, Liu J, Li J, Cao G (2012) Nanostructured carbon for energy storage and conversion. Nano Energy 1:195–220
115. Mabuchi A, Tokumitsu K, Fujimoto H, Kasuh T (1995) Charge-discharge characteristics of the mesocarbon microbeads heat-treated at different temperatures. J Electrochem Soc 142:1041–1046
116. Nagao M, Pitteloud C, Kamiyama T, Otomo T, Itoh K, Fukunaga T, Tatsumi K, Kanno R (2006) Structure characterization and lithiation mechanism of nongraphitized carbon for lithium secondary batteries, fuel cells, and energy conversion. J Electrochem Soc 153: A914–A919
117. Sun J, Liu H, Chen X, Evans DG, Yang W, Duan X (2013) Carbon nanorings and their enhanced lithium storage properties. Adv Mater 25:1124–1130
118. Yu Y, Cui C, Qian W, Xie Q, Zheng C, Kong C, Wei F (2013) Carbon nanotube production and application in energy storage. Asia Pac J Chem Eng 8:234–245
119. Meunier V, Kephart J, Roland C, Bernholc J (2002) Ab initio investigations of lithium diffusion in carbon nanotube systems. Phys Rev Lett 88:075506
120. Schauerman CM, Ganter MJ, Gaustad G, Babbitt CW, Raffaelle RP, Landi BJ (2012) Recycling single-wall carbon nanotube anodes from lithium ion batteries. J Mater Chem 22:12008–12015
121. Nishidate K, Hasegawa M (2005) Energetics of lithium ion adsorption on defective carbon nanotubes. Phys Rev B 71:245418

122. Zhao J, Buldum A, Han J, Ping Lu J (2000) First-principles study of Li-intercalated carbon nanotube ropes. Phys Rev Lett 85:1706–1709
123. DiLeo RA, Castiglia A, Ganter MJ, Rogers RE, Cress CD, Raffaelle RP, Landi BJ (2010) Enhanced capacity and rate capability of carbon nanotube based anodes with titanium contacts for lithium ion batteries. ACS Nano 4:6121–6131
124. Lv R, Zou L, Gui X, Kang F, Zhu Y, Zhu H, Wei J, Gu J, Wang K, Wu D (2008) High-yield bamboo-shaped carbon nanotubes from cresol for electrochemical application. Chem Commun 17:2046–2048
125. Zhou J, Song H, Fu B, Wu B, Chen X (2010) Synthesis and high-rate capability of quadrangular carbon nanotubes with one open end as anode materials for lithium-ion batteries. J Mater Chem 20:2794–2800
126. Oktaviano HS, Yamada K, Waki K (2012) Nano-drilled multiwalled carbon nanotubes: characterizations and application for LIB anode materials. J Mater Chem 22:25167–25173
127. Lahiri I, Oh S-M, Hwang JY, Cho S, Sun Y-K, Banerjee R, Choi W (2010) High capacity and excellent stability of lithium ion battery anode using interface-controlled binder-free multiwall carbon nanotubes grown on copper. ACS Nano 4:3440–3446
128. Lahiri I, Oh S-M, Hwang JY, Kang C, Choi M, Jeon H, Banerjee R, Sun YK, Choi W (2011) Ultrathin alumina-coated carbon nanotubes as an anode for high capacity Li-ion batteries. J Mater Chem 21:13621–13626
129. Leung K, Qi Y, Zavadil KR, Jung YS, Dillon AC, Cavanagh AS, Lee S-H, George SM (2011) Using atomic layer deposition to hinder solvent decomposition in lithium ion batteries: first-principles modeling and experimental studies. J Am Chem Soc 133:14741–14754
130. Jung YS, Cavanagh AS, Riley LA, Kang S-H, Dillon AC, Groner MD, George SM, Lee SH (2010) Ultrathin direct atomic layer deposition on composite electrodes for highly durable and safe Li-ion batteries. Adv Mater 22:2172–2176
131. Liu Y, Zheng Z, Liu XH, Huang S, Zhu T, Wang J, Kushim A, Hudak NS, Huang X, Zhang S, Mao SX, Qian X, Li J, Huang JY (2011) Lithiation-induced embrittlement of multiwalled carbon nanotubes. ACS Nano 5:7245–7253
132. Gu Y, Wu F, Wang Y (2013) Confined volume change in Sn-Co-C ternary tube-in-tube composites for high-capacity and long-life lithium storage. Adv Funct Mater 23:893–899
133. Yoon TH, Park YJ (2012) Electrochemical properties of CNTs/Co_3O_4 blended-anode for rechargeable lithium batteries. Solid State Ionics 225:498–501
134. Wu Y, Wei Y, Wang J, Jiang K, Fan S (2013) Conformal Fe_3O_4 sheath on aligned carbon nanotube scaffolds as high-performance anodes for lithium ion batteries. Nano Lett 13:818–823
135. Bindumadhavan K, Srivastava SK, Mahanty S (2013) MoS_2-MWCNT hybrids as a superior anode in lithium-ion batteries. Chem Commun 49:1823–1825
136. Liang M, Zhi L (2009) Graphene-based electrode materials for rechargeable lithium batteries. J Mater Chem 19:5871–5878
137. Brownson DAC, Kampouris DK, Banks CE (2011) An overview of graphene in energy production and storage applications. J Power Sourc 196:4873–4885
138. Liu Y, Artyukhov VI, Liu M, Harutyunyan AR, Yakobson BI (2013) Feasibility of lithium storage on graphene and its derivatives. J Phys Chem Lett 4:1737–1742
139. Hwang HY, Koo J, Park M, Park N, Kwon Y, Lee H (2013) Multilayer graphynes for lithium ion battery anode. J Phys Chem C 117:6919–6923
140. Pan D, Wang S, Zhao B, Wu M, Zhang H, Wang Y, Jiao Z (2009) Storage properties of disordered graphene nanosheets. Chem Mater 21:3136–3142
141. Yoo E, Kim J, Hosono E, Zhou H, Kudo T, Honma I (2008) Large reversible Li storage of graphene nanosheet families for use in rechargeable lithium ion batteries. Nano Lett 8:2277–2282
142. Bhardwaj T, Antic A, Pavan B, Barone V, Fahlman BD (2010) Enhanced electrochemical lithium storage by graphene nanoribbons. J Am Chem Soc 132:12556–12558

143. Wu ZS, Ren W, Wen L, Gao L, Zhao J, Chen Z, Zhou G, Li F, Cheng HM (2010) Graphene anchored with Co3O4 nanoparticles as anode of lithium ion batteries with enhanced reversible capacity and cyclic performance. ACS Nano 4:3187–3194
144. Wang ZL, Xu D, Wang HG, Wu Z, Zhang XB (2013) In situ Fabrication of porous graphene electrodes for high-performance energy storage. ACS Nano 7:2422–2430
145. Lee SU, Belosludov RV, Mizuseki H, Kawazoe Y (2009) Designing nanogadgetry for nanoelectronic devices with nitrogen-doped capped carbon nanotubes. Small 5:1769–1775
146. Mahmood N, Zhang C, Liu F, Zhu J, Hou Y (2013) Hybrid of Co_3Sn_2-Co nanoparticles and nitrogen-doped graphene as a lithium ion battery anode. ACS Nano 7:10307–10318
147. Mukherjee R, Thomas AV, KrishnamurthY A, Koratkar N (2012) Photothermally reduced graphene as high power anodes for lithium-ion batteries. ACS Nano 6:7876–7878
148. Zhang H-L, Liu S-H, Li F, Bai S, Liu C, Tan J, Cheng H-M (2006) Electrochemical performance of pyrolytic carbon-coated natural graphite spheres. Carbon 44:2212–2218
149. Fu LJ, Liu H, Li C, Wu YP, Rahm E, Holze R, Wu HQ (2006) Surface modifications of electrode materials for lithium ion batteries. Solid State Sci 8:113–128
150. Wang J, Liu J-L, Wang Y-G, Wang C-X, Xia Y-Y (2012) Pitch modified hard carbons as negative materials for lithium-ion batteries. Electrochim Acta 74:1–7
151. Ge M, Rong J, Fang X, Zhou C (2012) Porous doped silicon nanowires for lithium ion battery anode with long cycle life. Nano Lett 12:2318–2323
152. Ge MY, Lu YH, Ercius P, Rong JP, Fang X, Zhou CW, Mecklenburg M (2014) Large-scale fabrication, 3D tomography, and lithium-ion battery application of porous silicon. Nano Lett 14:261–268
153. Besenhard JO, Yang J, Winter M (1997) Will advanced lithium-alloy anodes have a chance in lithium-ion batteries? J Power Sourc 68:87–90
154. Beaulieu LY, Eberman KW, Turner RL, Krause LJ, Dahn JR (2001) Colossal reversible volume changes in lithium alloys. Electrochem Solid State Lett 4:A137–A140
155. Beaulieu LY, Hatchard TD, Bonakdarpour A, Fleischauer MD, Dahn JR (2003) Reaction of Li with alloy thin films studied by in situ AFM. J Electrochem Soc 150:A1457–A1464
156. Zhang XW, Patil PK, Wang CS, Appleby AJ, Little FE, Cocke DL (2004) Electrochemical performance of lithium ion battery, nano-silicon-based, disordered carbon composite anodes with different microstructures. J Power Sourc 125:206–213
157. Chan CK, Peng HL, Liu G, McIlwrath K, Zhang XF, Huggins RA, Cui Y (2008) High-performance lithium battery anodes using silicon nanowires. Nat Nanotechnol 3:31–35
158. McDowell MT, Lee SW, Wang C, Cui Y (2012) The effect of metallic coatings and crystallinity on the volume expansion of silicon during electrochemical lithiation/delithiation. Nano Energy 1:401–410
159. Maver U, Znidarsic A, Gaberscek M (2011) An attempt to use atomic force microscopy for determination of bond type in lithium battery electrodes. J Mater Chem 21:4071–4075
160. Soni SK, Sheldon BW, Xiao XC, Verbrugge MW, Ahn D, Haftbaradaran H, Gao HJ (2012) Stress mitigation during the lithiation of patterned amorphous Si islands. J Electrochem Soc 159:A38–A43
161. Lee KL, Jung JY, Lee SW, Moon HS, Park JW (2004) Electrochemical characteristics of a-Si thin film anode for Li-ion rechargeable batteries. J Power Sourc 129:270–274
162. Park MS, Wang GX, Liu HK, Dou SX (2006) lectrochemical properties of Si thin film prepared by pulsed laser deposition for lithium ion micro-batteries. Electrochim Acta 51:5246–5249
163. Raimann PR, Hochgatterer NS, Korepp C, Moller KC, Winter M, Schrottner H, Hofer F, Besenhard JO (2006) Monitoring dynamics of electrode reactions in Li-ion batteries by in situ ESEM. Ionics 12:253–255
164. Kim H, Choi J, Sohn HJ, Kang T (1999) The Insertion mechanism of lithium into Mg_2Si anode material for Li-ion batteries. J Electrochem Soc 146:4401–4405
165. Wachtler M, Winter M, Besenhard JO (2002) Anodic materials for rechargeable Li-batteries. J Power Sourc 105:151–160

166. Kim JW, Ryu JH, Lee KT, Oh SM (2005) Improvement of silicon powder negative electrodes by copper electroless deposition for lithium secondary batteries. J Power Sourc 147:227–233
167. Simon GK, Goswami T (2011) Improving anodes for lithium ion batteries. Metall Mater Trans A 42:231–238
168. Hovington P, Dontigny M, Guerfi A, Trottier J, Lagacé M, Mauger A, Julien CM, Zaghib K (2014) In situ Scanning electron microscope study and microstructural evolution of nano silicon anode for high energy Li-ion batteries. J Power Sourc 248:457–464
169. Lee SW, McDowell MT, Berla ML, Nix WD, Cui Y (2012) Fracture of crystalline silicon nanopillars during electrochemical lithium insertion. Proc Natl Acad Sci U S A 109:4080–4085
170. Liu XH, Zhong L, Huang S, Mao SX, Huang JH (2012) Size-dependent fracture of silicon nanoparticles during lithiation. ACS Nano 6:1522–1531
171. Soni K, Sheldon BW, Xiao X, Bower AF, Verbrugge MW (2012) Diffusion mediated lithiation stresses in Si thin film electrodes batteries and energy storage. J Electrochem Soc 159:A1520–A1527
172. Ryu JH, Kim JW, Sung YE, Oh SM (2004) Failure modes of silicon Powder Negative Electrode in Lithium secondary Batteries. Electrochem Solid State Lett 7:A306–A309
173. Goldman JL, Long BR, Gewirth AA, Nuzzo RG (2011) Strain anisotropies and self-limiting capacities in single-crystalline 3D silicon microstructures: models for high energy density lithium-ion battery anodes. Adv Funct Mater 21:2412–2422
174. Si Q, Hanna K, Imanishi N, Kubo M, Hirano A, Takeda Y, Yamamotao O (2009) Highly reversible carbon-nano-silicon composite anodes for lithium rechargeable batteries. J Power Sourc 189:761–765
175. Yang J, Winter M, Besenhard JO (1996) Small particle size multiphase Li-alloy anodes for lithium-ion batteries. Solid State Ionics 90:281–287
176. Trifonova A, Wachtler M, Wagner MR, Schroettner H, Mitterbauer C, Hofer F, Moller KC, Winter M, Besenhard JO (2004) Influence of the reductive preparation conditions on the morphology and on the electrochemical performance of Sn/SnSb. Solid State Ion 168:51–59
177. Ruffo R, Hong SS, Chan CK, Huggins RA, Cui Y (2009) Impedance analysis of silicon nanowire lithium ion battery anodes. J Phys Chem C 113:11390–11398
178. Chan CK, Ruffo R, Hong SS, Cui Y (2009) Surface chemistry and morphology of the solid electrolyte interphase on silicon nanowire lithium-ion battery anodes. J Power Sourc 189:1132–1140
179. Wu XD, Wang ZX, Chen LQ, Huang XJ (2003) Ag-enhanced SEI formation on Si particles for lithium batteries. Electrochem Commun 5:935–939
180. Stjerndahl M, Bryngelsson H, Gustafsson T, Vaughey JT, Tackeray MM, Edstrom K (2007) Surface chemistry of intermetallic AlSb-anodes for Li-ion batteries. Electrochim Acta 52:4947–4955
181. Obrovac MN, Christensen L (2004) Structural changes in silicon anodes during lithium insertion/extraction. Electrochem Solid State Lett 7:A93–A96
182. Obrovac MN, Krause JL (2007) Reversible cycling of crystalline silicon powder. J Electrochem Soc 154:A103–A108
183. Bridel J-S, Azaïs T, Morcrette M, Tarascon J-M, Larcher D (2011) In situ observation and long-term reactivity of Si/C/CMC composites electrodes for Li-ion batteries. J Electrochem Soc 158:A750–A759
184. Jung H, Park M, Yoon YG, Joo GB, Kim SK (2003) Amorphous silicon anode for lithium-ion rechargeable batteries. J Power Sourc 115:346–351
185. Yin J, Wada M, Yamamoto K, Kitano Y, Tanase S, Sakai T (2006) Micrometer-scale amorphous Si thin-film electrodes fabricated by electron-beam deposition for Li-ion batteries. J Electrochem Soc 153:A472–A477
186. Wang JS, Liu P, Sherman E, Verbrugge M, Tataria H (2011) Formulation and characterization of ultra-thick electrodes for high energy lithium-ion batteries employing tailored metal foams. J Power Sourc 196:8714–8718

187. Lee SW, McDowell MT, Choi JW, Cui Y (2011) Anomalous shape changes of silicon nanopillars by electrochemical lithiation. Nano Lett 11:3034–3040
188. Wagesreither S, Lugstein A, Bertagnolli E (2012) Anisotropic lithiation behavior of crystalline silicon. Nanotechnology 23:495716
189. Liu XH, Wang JW, Huang S, Fan FF, Huang X, Liu Y, Krylyuk S, Yoo J, Dayeh SA, Davydov AV, Mao SX, Picraux ST, Zhang SL, Li J, Zhu T, Huang JY (2012) In situ atomic-scale imaging of electrochemical lithiation in silicon. Nat Nanotechnol 7:749–756
190. Baranchugov V, Markevich E, Pollak E, Salitra G, Aurbach D (2007) Amorphous silicon thin films as a high capacity anodes for Li-ion batteries in ionic liquid electrolytes. Electrochem Commun 9:796–800
191. Liu XH, Liu Y, Kushima A, Zhang SL, Zhu T, Li J, Huang HY (2012) In situ TEM sxperiments of electrochemical lithiation and delithiation of individual nanostructures. Adv Energy Mater 2:722–741
192. Ohara S, Suzuki J, Sekine K, Takamura T (2004) A thin film silicon anode for Li-ion batteries having a very large specific capacity and long cycle life. J Power Sourc 136:303–306
193. Takamura T, Ohara S, Uehara M, Suzuki J, Sekine K (2004) A vacuum deposited Si film having a Li extraction capacity over 2000 mAh/g with a long cycle life. J Power Sourc 129:96–100
194. Maranchi JP, Hepp AF, Kumta PN (2003) High capacity, reversible silicon thin-film anodes for lithium-ion batteries. Electrochem Solid State Lett 6:A198–A201
195. Kim JB, Lee H-Y, Lee KS, Lim SH, Lee S-M (2003) Fe/Si multi-layer thin film anodes for lithium rechargeable thin film batteries. Electrochem Commun 5:544–548
196. Lee HY, Lee SM (2002) Graphite-FeSi alloy composites as anode materials for rechargeable lithium batteries. J Power Sourc 112:649–654
197. Ohara S, Suzuki J, Sekine K, Takamura T (2003) Li insertion/extraction reaction at a Si film evaporated on a Ni foil. J Power Sourc 119–121:591–596
198. Chen LB, Xie JY, Yu HC, Wang TH (2009) An amorphous Si thin film anode with high capacity and long cycling life for lithium ion batteries. J Appl Electrochem 39(8):1157–1162
199. Schmidt V, Wittemann JV, Gösele U (2010) Growth, thermodynamics, and electrical properties of silicon nanowires. Chem Rev 110:361–388
200. Nguyen HT, Yao F, Zamfir MR, Biswas C, So KP, Lee YH, Kim SM, Cha SN, Kim JM, Pribat D (2011) Highly interconnected Si nanowires for improved stability Li-ion battery anodes. Adv Energy Mater 1:1154–1161
201. Cui LF, Ruffo R, Chan CK, Peng HL, Cui Y (2009) Crystalline-amorphous core−shell Silicon nanowires for high capacity and high current battery electrodes. Nano Lett 9:491–495
202. Mc Dowell MT, Lee SW, Harris JT, Korgel BA, Wang C, Nix WD, Cui Y (2013) In situ TEM of two-phase lithiation of amorphous silicon nanospheres. Nano Lett 13:758–764
203. Chockla AM, Bogart TD, Hessel CM, Klavetter KC, Mullins CB, Korgel BA (2012) Influences of gold, binder and electrolyte on silicon nanowire performance in Li-ion batteries. J Phys Chem C 116:18079–180086
204. Kovalenko I, Zdyrko B, Magasinski A, Hertzberg B, Milicev Z, Burtovyy R, Luzinov I, Yushin G (2011) A Major constituent of brown algae for use in high-capacity Li-ion batteries. Science 334:75–79
205. Bang BM, Kim H, Song HK, Cho J, Park S (2011) Scalable approach to multi-dimensional bulk Si anodes *via* metal-assisted chemical etching. Energ Environ Sci 4:5013–5019
206. Kim H, Han B, Choo J, Cho J (2008) Three-dimensional porous silicon particles for use in high-performance lithium secondary batteries. J Angew Chem Int Ed 47:10151–10154
207. Yao Y, McDowell MT, Ryu I, Wu H, Liu N, Hu L, Nix WD, Cui Y (2011) Interconnected silicon hollow nanospheres for lithium-ion battery anodes with long cycle life. Nano Lett 11:2949–2954
208. Wang XL, Han WQ (2010) Graphene enhances Li storage capacity of porous single-crystalline silicon nanowires. ACS Appl Mater Interfaces 2:3709–3713

209. Rong JP, Masarapu C, Ni J, Zhang ZJ, Wei BQ (2010) Tandem structure of porous silicon film on single-walled carbon nanotube macrofilms for lithium-ion battery applications. ACS Nano 4:4683–4690
210. Guo J, Sun A, Wang C (2010) A porous silicon-carbon anode with high overall capacity on carbon fiber current collector. Electrochem Commun 12:981–984
211. Ma H, Cheng FY, Chen J, Zhao JZ, Li CS, Tao ZL, Liang J (2007) Nest-like silicon nanospheres for high-capacity lithium storage. Adv Mater 19:4067–4070
212. Ge M, Rong J, Fang X, Zhang A, Lu Y, Zhou C (2013) Scalable preparation of porous silicon nanoparticles and their application for lithium-ion battery anodes. Nano Res 6:174–181
213. Peng KQ, Hu JJ, Yan YJ, Wu Y, Fang H, Xu Y, Lee ST, Zhu J (2006) Fabrication of single-crystalline silicon nanowires by scratching a silicon surface with catalytic metal particles. Adv Func Mater 16:387–394
214. Zhao Y, Liu XZ, Li HQ, Zhai TY, Zhou HS (2012) Hierarchical micro/nano porous silicon Li-ion battery anodes. Chem Commun 48:5079–5081
215. Bang BM, Lee JI, Kim H, Cho J, Park S (2012) High-performance macroporous bulk silicon anodes synthesized by template-free chemical etching. Adv Energy Mater 2:878–883
216. Thakur M, Pernites RB, Nitta N, Isaacson M, Sinsabaugh SL, Wong MS, Biswal SL (2012) Freestanding macroporous silicon and pyrolyzed polyacrylonitrile as a composite anode for lithium ion batteries. Chem Mater 24:2998–3003
217. Thakur M, Isaacson M, Sinsabaugh SL, Wong MS, Biswal SL (2012) Gold-coated porous silicon films as anodes for lithium ion batteries. J Power Sourc 205:426–432
218. Thakur M, Sinsabaugh SL, Isaacson MJ, Wong MS, Biswal SL (2012) Inexpensive method for producing macroporous silicon particulates (MPSPs) with pyrolyzed polyacrylonitrile for lithium ion batteries. Sci Rep 2:00795
219. Zhang HG, Braun PV (2012) Three-dimensional metal scaffold supported bicontinuous silicon battery anodes. Nano Lett 12:2778–2783
220. Gowda SR, Pushparaj V, Herle S, Girishkumar G, Gordon JG, Gullapalli H, Zhan XB, Ajayan PM, Reddy ALM (2012) Three-dimensionally engineered porous silicon electrodes for Li ion batteries. Nano Lett 12:6060–6065
221. Chan CK, Patel RN, O'Connell MJ, Korgel BA, Cui Y (2010) Solution-grown silicon nanowires for lithium-ion battery anodes. ACS Nano 4:1443–1450
222. Kim H, Cho J (2008) Superior Lithium electroactive mesoporous Si-carbon core – shell nanowires for lithium battery anode material. Nano Lett 8:3688–3691
223. Song T, Cheng HY, Choi H, Lee JH, Han H, Lee DH, Yoo DS, Kwon MS, Choi JM, Doo SG, Chang H, Xiao JL, Huang YG, Park WI, Chung YC, Kim H, Rogers JA, Paik U (2012) Si/Ge double-layered nanotube array as a lithium ion battery anode. ACS Nano 6:303–309
224. Song T, Xia JL, Lee JH, Lee DH, Kwon MS, Choi JM, Wu J, Doo SK, Chang H, Park W, Il Zang DS, Kim H, Huang YG, Hwang KC, Rogers JA, Paik U (2010) Arrays of sealed silicon nanotubes as anodes for lithium ion batteries. Nano Lett 10:1710–1716
225. Park MH, Kim MG, Joo J, Kim K, Kim J, Ahn S, Cui Y, Cho J (2009) Silicon nanotube battery anodes. Nano Lett 9:3844–3847
226. Cui LF, Hu LB, Wu H, Choi JW, Cui Y (2011) Inorganic glue enabling high performance of silicon particles as lithium ion battery anode. J Electrochem Soc 158:A592–A596
227. Hu LB, Wu H, Hong SS, Cui LF, McDonough JR, Bohy S, Cui Y (2011) Si nanoparticle-decorated Si nanowire networks for Li-ion battery anodes. Chem Commun 47:367–369
228. Nadimpalli SP, Sethuraman VA, Dalavi S, Lucht B, Chon MJ, Shenoy VB, Guduru PR (2012) Quantifying capacity loss due to solid-electrolyte-interphase layer formation on silicon negative electrodes in lithium-ion batteries. J Power Sourc 215:145–151
229. Liu N, Wu H, McDowell MT, Yao Y, Wang C, Cui Y (2012) Kinetic competition model and size-dependent phase selection in 1-D nanostructures. Nano Lett 12:3315–3322
230. Zhou XY, Tang JJ, Yang J, Xie J, Ma L-L (2013) Silicon-carbon hollow core-shell heterostructures novel anode materials for lithium ion batteries. Electrochim Acta 87:663–668

231. Zhao K, Pharr M, Hartle L, Vlassak JJ, Suo Z (2012) Fracture and debonding in lithium-ion batteries with electrodes of hollow core-shell nanostructures. J Power Sourc 218:6–14
232. Hao F, Fang D (2013) Diffusion-induced stresses of spherical core-shell electrodes in lithium-ion batteries: the effects of the shell and surface/interface stress batteries and energy storage. J Electrochem Soc 160:A595–A600
233. Chen S, Gordin ML, Yi R, Howlett G, Sohn H, Wang D (2012) Silicon core-hollow carbon shell nanocomposites with tunable buffer voids for high capacity anodes of lithium-ion batteries. Phys Chem Chem Phys 14:12741–12745
234. Li X, Meduri P, Chen X, Qi W, Engelhard MH, Xu W, Ding F, Xiao J, Wang W, Wang C (2012) Hollow core-shell structured porous Si-C nanocomposites for Li-ion battery anodes. J Mater Chem 22:11014–11017
235. Chen HX, Dong ZX, Fu YP, Yang Y (2010) Silicon nanowires with and without carbon coating as anode materials for lithium-ion batteries. J Solid State Electrochem 14:1829–1834
236. Chen H, Xiao Y, Wang L, Yang Y (2011) Silicon nanowires coated with copper layer as anode materials for lithium-ion batteries. J Power Sourc 196:6657–6662
237. Sethuraman VA, Kowolik K, Srivinasan V (2011) Increased cycling efficiency and rate capability of copper-coated silicon anodes in lithium-ion batteries. J Power Sourc 196: 393–398
238. Yao Y, Liu N, McDowell MT, Pasta M, Cui Y (2012) Improving the cycling stability of silicon nanowire anodes with conducting polymer coatings. Energ Environ Sci 5:7927–7930
239. Memarzadeh EL, Kalisvaart WP, Kohandehghan A, Zahiri B, Holt CMB, Mitlin D (2012) Silicon nanowire core aluminum shell coaxial nanocomposites for lithium ion battery anodes grown with and without a TiN interlayer. J Mater Chem 22:6655–6668
240. Ryu I, Choi JW, Cui Y, Nix WD (2011) Size-dependent fracture of Si nanowire battery anodes. J Mech Phys Solids 59:1717–1730
241. Liu XH, Zheng H, Zhong L, Huang S, Karki K, Zhang LQ, Liu Y, Kushima A, Liang WT, Wang JW, Cho JH, Epstein E, Dayeh SA, Picraux ST, Zhu T, Li J, Sullivan JP, Cumings J, Wang C, Mao SX, Ye ZZ, Zhang S, Huang JH (2011) Anisotropic swelling and fracture of silicon nanowires during lithiation. Nano Lett 11:3312–3318
242. Xiao X, Lu P, Dahn J (2011) Ultrathin multifunctional oxide coatings for lithium ion batteries. Adv Mater 23:3911–3915
243. He Y, Yu X, Wang Y, Li H, Huang X (2011) Alumina-coated patterned amorphous silicon as the anode for a lithium-ion battery with high coulombic efficiency. Adv Mater 23:4938–4941
244. Nguyen HT, Zamfir MR, Duong LD, Lee YH, Bondavalli P, Pribat D (2012) lumina-coated silicon-based nanowire arrays for high quality Li-ion battery anodes. J Mater Chem 22: 24618–24626
245. Liu Y, Hudak NS, Huber DL, Limmer SJ, Sullivan JP, Huang JY (2011) In situ transmission electron microscopy observation of pulverization of aluminum nanowires and evolution of the thin surface Al_2O_3 layers during lithiation-delithiation cycles. Nano Lett 11:4188–4194
246. Wu H, Chan G, Choi JW, Ryu I, Yao Y, McDowell MT, Lee SW, Jackson A, Yang Y, Hu LB, Cui Y (2012) Stable cycling of double-walled silicon nanotube battery anodes through solid-electrolyte interphase control. Nat Nanotechnol 7:310–315
247. Rong J, Fang X, Ge M, Chen H, Xu J, Zhou C (2013) Coaxial Si/anodic titanium oxide/Si nanotube arrays for lithium-ion battery anodes. Nano Res 6:182–190
248. Choi N-S, Yao Y, Cui Y, Cho J (2011) One dimensional Si/Sn-based nanowires and nanotubes for lithium-ion energy storage materials. J Mater Chem 21:9825–9840
249. Liu XH, Zhang LQ, Zhong L, Liu Y, Zheng H, Wang JW, Cho JH, Dayeh SA, Picraux ST, Sullivan JP, Mao SX, Ye ZZ, Huang JY (2011) Ultrafast electrochemical lithiation of individual Si nanowire anodes. Nano Lett 11:2251–2258
250. Fuchsbichler B, Stangl C, Kren H, Uhlig F, Koller S (2011) High capacity graphite-silicon composite anode material for lithium-ion batteries. J Power Sourc 196:2889–2892
251. Jung DS, Hwang TH, Park SB, Choi JW (2013) Spray drying method for large-scale and high-performance silicon negative electrodes in Li-ion batteries. Nano Lett 13:2092–2097

252. Magasinski A, Dixon P, Hertzberg B, Kvit A, Ayala J, Yushin G (2010) High-performance lithium-ion anodes using a hierarchical bottom-up approach. Nat Mater 9:353–358
253. Nyholm L, Nyström G, Mihranyan A, Stromme M (2011) Toward flexible polymer and paper-based energy storage devices. Adv Mater 23:3751–3769
254. Chou SL, Zhao Y, Wang J-Z, Chen ZX, Liu H-K, Dou S-X (2010) Silicon/single-walled carbon nanotube composite paper as a flexible anode material for lithium ion batteries. J Phys Chem C 114:15862–15867
255. Li X, Cho J-H, Li N, Zhang Y, Williams D, Dayeh SA, Picraux ST (2012) Carbon nanotube-enhanced growth of silicon nanowires as an anode for high-performance lithium-ion batteries. Adv Energy Mater 2:87–93
256. Evanoff K, Kahn J, Balandin AA, Magasinski A, Ready WJ, Fuller TF, Yushin G (2012) Towards ultrathick battery electrodes: aligned carbon nanotube, enabled architecture. Adv Mater 24:533–537
257. Wen Z, Lu G, Mao S, Kim H, Cui S, Yu K, Huang X, Hurle PT, Mao O, Chen J (2013) Silicon nanotube anode for lithium-ion batteries. Electrochem Commun 29:67–70
258. Baggetto L, Notten PHL (2009) Lithium-ion (de)insertion reaction of germanium thin-film electrodes: an electrochemical and in situ XRD study batteries and energy storage. J Electrochem Soc 156:A169–A175
259. Seo M-H, Park M, Lee KT, Kim K, Kim J, Cho J (2011) High performance Ge nanowire anode sheathed with carbon for lithium rechargeable batteries. Energ Environ Sci 4:425–428
260. Park M, Cho Y, Kim K, Kim J, Liu M, Cho J (2011) Germanium nanotubes prepared by using the Kirkendall effect as anodes for high-rate lithium batteries. Angew Chem Int Ed 50:9647–9650
261. Liu XH, Huang S, Picraux ST, Li J, Zhu T, Huang JY (2011) Reversible nanopore formation in Ge nanowires during lithiation-delithiation cycling: an in situ transmission electron microscopy study. Nano Lett 11:3991–3997
262. Liang W, Yang H, Fan F, Liu Y, Liu XH, Huang XH, Zhu T, Zhang S (2013) Tough germanium nanoparticles under electrochemical cycling. ACS Nano 7:3427–3433
263. Graetz J, Ahn CC, Yazami R, Fultz B (2004) Nanocrystalline and thin film Germanium electrodes with high lithium capacity and high rate capabilities. J Electrochem Soc 151: A698–A702
264. Abel PR, Chockla AM, Lin Y-M, Holmberg VC, Harris JT, Korgel BA, Heller A, Mullins CB (2013) Nanostructured $Si_{(1-x)}Ge_x$ for tunable thin film lithium-ion battery anodes. ACS Nano 7:2249–2257
265. Zhang C, Pang S, Kong Q, Liu Z, Hu H, Jiang W, Han P, Wang D, Cui G (2013) An elastic germanium-carbon nanotubes-copper foam monolith as an anode for rechargeable lithium batteries. RSC Adv 3:1336–1340
266. Ren J-G, Wu Q-H, Tang H, Hong G, Zhang W, Lee S-T (2013) Germanium-graphene composite anode for high-energy lithium batteries with long cycle life. J Mater Chem A 1:1821–1826
267. Chockla AM, Klavetter KC, Mullins CB, Korgel BA (2012) Solution-grown germanium nanowire anodes for lithium-ion batteries. ACS Appl Mater Interfaces 4:4658–4664
268. Zaghib K, Dontigny M, Guerfi A, Trottier J, Hamel-Paquet J, Gariepy V, Galoutov K, Hovington P, Mauger A, Groult H, Julien CM (2012) An improved high-power battery with increased thermal operating range: C-$LiFePO_4$//C-$Li_4Ti_5O_{12}$. J Power Sourc 216:192–200
269. Yan C, Xi W, Si W, Deng J, Schmidt OG (2013) Highly conductive and strain-released hybrid multilayer Ge/Ti nanomembranes with enhanced lithium-ion-storage capability. Adv Mater 25:539–544
270. Yuan FW, Yang HJ, Tuan HY (2012) Alkanethiol-passivated Ge nanowires as high-performance anode materials for lithium-ion batteries: the role of chemical surface functionalization. ACS Nano 6:9932–9942
271. Xue DJ, Xin S, Yan Y, Jiang KC, Yin YX, Guo YG, Wan LJ (2012) Improving the electrode performance of Ge through Ge-C core-shell nanoparticles and graphene networks. J Am Chem Soc 134:2512–2515

272. Hwang IS, Kim J-C, Seo SD, Lee S, Lee JH, Kim DW (2012) A binder-free Ge-nanoparticle anode assembled on multiwalled carbon nanotube networks for Li-ion batteries. Chem Commun 48:7061–7063
273. Chan CK, Zhang XF, Cui Y (2008) High capacity Li ion battery anodes using Ge nanowires. Nano Lett 8:307–309
274. Yu Y, Gu L, Wang C, Dhanabalan A, Aken PAV, Maier J (2009) Encapsulation of Sn-carbon nanoparticles in bamboo-like hollow carbon nanofibers as an anode material in lithium-based batteries. Angew Chem Int Ed 48:6485–6489
275. Wang Y, Wu M, Jiao Z, Lee JY (2009) Sn-CNT and Sn-C-CNT nanostructures for superior reversible lithium ion storage. Chem Mater 21:3210–3215
276. Kumar TP, Ramesh R, Lin YY, Fey GTK (2004) Tin-filled carbon nanotubes as insertion anode materials for lithium-ion batteries. Electrochem Commun 6:520–525
277. Zhao H, Jiang C, He X, Ren J, Wan C (2007) Advanced structures in electrodeposited tin base anodes for lithium ion batteries. Electrochim Acta 52:7820–7826
278. Chen Z, Cao Y, Qian J, Ai X, Yang H (2012) Pb-sandwiched nanoparticles as anode material for lithium-ion batteries. J Solid State Electrochem 16:291–295
279. Pfanzelt M, Kubiak P, Fleischhammer M, Wohlfahrt-Mehrens M (2011) TiO_2 rutile – an alternative anode material for safe lithium-ion batteries. J Power Sourc 196:6815–6821
280. Belharouak I, Sun Y-K, Lu W, Amine K (2007) On the Safety of the $Li_4Ti_5O_{12}$/$LiMn_2O_4$ lithium-ion battery system batteries and energy storage. J Electrochem Soc 154:A1083–A1087
281. Chen JZ, Yang L, Tang YF (2010) Electrochemical lithium storage of TiO_2 hollow microspheres assembled by nanotubes. J Power Sourc 195:6893–6896
282. Lai C, Li GR, Dou YY, Gao XP (2010) Mesoporous polyaniline or polypyrrole/anatase TiO_2 nanocomposite as anode materials for lithium-ion batteries. Electrochim Acta 55:4567–4572
283. Gnanasekar KI, Subramanian V, Robinson J, Jiang JC, Posey FE, Rambabu B (2002) Direct conversion of TiO_2 sol to nanocrystalline anatase at 85 °C. J Mater Res 17:1507–1512
284. Subramanian V, Karki A, Gnanasekar KI, Eddy FP, Rambabu B (2006) Nanocrystalline TiO_2 (anatase) for Li-ion batteries. J Power Sourc 159:186–192
285. Wang JP, Bai Y, Wu MY, Yin J, Zhang WF (2009) Preparation and electrochemical properties of TiO_2 hollow spheres as an anode material for lithium-ion batteries. J Power Sourc 191:614–618
286. Kubiak P, Pfanzelt M, Geserick J, Hormann U, Husing N, Kaiser U, Wohlfahrt-Mehrens M (2009) Electrochemical evaluation of rutile TiO_2 nanoparticles as negative electrode for Li-ion batteries. J Power Sourc 194:1099–1104
287. Mancini M, Kubiak P, Geserick J, Marassi R, Husing N, Wohlfahrt-Mehrens M (2009) Mesoporous anatase TiO_2 composite electrodes: electrochemical characterization and high rate performances. J Power Sourc 189:585–589
288. Saravanan K, Ananthanarayanan K, Balaya P (2010) Mesoporous TiO_2 with high packing density for superior lithium storage. Energ Environ Sci 3:939–948
289. Beuvier T, Richard-Plouet M, Mancini-Le Granvalet M, Brousse T, Crosnier O, Brohan L (2010) TiO_2(B) nanoribbons as negative electrode material for lithium ion batteries with high rate performance. Inorg Chem 49:8457–8464
290. Inaba M, Oba Y, Niina F, Murota Y, Ogino Y, Tasaka A, Hirota K (2009) TiO_2(B) as a promising high potential negative electrode for large-size lithium-ion batteries. J Power Sourc 189:580–584
291. Jin YH, Lee SH, Shim HW, Ko KH, Kim DW (2010) Tailoring high-surface-area nanocrystalline TiO_2 polymorphs for high-power Li ion battery electrodes. Electrochim Acta 55:7315–7321
292. Wei Z, Liu Z, Jiang R, Bian C, Huang T, Yu A (2010) TiO_2 nanotube array film prepared by anodization as anode material for lithium ion batteries. J Solid State Electrochem 14:1045–1050
293. Kim HS, Kang SH, Chung YH, Sung YE (2010) Conformal Sn coated TiO_2 nanotube arrays and Its electrochemical performance for high rate lithium-ion batteries and energy storage. Electrochem Solid State Lett 13:A15–A18

294. Reddy MV, Jose R, Teng TH, Chowdari BVR, Ramakrishna S (2010) Preparation and electrochemical studies of electrospun TiO_2 nanofibers and molten salt method nanoparticles. Electrochim Acta 55:3109–3117
295. Li H, Martha S, Unocic RR, Luo H, Dai S, Qu J (2012) High cyclability of ionic liquid-produced TiO_2 nanotube arrays as an anode material for lithium-ion batteries. J Power Sourc 218:88–92
296. Nam SH, Shim H-S, Kim YS, Dar MA, Kim JG, Kim WB (2010) Ag or Au nanoparticle-embedded one-dimensional composite TiO_2 nanofibers prepared via electrospinning for use in lithium-ion batteries. ACS Appl Mater Interfaces 2:2046–2052
297. Zhou WJ, Liu H, Boughton RI, Du GJ, Lin JJ, Wang JY, Liu D (2010) One-dimensional single-crystalline Ti-O based nanostructures: properties, synthesis, modifications and applications. J Mater Chem 20:5993–6008
298. Wagemaker M, Borghols WJH, Mulder FM (2007) Large impact of particle size on insertion reactions. A case for anatase Li_xTiO_2. J Am Chem Soc 129:4323–4327
299. Luca V, Hunter B, Moubaraki B, Murray KS (2001) Lithium intercalation in anatase-structural and magnetic considerations. Chem Mater 13:796–801
300. Gubbens PCM, Wagemaker M, Sakarya S, Blaauw M, Yaouanc A, de Reotier PD, Cottrell PS (2006) Muon spin relaxation in $Li_{0.6}TiO_2$ anode material. Solid State Ionics 177:145–147
301. Wagemaker M, Borghols WJH, van Eck ERH, Kentgens APM, Kearley GL, Mulder FM (2007) The influence of size on phase morphology and Li-ion mobility in nanosized lithiated anatase TiO_2. Chem Eur J 13:2023–2028
302. Borghols WJH, Lutzenkirchen-Hecht D, Haake U, van Eck ERH, Mulder FM, Wagemaker M (2009) The electronic structure and ionic diffusion of nanoscale $LiTiO_2$ anatase. Phys Chem Chem Phys 11:5742–5748
303. Ganapathy S, van Eck ERH, Kentgens PM, Mulder FM, Wagemaker M (2011) Equilibrium lithium-ion transport between nanocrystalline lithium-inserted anatase TiO_2 and the electrolyte. Chem Eur J 17:14811–14816
304. Jung HG, Oh SW, Ce J, Jayaprakash N, Sun YK (2009) Mesoporous TiO_2 nano networks: anode for high power lithium battery applications. Electrochem Commun 11:756–759
305. Ren Y, Hardwick LJ, Bruce PG (2010) Lithium intercalation into mesoporous anatase with an ordered 3D pore structure. Angew Chem Int Ed 49:2570–2574
306. Zhong L-S, Hu J-S, Wan L-J, Song WG (2011) Nanoflower arrays of rutile TiO_2. Chem Commun 2008:1184–1186
307. Shin JY, Samuelis D, Maier J (2011) Sustained lithium-storage performance of hierarchical, nanoporous anatase TiO_2 at high rates: emphasis on Interfacial storage phenomena. Adv Funct Mater 2:3464–3472
308. Reddy MV, Teoh XWV, Nguyen TB, Lim YYM, Chowdari BVR (2012) Effect of 0.5 M $NaNO_3$: 0.5 M KNO_3 and 0.88 M $LiNO_3$:0.12 M LiCl molten salts, and heat treatment on electrochemical properties of TiO_2 batteries and energy storage. J Electrochem Soc 159:A762–A769
309. Reddy MV, Pei Theng L, Soh H, Beichen Z, Jiahuan F, Yu C, Ling YA, Andreea LY, Justin NCH, Liang TILG, Ian MF, An HVT, Ramanathan K, Kevin CWJ, Daryl TYW, Hao TY, Loh KP, Chowdari BVR (2012) In: Chowdari BVR, Kawamura J, Mizusaki J (eds) Solid State ionics: ionics for sustainable world, proceedings of the 13th Asian conference. World Scientific Publishing Co, Singapore, p 265
310. Zhang F, Zhang Y, Song SY, Zhang HJ (2011) Superior electrode performance of mesoporous hollow TiO_2 microspheres through efficient hierarchical nanostructures. J Power Sourc 196:8618–8624
311. Wang HE, Cheng H, Liu CP, Chen X, Jiang QL, Lu ZG, Li YY, Chung CY, Zhang WY, Zapien JA, Martinu L, Bello I (2011) Facile synthesis and electrochemical characterization of porous and dense TiO_2 nanospheres for lithium-ion battery applications. J Power Sourc 196:6394–6399
312. Kang JW, Kim DH, Mathew V, Lim JS, Gim JH, Kimz J (2011) Particle size effect of anatase TiO_2 nanocrystals for lithium-ion batteries and energy storage. J Electrochem Soc 158:A59–A62

313. Shin JY, Joo JH, Samuelis D, Maier J (2012) Oxygen-deficient $TiO_{2-\delta}$ nanoparticles via hydrogen reduction for high rate capability lithium batteries. Chem Mater 24:543–551
314. Park SJ, Kim H, Kim YJ, Lee H (2011) Preparation of carbon-coated TiO_2 nanostructures for lithium-ion batteries. Electrochim Acta 56:5355–5362
315. Jiang YM, Wang KX, Guo XX, Wei X, Wang JF, Chen JS (2012) Mesoporous titania rods as an anode material for high performance lithium-ion batteries. J Power Sourc 214:298–302
316. Ryu WH, Nam DH, Ko YS, Kim RH, Kwon HS (2012) Electrochemical performance of a smooth and highly ordered TiO_2 nanotube electrode for Li-ion batteries. Electrochim Acta 61:19–24
317. Panda SK, Yoon Y, Jung HS, Yoon WS, Shin H (2012) Nanoscale size effect of titania (anatase) nanotubes with uniform wall thickness as high performance anode for lithium-ion secondary battery. J Power Sourc 204:162–167
318. Ortiz GF, Hanzu I, Lavela P, Tirado JL, Knauth P, Djenizian T (2012) Novel fabrication technologies of 1D TiO_2 nanotubes, vertical tin and iron-based nanowires for Li-ion microbatteries. Int J Nanotechnol 9:260–294
319. Gonzalez JR, Alcantara R, Nacimiento F, Ortiz GF, Tirado JL, Zhecheva E, Stoyanova R (2012) Long-length titania nanotubes obtained by high-voltage anodization and high-intensity ultrasonication for superior capacity Electrode. J Phys Chem C 116:20182–20190
320. Han H, Song T, Lee EK, Devadoss A, Jeon Y, Ha J, Chung YC, Choi YM, Jung YG, Paik U (2012) Dominant factors governing the rate capability of a TiO_2 nanotube anode for high power lithium ion batteries. ACS Nano 6:8308–8315
321. Chen JS, Tan YL, Li CM, Cheah YL, Luan D, Madhavi S, Boey FYC, Archer LA, Lou XW (2010) Constructing hierarchical spheres from large ultrathin anatase TiO_2 nanosheets with nearly 100 % exposed (001) facets for fast reversible lithium storage. J Am Chem Soc 132:6124–6130
322. Wang DH, Choi DW, Li J, Yang ZG, Nie ZM, Kou R, Hu DH, Wang CM, Saraf LV, Zhang JG, Aksay IA, Liu J (2009) Self-assembled TiO_2-graphene hybrid nanostructures for enhanced Li-ion insertion. ACS Nano 3:907–914
323. Yang SB, Feng XL, Ivanovici S, Müllen K (2010) Fabrication of graphene-encapsulated oxide nanoparticles: towards high-performance anode materials for lithium storage. Angew Chem 122:8586–8589
324. Yang SB, Feng XL, Ivanovici S, Müllen K (2010) Fabrication of graphene-encapsulated oxide nanoparticles: towards high-performance anode materials for lithium storage. Angew Chem Int Ed 49:8408–8411
325. Qiu YC, Yan KY, Yang SH, Jin LM, Deng H, Li WS (2010) Synthesis of size-tunable Anatase TiO_2 nanospindles and their assembly into anatase-titanium oxynitride/titanium nitride – graphene nanocomposites for rechargeable lithium ion batteries with high cycling performance. ACS Nano 4:6515–6526
326. Lee JM, Kim IY, Han SY, Kim TW, Hwang S-J (2012) Graphene nanosheets as a platform for the 2D ordering of metal oxide nanoparticles: mesoporous 2D aggregate of anatase TiO_2 nanoparticles with improved electrode Performance. Chem Eur J 18:13800–13809
327. Wang J, Zhou Y, Xiong B, Zhao Y, Huang X, Shao Z (2013) Fast lithium-ion insertion of TiO_2 nanotube and graphene composites. Electrochim Acta 88:847–857
328. Yang SB, Feng XL, Mullen K (2011) Sandwich-like, graphene-based titania nanosheets with high surface Area for fast lithium storage. Adv Mater 23:3575–3579
329. Qiu JX, Zhang P, Ling M, Li S, Liu PR, Zhao HJ, Zhang SQ (2012) Photocatalytic synthesis of TiO_2 and reduced graphene oxide nanocomposite for lithium ion battery. ACS Appl Mater Interfaces 4:3636–3642
330. Cao HQ, Li BJ, Zhang JX, Lian F, Kong XH, Qu MZ (2012) Synthesis and superior anode performance of TiO_2-reduced graphene oxide nanocomposites for lithium ion batteries. J Mater Chem 22:9759–9766
331. Tao HC, Fan LZ, Yan XQ, Qu XH (2012) In situ synthesis of TiO_2-graphene nanosheets composites as anode materials for high-power lithium ion batteries. Electrochim Acta 69:328–333

332. Shah M, Park AR, Zhang K, Park JH, Yoo PJ (2012) Green synthesis of biphasic TiO_2-reduced graphene oxide nanocomposites with highly enhanced photocatalytic activity. ACS Appl Mater Interfaces 4:3893–3901
333. Das SK, Bhattacharyya AJ (2011) Influence of mesoporosity and carbon electronic wiring on electrochemical performance of anatase titania. J Electrochem Soc 158:A705–A710
334. Chang PY, Huang CH, Doong RA (2012) Ordered mesoporous carbon-TiO_2 materials for improved electrochemical performance of lithium ion battery. Carbon 50:4259–4268
335. Yang ZX, Du GD, Meng Q, Guo ZP, Yu XB, Chen ZX, Guo TL, Zeng R (2012) Synthesis of uniform TiO_2-carbon composite nanofibers as anode for lithium ion batteries with enhanced electrochemical performance. J Mater Chem 22:5848–5854
336. Moriguchi I, Hidaka R, Yamada H, Kudo T, Murakami H, Nakashima N (2006) Mesoporous nanocomposite of TiO_2 and carbon nanotubes as a high-rate Li-intercalation electrode material. Adv Mater 18:69–73
337. Cao FF, Guo YG, Zheng SF, Wu XL, Jiang LY, Bi RR, Wan LJ, Maier J (2010) Symbiotic coaxial nanocables: facile synthesis and an efficient and elegant morphological solution to the lithium storage problem. Chem Mater 22:1908–1914
338. Guo YG, Hu YS, Sigle W, Maier J (2007) Superior electrode performance of nanostructured mesoporous TiO_2 (anatase) through efficient hierarchical mixed conducting networks. Adv Mater 19:2087–2091
339. Wang W, Tian M, Abdulagatov A, George SM, Lee YC, Yang RG (2012) Three-dimensional Ni/TiO_2 nanowire network for high areal capacity lithium ion microbattery applications. Nano Lett 12:655–660
340. Cherian CT, Reddy MV, Magdaleno T, Sow CH, Ramanujachary KV, Subba Rao GV, Chowdari BVR (2012) (N, F)-Co-doped TiO2: synthesis, anatase-rutile conversion and Li-cycling properties. CrystEngComm 14:978–986
341. Barreca D, Carraro G, Gasparotto A, Maccato C, Cruz-Yusta M, Gomez-Camer JL, Morales J, Sada C, Sanchez L (2012) On the performances of Cu_xO-TiO_2 ($x = 1, 2$) nanomaterial as innovative anodes for thin film lithium batteries. ACS Appl Mater Interfaces 4:3610–3619
342. Bach S, Pereira-Ramos JP, Willman P (2010) Investigation of lithium diffusion in nano-sized rutile TiO_2 by impedance spectroscopy. Electrochim Acta 55:4952–4959
343. Zhao B, Cai R, Jiang S, Sha Y, Shao Z (2012) Highly flexible self-standing film electrode composed of mesoporous rutile TiO_2/C nanofibers for lithium-ion batteries. Electrochim Acta 85:636–643
344. Pfanzelt M, Kubiak P, Wohlfahrt-Mehrens M (2010) Nanosized TiO_2 rutile with high capacity and excellent rate capability batteries and energy storage. Electrochem Solid State Lett 13:A91–A94
345. Marinaro M, Pfanzelt M, Kubiak P, Marassi R, Wohlfahrt-Mehrens M (2011) ow temperature behaviour of TiO_2 rutile as negative electrode material for lithium-ion batteries. J Power Sourc 196:9825–9829
346. Liu H, Bi Z, Sun X-G, Unocic RR, Paranthaman MP, Dai S, Brown GM (2011) Mesoporous TiO_2-B microspheres with superior rate performance for lithium ion batteries. Adv Mater 23:3450–3454
347. Liu SH, Jia HP, Han L, Wang JL, Gao PF, Xu DD, Yang J, Che SN (2012) Nanosheet-constructed porous TiO_2-B for advanced lithium ion batteries. Adv Mater 24:3201–3204
348. Jang H, Suzuki S, Miyayama M (2012) Synthesis of open tunnel-structured TiO_2(B) by nanosheets processes and its electrode properties for Li-ion secondary batteries. J Power Sourc 203:97–102
349. Yang Z, Du G, Guo Z, Yu X, Chen Z, Guo T, Liu H (2011) TiO_2(B)-carbon composite nanowires as anode for lithium ion batteries with enhanced reversible capacity and cyclic performance. J Mater Chem 21:8591–8596

350. Yang Z, Du G, Guo Z, Yu X, Chen Z, Guo T, Sharma N, Liu H (2011) TiO_2(B)-anatase hybrid nanowires with highly reversible electrochemical performance. Electrochem Commun 13:46–49
351. Guo Z, Dong X, Zhou D, Du Y, Wang Y, Xia Y (2013) TiO_2(B) Nnanofiber bundles as a high performance anode for a Li-ion battery. RSC Adv 3:3352–3358
352. Li X, Wang C (2013) Engineering nanostructured anodes via electrostatic spray deposition for high performance lithium ion battery application. J Mater Chem A 1:165–182
353. Yu Y, Shui JL, Chen CH (2005) lectrostatic spray deposition of spinel $Li_4Ti_5O_{12}$ thin films for rechargeable lithium batteries. Solid State Commun 135:485–489
354. Prakash AS, Manikandan P, Ramesha K, Sathiya M, Tarascon JM, Shukla AK (2010) Solution-combustion synthesized nanocrystalline $Li_4Ti_5O_{12}$ as high-rate performance Li-ion battery anode. Chem Mater 22:2857–2863
355. Shen LF, Yuan CZ, Luo HJ, Zhang XG, Xu K, Xia YY (2010) acile synthesis of hierarchically porous $Li_4Ti_5O_{12}$ microspheres for high rate lithium ion batteries. J Mater Chem 20:6998–6704
356. Lin C-Y, Duh J-G (2011) Porous $Li_4Ti_5O_{12}$ anode material synthesized by one-step solid state method for electrochemical properties enhancement. J Alloys Compd 509:3682–3685
357. Chen JZ, Yang L, Fang SH, Hirano S, Tachibana K (2012) Synthesis of hierarchical mesoporous nest-like $Li_4Ti_5O_{12}$ for high-rate lithium ion batteries. J Power Sourc 200:59–66
358. Lin YS, Tsai MC, Duh JG (2012) Self-assembled synthesis of nanoflower-like $Li_4Ti_5O_{12}$ for ultrahigh rate lithium-ion batteries. J Power Sourc 214:314–318
359. Cheng L, Yan J, Zhu G-N, Luo JY, Wang CX, Xia YY (2010) General synthesis of carbon-coated nanostructure $Li_4Ti_5O_{12}$ as a high rate electrode material for Li-ion intercalation. J Mater Chem 20:595–602
360. Zhu GN, Liu HJ, Zhang JH, Wang CX, Wang YG, Xia YY (2011) Carbon-coated nano-sized $Li_4Ti_5O_{12}$ nanoporous micro-sphere as anode material for high-rate lithium-ion batteries. Energ Environ Sci 4:4016–4022
361. He YB, Ning F, Li B, Song QS, Lv W, Du H, Zhai D, Su F, Yang QH, Kang F (2012) Carbon coating to suppress the reduction decomposition of electrolyte on the $Li_4Ti_5O_{12}$ electrode. J Power Sourc 202:253–261
362. Xie G, Ni J, Liao X, Gao L (2012) Filter paper templated synthesis of chain-structured $Li_4Ti_5O_{12}$/C composite for Li-ion batteries. Mater Lett 78:177–179
363. Jung HG, Myung ST, Yoon CS, Son SB, Oh KH, Amine K, Scrosati B, Sun YK (2011) Microscale spherical carbon-coated $Li_4Ti_5O_{12}$ as ultra high power anode material for lithium batteries. Energ Environ Sci 4:1345–1351
364. Shen L, Yuan C, Luo H, Zhang X, Chen L, Li H (2011) ovel template-free solvothermal synthesis of mesoporous $Li_4Ti_5O_{12}$-C microspheres for high power lithium ion batteries. J Mater Chem 21:14414–14416
365. Zhao L, Hu YS, Li H, Wang ZX, Chen LQ (2011) Porous $Li_4Ti_5O_{12}$ coated with N-doped carbon from ionic liquids for Li-ion batteries. Adv Mater 23:1385–1388
366. Li B, Han C, He Y-B, Yang C, Du H, Yang QH, Kang F (2012) Facile synthesis of $Li_4Ti_5O_{12}$/C composite with super rate performance. Energ Environ Sci 5:9595–9602
367. Zhu N, Liu W, Xue MQ, Xie ZA, Zhao D, Zhang MN, Chen JT, Cao TB (2010) Graphene as a conductive additive to enhance the high-rate capabilities of electrospun $Li_4Ti_5O_{12}$ for lithium-ion batteries. Electrochim Acta 55:5813–5818
368. Zhang BA, Liu YS, Huang ZD, Oh S, Yu Y, Mai YW, Kim JK (2012) Urchin-like $Li_4Ti_5O_{12}$–carbon nanofiber composites for high rateperformance anodes in Li-ion batteries. J Mater Chem 22:12133–12140
369. Kim HK, Bak SM, Kim KB (2010) $Li_4Ti_5O_{12}$/reduced graphite oxide nano-hybrid material for high rate lithium-ion batteries. Electrochem Commun 12:1768–1771
370. Jhan YR, Duh JG (2012) Synthesis of entanglement structure in nanosized $Li_4Ti_5O_{12}$/multi-walled carbon nanotubes composite anode material for Li-ion batteries by ball-milling-assisted solid-state reaction. J Power Sourc 198:294–297

371. Huang J, Jiang Z (2008) The preparation and characterization of $Li_4Ti_5O_{12}$/carbon nano-tubes for lithium ion battery. Electrochim Acta 53:7756–7759
372. Shi Y, Wen L, Li F, Chen HM (2011) Nanosized $Li_4Ti_5O_{12}$/graphene hybrid materials with low polarization for high rate lithium ion batteries. J Power Sourc 196:8610–8617
373. Li X, Qu M, Huai Y, Yu Z (2010) Preparation and electrochemical performance of $Li_4Ti_5O_{12}$/carbon/carbon nanotubes for lithium ion battery. Electrochim Acta 55:2978–2982
374. Ni H, Fan LZ (2012) Nano-$Li_4Ti_5O_{12}$ anchored on carbon nanotubes by liquid phase deposition as anode material for high rate lithium-ion batteries. J Power Sourc 214:195–199
375. Shen L, Yuan C, Luo H, Zhang X, Xu K, Zhang F (2012) In situ growth of $Li_4Ti_5O_{12}$ on multi-walled carbon nanotubes: novel coaxial nanocables for high rate lithium ion batteries. J Mater Chem 21:761–767
376. Li X, Lai C, Xiao CW, Gao XP (2011) Enhanced high rate capability of dual-phase $Li_4Ti_5O_{12}$–TiO_2 induced by pseudocapacitive effect. Electrochim Acta 56:9152–9158
377. Rahman MM, Wang JZ, Hassan MF, Wexler D, Liu HK (2011) Amorphous carbon coated high grain boundary density dual phase $Li_4Ti_5O_{12}$-TiO_2: a nanocomposite anode material for Li-ion batteries. Adv Energy Mater 1:212–220
378. Shen L, Uchaker E, Zhang X, Cao G (2012) Hydrogenated $Li_4Ti_5O_{12}$ nanowire arrays for high rate lithium ion batteries. Adv Mater 24:6502–6506
379. Wang Y, Gu L, Guo YG, Li H, He XQ, Tsukimoto S, Ikuhara I, Wan LJ (2012) Rutile-TiO_2 nanocoating for a high-rate $Li_4Ti_5O_{12}$ anode of a lithium-ion battery. J Am Chem Soc 134:7874–7879
380. Shen LF, Zhang XG, Uchaker E, Yuan CZ, Cao GZ (2012) $Li_4Ti_5O_{12}$ Nanoparticles embedded in a mesoporous carbon matrix as a superior anode material for high rate lithium ion batteries. Adv Energy Mater 2:691–698
381. Shen LF, Yuan CZ, Luo HJ, Zhang XG, Yang SD, Lu XJ (2011) In situ synthesis of high-loading $Li_4Ti_5O_{12}$-graphene hybrid nanostructures for high rate lithium ion batteries. Nanoscale 3:572–574
382. Wang YG, Liu HM, Wang K, Eiji H, Wang Y, Zhou HS (2009) Synthesis and electrochemical performance of nano-sized $Li_4Ti_5O_{12}$ with double surface modification of Ti(III) and carbon. J Mater Chem 19:6789–6795
383. Jo MR, Nam KM, Lee Y, Song K, Park JT, Kang YM (2011) Phosphidation of $Li_4Ti_5O_{12}$ nanoparticles and their electrochemical and biocompatible superiority for lithium rechargeable batteries. Chem Commun 47:11474–11476
384. Kim J, Kim SW, Gwon H, Yoon WS, Kang K (2009) Comparative study of $Li(Li_{1/3}Ti_{5/3})O_4$ and $Li(Ni_{1/2-x}Li_{2x/3}Ti_{x/3})Ti_{3/2}O_4$ ($x = 1/3$) anodes for Li rechargeable batteries. Electrochim Acta 54:5914–5918
385. Tian BB, Xiang HF, Zhang L, Li Z, Wang HH (2010) Niobium doped lithium titanate as a high rate anode material for Li-ion batteries. Electrochim Acta 55:5453–5458
386. Yi TF, Xie Y, Shu J, Wang Z, Yue CB, Zhu R-S, Qiao HB (2011) Structure and Electrochemical Performance of Niobium-Substituted Spinel Lithium Titanium Oxide Synthesized by Solid-State Method Batteries and Energy Storage. J Electrochem Soc 158:A266–A274
387. Yu ZJ, Zhang XF, Yang GL, Liu J, Wang JW, Wang RS, Zhang JP (2011) High rate capability and long-term cyclability of $Li_4Ti_{4.9}V_{0.1}O_{12}$ as anode material in lithium ion battery. Electrochim Acta 56:8611–8617
388. Yi TF, Shu J, Zhu YR, Zhu X-D, Yue CB, Zhou AN, Zhu RS (2009) High-performance $Li_4Ti_{5-x}V_xO_{12}$ ($0 \le x \le 0.3$) as an anode material for secondary lithium-ion battery. Electrochim Acta 54:7464–7470
389. Gu F, Chen G, Wang ZH (2012) Synthesis and electrochemical performances of $Li_4Ti_{4.95}Zr_{0.05}O_{12}$/C as anode material for lithium-ion batteries. J Solid State Electrochem 16:375–382
390. Li X, Qu M, Yu Z (2009) Structural and electrochemical performances of $Li_4Ti_{5-x}Zr_xO_{12}$ as anode material for lithium-ion batteries. J Alloys Compd 487:L12–L17

391. Chen CH, Vaughey JT, Jansen AN, Dees DW, Kahaian AJ, Goacher T, Thackeray MM (2001) Studies of Mg-substituted $Li_{4-x}Mg_xTi_5O_{12}$ spinel electrodes ($0 \leq x \leq 1$) for lithium batteries. J Electrochem Soc 148:A102–A104
392. Huang S, Wen Z, Gu Z, Zhu X (2005) Preparation and cycling performance of Al^{3+} and F^- co-substituted compounds $Li_4Al_xTi_{5-x}F_yO_{12-y}$. Electrochim Acta 50:4057–4062
393. Wang Z, Chen G, Xu J, Lv Z, Yang W (2011) Synthesis and electrochemical performances of $Li_4Ti_{4.95}Al_{0.05}O_{12}$/C as anode material for lithium-ion batteries. J Phys Chem Solids 72:773–778
394. Huang S, Wen Z, Zhu X, Lin Z (2007) Effects of dopant on the electrochemical performance of $Li_4Ti_5O_{12}$ as electrode material for lithium ion batteries. J Power Sourc 165:408–412
395. Hao YJ, Lai Q-Y, Lu JZ, Ji XY (2007) Effects of dopant on the electrochemical properties of $Li_4Ti_5O_{12}$ anode materials. Ionics 13:369–373
396. Robertson AD, Trevino L, Tukamoto H, Irvine JTS (1999) New inorganic spinel oxides for use as negative electrode materials in future lithium-ion batteries. J Power Sourc 81–82:352–357
397. Yi TF, Xie Y, Wu Q, Liu H, Jiang L, Ye M, Zhu R (2012) High rate cycling performance of lanthanum-modified $Li_4Ti_5O_{12}$ anode materials for lithium-ion batteries. J Power Sourc 214:220–226
398. Gao J, Ying JR, Jiang CY, Wan CR (2009) Preparation and characterization of spherical La-doped $Li_4Ti_5O_{12}$ anode material for lithium ion batteries. Ionics 15:597–601
399. Gao J, Jiang CY, Wan CR (2010) Synthesis and characterization of spherical La-doped nanocrystalline $Li_4Ti_5O_{12}$/C compound for lithium-ion batteries. J Electrochem Soc 157: K39–K42
400. Bai YJ, Gong C, Qi YX, Lun N, Feng J (2012) Excellent long-term cycling stability of La-doped $Li_4Ti_5O_{12}$ anode material at high current rates. J Mater Chem 22:19054–19060
401. Zhang B, Du H, Li B, Kang F (2010) Structure and electrochemical properties of Zn-doped $Li_4Ti_5O_{12}$ as anode materials in Li-ion battery. Electrochem Solid State Lett 13:A36–A38
402. Yi TF, Liu H, Zhu YR, Jiang LJ, Xie Y, Zhu RS (2012) Improving the high rate performance of $Li_4Ti_5O_{12}$ through divalent zinc substitution. J Power Sourc 215:258–265
403. Yi TF, Xie Y, Jiang LJ, Shu J, Yue CB, Zhou AN, Ye MF (2012) Advanced electrochemical properties of Mo-doped $Li_4Ti_5O_{12}$ anode material for power lithium ion battery. RSC Adv 2:3541–3547
404. Zhong Z (2007) Synthesis of Mo^{4+} substituted spinel $Li_4Ti_{5-x}Mo_xO_{12}$ batteries and energy storage. Electrochem Solid State Lett 10:A267–A269
405. Zhang B, Huang Z-D, Oh S, Kim JK (2011) Improved rate capability of carbon coated $Li_{3.9}Sn_{0.1}Ti_5O_{12}$ porous electrodes for Li-ion batteries. J Power Sourc 196:10692–10697
406. Wolfenstine J, Allen JL (2008) Electrical conductivity and charge compensation in Ta doped $Li_4Ti_5O_{12}$. J Power Sourc 180:582–585
407. Jhan YR, Lin CY, Duh JG (2011) Preparation and characterization of ruthenium doped $Li_4Ti_5O_{12}$ anode material for the enhancement of rate capability and cyclic stability. Mater Lett 65:2502–2505
408. Qi Y, Huang Y, Jia D, Bao SJ, Guo ZP (2009) Preparation and characterization of novel spinel $Li_4Ti_5O_{12-x}Br_x$ anode materials. Electrochim Acta 54:4772–4776
409. Bai YJ, Gong C, Lun N, Qi YX (2013) Yttrium-modified $Li_4Ti_5O_{12}$ as an effective anode material for lithium ion batteries with outstanding long-term cyclability and rate capabilities. J Mater Chem A 1:89–96
410. Han JT, Huang YH, Goodenough JB (2011) New anode framework for rechargeable lithium batteries. Chem Mater 23:2027–2029
411. Yamamura H, Nobuhara K, Nakanishi S, Iba H, Okada S (2011) Investigation of the irreversible reaction mechanism and the reactive trigger on SiO anode material for lithium-ion battery. J Ceram Soc Jpn 119:855–860
412. Guo BK, Shu J, Wang ZX, H Y, Shi LH, Liu YN, Chen LQ (2008) Electrochemical reduction of nano-SiO_2 in hard carbon as anode material for lithium ion batteries. Electrochem Commun 10:1876–1878

413. Park CM, Choi W, Hwa Y, Kim JH, Jeong G, Sohn HJ (2010) Characterizations and electrochemical behaviors of disproportionated SiO and its composite for rechargeable Li-ion batteries. J Mater Chem 20:4854–4860
414. Feng X, Yang J, Lu Q, Wang J, Nuli Y (2013) Facile approach to SiO*x*/Si/C composite anode material from bulk SiO for lithium ion batteries. Phys Chem Chem Phys 15:14420–14426
415. Lee DJ, Ryou MH, Lee JN, Kim BG, Lee YM, Kim HW, Kong BS, Park JK, Choi JW (2013) Nitrogen-doped carbon coating for a high-performance SiO anode in lithium-ion batteries. Electrochem Commun 34:98–101
416. Lee JI, Park S (2013) High-performance porous silicon monoxide anodes synthesized via metal-assisted chemical etching. Nano Energy 2:146–152
417. Yamada M, Ueda A, Matsumoto K, Ohzuku T (2011) Silicon-based negative electrode for high-capacity lithium-ion batteries: "SiO"-carbon composite. J Electrochem Soc 158: A417–A421
418. Si Q, Hanai K, Ichikawa T, Phillipps MB, Hirano A, Imanishi N, Yamamoto O, Takeda Y (2011) Improvement of cyclic behavior of a ball-milled SiO and carbon nanofiber composite anode for lithium-ion batteries. J Power Sourc 196:9774–9779
419. Ren Y, Ding J, Yuan N, Jia S, Qu M, Yu Z (2012) Preparation and characterization of silicon monoxide/graphite/carbon nanotubes composite as anode for lithium-ion batteries. J Solid State Elecrochem 16:1453–1460
420. Guo C, Wang D, Wang Q, Wang B, Liu T (2012) A SiO/graphene nanocomposite as a high stability anode material for lithium-ion batteries. Int J Electrochem Sci 7:8745
421. Yamamura H, Nobuhara K, Nakanishi S, Iba H, Okada S (2011) Investigation of the irreversible reaction mechanism and the reactive trigger on SiO anode materials for lithium-ion battery. J Ceram Soc Jpn 119:845–849
422. Jeong J, Kim YU, Krachkovskiy SA, Lee CK (2010) A nanostructured $SiAl_{0.2}O$ anode material for lithium batteries. Chem Mater 22:5570–5579
423. Komaba S, Shimomura K, Yabuuchi N, Ozeki T, Yui H, Konno K (2011) Study on polymer binders for high-capacity SiO negative electrode of Li-ion batteries. J Phys Chem 115:13487–13495
424. Miyuki T, Okuyama Y, Sakamoto T, Eda Y, Kojima T, Sakai T (2012) Characterization of heat treated SiO powder and development of a $LiFePO_4$/SiO lithium ion battery with high-rate capability and thermostability. Electrochemistry 80:401–404
425. Jeong G, Kim JH, Kim Y-U, Kim YJ (2012) Multifunctional TiO_2 coating for a SiO anode in Li-ion batteries. J Mater Chem 22:7999–8004
426. Song K, Yoo S, Kang K, Heo H, Kang YM, Jo MH (2013) Hierarchical SiO_x nanoconifers for Li-ion battery anodes with structural stability and kinetic enhancement. J Power Sourc 229:229–233
427. Hwang SW, Lee JK, Yoon Y (2013) Electrochemical behavior of carbon-coated silicon monoxide electrode with chromium coating in rechargeable lithium cell. J Power Sourc 244:620–624
428. Liu B, Abouimrane A, Brown DE, Zhang X, Ren Y, Fang ZZ, Amine K (2013) Mechanically alloyed composite anode materials based on $SiO–Sn_xFe_yC_z$ for Li-ion batteries. J Mater Chem A 1:4376–4382
429. Yan N, Wang F, Zhong H, Li Y, Wang Y, Hu L, Chen Q (2013) Hollow porous SiO_2 nanocubes towards high-performance anodes for lithium-ion batteries. Nat Sci Rep 3:1568
430. Favors Z, Wang W, Bay HH, George A, Ozkan M, Ozkan CS (2013) Stable cycling of SiO_2 nanotubes as high-performance anodes for lithium-ion batteries. Sci Rep 4:4605
431. Pena JS, Sandu I, Joubert O, Pascual FS, Arean CO, Brousse T (2004) Electrochemical reaction between lithium and β-quartz GeO_2. Electrochem Solid State Lett 7:A278–A281
432. Seng KH, Park MH, Guo ZP, Liu HK, Cho J (2013) Catalytic role of Ge in highly reversible GeO_2/Ge/C nanocomposite anode material for lithium batteries. Nano Lett 13:1230–1236
433. Feng JK, Xia H, Lai MO, Lu L (2009) NASICON-structured $LiGe_2(PO_4)_3$ with improved cyclability for high-performance. J Phys Chem C 113:20514–20520

434. Feng JK, Lu L, Lai MO (2010) Lithium storage capability of lithium-ion conductor $Li_{1.5}Al_{0.5}Ge_{1.5}(PO_4)_3$. J Alloys Compd 501:255–258
435. Huang JY, Zhong L, Wang CM, Sullivan JP, Xu W, Zhang LQ, Mao SX, Hudak NS, Liu XH, Subramanian A, Fan HY, Qi LA, Kushima A, Li J (2010) In situ observation of the electrochemical lithiation of a single SnO_2 nanowire electrode. Science 330:1515–1520
436. Zhong L, Liu XH, Wang GF, Mao SX, Huang JY (2011) Multiple-stripe lithiation mechanism of individual SnO_2 nanowires in a flooding geometry. Phys Rev Lett 106:248302
437. Liu XH, Huang JY (2011) In-situ TEM electrochemistry of anode materials for lithium ion batteries. Energ Environ Sci 4:3844–3860
438. Liu J, Li Y, Huang X, Ding R, Hu Y, Jiang J, Liao L (2009) Direct growth of SnO_2 nanorod array electrodes for lithium-ion batteries. J Mater Chem 19:1859–1864
439. GuO ZP, Guo DD, Nuli Y, Hassan MF, Liu HK (2009) Ultra-fine porous SnO_2 nanopowder prepared via a molten salt process: a highly efficient anode material for lithium-ion batteries. J Mater Chem 19:3253–3257
440. Yin X, Chen L, Li C, Hao Q, Liu S, Li Q, Zhang E, Wang T (2011) Synthesis of mesoporous SnO_2 spheres via self-assembly and superior lithium storage properties. Electrochim Acta 56:2358–2363
441. Yang ZX, Du GD, Feng CQ, Li SA, Chen ZX, Zhang P, Guo ZP, Yu XB, Chen GN, Huang SZ, Liu HK (2010) Synthesis of uniform polycrystalline tin dioxide nanofibers and electrochemical application in lithium-ion batteries. Electrochim Acta 55:5485–5491
442. Zhu XJ, Guo ZP, Zhang P, Du GD, Zeng R, Chen ZX, Li S, Liu HK (2009) Highly porous reticular tin–cobalt oxide composite thin film anodes for lithium ion batteries. J Mater Chem 19:8360–8365
443. Zhu XJ, Guo ZP, Zhang P, Du GD, Poh CK, Chen ZX, Li S, Liu HK (2010) Three-dimensional reticular tin–manganese oxide composite anode materials for lithium ion batteries. Electrochim Acta 55:4982–4986
444. Chen JS, Cheah YL, Chen YT, Jayaprakash N, Madhavi S, Yang JH, Lou XW (2009) SnO_2 nanoparticles with controlled carbon nano-coating as high-capacity anode materials for lithium-ion batteries. J Phys Chem 113:20504–20508
445. Liu B, Guo ZP, Du G, Nuli Y, Hassan MF, Jia D (2010) In situ synthesis of ultra-fine, porous, tin oxide-carbon nanocomposites via a molten salt method for lithium-ion batteries. J Power Sourc 195:5382–5386
446. He M, Yuan L, Zhang W, Shu J, Huang Y (2013) A SnO_2-carbon nanocluster anode material with superior cyclability and rate capability for lithium-ion batteries. Nanoscale 5:3298–3305
447. Hassan MF, Rahman MM, Guo Z, Chen Z, Liu H (2010) SnO_2–NiO–C nanocomposite as a high capacity anode material for lithium-ion batteries. J Mater Chem 20:9707–9712
448. Yesibolati N, Shahid M, Chen W, Hedhili MN, Reuter MC, Ross FM, Alshareef HN (2014) SnO_2 anode surface passivation by atomic layer deposited HfO_2 improves Li-ion battery performance. Small 10:2849–2858
449. Yan J, Sumboja A, Khoo E, Lee PS (2011) V_2O_5 loaded on SnO_2 nanowires for high-rate Li ion batteries. Adv Mater 23:746–750
450. Li C, Wei W, Fang SM, Wang HX, Zhang Y, Gui YH, Chen RF (2010) A novel CuO-nanotube/SnO_2 composite as the anode material for lithium ion batteries. J Power Sourc 195:2939–2944
451. Xu W, Canfield NL, Wang DY, Xiao J, Nie ZM, Zhang JG (2010) A three-dimensional macroporous Cu/SnO_2 composite anode sheet prepared via a novel method. J Power Sourc 195:7403–7408
452. Du Z, Zhang S, Jiang T, Wu X, Zhang L, Fang H (2012) Facile synthesis of SnO_2 nanocrystals coated conducting polymer nannowires for enhanced lithium storage. J Power Sourc 219:199–203
453. Yim CH, Baranova EA, Courtel FM, Abu-Lebdeh Y, Davison IJ (2011) Synthesis and characterization of macroporous tin oxide composite as an anode material for Li-ion batteries. J Power Sourc 196:9731–9736

454. Wang J, Zhao HL, Liu XT, Wang CM (2011) Electrochemical properties of SnO_2/carbon composite materials as anode material for lithium-ion batteries. Electrochim Acta 56:6441–6447
455. Li MY, Liu CL, Wang Y, Dong WS (2011) Simple synthesis of carbon/tin oxide composite as anodes for lithium-ion batteries. J Electrochem Soc 158:A296–A301
456. Du G, Zhong C, Zhang P, Guo Z, Chen Z, Liu H (2010) Tin dioxide/carbon nanotube composites with high uniform SnO_2 loading as anode materials for lithium ion batteries. Electrochim Acta 55:2582–2586
457. Zhu CL, Zhang ML, Qiao YJ, Gao P, Chen YJ (2010) High capacity and good cycling stability of multi-walled carbon nanotube/SnO_2 core–shell structures as anode materials of lithium-ion batteries. Mater Res Bull 45:437–441
458. Wang Y, Zeng HC, Lee JY (2006) Highly reversible lithium storage in porous SnO_2 nanotubes with coaxially grown carbon nanotube overlayers. Adv Mater 18:645–649
459. Ren J, Yang J, Abouimrane A, Wang D, Amine K (2011) SnO_2 Nanocrystals deposited on multiwalled carbon nanotubes with superior stability as anode material for Li-ion batteries. J Power Sourc 196:8701–8705
460. Alaf M, Akbulut H (2014) Electrochemical energy storage behavior of Sn/SnO_2 double phase nanocomposite anodes produced on the multiwalled carbon nanotube bucky papers for lithium-ion batteries. J Power Sourc 247:692–702
461. Bonino CA, Ji L, Lin Z, Toprakci O, Zhang X, Khan SA (2011) Electrospun carbon-tin oxide composite nanofibers for use as lithium ion battery anodes. Appl Mater Interfaces 3:2534–2542
462. Dirican M, Yanilmaz M, Fu K, Lu Y, Kizil H, Zhang X (2014) Carbon-enhanced electrodeposited SnO_2/carbon nanofiber composites as anode for lithium-ion batteries. J Power Sourc 264:240–247
463. Zhou X, Dai Z, Liu S, Bao J, Guo Y-G (2014) Ultra-Uniform SnO_x/Carbon Nanohybrids toward Advanced Lithium-Ion Battery Anodes. Adv Mater 26:3943–3949
464. Lou XW, Li CM, Archer LA (2009) Designed synthesis of coaxial SnO_2-carbon hollow nanospheres for highly reversible lithium storage. Adv Mater 21:2536–2539
465. Li YM, Lv XJ, Lu J, Li JH (2010) Preparation of SnO_2-nanocrystal/graphene-nanosheets composites and their lithium storage ability. J Phys Chem C 114:21770–21774
466. Zhao B, Zhang GH, Song JS, Jiang Y, Zhuang H, Liu P, Fang T (2011) Bivalent tin ion assisted reduction for preparing graphene/SnO_2 composite with good cyclic performance and lithium storage capacity. Electrochim Acta 56:7340–7346
467. Zhong C, Wang JZ, Chen ZX, Liu HK (2011) Photoinduced optical transparency in dye-sensitized solar cells containing graphene nanoribbons. J Phys Chem C 115: 25115–25131
468. Lian PC, Zhu XF, Liang SZ, Li Z, Yang WS, Wang HH (2011) High reversible capacity of SnO_2/graphene nanocomposite as an anode material for lithium-ion batteries. Electrochim Acta 56:4532–4539
469. Huang XD, Zhou XF, Zhou LA, Qian K, Wang YH, Liu ZP, Yu CZ (2011) A facile one-step solvothermal synthesis of SnO_2/graphene nanocomposite and its application as an anode material for lithium-ion batteries. ChemPhysChem 12:278–281
470. Xie J, Liu SY, Chen XF, Zheng YX, Song WT, Cao GS, Zhu TJ, Zhao XB (2011) Nanocrystal-SnO_2-loaded graphene with improved Li-storage properties prepared by a facile one-pot hydrothermal route. Int J Electrochem Sci 6:5539–5549
471. Baek S, Yu SH, Park SK, Pucci A, Marichy C, Lee DC, Sung YE, Piao Y, Pinna N (2011) A one-pot microwave-assisted non-aqueous sol–gel approach to metal oxide/graphene nanocomposites for Li-ion batteries. RSC Adv 1:1687–1690
472. Wang XY, Zhou XF, Yao K, Zhang JG, Liu ZP (2011) A SnO_2/graphene composite as a high stability electrode for lithium ion batteries. Carbon 49:133–139
473. Xu CH, Sun J, Gao L (2012) Direct growth of monodisperse SnO_2 nanorods on graphene as high capacity anode materials for lithium ion batteries. J Mater Chem 22:975–979

474. Lin J, Peng Z, Xiang C, Ruan G, Yan Z, Natelson D, Tour JM (2013) Graphene nanoribbon and nanostructured SnO_2 composite anodes for lithium ion batteries. ACS Nano 7:6001–6007
475. Thaisar C, Barone V, Peralta JE (2009) Lithium adsorption on zigzag graphene nanoribbons. J Appl Phys 106:113715–113716
476. Zhou X, Wan LJ, Guo YG (2013) Binding SnO_2 nanocrystals in nitrogen-doped graphene sheets as anode materials for lithium-ion batteries. Adv Mater 25:2152–2157
477. Wu ZS, Sun Y, Tan YZ, Yang S, Feng X, Müllen K (2012) Three-dimensional graphene-based macro- and mesoporous frameworks for high-performance electrochemical capacitive energy storage. J Am Chem Soc 134:19532–19535
478. Liu S, Wang R, Liu M, Luo J, Sun J, Gao L (2014) Fe_2O_3-SnO_2 nanoparticle decorated graphene flexible films as high-performance anode materials for lithium-ion batteries. J Mater Chem A 2:4598–4604
479. Bhaskar A, Deepa M, Ramakrishna M, Rao TN (2014) Poly(3,4-ethylenedioxythiophene) sheath over a SnO_2 hollow spheres/graphene oxide hybrid for a durable anode in Li-ion batteries. J Phys Chem C 118:7296–7306
480. Poizot P, Laruelle S, Grugeon S, Dupont L, Tarascon JM (2000) Nano-sized transition-metal oxides as negative-electrode materials for lithium-ion batteries. Nature 407:496–499
481. Poizot P, Laruelle S, Grugeon S, Dupont L, Tarascon JM (2001) Searching for new anode materials for the Li-ion technology: time to deviate from the usual path. J Power Sourc 97–98:235–239
482. Grugeon S, Laruelle S, Dupont L, Tarascon JM (2003) An update on the reactivity of nanoparticles Co-based compounds towards Li. Solid State Sci 5:895–904
483. Badway F, Plitz I, Grugeon S, Laruelle S, Dolle M, Gozdz AS, Tarascon JM (2002) Metal oxides as negative electrode materials in Li-ion cells. Electrochem Solid State Lett 5:A115–A119
484. Chen CH, Hwang BJ, Do JS, Weng JH, Venkateswarlu M, Cheng MY, Santhanam R, Ragavendran K, Lee JF, Chen JM, Liu DG (2010) An understanding of anomalous capacity of nano-sized CoO anode materials for advanced Li-ion battery. Electrochem Commun 12:496–498
485. Yu Y, Chen CH, Shui JL, Xie S (2005) Nickel-foam-supported reticular CoO-Li_2O composite anode materials for lithium ion batteries. Angew Chem Int Ed 44:7085–7089
486. Reddy MV, Prihvi G, Loh KP, Chowdari BVR (2014) Li storage and impedance spectroscopy studies on Co_3O_4, CoO, and CoN for Li-ion batteries. ACS Appl Mater Interfaces 6:680–690
487. Nam KM, Choi YC, Jung SC, Kim YI, Jo MR, Park SH, Kang YM, Han YK, Park JT (2012) [100] Directed Cu-doped h-CoO nanorods: elucidation of the growth mechanism and application to lithium-ion batteries. Nanoscale 4:473–477
488. Jiang J, Liu J, Ding R, Ji X, Hu Y, Li X, Hu A, Wu F, Zhu Z, Huang X (2010) Direct synthesis of CoO porous nanowire arrays on Ti substrate and their application as lithium-ion battery electrodes. J Phys Chem C 114:929–932
489. Sun Y, Luo W, Huang Y (2012) Self-assembled mesoporous CoO nanodisks as a long-life anode material for lithium-ion batteries. J Mater Chem 22:13826–13831
490. Zhang L, Hu P, Zhao X, Tian R, Zou R, Xia D (2011) Controllable synthesis of core–shell Co-CoO nanocomposites with a superior performance as an anode material for lithium-ion batteries. J Mater Chem 21:18279–18283
491. Xiong S, Chen JS, Lou XW, Zeng HC (2012) Mesoporous Co_3O_4 and CoO-C topotactically transformed from chrysanthemum-like $Co(CO_3)_{0.5}(OH)\cdot 0.11H_2O$ and their lithium-storage properties. Adv Funct Mater 22:861–871
492. Qi Y, Du N, Zhang H, Fan X, Yang Y, Yang D (2012) CoO/$NiSi_x$ core–shell nanowire arrays as lithium-ion anodes with high rate capabilities. Nanoscale 4:991–996
493. Qi Y, Du N, Zhang H, Wang J, Yang Y, Yang D (2012) Nanostructured hybrid cobalt oxide/copper electrodes of lithium-ion batteries with reversible high-rate capabilities. J Alloys Compd 521:83–89

494. Wu FD, Wang Y (2011) Self-assembled echinus-like nanostructures of mesoporous CoO nanorod-CNT for lithium-ion batteries. J Mater Chem 21:6636–6641
495. Qi Y, Zhang H, Du N, Yang D (2013) Highly loaded CoO/graphene nanocomposites as lithium-ion anodes with superior reversible capacity. J Mater Chem A 1:2337–2342
496. Zhu J, Zhu T, Zhou X, Zhang Y, Lou X, Chen X, Zhang H, Hng H, Yan Q (2011) Facile synthesis of metal oxide/reduced graphene oxide hybrids with high lithium storage capacity and stable cyclability. Nanoscale 3:1084–1089
497. Peng C, Chen B, Qin Y, Yang S, Li C, Zuo Y, Liu S, Yang J (2012) Facile ultrasonic synthesis of CoO quantum dot/graphene nanosheet composites with high lithium storage capacity. ACS Nano 6:1074–1081
498. Sun Y, Hu X, Luo W, Huang Y (2012) Ultrathin CoO/graphene hybrid nanosheets: a highly stable anode material for lithium-ion batteries. J Phys Chem C 116:20794–20799
499. Li XF, Dhanabalan A, Bechtold K, Wang CL (2010) Binder-free porous core-shell structured Ni/NiO configuration for application of high performance lithium ion batteries. Electrochem Commun 12:1222–1225
500. Zhong C, Wang JZ, Chou SL, Konstantinov K, Rahman M, Liu HK (2010) Nanocrystalline NiO hollow spheres in conjunction with CMC for lithium-ion batteries. J Appl Electrochem 40:1415–1419
501. Liu L, Li Y, Yuan SM, Ge M, Ren MM, Sun CS, Zhou Z (2010) Nanosheet-based NiO microspheres: controlled solvothermal synthesis and lithium storage performance. J Phys Chem C 114:251–255
502. Cheng MY, Hwang BJ (2010) Mesoporous carbon-encapsulated NiO nanocomposite negative electrode materials for high-rate Li-ion battery. J Power Sourc 195:4977–4983
503. Qiao H, Wu N, Huang FL, Cai YB, Wei QF (2010) Solvothermal synthesis of NiO/C hybrid microspheres as Li-intercalation electrode material. Mater Lett 64:1022–1024
504. Rahman MM, Chou SL, Zhong C, Wang JZ, Wexler D, Liu HK (2010) Spray pyrolyzed NiO-C nanocomposite as an anode material for the lithium-ion battery with enhanced capacity retention. Solid State Ionics 180:1646–1651
505. Wang C, Wang DL, Wang QM, Chen HJ (2010) Fabrication and lithium storage performance of three-dimensional porous NiO as anode for lithium-ion battery. J Power Sourc 195:7432–7437
506. Yuan YF, Xia XH, Wu JB, Yang JL, Chen YB, Guo SY (2010) Hierarchically ordered porous nickel oxide array film with enhanced electrochemical properties for lithium-ion batteries. Electrochem Commun 12:890–893
507. Huang XH, Tu JP, Xia XH, Wang XL, Xiang JY, Zhang L, Zhou Y (2009) Morphology effect on the electrochemical performance of NiO films as anodes for lithium-ion batteries. J Power Sourc 188:588–591
508. Huang XH, Tu JP, Xia XH, Wang XL, Xiang JY, Zhang L (2010) Porous NiO/poly (3,4-ethylenedioxythiophene) films as anode materials for lithium ion batteries. J Power Sourc 195:1207–1210
509. May YJ, Tu JP, Xia XH, Gu CD, Wang XL (2011) Co-doped NiO nanoflake arrays toward superior anode materials for lithium ion batteries. J Power Sourc 196:6388–6393
510. Wu H, Xu M, Wu H, Xu J, Wang Y, Peng Z, Zhzng G (2012) Aligned NiO nanoflake arrays grown on copper as high capacity lithium-ion battery anodes. J Mater Chem 22:19821–19825
511. Liu H, Wang G, Liu J, Qiao S, Ahn H (2011) Highly ordered mesoporous NiO anode material for lithium ion batteries with an excellent electrochemical performance. J Mater Chem 21:3046–3052
512. Ni S, Li T, Yang X (2012) Fabrication of NiO nanoflakes and its application in lithium ion battery. Mat Chem Phys 132:1108–1111
513. Chen X, Zhang N, Sun K (2012) Facile ammonia-induced fabrication of nanoporous NiO films with enhanced lithium-storage properties. Electrochem Commun 20:137–140
514. Sun X, Yan C, Chen Y, Si W, Deng J, Oswald S, Liu L, Schmidt OG (2014) Tree-dimensionally curved NiO nanomembranes as ultrahigh rate capability anodes for Li-ion batteries with long cycle lifetimes. Adv Energy Mater 4. doi:10.1002/aenm.201300912

515. Bai Z, Ju Z, Guo C, Qian Y, Tang B, Xiong S (2014) Direct large-scale synthesis of 3D hierarchical mesoporous NiO microspheres as high- performance anode materials for lithium ion batteries. Nanoscale 6:3268–3273
516. Liu L, Guo Y, Wang Y, Yang X, Wang S, Guo H (2013) Hollow NiO nanotubes synthesized by bio-templates as the high performance anode materials of lithium-ion batteries. Electrochim Acta 114:42–47
517. Wang N, Chen L, Ma X, Yue J, Niu F, Xu H, Yang J, Qian Y (2014) Facile synthesis of hierarchically porous NiO micro-tubes as advanced anode materials for lithium-ion batteries. J Mater Chem A 2:16847–16850. doi:10.1039/C4TA04321A
518. Huang XH, Yuan YF, Wang Z, Zhang SY, Zhou F (2011) Electrochemical properties of NiO/Co–P nanocomposite as anode materials for lithium ion batteries. J Alloys Compd 509:3425–3429
519. Wen W, Wu JM (2011) Eruption combustion synthesis of NiO/Ni nanocomposites with enhanced properties for dye-absorption and lithium storage. ACS Appl Mater Interfaces 3:4112–4119
520. Li X, Dhanabalan A, Wang C (2011) Enhanced electrochemical performance of porous NiO–Ni nanocomposite anode for lithium ion batteries. J Power Sourc 196:9625–9630
521. Mai YJ, Xia XH, Chen R, Gu CD, Wang XL, Tu JP (2012) Self-supported nickel-coated NiO arrays for lithium-ion batteries with enhanced capacity and rate capability. Electrochim Acta 67:73–78
522. Kottegoda IRM, Idris NH, Lu L, Wang J-Z, Liu H-K (2011) Synthesis and characterization of graphene–nickel oxide nanostructures for fast charge–discharge application. Electrochim Acta 56:5815–5822
523. Mai YJ, Shi SJ, Zhang D, Lu Y, Gu CD, Tu JP (2012) NiO-graphene hybrid as an anode material for lithium ion batteries. J Power Sourc 204:155–161
524. Mai YJ, Tu JP, Gu CD, Wang XL (2012) Graphene anchored with nickel nanoparticles as a high-performance anode material for Li ion batteries. J Power Sourc 209:1–6
525. Qiu D, Xu Z, Zheng M, Zhao B, Pan L, Pu L, Shi Y (2012) Graphene anchored with mesoporous NiO nanoplates as anode material for lithium-ion batteries. J Solid State Electrochem 16:1889–1892
526. Zou Y, Wang Y (2011) NiO nanosheets grown on graphene nanosheets as superior anode materials for Li-ion batteries. Nanoscale 3:2615–2620
527. Huang Y, Huang X-L, Lian J-S, Xu D, Wang L-M, Zhang X-B (2012) Self-assembly of ultrathin porous NiO nanosheets/graphene hierarchical structure for high-capacity and high-rate lithium storage. J Mater Chem 22:2844–2847
528. Zhu XJ, Hu J, Dai HL, Ding L, Jiang L (2012) Reduced graphene oxide and nanosheet-based nickel oxide microsphere composite as an anode material for lithium ion battery. Electrochim Acta 64:23–28
529. Choi SH, Ko YN, Lee J-K, Kang YC (2014) Rapid continuous synthesis of spherical reduced graphene ball-nickel oxide composite for lithium ion batteries. Sci Rep 4:5786
530. Zhou G, Wang D-W, Yin L-C, Li N, Cheng H-M (2012) Oxygen bridges between NiO nanosheets and graphene for improvement of lithium storage. ACS Nano 6:3214–3223
531. Wang C, Li Q, Wang F, Xia G, Liu R, Li D, Li N, Spendelow S, Wu G (2014) Morphology-dependent performance of CuO anodes via facile and controllable synthesis for lithium-ion batteries. ACS Appl Mater Interfaces 6:1243–1250
532. Xiang JY, Tu JP, Zhang J, Zhong J, Zhang D, Cheng JP (2010) Incorporation of MWCNTs into leaf-like CuO nanoplates for superior reversible Li-ion storage. Electrochem Commun 12:1103–1107
533. Dar MA, Nam SH, Kim YS, Kim WB (2010) Synthesis, characterization, and electrochemical properties of self-assembled leaf-like CuO nanostructures. J Solid State Electrochem 14:1719–1726
534. Xiang JY, Tu JP, Zhang L, Zhou Y, Wang XL, Shi SJ (2010) Self-assembled synthesis of hierarchical nanostructured CuO with various morphologies and their application as anodes for lithium ion batteries. J Power Sourc 195:313–319

535. Chen LB, Lu N, Xu CM, Yu HC, Wang TH (2009) Electrochemical performance of polycrystalline CuO nanowires as anode material for Li ion batteries. Electrochim Acta 54:4198–4201
536. Ke FS, Huang L, Wei GZ, Xue LJ, Li JT, Zhang B, Chen SR, Fan XY, Sun SG (2009) One-step fabrication of CuO nanoribbons array electrode and its excellent lithium storage performance. Electrochim Acta 54:5825–5829
537. Reddy MV, Yu C, Jiahuan F, Loh KP, Chowdari BVR (2013) Li-cycling properties of molten salt method prepared nano/submicrometer and micrometer-sized CuO for lithium batteries. ACS Appl Mater Interfaces 5:4361–4366
538. Mai JY, Wang XL, Xiang JY, Qiao YQ, Zhang D, Gu CD, Tu JP (2011) CuO/graphene composite as anode materials for lithium-ion batteries. Electrochim Acta 56:2306–2311
539. Guo Z, Reddy MV, Goh BM, San AK, Bao Q, Loh KP (2013) Electrochemical performance of graphene and copper oxide composites synthesized from a metal–organic framework (Cu-MOF). RSC Adv 3:19051–19056
540. Wang B, Wu X-L, Shu C-Y, Guo Y-G, Wang C-R (2010) Synthesis of CuO/graphene nanocomposite as a high-performance anode material for lithium-ion batteries. J Mater Chem 20:10661–10664
541. Zhou J, Ma L, Song H, Wu B, Chen X (2011) Durable high-rate performance of CuO hollow nanoparticles/graphene-nanosheet composite anode material for lithium-ion batteries. Electrochem Commun 13:1357–1360
542. Lu LQ, Wang Y (2012) Facile synthesis of graphene-supported shuttle- and urchin-like CuO for high and fast Li-ion storage. Electrochem Commun 14:82–85
543. Zhou WC, Upreti S, Whittingham MS (2011) High performance Si/MgO/graphite composite as the anode for lithium-ion batteries. Electrochem Commun 13:1102–1104
544. Lu LQ, Wang Y (2011) Sheet-like and fusiform CuO nanostructures grown on graphene by rapid microwave heating for high Li-ion storage capacities. J Phys Chem 21:17916–17921
545. Ji LW, Medford AJ, Zhang XW (2009) Porous carbon nanofibers loaded with manganese oxide particles: formation mechanism and electrochemical performance as energy-storage materials. J Mater Chem 19:5593–5601
546. Liu J, Pang Q (2010) MnO/C nanocomposites as high capacity anode materials for Li-ion batteries. Electrochem Solid State Lett 13:A139–A142
547. Zhong KF, Xia X, Zhang B, Li H, Wang ZX, Chen LQ (2010) MnO powder as anode active materials for lithium ion batteries. J Power Sourc 195:3300–3308
548. Ding YL, Wu CY, Yu HM, Xie J, Cao GS, Zhu TJ, Zhao XB, Zeng YW (2011) Coaxial MnO/C nanotubes as anodes for lithium-ion batteries. Electrochim Acta 56:5844–5848
549. Liu Y, Zhao X, Li F, Xia D (2011) Facile synthesis of MnO/C anode materials for lithium-ion batteries. Electrochim Acta 56:6448–6452
550. Zhong K, Zhang B, Luo S, Wen W, Li H, Huang X, Chen L (2011) Investigation on porous MnO microsphere anode for lithium ion batteries. J Power Sourc 196:6802–6808
551. Li SR, Sun Y, Ge SY, Qiao Y, Chen YM, Lieberwirth I, Yu Y, Chen CH (2012) A facile route to synthesize nano-MnO/C composites and their application in lithium ion batteries. Chem Eng J 192:226–231
552. Sun B, Chen Z, Kim H-S, Ahn H, Wang G (2011) MnO/C core–shell nanorods as high capacity anode materials for lithium-ion batteries. J Power Sourc 196:3346–3349
553. Xu GL, Xu YF, Sun H, Fu F, Zheng XM, Huang L, Li JT, Yang SH, Sun SG (2012) Facile synthesis of porous MnO/C nanotubes as a high capacity anode material for lithium ion batteries. Chem Commun 48:8502–8504
554. Zhang X, Xing Z, Wang L, Zhu Y, Li Q, Liang J, Yu Y, Huang T, Tang K, Qian Y, Shen X (2012) Synthesis of MnO-C core–shell nanoplates with controllable shell thickness and their electrochemical performance for lithium-ion batteries. J Mater Chem 22:17864–17869
555. Li X, Li D, Qiao L, Wang X, Sun X, P W, He D (2012) Interconnected porous MnO nanoflakes for high-performance lithium ion battery anodes. J Mater Chem 22: 9189–9194

556. Xia Y, Xiao Z, Dou X, Huang H, Lu XH, Yan R, Gan Y, Zhu W, Tu J, Zhang W, Tao X (2013) Green and facile fabrication of hollow porous MnO/C microspheres from microalgaes for lithium-ion batteries. ACS Nano 7:7083–7092
557. Yue J, Gu X, Wang N, Jiang X, Xu H, Yang J, Qian Y (2014) General synthesis of hollow MnO_2, Mn_3O_4 and MnO nanospheres as superior anode materials for lithium ion batteries. J Mater Chem A 2:17421–17426. doi:10.1039/c0xx00000x
558. Liu B, Hu X, Xu H, Luo W, Sun Y, Huang Y (2014) Encapsulation of MnO nanocrystals in electrospun carbon nanofibers as high-performance anode materials for lithium-ion batteries. Sci Rep 4:4229
559. Sun Y, Hu X, Luo W, Xia F, Huang Y (2013) Reconstruction of conformal nanoscale MnO on graphene as a high-capacity and long-life anode material for lithium ion batteries. Adv Func Mater 23:2436–2443
560. Hsieh CT, Lin CY, Lin JY (2011) High reversibility of Li intercalation and de-intercalation in MnO-attached graphene anodes for Li-ion batteries. Electrochim Acta 56:8861–8867
561. Zhang KJ, Han PX, Gu L, Zhang LX, Liu ZH, Kong QS, Zhang CJ, Dong SM, Zhang ZY, Yao JH, Xu HX, Cui GL, Chen LQ (2012) Synthesis of nitrogen-doped MnO/graphene nanosheets hybrid material for lithium ion batteries. ACS Appl Mater Interfaces 4:658–664
562. Mai YJ, Zhang D, Qiao YQ, Gu CD, Wang XL, Tu JP (2012) MnO/reduced graphene oxide sheet hybrid as an anode for Li-ion batteries with enhanced lithium storage performance. J Power Sourc 216:201–207
563. Qiu DF, Ma LY, Zheng MB, Lin ZX, Zhao B, Wen Z, Hu ZB, Pu L, Shi Y (2012) MnO nanoparticles anchored on graphene nanosheets via in situ carbothermal reduction as high-performance anode materials for lithium-ion batteries. Mater Lett 84:9–12
564. Tang QW, Shan ZQ, Wang L, Qin X (2012) MoO_2-graphene nanocomposite as anode material for lithium-ion batteries. Electrochim Acta 79:148–153
565. Li Y, Tan B, Wu Y (2007) Mesoporous Co_3O_4 nanowire arrays for lithium ion batteries with high capacity and rate capability. Nano Lett 8:265–270
566. Li C, Yin X, Chen L, Li Q, Wang T (2010) Synthesis of cobalt ion-based coordination polymer nanowires and their conversion into porous Co_3O_4 nanowires with good lithium storage properties. Chem Eur J 16:5215–5221
567. Zhuo L, Ge J, Cao L, Tang B (2009) Solvothermal synthesis of CoO, Co_3O_4, $Ni(OH)_2$ and $Mg(OH)_2$ nanotubes. Cryst Growth D 9:1–6
568. Du N, Zhang H, Chen BD, Wu JB, Ma XY, Liu ZH, Zhang YQ, Yang DR, Huang XH, Tu JP (2007) Porous Co_3O_4 nanotubes derived from $Co_4(CO)_{12}$ clusters on carbon nanotube templates: a highly efficient material for Li-battery applications. Adv Mater 19:4505–4509
569. Tian L, Zou H, Fu J, Yang X, Wang Y, Guo H, Fu X, Liang C, Wu M, Shen PK, Gao Q (2010) Topotactic conversion route to mesoporous quasi-single-crystalline Co_3O_4 nanobelts with optimizable electrochemical performance. Adv Funct Mater 20:617–623
570. Liu J, Xia H, Lu L, Xue D (2010) Anisotropic Co_3O_4 porous nanocapsules toward high-capacity Li-ion batteries. J Mat Chem 20:1506–1510
571. Fan Y, Shao H, Wang J, Liu L, Zhang J, Cao C (2011) Synthesis of foam-like freestanding Co_3O_4 nanosheets with enhanced electrochemical activities. Chem Commun 47:3469–3471
572. Shaju KM, Jiao F, Débart A, Bruce PG (2007) Mesoporous and nanowire Co_3O_4 as negative electrodes for rechargeable lithium batteries. Phys Chem Chem Phys 9:1837–1842
573. Lou XW, Deng D, Lee JY, Feng J, Archer LA (2008) Self-supported formation of needlelike Co_3O_4 nanotubes and their application as lithium-ion battery electrodes. Adv Mater 20:258–262
574. Yan N, Hu L, Li Y, Wang Y, Zhong H, Hu X, Kong X, Chen Q (2012) Co_3O_4 nanocages for high-performance anode material in lithium-ion batteries. J Phys Chem C 116:7227–7235
575. Zhang XX, Xie QS, Yue GH, Zhang Y, Zhang XQ, Lu AL, Peng DL (2013) A novel hierarchical network-like Co_3O_4 anode material for lithium batteries. Electrochim Acta 111:746–754

576. Yang S, Cui G, Pang S, Cao Q, Kolb U, Feng X, Maier J, Mullen K (2010) Towards high-performance anode materials for lithium ion batteries. ChemSusChem 3:236–239
577. Li B, Shao J, Li G, Qu M, Yin G (2011) Co_3O_4-graphene composites as anode materials for high-performance lithium ion batteries. Inorg Chem 50:1628–1632
578. Wang B, Wang Y, Park H, Ahn H, Wang G (2011) In situ synthesis of Co_3O_4/graphene nanocomposite material for lithium-ion batteries and supercapacitors with high capacity and supercapacitance. J Alloys Compd 509:7778–7783
579. Choi B, Chang S, Lee Y, Bae J, Kim H, Huh Y (2012) 3D heterostructured architectures of Co_3O_4 nanoparticles deposited on porous graphene surfaces for high performance of lithium ion batteries. Nanoscale 4:5924–5930
580. Mei W, Huang J, Zhu L, Ye Z, Mai Y, Tu J (2012) Synthesis of porous rhombus-shaped Co_3O_4 nanorod arrays grown directly on a nickel substrate with high electrochemical performance. J. Mater Chem 22:9315–9321
581. Wang F, Lu C, Qin Y, Liang C, Zhao M, Yang S, Sun Z, Song X (2013) Solid state coalescence growth and electrochemical performance of plate-like Co_3O_4 mesocrystals as anode materials for lithium-ion batteries. J Power Sourc 235:67–73
582. Shim H-W, Jin Y-H, Seo S-D, Lee S-H, Kim D-W (2011) Highly reversible lithium storage in bacillus subtilis-directed porous Co_3O_4 nanostructures. ACS Nano 5:443–449
583. Huang H, Zhu WJ, Tao XY, Xia Y, Yu ZY, Fang JW, Gan YP, Zhang WK (2012) Nanocrystal-constructed mesoporous single-crystalline Co_3O_4 nanobelts with superior rate capability for advanced lithium-ion batteries. ACS Appl Mater Interfaces 4:5974–5980
584. Ge D, Geng H, Wang J, Zheng J, Pan Y, Cao X, Gu H (2014) Porous nano-structured Co_3O_4 anode materials generated from coordination-driven self- assembled aggregates for advanced lithium ion batteries. Nanoscale 6:9689–9694
585. Pan A, Wang Y, Xu W, Nie Z, Liang S, Nie Z, Wang C, Cao G, Zhang J-G (2014) High-performance anode based on porous Co_3O_4 nanodiscs. J Power Sourc 255:125–129
586. Rui X, Tan H, Sim D, Liu W, Chen X, Hng HH, Yazami R, Lim TM, Yan Q (2013) Template-free synthesis of urchin-like Co_3O_4 hollow spheres with good lithium storage properties. J Power Sourc 222:97–102
587. Wang J, Yang N, Tang H, Dong Z, Jin Q, Yang M, Kisailus D, Zhao H, Tang Z, Wang D (2013) Accurate control of multishelled Co_3O_4 hollow microspheres as high-performance anode materials in lithium-ion batteries. Angew Chem Int Ed 52:6417–6420
588. Wang Y, Xia H, Lu L, Lin J (2010) Excellent performance in lithium-ion battery anodes: rational synthesis of $Co(CO_3)_{0.5}(OH)_{0.11}H_2O$ nanobelt array and its conversion into mesoporous and single-crystal Co_3O_4. ACS Nano 4:1425–1432
589. Huang G, Xu S, Lu S, Li L, Sun H (2014) Porous polyhedral and fusiform Co_3O_4 anode materials for high-performance lithium-ion batteries. Electrochem Acta 135:420–427
590. Wang H, Ma D, Huang Y, Zhang X (2012) General and controllable synthesis strategy of metal oxide/TiO_2 hierarchical heterostructures with improved lithium-ion battery performance. Nat Sci Rep 2:701
591. Zhang L, Wu HB, Lou XW (2014) Iron-oxide-based advanced materials for lithium-ion batteries. Adv Energy Mater 4:4. doi:10.1002/aenm.201300958
592. He Y, Huang L, Cai JS, Zheng XM, Sun SG (2010) Structure and electrochemical performance of nanostructured Fe_3O_4/carbon nanotube composites as anodes for lithium ion batteries. Electrochim Acta 55:1140–1144
593. Biswal M, Suryawanshi A, Thakare V, Jouen S, Hannoyer B, Aravindan V, Madhavi S, Ogale S (2013) Mesoscopic magnetic iron oxide spheres for high performance Li-ion battery anode: a new pulsed laser induced reactive micro-bubble synthesis process. J Mater Chem A 1:13932–13940
594. Lee SH, Yu S-H, Lee JE, Jin A, Lee DJ, Lee N, Jo H, Shin K, Ahn T-Y, Kim Y-W, Choe H, Sung Y-E, Hyeon T (2013) Self-assembled Fe_3O_4 nanoparticle clusters as high-performance anodes for lithium Ion batteries via geometric confinement. Nano Lett 13:4249–4256

595. Xu JS, Zhu YJ (2012) Monodisperse Fe_3O_4 and γ-Fe_2O_3 magnetic mesoporous microspheres as anode materials for lithium-ion batteries. ACS Appl Mater Interfaces 4:4752–4757
596. Wang R, Xu C, Sun J, Gao L, Lin C (2013) Flexible free-standing hollow Fe_3O_4/graphene hybrid films for lithium-ion batteries. J Mater Chem A 1:1794–1800
597. Zhuo L, Wu Y, Wang L, Ming J, Yu Y, Zhang X, Zhao F (2013) CO_2–expanded ethanol chemical synthesis of a Fe_3O_4-graphene composite and its good electrochemical properties as anode material for Li-ion batteries. J Mater Chem A 1:3954–3960
598. Zhao J, Yang B, Zheng Z, Yang J, Yang Z, Zhang P, Ren W, Yan X (2014) Facile preparation of one-dimensional wrapping structure: graphene nanoscroll-wrapped of Fe_3O_4 nanoparticles and its application for lithium-ion battery. ACS Appl Mater Interaces 6:9890–9896
599. Ke FS, Huang L, Zhang B, Wei GZ, Xue LJ, Li JT, Sun SG (2012) Nanoarchitectured Fe_3O_4 array electrode and its excellent lithium storage performance. Electrochim Acta 78:585–591
600. Gao J, Lowe MA, Abruna HD (2011) Spongelike nanosized Mn_3O_4 as a high-capacity anode material for rechargeable lithium batteries. Chem Mater 23:3223–3227
601. Bai Z, Zhang X, Zhang Y, Guo C, Tang B (2014) Facile synthesis of mesoporous Mn_3O_4 nanorods as a promising anode material for high performance lithium-ion batteries. J Mater Chem A 2:16755–16770. doi:10.1039/c4ta03532a
602. Wang ZH, Yuan LX, Shao QG, Huang F, Huang YH (2012) Mn_3O_4 nanocrystals anchored on multi-walled carbon nanotubes as high-performance anode materials for lithium-ion batteries. Mater Lett 80:110–113
603. Li Z, Liu N, Wang X, Wang C, Qi Y, Yin L (2012) Three-dimensional nanohybrids of Mn_3O_4/ordered mesoporous carbons for high performance anode materials for lithium-ion batteries. J Mater Chem 22:16640–16648
604. Lavoie N, Malenfant PRL, Courtel FM, Abu-Lebdeh Y, Davidson IJ (2012) High gravimetric capacity and long cycle life in Mn_3O_4/graphene platelet/LiCMC composite lithium-ion battery anodes. J Power Sourc 213:249–254
605. Reddy MV, Yu T, Sow CH, Shen ZX, Lim CT, Subba Rao GV, Chowdari BVR (2007) α-Fe_2O_3 nanoflakes as an anode material for Li-ion batteries. Adv Func Mater 17:2792–2799
606. Jiao F, Bao JL, Bruce PG (2007) Factors influencing the rate of Fe_2O_3 conversion reaction. Electrochem Solid State Lett 10:A264–A266
607. Zhang J, Huang T, Liu Z, Yu A (2013) Mesoporous Fe_2O_3 nanoparticles as high performance anode materials for lithium-ion batteries. Electrochem Commun 29:17–20
608. Jia X, Chen J, Xu J, Shi Y, Fan Y, Zheng M, Dong QF (2012) Fe_2O_3 xerogel used as the anode material for lithium ion batteries with excellent electrochemical performance. Chem Commun 48:7410–7412
609. Cherian CT, Sundaramurthy J, Kalaivani M, Ragupathy P, Kumar PS, Thavasi V, Reddy MV, Sow CH, Mhaisakrishna S, Chowdari BVR (2012) Electrospun α-Fe_2O_3 nanorods as a stable, high capacity anode material for Li-ion batteries. J Mater Chem 22:12198–12204
610. Kang N, Park JH, Choi J, Jin J, Chun J, Jung IG, Jeong J, Park JG, Lee SM, Kim HJ, Son SU (2012) Nanoparticulate iron oxide tubes from microporous organic nanotubes as stable anode materials for lithium ion batteries. Angew Chem Int Ed 51:6626–6630
611. Zhu J, Yin Z, Yang D, Sun T, Yu H, Hoster HE, Hng HH, Zhang H, Yan Q (2013) Hierarchical hollow spheres composed of ultrathin Fe_2O_3 nanosheets for lithium storage and photocatalytic water oxidation. Energ Environ Sci 6:987–993
612. Xu S, Hessel CM, Ren H, Yu R, Jin Q, Yang M, Zhao H, Wang D (2014) γ-Fe_2O_3 multi-shelled hollow microspheres for lithium ion battery anodes with superior capacity and charge retention. Energ Environ Sci 7:632–637
613. Wang ZY, Luan DY, Madhavi S, Hu Y, Lou XW (2012) Assembling carbon-coated γ-Fe_2O_3 hollow nanohorns on the CNT backbone for superior lithium storage capability. Energ Environ Sci 5:5252–5256
614. Ji L, Toprakci O, Alcoutlabi M, Yai Y, Li Y, Zhang S, Guo B, Lin Z, Zhang X (2012) α-Fe_2O_3 nanoparticle-loaded carbon nano fibers as stable and high-capacity anodes for rechargeable lithium-ion batteries. ACS Appl Mater Interfaces 4:2672–2679

615. Cao Z, Qin M, Jia B, Zhang L, Wan Q, Wang M, Volinsky A, Qu X (2014) Facile route for synthesis of mesoporous Cr_2O_3 sheet as anode materials for Li-ion batteries. Electrochim Acta 139:76–81
616. Zhao G, Wen T, Zhang J, Li J, Dong H, Wang X, Guo Y, Hu W (2014) Two-dimensional Cr_2O_3 and interconnected graphene-Cr_2O_3 nanosheets: synthesis and their application in lithium storage. J Mater Chem A 2:944–948
617. Guo B, Chi M, Sun XG, Dai S (2012) Mesoporous carbon-Cr_2O_3 composite as an anode material for lithium ion batteries. J Power Sourc 205:495–499
618. Qiu YC, Xu GL, Yan KY, Sun H, Xiao JW, Yang SH, Sun SG, Jin LM, Deng H (2011) Morphology-conserved transformation: synthesis of hierarchical mesoporous nanostructures of Mn_2O_3 and the nanostructural effects on Li-ion insertion/deinsertion properties. J Mater Chem 21:6346–6353
619. Deng Y, Li Z, Shi Z, Xu H, Peng F, Chen G (2012) Porous Mn_2O_3 microsphere as a superior anode material for lithium ion batteries. RSC Adv 2:4645–4647
620. Chang L, Mai L, Xu X, An Q, Zhao Y, Wang D, Feng X (2013) Pore-controlled synthesis of Mn_2O_3 microspheres for ultralong-life lithium storage electrode. RSC Adv 3:1947–1952
621. Hu L, Sun Y, Zhang F, Chen Q (2013) Facile synthesis of porous Mn_2O_3 hierarchical microspheres for lithium battery anode with improved lithium storage properties. J Alloys Compd 576:86–92
622. Zhang Y, Yan Y, Wang X, Li G, Deng D, Jiang L, Shu C, Wang C (2014) Facile synthesis of porous Mn_2O_3 nanoplates and their electrochemical behavior as anode materials for lithium ion batteries. Chemistry 20:6126–6130
623. Deng Y, Wan L, Xie Y, Qin X, Chen G (2014) Recent advances in Mn-based oxides as anode materials for lithium ion batteries. RSC Adv 4:23914–23935
624. Gao QS, Yang LC, Lu XC, Mao JJ, Zhang YH, Wu YP, Tang Y (2010) Synthesis, characterization and lithium-storage performance of MoO2/carbon hybrid nanowires. J Mater Chem 20:2807–2812
625. Wang ZY, Chen JS, Zhu T, Madhavi S, Lou XW (2010) One-pot synthesis of uniform carbon-coated MoO_2 nanospheres for high-rate reversible lithium storage. Chem Commun 46:6906–6908
626. Yoon S, Manthiram A (2011) Microwave-hydrothermal synthesis of $W_{0.4}Mo_{0.6}O_3$ and carbon-decorated WO_x-MoO_2 nanorod anodes for lithium ion batteries. J Mater Chem 21: 4082–4085
627. Bhaskar A, Deepa M, Rao TN, Varadaraju UV (2012) Enhanced nanoscale conduction capability of a MoO_2/Graphene composite for high performance anodes in lithium ion batteries. J Power Sourc 216:169–178
628. Chen A, Li C, Tang R, Yin L, Qi Y (2013) MoO_2-ordered mesoporous carbon hybrids as anode materials with highly improved rate capability and reversible capacity for lithium-ion battery. Phys Chem Chem Phys 15:13601–13610
629. Cherian CT, Sundaramurthy J, Reddy MV, Kumar PS, Mani K, Pliszka D, Sow CH, Ramakrishna S, Chowdar BVR (2013) Morphologically robust $NiFe_2O_4$ nano fibers as high capacity Li-ion battery anode material. ACS Appl Mater Interfaces 5:9957–9963
630. Zhao Y, Li J, Ding Y, Guan L (2011) Enhancing the lithium storage performance of iron oxide composites through partial substitution with Ni^{2+} or Co^{2+}. J Mater Chem 21: 19101–19105
631. Kumar PR, Kollu P, Santhosh C, Rao KEV, Kim DK, Grace AN (2014) Enhanced properties of porous $CoFe_2O_4$-reduced graphene oxide composites with alginate binders for Li-ion battery applications. New J Chem 38:3654–3661
632. Yao X, Kong J, Tang X, Zhou D, Zhao C, Zhou R, Lu X (2014) Facile synthesis of porous $CoFe_2O_4$ nanosheets for lithium-ion battery anodes with enhanced rate capability and cycling stability. RSC Adv 4:27488–27492
633. Lavela P, Tirado JL (2007) $CoFe_2O_4$ and $NiFe_2O_4$ synthesized by sol–gel procedures for their use as anode materials for Li ion batteries. J Power Sourc 172:379–387

634. Cherian CT, Reddy MV, Sow CH, Chowdari BVR (2013) Interconnected network of $CoMoO_4$ submicrometer particles as high capacity anode material for lithium ion batteries. ACS Appl Mater Interfaces 5:918–923
635. Yu H, Guan C, Rui X, Ouyang B, Yadian B, Huang Y, Zhang H, Hoster HE, Fan HJ, Yan Q (2013) Hierarchically porous three-dimensional electrodes of $CoMoO_4$ and $ZnCo_2O_4$ and their high anode performance for lithium ion batteries. Nanoscale 6:10556–10561
636. Lee SH, Kim YH, Deshpande R, Parilla PA, Whitney E, Gillaspie DT, Jones KM, Mahan AH, Zhang SB, Dillon AC (2008) Reversible lithium-ion insertion in molybdenum oxide nanoparticles. Adv Mater 20:3627–3632
637. Meduri P, Clark E, Kim JH, Dayalan E, Sumanasekera GU, Sunkara MK (2012) MoO_{3-x} nanowire arrays as stable and high-capacity anodes for lithium ion batteries. Nano Lett 12:1784–1788
638. Sasidharan M (2012) Gunawardhana, N, Noma H, Yoshio M, Nakashima K (2012) α-MoO_3 hollow nanospheres as an anode material for Li-ion batteries. Bull Chem Soc Jpn 85:642–646
639. Wang ZY, Madhavi S, Lou XW (2012) Ultralong α-MoO_3 nanobelts: synthesis and effect of binder choice on their lithium storage properties. J Phys Chem C 116:12508–12513
640. Riley LA, Cavanagh AS, George SM, Jung YS, Yan YF, Lee SH, Dillon AC (2010) Conformal surface coatings to enable high volume expansion Li-ion anode materials. ChemPhysChem 11:2124–2130
641. Hassan MF, Guo ZP, Chen Z, Liu HK (2010) Carbon-coated MoO_3 nanobelts as anode materials for lithium-ion batteries. J Power Sourc 195:2372–2376
642. Yu X, Wang L, Liu J, Sun X (2014) Porous MoO_3 film as a high-performance anode material for lithium-ion batteries. ChemElectroChem 1:1476–1479
643. Mondal AK, Chen S, Su D, Liu H, Wang G (2014) Fabrication and enhanced electrochemical performances of MoO_3/graphene composite as anode material for lithium-ion batteries. Int J Smart Grid Clean Energ 3:142–148
644. Sun Y, Hu X, Luo W, Huang Y (2011) Hierarchical self-assembly of $Mn_2Mo_3O_8$–graphene nanostructures and theirenhanced lithium-storage properties. J Mater Chem C 21:17229–17235
645. Sharma Y, Sharma N, Subba RGV, Chowdari BVR (2007) Nanophase $ZnCo_2O_4$ as a high performance anode material for Li-ion batteries. Adv Func Mater 17:2855–2861
646. Reddy MV, Kenrick KYH, Wei TY, Chong GY, Leong GH, Chowdari BVR (2011) Nano-$ZnCo_2O_4$ material preparation by molten salt method and its electrochemical properties for lithium batteries and energy storage. J Electrochem Soc 158:A1423–A1428
647. Deng D, Lee JY (2011) Linker-free 3D assembly of nanocrystals with tunable unit size for reversible lithium ion storage. Nanotechnology 22:355401–355410
648. Du N, Xu YF, Zhang H, Yu JX, Zhai CX, Yang DR (2011) Porous $ZnCo_2O_4$ nanowires synthesis via sacrificial templates: high-performance anode materials of Li-ion batteries. Inorg Chem 50:3320–3324
649. Qiu YC, Yang SH, Deng H, Jin LM, Li WS (2010) A novel nanostructured spinel $ZnCo_2O_4$ electrode material: morphology conserved transformation from a hexagonal shaped nanodisk precursor and application in lithium ion batteries. J Mater Chem 20:4439–4444
650. Hu LL, Qu BH, Li CC, Chen YJ, Mein L, Lei DN, Chen LB, Li QH, Wang TH (2013) Facile synthesis of uniform mesoporous $ZnCo_2O_4$ microspheres as a high-performance anode material for Li-ion batteries. J Mater Chem A 1:5596–5602
651. Liu B, Zhang J, Wang XF, Chen G, Chen D, Zhou CW, Shen GZ (2012) Hierarchical three-dimensional $ZnCo_2O_4$ nanowire arrays/carbon cloth anodes for a novel class of high-performance flexible lithium-ion batteries. Nano Lett 12:3005–3011
652. Bai J, Liu G, Qian Y, Xiong S (2014) Unusual formation of $ZnCo_2O_4$ 3D hierarchical twin microspheres as a high-rate and ultralong-life lithium-ion battery anode material. Adv Funct Mater 24:3012–3020
653. Bresser D, Paillard E, Kloepsch R, Krueger S, Fiedler M, Schmitz R, Baither D, Winter M, Passerini S (2013) Carbon coated $ZnFe_2O_4$ nanoparticles for advanced lithium-ion anodes. Adv Energy Mater 3:513–523

654. Martinez-Julian F, Guerrero A, Haro M, Bisquert J, Bresser D, Paillard E, Passerini S, Garcia-Belmonte G (2014) Probing lithiation kinetics of carbon-coated $ZnFe_2O_4$ nanoparticle battery anodes. J Phys Chem C 118:6069–6072
655. Mueller F, Bresser D, Paillard E, Winter M, Passerini S (2013) Influence of the carbonaceous conductive network on the electrochemical performance of $ZnFe_2O_4$ nanoparticles. J Power Sourc 236:87–94
656. Rai AK, Kim S, Gim J, Alfaruqi MH, Mathew V, Kim J (2014) Electrochemical lithium storage of $ZnFe_2O_4$/graphene nanocomposite as an anode material for rechargeable lithium ion batteries. RSC Adv 4:47087–47095. doi:10.1039/c0xx00000x
657. Xia H, Qian Y, Fu Y, Wang X (2013) Graphene anchored with $ZnFe_2O_4$ nanoparticles as a high-capacity anode material for lithium-ion batteries. Solid State Sci 17:67–71
658. Ding Y, Yang Y, Shao H (2011) High capacity $ZnFe_2O_4$ anode material for lithium ion batteries. Electrochim Acta 56:9433–9438
659. Sui J, Zhang C, Hong D, Li J, Cheng Q, Li Z, Cai W (2012) Facile synthesis of MWCNT–$ZnFe_2O_4$ nanocomposites as anode materials for lithium ion batteries. J Mater Chem 22:13674–13681
660. Yao L, Hou X, Hu S, Wang J, Li M, Su C, Tade MO, Shao Z, Liu X (2014) Green synthesis of mesoporous $ZnFe_2O_4$/C composite microspheres as superior anode materials for lithium-ion batteries. J Power Sourc 258:305–318

Chapter 11
Electrolytes and Separators for Lithium Batteries

11.1 Introduction

Rechargeable lithium batteries are basically of two types; lithium metal batteries, and, lithium-ion batteries. Lithium metal batteries (LMB) provide a higher theoretical energy density than the alternatives: their wide commercial availability is limited, however, by the tendency to grow dendrites during cycling. This is a potential hazard and also reduces cycle lifetime. Attempts are being made to suppress dendritic growth either by using solid electrolytes that act as mechanical barriers, or by choosing electrolytes that produce a suitable passivation layer called the solid-electrolyte interphase (SEI). Since there is no entirely successful strategy to inhibit the growth of dendrites, safety concerns have led to the use of the other kind of lithium battery, namely, the lithium-ion battery (LiB).

Lithium-ion batteries are now widely employed for a variety of applications in electronic devices, mobile telephones, laptop computers and a large variety of other portable appliances. They possess a very high energy density, are light and compact and show excellent cyclability and reliability. The current commercial Li-ion batteries are based on aprotic organic liquids such as ethylene carbonate or dimethyl carbonate which have high dielectric constant and are thus good solvents for salts; they also show a large window of electrochemical stability. However, their vapor pressure is high, so that they can provoke fires and explosions in case of accidental battery shorts, when low-stability cathodes are used such as oxides. Such safety issues become accentuated in large lithium-ion batteries of interest in electric cars, especially if charge–discharge is carried out at high rates. The safety aspect has thus become a paramount issue in the development of this technology. Another component important for safety issue is the separator. This element must have, among other properties, a good wettability with the electrolyte, so that the choice of the separator is dependent on the choice of the electrolyte, one reason why we have chosen to include them in the same chapter.

C. Julien et al., *Lithium Batteries*, DOI 10.1007/978-3-319-19108-9_11

With these introductory remarks, one can provide a concise description of the major issues involved in the choice and use of various classes of electrolytes in lithium batteries. It should be immediately stated that most of the work in the literature pertains to the dominant class of these batteries, namely, lithium-ion batteries. These are the intercalation batteries in which both the anode and the cathode are hosts for the lithium ions and no metallic lithium or its alloys are involved.

11.2 Characteristics of an Ideal Electrolyte

Like any electrochemical device, a lithium battery uses two electrodes (anode and cathode) and an electrolyte: it is thus obvious that the choice of electrolyte components is dictated by the electrode materials in use. In other words the chemistry of the two electrode–electrolyte interfaces involved in the battery ultimately determines the optimum electrolyte. In principle, however, one may choose to define an "ideal" electrolyte (which is usually only a "wish list"!) that would have the following properties: (1) a large window of phase stability, i.e., no vaporization or crystallization, (2) non-flammability, (3) a wide electrochemical stability window, (4) non-toxicity, (5) abundant availability, (6) non-corrosive to battery components, (7) environmentally friendly, (8) robust against various abuses, such as electrical, mechanical, and thermal ones, and (9) good wetting properties at the electrolyte–electrode interface.

The vast amount of work published on lithium batteries shows that an "ideal" electrolyte does not exist. What one hopes to achieve is a "workable" electrolyte which has enough combination of desirable properties for an acceptable commercial battery. The literature on the electrolytes for lithium batteries is extremely vast, covering perhaps well over a thousand papers and reviews. No attempt is made here to survey all these publications. The approach adopted is to give a brief synopsis of the main points by giving reference and literature entries to some key papers, especially a few critical reviews that survey the huge amount of literature. A most excellent review was published by Xu in 2004 [1] and this chapter draws heavily upon this publication for the earlier work. More recent work, especially on electrolytes involving ionic liquids is drawn from original publications and our own recent review [2].

11.2.1 Electrolyte Components

In the electrolytes used in lithium batteries, formulations based on single solvents are very rare. Most batteries employ electrolytes that are based on two or more solvents in which one ore more lithium salts are dissolved. Mixed solvents provide a strategy to meet diverse and often contradictory requirements for battery applications, for example, high fluidity vs. high dielectric constant. Thus, solvents of very different physical and chemical properties are used together to attain various

functional aims simultaneously. Fundamentally, solid polymer and gel-polymer electrolytes behave like solution-type electrolytes: the polar macromolecules of the polymer are solvents that dissolve salts by *solvating* the anions and cations, whereas in the gel, a small portion of the high polymer provides the mechanical matrix which is soaked with or swollen by the liquid electrolyte. Ionic liquids (i.e., room temperature molten salts), however, are quite different in principle: no solvent is involved and the salt lattice dissociates into ions of opposite charges, by thermal disintegration only (melting).

11.2.2 Solvents

An ideal solvent should possess the following characteristics: (1) high dielectric constant so that it is able to dissolve salts at sufficient concentrations, (2) high fluidity (low viscosity) so that ion transport is facile, (3) inert to all cell components, (4) liquid in a wide temperature range, i.e., low melting point (T_m) and high boiling point, T_b, (5) should be safe (high flash point, T_f), nontoxic, and low cost. Most good solvents, in general, contain active protons (e.g., water and ethanol) but are unsuitable for LMB) or LiB. This is due to the extremely reactive nature of the strongly reducing anode (lithium metal or highly lithiated carbon) and the strongly oxidizing cathodes (transition metal based oxides): proton-containing solvents undergo electrochemical reactions generally within 2–4 V vs. Li^0/Li^+, i.e., in the range (0.0–4.5 V) in which rechargeable lithium batteries operate. Therefore, one must use aprotic nonaqueous solvents. However, these solvents must have the ability to dissolve sufficient amounts of lithium salts: only those with polar groups such as carbonyl (C = O), nitrile (C = N), sulfonyl (S = O), and ether-linkage (-0-) meet this requirement. Over the years an enormous range of solvents has been tried and the majority of them involve organic esters and ethers. Currently, solvents from these families are being used in lithium batteries and the most common ones are presented in Tables 11.1 and 11.2, taken from the excellent review of Xu [1].

11.2.3 Solutes

For a LiBs or LMBs, the aprotic nonaqueous solvent chosen must be combined with a suitable lithium salt (solute) to obtain an electrolyte appropriate for the anode/cathode combination chosen for the battery. For an ambient temperature rechargeable battery, an ideal solute should be aimed to meet the following requirements: (1) complete dissociation in the solvent at a fairly high concentration, (2) lithium (Li, Na, Zn, etc.) cation should be able to move with high mobility, (3) anion should be stable against oxidation reaction at the cathode, (4) anion should be inert to the solvent, (5) both anion and cation should remain inert towards all cell components, i.e., separator, (electrode substrate, current collectors: the electrode substrate and

Table 11.1 Organic carbonates and esters as electrolyte solvents [1] with *EC* ethylene carbonate, *PC* propylene carbonate, *BC* butylene carbonate, *γBC* γ butylene carbonate, *γVC* γ-valerolactone, *NMO N*-methyl-2-oxazolidinone, *DMC* dimethyl carbonate, *DEC* diethyl carbonate, *EMC* ethyl methyl carbonate, *EA* ethyl acetate, *MB* methyl butyrate, *EB* ethyl butyrate

Solvent	M_w (g mol^{-1})	T_m (°C)	T_b (°C)	η/cP @25 °C	ε @25 °C	Dipole moment (Debye)	T_f (°C)	Density (g cm^{-3}) @25 °C
EC	88	36.4	248	1.90[a]	89.78	4.61	160	1.321
PC	102	−48.8	242	2.53	64.92	4.81	132	1.2
BC	116	−53	240	3.2	53	–	–	–
γBC	86	−43.5	204	1.73	39	4.23	97	1.199
γVC	100	−31	208	2	34	4.29	81	1.057
NMO	101	15	270	2.5	78	4.52	110	1.17
DMC	90	4.6	91	0.59[b]	3.107	0.76	18	1.063
DEC	118	−74.3	126	0.75	2.805	0.96	31	0.969
EMC	104	−53	110	0.65	2.958	0.89	–	1.006
EA	88	−84	77	0.45	6.02	–	3	0.902
MB	102	−84	102	0.6	–	–	11	0.898
EB	116	−93	120	0.71	–	–	19	0.878

[a]At 40 °C
[b]At 20 °C

Table 11.2 Organic ethers as electrolyte solvents [1] with *DMM* 2-methyl-tetrahydrofuran, *DME* dimethyl ether, *DEE* diethyl ether, *THF* tetrahydrofuran, *2-Me-THF* 2-methyl-tetrahydrofuran, *1,3-DL* 1,3-dioxolane, *4-Me-1,3-DL* 4-methyl-1,3-dioxolane, *2-Me-1,3-DL* 2-methyl-1,3-dioxolane

Solvent	M_w (g mol^{-1})	T_m (°C)	T_b (°C)	η/cP @25 °C	ε @25 °C	Dipole moment (Debye)	T_f (°C)	Density (g cm^{-3}) @25 °C
DMM	76	−105	41	0.33	2.7	2.41	−17	0.86
DME	90	−58	84	0.46	7.2	1.15	0	0.86
DEE	118	−74	121				20	0.84
THF	72	−109	66	0.46	7.4	1.7	−17	0.88
2-Me-THF	86	−137	80	0.47	6.2	1.6	−11	0.85
1,3-DL	74	−95	78	0.59	7.1	1.25	1	1.06
4-Me-1,3-DL	88	−125	85	0.6	6.8	1.43	−2	0.983
2-Me-1,3-DL	88			0.54	4.39			

current collector are the meaning) and cell packaging materials etc., and (6) the solute should be nontoxic and stable against overheating of the battery etc. during abuse or short-circuiting etc.

The above criteria limit the choice of solutes for lithium batteries. Owing to a small radius of lithium cation, simple salts such as halides fail to show minimum

Table 11.3 Lithium salts as electrolyte solutes [1] with *LiBF*$_4$ lithium tetrafluoroborate, *LiBF*$_6$ lithium hexafluorophosphate, *LiAsF*$_6$ lithium hexafluoroarsenate, *LiClO*$_4$ lithium perchlorate, *Li-triflate* lithium trifluoromethanesulfonate; *Li imide* (*LiTFSI*) BIS (trifluoromethane) sulfonimide lithium

Salt	M_w (g mol^{-1})	T_m(°C)	T_{decomp} (°C) in solution	Al-corrosion	σ (mS cm^{-1}) (1.0 M, 25 °C)	
					In PC	In EC/DMC
$LiBF_4$	93.9	293	>100	No	3.4	4.9
$LiBF_6$	151.9	200	~8[a]	No	5.8	10.7
$LiAsF_6$	195.9	340	>100	No	5.7	11.1
$LiClO_4$	106.4	236	>100	No	5.6	8.4
Li-triflate	155.9	>300	>100	Yes	1.7	–
Li imide	286.9	234	>100	Yes	5.1	9.0

[a]In EC/DMC

solubility in low dielectric constant media. Salts containing anions called "soft Lewis base," which are bulkier such as Br^-, I^-, S^{2-}, $RCOO^-$ (carboxylates) show better solubility but are easily oxidized on the cathodes at potentials of interest in the lithium batteries. It is found that solubility requirements are met by complex anions such as in lithium hexafluorophosphate ($LiPF_6$), which is a F^- complexed by the Lewis acid PF_5. In such an anion, called anions of superacids, the single negative charge is well distributed by the electron-withdrawing Lewis acid ligands; these complex salts have usually lower melting points and show better solubility in low dielectric constant media.

It is observed that anions based on milder Lewis acids are stable in organic solvents at room temperature and have been extensively investigated by workers in this field. Examples of these salts include lithium perchlorate and lithium borates, arsenates, phosphates, and antimonates. Following Xu [1], some examples of these salts are presented in Table 11.3, together with some of their basic physical properties; also shown are their ion conductivity data in PC, and EC/DMC (1:1) the two solvents well studied by investigators in the area of lithium battery research. In general, carbonates and esters are more anodically stable while ethers are more resistant to cathodic decompositions [1]. Thus, solvents used in most commercial batteries are mixtures of solvents, plus some additives, in order to obtain various desirable properties; their compositions are usually kept as proprietary information.

11.2.4 Electrolytes with Ionic Liquids

Ionic liquids are constituted by multi-atomic organic ions, which have a low melting point, ideally much lower than room temperature: thus, these salts are liquids at ambient temperatures at which batteries are required to operate. They are the solvent

part of the electrolyte in the battery. Ionic liquids (ILs) show properties that make them attractive in Li-ion batteries. Some of these characteristics are [2]: (1) non flammability; (2) low vapor pressure; (3) low toxicity and high environmental compatibility, (4) large potential window/electrochemical stability, (5) high thermal stability, (6) acceptably conductivity, and (7) materials compatibility with the anodes and cathodes during charge–discharge. The ionic liquids do possess some disadvantages: high cost; high viscosity; low conductivity at low temperature; high contact angle (and thence poor wetting) with some electrode materials/configurations.

Ionic liquid salts have low melting temperatures because their components are large, non-symmetric ions possessing a univalent charge. A very low charge to radius ratio of both the cation and the anion leads to very low lattice energy of the salts with consequent low melting point and very low cation–anion electrostatic forces. Such cations and anions also are difficult to discharge on the electrodes, at least at lower potentials, so that a large window of electrochemical stability is obtained. Since these ionic liquids are essentially molten ionic salts they have little vapor pressure, in contrast to covalently bonded liquids such as ethylene carbonate, propylene carbonate, or water. Structures, of some typical ionic liquids are shown in Fig. 11.1.

11.2.4.1 Lithium Metal Rechargeable Batteries in Ionic Liquids

Rechargeable batteries based on lithium metal [LMB] are sought because they provide a higher theoretical energy density than the alternatives. The key limitation in commercializing such batteries is the growth of dendrites during cycling: this

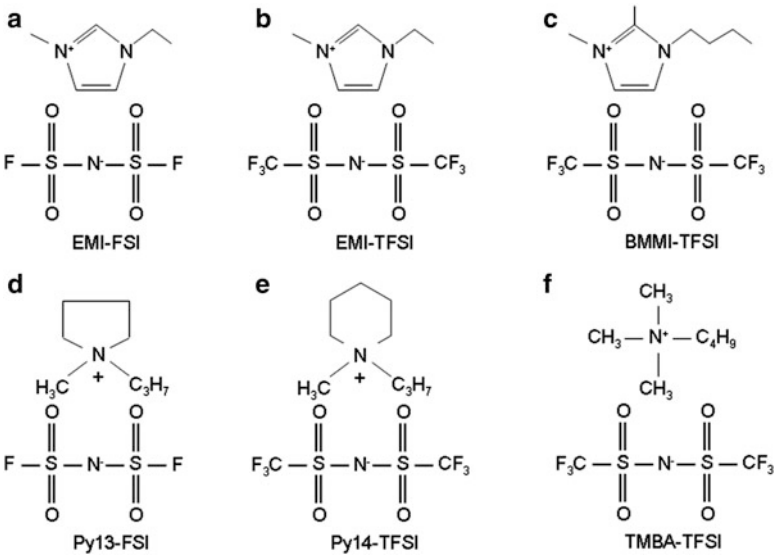

Fig. 11.1 Cation–anion combinations of some ionic liquids of interest in lithium-ion batteries. Reproduced with permission from [2]. Copyright 2010 Elsevier

poses potential hazard (internal shorts) and leads to reduced cycle lifetime. Several strategies have been attempted to suppress dendritic growth. Use of solid electrolytes to act as mechanical barriers, or choosing electrolytes that provide a suitable passivation layer called the solid-electrolyte-interphase (SEI) are the more popular strategies. Such SEI layers are obtained in high-dielectric constant aprotic organic electrolyte compositions based on compounds such as ethylene carbonate (EC) or diethyl carbonate (DEC) mixtures. These electrolytes have high vapor pressures and are flammable, thus potentially hazardous. To overcome these problems, use of ionic liquids [IL's] has been proposed by a number of workers [3, 4]. To enhance lithium-ion transport in ionic liquids of interest in batteries, addition of zwitterions to the electrolyte has been proposed [2]; zwitterionic compounds are designed to tether together the anion and cation constituting the battery ionic liquid. The mechanism of the enhancement of lithium ion transport in ionic liquids by zwitterions is not known, except for the speculation that they prevent the migration of the ionic liquid under the influence of an electric field [2]; more likely, they provide "bridges" of charges for the diffusing lithium ions somewhat similar to proton conduction in ice [5]. Owing to the aforementioned difficulties in cycling lithium metal anodes, they are used mostly in primary batteries; the same is true of lithium-metal alloys [6]. Commercial rechargeable lithium batteries invariably use graphite intercalation compounds as the active anode materials and not the lithium metal electrodes; the latter are used in some batteries using solid polymer electrolytes although some unresolved interfacial problems still exist in them.

11.2.4.2 Lithium Intercalation Rechargeable Batteries Involving Ionic Liquids

Over the years, extensive work has been carried out at the Hydro-Quebec Institute of Research [7, 8], as well as by other investigators [9] on the Li-ion batteries involving ionic liquids; this work has been reviewed recently [2]. It should be added that this work is not on the LiB as such but rather examines the electrochemistry of the anode and cathode half-cell reactions of interest in lithium intercalation batteries. Some solvent mixture compositions have been discovered, containing both ionic liquids and the organic solvents, which in the same time diminish enormously the problem of flammability faced in pure organic solvents and maintaining good conductivity close the organic solvent [8]. These solvent mixtures and their conductivities, viscosities, and flammability/non-flammability are summarized in Table 11.4, based on our previous work [2, 8].

11.2.5 Polymer Electrolytes

A major thrust of research on lithium-ion batteries is to create safe batteries by replacing the organic solvents, or at least, by diminishing their flammability and

Table 11.4 Viscosity, ionic conductivity, and flammability at 25 °C as function of % IL in EC-DEC-VC-$LiPF_6$ compositions electrolytes. Reproduced with permission from [2]. Copyright 2010 Elsevier

Ionic liquid[a]	Viscosity (Pa-S)	Conductivity (mS cm^{-1})	Flammability
0 % EMI-TSFI	12.1	8.5	YES
11 % EMI-TSFI	12.7	9.45	YES
20 % EMI-TSFI	13.7	9.31	YES
30 % EMI-TSFI	14.1	9.41	YES
40 % EMI-TSFI	14.9	11.09	NO
50 % EMI-TSFI	16.3	10.11	NO
60 % EMI-TSFI	17	10.45	NO
70 % EMI-TSFI	19.9	10.26	NO
80 % EMI-TSFI	24.5	10.13	NO
90 % EMI-TSFI	30.5	9.78	NO
100 % EMI-TSFI	36.3	8.61	NO

[a]*EMI-TFSI* 1-ethyl-3-methylimidazolium-bis(trifluoromethyl-sulfonyl)imide

high vapor pressure. One approach is to use solid electrolytes based on polymers, especially in batteries containing lithium metal anodes in so-called LMP (lithium metal polymer) batteries. Wright and coworkers discovered in 1973 [10] that the ether-based polymer poly(ethylene oxide) (PEO) was able to dissolve inorganic salts and exhibit ionic conduction at room temperature: thus polymer electrolytes were born. However, the credit for proposing the use of these electrolytes in batteries belongs to Armand et al. [11]. A vast number of publications and reviews have appeared on the subject [12]. These electrolytes offer many advantages: excellent process ability; absence of flammable liquids; possible prevention of dendrites; high dimensional stability that could lead to the elimination of a separator. Ion conduction in PEO and other similar polyether based media, polyacrylonitrile (PAN), poly(methyl methacrylate) PMMA, poly(vinylidene fluoride) (PVdF), mainly occur in the amorphous phases. Ion conductivities at ambient temperatures are rather low and dendrite formation during cycling is still an issue. Recent promising progress to tackle these problems involve perfluoropolyether based electrolytes [13], or the use of cross-linked polyethylene/(polyethylene oxide) electrolytes [14].

Solid polymer electrolytes are preferentially used in microelectronics and for portable use, because they make possible the production of ultrathin batteries, and have no risk of leaking. Higher ionic conductivities the order of 10^{-3} S cm^{-1} required for high-power batteries are not reached with solid-polymer batteries, and liquid organic electrolytes are preferred in this case. Gel polymer electrolytes are produced by combining both of them, i.e., by mixing organic electrolytes with solid polymer matrices, aiming to encompass both advantages: obtain the high ionic conductivity of 10^{-3} S cm^{-1} owing to the organic liquid, despite the fact that they are under the form of solid film since the liquid electrolyte is encapsulated in polymer chains that maintain the mechanical strength of the film. The cross-linked

structure of the film can be obtained when polymer chains become entangled upon heating and then turned into gel form upon cooling. The most studied gel polymer electrolyte obtained by this process is the poly(vinylidene fluoride-co-hexafluoropropylene) (PVdF-HFP) thermoplastic copolymer [15]. The advantage of choosing such a co-polymer, or PAN [16], and their related blends [17], is that they can be gelled by the liquid electrolyte to form in situ a microporous gel polymer electrolyte inside the batteries [18]. Nevertheless, the mechanical properties of such a physical cross-linking formed by the partial orientation of molecular chains are weak. To overcome this problem, the lithium-ion polymer batteries are manufactured by coating a polyolefin separator or electrode with gel-polymer electrolytes [19]. This gel coating compensates for the weakness of the mechanical stress of the electrolyte, and improves safety, and enhances the adhesive properties of the electrodes. The impregnation of GPE into the micropores of polyolefin membrane can be carried out through dipping [20–22] and in situ polymerization [23, 24]. Note that the nonpolar polyolefin is hydrophobic, so that the electrolytes with important content of EC or PC, etc. exhibit a poor wettability, but this drawback has been solved by a surface modification treating the polyolefin film with a wetting agent, mostly a surfactant [25] or grafting hydrophilic functional groups onto the surface and pore wells [26–33]. Since the surfactant is subjected to washing away by the liquid electrolyte upon cycling or storage, permanent grafting of hydrophilic functional groups is preferred. This grafting is carried out between two electrode plates and applied with a radio-frequency field in a gas atmosphere [27, 34].

Another route to overcome the problem of the weakness of the physical cross leaking is to use a chemical cross-linking, by dissolving a polymer precursor capable of chemical cross-linking into the electrolyte. An example is provided by gel polymer electrolytes based on PVdF-HFP as a polymer matrix, polyethylene glycol (PEG) as a plasticizer, and polyethylene glycol dimethacrylate (PEGDMA) as a chemical cross-linking oligomer. With these polymer electrolytes, rechargeable lithium batteries composed of carbon anode and $LiCoO_2$ cathode have acceptable cyclability and a good rate capability [35]. However, the structural changes needed to accommodate the variations of volume of the electrodes upon cycling are more difficult because the chemical cross-linking is based on chemical bonds instead of Van der Waals interactions. Also the terminal step of the preparation is heating and ultraviolet irradiation, the thermal and light initiators being azobisbutylonitrile and aromatic ketone, respectively. The long exposure at high temperature required for cross-linking is damageable to the productivity. Another weakness is the difficulty to remove non-reactive monomers from the polymer precursor. In the same spirit, Song et al. [36] impregnated a blend of polyethylene glycol diacrylate (PEGDA), PVdF, and poly(methyl methacrylate) (PMMA) into an 85 m poly(ethylene terephthalate) (PET) non-woven by ultraviolet (UV) cross-linking method. In addition to the improvement of the mechanical strength, a good conductivity and liquid electrolyte retention at high temperature was found with respect to untreated gel polymer electrolyte. Thus treated, the gel polymer can be considered as a separator which, however, does not act as a fuse and does not play a role

for the safety of the battery. In the present case, it is thus recommended to disperse polyethylene particles in the gel polymer electrolyte. The melting of these particles at 100 °C results in a rapid increase of the resistivity, so that they actually act as a fuse [37].

11.3 Passivation Phenomena at Electrode–Electrolyte Interfaces in Li Batteries

In a lithium-ion battery, in the first few cycles, the electrolyte reacts with both the anode and the cathode to form protective passivating layers. These layers prevent the uncontrolled destructive corrosion of the electrodes and consumption of the electrolyte. It also permits more appropriate rates of the battery reactions by allowing ionic conduction through the films. Aurbach et al. have studied the surface chemistry of this phenomenon extensively. Indeed Aurbach and Cohen open one of their major chapters by stating [38]: "Passivation phenomena in electrochemistry and electrochemical systems controlled by surface films are widely dealt with and extensively studied over the years." They refer (as reference 1 in their chapter, quoted here as our Ref. [38]), to the original work of Vijh, as also summarized in his book [39]. Since passivation layers on electrodes in lithium-ion batteries are central to the successful operation of these batteries, it is appropriate to delineate here the origins of this work, and, provide a description of the nature and function of these layers. It should be noted that the initial reactions of electrodes with nonaqueous electrolytes in LiB produce surface layers which are insulating so that they exhibit low electronic conductivity and, under applied electric field, high ionic conduction. That in nonaqueous solvents, metals react with the electrolyte to produce such passivating layers was first proposed by Vijh in 1968 [40].

The same author also showed that the bandgap of materials, including semiconducting layers, can be estimated from their heats of formation [41] and bond energies [42]; this work [41, 42] was also brought to the attention of the electrochemical community [43] and reviewed in a book [39]. Subsequently, the qualitative role of these surface films in electrochemical reactions [40] was quantified as a theory of "demetallized surfaces" [44]: these were the surfaces formed by the reaction of the electrodes with electrolytes, having semiconducting/insulating properties and which control the rates of the electrochemical reactions—exactly the situation obtaining in LiB, but developed for a more generalized case of a wide range of electrode reactions. More specifically, these concepts were shown also to be central to the battery reactions on active metals, as early as in 1974 [45]. For the case of anodic dissolution and electropolishing of metals in nonaqueous media, the role of these films was published in 1971 [46], and developed further in 1972 [47]. Thus, several cases of these films in electrode reactions, including specifically in batteries [45], have already been published and reviewed in a book, in 1974 [39]. With this background on the central kinetic participation of

semiconducting/insulating surface layers on electrodes in nonaqueous (as well as aqueous) solutions, a more specific situation of lithium ion batteries may now be placed in its proper context.

In 1979, Peled suggested that "in practical non-aqueous battery systems, the alkali and alkaline earth metals are always covered by a surface layer which is instantly formed by the reaction of the metal with the electrolyte" [48]. He went on to state that this passivating layer controls the rate of the battery reaction. He is essentially restating the same conclusion already demonstrated to be valid for a whole range of electrode reactions [39, 40, 43–47], including batteries [45], published several years before his paper [48]. One has thus to assume that Peled had not read the relevant electrochemical literature before "re-discovering" [48] the well-known role of surface films in electrode reactions [39–47], focused more narrowly in his case for the lithium batteries [48]. What was termed by Vijh [44] as a "demetallized surface" was coined by Peled [48], as a SEI: since the battery community, largely unaware of the foundational electrochemical work on this subject [39, 40, 43–47]—with the conspicuous exception of Aurbach [38]—has adopted Peled's terminology, we deal in the rest of this section with the nature, properties, and the role of SEI. Keep in mind, however, that SEI was not discovered by Peled [48] but "re-discovered" by him and given a new name.

As outlined above, metals, especially the more active alkali and alkaline earth metals but more generally all metals, react with the electrolyte components so that the electrode surfaces become demetallized [44], i.e., covered by a solid semiconduction/insulating layer [39]; the SEI layer proposed by Peled [48] on lithium in nonaqueous aprotic batteries is merely a case in point. The original contribution of Peled [48], however, lies in the fact that he regarded this film as analogous to a solid electrolyte constituting the interphasial region. He further made the point that the rate-determining process for a redox reaction on such a surface would be the diffusion of lithium ions through SEI: this point, again, had already been well-established in the electrochemical literature dealing with, for example, a variety of electrodes covered by insulating films, especially on anodes, as in the classic book by Young published in 1961.

Regarding the properties of SEI, the chemical composition of this film is closely related to the electrolyte used. It usually attains thickness in 25–100 Å range. Electrons do not show any appreciable tunneling trough an insulating film of this thickness [1]. Ideally, the electrolyte chosen should give rise to a SEI in which the cation transport number for the migration of lithium ions approaches unity. The structures and compositions of SEI formed on Li in various electrolytes have been extensively studied by many workers, most notably by Aurbach and coworkers [38]. A useful book surveying the work on SEI is available [49, 50]. It has been argued by Xu [1] that two aspects of SEI are central to its behavior: (1) static stability of SEI that relates to the standing storage of the battery and (2) dynamic stability that relates to its reversibility. SEI formation gives lithium electrodes static stability in nonaqueous solvents. However, SEI also gives rise to a nonuniform surface morphology on the lithium metal surface for the deposition of lithium: thus,

the current density across the surface is nonuniformly distributed during lithium stripping/deposition, with the direct consequence being dendritic growth.

For the lithium ion intercalation batteries, the limitations of uneven morphology of SEI on the electrodes are less serious since dendrite formation situation does not normally arise, except under extreme conditions, e.g., very low temperatures where lithium can deposit on the carbon anode.

For an ideal SEI for lithium ion batteries, the following requirements must be met: (1) electron transference number, $t_e = 0$; (2) high ionic conductivity; (3) uniform morphology and chemical composition; (4) good adhesion to the anode materials (C, Si, Sn, ...) surface; (5) Good mechanical strength and flexibility; (6) low solubility in electrolytes. It should be pointed out that although SEI layers are of paramount importance on anodes, they do exist on cathodes also [51] in lithium ion batteries. Further details are available in the previous reviews [1, 49, 50].

11.4 Some Problems with the Current Commercial Electrolyte Systems

It is generally realized that the current state-of-the-art electrolyte systems for lithium batteries are far from perfect and improvements/new electrolyte systems are being sought constantly. Some major problems needing attention are as follows.

11.4.1 Irreversible Capacity Loss

SEI surface films form both on the anode and the cathode and this means that a certain amount of electrolyte is permanently consumed. The irreversible process of SEI formation immobilizes a certain amount of lithium ions within the insoluble salt that constitutes the SEI. Since most LiBs are built as cathode-limited, in an attempt to avoid the lithium metal deposition on the carbonaceous anode at the end of charging, the consumption of the limited lithium ion source during the initial cycles leads to some permanent capacity loss of the cell. Thus, cell energy density and the corresponding cost are compromised. The extent of this irreversible capacity loss depends on the anode-electrolyte-cathode combination chosen.

11.4.2 Temperature Range

Most commercial battery electrolytes contain two indispensable components: $LiPF_6$ as salt and mixed organic solvent; at least binary mixing where the EC is an important component. It is found that, as an over simplified generalization, EC is

responsible for lower temperature and $LiPF_6$ for the higher temperature, instabilities. Some attempted solutions to minimize these instabilities involve use of additives to obtain so-called "functional electrolytes" [1].

11.4.3 Thermal Runaway: Safety and Hazards

When lithium cells are subjected to various abuses, thermal runaway can occur which causes safety hazards. This is a huge issue, especially in the use of these batteries in electric cars and in some aircrafts. A number of flame-retarded or nonflammable electrolytes are being developed by employing additives [1] or ionic liquids [2].

11.4.4 Enhanced Ion Transport

Although impedances at the anode–electrolyte and cathode–electrolyte interfaces are the limiting factor, ion transport within the bulk electrolyte is also an important consideration. Ion conductivity in nonaqueous solutions is much lower than in aqueous solutions: in fact the part of the current carried by the lithium ions in the battery electrolytes is always less than half. A semiempirical rule has been observed: the higher the bulk ion conductivity of the battery nonaqueous electrolyte, the more conductive the SEI formed on the electrode in this electrolyte [1]. In other words, more ionic conductivity desired in the SEI is heralded by higher lithium ion conductivity of the bulk electrolyte.

11.5 Electrolyte Designs

For small batteries that do not require much power or energy, solid electrolytes may be sufficient. For more demanding applications, more conductive electrolytes based on organic liquids must be used [52]. Nonaqueous electrolytes with high ionic conductivity include carbonate-based aprotic solvents such as: propylene carbonate (PC), ethylene carbonate (EC), diethyl carbonate (DEC), ethyl-methyl carbonate (EMC), or dimethylene carbonate (DMC) and blend of them. Liquid carbonates can dissolve a sufficient concentration of Li salts to give the conductivities required for electric transportation ($\sigma > 10^{-3}$ S cm^{-1}). The stabilization and control of the SEI in that case is crucial, not only to improve the cyclability and the performance of the cell but also to make it safer, since flammable gas can be generated during SEI formation, and the SEI can be resistive, thus increasing locally the temperature. That is why many efforts have been made to understand the mechanism of SEI formation and to put additives in the electrolyte to control and stabilize it. The

dynamic study shows that SEI formation takes place in two stages. The first stage occurs before Li^+ intercalation into graphite and the SEI formed in this stage is structurally porous, highly resistive, and unstable. The second stage occurs simultaneously with the intercalation of Li^+ and the resulting SEI is more compact and highly conductive [53]. Better stability of the latter is attributed to the formation of a network of organic compounds through the coordination of Li^+ ions and organic carbonate anions [54]. Therefore, attention is focused on the first stage for safety concerns.

11.5.1 Control of the SEI

The SEI formed in the first stage is more enriched with inorganic components than in second stage at high (lower if measured vs. Li^0/Li^+) voltage. Furthermore, this period produces more gaseous products, especially for PC-containing electrolytes. The SEI formation can be facilitated by chemically coating an organic film onto the surface of graphite through an electrochemical reduction of additives. This can be achieved by polymerizable additives that are preferably reduced to form an insoluble solid product, which subsequently is covered onto the surface of graphite as a preliminary film to deactivate catalytic activity. Therefore, use of these additives not only reduces gas generation but also increases the stability of the SEI due to the participation of additive molecular moieties to the SEI. Such additives contain one or more carbon–carbon double bonds in their molecules, and include vinylene carbonate [55–60], vinyl ethylene carbonate [59, 61], allyl ethyl carbonate [62], vinyl acetate [63], divinyl adipate [64], acrylic acid nitrile [64], 2-vinyl pyridine [65], maleic anhydride [66], methyl cinnamate [1], phosphonate [67], and vinyl-containing silane-based compounds [68, 69], and furan derivatives [70]. However, in addition to the reductive polymerization, the opposite oxidative polymerization can also occur on the positive electrode, which inevitably increases impedance and irreversibility of the cathode. Therefore, a reasonable amount of such additives in the electrolyte is not to exceed 2 wt%. Since the reductive polymerization takes place at higher potential than the solvent reduction, these additives operate on the initial stage of the SEI formation, resulting in a reduction of gas generation and stabilization of the SEI, thus improving the safety. Other additives operate differently, through absorption of their reduced products onto the graphite surface. They include sulfur-based compounds like SO_2 [71], CS_2 [72], polysulfide [73], cyclic alkyl sulfites [74], and aryl sulfites [75]. All of them must be strictly limited because they are soluble in organic electrolytes and anodically unstable at high potential. Another example is 5 wt% $AgPF_6$ that is able to suppress PC reduction and graphite exfoliation in 1 mol L^{-1} $LiPF_6$ PC–DEC (3:2 in vol.) electrolyte [76], due to the deposition of Ag at 2.15 V vs. Li^0/Li^+. Nitrogen compounds [73, 77] and carbonyl-based compounds [78–80] can also be used as reducing agents. Finally, another type of additive, named reaction-type additive [53], acts by scavenging radical ions [81], or by combining with the final products of the SEI. Such is the case for

CO_2-providers [82], as CO_2 facilitates the formation of the SEI formed with EC- and PC-based electrolytes [72, 83, 84]. A similar approach is the saturation of the electrolyte with Li_2CO_3 [85, 86].

11.5.2 Safety Concerns with Li Salts

The Li salt in the electrolyte also plays a role in the safety of the battery. For the SEI formed with $LiPF_6$-carbonate electrolyte, isolated LiF is the important factor producing unstable SEI [87]. For this reason, many boron-based anion receptors have been developed to dissolve LiF [88]. The most representative compound is tris (pentafluorophenyl) borane (TPFPB) [89] that dissolves LiF not only in electrolytes with $LiPF_6$ [89] but also with $LiBF_4$ salt [90, 91]. The drawback is that it also captures LiF from $LiPF_6$ to release highly reactive PF_5 [92]. A solution for this undesirable side effect may come from aromatic isocyanate compounds, which deactivate the reactivity of electron deficient PF_5 with the electrolyte solvents, and also stabilizes the SEI through the reactions with the chemisorbed oxygen groups on the surface of graphite particles [93]. It also scavenges water and acidic HF from the electrolyte due to its extremely high reactivity to these impurities. PF_5 can also deteriorate the stability of the SEI via reactions with its components. The consequence is safety hazard caused by the generation of gaseous products that build-up pressure inside the battery. Weakening the reactivity and acidity of PF_5 is possible by adding a weak Lewis base such as tris(2,2,2-trifluoroethyl)phosphite (TTFP) [93] to which we return in Sect. 11.5.4, devoted to fire retardants, or amide-based compounds such as 1-methyl-2-pyrrolidinone [94], fluorinated carbamate [95], and hexamethyl-phosphoramide [96].

To overcome the difficulties met with $LiPF_6$, attempts have been made to replace it by another salt without any fluorine in the chemical formula. Lithium bis (oxalato) borate (LiBOB) was initially studied as an alternative salt to improve the high temperature performance of Li-ion batteries [97], but it also significantly stabilizes the SEI during extended cycling [98]. Jiang and Dahn systematically investigated the safety feature of LiBOB with various electrode materials by means of accelerated-rate calorimetry (ARC) [99]. It was found that, while enhanced safety could be obtained with fully lithiated graphitic anode and LiBOB-electrolytes, there were safety concerns whit most of the tested cathode materials, as they showed higher self-heating rate, thus indicating higher reactivity between LiBOB and these metal oxides. The only exception is $LiFePO_4$ that showed much higher onset temperature in the presence of LiBOB. Thus, Dahn and coworkers proposed a so-called "thermally stable lithium-ion cell" with the configuration of graphite/LiBOB/EC/DEC/$LiFePO_4$ [89]. In addition, LiBOB is a very efficient protector against overcharge, at contrast with $LiPF_6$. We discuss this effect in the next section devoted to overcharge protection. LiBOB can even be efficient at an additive level (1 mol%) in a 1 mol L^{-1} $LiPF_6$ or a 1 mol L^{-1} $LiBF_4$ [100, 101] PC-EC electrolyte. Lithium oxaltodifluoroborate (LiODFB) has the same property, but provides better performance than LiBOB at low temperature. Note that we have

again shifted to salts that contain fluorine. Indeed, it is difficult to get rid of it, because, despite the safety problems that it induces, it has a very benefic effect: it passivates the aluminum collector by plating an AlF_3 layer at its surface, thus protecting the collector against corrosion. However, Al passivation can be achieved without the presence of fluorine: not only LiODFB but also LiBOB is able to suppress Al corrosion in the PC–DEC or EC–DMC electrolyte [101]. In that case, this is due to the anion break of O-B bonds and the new anion constantly combines with Al^{3+} to form a very stable passivation layer. Nevertheless, LiBOB has also some defects that limit its use: its low solubility in solvents with low dielectric constant, lower conductivity of their solutions in typical carbonate mixtures as compared to $LiPF_6$, easy hydrolyzability, and difficult large-scale synthesis of high-purity LiBOB [101, 102]. Safety features of LiBOB-bearing cells are being evaluated [103]: concerns remain in the case of cathodes where a higher self-heating rate is observed, including $Li_xMn_2O_4$ at small values of x [104], which suggests reactions between LiBOB and oxide cathodes.

$LiBF_4$ is known to have a much better thermal stability than $LiPF_6$ [105]. In particular, its stability in EC + γ-butyrolactone (GBL) has insured very low anode swelling during high-temperature storage, has improved the safety performance with a $LiCoO_2$ cathode, and very good results were obtained with $LiFePO_4$ as well [106]. Earlier works also motivate the alternative choice of lithium bis(trifluoromethanesulfonyl)imide (LiTFSI) instead of $LiBF_4$. The conductivity of the LiTFSI-based electrolyte is about 8×10^{-3} S cm^{-1} [107], and its molecular weight is only 197 g. In GBL-EC mixtures, however, $LiBF_4$ is preferred to LiTFSI because it is the only salt that permits full charge–discharge cycles with graphite anodes [108], and GBL is an interesting solvent because of its high flame point, high boiling point, low vapor pressure, and high conductivity at low temperatures [109].

A new class of compounds known as lithium fluoroalkylphosphates was introduced [110]. The premise for their development was that the substitution of one or more fluorine atoms in $LiPF_6$ with electron-withdrawing perfluorinated alkyl groups should stabilize the P–F bond, rendering it stable against hydrolysis and resulting in an improved thermal stability of the salt. The hydrophobic perfluorinated alkyl groups sterically shield phosphorus against hydrolysis. The new compounds also have conductivity comparable to that of $LiPF_6$. Oesten et al. [111] showed that $LiPF_3(C_2F_5)_3$ (LiFAP) has a combination of flame-retardant moieties, fluorinated derivatives and phosphoric acid esters. Gnanaraj et al. [112], who investigated the thermal stability of solutions of $LiPF_6$ and LiFAP in EC–DEC–DMC mixtures, showed that the onset temperature for thermal reactions of LiFAP solutions were higher than 200 °C, although their self-heating rate was very high.

11.5.3 Protection Against Overcharge

Safety hazards may also come from overcharge, and the life of the battery would anyway be reduced if high potentials were achieved. Additives in the electrolyte

have improved protection against overcharge. In particular, redox shuttle additives can do this reversibly: when overcharging, the shuttle molecules are oxidized at the positive electrode and the oxidized species diffuse to the negative electrode and are reduced back to the neutral molecule. The difficulty comes from the severe conditions that the shuttle additive should fulfill: (a) the shuttle reaction must be highly reversible, (b) its oxidation potential must be slightly higher than the normal end-of-charge potential of the positive electrode (c) it must be electrochemically stable within the cell operating potentials, and (d) its oxidized and reduced forms must be highly soluble and mobile. The anisole-family compounds belong to the small family of the few organic molecules that satisfy simultaneously all these conditions [113], and have thus been extensively studied [114]. Their potential in most cases are in the range 3.8–4.0 V and are thus suitable for $LiFePO_4$-based Li-ion batteries. Other aromatic compounds have similar functionalities. For $LiMn_2O_4$ cathode, however, the higher working potential requires a different additive. The only solution so far is provided by lithium fluorododecaborates ($Li_2B_{12}F_xH_{12-x}$) that act as a lithium salt but also as a redox shuttle at 4.5 V. This is the highest potential that redox shuttle molecules can undergo without structural deterioration.

In contrast with redox shuttle additives, shutdown additives terminate the cell operation permanently: at high potentials, the additive molecules polymerize to release gas, which activates the current interrupting device (disconnection of the pressure safety valves), while the resulting polymer is plated onto the surface of the cathode to isolate it from further overcharge. Most of these additives are aromatic compounds, such as xylene [115], cyclohexylbenzene [116], biphenyl [117–120] 2,2-diphenylpropane, phenyl-R-phenyl compounds (R = aliphatic hydrocarbon, fluorine substituted) and 3-thiopheneacetonitrile [120]. However, these compounds reduce the calendar life of the batteries due to their irreversible oxidation. On the other hand, LiBOB acts as a shutdown additive [1], as it begins to decompose and release gases (mainly CO_2 and CO) at a voltage of about 4.5 V. In a 1*C*-overcharge test on 8 Ah Li-ion batteries, the LiBOB battery only experienced mild vent with the maximum temperature not exceeding 100 °C and did not catch fire, while the $LiPF_6$-containing battery not only caught fire but exploded with the maximum temperature reaching 400 °C [1]. This excellent overcharge tolerance of LiBOB batteries, also observed with spinel cathode [121], is attributed to the fact that the oxalate molecular moieties of LiBOB are preferably oxidized to produce CO_2 by the oxygen released from the cathode [122].

11.5.4 Fire Retardants

Thermal runaway and battery fires are the main obstacle for the application of Li-ion batteries to electric vehicles, due in particular to the flammability of the organic liquids. Therefore many efforts have been made to find fire-retardant additives aiming at reducing the self-heat rate and delaying the onset of thermal runaway. The first strategy aims at using a chemical radical-scavenging process,

which terminates radical chain reactions responsible for the combustion reaction in the gas phase [123, 124]. The additives in that case are mainly organic phosphorous compounds. Partially fluorinated alkyl phosphates are successful not only as a retardant additive but also to improve the reductive stability [125]. When 20 wt% of tris(2,2,2-trifluoroethyl)phosphate was added, for example, the electrolyte became nonflammable while having no adverse impacts on both graphite anode and cathode [125]. Cyclophosphazene family compounds are also promising fire retardants [126, 127] due to the high content of phosphorus related to their ring structure, especially hexamethoxycyclotriphosphazene that is stable up to 5 V against the anodic potential [126]. Besides the P^{5+}-phosphates, the P^{3+}-phosphites have also a fire retardant power, with the advantage that they facilitate the formation of SEI [128], and can deactivate PF_5 [92]. The best example is tris(2,2,2-trifluoroethyl)phosphite (TTFP) [129]. Fluorinated propylene carbonates also act as non-phosphorus fire retardants [130].

Another strategy currently investigated to reduce electrolyte flammability is mixing with ionic liquids (IL), since room temperature ionic liquids are known for their non-volatility and inflammability. However, most ILs do not form a robust solid electrolyte interface on carbon during the first lithiation. Many efforts are then currently made to identify ILs improving cycling performance. 1-ethyl-3-methylimidazolium (EMI), 1-propyl-1-methylpyrrolidinium (Py13) have been chosen as cations, and bis(fluorosulfonyl)imide (PSI) for the anion and compared to conventional electrolytes: 1 mol L^{-1} $LiPF_6$ in EC-DEC or lithium bis (fluorosulfonyl) LiFSI salt [131]. The study has been extended to *N*-trimethyl-*N*-butylammonium (TMBA) cation, and bis(trifluoromethanesulfonyl)imide (TFSI) anion [132]. As a result, ionic liquids with $TFSI^-$ are safer than those with FSI^-, and IL with EMI^+ are worse than those with 1-butyl-3-methylimidazolium $BMIM^+$, $Py13^+$, and $TMBA^+$. The better stability of $TFSI^-$ comes from the fact that it contains more F atoms than FSI^-. At Li-containing negative electrodes, these F atoms may react to form LiF, which is an effective component of the passivation film. Then, TFSI with a higher fluorine content than FSI can form a thicker and more stable film of reaction products. In any case, these experiments also show that IL cannot be used at 100 % concentration in Li-ion batteries, because of their high viscosity and relatively low conductivity; in addition their conductivity decreases when a salt (e.g., LiTFSI) is added to make an electrolyte solution. This behavior is contrary to that of conventional aqueous and nonaqueous solvents. One way to overcome this difficulty is to add organic solvents such as EC and DEC. The conductivity and viscosity as a function of the rate of dilution of EMI-FTSI with the organic electrolyte ethylene carbonate/diethyl carbonate plus 2 % vinyl carbonate (EC-DEC VC-1 mol L^{-1} $LiPF_6$) has been investigated [8]. The result is reported in Fig. 11.2. When IL in the mixture increases up to 60 %, the conductivity rises much faster than the viscosity. Further increase of IL leads to a decrease in conductivity because there is no sufficient organic solvent available to solvate all the IL present, so the conductivity approaches that of pure IL. Correspondingly, there is a steep rise in viscosity of the mixtures with increasing IL fraction. The expected inverse correlation between conductivity and viscosity of the electrolytes

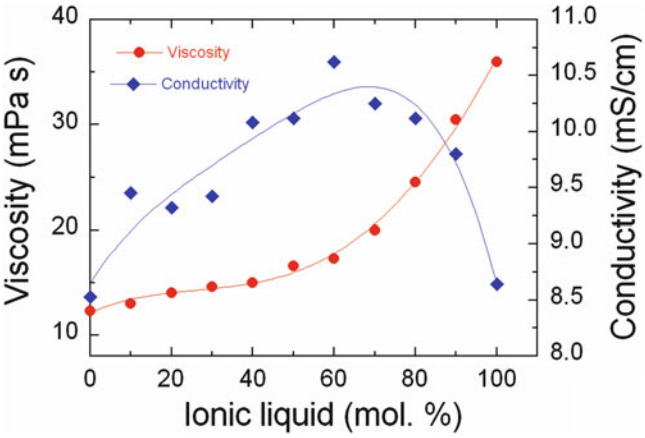

Fig. 11.2 Conductivity and viscosity of EC–DEC–VC–1 mol L^{-1} $LiPF_6$ with EMI-TFSI. Reproduced with permission from [8]. Copyright 2010 Elsevier

is not followed in the mixtures, because the organic solvent has covalent bonding and few ions (by auto-solvation), and hence low conductivity, whereas ionic liquids are by definition rich of ions, and therefore have higher conductivities than organic solvents. Therefore, there is a remarkable optimum concentration range for a promising battery application when the proportion of IL in the mixture is 40–60 %, which provides the key desirable properties: high conductivity and low viscosity. Upon exposure of the mixture to a direct flame, the electrolyte flammability occurred with pure organic electrolyte in the first second of ignition; as soon as IL is added in the electrolyte, the flame exposure time increases before flammability occurs. After adding 40 % IL in the electrolyte, no flammability is observed within the test periods (25 s). In addition, the high rate capability of $LiFePO_4$, which was reduced in pure IL, is recovered in the mixture when the IL concentration is 40 %; moreover, with increasing discharge rate, the capacity is maintained close to that in the organic solvent up to 2*C* rate [8]. Note that the mixed electrolyte is not a new phase, so that heating the mixture up to 100 °C does not prevent the decomposition of the salt and the organic solvent inside the mixture. However, adding 40–60 % IL in the organic electrolyte obviously increases the battery safety without damaging the performance up to 2*C* rate.

11.6 The Separators

We have already mentioned the interest of the separator in the case of gel-polymer electrolytes. This element is critical in the case of liquid electrolytes. The function of this membrane is to separate to prevent physical contact of the positive and negative electrodes. It must permit free ion flow, so that it must be porous. On the other hand, it should be an electrical insulator to prevent any electronic flow that

would result in a self-discharge process. The requirements in terms of chemical stability, porosity, pore size, permeability of the separators and the different materials that are used have been reviewed by Zhang [133]. The separator is also required to be capable of battery shutdown at a temperature smaller than that of the onset of thermal runaway, without loosing its mechanical stability. This condition is more or less stringent, depending on the choice of the electrodes, and is usually fulfilled by microporous polymer membranes Almost all such membranes used in the current Li-ion batteries are based on semi-crystalline polyolefin materials, such as polyethylene (PE), polypropylene (PP), and their combination under the form of PE-PP bilayer [134, 135] or PP-PE-PP trilayer [136–142] separators commonly used by manufacturers. Their shutdown temperature is ~130 °C (melting point of PE), and the melting temperature is that of PP, namely 165 °C. The PE layer is capable of melting and filling the pores at a temperature lower than thermal runway, which, as a result, considerably increases the resistance of the electrolyte layer between the two electrodes to terminate the operation of the battery, while the PP layer still has sufficient mechanical strength to prevent a short circuit between the electrodes. About a 35 °C buffer between the PE shutdown and PP melting may be enough for the protection of most Li-ion batteries, except if the overheating is so important that the separator shrinks or even melt, a situation that can be met during the nail penetration test and short-circuit test on batteries that include lamellar compounds as active particles of cathode elements, in which case the thermal runaway is inevitable.

The physical properties of the separators also depend on the preparation process, which determines the size of the pores and their orientation. Two modes of preparation are currently used, the dry process (separators commercialized by Celgard with the composition PP-PE-PPP), and the wet process (separators commercialized by Exxon Mobil with the composition PE alone). The details on these two processes and a comparison of the properties of the membranes commercialized by these two companies can be found in ref. [133]. From the viewpoint of microporous structure, the membranes made by the dry process seem to be more suitable for a high power density battery due to their open and straight porous structure, while those made by the wet process are more suitable for a long cycle life battery because of their tortuous and interconnected porous structure that is helpful in suppressing the growth of dendritic Li on the graphite anode during fast charging or low temperature charging. The polyolefin membranes used in Li-ion batteries have a typical thickness of 25 μm, decreasing towards 10 μm for the higher energy density batteries. This is a limit, since smaller thickness would raise a safety risk regarding mechanical penetration. For instance, the Celgard 2325, which is the reference of the PP-PE-PP membrane, has a thickness of 25 μm. In the first step of the preparation of this membrane by the dry process, the polymer resins are melt-extruded into a uniaxially oriented tubular film. The resulting film is required to have a crystalline row structure with lamellae arranged in rows with their long axis along the transverse direction (TD) perpendicular to the machine direction (MD). The consequence is a large difference between the tensile strength in the MD direction: 1900 kg cm^{-2} and the TD direction: 135 kg cm^{-2}. This is a major

difference with the membranes prepared by the wet method which are much more isotropic: the tensile strength of Exxon Mobil membranes are in the range 1200–1500 kg cm^{-2} in both MD and TD directions.

For high-power applications that require separators with an excellent thermal stability, such as electric vehicle applications for instance, inorganic composite separators are an alternative. They are made of ultra-thin particles bonded using a small amount of binder. The particles are oxides of transition metal, such as MgO [143], TiO_2 [144], Al_2O_3 [145], or $CaCO_3$ [146, 147]. The binder is usually PVdF or PVdF-HPF already mentioned in the context of gel-polymer electrolytes in Sect. 11.2.5. These separators have extreme thermal stability and show zero-dimensional shrinkage at high temperatures. Another advantage is their outstanding wettability with all the liquid electrolytes, in particular, they contain high concentration of cyclic carbonate solvents such as EC and γ-butyrolactone (GBL) that are unable to wet the nonpolar polyolefin separators, and permits the use of a high content of EC in the liquid electrolytes. In addition, the extreme thermal stability offers the batteries excellent temperature tolerance. However, these composite separators are not mechanically strong enough to fully withstand handling and manufacturing. In the case of their use as gel polymers, we have mentioned that one solution was the addition of a cross-linking oligomer.

To solve the problem for separators, Degussa developed a series of Separion (a trade name) separator by combining the characteristics of polymeric non-woven poly(ethylene terephthalate) (PET) and nanoparticles of ceramic materials (alumna, silica, zirconia nanoparticles) [148–152]. This separator is illustrated in Fig. 11.3. As an example [152], the inorganic binder sol can be prepared by hydrolyzing a mixture of tetraethoxysilane, methyltriethoxysilane and (3-glycidyloxypropyl) trimethoxysilane in the presence of HCl aqueous solution. The resulting sol was used to suspend aluminum oxide powders, and then the homogenized suspension

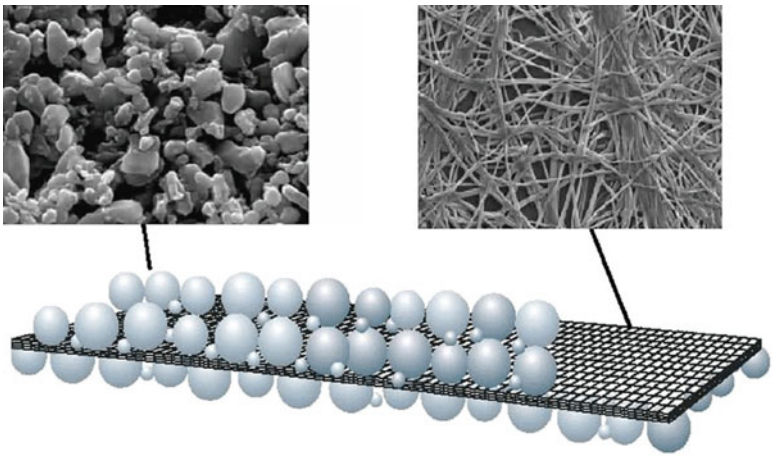

Fig. 11.3 Schematic structure of the Separion separators. This figure was redrawn in ref. [133] based on Fig. 1 of Ref. [148] and product brochure of Separion separators

Table 11.5 Comparison of the properties of the Separion and Celgard separators

Trade name	Separion	Separion	Celgard	Celgard
Separator brand	S240-P25	S240-P35	Celgard 2340	Celgard 2500
Composition	Al_2O_3/SiO_2	Al_2O_3/SiO_2	PP–PE–PP	PP
Support matrix	PET non-woven	PET non-woven	N/A	N/A
Thickness (μm)	25 ± 3	25 ± 3	38	25
Average pore size (μm)	0.24	0.45	0.038×0.90	0.209×0.054
Gurley value (s)	10–20	5–10	31	9
Porosity (%)	>40	>45	45	55
Temperature stability (°C)	210	210	135/163	163
Thermal shrinkage (%)	<1	<1	5	3
Tensile strength (MD)	>3 N cm^{-1}	>3 N cm^{-1}	2100 kg cm^{-2}	1200 kg cm^{-2}
Tensile strength (TD)			100 kg cm^{-2}	115 kg cm^{-2}

The data were cited directly from the product brochures. Gurley value was expressed as the time in seconds required to pass 100 mL of air through 6.45 cm^2 (1 $in.^2$) of membrane under a pressure of 31.0 cm (12.2 in.) of water

was coated on a porous non-woven PET, followed by drying at 200 °C to obtain the separator. This method resulted in a separator having an average pore size of 0.08 μm, a thickness of about 24 μm and a Gurley value of about 65 s, and the separator thus made was thermally stable up to 210 °C, which is limited by the melting point of PET non-woven matrix. The comparison between Separion and Celgard membranes in Table 11.5 shows the remarkable improvements of the Separion separators in terms of wettability, permeability (low Gurley value), meltdown temperature. In addition, all the abuse tests give evidence of the remarkable improvement in the safety of the batteries equipped with this separator. In a nail penetration test on the 8 Ah Li-ion pouch cells, the maximum temperature of the cell using Separion separators is only 58 °C against 500 °C for the cell using PE separators [150, 151].

11.7 Summary and Conclusions

In various commercial lithium ion batteries, the exact electrolyte composition differs from manufacturer to another, and the compositions employed remain proprietary information, involving secret formulas and additives etc. However, the majority of these electrolytes involve two indispensable components: EC as a solvent and $LiPF_6$ as the solute. It is believed that all manufacturers also use co-solvents involving one or more linear carbonates such as DMC, DEC or EMC; these co-solvents increase fluidity and decrease the melting point of the electrolyte. The commercialized lithium ion batteries deliver their rated capacity and power in the temperature range −20 to 50 °C: the lower temperature limit (−20 °C) is set by

EC owing to the high melting point and high liquid temperature it confers on the solvent mixture, and the high-temperature limit (50 °C) is due to $LiPF_6$ owing to its reactivity with solvents. At temperatures above 60 °C the performance deterioration of these batteries is permanent. However, the reduction in performance at low temperatures between −20 and −30 °C is usually temporary and can be recovered once the battery is brought back to temperatures above 20 °C. The struggle to obtain better and high performance electrolytes for lithium batteries is a highly complex area full of very intensive activity [132]. Some recent activity involving ceramic electrolytes in all solid-state lithium batteries may also be mentioned [132–156]. This chapter has been conceived as a survey on the electrolytes, with attention focussed on the basics regarding their constitution in relation to the safety concern and to their impact on the performance of the batteries. The reader who would be interested in more details and knowledge is invited to read a recent book that has been written for this purpose [157].

References

1. Xu K (2004) Non-aqueous liquid electrolytes for lithium-based rechargeable batteries. Chem Rev 104:4303–4417
2. Guerfi A, Vijh A, Zaghib K (2013) Safe lithium re-chargeable batteries based on ionic liquids. In: Scrosati B, Abraham KM, Schalkwijk WV, Hassoun J (eds) Lithium batteries. Advanced technologies and applications. Wiley, New York, pp 291–326
3. Lewandowski A, Swiderska-Mocek A (2009) Ionic liquids as electrolytes in lithium-ion batteries – an overview of electrochemical studies. J Power Sourc 194:601–609
4. Howlett PC, MacFarlane DR, Hollenkamp AF (2004) High lithium metal cycling efficiency in a room temperature ionic liquid. Electrochem Solid-State Lett 7:A97–A101
5. Conway BE (1964) Modern aspects of electrochemistry, vol 3. Butter-Worths, London, p 43
6. Schalkwijk WV, Scrosati B (eds) (2002) Advanced lithium-ion batteries. Kluwer, New York, p 3
7. Guerfi A, Dontigny M, Kobayashi Y, Vijh A, Zaghib K (2009) Investigations on some electrochemical aspects of lithium-ion ionic liquid/gel polymer battery systems. J Solid State Electrochem 13:1003–1014
8. Guerfi A, Dontigny M, Charest P, Peticlerc M, Lagacé M, Vijh A, Zaghib K (2010) Improved electrolytes for Li-ion batteries: mixtures of ionic liquid and organic electrolyte with enhanced safety and electrochemical performance. J Power Sourc 195:845–852
9. Fernicola A, Croce F, Scrosati B, Watanabe T, Ohno H (2007) Li TFSI-BEPy TFSI as an improved ionic liquid electrolyte for rechargeable lithium batteries. J Power Sourc 174:342–348
10. Wright PV (1975) Electrical conductivity in ionic complexes of poly (ethylene oxide). Br Polym J 7:319–325
11. Armand MB, Chabagano JM, Duclot M (1979) Poly-ethers as solid electrolytes. In: Vashishta P, Mundy JN, Shenoy GK (eds) Fast ion transport in solids. North Holland, Amsterdam, pp 131–136
12. Ratner MA, Shriver DF (1988) Ion transport in solvent – free polymers. Chem Rev 88:109–124

13. Wong DHC, Thelen JL, Fu Y, Devaux D, Pandya AA, Battaglia VS, Balsara NP, DeSimone JM (2014) Non-flammable perfluoropolyether – based electrolytes for lithium batteries, PNAS, doi: 10.1073/pnas.1314615111
14. Khurana R, Schaefer JL, Archer LA, Coates GW (2014) Suppression of lithium dendritic growth using cross-linked polyethylene/poly (ethylene oxide) electrolytes: a new approach for practical lithium-metal polymer batteries. J Am Chem Soc doi.org/10.1021/Ja502133j
15. Lee WJ, Kim SH (2008) Polymer electrolytes based on poly(vinylidenefluoride-hexafluoropropylene) and cyanoresin. Macromol Res 16:247–252
16. Min HS, Ko JM, Kim D (2003) Preparation and characterization of porous polyacrylonitrile membranes for lithium-ion polymer batteries. J Power Sourc 119–121:469–472
17. Subramania A, Sundaram NTK, Kumar GV (2006) Structural and electrochemical properties of micro-porous polymer blend electrolytes based on PVdF-co-HFP-PAN for Li-ion battery applications. J Power Sourc 153:177–182
18. Zhang SS, Xu K, Foster DL, Ervin MH, Jow TR (2004) Microporous gel electrolyte Li-ion battery. J Power Sourc 125:114–118
19. Jeong YB, Kim D-W (2004) Effect of thickness of coating layer on polymer-coated separator on cycling performance of lithium-ion polymer cells. J Power Sourc 128:256–262
20. Kim DW, Oh B, Park JH, Sun YK (2000) Gel-coated membranes for lithium-ion polymer batteries. Solid State Ionics 138:41–49
21. Wang Y, Travas-Sejdic J, Steiner R (2002) Polymer gel electrolyte supported with microporous polyolefin membranes for lithium ion polymer battery. Solid State Ionics 148:443–449
22. Oh JS, Kang YK, Kim DW (2006) Lithium polymer batteries using the highly porous membrane filled with solvent-free polymer electrolyte. Electrochim Acta 52:1567–1570
23. Abraham KM, Alamgir M, Hoffman DK (1995) Polymer electrolytes reinforced by Celgard® membranes. J Electrochem Soc 142:683–687
24. Morigaki K, Kabuto N, Haraguchi K (1997) Manufacturing method of a separator for a lithium secondary battery and an organic electrolyte lithium secondary battery using the same separator. U.S. Patent 5,597,659
25. Taskier HT (1982) Hydrophilic polymer coated microporous membranes capable of use as a battery separator. U.S. Patent 4,359,510
26. Gineste JL, Pourcelly G (1995) Polypropylene separator grafted with hydrophilic monomers for lithium batteries. J Membrane Sci 107:155–164
27. Urairi M, Tachibana T, Matsumoto K, Shinomura T, Iida H, Kawamura K, Yano S, Ishida O (1996) Process for producing a wind-type alkaline secondary battery. U.S. Patent 5,558,682
28. Senyarich S, Viaud P (2000) Method of forming a separator for alkaline electrolyte secondary electric cell. U.S. Patent 6,042,970
29. Choi SH, Lee KP, Lee JG, Nho YC (2000) Graft copolymer-metal complexes obtained by radiation grafting on polyethylene film. J Appl Polym Sci 77:500–508
30. Choi SH, Park SY, Nho YC (2000) Electrochemical properties of polyethylene membrane modified with carboxylic acid group. Radiat Phys Chem 57:179–186
31. Choi SH, Kang HJ, Ryu EN, Lee KP (2001) Electrochemical properties of polyolefin nonwoven fabric modified with carboxylic acid group for battery separator. Radiat Phys Chem 60:495–502
32. Ko JM, Min BG, Kim DW, Ryu KS, Kim KM, Lee YG, Chang SH (2004) Thin-film type Li-ion battery, using a polyethylene separator grafted with glycidyl methacrylate. Electrochim Acta 50:367–370
33. Gao K, Hu KG, Yi TF, Dai CS (2006) PE-g-MMA polymer electrolyte membrane for lithium polymer battery. Electrochem Acta 52:443–449
34. Takeuchi Y, Kawabe M, Yamazaki H, Kaneko M, Anan G, Sato K (2001) Sulfur containing atomic group introduced porous article U.S. Patent 6,171,708
35. Cheng CL, Wang YY (2004) Preparation of porous, chemically cross-linked, PVdF-based gel polymer electrolytes for rechargeable lithium batteries. J Power Sourc 134:202–210

36. Song MK, Kim YT, Cho J-Y, Cho BW, Popov BN, Rhee HW (2004) Composite polymer electrolytes reinforced by non-woven fabrics. J Power Sourc 125:10–16
37. Gee MA, Olsen I (1996) Battery with fusible solid electrolyte. US Patent 5534365
38. Aurbach D, Cohen YS (2004) Identification of surface films on electrodes in non-aqueous electrolyte solutions: spectroscopic, electronic and morphologic studies. In: Balbuena PB, Wang Y (eds) Lithium-ion batteries: solid electrolyte interphase. Imperial College Press, London, pp 70–139
39. Vijh AK (1973) Electrochemistry of metals and semiconductors. Marcel Dekker, New York, 297 p
40. Vijh AK (1968) Relation between solid-state cohesion of metal fluorides and the electrochemical behaviour of metals in anhydrous hydrogen fluoride. J Electrochem Soc 115:1096–1098
41. Vijh AK (1968) Comments on the relation between band gap energy in semiconductors and heats of formation. J Phys Chem Solids 29:2233–2236
42. Vijh AK (1969) Correlation between bond energies and forbidden gaps of inorganic binary compounds. J Phys Chem Solids 116:972–975
43. Vijh AK (1970) Chemical approaches to the approximate prediction of band gaps of semiconductors and insulators. J Electrochem Soc 117:173C–178C
44. Vijh AK (1972) Electrode reactions on demetallized surfaces. J Electrochem Soc 119:1498–1502
45. Vijh AK (1974) A possible role of corrosion reaction products in passivation electrodes in high energy density battery systems. Corrosion Sci 14:169–173
46. Vijh AK (1971) Role of semiconducting films in the electropolishing of metals in sulphamic acid-formamide solutions. Electrochim Acta 16:1427–1435
47. Vijh AK (1972) An interpretation of corrosion and anodic dissolution of some film-covered metals. J Electrochem Soc 119:1187
48. Peled E (1979) The electochemical behaviour of alkali and alkaline earth metals in non-aqueous battery systems – the solid-electrolyte interphase model. J Electrochem Soc 126:2047–2051
49. Young L (1961) Anodic oxide films. Academic, New York
50. Balbuena PB, Wang Y (eds) (2004) Lithium-ion batteries: solid-electrolyte interphase. Imperial College Press, London
51. Choi NS, Chen Z, Freunberger SA, Ji X, Sun Y, Amine K, Yushin G, Nazar LF, Cho J, Bruce PG (2012) Challenges facing lithium batteries and electrical double layer capacitors. Angew Chem Int Ed 51:9994–10024
52. Goodenough JB, Kim Y (2011) Challenges for rechargeable batteries. J Power Sourc 196:6688–6694
53. Zhang SS, Xu K, Jow TR (2006) EIS study on the formation of solid electrolyte interface in Li-ion battery. Electrochim Acta 51:1636–1640
54. Matsuta S, Asada T, Kitaura K (2000) Vibrational assignments of lithium alkyl carbonate and lithium alkoxide in the infrared spectra an Ab initio MO study. J Electrochem Soc 147:1695–1702
55. Simon B, Boeuve JP (1997) Rechargeable lithium electrochemical cell. US Patent 5,626,981. Accessed 6 May 1997
56. Aurbach D, Gamolsky K, Markovsky B, Gofer Y, Schmidt M, Heider U (2002) On the use of vinylene carbonate (VC) as an additive to electrolyte solutions for Li-ion batteries. Electrochim Acta 47:1423–1439
57. Contestabile M, Morselli M, Paraventi R, Neat RJ (2003) A comparative study on the effect of electrolyte/additives on the performance of ICP383562 Li-ion polymer (soft-pack) cells. J Power Sourc 119–121:943–947
58. Aurbach D, Gnanaraj JS, Geissler W, Schmidt M (2004) Vinylene carbonate and Li salicylatoborate as additives in $LiPF_3$ $(CF_2CF_3)_3$ solutions for rechargeable Li-ion batteries. J Electrochem Soc 151:A23–A30

59. Chen G, Zhuang GV, Richardson TJ, Liu G, Ross PNJ (2005) Anodic polymerization of vinyl ethylene carbonate in Li-ion battery electrolyte. Electrochem Solid State Lett 8:A344–A347
60. Sasaki T, Abe T, Iriyama Y, Inaba M, Ogumi Z (2005) Suppression of an alkyl dicarbonate formation in Li-ion cells. J Electrochem Soc 152:A2046–A2050
61. Hu YS, Kong WH, Wang ZX, Li H, Huang X, Chen LQ (2004) Effect of morphology and current density on the electrochemical behaviour of graphite electrodes in PC-based electrolyte containing VEC additive. Electrochem Solid State Lett 7:A442–A446
62. Lee JT, Lin YW, Jan YS (2004) Allyl ethyl carbonate as an additive for lithium-ion battery electrolytes. J Power Sourc 132:244–248
63. Abe K, Yoshitake H, Kitakura T, Hattori T, Wang H, Yoshio M (2004) Additives-containing functional electrolytes for suppressing electrolyte decomposition in lithium-ion batteries. Electrochim Acta 49:4613–4622
64. Santner HJ, Moller KC, Ivanco J, Ramsey MG, Netzer FP, Yamaguchi S, Besenhard JO, Winter M (2003) Acryl acid nitrile, a film-forming electrolyte component for lithium-ion batteries, which belongs to the family of additives containing vinyl groups. J Power Sourc 119–121:368–372
65. Komaba S, Itabashi T, Ohtsuka T, Groult H, Kumagai N, Kaplan B, Yashiroa H (2005) Impact of 2-vinylpyridine as electrolyte additive on surface and electrochemistry of graphite for C/$LiMn_2O_4$ Li-ion cells. J Electrochem Soc 152:A937–A946
66. Ufheil J, Baertsch MC, Würsig A, Novak P (2005) Maleic anhydride as an additive to γ-butyrolactone solutions for Li-ion batteries. Electrochim Acta 50:1733–1738
67. Gan H, Takeuchi ES (2002) Phosphonate additives for nonaqueous electrolyte in rechargeable electrochemical cells. US Patent 6,495,285 B2. Accessed 17 Dec 2002
68. Yamada M, Usami K, Awano N, Kubota N, Takeuchi Y (2005) Nonaqueous electrolytic solution and nonaqueous secondary battery. US Patent 6,872,493. Accessed 29 Mar 2005
69. Schroeder G, Gierczyk B, Waszak D, Kopczyk M, Walkowiak M (2006) Vinyl tris-2-methoxyethoxy silane – a new class of film-forming electrolyte components for Li-ion cells with graphite anodes. Electrochem Commun 8:523–527
70. Korepp C, Santner HJ, Fujii T, Ue M, Besenhard JO, Moller KC, Winter M (2006) 2-Cyanofuran – a novel vinylene electrolyte additive for PC-based electrolytes in lithium-ion batteries. J Power Sourc 158:578–582
71. Ein-Eli Y, Thomas SR, Koch VR (1997) The role of SO_2 as an additive to organic Li-ion batter electrolytes. J Electrochem Soc 144:1159–1165
72. Ein-Eli Y (2002) Dithiocarbonic anhydride (CS_2) – a new additive in Li-ion battery electrolytes. J Electroanal Chem 531:95–99
73. Besenhard JO, Wagner MW, Winter M, Jannakoudakis AD, Jannakoudakis PD, Theodoridou E (1993) Inorganic film-forming electrolyte additives improving the cycling behavior of metallic lithium electrodes and the self-discharge of carbon-lithium electrodes. J Power Sourc 44:413–414
74. Wrodnigg GH, Besenhard JO, Winter M (1999) Ethylene sulfite as electrolyte additive for lithium-ion cells with graphitic anodes. J Electrochem Soc 146:470–472
75. Wrodnigg GH, Besenhard JO, Winter M (2001) Cyclic and acyclic sulfites: new solvents and electrolyte additives for lithium ion batteries with graphitic anodes? J Power Sourc 97–98:592–594
76. Gan H, Takeuchi ES (2000) Electrolytic cell containing an anode and a cathode made up of active material capable of intercalating with alkali metal, a nonaqueous electrolyte activating both electrodes and a organic nitrate additive in the electrolyte. US Patent 6,136,477 A. Accessed 24 Oct 2000
77. Shu ZX, McMillan RS, Murray JJ, Davidson IJ (1996) Use of chloroethylene carbonate as an electrolyte solvent for a graphite anode in a lithium-ion battery. J Electrochem Soc 143:2230–2235
78. McMillan R, Slegr H, Shu ZX, Wang WD (1999) Fluoroethylene carbonate electrolyte and its use in lithium ion batteries with graphite anodes. J Power Sourc 81–82:20–26

79. Naji A, Ghanbaja J, Willmann P, Billaud D (2000) New halogenated additives to propylene carbonate-based electrolytes for lithium-ion batteries. Electrochim Acta 45:1893–1899
80. Lee JT, Wu MS, Wang FM, Lin YW, Bai MY, Chiang PC (2005) Effects of aromatic esters as propylene carbonate-based electrolyte additives in lithium-ion batteries. J Electrochem Soc 152:A1837–A1843
81. Levi MD, Markevich E, Wang C, Koltypin M, Aurbach D (2004) The effect of dimethyl pyrocarbonate on electroanalytical behaviour and cycling of graphite electrodes. J Electrochem Soc 151:A848–A856
82. Simon B, Boeuve JP, Broussely M (1993) Electrochemical study of the passivating layer on lithium intercalated carbon electrodes in nonaqueous solvents. J Power Sourc 43–44:65–74
83. Ein-Eli Y, Markovsky B, Aurbach D, Carmeli Y, Yamin H, Luski S (1994) The dependence of the performance of Li-C intercalation anodes for Li-ion secondary batteries on the electrolyte solution composition. Electrochim Acta 39:2559–2569
84. Shin JS, Han CH, Jung UH, Lee SI, Kim HJ, Kim K (2002) Effect of Li_2CO_3 additive on gas generation in lithium-ion batteries. J Power Sourc 109:47–52
85. Choi YK, Chung KI, Kim WS, Sung YE, Park SM (2002) Suppressive effect of Li_2CO_3 on initial irreversibility at carbon anode in Li-ion batteries. J Power Sourc 104:132–139
86. Andersson AM, Edstrom K (2001) Chemical composition and morphology of the elevated temperature SEI on graphite. J Electrochem Soc 148:A1100–A1109
87. Sun X, Lee HS, Yang XQ, McBreen J (2002) Using a boron-based anion receptor additive to improve the thermal stability of $LiPF_6$-based electrolyte for lithium batteries. Electrochem Solid State Lett 5:A248–A251
88. Sun X, Lee HS, Yang XQ, McBreen J (2003) The compatibility of a boron-based anion receptor with the carbon anode in lithium-ion batteries. Electrochem Solid State Lett 6:A43–A46
89. Herstedt M, Stjerndahl M, Gustafsson T, Edstrom K (2003) Anion receptor for enhanced thermal stability of the graphite anode interface in a Li-ion battery. Electrochem Commun 5:467–472
90. Sun X, Lee HS, Yang XQ, McBreen J (1999) Comparative studies of the electrochemical and thermal stability of two types of composite lithium battery electrolytes using boron-based anion receptors. J Electrochem Soc 146:3655–3659
91. Zhang SS, Xu K, Jow TR (2002) A thermal stabilizer for $LiPF_6$-based electrolytes of Li-ion cells. Electrochem Solid State Lett 5:A206–A208
92. Jow TR, Zhang SS, Xu K, Ding MS (2005) Non-aqueous electrolyte solutions comprising additives and non-aqueous electrolyte cells comprising the same. US Patent 6,905,762 B1. Accessed 14 June 2005
93. Wang X, Naito H, Sone Y, Segami G, Kuwajima S (2005) New additives to improve the first-cycle charge-discharge performance of a graphite anode for lithium-ion cells. J Electrochem Soc 152:A1996–A2001
94. Appel K, Pasenok S (2000) Electrolyte system for lithium batteries and use of said system, and method for increasing the safety of lithium batteries. US Patent 6,159,640. Accessed 12 Dec 2000
95. Li W, Campion C, Lucht BL, Ravdel B, DiCarlo J, Abraham KM (2005) Additives for stabilizing $LiPF_6$-based electrolytes against thermal decomposition. J Electrochem Soc 152: A1361–A1365
96. Xu K, Zhang SS, Jow TR, Xu W, Angell CA (2002) LiBOB as salt for lithium-ion batteries: a possible solution for high temperature operation. Electrochem Solid State Lett 5:A26–A29
97. Xu K, Zhang SS, Poese BA, Jow TR (2002) Lithium bis(oxalate)borate stabilizes graphite anode in propylene carbonate. Electrochem Solid State Lett 5:A259–A262
98. Jiang J, Dahn JR (2003) Comparison of the thermal stability of lithiated graphite in LiBOB EC/DEC and in $LiPF_6$ EC/DEC. Electrochem Solid State Lett 6:A180–A182
99. Heider U, Schmidt M, Amann A, Niemann M, Kühner A (2003) Use of additives in electrolyte for electrochemical cells. US Patent 6,548,212. Accessed 15 Apr 2003

100. Wiesboeck RA (1972) Tetraacetonitrilolithium hexafluorophosphate, tetraacetonitrillithium hexafluoroarsenate and method for the preparation thereof. US Patent 3,654,330. Accessed 4 Apr 1972
101. Lee HS, Yang XQ, Nam KW, Wang X (2012) Fluorinated arylboron oxalate as anion receptors and additives for non-aqueous battery electrolytes. US Patent 2012/0183866 A. Accessed 19 July 2012
102. Xu K, Zhang SS, Lee U, Allen JL, Jow TR (2005) LiBOB: is it an alternative salt for lithium ion chemistry? J Power Sourc 146:79–85
103. Dahn JR, EFuller EW, Obrovac M, von Sacken U (1994) Thermal stability of Li_xCoO_2, Li_xNiO_2 and λ-MnO_2 and consequences for the safety of Li-ion cells. Solid State Ionics 69:265–270
104. Jang DH, Shin YJ, Oh SM (1996) Dissolution of spinel oxides and capacity losses in 4 V $Li/Li_xMn_2O_4$ cells. J Electrochem Soc 143:2204–2211
105. Zaghib K, Striebel K, Guerfi A, Shim J, Armand M, Gauthier M (2004) $LiFePO_4$/polymer/natural graphite: low cost Li-ion batteries. Electrochim Acta 50:263–270
106. Zaghib K, Charest P, Guerfi A, Shim J, Perrier M, Striebel K (2005) $LiFePO_4$ safe Li-ion polymer batteries for clean environment. J Power Sourc 146:380–385
107. Chagnes A, Carré B, Willmann P, Dedryvère R, Gonbeau D, Lemordant D (2003) Cycling ability of γ-butyrolactone-ethylene carbonate based electrolytes. J Electrochem Soc 150: A1255–A1261
108. Takami N, Sekino M, Ohsaki T, Kanda M, Yamamoto M (2001) New thin lithium-ion batteries using a liquid electrolyte with thermal stability. J Power Sourc 97–98:677–680
109. Schmidt M, Heider U, Kuehner A, Oesten R, Jungnitz M, Ignatev N, Sartori P (2001) Lithium fluoroalkylphosphates: a new class of conducting salts for electrolytes for high energy lithium-ion batteries. J Power Sourc 97–98:557–560
110. Oesten R, Heider U, Schmidt M (2002) Advanced electrolytes. Solid State Ionics 148:391–397
111. Gnanaraj JS, Zinigrad E, Asraf L, Gottlieb HE, Sprecher M, Aurbach D, Schmidt M (2003) The use of accelerating rate calorimetry (ARC) fort he study of the thermal reactions of Li-ion battery electolyte solutions. J Power Sourc 119–121:794–798
112. Buhrmester C, Chen J, Moshurchak L, Jiang J, Wang RL, Dahn JR (2005) Studies of aromatic redox shuttle additives for $LiFePO_4$-based Li-ion cells. J Electrochem Soc 152:A2390–A2399
113. Dahn JR, Jiang J, Fleischauer MD, Buhrmester C, Krause LJ (2005) High-rate overcharge protection of $LiFePO_4$-based Li-ion cells using the redox shuttle additive 2,5-ditertbutyl-1,4-dimethoxybenzene. J Electrochem Soc 152:A1283–A1289
114. Feng XM, Ai XP, Yang HX (2004) Possible use of methylbenzenes as electrolyte additives for improving the overcharge tolerances of Li-ion batteries. J Appl Electrochem 34:1199–1203
115. Lee H, Lee JH, Ahn S, Kim HJ, Cho JJ (2006) Co-use of cyclohexyl benzene and biphenyl for overcharge protection of lithium-ion batteries. Electrochem Solid State Lett 9:A307–A310
116. Xiao L, Ai X, Cao Y, Yang H (2004) Electrochemical behavior of biphenyl as polymerizable additive for overcharge protection of lithium ion batteries. Electrochim Acta 49:4189–4196
117. Choy SH, Noh HG, Lee HY, Sun HY, Kim HS (2005) Nonaqueous electrolyte composition for improving overcharge safety and lithium battery using the same. U.S. Patent 6,921,612. Accessed 26 July 2005
118. Mao H, Wainwright DS (2000) Improvement comprises a monomer additive mixed in nonaqueous electrolyte which polymerizes to form electroconductive polymer at battery voltages greater than maximum operating charging voltage and creates an internal short circuiting. US Patent 6,074,776 A. Accessed 13 June 2000
119. Reimers JN, Way BM (2000) Additives selected from the group consisting of phenyl-aliphatic hydrocarbon-phenyl compounds, fluorine substituted biphenyl compounds, and

3-thiopheneacetonitrile can provide better cycling performances; fireproofing. US Patent 6,074,777 A. Accessed 13 June 2000
120. Amine K, Liu J, Belharouak I, Kang SH, Bloom I, Vissers D, Henriksen G (2005) Advanced cathode materials for high-power applications. J Power Sourc 146:111–115
121. Zhang SS (2006) An unique lithium salt for the improved electrolyte of Li-ion battery. Electrochem Commun 8:1423–1428
122. Granzow A (1978) Flame retardation by phosphorus compounds. Chem Res 11:177–183
123. Xu K, Ding MS, Zhang SS, Allen JL, Jow TR (2002) An attempt to formulate non-flammable lithium ion electrolytes with alkyl phosphates and phosphazenes. J Electrochem Soc 149: A622–A626
124. Xu K, Zhang SS, Allen JL, Jow TR (2002) Nonflammable electrolytes for Li-ion batteries based on a fluorinated phosphate. J Electrochem Soc 149:A1079–A1082
125. Lee CW, Venkatachalapathy R, Prakash J (2000) A novel flame-retardant additive for lithium batteries. Electrochem Solid State Lett 3:63–65
126. Prakash J, Lee CW, Amine K (2002) Flame-retardant additive for Li-ion batteries. US Patent 6,455,200 B1. Accessed 24 Sept 2002
127. Yao XL, Xie S, Chen CH, Wang QS, Sun JH, Li YL, Lu SX (2005) Comparative study of trimethyl phosphate and trimethyl phosphate as electrolyte additives in lithium ion batteries. J Power Sourc 144:170–175
128. Xu W, Deng Z (2007) Stabilized nonaqueous electrolytes for rechargeable batteries. World Patent 2007109435 A2. Accessed 27 Sept 2007
129. Yokoyama K, Sasano T, Hiwara A (2000) Fluorine-substituted cyclic carbonate electrolytic solution and battery containing the same. US Patent 6,010,806. Accessed 4 Jan 2000
130. Guerfi A, Duchesne S, Kobayashi Y, Vijh A, Zaghib Z (2008) $LiFePO_4$ and graphite electrodes with ionic liquids based on bis(fluorosulfonyl)imide $(FSI)^-$ for Li-ion batteries. J Power Sourc 175:866–873
131. Wang Y, Zaghib K, Guerfi A, Bazito FC, Torresi RM, Dahn JR (2007) Accelerating rate calorimetry studies of the reactions between ionic liquids and charged lithium ion battery electrode materials. Electrochim Acta 52:6346–6352
132. Sakuda A, Hagashi A, Tatsumisago M (2013) Sulfide solid electrolyte with favourable mechanical property for all-solid-state lithium battery. Sci Rep 3:2261–2266. doi:10.1038/svep 02261
133. Zhang SS (2007) A review on the separators of liquid electrolyte Li-ion batteries], together with the manufacturing processes. J Power Sourc 164:351–364
134. Lundquist JT, Lundsager B, Palmer NI, Troffkin HJ, Howard J (1987) Battery separator. U.S. Patent 4,650,730
135. Yu WC, Geiger MW (1996) Shutdown, bilayer battery separator. U.S. Patent 5,565,281
136. Lundquist JT, Lundsager CB, Palmer NI, Troffkin HJ (1988) Dimensional stability. U.S. Patent 4,731,304
137. Yu WC, Dwiggins CF (1997) Methods of making cross-ply microporous membrane battery separator, and the battery separators made thereby. U.S. Patent 5,667,911
138. Yu WC (1997) Shutdown, trilayer battery separator. U.S. Patent 5,691,077
139. Yu TH (2000) Microporous polypropylene coatings; shutdown layer blend of low density polyethylene and calcium carbonate. U.S. Patent 6,080,507
140. Yu WC (2005) Continuous methods of making microporous battery separators. U.S. Patent 6,878,226
141. Callahan RW, Call RW, Harleson KJ, Yu TH (2003) Battery separators with reduced splitting propensity. U.S. Patent 6,602,593
142. Kinouchi M, Akazawa T, Oe T, Kogure R, Kawabata K, Nakakita Y (2003) Battery separator and lithium secondary battery. U.S. Patent 6,627,346
143. Prosini PP, Villano P, Carewska M (2002) A novel intrinsically porous separator for self-standing lithium-ion batteries. Electrochim Acta 48:227–233

144. Kim KM, Park NG, Ryu KS, Chang SH (2006) Characteristics of PVdF-HFP/TiO_2 composite membrane electrolytes prepared by phase inversion and conventional casting methods. Electrochim Acta 51:5636–5644
145. Takemura D, Aihara S, Hamano K, Kise M, Nishimura T, Urushibata H, Yoshiyasu H (2005) A powder particle size effect on ceramic powder based separator for lithium rechargeable battery. J Power Sourc 146:779–783
146. Zhang SS, Xu K, Jow TR (2003) Alkaline composite film as a separator for rechargeable lithium batteries. J Solid State Electrochem 7:492–496
147. Zhang SS, Xu K, Jow TR (2005) An inorganic composite membrane as the separator of Li-ion batteries. J Power Sourc 140:361–364
148. Augustin S, Hennige VD, Horpel G, Hying C (2002) Ceramic but flexible: new ceramic membrane foils for fuel cells and batteries. Desalination 146:23–28
149. Augustin S, Hennige VD, Horpel G, Hying C, Tarabocchia J, Swoyer J, Saidi MY (2006) Performance of saphion type batteries using SEPARION separators. Meet Abstr Electrochem Soc 502 Abstract 80
150. Augustin S, Hennige VD, Horpel G, Hying C, Haug P, Perner A, Pompetzki M, Wohrle T, Wurm C, Ilic D (2006) Improved abuse tolerance of PoLiFlex batteries using SEPARION separators. Meet Abstr Electrochem Soc 502 Abstract 84
151. Augustin S (2006) Ceramic separator for large lithium ion batteries. Advanced automotive battery and ultracapacitor conference (AABC-06), Baltimore MD. Accessed 15–19 May 2006
152. Hennige V, Hying C, Horpel G, Novak P, Vetter J (2006) Separator provided with asymmetrical pore structures for an electrochemical cell. U.S. Patent 20,060,078,791
153. West WC, Whitacre JF, Lim JR (2004) Chemical stability enhancement of lithium conducting solid electrolyte plates using sputtered LiPON thin films. J Power Sourc 126:134–138
154. Thangadurai V, Weppner W (2005) Investigations on electrical conductivity and chemical compatibility between fast lithium ion conducting garnet-like $Li_4BaLa_2Ta_2O_{12}$ and lithium battery cathodes. J Power Sourc 142:339–344
155. Fergus JW (2010) Ceramic and polymeric solid electrolytes for lithium-ion batteries. J Power Sourc 195:4554–4569
156. Kotobuki M, Kanamura K (2013) Fabrication of all-solid-state battery using $Li_5La_3Ta_2O_{12}$ ceramic electrolyte. Ceramic Intern 39:6481–6487
157. Jow RY, Ksu K, Borodin O, Ue M (2014) Electrolytes for lithium and lithium-ion batteries. Springer, New York, pp 1–467

Chapter 12
Nanotechnology for Energy Storage

12.1 Introduction

Nanomaterials of metal oxides have been intensively studied as anode and cathode materials for lithium-ion batteries (LiBs) aimed at achieving higher specific capacities and high power density. It is worth pointing out that the word "nanotechnology" has become very popular and is used to describe many types of research where the characteristic dimensions are much less than 1 μm. For example, continued improvements in lithography to design computer components have resulted in line widths that are less than one micron: this work is often called "nanotechnology." Many of the exponentially improving trends in computer hardware capability have remained steady for the last 50 years. Today "nanosciences" are fairly widespread with the belief that these trends are likely to continue for at least several years; however, new aspects are now considered in the field of energy transformation. In this respect, the classic 1959 article "There's plenty of room at the bottom" by Richard P. Feynman discusses the limits of miniaturization and forecast the ability to ". . .arrange the atoms the way we want; the very atoms, all the way down!" [1].

Nano-structured materials are distinguished from conventional polycrystalline materials by the size of the structural entities that comprises them, microstructures comprising nanoscale domains in at least one dimension. The ability to control a material's structure and composition at the nano-level has demonstrated that materials and devices having properties intrinsically different from their polycrystalline counterparts can be fabricated. As tailoring of fundamental properties becomes possible at the atomic level, the prospect of developing novel materials and devices with new applications become viable.

Conventional rechargeable Li batteries exhibit rather poor rate performance, even compared with old technologies such as lead-acid [2]. Achieving high rate rechargeable Li-ion batteries depends ultimately of the dimension of the active particles for both negative and positive electrodes. One of the prospective solutions for the preparation of electrodes with high power density is the choice of

C. Julien et al., *Lithium Batteries*, DOI 10.1007/978-3-319-19108-9_12

nanocomposite materials because the geometric design of the insertion compound is a crucial intrinsic property. The performance of electrode materials for Li-ion batteries reached today is the result of intensive research to reduce the size of the particles to the nanoscale. It is important, however, to specify what "nano" means here. In electronics, for instance, it signifies particles that are so small the electronic or the magnetic properties are modified by quantum confinement of the electrons. It means particles smaller than 10 nm. In the physics and electrochemistry of the cathode elements of Li-ion batteries, however, the term is used to signify particles so small that their properties depend importantly on surface effects. Typically, the surface layer is about 3 nm thick, so that particles are labeled "nano" in the literature if their size is smaller than 100 nm, and usually in the range 20–100 nm. So far, there has been little interest to synthesize smaller particles because too small particles have been reported to reduce the tap density [3] and they are much more difficult to handle in making electrodes for the industry of Li-ion batteries. It turns out that some size effects on the physical and chemical properties of the particles have been observed in this "nano" range, as we see later in this review, but they were not necessarily expected and may not be totally understood. Still, there have been many efforts through the years to decrease the size of the particles from a few microns to this "nano" range, for several reasons. One is the increase of the effective contact area of the powder with the electrolyte. A larger effective contact surface with the electrolyte means a greater probability to drain Li^+ ions from the electrode, which increases the power density of the cell. A smaller particle size also reduces the Li diffusion length to the interior of the particle, which leads to a greater capacity at higher charge–discharge rates and therefore to a larger power density. Reducing the dimensions of the active particles to nanoscale means, for a given chemical diffusion coefficient of Li^+ ions, D^*, the characteristic time, τ, for the intercalation reaction decreases by a factor of 10^6, since the characteristic time constant for intercalation is expressed by:

$$\tau = L^2/4\pi D^*, \tag{12.1}$$

where L is the diffusion length [4]. Nanoparticles, as well as more tailored nanostructures, are being explored and exploited to enhance rate, even for materials with poor intrinsic electronic conductivity such as olivine frameworks. For such a compound, by preparing the materials at the nanoscale form and by carbon coating, high rate are achievable [5]. In addition, the small electronic conductivity of the olivine particles that results from a two-phase $FePO_4/LiFePO_4$ reaction has led to coating of the particles with a thin layer that is conductive of both electrons and Li, usually an amorphous carbon layer [6]. Decreasing the particle size reduces the length of the tunneling barrier for electrons to travel from/to the surface layer or to/from the core of the particle, which also increases the power density. The coat may also decrease the activation energy for Li^+ transfer across the electrode–electrolyte interfaces.

This chapter is organized as follows. The first part is devoted to the synthesis and physicochemical properties of nanoscale functional electrode materials in various

shapes, i.e., nanoparticles, nanofibers, nanobelts. Compounds such as LiMO_2 with M = (Ni,Co), (Ni,Mn,Co), MnO_2, $LiFePO_4$, WO_3-SiO_2 nanocomposite, WO_3 nanorods, and Li_2MnO_3 rock-salt nanoparticles are examined. Various parameters that influence electrochemical performance such as particle morphology, particle size distribution are discussed. In the second part we present a specific technique of characterization that is vibrational spectroscopy (FTIR and Raman), a powerful tool for investigating the structural properties at the local scale of nanomaterials.

12.2 Synthesis Methods of Nanomaterials

The fabrication of low-dimensional nanostructures such as nanotubes, nanorods, nanofibers, nanoneedles, and nanowires had achieved a lot of attention among the researchers due to their promising applications in many advanced systems. There are two major categories into which preparative technique of nanomaterials can be classified: the physical "top-down" approach such as milling, and the chemical "bottom-up" approach such as sol–gel wet chemistry. Note that the former physical technique receives a great deal more interest in the industrial sector [7]. As a general rule, lower temperature reactions and shorter reaction times are then possible and they yield materials of higher homogeneity and higher specific area [8].

12.2.1 Wet-Chemical Methods

Wet-chemistry, also named soft-chemistry or "chimie douce," refers to synthetic technique that implies a liquid phase. There has been a great deal of interest in preparation of polycrystalline materials, particularly oxides synthesized at low temperature ($T > 200$ °C). This method consists of acidification of aqueous solutions of the starting materials. The overall process includes several steps as shown in the schematic chart Fig. 12.1: (1) mixing of starting materials in the liquid phase, (2) formation of the gel by evaporation, (3) formation of the precursor by heating the gel at low temperature and (4) calcination procedure at different firing temperatures to obtain the final product. The wet-chemical techniques could be classified in four groups according the salts and complexing agent used (Table 12.1). They are namely sol–gel [9, 10], co-precipitation [11, 12], combustion [13], pyrolysis [14], polyol [15], Pechini process [16, 17], etc.; they were employed for the preparation of nanostructured metal oxides devoted to electrodes for Li-ion batteries. These techniques are assisted by chelating agents that are carboxylic acids like citric, oxalic, malic, tartaric, and succinic [18]. Pereira-Ramos has critically discussed the impact afforded by soft-chemistry techniques especially sol–gel synthesis and precipitation techniques on the electrochemical behavior of the oxide materials as prepared [19]. Solution preparative techniques allow a better mixing of the

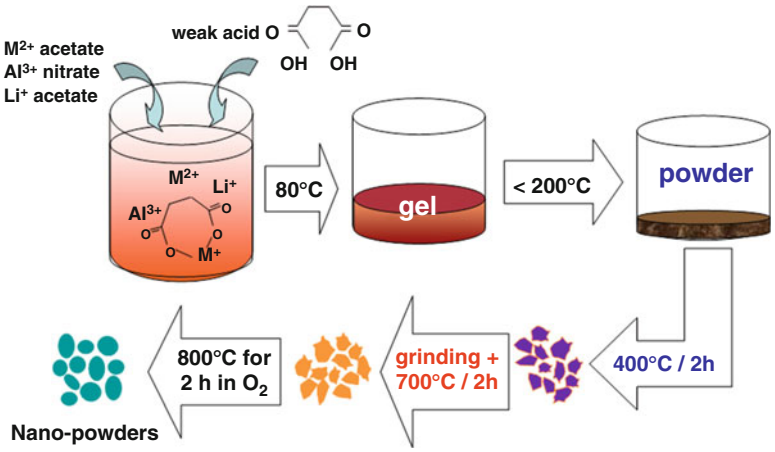

Fig. 12.1 Wet-chemical method assisted by carboxylic acid

Table 12.1 The various wet-chemistry methods used to growth transition-metal oxide powders

Method	Salts	Complexing agent	Molecular weight (g mol^{-1})	Molecular formula
Sol–gel	Acetates	Citric acid	192.43	$HOC(COOH)(CH_2COOH)_2$
Co-precipitation	Acetates	Oxalic acid	90.04	HOOCCOOH
Combustion	Nitrates	Glycine	75.07	NH_2CH_2COOH
Pyrolysis	Acetates	Succinic acid	118.09	$HOOCCH_2CH_2COOH$

elements and thus a better reactivity of the mixture to obtain purer reaction products. Lower reaction temperature and shorter reaction time are then possible to yield a compound of high homogeneity and high specific area. Moreover, these low-temperature methods make use of lower calcination temperatures resulting in particles of smaller size and a highly strained lattice.

12.2.1.1 Sol–Gel Method

The sol–gel method is based on the preparation of a colloidal suspension, a sol, and its transition to a gel from which the polycrystalline material can be obtained via inorganic polymerization reactions in solution. In the sol–gel process, a solid phase is formed through gelation of a colloidal suspension. Drying of the gel can then give "dry gel" (xerogel) state and subsequent heat treatment can be used to remove unreacted organic residues, stabilize the gel, densify it, and induce crystallinity. As an example, Fig. 12.2 shows the DTA-TG curves of the $LiNi_{0.5}Co_{0.5}O_2$ xerogel. The weak endothermic effect associated with a small weight loss of about 9 % for $T < 250$ °C are attributed to departure of residual water. A strong exothermic peak appears at 316 °C after the departure of the remaining water molecule. This

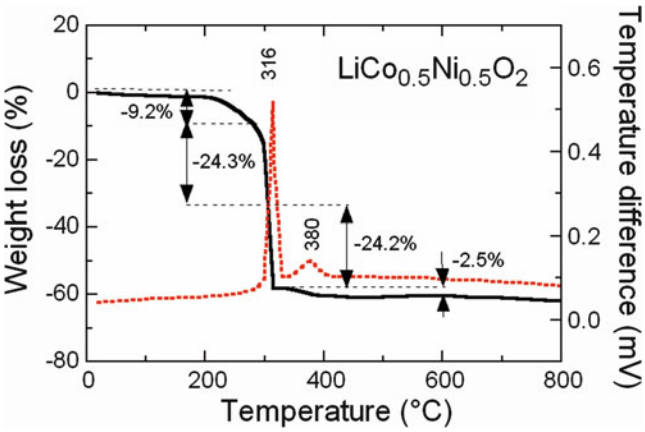

Fig. 12.2 TG-DTA curves of the $LiNi_{0.5}Co_{0.5}O_2$ xerogel. Measurements were carried out at heating rate of 10 °C per min with oxygen flow

exothermic effect corresponds to the combustion of citric acid and acetate ions xerogel. More than half of the weight loss occurs during this stage because of a violent oxidation decomposition reaction. It appeared that citric acid (formed by –COOH– groups) acts as a fuel in the pyrolysis of the gel precursor, accelerating the decomposition of acetate ions. It was reported that chelating agent (carboxylic acid) provides combustion heat for calcination in the synthesis of oxide powders [20]. The gel precursor was self-burning once ignited, because the decomposed acetate ions acted as oxidizer. The weight loss in the temperature range 330–400 °C corresponds to the decomposition of the remaining organic constituents. Even though the crystallization starts below 400 °C; thus well-crystallized and pure phases have been obtained at 600 °C. While the pyrolysis at this stage was very complicated, it could be presumed that the last weak exothermic at ca. 380 °C in the DTA curve corresponds to the crystallization of the $LiNi_{0.5}Co_{0.5}O_2$ phase [9].

12.2.1.2 Pechini Technique

In 1967, in manufacturing ceramic capacitors, Maggio Pechini developed a sol–gel technique for synthesis of alkaline-earth titanates and niobates, materials which do not have favorable hydrolysis equilibrium [21]. In the Pechini method, otherwise *polymerizable complex method*, chelating of cations is realized with the aid of poly-alcohols to create a gel through esterification. The most popular chelating agent which has four carboxylate groups is ethylenediamine tetra-acetate (EDTA). After formation, the gelled composite is sintered, pyrolysing the organic species and leaving nanoparticles. In the Pechini method the metal cations are trapped in the polymer gel, while in the traditional sol–gel methods, the gel is part of the gel structure. The Pechini process uses poly-hydroxyl alcohols such as ethylene glycol

and polyvinyl alcohol as polymerizing agent in order to enhance the uniform distribution of metal ions and avoid their precipitation during evaporation [22]. Note that oxides can be prepared by the conventional acid pH Pechini process and a modified basic pH Pechini process. Higher pH of the starting solution resulted in significantly finer grains in the sintered powders. Zinc oxide (ZnO) nanorods have been successfully synthesized by modified Pechini process using ethylene glycol [23].

12.2.1.3 Precipitation Method

Precipitation processes are among the oldest of techniques for the synthesis of nanomaterials. Precipitation synthesis consists of the condensation of a solid oxide network (the precipitate) starting from soluble species. The condensation of the species is initiated by a redox reaction or by a change of pH. Precipitate containing transition-metal ions show typical colors: pink for cobalt, reddish brown for Fe^{III}, pale pink for manganese, green for nickel, etc. Different cations form precipitates at different pH values. For example, Fe commences to precipitate at $pH \approx 2.5$ as hydroxide, while at $pH \approx 1.8$ as phosphate. Zhang et al. [24] synthesized $Li_{1+x}(Ni_{1/3}Mn_{1/3}Co_{1/3})_{1-x}O_2$ powders by a two-step combustion method using the hydroxide route by mixing $(Ni_{1/3}Mn_{1/3}Co_{1/3})(OH)_2$ transition-metal hydroxides and lithium carbonate starting materials dissolved in distilled water. NaOH and NH_4OH solution was also fed into the reactor, in which the pH of the precipitate was controlled with care to its optimized value, namely $pH = 11$ [25]. After suitable grounding and stirring, the precursor was heated at 500 °C for 5 h. The final products were fired at 950 °C for 10 h in air. The mean crystallite size L_{003} in the <001> direction is about 80 Å larger than in the perpendicular direction, which is linked to the elongated shape of the crystallites. Solid solution material $0.5Li_2MnO_3$-$0.5LiNi_{0.33}Co_{0.33}Mn_{0.33}O_2$, the so-called lithium-rich compound, was prepared via a modified co-precipitation method, which takes sulfates with high solubility as the transition-metal sources of mixed hydroxide precursor [26]. This process uses desired amounts of KOH and NH_4OH, which act as a chelating agent separately fed in the reactor.

12.2.1.4 Polyol Process

The polyol process is a soft-chemical method using glycol-based solvents such as diethylene glycol (DEG), triethylene glycol (tEG), and tetraethylene glycol (TEG). The polyol process consists of the reduction of metallic compounds such as oxides and salts in a liquid alcohol medium maintained at its boiling points [27]. The action of polyol medium is twofold for the formation of monodisperse nanoparticles: a solvent and a stabilizer that limits particle growth and prohibits agglomeration. In order to achieve rapid nucleation in polyol reactions, a general rule of thumb is that

the higher the temperature of the glycol, the faster the nucleation and the more uniform the nanoparticles formed. Kim et al. [28] synthesized $LiFePO_4$ nanoparticles prepared by the polyol process without post heat treatments. The particles showed highly crystalline nature of rod and plate like morphologies with an average size of 300 nm. Badi et al. [29] reported modified polyol syntheses which produce nanocrystalline $Li_{1-y}FePO_4$ directly, where the maximum Li substoichiometry on thr M1 site sustained at synthesis temperatures of 320 °C is about 10 %. LFP nanocrystals of relatively uniform morphology were grown with an average width of 20 nm and a length of 40 nm of a very narrow particle size distribution [30].

12.2.1.5 Combustion Method

Combustion method involves exothermic redox reaction of an oxidizer (metal nitrate) and an organic fuel (carboxylic acid, carbo hydrazide (CH), oxalyl dihydrazide (ODH), tetra formal tri-azine (TFTA), acid dihydrazide, urea, etc.) to obtain the desired phase. The stoichiometry of metal nitrate to fuel is calculated assuming the complete combustion to yield metal oxide phase, and CO_2, N_2, and H_2O as by-products. Some of the fuels used were found to be specific for a particular class of oxides, e.g., urea for alumina and related oxides, carbo hydrazide for zirconia, ODH for Fe_2O_3 and ferrites, TFTA for TiO_2, glycine for chromium and related oxides [31]. Combustion synthesis can occur by two modes: self-propagating high-temperature synthesis (SHS) and volume combustion synthesis (VCS). The samples are heated by an external source either locally (SHS) or uniformly (VCS) to initiate en exothermic reaction. VCS is more appropriate for weakly exothermic ractions that require preheating prior ignition, and is sometimes referred to as "thermal explosion" mode [32]. Typical products synthesized by combustion reaction are submicron size with large surface area that both are function of the gaseous products evolved during combustion. As an example, the combustion of γ-Fe_2O_3 using a redox compound such as iron hydrazinium $FeN_2H_5(N_2H_3COO)_3$ liberates 30 mol of gases per Fe_2O_3, i.e., $6CO_2 + 8\ N_2 + 16H_2O$, whereas the redox mixture iron nitrate plus malonohydrazide $C_3H_8N_4O_2$ gives only 20 mol [33]. Julien et al. [34] prepared substituted lithium cobalt oxides, $LiCo_{0.5}M_{0.5}O_2$ (M = Ni, Mg, Mn, Zn) using urea as fuel for cathode materials in Li-ion batteries. Nanopowders 30–60 nm sized of spinel $LiMn_2O_4$ were synthesized using poly acrylic acid (PAA) [35]. The high-voltage cathode material, $LiNiVO_4$, was synthesized at temperatures as low as 320 °C using the aqueous glycine–nitrate combustion process [36]. The synthesis procedure was as follows: the aqueous solution of metal nitrate and ammonium metavanadate was mixed with glycine (aminoacetic acid) solution in the stoichiometric ratio 1:2 and heated to boiling and underwent dehydrated green-black sticky paste. This paste was decomposed at around 250 °C accompanied by a mass od small bubbles (foams) followed by the generation of combustible gases such as NO_x and ammonia, which ultimately gave rise to a pale brown powder, referred to as the precursor. The desired phase of the final product $LiNiVO_4$ was

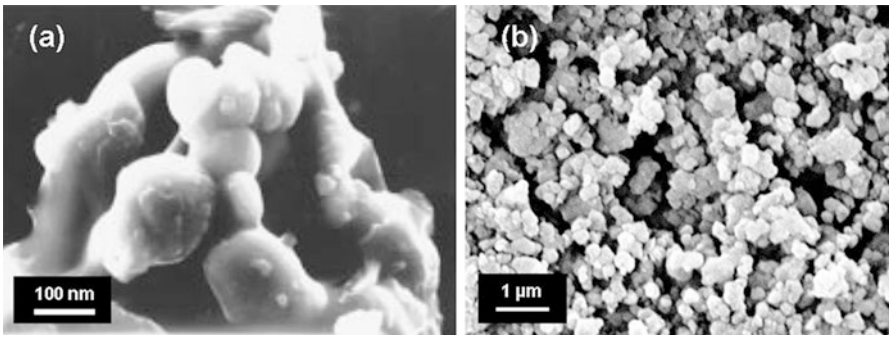

Fig. 12.3 Micrographs of (**a**) inverse spinel $LiNiVO_4$ synthesized by the glycine-assisted combustion method. (**b**) $LiMn_2O_4$ spinel nanopowders prepared by combustion method using urea as a fuel

obtained after annealing at 500 °C in air for 6 h. A theoretical reaction, assuming complete thermal decomposition of the starting materials, may be written as:

$$\begin{aligned} LiNO_{3(aq)} + Ni(NO_3)_{2(aq)} + NH_4VO_{3(aq)} + 6NH_2CH_2COOH_{(aq)} &\rightarrow^{heat}\nabla_{air} \\ \rightarrow LiNiVO_{4(s)} + 5N_{2(g)} + 12CO_{2(g)} + 17H_2O_{(g)}&. \end{aligned} \quad (12.2)$$

SEM analysis reveals the formation of spherical of spherical grains of submicronic size, average size of grains 80–180 nm (Fig. 12.3a). $LiNi_{0.3}Co_{0.7}O_2$ layered material was prepared by the glycine-assisted combustion method [37]. The carboxylic acid groups (–COOH–) that forms viscous resins act as a fuel during the crystallization process at lower temperature $T < 250$ °C providing nanostructured particles. Chitra et al. [13] have developed a new combustion method using urea as a fuel for the synthesis of spinel $LiMn_2O_4$. Nanopowders were formed around 500 °C have spherical shape (Fig. 12.3b) with nearly pore-free state and high surface area ($S_{BET} \approx 13\ cm^2\ g^{-1}$). A modified combustion synthesis, namely PVA-gel method using a solution metal nitrates containing polyvinyl alcohol (PVA) has been proposed to prepare nanostructured $LiMn_2O_4$ with loosely agglomerated spherical 30-nm sized particles [38].

12.2.1.6 Pyrolysis Method

Pyrolysis method, otherwise *wet-chemical reaction succinic acid assisted*, consists of ignition of a resin that removes the organic portion, leading the selected composition of mixed oxides chemically combined. This method with proper amount of chelating agent results in much lower calcination temperature and shorter time of calcinations and mechanically-grinding for producing single-phased nanomaterials compared with other processes. It has been found that the bulk quantities of submicron-sized particles can be obtained at a modest temperature as low as 300 °C, with the highest level of phase purity. This technique describes a simple solution mixing procedure

[39, 40]. For example, in the succinic-assisted process of $LiNi_{0.5}Co_{0.5}O_2$ the ignition occurs at 277 °C compared to 296 and 315 °C for the sol–gel and combustion method, respectively [14]. The pyrolysis method consists of metal acetates dissolved in a methanolic aqueous solution mixed with a solution of succinic acid. Care was exercised in adjusting the concentration of the complexing agent by controlling the pH of the mixed solution that forms an extremely viscous paste-like substance upon slow evaporation of methanol and acetic acid. The $(COOH)_2$ carboxylic groups of the succinic acid form chemical bonds with the metal ions in developing an extremely viscous paste-like substance upon slow evaporation of methanol and acetic acid. The paste was further dried at 120 °C to obtain the dried precursor mass. The precursor decomposition resulted in a huge exothermic reaction as exemplified by the combustion of organic species present in the precursor mass. In the case of $LiNi_{0.5}Co_{0.5}O_2$, this exothermic process yielding a brownish black colored powder enhances the oxidation reaction and onsets the phase formation of the crystalline phase. In the case of the pyrolysis synthesis of nanocrystalline $LiFePO_4$ the pH of the solution with succinic acid was adjusted, ranging between 5.0 and 5.5 using liquid NH_3 because weak acid or neutral or weak basic precursor solutions are preferable to obtain single phase $LiFePO_4$ [41] and strong basic condition should be avoided to prepare $LiFePO_4$ without impurity phase [42].

12.2.2 Template Synthesis

Ordered nanostructured materials were prepare by the template technique. This method consists of a thermal decomposition of the sol–gel precursor within the pores of a membrane. The template is dipped into the sol for 10 min and taken out for heating at $T > 400$ °C resulting in the formation of nanomaterial within the template pores. Different types of template have been widely investigated such as anodic aluminum oxides (AAO), porous polymer and nano-channel glass templates. The final nano-specimens are obtained by dissolution the template composites in 6 mol L^{-1} NaOH solution. The template method with porous membranes of AAO has been successfully used to prepare nanotubes. Li et al. [43] reported the template synthesis of $LiCoO_2$, $LiMn_2O_4$, and $LiNi_{0.8}Co_{0.2}O_2$ nanotubes by heat treatment at 500 °C for 8 h in air. Zhou et al. [44] prepared high-ordered $LiMn_2O_4$ nanowire arrays by AAO template from a polymeric matrix formed by mixture of metal acetates as the cationic sources and citric acid and ethylene glycol as the monomers. The as-produced nanowires were uniformly distributed and had a diameter of around 100 nm.

12.2.3 Spray-Pyrolysis Method

Spray-pyrolysis method is a useful method for the synthesis of high purity, narrow size distribution, homogeneous composition of oxide particles with spherical morphology.

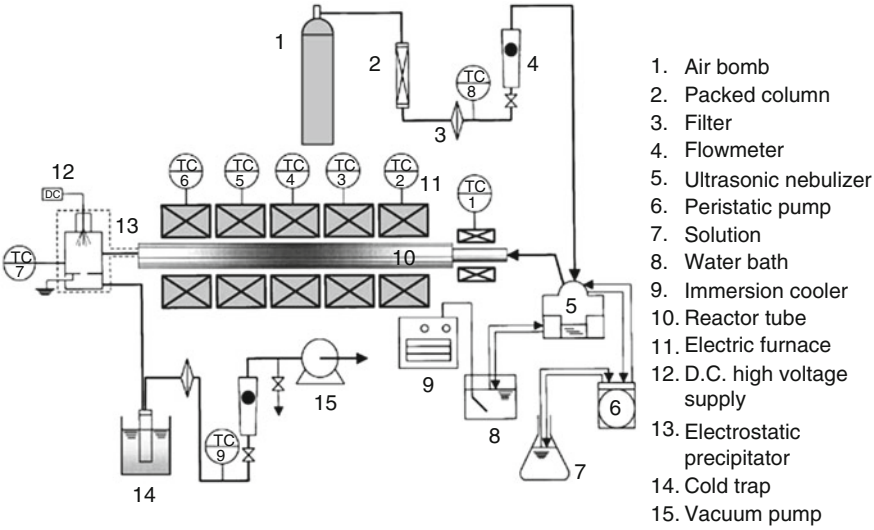

Fig 12.4 Schematic diagram of the experimental apparatus for ultrasonic spray pyrolysis synthesis. Reproduced with permission from [45]. Copyright 2002 Elsevier

The schematic diagram of the experimental apparatus is presented in Fig. 12.4. This setup is divided into three parts such as droplet generator, pyrolysis reactor, and particle collector. The droplet generator consists of an ultrasonic nebulizer, a peristaltic pump for supplying the precursor solution and thermostat circulation parts. The pyrolysis reactor tube is formed by putting a quartz tube (186 cm length) into a horizontal furnace, which is divided into five heating zones. Taniguchi et al. [45] reported that spherical spinel $LiMn_2O_4$ powders could be synthesized using this method by varying gas flow rates and temperature profiles in the reactor. The crystallite size was approximately 30 nm and the specific area of the particles ranges from 5.7 top 12.7 $m^2\ g^{-1}$. $Li[Ni_{1/3}Mn_{1/3}Co_{1/3}]O_2$ was prepared by a two-step synthesis: firstly the precursor $[Ni_{1/3}Mn_{1/3}Co_{1/3}]O_2$ was prepared using the spray method from an aqueous solution including hydrated metal nitrates and citric acid (molar ratio of total metal to citric acid fixed at 0.2) as a polymeric agent. The solution was atomized using an ultrasonic nebulizer with a resonant frequency of 1.7 MHz. The aerosol stream was introduced into the vertical quartz reactor heated at 500 °C. The flow rate of air used as a carrier gas was 10 L min^{-1}. The final products were obtained by mixing the precursor with excess amount of $LiOH{\cdot}H_2O$ followed by calcination at 900 °C. The powders consisted of polycrystalline aggregates (~500 nm) composed of 50-nm primary particles [46]. In the spray-drying method, dried particles with a desired diameter are instantly obtained by controlling the diameter of the spray nozzle. $LiNi_{1/3}Mn_{1/3}Co_{1/3}O_2$ was synthesized by mixing the aqueous solution of metal nitrates and succinic acid using an atomizing nozzle in combination with compressed air. The liquid is deposited at a rate of 100 ml min^{-1} and the spraying is carried out at a pressure of 2 MPa in the reactor maintained at 220 °C [47].

12.2.4 Hydrothermal Method

Since more than one century, hydrothermal synthesis was clearly identified as an important technology for preparation of nanometer-sized particles than can be quenched to form nanoparticle powder, or cross linked to produce nanocrystalline structures [48, 49]. Among the various synthesis approaches pursued in the fabrication of electrode materials for Li-ion batteries, the hydrothermal route is particularly successful with respect to controlling the chemical composition, crystallite size, and particle shape. Hydrothermal synthesis (HTS) is a process that utilizes single or heterogeneous phase reactions in aqueous media at elevated temperature ($T > 25\,^{\circ}\mathrm{C}$) and pressure ($p > 100$ kPa) to crystallize ceramic materials directly from solution [50]. HTS takes place in a wide variety of liquid media: aqueous- and solvent-based systems. HTS offers other advantages over conventional ceramic methods. All forms of nanoscale materials can be prepared, namely nanopowders [51], nanofibers [52], nanobelts [53], nanoplates [54], nanowires [55], nanorods [56], nanovesicles [57], etc. The use of inexpensive, environmentally benign water as a solvent offers a "green" manufacturing approach for large-scale production of Li(Fe,Mn)PO_4/C cathodes for high-power hybrid electric vehicle and plug-in hybrid electric vehicle applications. Further energy-consuming processing steps are reduced such as longer time high temperature calcination. HTS eliminates the formation of agglomerates and produces nanoparticles with narrow particle size distribution. Precise well-defined powder morphology can be also significant. Another merit is that the purity of hydrothermally prepared powders significantly exceeds the purity of the starting substances because the hydrothermal crystallization is a self-purifying process that rejects impurities. However, the conventional hydrothermal process involves a longer reaction time. For instance, it is 5–12 h to synthesize $LiFePO_4$ [58–60]. In this regard, microwave-assisted synthesis approaches will be appealing because they can shorten the reaction time to a few minutes with significant energy savings. The one-pot synthesis was developed for preparing Li$M$$PO_4$/C ($M$ = Mn, Fe, Co) nanocomposites by a microwave assisted hydrothermal process involving hydrothermal carbonization of glucose [61]. Recently, Beninati et al. [62] and Wang et al. [63] reported the synthesis of $LiFePO_4$ by irradiating the solid-state raw materials with carbon in a domestic microwave oven. An in situ coating of carbon on $LiFePO_4$ was attempted during the MW-HT process, employing glucose as the carbon source. An aqueous solution of LiOH, H_3PO_4, and glucose was first stirred for a few minutes. An aqueous solution of the sulfates of Mn^{2+}, Fe^{2+}, or Co^{2+} was then added to this mixture so that the Li:M:P molar ratio was 3:1:1 and the M^{2+} to glucose molar ratio was 2:1, which resulted in a carbon content of 5 wt% in the final product. Although, the synthesis of transition-metal oxides or olivine phosphates requests a careful control of the pH of the solution. Reaction mixtures are acidic for M = Mn (pH = 6.1) and Fe (pH = 6.7), while they are kept basic (pH = 9.9) for M = Co by adding ammonium hydroxide. Because cobalt phosphate hydrate without lithium is known to be formed under acidic conditions for M = Co, a basic condition was employed to obtain $LiCoPO_4$ [64]. During the synthesis of $LiFePO_4$, the pH

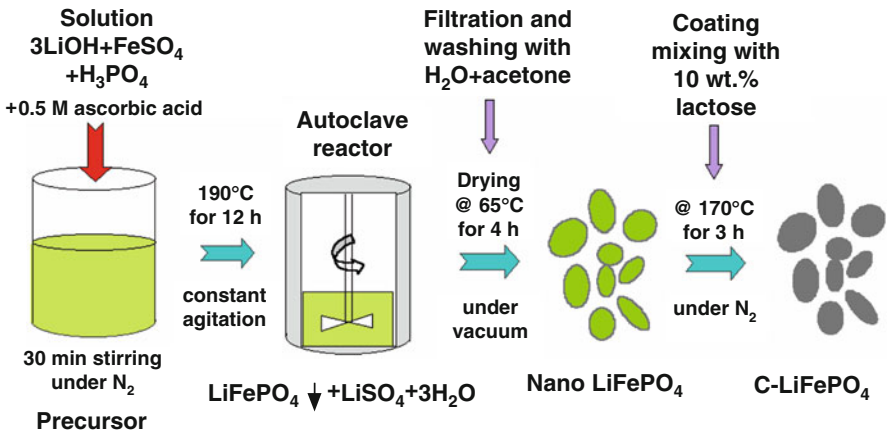

Fig. 12.5 Schematic picture of synthesis procedure of LFP particles using a stirring hydrothermal method

value of the reaction precursor solution was measured before and after hydrothermal synthesis. Supercritical hydrothermal synthesis introduces organic ligands (amino acids, carboxylic acids, or alcohols) into supercritical hydrothermal conditions, in which the water is in a state above the critical temperature (374 °C) and pressure (22.1 MPa). Because the drastic change in density, the solubility is greatly enhanced and phase behavior changes largely around the critical point. Consequently particle size is in the range from 2.5 to 10 nm and particle size dispersion is extremely narrow. Crystal shape can be controlled by changing concentration of organic modifiers such as nanosphere and nanocube [64]. Numerous investigations have been devoted to synthesize electrode materials for Li-ion batteries such as $LiFePO_4$ [65], $LiMn_2O_4$ [66], $LiCoO_2$ [67], and $Li_4Ti_5O_{12}$ [68].

$LiFePO_4$-C cathode materials were prepared by hydrothermal synthesis assisted by rotating/stirring tests at different agitation speeds (Fig. 12.5) [69]. The hydrothermal processes were carried out at 190 °C for 12 h with a solution chemistry of $LiOH{\cdot}H_2O$, $FeSO_4 \cdot 7H_2O$, H_3PO_4 (85 wt%), and ascorbic acid (as reducing agent) in the stoichiometry 3Li:1Fe:1P:0.2C. Annealing was done at 700 °C under nitrogen atmosphere using lactose as carbon coating source. The $LiFePO_4$-C electrodes prepared by employing agitation during hydrothermal synthesis were found to exhibit higher discharge capacities (137.6 mAh g^{-1} at *C*/12) than those prepared without agitation (106.2 mAh g^{-1}). This was equally true for higher current rates, namely *C*/5 and *C*/3. Via a series of tests at different speeds (260–1150 rpm) and different concentrations (0.4, 0.5, 0.6 mol dm^{-3}) the optimum solution rotating agitation/concentration conditions were determined to be 260–380 rpm and 0.5 mol dm^{-3}, respectively. Under these conditions $LiFePO_4$-C materials with excellent capacity retention (~130 mAh g^{-1} at coulombic efficiency >99 %), and better cycling stability at high current rates (1*C*) were obtained. The improved performance of the $LiFePO_4$-C material obtained by controlled rotating

agitation-hydrothermal solution synthesis is attributed to production of less aggregated particles with high surface area and less impurity. Hence, the controlled rotating agitation solution synthesis method provides a scalable and eco-friendly way in producing better performing cathode particles for use in Li-ion batteries [69].

12.2.5 Jet Milling

Micronization of materials is a common process in many aspects of manufacturing pharmaceuticals, toners, ceramics, cosmetics, and paints. The principle of micronization by jet milling is the collision of particles within a fast gas jet. The processes responsible for size reduction and separation within the milling chamber were investigated intensively in the 1960s by Rumpf and Kuerten [70]. Although much is known on the particle size reduction of hard and crystalline materials, the jet milling is a grinding process of using highly compressed air or other gases, usually in a vortex motion, to impact fine particles against each other in a chamber [71–74]. This technique involves a grinding energy created by gas streams from horizontal grinding air nozzles, whose main interest is the very low pollution of ground powders. It allows the production of very fine powders with relatively hard materials. The principle is as follows. The sample material is sucked into a grinding chamber. Jets of compressed air or another inert gas accelerate the particles which collide in an area of maximum turbulence. The powders are then recovered by cyclone systems. This technique has some advantages: small particle size, particle spherical and uniform, grinding materials temperature-sensitive, low pollution of ground powders, tight particle size control, large and small batch quantities, easy cleaning and maintenance of the mill (Fig. 12.6).

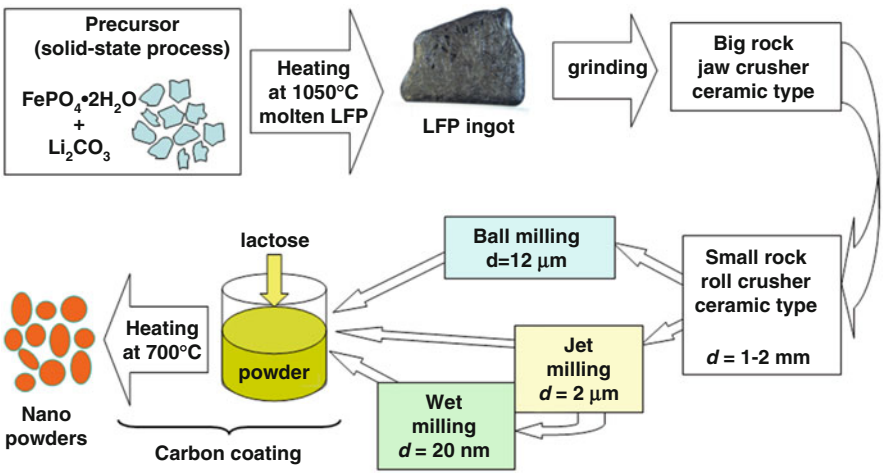

Fig. 12.6 Synthesis from molten ingot. Nanopowders are obtained using crusher ceramic liner and jet milling

$LiFePO_4$ (LFP) nanoparticles have been obtained by grinding ingot synthesized in the molten state (Fig. 12.6). This process, followed by jet milling, and then wet milling, provides a simple way to obtain powders with monitored size of the particles in the whole range from macroscopic to 25 nm, although at this stage, we find that these particles tend to segregate to form secondary particles of size ~100 nm [75]. The synthesis procedure was as follows. First, the ingot obtained by heating a mixture $FePO_4{\cdot}2H_2O$ and Li_2CO_3 at 1050 °C for 5 min and cooled in Ar atmosphere. Then the ingot was crashed into centimeter-sized particles by using a jaw-crusher with ceramic liner to avoid metal contamination. The third process used a roll crusher (ceramic type) to obtain millimeter-sized particles. The millimeter-sized particles are further ground by using jet-mill to achieve micrometer-sized particles. In the process, the grains enter the grading wheel and are blasted to cyclone separator and collector. The smallest particle size (25 nm) was reached by jet milling of microsized particles dispersed in isopropyl alcohol (IPA) solution at 15 % of solid concentration and ground on a bead mill using 0.2 mm zironial's beads. Finally the carbon-coating was realized by mixing nanoparticles with carbon precursor (lactose) in acetone solution after drying, the blend is heated at 700 °C for 45 h in neutral atmosphere [75]. Core–shell nanostructured xLi_2MnO_3 $(1-x)LiMO_2$ (M = Ni, Co, Mn) composite cathode materials were synthesized through a simple solid-state reaction using a mechanochemical ball-milling process [76]. TEM analysis shows primary particles smaller (<100 nm) than of the starting material because the low temperature synthesis (~400 °C) of the Li_2MnO_3 powders.

12.3 The Disordered Surface Layer

12.3.1 General Considerations

The increase of rate capability of cathode materials (for use in hybrid electric vehicles for instance) could be achieved by decreasing as much as possible the size of the particles to improve the effective surface that is active for electrochemical reactions. In addition, smaller size means reduced path for the electrons and the Li^+ ions inside the particles. Since the electronic and ionic conductivity are small [30], this reduction is expected to benefit the performance, especially at high C-rates. The experimental results, however, are not as simple as one might have expected, because the reduction in size implies that surface effects become more important, and the surface layer does not necessarily have the same properties as the bulk, with important impact on the electrochemical properties. The bulk properties (i.e., physical and chemical properties big enough so that surface effects are negligible) are now well understood. That is not the case, yet, for surface effects that are still under debate.

Several experiments have evidenced the existence of a disordered layer (DSL) at the surface of particles of oxide, typically few nanometers that modified the intrinsic properties of electrode material for Li-ion batteries [77–83]. Yet attention must be

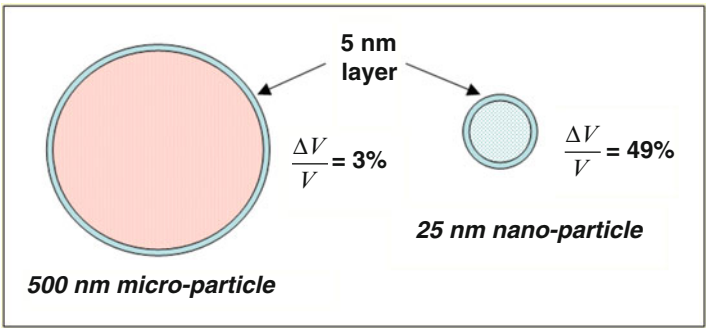

Fig. 12.7 Schematic representation of the simple core–shell model for description of the importance of the disordered surface layer in nanoparticle

paid to the quality of the surface, especially as the importance of the surface-to-volume ratio increases for nanomaterials, in order to prevent the surface from acting as a barrier to transfer of lithium ions and/or electrons during the charging and discharging of lithium batteries. Figure 12.7 depicts a simple model of the shell–core volume ratio, R_{SC}, for a 5-nm thick surface layer: in the case of a big enough particle (0.5 μm diameter) $R_{SC} = 3$ %, while it becomes 49 % for a nanoparticle (25 nm diameter). In this context, it is obvious that the nanoparticle behaves differently than the big one. Aurbach et al. [84] have suggested that the capacity retention of a cathode active material is strongly dependent on the surface chemistry of the particles of the insertion material, which are always covered by surface films limiting the Li-ion migration and their charge transfer across the active interface.

To illustrate this complex situation, let see the case of olivine material. In particular, the phase diagram of Li_xFePO_4 shows that the solid solution is unstable at room temperature for big particles (say, particles of size $d \geq 100$ nm). As a consequence, a rapid demixing occurs upon cooling, and we are left with two phases, namely $Li_{1-\alpha}FePO_4$ and $Li_\beta FePO_4$, where α, β denote the width of the single-phase regions [85]. Yet these parameters are small for large particles, say of diameter $d \leq 100$ nm, in which case, in first approximation, the lithiation–delithiation process involves $x\text{LiFePO}_4 + (1-x)\text{FePO}_4$ and not Li_xFePO_4 solid solutions. This separation, which takes its origin in Coulomb correlation [86], has an important impact on electrochemical properties, since it results in the plateau Li^0/Li^+ voltage vs. x at 3.4 V. However, upon decreasing the size of the particles, experiments reported in the literature show that the plateau is shrinking, which has been interpreted as the sign that the miscibility gap decreases with d. This has been confirmed by Gibot et al. [87] according to which the voltage plateau is no longer observed in particles with $d \approx 40$ nm. Amorphizationn of the particle was observed upon cycling for crystallite size in the range $d \leq 100$ nm, which has been interpreted in terms of nucleation limited phase transition pathways [88]. This amorphization, however, has not been observed in particles of size $d \approx 100$ nm, in which case well crystallized $LiFePO_4$ and $FePO_4$ domains have been observed at any stage of lithiation/delithiation process [89].

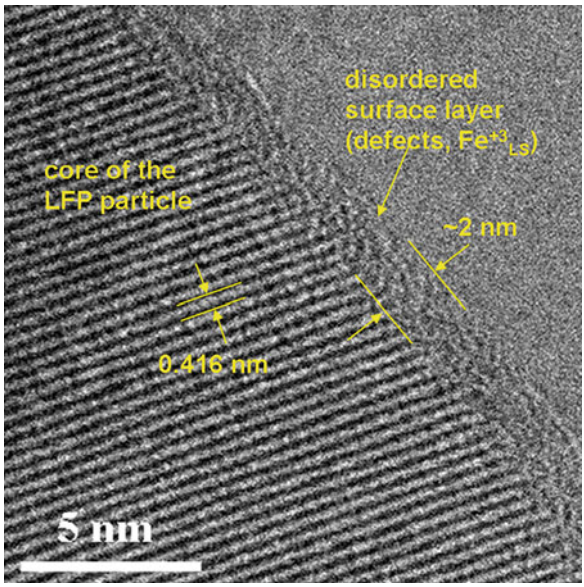

Fig. 12.8 HRTEM image showing the disordered surface layer for an as-prepared $LiFePO_4$ particle

High-resolution transmission electronic microscope (HRTEM) image (Fig. 12.8) shows that a surface layer of about 2-nm thick is strongly disordered, but not amorphous [77]. Note that the core of the particles below the surface has a size that is the same as the coherence length deduced from the XRD analysis. Therefore, the particles are crystallites surrounded by a disordered surface layer. The HRTEM image after carbon coating shows the same particle, now covered with a 3-nm thick carbon layer, and a less-disordered surface layer. It is now possible to investigate the role of the carbon coating by comparison of the physical and chemical properties between the $LiFePO_4$ particles before and after carbon coating [80]. Since the surface layer is only about 3 nm wide and not well ordered, however, XRD experiments are not sensitive to the surface layer. The investigation of the magnetic properties is a good strategy for this purpose, since iron is a magnetic ion. In the bulk, iron is known to be in the Fe^{2+} high spin state and thus carries the spin $S = 5/2$ (the orbital momentum is quenched by the crystal field and is thus negligible). The magnetic properties associated to the spin of a given iron ion are quite sensitive to its local environment. That is why they can be used as a probe of any defect or impurity in its vicinity. This strategy was successful for the bulk [5], but also for the surface [77], with which we are concerned hereunder.

12.3.2 DSL of $LiFePO_4$ Nanoparticles

The preparation and characterization of nanoparticles of $LiFePO_4$ is then of primary importance, in as much as their structural properties may depend on their size.

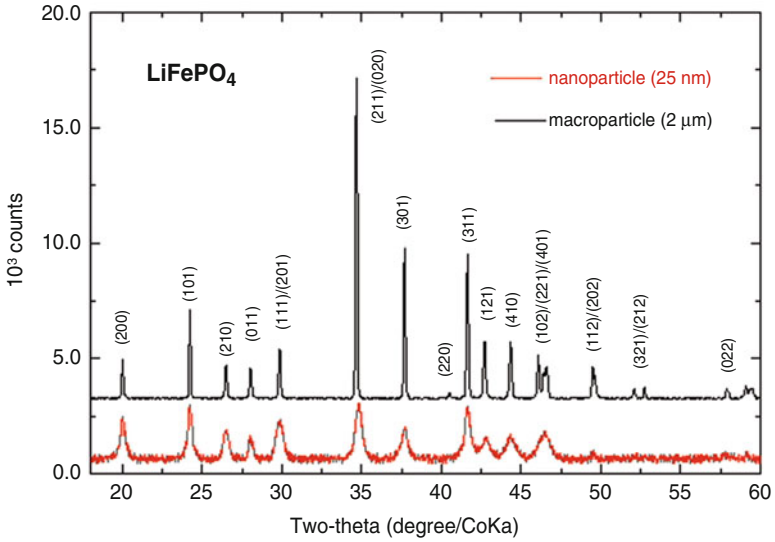

Fig. 12.9 XRD patterns of $LiFePO_4$ sample with primary particles 25 nm size, secondary particles of size 100 nm (*lower spectrum*) obtained after jet milling and of sample with 2-µm particle size (*upper spectrum*) for comparison

$LiFePO_4$ particles of sizes in the range 30–40 nm have been prepared by jet-milling route with carbon coating for optimization of the electrochemical performance [75]. The XRD pattern of 25-nm sized nanoparticles is shown in Fig. 12.9 with the spectrum of particle of 2 µm for comparison. The local structure was studied by FTIR spectroscopy of the samples obtained just after roll, jet and wet milling as shown in Fig. 12.10. The positions of the intrinsic bands in the spectra of $LiFePO_4$ are well known: the bands in the range 372–647 cm^{-1} are bending modes (ν_2 and ν_4) involving $(PO_4)^{3-}$ symmetric and asymmetric modes and Li vibrations, while the part of the spectrum in the range 945–1139 cm^{-1} corresponds to the stretching modes of the $(PO_4)^{3-}$ units. They involve symmetric and asymmetric modes of the P–O bonds at frequencies closely related to those of the free molecule. There is a band broadening as d increases: the most resolved spectra are observed in the wet-milled case. The broadening is the signature to a shorter lifetime of the vibration modes due to solid friction associated to defects. The more resolved spectrum observed for smaller values of d is then attributable to the fact that smaller particles have less structural defects such as grain boundaries in the vicinity of which the lattice is less ordered (in the limit of nanoparticles $d = 25$ nm, the particles are also crystallites ($d \approx l$), and thus without any structural defect in the bulk of the particles). The only disorder for such small particles is located in the surface layer, inside which the iron ions are in the Fe^{3+} low spin ($S = 1/2$) configuration. The disorder is found to have dramatic effects on the electrochemical properties as it stabilizes the solid solution inside the passivation layer. This disorder is strongly reduced by the carbon coating at 750 °C, which switches the

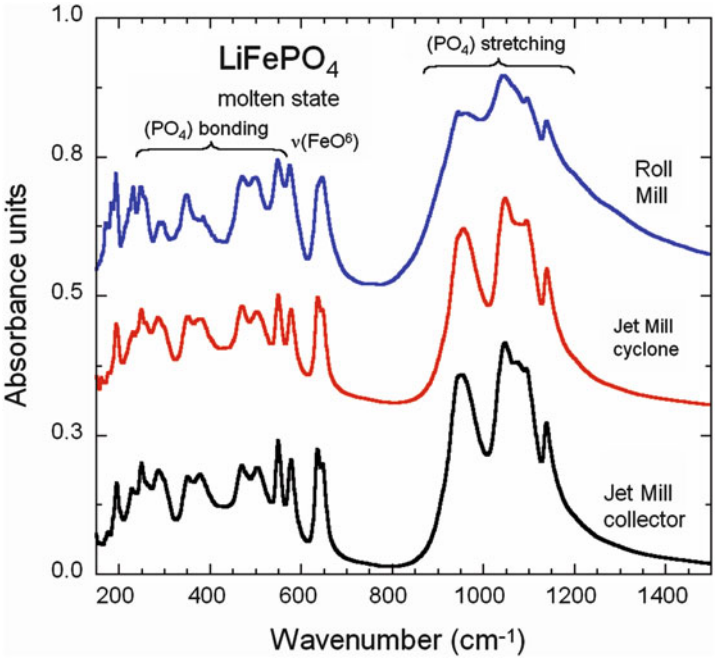

Fig 12.10 FTIR absorption spectra of molten-state samples at different stages of the grinding process (before carbon coating): roll mill, jet mill cyclone, and jet mill collector

Fe^{3+} ions in the surface layer to the high spin ($S = 5/2$) configuration, and restores the plateau of the voltage vs. capacity. The results are discussed in the context of the controversy on the shrinking of the miscibility gap upon decreasing the size of the particles to the nanoscale.

For nanoparticles, the fraction $(1 - y)$ of iron ions in the surface layer is not negligible, and we found that this contribution is different from that of the bulk that was investigated by magnetic measurements [80]. The response of the magnetic moments of the iron ions is thus different for the ions in the bulk and the ions in the surface layer. Therefore, one has to add to the bulk contribution to the magnetic susceptibility the contribution coming from the iron ions inside the surface layer (Fig. 12.11). We found that this contribution satisfies the Curie law, so that $\chi(T)$ takes the form:

$$\chi(T) = y\,\frac{C_0}{T + \theta_0} + (1 - y)\,\frac{C'}{T}, \tag{12.3}$$

for $T \geq 100$ K. There are two fitting parameters, the fraction y of iron ions in the bulk, and C'. We have shown that the solution for the set (y, C') is unique, and for particles with diameter 40 nm, it is [75]:

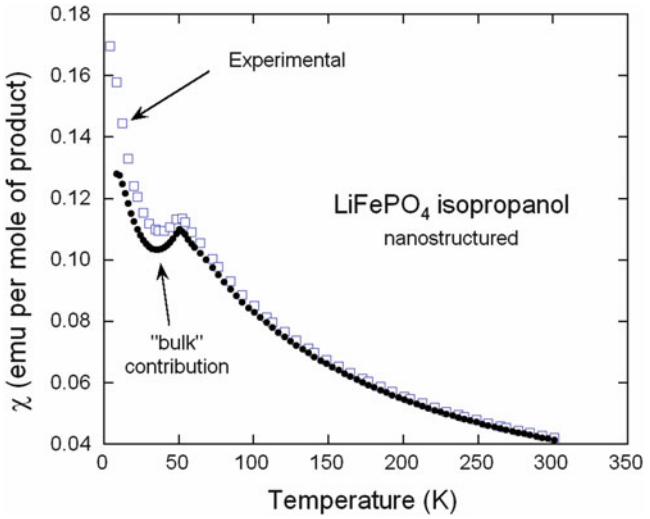

Fig. 12.11 Magnetic susceptibility of $LiFePO_4$. The *solid circles* are the contribution of the core region, and match the results observed for particles without surface effects. The *open squares* are experimental data for the 40 nm sized particles before carbon coating. The difference is quantitatively fit by the second term in Eq. (12.3)

$$y = 0.89,\ C^{'} = 0.37 \text{ emu K mol}^{-1}. \tag{12.4}$$

It should be noticed that the contribution of the core region to the magnetic susceptibility reduced to the Curie–Weiss expression only in the paramagnetic regime. On the other hand, the absence of spin correlations evidenced by the Curie law implies that, at any temperature, including below the Néel temperature T_N:

$$\chi(T) - \chi_{\text{bulk}}(T) = (1-y)\frac{C^{'}}{T}, \forall T, \tag{12.5}$$

which has been verified [75]. This behavior at low temperature allows us to distinguish between the increase of the effective moment due to the magnetic polarons (investigated in the previous section) and surface effects, since the polarons care spin-frozen at low temperature and do not give a Curie contribution to the susceptibility. The value of y is self-consistent with the ratio N_S/N_B, with N_S the number of iron ions in the 3-nm thick surface layer and N_B the number of iron ions in the core region of a spherical particle of 40 nm in diameter. The value of C', however, was not necessarily expected, as it corresponds to a spin $S = 1/2$, implying that iron in the surface layer of uncoated particles is Fe^{3+} in the low spin state. On this example, the magnetic properties of uncoated particles have revealed important properties. First of all, the iron in the surface layer is trivalent. A significant amount of Fe^{3+} is systematically detected in $LiFePO_4$ by Mössbauer experiments although they do not give any information on their location [5]. The magnetic properties are

the first evidence that these Fe^{3+} ions are localized in the surface layer. In addition, the analysis of $\chi(T)$ has shown that the Fe^{3+} ions are uncorrelated, since there contribution is a Curie law C'/T with vanishing Curie–Weiss temperature (at least down to 10 K). This is the evidence for important frustration of the magnetic interactions in the surface layer: the decorrelation of the magnetic spins is the translation on the magnetic properties of the structural disorder that affects the surface layer. Finally, the Fe^{3+} ions are in the low-spin state. Remember that a free ion, i.e., ion not submitted to the crystal field, is always in the high spin state due to the Hund's rule. The low spin state is then signature that the crystal field is big enough to break the Hund's rule. This is another signature of an important structural disorder that enhances crystal-field effects in the surface layer. The fact that the iron ions are in the trivalent state means that the surface layer has been delithiated.

After carbon coating, the magnetic response of the coated particles is closer to the result predicted for intrinsic $LiFePO_4$ with, however, an effective moment 5.02 μ_B still slightly larger than the theoretical value 4.90 μ_B. Since Fe^{3+} in the high-spin state is 5/2, its effective moment is 5.92, and we note that:

$$y(4.9)^2 + (1-y)(5.92)^2 = (5.02)^2, \tag{12.6}$$

which means that the excess in magnetic moment with respect to the theoretical value is entirely attributable to the conversion of $Fe^{3+}(S = 1/2)$ in $Fe^{3+}(S = 5/2)$ in the surface layer. This is actually the "normal" state for iron in the surface layer. In particular, we have shown that exposure to moisture, even for short period of time, oxidizes the iron at the surface, with the consequence that iron is in the $Fe^{3+}(S = 5/2)$ in the surface layer. Note that the study of the degradation of the particles upon exposure to moisture has shown that the surface layer is completely delithiated very fast, but after that, no further delithiation is observed at the scale of few days because the $FePO_4$ surface layer is waterproof and protects the core [78]. The same magnetic analysis has been performed on lamellar compounds, and they have shown that the exposure to moisture induces a delithiation over a thickness of 10 nm in that case [81], larger than the 3 nm in $LiFePO_4$, so that the lamellar compounds are more sensitive to moisture than olive samples.

12.3.3 DSL of $LiMO_2$ Layered Compounds

Actually, not even the transition-metal oxides, but also carbon coating is efficient to improve the cycle life of Li-ion batteries with $LiN_{1/3}Mn_{1/3}Co_{1/3}O_2$ (NMC) and $LiCoO_2$ (LCO) as well. Even a simple heating in presence of an organic compound is sufficient because it has an annealing effect that re-crystallizes the surface layer that is otherwise disordered. The surface of NMC particles were studied for material synthesized at 900 °C by a two-step process from a mixture of $LiOH{\cdot}H_2O$ and metal oxalate $[(Ni_{1/3}Co_{1/3}Mn_{1/3})C_2O_4]$ obtained by co-precipitation [82]. The effect of the

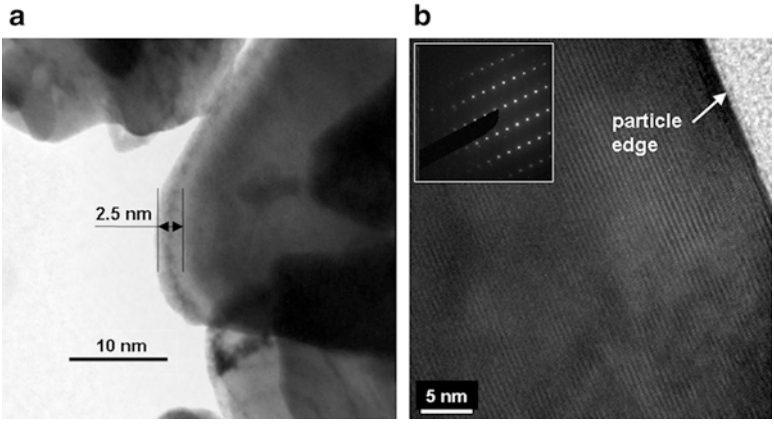

Fig. 12.12 TEM images of NMC powders showing the surface modification of 250-nm sized particle. Images (**a**) and (**b**) display the HRTEM features of NMC powders for as-grown and heat treated sample with sucrose at 600 °C for 30 min in air, respectively. Reproduced with permission from [82]. Copyright 2011 Elsevier

heat treatment at 600 °C with organic substances, such as sucrose and starch, investigated by HRTEM images and Raman spectra, indicate that the surface of particles has been modified. The annealing process does not lead to any carbon coating but it leads to the crystallization of the thin disordered layer on the surface of NMC. The analysis of the HRTEM images (Fig. 12.12) gives evidence that the surface of the particles have been modified by the calcination at 600 °C. Before carbon treatment, we observe the presence of an amorphous-like layer, typically 2.5-nm thick that covers the NMC particle. In the micrograph, this surface layer appears as a greyish region at the edge of NMC crystallites, while the core of the primary particle is the dark region. After the heat-treatment at moderate temperature with an organic substance such as sucrose or starch, we observe the disappearance of disordered layer. Thus the edge of the particle displays well-defined election diffraction patterns (insert of Fig. 12.12). The beneficial effect has been tested on the electrochemical properties of the NMC cathode materials in half lithium cell. For rate performance comparison, the modified Peukert plots, i.e., the specific capacity vs. *C*-rate, are shown in Fig. 12.13. A capacity 107 mAh g^{-1} is delivered in the voltage range 2.5–4.2 V at 10*C* rate from the cell with surface-modified NMC, while it is only 81 mAh g^{-1} with the non-treated NMC electrode at the same *C*-rate.

The effect of H_2O on NMC in humid atmosphere was investigated by structural, magnetic and electrochemical analysis on $LiNi_{1/3}Mn_{1/3}Co_{1/3}O_2$ (NMC) compounds synthesized by the co-precipitation method [81]. The consequence is that immersion of NMC to H_2O and exposure of NMC to humid atmosphere led to a rapid attack that manifests itself by the delithiation of the surface layer of the particles. This aging process occurred during the first few minutes, then it is saturated, and the thickness of the surface layer at saturation is 10 nm. The quantitative analysis of the Raman spectrum of NMC samples was reported in ref. [81]. Upon exposure to ambient atmosphere for 1 day, the spectrum of the same sample shows three

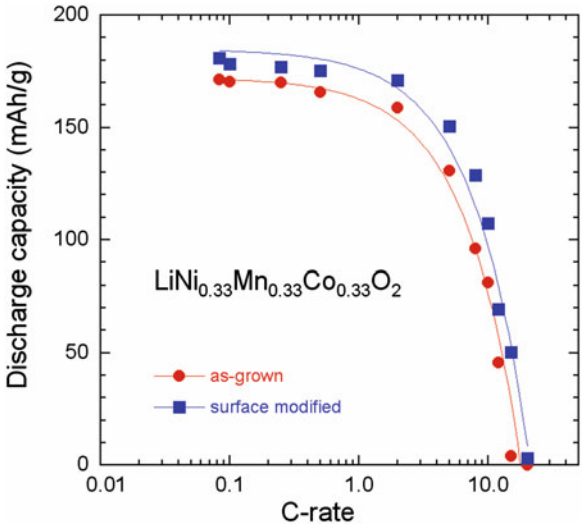

Fig. 12.13 Modified Peukert plots of Li//NMC coin cells for the as-grown and the surface modified NMC cathode material. Reproduced with permission from [82]. Copyright 2011 Elsevier

additional bands that are characteristic of LiOH, and another band characteristic of CO_3 molecular unit, which confirms the presence of Li_2CO_3 in addition of the lithium hydroxide. The general trend in intercalation compounds is recovered, whether they are lamellar or not, according to which the reaction of lithium with H_2O at the surface results in the delithiation of the surface layer, the lithium involved in the process forming LiOH and Li_2CO_3 at the surface. The degradation of the surface of $LiNi_{1/3}Mn_{1/3}Co_{1/3}O_2$ affects the electrochemical properties of the material as a cathode element. After aging, an initial discharge capacity of 139 mAh g^{-1} was delivered at 1*C*-rate in the cutoff voltage of 3.0–4.3 V. About 95 % of its initial capacity was retained after 30 cycles.

12.4 Electrochemical Properties of Nanoparticles

In this section, first we present the effect of surface modification by carbon coating of $LiFePO_4$ nanoparticles and secondly the comparison between energy- and power-grade LFP materials. Figure 12.14 shows the typical charge–discharge voltage profile of the $LiFePO_4$ cathode material investigated here before carbon coating (a) and after carbon-coating (b), using LFP/$LiPF_6$-EC-DEC/Li cell. The test was performed galvanostatically at charge–discharge rate *C*/24 that is very slow, to insure that equilibrium has been reached. The voltage range is 2.2–4.0 V vs. Li^0/Li^+. The charge–discharge profile appears with the typical voltage plateau (at ca. 3.45 V vs. Li^0/Li^+) attributed to the two-phase reaction $FePO_4$-$LiFePO_4$ system. However, the plateau has been shrunk, especially on the side of low Li concentrations (charged state). However, after carbon-coating, the full width of the plateau has been

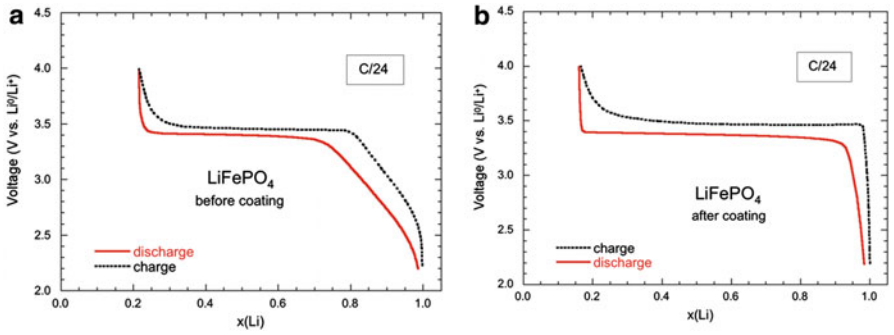

Fig. 12.14 Charge–discharge voltage profile of $LiFePO_4$ before (**a**) and after (**b**) carbon coating cathode material using LFP/$LiPF_6$-EC-DEC/Li cell at room temperature. The test was performed galvanostatically at charge–discharge rate *C*/24

recovered. The carbon-coated material exhibits a reversible capacity 160 mAh g^{-1} that amounts to a utilization efficiency of 94 %. Zaghib et al. [77] shed light on the conflicting results found by different groups on the phase diagram and electrochemical properties of $LiFePO_4$ particles of size $d \approx 40$ nm. Degraded electrochemical properties and slope in the charge–discharge profile are due to the stabilization of the solid solution, in the region of the particle where a sever disorder exists. With the synthesis process we have used, in the present work, this region is limited to the surface layer only, before carbon-coating. On the other hand, the treatment associated to the carbon-coating cures this disorder, so that we have obtained particles well crystallized and free from impurity and defect. For such particles, we find, in agreement with theoretical models that the small size of the particles has not modified significantly the electrochemical properties of material. Since in addition, the aggregation of the particles is small and the dispersion of the particles is small, this synthesis process opens the route to the preparation of nano-structured particles of $LiFePO_4$ for use as the active element in future Li-ion batteries with high power.

Figure 12.15 displays the SEM images of two types of LFP particles: LFP synthesized by solid-state reaction via the polymer-precursor method showing particles of 2–5 μm size and LFP synthesized by hydrothermal method showing particles with an average size of 300 nm. The modified Peukert plots are shown in Fig. 12.16. It is remarkable that the power-grade powders 75 % of the initial capacity at 10*C*-rate.

12.5 Nanoscale Functional Materials

12.5.1 WO_3 Nanocomposites

Tungsten trioxide is an n-type semiconductor which has found a great deal of interest in several applications including electrochromic displays, smart windows,

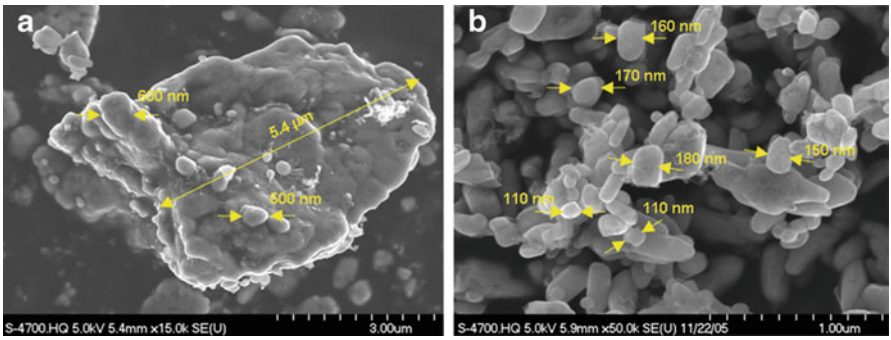

Fig. 12.15 SEM images of $LiFePO_4$ powders. (**a**) Energy grade and (**b**) power grade powders

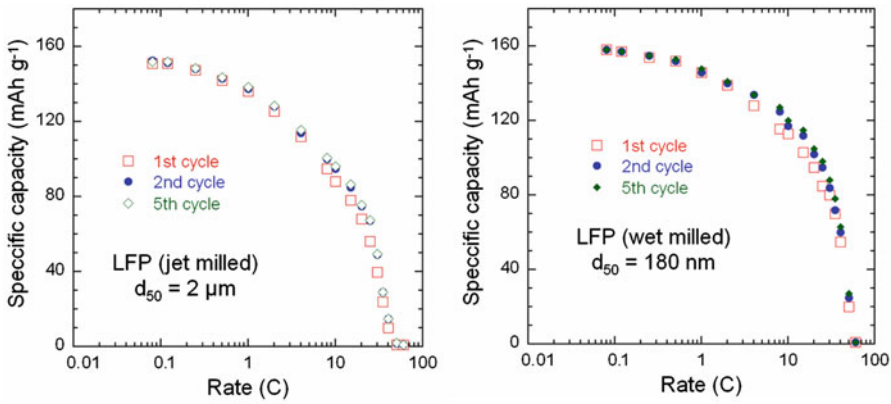

Fig. 12.16 Modified Peukert plots of $LiFePO_4$ cathode materials as a function of the particle size: (*left*) energy grade and (*right*) power grade powders

gas detectors, and electrochemical capacitors. The optimal performance of the WO_3 nanomaterials in the sensor devices depends on the electrical conductivity and surface adsorption properties, which are closely related to the structure, morphology and size of the particles. Ag-doped WO_3 nanomaterials have been studied as sensing element to detect relative humidity (RH) with an average sensitivity of 2.14 MW%RH in the 20–90 % range. The Ag:WO_3 bronze was prepared by soft-chemical route with 147-nm particle size [90]. WO_3 nanomaterials were synthesized via a sol–gel method and calcination for use as a CO gas sensor. The sensitivity of WO_3 sensor ships was determined by comparing the changes in electrical resistance in the absence and presence of 50 ppm of CO gas at 200 °C [91]. Nanocrystalline WO_3 films prepared by gas evaporation show enhanced gas-sensing properties; when doped with Al or Au, 5 ppm of H_2S yielded a conductance increase by ~250 times even at room temperature [92].

Among materials for electrochromic display devices (ECDs), WO_3 has attracted the most attention, so far. It is well-known that better electrochromic reversibility and relatively short response time depends on the structure and morphology of the films. An attempt at surface modification of WO_3 films and enhancement of the diffusion rate of Li ions in an electrochromic device was realized using by incorporating nanoscopic silicon oxide particles into WO_{3-x}-0.1TiO_2 thin films prepared by the sol–gel route, which exhibit increase of lifetime and stability. The sol–gel solution with nano-sized SiO_2 particles (40 nm) was spin-coated onto indium-tin-oxide covered glass substrate [93]. The variation of the optical density of surface-developed of WO_{3-x}-0.1TiO_2 thin films during coloring ($E = -2.5$ V) and bleaching ($E = +1.5$ V) was studied in lithium cell using nonaqueous electrolyte of 1 mol L^{-1} $LiClO_4$ in propylene carbonate. Saturation of the coloration is almost reached after 1.5 s for the nanocomposite films, while pure WO_{3-x} takes ≈ 4 s. The improvement of specific charge density from $Q = 9.4$–41 mC cm^{-2} observed for pure and surface developed films could be explained as follows (1). The response time is improved due to the extremely high surface area of the composite, leading to the enhancement of ion insertion through the film–electrolyte interface (2). The presence of SiO_2 nanoparticle results a more open xerogel amorphous structure of WO_{3-x} films. This is the enhancement effect that has been observed in the ionic conduction of LiI-Al_2O_3 composite [94].

12.5.2 WO_3 Nanorods

The Li-driven electrochemical properties of monoclinic WO_3 nanorods prepared by a solution-base colloidal approach have been studied and the relationship between the properties and the nano-structures of the materials has been established [95]. WO_3 nanorods with a high aspect ratio were found to yield an intercalation capacity up to 1.12 Li per formula unit, much higher than the value of 0.78 Li for bulk WO_3. This can be explained on the basis of the unique rod-like structure that effectively enhanced structure stability. The evolution of Li-driven reaction kinetics further illustrated benefits of WO_3 nanorods owing to the increased edge and corner effects. WO_3 nanorods were synthesis by using hydrothermal process without any surfactants. The nanorod film deposited on ITO exhibits high electrochromic stability and comparable color display, contrast, and coloration/bleaching response. The maximum transmittance wave-lengths have obvious blue-shifts and the transmittance intensities decrease with the increase of the applied negative voltages within the spectra of 500–900 nm. The electrochromic device was cycled more than 3000 cycles with a coloration/bleaching response of 8 s [96].

12.5.3 WO_3 Nanopowders and Nanofilms

Different forms of nanomaterials were synthesized for optical applications in lithium-based devices. Mixed WO_3–TiO_2 oxides have been prepared from aqueous solutions of tungstic acid and titanium isopropoxide in H_2O_2. Peroxopolytungstic acids were obtained from pure tungstic acid whereas $WO_3 \cdot 1/3H_2O$ is formed in the presence of Ti^{VI}. Three crystalline oxides are formed successively upon heating Ti doped $WO_3 \cdot 1/3H_2O$, namely h-WO_3, o-WO_3, and m-WO_3. The intermediate metastable o-WO_3 phase has not been observed in the absence of titanium. The cathodic behavior of these oxides shows that the discharge curves corresponding to the electrochemical insertion of Li are noticeably different [97, 98]. In the course of the preparation of WO_3 by sol–gel technique, kinetics of its synthesis and the structural changes were studied by in situ Raman spectroscopy during the transition from colloidal solution to gel. The removal of water molecules affects the symmetric W = O stretching mode. The Raman spectrum of a gelified sample shows peaks attributed to the O-W-O bending mode and the disappearance of the high-frequency mode attributed to polyanionic species. After 2 days the gelified sample became a precipitated material, which exhibited the Raman spectrum of a crystalline tungsten oxide hydrate [99]. Another potential application of WO_3 thin films is in aerospace industry for infrared emissivity modulation and temperature control in spacecraft [100]. WO_3 500-nm thick films were fabricated by the pulsed-laser deposition (PLD) technique. The compositional studies using X-ray photoelectron spectroscopy and electron probe microanalysis (EPMA) measurements indicated that the grown films were nearly stoichiometric with small amount of oxygen vacancies. Figure 12.17a shows the bright field TEM image of the sample structure. The morphology of the PLD WO_3 films is characterized by the grains of 60–70 nm in size and root-mean-square (rms) surface roughness value of 10 nm. HRTEM image (Fig. 12.17b) confirms that the film consists of a well-crystallized WO_3, which is identified as the monoclinic phase [101].

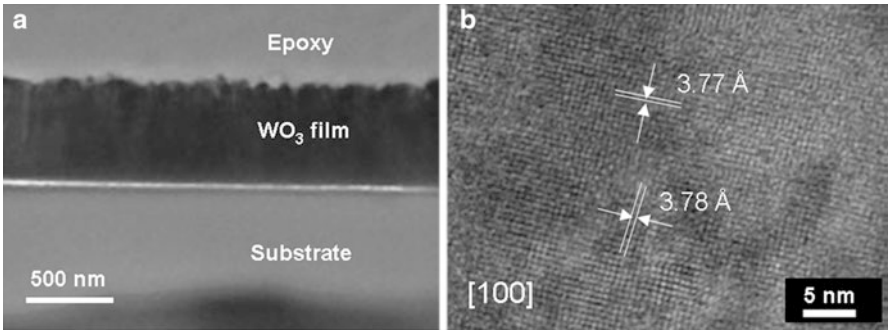

Fig. 12.17 Electron micrographs of WO_3 thin films. Image (**a**) is the bright field view of the sample structure. The substrate, the WO_3 thin film, and the epoxy regions are indicated in the micrograph. Image (**b**) is the HRTEM image of the WO_3 thin film with lattice fringes corresponding to the monoclinic structure

12.5.4 Li_2MnO_3 Rock-Salt Nano-structure

Among the lithium insertion oxides, Li_2MnO_3 is one of the most interesting compounds from the point of view of its structure and electrochemical behavior [102, 103]. Indeed, this oxide, in its microcrystalline form, is electrochemically inactive for lithium insertion and extraction between 2.0 and 4.4 V; however it delivers a high theoretical capacity of 460 mAh g^{-1} for total Li extraction. Li_2MnO_3 (or alternatively $Li[Li_{1/3}Mn_{2/3}]O_2$) has a rock-salt structure containing layers of Li^+ and Mn^{4+} cations between close-packed arrays of oxygen anions; all the octahedral sites are occupied by cations. A layer of lithium ions and a mixed layer of (1:2) lithium and manganese ions alternate between close-packed oxygen layers (see the structural representation in Fig. 5.24). This compound is electrochemically inactive. Insertion of Li^+ ions into a stoichiometric rock-salt phase is not possible because all the octahedral sites are fully occupied. Li extraction is not energetically feasible because all the manganese cations are tetravalent. Nanoparticles (20–80 nm) of Li_2MnO_3 were synthesized using the self-combustion reaction and studied the electrochemical activity of electrodes prepared from this nano-material at 30, 45, and 60 °C [103]. It was shown that the first Li-extraction from nano-Li_2MnO_3 occurs at much lower potentials (by 180–360 mV) in comparison with micron-sized Li_2MnO_3 electrodes. This can be associated with the higher surface-to-volume ratio, much shorter the diffusion path and the increased surface concentration of the electrochemically active sites. Figure 12.18 shows a comparison of the XRD patterns from the nano-sized Li_2MnO_3 material with that obtained from the micron-sized Li_2MnO_3 material. The nano-sized material is characterized by significant broadening of the peaks.

On the basis of magnetic susceptibility studies of nano-Li_2MnO_3 we proposed a model of disordered surface layer, containing Mn^{3+} or Mn^{2+} ions, both at low spin state, at the surface of these nanoparticles. From the results of structural analysis

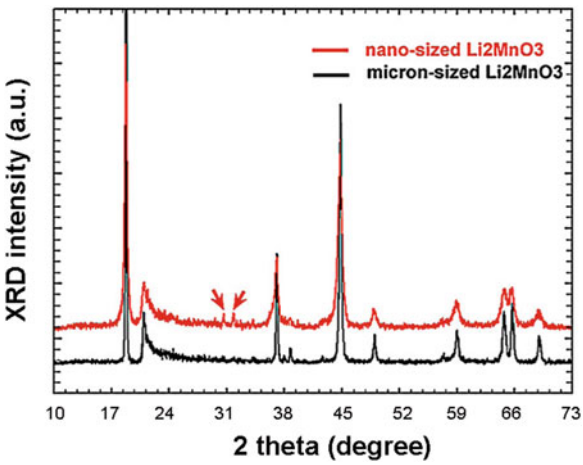

Fig. 12.18 The XRD patterns of nano-sized Li_2MnO_3 (*upper curve*) compared with micron-sized material (*lower curve*). Two peaks marked by arrows at $2\theta = 30.5$ and 31.6° belong to Li_2CO_3 impurity that can be formed during the synthesis due to some excess of the lithium

(by X-ray and electron diffraction and vibrational Raman spectroscopy) of galvanostatically cycled nano-Li_2MnO_3 electrodes in Li-cells we came to a conclusion of partial transition of layered $LiMnO_2$ to spinel-type ordering during delithiation/lithiation. This was confirmed also by analysis of Raman spectroscopy of these materials that demonstrated a strong blue-shift of the main Raman band (A_{1g} mode) attributed to formation of the spinel-type structural ordering.

12.5.5 *Aluminum Doping Effect in NCA Materials*

Aluminum doped $LiNi_yCo_{1-y}O_2$ (NCA) oxides prepared by wet-chemical method from citrate precursor displays a nano-structured phase. The influence of Al doping on particle size and morphologies is clearly evidenced in Fig. 12.19. The net result of incorporation of a small amount of 0.05 mol% Al is the decrease of the grain size from 300 nm for $LiNi_{0.7}Co_{0.3}O_2$ to 80 nm for $LiNi_{0.70}Co_{0.25}Al_{0.05}O_2$. In addition the particle size distribution is narrow. XRD patterns show that the doped sample belongs to the $LiNiO_2$-$LiCoO_2$-$LiAlO_2$ solid solution and has the layered rhombohedral structure ($R\bar{3}m$ S.G.).

The charge–discharge profiles of Li//$LiNi_{0.70}Co_{0.25}Al_{0.05}O_2$ and Li//$LiCoO_2$ cells in the potential range 2.5–4.3 V are shown in Fig. 12.19. Replacing a small amount of Co demonstrates higher capacity retention compared with $LiCoO_2$ electrode (≈50 mV) At cutoff voltage of 4.3 V ($\Delta x = 0.72$), the specific capacity delivered by the Li//$Li_xNi_{0.6}Co_{0.35}Al_{0.05}O_2$ cell is ca. 195 mAh g^{-1}, which is a larger value than the Li//Li_xCoO_2 system with $\Delta x = 0.5$. Due to the nanosized particle the capacity retention is less than NCA materials with $y = 0.7$. The trends for the Al^{3+}-doped materials show that lower capacities were obtained with an increase in y(Al) because Al^{3+} cation cannot be oxidized, so it is an

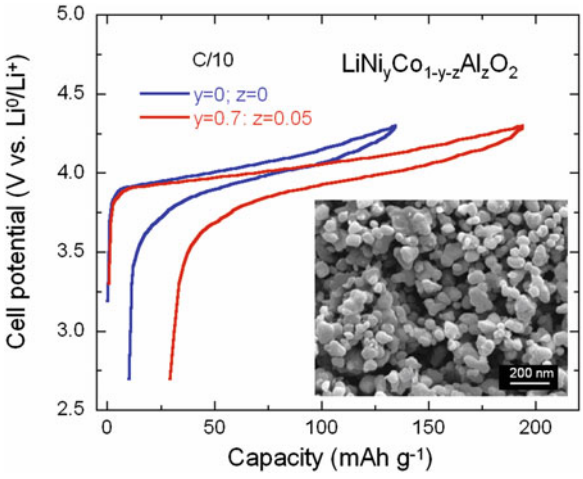

Fig. 12.19 First charge–discharge curve of the Li//$LiNi_{0.70}Co_{0.25}Al_{0.05}O_2$ cell compared with the voltage-composition profile of Li//$LiCoO_2$. The insert shows the SEM image of NCA powders

electrochemically inactive element. Long life electrochemical data showed that the cell using $LiNi_{0.70}Co_{0.25}Al_{0.05}O_2$ powders performed slightly better than the other ones. This means that for Al^{3+} doping, the optimum doping level for gravimetric capacity and life cycle ability would be approximately $y = 0.05$. No reason could be given for such a trend. However, the rechargeability of the $Li//LiNi_{0.70}Co_{0.25}Al_{0.05}O_2$ cells seems better than $LiCoO_2$ because the lack of the two-phase behavior in the high voltage region ($x \approx 0.5$). In addition, the electronic resistivity of the cathode material increases at the end of the charge, which is an advantageous property for preventing overcharge. Thus safety appears to be better with Al-doped $LiNi_yCo_{1-y}O_2$ for fully charge state when Li ions cannot be extracted from the host matrix because no electrons are removed from either Al^{+3} or Co^{4+} state [104, 105].

12.5.6 MnO_2 Nanorods

As an important inorganic compound, MnO_2 has been extensively used in many fields including primary batteries, lithium batteries, water treatment, supercapacitors, sensors, because its specific chemical structures and physical properties. Attractive features for implementing MnO_2 based materials for battery applications is the low cost, and also a highly abundant transition metal compared to for example cobalt, nickel, and vanadium. Hence, MnO_2-type batteries are attractive for energy storage applications like electric vehicles that require large amounts of materials in the market [106]. Substituted MDO nanowires with various elements, Cr, Al, Ni and Co, were prepared through the redox reactions of solid-state precursors or ion-adduct precursors under hydrothermal or non-hydrothermal condition. It was found that the partial replacement of Mn with transition-metal ions could improve the electrode performance of 1D-nanostructured manganates [107]. Nanosized pure, Ag-coated and doped manganese dioxides (MDO) were prepared through a redox reaction between $KMnO_4$ and fumaric acid. XRD analysis showed cryptomelane crystal structure for pure, coated and doped α-phases. Chemical analysis detected the presence of silver in doped and coated MDO. Scanning electron microscope and energy-dispersive spectroscopy analyses confirmed the presence of silver in doped and coated oxides. TEM images showed that the pure MnO_2 particles were synthesized in nanoscale with about 20 nm and agreed with calculated value by Scherrer's formula. From the representative TEM image (Fig. 12.20a) doped-MnO_2 sample has a rod-like shape. The average size of these nanorods is about 25 nm in diameter and 90 nm in length. Magnetic measurements showed reduction in Mn^{3+} ions in the crystal structure after coating and doping with silver. The electrochemical performance showed that Ag-coated and doped MnO_2 samples have better initial capacities than pristine MnO_2. Ag-coated MnO_2 material

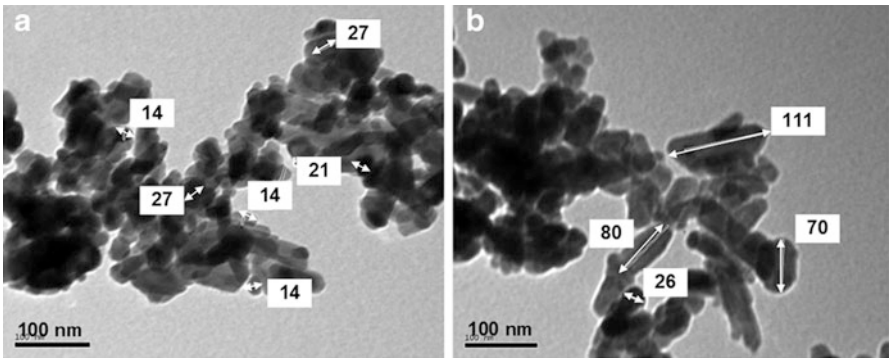

Fig. 12.20 TEM images of (**a**) Ag-coated and (**b**) Ag-doped nanorod-like MnO_2 prepared by redox reaction between $KMnO_4$ and fumaric acid

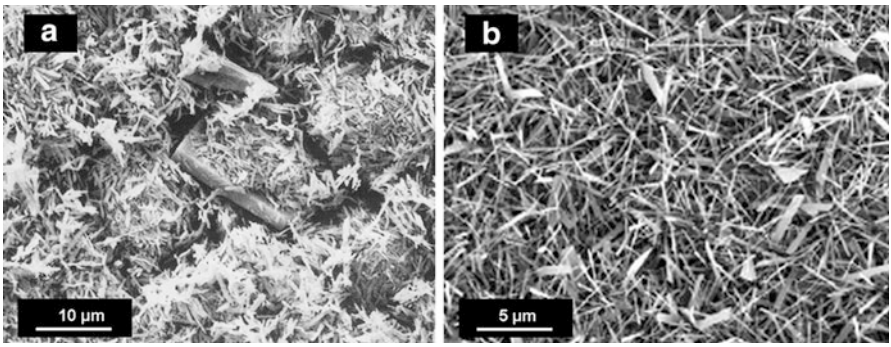

Fig. 12.21 SEM images of (**a**) The intermediate compound was placed in the autoclave heated at 170 °C and (**b**) The nanofibers synthesized in the autoclave heated at 185 °C for 6 days

showed the best capacity retention upon cycling among all prepared MnO_2 oxides, i.e., 140 mAh g^{-1} after the 40th cycle at *C*/5 rate in the potential window 1.5–4.0 V vs. Li^0/Li^+ [56, 108].

12.5.7 MoO_3 Nanofibers

MoO_3 nanofibers were synthesized by hydrothermal reaction from acidified ammonium heptamolybdate tetrahydrate precursor (Fig. 12.21). Structural analysis shows that MoO_3 nanofibers 50–80 nm in diameter and a several micrometers in length are crystallized with the α-form in the orthorhombic system (*Pbnm* S.G.). The composition $MoO_{2.9975}$ was determined by Rietveld refinement and magnetic susceptibility measurements. The electrochemical performance of Li//MoO_3 cells with

nanofibers deliver a better discharge capacity after 40 cycles than MoO_3 bulk. Nanofibers show a specific capacity 265 mAh g^{-1} for the first discharge in the potential range 3.5–1.5 V with Li uptake of 1.5 Li/Mo. Thus, the electrochemical features of nanofibers are characteristic of a two-phase domain similar to that of bulk α-MoO_3. However, we notice that, as expected, the discharge curve exhibits larger cell polarization for high *C*-rate, i.e., about 0.6 V at 2*C*. Structural evolution of this domain corresponds to a solid solution involving $Li_{0.08}MoO_3$ and $Li_{0.2}MoO_3$ (called α′-MoO_3). The evolution of the local structure of cathode materials during the first discharge has been studied by Raman spectroscopy. Results describe that the lithium insertion process consists in rather moderate local distortions allowing the accommodation of 1.5 Li/mol of oxide without breaking of the orthorhombic symmetry [109].

12.6 Concluding Remarks

One of the challenges in the field of rechargeable lithium-ion batteries is the use of nanoparticles for cathode and anode materials. This in general should be considered as favorable for achieving high rate capability, since solid-state Li-ion transport in the bulk materials may be the rate-determining step for the entire intercalation–deintercalation processes. The use of nanoparticles leads to reducing to minimum the diffusion path for the electrons and the Li-ion transport, and to better accommodation of strain during Li^+ extraction/insertion. Furthermore, since the electrochemical active surface area is inversely proportional to the particle size, the electrodes comprising nanoparticles posses significantly larger surface area and have more active sites for the electrochemical reactions. Hence for nanoparticles, surface effects become more important than the bulk properties and they are still under debate in the literature. In regard of the materials for positive electrodes in lithium cells, it was demonstrated that the cathodes comprising nanoparticles of $LiMn_{0.5}Ni_{0.5}O_2$ and $LiMn_{1.5}Ni_{0.5}O_4$ display faster kinetics than electrodes based on micrometric-size particles. It was also shown that the electrodes prepared from the spinel $LiMn_2O_4$ nanoparticles exhibited improved cycling performance, small charge-transfer resistance at the electrode–solution interface, a reduced the Jahn–Teller effect, and stabilization of the nano-$LiMn_2O_4$ cathodes in cycling at 60 °C. In the case of nano-crystalline $LiCoO_2$ electrodes, the increased values of the discharge capacity were attributed to shorter diffusion distances that promote faster and more uniform Li^+ intercalation. The dramatic effect of the small grain-size material (<20 nm) on increasing the electrochemical activity (capacity) has been established recently for the lithium extraction/insertion reactions of $LiCrO_2$ electrodes. On the other hand, nanoparticles with a relatively high surface area may be reactive with electrolyte solutions based on alkyl carbonate solvents and $LiPF_6$

(which unavoidably contain detrimental contaminants such as HF, trace water, PF_5 and POF_3). Possible reactions with solution species may develop undesirable detrimental side reactions (especially on the high surface area particles) leading to the passivation phenomena and high electrode impedance. In these systems, the irreversible oxidation of alkyl carbonate solvents resulting in the evolution of CO_2 accompanies the electrochemical processes at high anodic potentials. For more than a decade, researchers have accumulated lots of information and reported numerous papers on the synthesis of nanoparticles of the lithiated transition-metal oxides, their magnetic properties, vibrational modes studied by infra-red and Raman spectroscopy, and on the electrochemical performance of positive electrodes comprising nanoparticles of the active material in lithium cells. Based on the literature reports in the field, it can be concluded that the possible use of nanomaterials in electrodes for Li-ion batteries should be studied rigorously and specially for each electrode material individually taking into account the balance between the pros and cons. In regard of the Li_2MnO_3 nanoparticles, we realized that the literature data on their characterization and electrochemical performance are scarce. It was shown, for instance that the electrochemical behavior of the nanocrystalline Li_2MnO_3 electrodes depends upon the particles morphology, specific surface area, and annealing temperature of the as-prepared material. The authors synthesized nano-Li_2MnO_3 by the solid-state reaction and studied the structural transformation of this material between layered $LiMnO_2$ and cubic $LiMn_2O_4$ spinel-type phases.

References

1. Feynman RP (1992) There's plenty of room at the bottom. J Microelectromech Syst 1:60–66
2. Zaghib K, Julien CM, Prakash J (2003) New trends in intercalation compounds for energy storage and conversion. The Electrochem Society, Pennington
3. Chen Z, Dahn JR (2002) Reducing carbon in $LiFePO_4$/C composite electrodes to maximize specific energy, volumetric energy and tap density. J Electrochem Soc 149:A1184–A1189
4. Weppner W, Huggins RA (1977) Determination of the kinetic parameters of mixed-conducting electrodes and application to the system Li_3Sb. J Electrochem Soc 124:1569–1578
5. Julien CM, Mauger A, Ait-Salah A, Massot M, Gendron F, Zaghib K (2007) Nanoscopic scale studies of $LiFePO_4$ as cathode material in lithium-ion batteries for HEV application. Ionics 13:395–411
6. Ravet N, Goodenough J.B, Besner S, Simoneau M, Hovington P, Armand M (1999) Improved iron based cathode material. In: Proceedings of the 196th ECS meeting, Honolulu, extended abstract n° 127. Accessed Oct 1999
7. Lalena JN, Clearly DA (2010) Principles of inorganic materials design. Wiley, Hoboken, NJ
8. Huang B, Jang YI, Chiang YM, Sadoway DR (1998) Electrochemical evaluation of $LiCoO_2$ synthesized by decomposition and intercalation of hydroxides for lithium-ion battery applications. J Appl Electrochem 28:1365–1369

9. Julien C, El-Farh L, Rangan S, Massot M (1999) Synthesis of $LiNi_{1-y}Co_yO_2$ cathode materials prepared by a citric acid-assisted sol-gel method for lithium batteries. J Sol Gel Sci Technol 15:63–72
10. Abdel-Ghany AE, Hashem AM, Abuzeid HA, Eid AE, Bayoumi HA, Julien CM (2009) Synthesis, structure characterization and magnetic properties of nanosized $LiCo_{1-y}Ni_yO_2$ prepared by sol-gel citric acid route. Ionics 15:49–59
11. Garcia B, Barboux P, Ribot F, Kahn-Harari A, Mazerolles L, Baffier N (1995) The structure of low temperature crystallized $LiCoO_2$. Solid state Ionics 80:111–118
12. Myung ST, Kim GH, Sun YK (2004) Synthesis of $Li[Ni_{1/3}Co_{1/3}Mn_{1/3}]O_{2-z}F_z$ via coprecipitation. Chem Lett 33:1388–1389
13. Chitra S, Kalyani P, Mohan T, Gangadharan R, Yebka B, Castro-Garcia S, Massot M, Julien C, Eddrief M (1999) Characterization and electrochemical studies of $LiMn_2O_4$ cathode materials prepared by combustion method. J Electroceram 3:433–441
14. Julien C, Letranchant C, Rangan S, Lemal M, Ziolkiewicz S, Castro-Garcıa S, El-Farh L, Benkaddour M (2000) Layered $LiNi_{0.5}Co_{0.5}O_2$ cathode materials grown by soft-chemistry via various solution methods. Mater Sci Eng B 76:145–155
15. Azib T, Ammar S, Nowak S, Lau-Truing S, Groult H, Zaghib K, Mauger A, Julien CM (2012) Crystallinity of nano C-$LiFePO_4$ prepared by the polyol process. J Power Sourc 217:220–228
16. Liu W, Farrington GC, Chaput F, Dunn B (1996) Synthesis and electrochemical studies of spinel phase $LiMn_2O_4$ cathode materials prepared by the Pechini process. J Electrochem Soc 143:879–884
17. Vivekanandhan S, Venkateswarlu M, Satyanarayana N (2005) Effect of different ethylene glycol precursors on the Pechini process for the synthesis of nano-crystalline $LiNi_{0.5}Co_{0.5}VO_4$ powders. Mater Chem Phys 91:54–59
18. Kwon SW, Park SB, Seo G, Hwang ST (1998) Preparation of lithium aluminate via polymeric precursor routes. J Nucl Mater 257:172–179
19. Pereira-Ramos JP (1995) Electrochemical properties of cathodic materials synthesized by low-temperature techniques. J Power Sourc 54:120–126
20. Taguchi H, Yoshioka H, Matsuda D, Nagao M (1993) Crystal structure of $LaMnO_{3+\delta}$ synthesized using poly(acrylic acid). J Solid State Chem 104:460–463
21. Pechini MP (1967) Method of preparing lead and alkaline-earth titanates and niobates and coating method using the same to form a capacitor. US Patent 3,330,697. Accessed 11 Jul 1967
22. Tai LW, Lessing PA (1992) Modified resin-intermediate processing of perovskite powders: part I. Optimization of polymeric precursors. J Mater Res 7:511–519
23. Ramasamy Devaraj R, Karthikeyan K, Jeyasubramanian K (2013) Synthesis and properties of ZnO nanorods by modified Pechini process. Appl Nanosci 3:37–40
24. Zhang X, Jiang WJ, Mauger A, Qi L, Gendron F, Julien CM (2010) Minimization of the cation mixing in $Li_x(NMC)_{1-x}O_2$ as cathode materials. J Power Sourc 195:1292–1301
25. Lee KS, Myung ST, Prakash J, Yashiro H, Sun YK (2008) Optimization of microwave synthesis of $Li[Ni_{0.4}Co_{0.2}Mn_{0.4}]O_2$ as a positive electrode material for lithium batteries. Electrochim Acta 53:3065–3074
26. Chen Y, Xu G, Li J, Zhang Y, Chen Z, Kang F (2013) High capacity $0.5Li_2MnO_3$-$0.5LiNi_{0.33}Co_{0.33}Mn_{0.33}O_2$ cathode material via a fast co-precipitation method. Electrochim Acta 87:686–692
27. Larcher D, Patrice R (2000) Preparation of metallic powders and alloys in polyol media: a thermodynamic approach. J Solid State Chem 154:405–411
28. Kim DH, Kim TR, Im JS, Kang JW, Kim J (2007) A new method to synthesize olivine phosphate nanoparticles. J Phys Scripta T 129:31–34
29. Badi SP, Wagemaker M, Ellis BL, Singh DP, Borghols WJH, Kan WH, Ryan DH, Mulder FM, Nazar LF (2011) Direct synthesis of nanocrystalline $Li_{0.90}FePO_4$: observation of phase segregation of anti-site defects on delithiation. J Mater Chem 21:10085–10093

30. Kim DH, Kim J (2006) Synthesis of $LiFePO_4$ nanoparticles in polyol medium and their electrochemical properties. Electrochem Solid State Lett 9:A439–A442
31. Patil KC, Aruna ST, Mimani T (2002) Combustion synthesis: an update. Curr Opinion Solid State Mater Sci 6:507–512
32. Varma A, Rogachev AS, Mukasyan AS, Stephen Hwang S (1998) Combustion synthesis of advanced materials: principles and applications. Adv Chem Eng 24:79–226
33. Patil KC (1993) Advanved ceramics: combustion synthesis and properties. Bull Mater Sci 16:533–541
34. Julien C, Camacho-Lopez MA, Mohan T, Chitra S, Kalayani P, Gopakumar S (2001) Combustion synthesis and characterization of substituted lithium cobalt oxides in lithium batteries. Solid State Ionics 141–142:549–557
35. Hyu-Bum P, Kim J, Chi-Woo L (2001) Synthesis of $LiMn_2O_4$ powder by auto-ignited combustion of poly(acrylic acid)-metal nitrate precursor. J Power Sourc 92:124–130
36. Prabaharan SRS, Michael MS, Radhakrishna S, Julien C (1997) Novel low-temperature synthesis and characeterization of $LiNiVO_4$ for high-voltage Li ion batteries. J Mater Chem 7:1791–1796
37. Julien C, Michael SS, Ziolkiewicz S (1999) Structural and electrochemical properties of $LiNi_{0.3}Co_{0.7}O_2$ synthesized by different low-temperature techniques. Int J Inorg Mater 1:29–37
38. Lu CH, Saha SK (2001) Low temperature synthesis of nano-sized lithium manganese oxide powder by the sol-gel process using PVA. J Sol Gel Sci Technol 20:27–34
39. Prabaharan SRS, Saparil NB, Michael SS, Massot M, Julien C (1998) Soft chemistry synthesis of electrochemically-active spinel $LiMn_2O_4$ for Li-ion batteries. Solid State Ionics 112:25–34
40. Julien C (2000) 4-Volt cathode materials for rechargeable lithium batteries, wet-chemistry synthesis, structure and electrochemistry. Ionics 6:30–46
41. Higuchi M, Katayama K, Azuma Y, Yukawa M, Suhara M (2003) Synthesis of $LiFePO_4$ cathode material by microwave processing. J Power Sourc 119:258–261
42. Lee J, Teja AS (2005) Characteristics of lithium iron phosphate ($LiFePO_4$) particles synthesized in subcritical and supercritical water. J Supercrit Fluids 35:83–90
43. Li X, Cheng F, Guo B, Chen J (2005) Template-synthesized of $LiCoO_2$, $LiMn_2O_4$ and $LiNi_{0.8}Co_{0.2}O_2$ nanotubes as the cathode materials of lithium ion batteries. J Phys Chem B 109:14017–014024
44. Zhou YK, Shen CM, Huang J, Li HL (2002) Synthesis of high-ordered $LiMn_2O_4$ nanowire arrays by AAO template and its structural properties. Mater Sci Eng B 95:77–82
45. Taniguchi T, Song D, Wakihara M (2002) Electrochemical properties of $LiM_{1/6}Mn_{11/6}O_4$ (M = Mn, Co, Al, and Ni) as cathode materials for Li-ion batteries prepared by ultrasonic spray pyrolysis method. J Power Sourc 109:333–339
46. Park SH, Yoon CS, Kang SG, Kim HS, Moon SI, Sun YK (2004) Synthesis and structural characterization of layered $Li[Ni_{1/3}Mn_{1/3}Co_{1/3}]O_2$ cathode material by ultrasonic spray pyrolysis method. Electrochim Acta 49:557–563
47. Guo ZP, Liu H, Liu HK, Dou SX (2003) Characterization of layered $LiNi_{1/3}Mn_{1/3}Co_{1/3}O_2$ cathode materials prepared by spray-drying method. J New Mat Electrochem Syst 6:263–266
48. Byrappa K, Yoshimura M (2001) Handbook of hydrothermal technology. William Andrew Publishing, Norwich
49. Yoshimura M, Suchanek WL, Byrappa K (2000) Soft solution processing: a strategy for one-step processing of advanced inorganic materials. MRS Bull 25:17–25
50. Suchanek WL, Riman RE (2006) Hydrothermal synthesis of advanced ceramic powders. Adv Sci Technol 45:184–193
51. Brochu F, Guerfi A, Trottier J, Kopeć M, Mauger A, Groult H, Julien CM, Zaghib K (2012) Structure and electrochemistry of scaling nano C-$LiFePO_4$ synthesized by hydrothermal route: complexing agent effect. J Power Sourc 214:1–6

52. Eftekhari A (2006) Bundled nanofibers of V-doped $LiMn_2O_4$ spinel. Solid State Commun 140:391–394
53. Ma R, Bando Y, Zhang L, Sasaki T (2004) Layered MnO_2 nanobelts: hydrothermal synthesis and electrochemical measurements. Adv Mater 16:918–922
54. Xiao X, Liu X, Wang L, Zhao H, Hu Z, He X, Li Y (2012) $LiCoO_2$ nanoplates with exposed (001) planes and high rate capability for lithium-ion batteries. Nano Res 5:395–401
55. Xiao X, Yang L, Zhao H, Hu Z, Li Y (2012) Facile synthesis of $LiCoO_2$ nanowires with high electrochemical performance. Nano Res 5:27–32
56. Hashem AM, Abuzeid HM, Abdel-Latif AM, Abbas HM, Ehrenberg H, Indris S, Mauger A, Groult H, Julien CM (2013) MnO_2 nanorods prepared by redox reaction as cathodes in lithium batteries. ECS Trans 50–24:125–130
57. Li Q, Gao F, Zhao D (2002) One-step synthesis and assembly of copper sulphide nanoparticles to nanowires, nanotubes and nanovesicles by a simple organic amine-assisted hydrothermal process. Nano Lett 2:725–728
58. Shiraishi K, Dokko K, Kanamura K (2005) Formation of impurities on phospho-olivine $LiFePO_4$ during hydrothermal synthesis. J Power Sourc 146:555–558
59. Lee J, Teja AS (2006) Synthesis of $LiFePO_4$ micro and nanoparticles in supercritical water. Mater Lett 60:2105–2109
60. Jun B, Gu HB (2008) Preparation and characterization of $LiFePO_4$ cathode materials by hydrothermal method. Solid State Ionics 178:1907–1914
61. Vadivel-Murugan A, Muraliganth T, Manthiram A (2009) One-pot microwave-hydrothermal synthesis and characterization of carbon-coated $LiMPO_4$/C (M=Mn, Fe, Co) cathodes. J Electrochem Soc 156:A79–A83
62. Beninati S, Damen L, Mastragostino M (2008) MW-assisted synthesis of $LiFePO_4$ for high power applications. J Power Sourc 180:875–879
63. Wang L, Huang Y, Jiang R, Jia D (2007) Preparation and characterization of nano-sized $LiFePO_4$ by low heating solid-state coordination method and microwave heating. Electrochim Acta 52:6778–6783
64. Hayashi H, Hakuta Y (2010) Hydrothermal synthesis of metal oxide nanoparticles in supercritical water. Materials 3:3794–3817
65. Xu CB, Lee J, Teja AS (2008) Continuous hydrothermal synthesis of lithium iron phosphate particles in subcritical and supercritical water. J Supercrit Fluid 44:92–97
66. Lee JH, Ham JY (2006) Synthesis of manganese oxide particles in supercritical water. Korean J Chem Eng 23:714–719
67. Shin YH, Koo SM, Kim DS, Lee YH, Veriansyah B, Kim J, Lee YW (2009) Continuous hydrothermal synthesis of HT-$LiCoO_2$ in supercritical water. J Supercrit Fluids 50:250–256
68. Zhu W, Yang M, Yang X, Xu X, Xie J, Li Z (2014) Supercritical continuous hydrothermal synthesis of lithium titanate anode materials for lithium-ion batteries. US Patent 20140105811 A1. Accessed 17 Apr 2014
69. Vediappan K, Guerfi A, Gariépy V, Demopoulos GP, Hovington P, Trottier J, Mauger A, Julien CM, Zaghib K (2014) Stirring effect in hydrothermal synthesis of C-$LiFePO_4$. J Power Sourc 266:99–106
70. Kuerten H, Rumpf H (1966) Zerkleinerungsuntersuchungen mit tribolumineszierenden Stoffen. Chemie Ing Techn 38:331–342
71. Tanaka T, Kanda Y (2006) Crushing and grinding. In: Masuda H, Higashitani K, Yoshida H (eds) Powder technology handbook, vol 3. CRC Taylor and Francis, New York
72. Saleem IY, Smyth HDC (2010) Micronization of a soft material: air-jet and micro-ball milling. AAPS Pharm Sci Tech 11:1642–1649
73. Hosokawa Micron Powder Systems (1996) Fluidized bed jet milling for economical powder processing. Ceram Ind. http://hmicronpowder.com/fluidized.pdf. Accessed Apr 1996
74. Comex (2014) Jet milling. http://www.comex-group.com/Comex/files/78/Brochure%20JMX.pdf

75. Zaghib K, Charest P, Dontigny M, Guerfi A, Lagace M, Mauger A, Kopec M, Julien CM (2010) $LiFePO_4$: from molten ingot to nanoparticles with high-rate performance in Li-ion batteries. J Power Sourc 195:8280–8288
76. Noh JK, Kim S, Kim H, Choi W, Chang W, Byun D, Cho BW, Chung KY (2014) Mechanochemical synthesis of Li_2MnO_3 shell/$LiMO_2$ (M = Ni, Co, Mn) core-structured nanocomposites for lithium-ion batteries. Sci Rep 4:4847
77. Zaghib K, Mauger A, Gendron F, Julien CM (2008) Surface effects on the physical and electrochemical properties of thin $LiFePO_4$ particles. Chem Mater 20:462–469
78. Zaghib K, Dontigny M, Charest P, Labrecque JF, Guerfi A, Kopec M, Mauger A, Gendron F, Julien CM (2008) Aging of $LiFePO_4$ upon exposure to H_2O. J Power Sourc 185:698–710
79. Axmann A, Stinner C, Wohlfahrt-Mehrens M, Mauger A, Gendron F, Julien CM (2009) Non-stoichiometric $LiFePO_4$: defects and related properties. Chem Mater 21:1636–1644
80. Julien CM, Mauger A, Zaghib K (2011) Surface effects on electrochemical properties of nano-sized $LiFePO_4$. J Mater Chem 21:9955–9968
81. Zhang X, Jiang WJ, Zhu XP, Mauger A, Lu D, Julien CM (2011) Aging of $LiNi_{1/3}Mn_{1/3}Co_{1/3}O_2$ cathode material upon exposure to H_2O. J Power Sourc 196:5102–5108
82. Hashem AMA, Abdel-Ghany AE, Eid AE, Trottier J, Zaghib K, Mauger A, Julien CM (2011) Study of the surface modification of $LiNi_{1/3}Co_{1/3}Mn_{1/3}O_2$ cathode material for lithium ion battery. J Power Sourc 196:8632–8637
83. Mauger A, Zaghib K, Groult H, Julien CM (2013) Surface and bulk properties of $LiFePO_4$: the magnetic analysis. ECS Trans 50–24:115–123
84. Aurbach D, Gamolsky K, Markovsky B, Salitra G, Gofer Y, Heider U, Oesten R, Schmidt M (2000) The stydy of surface phenomena related to electrochemical lithium intercalation into Li_xMO_y host materials (M = Ni, Mn). J Electrochem Soc 147:1322–1331
85. Yamada A, Koizumi H, Nishimura S, Sonoyama N, Kanno R, Yonemura M, Nakamura T, Kobayashi T (2006) Room-temperature miscibility gap in Li_xFePO_4. Nat Mater 5:357–360
86. Zhou F, Marianetti CA, Cococcioni M, Morgan D, Ceder G (2004) Phase separation in Li_xFePO_4 induced by correlation effects. Phys Rev B Condens Matter 69:201101
87. Gibot P, Casas-Cabanas M, Laffont L, Levasseur S, Carlac P, Hamelet S, Tarascon JM, Masquelier C (2008) Room-temperature single-phase Li insertion/extraction in nanoscale Li_xFePO_4. Nat Mater 7:741–747
88. Tang M, Huang HY, Meethong N, Kao YH, Carter WC, Chiang YM (2009) Model for the particle size, overpotential and strain dependence of phase transition pathways in storage electrodes: application to nanoscale olivines. Chem Mater 21:1557–1571
89. Zaghib K, Mauger A, Goodenough JB, Gendron F, Julien CM (2009) Positive electrode: lithium iron phosphate. In: Garche J, Dyer C, Moseley P, Ogumi Z, Rand D, Scrosati B (eds) Encyclopedia of electrochemical power sources, vol 5. Elsevier, Amsterdam, pp 264–296
90. Pandey NK, Tiwari K, Roy A (2011) Ag doped WO_3 nanomaterials as relative humidity sensor. Sensors J IEEE 11:2911–2918
91. Suisanti D, Diputra AA, Tananta L, Purwaningsih H, Kusuma GE, Wang C, Shih S, Huanf Y (2014) WO_3 nanomaterials synthesized via a sol-gel method and calcination for use as a CO gas sensor. Front Chem Sci Eng 8:179–187
92. Hoel A, Reyes LF, Heszler P, Lantto V, Granqvist CG (2004) Nanomaterials for environmental applicationq: novel WO_3-based gas sensors made by advanced gas deposition. Curr Appl Phys 4:547–553
93. Aliev AE, Park C (2000) Deveopment of WO_3 thin films using nanoscale silicon particles. Jpn J Appl Phys 39:3572–3578
94. Liang CC (1973) Conduction characteristics of the lithium iodide-aluminium oxide solid electrolytes. J Electrochem Soc 120:12891292
95. Wang Q, Wen Z, Jeong Y, Choi J, Lee K, Li J (2006) Li driven electrochemical properties of WO_3 nanorods. Nanotechnology 17:3116–3120
96. Wang J, Eugene Khoo E, Lee PS, Ma J (2008) Synthesis, assembly, and electrochromic properties of uniform crystalline WO_3 nanorods. J Phys Chem C 112:14306–14312

97. Yebka B, Pecquenar B, Julien C, Livage J (1997) Electrochemical Li^+ insertion in WO_3-xTiO_2 mixed oxides. Solid State Ionics 104:169–175
98. Pecquenard B, Lecacheux H, Livage J, Julien C (1998) Orthorhombic WO_3 formed via a Ti-stabilized $WO_3 \cdot 1/3H_2O$ phase. J Solid State Chem 135:159–168
99. Picquart M, Castro-Garcia S, Livage J, Julien C, Haro-Poniatowski E (2000) Sol-gel transition kinetics in WO_3 investigated by in-situ Raman spectroscopy. J Sol Gel Sci Technol 18:199–206
100. Ramana CV, Utsunomiya S, Ewing RC, Julien CM, Becker U (2005) Electron microscopy investigation of structural transformations in tungsten oxide (WO_3) thin films. Phys Status Sol A 202:R108–R110
101. Ramana CV, Utsunomiya S, Ewing RC, Julien CM, Becker U (2006) Structural stability and phase transitions in WO_3 thin films. J Phys Chem B 110:10430–10435
102. Yu DYW, Yanagida K (2011) Structural analysis of Li_2MnO_3 and related Li-Mn-O materials. J Electrochem Soc 158:A1015–A1022
103. Amalraj SF, Sharon D, Talianker M, Julien CM, Burlaka L, Lavi R, Zhecheva E, Markovsky B, Zinigrad E, Kovacheva D, Stoyanova R, Aurbach D (2013) Study of the nanosized Li_2MnO_3: electrochemical behaviour, structure, magnetic properties and vibrational modes. Electrochim Acta 97:259–270
104. Amdouni N, Zarrouk H, Soulette F, Julien C (2003) $LiAl_yCo_{1-y}O_2$ ($0.0 \leq y \leq 0.3$) intercalation compounds synthesized from the citrate precursors. Mater Chem Phys 80:205–214
105. Amdouni N, Zarrouk H, Julien CM (2003) Structural and electrochemical properties of $LiCoO_2$ and $LiAl_yCo_{1-y}O_2$ ($y = 0.1$ and 0.2) oxides. A comparative study of electrodes prepared by the citrate precursor route. Ionics 9:47–55
106. Minakshi M, Blackford M, Ionescu M (2011) Characterization of alkaline-earth oxide additions to the MnO_2 cathode in an aqueous secondary battery. J Alloys Compd 509:5974–5980
107. Park DH, Ha HW, Lee SH, Choy JH, Hwang SJ (2008) Transformation from microcrystalline $LiMn_{1-x}Cr_xO_2$ to 1D nanostructured β-$Mn_{1-x}Cr_xO_2$: promising electrode performance of β-MnO_2-type nanowires. J Phys Chem C 112:5160–5164
108. Abuzeid HM, Hashem AM, Narayanan N, Ehrenberg H, Julien CM (2011) Nanosized silver-coated and doped manganese dioxide for rechargeable lithium batteries. Solid State Ionics 182:108–115
109. Hashem AM, Groult H, Mauger A, Zaghib K, Julien CM (2012) Electrochemical properties of nanofibers α-MoO_3 as cathode materials for Li batteries. J Power Sourc 219:126–132

Chapter 13
Experimental Techniques

13.1 Introduction

The incremental capacity of an insertion electrode material used in ambient temperature batteries can be estimated from voltage spectroscopy measurements which can help to the determination of phase diagram of the insertion compound [1]. In the first section, we examine the various aspects of electrochemical lithium insertion into a number of electrode materials. The experimental techniques of solid-state electrochemistry are presented in the second section. Voltage spectroscopy and phase diagram during Li intercalation into cathode materials are investigated. Finally, the experimental determination of the diffusion coefficient of ions in solid materials is investigated.

A large class of ambient temperature batteries involves electrode insertion reaction, where a fraction (x) of foreign cations (Li^+) together with compensating electrons (e^-) are incorporated into the lattice of a host electrode material (H) forming a nonstoichiometric compound:

$$x\mathrm{Li}^+ + xe^- + \mathrm{H} \leftrightarrow \mathrm{Li}_x\mathrm{H}. \tag{13.1}$$

In case the reaction product bears a close structural relationship to the pristine electrode (unreacted) material (H), this type of reaction is classified as topochemical [2]. A special case of the topochemical process is the intercalation or insertion reaction which proceeds without any breakage of bonds in the host structure. This reaction (Eq. 13.1) is generally reversible.

13.2 Theory

The equilibrium potential of a solid-state redox reaction associated with Li ions insertion and extraction usually shows subtle dependence on the reaction parameter, x (concentration of ions and electrons in the host matrix). This often makes

C. Julien et al., *Lithium Batteries*, DOI 10.1007/978-3-319-19108-9_13

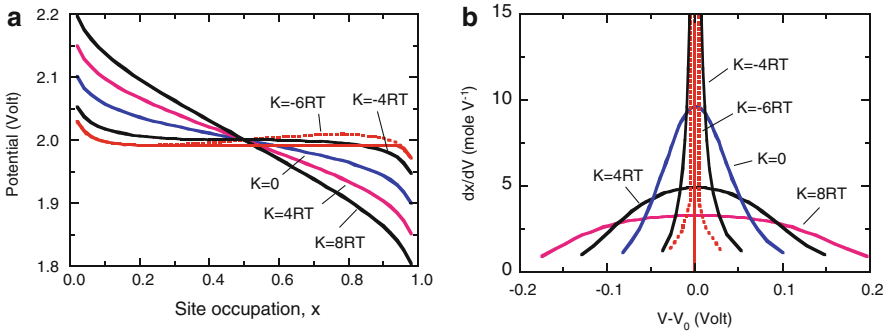

Fig. 13.1 (**a**) Open-circuit voltage vs. composition curves according to Eq. (13.2) for different values of the interaction parameter K and $E_o = 2$ V. (**b**) Normalized capacity vs. $V - V_o$ curves for different values of K

deviations from the simple Nernst law due to interactions between the inserted species and the host lattice [3]. The open-circuit voltage (OCV) vs. composition, $V(x)$, can be separated into three terms: a standard electrode potential V_o, a configurational term accounting for the distribution over ideal equivalent sites, and a term K accounting for the interactions between inserted ions:

$$V(x) = V_o - \frac{RT}{F}\left[\ln\left(\frac{x}{1-x}\right) - \frac{K}{F}\left(x - \frac{1}{2}\right)\right], \tag{13.2}$$

where both the configurational and the interaction term are functions of the degree of intercalation, x. The interaction parameter, K, may be either positive (repulsion) or negative (attraction). Figure 13.1a shows the open-circuit voltage OCV vs. composition curves according to Eq. (13.2) for different values of the interaction parameter. OCV is continuously decreasing, with a S-shaped equilibrium potential vs. capacity curve, for a single phase intercalation process. It is constant if two phases are present simultaneously, exhibiting a L-shaped curve. The normalized differential capacity, $C^* = (-dx/dV)$, also named *incremental capacity*, is given by:

$$C^* = -\frac{dx}{dV} = \frac{F}{RT}\left[1 + \frac{x}{1-x} + Kx\right]^{-1}, \tag{13.3}$$

where dx/dV indicates an electrochemical density of states at V for a system. For values of K greater than -4, this relation predicts the differential capacity curve to be bell-shaped, with the maximum at the potential where x is equal to 0.5. Normalized capacity curves for different values of K are shown in Fig. 13.1b. C^* as given by Eq. (13.3) has a singularity at $x = 0.5$ for $K = -4RT$, corresponding to the onset of condensation of the intercalated Li ions due to strong attractive interaction. At this point, the OCV vs. composition curve has zero slope. The states corresponding to this region cannot be realized, but will separate into a lithium-rich

and a lithium-poor phase, each with same lithium activity. The differential capacity corresponding to this two-phase region is infinite, and can be described as a delta function (Fig. 13.1b).

13.3 Measurements of Insertion Kinetics

The composition-dependent electrode potential, $E(x)$, can be determined by preparing either chemically or electrochemically specimens of different compositions and by measuring their OCV against a suitable reference electrode in an electrochemical cell. The average composition is estimated by chemical analysis or coulometric titration for electrochemically prepared samples [4, 5]. In both cases, sufficient time is required to be in a thermodynamic equilibrium regime. Coulometric techniques are essentially point-to-point methods allowing the determination of the electromotive force (emf) curves at closely spaced points. They are galvanostatic intermittent titration technique (GITT) and electrochemical potential spectroscopy (EPS) [4–9].

13.3.1 Electrochemical-Potential Spectroscopy (EPS)

A powerful electrochemical technique involves the application of a series of constant potential steps to an electrochemical cell [7]. On each potential step the cell is permitted to attain quasi open-circuit conditions by letting the current decay to a small, but finite, value. When small voltage steps are made, the voltage-charge relation is a highly precise and accurate approximation to the thermodynamic properties of the cell. Application to the Li-TiS_2 couple shows that the charge accumulated on each voltage step resembles an electrochemical potential spectrogram that provides evidence for the structural ordering of lithium in Li_xTiS_2. The technique can be used to study the potential-dependent cell kinetics, the thermodynamics of adsorption on surfaces, and the phase diagrams of cathode materials.

The voltage of a lithium intercalation battery varies with its state of discharge, i.e., the intercalant composition x. Subsequently more careful experiments have shown fine structure in $V(x)$ for many intercalation system [4, 5, 7, 10] clearly observed in plots of dx/dV vs. x or V, which can be caused by a variety of physical mechanisms such as the interactions between intercalated atoms within the host or intercalation-induced structural phase transitions in the host. Therefore, careful measurements of dx/dV can be used a study the physics and chemistry of the intercalation process.

Experimental details of EPS are given in ref. [7]. Let us describe the basic considerations as follows with $dQ = I_o dt$ and $dQ = Q_o dx$. When a cell based on

intercalation is charged or discharged at constant current, the rate of change of cell voltage with time is:

$$\frac{dV}{dt} = \frac{dV}{dQ}\frac{dQ}{dt} = \frac{I_o}{Q_o}\frac{dV}{dx}, \tag{13.4}$$

where V is the cell voltage, I_o, the constant current, Q_o the charge corresponding to a change, $\Delta x = 1$ in the intercalation electrode:

$$Q_o = \frac{mF}{M_w}. \tag{13.5}$$

In this equation, m is the mass of the active element of the electrode, and M_w is its molar mass (we assume that there is one Li^+ ion per chemical formula), and F is the Faraday's constant. By monitoring the cell voltage as a function of time, one can obtain dx/dV since:

$$\frac{dx}{dV} = \frac{I_o}{Q_o}\left(\frac{dV}{dt}\right)^{-1}. \tag{13.6}$$

With measurement of dx/dV at high resolution in V and x, we monitor the voltage of the cell as a function of time with a computer-controlled voltmeter. In the standard terminology, this method of measuring dx/dV is called derivative constant current chronopotentiometry.

From Eqs. (13.4) and (13.6), we assume that the integral of the current can be directly related to the change of composition that occurs within the insertion electrode. By examining the derivative quantity, dx/dV, measured at different current values, one can usually determine the effects of the finite rate and obtain the equilibrium dx/dV. The same studies can also be made as a function of voltage sweep rate using linear sweep voltammetry (LSV).

The experimental procedure consists in a series of constant voltage steps ΔV applied to the galvanic cell as shown in Fig. 13.2. At each voltage stage $V_i + \delta V = V_{i+1}$ the decreasing current output is recorded and integrated in time to give the corresponding change of stoichiometry Δx up to a predefined small current value I_{min}. Then the corresponding charge variation in the cell is given by:

$$\Delta q = \frac{mF}{M_w}\Delta x, \tag{13.7}$$

where M_w, m and F are the atomic weight, the mass of the cathode material and the Faraday's constant, respectively. The smaller I_{min}, the closest the cell is to the thermodynamic equilibrium, so the voltage V vs. x relation in the host can be

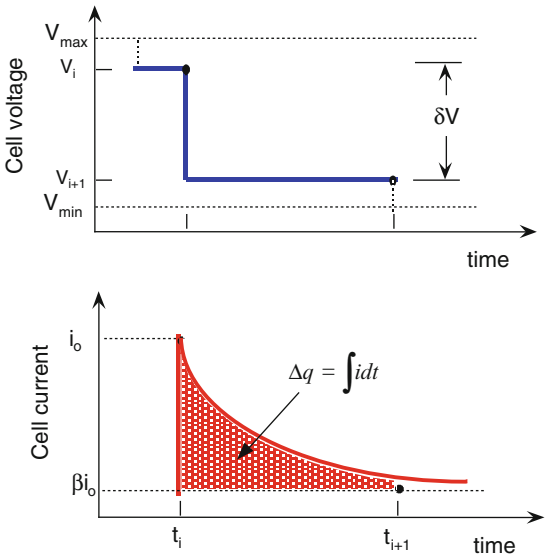

Fig. 13.2 Schematic illustration of the voltage-stepped cycling method, electrochemical-potential spectroscopy (EPS) and the corresponding current passing the cell

considered as a good approximation to the thermodynamic EMF of the cell. We can obtain very precise thermodynamic data like:

1. Cell voltage with an error equal to the voltage resolution given by the source unit, e.g., 0.5 mV in our experiment, which is such smaller than the error of few μV in the galvanostatic method.
2. Derivative incremental capacity $-dx/dV$ vs. V or x almost free of error. This is important in the case where there exist two sequential phases having small difference or a single-phase with small free energy of formation, e.g., in Li ordering.

Another advantage, mentioned below, is the speed of this method. In EPS the experimental time is consumed only at the potentials where the cell presents large capacity. On the contrary, the current falls quickly and the system proceeds readily to the next potential step. In other words, the system presents voltage scanning rate. In practice one can obtain results similar to the galvanostatic method's results in the one fifth or even less of time, because at the beginning of each step the current output of the cell is much higher than $I_{\min}$ which is the actual value of the current when the step ends. Finally the EPS is the most appropriate method for the first study of an unknown cathodic material and for the study of slower reactions that are met in a lot of solid state systems.

Within the EPS investigations, the conditions of validity and calculation of intensity time functions have been discussed [11, 12]. In particular, a fast diffusion of Li in the host material depends on the nature of the host, but more drastically on the grain size of the cathode when constituted by powdered or polycrystalline form. Therefore, one has to check in each case that the increments of the applied voltage and the value of the cut-off current are small enough to make sure that the kinetic

values are almost identical to the equilibrium ones. In other words, the time scale of the experiments must be the small compared to the characteristic time $\tau \ll L^2/4\widetilde{D}_i$ with $\widetilde{D}_i$ the chemical diffusion coefficient. τ is the time that the lithium ions need to go from one electrode to the other with L the length of the lithium path inside the solid (when the travel time inside the electrolyte is negligible). In particular, the C-rate at which the experiment is performed must be small compared to $1/\tau$ (with τ expressed in hours in that case, according to the convention on the C-rate). Experimentally this means that when the increments of voltage are too large or when the reaction process is impeding the Li-diffusion, the EPS method cannot be used.

13.3.2 Galvanostatic Intermittent Titration Technique (GITT)

The theory and the experimental procedure of the galvanostatic intermittent titration technique (GITT) have been well developed by Weppner and Huggins [4]. The application of this technique has been successful for the kinetic studies of numerous lithium intercalated compounds such as TiS_2 and TaS_2. An extension of the GITT method has been presented by Honders et al. [13, 14] with application to Li_xTiS_2 and Li_xCoO_2. The advantage of this extended method with respect to the more conventional techniques, which involve only semi-infinite diffusion is that both the chemical diffusion coefficient $\left(\widetilde{D}_i\right)$ for species i and the enhancement factor (W) can be determined from kinetic data only, with $\widetilde{D}_i = D_i^0 W$. Furthermore, the determination of $\widetilde{D}_i$ only requires an estimation of the effective length of the diffusion path, instead of an active electrode area.

The self-diffusion coefficient or diffusivity D_i^0 is defined by the first Fick's law applied to the chemical:

$$J_i = -c_i \frac{D_i^0}{RT} \frac{d\mu_i}{dx}, \tag{13.8}$$

where J_i is the amount of substance i (in mol) per unit area and unit time, c_i the concentration (in mol m^{-3}), R the universal gas constant. μ_i is the chemical potential given by the relation:

$$\mu_i = \mu_i^0 + RT\ln a_i. \tag{13.9}$$

This relation defines the activity a_i for the species i. By combining these two equations, we find:

$$J_i = -\widetilde{D}_i \frac{dc_i}{dx}, \tag{13.10}$$

with the chemical diffusion coefficient for the species i:

$$\widetilde{D}_i = D_i \frac{d(\ln a_i)}{d(\ln c)} = D_i K_t, \tag{13.11}$$

where K_t is the Darken or thermodynamic factor for the species i. According the development in ref. [13], the enhancement factor W of the total diffusion throughout the structure is:

$$W = \left[(1 - t_i) \frac{\partial \ln a_i}{\partial \ln c_i} - \sum_{j \neq i,\, e,\, h} t_j \frac{z_i}{z_j} \times \frac{\partial \ln a_i}{\partial \ln c_i} \right], \tag{13.12}$$

where t_i is charge transfer coefficient (or transference number) of the species i. For the case in which only one ionic i and one electronic species e have to be considered, so that $t_e = 1 - t_i$, the diffusion coefficient becomes:

$$\widetilde{D} = D_i^o t_e \frac{\partial \ln a_i}{\partial \ln c_i}. \tag{13.13}$$

If the sample is predominantly an electronic conductor (electronic conductivity large compared with the ionic conductivity), so that $t_e \rightarrow 1$, so that:

$$D = D_i, \tag{13.14}$$

which means that the ionic conductivity is not affected by the electrons. In this case, the electrons respond instantaneously to the motion of the ions to keep local charge neutrality, so that the diffusion is only limited by the motion *f* the ions. On the other hand, if the transference number of the ionic species is much larger than for the electronic species, Eq. (13.12) can be rewritten as:

$$\widetilde{D} = \frac{C_e D_e^o}{z_i^2 C_i} \times \frac{\partial \ln a_i}{\partial \ln c_i}, \tag{13.15}$$

in which the chemical diffusion coefficient for the ionic species is affected by the electronic kinetics. The reason is that the limited diffusion of the electrons implies a delay between the motion of the ions and electrons, which generates an internal electric field and a Coulomb interaction between ions and electrons, so that their motion is interdependent.

The schematic illustration of a single step of the GITT method is shown in Fig. 13.3. An electric current I_o is driven through the galvanic cell by an external

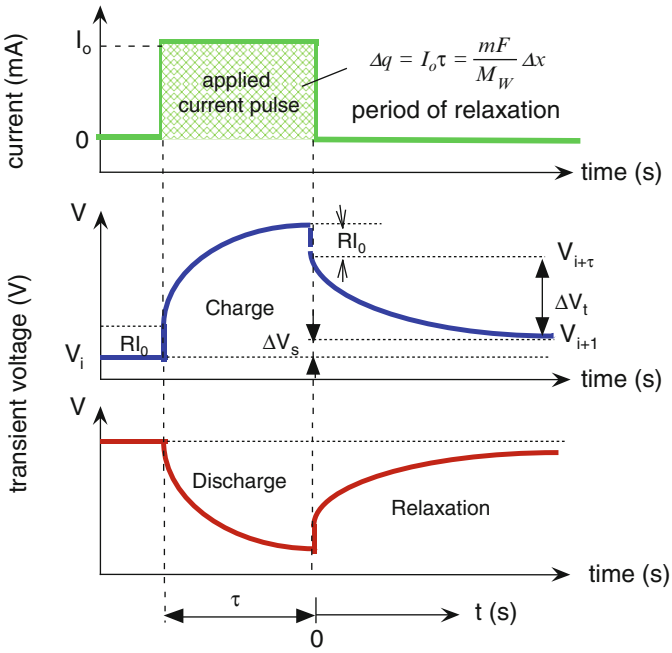

Fig. 13.3 Schematic illustration of the galvanostatic intermittent titration technique (GITT)

source during time interval τ. The change in stoichiometry Δx caused by the coulometric titration is given by the Faraday's law:

$$\Delta x = \frac{I_0 \tau M_w}{zmF}, \tag{13.16}$$

where τ is the duration of the current pulse (see Fig. 13.3).

Thus ΔV_t is the total transient voltage change of the galvanic cell for the applied current I_o. ΔV_s is the change of the steady-state voltage of the cell for this step i [6] as shown in Fig. 13.3 that is:

$$\begin{aligned} \Delta V_t &= V_{i+1} - V_i, \\ \Delta V_s &= V_{i+1} - V_{i+\tau} \end{aligned}. \tag{13.17}$$

The temporal response of the voltage decay is expressed by:

$$\Delta V_t = \frac{I_0 RT}{AF^2 x} W \left[\sqrt{\frac{4t}{\pi \widetilde{D}}} - \frac{t}{L} \right]. \tag{13.18}$$

L is the size of the particles in contact with the electrolyte, also called solid state-diffusion length.

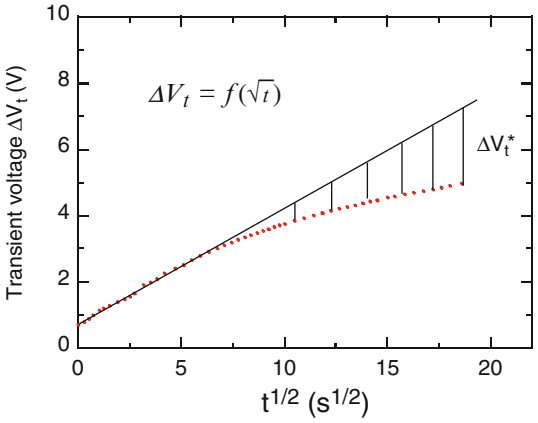

Fig. 13.4 Plot of the transient voltage $\Delta E_t = f(\sqrt{t})$

13.3.2.1 Short Relaxation Time $\left(t \ll L^2/\widetilde{D}\right)$

After a time interval τ, the current flux is interrupted, and the composition within the sample tends to homogenize by diffusion of the mobile species, while the voltage decays because of relaxation of the generated concentration gradient. If ΔV_t vs. $\sqrt{t}$ shows the expected straight line behavior (Fig. 13.4), the diffusion coefficient can be calculated by solving the second Fick's law, because all other quantities are known or measurable:

$$\widetilde{D} = \frac{4}{\pi\tau}\left(\frac{mV_m}{M_w A}\right)^2 \left(\frac{\Delta V_s}{\Delta V_t}\right)^2, \tag{13.19}$$

where A is the area of the sample-electrolyte interface. With the condition $L^2/t\widetilde{D} \gg 1$, an electrode 1 μm-thick and $\widetilde{D} = 10^{-10}\text{cm}^2/\text{s}$ gives $t \ll 100$ s. Note that the enhancement factor is included in the slope of the coulometric titration $\Delta V_s/\Delta x$. From the slope of the linear part (Fig. 13.4) the value of $\widetilde{D}/W^2$ can be found as

$$\frac{\widetilde{D}}{W^2} = \frac{4}{\pi}\left(\frac{I_0 RT}{AF^2 x}\right)^2 \left(\frac{\Delta\left(\sqrt{t}\right)}{\Delta V_t}\right)^2. \tag{13.20}$$

13.3.2.2 Long Relaxation Time $\left(t \gg L^2/\widetilde{D}\right)$

For longer time, the deviations of the linearity (vertical lines in the figure) are then plotted as a function of t. The new overpotential ΔV_t^* is a linear function of time expressed by:

$$\Delta E_t^* = \left(\frac{\partial(\Delta V_t)}{\partial\left(\sqrt{t}\right)}\right)\sqrt{t} - \Delta V_t = \left[\frac{I_o RTW}{AF^2 xL}\right]t + \eta, \tag{13.21}$$

where η is the constant voltage term. Thus, the slope of the new function ΔV_t^* vs. t provides the enhancement factor expressed by:

$$W = \left[\frac{AFxL}{I_o RT}\right]\left(\frac{\partial(\Delta V_t)}{\partial t}\right). \tag{13.22}$$

13.3.3 Electrochemical Impedance Spectroscopy

Li-ion and electrode kinetic studies are also carried out by means of the electrochemical impedance spectroscopy (EIS). Both measurements are currently performed in cells with Li-metal anode as reference electrode. The EIS is done using an impedance/gain-phase analyzer coupled with the battery tester unit. The measurements are usually carried out in the frequency range 350 kHz to 3 mHz with an ac signal amplitude of few mV (typically 5 mV). Figure 13.5 shows the typical impedance spectra (Nyquist plots) obtained for pristine and carbon-coated $LiNi_yMn_zCo_{1-y-z}O_2$ samples. Both of them exhibit a semicircle in the high-frequency region and a straight line (Warburg diffusion) in the low-frequency range (ω <1 Hz). After carbon coating, impedance of the $LiNi_yMn_zCo_{1-y-z}O_2$ particles has markedly decreased and the Warburg component has changed.

The impedance of the cell is the complex quantity, $Z_c = \mathrm{Re}(Z_c) + \mathrm{Im}(Z_c)$, where the real part is the sum of the internal resistance, in practice the sum of the charge transfer resistance R_1 and R_2 at the interface with the two electrodes, plus the Warburg contribution due to diffusive process:

$$\mathrm{Re}(Z_c) = R_1 + R_2 + \frac{\sigma}{\sqrt{\omega}}, \tag{13.23}$$

where σ is the Warburg coefficient, which can be determined as the slope of the straight line obtained by plotting Z_c vs. $\omega^{-1/2}$ in the low-frequency range according

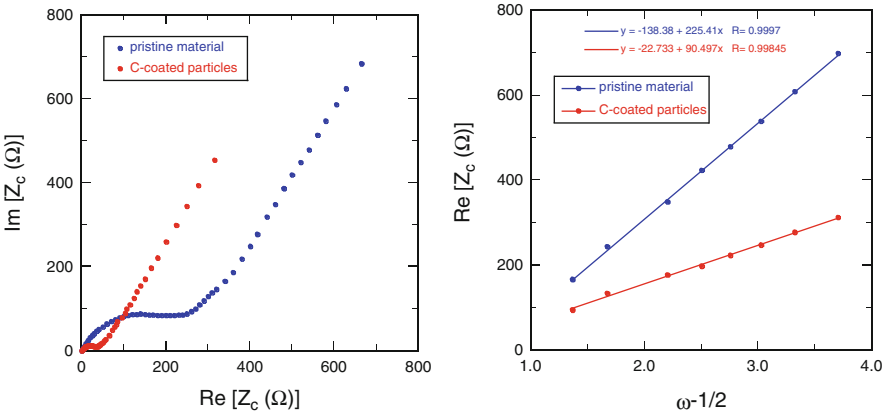

Fig. 13.5 (**a**) Impedance spectra for pristine and carbon-coated $LiNi_yMn_zCo_{1-y-z}O_2$ samples. (**b**) Plots of real part of Z_c vs. $\omega^{-1/2}$. The slope σ is the Warburg coefficient

to (Fig. 13.5b). The diffusion coefficient of ionic species can then be calculated from the equation [15]:

$$\widetilde{D} = \frac{R^2T^2}{2n^4F^4} \times \left(\frac{1}{AC\sigma}\right)^2, \tag{13.24}$$

where R, T and F have their usual meaning. n is the number of electrons per molecule oxidized, A is the surface area of the interface between the particles and the electrolyte, like in the previous section, c is the concentration of Li^+ ions. Note that this relation between the Warburg and the diffusion coefficients is only valid if the diffusion layer has an infinite thickness. In practice, this condition is met if the characteristic time of the experiments is $\omega^{-1} \leq L^2/\widetilde{D}$. It is clear that the diffusion coefficient of Li^+ ions is enhanced by carbon deposit at the surface of particles (Fig. 13.5b). This increase in the diffusivity can be attributed to the increase of the Darken factor which results from the enhancement of the electronic conduction. This effect appears to be favorable for the electrochemical performance of the NMC particles during cycling at high rate.

13.4 Application: Kinetics in MoO_3 Electrode

In this section we present the advantage of the above methods involving only semi-infinite diffusion for the determination of both the chemical diffusion coefficient and the enhancement (or thermodynamic) factor of MoO_3 electrode materials inserted by Li^+ ions. MoO_3 crystals and films are considered [15, 16].

13.4.1 MoO_3 Crystal

Typical discharge–charge curves of a Li//MoO_3 have been shown previously (see Chap. 9). Kinetics measurements performed on anhydrous α-Li_xMoO_3 phase show the fast motion of Li^+ ions in the van der Waals plane of the layered framework. The chemical diffusion coefficient varies from 2×10^{-10} to 6×10^{-11} cm^2 s^{-1} in the compositional range $0.05 \leq x \leq 1.35$ with a maximum value $\widetilde{D} = 1 \times 10^{-9} cm^2 s^{-1}$ at $x = 0.75$, while the enhancement factor varies in the range $1 \leq W \leq 17$ as shown in Fig. 13.6. As the compositional dependence of $\widetilde{D}$ is due to the nature of empty sites in the host, the variation of the chemical diffusion coefficient of Li^+ ions in α-Li_xMoO_3 can be expressed as a quadratic function of x:

$$\widetilde{D} = \beta x^2(1-x) + x\left(1-x^2\right), \tag{13.25}$$

where β is a parameter related to the repulsive interaction energy between alkali ions in the host structure. Note that x from now on will mean the Li concentration,

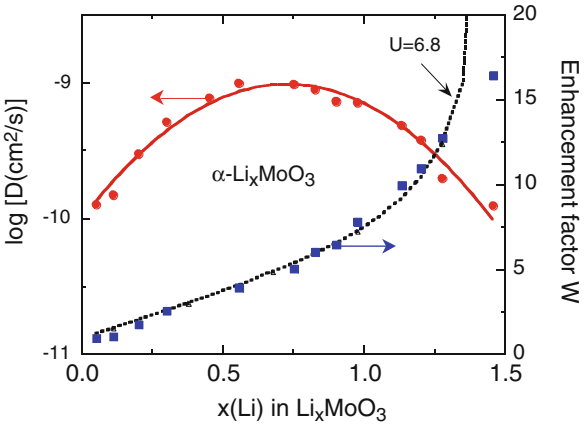

Fig. 13.6 Compositional dependence of $\widetilde{D}$ and W for α-Li_xMoO_3 single crystal

while x was a position in Eqs. (13.8) and (13.10). Since, however, these two equations will not be used in this section, there should not be any confusion. $\widetilde{D}$ shows a maximum value at the half-filling site number [12].

The chemical potential is given by the equation:

$$\mu = \mu_0 + RT\ln a = -FV(x), \tag{13.26}$$

which, combined with Eq. (13.11), gives the enhancement factor under the form:

Combining Eqs. (13.11) and (13.2), we find the expression of the x-dependence of the enhancement factor:

$$W = -\frac{F}{RT}\frac{\partial V}{\partial \ln x} = 1 + \frac{x}{1-x} + Kx. \tag{13.27}$$

This simple expression applied to data of Fig. 13.6, gives the interaction parameter, K, accounting for the electrostatic repulsion between the insertion Li^+ ion. For α-Li_xMoO_3 the result is $K = 6.8$.

13.4.2 MoO_3 Films

Let consider a cathode material with a planar configuration such as MoO_3 thin film for instance, for which the cell voltage vs. Li insertion is given in Fig. 13.7a. MoO_3 films were grown onto silicon wafer by rf-sputtering technique into an evaporation chamber filled with a mixture of argon and oxygen. It appears that optimization of grown parameters include the substrate temperature T_s and the oxygen partial pressure $p(O_2)$.

Figure 13.7a shows that the potential profile depends strongly on the partial oxygen pressure in the deposition chamber. Changes in the standard potential E^0 are

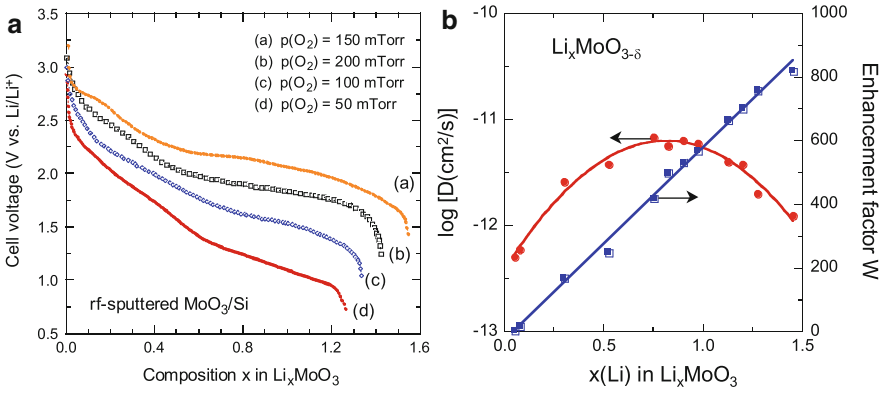

Fig. 13.7 (**a**) Discharge profiles of Li//MoO_3 cells fabricated with rf-sputtered films deposited onto Si wafer in different oxygen ambient. (**b**) x-dependence of the chemical diffusion coefficient and enhancement factor in Li_xMoO_3 films

due to the variation in the stoichiometry of the $MoO_{3-\delta}$ films. With $p(O_2) =$ 150 mTorr, the film composition is close to the ideal stoichiometry with $\delta = 0$. The kinetics of Li^+ ions in Li_xMoO_3 cathode material have been studied in the intercalation range $0 \leq x \leq 1.5$ during the relaxation periods of the discharge [16]. The chemical diffusion coefficient $\widetilde{D}$, the component diffusion D_o, and the enhancement factor (or thermodynamic factor) $W = \widetilde{D}/D_o$ are evaluated using the modified galvanostatic intermittent titration technique (GITT) with a long duration pulse excitation. According to Eq. (13.20), the transient voltage ΔE is a linear function of the square root of time, $\sqrt{t}$, like in Fig. 13.4, and the slope can be used to calculate the chemical diffusion coefficient $\widetilde{D}$ if the thermodynamic factor is known from the cell potential versus x relation.

The x-dependence of the chemical diffusion coefficient $\widetilde{D}$ and the enhancement factor W in Li_xMoO_3 film is shown in Fig. 13.7b. The maximum value of 6.8×10^{-12} cm^2 s^{-1} is obtained at $x = 0.75$ and at higher concentrations $\widetilde{D}$ decreases according to a quadratic law:

$$\widetilde{D} = x(5.3 - 2.8x)10^{-12}. \tag{13.28}$$

In this case, the intercalation process is essentially controlled by the Li concentration in the host lattice. As shown in Fig. 13.7b the thermodynamic factor, W, varies linearly with the degree of Li intercalation from 10 to 820 in the range $0.05 \leq x \leq 1.5$. This x-dependence of W can be associated with the large decrease of the electronic mobility in Li_xMoO_3 film. Considering that MoO_3 films are oxygen-deficient materials, the model of charge transport in internal defect compounds can be applied [14–18]. Defects are Li interstitials, Li*, and conduction electrons, e'. It has been shown [17] that, in a solid solution where no internal defect reactions

occur, the thermodynamic factor is related to the defect concentration (if dilute defects exist) as:

$$W = \Phi_{\mathrm{Li}}^{-1} + \Phi_{e'}^{-1}, \tag{13.29}$$

where $\Phi_{\mathrm{Li}} = c_{\mathrm{Li}^*}/c_{\mathrm{Li}^+}$ and $\Phi_{e'} = c_{e'}/c_{\mathrm{Li}^+}$. Equation (13.29) explains the linear variation of W with the degree of intercalation as shown in Fig. 13.7b. The large increase of W is associated with the decrease of the electronic mobility in the Li_xMoO_3 film.

13.5 Incremental Capacity Analysis (ICA)

13.5.1 Introduction

Thermodynamic data are needed to determine the nature of the intercalation–deintercalation mechanism of electrodes. The concept of electrochemical potential spectroscopy (EPS) was introduced in 1979 by Thomson [7] taking detailed data related to both kinetic and thermodynamic parameters in a single, slow voltage cycle. EPS is also referred as incremental capacity analysis (ICA) or differential voltage analysis (DVA). OCV data often reflect battery aging and performance degradation [19]; by using the ICA technique [10], which differentiates the battery charged capacity (Q) with respect to the terminal voltage (V) and transforms voltage plateaus on the $V - Q$ (voltage-charged vs. capacity) curve into clearly identifiable dQ/dV peaks on the differential capacity curve, gradual changes in cell behavior can be detected, based on life cycle test data, with greater sensitivity than those based on conventional methods.

The redox potential of insertion electrodes is normally represented by the derived form of Eq. (3.12), which, when $K = 0$, can be written under the form:

$$\frac{dx}{dV} = \frac{F}{RT}x(1-x). \tag{13.30}$$

Equation (13.30) predicts an S-shaped potential curve as a function of moles of species involved in the insertion process. In such a case, (dx/dV) defines the capability of storing or delivering charge at a potential V. In practice, however, the interaction K-term is not negligible, so that the full Eq. (13.2) must be written at each incremental step i, letting K depend on i, since the interaction may depend on the lithium concentration. To make contact with [20, 21], we use their notations, and write the electrode potential for $x_{i-1} < x_i < x_{i+1}$ under the form:

$$V(x) = V_{0i} - \frac{RT}{F}\ln\left(\frac{x_i}{1-x_i}\right) - \frac{z\phi_i}{F}(1-2x_i), \tag{13.31}$$

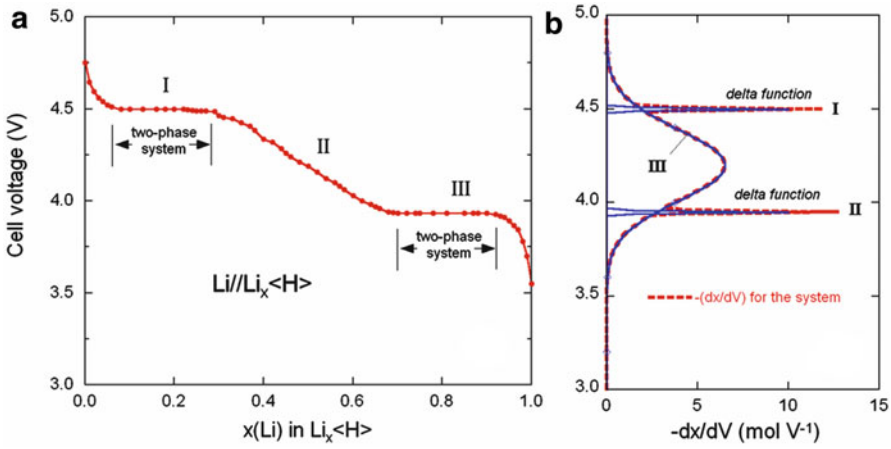

Fig. 13.8 (**a**) Voltage-composition profile for the solid-state redox reaction of an insertion compound $Li_x < H >$ showing three potential region and (**b**) corresponding differential capacity (dx/dV) curve

which is just Eq. (13.2) with $\phi_1 = -K_i/(2z)$, so that, now, ϕ_i is the interaction energy ($\phi_i < 0$ repulsive and $\phi_i > 0$ attractive), z is the number of nearest neighbor sites, x_i is the ratio of occupied sites to available sites of a given energy in a system, and V_{0i} is the standard potential given at $x = 1/2$ for the ith redox couple. Therefore:

$$\frac{dx_i}{dV} = -\left[\frac{RT}{F}\frac{1}{x_i(1-x_i)} - \frac{2z\phi_i}{F}\right]^{-1}. \tag{13.32}$$

Figure 13.8 displays the analytical result of redox potentials observed for an insertion compound $Li_x < H >$ including two plateaus separated by an S-shaped solid-solution reaction that is the typical situation of Li_xMO_2 electrodes (M = Co, $Ni_{0.5}Co_{0.5}$ or Ni). In such a layered framework, a $[2 \times 2]$ sublattice with respect to a basal triangular lattice is most probable due to the occupation of Li ions at all the $[2 \times 2]$ sublattice sites giving the composition $Li_{0.25}MO_2$ and $Li_{0.75}MO_2$ (Fig. 13.8b) owing to a particle–hole interaction [21]. As the system shown in Fig. 13.8 can be decomposed into three parts, this situation is formulated using the general principle of superposition of states. Consequently, the normalized concentration x in Li_xMO_2 at potential $V(y)$ is given by:

$$x = \int_{\infty}^{V} \sum_{i=1}^{3} \left(\frac{\partial x_i}{\partial V}\right) dV. \tag{13.33}$$

The parameters obtained from the analytical data of Fig. 13.8 are $V_{01} = 4.50$ V and $z\phi_1/F = +0.25$ V for system I, $V_{02} = 4.18$ V and $z\phi_2/F = -0.25$ V for the system in the composition range II, and $V_{03} = 3.91$ V and $z\phi_3/F = +0.25$ V in the composition

range III. The interaction-energy parameters are thus attractive in both regions I and III. In this following, we illustrate the investigations of ICA of positive and negative electrodes by considering the mechanism of lithium-ion insertion in their frameworks; $Li_xV_6O_{13}$, $Li_{1-x}NiO_2$, $Li_{1-x}Ni_{1/2}Mn_{1/2}O_2$, $Li_3V_2(PO_4)_3$ and silicon nanowires are considered. We also present the estimation of the state-of-health (SOH) of Li-ion full cell by considering the cycle life of a $LiFePO_4$//graphite battery.

13.5.2 Incremental Capacity Analysis of Half Cell

13.5.2.1 V_6O_{13}

The use of V_6O_{13} as active material for positive electrodes in secondary lithium batteries was first suggested in 1979 by Murphy et al. [22]. The property most in favor of V_6O_{13} is the high stoichiometric energy density 0.89 Wh g^{-1}. However, when highly lithiated $Li_6V_6O_{13}$ is a poor electronic conductor [23]. Therefore, the addition of electronically conductive material, e.g., graphite or carbon is mandatory, which reduces the practical energy density. The structure of V_6O_{13} contains edge-shared octahedra forming single and double zig–zag chains linked together by further edge sharing. The resulting sheets (single and double) are interconnected by corner sharing, thus giving a 3-D framework [24]. This structure contains tri-capped cavities joined through shared square faces. The three open faces of the cavity should permit lithium-ion diffusion along (010) with the possibility of exchange between pairs of adjacent channels.

Figure 13.9 shows the first discharge–charge characteristics of a Li//V_6O_{13} cell. The lithium insertion reaction, 1Li per V atom, is found to be reversible in the

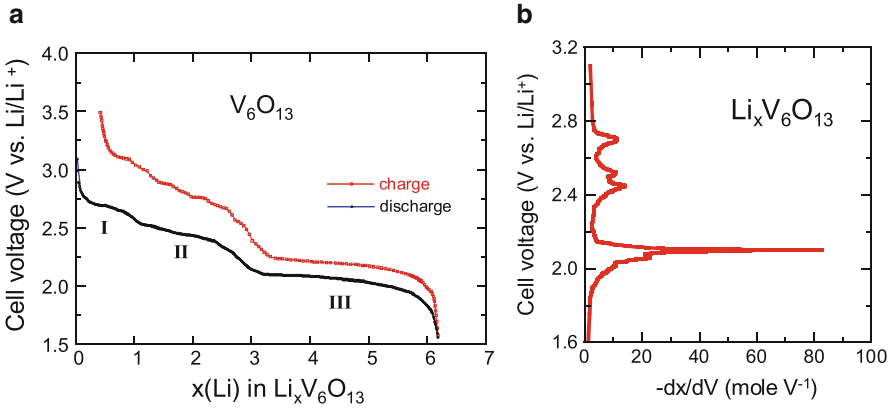

Fig. 13.9 (**a**) First discharge–charge curve of Li//V_6O_{13} cell. (**b**) Incremental capacity of Li insertion in V_6O_{13}

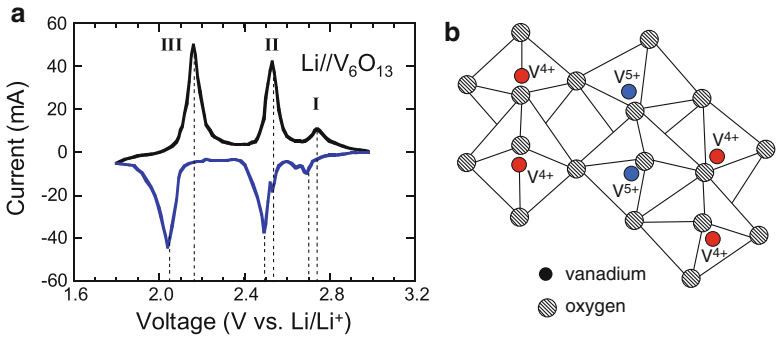

Fig. 13.10 (**a**) Voltammogram of Li//V_6O_{13} cell recorded at sweep rate 10 μV/s. The current is normalized as dQ/dV, assuming that the composition at 2.2 V vs. Li^0/Li^+ is $Li_4V_6O_{13}$. (**b**) Schematic representation of the crystal structure of V_6O_{13} showing the nonequivalent vanadium sites

voltage range 3.2–1.5 V. Theoretically the maximum limit of lithium uptake by the stoichiometric V_6O_{13} structure is believed to be 8 per formula unit as determined by the available electronic sites rather than the structural cavities [25]. The limit corresponds to a situation when all the vanadium ions are present in the trivalent V^{3+} state. As a function of the stoichiometry, the maximum uptake goes to 1.35Li for $VO_{2.18}$ oxide. As pointed out by West et al. [6], the structure of V_6O_{13} can be also visualized as a stack of VO_2(B) and α-V_2O_5 sheets joined at octahedra corners; so, V_6O_{13} can be considered as an intergrowth of single (α-V_2O_5) and double (VO_2(B)) layers of VO_6 octahedra. The discharge curve (insertion reaction) occurs in three steps that correspond to the reduction of V cations. As the pristine material can be expressed $\left[V_4^{4+}V_2^{5+}\right]O_{13}$, the final product of the insertion reaction $Li_6\left[V_4^{3+}V_2^{4+}\right]O_{13}$ implies three steps in the voltage profile, associated to the insertion of Li at different lattice sites, accompanied with the reduction $V^{5+} \rightarrow V^{4+}$, $V^{4+} \rightarrow V^{3+}$ (Fig. 13.10). In particular, the large plateau at 2.1 V is attributed to the $V^{4+} \rightarrow V^{3+}$ reduction process [26].

13.5.2.2 $LiNiO_2$

The layered transition-metal oxides such as $LiCoO_2$ (LCO) and $LiNiO_2$ (LNO) are the most attractive cathode materials for the rechargeable lithium batteries, because they have high specific capacity (273 mAh g^{-1}), high operating cell voltage (~4 V), and excellent rechargeability. The $LiNiO_2$ is a more attractive choice because of lower cost as compared with that of $LiCoO_2$. $LiNiO_2$ crystallizes in the layered rock-salt structure (α-$NaFeO_2$-like structure). This structure is based on the close-packed network of oxygen atoms with the Li^+ and Ni^{3+} ions ordering on alternating (111) planes of the cubic rock-salt structure. This (111) ordering introduces a slight distortion of the lattice to hexagonal symmetry with cell constants $a = 2.816$ Å and

$c = 14.08$ Å [27]. The structure of layer-like $LiNiO_2$ is constituted by packing of $(NiO_2)^{2-}$ slabs with Li^+ inserted within the interslab space. A study of the electronic and magnetic properties of the Li_xNiO_2 system has been recently reported by Dutta et al. [28]. This material behaves as a small-polaron semiconductor with holes in the $Ni^{4+/3+}$ couple and a massive Ni-O covalent mixing.

The formation of low lithium content Li_xNiO_2 ($x < 0.2$) causes cycle life failure. In addition, the material becomes highly catalytic toward electrolyte oxidation and some of the nickel ions may migrate to lithium sites. The formation of pure LNO is difficult, and residual Ni^{II} (up to 1–2 %) exists between the NiO_2 slabs. In fact, the first cycle irreversibility during charge–discharge is mainly related to the amount of Ni^{II} between the slabs of NiO_2, which requires extra charge for oxidation to higher valency state, when electrolyte decomposition is controlled. Through careful synthesis and adjustment of lithium concentration in the material during heat treatment, we obtained $LiNiO_2$ very close to stoichiometry. Figure 13.11a shows first charge–discharge profile of the LNO cathode cycled at current density 0.1 mA cm^{-2}. The total irreversibility of the first cycle is an indicative of the stoichiometric compound with negligible amount of Ni^{II} in the lithium layer.

The voltamogram (Fig. 13.11b) shows that various phase transitions occur upon Li extraction from $Li_{1-x}NiO_2$. Zhong and von Sacken have shown that $LiNiO_2$ charged to 4.1 V vs. Li^0/Li^+ can deintercalate $x = 0.7$ [29]. The reaction mechanism is explained in terms of topotactic process: hexagonal R-3m $LiNiO_2$ is oxidized to NiO_2 (R-3m, $a = 2.81$ Å, $c = 13.47$ Å) via $Li_{1-x}NiO_2$ ($0.25 \leq x \leq 0.55$) having monoclinic lattice ($C2/m$) [30]. Ordered structures for Li_yNiO_2 have been experimentally reported at $y = 0.25$; 0.33 and $y = 0.63$ [31]. Additional Li can be removed above 4.1 V but this degrades cell performance because the cathode structure is destabilized beyond $x = 0.7$. In an overcharged $Li_{1-x}NiO_2$ cathode most of the Ni atoms are in the unstable Ni^{4+} state. Manthiram et al. [32] have shown that $Li_{0.5}NiO_2$ is unsafe because this oxide can transform to cubic spinel-like structure under mild heating at 150 °C.

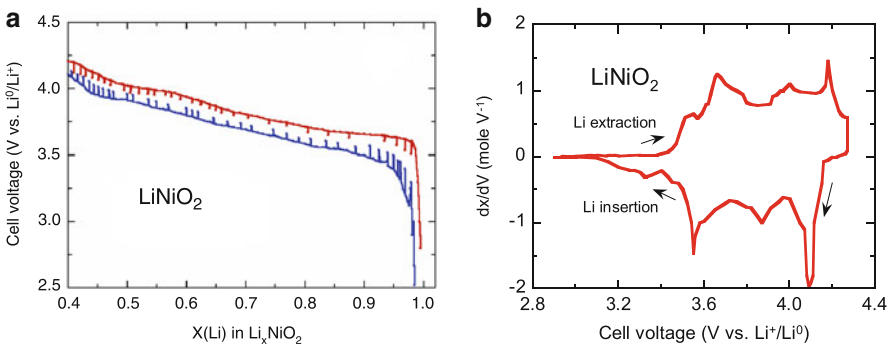

Fig. 13.11 (**a**) Charge–discharge profile of Li//$LiNiO_2$ electrochemical cell. Current density of 0.1 mA/cm^2 in 1 *M* $LiPF_6$ + 65/35 EC-DMC. (**b**) Voltammogram of Li//$LiNiO_2$ cell recorded at sweep rate 10 μV/s

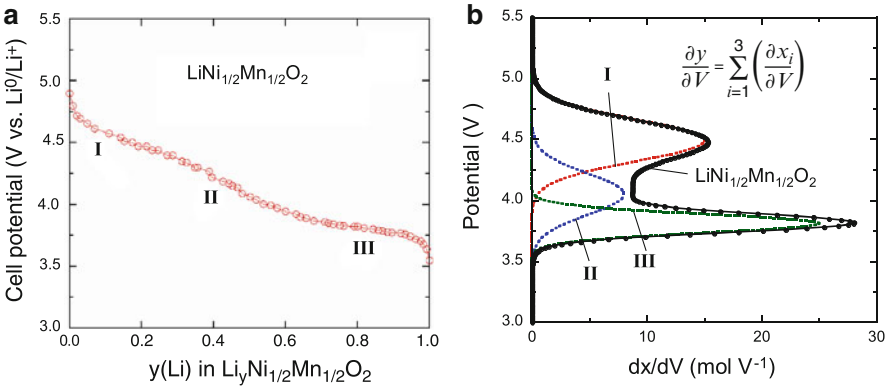

Fig. 13.12 (**a**) Discharge vs. composition curve of $LiNi_{0.5}Mn_{0.5}O_2$ cathode material. (**b**) Incremental capacity curve showing the three regions of the redox reaction

13.5.2.3 $LiNi_{0.5}Mn_{0.5}O_2$

Lithium nickel manganese oxides without cobalt have been investigated as cathode materials for advanced lithium-ion batteries [33]. Koyama et al. [34] have shown that $LiNi_{0.5}Mn_{0.5}O_2$ is a stable compound consisting of Ni^{2+} and Mn^{4+}, not a solid solution of $LiNiO_2$ and $LiMnO_2$, whereas $LiCo_{0.5}Ni_{0.5}O_2$ is a one-to-one solid solution of $LiCoO_2$ and $LiNiO_2$. As shown in Fig. 13.12, the solid-state redox reaction of $LiNi_{0.5}Mn_{0.5}O_2$ can be presented by decomposing the incremental capacity curve into three parts at $y = 1/3$, 1/2 and 2/3 in $Li_xNi_{0.5}Mn_{0.5}O_2$, which are characterized by redox levels at 4.49, 4.05, and 3.81 V vs. Li^0/Li^+. Using Eq. (13.29) the negative interaction parameters of $z\phi_i/F$ mean repulsive interaction, i.e., one-phase reaction over an entire range. Similarly, one observes three redox levels in $LiNiO_2$ and $LiNi_{0.5}Co_{0.5}O_2$ systems but at different voltages that are 4.23, 3.93 and 3.63 V for $LiNiO_2$ and 4.58, 4.05, 3.58 V for $LiNi_{0.5}Co_{0.5}O_2$. Note that (1) the solid-state redox reaction for $LiNiO_2$ formally consists ofNi^3+/Ni^{4+}, while that for $LiNi_{1/2}Mn_{1/2}O_2$ seemingly consists of Ni^2+/Ni^{3+} and Ni^{3+}/Ni^{4+} and (2) The average voltage of 4.10 V for $LiNi_{1/2}Mn_{1/2}O_2$ is higher than 3.90 V for $LiNiO_2$.

13.5.2.4 $Li_3V_2(PO_4)_3$

The monoclinic lithium vanadium phosphate $Li_3V_2(PO_4)_3$ exhibits an excellent reversibility when the charge extracted is limited to the value equivalent to two Li per formula unit. The extraction of the last lithium is observed at a potential greater than 4.6 V vs. Li^0/Li^+ and involves a significant overvoltage [35]. In $Li_xV_2(PO_4)_3$, the $V^{3+/4+}$ redox couple takes place in the range $x = 1$–3.

Both voltage profile and incremental capacity are shown in Fig. 13.13. The experimental titration curve for $LiV_2(PO_4)_3$ displays three regions, which span in the composition ranges: $x_1 = 0$–0.5, $x_2 = 0.5$–1, and $x_3 = 1$–2 in $Li_{(3-x)}V_2(PO_4)_3$,

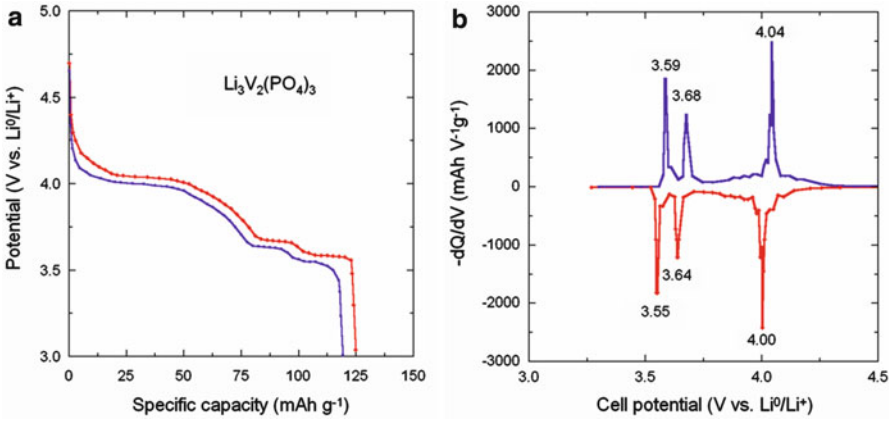

Fig. 13.13 (**a**) Discharge–charge curve vs. composition of monoclinic $Li_3V_2(PO_4)_3$ cathode material recorded at *C*/20 rate. (**b**) Incremental capacity curve showing the three regions of the redox reaction. Numbers are the redox potential in volt

respectively. In each region, plateaus are observed, substantiating the two phase character of the electrochemical redox reaction with little lithium solubility in each phase. Under the low current regime used (*C*/20), the first two Li ions are extracted at an average voltage of 3.64 and 4.09 V vs. Li^0/Li^+, respectively. In turn, the first lithium is removed in two steps, i.e., 3.61 and 3.69 V vs. Li^0/Li^+. The second lithium; however; is extracted over one single step, 4.09 V vs. Li^0/Li^+. Almost all of the lithium ions equivalent to 2 mol per formula unit have been extracted ~125 mAh g^{-1} for a theoretical of 133 mAh g^{-1}. Both plateaus correspond to lithium extraction associated with the $V^{3+/4+}$ redox couple.

13.5.2.5 Silicon Nanowires

Silicon is currently investigated as a replacement for graphite for the negative electrode of Li-ion batteries (see Chap. 10). The incorporation of 4.4 Li atoms per Si provides a specific discharge capacity of 4200 $mAhg^{-1}$ in the relatively low potential below 0.5 V. An important feature of Si anode materials is the large inherent change in specific volume (up to about 400 %) during the insertion and extraction of large amounts of Li ions. This causes pulverization or crumbling, and a loss of electrical contact between the active material and the current collector. The result is a reduction in the effective capacity during cycling. A adequate way to accommodate the large volume evolution is the use of nanosized particles such as Si nanowires [36] and nanoporous Si [37] (see Chap. 10 devoted to anodes).

Electrochemical potential spectroscopy was successfully used to study the differential capacity *dQ*/*dV* as a function of potential in the silicon nanowires (SiNw) that provides information about the structural transformations during lithiation and delithiation. The voltage vs. capacity profile and the corresponding

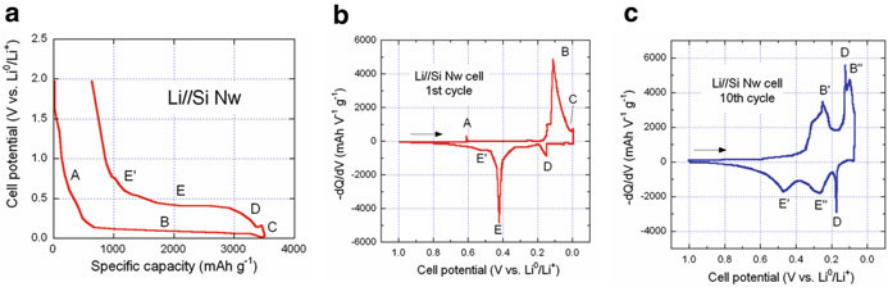

Fig. 13.14 Electrochemical features of Si nanowires. (**a**) Potential vs. specific capacity profile, (**b**) *dQ*/*dV* curve for the first cycle and (**c**) *dQ*/*dV* curve for the 10th cycle that shows the amorphization of the material

dQ/*dV* vs. voltage curves are shown in Fig. 13.14. During the charge (Li insertion), a small peak (noted A) is observed at 0.62 V and a larger peak (noted B) at 0.125 V (Fig. 13.14b). The peak at 0.62 V has been reported to be due to SEI formation on the Si surface, whereas the peak at 0.125 V is a two-phase region where crystalline Si (c-Si) reacts with Li to form an amorphous lithium silicide, a-Li_xSi. During the discharging (Li extraction) process, two peaks (D and E) are observed in the differential capacity curve, which correspond to plateaus in the voltage vs. capacity curve. The two-phase region at E looks similar to the reported [38] delithiation of crystalline $Li_{15}Si_4$ to form amorphous Si. After few cycles, the *dQ*/*dV* curve (Fig. 13.14c) shows that the crystalline Si has been converted to amorphous Si. During the charge, lithiation into the amorphous Si occurs in two sloping single-phase regions, as indicated by B′ and B″. Chan et al. [39] reported the a-$Li_x'Si$ and a-$Li_{(x'+x'')}Si$ phases to identify the phases formed at B′ and B″, respectively. Below 50 mV, the same transformation to a-Li_ySi occurs and delithiation of this phase occurs in a two-phase region.

13.5.3 ICA and DVA of Full Cell

Recently incremental capacity analysis (ICA) has been demonstrated [40–43] to be explicitly capable of identifying degradation mechanism in combination with high fidelity and accurate computer model simulation. The ICA is a method widely used to highlight the different areas in a voltage profile where the voltage derivative with respect to capacity is plotted as a function of capacity. Following the cell voltage relation to electrode voltage:

$$V_{\text{cell}} = V_{\text{cathode}} - V_{\text{anode}}, \tag{13.34}$$

and the definition of individual electrode ICA:

$$\mathrm{ICA}_{\mathrm{anode}} = \frac{dQ_{\mathrm{anode}}}{dV_{\mathrm{anode}}} = f(V), \tag{13.35}$$

$$\mathrm{ICA}_{\mathrm{cathode}} = \frac{dQ_{\mathrm{cathode}}}{dV_{\mathrm{cathode}}} = f(V), \tag{13.36}$$

the cell ICA is a linear combination of the two according to:

$$\mathrm{ICA}_{\mathrm{cell}} = \left[\frac{1}{\mathrm{ICA}_{\mathrm{cathode}}} - \frac{1}{\mathrm{ICA}_{\mathrm{anode}}}\right] = f(V). \tag{13.37}$$

Several reports have shown the strength of ICA for the evaluation of the on-board state of health monitoring of lithium-ion batteries [44, 45] has illustrated advancement in applying ICA (or DVA) to decipher aging and degradation mechanisms on large format commercial $LiFePO_4$-based lithium-ion cells. The incremental capacity signature at $C/25$ (Fig. 13.15) are consistent with the characteristics of a typical graphite—$LiFePO_4$ chemistry [46] in which the staging phenomena can be clearly identified. In the negative electrode, the lithium intercalation transforms C to LiC_6 in at least five distinct staging processes (which transform one stage compound to another). A peak in the ICA spectrum denotes a flat region in a voltage profile. For

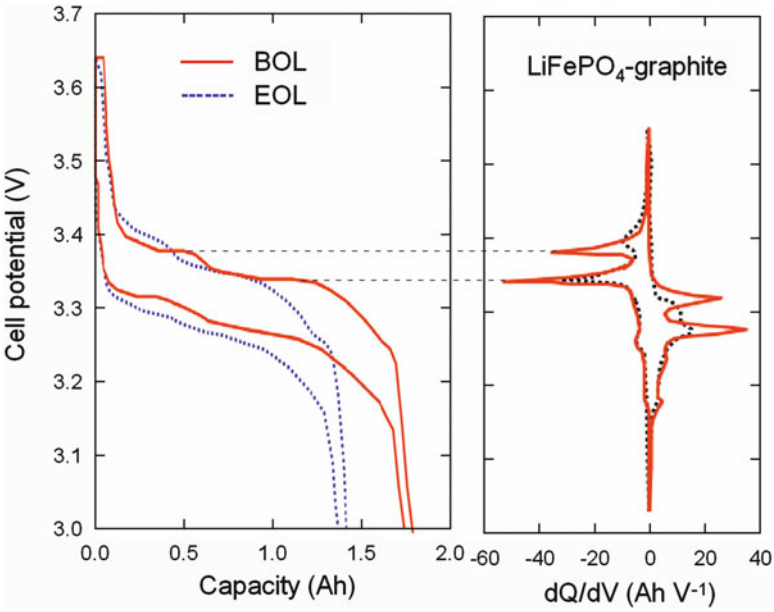

Fig. 13.15 ICA of $LiFePO_4$//graphite full cell at BOL and ECL. The 18650-type battery was charge and discharge at $C/25$ rate. Cell aging is clearly identified by the ICA curve at the beginning-of-life (BOL) compared with that at the end-of-life (EOL)

voltage profile recorded at sufficiently low current rate, it is possible to distinguish the different voltage plateaus associated to the staging of the graphite anode (Fig. 13.15) as peaks at defined voltage levels. A symmetric reduction of the peak intensity is an indication of an aging regime where the cell is symmetrically aged as expected if the activity of both anode and cathode materials is lost at the same rate, thereby causing a loss of total cell capacity. In the example shown in Fig. 13.15, the peaks at 3.35–3.38 V for are significantly affected during aging.

Similarly, the full cells can be characterized in terms of differential voltage using a low rate ($C/25$) for capacity vs. voltage measurement. These data are then analyzed in terms of their time dependence and by differential voltage (dV/dQ) analysis to elucidate some of the capacity fade mechanisms in the cells. Then the voltage of a cell (Eq. 13.36), the derivative of voltage with respect to capacity, dV/dQ, is well suited for graphical analysis of battery; (dV/dQ) cell can be written as:

$$\left(\frac{dV}{dQ}\right)_{\text{cell}} = \left(\frac{dV}{dQ}\right)_{\text{cathode}} - \left(\frac{dV}{dQ}\right)_{\text{anode}}. \tag{13.38}$$

That is, the contributions from the anode and cathode electrodes add linearly. This is in contrast with the way the contributions add when using dQ/dV given in Eq. (13.37).

In a dV/dQ curve, the peaks are from phase transitions, whereas the peaks in a dQ/dV curve are from phase equilibrium. At equilibrium, two or more coexisting phases have the same lithium chemical potential. Thus, $dV = 0$ at equilibrium, making dQ/dV undefined. On the other hand, dQ is never zero using a constant-current discharge or charge. The peaks in the dV/dQ curves were assigned to the positive electrode, to the negative electrode, or to their sum by comparison with half-cell data. In the work that follows, we continue the discussion of the technique and show how to use dV/dQ analysis in a case where side reactions occur at the negative electrode [47–51].

13.6 Transport Measurements in Solids

The first parameter to determine in experiments is the free carrier concentration, n or p. The direct measurement is based on the Hall effect. We discuss this effect in the first section. However, this type of measurement requires that we can make ohmic contacts on the sample. It is not always possible even on “big” well-crystallized samples, and it becomes very difficult if not impossible on nanoscopic powders, in which case optical spectroscopy is the tool that may be used to determine n or p.

13.6.1 Resistivity Measurements

The simplest way to measure the resistivity of a solid material is to cut a bar-shaped sample, and to make separate current contacts on the short edges and voltage contacts on the surface, as shown in Fig. 13.16. The use of four terminals ensures that the measured voltage does not include the voltage drop due to the current contacts. The resistivity is given by:

$$\rho = \frac{V_C - V_D}{i} \frac{S}{l_{CD}}, \tag{13.39}$$

where l_{CD} is the distance between points C and D and S is the cross-section of the sample in the direction of the current flow. The possible contribution of thermoelectric effect can be eliminated by inversion of the current flow is strongly advisable. Note that a precise knowledge of the placement of the contacts and of the sample geometry is requested. This is a strong limit to the technique when the material under study is difficult to cut with great precision. Moreover, for Eq. (13.42) is valid only if the current density is equal on each point of the sample cross-section and the equipotentials are parallel to the current electrodes.

13.6.2 Hall Effect

Suppose we can make ohmic contacts on a sample. The idea is make a direct measurement of the electric current j_x that crosses the sample when an electric field is applied in a direction x. A uniform magnetic field H is applied in the direction z, which creates a voltage measured in the direction y. The scheme is given by Fig. 13.17.

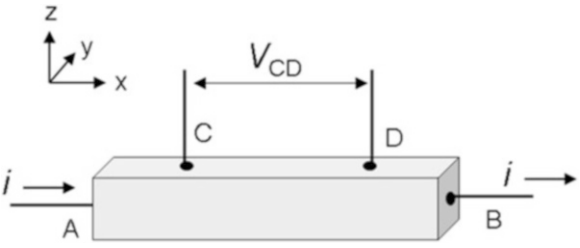

Fig. 13.16 Conventional four-probe method for the measurement of the resistivity. Current is injected through contact A and drained from contact B. The voltage drop is measured between contact C and D

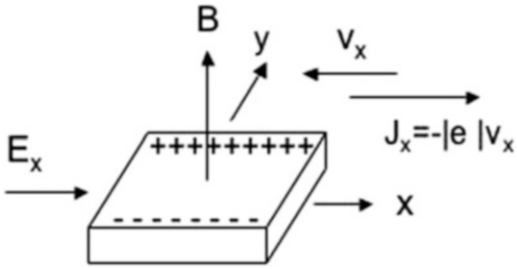

Fig. 13.17 Principle of the Hall effect

Consider the case where we have a concentration n of electrons in the sample. Since they are submitted to the electric field supposed to be in the direction $+x$, they acquire a drift velocity v in the direction $-x$. The Lorentz force applied to the electrons is $-|e|\vec{v} \wedge \vec{B}$ which is then along the direction $-y$, which in turn creates an electric field E_y in the y-direction, hence an accumulation of charge at the edges of the sample in the y direction (Fig. 13.13). The resulting electric potential opposes the motion of the electrons due to the Lorentz force, and at equilibrium, the current along y must vanish due to the exact compensation between the Lorentz force and the electric force eE_y according the relation:

$$-|e|\left(\vec{E}_y + \vec{v} \wedge \vec{B}\right) = 0 \Rightarrow E_y = v_x B. \tag{13.40}$$

Since $j_x = -|e|nv_x$, we find $\frac{E_y}{j_x B} = R_H = -\frac{1}{n|e|}$. We measure $E_y = V/L_y$ with L_y the dimension of the sample in this direction. B is known; j_x is the current that can be deduced from measurement of the conductivity, so that the Hall coefficient R_H can be readily obtained. For electrons, R_H is negative, but if the free carriers are holes, $R_H = 1/(p|e|)$. Therefore the Hall constant gives directly the carrier concentration, but also the sign of the Hall coefficient tells whether we have electrons of holes. In addition, once n or p is known from R_H, we can deduce the mobility μ_e or μ_p from j_x.

If there are both electrons and holes, the situation is more complex, but still it is possible to deduce the four parameters n or p, μ_e, μ_p. The price to pay to determine these four parameters instead of the two that we have with only one type of carrier is that both the conductivity and Hall coefficient must now be measured as a function of the magnetic field [52]. Theoretically, two electrodes along y at both ends should be sufficient to measure E_y. In practice, however, we need to duplicate them, and have 4 contacts. The reason is that it is not possible to have two contacts exactly along the y axis, so that we measure not only the voltage due to E_y, but also a parasitic tension associated to E_x due to the nonsymmetrical contact placement. Sample shape may also be a problem, since we have made the calculation for an ideal parallelepiped sample. The most common way to control these problems is to acquire two sets of Hall measurements, one for positive and one for negative magnetic field direction, and have four contacts instead of two. Then the experimental procedure to be used is detailed in [53]. Sometimes, it is more convenient to measure a layer or sheet conductivity than bulk conductivity. In that case, use the Van der Pauw technique, which is also based on the Hall effect [54].

13.6.3 Van der Pauw Method

The advantage of the van der Pauw technique is that it allows resistivity measurements avoiding problems due to the nonclassical bar- or bridge-shaped geometry of sample (Fig. 13.18). The technique was developed in order to measure the resistivity (and the sheet resistance) of thin and flat samples of semiconductors.

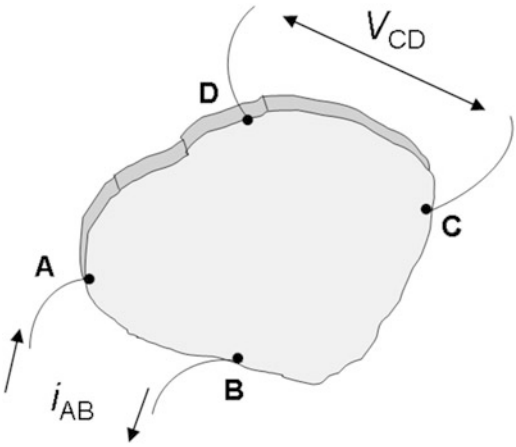

Fig. 13.18 Disposition of the contacts on the edge of an arbitrarily shaped sample, as in the van der Pauw technique. The current flows from A to B and the voltage is measured across C and D: the resistance $R_{AB,CD}$ is given by $(V_D - V_C)/i_{AB}$

Van der Pauw [30] showed that determination of the resistivity of samples of arbitrary shape requires: (1) the contacts realized on the edge of the specimen, (2) the contact sufficiently small (point-like), (3) the sample with homogeneous thickness d, and (4) the sample without isolated holes (surface connected). Fulfilled conditions allow the van der Pauw theorem:

$$\exp\left(-\pi\frac{R_{AB,CD}d}{\rho}\right)+\exp\left(-\pi\frac{R_{BC,AD}d}{\rho}\right)=1, \tag{13.41}$$

where

$$R_{AB,CD}=\frac{V_D-V_C}{i_{AB}}, \tag{13.42}$$

and i_{AB} is the current fed in the specimen through A and drained from B. A similar relation defines $R_{BC,AD}$. Currently, the absence of contact symmetry, requests dual measurements $R_{BC,AD}$ and $R_{AB,CD}$; thus the resistivity is written in the form:

$$\rho=\frac{\pi d}{\ln 2}\frac{R_{AB,CD}+R_{BC,AD}}{2}\times f\left(\frac{R_{AB,CD}}{R_{BC,AD}}\right), \tag{13.43}$$

where the correction function f expressed from Eq. (13.46) can be deduced from the graph in Fig. 13.19 [54–56].

Using the van der Pauw method of conformal mapping with the contacts, A, B, C, and D placed successively along the periphery of a sample, the Hall coefficient is given by [57]:

$$R_H=d\Delta(R_{BD,AC})/H. \tag{13.44}$$

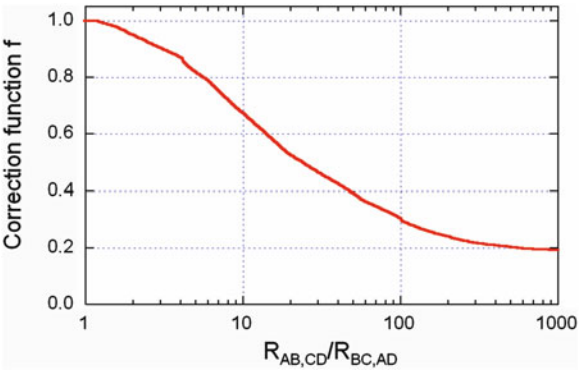

Fig. 13.19 Graph of the correction function vs. the ratio of measured resistances $R_{AB,CD}/R_{BC,AD}$

Here $R_{BD,AC}$ is the potential difference V_{AC} between contacts A and C per unit current between contacts B and $\Delta(R_{BD,AC})$ is the change in $R_{BD,AC}$ due to a magnetic field H applied perpendicular to the plane of the sample (Fig. 13.14). The van der Pauw technique has been successively applied to study the semiconducting properties of lithium intercalation compounds [58–61].

13.6.4 Optical Properties

If ohmic electric contacts cannot be obtained, the solution is provided by optical properties. An example has been provided in Chap. 4. So far, we had only considered static properties; now we have to investigate the response of the semiconductor to an electromagnetic wave of angular frequency $\omega : E(t) = E(\omega)e^{-i\omega t}$. The equation of motion of the electron is still given by the dynamics law:

$$m\frac{dv}{dt} = eE(t) - \frac{mv}{\tau}, \tag{13.45}$$

with τ the relaxation time. The response of the electron to this excitation is at the same frequency: $v(t) = v(\omega)e^{-i\omega t}$, and Eq. (13.45) gives:

$$p(\omega) = mv(\omega) = \frac{e\tau E(\omega)}{1 - i\omega\tau}. \tag{13.46}$$

The electric current generated this electromagnetic wave is: $j(t) = nev(t) = \sigma(t)E$, with σ the conductivity:

$$\sigma(t) = \frac{ne^2\tau}{m(1 - i\omega\tau)}. \tag{13.47}$$

If $\omega\tau \ll 1$, we recover the Ohm's law, as expected. Otherwise, friction prevents the electron from "following" the field: the imaginary part in Eq. (13.47) implies an out-of-phase response of the electron gas. If we consider the trajectory of the electron, we write that the position x of the electron oscillate at the same frequency, i.e., $x(t) = x(\omega)e^{-i\omega t}$ so that $v(t) = dx/dt = -i\omega x(t)$, which can be inserted in Eq. (13.46) to obtain:

$$x = -\frac{e\tau E}{m(i\omega + \omega^2\tau)}. \tag{13.48}$$

This displacement means a polarization of the medium:

$$P = nex = -\frac{ne^2/m}{\omega^2 + i\omega/\tau}E, \tag{13.49}$$

and thus a displacement field $D = \varepsilon_0 E + P$, which enters in the Gauss's law $\nabla \cdot D = \rho_f$ of the Maxwell equations, with ρ_f is the density of free charges. After Eq. (13.49), the dielectric constant $\varepsilon = D/E$ is then:

$$\varepsilon = 1 - \frac{\omega_p^2}{\omega^2[1 + i/(\omega\tau)]}, \tag{13.50}$$

with ω_p the plasma frequency: $ne^2/m\varepsilon_0$. Equation (13.50) is the Drude–Zener formula. We have written the equations (and thus ω_p) in the international system of units (MKSA). However, in solid-state physics, this system of units is never used. Instead, the system of units that is used is cgs units in which we set $4\pi\varepsilon_0 = 1$. Therefore, the expression usually reported in books on this subject (and papers) is obtained by the formula we have displayed, in which ε_0 is replaced by $1/4\pi$:

$$\omega_p{}^2 = \frac{4\pi ne^2}{m}. \tag{13.51}$$

It is important to remember the system of units when some numerical application is needed. To avoid any problem linked to the units, you may simply use the formula:

$$\omega_p/2\pi \approx 0.9 \times 10^4 n^{1/2}, \tag{13.52}$$

with n in cm^{-3}, the result is in Hz.

13.6.4.1 Limit $\omega\tau >> 1$ for the Free Electron Gas (No Mixing with Phonons)

The high frequency limit is the case $\omega\tau >> 1$, in which case Eq. (13.50) reduces to:

$$\varepsilon = 1 - \frac{{\omega_p}^2}{\omega^2}. \tag{13.53}$$

To explore Eq. (13.53), we have to remember some basics on optics, namely:

- The dispersion relation for an electromagnetic wave, as deduced from the Maxwell equations is: $c^2q^2 = \omega^2\varepsilon$.

$$E = E_0 \exp(iqx - iwt).$$

- The wave vector is $q = \omega\hat{n}(\omega)/c$, with the complex refraction index $\hat{n}(\omega) = \sqrt{\varepsilon}$.

Therefore, if $\varepsilon > 0$, q is real, and the medium is transparent: the electromagnetic wave propagates without any absorption. After Eq. (13.53), this is the case when $\omega > \omega_p$. For the high carrier densities met in metals, the plasma frequency is in the visible of near ultraviolet, which explains the transparency of alkali metals (Li, K,) in the UV. On the other hand, if $\omega < \omega_p$ Eq. (13.53) shows that ε is real but negative so that $\hat{n}(\omega)$ and q are pure imaginary. In that case, E is an evanescent wave that is just needed to fulfill the boundary conditions (continuity of the fields) at the surface when the sample is illuminated by a beam at this frequency: the light cannot penetrate in the sample, and is totally reflected at the surface. That is why well-polished metallic surfaces are mirrors.

In semiconductors where the concentration n is much smaller, the plasma frequency may fall in the infrared; in that case, the optical effects associated to the plasma frequency may interfere with the absorption/excitation of phonons in the crystal, which adds another frequency-dependence of the dielectric constant. That is why we have specified in the title that we consider the case where the plasma frequency and phonon frequencies are sufficiently different to avoid interference effects. Note that the displacement field and the motion of the electrons are in the same x-direction, which means that we are dealing with a charge density wave that is longitudinal. Another way is to do the opposite: consider such a charge density wave with angular frequency ω, $\rho = \rho_\omega e^{i\omega t}$. Remember the equation of conservation or continuity is:

$$\text{div}\ \ j + \partial\rho/\partial t = 0 = \text{div}\ \ j + i\omega\rho_\omega e^{i\omega t}. \tag{13.54}$$

If we neglect the polarization of the ions to keep only that of the electron gas (plasma), the Maxwell equation is:

$$\text{div } E = \frac{\rho}{\varepsilon_0} = \frac{\rho_\omega}{\varepsilon_0} e^{i\omega t}, \tag{13.55}$$

or, taking the equation of continuity into account: $\text{div } E = \frac{\text{div } j}{-i\varepsilon_0\omega}$, which can be written:

$$\text{div}\left(E + \frac{j}{i\varepsilon_0\omega}\right) = 0. \tag{13.56}$$

Taking into account Eq. (13.47):

$$j = \sigma(\omega)E = \frac{ne^2\tau}{m(1 + i\omega\tau)}E, \tag{13.57}$$

we find, in the limit $\omega\tau >> 1$:

$$\text{div}\left(E + \frac{1}{i\varepsilon_0\omega}\frac{ne^2\tau E}{i\omega\tau m}\right) = \text{div } E\left(1 - \frac{ne^2\tau}{m\omega^2\varepsilon_0}\right) = 0, \tag{13.58}$$

we recover the expression of the dielectric constant. The solution of this equation is equation is satisfied for $\varepsilon = 0$, i.e., at $\omega = \omega_p$. Therefore, at the plasma, a longitudinal charge density wave propagates in the electron gas.

13.6.4.2 Reflectivity Near the Plasma Edge in a Solid

We have considered so far the case of free electrons. In a solid, however, there are not only the conduction electrons that can be considered as free, there are also the electrons in the core orbits. And they contribute to the dielectric constant. At frequencies the order of the plasma frequency, the contribution of the core electrons do not depend significantly on ω; this dependence occurs at much larger frequencies only. However, Eq. (13.50) implies that $\varepsilon(\omega >> \omega_p) = 1$. In practice, the optical spectra are measured at frequencies ω that, even significantly larger than ω_p, still remain in the domain where the core contribution remains independent of ω. Therefore, what the opticians call naturally ε_∞, i.e., the value of ε they measure at $\omega >> \omega_p$ is in reality this contribution of the core electrons; it is only at much larger frequencies that ε will decreases to unity. We keep this definition of ε_∞ that is conventional, and it means that in Eq. (13.50), we have to replace 1 by ε_∞:

$$\varepsilon = \varepsilon_\infty - \frac{\omega_p^2}{\omega^2[1 + i/(\omega t)]}. \tag{13.59}$$

(a) Case $\omega\tau >> 1$. If we are still in the situation $\omega\tau >> 1$ in Eq. (13.59), we find that:

- The sample is transparent if $\omega > \omega_p[\varepsilon_\infty]^{-1/2}$.
- The sample is totally reflecting if $\omega < \omega_p[\varepsilon_\infty]^{-1/2}$.

The frequency at which the sample shifts form mirror to transparent is thus renormalized by the factor $\varepsilon_\infty^{1/2}$ in the solid. Another important frequency is obtained when $n = \varepsilon = 0$, because, it corresponds to a reflection coefficient $R = 0$. It happens at frequency:

$$\omega = \omega_{\min} = \omega_p[\varepsilon_\infty - 1]^{-1/2}. \tag{13.60}$$

(b) General case. In some cases, we cannot neglect τ. Finite τ means that ε has a real and an imaginary part, so that we have to take the general optical formula:

$$\hat{n} = \varepsilon^{1/2} = n + ik, \tag{13.61}$$

with n the refraction index and k the absorption coefficient. The notation is unfortunate, because n was already employed as the electron concentration, but this is the conventional notation in the literature, and this should not lead to any confusion. Equation (13.59) can be written:

$$\mathrm{Re}(\varepsilon) = \varepsilon_\infty - \frac{\omega_p^2}{\left(\omega^2 + \gamma_p^2\right)}, \qquad \mathrm{Im}(\varepsilon) = \frac{\gamma_p \omega_p^2}{\left(\omega^2 + \gamma_p^2\right)}, \tag{13.62}$$

with $\gamma_p^2 = \omega/\tau$ and γ_p is the damping factor. In experiments, the physical property that is measured is the reflectivity. The reflection coefficient is:

$$R = \left|\frac{1-\hat{n}}{1+\hat{n}}\right|^2 = \frac{(n-1)^2 + k^2}{(n+1)^2 + k^2}. \tag{13.63}$$

The reflectivity curve $R(\omega)$ can then be computed from Eqs. (13.61) to (13.63), and compared with experiments to deduce the two fitting parameters τ (entering γ_p) and ω_p, provided that the experiments have been made up to frequencies large enough to deduce ε_∞ from the relation:

$$R_\infty = \left[\left(\varepsilon_\infty^{1/2} - 1\right)/\left(\varepsilon_\infty^{1/2} + 1\right)\right]^2. \tag{13.64}$$

We can summarize the results by drawing the shape of the $R(\omega)$ curves shown in Fig. 13.20. Note that ω_p gives n/m. Since the static electric conductivity is $ne^2\tau/m$, the analysis of the optical properties allows us to determine the electric conductivity even when it is not possible to make ohmic contacts. On the other hand, this

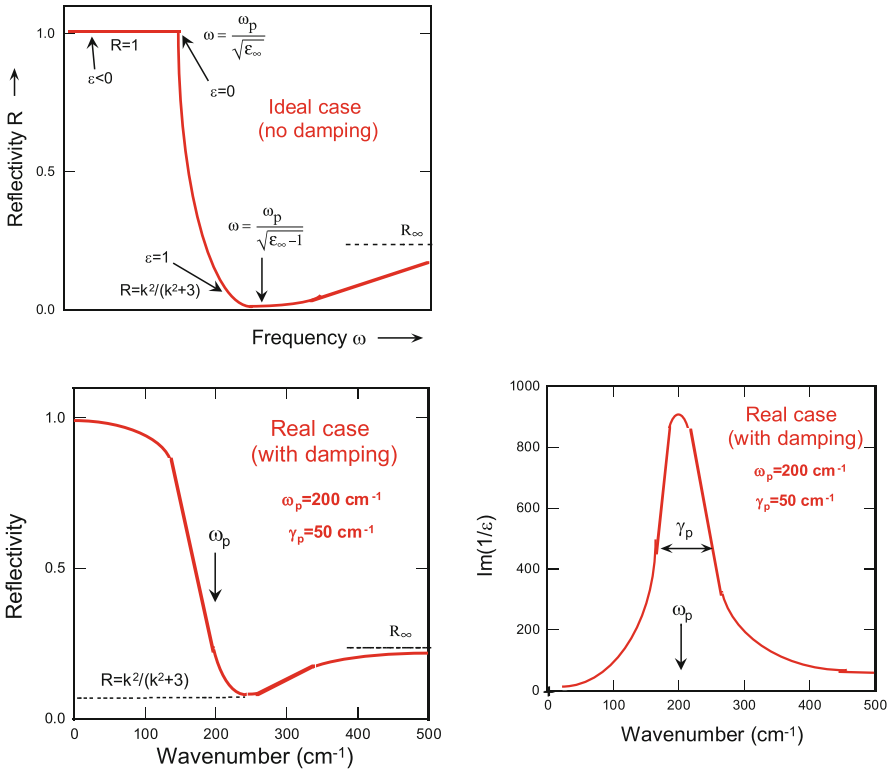

Fig. 13.20 Reflectivity vs. frequency showing the Drude edge of semiconductor materials in the infrared spectral region

experiment does not allow us to separate between n and m, while the measurement of the Hall gives access to n alone. The best is to do both: Hall effect measurements plus the analysis of the reflectivity near the plasma give the three parameters get n, m and μ.

Finally, in case n, μ are small, optical measurements can be replaced by measurements of ε (measure of capacity in which the material is placed). In semiconductors, optics is the convenient tool to measure ω_p since it is located at frequencies that are of easy access to optical devices. In metals where the plasma frequency is in the near UV, it may be more convenient to if the plasma edge is the near UV, it may be more convenient to send an electron beam on the metal, at normal incidence, and look at the spectral energy of the reflected beam. Normal incidence is needed to excite the plasma wave at the plasma frequency, because it is a longitudinal wave. Like any wave, the electron motion must be quantified, which means that the incident beam can create quanta of vibrations of the plasma, quasiparticles named plasmons, of energy $h\omega_p$. In the process, some of the reflected electrons have lost the kinetic energy $h\omega_p$, which can be detected by analysis of the energy profile of the reflected beam.

13.6.5 Ionic Conductivity: Complex Impedance Technique

Usually, the ionic conductivity is much smaller than that of the electrons. To determine it, the convenient tool is the complex impedance technique, because it requires very small current (prevents heating) and very small ionic motion. The a.c. method is called electrochemical impedance spectroscopy (EIS) because the impedance spectrum measured in a wide frequency range evaluates the performance of batteries and characterizes the various elements such as electrode, electrolyte and electrolyte/electrode interface. First, let us consider the ionic conductivity in a solid electrolyte. The complex impedance due to the Li-motion is:

$$Z = \frac{Z_{\omega=0}}{1 + i\omega\tau} = \frac{R}{1 + i\omega\tau}, \tag{13.65}$$

with R the resistance of the medium and τ the relaxation time (associated to the ionic mobility). This expression is identical to the complex impedance of a RC circuit (resistance R and capacity C in parallel), since in that case:

$$Z = \frac{R}{1 + i\omega RC}. \tag{13.66}$$

Therefore, the determination of R and τ is reduced to the measurement of a resistance and a capacitance. The way to do it is to make a "Cole–Cole plot." For that purpose, we write Eq. (13.68) under the more symmetric form:

$$\begin{aligned} \mathrm{Re}(Z) - R/2 &= R\left(\frac{1}{1 + (RC\omega)^2} - \frac{1}{2}\right) = \frac{R}{2}\left[\frac{1 - (RC\omega)^2}{1 + (RC\omega)^2}\right], \\ -\mathrm{Im}(Z) &= \frac{\omega RC}{1 + (\omega RC)^2}. \end{aligned} \tag{13.67}$$

Therefore,

$$[\mathrm{Re}(Z) - R/2]^2 + [\mathrm{Im}(Z)]^2 = \frac{R^2}{4}. \tag{13.68}$$

This is the equation of a circle in the Re(Z), Im(Z) plane, centered at $R/2$, of radius $R/2$; Note RC (or τ) are positive, so that only half of the circle has a physical meaning. Measurements of Z as a function of the frequency scan this semi-circle when plotting –Im(Z) as a function of Re(Z); This is the Cole–Cole plot (Fig. 13.21).

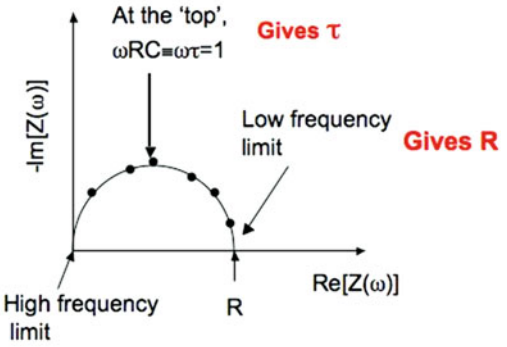

Fig. 13.21 Principle of the Cole–Cole plot

This is, however, the "ideal" case. In practice, situations more difficult to analyze may happen. For instance, in some cases, we observe an impedance of the form:

$$Z = \frac{R}{1 + (i\omega\tau)^{1-\alpha}}, \tag{13.69}$$

with $\alpha \neq 0$. This situation is very common in glasses, where it is due to a broad distribution of relaxation times. It is thus characteristics of disorder, often met in the surface layer of cathode materials. On an experimental point of view, this situation is easily detected by the fact that the Cole–Cole plot is still part of a circle, but the diameter has rotated by an angle $\pi\alpha/2$. Another situation is met when at the low frequency limit, the data in the Cole–Cole plot are aligned quasi linearly on a line almost vertical. In this region, Z is a pure capacitance $1/(i\omega C)$; the ions cannot move: this the case of a blocking electrode, i.e., the Li^+ ions are blocked at the surface. These two situations are illustrated below (Figs. 13.21 and 13.22). Another case is met when, instead of one semi-circle, there are several of them due to different events that the ions experience when they travel between the electrodes, which can be summarized in Fig. 13.23.

Let us finish with a true experimental result, illustrating that the method is powerful Fig. 13.24 shows the impedance spectra as a function of temperature for lithium borate B_2O_3-Li_2O-Li_2SO_4 glass. We recognize the features predicted by the formalism. The variation as a Cole–Cole curve gives evidence that the ionic conduction is activated and the activation energy can be deduced from these experiments [62, 63].

The electrical conductivity of thermally evaporated thin films of the binary borate glass system $B_2O_3 \cdot xLi_2O$ for various concentration of lithium oxide $0.7 \leq x \leq 5$ was been studied by Dzwonkowski et al. [63]. Complex impedance experiments have been carried out on films in a planar configuration using thin film blocking electrodes. The data were described using the electric modulus formalism for which two approaches are investigated. The first model uses a decay function as a fractional

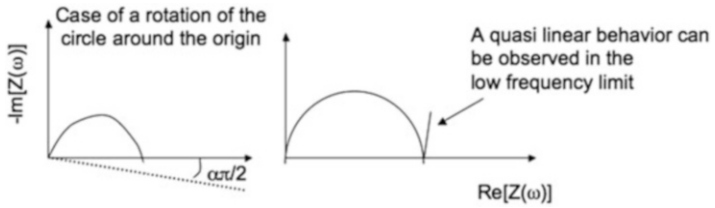

Fig. 13.22 Two configurations of the Cole–Cole plot

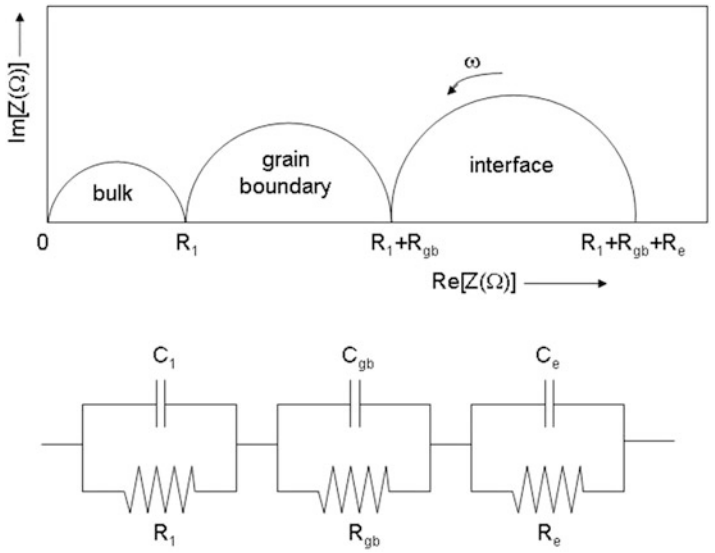

Fig. 13.23 The Cole–Cole plot of a polycrystalline material with the corresponding equivalent circuit that fits the experimental data

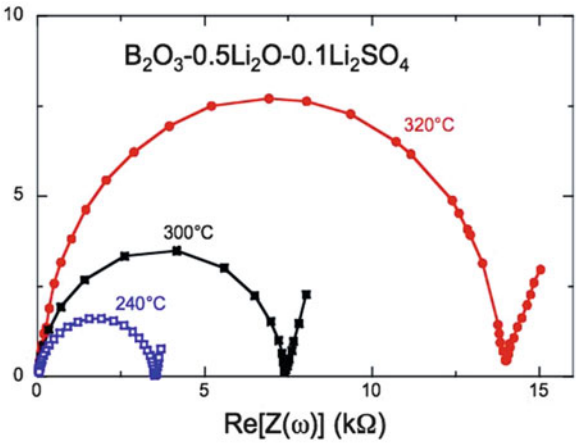

Fig. 13.24 Impedance spectra as a function of temperature for B_2O_3-Li_2O-Li_2SO_4 glass

exponential function and the second uses the Gaussian-like distribution function of the relaxation time. Both are compared with the complex impedance plane method. The experimental complex impedance data are modified by the electrode effect even in the frequency range of the dielectric relaxation. An easy way to calculate the non-modified dielectric parameters is proposed. The imaginary and real parts of the electric modulus are simultaneously treated by the fitting procedure.

The real part of the conductivity varies with frequency as a result of the distribution of relaxation times [62]. The usually accepted formula proposed by Jonscher [64] is:

$$\sigma(\omega) = \sigma(0) + A\omega^n, \tag{13.70}$$

where n is the exponential factor that depends of the hopping mechanism of alkali ions. This is the way to extract the dielectric relaxation effect from the experimental data. The exponential factors n are found to be between 0.6 and 0.7 for $B_2O_3 \cdot xLi_2O$ glasses. It is important to note that in the basis of the electric modulus formalism alone it is impossible to distinguish the local dielectric relaxation coupled with the non-charge transporting mechanisms from the static conductivity relaxation characterized by a distribution of relaxation time [63]. The conductivity as well as the average relaxation time of $B_2O_3 \cdot xLi_2O$ glasses are thermally activated with activation energies in the range 0.6–0.7 eV.

13.7 Magnetism as a Tool in the Solid-State Chemistry of Cathode Materials

The cathode elements for lithium batteries include oxygen and a transition element is their chemical formula. The transition ion is magnetic (with only few exceptions like Fe^{2+} of Co^{3+} in the low-spin state). In addition, the materials are often semiconductors with small electron (or hole) concentration, so that the magnetic exchange interactions are essentially superexchange interactions that are short-range. The magnetic properties of the cathode material will then be dominated by the interaction between each magnetic ion and the other ions close to it. It gives us the opportunity to use the magnetic ion as a probe of the atoms in its vicinity at the atomic scale. That is why it is an important tool to characterize the sample, by detecting impurity phases or local defects. It comes in complement to other more conventional tools. An example has been provided in the chapter on olivine cathode elements, as the investigation of the magnetic properties have been determinant to identify the different impurities that poisoned this material and to quantify their concentrations. This information allowed the chemists to adjust the synthesis parameters to get rid of them, to finally reach the situation where the material could be prepared free of defects, opening the route to its commercialization. The XRD, SEM, TEM are probes of the crystallinity of the samples at the nanometer

scale; the infrared optical spectroscopy is a probe at the molecular scale; the magnetism is a probe at the atomic scale, and it thus nicely complementary to the other tools.

The purpose of this section is to show through different examples how to use this powerful means of investigation to characterize the cathode materials. Of course it cannot be complete. It is limited to the information we can get from the simplest magnetic measurements: the magnetization $M(H,T)$ and the magnetic susceptibility $\chi(H,T)$ as a function of temperature and magnetic field. They are the basic experimental set-ups that should be available in research center in solid-state chemistry. There are also more sophisticated tools, such as Mössbauer spectroscopy, nuclear magnetic resonance, both related to magnetic properties. However, they come in complement to the measurements of $M(H,T)$ and $\chi(H,T)$, and are then out of the scope of this section that we wanted to be basic. In addition, these more sophisticated approaches require some expertise, so that collaboration with people specialized in this field is highly recommended. That is also the case to some extent for the electron spin resonance (ESR) spectroscopy.

13.7.1 $LiNiO_2$

Let us start with this material with which we are familiar since the Sect. 13.5.2.2 of this chapter. We have already noted that the lattice of this compound is fragile, with a problem that is recurrent in Ni-based cathode materials: Ni has a tendency to occupy Li lattice sites [65]. The problem with Ni^{2+} is that it has a tendency to mix up with Li, so that instead of having all the Li^+ ions on their (*b*)-lattice sites, and Ni^{2+} on their (*a*)-sites, part of Ni^{2+} ions are found on the lattice sites of the lithium, forming Ni(3b) defects, also named Ni_{Li}. The reason is that the ionic radii of Li^+ and Ni^{2+} are almost the same: 0.76 Å for Li^+, 0.69 Å for Ni^{2+}. This is damageable the electrochemical properties, because the Ni_{Li} defect is a diffusing center for the Li^+ ions, which affects their mobility. As a consequence, it is very difficult to prepare stoichiometric $LiNiO_2$ and the actual chemical composition of the final product after synthesis is usually $Li_{1-z}Ni_{1+z}O_2$. The parameter z is thus very important. The most accurate determination of z is obtained by the analysis of magnetic properties.

The magnetic susceptibility satisfies the Curie–Weiss law above $T = 50$ K, up to room temperature [66]. This large range of temperature allows for the determination of the slope of $\chi^{-1}(T)$, and thus of the Curie constant with a very good accuracy. The result is $C_p = 4.26 \times 10^{-3}$ emu g^{-1}, from which we deduce the effective magnetic moment carried by Ni^{2+} : $\mu_{eff}^{exp} = 1.81\mu_B$. The paramagnetic Curie temperature is $\theta_p = +30$ K, indicating the presence of ferromagnetic interactions; we shall return to it later. Let us first discuss the value of μ_{eff}. It is larger than expected, because in stoichiometric $LiNiO_2$, the charge neutrality implies that all the nickel ions are in the Ni^{3+} state of charge. Ni^{3+} in the low spin state has

1 unpaired electron, so $S = 1/2$, and the effective magnetic moment associated to it is $\mu_{\text{eff}} = S(S+1)]^{1/2}\ \mu_B = 1.73\ \mu_B$. The experimental value $\mu_{\text{eff}} = 1.81\ \mu_B$ is then evidence that all the nickel ions are not in the Ni^{3+} configuration: only a fraction x of them is in the Ni^{3+} state, the other fraction $1 - x$ is in the Ni^{2+} state due to some deviation from stoichiometry. According to the chemical formula $Li_{1-z}Ni_{1+z}O_2$, the charge neutrality equation is:

$$1 - z + (1+z)[3x + 2(1-x)] - 4 = 0 \ \text{ or : } x + 2 = (z+3)/(1+z). \quad (13.71)$$

Since, z is very small, as we shall see, we can make a development to first order:

$$x + 2 \approx (z+3)(1-z) \approx 3 - 2z \rightarrow x = 1 - 2z; 1 - x = 2z. \quad (13.72)$$

Therefore:

$$\mu_{\text{eff}}^{\text{exp}} = \left[(1-2z)\mu_{\text{eff}}^2\left(Ni^{3+}\right) + 2z\mu_{\text{eff}}^2\left(Ni^{3+}\right)\right]^{1/2}. \quad (13.73)$$

Taking into account that $\mu_{\text{eff}}(Ni^{3+}) = 1.73$, $\mu_{\text{eff}}(Ni^2+) = 2.83$, $\mu_{\text{eff}}^{\text{exp}} = 1.81\mu_B$, Eq. (13.73) gives the value $z = 0.027$. Note the slope of Curie constant is proportional to $(\mu_{\text{eff}})^2$, so the difference between $1.81\mu_B$ with respect to 1.73 means a change in the slope of the $\chi^{-1}(T)$ curve by a factor $(1.81/1.73)^2$, i.e., a 9 % change in the slope that is easily detected. That is why magnetic properties are so sensitive to the deviation from stoichiometry.

Let us now investigate the magnetic properties at low temperature. At temperature $T_B = 8$ K a peak of susceptibility is observed (see Fig. 13.25). In that case it is important to use two experimental procedures referred field cooled (FC) and zero-field cooled (ZFC). In the FC experiment, the magnetic field is applied at high

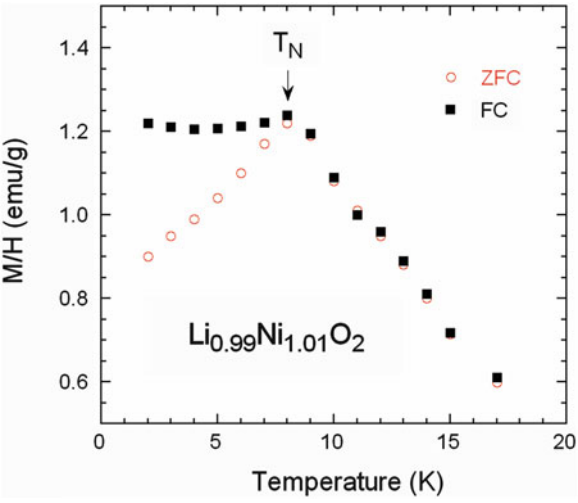

Fig. 13.25 M/H where M is the magnetization measured at the magnetic field $H = 10$ kOe for an off-stoichiometric $LiNO_2$. ZFC and FC stand for zero-field cooled and field cooled, respectively, as explained in the text

temperature, i.e., at a temperature larger than T_B. Then, the magnetization is measured during cooling. In the ZFC experiment, the sample is first cooled down to the lowest temperature available in the experiments, and no magnetic field is applied during the cooling process. Then the magnetic field is applied, and the magnetization is recorded during the heating, up to a temperature larger than T_B. If the peak of susceptibility is associated to an antiferromagnetic ordering at the Néel temperature, there should be no difference between FC and ZFC results. The measurement of FC and ZFC susceptibility curves in $Li_{1-z}Ni_{1+z}O_2$ reveals that the physical meaning of the peak at 8 K is different, since this is the temperature where magnetic irreversibility occurs, evidenced by a departure between FC and ZFC curves. This is characteristic of the blocking of ferromagnetic nanoparticles. These "particles" here are due to the ferromagnetic coupling of the Ni on site Li (noted Ni_{Li}), with the neighboring Ni ions in the Ni layers. At $T > 8$ K, these domains are in the superparamagnetic state, and T_B is their blocking temperature. At high temperature where the ferromagnetic ordering between Ni_{Li} and the neighboring Ni ions is broken by thermal fluctuations, their response is paramagnetic. It is presumably responsible for the positive value of θ_p found for this sample. Since the number of next-nearest neighbors of a Ni_{Li} site is known from the geometry of the lattice, the number of Ni ions involved in each cluster is known; it is then straightforward to determine the concentration of Ni_{Li} from the magnetization curves $M(H)$ at low temperature $T << 8$ K, by following the same analysis that we have illustrated in Chap. 7 to determine the concentration of different impurities in $LiFePO_4$.

13.7.2 $LiNi_{1-y}Co_yO_2$

$LiNiO_2$ has two problems. We have just evidenced that Ni has a tendency to occupy Li sites and generate a deviation from stoichiometry, which alters the electrochemical properties. The second problem is due to the fact that Ni^{3+} is a Jahn–Teller ion, which means that the d-electrons in this configuration create a local lattice distortion. The accumulation of such distortions upon cycling favors the formations of cracks, grain boundaries and other extended defects that reduce the lifetime of the battery when this material is used as the active element of the cathode.

That is why efforts have been made to reduce the concentration of Ni^{3+} ions by substitution of Ni for another transition element. Let us illustrate the case where the cobalt is chosen as the ion for substitution [67]. This is a natural choice since the end the series, $LiCoO_2$ is a well-known cathode element of the first generation of Li-ion batteries. The magnetization curve $M(H)$ of $LiNi_{1-y}Co_yO_2$ is illustrated in Fig. 13.26 for $y = 0.2$. We recover the typical magnetization curve characteristic of the presence of magnetic clusters. At small magnetic field, the magnetization M increases strongly with H. This is due to the ferromagnetic clusters (the same clusters as in $Li_{1-z}Ni_{1+z}O_2$) in a superparamagnetic state: the large magnetic moment associated to each isolated ferromagnetic cluster aligns along the applied magnetic field. Above 30 kOe, the magnetization associated to the ferromagnetic

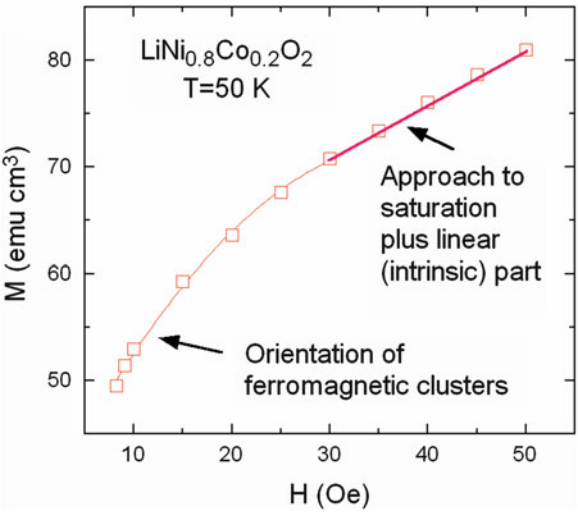

Fig. 13.26 Magnetization curve of $LiNi_{0.8}Co_{0.2}O_2$

clusters is almost (but not completely) saturate. At larger field, the variations of $M(H)$ are dominated by the intrinsic contribution $\mu_{\text{int}}H$ of $LiNi_{1-y}Co_yO_2$, which is linear in field since the material is paramagnetic at this temperature. However, the fact that the magnetization of the magnetic clusters does not saturate completely contrary to the cases we have met in $LiFePO_4$ or in the Sect. 13.7.1 implies that we have to use a more elaborate model that takes into account the magnetic anisotropy. The approach to saturation of ferromagnetic clusters can be written [68, 69]: $M_s(1-a/H-b/H^2)$, so that the magnetization at $H > 30$ kOe takes the form:

$$M(H) = M_{\text{s}}\left(1 - \frac{a}{H} - \frac{b}{H^2}\right) + \chi_{\text{int}}H; \quad b = \beta\left(\frac{K}{M_{\text{s}}}\right)^2. \tag{13.74}$$

The a-term comes from the series development of the Langevin function, the b-term is the anisotropy effect, with K the anisotropy constant. β is a constant that depends only on the material. The fit of the experimental curve with Eq. (13.74) leads to the determination of the fitting parameters M_s and b. On the other hand, the Néel relaxation time for a superparamagnetic particle to respond to the magnetic field is [70]:

$$\tau = \tau_0 \exp\left(\frac{E_{\text{a}}}{k_{\text{B}}T}\right), \tag{13.75}$$

where $\tau_0 = 10^{-9}$ s is an atomic relaxation time. τ is equal to a typical measurements time 100 s when:

$$E_{\text{a}} = 25k_{\text{B}}T. \tag{13.76}$$

This relation defines the temperature T_B at which the magnetization of the particle does not have time to reach equilibrium before its measurement. The energy barrier is proportional to the volume V of the particle and to the magneto-crystalline energy density, taking the simple form $E_a = VK = 25k_BT_B$ in case of uniaxial anisotropy. It is also responsible for de deviation of M from M_S according to Eq. (13.74). The link between the two can be written:

$$V = \frac{25k_BT_B}{M_s}\sqrt{\frac{\beta}{b}}, \tag{13.77}$$

T_B is the blocking temperature determined experimentally like in $Li_{1-z}Ni_{1+z}O_2$, and $\beta = 0.0762$ in the present case. This relation can then be used to determine the average volume V of the ferromagnetic clusters, once the parameter b has been determined by fitting the magnetization curve, and finally the radius of the clusters assuming they are spherical, reported in Fig. 13.27.

The variation of the size of the clusters is not necessarily expected and has not been discussed in the original paper [67]. Indeed, if the clusters are far from each other, their size is just dictated by the geometry of the lattice: Ni_{Li} and the surrounding Ni^{3+} ions. The increase in size when the cobalt concentration is already an evidence that the nature of the ferromagnetic clusters is different from the clusters met in [65, 66], a difference linked to the fact that the synthesis process used both works are different. The information on the origin of the clusters can be deduced from the blocking temperature. The onset of irreversibility, determined by the onset of a difference between FC and ZFC curves in Fig. 13.28, takes place at $T_B = 220$ K.

The magnetization curve (not reported here) shows that M is linear in H at room temperature even at low magnetic field, which implies that there is no ferromagnetic cluster with Curie temperature as large as 300 K, which excludes

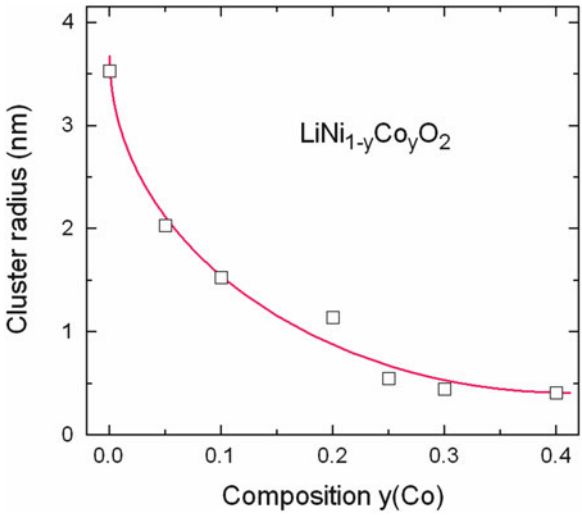

Fig. 13.27 Size of the magnetic clusters as a function f the composition in $LiNi_{1-y}Co_yO_2$

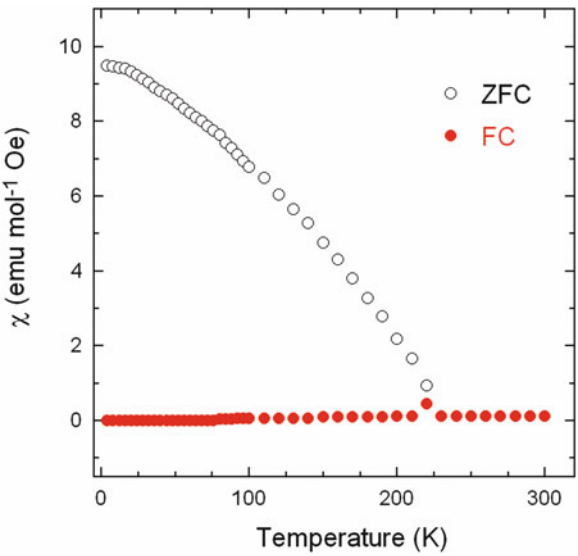

Fig. 13.28 Magnetic susceptibility M/H measured at $H = 10$ kOe of $LiNi_{1-y}Co_yO_2$ (case $y = 0$)

nanoparticles of nickel. Actually, a ferromagnetic moment takes place approximately at T_B. Therefore, as soon as the ferromagnetic clusters are formed, they "block," proving that the particles are actually large (remember that $V = 25k_BT_B/K$ with K the anisotropy constant, so that the size d of the particle is proportional to $T_B^{1/3}$ for clusters with the same composition, i.e., same factor K). This is consistent with the values $d(y)$ in Fig. 13.27. The large value of the Curie temperature $T_C \sim T_B \sim 220$ K definitely excludes the possibility that they take their origin from Ni_{Li}. In effect, we have seen in Sect. 13.7.1 that, in presence of Ni_{Li}, the system remains paramagnetic, and the Curie–Weiss law remains valid down to 50 K. We are thus in presence of ferromagnetic clusters of a secondary phase. To identify it, we have to look in the literature for some Ni compounds with a magnetic ordering at about the same temperature. The answer is provided in Fig. 13.29, which illustrates the magnetic properties of NiO with some impurities in it [71]. The analogy is obvious, even if the Curie temperature is 250 K rather than 220 K. This shift can easily be understood if we note that the Curie temperature is very sensitive to the actual composition of the NiO-based material. Therefore, the nature of the clusters of size larger than 1 nm evidenced in $LiNi_{1-y}Co_yO_2$ for $y < 0.25$ in [2] is attributable to non stoichiometric NiO with some Li in it like in the $Li_{0.05}Fe_{0.02}Ni_{0.93}O$ sample above mentioned (note surprising since there is one Li per chemical formula in $LiNi_{1-y}Co_yO_2$), and eventually some impurity in it (Fe or another ion).

These clusters, however, are observed in $LiNi_{1-y}Co_yO_2$ only at small concentrations of cobalt. On the other hand, in the curve illustrating the variation of the size $d(y)$, we can see that d is almost independent of y for $y > 0.25$, and is typically 1 nm. In addition, the blocking temperature 8–10 K for such large values of y is about the same as in the $Li_{1-z}Ni_{1+z}O_2$ sample studied in the previous section, which

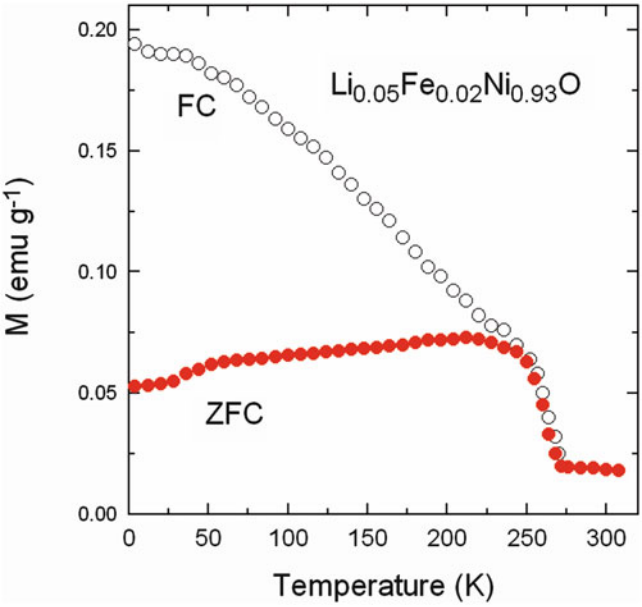

Fig. 13.29 Magnetization of $Li_{0.05}Fe_{0.02}Ni_{0.93}O$. Reproduced with permission from [71]. Copyright 2009 Elsevier

proves that the ferromagnetic clusters are the same: we recover the ferromagnetic clusters due to Ni_{Li} defects.

We can thus draw the following conclusions:

(a) In $LiNi_{1-y}Co_yO_2$, the Ni_{Li} defects spin-polarize the Ni spins in their vicinity form ferromagnetic clusters of typical size 1 nm. They give a superparamagnetic contribution to the magnetic properties down to the blocking temperature (about 8–10 K for this size of temperature). That is the case for the sample $y = 0$ in refs. [65, 66] and also in the samples $y > 0.2$ in ref. [67].

(b) On the other hand, the preparation process used in ref. [2] induces a secondary phase, under the form of particles of nonstoichiometric NiO. The size of the NiO-based nanoclusters may reach about 3 nm in that case. However, the introduction of Co in substitution for Ni reduces this secondary phase, and is evidenced by a decrease in the size of the NiO-based nanoclusters that eventually disappear at $y \sim 0.2$. On the other hand, the introduction of Co did not allow us to get rid of the Ni_{Li} defects that are still observe at higher Co concentrations.

13.7.3 Boron-Doped $LiCoO_2$

In continuity with the previous section, let us now consider $LiCoO_2$. It is the case $y = 1$ of the previous section, except hat we consider the case where boron doping has been added, because it improves the electrochemical properties, by preventing

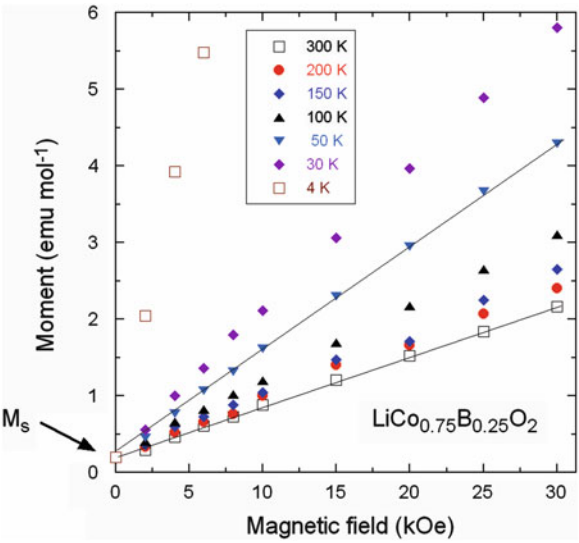

Fig. 13.30 Isothermal magnetization curves of $LiCo_{0.75}B_{0.25}O_2$ cathode material. The saturation moment is due to Ni clusters (60 ppm of Ni) that come from the Ni impurities in commercial cobalt oxide (<0.4 %)

the Verwey transition upon delithiation. The Verwey transition, originally discovered by Verwey in Fe_3O_4 is a generic name for the charge ordering that happens when the magnetic ion is 50 % in one state of charge and 50 % in another one. This situation is met in $Li_{0.5}CoO_2$ (Co^{3+} and Co^{4+}), which means that it is not possible to decrease the delithiation process beyond this composition.

The analysis of the magnetic properties of boron-doped $LiCoO_2$ has been made in [72]. The magnetization curves are reported in Fig. 13.30 for the composition $LiCo_{0.75}B_{0.25}O_2$ chosen as an example. The curves are linear in H, but extrapolates to a magnetization M_S, again an evidence of ferromagnetic clusters. Note the value of M_S does not depend on temperature up to rrom temperature, so that the Curie temperature of the magnetic impurity is much larger than 300 K. This information tells us that it can be identified as nickel under the form of Ni nanoparticles due to the presence of Ni as a residual impurity in the commercial cobalt used as a precursor to prepare the samples. Of course the quantity of nickel is not large, its amount deduced from the experimental value of M_S, is 60 ppm of Ni in the sample. It is, however, sufficient to give rise to this parasitic magnetic signal, another illustration of the sensitivity of the magnetic properties. Also the Ni particles are very small (not surprising since the amount of Ni is so small), so that he blocking temperature is too small to be detected in the experiments.

The second step is the study of the intrinsic magnetic susceptibility defined as $\chi = (M - M_s)/H$. Note that the subtraction of M_s is important and χ is actually markedly different from M_s/H because the magnetic susceptibility of the material is small. The reason is that Co is trivalent and its ground state is nonmagnetic ($S = 0$). However, an exited state is magnetic, giving rise to a Van Vleck paramagnetism that overcomes the diamagnetic contribution of the core. The particularity of the Van Vleck paramagnetism is that it does not depend on the temperature, and its

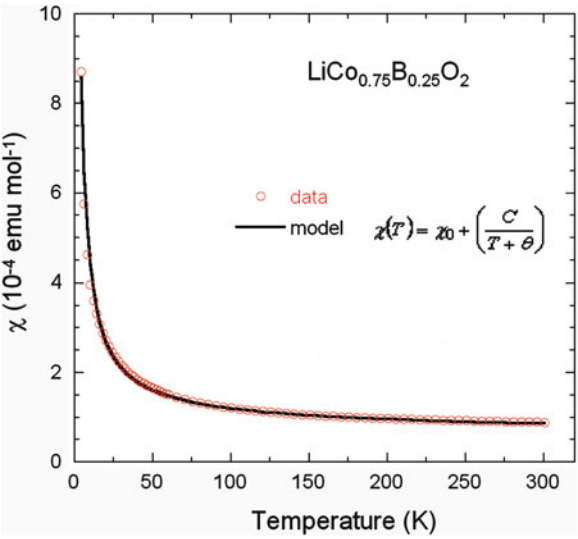

Fig. 13.31 Intrinsic magnetic susceptibility of $LiCo_{0.75}B_{0.25}O_2$ cathode material

contribution to the magnetic susceptibility is thus a constant χ_0 [73]. However, χ depends strongly on temperature, as it can be seen in Fig. 13.31.

We are thus obliged to add a Curie–Weiss term to χ_0, which must come from a defect, and write $\chi(T)$ under the form:

$$\chi(T) = \chi_0 + \left(\frac{C}{T+\theta}\right). \tag{13.78}$$

The experimental value of the Curie constant is so small that it should not come from any impurity. We presume it is due to the presence of Co^{4+} in concentration 0.09 % due to the same amount of Li vacancies. The fit obtained for this concentration and the value $\chi_0 = 5 \times 10^{-5}$ emu/mol (the value expected for Co^{3+}) is excellent. The last fitting parameter is $\theta = 2$ K. Such a small value is expected, because the concentration of Co^{4+} spins is so small that they do not interact significantly, which implies that their contribution to the magnetic properties is close to that of the Curie law C/T.

13.7.4 $LiNi_{1/3}Mn_{1/3}Co_{1/3}O_2$

This is the last lamellar compound that we shall consider here, but also the most promising as a cathode element. The formula is issued from the following considerations: Ni is the active element for electrochemistry (see Sect. 13.7.1), Co is introduced to reduce the amount of Ni on lithium 3*b* sites (see Sect. 13.7.2), Mn is introduced for stabilization of the lattice. Ni(3*b*) forms Mn^{4+}-Ni^{2+} pairs with

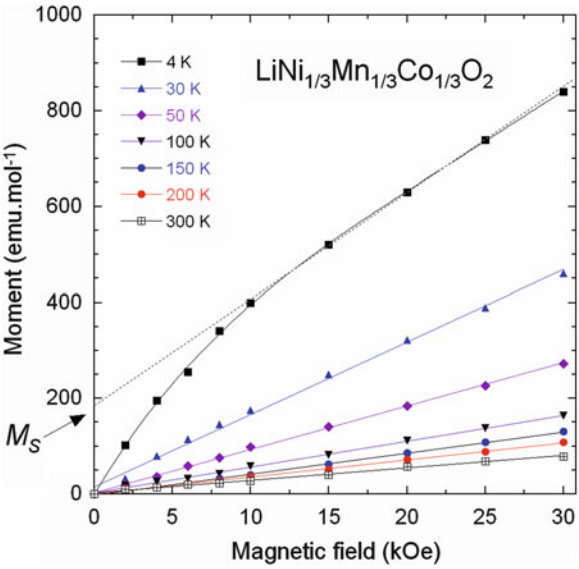

Fig. 13.32 Isothermal magnetization curves of $LiNi_{1/3}Mn_{1/3}Co_{1/3}O_2$ cathode material. Concentration of Ni^{2+} defects in the (3b) Li sites is estimated from M_s

neighboring manganese ions, and these pairs are ferromagnetic after the Goodenough rules. Therefore, the magnetic properties are well suited to the detection of Ni(3*b*) [74, 75]. The magnetization curves in Fig. 13.32 have a shape similar to those of the previous lamellar compound $LiNi_{1-y}Co_{1-y}O_2$ with Ni_{Li} defects, and for the reason: ferromagnetic clusters due to Ni_{Li} defects. The only difference is that, in the present case, the ferromagnetic cluster is a Mn^{4+}-Ni^{2+} pair. We might do the same analysis as in the previous materials, but we can even do simpler: since the magnetic fields available are large enough to reach technical saturation of the magnetization associated to the ferromagnetic clusters, we can obtain M_S by interpolation of the linear (intrinsic part) of the magnetization curve at high fields, at it is illustrated in the figure. Note it has to be done at the lowest temperature (4.2 K) available in the experiments, since the saturation of the extrinsic part is reached only at higher fields at larger temperature. Since the spins of the ions involved in the ferromagnetic pair are $S(Mn^{4+}) = 3/2$, $S(Ni^{2+}) = 1$, the total spin of the ferromagnetic pair is $3/2 + 1 = 5/2$, so that the magnetic moment associated to each ferromagnetic pair generated by Ni(3*b*) is 5 μ_B. The concentration of Ni(3b) defects is thus equal to the ratio between M_S and 5 μ_B. The result for this sample is 1.8 % of Ni in the (3b) site. This value is in quantitative agreement with the value given by Rietveld analysis of the XRD spectra, and in the present case, it proves that the sample preparation has been optimized (we have found that a concentration of Ni(3b)lower than 2 % is not damageable for the electrochemistry).

The analysis of magnetic properties is also useful to study the local structure of the lamellar materials at different stages of the lithiation/delithiation process [76]. It has also been used successfully to characterize electrode materials of different families. In spinel compounds, for instance, we can mention the detection of

MnO_3 impurities the $LiMn_2O_4$ spinel [77], or Li_2MnO_3 impurity that disproportionates in $Li_{1+y}Mn_{2-y}O_4$ [78]. More recently, it has also been used to study the phase transitions in Li_2MnO_3 electrodes at various states-of-charge [79].

References

1. Julien C, Nazri GA (2001) Intercalation compounds for advanced lithium batteries. In: Nalwa HS (ed) Handbook of advanced electronic and photonic materials, vol 10. Academic Press, San Diego, pp 99–184
2. Julien CM (2003) Lithium intercalated compounds charge transfer and related properties. Mat Sci Eng R 40:47–102
3. Armand M (1980) Intercalation electrodes. In: Murphy DW, Broadhead J, Steele BCH (eds) Materials for advanced batteries. Plenum Press, New York, pp 145–161
4. Coleman ST, McKinnon WR, Dahn JR (1984) Lihtium intercalation in $Li_xMo_6Se_8$: a model mean-field lattice gas. Phys Rev B 29:4147–4149
5. Berlinsky AJ, Unruh WG, McKinnon WR, Haering RR (1979) Theory of lithium ordering in Li_xTiS_2. Solid State Commun 31:135–138
6. Weppner W, Huggins R (1977) Determination of the kinetic parameters of mixed-conducting electrodes and applications to the system Li_3Sb. J Electrochem Soc 124:1569–1578
7. Thompson AH (1979) Electrochemical potential spectroscopy: a new electrochemical measurement. J Electrochem Soc 126:608–616
8. Dalard F, Deroo D, Sellani A, Mauger R, Mercier J (1982) Thermodynamical insertion of lithium in V_5O_8. Validity domain of the Thompson method. Solid State Ionics 7:17–22
9. West K, Jacobsen T, Zachau-Christiansen B, Atlung S (1983) Determination of the differential capacity of intercalation electrode materials by slow potential scans. Electrochim Acta 28:97–107
10. Roscher MA, Assfalg J, Bohle OS (2011) Detection of utilizable capacity deterioration in battery systems. IEEE Trans Veh Technol 60:98–103
11. Dines MB (1975) Lithium intercalation via n-butyllithium of the layered transition metal dichalcogenides. Mater Res Bull 10:287–291
12. Basu S, Worrell WL (1979) Chemical diffusion of lithium in Li_xTaS_2 and Li_xTiS_2 at 30 °C. In: Vashishta P, Mindy JN, Shenoy GK (eds) Fast ion transport in solids. North-Holland, Amsterdam, pp 149–152
13. Honders A, Young EWA, Van Heeren AH, de Wit JHW, Broers GHJ (1983) Several electrochemical methods for the measurement of thermodynamic activity and effective kinetic properties of inserted ions in solid solution electrodes. Solid State Ionics 9–10:375–382
14. Honders A, der Kinderen JM, Van Heeren AH, de Wit JHW, Broers GHJ (1985) Bounded diffusion in solid solution electrode powder compacts. Part II. The simultaneous measurement of the chemical diffusion coefficient and the thermodynamic factor in Li_xTiS_2 and Li_xCoO_2. Solid State Ionics 15:265–276
15. Bard AJ, Faukner LR (1980) Electrochemical methods. Wiley, New York
16. Julien C, Nazri GA (1994) Transport properties of lithium-intercalated MoO_3. Solid State Ionics 68:111–116
17. Julien C, Nazri GA, Guesdon JP, Gorenstein A, Khelfa A, Hussain OM (1994) Influence of the growth conditions on electrochemical features of MoO_3 film-cathodes in lithium microbatteries. Solid State Ionics 73:319–326
18. Honders A, Young EWA, Hintzen AJH, de Wit JHW, Broers GHJ (1985) Bounded diffusion in solid solution electrode powder compacts. Part II. The kinetic prperties of Ag_xTiS_2 and Ag_xNiPS_3. Solid State Ionics 15:277–286

19. Maier J (1991) Diffusion in materials with ionic and electronic disorder. In: Nazri GA, Huggins RA, Shriver DF (eds) Solid state ionics II, vol 210. Materials Research Society, Pittsburgh, pp 499–510
20. Dubarry M, Svoboda V, Hwu R, Liaw BY (2006) Incremental capacity analysis and close-to-equilibrium OCV measurements to quantify capacity fade in commercial rechargeable lithium batteries. Electrochem Solid State Lett 9:A454–A457
21. Jacobsen T, West K, Atlung S (1979) Electrochemical potential spectroscopy: a new electrochemical measurement. J Electrochem Soc 126:2169–2170
22. Ohzuku T, Ueda A (1997) Phenomenological expression of solid-state redox potentials of $LiCoO_2$, $LiCo_{1/2}Ni_{1/2}O_2$ and $LiNiO_2$ insertion electrodes. J Electrochem Soc 144:2780–2785
23. Murphy DW, Christian PA, DiSalvo FJ, Carides JN (1979) Vanadium oxide cathode materials for secondary lithium cells. J Electrochem Soc 126:497–499
24. West K, Zachau-Christiansen B, Jacobsen T (1983) Electrochemical properties of non-stoichiometric V_6O_{13}. Electrochim Acta 28:1829–1833
25. West K, Zachau-Christiansen B, Jacobsen T, Atlung S (1985) V_6O_{13} as cathode material for lithium cells. J Power Sourc 14:235–245
26. Lampe-Önnerud C, Thomas JO, Hardgrave M, Yde-Andersen S (1995) The Performance of single phase V_6O_{13} in the lithium/polymer electrolyte battery. J Electrochem Soc 142:3648–3651
27. Mizushima K, Jones PC, Wiseman PJ, Goodenough JB (1980) Li_xCoO_2 ($0 < x < 1$): a new cathode material for batteries of high energy density. Mater Res Bull 15:783–789
28. Dutta G, Manthiram A, Goodenough JB, Grenier JC (1992) Chemical synthesis and properties of $Li_{1-\delta-x}Ni_{1+\delta}O_2$ and $Li[Ni_2]O_4$. J Solid State Chem 96:123–131
29. Zhong Q, von Sacken U (1995) Crystal structure and electrochemical properties of $LiAl_yNi_{1-y}O_2$ solid solution. J Power Sourc 54:221–223
30. Ohzuku T, Ueda A, Nagayama M (1993) Electrochemistry and structural chemistry of $LiNiO_2$ (R-3m) for 4 volt secondary lithium cells. J Electrochem Soc 140:1862–1870
31. Arroyo ME, Ceder G (2003) First principles calculations of Li_xNiO_2: phase stability and monoclinic distortion. J Power Sourc 119–121:654–657
32. Chebiam RV, Prado F, Manthiram A (2001) Structural instability of delithiated $Li_{1-x}Ni_{1-y}Co_yO_2$ cathodes. J Electrochem Soc 148:A49–A53
33. Lu Z, MacNeil DD, Dahn JR (2001) Layered cathode materials $Li[Ni_xLi_{(1/3-2x)}Mn_{(2/3-x/3)}]O_2$ for lithium-ion batteries. Electrochem Solid State Lett 4:A191–A194
34. Koyama Y, Makimura Y, Tanaka I, Adachi H, Ohzuku T (2004) Systematic research on insertion materials based on superlattice models in a phase triangle of $LiCoO_2$-$LiNiO_2$-$LiMnO_2$: I. First-principles calculation on electronic and crystal structures, phase stability and new $LiNi_{1/2}Mn_{1/2}O_2$ material. J Electrochem Soc 151:A1499–A1508
35. Saidi MY, Barker J, Huang H, Swoyer JL, Adamson G (2002) Electrochemical properties of lithium vanadium phosphate as a cathode material for lithium-ion batteries. Electrochem Solid State Lett 5:A149–A151
36. Nguyen HT, Yao F, Zamfir MR, Biswas C, So KP, Lee YH, Kim SM, Cha SN, Kim JM, Pribat D (2011) Highly interconnected Si nanowires for improved stability Li-ion battery anodes. Adv Energy Mater 1:1154–1161
37. Ge M, Rong J, Fang X, Zhang A, Lu Y, Zhou C (2013) Scalable preparation of porous silicon nanoparticles and their application for lithium-ion battery anodes. Nano Res 6:174–181
38. Obrovac MN, Krause JL (2007) Reversible cycling of crystalline silicon powder. J Electrochem Soc 154:A103–A108
39. Chan CK, Riccardo Ruffo R, Hong SS, Huggins RA, Cui Y (2009) Structural and electrochemical study of the reaction of lithium with silicon nanowires. J Power Sourc 189:34–39
40. Dubarry M, Liaw BY (2009) Identify capacity fading mechanism in a commercial $LiFePO_4$ cell. J Power Sourc 194:541–549
41. Roscher MA, Assfalg J, Bohle OS (2011) Detection of utilizable capacity deterioration in battery systems. IEEE Trans Veh Technol 60:98–103

42. Dubarry M, Svoboda V, Hwu R, Liaw BY (2006) Incremental capacity analysis and close-to-equilibrium OCV measurements to quantify capacity fade in commercial rechargeable lithium batteries. Electrochem Solid State Lett 9:A454–A457
43. Weng C, Cui Y, Sun J, Peng H (2013) On-board state of health monitoring of lithium-ion batteries using incremental capacity analysis with support vector regression. J Power Sourc 235:36–44
44. Dubarry M, Liaw BY, Chen MS, Chyan SS, Han KC, Sie WT, Wu SH (2011) Identifying battery aging mechanisms in large format Li ion cells. J Power Sourc 196:3420–3425
45. Weng C, Cui Y, Sun J, Peng H (2013) On-board state of health monitoring of lithium-ion batteries using incremental capacity analysis with support vector regression. J Power Sourc 235:36–44
46. Zaghib K, Dubé J, Dallaire A, Galoustov K, Guerfi A, Ramanathan M, Benmayza A, Prakash J, Mauger A, Julien CM (2012) Enhanced thermal safety and high power performance of carbon-coated $LiFePO_4$ olivine cathode for Li-ion batteries. J Power Sourc 219:36–44
47. Bloom I, Jansen AN, Abraham DP, Knuth J, Jones SA, Battaglia VS, Henriksen GL (2005) Differential voltage analyses of high-power, lithium-ion cells 1. Technique and application. J Power Sourc 139:295–303
48. Bloom I, Christophersen J, Gering K (2005) Differential voltage analyses of high-power lithium-ion cells 2. Applications. J Power Sourc 139:304–313
49. Bloom I, Christophersen JP, Abraham DP, Gering KL (2006) Differential voltage analyses of high-power lithium-ion cells 3. Another anode phenomenon. J Power Sourc 157:537–542
50. Bloom I, Walker LK, Basco JK, Abraham DP, Christophersen JP, Ho CD (2010) Differential voltage analyses of high-power lithium-ion cells. 4. Cells containing NMC. J Power Sourc 195:877–882
51. Kassem M, Bernard J, Revel R, Pelissier S, Duclaud F, Delacourt C (2012) Calendar aging of a graphite/$LiFePO_4$ cell. J Power Sourc 208:296–305
52. Kwan CCY, Basinski J, Wooley JC (1971) Analysis of the two-rand Hall effect and magnetoresistance. Phys Status Solidi 48:699–704
53. Smits FM (1958) Measurement of sheet resistivities with the four-point probe. Bell Syst Tech J 34:711–718
54. Van der Pauw LJ (1958) A method of measuring the resistivity and Hall coefficient on lamellae of arbitrary shape. Philips Tech Rev 26:220–224
55. Chwang R, Smith BJ, Crowell CR (1974) Contact size effects on the van der Pauw method for resistivity and Hall coefficient measurement. Solid State Electron 17:1217–1227
56. Ramadan AA, Gould RD, Ashour A (1994) On the Van der Pauw method of resistivity measurements. Thin Solid Films 239:272–275
57. Levy M, Sarachik MP (1989) Measurement of the Hall coefficient using van der Pauw method without magnetic field reversal. Rev Sci Instrum 60:1342
58. Julien C, Hatzikraniotis E, Chevy A, Kambas K (1985) Electrical behaviour of lithium intercalated layered In-Se compounds. Mat Res Bull 20:287–292
59. Julien C, Hatzikraniotis E, Balkanski M (1986) Electrical properties of lithium intercalated p-type GaSe. Mater Lett 4:401–403
60. Klipstein PC, Friend RH (1987) Transport properties of Li_xTiS_2 ($0 < x < 1$): a metal with a tunable Fermi level. J Phys C 20:4169–4180
61. Julien C, Samaras I, Gorochov O, Ghorayeb AM (1992) Optical and electrical-transport studies on lithium-intercalated TiS_2. Phys Rev B 45:13390–13395
62. Julien C, Massot M (1990) Complex impedance spectroscopy. In: Balkanski M (ed) Microionics: solid state integrable batteries. North-Holland, Amsterdam, pp 173–195
63. Dzwonkowski P, Eddrief M, Julien C, Balkanski M (1991) Electrical ac conductivity in B_2O_3-xLi_2O glass thin films and analysis using the electric modulus formalism. Mater Sci Eng B 8:193–200
64. Jonscher AK (1977) The universal dielectric response. Nature 267:673–679

65. Chappel E, Nunez-Regueiro MD, de Brion S, Chouteau G, Bianchi V, Caurant D, Baffier N (2002) Interlayer magnetic frustration in quasistoichiometric $Li_{1-x}Ni_{1+x}O_2$. Phys Rev B66:132412
66. Julien CM, Ait-Salah A, Mauger A, Gendron F (2006) Magnetic properties of intercalation compounds. Ionics 12:21–32
67. Senaris-Rodrigues MA, Castro-Garcia S, Castro-Couceiro A, Julien C, Hueso LE, Rivas J (2003) Magnetic clusters in $LiNi_{1-y}Co_yO_2$ nanomaterials used as cathodes in lithium-ion batteries. Nanotechnol 14:277–282
68. Grossinger R (1981) A critical examination of the law of approach to saturation. I. Fit procedure. Phys Status Solidi A 66:665–674
69. Grossinger R (1982) Correlation between the inhomogeneity and the magnetic anisotropy in polycrystalline ferromagnetic materials. J Magn Magn Mater 28(1982):137–142
70. Néel L (1949) Théorie du traînage magnétique des ferromagnétiques en grains fins avec application aux terres cuites. Ann Geophys 5:99–136
71. Mana S, De SK (2009) Magnetic properties of Li and Fe co-doped NiO. Solid State Commun 149:297–300
72. Julien CM, Mauger A, Groult H, Zhang X, Gendron F (2011) $LiCo_{1-y}B_yO_2$ cathode materials for rechargeable lithium batteries. Chem Mater 23:208–218
73. Kittel C (2004) Introduction to solid state physics, 8th edn. Wiley, Hoboken
74. Zhang X, Mauger A, Lu Q, Groult H, Perrigaud L, Gendron F, Julien CM (2010) Synthesis and characterization of $LiNi_{1/3}Mn_{1/3}Co_{1/3}O_2$ by wet-chemical method. Electrochim Acta 55:6440–6449
75. Zhang X, Jiang WJ, Mauger A, Lu Q, Gendron F, Julien CM (2010) Minimization of the cation mixing in $Li_{1+x}(NMC)_{1-x}O_2$ as cathode material. J Power Sourc 195:1292–1301
76. Ben-Kamel K, Amdouni N, Mauger A, Julien CM (2012) Study of the local structure of $LiNi_{0.33+\delta}Mn_{0.33+\delta}Co_{0.33-2\delta}O_2$ ($0.025 \leq \delta \leq 0.075$) oxides. J Alloys Comp 528(2012):91–98
77. Kopec M, Dygas JR, Krok F, Mauger A, Gendron F, Julien CM (2008) Magnetic characterization of $Li_{1+x}Mn_{2-x}O_4$ spinel ($0 \leq x \leq 1/3$). J Phys Chem Solids 69:955–966
78. Kopec M, Dygas JR, Krok F, Mauger A, Gendron F, Jaszczak-Figiel B, Gagor A, Zaghib K, Julien CM (2009) Heavy-fermion behavior and electrochemistry of $Li_{1.27}Mn_{1.73}O_4$. Chem Mater 21:2525–2533
79. Amalraj FS, Burlaka L, Julien CM, Mauger A, Kovacheva D, Talianker M, Markovsky B, Aurbach D (2014) Phase transitions in Li_2MnO_3 electrodes at various states-of-charge. Electrochim Acta 123:395–404

Chapter 14
Safety Aspects of Li-Ion Batteries

14.1 Introduction

Lithium-ion batteries have dominated the battery industry for the past several years in portable electronic devices due to their high volumetric and gravimetric energy densities. It was expected that the success of these batteries in small scale applications would translate to large scale applications, which would have an important impact in the future of the environment by improving energy efficiency and reducing pollution. Safety of lithium-ion rechargeable batteries has been the technical obstacle for high power demand applications [1]. Lithium ion batteries under normal usage are generally safe. However, safety of Li-ion battery under abusive conditions is still a technical barrier for applications such as hybrid electric vehicles (HEV) and electric vehicles (EV), and the safety too often relies on the battery monitoring system (BMS). This thermal runaway not only is a safety hazard but also hinders the performance of lithium ion batteries eventually.

Even though the mechanism of thermal runaway is initiated by the anode in combination with the electrolyte [2], the rapid temperature rise in the cell, which dominates the overall heat generated during this process, is produced by the cathode reacting with the electrolyte [3, 4]. Therefore, it is of utmost importance to find a more structurally stable cathode in order to use lithium batteries at their fullest potential [5].

Lithium ion cells have historically used lithium metal oxides as cathode materials due to their high capacity for lithium intercalation, and suitable chemical and physical properties required for Li-ion electrodes. Layered materials with $LiMO_2$ structure, where $M = $ Co, Ni, Mn, or a combination of these metals, have been the most extensively used and investigated cathodes. These types of cathodes show excellent performance, but suffer from higher cost, toxicity ($LiCoO_2$), and thermal instability ($LiNiO_2$). In order to avoid these problems, another lithium metal oxide material with spinel structure $LiMn_2O_4$ has been proposed to substitute the layered materials. This oxide is inexpensive and environmentally friendly, but has

C. Julien et al., *Lithium Batteries*, DOI 10.1007/978-3-319-19108-9_14

disadvantages related to capacity fade issues, especially at high temperatures. Recently, an olivine structure material ($LiFePO_4$) has emerged as a possible cathode replacement, and abundant focus of research [6–12] on $LiFePO_4$ in the past and in recent years has been made owing to its desirable properties such as (1) relatively inexpensive material cost, (2) high average cycling voltage due to flat potential of 3.4 V vs. Li^0/Li^+, (3) reasonably high theoretical capacity 170 mAh g^{-1}, (4) relatively less toxic compared to $LiCoO_2$ systems, and (5) most of all, ability to suppress thermal runaway to make the Li-ion battery thermally safe. This property is attributed to the high covalent feature of the P–O bonds in the tetrahedral (PO_4) units, which stabilizes the olivine structure and prevents oxygen release from the charged (delithiated) olivine materials up to 600 °C [13, 14]. This is still controversial in other members of the olivine family Li*M*PO_4. In particular, a thermal instability has been reported in the charged (i.e. delithiated) state of $LiMnPO_4$ and $LiCoPO_4$ [15–18]. However, in a recent study, the $LiFePO_4$ and $LiMnPO_4$ cathode materials were found to have comparable thermal stability in their pristine and fully delithiated states [19]. On the other hand, there is an overall agreement on the remarkable thermal stability of $LiFePO_4$ and its delithiated counterpart [15, 16], and the recognition that $LiFePO_4$ is a safer cathode material than the commonly used lithium metal oxide cathodes with layered structures [3, 20, 21].

Nevertheless, $LiFePO_4$ material suffers from poor electronic conductivity [22]. This leads to poor rate capability that has limited the use of $LiFePO_4$ for high power density HEV and EV applications. Hence, a conductive carbon coating on the surface of $LiFePO_4$ was introduced to enhance the conductivity of the electrode and tailor $LiFePO_4$ electrode more suitable to high power density HEV and EV applications [8–12, 24–26]. This chapter discusses the improvement in electrochemical and thermal properties of Lithium iron phosphate ($LiFePO_4$) protected with a thin layer of carbon as a cathode material.

14.2 Experiments and Methods

14.2.1 Coin Cell Fabrication

$LiFePO_4$/Li and graphite/Li half-cells were prepared using a carbon-coated $LiFePO_4$ electrode and graphite anode supplied by Hydro-Quebec, Canada. The scanning electron microscope (SEM) image in Fig. 14.1 shows that the average size of the carbon-coated $LiFePO_4$ particles is 150 nm. The positive electrode contained 89 % $LiFePO_4$ particles 150 nm in diameter coated with carbon as active cathode material, 3 % vapor grown carbon fiber, 3 % carbon acetylene black (CAB) and 5 % PVdF binder and metallic lithium foil was used as negative electrode. The electrodes were dried at 120 °C under a vacuum and then transferred to argon filled glove box. The coin cells were 20 mm in diameter and 3.2 mm thick (2032-size coin cells). A Celgard (3501) surfactant coated porous polypropylene separator,

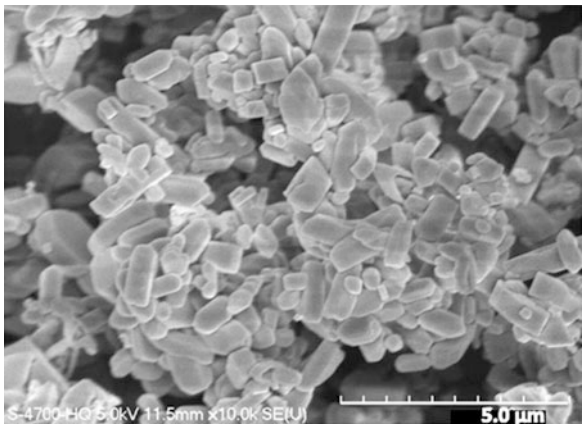

Fig. 14.1 SEM image of the C-$LiFePO_4$ particles used as the active cathode element of the $LiFePO_4$//Li coin cells and the $LiFePO_4$// C 18650-type cells in the present work

1.2 mol L^{-1} $LiPF_6$ in ethylene carbonate (EC) and ethyl methyl carbonate (EMC) (wt% 3:7) electrolyte, and lithium metal foil were also used within the stainless steel case to fabricate 2032-size coin cell. All cells were assembled in an argon-filled glove box and galvanostatically cycled at 0.1*C* rate from 2.5 to 4 V five times at constant temperature of 25 °C in a BT-2043 Arbin cycler. The graphite anode laminate was composed of carbon-coated graphite, VGCF, and binder. The anode half-cell preparation also went through the same process as the cathode half-cell. The cells were cycled five times at constant temperature of 25 °C at rate of 0.1*C* from 1 to 10^{-3} V in BT-2043 Arbin cycler. Fully delithiated cathode material from coin cells was used to measure thermal stability of cathode using DSC. Coin cells using spinel ($LiMn_2O_4$) and layered ($LiNi_{0.8}Co_{0.15}Al_{0.05}O_2$) oxides synthesized at Illinois Institute of Technnology, Chicago, were also prepared to compare thermal stability of different cathode chemistries.

14.2.2 Differential Scanning Calorimetry

The thermal stability of the $LiFePO_4$ cathode, along with other cathode materials and anode material was studied using differential scanning calorimetry (DSC-Perkin-Elmer Pyris 1 differential scanning calorimeter). After cycling the cells five times at 0.1*C* rate and obtaining the proper capacity, the cells were fully-charged and subsequently subjected to 8 h of trickle charge at constant voltage of 4.2 V to ensure the cathode material is completely delithiated. Then, they were introduced into the dry glove box. The cells were opened carefully and the cathode material was recovered. The electrodes were slightly dried and then scratched to obtain the cathode material. Three to six milligrams of active material samples from each electrode were packed into small stainless steel DSC capsules and then hermetically sealed. The samples were scanned in the DSC equipment under nitrogen purging from 50 to 400 °C at a 10 °C min^{-1} heating rate.

14.2.3 Experiments on Commercial 18650 Cells

Hydro-Quebec (HQ), Canada, supplied the cylindrical 18650-size cells consisting of carbon-coated $LiFePO_4$ as the cathode material and the carbon-coated graphite as the anode material. The laminate composition in the 18650-cell was the same as used in the coin cell mentioned in Sect. 14.2.1. The thermal properties of HQ cylindrical 18650-size cells of 1.4 Ah capacity were investigated under various states of charge and discharge using an isothermal calorimeter (IMC). The thermal runaway behavior of the same cell at fully charged state was investigated using an accelerating rate calorimeter (ARC). The dynamic power capabilities of carbon-coated $LiFePO_4$//graphite based commercial 18650-size cells, supplied by Hydro-Quebec were studied with HPPC test [27].

14.2.3.1 Hybrid Pulse Power Characterization

One of the applications where Li-ion batteries are considered as an immediate solution is in large-scale applications where high power is required. HPPC test emulates the requirements of cells used in HEVs and PHEVs on the road. HPPC test was performed on fully charged cell by applying sequence of pulse containing discharge 10 % of capacity, followed by 1 h rest, 3*C* discharge pulse for 18 s, 32 s rest, and series of regenerative charging pulses for 10 s. The next pulse begins again after 10 s rest and discharges again 10 % capacity of the cell. The scheme of the HPPC profile is illustrated in Fig. 14.2. The HPPC test profile was developed to study the useable power and voltage range of cells at different depths of discharge (DOD).

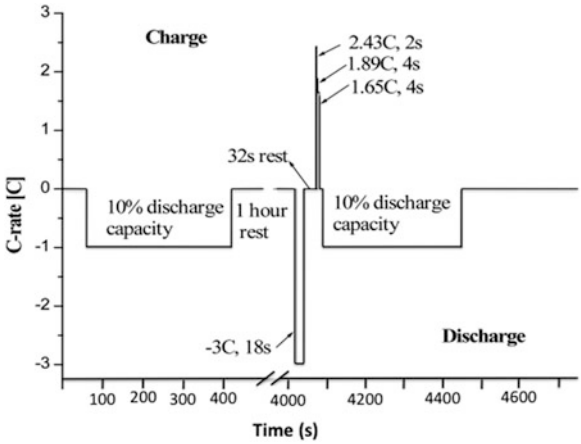

Fig. 14.2 Hybrid pulse power characterization (HPPC) profile [27] for cylindrical 18650 cells

14.2.3.2 Isothermal Microcalorimetry

The isothermal microcalorimeter (IMC, Model CSC 4400, Calorimetry Science Corp.) was used to measure the rate of heat released/absorbed by the 18650 cell during charge–discharge process, monitored simultaneously in a BT-2043 Arbin cycler. The cell chamber temperature of the IMC was controlled to be at 25 °C. The difference in the heat flow rate between the sample cylindrical cell and the reference cylindrical cell was recorded as the output heat flow rate from cell reactions. To examine the effect of discharge rate on the heat flow rate, the 18650 cell was cycled at different discharge rates (0.1, 0.2, and 0.5*C*). Two hours of rest was maintained between every charge and discharge to recover the residual heat completely from the cell. This relaxation period ensures prevention of mixing of charge and discharge heats.

14.2.3.3 Accelerating Rate Calorimeter

Accelerating Rate Calorimeter (Arthur D. Little ARC2000) was used to measure the thermal stability of the commercial cylindrical 18650-size cell. The 18650 cell was fully charged to 4.0 V, followed by 24 h of trickle charge at constant voltage of 4.0 V and subsequently transferred to ARC. The ARC setup consists of three heaters, top, base and side heaters, each equipped with individual thermocouples to ensure uniform heating across the entire chamber and thus the cell is heated uniformly as well. The ARC was operated based on Heat-Wait-Search (HWS) mode which consists of heating the cell from 40 to 450 °C at a heating rate of 5 °C min^{-1} in the heating mode for every 10 °C step. The waiting mode allows the temperature to equilibrate for 20 min and then ARC searches for an exothermal heat release from the cell (>0.02 °C min^{-1}) for 15 min during the search mode. If the calorimeter detects self-heat rate greater than or equal to 0.02 °C min^{-1}, it will track that exothermic heat released by the cell reactions, otherwise the temperature is stepped up by 10 °C for the next HWS mode. Thus the HWS mode continues until the cell undergoes thermal decomposition (sample-to-chamber temperature difference >100 °C) is detected or the final temperature (450 °C) is reached.

14.2.3.4 Safety Tests

Video of nail penetration, which was performed to investigate the safety behavior of a cell under penetration of a strong nail into the cell, is shown in the results section of this article. Prior to the test, the cell was fully-charged at a rate of *C*/6. Once the desired state of charge was reached, the cell was carefully placed and safely fastened on to a specially designed stand. The thermocouple was placed behind the cell, which makes it not visible in the attached video. During the nail penetration test, the cell was perforated with nail and the position of the nail was

maintained inside the cell for the entire duration of the experiment. The voltage, current, and temperature of the cell were measured over time to assess the damage induced during and after nail penetration. For the crush test, the cell was crushed to approximately 50 % of its thickness. Both the nail penetration and crush test were performed in a way to emulate enforced internal short-circuit of the cell. After the test, the cell was allowed to cool in ambient conditions for a minimum of 1 h so that the temperature drops and no further reaction occurs. The experiments were performed in a closed room specifically designed for destructive tests. The room was ventilated after the tests to evacuate any gases that were liberated during the experiment.

14.3 Safety of $LiFePO_4$-Graphite Cells

Figure 14.3 shows the electrochemical performance of the carbon-coated $LiFePO_4$ in a half-cell for the first seven charge–discharge cycles at *C*/10 rate. The behavior clearly indicates a single long plateau around 3.4 V vs. Li^0/Li^+. Carbon-coated $LiFePO_4$ exhibited more than 97 % coulombic efficiency and a consistent reversible discharge capacity ~152 mAh g^{-1}, which is more than 89 % of its theoretical capacity, when cycled between 2.5 and 4.0 V. This capacity is in agreement with our prior works [28]. It is, however, significantly smaller than the theoretical value close to 170 mAh g^{-1} because the tests were performed on a 2032 coin cell, and we have already reported that the capacity in such cells is systematically smaller by about 10 mAh g^{-1} lower than the value measured in 18650 cells with the same powder [29]. It can be seen that the carbon-coated $LiFePO_4$ electrode exhibited a discharge voltage plateau at 3.43 V vs. Li^0/Li^+ corresponding to the two-phase $LiFePO_4/FePO_4$ transformation [12]. These results are an improvement of the performance of uncoated $LiFePO_4$ electrodes [12, 23, 30, 31] and some carbon-coated electrodes [24] found in literature.

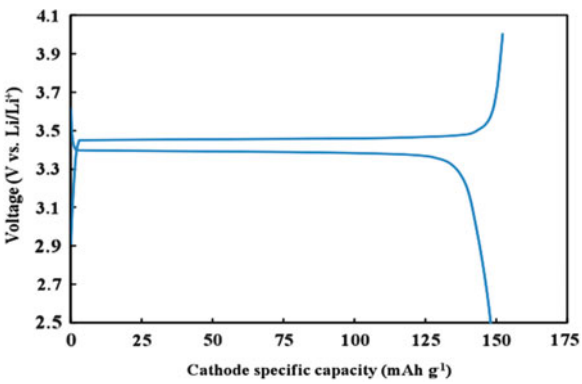

Fig. 14.3 Electrochemical Performance of initial seven 0.1*C* rate charge–discharge cycles for carbon-coated $LiFePO_4$/Li 2032 coin cell (the curves of the seven cycles are superposed)

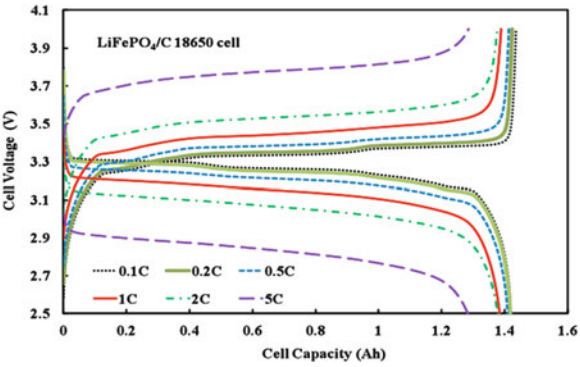

Fig. 14.4 Rate capability result on C-$LiFePO_4$// graphite 18650 cell at different discharge rates. The different plateaus at low *C*-rates correspond to the different phases of Li_xC_6 on the negative electrode

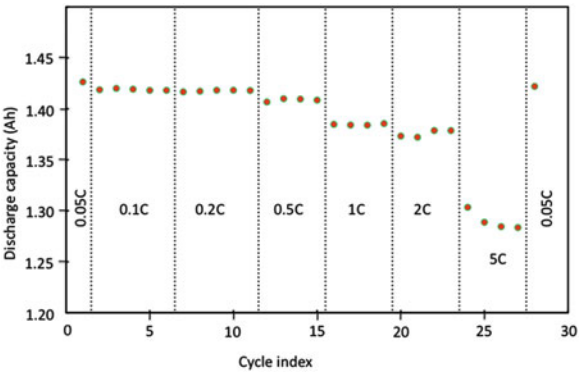

Fig. 14.5 Discharge capacity of C-$LiFePO_4$// graphite 18650 cell for different *C*-rates to illustrate capacity retention at higher *C*-rates

Figure 14.4 shows the rate capability of the carbon-coated $LiFePO_4$//graphite cylindrical 18650 cell at 0.1, 0.2, 0.5, 1, 2, and 5*C* rates. The same cycling rates during charge and discharge were used for all measurements and the cells were cycled in the same potential window as used in coin cells. The cell had consistently high reversible discharge capacity of 1.42 Ah when discharged at 0.1*C* rate. These cylindrical cells also showed very good capacity retention when cycled at 0.1*C* rate and only 1.3 % capacity loss was observed after 70 cycles of charge and discharge at 0.1*C* rate. The coulombic efficiencies obtained at all the different charge–discharge rates exceeded 99.3 %. Figure 14.5 shows the discharge capacity of C-$LiFePO_4$//graphite 18650-size cell at various cycling rates and for multiple cycles. It can be seen that the cell maintained similar discharge capacities when cycled at rates slower than 1*C*-rate, and the cell was able to retain 90 % of the initial capacity for rates up to 5*C* rate. These results just illustrate that carbon-coated active material exhibited higher capacity retention at higher discharge currents, compared with non-coated particles [32, 33]. Most importantly, the cell regained the 1.42 Ah capacity when the cell was cycled at the initial 0.1*C* charge and discharge rate. The loss of capacity at high discharge rates is attributed to the increase in the internal resistance and is followed by full capacity recovery.

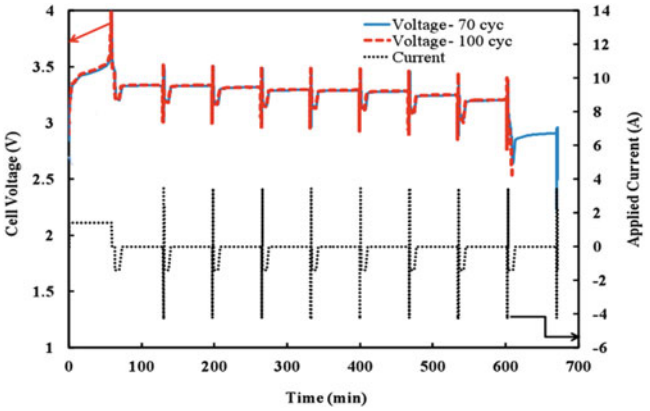

Fig. 14.6 HPPC results for a C-$LiFePO_4$//graphite 18650 cell after 70 and 100 cycles of charge–discharge at 0.1*C* rate. The results after 70 cycles and 100 cycles cannot be distinguished, and the two voltage–time profiles are superposed

Post rate capability tests indicated that the cathode material did not undergo any degradation during high discharge rates.

A cylindrical 18650-size cell using carbon-coated HQ $LiFePO_4$ as positive electrode was subjected to HPPC test after 70 cycles at 0.1*C* rate, and then cycled again up to 100 cycles at 0.1*C* rate, after which one more HPPC test was performed on the 18650-size cylindrical cell. Figure 14.6 illustrates the applied current and measured voltage profile after the cylindrical cells were cycled up to 70 and 100 cycles. Even after 70 cycles of charge and discharge, the HQ cell was able to withstand nine high-rate discharge and regenerative charge pulses and the cell was able to withstand eight high-rate pulses after 100 cycles.

This cell was able to deliver 3.2 V down to 80 % DOD and the calculated cell resistances ($\Delta V/\Delta I$) at different SOC indicated that cell resistance remained lower than 34.3 mΩ to 80 % DOD for both 18 s discharge pulses and 10 s regenerative charge pulses. Again cell resistance of discharge pulses were consistently higher than that of regenerative charge pulse and the values ranged between 14 and 34 mΩ only. The difference between the resistance of charge and discharge is due to the HPPC procedure reported in Fig. 14.1: the discharge is a continuous process while the charge is pulsed regime. This cell also showed consistent pulse power capacity as evident from very low differential discharge pulse power drop and regenerative pulse power gain, which is illustrated in Fig. 14.7. Average power values indicated that 80 % of discharge power can be applied back to the cell in the form of regenerative charging on this cell. Again no significant change in resistances and pulse power capacity were observed in both 18 s discharge pulse (DP) and 10 s regenerative charge pulse (RGP) down to 80 % depth of discharge (DOD) for cell tested after 70 and 100 cycles. HPPC results indicated that carbon-coated $LiFePO_4$ electrodes are very well suited for HEV applications. The performance of $LiFePO_4$ electrodes at high discharge rates and the high power of the 18650 cell were

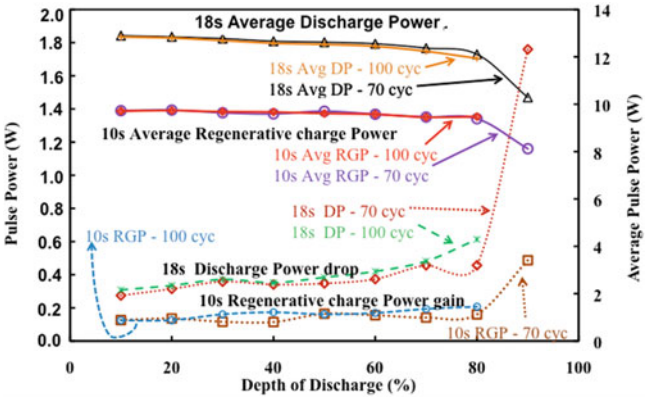

Fig. 14.7 Differential Pulse power drop/gain (*left* scale) and pulse power capacity (*right* scale) of the C-$LiFePO_4$//graphite 18650 cell at different states of charge. The symbols are experimental results under the conditions defined as ns (duration in number of seconds) of the discharge pulse (DP) or regenerating charge pulse (RGP) after 70 and 100 cycles (cyc)

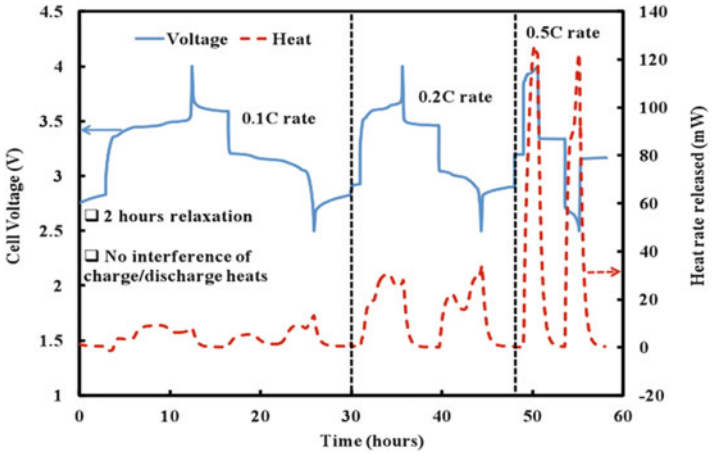

Fig. 14.8 Generated heat rate (broken curve, *right* scale) and voltage profiles (full curve *left* scale) of a cylindrical 18650 size C-$LiFePO_4$//graphite cell during cycling using an isothermal microcalorimeter

attributed mainly to the electronic conductivity improvement achieved through carbon-coating of the positive electrode.

Figure 14.8 shows the generated heat rate and the voltage profiles of a cylindrical 18650 size cell at different rates (0.1, 0.2, and 0.5*C*) at 25 °C. Two hours rest period of time was left between each charge and discharge, so that there is no overlap between charge–discharge heats. These profiles were reproducible for up to three cycles for each rate. It can be seen from the figure that the overall exothermic heat generated during charge and discharge process increased with respect to the *C*-rate.

Table 14.1 Accumulated heat released and the estimated cell temperature rise during charge–discharge of the cylindrical 18650 size C-$LiFePO_4$//graphite cell at different *C*-rate

	Accumulated heat (J)		Estimated ΔT (°C)	
C-rate	Charge	Discharge	Charge	Discharge
C/10	216	197	2.9	2.6
C/5	420	375	5.6	5.0
C/2	689	645	9.3	8.5

This overall heat released from the cylindrical 18650-size cell includes the reversible heat due to the entropic change of the cell reaction, and the irreversible heat due to the deviation of the cell potential from its equilibrium potential [34]. Table 14.1 shows the accumulated exothermic heat values obtained by the calculation of the area under the heat rate profile during the charge–discharge process. The cell relaxation heat released during the 2 h rest period between every charge and discharge was also included in the estimation of accumulated heat during charge–discharge.

At low *C*-rate, the generated heat during discharge process was increased by 90 % from 0.1*C* to 0.2*C*. This heat, at low *C*-rates, includes the nearly balanced contribution of both the reversible entropic and irreversible resistive heat, as the heat rate profiles show non-monotonous behavior which is attributed to the sign changes of entropy values [35] occurring during charge–discharge. However, at higher rate, 0.5*C*, the generated heat was increased by 227 %, and this was mainly due to the dominance of the irreversible resistive heat over the reversible entropic heat, because of the significant increase of the overpotential caused by the enormous rise in the ohmic resistance and also the electrodes polarization as a result of conversion to $FePO_4$ phase [34]. This conversion is achieved at 3.6 V vs. Li^0/Li^+, and $FePO_4$ is known to be very resistive acting as a limiting current element. The delithiated material does not generate exothermic reaction because of the absence of Li ions [36]. Nevertheless, the heat generated at 0.5*C* rate remains very moderate, and actually too small to cause any thermal runaway. The estimated cell temperature showed rise of 9.3 °C during charge and 8.5 °C during discharge at 0.5*C* rate, which indicates the cell temperature at the surface will reach 34 °C when no external cooling is applied during charge–discharge. The cell surface temperatures were estimated using cell average heat capacity value 75 J g^{-1} reported elsewhere [37] and the integrated heat values. The estimated cell temperatures at the surface were found to be less than SEI decomposition temperature and hence carbon-coated $LiFePO_4$ is considered to be a safe material that retains its reversible chemical structure during the continuous charge and discharge processes.

Figure 14.9 illustrates the DSC spectra of the fully delithiated and overcharged carbon-coated $LiFePO_4$ and the spectra of the fully lithiated carbon-coated graphite, both electrodes with traces of 1.2 mol L^{-1} $LiPF_6$ in EC-EMC (3:7), measured at a scan rate of 10 °C min^{-1} from 50 to 400 °C. The traces of electrolyte in the samples prepared for DSC were calculated to be between 15 and 20 % weight of the electrode tested. The onset temperature of the lithiated anode and delithiated cathode was

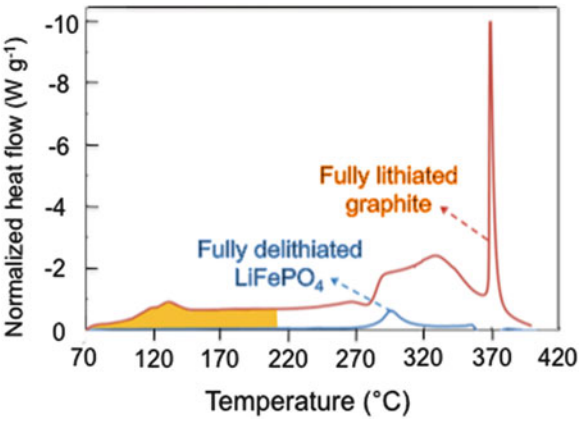

Fig. 14.9 DSC spectra of fully lithiated graphite and overcharged $LiFePO_4$ with traces of 1.2 mol L^{-1} $LiPF_6$ in EC-EMC (3:7) electrolyte at 10 °C min^{-1}

Table 14.2 Flow of enthalpy deduced from the DSC spectra of the fully delithiated and overcharged carbon-coated $LiFePO_4$ and the fully lithiated carbon-coated graphite (see Fig. 14.8); that of the overcharged cathode elements investigated (see Fig. 14.9) are reported in the three last columns

Cell	Temperature range (°C)	ΔH (J g^{-1})
$LiFePO_4$//graphite	250 °C $\leq T \leq$ 360 °C	−96.6
Graphite//Li	250 °C $\leq T \leq$ 360 °C	−170
Cathode material	Onset T (°C)	Overall ΔH (J g^{-1})
$LiNi_{0.8}Co_{0.15}Al_{0.05}O_2$	170	−941
$LiMn_2O_4$	264	−439
$LiFePO_4$	245	−250

detected at 80 and 245 °C, respectively. By convention, we note with a negative sign the heat that is lost by the system under consideration, i.e. a negative peak in the figure means an exothermic peak. The variation of enthalpy is reported in Table 14.2. In particular, the heat generated from the lithiated graphite was −170 J g^{-1} for temperatures between 67 and 200 °C, which corresponds to the SEI layer decomposition interval; this heat represents the contribution of the lithiated graphite to initiate the overall thermal runaway in a full cell. Enthalpy of anode reaction beyond 200 °C was not included, as most of the cathode chemistries start degrading at this temperature. However, the delithiated cathode, the most responsible electrode in the thermal runaway, showed very good stability under the DSC test. The calculated enthalpy of cathode reaction in the range of 50–400 °C was −250 J g^{-1} and this heat is a result of higher oxidation state of Fe occurring in fully charged cathode, which undergoes exothermic reaction with the electrolyte. These results are in good agreement with early studies [38] and indicate a significant improvement in the thermal properties of $LiFePO_4$ cathode compared to the commonly used lithium metal oxide layered materials [39]. This result proved that the lithium iron phosphate is distinguished material cathode in term of safety due to the strong P–O covalent bonds in $(PO_4)^{3-}$ polyanion, which prohibits the oxygen liberation [40]. Delayed reaction onset

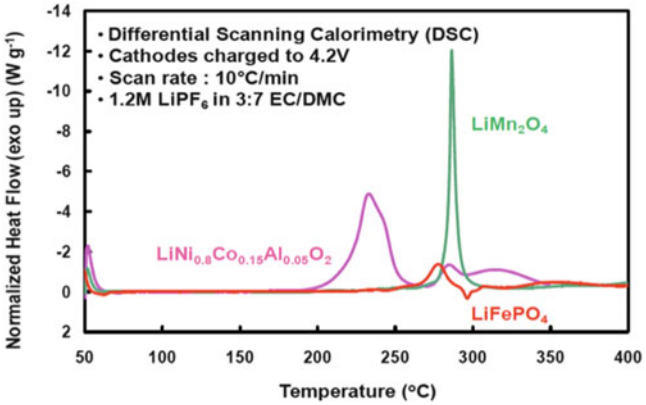

Fig. 14.10 DSC spectra of overcharged layered, spinel, and olivine cathodes with traces of 1.2 mol L^{-1} $LiPF_6$ in EC-EMC (3:7) electrolyte at 10 °C min^{-1}

temperature and considerably smaller reaction enthalpy for $LiFePO_4$ cathode is mainly attributed to high activation energy needed to break the strong P–O bond for oxygen release. It can also be seen that reaction enthalpy of cathode was found to be lesser than that of graphite anode and any effects of the combination can be observed in ARC measurements discussed later in this chapter.

Figure 14.10 shows DSC spectra of the overcharged spinel ($LiMn_2O_4$), layered ($LiNi_{0.8}Co_{0.15}Al_{0.05}O_2$) cathode, and carbon-coated $LiFePO_4$, all electrodes with traces of 1.2 mol L^{-1} $LiPF_6$ in EC-EMC (3:7), measured at a scan rate of 10 °C min^{-1} from 50 to 400 °C. We can observe that both spinel and olivine cathodes have delayed onset temperature by at least 70 °C with respect to the layered cathode. The layered cathode was found to be thermally unsafe, as this cathode undergoes its exothermic reaction with very large enthalpy (−941 J g^{-1}) and the reaction gets completed at much earlier temperature, lower than the onset temperature of spinel and olivine. Spinel cathode showed roughly half the exothermic reaction enthalpy (−439 J g^{-1}), whereas carbon-coated olivine showed even lesser exothermic reaction enthalpy (−250 J g^{-1}). The results are summarized in Table 14.2.

Based on their previous experimental results, Prakash et al. [39] proposed that a possible mechanism leading to the thermal runaway of the layered cathode consists of the following four steps:

- *Step 1*: The first step involves a partial structural deformation of $Li_xNi_{0.8}Co_{0.15}Al_{0.05}O_2$ into disorder oxide (spinel-like structure) and liberation of small amount of oxygen from it as a result of this structural deformation.
- *Step 2*: This step entails the reaction of the oxygen produced in step-1 with the ethylene carbonate due to its lower flash point of 150 °C:

$$C_3H_4O_3 + 2.5O_2 \rightarrow 3CO_2 + 2H_2O. \tag{14.1}$$

The continuous reaction of the oxygen with EC and possibly EMC releases combustion heat in the system and raises the temperature.

- *Step 3*: The heat released in the above reaction further accelerates the structural deformation, which finally leads to complete structural collapse of the oxide:

$$Li_{0.36}Ni_{0.8}Co_{0.15}Al_{0.05}O_2 \rightarrow 0.18Li_2O + 0.8NiO + 0.05Co_3O + 0.025Al_2O_3 + 0.375O_2. \quad (14.2)$$

- *Step 4*: The large amount of oxygen and heat produced in the above reaction helps the combustion of the remaining electrolyte (EC, EMC, and $LiPF_6$) to produce thermal runaway:

$$C_3H_4O_3 + 2.5O_2 \rightarrow 3CO_2 + 2H_2O, \quad (14.3)$$

$$C_3H_8O_3 + 2.5O_2 \rightarrow 3CO_2 + 2H_2O. \quad (14.4)$$

However, in $LiFePO_4$, phase transformation to $FePO_4$ is considered to occur in step 1 rather than structure disordering observed in layered cathode. Step 2 is observed to the same extent found in layered cathode, whereas step 3 is mostly prevented as the heat released from combustion of the solvents with O_2 is used to maintain the $FePO_4$ phase, hence the structural stability of the $LiFePO_4/FePO_4$ cathode. Again, the strong P–O covalent bonds in $(PO_4)^{3-}$ polyanion found in $LiFePO_4$ significantly reduce the rate of O_2 release, thereby reducing the combustion step itself and causing no further damage to the cathode structure.

It was observed in IMC results on $LiFePO_4$ that the cell temperature is raised to not more than 34 °C during charge and discharge at 0.5*C* rate, and DSC measurements showed that $LiFePO_4$ is less reactive with electrolyte at high temperatures than spinel and layered cathodes. Moreover fully lithiated graphite was observed to show more exothermic heat than $LiFePO_4$ cathode itself, resulting from SEI layer decomposition. So a fully charged cylindrical 18650 cell using $LiFePO_4$/graphite was tested in Accelerating Rate Calorimeter (ARC) to realize the overall combination of exothermic reaction heats of $LiFePO_4$, graphite and electrolyte. The simultaneous cell temperature and heater temperature and in situ cell open-circuit potential recorded during ARC test of the cell is reported in Fig. 14.11. It shows that the cell was heated uniformly as the thermocouples placed in top, side and base of the heater indicated the same temperature during the course of the experiment, and the cell temperature also closely followed the heater temperature until any self-heat was released from the cell. Open-circuit potential remained constant around 3.3 V during this period. At temperature about 80 °C after 160 min from the start of the experiment, the cell started to show self-heat at a rate greater than 0.02 °C min^{-1}. Once the self-heat is released from the cell and is sustained for more than 30 min, the heater begins to follow the cell temperature to the same rate of self-heat. Open-circuit potential also began to gradually drop due to the resistive heating of the cell.

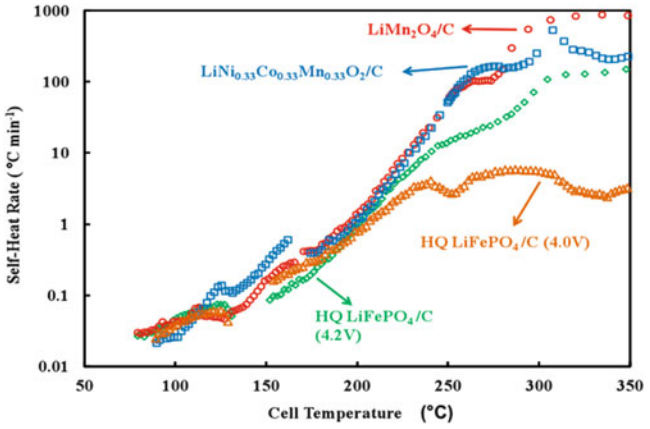

Fig. 14.11 Cell temperature measured at side, top, and base of the heater (the curves are superposed) and in situ open-circuit potential chronological record of $LiFePO_4$/C 18650 cell subjected to ARC test

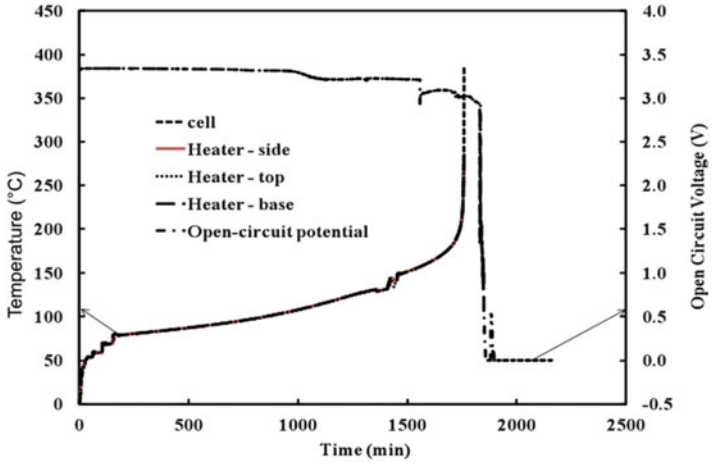

Fig. 14.12 Self-heat rates of fully charged 18650 cells with spinel, layered, and olivine cathodes measured in ARC. Self-heat rates of olivine cathode overcharged to 4.2 V are also shown

After 1455 min of testing, the cell temperature began to rise sharply at a temperature of 150 °C and open-circuit potential began to drop rapidly. This behavior of the cell was attributed to internal short-circuit of the cell owing to the melting of the separator. At 1756 min of test, the cell completely decomposed and the cell temperature completely shot off from that of the heater temperature by more than 80 °C; the cell voltage abruptly fell close to zero in few minutes later.

Figure 14.12 shows the self-heat rate (SHR) released from the 18650 cell ($LiFePO_4$//graphite) fully charged to 1.42 Ah capacity, when heated up to

Table 14.3 Comparison of accelerating rate calorimeter parameters for the different chemistries (anode in graphite): T_{Onset} is the temperature at the onset of self-heat rate (SHR), the next column is the maximum value of the SHR, which occurs at the temperature given in the last column

Cathode	T_{Onset} (°C)	Max SHR (°C/min)	$T_{Max\ SHR}$ (°C)
$LiNi_{0.8}Co_{0.15}Al_{0.05}O_2$//C	74	532	307
$LiMn_2O_4$//C	79	878	334
$LiFePO_4$//C (4.0 V)	89	6.1	286
$LiFePO_4$//C (4.2 V)	89	158	353

450 °C in ARC. The figure illustrates three different exothermic reactions. The first self-heat exotherm was observed between 90 and 130 °C, and it is mainly attributed to the reaction of the carbonaceous material in combination with the electrolyte caused by the SEI layer decomposition [40]. At temperatures above 150 °C, which corresponds to the melting temperature of the separator, the second self-heat exotherm was initiated, causing the cathode to be exposed to reaction with electrolyte. Cathode was subsequently decomposed at temperatures larger than 245 °C and reacted with the electrolyte, releasing more heat and increasing the cell temperature further up. At temperatures above 260 °C, the oxygen released from the composed cathode reacted with the organic solvents, initiating the third self-heat exotherm that corresponds to the beginning of the thermal runaway. However, the cell remained safe and did not explode for temperatures up to 450 °C, since the maximum self-heat rate of the cell was found to be less than 6 °C min^{-1} only. It is deduced that the peak producing the maximum self-heat rate of 6 °C per minute at 286 °C corresponds to the major exothermic reaction as described in the DSC study. The SHR observed in the ARC study of $LiFePO_4$ cathode was significantly lower than the layered oxide and spinel cathodes, indicating the thermal stability of the olivine cathode. The onset temperature and maximum SHR for different cathode chemistries are listed in Table 14.3. It is observed that even an overcharged (to 4.2 V) $LiFePO_4$//C cell showed only 158 °C min^{-1} maximum SHR, compared to 532 and 878 °C min^{-1} maximum SHR observed in layered and spinel oxide cathodes.

DSC results indicated higher exothermic reaction enthalpy for layered oxide than spinel cathode, but the maximum SHR of spinel was found to be higher than that of the layered oxide. On the other hand, the maximum SHR temperature in ARC and the exothermic reaction peak temperature in DSC were found to be consistent. To study this inconsistency of reaction enthalpy and maximum SHR, a DSC experiment was performed for fully-delithiated cathode, $Li_{0.36}Ni_{0.8}Al_{0.05}O_2$, in the presence and absence of the electrolyte. Figure 14.13 shows the DSC traces of $Li_xNi_{0.8}Co_{0.15}Al_{0.05}O_2$ in the presence and absence of electrolyte (1.2 mol L^{-1} $LiPF_6$ in EC-EMC (3:7)). One major exothermic reaction is detected at 225 °C, followed by complex small peaks. The major exothermic peak (−731 J g^{-1}), starting at 204 °C and reaching a maximum at 224 °C, is attributed to the structural change of the delithiated cathode accompanying the oxygen liberation and combustion of the electrolyte with the liberated oxygen [39]. The following multiple

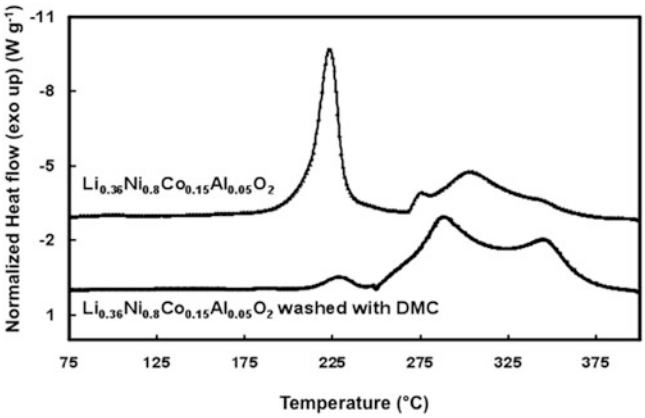

Fig. 14.13 DSC traces of $Li_xNi_{0.8}Co_{0.15}Al_{0.05}O_2$ in the presence and absence of electrolyte (1.2 mol L^{-1} $LiPF_6$ in EC-EMC (3:7))

peaks are attributed to the reaction of the remaining electrolyte with the continuous decomposition of the cathode. A decrease in the heating rate of the rinsed sample as shown in Fig. 14.13 suggests that the major exothermic reaction at about 225 °C is due to the reaction of the delithiated cathode and the electrolyte.

Hence it is clear that the layered cathode material reacts prematurely with the electrolyte and in the process does not have enough electrolyte to react further. This behavior is consistent with the maximum SHR observed for layered oxide at a much earlier temperature 307 °C than spinel, and the SHR was not sustained after the complete exhaustion of electrolyte at 307 °C. Hence, the $LiFePO_4$ cell exhibited excellent safety, much better than other chemistries, considering the facts that they have very large onset temperature and very low self-rate to remotely cause any thermal runaway of the Li-ion cell.

Safety tests were performed for $LiCoO_2$ and carbon-coated $LiFePO_4$ based 18650 cells in their fully charged state. The resulting videos of the crush and nail penetration tests are provided in the supplementary information. Before the crush test, the cell was charged to 3.7 V and the cell temperature was 26 °C. For the cell with $LiCoO_2$ cathode, the crush test resulted in immediate spark and lot of smoke, causing the cell temperature to increase from 27 to 352 °C in 14 s and the cell voltage dropped from 4.46 to 0 V in few seconds. On the other hand, the crush test for the cell with olivine oxide cathode produced a maximum temperature of 98 °C in 24 s with cell voltage still showing 0.05 V for carbon-coated $LiFePO_4$ cell). Nail penetration on cells fabricated with $LiCoO_2$ cathode showed immediate spark and smoke, causing the cell temperature to increase from 27 to 352 °C in 14 s and the cell voltage dropped from 4.46 to 0 V in few seconds. The nail penetration test on cells fabricated with $LiFePO_4$ cathode revealed that the cell reached a maximum temperature of 103 °C, with a small amount of electrolyte escaping from the cell. For both the tests on $LiFePO_4$ cell, no smoke, no flame, and no explosion were observed. The thermal studies carried out on Li_xCoO_2 show that the delithiated

$LiCoO_2$ decomposes to CoO or Co_2O_3 and releases O_2 at about 240 °C [41, 42]. As a result, an extensive amount of heat is produced when the remaining electrolyte reacts with the released O_2 [41–44]. The DSC results in Fig. 14.12 show very similar trend as observed in other studies for $LiNiO_2$ [41–43]. In spite of the doping of the present cathode with cobalt and aluminum, it seems that the thermal stability of $LiNi_{0.8}Co_{0.15}Al_{0.05}O_2$ has similar reaction mechanisms to Li_xNiO_2. On the other hand, the strong nature of P–O bond in $(PO_4)^{3-}$ polyanion results in less rate of O_2 release and thus prevents $LiFePO_4$ cell from thermal runaway, unlike in the case of $LiCoO_2$.

14.4 Li-Ion Batteries Involving Ionic Liquids

Conventional electrolyte for Li-ion batteries, i.e., ethylene carbonate or dimethyl carbonate, are organic solvents with high vapor pressure, and in case of accidental battery shorts or thermal runaway, can lead to fires and explosions. Some of these dramatic accidents have occurred from time-to-time, leading to recalls of millions of batteries and creating concern, even panic among the consumers. Such safety issues become paramount in large lithium-ion batteries of interest in electric cars, especially if charge–discharge is carried out at high rates. Thus safety has become a central issue in the development of this technology. A major avenue for creating a safe lithium-ion battery is to replace organic solvents or at least to diminish their flammability and high vapor pressure. The approach adopted at Hydro-Québec (HQ), through its research institute, is to use ionic liquids as solvents in these batteries; we have also discovered some solvent mixture compositions of organic solvents and ionic liquids which retain the best characteristics of both constituents and provide safe battery electrolytes [45].

Ambient temperature ionic liquid based on bis(fluorosulfonyl)imide (FSI) as anion and 1-ethyl-3-methyleimidazolium (EMI) or *N*-methyl-*N*-propylpyrrolidinium (Py13) as cation were investigated with natural graphite anode and $LiFePO_4$ cathode in lithium cells. The electrochemical performance was compared to the conventional solvent EC/EDC with 1 mol L^{-1} $LiPF_6$ or 1 mol L^{-1} LiFSI. The ionic liquid showed lower first coulombic efficiency at 80 % compared to EC-DEC at 93 %. The impedance spectroscopy measurement showed higher resistance of the diffusion part and it increased in the following order:

$$\begin{aligned} \mathrm{EC/DEC-LiFSI} &< \mathrm{EC/DEC-LiPF_6} < \mathrm{Py13(FSI)-LiFSI} \\ &= \mathrm{EMI(FSI)-LiFSI}, \end{aligned} \tag{14.5}$$

however a comparable reversible capacity was found in EC/DEC and EMI(FSI)-LiFSI. The high viscosity of the ionic liquids (IL) suggested using different conditions such as vacuum and 60 °C, to improve the impregnation of IL in the electrodes, and the reversible capacity was improved to 160 mAh g^{-1} at *C*/24.

The high rate capability of $LiFePO_4$ was evaluated in polymer-IL and compared to the pure IL cells configuration. The power performance was decreased when the polymer is added, at $C/10$ only 126 mAh g^{-1} was delivered compared to 155 mAh g^{-1}.

14.4.1 Graphite Anode against Different Electrolytes

The impedance measurement is shown in Fig. 14.14. A comparable interface resistance is observed with graphite anode vs. Li, between ionic liquid and reference electrolyte EC/DEC-$LiPF_6$ at 80 Ω. However, EC/DEC-LiFSI based salt showed a lower interface impedance at 65 Ω. In the diffusion part, the ionic liquids show higher resistance (20 Ω) and it increases in the order given in Eq. (14.5). Due to the high viscosity of the IL, the diffusion resistance is consequently higher.

Figure 14.15 shows the first two cycles of discharge–charge curves of anode graphite (a) in EC-DEC-$LiPF_6$, (b) in EC/DEC-LiFSI, (c) in EMI(FSI) and (d) in Py13(FSI). These charge–discharge cycles were obtained at $C/24$ rate between 0 and 2.5 V at ambient temperature. For the standard cell (curve a), a reversible capacity that obtained at the second discharge of 365 mAh g^{-1} was obtained very close to theoretical capacity, with high coulombic efficiency in the first cycle (CE1) at 92.7 %. These data reflect the performance of our electrodes in the standard electrolyte which was used as reference for comparison in this study. When $LiPF_6$ is replaced by LiFSI salt (curve b), the anode shows excellent performance with reversible capacity close to the theoretical capacity of 369 mAh g^{-1} and 93 % of coulombic efficiency in the first cycle. The LiFSI salt has a positive effect on the formation of coherent passive layer on the graphite. Curve (c) represents the cell

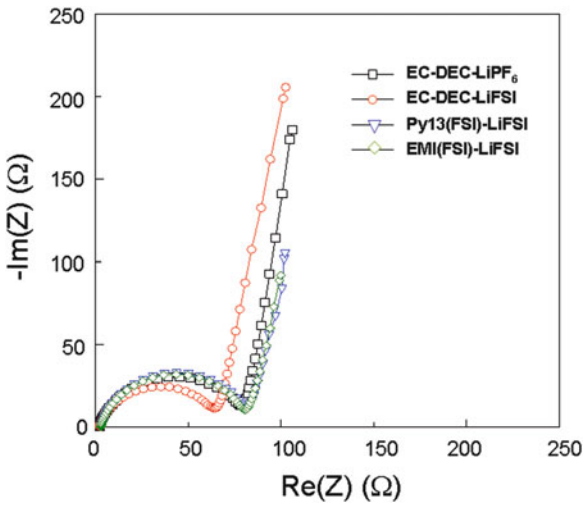

Fig. 14.14 Impedance spectra of Li//graphite anodes before cycling in different electrolytes

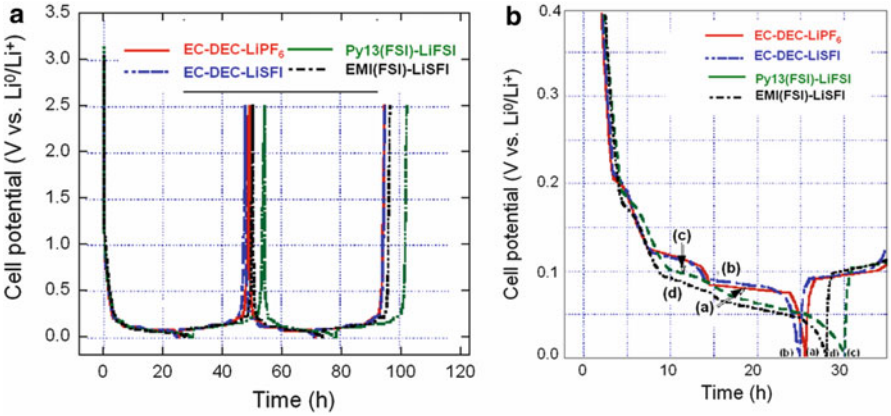

Fig. 14.15 (**a**) The first discharge–charge cycles for Li//graphite anodes in different electrolytes and (**b**) the expanded version of the first cycle in the potential range 0.5–0 V

Table 14.4 The first electrochemical characteristics of the graphite anode

Electrolyte	1st discharge (mAh/g)	CE1 (%)	Reversible capacity (mAh/g)	CE2 (%)
EC-DEC-1MLiPF$_6$	398	92.7	365	100
EC-DEC-1MLiFSI	382	93.0	369	100
Py13-FSI +0.7MLiFSI	468	80	367	98.3
EMI-FSI +0.7MLiFSI	432	80.5	362	97.6

with IL based on EMI-FSI that shows 362 mAh g^{-1} as reversible capacity but only 80.5 % of coulombic efficiency. However, for the ionic liquid Py13 (curve d), the reversible capacity is close to the theoretical with 367 mAh g^{-1}, while the first coulombic efficiency was 80 %. All these data explain well that LiFSI salt in FSI-based ionic liquid is suitable to be used in the anode graphite side without any secondary reaction. In Table 14.4, we summarize the first electrochemical data for the graphite anode for the first cycle. The coulombic efficiency in the second cycle (CE2) still does not reach 100 % which probably is associated with some side reactions, and then the passivation layer on the graphite cannot be established during the first cycles (Fig. 14.15b).

The cyclability of the cells was evaluated at 1*C* in discharge and charging at *C*/4. The capacity evolution was quite stable for organic electrolyte during cycling. The reversible discharge capacity was slightly lower in LiFP$_6$ compared to LiFSI salt. On the other hand, when the electrolyte is an ionic liquid, the discharge capacity still increased during the first five cycles for Py13(FSI) and ten cycles for EMI(FSI). This result indicates that IL Py13(FSI) electrolyte needs more cycles to form the

passivation layer on the graphite surface particles. For the IL EMI(FSI), the capacity increases can be attributed to the improvement of the wettability in the a electrode bulk with lithium intercalation–deintercalation in graphite. However, Ishikawa et al. [46] reported quite stable cyclability of the Li/graphite anode with ionic liquid EMI(FSI) with 0.8 mol L^{-1} LiTFSI salt and they show a stable capacity of 360 mAh g^{-1} at *C*/5. These data suggest probably the combined stabilizing effect of FSI cation in ionic liquid and the additive salt type on the anode graphite to the SEI layer and thus quite high reversible capacity.

14.4.2 $LiFePO_4$ Cathode Against Different Electrolytes

In the cells, the $LiFePO_4$ cathode side exhibited interface resistance behavior different from that of the graphite anode side (Fig. 14.16). The highest interface resistance with reference electrolyte was obtained at 240 Ω. The ionic liquids both show a lower interface resistance at 54 and 64 Ω, respectively, for Py13(FSI) and EMI(FSI). This result can probably be explained by the fact that the cathode bulk was not completely wetted in the ionic liquid configuration cells when the cathode was simply dipped in IL under normal conditions. Perhaps some $LiFePO_4$ particles did not have any passivation layer yet and thus did not contribute to the total resistance of the cathode interface. For the cathode, the electrochemical performance of the Li//$LiFePO_4$ cells was examined with ionic liquids and compared to that in the conventional organic solvent. Figure 14.17 shows the first charge–discharge curves at *C*/24 between 4 and 2.5 V.

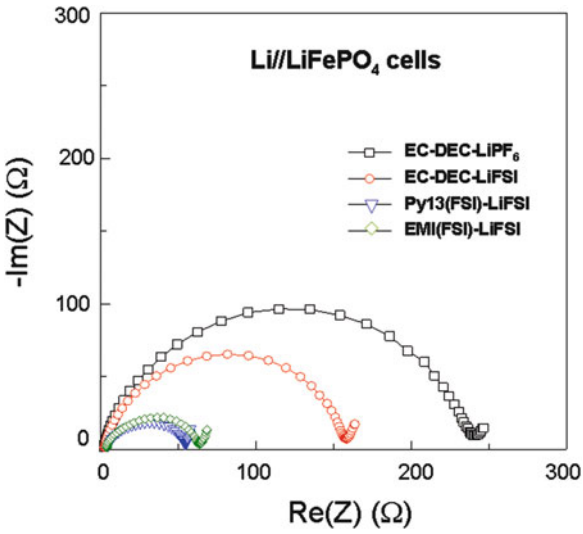

Fig. 14.16 Impedance profiles of Li//$LiFePO_4$ cathodes in different electrolytes

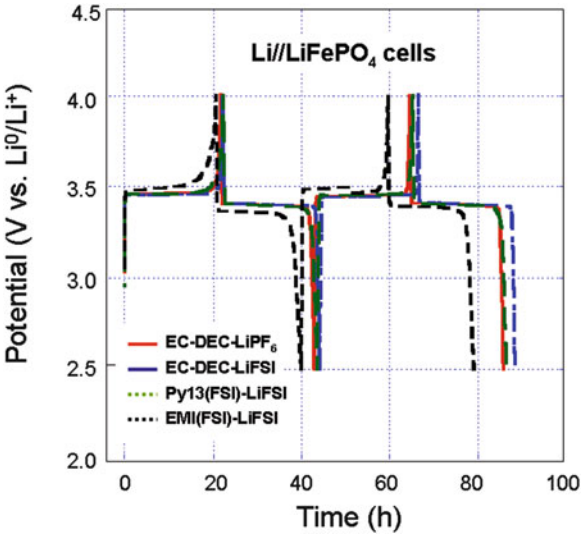

Fig. 14.17 The first charge–discharge cycle of Li//$LiFePO_4$ cells in different electrolytes

Table 14.5 The first electrochemical characteristics of the $LiFePO_4$ cathode

Electrolyte	1st discharge (mAh g^{-1})	CE1 (%)	Reversible capacity (mAh g^{-1})	CE2 (%)
EC/DEC-1MLiPF_6	158.2	97.5	158.0	98.0
EC/DEC-1MLiFSI	156.5	98.05	156.5	98.0
Py13-FSI + 0.7MLiFSI	151.3	93.0	143.3	98.3
EMI-FSI + 0.7MLiFSI	164.0	95.0	160.0	97.0

The reversible capacity with EC/DEC-LiPF6 (a) was 158 mAh g^{-1} with 97.5 % as coulombic efficiency in the first cycle (CE1). In curve of charge–discharge (b) with LiFSI salt, the reversible capacity was quite comparable to EC-DEC-LiPF_6 electrolyte at 156.5 mAh g^{-1} and 98 % in the first cycle coulombic efficiency. With the ionic liquid Py13-FSI (c), a lower reversible capacity of 143 mAh g^{-1} was obtained with only 93 % coulombic efficiency. However, with ionic liquid EMI (FS), curve (d), higher reversible capacity and coulombic efficiency, respectively, with 160 mAh g^{-1} and 95 % were obtained. The reversible capacity and the coulombic efficiency are summarized in Table 14.5. The high viscosity of Py13 (FSI), two times that of EMI(FSI) can make the lithium extraction from $LiFePO_4$ structure more difficult even at low rate like *C*/24. This result is clearly described on the charge curve with not well defined curvature at the end of the charging plateau.

In the $LiFePO_4$ cells, the viscosity perhaps affects the performance also due to the carbon coating on the surface of $LiFePO_4$ particles. When electrolyte has high viscosity like an ionic liquid, the wettability of the carbon layer is more difficult due to its large surface area. Then the lithium ion cannot migrate easily across this layer, particularly in the first cycles. Moreover, the viscosity can prohibit also the wettability of all the electrodes in depth, both anode and cathode because of the quasi

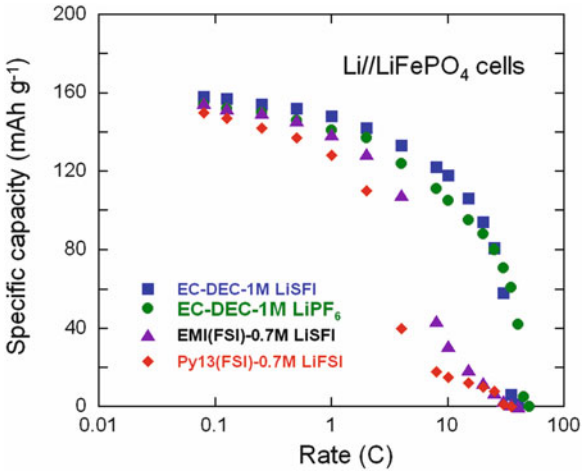

Fig. 14.18 Rate capability of Li/$LiFePO_4$ cells at different discharge rate in different electrolytes

three-dimensional fractal nature of the electrodes. The highest capacity was obtained with EMI(FSI) at 145 mAh g^{-1} compared to EC-DEC-$LiPF_6$ and EC-DEC-LiFSI which give around 137 and 139 mAh g^{-1}, respectively. However, Py13 (FSI) shows a capacity decrease to 105 mAh g^{-1}. The coulombic efficiency for all the electrolytes found stabilized at 100 % in the second cycle, except for the Py13 (EMI) for which the coulombic efficiency reaches 100 % only in the sixth cycle. Since ionic conductivity is inversely related to the viscosity, the Py13(FSI) tends not to yield good capacity at 1*C* compared to other electrolytes. Thus, it is necessary to evaluate the cathode in these electrolytes with different increasing discharge rates in order to push the power limitation of these electrolytes. In order to investigate the power performance of $LiFePO_4$ in different electrolytes, a rate capability test was applied. The rate dependence of the different electrolytes is summarized in Fig. 14.18 as Peukert plots. The discharge current was varied at different rates where as the charge current was maintained constant at *C*/4.

The organic solvent EC/DEC with LiFSI salt shows a quite reasonable performance at high rate, e.g., at 15*C* rate high discharge capacities were delivered by the cell having LiFSI with 105 mAh g^{-1}. For the rates above 20*C*, the capacity starts diverging from the cell having $LiPF_6$ as salt. With ionic liquids when higher viscosity is used, EMI(FSI) shows a comparable performance until 1*C* rate; at rate over 4*C*, the capacity dropped to 45 mAh g^{-1}. For a more viscous electrolyte such as Py13(FSI), the *C*-rate performance was lower and the gap with other cells starts at *C*/2 rate. At 4*C*, the capacity dropped to low value of 40 mAh g^{-1}. From these data, it is clear that the power performance is depends on the viscosity and the ionic conductivity. Furthermore, the LiFSI salt has shown a good result for both organic and ionic electrolytes [47] has compared the performance at high rate of the Li/LiFSI-EMI/$LiCoO_2$ with FSI or TFSI as anion. He confirmed the higher

performance of EMI when FSI anion is used. He found the capacity retention ratio 1/0.1*C* for EMI(FSI) and Py13(FSI) cells was 93 and 87 % respectively. However, when TFSI anion is used, the EMI(TFSI) cell has shown lower capacity retention ratio 1/0.1*C* with only 43 %. Furthermore, the performance of these ionic liquids not only depends on the viscosity and conductivity, but also on the anion and on the salt additive types. For further tests, we have selected the Py13(FSI) IL based on its higher safety level as reported by Wang et al. [48]. In order to improve the wettability of the cathodes with the ionic liquid, $LiFePO_4$ cathode was pre-treated by immersing it in Py13(FSI)-LiFSI IL, then putting under vacuum at 60 °C for 8 h. This cathode was then evaluated with a lithium metal cell.

The first charge–discharge cycles of the pre-treated cell, realized at 25 °C, are shown in Fig. 14.19 compared to the cell prepared without vacuum at 25 °C. The coulombic efficiency was improved in the first and second cycles to 100 % compared to 92.6 and 98.3 %. The impedance spectra of these cells before and after cycling are shown in Fig. 14.20. The interface resistance is higher when the cathode is pre-treated under vacuum 70 Ω vs. 50 Ω. However, after two cycles at *C*/24, the interface impedance is lower in the pre-treated cathodes. The reversible capacity was increased by 14 to 160 mAh g^{-1}. The viscosity limitation of the IL Py13(FSI) was two times that of EMI(FSI). The high rate capability shows small increase in the power performance until 2*C* rate (Fig. 14.21). Above 2*C* rate, high jump in the capacity was delivered from 40 to 80 mAh g^{-1}. However for the higher rates, the capacity dropped comparably to the same level as in cells in which the cathode wetting was not improved with vacuum pre-treatment as described above.

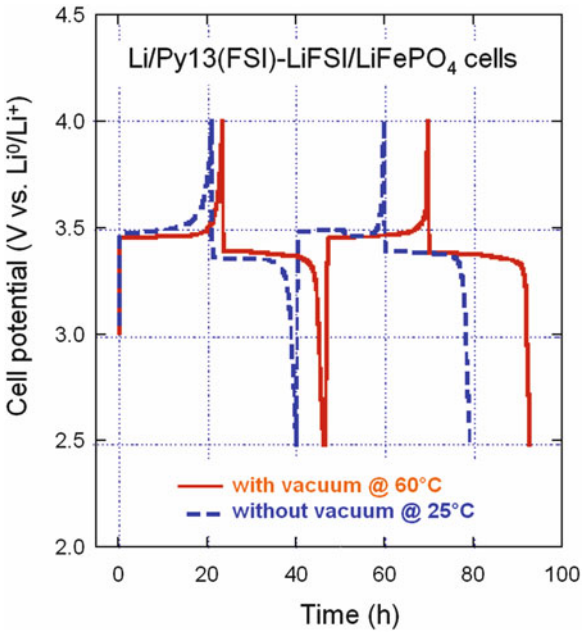

Fig. 14.19 The first charge–discharge of $Li/LiFePO_4$ cells with Py13(FSI)-LiFSI with and without vacuum

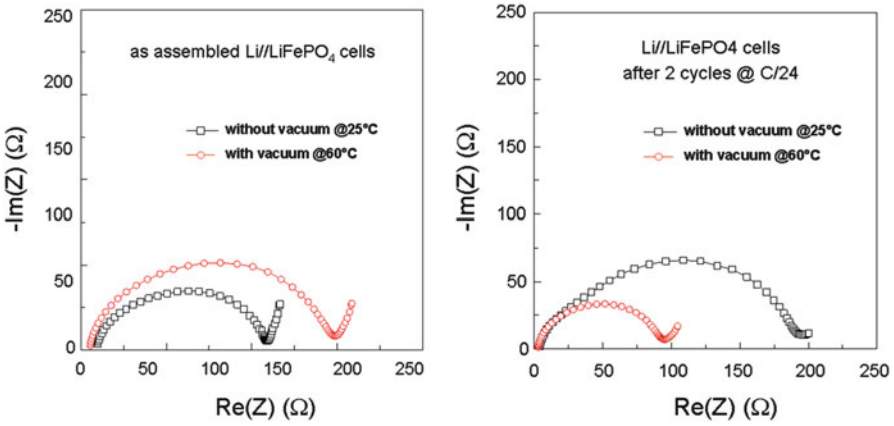

Fig. 14.20 Impedance of Li/$LiFePO_4$ cells with Py13(FSI)-LiFSI, (**a**) freshly assembled cells, and (**b**) after two cycles

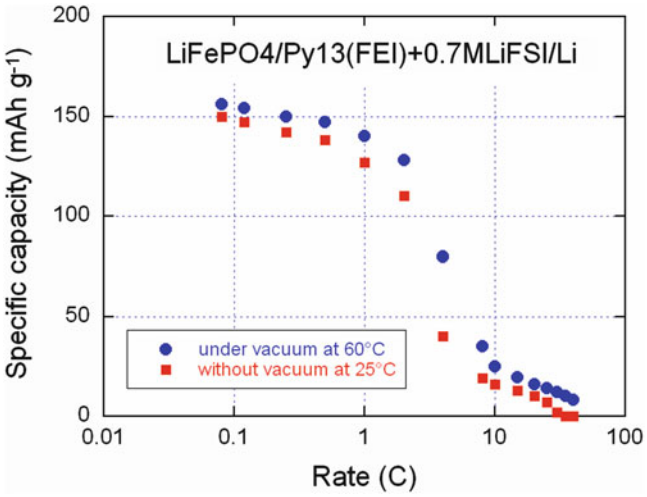

Fig. 14.21 Rate capability of Li/$LiFePO_4$ cells with Py13(FSI)-LiFSI with and without vacuum

14.5 Surface Modification

Attempts to increase the energy density by increasing the voltage of the cells did not lead so far competing products, because the gain in energy is accompanied by a decrease of the cycling life, and also problems in safety issues [49, 50]. Thus another route that has been explored is the surface modification of the active particles of the positive electrode. The idea is either to reduce the interface resistance by crystallization of the surface layer, or to coat the particles with something that would protect the particles against side reactions with the

electrolyte, avoid the loss of transition-metal ions or of oxygen, without altering the electronic and ionic conductivities. This route turned out to be more efficient than the doping process to improve the electrochemical properties and the safety of Li-ion batteries [51].

14.5.1 Energy Diagram

It has been suggested that in practical non-aqueous lithium battery systems the anode (Li or graphite) is always covered by a surface layer named the solid electrolyte interphase (SEI), 1–3 nm thick, which is instantly formed by the reaction of the metal with the electrolyte. This film, which acts as an interphase between the metal and the solution, has the properties of a solid electrolyte. This layer has a corrosive effect and grows with the cycling life of the battery [52]. Thermodynamic stability of a lithium cell requires the electrochemical potentials of electrodes E_A and E_C located within the energetic window of the electrolyte, which contrains the cell voltage V_o of the electrochemical cell to:

$$eV_o = E_C - E_A \geq E_g, \tag{14.6}$$

where e is the elementary electronic charge and E_g is the energy separation $E_L - E_H$ between the lowest unoccupied molecular orbital (LUMO) and the highest occupied molecular orbital (HOMO) [53]. The SEI passivating layer at the electrode/electrolyte boundary gives a kinetic stability to the cell for V_o larger than E_g. The design of electrodes must match the LUMO and HOMO level of the electrolyte. Figure 14.22 shows the schematic energy diagram of Li-ion cells with two different chemistries. For the graphite//$LiCoO_2$ cell (Fig. 14.22a), graphite has E_A lying

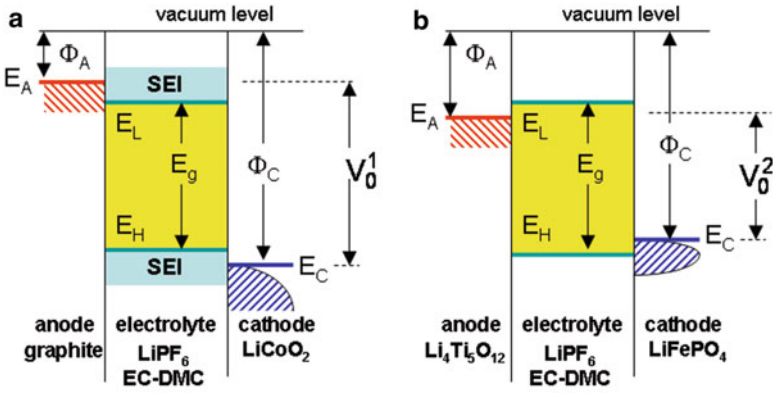

Fig. 14.22 Electronic band diagrams of Li-ion batteries: (**a**) graphite//$LiCoO_2$ and (**b**) LTO//LFP cells. E_A and E_C represent the Fermi level of anode and cathode respectively. E_g is the electrolytic window that ensures the thermodynamic stability, while $E_A > E_L$ and $E_C < E_H$ requires a kinetic stability by the formation of an SEI layer

above the LUMO of used non-aqueous electrolytes. Similarly, E_C of the cathode lies below the HOMO level. Thus, both graphite and $LiCoO_2$ electrodes are possible because a passivating SEI film has grown. The SEI requires properties as follows: (1) it must have good mechanical stability when changes in electrode volume occur upon cycling life, (2) ensure fast Li^+-ion transfer from the electrolyte to the electrode and (3) good ionic conductivity over the temperature range $-40 < T < 60$ °C. On the other hand, the $Li_4Ti_5O_{12}$//$LiFePO_4$ (LTO//LFP) cell does not have SEI formation (Fig. 14.22b) because the electrode energy levels E_C and E_A match well with the electrolytic window which provides very high safety. But the price to pay is a lower open-circuit voltage, i.e., 2 V against 4 V for the graphite//$LiCoO_2$ battery.

14.5.2 Surface Coating of Layered Electrodes

14.5.2.1 $LiCoO_2$

While $LiCoO_2$ is currently used in commercial Li-ion batteries with good rate capability, its function is limited (Li_xCoO_2, $x > 0.5$; potential >4.2 V vs. Li^0/Li^+) because Co^{4+} ion dissolution into the electrolyte that deteriorate the battery performance. The surface modification of $LiCoO_2$ by different substances such as metal oxides, carbon, and phosphates has various beneficial effects. It prevents the Co dissolution and electrolyte decomposition that helps the battery safety, the energy density, and working voltage. Other results are the suppression of the undesired SEI layer, protection of particles against side reaction with electrolyte and avoid the loss of oxygen. Typical surface modification is a 2–3 nm thick coating layer that corresponds to 1–2 % in weight [54–57].

Figure 14.23 displays the differential scanning calorimetry (DSC) measurements of a fully-charge electrode at 4.4 V vs. Li^+/Li^0 for bare, Al_2O_3- and MgO-coated

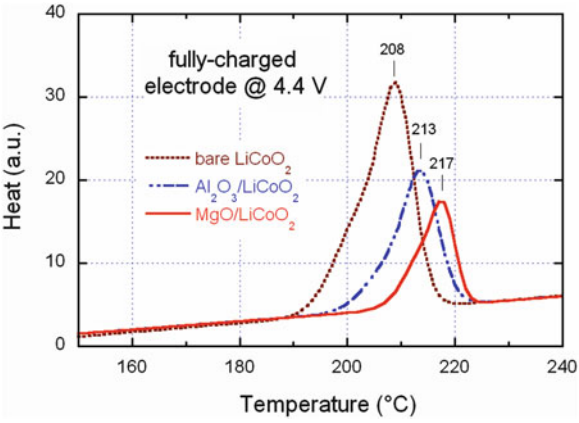

Fig. 14.23 DSC of a fully charged electrode at 4.4 V vs. Li^+/Li^0 for bare and Al_2O_3- and MgO-coated $LiCoO_2$ particles. The electrodes were cycled in coin cells with 1 mol L^{-1} $LiPF_6$ solution in EC-DMC (1:1) as electrolyte

$LiCoO_2$ particles. The electrodes were cycled in coin cells with 1 mol L^{-1} $LiPF_6$ solution in EC-DMC (1:1) as electrolyte. DSC curves show that the decomposition temperature has increased and the total amount of the reaction heat is reduced by the coatings. These results suggest that the safety of MgO-coated LCO electrode is improved. However, the coating also decreases the activation energy of lithium ion transfer reaction at the $LiCoO_2$ thin film electrode–electrolyte interface, indicating that the modification by MgO affects the kinetics of lithium ion transfer reaction at the $LiCoO_2$–electrolyte interface [57].

14.5.2.2 $LiNi_{0.7}Co_{0.3}O_2$

Not surprisingly, the same coatings as those reviewed for $LiCoO_2$ have been tested on the $LiNiO_2$ family, aiming to the same purpose: improve the electrochemical performance and find a solution to the thermal instability that hinders its use. For instance, Yoon et al. reported that MgO-coating of $LiNi_{0.8}Co_{0.2}O_3$ can suppress the formation of NiO-like rock-salt structure when heated at 450 °C [58]. $AlPO_4$ coating can also be done on $LiNi_{0.8}Co_{0.1}Mn_{0.1}O_2$ that has a larger capacity than $LiCoO_2$ [59]. Figure 14.24 presents the DSC curves of bare, Al_2O_3- and $AlPO_4$-coated $LiNi_{0.8}Co_{0.2}O_2$ electrode in the charge state at 2.6 V. These results show the beneficial effect of coating on the total amount of the reaction heat.

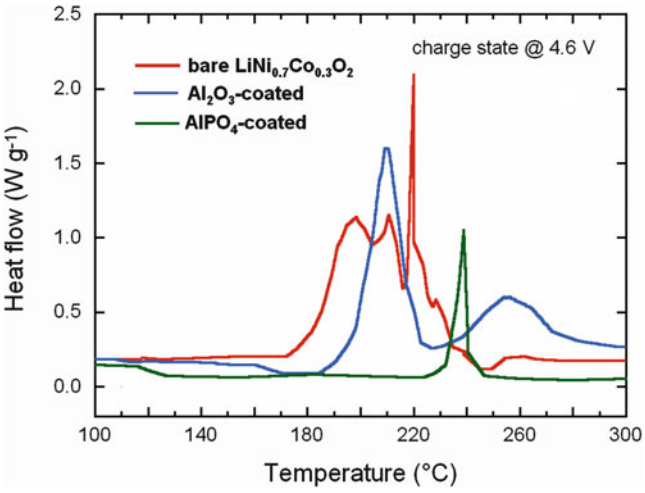

Fig. 14.24 DSC curves of bare, Al_2O_3- and $AlPO_4$-coated $LiNi_{0.8}Co_{0.2}O_2$ electrode in the charge state at 2.6 V

14.5.3 Surface Modifications of Spinel Electrodes

14.5.3.1 $LiMn_2O_4$

The spinel $LiMn_2O_4$ (LMO) is an attractive cathode element, mainly because its thermal stability is much better than that of the lamellar compounds [60]. However, it suffers from poor cycling behavior. The dissolution of manganese in the electrolyte is of major concern [61], since it reduces the calendar life of the battery. In addition, the kinetics of this reaction of $LiMn_2O_4$ with the electrolyte increases with the temperature, so that $LiMn_2O_4$-based batteries need to be maintained at room temperature. In this context, the study of surface modifications of LMO is of primary importance to protect the material against reactions with the electrolyte and avoid the dissolution of Mn^{3+} in order to achieve two goals: (1) improve the calendar life and cycling life to make it competitive with other cathode elements, and (2) make it possible to get rid of the lamellar component in the cathode, to restore the thermal safety of the battery. The most commonly used coating materials are metal oxides such as Al_2O_3, ZrO_2, ZnO, SiO_2, and Bi_2O_3, which can successfully protect electrode from HT attack. Developments in the surface modification of $LiMn_2O_4$ as cathode material of power lithium-ion battery have been reviewed by Yi et al. [62].

To explore the change in the electrochemical properties of the spinel electrodes, electrochemical impedance spectroscopy (EIS) was carried out for the pristine and coated material upon cycling in the charged state for cells maintained at 55 °C. Nyquist plots derived from the analyses of uncoated and ZrO_2-coated $LiMn_2O_4$ are shown in Fig. 14.25. Each EIS spectrum consists of two semicircles and a slope. The first semicircle in the high-to-medium frequency region is attributed to resistance of surface film (R_{sf}) that covers the electrode particle, while the semicircle at medium-to-low frequency region is associated with the charge transfer resistance (R_{ct}) coupled with a double-layer capacitance and the slope at the low-frequency region is assigned to lithium-ion diffusion in the bulk material. On the basis of this mechanism, the equivalent circuit used for analysis is given as insert. R_w represents the electrolyte resistance, CPE_{dl} is a constant phase element and W_z is the Warburg element corresponding to the Li^+ ion diffusion in the host material. After 50 cycles, the increase of R_{ct} of the uncoated material is due to the chemical evolution at the electrode–electrolyte interface rather than Mn(II) migration. The impedance spectra of ZrO_2-coated $LiMn_2O_4$ clearly display the contribution of the low frequency element due to the modified SEI layer, which reduces the Li^+-ion transport through the coating.

It has been reported that LMO particles coated with either borate glass Li_2O-$2B_2O_3$ (LBO) or with fluorine exhibit good high-temperature electrochemical performance. LBO-coated LMO electrode via solution method has an excellent cycling behavior (112 mAh g^{-1}) without any capacity loss even after 30 cycles at 1*C* rate [63]. Fluoride is also used to coat LMO to improve its cyclability because it is very stable even in HF. Lee et al. [64] reported that the BiOF-coated spinel

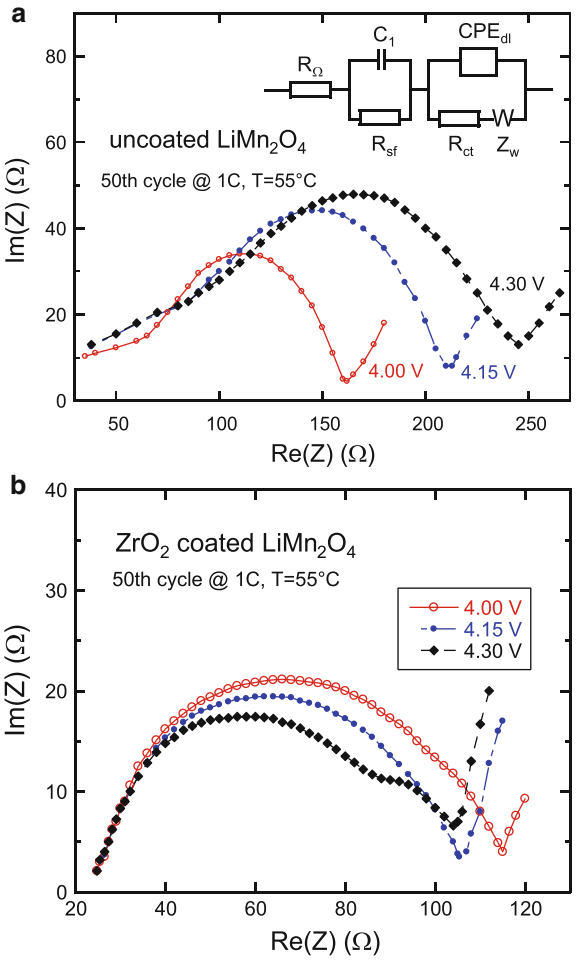

Fig. 14.25 Nyquist diagrams of (**a**) uncoated $LiMn_2O_4$ as a function of the state of charge after 50 cycles in the potential range 4.0–4.3 V and (**b**) after ZrO_2 coating. Cells were cycled at 1*C* rate and maintained at $T = 55$ °C. The equivalent circuit used for the analysis is shown as insert (see text for symbol meaning)

electrode had excellent capacity retention at 55 °C, maintaining its initial discharge capacity of 96 % after 100 cycles against 84 % for the pristine material because the oxyfluoride layer provides a strong protection against HF attack and scavenges HF.

14.5.3.2 $LiNi_{0.5}Mn_{1.5}O_4$

$LiNi_{0.5}Mn_{1.5}O_4$ (LNM) is considered as the most promising cathode to increase the density energy, as it operates at 4.7 V [65]. Unfortunately, its use is still postponed, mainly because of a significant capacity loss at elevated temperature $T > 50$ °C, which is a critical environment for HEV and EV applications. As for the $LiMn_2O_4$ spinel, the remedy envisioned for canceling the electrode-electrolyte reactions is the same for both materials, namely coat the particles with a protective layer.

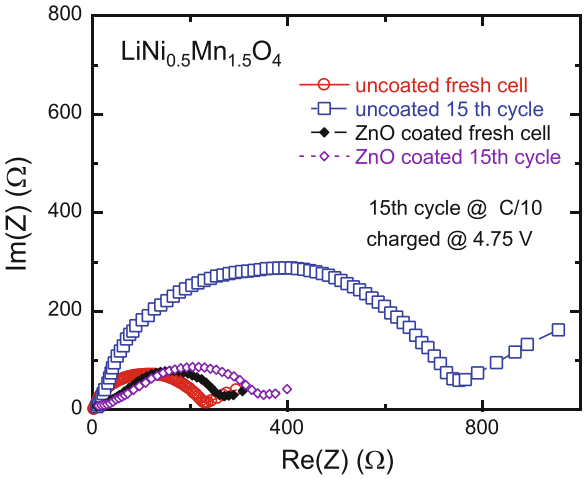

Fig. 14.26 Nyquist plots of uncoated and ZnO-coated $LiNi_{0.5}Mn_{1.5}O_4$ of fresh electrode and after 15 cycles at *C*/10 rate. EIS measurements were carried out in the charged state (4.75 V vs. Li^+/Li^0) at 55 °C

Like in the case of LCO, numerous coatings have been experimented such as ZnO, $AlPO_4$, $FePO_4$ that improved the electrochemical properties but not as much as Al_2O_3 [66]. As an example, the effect of ZnO coating on LMN electrode in the charged state at 4.75 V is depicted in Fig. 14.26. The pristine and coated materials were cycled at *C*/10 rate in cells maintained at 55 °C. After 15 cycles, it is observed that the spectrum of uncoated LNM electrode due to the big change of the R_{ct} resistance. Although the interpretation of the EIS results can be made using the equivalent circuit presented in Fig. 14.25. The Nyquit plots show that the initial R_{ct} value for the ZnO-coated LNM electrode is higher that for the uncoated sample because the coating formation. However, little change is observed upon cycling. In the case of the coated sample, both R_{cf} remains almost constant and R_{ct} slighly increases that obviously shows the more stable electrode–electrolyte interface.

14.6 Concluding Remarks

Lithium battery safety has raised a large interest in the recent years. The safety protection is a fundamental issue in the lithium-ion battery technology and the risks associated with it are managed in order to guarantee a safe use of the cells. Prevention includes many factors such as minimization of temperature runaway, internal shorts, mechanical damage, and control of the state of charge. Potential hazards include: oxygen gas release, corrosive electrolyte released, fire, and explosion. The diagram of the temperature runaway in Li-ion batteries as a function of the different positive electrode materials is shown in Fig. 14.27. We note that the electrode instability mainly due to structural breakdown and release oxygen appears to be a function of the metal-oxygen bonding in the order layered materials ($LiMO_2$-type) → spinel ($LiMn_2O_4$) → olivine ($LiMPO_4$).

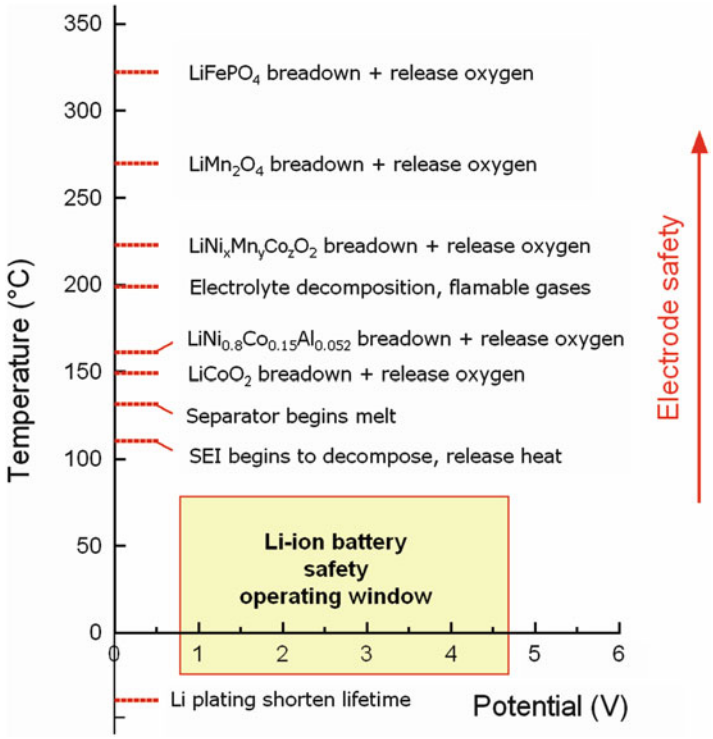

Fig. 14.27 Diagram of the temperature runaway in Li-ion batteries as a function of the different positive electrode materials with the range of voltage/temperature for battery safety

The carbon-coated $LiFePO_4$ showed excellent electrochemical performance reaching 152 mAh g^{-1}. This electrode also exhibited a reversible capacity corresponding to more than 89 % of the theoretical capacity when cycled between 2.5 and 4.0 V. Cylindrical 18650 cells with carbon-coated $LiFePO_4$ showed only 1.3 % discharge capacity loss for 100 cycles at 0.1*C* rate and also delivered 90 % of capacity retention at higher discharge rates up to 5*C* rate with 99.3 % coulombic efficiency, implying that the carbon coating improves the electronic conductivity. Low cell resistances and 80 % recovery of discharge pulse power through regenerative charge pulse during HPPC test performed on $LiFePO_4$ 18650-size cell indicated the suitability of this carbon-coated $LiFePO_4$ for high power HEV applications. The heat generation during charge and discharge at 0.5*C* rate, studied using IMC, indicated that the cell temperature is not raised above 34 °C in absence of external cooling. Thermal studies were also investigated by DSC and ARC, which showed that $LiFePO_4$ is safer, upon thermal and electrochemical abuse, than the commonly used lithium metal oxide cathodes with layered and spinel structures. Safety tests performed on $LiFePO_4$ cathode based cells, indicated that $LiFePO_4$ cells withstand physical abuse without causing any safety hazard, whereas $LiCoO_2$ causes instantaneous fire and smoke upon safety tests. In addition, the investigation

of $LiNi_{0.8}Co_{0.15}Al_{0.05}O_2$ has revealed that the introduction of Ni and Al as the doping element did not improve the thermal stability, which is then a recurrent problem in layered compounds. The dissolution of manganese in the electrolyte of $LiMn_2O_4$ spinel//graphite cells has been the motivation to add to the spinel a layer compound acting as a trap of manganese, in order to decrease the capacity fade. The present work, however, shows that it amounts to introduce in the cells an unstable element with very poor thermal stability. Therefore, delivery of high power and safety upon thermal, electrochemical, and physical abuse makes carbon-coated $LiFePO_4$ more suitable for HEV applications.

References

1. Joachin H, Kaun TD, Zaghib K, Prakash J (2008) Electrochemical and thermal studies of $LiFePO_4$ cathode in lithium-ion cells. ECS Trans 6–25:11–16
2. Yang H, Bang HJ, Amine K, Prakash J (2005) Investigations of the exothermic reactions of natural graphite anode for Li-ion batteries during thermal runaway. J Electrochem Soc 152: A73–A79
3. Joachin H, Kaun TD, Zaghib K, Prakash J (2009) Electrochemical and thermal studies of carbon-coated $LiFePO_4$ cathode. J Electrochem Soc 156:A401–A406
4. Lee CW, Venkatachalapathy R, Prakash J (2000) A novel flame-retardant additive for lithium batteries. Electrochem Solid State Lett 3:63–65
5. MacNeil DD, Lu Z, Chen Z, Dahn JR (2002) A comparison of the electrode/electrolyte reaction at elevated temperatures for various Li-ion cathodes. J Power Sourc 108:8–14
6. Li J, Suzuki T, Naga K, Ohzawa Y, Nakajima T (2007) Electrochemical performance of $LiFePO_4$ modified by pressure-pulsed chemical vapor infiltration in lithium-ion batteries. Mater Sci Eng B 142:86–92
7. Takahashi M, Otsuka H, Akuto K, Sakurai Y (2005) Confirmation of long-term cyclability and high thermal stability of $LiFePO_4$ in prismatic lithium-ion cells. J Electrochem Soc 152: A899–A904
8. Yonemura M, Yamada A, Takei Y, Sonoyama N, Kanno R (2004) Comparative kinetic study of olivine Li_xMPO_4 (M = Fe, Mn). J Electrochem Soc 151:A1352–A1356
9. Zaghib K, Shim J, Guerfi A, Charest P, Striebel KA (2005) Effect of carbon source as additive in $LiFePO_4$ as positive electrode for Li-ion batteries. Electrochem Solid State Lett 8: A207–A210
10. Belharouak I, Johnson C, Amine K (2005) Synthesis and electrochemical analysis of vapor-deposited carbon-coated $LiFePO_4$. Electrochem Commun 7:983–988
11. Jiang J, Dahn JR (2004) ARC studies of the thermal stability of three different cathode materials $LiCoO_2$, $Li[Ni_{0.1}Co_{0.8}Mn_{0.1}]O_2$ and $LiFePO_4$ in $LiPF_6$ and LiBoB EC/DEC electrolytes. Electrochem Commun 6:39–43
12. Padhi AK, Nanjundaswamy KS, Masquelier C, Goodenough JB (1997) Mapping of transition metal redox energies in phosphates with NASICON structure by lithium intercalation. J Electrochem Soc 144:2581–2586
13. Yamada A, Chung SC, Hinokuma K (2001) Optimized $LiFePO_4$ for lithium battery cathodes. J Electrochem Soc 148:A224–A229
14. Armand M, Tarascon JM (2008) Building better batteries. Nature 451:652–657
15. Chen G, Richardson TJ (2010) Thermal instability of olivine-type $LiMnPO_4$ cathodes. J Power Sourc 195:1221–1224
16. Chen G, Richardson TJ (2009) Solid solution phases in the olivine-type $LiMnPO_4/MnPO_4$ system. J Electrochem Soc 156:A756–A762

17. Kim SW, Kim J, Gwon H, Kang K (2009) Phase stability study of $Li_{1-x}MnPO_4$ ($0 \leq x \leq 1$) cathode for Li rechargeable battery. J Electrochem Soc 156:A635–A638
18. Bramnik NN, Nikolowski K, Trots DM, Ehrenberg H (2008) Thermal stability of $LiCoPO_4$ cathodes. Electrochem Solid State Lett 11:A89–A93
19. Martha SK, Haik O, Zinigrad E, Exnar I, Drezen T, Miners JH, Aurbach D (2011) On the thermal stability of olivine cathode materials for lithium-ion batteries. J Electrochem Soc 158: A1115–A1122
20. Martha SK, Markovsky B, Grinblat J, Gofer Y, Hai O, Zinigrad E, Aurbach D, Drezen T, Wang D, Deghenghi G, Exnar I (2009) $LiMnPO_4$ as an advanced cathode material for rechargeable lithium batteries. J Electrochem Soc 156:A541–A552
21. Martha SK, Grinblat J, Haik O, Zinigrad E, Drezen T, Miners JH, Exnar I, Kay A, Markovsky B, Aurbach D (2009) $LiMn_{0.8}Fe_{0.2}PO_4$: an advanced cathode material for rechargeable lithium batteries. Angew Chem Int Ed 48:8559–8563
22. Zaghib K, Mauger A, Goodenough JB, Gendron F, Julien CM (2007) Electronic, optical, and magnetic properties of $LiFePO_4$: small magnetic polaron effects. Chem Mater 19:3740–3747
23. Nakamura T, Miwa Y, Tabuchi M, Yamada Y (2006) Structural and surface modifications of $LiFePO_4$ olivine particles and their electrochemical properties. J Electrochem Soc 153: A1108–A1114
24. Yang S, Song Y, Zavalij PY, Whittingham MS (2002) Reactivity, stability and electrochemical behavior of lithium iron phosphates. Electrochem Commun 4:239–244
25. Ravet N, Chouinard Y, Magnan JF, Besner S, Gauthier M, Armand M (2001) Electroactivity of natural and synthetic triphylite. J Power Sourc 97:503–507
26. Zaghib K, Mauger A, Kopec M, Gendron F, Julien CM (2009) Intrinsic properties of 40 nm-sized $LiFePO_4$ particles. ECS Trans 16–42:31–41
27. Wu Q, Lu W, Prakash J (2000) Characterization of a commercial size Li-ion cell with a reference electrode. J Power Sourc 88:237–242
28. Trudeau ML, Laul D, Veillette R, Serventi AM, Mauger A, Julien CM, Zaghib K (2011) In-situ HRTEM synthesis observation of nanostructured $LiFePO_4$. J Power Sourc 196:7383–7394
29. Zaghib K, Dontigny M, Guerfi A, Charest P, Rodrigues I, Mauger A, Julien CM (2011) Safe and fast-charging Li-ion battery with long shelf life for power applications. J Power Sourc 196:3949–3954
30. Shin HC, Cho WI, Jang H (2006) Electrochemical properties of the carbon-coated $LiFePO_4$ as a cathode material for lithium-ion secondary batteries. J Power Sourc 159:1383–1388
31. Gao F, Tang Z (2008) Kinetic behavior of $LiFePO_4$/C cathode material for lithium-ion batteries. Electrochim Acta 53:5071–5075
32. Zaghib K, Dontigny M, Charest P, Labrecque JF, Guerfi A, Kopec M, Mauger A, Gendron F, Julien CM (2010) $LiFePO_4$: from molten ingot to nanoparticles with high-rate performance in Li-ion batteries. J Power Sourc 195:8280–8288
33. Julien CM, Mauger A, Zaghib K (2011) Surface effects on electrochemical properties of nano-sized $LiFePO_4$. J Mater Chem 21:9955–9968
34. Yang H, Prakash J (2004) Determination of the reversible and irreversible heats of a $LiNi_{0.8}Co_{0.1}5Al_{0.05}O_2$/natural graphite cell using electrochemical-calorimetric technique. J Electrochem Soc 151:A1222–A1229
35. Lu W, Yang H, Prakash J (2006) Determination of the reversible and irreversible heats of $LiNi_{0.8}Co_{0.2}O_2$/mesocarbon microbead Li-ion cell reactions using isothermal microcalorimetry. Electrochim Acta 51:1322–1329
36. Whitacre JF, Zaghib K, West WC, Ratnakumar BV (2008) Dual active material composite cathode structures for Li-ion batteries. J Power Sourc 177:528–536
37. Forgez C, Do DV, Friedrich G, Morcrette M, Delacourt C (2010) Thermal modeling of a cylindrical $LiFePO_4$/graphite lithium-ion battery. J Power Sourc 195:2961–2968
38. Jin EM, Jin B, Jun DK, Park KH, Gu HB, Kim KW (2008) A study on the electrochemical characteristics of $LiFePO_4$ cathode for lithium polymer batteries by hydrothermal method. J Power Sourc 178:801–806

39. Bang HJ, Joachin H, Yang H, Amine K, Prakash J (2006) Contribution of the structural changes of $LiNi_{0.8}Co_{0.15}Al_{0.05}O_2$ cathodes on the exothermic reactions in Li-ion cells. J Electrochem Soc 153:A731–A737
40. Dokko K, Koizumi S, Sharaishi K, Kananura K (2007) Electrochemical properties of $LiFePO_4$ prepared via hydrothermal route. J Power Sourc 165:656–659
41. Dahn JR, Fuller EW, Obrovac M, von Sacken U (1994) Thermal stability of Li_xCoO_2, Li_xNiO_2 and λ-MnO_2 and consequences for the safety of Li-ion cells. Solid State Ionics 69:265–270
42. McNeil DD, Dahn JR (2001) The reaction of charged cathodes with nonaqueous solvents and electrolytes: I. $Li_{0.5}CoO_2$. J Electrochem Soc 148:A1205–A1210
43. Lee KK, Yoon WS, Kim KB, Lee KY, Hong ST (2001) A study on the thermal behaviour of electrochemically delithiated $Li_{1-x}NiO_2$. J Electrochem Soc 148:A716–A722
44. Baba Y, Okada S, Yamaki JI (2002) Thermal stability of Li_xCoO_2 cathode for lithium ion battery. Solid State Ionics 148:311–316
45. Guerfi A, Dontigny M, Charest P, Petitclerc M, Legacé M, Vijh A, Zaghib Z (2010) Improved electrolytes for Li-ion batteries: mixtures of ionic liquid and organic electrolyte with enhanced safety and electrochemical performance. J Power Sourc 195:845–852
46. Ishikawa M, Sugimoto Y, Kikuta M, Ishiko E, Kono M (2006) Pure ionic liquid electrolyte compatible with a graphitized carbon negative electrode in rechargeable lithium-ion batteries. J Power Sourc 162:658–662
47. Matsumoto H, Sakaebe H, Tatsumi K, Kikuta M, Ishiko E, Kono M (2006) Fast cycling of $Li/LiCoO_2$ cell with low-viscosity ionic liquids based on bis(fluorosulfonyl)imide $[FSI]^-$. J Power Sourc 160:1308–1313
48. Wang Y, Zaghib Z, Guerfi A, Bazito FFC, Torresi RM, Dahn JR (2007) Accelerating rate calorimetry studies of the reactions between ionic liquids and charged lithium ion battery electrode materials. Electrochim Acta 52:6346–6352
49. Zaghib K, Dubé J, Dallaire A, Galoustov K, Guerfi A, Ramanathan M, Benmayza A, Prakash J, Mauge A, Julien CM (2012) Enhanced thermal safety and high power performance of carbon-coated $LiFePO_4$ olivine cathode for Li-ion batteries. J Power Sourc 219:36–44
50. Zaghib K, Dubé J, Dallaire A, Galoustov K, Guerfi A, Ramanathan M, Benmayza A, Prakash J, Mauger A, Julien CM (2014) Lithium ion cell components and their effect on high-power battery safety. In: Pistoia G (ed) Lithium-ion batteries: advances and applications. Elsevier, New York, pp 437–460
51. Li C, Zhang HP, Fu LJ, Liu H, Wu YP, Rahm E, Holze R, Wu HQ (2006) Cathode materials modified by surface coating for lithium ion batteries. Electrochim Acta 51:3872–3888
52. Cho J, Kim YJ, Park B (2000) Novel $LiCoO_2$ cathode material with Al_2O_3 coating for a Li ion cell. Chem Mater 12:3788–3791
53. Liu LJ, Chen Q, Huang XJ, Yang XQ, Yoon WS, Lee HS, McBreen J (2004) electrochemical and in situ synchrotron XRD studies on Al_2O_3-coated $LiCoO_2$ cathode material. J Electrochem Soc 151:A1344–A1351
54. Oh S, Lee JK, Byuna D, Cho W, Cho BW (2004) Effect of Al_2O_3 coating on electrochemical performance of $LiCoO_2$ as cathode materials for secondary lithium batteries. J Power Sources 132:249–255
55. Chen ZH, Dahn JR (2002) Effect of a ZrO_2 coating on the structure and electrochemistry of Li_xCoO_2 when cycled to 4.5 V. Electrochem Solid State Lett 5:A213–A216
56. Chang W, Choi JW, Im JC, Lee JK (2010) Effects of ZnO coating on electrochemical performance and thermal stability of $LiCoO_2$ as cathode material for lithium-ion batteries. J Power Sourc 195:320–326
57. Wang Z, Wu C, Liu L, Wu F, Chen L, Huang X (2002) Electrochemical evaluation and structural characterization of commercial $LiCoO_2$ surfaces modified with MgO for lithium-ion batteries. J Electrochem Soc 149:A466–A471
58. Yoon WS, Nam KW, Jang D, Chung KY, Hanson J, Chen JM, Yang XQ (2012) Structural study of the coating effect on the thermal stability of charged MgO-coated $LiNi_{0.8}Co_{0.2}O_2$ cathodes investigated by in situ XRD. J Power Sourc 217:128–134

59. Cho J, Kim H, Park B (2004) Comparison of overcharge behavior of $AlPO_4$-coated $LiCoO_2$ and $LiNi_{0.8}Co_{0.1}Mn_{0.1}O_2$ cathode materials in Li-ion cells. J Electrochem Soc 151: A1707–A1711
60. Wohlfahrt-Mehrens M, Vogler C, Garche J (2004) Aging mechanisms of lithium cathode materials. J Power Sourc 127:58–64
61. Amatucci GG, Schmutz CN, Blyr A, Sigala C, Gozdz AS, Larcher D, Tarascon JM (1997) Materials effects on the elevated and room temperature performance of C-$LiMn_2O_4$ Li-ion batteries. J Power Sourc 69:11–25
62. Yi TF, Zhu YR, Zhu XD, Shu J, Yue CB, Zhou AN (2009) A review of recent developments in the surface modification of $LiMn_2O_4$ as cathode material of power lithium-ion battery. Ionics 15:779–784
63. Sahan H, Göktepe H, Patat S, Ülgen A (2008) Solid State Ionics 178:1837–1842
64. Lee KS, Myung ST, Amine K, Yashiro H, Sun YK (2009) Dual functioned BiOF-coated Li $[Li_{0.1}Al_{0.05}Mn_{1.85}]O_4$ for lithium batteries. J Mater Chem 19:1995–2005
65. Julien CM, Mauger A (2013) Review of 5-V electrodes for Li-ion batteries: status and trends. Ionics 19:951–988
66. Liu D, Bai Y, Zhao S, Zhang W (2012) Improved cycling performance of 5 V spinel $LiMn_{1.5}Ni_{0.5}O_4$ by amorphous $FePO_4$ coating. J Power Sourc 219:333–338

Chapter 15
Technology of the Li-Ion Batteries

15.1 The Capacity

The irreversible capacity that is measured by the loss of capacity delivered by the battery during the first cycle (eventually also the second cycle) may have different causes. For the positive electrode, the loss of capacity during the first two cycles is often due to the fact that, when the cell is charged for the first time, the de-intercalation of lithium is accompanied with a structure modification that is not totally reversible, so that during the first discharge, some lattice distortion remains, even if the lithium can reenter into the active element of the positive electrode. As a consequence, some of the Li^+ ions will remain trapped into the particles. The irreversible capacity of $LiCoO_2$, for instance, is typically 3–5 mAh g^{-1}. Yet, this loss is relatively small, but it increases for materials that have a smaller structural stability such as $LiNiO_2$, in which case, the irreversible capacity raises up to 20–30 mAh g^{-1}. On the negative electrode side, the cause for the irreversible loss of capacity is different. In particular, for carbon-based anodes, the initial irreversibility is due to the formation of the solid-electrolyte interface (SEI) caused by the reduction of the electrolyte at the surface of the anode. The exact value of the irreversible capacity in this case depends on the shape, size and crystallinity of the carbon particles, but it remains in the range 20–30 mAh g^{-1}. Note that this part of the irreversible loss of capacity is due to the Li^+ ions that are trapped in the SEI on the anode, but these Li^+ ions have been supplied by the positive electrode during the first charge. On the other hand, Chap. 10 gives examples of situations where the initial irreversibility is huge, either because of the destruction of the crystallinity (amorphization) of the anode material during the first charge (for example: Si), or because of irreversible chemical reactions during the first discharge (for example: anodes based on alloying/de-alloying reactions). The irreversible capacity for such anodes is so large that attention is focused on the

C. Julien et al., *Lithium Batteries*, DOI 10.1007/978-3-319-19108-9_15

reversible capacity measured after the first or second cycle of the half cell, since it is the capacity that can be delivered during the life of the battery. In any case, the coulombic efficiency after the two first cycles for a battery of interest (i.e., already commercialized or under investigation in research laboratories) is close to 100 %.

15.2 Negative/Positive Capacity Ratio

The negative electrode/positive electrode ratio N/P is also called the balance of the battery. To understand the importance of this parameter, let us first consider the case of a negative electrode with initial capacity 100 mAh with irreversible capacity 10 mAh. This means that, in an experience made on a cell with this electrode and Li-metal as the counter-electrode, the measurements have shown that the formation of the SEI has consumed 10 mAh, so that the capacity delivered by the electrode after formation of the SEI is 90 mAh. For this half-cell, the formation of the SEI has no consequence, and does not limit the capacity of the half-cell, because the metal-Li is a reservoir that can provide as much of Li^+ ions as we need. This, however, is not true for the full cell. To see the effect, let us consider now the full cell with this negative electrode, and a positive electrode with an initial capacity 100 mAh and irreversible capacity 20 mAh, so that its reversible capacity is 80 mAh. During the first charge, the capacity of the positive electrode is just sufficient to allow for the formation of the SEI that consumes 10 mAh, plus fully charge the negative electrode with an amount of Li^+ ions corresponding to a capacity of 90 mAh. Upon discharging, these Li^+ ions will be delivered by the negative electrode to the positive electrode, so that only the amount of lithium inside the positive electrode now corresponds to a capacity of 100-10 = 90 mAh. However, a part of them corresponding to the irreversible capacity 20 mAh will be trapped, so that the capacity of the battery will be 90-20 = 70 mAh, while the negative electrode has a larger capacity. Therefore, the formation of the SEI has now contributed to a decrease of the reversible capacity of the full cell.

It might be tempting to increase the amount of active product in the positive electrode to increase the capacity of the battery. However, this may be not a good idea. Let us assume for instance that we increase the capacity of the positive electrode by 50 %. Then the initial capacity of the positive electrode is 150 mAh, and the irreversible capacity is 30 mAh. During the first charge, 100 mAh out of the 150 mAh available will be delivered by the positive electrode like before. Actually, if the charge is stopped at this stage, then, during the first discharge, 90 mAh will return to the negative electrode. The amount of lithium that the positive electrode can deliver in the second charge corresponds to a capacity of 140-30 = 110 mAh capacity available to proceed reversibly upon cycling, larger than the 90 mAh that the negative electrode can absorb, so that the reversible capacity is simply the reversible capacity of the negative electrode: 90 mAh. However, batteries are used usually under conditions of deep charging and discharging. In the case of the cell we have chosen, after an amount of lithium corresponding to 100 mAh have been

transferred to the negative electrode, further charging will still move the lithium remaining in the positive electrode to the negative electrode. Since, however, there is no more room for additional Li in this negative electrode, the lithium will accumulate at the surface of the negative electrode, and will thus form a Li-metal film. This effect known as lithium plating, results in a serious threat for the safety of the battery because of the possible formation of lithium oxides, so that this situation is actually prohibited. Therefore, the first criterion in the design of a battery is that the capacity of the negative electrode must be larger than the capacity of the positive electrode, despite the advantage of a gain in capacity of the battery that a larger capacity of the positive electrode might induce.

Taking this rule into account, let us see if we can increase the capacity of the initial battery we has envisioned, by increasing the capacity of the negative electrode by 50 %, instead of that of the positive electrode. Then we are left with a positive electrode with capacity 100 mAh, irreversible capacity 10 mAh, and the negative electrode now has a capacity 150 mAh, and irreversible capacity 15 mAh. Now, the same considerations as before show immediately that after the end of the first cycle, the capacity is 100-15-20 = 65 mAh instead of the initial 70 mAh when the capacity of the negative electrode was only 100 mAh. Therefore the increase of capacity of the negative electrode has actually led to a decrease of the capacity of the battery. This is due to the increase of the irreversible capacity due to the formation of the SEI that increases in the same proportion as the reversible capacity of the negative electrode, when it is obtained by simply adding active particles (same size and same shape).

Of course the example we have chosen is oversimplified: there are some degradations of the capacity upon cycling and in time, also we have assumed that the loss of irreversible capacity on the anode side was only due to the formation of the SEI supposed to be stable, and so on. It is sufficient, however, to illustrate the importance of the choice of the balance of the electrodes to determine both the safety and the capacity of the batteries.

Since the balance of the battery is a very important parameter, the battery manufacturers are usually reluctant to communicate on it. The information is released for the old-fashioned $LiCoO_2$//graphite cell that has been used for 30 years. For a standard "18650" cell (i.e., cylindrical, diameter: 18 mm, length 65 mm), the width of the anode is ~59 mm, slightly larger than the width of the cathode ~58 mm, so that the condition of a capacity of the negative electrode larger than that of the positive electrode is fulfilled, with the ratio N/P = 1.1.

15.3 Electrode Loading

The electrode loading refers to the quantity of electrode material that is deposited per unit area of the current conductor foil. This is also an important parameter that needs to be optimized. Too large loading levels introduce excessive resistance within the electrode layer and thus limits the electrical current that can cross the electrode, i.e.,

reduces the rate capability of the battery. On the other hand, decreasing the loading level increases the rate capability, but it also reduces the mass of active materials and thus the energy density. Therefore, an increased electrode area is required to compensate this reduction in order to keep the same capacity, which in turn requires a larger amount of metal foil on the current collector, and thus a mass penalty that may be larger than the reduction of the gain of mass associated with the decrease of the loading. One might wish to decrease the thickness of the metal foil to overcome this difficulty, but of course, there is a limitation imposed by the need to handle the foil during the manufacturing process of the battery. We recover here the basic conflict in Li-ion batteries between high power and high energy. Therefore, the loading level (in g cm^{-2}) is always a compromise, and its optimization is again specific to the powder that is used for the electrode, since the effective surface area also depends on the size and shape of the particles.

15.4 Degradations

The loss of capacity either with cycling (cycle life) or simply with time (calendar life) has different causes, we review in this section.

15.4.1 Damage of the Crystalline Structure

With the noticeable exception of $Li_4Ti_5O_{12}$, the active anode materials change volume when they absorb or release lithium. Upon cycling, this results in a fatigue of these active materials. In extreme cases, the result is a pulverization of the particles (see the case of Si anodes, Chap. 10). More often, like in graphite, it results in micro-cracks, exposing new parts of the particles to the electrolyte, in particular at the end of deep discharge where the variation of volume is the largest. The interaction of this new part of the active particles with the electrolyte results in the formation of additional SEI when the battery is recharged, which requires a consumption of Li, and thus a decrease of the capacity. Meanwhile the increase of the SEI leads to an increase of the resistance of the battery, and thus lowers the rate capability. In addition, this aging of the surface of the particles also results in modified electrochemical properties and thus aging of the battery.

15.4.2 Dissolution of the SEI

Traces of contaminants can be introduced in the electrolyte during manufacturing. They also can simply result from dissolved species from the positive electrode. The reason is that the positive electrode is susceptible to oxidation at the end of charge.

The dissolved species, in some cases, act as catalysts that dissolve the SEI, in particular at the end of the discharge where the SEI is less stable. To understand the consequence of such an effect on the battery, let us return to the same example similar to the one we used before, with a full cell doted with a positive electrode of initial capacity 110 mAh, irreversible capacity 10 mAh, so that its reversible capacity is 100 mAh, and a negative electrode of initial capacity 130 mAh, including an irreversible capacity 50 mAh required for the formation of the initial SEI. After the first cycle, the capacity of the cell is thus 110-10-30 = 70 mAh, smaller than the capacity 80 mAh of the negative electrode as required. Now we assume a degradation of the positive electrode so that, after 100 cycles, the SEI has been partly dissolved and the irreversible capacity associated to it has been reduced by 10 mAh. Then, if this is the only modification in the cell, the capacity after 100 cycles has increased to 80 mAh, just equal to the capacity that the negative electrode can afford, so that further degradation will result in the formation of a lithium plating at the surface of the negative electrode, just what we do not want. Of course, this is an extreme situation, but it illustrates the damage that may result from the degradation of the cathode if the resulting species dissolved in the electrolyte dissolve the SEI. It also points to the importance of choosing the couple positive-negative electrodes so that a stable SEI is formed (see Chap. 1).

15.4.3 Migration of Cathode Species

The dissolved species from the positive electrode can also migrate from the positive to the negative electrode. In this case, they can undergo reduction and produce additional surface layer. An example is the dissolution of manganese into the electrolyte in case of the $LiMn_2O_4$ spinel. As any chemical reaction, this oxidation accelerates with temperature. The experience has been made after a hot summer in the USA, where the electric cars equipped with this anode were recalled by the car maker for change of the batteries out of use. In more dramatic cases, met in particular with Ni-rich layered metal oxides, the oxygen may be released form the positive electrode, move to the carbon anode with which it will react to form CO_2.

15.4.4 Corrosion

Any residual presence of water will engender corrosion of the collectors. The lithium salt used in the Li-ion batteries is normally $LiPF_6$, which has a very good conductivity, and presents the advantage of protecting the collector in aluminum from corrosion. However, it reacts with water to form hydrofluoric acid HF that is very corrosive and thus attacks metallic collectors according to the reaction:

$$LiPF_6 + 4H_2O \rightarrow 5HF + LiF + H_3PO_4. \quad (15.1)$$

It is thus primordial to take care during the manufacturing of the battery to avoid the introduction of any trace of water.

15.5 Manufacturing and Packaging

The components of a cell are the two electrodes, the separator, and the electrolyte. The choice and role and choice of the separator have been reviewed in the chapter devoted to the safety. In this section, we review the different steps to assembly these elements in the manufacturing of the cells.

15.5.1 Step 1: Preparation of the Active Particles of the Electrodes

The synthesis of the active particles used as active elements of the electrodes, and their performance depending on the size, shape, composition, is the topic treated in the chapters devoted to anodes and cathodes. We have shown in these chapters that the active particles for both the positive and the negative electrodes are now nanoparticles. The technology of the nanoparticles is a domain in itself, and we engage the reader to read specialized books devoted to the subject [1]. We thus assume here that the step of the preparation of the active nanoparticles is achieved. In the chapters devoted to the positive and negative electrodes chapters, however, the electrodes were built with homogeneous powder since the purpose was to test the active elements and to compare their electrochemical properties. We have seen, however, that each material has its advantage and inconvenience, so that the choice depends on the application of the battery. In many applications that rely on Li-ion batteries for energy storage, the nominal duty cycle consists of a long-duration base load (typically to support ancillary or standby functions) punctuated by shorter durations of higher power demand for events such as physical actuation or communication uplink [2–4]. In the absence of electrode materials that can deliver both very high energy specific energy as well as high-rate capability, this type of power profile has led system designers to select either lower energy density systems that can support high discharge rates, or to specify dual-rate hybrid energy storage systems that use two independent storage devices: one low-rate high energy, the other high-rate low energy [5–7]. This solution leads to increased complexity at the systems level, where separate charge control electronics, packaging and wiring are needed. There is, however, another possible solution: a dual-rate hybrid battery that is based on two different active cathode materials that are incorporated into the same positive electrode structure and work in concert. The approach is not new, as there are many publications, both in the academic and patent arenas, which describe

the idea in different forms. For example, several groups have examined mixing layered $LiMO_2$ ($M = Ni, Co, Mn$) and spinel $LiMn_2O_4$ in the same cathode structure [8–10]. Other groups examined mixing $LiMO_2$ and Li_2RuO_3 in a similar fashion [11]. A use of $LiFePO_4$:$LiCoO_2$ multi-layered structure has also been proposed to increase cell tolerance to overcharge [12]. A US patent covers a broad range of possible electrode compositions and describes in detail specific cathode active material blends, including mixed $LiMO_2$ layered materials hybridized with $LiMPO_4$ materials [13]. This is a process increasingly popular for the positive electrode. For instance, the carbon-coated $LiFePO_4$ is known to be the safest cathode element, and it can deliver very high power up to 50*C* rate [14, 15]. This is thus the best cathode active element for batteries in hybrid vehicles for instance [16, 17], since this battery should be able to support a large *C*-rate upon charging to recuperate the maximum energy during the braking phase, and fast discharge during accelerations of the car. The energy density of $LiFePO_4$, however, is rather small, since the operating voltage is 3.5 V, and the capacity is 160 mAh g^{-1}. This is a limit for use in electric cars, since the driver wants the largest possible autonomy. For the lamellar compounds, it is just the opposite: they are not safe, have poor rate capability, but large capacities. In particular, the pseudo-binary system $xLi[Ni_{0.5}Mn_{0.5}]O_2$:$y[Li[Li_{0.33}Mn_{0.67}]O_2$ has been found to have particularly large capacities, reaching 250 mAh g^{-1} for $x = y = 0.5$, i.e., for $Li[Li_{0.17}Mn_{0.58}Ni_{0.25}]O_2$ (when charged to 4.8 V) at low *C*-rate [18–20]. Therefore, it is tempting to build a positive electrode in which both of these active elements are present to find a compromise between their advantages and disadvantages. There are three different means of preparing this electrode, shown in Fig. 15.1 [21]. The two active materials can be (a) completely mixed in a single monolithic electrode; (b) segregated into two different areas; (c) layered with the $LiFePO_4$ at the bottom, i.e., in contact with the aluminum in all these cases. The tests performed on the cells with the electrodes prepared in the three configurations have shown that it is less advantageous to mix or layer the two active elements. This is easily understood as follows. When the Li

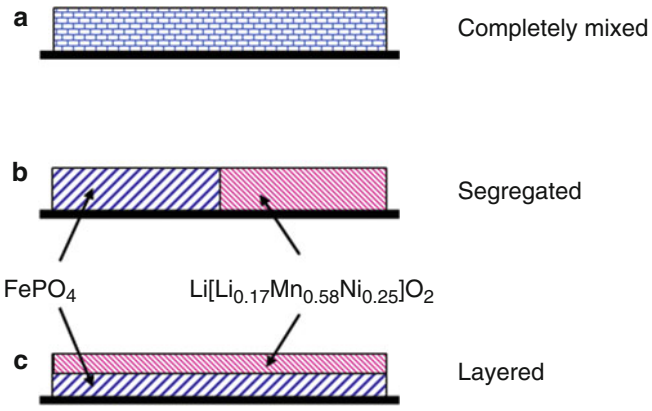

Fig. 15.1 The different means of preparing a $Li[Li_{0.17}Mn_{0.58}Ni_{0.25}]O_2$ electrode

$[Li_{0.17}Mn_{0.58}Ni_{0.25}]O_2$ and the $LiFePO_4$ are mixed intimately, all the particles are forced to be equipotential with their neighboring particles because they are in electrical contact via the high surface area conductive diluents. The consequence is an increased degree of overall electrode polarization, though the higher conductivity of the C-$LiFePO_4$ material was still able to combat severe polarization to some degree, as it likely offered a direct conductive route through the thickness of the electrode.

The layered case is more extreme: here both the electronic and the ionic conductivities of both of the constituents are manifested, as the C-$LiFePO_4$ is not present throughout the electrode to aid in electrical conductivity. All cell current is then forced to pass through the $Li[Li_{0.17}Mn_{0.58}Ni_{0.25}]O_2$ material, damming the rate capability of the electrode.

On the other hand, in the case of the physically segregated electrodes, the entire $Li[Li_{0.17}Mn_{0.58}Ni_{0.25}]O_2$ electrode can be polarized as a single body under higher discharge rates, thereby driving most current through the $LiFePO_4$ electrode. In this case, it s not requisite that all of the $Li[Li_{0.17}Mn_{0.58}Ni_{0.25}]O_2$ and $LiFePO_4$ active particles be held at the same potential within their separate electrodes.

In conclusion, mixing two active materials with disparate rate capabilities into a composite electrode is not equivalent to placing the electrodes in parallel at either an electrode or cell level. The best electrode configuration consists of segregated active materials contacting a common current collector. This arrangement allows the high-rate material to contribute fully under high current loads, without suffering the significant polarization effects associated with the low-rate material. This configuration is most similar to putting separate cells made using pure positive electrodes of the specific materials in parallel at the circuit level, a solution that is less appealing for applications requiring compact energy storage devices and simple charge control electronics. The voltage profile of the Li $[Li_{0.17}Mn_{0.58}Ni_{0.25}]O_2$—carbon coated $LiFePO_4$ in 50:50 wt% ratio built in this configuration with Li metal counter-electrode is shown in Fig. 15.2. The results were obtained by spray-deposition of the powders mixed in NMP solvent bath with 10 wt% binder and 10 wt% carbon black conductive diluents (see the next step devoted to the preparation of this laminate). The data were collected after several low-rate formation cycles were completed on the cells to encourage electrode SEI stabilization. One recognizes the voltage plateau at 3.45 V corresponding to the contribution of the $LiFePO_4$ part, to which is superposed the contribution of the Li $[Li_{0.17}Mn_{0.58}Ni_{0.25}]O_2$ component. A battery obtained by assembling such cells delivers over 700 W/kg at low rates and 300 W kg^{-1} at the rate of 3*C*.

15.5.2 Step 2: Preparation of the Electrode Laminates

The preparation is similar for both electrodes. First a conductive agent (usually carbon, acetylene black) is added to the powder in order to absorb the dilatation-contraction of the particles, and improve the electrical conductivity of the powder. Then a binder is added to plasticize the electrode, so that it can be handled.

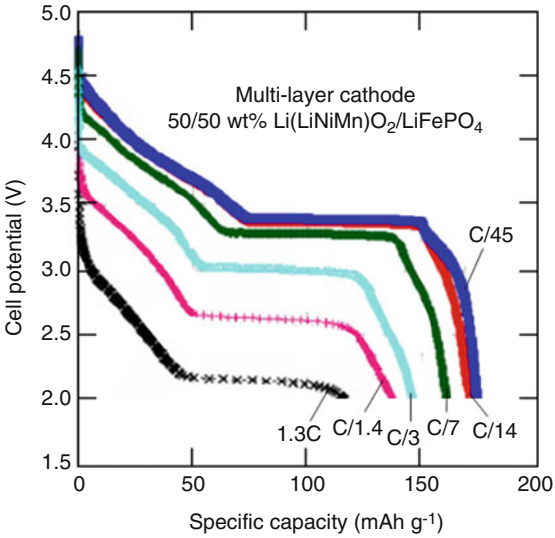

Fig. 15.2 Voltage profile of the $Li[Li_{0.17}Mn_{0.58}Ni_{0.25}]O_2$—carbon coated $LiFePO_4$ in 50:50 wt% ratio built in this configuration with Li metal counter-electrode

15.5.2.1 The Binder

The typical binder is the polyvinylidene fluoride (PVdF). In the cell manufacturing processes, *N*-methyl-2-pyrrolidone (NMP) is generally used as a solvent to dissolve the PVdF binder. Despite the widespread use of NMP, it has some disadvantages such as high cost, environmental issue associated with NMP recovery, and the severe processing control of the relative humidity (to be <2 %) to avoid the corrosion effects discussed earlier in this chapter. Also, the PVdF has strong binding strength, but low flexibility. The low flexibility can easily deteriorate cycle life characteristics of the battery due to the breaking of the bonds between active particles when important expansion/contraction process occurs during charging and discharging process. Therefore, a new trend is being developed to substitute the PVdF binder by another binder having a better elasticity to absorb the expansion and contraction stresses during cycling, in particular in anodes [22, 23]. In the case of Si-anodes, in particular, where the change of volume upon insertion or de-intercalation of lithium is very high, PVdF does not lead to good results. In such a case, the selection of a more flexible binder is very important for the electrochemical performance of anode electrodes [24–27]. So far, candidates for various new binders for Si anodes have included styrene butadiene rubber-sodium carboxymethyl cellulose (SBR-SCMC), sodium carboxymethyl cellulose (SCMC), polyamide imide (PAI), and polyacrylic acid (PAA), polyimide (PI), algae, among others [27–35] (see also Chap. 10).

Other reasons have been brought up to substitute PVdF: safety aspect of the battery, its high cost [36, 37]. Fluorine is one of the degradation products in the battery that produces stable LiF. Depending on liquid electrolytes, the formation of LiF and other harmful products with double bond ($C=CF^{-}$) is accelerated [38–40].

Further, self-heating thermal runaway can be induced. With respect to safety, a binder such as PVdF, which is soluble in organic solvent, is dangerous to humans and the environment. Consequently, many efforts have been done to identify suitable alternative non-fluorinated binders soluble in agent friendlier than an organic solvent. Such aqueous binders have been successfully tested and are increasingly popular for the negative electrode materials [23, 37] since some time. Their advantages are as follows: (1) low cost, (2) no pollution problem, (3) enhancement in the active material ratio in a cell owing to the reduction of binder content, (4) no requirement for strict control of the processing humidity, and (5) fast drying speed in electrode fabrication. SBR/CMC composite agent is the most popular aqueous binder, where styrene-butadiene rubber (SBR) is the primary binder, and sodium carboxymethyl cellulose (CMC) is the thickening/setting agent. Nowadays, some elastomers are commercially used as a binder for anodes in Li-ion batteries.

Recently, effort has started in the preparation of the positive electrode slurry as well [41]. However, the transition from nonaqueous to aqueous coating process has encountered some unexpected difficulties related so slurry formulation, viscosity control and film processing, which must be overcome for successful implementation in Li-ion batteries. Looking as an example the at the case of $LiFePO_4$ which is a recently commercialized positive electrode, we find that the compatibility of the elastomer binder compared to the PVdF binder, and how they connect or interact with the $LiFePO_4$ particles is different. Figure 15.3 illustrates the binding models with elastomer and PVdF binders. Regarding the CMC, it is very difficult to observe it directly in the electrode structure. We speculate that very thin CMC layer is coated at the active material of $LiFePO_4$, and some part acts as a rigid binder. During the aqueous slurry preparation process, the CMC is very important as a thickener to control the viscosity, but after coating the CMC stays almost unchanged in the electrode. CMC is an electrochemically inert part in the electrode and then eventually has no significant role in the dried electrode. We consider that the elastomer contacts quite a small surface area of each particle. This contact is enough to ensure good binding and still gives flexibility to the electrodes. The high flexibility is confirmed by the smaller electrode density when CMC is used instead of PVdF with the same active particles, and the elastomer was found to be twice

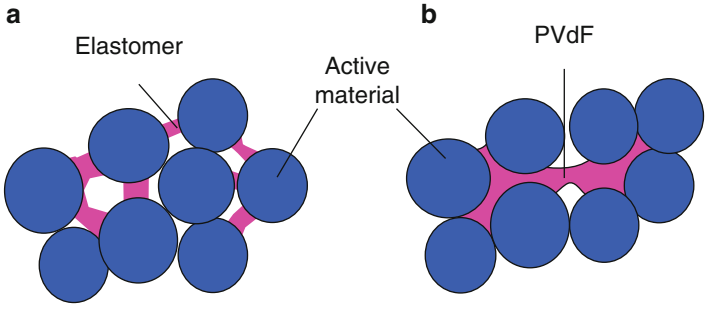

Fig. 15.3 Illustration of the binding models with (**a**) elastomer and (**b**) PVdF binder

more flexible than the PVdF [41]. Thus, the binder absorbs the expansion and the contraction of the active particles during the repeated charge and discharge since its flexibility is increased, so a battery having improved cycle life characteristics can be fabricated. In contrast, PVdF contacts a larger surface area that affects the electrode flexibility and battery cycling life. Moreover, the elastomer shows good oxidation stability up to 6 V, while PVdF shows degradation at 5.4 V. Therefore, this elastomer can be used as a binder for the next generation of 5 V-negative electrodes, while PVdF cannot be used with them, since PVdF oxidation forms a degraded fluorinated polymer, and then eventually to HF [41]. Even at the higher voltage where the elastomer degrades, the main degradation product is based on the aromatic hydrocarbon structure. This then should be the future binder not only for the negative, but also for the positive electrodes as well. However, the drawback of the aqueous suspension is the tendency of the powder to agglomerate because of the strong hydrogen bonding and electrostatic interactions [42]. Therefore, attention must be paid in implementing elastomers to control the dispersion in order to avoid the agglomeration during the preparation of the slurry. The typical mass of active materials, binder, and carbon black in dry components ranges from 75 to 90 %, 5 to 10 %, and 5 to 15 %, respectively.

15.5.2.2 Deposition on the Current Collector

The mixing of the active power, the carbon additive, and the polymer binder dissolved in a solvent is done by a planetary mixer. At the exit of the planetary mixer, the mixture that has the consistency of an ink must be deposited on the aluminum foil (positive electrode) of copper (negative electrode). This can be done by casting, coating of printing processes.

(a) *Casting*. Tape casting can be used to produce films as thin as 5 μm, while the typical thickness after drying is in the range 1.3–25 μm [43]. In this process, the slurry for the positive electrode is poured in a reservoir behind a "doctor blade" tool [44], and then cast on a moving Al foil carrier. When the slurries pass under a doctor blade, they will display a lower viscosity under the shear of the blade and a higher viscosity downstream from the blade. This prevents the slurries from spreading out of the cast region. The thickness of the wet film is given by the gap between the doctor blade and Al foil and the speed at which the Al foil moves. After the casting, the wet electrode is moved is dried so that the solvent is evaporated from the surface. At this stage, the pre-dried tape is transferred in a vacuum oven for further drying. The drying process is due to two mechanisms: evaporation of the solvent from the surface, and diffusion of the solvent through the tape to the surface. The fastest way to dry a tape is to heat the bottom of the tape without heating the air to enhance the solvent mobility in the tape, but the drying rate remains small enough so that the solvent concentration remains more or less uniform throughout the tape during the drying process.

Fig. 15.4 Image of the positive electrode formed by the deposition of the slurry onto an aluminum foil from a reservoir through a slot-die under hydraulic "pump" pressure

(b) *Coating*. The coating is quite an important process. The reader that wants more details can consult a book of 784 pages [45] devoted to the problem. Here, we simply give the basics of the process concerning the manufacturing of Li-ion batteries. Slot-die coating is another means of preparation of the negative electrodes [46]. In this process, the coating is squeezed out from a reservoir through a slot-die under hydraulic "pump" pressure onto a moving aluminum foil (Fig. 15.4). The slot is oriented perpendicular to the direction of aluminum foil movement. The success to obtain a uniform film is conditioned by the stability of the coating bead that fills the gap between the slot-die and the aluminum foil. The coating speed can be increased by applying vacuum underneath the coating bead [47]. The horizontal position of the slot-die provides the best combination of air purging at start-up and clean operation that are mandatory to make sure that the deposited film is free of any impurity. Indeed, one advantage of the slot-die method is the low contamination of the coating layer, as the entire slurry flow path is sealed against the environment until the slurry reaches the aluminum foil. Another advantage of this process is that it is contact-less because there is no doctor blade resting on the substrate, it generates no additional tensile stress in the substrate foil. Also, the coating thickness is determined by flow rate and web speed rather than gap thickness, which facilitates the obtaining of a uniform and defect-free film. The optimum operating coating parameters have been investigated in [48]. The limits of the method have been studied by Lee et al. [49]. In particular, the higher viscosity decreases the maximum operational coating speed above which the coating fails. Note this viscosity depends on the choice and concentration of the binder, but also on the size and shape of the active particles, so that it is specific to each slurry. The minimum coating thickness is also related to capillary number. One reason for the failure above the maximum speed limit is that air en entrained [50]. Air entrainment may also happen for other reasons, when the dynamic contact angle reaches 180° [50], surface roughness of the substrate [51], surface tensions of the liquid [52].

(c) *Printing*. Printing techniques (gravure or silkscreen printing, flexography) can also be used. In this case, the deposition is done by rollers covered with the ink-like slurry. After passage through a drying tunnel, the solvent has

evaporated, and a dry electrode roller is obtained. The most popular printing process is the screen printing, which is simple, highly reproducible, and efficient in large-scale production [53]. In addition no post-annealing is needed [54]. Like in the previous processes, a key issue is the obtaining of a homogeneous and stable paste with the appropriate viscosity. Also, it is important to optimize the adhesion strength between the substrate and the printed thick film. Otherwise, the film can delaminate.

A method tested on $LiCoO_2$ to increase the adhesion strength is the introduction to the slurry of a *bis*-phenol epoxy, plus dicyandiamide serving as a curing agent to remove the epoxy ring, in epoxy over dicyandiamide ratio 1/0.1 [55]. However, epoxy tended to segregate while curing and increased the surface roughness of the film. This problem could be overcome by adding ethyl cellulose resin to the paste, with a ratio of epoxy/ethyl cellulose of 1/3.

15.5.2.3 Roll Pressing Process

After deposition of the film, the strip of the electrode must be compressed, decreasing from 70 to 20–40 % the porosity, another important parameter that needs to be adjusted: the porosity must be large enough to allow for a good contact between the particles and the electrolyte, and thus a large effective surface area available for the electrochemical reactions; but is has to be small enough so that it does not impair the electrical contact between the active particles and the current collector. First, the edges of the strip are trimmed away to remove creases arising from thickness differences between coated and uncoated areas. The next step is to divide the strip lengthwise to obtain the electrode. Then, the electrode is preheated before introduction into the roll, so as to press the electrode well. A non-woven cleaning process removes impurities from the electrode surface, and finally, this electrode is wound onto a roll while maintaining tension.

15.5.3 Assembly Process

The winding process produces a jelly roll by attaching a tab to the electrode and placing the separator between the two electrodes followed by cylindrical winding. Ultrasonic welding is used to attach an aluminum and a nickel tab to the positive electrode and negative electrode, respectively. The reforming center process removes creases at the center of the jelly roll, and creates space to insert the welding tip. At this stage, the jelly roll is tested. Its electrical resistance is measured to check that it is larger than tens of MΩ. If the cell that is going to be manufactured is of cylindrical shape, the jelly roll is now ready for insertion in the can. However, when packs of many cells are required to make a battery, like in the case of electric vehicles, for instance, the cylindrical shape is not the most convenient because of

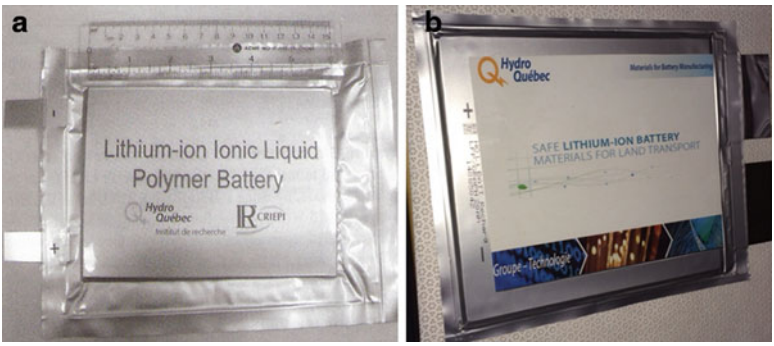

Fig. 15.5 (**a**) Li-ion flat aluminum bag cell (Ionic liquid/polymer type) with an active surface area of 104 cm^2 and (**b**) prismatic 20-Ah Li-ion cell (A4 format)

the low packing density. For this purpose, the cells are rather prepared in prismatic shape, in which case the jelly roll is pressed before insertion in the can (Fig. 15.5).

The jelly roll is inserted in the can to a certain depth that is controlled by X-ray inspection. The anode tab is bent for welding to the floor of the can. In the assembly of a cylindrical cell, the beading process creates a bent groove for the gasket to reach the top the can.

It is then time to inject the electrolyte. In the process, the internal pressure is kept lower then the atmospheric pressure, and the electrolyte is allowed to be impregnated into the jelly roll by introducing air into the can. After the electrolyte injection, electrolyte surrounding the electrode tap and beading area is wiped with a non-woven cleaning. Finally, the gasket is inserted.

The negative electrode tap welding process includes the bottom of the current break assembly. The current break is enabled by ultrasonic welding of the central area of the safety vent assembly (see Chap. 14).

The crimping process applied pressure to the top part of the battery containing the current break assembly, the positive temperature coefficient (PTC) and cap-up. After sealing the current break, the PTC, and the cap-up either soldered shut by a laser beam or into a heat-sealed soft pouch, the crimped cell is pressed to maintain a constant height. The cell is ready for inspection by X-rays to check for any defect and verify the internal assembly of all these elements. After washing with water to remove electrolyte and any impurity at the surface, the cell is dried to eliminate moisture. Finally, the battery in imprinted with the manufacturing factory, line number and date.

15.5.4 Formation Process

Since the SEI is formed during the initial charging, it is of primary importance for the future performance and the life of the battery that the first cycles to be done according to a protocol that permits the SEI to be well formed and stabilized to

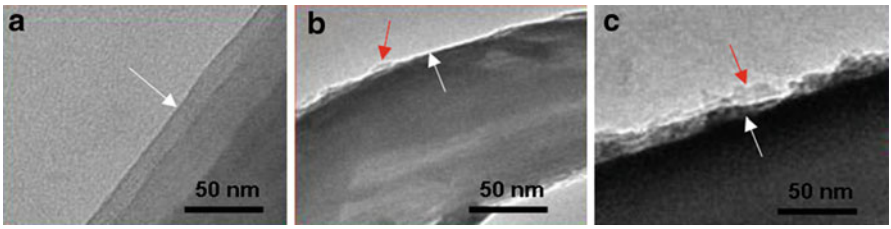

Fig. 15.6 TEM images showing the SEI formation onto the surface of graphite electrode. (**a**) Fresh electrode, (**b**) after discharge at 1.2 V and (**c**) after discharge at 0.05 V. *White* and *red arrows* indicate the edge of graphite and SEI layer, respectively

avoid decomposition of the electrolyte (Fig. 15.6). That is this formation test is made by the manufacturer, and must then be considered a part of the manufacturing process. Some of the faulty cells can also be detected during this procedure, because the main cause of failure is internal short-circuits, leading to drop in the open circuit voltage and discharge capacity. These faulty batteries are discarded, and the tolerance on the capacity is small, because when they are connected in parallel or in series inside a pack, they must have the same characteristics, and in particular the same capacity within 3 %. Therefore, when the battery has been prepared by following the previous steps described in Sects. 15.4.1–15.4.4, it is fully charged and stabilized for few hours. After elimination of any faulty cell, the fully charged cells are then kept under constant temperature and humidity for a month and controlled. Then the battery is fully discharged to check for its capacity, and the battery is classified according to its discharge capacity, one level corresponding to 3 % discharge capacity. The battery is now ready to be commercialized, and in the discharged state.

15.5.5 The Charger

The first task of the consumer after he/she has bough a battery is then to charge it. This operation is done by a charger. Inside this device, electronics protect the battery from overcharge that, by definition, occurs when too much of lithium is sent to the negative electrode. As we have seen in the section devoted to the capacity and balance between the electrode, the negative electrode, by construction, should have a capacity larger that the positive electrode. Therefore, it is not possible in principle to reach a situation where an excess of lithium coming from the positive electrode would form of lithium layer at the surface of the negative electrode. Nevertheless, overcharge results in a sharp increase in the voltage associated to the rise in the internal resistance of the battery, resulting in an increase of the internal temperature and possible thermal runaway and battery fire, because when the active particles of the positive electrode have been emptied from their lithium content,

they are insulating. In some cases, it also results in a structural collapse of the active particles of the positive electrode, with the risk of explosion. The battery charge is thus equipped with an electronic device to control carefully the charge of the battery. In case the lithium intercalation/extraction of lithium of the active particles of at least one of the two electrodes proceeds through a solid solution, the voltage of the cell depends on the charge of the cell. The control can then be made by measurements of the voltage. In case the lithium intercalation/extraction proceeds with a two-phase reaction, we have seen in Chaps. 1 and 2 that the voltage profile is a plateau; in this case, met in the new generation of batteries with $LiFePO_4$ as a cathode in particular, the control is done by measurements of the current, which, integrated over time, determines directly the amount of Li^+ ions that have been transferred to the negative electrode. In any case, the operational voltage at a given state of charge is specific to the each positive-negative electrode couple. In addition, the current that cross the battery during the charge must be controlled and limited so that the battery is not too far from thermodynamic equilibrium during the charge process, otherwise large over-potential would occur. The charger is also equipped with electronics to control the dynamics of the charge process. Usually, the charge is triggering process, in which the charge proceeds by steps, each step being defined by charging controlled by the current followed by a period of time where the battery is left at rest for equilibration. Again, the kinetics of the motion of the lithium inside the battery is specific to the choice of the electrodes. For these reasons, it is mandatory to charge the battery with the charger delivered by the constructor, i.e., the charger that has been adapted specifically to this particular battery.

References

1. Hosakawa M, Nogi K, Naito M, Yokoyama T (eds) (2008) Nanoparticles technology handbook. Elsevier, New York
2. Mayo RN, Ranganathan P (2005) Energy consumption in mobile devices: why future systems need requirements – aware energy scale-down. In: Salsafi B, Vijaykumar TN (eds) Power – aware computer systems. Lect Notes Comput Sci 3164:26–39
3. Verbrugge M, Frisch D, Koch B (2005) Adaptive energy management of electric and hybrid electric vehicles. J Electrochem Soc 152:A333–A342
4. Harrison AI (2003) The changing world of standby batteries in telecoms applications. J Power Sourc 116:232–235
5. Lam LT, Louey R (2006) Development of ultra-battery for hybrid-electric vehicle applications. J Power Sourc 158:1140–1148
6. Chandrasekaran R, Sikha G, Popov BN (2005) Capacity fade analysis of a battery/super capacitor hybrid and a battery under pulse loads – full cell studies. J Appl Electrochem 35:1005–1013
7. Han J, Park ES (2002) Direct methanol fuel-cell combined with a small back-up battery. J Power Sourc 112:477–483
8. Park SH, Kang SH, Johnson CS, Amine K, Tackeray MM (2007) Lithium-manganese-nickel-oxide electrodes with integrated layered-spinel structures for lithium batteries. Electrochem Commun 9:262–268

9. Arrebola JC, Caballero A, Hernan L, Morales J (2005) Expanding the rate capabilities of the $LiNi_{0.5}Mn_{1.5}O_4$ spinel by exploiting the synergistic effect between nano and microparticles. Electrochem Solid State Lett 8:A461–A645
10. Ma ZF, Yang XQ, Liao XZ, Sun X, McBreen J (2001) Electrochemical evaluation of composite cathodes base on blends of $LiMn_2O_4$ and $LiNi_{0.8}Co_{0.2}O_2$. Electrochem Commun 3:425–428
11. Stux AM, Swider-Lyons KE (2005) Li-ion capacity enhancement in composite blends of $LiCoO_2$ and Li_2RuO_3. J Electrochem Soc 152:A2009–A2016
12. Imachi N, Takano Y, Fujimoto H, Kida Y, Fujutani S (2007) Layered cathode for improving safety of Li-ion batteries. J Electrochem Soc 154:A412–A416
13. Barker J, Saidi MY, Tracey EK (2006) Electrodes comprising mixed active particles. US Patent 7,041,239. Accessed 9 May 2006
14. Zaghib K, Dontigny M, Guerfi A, Charest P, Rodrigues I, Mauger A, Julien CM (2011) Safe and fast-charging Li-ion battery with long shelf life for power applications. J Power Sourc 196:3949–3954
15. Zaghib K, Dontigny M, Guerfi A, Trottier J, Hamel-Paquet J, Gariepy V, Galoutov K, Hovington P, Mauger A, Groult H, Julien CM (2012) An improved high-power battery with increased thermal operating range: C–$LiFePO_4$//C–$Li_4Ti_5O_{12}$. J Power Sourc 216:192–200
16. Zaghib K, Dubé J, Dallaire A, Galoustov K, Guerfi A, Ramanathan M, Benmayza A, Prakash J, Mauger A, Julien CM (2014) Enhanced thermal safety and high power performance of carbon-coated $LiFePO_4$ olivine cathode for Li-ion batteries. J Power Sourc 219:36–44
17. Zaghib K, Dontigny M, Perret P, Guerfi A, Ramanathan M, Prakash J, Mauger A, Julien CM (2014) Electrochemical and thermal characterization of lithium titanate spinel anode in C-$LiFePO_4$//C-$Li_4Ti_5O_{12}$ cells at sub-zero temperatures. J Power Sourc 248:1050–1057
18. Wu Y, Manthiram A (2006) High capacity, surface-modified layered $Li/Li[Ni_xLi_{(1/3-2x/3)}Mn_{(2/3-x/3)}]O_2$ cathodes with low irreversible capacity loss batteries, fuel cells, and energy conversion. Electrochem Solid State Lett 9:A221–A224
19. Lu ZH, Dahn JR (2002) Understanding the anomalous capacity of $Li/Li[Ni_xLi_{(1/3-2x/3)}Mn_{(2/3-x/3)}]O_2$ cells using in situ X-ray diffraction and electrochemical studies. J Electrochem Soc 149:A815–A822
20. Lu ZH, Beaulieu LJ, Donaberger RA, Thomas CL, Dahn JR (2002) Synthesis, structure, and electrochemical behavior of $Li[Ni_xLi_{(1/3-2x/3)}Mn_{(2/3-x/3)}]O_2$. J Electrochem Soc 149:A778–A791
21. Whitacre JF, Zaghib K, West WC, Ratnakumar BV (2008) Dual active material composite cathode structures for Li-ion batteries. J Power Sourc 177:528–536
22. Fukunaga M, Suzuki K, Kuroda A (2003) The 44th battery symposium in Japan. Abst #1D19, p 462
23. Zhang SS, Xu K, Jow TR (2004) Evaluation on a water-based binder for the graphite anode of Li-ion batteries. J Power Sourc 138:226–231
24. Chen Z, Chevrier V, Christensen L, Dahn JR (2004) Design of amorphous alloy electrodes for Li-ion batteries: a big challenge. Electrochem Solid State Lett 7:A310–A314
25. Chen Z, Christensen L, Dahn JR (2003) Comparison of PVDF and PVDF-TFE-P as binders for electrode materials showing large volume changes in lithium-ion batteries. J Electrochem Soc 150:A1073–A1078
26. Chen Z, Christensen L, Dahn JR (2003) Large-volume-change electrodes for Li-ion batteries of amorphous alloy particles held by elastomeric ethers. Electrochem Commun 5:919–923
27. Liu R, Yang MH, Wu HC, Chiao SM, Wu NL (2005) Enhanced cycle life of Si anode for Li-ion batteries by using modified elastomeric binder. Electrochem Solid State Lett 8: A100–A103
28. Li J, Lewis RB, Dahn JR (2007) Sodium carboxymethyl cellulose: a potential binder for Si negative electrodes for Li-ion batteries. Electrochem Solid State Lett 10:A17–A20
29. Bridel JS, Azaïs T, Morcrette M, Tarascon JM, Larcher D (2010) Key parameters governing the reversibility of Si/carbon/CMC electrodes for Li-ion batteries. Chem Mater 22:1229–1241

30. Choi NS, Yew KH, Choi WU, Kim SS (2008) Enhanced electrochemical properties of a Si-based anode using an electrochemically active polyamide imide binder. J Power Sourc 177:590–594
31. Magasinski A, Zdyrko B, Kovalenko I, Hertzberg B, Burtovyy R, Huebner CF, Fuller TF, Luzinov I, Yushin G (2010) Toward efficient binders for Li-ion battery Si-based anodes: polyacrylic acid. ACS Appl Mater Interfaces 2:3004–3010
32. Ding N, Xu J, Yao Y, Wegner G, Lieberwirth I, Chen C (2009) Improvement of cyclability of Si as anode for Li-ion batteries. J Power Sourc 192:644–651
33. Chong J, Xun S, Zheng H, Song X, Liu G, Ridgway P, Wang JQ, Battaglia VS (2011) A comparative study of polyacrylic acid and poly(vinylidene difluoride) binders for spherical natural graphite/$LiFePO_4$ electrodes and cells. J Power Sourc 196:7707–7714
34. Kiovelko I, Zdyrko B, Magasinski A, Hertzberg B, Milicev Z, Burtovyy R, Luzinov I (2011) A major constituent of brown algae for use in high-capacity Li-ion batteries. Science 334:75–79
35. Kim JS, Choi W, Cho KY, Byun D, Lim JC, Lee JK (2014) Effect of polyimide binder on electrochemical characteristics of surface-modified silicon anode for lithium ion batteries. J Power Sourc 244:521–526
36. Lee JH, Kim JS, Kim YC, Zang DS, Paik U (2008) Dispersion properties of aqueous-based $LiFePO_4$ pastes and their electrochemical performance for lithium batteries. Ultramicroscopy 108:1256–1259
37. Lee JH, Lee S, Paik U, Choi YM (2005) Aqueous processing of natural graphite particulates for lithium-ion battery anodes and their electrochemical performance. J Power Sourc 147:249–255
38. Maleki H, Deng G, Haller IK, Anami A, Howard JN (2000) Thermal stability studies of binder materials in anodes for lithium-ion batteries. J Electrochem Soc 147:4470–4475
39. Gaberscek BM, Drofenik J, Dominiko R, Pejovnik S (2000) Improved carbon anode for lithium batteries pretreatment of carbon particles in a polyelectrolyte solution. Electrochem Solid State Lett 3:171–173
40. Oskam G, Searson PC, Jow TR (1999) Sol-gel synthesis of carbon/silica gel electrodes for lithium intercalation articles. Electrochem Solid State Lett 2:610–612
41. Guerfi A, Kaneko M, Petitclerc M, Mori M, Zaghib K (2007) $LiFePO_4$ water-soluble binder electrode for Li-ion batteries. J Power Sourc 163:1047–1052
42. Nahass P, Rhine WE, Pober RL, Bowen HK, Robbins WL (1990) A comparison of aqueous and non-aqueous slurries for tape-casting, and dimensional stability in green tapes. In: Nair KM, Pohanka R, Buchanan RC (eds) Materials and processes in microelectronic systems, ceramic transactions, vol 15. American Ceramic Society, Westerville OH, pp 355–364
43. Mistler RE, Twiname ER (2000) Tape casting: theory and practice. American Ceramic Society, Westerville, OH
44. Berni A, Mennig M, Schmidt H (2004) Sol-gel technologies for glass producers and users. Springer, New York, pp 89–92
45. Tracton AA (ed) (2005) Coatings technology handbook. CRC Press, Taylor & Francis Group, Boca Raton
46. Hodges AM, Chambers G (2005) Multilayer; dielectric substrate overcoated with electroconductive layer US Patent 6,946,067. Accessed 20 Sept 2005
47. Chang YR, Chang HM, Lin CF, Liu TJ, Wu PY (2007) Three minimum wet thickness regions of slot die coating. J Colloid Interface Sci 308:222–230
48. Chu WB, Yang JW, Wang YC, Liu TJ, Tiu C, Guo J (2006) The effect of inorganic particles on slot die coating of poly(vinyl alcohol) solutions. J Colloid Interface Sci 297:215–225
49. Lee KY, Liu LD, Ta-Jo L (1992) Minimum wet thickness in extrusion slot coating. Chem Eng Sci 47:1703–1713
50. Deryagin BV, Levi SM (1964) Film coating theory. The Focal Press, New York
51. Buonopane RA, Gutoff EB, Rimore MMT (1986) Effect of pumping tape surface properties on air entrainment velocity. AIChE J 32:682–683

52. Burley S, Kennedy BS (1976) An experimental study of air entrainment at a solid/liquid/gas interface. Chem Eng Sci 31:901–911
53. Tymecki L, Zwierkowska E, Koncki R (2004) Screen-printed reference electrodes for potentiometric measurements. Anal Chim Acta 526:3–11
54. Park MS, Hyun SH, Nam SC (2006) Preparation and characteristics of $LiCoO_2$ paste electrodes for lithium ion micro-batteries. J Electroceramics 17:651–655
55. Park MS, Hyun SH, Nam SC (2007) Mechanical and electrical properties of a $LiCoO_2$ cathode prepared by screen-printing for a lithium-ion micro-battery. Electrochim Acta 52:7895–7902

Acronyms

a.c.	Alternative current
AFM	Antiferromagnetism
ALD	Atomic layer deposition
ARC	Accelerating rate calorimeter
ASTM	American society for testing and materials
BET	Brunauer–Emmett–Teller
BMS	Battery management system
ccp	Cubic close-packed array
CDMO	Composite dimensional manganese dioxide
CE	Coulombic efficiency
CMD	Chemical manganese dioxide
CMOS	Complementary metal oxide semiconductor
CN	Coordination number
CNT	Carbon nanotube
CPE	Constant phase element
CPO	Close-packed oxygen
CVD	Chemical vapor deposition
d.c.	Direct current
DEC	Diethyl carbonate
DEG	Diethyleneglycol
DHPG	Doped hierarchically porous graphene
DMC	Dimethyl carbonate
DMF	*N*-dimethylformamide
DOD	Depth of discharge
DSC	Differential scanning calorimetry
DSL	Disordered surface layer
DVA	Differential voltage analysis
EC	Ethylene carbonate
EDS	Energy dispersive spectroscopy

C. Julien et al., *Lithium Batteries*, DOI 10.1007/978-3-319-19108-9

EIS	Electrochemical impedance spectroscopy
EMC	Ethylmethyl carbonate
EMD	Electrolytic manganese dioxide
EMI	1-Ethyl-3-methylimidazolium
EPR	Electron paramagnetic resonance
ES	Energy storage
ESCA	Electron spectroscopy for chemical analysis
ESR	Electron spin resonance
EV	Electric vehicle
EXAFS	Extended X-ray absorption fine structure
FC	Field cooling
fcc	Face cubic centered
FEC	Fluorinated ethylene carbonate
FM	Ferromagnetism
FTIR	Fourier transform infrared
Fwhm	Full width at half maximum
GBL	γ-Butyrolactone
GHG	Greenhouse gases
GITT	Gavanostatic intermittent titration technique
GNR	Graphene nanoribbon
GNS	Graphene nanoscroll
GS	Graphene sheet
HEV	Hybrid electric vehicles
HPPC	Hybrid pulse power characterization
HOMO	Highest occupied molecular orbit
HRTEM	High-resolution transmission electron microscopy
HTR	Hydrothermal reaction
HWS	Heat-wait-search
HWHM	Half width at half-maximum
IEA	International Energy Agency
IC	Intercalation compound
ICA	Incremental capacity analysis
ICM	Isothermal microcalorimeter
ICP	Inductively coupled plasma
IPA	Isopropyl alcohol
ITO	Indium tin oxide (tin-doped indium oxide)
JCPDS	Joint committee on powder diffraction standard
JT	Jahn-Teller
LCO	$LiCoO_2$
LCP	$LiCoPO_4$
LFP	$LiFePO_4$
LIB	Lithium-ion batteries
LiBOB	Lithium bis(oxalato)borate
LiFAP	$LiPF_3(C_2F_5)_3$

LiTFSI	Lithiumbis(trifluoromethane) sulfonamide
LMB	Lithium-metal batteries
LMO	$LiMn_2O_4$
LMP	$LiMnPO_4$
LNM	$LiNi_{0.5}Mn_{1.5}O_4$
LNMC	Li-rich NMC
LNO	$LiNiO_2$
LNP	$LiNiPO_4$
LTO	$Li_4Ti_5O_{12}$
LUMO	Lowest unoccupied molecular orbital
LVP	$Li_3V_2(PO_4)_3$
MAS	Magic angle spinning
MDO	Manganese dioxide
MOC	Mesoporous carbon
MWCNT	Multi-walled carbon nanotube
NaCMC	Sodium carboxymethyl cellulose
NASICON	Na^+ superionic conductor
NC	Nitrogen-doped carbon
NCA	$LiNi_{0.8}Co_{0.15}Al_{0.05}O_2$
NCO	$LiNi_{1-y}Co_yO_2$
NIR	Near infrared
NMC	$LiNi_xCo_yMn_zO_2$
NMO	$LiNi_{0.5}Mn_{0.5}O_2$
NMP	*N*-methyl-2-pyrrolidone
NMR	Nuclear magnetic resonance
Nn	Nearest neighbouring
NRA	Nanoribbons array
Nw	Nanowire
OCV	Open-circuit voltage
PAA	Poly(acrylic acid)
PbBat	Lead acid battery
PC	Propylene carbonate
PCNF	Porous carbon nanofibers
PEDOT	Poly(3,4-ethylenedioxythiophene)
PEO	Polyethylene oxide
PHEV	Plug hybrid electric vehicles
PLD	Pulse-laser deposition
PMMA	Poly(methyl methacrylate)
ppm	Part per million
PVA	Poly(vinyl alcohol)
PVdF	Polyvinylidene fluoride
PVP	Poly-vinyl-pyridine
RBM	Rigid-band model
rf	Radio frequency

rms	Root-mean-square
RS	Raman scattering
SAED	Selected area electron diffraction
SDR	Self-discharge rate
SEI	Solid electrolyte interphase
SEM	Scanning electron microscopy
SFLS	Supercritical fluid–liquid–solid
S.G.	Space group
SOC	State of charge
SQUID	Superconducting quantum interference device
SSR	Solid state reaction
SVO	$Ag_2V_4O_{11}$
SWNT	Single-walled carbon nanotubes
tEG	Triethyleneglycol
TEG	Tetrathyleneglycol
TEM	Transmission electron microscopy
TF	Thin film
TM	Transition metal
TMD	Transition-metal dichalcogenide
TMO	Transition-metal oxide
TNO	$TiNb_2O_7$
TTFP	Tris(2,2,2-trifluoroethyl)phosphate
USABC	United States advanced battery consortium
USP	Ultrasonic spray pyrolysis
V2G	Vehicle-to-Grid
VC	Voltammetry cyclic
vdW	van der Waals
VLS	Vapor–solid–liquid
XANES	X-ray absorption near-edge structure
XPS	X-ray photoelectron spectroscopy
XRD	X-ray diffraction
XRPD	X-ray powder diffraction
ZFC	Zero-field cooling
1D	One dimensional
2D	Two dimensional
3D	Three dimensional

Index

C. Julien et al., *Lithium Batteries*, DOI 10.1007/978-3-319-19108-9